ISTITUTO NAZIONALE DI FISICA NUCLEARE

Sezione di Pisa

INFN-13-01/PI
20th february 2013

Super*B* Detector
Technical Design Report

SuperB Collaboration (F. Forti et al.)

Abstract

In this Technical Design Report (TDR) we describe the Super*B* detector to be installed on the Super*B* e^+e^- high luminosity collider. The Super*B* asymmetric collider, foreseen to be constructed on the Tor Vergata campus near the INFN Frascati National Laboratory, is designed to operate both at the $\Upsilon(4S)$ energy in the center of mass with a luminosity of 10^{36} $cm^{-2}s^{-1}$ and at the τ/charm production threshold with a luminosity of 10^{35} $cm^{-2}s^{-1}$. This high luminosity, producing a data sample about a factor 100 larger than present *B* Factories would allow investigation of new physics effects in rare decays, CP Violation and Lepton Flavour Violaion. This document details the detector design presented in the Conceptual Design Report (CDR) in 2007. The R&D and engineering studies perfomed to arrive at the full detector design are described, and an updated cost estimate is presented.

*Published by **SIDS–Pubblicazioni***
Laboratori Nazionali di Frascati

INFN-13-01/PI, LAL 13-01, SLAC-R-1003

Technical Design Report

SuperB Detector

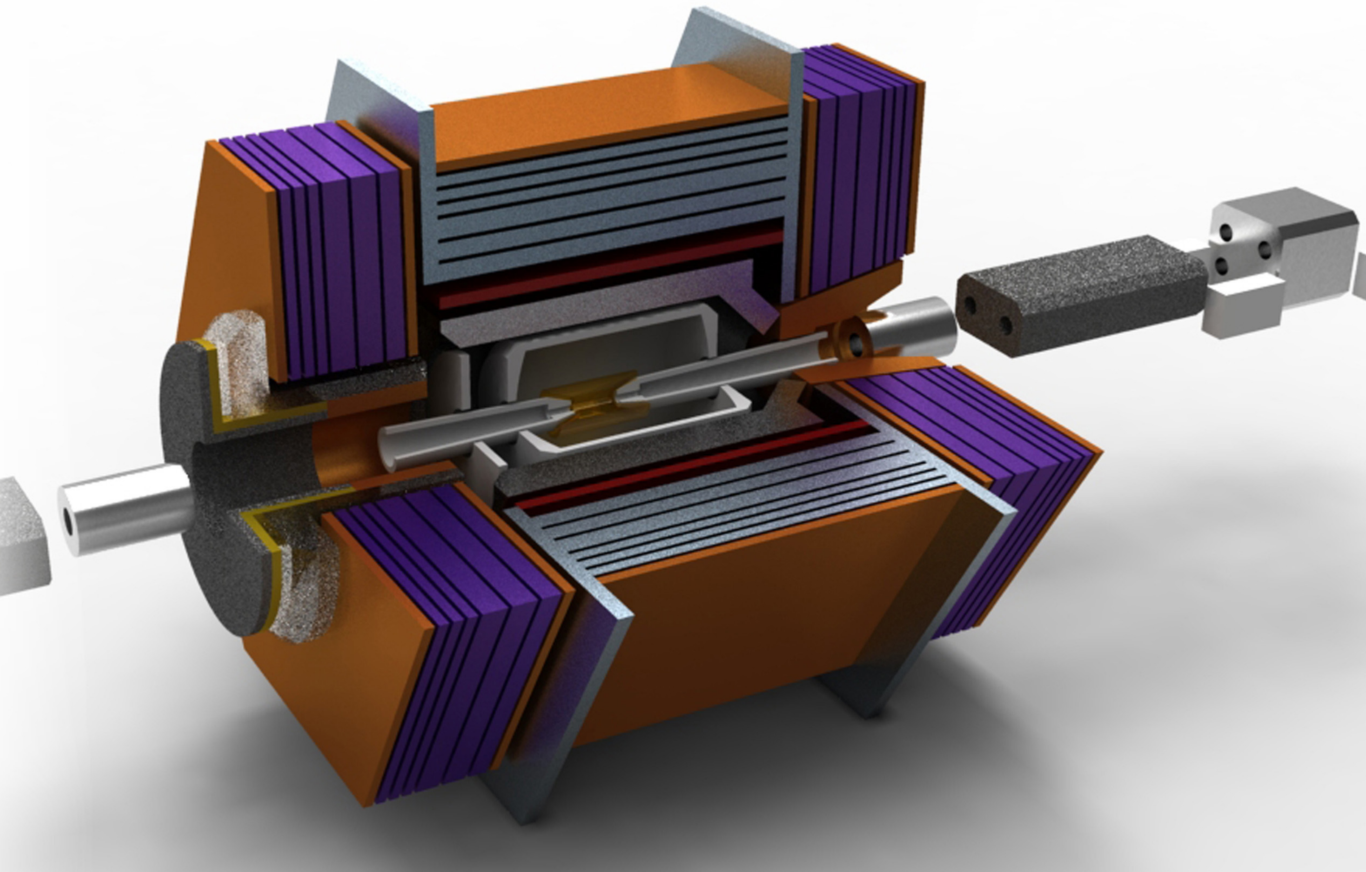

A High-Luminosity Asymmetric $e^+ e^-$ Super Flavour Factory

INFN-13-01/PI, LAL 13-01, SLAC-R-1003

Super*B* Detector
Technical Design Report

Abstract

In this Technical Design Report (TDR) we describe the Super$B$ detector to be installed on the Super$B$ e^+e^- high luminosity collider. The Super$B$ asymmetric collider, foreseen to be constructed on the Tor Vergata campus near the INFN Frascati National Laboratory, is designed to operate both at the $\Upsilon(4S)$ energy in the center of mass with a luminosity of $10^{36}\,\mathrm{cm}^{-2}\mathrm{s}^{-1}$ and at the τ/charm production threshold with a luminosity of $10^{35}\,\mathrm{cm}^{-2}\mathrm{s}^{-1}$. This high luminosity, producing a data sample about a factor 100 larger than present B Factories would allow investigation of new physics effects in rare decays, CP Violation and Lepton Flavour Violaion. This document details the detector design presented in the Conceptual Design Report (CDR) in 2007. The R&D and engineering studies perfomed to arrive at the full detector design are described, and an updated cost estimate is presented .

Preface

Flavour physics not only provides insight in the physics of the standard model but also offers great discovery potential for new physics processes, as the B-Factories experiments, *BABAR* at SLAC and Belle at KEK, have demonstrated very effectively. Increasing the luminosity has been identified from the very beginning as the key element to extend the physics reach of these machines. Since 2003 a group of physicists began to explore the physics potential of very high luminosity B-Factory machines. An upgrade of the the PEP-II accelerator was initially investigated; then the *BABAR* and Belle community started in 2004 a series of joint workshops in Hawaii.

The Super$B$ Project was formally born in 2005 when INFN inserted in its three-years planning document the intention of building a high luminosity flavour factory in the Frascati area. In the course of the years Super$B$ has evolved from an intention into a full-fledged project, with a Conceptual Design Report published in 2007, progress reports in 2009, and a formal collaboration structure setup in 2010 with hundreds of members from several countries. All aspects of the project, physics potential, accelerator design, detector design, successfully passed several international reviews setup by INFN. In 2010 Super$B$ was inserted in the Italian Research Ministry National Research Plan as Flagship Project, and a good fraction of the required funds were allocated, although not the full amount. The decision to build Super$B$ on the land of the University of Rome Tor Vergata led, in 2011, to the formation of the Cabibbo Laboratory consortium between INFN and TorVergata, with the explicit mission of constructing and managing a new research infrastructure for flavour physics. A ministerial cost and schedule review of the accelerator project was held in fall 2012. A combination of a more realistic cost estimates and the unavailability of funds due of the global economic climate led to a formal cancelation of the project on Nov 27, 2012.

The community who had been committed to the project for so long, although devastated by the sudden cancelation, decided to try to preserve and document as much as possible of the work done in Super$B$, both to retain a lasting trace of the committment of the group and, more importantly, to provide a written basis of the technical achievements for the use of future scientific endavours. It is in this spirit that this Detector Technical Design Report, whose preparation was quite advanced at the time of the cancelation of the project, has been completed and is being published. We felt that the tone and grammar of the text should remain that of a project that will be built rather than that of a project that would have been built. Therefore we kept the assertiveness and optimism of a community that was expecting to start constructing the machine and experiment within a few months. We sincerely hope that it can be of use to the scientific community.

Acknowledgements

Work supported in part by: the Italian Institute for Nuclear Physics, INFN; the U.S. Department of Energy under contract number DE-AC02-76SF00515 and other grants.

The TDR covers have been designed by Bruno Mazoyer, graphics designer at the Laboratoire de l'Accélérateur Linéaire (Orsay, France).

The authors would like to acknowledge the continuing support of Lucia Lilli, INFN-Pisa, as the project scientific secretary.

M. Baszczyk, P. Dorosz, J. Kolodziej, W. Kucewicz, M. Sapor
AGH University of Science and Technology, Kraków, Poland

A. Jeremie
LAPP - Annecy, Annecy-le-Vieux, France

E. Grauges Pous
Universitat de Barcelona, Barcelona, Spain

G. E. Bruno[ab], G. De Robertis[b], D. Diacono[b], G. Donvito[b], P. Fusco[ab], F. Gargano[b], F. Giordano[ab], F. Loddo[b], F. Loparco[ab], G. P. Maggi[b], V. Manzari[b], M. N. Mazziotta[b], E. Nappi[b], A. Palano[b], B. Santeramo[ab], I. Sgura[b], L. Silvestris[b], V. Spinoso[b]
[a]*Dipartimento di Fisica dell'Università e del Politecnico di Bari;* [b]*INFN - Sezione di Bari, Bari, Italy*

G. Eigen, J. Zalieckas, Z. Zhuo
University of Bergen, Bergen, Norway

L. Jenkovszky
Bogolyubov Institute for Theoretical Physics, Kiev, Ukraine

G. Balbi[c], M. Boldini[c], D. Bonacorsi[bc], V. Cafaro[c], I. D'Antone[c], G. M. Dallavalle[c], R. Di Sipio[bc], F. Fabbri[c], L. Fabbri[bc], A. Gabrielli[bc], D. Galli[bc], P. Giacomelli[c], V. Giordano[c], F. M. Giorgi[c], C. Grandi[c], I. Lax[c], S. Lo Meo[bc], U. Marconi[c], A. Montanari[c], G. Pellegrini[c], M. Piccinini[bc], T. Rovelli[bc], N. Semprini Cesari[bc], G. Torromeo[c], N. Tosi[bc], R. Travaglini[c], V. M. Vagnoni[c], S. Valentinetti[ac], M. Villa[bc], A. Zoccoli[ac]
[a]*università di Bologna;* [b]*Università di Bologna;* [c]*INFN - Sezione di Bologna, Bologna, Italy*

J.-F. Caron, C. Hearty[1], P. F.-T. Lu, T. S. Mattison, J. A. McKenna, R. Y.-C. So
University of British Columbia, Vancouver, British Columbia, Canada

M. Yu. Barnyakov, V. E. Blinov, A. A. Botov, V. P. Druzhinin, V. B. Golubev, S. A. Kononov, E. A. Kravchenko, E. B. Levichev, A. P. Onuchin, S. I. Serednyakov, D. A. Shtol, Y. I. Skovpen, E. P. Solodov
Budker Institute of Nuclear Physics, Novosibirsk, Russian Federation

A. Cardini[b], M. Carpinelli[ab]
[a]*Università di Sassari;* [b]*INFN - Sezione di Cagliari, Cagliari, Italy*

D. S.-T. Chao, C. H. Cheng, D. A. Doll, B. Echenard, K. Flood, J. Hanson, D. G. Hitlin, P. Ongmongkolkul, F. C. Porter, R. Y. Zhu
California Institute of Technology, Pasadena, CA, USA

N. Randazzo
INFN - Sezione di Catania, Catania, Italy

E. De La Cruz Burelo
Centro de Investigación y de Estudios Avanzados de IPN, Mexico City, Mexico

[1]Also with Institute of Particle Physics, Canada.

Y. Zheng
Graduate University of Chinese Academy of Sciences, Beijing, China

P. Campos, M. De Silva, A. Kathirgamaraju, B. Meadows, B. Pushpawela, Y. Shi, M. Sokoloff
University of Cincinnati, Cincinnati, OH, USA

G. Lopez Castro
Centro de Investigación y de Estudios Av. de IPN, Mexico City, Mexico

V. Ciaschini, P. Franchini, F. Giacomini, A. Paolini
INFN - CNAF, Bologna, Italy

G. A. Calderon Polania
Universidad Autónoma de Coahuila (UAdeC), Coahuila, Mexico

S. Laczek, P. Romanowicz, B. Szybinski
Cracow University of Technology, Kraków, Poland

M. Czuchry, L. Flis, D. Harezlak, J. Kocot, M. Radecki, M. Sterzel, T. Szepieniec, T. Szymocha, P. Wójcik
Academic Computer Center CYFRONET AGH, Kraków, Poland

M. Andreotti[ac], W. Baldini[c], R. Calabrese[ac], V. Carassiti[c], G. Cibinetto[c], A. Cotta Ramusino[c], F. Evangelisti[c], A. Gianoli[c], E. Luppi[ac], R. Malaguti[c], M. Manzali[ac][2], M. Melchiorri[c], M. Munerato[c], C. Padoan[ac], V. Santoro[c], L. Tomassetti[bc]
[a]*Dipartimento di Fisica e Scienze della Terra, Università di Ferrara;* [b]*Dipartimento di Matematica e Informatica, Università di Ferrara;* [c]*INFN - Sezione di Ferrara, Ferrara, Italy*

M. M. Beretta, M. Biagini, M. Boscolo, E. Capitolo, R. de Sangro, M. Esposito, G. Felici, G. Finocchiaro, M. Gatta, C. Gatti, S. Guiducci, S. Lauciani[3], P. Patteri, I. Peruzzi[4], M. Piccolo, P. Raimondi, M. Rama, C. Sanelli, S. Tomassini
INFN - LNF (Laboratori Nazionali di Frascati), Frascati, Italy

P. Fabbricatore
INFN - Sezione di Genova, Genova, Italy

D. Delepine, M. A. Reyes Santos
Universidad de Guanajuato Leòn, Guanajuato, Mexico

M. Chrzaszcz[5], R. Grzymkowski, P. Knap, J. Kotula, T. Lesiak, J. Ludwin, J. Michalowski, B. Pawlik, B. Rachwal, M. Stodulski, J. Wiechczynski, M. Witek, L. Zawiejski, M. Zdybal
H. Niewodniczanski Inst. of Nuclear Physics PAS, Kraków, Poland

V. Y. Aushev, A. Ustynov
Kiev Institute for Nuclear Research, Kiev, Ukraine

[2] Also with INFN - CNAF.
[3] Also with Laboratoire de l'Accélérateur Linéaire, Univ. Paris-Sud, CNRS/IN2P3, Orsay, France.
[4] Also with Università di Perugia.
[5] Also with University of Zurich, Zurich, Switzerland.

N. Arnaud, P. Bambade, C. Beigbeder, F. Bogard, M. Borsato, D. Breton, J. Brossard, L. Burmistrov, D. Charlet, V. Chaumat, O. Dadoun, M. El Berni, J. Maalmi, V. Puill, C. Rimbault, A. Stocchi, V. Tocut, A. Variola, S. Wallon, G. Wormser
Laboratoire de l'Accélérateur Linéaire, Univ. Paris-Sud, CNRS/IN2P3, Orsay, France

F. Grancagnolo
INFN - Sezione di Lecce, Lecce, Italy

E. Ben-Haim, S. Sitt
LPNHE - Paris, Paris, France

M. Baylac, O. Bourrion, J.-M. Deconto, Y. Gomez Martinez, N. Monseu, J.-F. Muraz, J.-S. Real, C. Vescovi
LPSC (UJF-CNRS/IN2P3-INPG), Grenoble, France

R. Cenci, A. Jawahery, D. Roberts, E. W. Twedt
University of Maryland, College Park, MD, USA

R. Cheaib, D. Lindemann, S. Nderitu, P. Patel[6], S. H. Robertson, D. Swersky, A. Warburton
McGill University, Montréal, Québec, Canada

E. Cuautle Flores, G. Toledo Sanchez
Universidad Nacional Autónoma de Mexico, Mexico City, Mexico

P. Biassoni[c], L. Bombelli[ac], M. Citterio[c], S. Coelli[c], C. Fiorini[ac], V. Liberali[bc], M. Monti[c], B. Nasri[ac], N. Neri[c], F. Palombo[bc], F. Sabatini[c], A. Stabile[bc]
[a]*Politecnico di Milano;* [b]*Università di Milano;* [c]*INFN - Sezione di Milano, Milano, Italy*

A. Berra[cd], A. Giachero[bd], C. Gotti[ad], D. Lietti[cd], M. Maino[bd], G. Pessina[bd], M. Prest[cd]
[a]*Dipartimento di Elettronica e Telecomunicazioni, Università degli Studi di Firenze;* [b]*Dipartimento di Fisica dell'Università di Milano-Bicocca;* [c]*Università degli Studi dell'Insubria di Como;* [d]*INFN - Sezione di Milano Bicocca, Milano, Italy*

J.-P. Martin, M. Simard, N. Starinski, P. Taras
Université de Montréal, Montréal, Québec, Canada

A. Drutskoy, S. Makarychev, A. V. Nefediev
ITEP - Moscow, Moscow, Russian Federation

A. Aloisio[c], S. Cavaliere[c], G. De Nardo[c], M. Della Pietra[bc], A. Doria[c], R. Giordano[ac], A. Ordine[c], S. Pardi[c], G. Russo[c], C. Sciacca[c]
[a]*Università di Napoli "Federico II";* [b]*Università Parthenope di Napoli;* [c]*INFN - Sezione di Napoli, Napoli, Italy*

I. I. Bigi, C. P. Jessop, W. Wang
University of Notre Dame, Notre Dame, IN, USA

[6]Deceased.

M. Bellato[b], M. Benettoni[b], M. Corvo[b7], A. Crescente[b], F. Dal Corso[b], U. Dosselli[b], C. Fanin[b], A. Gianelle[b], S. Longo[b], M. Michelotto[b], F. Montecassiano[b], M. Morandin[b], R. Pengo[b8], M. Posocco[b], M. Rotondo[b], G. Simi[ab], R. Stroili[ab]
[a]Università di Padova; [b]INFN - Sezione di Padova, Padova, Italy

L. Gaioni[c], A. Manazza[c], M. Manghisoni[ac], L. Ratti[bc], V. Re[ac], G. Traversi[ac], S. Zucca[c]
[a]Università di Bergamo; [b]Università di Pavia; [c]INFN - Sezione di Pavia, Pavia, Italy

S. Bizzaglia[b], M. Bizzarri[ab], C. Cecchi[ab], S. Germani[b9], M. Lebeau[b10], P. Lubrano[b], E. Manoni[b], A. Papi[b], A. Rossi[b], G. Scolieri[b]
[a]Università di Perugia; [b]INFN - Sezione di Perugia, Perugia, Italy

G. Batignani[bc], S. Bettarini[bc], G. Casarosa[c], A. Cervelli[c], A. Fella[c11], F. Forti[bc], M. Giorgi[bc], L. Lilli[c], A. Lusiani[ac], B. Oberhof[bc], A. Paladino[c], F. Pantaleo[c], E. Paoloni[bc], A. L. Perez Perez[c], G. Rizzo[bc], J. Walsh[c]
[a]Scuola Normale Superiore; [b]Università di Pisa; [c]INFN - Sezione di Pisa, Pisa, Italy

A. Fernández Téllez
Benemérita Universidad Autónoma de Puebla, Puebla, Mexico

G. Beck, M. Berman, A. Bevan, F. Gannaway, G. Inguglia, A. J. Martin, J. Morris
Queen Mary, Univ. of London, London, United Kingdom

V. Bocci[b], M. Capodiferro[b], G. Chiodi[b], I. Dafinei[b], N. V. Drenska[b], R. Faccini[ab], F. Ferroni[ab], C. Gargiulo[b], P. Gauzzi[ab], C. Luci[ab], R. Lunadei[b], G. Martellotti[b], F. Pellegrino[b], V. Pettinacci[b], D. Pinci[b], L. Recchia[b], D. Ruggeri[b], A. Zullo[b]
[a]Università di Roma; [b]INFN - Sezione di Roma, Roma, Italy

P. Camarri[ab], R. Cardarelli[b], C. De Santis[b], A. Di Ciaccio[ab], V. Di Felice[b], F. Di Palma[b], A. Di Simone[b], L. Marcelli[b], R. Messi[ab], D. Moricciani[b], R. Sparvoli[ab], S. Tammaro[b]
[a]Università di Roma Tor Vergata; [b]INFN - Sezione di Roma Tor Vergata, Roma, Italy

P. Branchini[b], A. Budano[b], S. Bussino[ab], M. Ciuchini[b], F. Nguyen[b], A. Passeri[b], F. Ruggieri[b], E. Spiriti[b]
[a]Università di Roma Tre; [b]INFN - Sezione di Roma Tre, Roma, Italy

F. Wilson
Rutherford Appleton Laboratory, Didcot, United Kingdom

I. Leon Monzon, J. R. Millan-Almaraz, P. L. M. Podesta-Lerma
Universidad Autónoma de Sinaloa, Sinaloa, Mexico

D. Aston, B. Dey, A. Fisher, P. D. Jackson, D. W. G. S. Leith, S. Luitz, D. MacFarlane, M. McCulloch, S. Metcalfe, A. Novokhatski, S. Osier, R. Prepost, B. Ratcliff, J. Seeman, M. Sullivan, J. Va'vra, U. Wienands, W. Wisniewski
SLAC, Menlo Park, CA, USA

[7]Also with Laboratoire de l'Accélérateur Linéaire, Univ. Paris-Sud, CNRS/IN2P3, Orsay, France.
[8]Also with INFN - LNL.
[9]Also with Laboratoire de l'Accélérateur Linéaire, Univ. Paris-Sud, CNRS/IN2P3, Orsay, France.
[10]Also with Caltech.
[11]Also with Università di Ferrara, Dipartimento di Matematica e Informatica and Laboratoire de l'Accélérateur Linéaire, Univ. Paris-Sud, CNRS/IN2P3, Orsay, France.

B. D. Altschul, M. V. Purohit
University of South Carolina, Columbia, SC, USA

J. Baudot, I. Ripp-Baudot
IPHC - Strasbourg, Strasbourg, France

G. A. P. Cirrone, G. Cuttone
INFN - LNS (Laboratori Nazionali del Sud), Catania, Italy

O. Bezshyyko, G. Dolinska
Taras Shevchenko National University of Kyiv, Kiev, Ukraine

A. Soffer
Tel Aviv University, Tel Aviv, Israel

F. Bianchi[ab], F. De Mori[ab], A. Filippi[b], D. Gamba[b], S. Marcello[ab]
[a]*Università di Torino;* [b]*INFN - Sezione di Torino, Torino, Italy*

M. Bomben[c], L. Bosisio[ac], P. Cristaudo[c], L. Lanceri[ac], B. Liberti[c], I. Rashevskaya[c], C. Stella[bc], E. S. Vallazza[c], L. Vitale[ac]
[a]*Università di Trieste;* [b]*Università di Udine;* [c]*INFN - Sezione di Trieste, Trieste, Italy*

G. Auriemma[ab], C. Satriano[ab]
[a]*Università degli Studi della Basilicata;* [b]*INFN - Sezione di Roma, Potenza, Italy*

F. Martinez Vidal, J. Mazorra de Cos, A. Oyanguren, P. Ruiz Valls
University of Valencia-CSIC, Valencia, Spain

A. Beaulieu, S. Dejong, J. Franta, M. J. Lewczuk, M. Roney, R. Sobie
University of Victoria, Victoria, British Columbia, Canada

Contents

1 Introduction **1**
- 1.1 The Physics Motivation 1
- 1.2 The Super$B$ Project Elements 1
- 1.3 The Detector Technical Design Report 2
- 1.4 Bibliography 2

2 Collider Overview **5**
- 2.1 The Super$B$ collision scheme 5
- 2.2 The accelerator complex 6
- 2.3 Bibliography 10

3 Detector Overview **11**
- 3.1 Physics Performance 13
- 3.2 Challenges on Detector Design 15
- 3.3 Detector R&D 16
  - 3.3.1 Machine Detector Interface (MDI) and Backgrounds Simulation 16
  - 3.3.2 Silicon Vertex Tracker (SVT) 18
  - 3.3.3 Drift Chamber (DCH) 19
  - 3.3.4 Particle Identification (PID) 20
  - 3.3.5 Electromagnetic Calorimeter (EMC) 21
  - 3.3.6 Instrumented Flux Return (IFR) 22
  - 3.3.7 Electronics, Trigger, and DAQ (ETD) 22
- 3.4 Bibliography 23

4 Physics with Super$B$ **25**
- 4.1 Introduction 25
- 4.2 B and D decays 26
  - 4.2.1 Rare B decays 26
  - 4.2.2 Rare D decays 28
  - 4.2.3 CKM matrix and unitarity triangle 29
  - 4.2.4 CP violation in B decays 30
  - 4.2.5 CP violation in D decays 30
  - 4.2.6 Other symmetry tests 31
  - 4.2.7 Charm mixing 32
  - 4.2.8 B physics at the $\Upsilon(5S)$ 32
- 4.3 τ physics at Super$B$ 33
  - 4.3.1 Lepton flavor violation in τ decay 33
  - 4.3.2 CP violation in τ decay 34
  - 4.3.3 Measurement of the τ $g{-}2$ and EDM form factors 34
- 4.4 Super$B$ Neutral Current Electroweak Physics Programme 36

4.5 Exotic Spectroscopy in Super$B$ . . . 37
4.6 Direct searches . . . 38
4.7 Executive Summary . . . 39
4.8 Bibliography . . . 43

5 Machine Detector Interface and Backgrounds **49**
5.1 Introduction . . . 49
5.2 Backgrounds Sources Overview . . . 49
5.3 Radiative Bhabha . . . 50
5.3.1 Simulation tools . . . 50
5.3.2 Losses at the beam-pipe . . . 51
5.3.3 Shield System . . . 52
5.4 Pairs production . . . 52
5.4.1 Cross section and spectrum comparison . . . 53
5.4.2 Impact of beam-beam effect on secondaries . . . 54
5.4.3 Beam pipe losses . . . 54
5.5 Touschek background . . . 55
5.6 Beam gas background . . . 60
5.7 SVT background overview . . . 63
5.8 DCH background overview . . . 65
5.9 FTOF background overview . . . 65
5.10 FDIRC background overview . . . 66
5.10.1 Shielding the FDIRC . . . 68
5.10.2 Background rates in the FDIRC . . . 69
5.10.3 Integrated charges and doses . . . 69
5.11 EMC background overview. . . . 70
5.12 IFR background overview . . . 71
5.12.1 Neutron Background . . . 71
5.12.2 Charged Particles . . . 72
5.12.3 Background remediation . . . 73
5.13 ETD background overview . . . 73
5.14 SVT radiation monitor . . . 74
5.15 Bibliography . . . 76

6 Silicon Vertex Tracker **79**
6.1 Overview . . . 79
6.1.1 SVT and Layer0 . . . 79
6.1.2 SVT Requirements . . . 81
6.1.2.1 Resolution . . . 81
6.1.2.2 Acceptance . . . 81
6.1.2.3 Efficiency . . . 81
6.1.2.4 Background & Radiation Tolerance . . . 82
6.1.2.5 Reliability . . . 82
6.1.3 Baseline Detector Concept . . . 83
6.1.3.1 Technology . . . 83
6.1.3.2 Layout . . . 83
6.1.3.3 Readout Electronics . . . 87
6.1.3.4 Module design and Mechanical Support . . . 87

6.1.4 Layer0 Pixel Upgrade . . . 88
6.1.4.1 Motivations . . . 88
6.1.4.2 Technology Options for Layer0 pixel upgrade . . . 90
6.1.4.3 Pixel Module & Material Budget . . . 91
6.2 Backgrounds . . . 93
6.3 Detector Performance Studies . . . 94
6.3.1 Introduction . . . 94
6.3.2 The SVT layout . . . 94
6.3.3 Impact of Layer0 on detector performance . . . 95
6.3.4 Tracking performance . . . 98
6.3.5 Impact of machine background on tracking performance . . . 98
6.3.6 Sensitivity studies for time-dependent analyses . . . 100
6.3.7 Performance with Layer0 pixel detectors . . . 101
6.3.8 Particle identification with dE/dx . . . 102
6.4 Silicon Sensors . . . 102
6.4.1 Requirements . . . 103
6.4.2 Sensor design and technology . . . 103
6.4.3 z-side strip connection options . . . 108
6.4.4 Wafer layout and quantities . . . 109
6.4.5 Prototyping and tests . . . 110
6.5 Fanout Circuits . . . 110
6.5.1 Fanouts for Layer0 . . . 111
6.5.1.1 Requirements and Technology . . . 111
6.5.1.2 Design . . . 112
6.5.1.3 Prototyping and tests . . . 112
6.5.2 Fanouts for outer layers . . . 113
6.5.2.1 Requirements . . . 113
6.5.2.2 Material and production technique . . . 113
6.5.2.3 Design . . . 114
6.5.2.4 Tests and prototyping . . . 114
6.6 Readout Electronics . . . 114
6.6.1 Readout chips for Strip and Striplet Detectors . . . 115
6.6.2 Readout chips requirements . . . 116
6.6.3 Readout Chip Implementation . . . 119
6.6.4 R&D for strip readout chips . . . 120
6.6.5 Hybrid Design . . . 122
6.6.5.1 Hybrid mechanical requirements . . . 122
6.6.5.2 Hybrid Electrical requirements . . . 124
6.6.5.3 Layout requirements and implementation . . . 125
6.6.6 Data Transmission . . . 126
6.6.6.1 The Tail . . . 126
6.6.6.2 The transition card . . . 128
6.7 Mechanical Support and Assembly . . . 131
6.7.1 IR Components & Constraints . . . 131
6.7.2 Module Layout & Assembly . . . 132
6.7.3 L1-L5 Half detector assembly . . . 134
6.7.4 Layer0 Half Detector Assembly . . . 136

6.7.5 Mount Layer0 on the Be-pipe and L1-L5 on the conical shield 138
6.7.5.1 Gimbal Rings 138
6.7.6 Installation & Removal of the Complete IR Assembly in Super*B* 139
6.7.6.1 Quick Demounting of the SVT, Layer0 and Be beam-pipe 139
6.7.6.2 Temporary Cage and Translation System 140
6.7.7 Detector Placement and Survey 141
6.7.8 Detector Monitoring 142
6.7.9 R&D Program 142
6.8 Layer0 Upgrade Options 143
6.8.1 Hybrid pixels 143
6.8.2 CMOS monolithic sensor options 145
6.8.2.1 Deep N-well CMOS MAPS 145
6.8.2.2 DNW MAPS in vertical integration technologies 146
6.8.2.3 Monolithic pixels in quadruple-well CMOS technology 146
6.8.3 Overview of the R&D activity 147
6.8.3.1 Front-end electronics for hybrid pixel detectors in 130 nm CMOS technology 147
6.8.3.2 The Apsel DNW MAPS series 148
6.8.3.3 The Apsel4well quadruple well monolithic sensor 152
6.8.3.4 Fast readout architecture for MAPS pixel matrices 154
6.8.4 Radiation tolerance 154
6.9 Services and Utilities 158
6.10 Bibliography 159

7 Drift Chamber **165**
7.1 Introduction 165
7.1.1 Physics Requirements 165
7.1.2 Design Overview 165
7.1.3 Cluster Counting 166
7.1.4 Geometrical Constraints 166
7.1.5 Machine Background Considerations 166
7.2 Design Optimization 169
7.2.1 Performance Studies 169
7.2.1.1 Radius and Thickness of the Inner Wall 169
7.2.1.2 Endcap shape and position 169
7.2.1.3 Wire and Gas Material 170
7.2.1.4 Stereo Angle Layout 171
7.2.1.5 Cluster Counting 171
7.2.2 Cell Design and Layer Arrangement 172
7.2.3 Gas Mixture 174
7.2.4 R&D and Prototype Studies 174
7.2.4.1 Prototype 1 174
7.2.4.2 Prototype 2 176
7.2.4.3 Single Cell Prototypes 178
7.2.4.4 Aging studies 180
7.2.5 R&D Future Developments 181

7.3 Mechanical Design . . . 181
7.3.1 Endplates . . . 182
7.3.2 Inner cylinder . . . 182
7.3.3 Outer Cylinder . . . 183
7.3.4 Analysis of Buckling Instabilities . . . 183
7.3.4.1 Endplates . . . 183
7.3.4.2 Inner Cylinder . . . 183
7.3.4.3 Outer Cylinder . . . 184
7.3.5 Choice of wire . . . 184
7.3.6 Feedthrough design . . . 186
7.3.7 Endplate systems . . . 186
7.3.7.1 Electronics enclosures . . . 186
7.3.7.2 Cooling . . . 186
7.3.7.3 Shielding . . . 187
7.3.7.4 Electromechanical boards . . . 187
7.3.8 Stringing . . . 188
7.4 Electronics . . . 189
7.4.1 Design Goals . . . 189
7.4.2 Standard Readout . . . 189
7.4.2.1 Charge measurement . . . 189
7.4.2.2 Time measurement . . . 189
7.4.2.3 Front End Electronics . . . 190
7.4.3 Cluster Counting . . . 191
7.4.3.1 Front End Electronics . . . 192
7.5 High Voltage system . . . 192
7.5.1 Main System and HV Distribution Boards . . . 192
7.6 Gas system . . . 192
7.7 Monitoring and Calibration . . . 194
7.7.1 Monitoring . . . 194
7.7.2 Calibration . . . 195
7.8 Integration . . . 195
7.8.1 Overall geometry and mechanical support . . . 195
7.8.2 Installation and alignment . . . 195
7.8.3 Services . . . 196
7.9 Bibliography . . . 197

8 Particle Identification **199**
8.1 Summary of Detector Performance goals . . . 199
8.1.1 DIRC Detector concept . . . 199
8.1.2 Charged Particle Identification . . . 200
8.2 Particle Identification Overview . . . 200
8.2.1 Experience with the *BABAR* DIRC . . . 200
8.2.2 Barrel PID: Focusing DIRC (FDIRC) . . . 201
8.3 The Barrel FDIRC Detector Overview . . . 206
8.3.1 Photodetectors . . . 206
8.3.2 Laser calibration system . . . 216
8.3.3 FDIRC Mechanical Design . . . 218

8.3.4 Electronics readout, High and Low voltage . . . 227
8.3.5 Integration issues . . . 235
8.3.6 FDIRC R&D Results . . . 235
8.3.7 Conclusion and ongoing FDIRC R&D . . . 239
8.3.8 System Responsibilities and Management . . . 239
8.3.9 Cost, Schedule and Funding Profile . . . 240
8.4 A possible PID detector on the Super$B$ forward side . . . 240
8.4.1 Physics motivation and detector requirements . . . 240
8.4.2 The Forward task force and the selection of a forward PID technology . . . 242
8.4.3 The DIRC-like forward time-of-flight detector (FTOF) . . . 244
8.4.4 Appendix: forward PID R&D activities . . . 252
8.5 Bibliography . . . 257

9 Electromagnetic Calorimeter 261
9.1 Overview . . . 261
9.1.1 Background and radiation issues . . . 262
9.1.2 Simulation tools . . . 262
9.1.2.1 FastSim . . . 262
9.1.2.2 FullSim . . . 263
9.2 Barrel Calorimeter . . . 264
9.2.1 Requirements for the Super$B$ Environment . . . 264
9.2.1.1 Crystal Aging in *BABAR* at PEP-II . . . 264
9.2.1.2 Backgrounds . . . 265
9.2.2 Description of *BABAR* Barrel Calorimeter . . . 266
9.2.2.1 Mechanical design . . . 266
9.2.2.2 Readout . . . 268
9.2.2.3 Low-energy Source Calibration . . . 268
9.2.2.4 Light Pulser . . . 269
9.2.3 Performance of the *BABAR* barrel . . . 270
9.2.3.1 Energy and position resolution . . . 270
9.2.3.2 $\gamma\gamma$ mass resolution . . . 270
9.2.3.3 Radiation Damage Effects on Resolution . . . 271
9.2.3.4 Expected Changes in Performance at Super$B$ . . . 272
9.2.4 Electronics changes . . . 273
9.2.4.1 Requirements . . . 273
9.2.4.2 Electronic noise measurements . . . 274
9.2.4.3 Readout design . . . 275
9.2.5 Disassembly at SLAC and Transport to Italy . . . 275
9.2.6 Electronics refurbishment . . . 276
9.2.7 Shipment, Refurbishing and Reassembly . . . 277
9.3 Forward Calorimeter . . . 277
9.3.1 LYSO Crystals . . . 278
9.3.1.1 Transmittance and Emission . . . 280
9.3.1.2 Decay time and Light Output . . . 282
9.3.1.3 Response Uniformity . . . 284
9.3.1.4 Radiation Hardness . . . 285
9.3.1.5 Specifications, Production and Testing . . . 287

9.3.2 Readout and Electronics . . . 288
9.3.2.1 APD Readout . . . 288
9.3.2.2 Electronics Block diagram . . . 288
9.3.2.3 Preamplifier and shaper . . . 289
9.3.2.4 Digitization . . . 289
9.3.2.5 Requirements on mechanics . . . 289
9.3.3 Calibration . . . 289
9.3.3.1 Initial LYSO calibration with sources . . . 289
9.3.3.2 Temperature monitoring and correction . . . 290
9.3.4 Mechanical Structure . . . 290
9.3.4.1 Crystals . . . 290
9.3.4.2 Modules . . . 292
9.3.4.3 Installation . . . 292
9.3.4.4 Refurbishment of the *BABAR* structure . . . 292
9.3.4.5 Tests of the Spare FWD modules . . . 293
9.3.5 Beam Tests . . . 293
9.3.5.1 Description of the apparatus . . . 293
9.3.5.2 Description of the beams . . . 295
9.3.5.3 Description of data and calibration . . . 296
9.3.5.4 Electronics noise measurements . . . 297
9.3.5.5 Temperature corrections . . . 297
9.3.5.6 Results . . . 297
9.3.6 Alternatives . . . 298
9.3.6.1 Full LYSO calorimeter . . . 298
9.3.6.2 Pure CsI . . . 301
9.3.6.3 BGO . . . 302
9.3.6.4 Comparison among options . . . 305
9.4 Backward Calorimeter . . . 306
9.4.1 Requirements . . . 307
9.4.1.1 Energy and angular resolution . . . 307
9.4.1.2 Background rates . . . 308
9.4.1.3 Radiation hardness . . . 308
9.4.1.4 Solid angle, transition to barrel . . . 308
9.4.2 Mechanical design . . . 309
9.4.2.1 Calorimeter construction . . . 310
9.4.2.2 Support and services . . . 310
9.4.3 SiPM/MPPC readout . . . 310
9.4.4 Electronics . . . 311
9.4.5 Calibration . . . 312
9.4.6 Backward simulation . . . 312
9.4.7 Performance in simulations . . . 312
9.4.8 Impact on physics results . . . 313
9.4.9 Use for particle identification . . . 314
9.4.10 Discussion of task force conclusions . . . 317
9.5 Environmental monitoring . . . 317
9.6 Bibliography . . . 318

10 Instrumented Flux Return **321**
10.1 Physics Goals and Performance Requirements . . . 321
10.2 Detector Overview . . . 322
10.2.1 The Absorber Structure . . . 322
10.2.2 The Active Detector Choice . . . 325
10.3 Backgrounds . . . 325
10.3.1 Neutron Background . . . 326
10.3.2 Charged Particles . . . 326
10.3.3 Photon Background . . . 326
10.4 Identification Performance . . . 327
10.4.1 Muon Detection . . . 327
10.4.2 K_L Detection . . . 331
10.5 Detector R&D . . . 332
10.5.1 Module Tests and Results . . . 332
10.5.1.1 Detection module R&D . . . 334
10.5.1.2 Radiation damage of photodetectors . . . 335
10.5.2 Prototype Test and Results . . . 337
10.5.2.1 Design and construction of the IFR prototype . . . 337
10.5.2.2 Beam Tests . . . 338
10.5.2.3 Tests Results . . . 340
10.6 Baseline Design of the IFR Detector . . . 342
10.6.1 Detector Layout . . . 342
10.6.2 Chamber Construction, Assembly and Quality Control . . . 345
10.7 Photodetectors and PCB . . . 347
10.7.1 Photodetector PCB and optical coupling to fibers . . . 347
10.7.2 Photodetector location . . . 348
10.7.3 Photodetector choice . . . 348
10.7.4 Aging and background issues . . . 349
10.7.5 Temperature requirements . . . 350
10.8 Front-End Electronics . . . 350
10.8.1 IFR channel count estimation . . . 350
10.8.2 Estimations of the IFR event size and data bandwidth . . . 351
10.8.3 Background radiation and electronics design constraints . . . 351
10.8.4 The IFR readout system . . . 355
10.9 Final assembly and installation . . . 365
10.10Bibliography . . . 365

11 Magnet and Flux Return **371**
11.1 Magnet main characteristics . . . 371
11.2 Magnetic forces on the solenoid . . . 373
11.3 Cryogenics . . . 373
11.4 Current supply and protection system . . . 374
11.5 Plan for reusing the *BABAR* magnet equipment. . . . 375
11.6 Bibliography . . . 377

12 Electronics, Trigger, Data Acquisition and Online **379**
12.1 Trigger Strategy and System Requirements . . . 379
12.1.1 Trigger Rate and Event Size Estimation . . . 379

12.1.2 Dead Time and Buffer Queue Depth Considerations 380
12.1.3 Choice of Global Clock Frequency 381
12.2 Architecture Overview 381
12.3 Trigger and Event Data Chain 382
12.3.1 Level-1 Trigger 382
12.3.1.1 Drift chamber trigger (DCT) 382
12.3.1.2 Electromagnetic Calorimeter Trigger (EMT) 385
12.3.1.3 L1 DCT and EMT trigger processors 387
12.3.1.4 Global Trigger (GLT) 387
12.3.1.5 L1 Trigger Latency 388
12.3.1.6 Monitoring the Trigger 388
12.3.1.7 L1 Trigger R&D 388
12.3.2 Fast Control and Timing System 388
12.3.3 Control and Data Links 391
12.3.4 Common Front-End Electronics 396
12.3.5 Read-Out Modules 398
12.3.6 Network Event Builder 399
12.3.7 High-Level Trigger Farm 400
12.3.8 Data Logging 400
12.3.9 Data Quality Monitoring System 401
12.4 System Integration and Error Handling 401
12.5 Control Systems 401
12.5.1 Electronics Control System 402
12.5.2 Detector Control System 403
12.5.3 Farm Control System 404
12.6 Support Systems 404
12.7 R&D for Electronics, Trigger and Data Acquisition and Online 404
12.8 Conclusions 405
12.9 Bibliography 405
12.A Appendix: ETD design rules for the FEE 407

13 Subdetector Electronics and Infrastructure **409**
13.1 Subsystem-specific Electronics 409
13.1.1 SVT Electronics 409
13.1.1.1 SVT Summary 411
13.1.2 DCH Electronics 411
13.1.2.1 Design Goals 411
13.1.2.2 DCH FEE (overall design) 412
13.1.2.3 Off Detector Electronics - Standard Readout 412
13.1.2.4 Off Detector Electronics - Cluster Counting 413
13.1.2.5 FEE Crates 414
13.1.2.6 Number of Crates and Links 414
13.1.2.7 ECS 414
13.1.2.8 Cabling 415
13.1.2.9 Power Requirements 415
13.1.2.10 DCH Summary 415

13.1.3 PID Electronics . . . 415
13.1.3.1 The Front-end Crate . . . 416
13.1.3.2 The Communication Backplane . . . 416
13.1.3.3 The PMT Backplane . . . 416
13.1.3.4 Cooling and Power Supply . . . 416
13.1.3.5 The Front-end Board . . . 418
13.1.3.6 The Crate Controller Board (FBC) . . . 418
13.1.3.7 PID Summary . . . 418
13.1.4 EMC Electronics . . . 418
13.1.4.1 EMC Summary . . . 420
13.1.5 IFR Electronics . . . 420
13.1.5.1 IFR Summary . . . 423
13.2 Electronics Infrastructure . . . 424
13.2.1 Power supplies, grounding and cabling . . . 424
13.2.1.1 Grounding and shielding . . . 424
13.2.1.2 Rules for cables . . . 424
13.2.1.3 Power Supply to the Front-end . . . 425
13.2.1.4 High Voltage Power Supply for the Detectors . . . 427
13.3 Bibliography . . . 427

14 Software and Computing **429**
14.1 Tools to support detector studies . . . 429
14.1.1 Full Simulation . . . 429
14.1.2 Fast Simulation . . . 432
14.1.3 Distributed computing tools . . . 437
14.1.4 Collaborative tools . . . 439
14.2 The Super$B$ baseline computing model . . . 440
14.2.1 Data processing strategy . . . 440
14.2.2 Resource estimate . . . 441
14.2.3 Computing Infrastructure . . . 442
14.3 The Super$B$ Computing R&D program . . . 443
14.3.1 Exploiting parallelism . . . 443
14.3.2 Distributed computing R&D: DIRAC framework evaluation . . . 445
14.3.3 Data management and distributed storage R&D . . . 446
14.4 Outlook . . . 448
14.5 Bibliography . . . 449

15 Facilities, Mechanical Integration and Assembly **453**
15.1 Introduction . . . 453
15.1.1 Magnet and Instrumented Flux Return . . . 453
15.2 Component Extraction . . . 454
15.3 Component Transport . . . 455
15.4 Detector Assembly . . . 456

16 The Super$B$ Collaboration and Project Management **457**
16.1 Collaboration Membership . . . 458
16.2 The Collaboration Council . . . 458
16.3 The Spokesperson . . . 459

16.4 The Executive Board . . . 459
16.5 The Management Team and Management Plan . . . 460
16.6 The International Finance Review Committee . . . 460
16.7 Interaction with the Cabibbo-Lab . . . 460
16.8 Construction Responsibilities . . . 460
16.9 Bibliography . . . 461

17 Cost and Schedule **463**
17.1 Detector Costs . . . 464
17.2 Basis of Estimate . . . 468
17.3 Schedule . . . 470
17.4 Bibliography . . . 470

1 Introduction

1.1 The Physics Motivation

The Standard Model successfully explains the wide variety of experimental data that has been gathered over several decades with energies ranging from under a GeV up to several hundred GeV. At the start of the millennium, the flavor sector was perhaps less explored than the gauge sector, but the PEP-II and KEK-B asymmetric B Factories, and their associated experiments BABAR and Belle, have produced a wealth of important flavor physics highlights during the past decade [1]. The most notable experimental objective, the establishment of the Cabibbo-Kobayashi-Maskawa phase as consistent with experimentally observed CP-violating asymmetries in B meson decay, was cited in the award of the 2008 Nobel Prize to Kobayashi and Maskawa [2].

The B Factories have provided a set of unique, over-constrained tests of the Unitarity Triangle. These have, in the main, been found to be consistent with Standard Model predictions. The B factories have done far more physics than originally envisioned; BABAR alone has published more than 480 papers in refereed journals to date. Some examples of important experimental results are measurements of all three angles of the Unitarity Triangle, including α and γ in addition to sin 2β; the establishment of $D^0\bar{D}^0$ mixing; the uncovering of intriguing clues for potential New Physics in $B \to K^{(\star)}l^+l^-$, $B \to K\pi$, $B \to D\tau\nu$, and $B \to D^{(\star)}\tau\nu$ decays; and the unveiling of an entirely unexpected new spectroscopy.

All present measurements confirm the Standard Model, reducing the parameter space for New Physics Models, whose signals remain elusive. With the LHC in full operation, we expect major experimental discoveries during the next few years at the energy frontier. We would hope not only to complete the Standard Model by confirming that the exciting recent observations by ATLAS and CMS around 126 GeV/c^2 indeed come from the Higgs boson, but also to find signals of New Physics, which are widely expected to lie around the 1 TeV energy scale. If found, the New Physics phenomena will need data from very sensitive heavy flavor experiments if they are to be understood in detail. Determining the flavor structure of the New Physics involved requires the information on rare b, c, and τ decays, and on CP violation in b and c quark decays that only a very high luminosity asymmetric B Factory can provide [3]. On the other hand, if such signatures of New Physics are not observed at the LHC, then the excellent sensitivity provided at the luminosity frontier by a next generation super B factory provides another avenue to observing New Physics at mass scales up to 10 TeV or more through observation of rare processes involving B and D mesons and studies of lepton flavour violation in τ decays.

1.2 The Super*B* Project Elements

It is generally agreed that the physics being addressed by a next-generation B factory requires a data sample that is some 50–100 times larger than the existing combined sample from BABAR and Belle, or at least 50–75 ab^{-1}. Acquiring such an integrated luminosity in a 5 year time frame requires that the collider run at a luminosity of at least $10^{36}\,\mathrm{cm}^{-2}\mathrm{s}^{-1}$.

For a number of years, an Italian led, INFN hosted, collaboration of scientists from Canada, Italy, Israel, France, Norway, Spain, Poland, UK, and USA has worked to design and propose a high luminosity 10^{36} asymmetric B Factory project, called Super$B$, to be built at or near the Frascati laboratory [4].

The accelerator portion of the project employs lessons learned from modern low-emittance synchrotron light sources and ILC/CLIC R&D, and an innovative new idea for the intersection region of the storage rings [5, 6], called crab waist, to reach luminosities over 50 times greater than those obtained by earlier B factories at KEK and SLAC. There is now an attractive, cost-effective accelerator design, including polarized beams, which is being further refined and optimized [7]. It is designed to incorporate many PEP-II components. This facility promises to deliver fundamental discovery-level science at the luminosity frontier.

There is also an active international collaboration working effectively on the design of the detector. The detector team draws heavily on its deep experience with the *BABAR* detector, which has performed in an outstanding manner both in terms of scientific productivity and operational efficiency, and which serves as the foundation of the design of the Super$B$ detector. Substantial R&D has been undertaking to understand the modifications and enhancements of the detector components required to deal with the much higher luminosity and the different physics and machine backgrounds.

The Super$B$ project has been developed over a substantial time frame. In 2010, the design and development of all elements of the project were described in the "Design Progress Reports", a set of several descriptive documents that summarized developments and status of each major division of the project: Physics [8], Accelerator [7], and Detector [9]. These documents present a snapshot of the entire project at an intermediate stage between the Conceptual Design Report [4], which was written in 2007, and the Technical Design Reports (TDRs).

1.3 The Detector Technical Design Report

This TDR describes the design and development of the Super$B$ detector, which is based on a major upgrade of *BABAR*. It begins with overviews of each of the elements of the project (Accelerator, Detector, and the Physics). In particular, the Detector section summarizes the base detector design, the challenges involved in detector operations at the luminosity frontier, the approach being taken to optimize remaining general design options, and the R&D program that is underway to validate the system and subsystem designs. A chapter detailing the many challenging issues involved in the machine detector interface at this high luminosity machine follows. Each of the detector subsystems and the general detector systems (especially electronics and Data Acquisition) are then described in more detail, followed by a discussion of the computing and software. The detector hall facilities are then described in the context of the integration and assembly of the full detector. Finally, the paper concludes with a discussion of project management, detector costs, and a schedule overview.

1.4 Bibliography

[1] J. Beringer et al., (Particle Data Group collaboration), "Review of particle physics", *Phys. Rev. D* 86:010001, 2012, doi:10.1103/PhysRevD.86.010001.

[2] http://nobelprize.org/nobel_prizes/physics/laureates/2008/press.html and http://www-public.slac.stanford.edu/babar/Nobel2008.htm.

[3] D. Hitlin, C. Cheng, D. Asner, T. Hurth, B. McElrath, et al., "New Physics at the Super Flavor Factory. Proceedings, 6th superB Workshop, Valencia, Spain, January 7-15, 2008", 2008, arXiv:0810.1312 [hep-ph].

[4] M. Bona et al., "Super$B$: A High-Luminosity Asymmetric e^+e^- Super Flavor Factory. Conceptual Design Report", 2007, arXiv:0709.0451 [hep-ex].

[5] P. Raimondi, *2nd LNF Workshop on SuperB, Frascati, Italy*, March 2006, http://www.lnf.infn.it/conference/superb06/talks/raimondi1.ppt.

[6] P. Raimondi, *Proceedings of Particle Accelerator Conference (PAC 07), Albuquerque, New Mexico, USA*, 2007.

[7] M. Biagini et al., (Super$B$ collaboration), "Super$B$ Progress Reports: The Collider", 2010, arXiv:1009.6178 [physics.acc-ph].

[8] B. O'Leary et al., (Super$B$ collaboration), "Super$B$ Progress Reports – Physics", 2010, arXiv:1008.1541 [hep-ex].

[9] E. Grauges et al., (Super$B$ collaboration), "Super$B$ Progress Reports – Detector", 2010, arXiv:1007.4241 [physics.ins-det].

2 Collider Overview

The main goal of the Super$B$ facility is to produce $\Upsilon(4S)$ mesons at a rate of $\sim 1\,\mathrm{kHz}$ by colliding electron on positron beams exploiting the process $e^+e^- \to \Upsilon(4S)$ whose maximum cross section ($\sim 1\,\mathrm{nb}$) is reached at $\sqrt{s} \sim 10.58\,\mathrm{GeV}$. This requirement set the design luminosity of the collider at $10^{36}\,\mathrm{cm}^{-2}\mathrm{s}^{-1}$, a two orders of magnitude increase with respect to the present generation B factories. Super$B$ will be able to operate in a $\sqrt{s}$ range spanning from below the $b\bar{b}$ threshold up the $\Upsilon(5S)$, moreover Super$B$ will be also able to run at the τ/charm threshold with a luminosity in the range of $10^{35}\,\mathrm{cm}^{-2}\mathrm{s}^{-1}$.

The $\Upsilon(4S)$ will be produced with a sizeable boost in the laboratory frame ($\beta\gamma \sim 0.28$) to allow for an accurate measurement of the longitudinal separation of the decay vertices of the two B mesons originating from the $\Upsilon(4S)$. The electron colliding beam will be longitudinally polarized at the Interaction Point (IP) to allow for a precise determination of the electroweak parameter $\sin\vartheta_{\mathrm{W}}$ and to provide additional kinematical informations useful to the searches of lepton flavour violating (LFV) decays of the τ leptons. These additional informations will be useful both for rejecting the dominant backgrounds minimising these decays and, in case of observation, for determining the Lorentz structure of the LFV coupling.

The followings sections will provide an overview of the novel crab-waist collision scheme with a brief summary of the test performed at DAΦNE with this new scheme. The accelerator complex and its main parameters are also presented.

2.1 The Super$B$ collision scheme

A Super$B$ factory can provide a uniquely sensitive probe of New Physics in the flavour sector of the Standard Model.

The two proposed second-generation B factory designs, Super$B$ and SuperKEKB, come after the successes of the first generation B factories PEP-II at SLAC and KEKB at KEK which, in turn, came after three former colliders which operated at the $\Upsilon(4S)$ resonance (DORIS-II at DESY, VEPP-4M at BINP and CESR at Cornell).

The two B factories PEP-II and KEKB were conceived in the 90's with very ambitious design parameters, that — compared to typical accelerator commissioning schedules — were reached very rapidly. Both colliders achieved very high peak luminosities with very good reliability, assuring their success. Both colliders are based on a similar design: double rings with asymmetric energies, flat beams and a multibunch regime. Key features of their design are also a low β^* at the IP with β_y^* between 1 and 2 cm. PEP-II adopted a head-on collision scheme and beams were separated off the IP by dipole magnets, while in KEKB beams were separated by a finite-angle crossing scheme with +/-11 mrad.

High luminosity is obtained essentially by high beam currents pushed to their maximum values. Of course, beam current cannot be increased infinitely, due to beam-beam interaction, but also to beam instabilities and to synchrotron radiation emission. As beam density is increased, beam-beam interaction gets stronger and other effects, such as electron cloud and fast ion, that cause beam instabilities get stronger. Also synchrotron radiation emission in the interaction region sets a limit to stored current. Bunch-by-bunch feedback systems have played a primary role for damping instabilities. Moreover, in B factories high currents induced also high Interaction Region (IR) backgrounds, that have been well handled, together with lifetime effects. First generation B factories PEP-II and KEKB, as for all the factories, namely the

Frascati Φ Factory DAΦNE and the Chinese Tau-Charm factory BTCF, are electron-positron colliders based on standard collision schemes. Some of the main parameters of the two B factories are reported in Table 2.1, with a comparison with one of the former colliders running at the $\Upsilon(4S)$ resonance CESR-Phase III.

A new collision scheme named *crab-waist* [1] opened the possibility of enhancing the luminosity by about two orders of magnitudes with no currents increase, making a breaktrough in the colliders design. This launched a new generation of B factories, namely Super$B$ and SuperKEKB, based on the new scheme proposed by Pantaleo Raimondi, that allows to step forward from factories to super factories. The *crab-waist* (CW) scheme combines several ingredients that together are very powerful for a luminosity increase: one is the tighter focus on beams at IP, a second one is the large Piwinski angle and the third and very important one is the twist of the beam waists at the IP obtained by placing two proper sextupoles per ring. Super$B$ is designed to fully accomplish the CW scheme.

First of all Super$B$ relies on two low emittance storage rings to provide small bunches (see the emittances in Table 2.1). The vertical dimension of the bunches will be demagnified down to 36 nm by a strong final focus doublet located half a meter from the IP. Higher luminosity will be obtained as a simple consequence that this scheme provides a smaller spot size at the IP, thus by exploiting the recent advances in damping rings and final focus design techniques.

The second ingredient of the CW scheme is the large Piwinski angle, with flat beams and small horizontal crossing angle, obtained by decreasing the horizontal beam size σ_x and increasing the crossing angle θ. This, in turn, brings a luminosity increase with a horizontal tune shift decrease, but, most importantly, at the same time the overlap area of the colliding bunches is decreased. So, the vertical beta function β_y^* can be of the same order of this overlap area, therefore much smaller than the longitudinal bunch length σ_z as in the standard collision scheme, where the bunch length is, for this reason, needed as small as possible. This is a good gain, as with longer bunches high order modes (HOM) heating is decreased together with coherent syncrotron radiation emission, power consumption and beam instabilities are less severe. Moreover, a lower β_y^* allows also for lower vertical beam-beam tune shift.

The last ingredient of the CW collision scheme is the crab waist transformation by means of two sextupole lenses (*crab sextupoles*) at the opposite sides of the IP that provide a waist rotation of one bunch to the axis of the other one. This translates into a luminosity gain due to a better overlap area, where both beams collide in the minimum β_y region. In addition, most importantly, these two crab sextupoles suppress very efficiently betatron and synchrobetatron resonances. They must have a π phase advance horizontally and $\pi/2$ vertically with respect to the IP, and a proper strength.

This new CW collision scheme has been successfully tested at DAΦNE after a shut-down in 2007 for the installation of the new experimental detector SIDDHARTA and for the major changes in the interaction region necessary to implement the new collision scheme [2]. The best peak luminosity of $4.53 \cdot 10^{32}\,\mathrm{cm}^{-2}\mathrm{s}^{-1}$ was obtained in June 2009, showing an increase of a factor 3 with respect to the peak luminosity reached before the upgrade. The luminosity gain came partly from the smaller vertical beta function with the high Piwinski angle, and partly from the beam-beam resonance suppression that happens with the crab sextupoles. The vertical beam-beam tune-shift has improved by about a factor 1.5, going to 0.044. Numerical beam-beam simulations are in good agreement (within 15-20%) with experimental data.

2.2 The accelerator complex

The Super$B$ accelerators complex consists of an injection system that will inject electrons and positrons into their respective rings at full energies. Electrons and positrons have a nominal energy of 4.2 GeVand 6.7 GeV, respectively. In addition, electrons will be polarized. The two

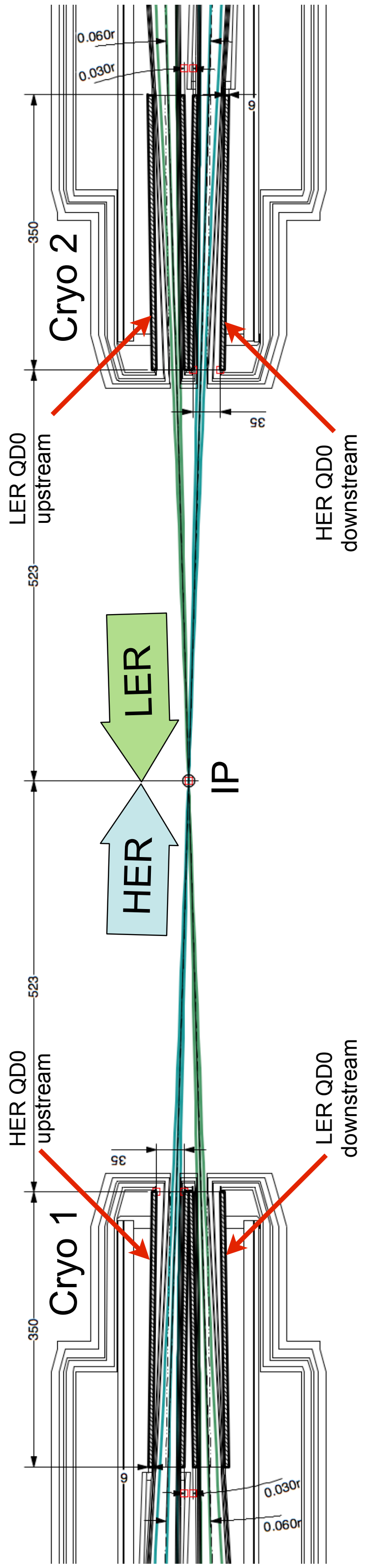

Figure 2.1: The SuperB interaction region layout.

Table 2.1: Main parameters of Super$B$. PEP-II, KEKB and CESR best achieved luminosity parameters are also reported.

Parameter	Super$B$		PEP-II		KEKB		CESR
	HER(e^+)	LER(e^-)	HER(e^-)	LER(e^+)	HER(e^-)	LER(e^+)	
Luminosity (10^{33} cm^{-2}s^{-1})	1000		12		17		1.2
Circumference (m)	1200		2200		3014		768
Energy (GeV)	6.7	4.18	8.97	3.12	8.0	3.5	5.29
Lorentz $\beta\gamma$ factor	0.238		0.553		0.426		—
Beam current (mA)	1900	2440	1875	2990	1330	1650	370
Particle per bunch ($\times 10^{10}$)	5.1	6.6	5.0	7.9	6.0	7.5	12
h/v emittance (nm / pm)	2.0/5.0	2.5/6.2	73/ 1000	36/ 1000	24/ 600	18/ 600	400/ 4500
h/v $\beta^\star$ (mm)	26/0.26	32/0.21	740/11	210/10	560/6.5	590/5.9	450/21
h/v beam size @ IP (μm/ nm)	7.2/36	8.9/36	147/5000		116/1900	103/1900	420/ 4000

main rings will have a circumference of about 1200 m.

The injection complex (Fig. 2.3) will consist of a polarized electron gun, a positron production system, electron and positron linac sections, a damping ring and the transfer lines connecting these systems to the collider main rings. Electrons will be accelerated in the linac and then into the damping ring; positrons, produced by accelerated electrons impinging on a positron converter target, will be accelerated and injected in the damping ring as for the elctrons.

To keep the ultra high luminosity nearly constant, continuous injection in both rings is necessary. The charge required for injection into the main rings is 300 pC/bunch in five bunches. All the three linac sections are based on S-band accelerating sections operating at a repetition frequency of 100 Hz. The injection repetition cycle is 30 ms for each beam; this provides a third time slot with 30 ms repetition cycle that can be used to accelerate an ultra-low emittance beam to drive a SASE-FEL facility. Electrons will be produced by a polarized gun similar to the SLC gun, where 80% polarization has been routinely achieved. At full luminosity and beam currents the lifetime of the beams in the two main rings is expected to be between 3 and 8 minutes. Therefore, to keep beam currents and luminosity nearly constant, the injection process must be continuous with top-up injection.

The Super$B$ HER and LER lattice designs have several constraints, like an extremely low emittance and small IP beam sizes needed for the high luminosity, as well as reasonable beam lifetimes and high electron beam polarization.

After intense work on the optimization of the lattice and beam parameters, asymmetric emittances and asymmetric beam currents for the two rings were chosen. The Super$B$ rings consist of two main lattice systems: arcs and final focus. The arcs bend the beams back into collisions and generate the horizontal emittance. The final focus consists of an extremely low-β insertion and a crab-waist scheme with special optics. The Super$B$ rings can be considered as two damping rings, similar to the ILC and CLIC ones, with the constraint of including a final focus section for collisions. So, the challenge is not only to achieve low emittance beams, but also to choose all the beam parameters to reach a very high luminosity with acceptable lifetimes and small beam degradation.

The Final Focus is the most crucial system for achieving the Super$B$ performance. Reaching the luminosity goal relies on the capability to de-magnify the vertical beam size down to 35 nm at the IP. Therefore, the Final Focus design has to provide small beta functions at the IP: β_x^* is 2.6 cm for the HER and 3.2 cm for the LER, while β_y^* is 0.23 mm for the HER and 0.20 mm for the LER. These small beta functions at the IP can be reached if the IR magnets are as close as possible to the IP.

The total length of the Final Focus is about $\pm$ 300 m around the IP and it includes the IR,

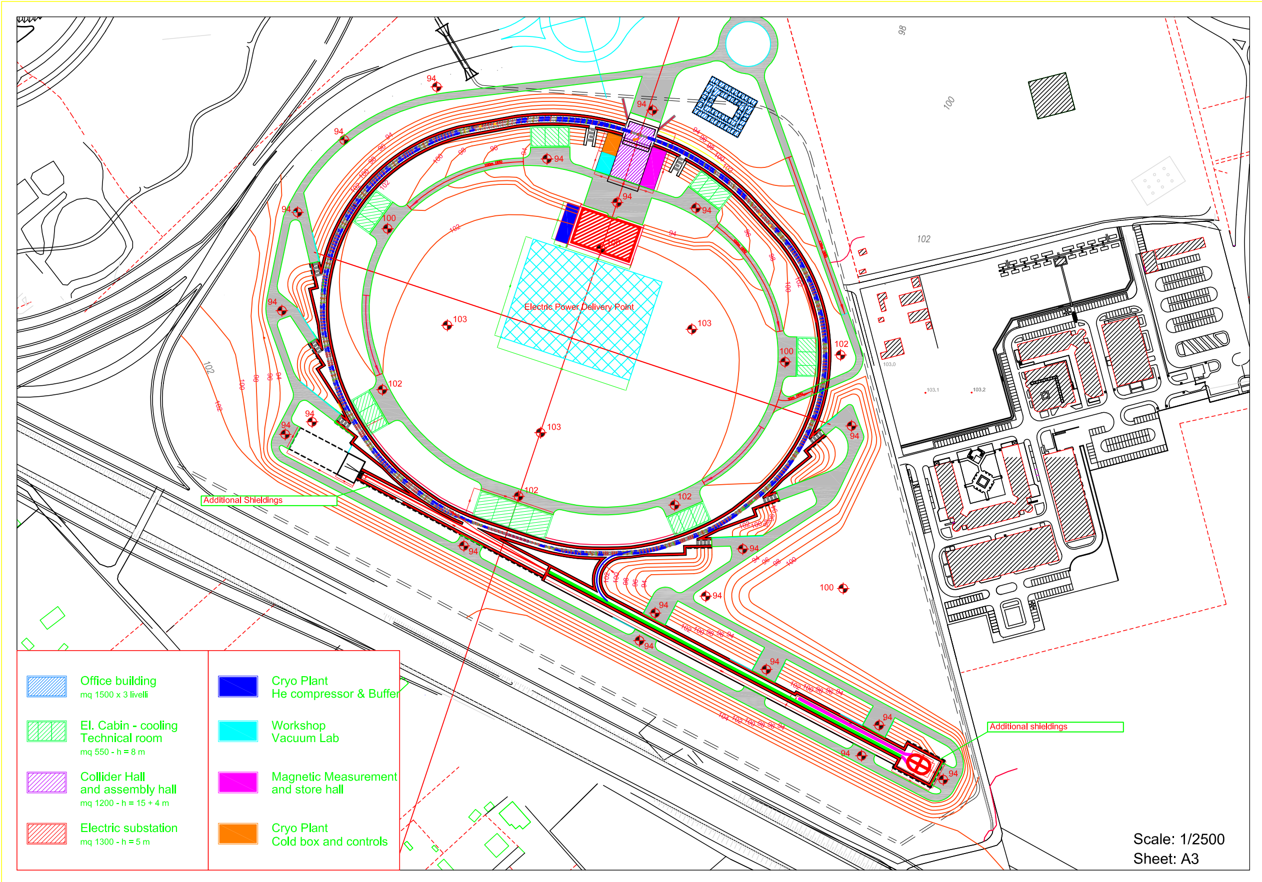

Figure 2.2: The Super$B$ site layout. The two main rings, the injection system and the positrons damping rings are represented together with the main services.

which is defined as a region of $\pm$ 5 m around the IP.

The IR is designed to have a total crossing angle at the IP of 60 mrad; this is the lowest value that allows for sufficient seperation of the beams to account for parasitic collisions, and to avoid synchrotron radiation backgrounds from large transverse orbits hitting the detector beam pipe. In the IR the two beams will be focused by two independent magnetic systems; no quadrupole will be shared among the LER and the HER. The advantage of this design choice with respect to most conventional designs is the smaller dispersion attainable inside of QD0. This is a bonus for both the machine (smaller equilibrium emittance) and the detector (lower background rates). In the present design the HER and LER permanent magnet quadrupoles will provide the first IP vertical focusing. The remaining vertical focusing strength will be provided by two superconducting quadrupoles for the HER and one for the LER. The HER and LER superconducting quadrupoles are installed in separate warm bore cryostats, respectively. Extra focusing for the HER is provided by two additional quadrupoles, named QD0H and QF1H. Soft upstream bend magnets are used to minimize as much as possible the synchrotron radiation power in the IP area.

The design of the superconducting quadrupoles (SCQ) is particularly challenging. The thermal load by synchrotron radiation on the beam pipe inside the SCQs will be $\tilde{2}00W$, so a cold bore design is not suitable. The horizontal beam clearance and the crossing angle at the IP fix both the warm bore diameter to

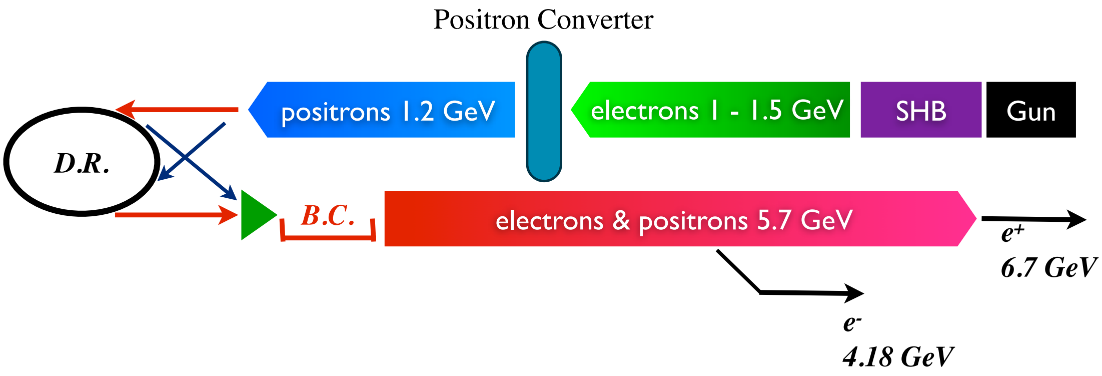

Figure 2.3: The Super$B$ injection system conceptual layout.

24 mm and the maximum thickness allowed for the cryostat and the SCQ cold mass to 22 mm. The SCQs will be built using a double helical winding scheme and a novel compensation technique to cancel out the cross talk between adjacent quadrupoles (i.e., LER QD0 upstream and HER QD0 downstream). A sketch of the IR layout is shown in in Fig.2.1.

In summary, the Super$B$ accelerator complex has been carefully studied and a mechanical layout provided, allowing for a rigorous cost estimate.

2.3 Bibliography

[1] P. Raimondi, *2nd LNF Workshop on SuperB, Frascati, Italy*, March 2006, http://www.lnf.infn.it/conference/superb06/talks/raimondi1.ppt.

[2] M. Zobov, D. Alesini, M. Biagini, C. Biscari, A. Bocci, et al., “Test of crab-waist collisions at DAFNE Phi factory”, *Phys.Rev.Lett.* 104:174801, 2010, doi:10.1103/PhysRevLett.104.174801.

3 Detector Overview

The Super$B$ detector concept is based on the *BABAR* detector, with those modifications required to operate at a luminosity of $10^{36}\,\mathrm{cm}^{-2}\mathrm{s}^{-1}$ or more, and with a reduced center-of-mass boost. Higher luminosity and machine-related backgrounds, as well as the need to improve detector hermeticity and performance, require significant R&D to implement this upgrade.

The *BABAR* detector, which operated on PEP-II from 1999 to 2008, consists of a tracking system with a five layer double-sided silicon strip vertex tracker (SVT) and a 40 layer drift chamber (DCH) inside a 1.5 T magnetic field, a Cherenkov detector with fused silica bar radiators (DIRC), an electromagnetic calorimeter (EMC) consisting of 6580 CsI(Tl) crystals and an instrumented flux-return (IFR) for K_L^0 detection and μ identification.

The Super$B$ detector concept reuses a number of components from *BABAR*: the flux-return steel, the superconducting coil, the barrel of the EMC and the fused silica bars of the DIRC. The flux-return will be augmented with additional absorber to increase the number of interaction lengths for muons to roughly 7λ. The DIRC camera will be replaced by a twelve-fold modular camera using multi-anode photo multipliers (MAPMT) photon detectors in a focusing configuration using fused silica optics to reduce the impact of beam related backgrounds and improve performance. The readout electronics will also be replaced with a much faster system. For the forward EMC, subject to higher particle rates and background, a replacement of the CsI(Tl) crystals with faster devices is required at least where the rates are highest. A solution based on cerium-doped LYSO (lutetium yttrium orthosilicate) crystals, which have a much shorter scintillation time constant, a lower Molière radius and much better radiation hardness than the current CsI(Tl) crystals, would give the ultimate detector performance. The high cost of this material has prompted the collaboration to also explore different solutions, and the present design is a hybrid of the existing CsI(Tl) in the outermost rings, plus LYSO in the inner rings where the rates are highest. Another attractive possibility is based on pure CsI crystals which, while featuring a fast response time, suffer from a low light yield, requiring R&D on the readout device.

The tracking detectors for Super$B$ will be new. The current SVT cannot operate at $\mathcal{L} = 10^{36}\,\mathrm{cm}^{-2}\mathrm{s}^{-1}$, and the DCH has reached the end of its design lifetime and must be replaced. To maintain sufficient proper-time difference (Δt) resolution for time-dependent *CP* violation measurements with the Super$B$ boost of $\beta\gamma = 0.24$, the vertex resolution will be improved by reducing the radius of the beam pipe, placing the innermost layer of the SVT at a radius of roughly 1.5 cm. This innermost layer of the SVT will be initially constructed of silicon striplets, with an upgrade path to Monolithic Active Pixel Sensors (MAPS) or other pixelated sensors, depending on the estimated background levels and the success of the connected R&D. Likewise, the design of the cell size and geometry of the DCH will be driven by occupancy considerations.

It is desirable to improve the hermeticity of the Super$B$ detector, and thereby its performance for certain physics channels, by including a backward "veto-quality" EMC detector comprising a lead-scintillator stack and a forward PID based on a fast Cherenkov light time-of-flight system with multichannel plate PMT readout. Currently a final decision on the inclusion of these two devices has not been taken, but enough space has been reserved to make their installation possible.

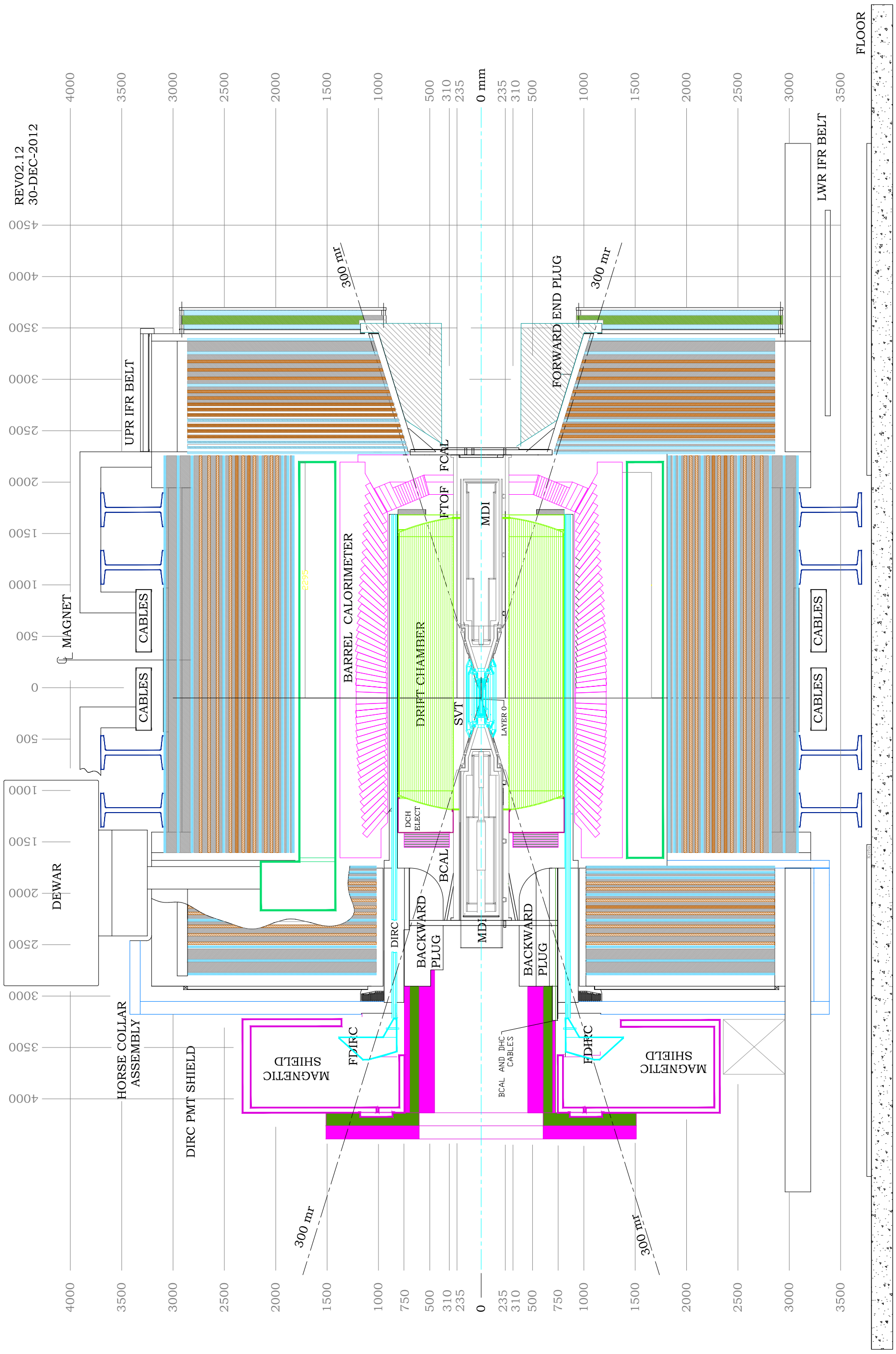

Figure 3.1: Concept for the Super$B$ detector. Space is reserved for the backwards calorimeter (BCAL) and the forward time-of-flight system (FTOF).

The Super$B$ detector concept is shown in Figure 3.1.

3.1 Physics Performance

The Super$B$ detector design, as described in the Conceptual Design Report [1], left open a number of issues that have a large impact on the overall detector geometry. These include the physics impact of a PID device in front of the forward EMC; the need for an EMC in the backward region; the position of the innermost layer of the SVT; the SVT internal geometry and the SVT-DCH transition radius; and the amount and distribution of absorber in the IFR.

These issues have been addressed by evaluating the performance of different detector configurations in reconstructing charged and neutral particles as well as the overall sensitivity of each configuration to a set of benchmark decay channels. To accomplish this task, a fast simulation code specifically developed for the Super$B$ detector has been used (see Section 14), combined with a complete set of analysis tools inherited, for the most part, from the *BABAR* experiment. GEANT4-based code has been used to simulate the primary sources of backgrounds—including both machine-induced and physics processes—in order to estimate the rates and occupancies of various sub-detectors as a function of position. The main results from these ongoing studies are summarized in this section.

Time-dependent measurements are an important part of the Super$B$ physics program. In order to achieve a Δt resolution comparable to that at *BABAR*, the reduced boost at Super$B$ must be compensated by improving the vertex resolution. This requires a thin beam pipe plus a SVT Layer0 that is placed as close as possible to the IP. The main factor limiting the minimum radius of Layer0 is the hit rate from $e^+e^- \to e^+e^-e^+e^-$ background events. Two candidate detector technologies with appropriate characteristics, especially in radiation length (X_0) and hit resolution, for application in Layer0 are (1) a hybrid pixel detector with 1.08% X_0 and 14 μm hit resolution, and (2) striplets with 0.40% X_0 and 8 μm hit resolution. Simulation studies of $B^0 \to \phi K^0_S$ decays have shown that with a boost of $\beta\gamma = 0.28$ the hybrid pixels (the striplets) reach a $\sin 2\beta_{\rm eff}$ per event error equal to *BABAR* at an inner radius of 1.5 cm (2.0 cm). With $\beta\gamma = 0.24$ the error increases by 7–8%. Similar conclusions also apply to $B^0 \to \pi^+\pi^-$ decays.

The *BABAR* SVT five-layer design was motivated both by the need for standalone tracking for low-p_T tracks as well as the need for redundancy in case several modules failed during operation. The default Super$B$ SVT design, consisting of a *BABAR*-like SVT detector and an additional Layer0, has been compared with two alternative configurations with a total of either five or four layers. These simulation studies, which used the decay $B \to D^*K$ as the benchmark channel, focused on the impact of the detector configuration on track quality as well as on the reconstruction efficiency for low p_T tracks. The studies have shown that, as expected, the low-p_T tracking efficiency is significantly decreased for configurations with reduced numbers of SVT layers, while the track quality is basically unaffected. Given the importance of low momentum tracking efficiency for the Super$B$ physics program, these results support a six-layer layout.

Studies have also shown that the best overall SVT+DCH tracking performance is achieved if the outer radius of the SVT is kept small (14 cm as in *BABAR* or even less) and the inner wall of the DCH is as close to the SVT as possible. However, as some space between the SVT and DCH is needed for the cryostats that contain the super-conducting magnets in the interaction region, the minimum DCH inner radius is expected to be about 27 cm.

The impact of a forward PID device is estimated using benchmark modes such as $B \to K^{(*)}\nu\bar{\nu}$, balancing the advantage of having better PID information in the forward region with the drawbacks arising from more material in front of the EMC and a slightly shorter DCH. Three detector configurations have been compared in these simulation studies: *BABAR*, the Super$B$ baseline (with no forward PID device), and a configuration that includes a time-of-flight (TOF) detector between the DCH and the forward EMC. The results, presented in terms of $S/\sqrt{S+B}$, for the decay mode $B \to K\nu\bar{\nu}$ with the tag side reconstructed in the semileptonic modes, are shown in Figure 3.2. In summary, while the default Super$B$ design leads to an improvement of about 7–8% in $S/\sqrt{S+B}$, primarily due the reduced boost in Super$B$, the configuration with the forward TOF provides an additional 5–6% improved sensitivity for this channel. Machine backgrounds have not been included in these simulations.

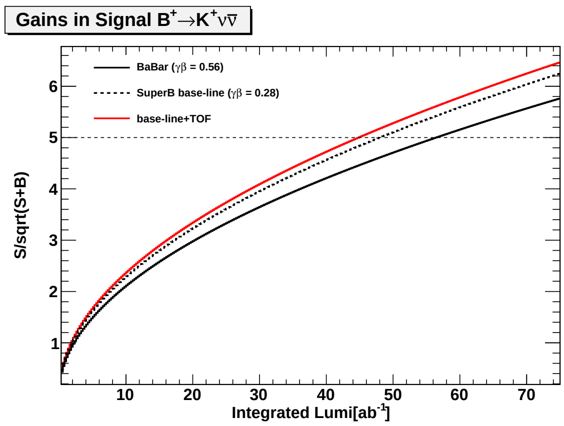

Figure 3.2: $S/\sqrt{S+B}$ of $B \to K\nu\bar{\nu}$ as a function of the integrated luminosity in three different detector configurations.

The backward calorimeter under consideration is designed to be used in veto mode. Its impact on physics can be estimated by studying the sensitivity of rare B decays with one or more neutrinos in the final state, which benefit from having more hermetic detection of neutrals to reduce the background contamination. One of the most important benchmark channels of this kind is $B \to \tau\nu$. Preliminary studies, not including the machine backgrounds, indicate that, when the backward calorimeter is installed, the statistical precision $S/\sqrt{S+B}$ is enhanced by about 8%. The results are summarized in Figure 3.3. The top plot shows how $S/\sqrt{S+B}$ changes as a function of the cut on $E_{\rm extra}$ (the total energy of charged and neutral particles that cannot be directly associated with the reconstructed daughters of the signal or tag B) with or without the backward EMC. The signal is peaked at zero. The bottom plot shows the ratio of $S/\sqrt{S+B}$ for detector configurations with and without a backward EMC, again as a function of the $E_{\rm extra}$ cut. This analysis did not include machine backgrounds, which could affect the $E_{\rm extra}$ distributions significantly. It is possible that the backward calorimeter could also be used as a PID time-of-flight device.

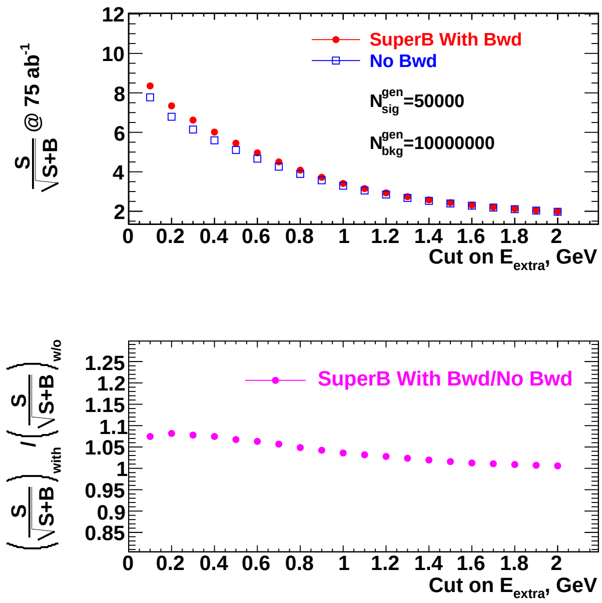

Figure 3.3: Top: $S/\sqrt{S+B}$ as a function of the cut on $E_{\rm extra}$ with (circles) and without (squares) the backward EMC. Bottom: ratio of $S/\sqrt{S+B}$ for detector configurations with or without a backward EMC as a function of the $E_{\rm extra}$ cut.

The presence of a forward PID or backward EMC affects the maximum extension of the DCH and therefore the tracking and dE/dx performance in those regions. The impact of a TOF PID detector is practically negligible because it only takes a few centimeters from the DCH. On the other hand, the effect of a forward RICH device (~ 20 cm DCH length reduction) or the backward EMC (~ 30 cm) is somewhat larger. For example, for tracks with polar angles $< 23°$ and $> 150°$, there is an increase in σ_p/p of 25% and 35%, respectively. Even in this case, however, the overall impact on the physics is generally quite limited because only a small fraction of tracks cross the extreme forward and backward regions.

The IFR system will be upgraded by replacing the *BABAR* RPCs and LSTs with layers of much faster extruded plastic scintillator coupled to WLS fibers read out by APDs operated in Geiger mode. The identification of muons and K_L^0 is optimized with a GEANT4 simulation by tuning the amount of iron absorber and the distribution of the active detector layers. The current baseline design has a total iron thickness of 92 cm interspersed with eight layers of scintillator. Preliminary estimates indicate a muon efficiency larger than 90% for $p > 1.5\,\mathrm{GeV}/c$ at a pion misidentification rate of about 2%.

3.2 Challenges on Detector Design

Machine background is one of the leading challenges of the Super*B* project: each subsystem must be designed so that its performance is minimally degraded because of the occupancy produced by background hits. Moreover, the detectors must be protected against deterioration arising from radiation damage. In effect, what is required is that each detector perform as well or better than *BABAR*, with similar operational lifetimes, but for two orders of magnitude higher luminosity. An extensive GEANT4-based background simulation effort has been undertaken to provide the parameters for detector and electronics design. The simulation takes into account both the overlap of background generated particles on physics events, with the consequent performance deterioration, and the overall ionizing and non-ionizing radiation levels (in particular neutrons) in the various locations of the detector.

Single beam backgrounds can be classified as follows:

- synchrotron radiation (SR) produced near the interaction region (IR). Although no bending is foreseen near the IR, the strong focusing required to obtain the high luminosity causes significant synchrotron radiation levels, which must be directed to absorber masks strategically located very close to the interaction point. Residual low energy photons, mainly generated in the backscattering of SR are absorbed by a coating of the beam pipe with high-Z material.
- beam-gas coulomb scattering and Touschek intra-beam scattering; these cause particle losses all around the rings, and require a careful collimator design to prevent these particles from reaching the interaction region or showering in the nearby machine elements.

Other very relevant backgrounds are related to the interaction of the primary particles and thus proportional to luminosity:

- radiative Bhabha scattering (*i.e.* $e^+e^- \to e^+e^-\gamma$) where one of the incoming beam particle looses a significant fraction of its energy by the emission of a photon. Both the photon and the radiating beam particles emerge from the IP traveling almost collinearly with respect to the beam-line. The magnetic elements downstream of the IP over-steer these primary particles into the vacuum chamber walls producing electromagnetic showers, whose final products are the background particles seen by the subsystems. The particles of these electromagnetic showers can also excite giant nuclear resonances in the material around the beam line expelling neutrons from the nucleus. Careful optimization of the mechanical apertures of the vacuum chambers and the optical elements is needed to keep a large stay-clear for the off-energy primary particles, hence reducing the background rate. The simulations indicate that a mechanically challenging 4.5 cm tungsten shield all around the machine elements near the IR is necessary to reduce this background source to an acceptable level.
- electron-positron pair production by the two photon process $e^+e^- \to e^+e^-e^+e^-$,

whose total cross section evaluated at leading order with the Monte Carlo generator DIAG36 [2] is 7.3 mb corresponding, at nominal luminosity, to a rate of 7.3 GHz. The pairs produced by this process are characterized by very soft transverse momenta particles which are for the most part confined inside the beam pipe by the 1.5 T solenoidal field. Those particles having a transverse momentum large enough to reach the beam pipe ($p_T > 2.5\,\mathrm{MeV}/c$) and with a polar angle inside the SVT Layer0 acceptance are expected to give a track rate of $2\,\mathrm{MHz/cm}^2$ at a radius of 1.5 cm, and are the driving element in the design of the segmentation and the read-out architecture for SVT Layer0.

- The elastic Bhabha process has also been considered. The cross section for producing a primary particle reconstructed by the detector via this process is $\sim$ 100 nb corresponding to a rate of about 100 kHz. This is expected to be the driving term for the level one trigger rate, which is nominally set at 150 kHz, more than an order of magnitude larger than in *BABAR*.

The Super*B* detector design poses therefore many challenges and requires some detector R&D to be finalized and optimized, although a baseline solution exists for all subsystems, as can been seen in Table 3.1, where the baseline solution, the main design challenges and required detector R&D are detailed for each subsystem.

3.3 Detector R&D

The basic geometry, structure and physics performance of the Super*B* detector is mainly predetermined by the retention of the solenoidal magnet, the return steel, and the support structure from the *BABAR* detector, and a number of its largest and most expensive subsystems. Even though this fixes both the basic geometry, and much of the physics performance, it does not really constrain the expected performance of the Super*B* detector in any important respect. *BABAR* was already an optimized *B*-factory detector for physics, and any improvements in performance that could come from changing the overall layout or rebuilding the large subsystems would be modest overall. The primary challenge for Super*B* is to retain physics performance similar to *BABAR* in the higher background environment while operating at much higher ($\sim \times 50$) data taking rates.

Subdetector envelopes have been defined for the most part, although some adjustements especially regarding the DCH length and inner radius might be necessary. The benefits of a backward EMC and forward PID have been evaluated and enough space has been left in the general layout to allow the installation of these devices, provided that enough resources can be found to build them. The TOF technology for the forward PID is particularly challenging and requires further R&D to arrive at a robust detector design. The inner radius of the DCH is determined by the dimensions of the cryostat for the final focus superconducting quadrupoles and of the tungsten shields.

The Super*B* detector concept rests, for the most part, on well-validated basic detector technology. Nonetheless, because of the high rates and demanding performance requirements, each of the sub-detectors has many challenges to tackle, with several R&D initiatives ongoing to improve the specific performance and optimize the overall detector design. These are described in more detail in each subsystem section.

3.3.1 Machine Detector Interface (MDI) and Backgrounds Simulation

The machine detector interface is a crucial element of both the accelerator and detector design. It contains the final focus, composed by several important magnetic elements: the focusing quadrupoles, the crab waist sextupoles, and the anti-solenoids compensating for the detector field. These elements are for the most part implemented with superconducting magnets contained in a single cryostat. Some permanent

Table 3.1: Baseline solution, main design challenges and required detector R&D for each subsystem

System	Baseline	Challenges and R&D
MDI	IR baseline designed	Magnetic elements and radiation masks. Design of tungsten shields. Cryostat radius. Background simulations: global map, detector occupancy.
SVT	6-layer silicon Striplets Layer 0	Technology for Layer 0: striplets or pixels. Thin pixels R&D. Readout chip for strips. Readout architecture. Mechanical design.
DCH	Stereo-axial He-based	Dimensions (inner radius, length). Mechanical structure. Cluster counting option.
PID	DIRC w/ FBLOCK	Focusing Block design. Photon detection. Mechanical structure. Forward PID: cost/benefit analysis. Prove TOF technology.
EMC	Barrel: CsI(Tl) Forw: LYSO+CsI(Tl)	Electronics and trigger. Mechanical structure. Transport and refurbishing. Crystal choice: LYSO, LYSO + CsI(Tl), pure CsI; photon detetector. Backward EMC: cost/benefit analysis.
IFR	Scintillator+ fibers	8 vs 9 layers. SiPM radiation damage and location. Extra 10 cm iron. Mechanical design and yoke reuse.
ETD	Synchronous const. latency	Fast link rad hardness. L1 Trigger (jitter and rate). ROM design. Link to computing for HLT.

magnets very close to the interaction point are also required.

The Interaction Region (IR) design is also crucial to keep backgrounds in the detector under control. The most notable elements in this respect are:

- the synchrotron radiation masks, carefully placed inside the primary vacuum to absorb radiation emitted during the steering and focusing of the beams

- the final focus quadrupoles (QD0), whose design has required a great deal of R&D. In fact, radiative Bhabha scattering will produce on-axis particles with reduced momentum that will be deviated by any residual dipole field component on the nominal trajectory. This implies that QD0 cannot be shared by the two beams, and complex twin quad design had to be developed with a distance of only a few cm between the two beam axes.

- the tungsten radiation shields absorb the showers produced by the particles that even in a careful QD0 design do get deviated out of the beam pipe in the vicinity of the IR. Simulation studies indicate that a 4.5 cm thick shield is adequate. The mechanical design of the support system for the shields and of the assembly system for the entire IR (including the SVT) is extremely challenging.

A cross section of the IR, including the tungsten shields, the cryostat, and the SVT is shown in Figure 3.4.

Backgrounds simulation is essential to provide guidance for both the machine and detector design. A GEANT4-based background simulation framework has been developed that can provide input to detector performance studies, provide radiation maps throughout the detector and experimental hall, as well as background frames to be superimposed to physics events for physics studies. Validation of these simulation results is very difficult, and has been realized through a combination of extrapolation from *BABAR* information, comparison with lower energy DaΦne running, and comparison with analogous simulations performed by the Belle-II collaboration [3]. In addition, some of the backgrounds critically depend on the placement accuracy of machine elements that might not be at their nominal position in reality. To account for all these uncertainties we require the detector to operate with a $\times 5$ safety factor over the simulated nominal background level.

3.3.2 Silicon Vertex Tracker (SVT)

The SVT baseline design is based on double-sided silicon microstrip detectors for all layers. The current Layer0 baseline configuration for the beginning of data taking is based on the double-sided silicon striplets technology, which is mature and has been shown to provide good physics performance thanks to the low material budget associated (*i.e.* no readout electronics in the active area). However, an upgrade to pixel sensors, hybrid pixels or thinner CMOS Monolithic Active Pixel Sensor (MAPS), more robust against background occupancy, is planned for the full luminosity run. Specific R&D programs are ongoing in order to meet the Layer0 requirements, which include low pitch and material budget, high readout speed and radiation hardness. If successful, this will allow the replacement of the Layer0 striplet modules in a second phase of the experiment. For this purpose, the Super*B* interaction region and the SVT mechanics will be designed to ensure a rapid access to the detector to ease a replacement of the Layer0.

The expected $2\,\mathrm{MHz/cm^2}$ track rate at 1.5 cm translates into a much larger hit rate once the hit multiplicity, loopers, and safety factor are taken into account, setting a requirement of $100\,\mathrm{MHz/cm^2}$ hit rate with a required module readout bandwidth of 5 Gbit/s. Material budget is the other essential element of the Layer0 design, with a requirement of about $0.5\%\,\mathrm{X_0}$.

The hybrid pixels technology represents a mature and viable solution but reduction in the front-end pitch and in the total material budget with respect to pixel systems developed for LHC experiments is required to meet the Layer0 requirements. The spatial resolution constraints of 10–15 μm set a limit to the area of the elementary readout cell and, as a consequence, to the amount of functionalities that can be included in the front-end electronics. For a $50\times50\,\mu\mathrm{m}^2$ pixel cell a planar 130 nm CMOS technology may guarantee the required density to implement in-pixel data sparsification and fast time stamping ($< 1\,\mu$s), meeting the Layer0 requirements.

Denser CMOS technologies (90 or 65 nm technology) can be used to increase the functional density in the readout electronics and include such functions as gain calibration, local threshold adjustment and amplitude measurement and storage. In this case, costs for R&D (and, eventually, production) would increase significantly.

Vertical integration (or 3D) CMOS technologies may represent a lower cost alternative to sub-100 nm CMOS processes to increase the functional density in the pixel cell [4, 5].

CMOS MAPS are very appealing for applications where the material budget is critical since in this technology the sensor and readout electronics share the same substrate that can be thinned down to several tens of microns. As the readout speed is another crucial aspect for application in Layer0 a new Deep NWell MAPS design approach has been developed in the last few years. This allowed for the first time the implementation of thin CMOS sensors with similar functionalities as in hybrid pixels, such as pixel-level sparsification and fast time stamping [6]. A limiting factor of this technology, though, is the presence of competitive N-Wells inside the pixel cell, that can subtract charge from the main collecting electrode leading to an efficiency of the

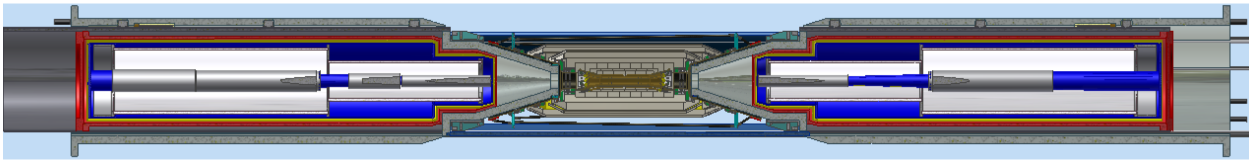

Figure 3.4: Cross section of the interaction region and machine-detector interface area.

order of 90%. A significant degradation of the charge collected (about 50%) has also been measured after neutron irradiation of 7×10^{12} n/cm^2, corresponding to about 1.5 years of operation in the Layer0 [7].

Further MAPS performance improvements are currently under investigation with two different approaches: the use of INMAPS CMOS process, featuring a quadruple well and a high resistivity substrate, and 3D CMOS MAPS, realized with vertical integration technology.

In order to increase the charge collection efficiency, the INMAPS 180 nm CMOS process is being explored: a deep P-well implant, deposited beneath the competitive N-Wells, can prevent them from stealing charge from the main collecting electrode. Moreover, the use of a high resistivity substrate, also available in this process, can further improve charge collection and radiation resistance with respect to standard CMOS devices.

The realization of 3D MAPS, using two CMOS layers interconnected with vertical integration technology, also offers several advantages with respect to standard 2D MAPS. In these devices, one CMOS tier is hosting the sensor with the analog front-end and the second tier is dedicated to the in-pixel digital front-end and the peripheral readout logic. With this splitting of functionalities the collection efficiency can be improved, significantly reducing the N-Well competitive area in the sensor layer, allowing the implementation of a more performant readout architecture, and minimizing the cross-talk between analog and digital blocks.

To keep material at a minimum it is essential to also develop low mass cooling systems as well as low mass cables and data transmission systems. A vigorous R&D program on single- and double-phase microchannel cooling is ongoing, with the final goal of integrating the microchannels directly on the silicon substrate, thus significantly reducing the extra material needed.

3.3.3 Drift Chamber (DCH)

In the DCH, many parameters must be optimized for Super$B$ running, such as the gas mixture and the cell layout. Precision measurements of fundamental gas parameters are ongoing, as well as studies with small cell chamber prototypes and simulation of the properties of different gas mixtures and cell layouts.

An improvement of the performance of the DCH could be obtained by using the innovative "Cluster Counting" method. Signals in drift chambers are usually split to an analog chain that integrates the charge and a digital chain that records the arrival time of the first electron, discriminated with a given threshold. The cluster counting technique consists instead in digitizing the full waveform to count and measure the time of all individual peaks. On the assumption that these peaks can be associated to the primary ionization acts along the track, the energy loss and to some extent the spatial coordinate measurements can be substantially improved. In counting the individual cluster, one indeed removes the sensitivity of the specific energy loss measurement to fluctuations in the amplification gain and in the number of electrons produced in each cluster, fluctuations which significantly limit the intrinsic resolution of conventional dE/dx measurements.

The ability to count the individual ionization clusters and measure their drift times strongly depends on the average time separation between them, which is, in general, relatively large in He-based gas mixtures thanks to their low primary yield and slow drift velocity. Other requirements for efficient cluster conting include good signal-to noise ratio but no or limited gas-gain saturation, high preamplifier bandwidth, and digitization of the signal with a sampling speed of the order of 1 Gs/sec. Finally, it is necessary to extract online the relevant signal features (*i.e.* the cluster times), because the DAQ system of the experiment would hardly be able to manage the enormous amount of data from the digitized waveforms of the about 10,000 drift chamber channels.

In order to optimize the gas mixture for the Super$B$ environment, and to assess both the feasibility and the operational improvements for the cluster counting technique an R&D program has been ongoing. The program includes both beam tests and cosmic ray stands to monitor performances of *ad hoc* built prototypes. While the $\mathrm{d}E/\mathrm{d}x$ resolution gain of the cluster counting method is in principle quite sizeable compared to the traditional total charge collection, the actual capability of the measured number of clusters might not retain the same analyzing power, due to a plethora of experimental effects that should be studied in detail so that the energy loss measurement derating should be assessed and, if possible, cured. Although this technique requires significant R&D, the cable plant is being designed to allow the upgrade of preamplifiers and readout system if cluster counting is proven feasible in the experiment.

3.3.4 Particle Identification (PID)

The DIRC (Detector of Internally Reflected Cherenkov light) is an example of innovative detector technology that has been crucial to the performance of the *BABAR* science program. The DIRC main performance parameters are the following: (a) a measured time resolution per photon of $\sim$1.7 ns, close to the photomultiplier (PMT) transit time spread of 1.5 ns, (b) a single photon Cherenkov angle resolution of 9.6 mrad for tracks from di-muon events, (c) a Cherenkov angle resolution per track of 2.5 mrad in di-muon events, and (d) a π/K separation greater than 2.5σ over the entire track momentum range, from the pion Cherenkov threshold up to 4.2 GeV/c.

A new Cherenkov ring imaging detector is being planned for the Super$B$ barrel, called the Focusing DIRC, or FDIRC. It will reuse the existing *BABAR* bar boxes and mechanical support structure. This structure will be attached to a new photon "camera", which will be optically coupled to the bar box exit window. The new camera design combines a small modular focusing structure that images the photons onto a focal plane instrumented with very fast, highly pixelated, photon detectors (MaPMTs) [8]. The readout electronics will be completely redesigned, bringing the time accuracy of the full readout chain to $200-250$ ps, which helps reduce the background and allows a correction for chromatic aberrations. These elements should combine to attain the same PID performance as the *BABAR* DIRC while being at least 100 times less sensitive to backgrounds.

Two FDIRC prototypes have been built. The first prototype, which used a spherical mirror design not suitable for Super$B$, was tested on a beam and with cosmic rays, giving the proof of principle of the FDIRC concept. The second is a full-scale prototype of a Super$B$ FDIRC sector. Being able to purchase parts matching the specifications and to build it is already a great achievement. The test of this final prototype will validate the detector and electronics design. Parallel to this effort, there are many detailed studies of the MaPMT ongoing in all major institutions involved in the FDIRC, addressing issues such as the the timing resolution and pixel cross-talk. The results of this complex R&D program will allow the finalization of the design of this novel and performant device.

The possibility of increasing the hermeticity of the detector by including a PID device in the forward area has been considered. The physics gain from such a device is about 4–5%, which is considered significant enough, provided that the device is sufficiently performant and does not degrade the performance of the rest of the apparatus. Different technologies have been examined: a Focusing Aerogel RICH, a scintillating detector coupled to SiPMT arrays, and a DIRC-like time of flight detector based on fused silica and MCP-PMT (FTOF). Given the space constraints and the performance requirements the FTOF is the chosen technology.

The FTOF [9, 10] belongs to the family of the DIRC detectors. Charged particles crossing a thin layer of fused silica emit Cherenkov light along their trajectories, provided that their momentum is high enough. A fraction of these photons are trapped by total internal reflection and propagate inside the quartz until an array of Multi-Channel Plate Photomultipliers (MCP-PMT), where they are detected. Unlike the (F)DIRC, no attempt is made to reconstruct Cherenkov angles: K/π separation is provided by time-of-flight. Given the short flight distance between the IP and the FTOF (about 2 meters, hence a 90 ps difference for 3 GeV/c particles), the whole detector chain must make measurements accurate at the 30 ps level or better. This is one of the main challenges of this design, the others being the photon yield, the sensitivity to the background (including ageing effects due to the charge integrated over time by the photon detectors) and the event reconstruction. Regarding the latter point, one should emphasize that the FTOF is a two-dimensional device: the PID separation uses both the timing and spatial distributions of the photons detected in the MCP-PMT arrays. A first prototype was built and tested with cosmic rays, giving an initial proof of principle of the method, but R&D is ongoing to build a full scale prototype and to study various design options and their performance in magnetic field, as well as their robustness against background and radiation damage.

3.3.5 Electromagnetic Calorimeter (EMC)

The Super$B$ EMC reuses the barrel part of the *BABAR* EMC detector consisting of 5760 CsI(Tl) crystals readout by PIN-diodes. The increased event and background rate requires a replacement of the readout electronics and a careful assessment of the effect of radiation damage on the *BABAR* crystals. In addition, there are several important technical issues related to the EMC barrel transportation and refurbishing.

On the other hand, the *BABAR* forward calorimeter will need to be partially replaced, due to the higher radiation and higher rates at Super$B$ compared with PEP-II. At least the innermost rings of the forward endcap will have to be replaced by new scintillating crystals, designed to work well in this new environment. After an intensive R&D program the baseline option for the inner rings of the forward EMC is to use the faster and more radiation resistant Ce-doped LYSO crystals readout by avalanche photo diodes (APD). This is the best choice in terms of performance and radiation hardness over the alternatives we have considered because of the faster response time and shorter Molière radius that address the higher event and background rates. LYSO is a fast scintillator largely used in medical applications with crystals of small size. The R&D was concentrated on the optimization of performance for large crystals (2 cm × 2 cm × 20 cm) with good light yield uniformity and optimized Ce doping, in order to have the best possible light output. Thanks to this effort, more than one producer is able to grow LYSO crystals of good quality that can be used in high energy physics applications. The high cost of LYSO has prompted the collaboration to examine other lower cost options, such as BGO and pure CsI. The latter is particularly attractive for its very fast response (30 ns compared to 40 ns of LYSO), while at the same time posing significant readout problems with a light yield a factor 20 less than LYSO and a factor 45 less than CsI(Tl). A vigorous R&D program has started to examine photo-pentodes and large area APDs as readout options for pure CsI. Neither solution at this time guarantees the required performance, and additional studies are needed. R&D is also needed to verify the radiation hardness of pure CsI.

A lead-scintillator-sandwich backward endcap calorimeter readout with SiPM/MPPC improves the hermeticity of the detector. The main purpose of this component is to detect energy in the backward endcap region, as a veto of events with “extra” energy. This is particularly important for studying channels with neutrinos in the final state. Because of the fast time response, the backward EMC may also have a role in particle identification by providing time-of-flight for the relatively slow backward-going charged particles.

3.3.6 Instrumented Flux Return (IFR)

The Instrumented Flux Return (IFR) is designed primarily to identify muons, and, in conjunction with the electromagnetic calorimeter, to identify neutral hadrons, such as K_L^0. The iron yoke of the detector magnet, providing the large amount of material needed to absorb hadrons, is segmented in depth, with large area extruded scintillator bars readout with Silicon Photo Multipliers.

The detector consists of a central part, the barrel, and of two endcaps, to cover the forward and backward regions. Both the barrel and the two endcaps, are made of $\sim 92\,\mathrm{cm}$ of iron interleaved by 9 layers of segmented scintillator planes (with a thickness of 2 cm). The use of plastic scintillator as active material ensures fast response, reliability, robustness and long term stability while the high granularity guarantees a good space resolution, very important to cope with the expected high particle flux. Each active plane provides both coordinates simultaneously, since it is made of two layers of orthogonal scintillator bars: the longitudinal bars are 5 cm wide while the transversal bars are 10 cm wide. The scintillation light is collected by three Wave Length Shifting fibers (Kuraray Y11, 1.2 mm), housed in surface grooves machined on each bar, and guided to the SiPM placed at one end of each bar.

The general layout outlined above is the result of extensive R&D studies, which concerned all the active parts of the detector. We compared fibers from different producers (Saint-Gobain and Kuraray) and with different diameters (1.0 mm and 1.2 mm), and we studied the optimal number of fibers to collect light from each scintillator bar. On the photodetectors side, we are still comparing the performance of devices from various producers (FBK-Advansid, Hamamatsu, SensL), with different pixel size (e.g. 25×25, 50×50, and $100\times100\,\mu\mathrm{m}^2$). A final decision has not been taken yet, as the performances of these recently developed devices are improving very rapidly, and more R&D studies are needed.

The performances of the detector have been studied through a full scale prototype, i.e. a prototype with the same iron-scintillator structure of the detector. It has been tested at the Fermilab Test Beam Facility, where muons and pions of energy in the range of interest for Super$B$ are available.

Given the very high luminosity and, as a consequence, the high level of background radiation, one of the most critical issues is to understand the radiation damage of all the sensitive detector components. For semiconductor devices like SiPMs and front end electronics, it is of particular importance the effect of neutrons, which are known to produce an increase in the dark count and a possible malfunctioning of FPGAs. A R&D program is ongoing to characterize devices from different vendors as well as to identify mitigation strategies, both in the SiPM design, and in their location and shielding.

3.3.7 Electronics, Trigger, and DAQ (ETD)

The Super$B$ Electronics, Trigger, Data acquisition and Online system (ETD) comprises the Level-1 trigger, the event data chain and their support systems. Event data corresponding to accepted Level-1 triggers move from the Front-End Electronics (FEE) through the Read-Out Modules (ROMs), the network event builder and the High Level Trigger (HLT) to a data logging buffer where they are handed over to the offline for archival and further processing. ETD also includes the hardware and software components that control and monitor the detector and data acquisition systems and perform near-real-time data quality monitoring and online calibration.

At present, the Electronics, DAQ, and Trigger (ETD), have been designed for the base luminosity of $1 \times 10^{36}\,\mathrm{cm}^{-2}\,\mathrm{s}^{-1}$, with adequate headroom. Further R&D is needed to understand the requirements at a luminosity up to 4 times greater, and to insure that there is a smooth upgrade path when the present design becomes inadequate. In particular, radiation levels in various areas of the detector are driving elements of many of the technical choices.

Data Links are the most subject to radiation and require R&D to qualify components and understand the possibility of using new generation FPGAs. A strong connection with LHC technology development is in place.

For the L1 trigger, the achievable minimum latency and physics performance will need to be studied. The studies require to address many factors including (1) improved time resolution and trigger-level granularity of the EMC and a faster DCH; (2) potential inclusion of SVT information at L1; (3) the possibility of a L1 Bhabha veto; (4) possibilities for handling pile-up and overlapping (spatially and temporally) events at L1; and (5) opportunities created by modern FPGAs to improve the trigger algorithms.

The main R&D topics for the Event Builder and HLT Farm are (1) the applicability of existing tools and frameworks for constructing the event builder; (2) the HLT farm framework; and (3), event building protocols and how they map onto the network hardware.

To provide the most efficient use of resources, it is important to investigate how much of the software infrastructure, frameworks and code implementation can be shared with Offline computing. This requires us to determine the level of reliability-engineering required in such a shared approach. We also must develop frameworks to take advantage of multi-core CPUs.

3.4 Bibliography

[1] M. Bona et al., (Super*B* Collaboration collaboration), "Super*B*: A High-Luminosity Asymmetric e^+e^- Super Flavor Factory. Conceptual Design Report", 2007, arXiv:0709.0451 [hep-ex].

[2] F. A. Berends, P. Daverveldt, and R. Kleiss, "Monte Carlo Simulation of Two Photon Processes. 2. Complete Lowest Order Calculations for Four Lepton Production Processes in electron Positron Collisions", *Comput.Phys.Commun.* 40:285–307, 1986, doi:10.1016/0010-4655(86)90115-3.

[3] "Joint Belle II & Super*B* Background Meeting", Vienna, February 9-10, 2012", 2012, http://background.hephy.at/.

[4] R. Yarema, D. Christian, M. Demarteau, G. Deptuch, J. Hoff, et al., "3D IC pixel electronics—the next challenge", *TWEPP08*, pp. 183-187, 2008, http://www.ntua.gr/twepp08/.

[5] "VIPIX Collaboration—Vertically Integrated PIXels", http://eil.unipv.it/vipix/.

[6] A. Gabrielli, F. Giorgi, F. Morsani, G. Rizzo, and M. Villa, "High efficiency readout circuits for large matrices of pixels", *Nucl. Instrum. Meth.* A658:141–144, 2011, doi:10.1016/j.nima.2011.04.048.

[7] L. Ratti et al., "Front-End Performance and Charge Collection Properties of Heavily Irradiated DNW MAPS", *IEEE Trans. Nucl. Sci.* NS-57(4):1781, 2010, doi:10.1109/RADECS.2009.5994549.

[8] J. Vavra, "PID techniques: Alternatives to RICH Methods", *Nucl. Instrum. Meth.* A639:193–201, 2011, doi:10.1016/j.nima.2010.09.062.

[9] J. Vavra, "Super*B* Workshop, Perugia, June 2009", 2009, http://agenda.infn.it/conferenceDisplay.py?confId=1161.

[10] J. Vavra, "Super*B* Workshop, SLAC, October 2009", 2009, http://agenda.infn.it/conferenceDisplay.py?confId=1742.

4 Physics with Super$B$

4.1 Introduction

The Super$B$ project consists of an e^+e^- collider with a general purpose detector dedicated to the study of precision flavor physics. This will be built at the Cabibbo Laboratory to commence taking data later this decade. Super$B$ is designed to accumulate: $75\,\text{ab}^{-1}$ of data at the $\Upsilon(4S)$, more than 100 times the BABAR data sample; $1000\,\text{fb}^{-1}$ at the $\psi(3770)$, 100 times the expected data sample from BES III; and several ab^{-1} at the $\Upsilon(5S)$, 15 times the data sample accumulated by Belle; as well as running at other center of mass energies. Using these data one will be able to search for New Physics (NP) and test the Standard Model (SM) in a multitude of ways.

This document is divided into summaries of the heavy quark flavour physics programme, i.e. $B_{u,d,s}$ and D decays (section 4.2), τ physics (section 4.3), precision electroweak physics (section 4.4), exotic spectroscopy (section 4.5), and direct searches (section 4.6). Finally section 4.7 gives a broad overview of the physics programme and how this fits into the context of furthering our understanding of nature at a fundamental level. The ensemble of precision measurements, studies of rare decays, CP and other symmetry violating observables all play a role in the process of trying to elucidate the nature of physics beyond the Standard Model. These are augmented by searches for processes forbidden within the SM, such as charged lepton flavour violation, Dark Matter, and Dark Forces. More detailed discussions of the Super$B$ project and physics programme can be found in Refs. [1, 2, 3, 4, 5, 6].

The recent discovery of a Higgs-like particle by ATLAS and CMS (presumed here to be the spin-zero SM Higgs particle) heralds a new era in particle physics. There are two ramifications of this discovery that relate to the Super$B$ physics programme, the first is that the SM Higgs is related to a number of flavour processes that will be studied at Super$B$, and so now that we know this particle exists, and have started to learn about its properties — we are compelled to check how this fits in with our understanding of the electroweak sector. The second ramification is that many scenarios of physics beyond the SM predict other Higgs particles, so while this discovery is profound, it is not the final missing piece of the puzzle required to explain the subatomic world. Some of these additional Higgs particles may be hard to study directly at the energy frontier, and Super$B$ is in a position to test such theories to constrain the presence of light ($< 10\,\text{GeV}/c^2$) Higgs particles and charged Higgs particles that may be present in nature.

The measurements relating to the SM Higgs particle that are of particular interest to this programme are determinations of $\sin^2\theta_W$, which at the center of mass energy corresponding to the $\Upsilon(4S)$ is devoid of hadronisation uncertainties that affect interpretation of the LEP/SLC measurements at the Z^0 pole in the $e^+e^- \to b\bar{b}$ transition. The weak angle can be measured for e^+e^-, $\mu^+\mu^-$, $c\bar{c}$ and $b\bar{b}$ final states at Super$B$. The interest in $\sin^2\theta_W$ is in inverting precision electroweak fits that have been used to infer the Higgs mass since the LEP-days to use the now-known mass to predict the weak angle as a function of $\sqrt{s}$. Hence one can test the running of the weak mixing angle. Looking at the measurements made at the Z^0 pole, it is the $e^+e^- \to b\bar{b}$ measurement that is furthest from expectation (and also has a limiting hadronisation uncertainty). A similar physics potential, albeit with larger uncertainty and not using the $b\bar{b}$ mode, exists for a run at the $\psi(3770)$ with a polarized electron beam. In terms of constraining charged Higgs particles, Super$B$ can study rare tree decays such as $B \to (D^{(*)})\tau\nu$, which are mediated by a W boson. Beyond the SM these decays could have additional contributions arising from the charged Higgs sector. Similarly *CP* violation can be introduced into τ decays via the presence of a charged Higgs, and could alter the expected asymmetry in decay modes such as $\tau \to K^0_S\pi\nu$. Loop-mediated Higgs transitions can also be detected using final states such as $b \to s\gamma$. Hence comparison of the decay rates and *CP* asymmetries measured in data, with those expected in the SM can be used to constrain m_{H+} as a function of the parameters of a given NP model. Many rare decay constraints on NP have direct parallels between B and Charm decays, and so larger samples of $D_{(s)}$ mesons accumulated at the $\psi(3770)$ and the $\Upsilon(4S)$ provide alternate ways to test the SM.

For example if one considers a type-II two-Higgs doublet model (2HDM), the decay $b \to s\gamma$ already excludes m_{H+} below about 300 GeV/c^2 for all values of the Higgs vacuum expectation value ($\tan\beta$), $B \to \tau\nu$ excludes masses below ~ 1 TeV/c^2 for large $\tan\beta$, and the combination of $B \to \tau\nu$, $B \to D\tau\nu$ and $B \to D^*\tau\nu$ disfavor the type II 2HDM model for any value of $\tan\beta$. Just as with this example, the combination of measurements of rare decays at Super$B$ will play a role in elucidating the charge partners of the SM Higgs. The results of these searches are expected to be available before the high luminosity running of the SLHC commences early next decade, and could shed light on the SM Higgs sector and beyond.

4.2 B and D decays

4.2.1 Rare B decays

Rare B decays provide an excellent opportunity to search for NP at a flavour factory. Processes highly suppressed in the SM, such as Flavour Changing Neutral Currents (FCNCs), could receive large NP contributions, often resulting in measurable deviations in the branching fractions and other observables.

The Super$B$ detector is designed to be well equipped to study a wide variety of rare B meson decays. Excellent reconstruction of charged and neutral particles, with very good particle identification and virtually fully efficient triggering for $B\overline{B}$ events, allow the study of complex decay chains that involve several charged and neutral particles. In addition, decay modes with missing neutrinos can be studied effectively by employing *hadronic* or *semileptonic tagging* techniques. This approach, which has been used very successfully at the current B Factories, entails fully reconstructing one of the two B meson decays in the event, thus assigning the remaining particles (including missing particles) to the signal decay under study. This powerful technique is used to identify decays with missing neutrinos. We discuss selected rare B decays in the following paragraphs, most of which can only be studied in an e^+e^- environment. These are important parts of the Super$B$ physics programme.

The decay mode $B^+ \to \tau^+\nu_\tau$ is sensitive to NP scenarios that include a charged Higgs boson, such as SUSY and two-Higgs doublet models. Currently, the branching fraction for this decay measured at *BABAR* and Belle, while current compatible with SM expectations, has at times been in tension with the SM value obtained from global fits to CKM quantities [7, 8]. The lower bound on the branching fraction provides the most stringent constraint on a charged Higgs (corresponding to the SM $W^\pm$ and non-SM $H^\pm$ amplitudes destructively interfering). In fact, the technique of hadronic or semileptonic tagging, where the non-signal B meson in the event is fully reconstructed, allows the search on the signal side of a single charged track and missing energy. With this method, Super$B$ will measure $\mathcal{B}(B^+ \to \tau^+\nu_\tau)$ with a precision of approximately 3%. The related channel $B^+ \to \mu^+\nu_\mu$, will be measured to about 5% at Super$B$, and will increase the overall sensitivity to the presence of charged Higgs bosons. Belle have recently updated their $B^+ \to \tau^+\nu_\tau$ measurement and obtain a result compatible with the SM [9], however the corresponding *BABAR* update remains in tension with the SM [10], prompting the need for further experimental investigation. Figure 4.1 shows the constraint on the charged Higgs mass vs $\tan\beta$ plane that would be obtained from a Super$B$ measurement of $B \to \tau\nu$ and $B \to \mu\nu$ consistent with the SM. A similar constraint would be obtained in the MSSM.

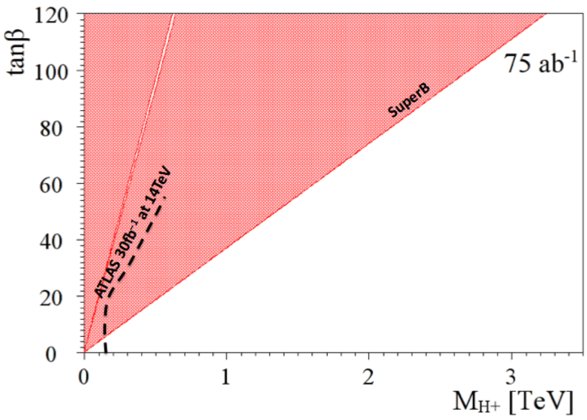

Figure 4.1: The constraint on the mass of a charged Higgs boson as a function of $\tan\beta$ in a 2HDM-II (95% C.L.). The constraint anticipated from the LHC with $30\,\mathrm{fb}^{-1}$ of data collected at a center of mass energy of 14 TeV is also shown for comparison. The Super$B$ constraint is dominated by $B \to \tau\nu$ up to luminosities $\sim 30\,\mathrm{ab}^{-1}$, and the $B \to \mu\nu$ contribution dominates above this. The ATLAS constraint is taken from arXiv:0901.0512.

Semileptonic B decays with a τ lepton in the final state are sensitive to NP effects, in particular those arising from the presence of a charged Higgs boson. The *BABAR* experiment recently reported an excess of $B \to D^{(*)}\tau\nu$ decays with respect to SM expectations, with a combined statistical significance of 3.4σ [11]. Interestingly, the results seem to exclude the simplest NP model with a charged Higgs, the Type II Two Higgs Doublet Model. More precise measurements of these channels are needed to determine if the discrepancy is more than a statistical fluctuation. The large data sample of Super$B$ will lead to greatly reduced uncertainties on these branching fractions and the determination of the q^2-dependence of the decay rate, an important measurement for unraveling the nature of possible NP effects.

The decays $B \to K^{(*)}\nu\overline{\nu}$ are interesting probes of NP, since they allow one to study Z penguin and other electroweak penguin effects in the absence of other operators that can dominate in $b \to s\ell^+\ell^-$ decays. Here again hadronic and semileptonic tagging will be used to isolate the non-signal B meson in the event. The signal signature then becomes a single kaon (or K^*) candidate accompanied by a momentum imbalance, and nothing else. Super$B$ will maximize sensitivity to NP by independently measuring the $B \to K\nu\overline{\nu}$ and $B \to K^*\nu\overline{\nu}$ branching fractions, along with F_L, the K^* longitudinal polarization fraction. Furthermore, it may be possible to measure the fully inclusive mode $B \to X_s\nu\overline{\nu}$ at Super$B$, increasing the sensitivity to NP effects in Z penguin processes. The expected constraints on the model-independent NP parameters ε and η introduced in [12] are shown in Figure 4.2.

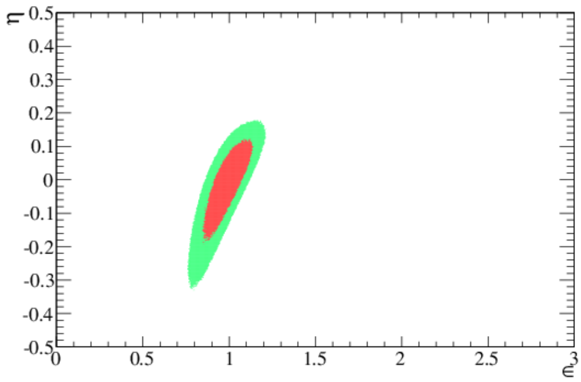

Figure 4.2: Expected constraints on the model-independent parameters ε and η describing NP contributions to $B \to K^{(*)}\nu\overline{\nu}$ [12] from Super$B$ measurements.

One fruitful area to look for NP is in $b \to s\ell^+\ell^-$ transitions, which occur in the SM via electroweak penguin loops and box diagrams. This transition represents a rather broad field of study since it comprises several different exclusive decays of charged and neutral B mesons, along with the fully inclusive channel, usually denoted $B \to X_s \ell^+\ell^-$. Super$B$ is expected to accumulate $10-15K$ events in each of the exclusive channels, including final states with an e^+e^- pair. The ratio $R_\mu^{(*)} = B(B \to K^{(*)}\mu^+\mu^-)/B(B \to K^{(*)}e^+e^-)$, an important observable sensitive to neutral Higgs particles in SUSY models, will only be measured precisely at future Super Flavour Factories. The event sample accumulated at Super$B$ will complement the current studies being performed on $B^0 \to K^{*0}\mu^+\mu^-$ at LHC [13]. Additionally, Super$B$ can make precise measurements of rates, asymmetries and angular distributions of the inclusive channel $B \to X_s\ell^+\ell^-$, exploiting the possibility of performing hadronic and semileptonic tagging in the e^+e^- environment. The inclusive channel is of interest because theoretical calculations of inclusive observables generally have lower uncertainties compared to the corresponding exclusive channels.

The study of $b \to s\gamma$ transitions has been one of the cornerstones of the B physics programmes at *BABAR* and Belle. The combination of precise measurements of the inclusive branching fraction along with its precise SM calculation, both at the level of about 7%, leads to strong constraints on Flavour Changing Neutral Currents in NP models. Super$B$ can measure this branching fraction to a precision of about 3%, increasing the constraints imposed by this transition. There is no consensus whether the theoretical uncertainty could match this precision or not. Additionally, the high statistics of the Super$B$ data sample will permit the measurement of the Cabibbo-suppressed $B \to X_d\gamma$ channel to good precision.

4.2.2 Rare D decays

For a long time the HEP community has worked on $K \to \pi\nu\overline{\nu}$ transitions and plans new projects to study this mode in greater detail. Here SM dynamics are greatly suppressed, and one can deal with the impact of long distance (LD) dynamics by using correlations with semileptonic decays. This situation is different for $D \to X_u\nu\overline{\nu}$: short distance dynamics are truly tiny with $\mathrm{BR_{SD}}(D \to X_u\nu\overline{\nu}) \sim O(10^{-15})$, and impact of LD contributions on inclusive final states is negligible in the SM. This rare charm decay mode is a good place to look for signs of NP which could enhance the branching fraction by many orders of magnitude above the SM expectation. For general models of NP like Little Higgs with T parity (LHT) or non-minimal charged Higgs models, one can have enhancements up to 10^4. More exotic models can lead to larger enhancements. This decay can be studied using fully reconstructed hadronically tagged D events at the $\psi(3770)$. Other advantages of studying rare charm decays at Super$B$ include final states with π, η, η' and 2π which can contribute around 10–20% for the inclusive width. This is sufficient to probe enhancements from NP. Direct and indirect *CP* violation can be compared using $D^\pm \to \pi^\pm\nu\overline{\nu}$ and $D^0/\overline{D}^0 \to \pi^0\nu\overline{\nu}$. At the $\psi(3770)$ one can use quantum correlations between $D\overline{D}$ pairs, e.g. at threshold one can analyze $D_L \to (\pi^0,\eta,\eta')\nu\overline{\nu}$ due to correlation with $D \to K^+K^-/\pi^+\pi^-$ to probe direct vs indirect *CP* violation in the case of large NP manifestations.

Another rare decay D that can be used to obtain an insight into physics beyond the SM is $D \to \gamma\gamma$. This channel is dominated by long distance transitions, however it is possible that NP could enhance the rate well above the SM expectation of a few $\times 10^{-8}$. Super$B$ is expected to be able to achieve a sensitivity that will enable a rudimentary measurement of this mode at the SM rate. If NP is not manifest, then this rate will provide a stringent constraint on the LD contribution to the decay $D \to \mu^+\mu^-$, which itself is a mode very sensitive to NP. The $D \to \mu^+\mu^-$ amplitude is dominated by the LD component, and so in order to interpret if any measured rate is compatible with the SM or not, one has to have a good understanding of $D \to \gamma\gamma$.

It is also possible to probe NP using the set of decays $D \to h\ell^+\ell^-$, where $h = \pi, \rho$. Even though the total rate is dominated by LD contributions, the shape of the q^2 distribution of the di-lepton pair is sensitive to NP, and in particular one may be able to learn about the underlying dynamics of these final states by comparing resonant to off-resonant features within the dilepton system.

Finally one can search for light dark matter particles by studying D decays to invisible, or invisible $+\gamma$ final states. Measurements made at the $\psi(3770)$ can complement the corresponding studies of rare $B_{d,s}$ mesons performed at the $\Upsilon(4S)$ and $\Upsilon(5S)$.

4.2.3 CKM matrix and unitarity triangle

Broadly speaking improved determinations of CKM matrix elements will lead to a better understanding of the SM, and in particular more precise tests of unitarity. It should be noted however that some of the rare decay searches that are sensitive probes of NP have significant theoretical uncertainties arising from the lack of precision CKM parameter determinations. Hence not only NP could show up in precision CKM matrix element measurements, but these measurements also play a significant role in the search for NP elsewhere. Super$B$ can improve the determination of four of the CKM matrix elements via measurements of $|V_{ub}|$, $|V_{cb}|$, $|V_{us}|$ and $|V_{cd}|$ as briefly summarized below.

At the end of the B Factory era there is still tension between inclusive and exclusive measurements of $|V_{ub}|$ and $|V_{cb}|$. In anticipation of larger data samples theorists have started working with experimentalists to understand how one can make measurements in the future that are both experimentally and theoretically more robust. Several promising ideas have been put forward that will require data samples comparable to that achievable at Super$B$. Unitarity tests are just one of the reasons why it is important to improve our understanding of these parameters. Precision measurements of these quantities will be beneficial to the Lattice community and enable a number of rare decay searches for NP.

The measurement of $|V_{us}|$ is currently dominated by the interpretation of semi-leptonic kaon decays. However the limiting factor in those measurements comes from theory and unless significant progress is made on that front there will be essentially no improvement on the precision of $|V_{us}|$ from more precise kaon measurements. If one wishes to make a significant improvement in the measurement of $|V_{us}|$ one has to resort to the use of τ leptons. Super$B$ with about 75 times the existing worlds sample of τ lepton pairs will be able to make a significant improvement on the determination of this parameter. A high statistics run at charm threshold would also lead to an improved constraint on $|V_{us}|$ from τ decays.

Data accumulated at the $\psi(3770)$ will enable one to determine $|V_{cd}|$ via the study of semileptonic D decays. This CKM factor is currently known to a precision of 4.8%. It is expected that BES III will be able to improve the precision on this quantity before Super$B$ starts to take data. However with an expected 100 times the data sample of BES III, Super$B$ will be able to perform a necessary cross check, and improve our understanding of this CKM element.

It should be noted that the ratio of $|V_{td}/V_{ts}|$ can be determined using radiative B decays via $b \to d$ and $b \to s$ transitions. Theoretical uncertainties that would otherwise limit the interpretation of these results cancel in the ratio of rates.

Super$B$ can improve the measurements of the unitarity triangle angles α, β and γ to expected precisions of 1°, 0.2°, and 1°, respectively. These estimates are for the most sensitive modes and are sufficient to perform a percent level determination of the apex of the unitarity triangle ($\sigma_{\overline{\eta}}/\overline{\eta} \sim 1\%$, $\sigma_{\overline{\rho}}/\overline{\rho} \sim 3\%$) using only angles, and will provide a precision input to global fits. The primary measurements of γ and β are expected to be theoretically clean in the context of the full Super$B$ data sample.

Current theory results in an uncertainty on α of about 1° from SU(2) symmetry breaking. There are four sets of modes that will be used to extract this angle: $B \to \pi\pi$, $B \to \rho\rho$, $B \to \pi^+\pi^-\pi^0$, and $B \to a_1\pi$, where SU(3) breaking affects the latter measurement. Consistency between modes will allow one to constrain NP entering through loop contributions, as any large difference in the measured central values would not be consistent with the SM. Theoretical uncertainties on α determination will be comparable in magnitude to the experimental precision attainable at Super$B$.

Current measurements of γ from the B Factories and LHCb highlight the (well known) need for diversity in channels used to measure γ. Dalitz methods can access the weak phase directly, however the most popular methods implemented (ADS and GLW) rely on reconstructing quasi-two-body $D^{(*)}K^{(*)}$ final states whereby the weak phase is measured as a term multiplied by a Cabibbo suppression factor r_B. This number is small $(1-2\%)$ and poorly determined, and so the constraint on γ is highly sensitive to the extracted value of this nuisance parameter. For that reason we expect that it will be necessary to continue to average together different sets of constraints on γ in order to obtain a robust measurement for the foreseeable future. With the full data sample from Super$B$ we expect to be able to measure γ to a precision of 1° in a given channel. The GGSZ (Dalitz) method for γ was expected to have a significant systematic uncertainty arising from limited knowledge of the strong phase difference as a function of position in the $D \to K^0_S h^+h^-$ Dalitz plot. The Super$B$ run at charm threshold is expected to provide 100 times the data available from BES III, which can be used to effectively remove this uncertainty and enable the continued use of this method. The GGSZ method currently dominates our knowledge of γ, so it is important that one retain this powerful approach in the determination of the angles. Also the assumption that *CP* violation in charm decays is negligible in the determination of γ is something that should be revisited in light of recent results from LHCb, CDF and Belle.

4.2.4 *CP* violation in B decays

It is important to compare tree- and loop-level processes which measure the same unitarity triangle angles in the SM. NP, more likely to affect loop-dominated processes, can then be revealed by a difference in the extracted angle for different modes.

Typical examples are the loop-dominated $b \to s$ transitions. These are a set of modes that are able to measure β_{eff} in the SM, where $\beta_{eff} \sim \beta$, up to hadronic uncertainties from higher order contributions. By testing the consistency with β from tree dominated charmonium + K^0 modes, one can search for signs of heavy particles with non-trivial quark flavour transitions in loops. The most promising "*golden*" modes are those that are both experimentally precise and theoretically clean. A full list of the golden modes is given in Ref. [5], and the highlights are (for $b \to s$ penguin transitions) $B \to \eta' K^0$ ($\sigma_S = 0.007$), $B \to \phi K^0$ ($\sigma_S = 0.02$), and (for $b \to d$ transitions) $B \to J/\psi \pi^0$ ($\sigma_S = 0.02$). The latter mode is used to bound theoretical uncertainties in the tree dominated $B \to J/\psi K^0$ channel.

A set of *CP* violating observables that are central to the B physics programme at Super$B$ are *CP* asymmetries in radiative decays. These include $a_{CP}(B \to X_s\gamma)$ and $a_{CP}(B \to X_{s+d}\gamma)$ which are predicted to be small in the SM. While the former seems theoretically limited, the latter has quite small theoretical uncertainty [5]. The experimental error on $a_{CP}(B \to X_{s+d}\gamma)$ at Super$B$ will be about 2%.

Furthermore, a time-dependent analysis of the *CP* asymmetry in the exclusive mode $B^0 \to K^0_s\pi^0\gamma$ will be very sensitive to the presence of right-handed currents arising from NP. For this decay, we estimate an uncertainty of 0.03 on the *CP* violation parameter C.

4.2.5 *CP* violation in D decays

The recent evidence for direct *CP* violation in charm decays using a time-integrated asymmetry ΔA_{CP} is extremely interesting[1]. It is clear from the response of the theoretical community that one needs to perform a detailed analysis of hadronic uncertainty before heralding this result as a sign of NP, since various conclusions have been reached either in favor of NP or of being compatible with the SM depending on how one treats the problem.

Shortly before the ΔA_{CP} result was announced a systematic evaluation of time-

[1] This is a difference in time-integrated rates of neutral D mesons decaying into K^+K^- and $\pi^+\pi^-$ final states.

dependent CP asymmetries in charm was proposed using data from $\psi(3770)$, $\Upsilon(4S)$ and at hadron machines [14]. There are at least thirty five neutral modes that provide interesting tests of the SM, and a number will only be accessible at e^+e^- machines, and will complement the work underway at the LHC. Unlike B decays where golden channels can be readily identified in time-dependent measurements, hadronic effects cloud ones ability to interpret any small (percent level or less) result given the data accessible today. To resolve the issue of hadronic uncertainties one needs to measure a multitude of final states, and once again Super$B$ can contribute to the endeavor. An important step forward would be to perform a time-dependent measurement of a single mode. Currently, in order to control of systematic uncertainties at the LHC, a difference is taken between two modes. One presumes it will soon be possible to extract the TDCP parameters from a single mode at LHCb without resorting to taking a difference. In the case of $D \to \pi^+\pi^-$ (which is more interesting in the context of the SM than the KK final state also used for ΔA_{CP} as it can be used to measure an angle of a unitarity triangle) one needs to control penguin contributions, and an Isospin analysis will result in an error of a few degrees. It has been suggested for example that a time-dependent analysis of $D \to \pi^+\pi^-$ and $D \to \pi^0\pi^0$ channels can be used to resolve this problem up to Isospin breaking from electroweak penguins. This residual contribution can be controlled using the direct CP violation measurement from $D \to \pi^+\pi^0$ decays.[2] It should also be noted that if a relatively large non-zero value of ΔA remains, then it is possible that TDCP parameters would be clearly non-SM when measured. Many of these issues can be resolved by Super$B$, and it would be possible to explore this new area in the full range of final states. It is also important to quantify CP violation in charm decays as the methods to measure γ using B decays assume this is negligible, and one must verify this is the case for precision measurements. A run at the $\psi(3770)$ lasting a year is expected to provide independent measurements of TDCP asymmetries with statistical precisions comparable to a five year run at the $\Upsilon(4S)$ for Super$B$ or using the full data sample expected at LHCb according to Ref. [14].

It is also possible to measure direct CP violation in charged D decays, however as with B and kaon manifestations of direct CP violation, detailed understanding of hadronic uncertainties and strong phase differences will be required in order to interpret any results in the context of the SM. Four body final states such as $D \to K^+K^-\pi^+\pi^-$ can be used to measure triple product asymmetries related to T odd, CP violating phenomena.

It should be possible for the low energy machine to reach 4.005 GeV, on doing so one could measure the CP asymmetry in $e^+e^- \to DD^* \to D\overline{D}\gamma$. It is possible to use the method proposed by Bondar *et al.* to measure charm mixing parameters using time-integrated observables at this energy [15].

4.2.6 Other symmetry tests

CPT is conserved in relativistic quantum field theories, and underpins the SM. Super$B$ will be able to test CPT using neutral B and D mesons created in collisions at the $\Upsilon(4S)$ and $\psi(3770)$, respectively. The most recent test of CPT from *BABAR* yields a deviation from the SM expectation of 2.8σ [16]. While this is not significant it is important to repeat this measurement to understand if this is an out lier, or if there is some contribution from NP.

If CPT is conserved, then given that CP is violated one can infer that T must also be violated. *BABAR* recently discovered T violation via a time-dependent asymmetry constructed from T conjugated pairs of neutral B meson decays [17]. This established the existence of T violation using a self-consistent approach, without invoking CPT to relate CP violation to T violation. This is a significant step forward in the field, and should be studied in greater detail. Super$B$ will be able to significantly improve the precision on this measurement, which can then

[2] For this mode in particular, the required precision of parts per mille is probably only possible with data from charm threshold.

be compared with complementary tests of *CP* violation and *CPT* to test the SM.

4.2.7 Charm mixing

Whatever the outcome of studies of direct and indirect *CP* violation, an open question remains whether mixing-induced *CP* violation can also be observed. An obvious sign of this phenomenon would be a mode dependence of the mixing parameters x_D or y_D, respectively related to mass and decay widths for the underlying D mass eigenstates. *CP* violation in mixing itself would show up in $D-\overline{D}$ differences in mixing rates $|q/p|$ and in the phase of this quantity. We anticipate [5] that Super$B$ should be sensitive to a value for $|q/p|_D$ differing from 1.0 by a few percent, or to a mixing phase $\arg(q/p)$ differing from zero by $\sim 1°$. Furthermore, we expect that such results can also be obtained in a variety of decay modes. We also anticipate measurements of x_D and y_D with precisions close to $\sim 1 \times 10^{-4}$, an improvement of an order of magnitude from current world averages. This precision compares well with expectations from LHCb but the comparison will depend on the ultimate LHCb trigger, whose present design limits their yield of decays to the "golden" *CP* self-conjugate modes (primarily $K^0_S\pi^+\pi^-$ or $K^0_S K^+K^-$). The e^+e^- data should, however, cover a considerably wider range of modes that will complement well the results from LHCb.

The Super$B$ estimates are derived from a robust extrapolation from charm mixing parameters measured by *BABAR* [5]. Specifically, we assume that sample sizes at the $\Upsilon(4S)$ will be larger, thereby improving statistical precision by a factor at least ~ 12 [3]. We expect most systematic effects to scale with square root of luminosity, but we do note that the time-dependent Dalitz plot analyses of decays to the golden modes, which are crucial, will be limited in precision by an irreducible systematic uncertainty in the nature of the Dalitz plot decay model. We estimate this limits precision in x_D to 7×10^{-4}, only a factor 4 improvement over *BABAR*. Replacing the Dalitz models with measurements of $D^0\overline{D}^0$ phases obtained from quantum correlations observed in $\psi(3770)$ data from BES III, should improve the precision on $x_D(y_D)$ to $4(2) \times 10^{-4}$. This model uncertainty would be virtually eliminated by the use of a 1 ab^{-1} Super$B$ run at charm threshold to reach precisions $\sim 2(1) \times 10^{-4}$.

The anticipated integrated luminosity at charm threshold from Super$B$ is expected to be 1 ab^{-1}. Previous estimates of the sensitivity to charm mixing have assumed half of this data sample in order to determine the anticipated precision on x and y. Figure 4.3 shows the corresponding constraint obtained when one uses the full 1 ab^{-1} sample.

[3]Simulation studies indicate that the improved time-resolution in Super$B$ could introduce further gains that we did not include in the estimates.

4.2.8 B physics at the $\Upsilon(5S)$

It is expected that Super$B$ will accumulate several ab^{-1} of data at the $\Upsilon(5S)$. The aim of the physics programme at this center of mass energy is to search for physics beyond the SM via rare decays and to perform precision tests

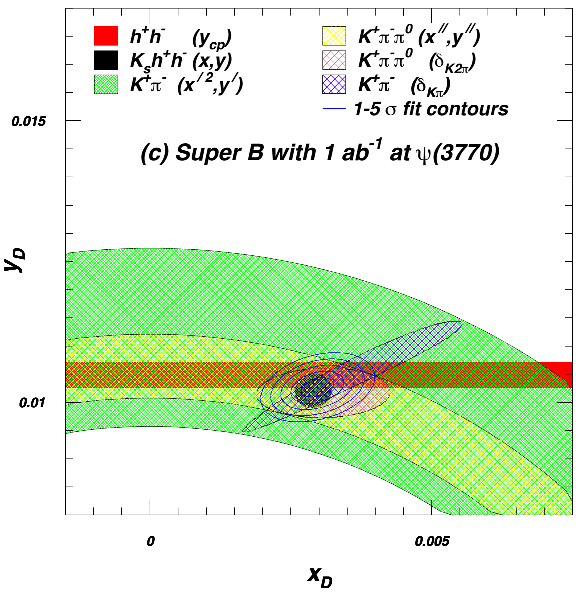

Figure 4.3: The expected constraint from Super$B$ on the charm mixing parameters x and y using the full 75 ab^{-1} sample from the $\Upsilon(4S)$, and 1 ab^{-1} from $\psi(3770)$.

of the SM. An example of a decay channel that may be affected by NP is $B_s \to \gamma\gamma$. Various NP scenarios suggest correlations between this B_s decay and $B_d \to X_s\gamma$. Hence, a branching fraction measurement of this decay is an important cross check of searches for NP performed using data collected at the $\Upsilon(4S)$. A number of rare decays with neutral final states or missing energy can be studied in this environment.

The semi-leptonic asymmetry a_{SL} in B_s decays is of interest as this is sensitive to NP and can be correlated with flavor observables measured at the $\Upsilon(4S)$. Super$B$ is expected to be able to measure a_{SL} to a precision of 0.006 with $1\,\mathrm{ab}^{-1}$ of data at the $\Upsilon(5S)$.

It will be possible to study B_s decays inclusively using data from the $\Upsilon(5S)$, and one can also search for the $B_s \to \tau^+\tau^-$ channel using kinematics of the final state to suppress background.

Finally, compared to B_d and B_u decays, knowledge of the decay modes of B_s is limited. With a data sample of this size, Super$B$ will be able to contribute to the general level of understanding of absolute branching fractions of B_s decays, which will enable theorists to improve their calculations and may reduce uncertainties on normalization channels for hadronic experiments to use (e.g. a precise measurement of the absolute value of the branching fraction of $B \to J/\psi\phi$ would be of particular interest as a normalization mode for LHC measurements of the rate of $B_s \to \mu^+\mu^-$).

4.3 τ physics at Super$B$

Measurements on τ leptons at the intensity frontier provide a powerful tool to search for NP effects in a way that is competitive and complementary with respect to LHC and other existing or planned experiments like MEG and Mu2e. Lepton Flavor violation (LFV) in τ decay is a measurable unambiguous signal for many NP models, and the expected sensitivities of the planned Super Flavor Factories is unrivaled. The large and clean dataset of $e^+e^- \to \tau^+\tau^-$ events will also permit additional NP searches based on precision measurements of CPV in τ decays, and of the τ $g-2$ and EDM form factors, with impressive improvements on the present experimental accuracy. Furthermore, Super$B$ offers the unique features of the largest design luminosity and of an 80% polarized electron beam, which provides an extra handle to identify sources of NP in LFV and to improve the experimental precision on the τ $g-2$ and EDM form factors.

In addition to being a powerful probe for NP, a high luminosity τ factory at the $\Upsilon(4S)$ peak represents an ideal facility for most τ physics measurements because the data analysis is facilitated from the fact that events consist in a correlated $\tau^+\tau^-$ pair in a well defined initial state with no superposition of background. And in the Super$B$ project, the information of the initial state is further refined in a useful way using a polarized electron beam. In these conditions, a large number of precision measurements are possible, such as $|V_{us}|$ from τ decays into strange final states, α_s, the $(g-2)_\mu$ hadronic contribution, and leptonic charged weak current couplings.

While the statistics of a $1\,\mathrm{ab}^{-1}$ run at the $\psi(3770)$ would be smaller than that obtained using a $75\,\mathrm{ab}^{-1}$ run at the $\Upsilon(4S)$, there are several instances where data collected at the lower energy would have a distinct advantage. This may become relevant should one discover new physics, and wish to perform precise cross checks in a cleaner environment than would be possible at the $\Upsilon(4S)$, or perform a high luminosity run at low energy, or at a high luminosity $\tau-$charm factory.

4.3.1 Lepton flavor violation in τ decay

The SM with neutrino mixing includes Lepton Flavor Violation (LFV) in τ decays, although at rates too small to be detected. On the other hand, measurable LFV rates can naturally arise for a variety of NP models, for instance MSSM [18, 19], MSSM with flavor symmetries [20, 21], Non Universal Higgs Masses (NUHM) SUSY [22, 23, 24], MSSM with R-parity violation (RPV) [25], LHT [26], Z' models [27]).

In many cases, the most sensitive mode is $\tau^{\pm} \to \mu^{\pm}\gamma$, and some important complementary modes are $\tau \to e\gamma$, $\tau \to \ell\ell\ell$, $\tau \to \mu\eta$. The planned Super Flavor Factories, Super$B$ and Belle II, have no significant competition in these NP searches, and Super$B$ has the advantage of a larger design luminosity and electron beam polarization, which can be used to distinguish between left and right handed NP currents.

LFV in muon decay is related to τ LFV in a way that is determined by the specific details of a NP model, on which there are no experimental clues so far. Therefore, LFV searches on $\mu \to e\gamma$ and $\mu \to e$ conversion in material are complementary in nature with the τ ones, and in order to understand NP in the long term one has to understand all three sets of measurements in detail. While for some specific NP models, with specific choices of parameters, the experimental sensitivity for LFV is larger for muon decays than for τ decays, in general searches for LFV τ decays remain important in understanding the underlying dynamics of NP models.

The Super$B$ design integrated luminosity of $75\,\mathrm{ab}^{-1}$, in combination with moderate improvements in the detector efficiency and resolution, provides a LFV sensitivity 10 times better than the B Factories for background-limited τ decay modes like $\tau^{\pm} \to \mu^{\pm}\gamma$ and up to 100 times better for the cleanest $\tau \to \ell\ell\ell$ searches. Figure 4.4 summarizes the expected LFV sensitivities from Super$B$ and the LHCb upgrade [28].

If one considers the search for $\tau \to \mu\gamma$: for data collected at the $\Upsilon(4S)$, this has an irreducible background from events with initial state radiation. Data collected at low energy (at or below about 4.0 GeV) can be used to isolate a clean (background free) sample of events. An extended run of several ab^{-1} at the $\psi(3770)$ would be competitive with limits achievable at the $\Upsilon(4S)$ using Super$B$. Such a run would be justified in the event of a discovery at the $\Upsilon(4S)$.

4.3.2 *CP* violation in τ decay

The SM predicts vanishingly small *CP* violation effects in τ decays, for instance, the *CP* asymmetry rate of $\tau^{\pm} \to K^{\pm}\pi^{0}\nu$ is estimated to be of order $\mathcal{O}(10^{-12})$ [30]. For the decay $\tau^{\pm} \to K_S\pi^{\pm}\nu$ the SM predicts, with a 2% relative precision, a *CP* asymmetry of 3.3×10^{-3} due to the known *CP*-violating phase of the $K^0\overline{K}^0$ mixing amplitude [31]. Any observed deviation from this clean, and precisely defined, picture would be a clear sign of NP. Specific NP models such as RPV SUSY [32, 25] and non-SUSY multi-Higgs models [33, 34, 35, 36] can accommodate *CP* violation in τ decays up to 10^{-1} or the present experimental limits [37], while satisfying other experimental constraints. Examples of decay modes with potentially sizable asymmetries are $\tau \to K\pi\nu_\tau$, $\tau \to K\eta^{(\prime)}\nu_\tau$, and $\tau \to K\pi\pi\nu_\tau$ [32, 33, 34, 35, 36].

The Belle and *BABAR* Collaborations have searched for *CP* violation in τ decay [37, 38] with different analyses on the same decay mode. *BABAR* measured the *CP* asymmetry in the total branching ratio, which is affected by the K_S *CP* violation amplitude and found a 2.8σ discrepancy with respect to the SM. Belle measured an angular dependent *CP* asymmetry where any detectable effect would correspond to NP, with a sensitivity of order 10^{-3}. Super$B$ can conceivably improve by an order of magnitude. As *CP* violation is an interference effect that is linear in the NP amplitude, a 10^{-4} precision on a *CP* asymmetry corresponds very roughly to measuring the $\tau \to \mu\gamma$ branching fraction with 10^{-10} precision [39].

4.3.3 Measurement of the τ $g-2$ and EDM form factors

The anomalous magnetic and the electric dipole moments of the τ are fundamental properties of the heaviest known lepton and are predicted with extreme precision within the SM both at zero and non-zero transferred momentum. They can be measured at transferred momenta of the order of the τ mass from the angular distributions of the τ decay products in $e^+e^- \to \tau^+\tau^-$ events. For this purpose having polarized beams represents a clear advantage [40, 41].

Within the SM, the τ $g-2$ has been computed with very good precision, $\Delta a_\tau = \Delta(g-2)_\tau/2 = 5 \times 10^{-8}$ [42]; its size is mainly determined by

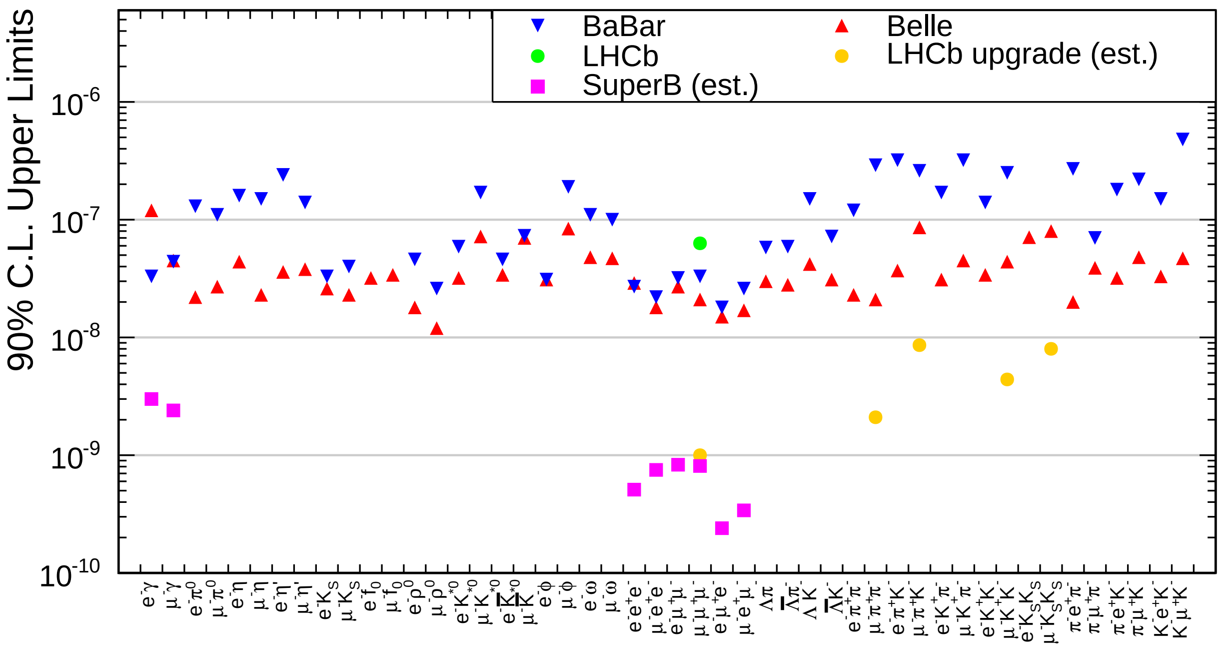

Figure 4.4: Summary of present upper limits on τ LFV compared with expected upper limits from Super$B$ and the LHCb upgrade. The latter estimates are the order-of-magnitude estimates listed in the letter of intent [28]. A naive LHCb-upgrade sensitivity estimate for $\tau \to 3\mu$ based on the 2012 LHCb 90% expected upper limit [29] extrapolated from $1\,\mathrm{fb}^{-1}$ to $50\,\mathrm{fb}^{-1}$ with the square root of the luminosity gives 1.5×10^{-8}, to be compared with 1.0×10^{-9} in the plot. In some cases, the *BABAR* results are hidden by very similar results by Belle, which are superposed in the plot.

the first perturbative term which is of order α and is the same for all leptons.

If one assumes that the present muon $g{-}2$ discrepancy is caused by NP corresponding to the MSSM with $\tan\beta \gtrsim 10$, one expects a much larger NP effect on the τ $g{-}2$, at the level of 10^{-6}.

There is limited experimental information on the τ $g{-}2$, the OPAL collaboration obtained a limit on the size of $F_2(q)$ [where $F_2(0) = (g{-}2)/2$] averaging transferred momenta between approximately the τ and the Z mass at the level of 7% [43]. For Super$B$ with $75\,\mathrm{ab}^{-1}$ of data and a 100% polarized electron beam, the real and imaginary part of the $g{-}2$ form factor F_2 can be measured assuming perfect reconstruction with a resolution in the range $[0.75 - 1.7] \times 10^{-6}$ [44]. When the design 80% beam polarization and realistic experimental reconstruction effects are included, the resolution is be estimated at about 2.4×10^{-6}, which is comparable to the size of possible NP MSSM contributions compatible with the muon $g{-}2$ discrepancy.

The τ EDM is expected to be vanishing small, and the existing upper limit on the electron EDM imposes severe constraints also on contributions from NP to about $d_\tau \lesssim 10^{-22} e\,\mathrm{cm}$. Experimentally, from a Belle analysis on $29.5\,\mathrm{fb}^{-1}$ of data [45] (unpolarized beams), we know that the experimental resolution on the real and imaginary parts of the τ EDM is between $0.9 \times 10^{-17}\,e\,\mathrm{cm}$ and $1.7 \times 10^{-17}\,e\,\mathrm{cm}$, including systematic effects.

Recent studies have provided an estimate of the Super$B$ upper limit sensitivity for the real part of the τ EDM $|\mathrm{Re}\{d_\tau^\gamma\}| \leq 7.2 \times 10^{-20}\,e\,\mathrm{cm}$ with $75\,\mathrm{ab}^{-1}$ [40]. The result assumes a 100% polarized electron beam colliding with unpolarized positrons at the $\Upsilon(4S)$ resonance. Uncertainty on the polarization is neglected, and a perfect reconstruction of the decay $\tau \to \pi\nu$ is assumed. A refined sensitivity estimate has been obtained assuming an electron beam with a polarization of 80% $\pm$ 1% and realistic experimental reconstruction efficiency and uncertainties at $\approx 10 \times 10^{-20} e\,\mathrm{cm}$. Such a measurement would constitute a remarkable experimental improvement over current constraints.

4.4 Super$B$ Neutral Current Electroweak Physics Programme

With its ultra-high luminosity, polarized beam, and the ability to run at both the b-quark and c-quark thresholds, Super$B$ is a unique and versatile facility and no other machine with all of these capabilities is planned. In particular, the polarization of the electron beam enables Super$B$ to measure the weak neutral current vector coupling constants of the b-quark, c-quark and muon at significantly higher precision than any previous experiment. The precision of the vector coupling to the tau and electron will be measured with a precision comparable to that attained at SLC and LEP. Within the framework of the SM these measurements of g_V^f can be used to determine the weak mixing angle, θ_W, through the relation: $g_V^f = T_3^f - 2Q_f \sin^2\theta_W$, where T_3^f is the 3^{rd} component of weak isospin of fermion f, Q_f is its electric charge in units of electron charge and higher order corrections are ignored here for simplicity. Figure 4.5 shows the determinations of $\sin^2\theta_W$ at present and future experimental facilities including Super$B$. If one were to run with a polarized electron beam at the $\psi(3770)$, then a similar programme could be exploited using c-quark and muon pairs. An interesting level of precision would be achievable in order to test the SM at an energy similar to the NuTeV result.

Super$B$ determines g_V^f by measuring the left-right asymmetry, A_{LR}^f, for each identified final-state fermion-pair in the process $e^+e^- \to f\overline{f}$.

$$A_{LR}^f = \frac{\sigma_L - \sigma_R}{\sigma_L + \sigma_R} = \frac{sG_F}{\sqrt{2}\pi\alpha Q_f} g_A^e g_V^f \langle Pol \rangle \quad (4.1)$$

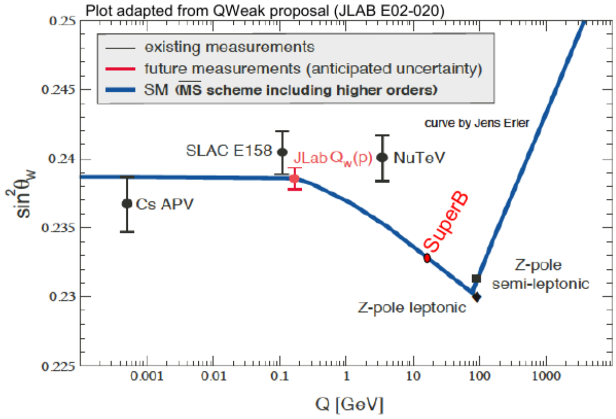

Figure 4.5: Determination of $\sin^2\theta_W$ at present and future experimental facilities.

where g_A^e is the neutral current axial coupling of the electron, $g_A^e = T_3^e$, G_F is the Fermi coupling constant, s is the square of the center-of-mass energy, and

$$\langle Pol \rangle = 0.5 \left[(N_{asym})_{RPB} - (N_{asym})_{LPB} \right], \quad (4.2)$$

is the average beam polarization, where N_{asym} is the asymmetry between N_{eR} and N_{eL}, and LPB and RPB indicate left or right polarized beams.

These asymmetries arise from $\gamma - Z$ interference and although the SM asymmetries are small (-3×10^{-4} for the leptons, -3×10^{-3} for charm and -1.3% for the b-quarks), the unprecedented precision is possible because of the high luminosity of Super$B$ together with a 70% beam polarization measured to $\pm 0.5\%$. To achieve the required precision all detector-related systematic errors are made to cancel by flipping the polarization from R to L in a random, but known, pattern through a run. $\langle Pol \rangle$ is measured with both a Compton Polarimeter, which has an uncertainty at the interaction point of $< 1\%$ and by measuring the forward-backward polarization asymmetry of the τ-pairs using the kinematic distributions of the decay products of the τ. The latter can be used to determine $\langle Pol \rangle$ to 0.5% at the interaction point in a manner entirely independent of the Compton Polarimeter.

The 3σ discrepancy between the LEP measurements of the right-handed b-quark couplings to the Z will be experimentally probed with higher precision at Super$B$. Also, measurements with the projected precision will enable Super$B$ to probe parity violation induced by the exchange of heavy particles such as Z-boson or hypothetical TeV-scale Z' boson(s). If such bosons only couple to leptons they will not be produced at the LHC. Moreover, the Super$B$ machine will have a unique possibility to probe parity violation in the lepton sector mediated by light and very weakly coupled particles often referred to as "dark forces" (Sec. 4.5). Recently, such forces have been entertained as a possible connecting link between normal and dark matter [46, 47]. The enhancement of parity violation in the muon sector has been an automatic consequence of some models [48] that aim at explaining the unexpected result for the recent Lamb shift measurement in muonic hydrogen [49]. The left-right asymmetry of the $e^-e^+ \to \mu^-\mu^+$ in such models is expected to be enhanced at low-to-intermediate energies, and the Super$B$ facility may provide a conclusive test of such models, as well as impose new constraints on parity-violating dark sector.

4.5 Exotic Spectroscopy in Super$B$

Although the SM is well-established, QCD, the fundamental theory of strong interactions, provides a quantitative comprehension only of phenomena at very high energy scales, where perturbation theory is effective due to asymptotic freedom. The description of hadron dynamics below the QCD dimensional transmutation scale is therefore far from being under full theoretical control.

Systems that include heavy quark-antiquark pairs (quarkonia) are a unique and, in fact, ideal laboratories for probing both the high energy regimes of QCD, where an expansion in terms of the coupling constant is possible, and the low energy regimes, where non-perturbative effects dominate. For this reason, quarkonia have been studied for decades in great detail. The detailed level of understanding of the quarkonia mass spectra is such that a particle mimicking quarkonium properties, but not fitting any quarkonium level, is most likely to be considered to be of a different nature.

In particular, in the past few years the B Factories and the Tevatron have provided evidence for a large number of states that do not admit the conventional mesonic interpretation and that instead could be made of a larger number of constituents. While this possibility has been considered since the beginning of the quark model [50], the actual identification of such states would represent a major revolution in our understanding of elementary particles. It would also imply the existence of a large number of additional states that have not yet been observed.

For an overview of the observed states and their interpretation we refer to [51], here we will discuss the Super$B$ potential and its interplay with the other planned experiments.

Regardless of the theoretical ansatz in which the observed states are interpreted, the existence of a new fundamental type of state implies the existence of a number of new states that is much larger than the set of states observed so far. For instance, as detailed in Ref. [51], under the assumption of the tetraquark nature of the observed new state there are at least 18 states predicted for each J^{PC}; similarly in the molecular model, the number of thresholds close to which a new state could be is extremely large.

The next generation of experiments ought therefore to make the leap from the discovery phase to the systematic investigation of the whole spectroscopy. As an example one should search for a charged state decaying into $J/\psi K$ and produced in B decays in conjunction to a ω. This search was not performed in BABAR and Belle both because of lack of a certain theoretical model, but above all because of lack of statistics.

In this process of building the complete picture Super$B$ plays a critical role because of the following characteristics:

- *large statistics.* The largest limitation of the current data sample is the low statistics. As a consequence, signals are still not well established, precision analyses for the determination of the quantum numbers is impossible and several states are likely not to have been observed because of a low branching fraction. In particular all final states with D and D_s mesons will be accessible for the first time at Super$B$.

- *clean environment.* Albeit the high luminosity, that will slightly degrade the detector performance, the experiment is a multipurpose one, like *BABAR*. It will therefore have detection capabilities for all neutral and charged particles. Detection efficiencies are not expected to vary significantly from the *BABAR* ones.

- *center-of-mass scan potential.* The cleanest way to study a particle is to produce it directly, and this is possible, for $J^{PC} = 1^{--}$ states if the machine can adjust its energy to match the mass of the state. This is the case for Super$B$ over a large range of energy, in the vicinity of the charm threshold and for energies above the Υ(4S), thus allowing for direct studies on any $J^{PC} = 1^{--}$ exotic state.

Super$B$ is not the only next generation experiment capable of investigating heavy quark spectroscopy.

The LHCb experiment is starting to investigate its potential in the field. The larger number of mesons produced allows detailed studies of the decay modes with final states made of charged particles. All other modes are best investigated by e^+e^- machines.

The only other next generation experiments at an e^+e^- machine are BES-III and Belle-II. BES-III is a τ-charm factory planning to run below the energies of interest, at the $\psi(3770)$ [52], where they expect to collect $5\,\mathrm{fb}^{-1}$ per year. Concerning Belle-II, the Super-KEKB accelerator is not designed to have the scan capabilities of Super$B$ and would not therefore be able to cover the corresponding physics.

A separate mention is deserved by the PANDA experiment at FAIR [53], a proton-antiproton collider which could produce the exotic resonances at threshold (i.e. $e^+e^- \to X, Y$). This innovative production mechanism allows for copious production without the hindrance of fragmentation products.

The complementarity of the two experiments is guaranteed by the fact that the final states that can be studied by the two experiments are different and that the PANDA experiment can more easily access the narrow states while Super$B$ can study in detail larger states if the production mechanism is favorable. Furthermore, in case the center-of-mass-energy of Super$B$ is changed to the $Y(4260)$ mass, assuming a factor 10 loss in luminosity with respect to running at the $\Upsilon(4S)$, the number of events produced in a few weeks would be equivalent to the PANDA dataset. Finally, PANDA can only reach center-of-mass energies as high as 5 GeV and therefore has no access to bottomonium spectroscopy.

4.6 Direct searches

Bottomonium decays can also be very sensitive to new particles that might have escaped direct searches at lower luminosity and higher energy facilities because of small couplings with ordinary matter. Among such searches we consider here the quest for dark matter and dark forces.

Two promising reactions for searching **low-mass dark matter** (χ) are the invisible and radiative decays of the $\Upsilon(1S)$ mesons, which can be measured in the mode $\Upsilon(3S) \to \pi^+\pi^- invisible$ [54]. The current best sensitivity to this process has been achieved by the *BABAR* experiment [55]; however, this result is still an order of magnitude above the SM prediction. The sensitivity is limited by the amount of background that needs to be subtracted, primarily due to undetected leptons from $\Upsilon(1S) \to \ell^+\ell^-$ decays. Achieving a $3-5\sigma$ sensitivity to the SM will require active background tagging down to 5-10 degrees above the beam-line in both the forward and backward directions. Also the searches for bino-like neutralino in radiative $\Upsilon(1S) \to \gamma + invisible$ decays require extended detector coverage in the forward and backward directions to reduce the dominant radiative QED backgrounds.

Concerning the search for **dark forces**, recent cosmic ray measurements of the electron and positron flux [56, 57, 58] have spectra which are not well described by galactic cosmic ray models and that lead to the introduction of a class of theories containing a new "dark force" and a light, hidden sector. In this model, the observed signals are due to dark matter particles with mass $\sim 400 - 800\,\mathrm{GeV}/c^2$ annihilating into the gauge boson force carrier with mass $\sim 1\,\mathrm{GeV}/c^2$, dubbed the A' (a "dark photon"), which subsequently decays to SM particles. If the A' mass is below twice the proton mass, decays to $p\overline{p}$ are kinematically forbidden allowing only decays to states like e^+e^-, $\mu^+\mu^-$, and $\pi\pi$.

The dark sector couples to the SM through kinetic mixing with the photon with a mixing strength ϵ. Low-energy, high luminosity e^+e^- experiments like the B Factories are in excellent position to probe these theories [59, 60] by searching the A' either in direct production, or in rare B mesons and light mesons decays.

It is possible to search for dark photon production in data from e^+e^- collisions (see [61] and references therein) where current limits on the kinetic mixing parameter ϵ are a few $\times 10^{-3}$. SuperB should be able to improve upon these limits by an order of magnitude.

Other possible search channels are:

- the dark Higgs-strahlung process: the combined production with a dark Higgs (h') (e.g. $e^+e^- \to A'h', h' \to A'A'$) where BABAR set a limit on the dark sector coupling constant and the mixing parameter at the level of $10^{-10} - 10^{-8}$ for $0.8 < m_{h'} < 10.0\,\mathrm{GeV}$ and $0.25 < m_{A'} < 3.0\,\mathrm{GeV}$ with the constraint $m_{h'} > 2m_{A'}$ and where Super$B$ could improve these limits by two orders of magnitude;

- very rare decays of the B meson, as resonances in the dilepton spectrum of $B \to Kl^+l^-$, $B^0 \to l^+l^-l^+l^-$ or $B \to Kl^+l^-l^+l^-$, where Super$B$ could probe couplings between a dark pseudoscalar and the top quark at the level of $1000 - 10000\,\mathrm{TeV}$, much larger than the scale accessible at LHC in direct collisions;

- rare meson decays [62] where the huge samples of lighter mesons such as π^0, η, K, ϕ, and $J\psi$ can be used to search for the channel $\pi^0/\eta \to \gamma A' \to \gamma l^+l^-$.

4.7 Executive Summary

Up to now the SM managed to pass all the experimental challenges unscathed, providing an overall good description of particle physics up to the energy scales probed in experiments, which is now approaching the TeV scale.

In spite of its phenomenological success, however, the SM is not satisfactory for several theoretical reasons, including the instability of the Fermi scale against radiative corrections, the lack of an explanation for the origin of flavour and *CP* violation and the non-unified description of the fundamental interactions, with gravity totally unaccounted for. In addition, the SM does have phenomenological problems when confronted with astrophysical and cosmological data: it cannot provide a viable dark matter candidate or an amount of *CP* violation large enough to account for the observed matter-antimatter asymmetry in the universe.

For these reasons, the SM is regarded as a low-energy theory bound to fail at some energy scale larger than the Fermi scale, where New Physics (NP) effects become important. The search for these effects is the main goal of particle physics in the next decades, both at present and future experimental facilities.

Flavor physics is the best candidate as a tool for indirect NP searches for several well-known reasons: FCNCs, neutral meson-antimeson mixing and *CP* violation occur at the loop level in the SM and therefore are potentially subject to large virtual corrections from new heavy particles. In addition, flavour violation in the SM is governed by weak interactions and, in the case of quarks, suppressed by small mixing angles.

All these features are not necessarily shared by NP which could then produce very large effects.

In spite of its potential, so far flavour physics has not provided a clear NP signal, although deviations with low significance are present here and there. This failure, however, should not be considered discouraging. Broadly speaking, flavour physics probed and excluded so far only the region of small NP scales and/or large NP flavour couplings. On the other hand, we should not forget that flavour physics successfully anticipated the existence and sometimes the mass range of all the heavy quarks which are nowadays part of the SM [63, 64, 65]. This may well happen again for heavy particles beyond the SM.

From a phenomenological point of view, flavour physics can be used in two modes. In the "NP discovery" mode, deviations from the SM expectation are looked for in each NP-sensitive measurement irrespective of their origin. The name of the game in this case is high precision and a control of the SM contributions which matches it. Depending on the NP at work, measurements in the B and D sectors at Super$B$ can be sensitive to contribution of new particles with masses up to tens or hundreds TeV [3, 5] (see the MSSM example in Figure 4.6). Although in general a precise determination of the NP masses is hindered by the unknown NP flavour couplings, even a broad indication of the NP mass range would be a most valuable information in the unfortunate case direct searches at the LHC will be unsuccessful. The "NP characterization" mode entails measuring significant deviations in several observables from different flavour sectors and studying the correlations among them. If some information on the NP mass spectrum is already available, this kind of analysis could provide crucial information to disentangle different NP contributions, elucidate the NP flavour structure and measure the NP flavour couplings [3, 5] (see the MSSM example in Figure 4.7). It is worth recalling that, on top of the intrinsic phenomenological interest, flavour is intimately related to NP symmetry properties in many extensions of the SM. For example, new flavour structures ap-

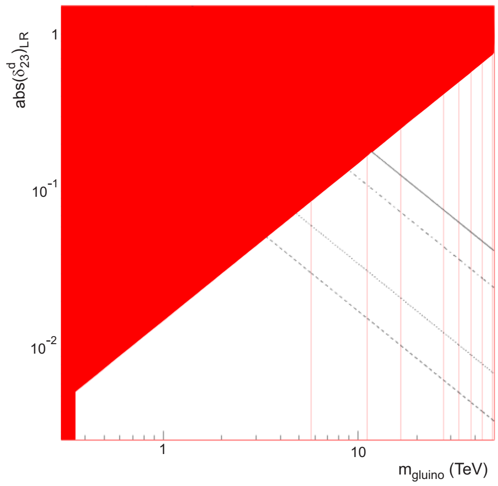

Figure 4.6: Region of the MSSM parameter space where a non-vanishing squark mass insertion parameter $(\delta^d_{23})_{LR}$ can be extracted with at least 3σ significance (in red) using $a_{\rm CP}(B_d \to X_s\gamma)$, $\mathcal{B}(B_d \to X_s\gamma)$ and $\mathcal{B}(B_d \to X_s\ell^+\ell^-)$ as constraints and assuming dominance of gluino-mediated contributions. For $m_{\tilde{g}} \sim 1$ TeV, Super$B$ is sensitive to $(\delta^d_{23})_{LR} \sim 10^{-2}$. For larger values of $(\delta^d_{23})_{LR}$, Super$B$ sensitivity extends to $m_{\tilde{g}} > 10$ TeV.

pearing in the MSSM originate from the soft SUSY-breaking sector. By measuring many NP-sensitive observables in different flavour sectors, Super$B$ can give a major contribution to this ambitious program, which needs combining all available flavour information, from kaon fixed-target experiments to hadronic collider results.

The Super$B$ physics programme sketched in this document extends over a large set of rare decays, FCNCs, CP-violation in the B_d/B_u, D and τ sectors, measured at the $\Upsilon(4S)$ and the $\psi(3770)$ resonances [3, 5]. The full set of measurements performed at the B factories can be repeated taking advantage of the much larger data samples which typically allows one to increase experimental precision/sensitivity by a factor 5 to 10. These include the unitarity triangle angles measured with various techniques, inclusive and exclusive semileptonic decays, $B \to X_s\gamma$, $B \to \tau\nu$, $B \to D\tau\nu$, several penguin-dominated $b \to s$ decays, τ flavour-violating decays, D–$\overline{D}$ mixing parameters, and many other processes. Indeed, with very few exceptions, these measurements are not severely limited by systematic or theoretical uncertainties. In addition, several new measurements, which were not feasible before, become possible: these include various observables in the decays $B \to K^{(*)}\nu\overline{\nu}$, $B \to X_s\ell^+\ell^-$, $B \to X_d\gamma$, CP violation in D mixing and decays, τ form factors, including EDM and $(g-2)_\tau$. Some LFV τ decay searches are expected to remain background free at Super$B$, and the corresponding limits are expected to be improved by two orders of magnitude on these modes (e.g. $\tau \to 3\mu$) relative to constraints from the B Factories. Some of these rare decays can be used to probe the nature of the Higgs sector, related to the recently discovered particle at CERN, by constraining charged and neutral partners of this Higgs which have been predicted by many postulated NP scenarios.

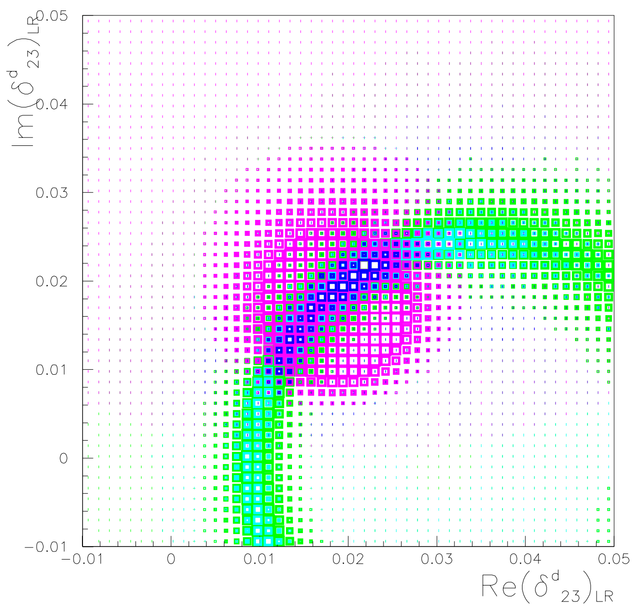

Figure 4.7: Extraction of $(\delta^d_{23})_{LR}$ from the measurements of $a_{\rm CP}(B_d \to X_s\gamma)$ (magenta), $\mathcal{B}(B_d \to X_s\gamma)$ (green) and $\mathcal{B}(B_d \to X_s\ell^+\ell^-)$ (cyan) with the errors expected at Super$B$. Central values are generated using $(\delta^d_{23})_{LR} = 0.028\,e^{i\pi/4}$ and squark and gluino masses at 1 TeV.

Within its physics programme, Super$B$ will explore to unprecedented precision a number of recent developments in the field of B and D physics that could be a hint of physics beyond the SM. The large $\mathcal{B}(B \to \tau\nu)$ measured at the B Factories and the recent evidence for an excess also in $B \to D^{(*)}\tau\nu$ decays reported by *BABAR* is something that needs to be verified and studied to high precision. The same holds true for the CP asymmetry of $\tau \to K_s\pi\nu$ which *BABAR* measured almost 3σ away from the SM and for the direct CP asymmetry in singly Cabibbo-suppressed D decay measured by LHCb. For the latter, an open issue is the actual SM prediction which is hindered by the theoretical inability to compute the relevant D decay amplitudes. Super$B$ will be able to perform time-dependent CP asymmetry studies in neutral D decays at the $\psi(3770)$ and $\Upsilon(4S)$, enabling one to exploit the different statistical data samples using complementary experimental techniques, as well as measuring hadronic modes required to constrain theoretical uncertainties relating to the interpretation of the measured observables.

Given the importance of controlling precisely the SM contributions, it is crucial to improve the determination of the CKM parameters ρ and η in the presence of NP, using fit strategies already applied successfully to B Factory data. By combining data taken at the $\psi(3770)$ as well as $\Upsilon(4S)$ one will be able to make competitive measurements of all the angles of the unitarity triangle (α, β, and γ) and the magnitude of several matrix elements (V_{ub}, V_{cb}, V_{us}, and V_{cd}), as well as the ratio $|V_{td}|/|V_{ts}|$. In particular, the crucial information on V_{ub} and V_{cb} coming from semileptonic decays can be improved only at flavour factories, where in addition the large data set can be used to control theoretical uncertainties in inclusive decays. Using this information, one can determine ρ and η with percent precision irrespective of possible NP contributions to $\Delta F = 2$ amplitudes. The reduced uncertainty on the CKM parameters allows one to boost the NP sensitivity of several observables measured at Super$B$ and elsewhere. One should not forget that the CKM fit itself is a test of NP in $\Delta F = 2$ amplitudes which could produce an unmistakable signal at Super$B$, like the one shown in Figure 4.8.

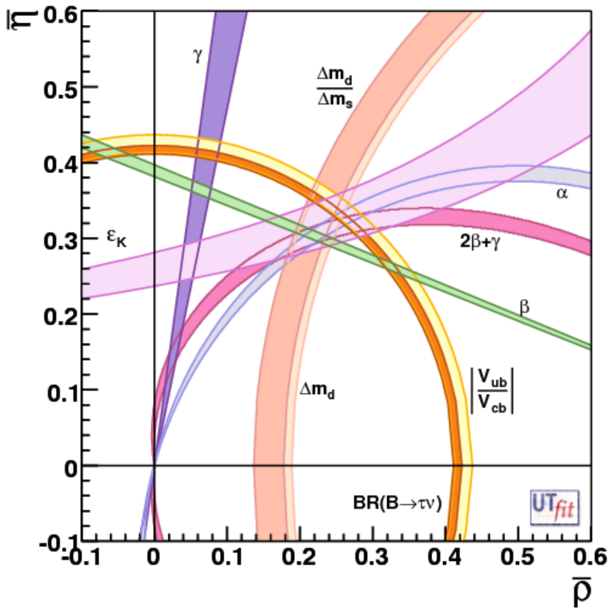

Figure 4.8: Constraints on the $(\bar{\rho}, \bar{\eta})$ plane using measurements from Super$B$. Existing central values are extrapolated to sensitivities expected from Super$B$ with 75 ab^{-1} and one can see that the constraints are not consistent with the CKM scenario. This highlights the importance of performing a precision CKM test with Super$B$.

τ physics is another prominent topic of the Super$B$ physics programme. Flavor-violating τ decays would be a clear and clean mark of new physics [3, 4, 5]. Super$B$ extends sensitivity for $\mathcal{B}(\tau \to \mu\gamma)$ down to the 10^{-9} region, where many NP models produce detectable signals. In addition, this region is complementary to the MEG sensitivity for $\mu \to e\gamma$ (10^{-13}) in some SM extensions, allowing one to probe the mechanism responsible for the LFV. In addition, the excellent performance of Super$B$ in measuring $\mathcal{B}(\tau \to 3\ell)$ not only gives an additional chance to detect LFV, but could also allow us to tell apart models where LFV is generated through magnetic dipole operators (such as the MSSM) from those using different mechanisms (for example little Higgs models). Finally, the τ physics programme does not only include LFV: a complete characterization of the τ properties to high precision can be carried out, including *CP* violation and form factor measurements, such as the EDM and $(g-2)_\tau$. Interestingly enough, assuming that the present deviation of $(g-2)_\mu$ from its SM prediction is a NP effect, then one expects the corresponding deviation in $(g-2)_\tau$ to be measurable at Super$B$ in many SM extensions.

In spite of the superior performance of hadronic colliders in the B_s sector, Super$B$ can still provide few complementary B_s measurements running at the $\Upsilon(5S)$. Examples are $\mathcal{B}(B_s \to \gamma\gamma)$ and the semileptonic asymmetry a_{SL} which can be used, together with $\Delta\Gamma_s$ and Δm_s, to determine the NP-sensitive phase $\phi_s = \arg(-M_{12}/\Gamma_{12})$. In addition, a precise measurement of the branching ratio of reference B_s decay modes would provide a valuable input to the LHCb-upgrade physics programme, allowing for a reduction of systematic uncertainties on high-precision measurements of absolute branching fractions (for example a precise measurement of the branching fraction of

$B_s \to J/\psi\phi$ will be useful to control systematic uncertainties in the measured branching fraction of $B_s \to \mu^+\mu^-$ from measurements made in the future at the LHC).

Polarization of the electron beam, a unique feature of Super$B$, makes it possible to measure the e^+e^- LR asymmetry in various channels. The bottom and charm NC vector couplings will be determined with unprecedented precision and $\sin^2\theta_W$ will be measured at the $\Upsilon(4S)$ using leptons with a precision comparable to that at the Z peak [5]. These unique measurements provide important EW precision tests which, after the measurement of the Higgs boson mass, become another powerful tool for indirect NP searches. Furthermore, polarization provides new handles for τ physics studies, in particular FV and form factor measurements.

Finally, Super$B$ can perform direct NP searches as well: elusive light particles like low-mass dark matter or light vector bosons, such as the "dark" photon, can be looked for in bottomonium decays and using data collected from the low energy run. In addition, a rich spectroscopy programme can be carried out at Super$B$. It is aimed at finding further unconventional states in the quarkonia mass spectra and possibly shedding light on the strong interaction mechanism leading to their formation. In this respect, the Super$B$ scan capabilities offer unique opportunities to study both the charmonium and bottomonium spectra with high statistics.

While there is a subset of Super$B$ measurements which can be interpreted with little or no theoretical input (for example: the CKM angles γ and α, flavour-violating τ decays, many CP violating D transitions), in order to exploit the full phenomenological potential of the Super$B$ program, one needs theoretical uncertainties to match the experimental precision to allow one to reveal and disentangling genuine NP effects. Extrapolation of the present systematics indicates that lattice QCD could reach the required precision on the relevant hadronic parameters in few years [3, 5]. It seems also possible to control theoretical uncertainties at the required level in inclusive semileptonic decays using data-driven methods based on the heavy quark expansion and the huge Super$B$ data set. Inclusive radiative decays, most notably the $B \to X_s\gamma$ rate, could be limited by theory uncertainties, although there is no general consensus on the ultimate theoretical error which could be obtained in the next years. Only for some two-body non-leptonic decays, in particular the penguin-dominated $b \to s$ transitions, theory seems not able, in the absence of a breakthrough, to match the experimental precision. Yet, even in this case, data and flavour symmetries can be sometimes used to bound the theoretical uncertainties and allow for the extraction of the NP signal.

In summary, we have shown that there are a significant number of golden modes for which Super$B$, collecting $75\,\mathrm{ab}^{-1}$ of data at the $\Upsilon(4S)$ and $1\,\mathrm{ab}^{-1}$ of data at the $\psi(3770)$, has the best expected sensitivities [6]. The physics potential of Super$B$ and Belle II are similar, but Super$B$ provides additional opportunities owing to its charm threshold running capability and beam polarization. As with BABAR and Belle, and ATLAS and CMS, there is a significant benefit in having two super flavour factories, as it will be possible to verify any discoveries made by one of the experiments. The super flavour factories and the LHCb upgrade physics programs are largely complementary and the overlap is confined to $B^0 \to K^{0*}\mu^+\mu^-$ and the charm mixing parameters, which the LHCb upgrade will eventually improve upon [6]. All together, Super$B$, Belle II, LHCb upgrade and experiments measuring ultra-rare K decays and searching for muon flavor violation, will be able to provide full and redundant coverage of all quark and charged lepton flavour sectors with high-precision measurements of rare decays, FCNCs, flavour and CP violating processes. These will be a key tool to characterize NP at the TeV scale or to start probing the multi-TeV region.

4.8 Bibliography

[1] M. E. Biagini et al., (Super$B$ collaboration), "Super$B$ Progress Reports – Acceler-

ator", 2010, arXiv:1009.6178 [physics.acc-ph].

[2] E. Grauges et al., (Super$B$ collaboration), "Super$B$ Progress Reports – Detector", 2010, arXiv:1007.4241 [physics.ins-det].

[3] M. Bona et al., (Super$B$ collaboration), "Super$B$: A High-Luminosity Asymmetric e^+e^- Super Flavor Factory. Conceptual Design Report", 2007, arXiv:0709.0451 [hep-ex].

[4] D. Hitlin et al., "New Physics at the Super Flavor Factory. Proceedings, 6th superB Workshop, Valencia, Spain, January 7-15, 2008", 2008, arXiv:0810.1312 [hep-ph].

[5] B. O'Leary et al., (Super$B$ collaboration), "Super$B$ Progress Reports – Physics", 2010, arXiv:1008.1541 [hep-ex].

[6] B. Meadows, M. Blanke, A. Stocchi, A. Drutskoy, A. Cervelli, et al., "The impact of Super$B$ on flavour physics", 2011, arXiv:1109.5028 [hep-ex].

[7] M. Bona et al., (UTfit collaboration), "An Improved Standard Model Prediction Of $BR(B \to \tau\nu)$ And Its Implications For New Physics", *Phys.Lett.* B687:61–69, 2010, doi:10.1016/j.physletb.2010.02.063, arXiv:0908.3470 [hep-ph].

[8] J. Charles et al., "Predictions of selected flavour observables within the Standard Model", *Phys.Rev.* D84:033005, 2011, doi:10.1103/PhysRevD.84.033005, arXiv:1106.4041 [hep-ph].

[9] See presentation by Y. Yook at ICHEP 2012.

[10] J. Lees et al., (BABAR collaboration), "Evidence of $B \to \tau\nu$ decays with hadronic B tags", 2012, arXiv:1207.0698 [hep-ex].

[11] J. Lees et al., (BaBar Collaboration collaboration), "Evidence for an excess of $\bar{B} \to D^{(*)}\tau^-\bar{\nu}_\tau$ decays", *Phys.Rev.Lett.* 109:101802, 2012, doi:10.1103/PhysRevLett.109.101802, arXiv:1205.5442 [hep-ex].

[12] W. Altmannshofer, A. J. Buras, D. M. Straub, and M. Wick, "New strategies for New Physics search in $B \to K^*\nu\bar{\nu}$, $B \to K\nu\bar{\nu}$ and $B \to X_s\nu\bar{\nu}$ decays", *JHEP* 04:022, 2009, doi:10.1088/1126-6708/2009/04/022, arXiv:0902.0160 [hep-ph].

[13] R. Aaij et al., (LHCb collaboration), "Differential branching fraction and angular analysis of the decay $B^0 \to K^{*0}\mu^+\mu^-$", *Phys.Rev.Lett.* 108:181806, 2012, doi:10.1103/PhysRevLett.108.181806, arXiv:1112.3515 [hep-ex].

[14] A. Bevan, G. Inguglia, and B. Meadows, "Time-dependent CP asymmetries in D and B decays", *Phys.Rev.* D84:114009, 2011, doi:10.1103/PhysRevD.84.114009, arXiv:1106.5075 [hep-ph].

[15] A. Bondar, A. Poluektov, and V. Vorobiev, "Charm mixing in the model-independent analysis of correlated D^0 $\overline{D}^0$ decays", *Phys.Rev.* D82:034033, 2010, doi:10.1103/PhysRevD.82.034033, arXiv:1004.2350 [hep-ph].

[16] B. Aubert et al., (BABAR collaboration), "Search for CPT and Lorentz violation in B0 - anti-B0 oscillations with dilepton events", *Phys.Rev.Lett.* 100:131802, 2008, doi:10.1103/PhysRevLett.100.131802, arXiv:0711.2713 [hep-ex].

[17] J. P. Lees et al., (BABAR collaboration), "Observation of Time Reversal Violation in the B^0 Meson System", 2012, arXiv:1207.5832 [hep-ex].

[18] S. Antusch, E. Arganda, M. J. Herrero, and A. M. Teixeira, "Impact of theta(13) on lepton flavour violating processes within SUSY seesaw", *JHEP* 11:090, 2006, arXiv:hep-ph/0607263.

[19] E. Arganda and M. J. Herrero, "Testing supersymmetry with lepton flavor violating tau and mu decays", *Phys. Rev.* D73:055003, 2006, hep-ph/0510405.

[20] L. Calibbi, J. Jones-Perez, and O. Vives, "Electric dipole moments from flavoured CP violation in SUSY", *Phys. Rev.* D78:075007, 2008, doi:10.1103/PhysRevD.78.075007, arXiv:0804.4620 [hep-ph].

[21] L. Calibbi et al., "FCNC and CP Violation Observables in a SU(3)-flavoured MSSM", 2009, arXiv:0907.4069 [hep-ph].

[22] P. Paradisi, "Higgs-mediated $\tau \to \mu$ and $\tau \to e$ transitions in II Higgs doublet model and supersymmetry", *JHEP* 02:050, 2006, hep-ph/0508054.

[23] E. Arganda, M. J. Herrero, and J. Portoles, "Lepton flavour violating semileptonic tau decays in constrained MSSM-seesaw scenarios", *JHEP* 06:079, 2008, doi:10.1088/1126-6708/2008/06/079, arXiv:0803.2039 [hep-ph].

[24] M. J. Herrero, J. Portoles, and A. M. Rodriguez-Sanchez, "Sensitivity to the Higgs Sector of SUSY-Seesaw Models in the Lepton Flavour Violating $\tau \to \mu f_0(980)$ decay", *Phys. Rev.* D80:015023, 2009, doi:10.1103/PhysRevD.80.015023, arXiv:0903.5151 [hep-ph].

[25] H. K. Dreiner, M. Kramer, and B. O'Leary, "Bounds on R-parity violation from leptonic and semi- leptonic meson decays", *Phys. Rev.* D75:114016, 2007, doi:10.1103/PhysRevD.75.114016, arXiv:hep-ph/0612278.

[26] M. Blanke, A. J. Buras, B. Duling, A. Poschenrieder, and C. Tarantino, "Charged Lepton Flavour Violation and $(g-2)_\mu$ in the Littlest Higgs Model with T-Parity: a clear Distinction from Supersymmetry", *JHEP* 05:013, 2007, arXiv:hep-ph/0702136.

[27] M. Raidal et al., "Flavour physics of leptons and dipole moments", 2008, arXiv:0801.1826 [hep-ph].

[28] LHCb Upgrade Collaboration, "Letter of intent", https://twiki.cern.ch/twiki/pub/LHCb/LHCbUpgrade/LOI.pdf.

[29] LHCb Collaboration, "Search for the lepton flavour violating decay $\tau^- \to \mu^+\mu^-\mu^-$", May 2012, LHCb-CONF-2012-015.

[30] D. Delepine, G. Lopez Castro, and L. T. Lopez Lozano, "CP violation in semileptonic tau lepton decays", *Phys. Rev.* D72:033009, 2005, arXiv:hep-ph/0503090.

[31] I. I. Bigi and A. I. Sanda, "A 'known' CP asymmetry in tau decays", *Phys. Lett.* B625:47–52, 2005, hep-ph/0506037.

[32] D. Delepine, G. Faisel, and S. Khalil, "SUSY R parity violation and CP asymmetry in semi-leptonic tau-decays", *Phys. Rev.* D77:016003, 2008, doi:10.1103/PhysRevD.77.016003, arXiv:0710.1441 [hep-ph].

[33] A. Datta, K. Kiers, D. London, P. J. O'Donnell, and A. Szynkman, "CP violation in hadronic tau decays", *Phys. Rev.* D75:074007, 2007, hep-ph/0610162.

[34] K. Kiers et al., "CP violation in $\tau \to K\pi\pi\nu_\tau$", *Phys. Rev.* D78:113008, 2008, doi:10.1103/PhysRevD.78.113008, arXiv:0808.1707 [hep-ph].

[35] D. Kimura, K. Y. Lee, T. Morozumi, and K. Nakagawa, "CP violation of $\tau \to K\pi(\eta,\eta')\nu$ decays", 2008, arXiv:0808.0674 [hep-ph].

[36] D. Kimura, K. Y. Lee, T. Morozumi, and K. Nakagawa, "CP violation in tau decays", 2009, arXiv:0905.1802 [hep-ph].

[37] M. Bischofberger et al., (Belle collaboration), "Search for CP violation in $\tau \to K^0_S\pi\nu_\tau$ decays at Belle", *Phys.Rev.Lett.* 107:131801, 2011, arXiv:1101.0349 [hep-ex].

[38] J. Lees et al., (*BABAR* collaboration), "Search for CP Violation in the Decay $\tau^- \to \pi^- K^0_S \nu_\tau$", *Phys.Rev.* D85:031102, 2012, doi:10.1103/PhysRevD.85.099904, 10.1103/PhysRevD.85.031102, arXiv:1109.1527 [hep-ex].

[39] I. Bigi, "'Ceterum censeo Fabricam Super Saporis esse faciendam' ('Moreover I advise a Super-Flavour Factory has to be built')", pp. 134-148, 2008, arXiv:0804.4612 [hep-ph].

[40] G. A. Gonzalez-Sprinberg, J. Bernabeu, and J. Vidal, "τ electric dipole moment with polarized beams", 2007, arXiv:0707.1658 [hep-ph].

[41] J. Bernabéu, G. A. Gonzalez-Sprinberg, and J. Vidal, "CP violation and electric-dipole moment at low energy tau production with polarized electrons", *Nucl. Phys.* B763:283–292, 2007, hep-ph/0610135.

[42] S. Eidelman and M. Passera, "Theory of the tau lepton anomalous magnetic moment", *Mod.Phys.Lett.* A22:159–179, 2007, doi:10.1142/S0217732307022694, arXiv:hep-ph/0701260 [hep-ph].

[43] K. Ackerstaff et al., (OPAL collaboration), "An Upper limit on the anomalous magnetic moment of the tau lepton", *Phys.Lett.* B431:188–198, 1998, arXiv:hep-ex/9803020 [hep-ex].

[44] J. Bernabeu, G. A. Gonzalez-Sprinberg, J. Papavassiliou, and J. Vidal, "Tau anomalous magnetic moment form factor at Super B/Flavor factories", *Nucl. Phys.* B790:160–174, 2008, doi:10.1016/j.nuclphysb.2007.09.001, arXiv:0707.2496 [hep-ph].

[45] K. Inami et al., (Belle collaboration), "Search for the electric dipole moment of the tau lepton", *Phys. Lett.* B551:16–26, 2003, hep-ex/0210066.

[46] M. Pospelov and A. Ritz, "Astrophysical Signatures of Secluded Dark Matter", *Phys. Lett.* B671:391–397, 2009, doi:10.1016/j.physletb.2008.12.012, arXiv:0810.1502 [hep-ph].

[47] N. Arkani-Hamed, D. P. Finkbeiner, T. R. Slatyer, and N. Weiner, "A Theory of Dark Matter", *Phys. Rev.* D79:015014, 2009, doi:10.1103/PhysRevD.79.015014, arXiv:0810.0713 [hep-ph].

[48] B. Batell, D. McKeen, and M. Pospelov, "New Parity-Violating Muonic Forces and the Proton Charge Radius", *Phys.Rev.Lett.* 107:011803, 2011, doi:10.1103/PhysRevLett.107.011803, arXiv:1103.0721 [hep-ph].

[49] R. Pohl, A. Antognini, F. Nez, F. D. Amaro, F. Biraben, et al., "The size of the proton", *Nature* 466:213–216, 2010, doi:10.1038/nature09250.

[50] M. Gell-Mann, "A Schematic Model of Baryons and Mesons", *Phys. Lett.* 8:214–215, 1964, doi:10.1016/S0031-9163(64)92001-3.

[51] N. Drenska, R. Faccini, F. Piccinini, A. Polosa, F. Renga, et al., "New Hadronic Spectroscopy", *Riv.Nuovo Cim.* 033:633–712, 2010, doi:10.1393/ncr/i2010-10059-8, arXiv:1006.2741 [hep-ph].

[52] D. M. Asner et al., "Physics at BES-III", 2008, arXiv:0809.1869 [hep-ex].

[53] M. F. M. Lutz, B. Pire, O. Scholten, and R. Timmermans, (PANDA collaboration), "Physics Performance Report for PANDA: Strong Interaction Studies with Antiprotons", 2009, arXiv:0903.3905 [hep-ex].

[54] B. McElrath, "Invisible quarkonium decays as a sensitive probe of dark matter", *Phys. Rev.* D72:103508, 2005, hep-ph/0506151.

[55] B. Aubert et al., (*BABAR* collaboration), "A Search for Invisible Decays of the Upsilon(1S)", *Phys. Rev. Lett.* 103:251801, 2009, doi:10.1103/PhysRevLett.103.251801, arXiv:0908.2840 [hep-ex].

[56] A. Chang et al., (ATIC collaboration), "An excess of cosmic ray electrons at energies of 300–800 GeV", *Nature* 456:362, 2008.

[57] A. A. Abdo et al., (Fermi LAT collaboration), "Measurement of the Cosmic Ray e+ plus e- spectrum from 20 GeV to 1 TeV with the Fermi Large Area Telescope", *Phys.Rev.Lett.* 102:181101, 2009, doi:10.1103/PhysRevLett.102.181101, arXiv:0905.0025 [astro-ph.HE].

[58] O. Adriani et al., (PAMELA collaboration), "An anomalous positron abundance in cosmic rays with energies 1.5-100 GeV", *Nature* 458:607–609, 2009, doi:10.1038/nature07942, arXiv:0810.4995 [astro-ph].

[59] B. Batell, M. Pospelov, and A. Ritz, "Probing a Secluded U(1) at B-factories", *Phys.Rev.* D79:115008, 2009, doi:10.1103/PhysRevD.79.115008, arXiv:0903.0363 [hep-ph].

[60] R. Essig, P. Schuster, and N. Toro, "Probing Dark Forces and Light Hidden Sectors at Low-Energy e+e- Colliders", *Phys.Rev.* D80:015003, 2009, doi:10.1103/PhysRevD.80.015003, arXiv:0903.3941 [hep-ph].

[61] J. D. Bjorken, R. Essig, P. Schuster, and N. Toro, "New Fixed-Target Experiments to Search for Dark Gauge Forces", *Phys.Rev.* D80:075018, 2009, doi:10.1103/PhysRevD.80.075018, arXiv:0906.0580 [hep-ph].

[62] M. Reece and L.-T. Wang, "Searching for the light dark gauge boson in GeV-scale experiments", *JHEP* 07:051, 2009, doi:10.1088/1126-6708/2009/07/051, arXiv:0904.1743 [hep-ph].

[63] S. L. Glashow, J. Iliopoulos, and L. Maiani, "Weak Interactions with Lepton-Hadron Symmetry", *Phys. Rev.* D2:1285–1292, 1970.

[64] M. Kobayashi and T. Maskawa, "CP Violation in the Renormalizable Theory of Weak Interaction", *Prog. Theor. Phys.* 49:652–657, 1973.

[65] I. I. Bigi, "B0 - anti-B0 mixing: A theoretical evaluation after ARGUS", *Conf.Proc.* C8708101, 1988.

5 Machine Detector Interface and Backgrounds

5.1 Introduction

The Super$B$ experiment consists of a detector and a collider that must be properly interfaced to guarantee optimal operations.

The set of constraints and requirements from both sides is managed by the Machine Detector Interface (MDI).

One of the leading challenges in designing the detector is the background model of the environment in which it will operate since both the large luminosity boost and the substantial emittance decrease with respect to the present generation facilities will put the detector in a dangerous unexplored realm.

In addition to the particles that are the main object of measurement, the detector will also be exposed to particles produced away from the IP that are an unpleasant but unavoidable side effect of the accelerator operations. These particles constitute the machine background. Super$B$ will also detect the particles produced at the IP by QED scattering processes that have cross sections of a few mbarn.

The machine background affecting Super$B$ is mainly the result of an electromagnetic shower initiated by a beam particle hitting the beam pipe somewhere along the ring. The machine lattice can provide stable orbits only for a limited region in phase space around the reference orbit. Either scattering processes occurring at the IP, or Touschek and beam-gas scattering taking place all around the ring can bring a beam particle outside the stability region making it eventually collides with the beam pipe.

In addition to these backgrounds the detector will be also exposed to the risks connected to the intense synchrotron radiation produced by the beams passing through the magnetic elements upstream the IP whose total power (in the kW range) and energy spectrum (spanning from the soft to the hard X-rays) constitute a serious concern for the inner detectors.

Background considerations influence several aspects of the design: readout segmentation, electronics shaping time, data transmission rate, triggering and radiation hardness.

The following sections will describe how these sources are simulated, how their effects on the detectors are mitigated and what is their impact on the subsystems.

5.2 Backgrounds Sources Overview

With the proposed collider design, the primary sources of background are scattering of the following type: radiative Bhabha, pairs production via 2-photon QED interactions, Touschek, and beam-gas. Photons from synchrotron radiation, if properly handled and kept away from sensitive areas, give smaller contributions limited to the innermost detectors (SVT). The heat load due to synchrotron radiation photons striking masks and primaries and secondaries particles hitting the super-conducting magnets must be also carefully evaluated. We have developed a detailed Geant4 based software called `Bruno` that is able to simulate the detector and the beam-line, described from -16 to 16 meters from the IP. `Bruno` has been used to estimate the impact of the different background sources on the operation of the detector. The relevant magnetic and physical elements used in the configuration are the quadrupoles of the final focus doublets closest to the IP and the dipoles of the first bends near the detector. Tungsten shields placed around the cryostat of the final focus super conducting doublet protect the detector on both sides of the interaction region (Sec. 5.3.3).

The background sources described below have been simulated separately with Bruno. The details of the simulated samples are reported in Table 5.1. Touschek scattering, beam scattering with residual gas, and photons from synchrotron radiation do not have an equivalent time because each event is rescaled with a statistical weight obtained from the dedicated simulation used to produce them, as described in Sec. 5.5 and 5.6.

5.3 Radiative Bhabha

Radiative Bhabha scattering $e^+e^- \to e^+e^-\gamma$ is expected to be one the dominant background sources for the detector since it is, along with Touschek scattering, the main mechanism by which beam particles are lost along the machine. Since the rings can provide stable orbits only for particles in a small range of energies (roughly $\pm 1\%$ from the nominal beam energy) the photon radiated by one of the incoming leptons can carry away enough energy to lead to the lepton loss at some point downstream of the IP. The particle loss cross section for this process in Super$B$ is roughly 170 mb [1, 2], that is order of 170 GHz per ring at nominal luminosity. This huge loss rate requires an accurate design of the final focus in order to transport most of these particles far away from the IP and minimize the detrimental effects on the detector. These reasons are a clear motivation to develop a reliable and accurate simulation tool for this kind of process.

5.3.1 Simulation tools

The effects on the detector of particles scattered by the radiative Bhabha processes is studied with Bruno, a Geant4 [3] based simulation program used in conjunction with the BBBREM generator [4]. BBBREM is a Monte Carlo generator which simulates at tree level single bremsstrahlung in Bhabha scattering in the very forward direction. BBBREM correctly takes into account the finite lepton masses, thus providing an accurate description of the angular distribution of the final products. BBBREM takes into account in its matrix element evaluation only the two t-channel Feynman graphs describing the photon emission by initial or final state radiation. This approximation is meaningful because the amplitude of the process is very large for photons emitted nearly parallel to the radiating beam. The typical photon emission angle with respect to the radiating lepton is order of $1/\gamma$ where γ is the Lorentz factor of the incoming radiating lepton. Hence, one expects negligible contributions to the total amplitude coming both from the s-channel Feynman graphs and from the interference terms among graphs describing the emission from the electron and the positron.

The BBBREM generator takes also into account the finite bunch density effect that reduces the radiative Bhabha cross-section. The effect is modeled by setting up an infrared cutoff on the transferred momentum squared (Q_0^2) that depends on the average distance among two electrons/positrons in the colliding section of the bunch.

The BBBREM generator uses the following input parameters:

- Total center-of-mass energy of the incoming e^+e^- system (including the energy spread of the electrons/positrons)
- The photon energy cutoff fraction κ_0. This is a minimum value of the energy fraction (in the CM) carried away by the radiated photon ($\kappa = \Delta E/E$). As the total radiative Bhabha cross-section is infrared divergent a sensitive minimum value needs to be set.
- The number of interactions to be simulated (N_{int}).

The BBBREM code is embedded in Bruno to generate the primaries. The beams nominal parameters at the IP are used to accurately simulate the statistical distribution of the primary vertex position and of the incoming particle momentum spread.

These parameters are also used to calculate the luminosity ($\mathcal{L}$) per bunch crossing. It has been checked that the main backgrounds

Table 5.1: Details of simulated samples for the the background sources: source name, description with parameters, number of events (or bunch-crossing), and equivalent time, if applicable.

Name	Brief description	# of events	Equivalent time
RadBhabha	Radiative Bhabha with $\Delta E/E > 30\%$	15k	66μs
RadBhabhaLowDE	Radiative Bhabha with $5\% < \Delta E/E <$ 30%	20k	88μs
Pairs	2-photon	100k	442μs
Touschek HER	Touschek scattering from HER	90k	N/A
Touschek LER	Touschek scattering from LER	198k	N/A
Beam gas HER	Beam gas scattering from HER	285k	N/A
Beam gas LER	Beam gas scattering from LER	283k	N/A
SyncRad HER	Synchrotron radiation from HER	9.8k	N/A
SyncRad LER	Synchrotron radiation from HER	9.6k	N/A

come from radiative Bhabha events with $\kappa > 0.3$ (High-κ radiative Bhabha). Events with $0.005 < \kappa < 0.3$ (Low-κ radiative Bhabha) give smaller but non-negligible contribution. Both of them have been simulated and considered in the detector studies.

5.3.2 Losses at the beam-pipe

The impact of this source of background extends to the whole detector. A large fraction of the off-energy electrons and positrons hit the downstream beam-line elements producing electromagnetic showers. Low energy particles from these showers hit all of the detector subsystems. An accurate evaluation requires a careful modeling of the final focus which includes the geometry (beam-pipe, magnets, shields, cryostat) and the magnetic field. The interaction of the beams with the material in the final focus produces mainly low-energy electrons and photons. Neutrons with a mean kinetic energy around 1 MeV are also produced via photo-nuclear reactions. Neutrons are produced along the beam line both near the IP and near the bending magnets downstream of the IP. These neutrons build up a neutron cloud that thermalize inside the detector hall for times up to tens of μs, causing delayed background hits at the EMC and IFR, and also affecting the front-end-electronics.

A very useful and efficient approach to understand how the radiative Bhabha background affects the detector is to estimate the particle loss rate along the beam pipe. This information is very valuable to decide where protective shields for the detector (see Sec. 5.3.3) have to be placed before proceeding with more time consuming simulations. The loss rate due to positrons (high-energy-ring or HER) and due to electrons (low-energy-ring or LER) as a function of the Z-coordinate is shown in Figure 5.1 in the region $-3\text{m} < Z < 3\text{m}$ (inside the detector).

Both plots show similar patterns. Only very low-energy (off-energy) particles hit the beam pipe near the interaction region. The contribution to the losses from higher energy particles increases far away the IP. The loss structure (the different peaks) is due to two effects: the beam-pipe profile (the beam pipe gets wider for higher $|Z|$); and the location of the magnets along the beam-line. Even for the losses occurring inside the Super$B$ detector, the lost particles are quite collimated along the beam-pipe, so the debris generated from them are the ones expected to affect the outer sub-detectors. Some debris produced outside of the detector ($|Z| > 3\text{m}$) produces background by back-scattering with the material around the final focus. Even though the back-scattering probability is small, the large loss cross-section makes this component non-negligible. This justifies the necessity of a model of the final focus up to 16 m from the IP.

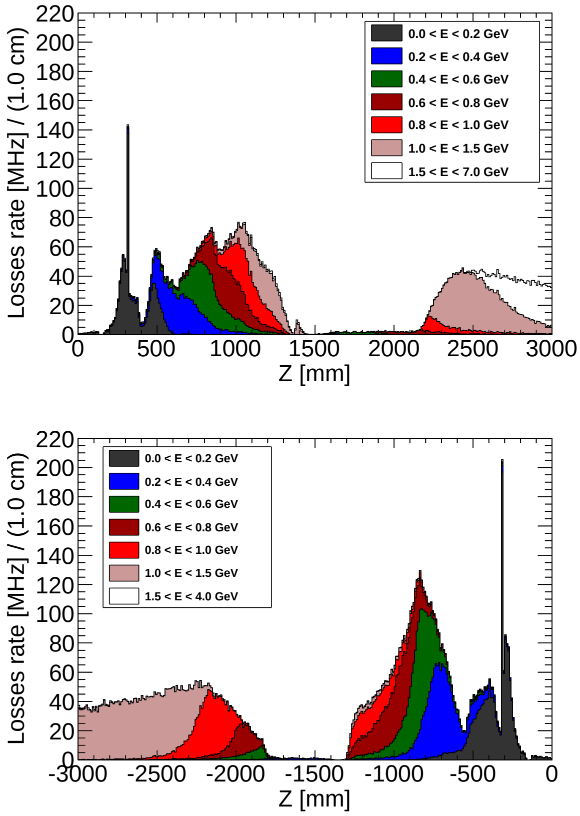

Figure 5.1: Rad-Bhabha loss rate at the beampipe due to positrons (top) and due to electrons (bottom) as a function of the Z coordinate.

Without any shield or mask the Super$B$ detector would be overwhelmed mainly by radiate Bhabha backgrounds. Some shields have been included to reduce this background source, and will be briefly described in the next section.

5.3.3 Shield System

Several types of shields are needed around the hot regions. A tungsten shield (W-shield) surrounds the final focus regions inside the detector. The aim of this shield is to reduce the amount of secondary electrons and photon coming from the interaction of the primary electrons/positrons with the final focus material around IP. The shield consists of two sections. The conical section is 3 cm thick and is as close as possible to the IP ($22 < |Z| < 80$ cm). It does not interfere with the SVT angular acceptance ($\pm$300 mrad). The cylindrical section has a 4.5 cm thickness, which is mainly limited by the geometrical constraints coming from the DCH inner radius and the final focus cryostats outer radius. The cylinder covers the regions $80 < Z < 280$ cm and $-220 < Z < -80$ cm. This thickness is sufficient to reduce backgrounds on the EMC/DCH up to acceptable levels with a reasonable safety margin.

A pair of lead-plugs in the forward and backward regions have been included following a similar design to *BABAR* in order to shield the detector from secondaries produced far away from the IP. All these shields reduce the radiative Bhabha background by a factor of 2–5 in most of the subsystems. The shields tailored for the FDIRC and IFR are described in the corresponding sections.

5.4 Pairs production

During high energy beam-beam interaction, electromagnetic secondary backgrounds are produced from Incoherent Pair Creation (IPC) processes [5], where e^+e^- pairs arise from interaction of both real or virtual photons of each beam with individual particles of the other beam. Three processes are responsible for IPC: the Breit-Wheeler process, in which two real beamstrahlung photons interact, the Bethe-Heitler one, where a real and a virtual photon collide and finally the Landau-Lifschitz (LL) process with two virtual photons. Hence, although almost no beamstrahlung is produced during beam-beam collision at Super$B$, pairs can be created through the processes involving virtual photons, in particular the Landau-Lifschitz one.

A fraction of the pairs are produced with transverse momentum large enough to reach the beam pipe. The large cross section combined with a high collision frequency can lead to an significant background rate that it is necessary to predict wll. Several simulation tools have been used to evaluate the production rate of the e^+e^- pairs and estimate backgrounds in the detector: two versions of the BDK four fermion generator [6], and the GUINEA-PIG++ (GP++) [7, 8] beam-beam interaction code, based on the Weizaecker-Williams approximation for the calculation of the processes involving virtual photons.

5.4.1 Cross section and spectrum comparison

BDK is a Monte-Carlo generator for four-fermion processes in e^+e^- interactions. It is based on complete calculations with leading-order massive matrix elements for all relevant electro-weak diagrams involved. Several adaptations of the initial code have been developed within lepton collider collaborations. For the present study, two of them have been used and compared, one retrieved from the Delphi repository and the other, DIAG36, from the *BABAR* one. The generations are performed in the center of mass of the two mother particles, each with an energy of 5.29 GeV.

GP++ is a beam-beam interaction program developed for high energy e^+e^- linear collider, including several secondary production processes. For the IPC, the three processes described above are calculated using the equivalent photon approximation for the processes involving virtual photons. This approximation treats virtual photons as real ones by convolving an equivalent spectrum for the virtual photons with the cross section for the real-real case. These photons are treated as being real as long as their virtuality remains below an upper limit, above which they are ignored. This limit is set to the half of the invariant mass squared. Once they are produced, the pairs are tracked through the electromagnetic field of the beams until the end of the interaction.

The cross section prediction is about 7.30 mbarn for both BDK simulations, and about 7.74 mbarn for the Landau-Lifshitz process in GP++, which represents 97% of the total IPC, the remainder being produced by the Bethe-Heitler process.

Figures 5.2–5.4 show the energy, transverse momentum and angular distributions of the lepton pairs produced by BDK, DIAG36 and GP++ at the production time. Good agreement can be observed between the three generators.

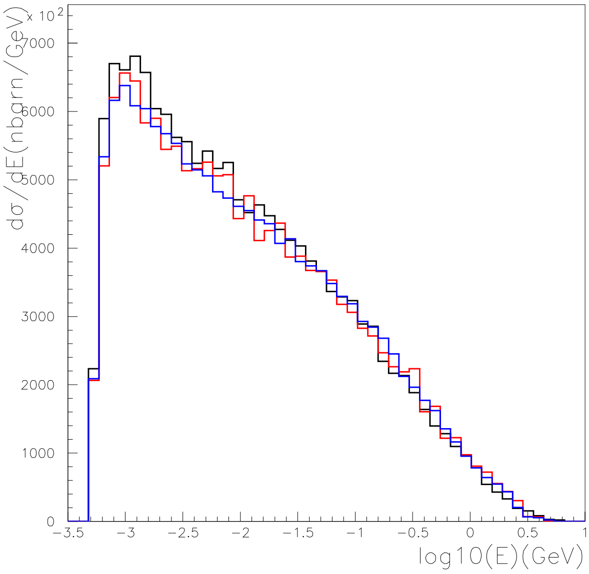

Figure 5.2: Comparison of energy distributions generated with BDK in blue, DIAG36 in red and GP++ in black.

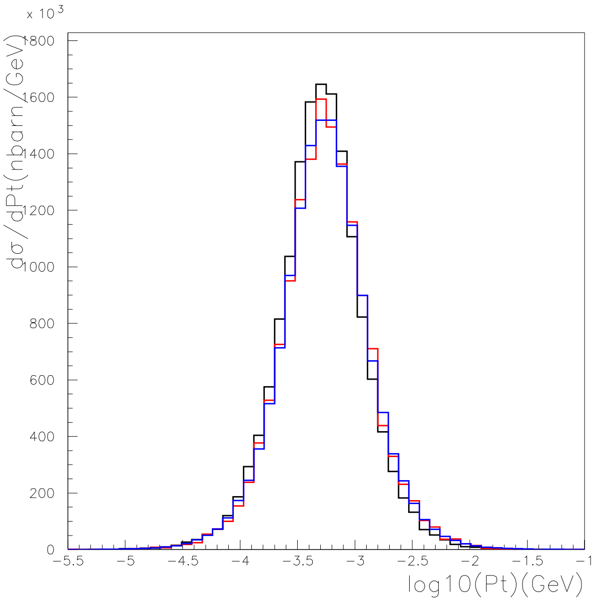

Figure 5.3: Comparison of transverse momentum distributions generated with BDK in blue, DIAG36 in red and GP++ in black.

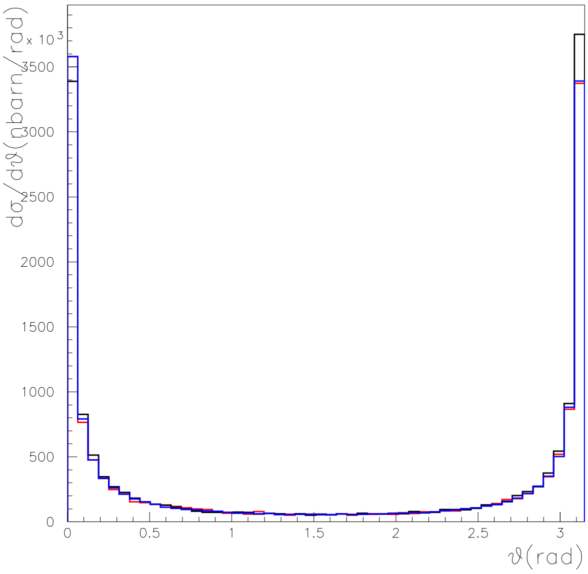

Figure 5.4: Comparison of angular pair distributions generated with BDK in blue, DIAG36 in red and GP++ in black.

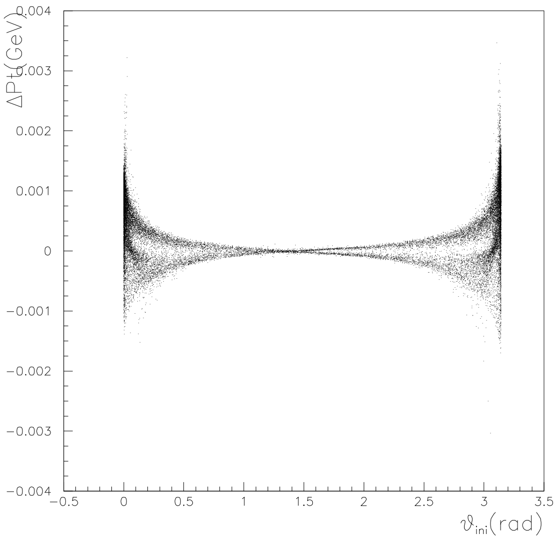

Figure 5.5: Difference between the final and initial transverse momentum as a function of initial angle of the pair particles.

The pairs are produced with a mean energy of 120 MeV and a mean transverse momentum of ≈ 1.5 MeV.

5.4.2 Impact of beam-beam effect on secondaries

Since the pairs are mostly produced at low energy and small angle, they are affected by the electromagnetic field of the oncoming beam, being either focused or defocused according to their charge. The most deflected particles are those produced at very low angle (Figure 5.5) and very low energy (Figure 5.6).

The global impact of electromagnetic deflections is shown on Figure 5.7. The transverse momentum is on average slightly increased of a few hundreds keV.

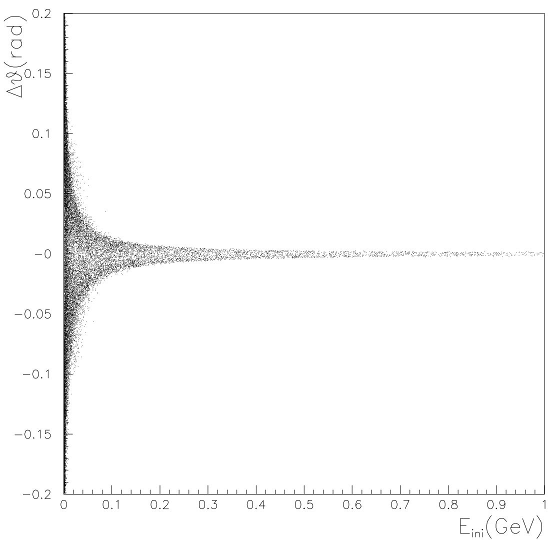

Figure 5.6: Deflection angle as a function of the pair particle energy.

5.4.3 Beam pipe losses

A fraction of the pair particles can reach the beam pipe (BP), whose inner radius is 10 mm.

In a magnetic field, the charged particles move along an helix of a radius $r_0 = 3.33 p_t / B$, r_0 being in meter, p_t in GeV/c and B in Tesla. The rates of particles reaching the beam pipe for a magnetic field of 1.5 T are presented in Table 5.2

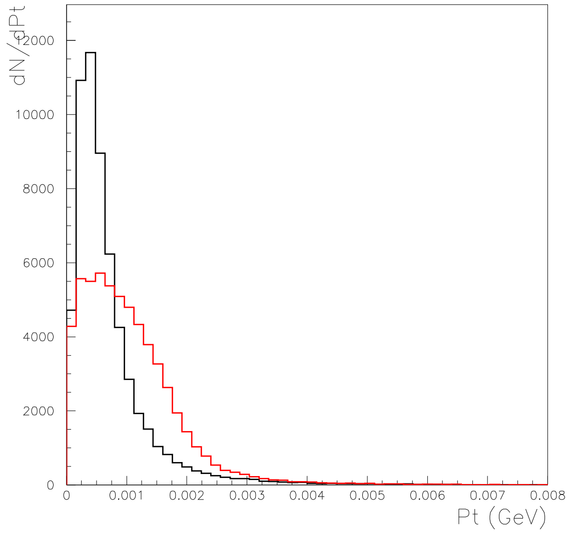

Figure 5.7: Comparison of transverse momentum distributions generated with GP++ at the creation time in black and the end of beam-beam interaction in red.

as obtained from DIAG36 and GP++ simulations, without angular cuts and within the angular acceptance of 100 mrad $< \theta < \pi - 100$ mrad, corresponding to a length of 20 cm. In addition to the Landau-Lifshitz process, the total Incoherent Pairs Creation cross-sections are also listed. The losses in the 20 cm long beam pipe are of the order of 400 MHz. The electromagnetic deflections, affecting the low energy particles produced at low angle, lead to an increase in the rate of around 10%.

5.5 Touschek background

The same ingredients that characterize the crab waist scheme directly affect the Touschek scattering, which is for this reason expected to be relevant for the Super$B$ rings, particularly for the LER. The Touschek effect is Coulomb scattering of charged particles in a stored bunch that induces energy exchange between transverse and longitudinal motions. Small transverse momentum fluctuations lead to larger longitudinal variations, as the effect is amplified by the Lorentz factor. After that, these off-momentum particles can exceed the RF momentum acceptance or they may hit the aperture when displaced by dispersion. In both cases they get lost. The features of the crab waist scheme on which Super$B$ design is based are—with respect to conventional collision schemes—the smaller emittance and the smaller transverse beam sizes, especially at the IP. But the achievement of the high luminosity that this collision scheme can provide is not enough: its use depends also on how well the backgrounds can be controlled. However, some remedies to counteract this effect can be undertaken, such as implementing proper shielding to decrease the impact of backgrounds on the detector performance.

Several studies have been performed to control and reduce the background induced by the Touschek effect together with the beam related lifetime, by means of a numerical code named STAR [9] which has been developed for $DA\Phi NE$[10] and tested with the KLOE data and, more recently, on the crab waist collision scheme [11] .

At the LER and HER of the Super$B$ accelerator, the Touschek Interaction Region (IR) particle losses and lifetime have been optimized numerically by means of a trade-off between critical parameters, such as emittance, bunch current and bunch length. The Touschek scattered particles are simulated from their generation to their loss point in the beam pipe; secondary particles are then propagated through the IR up to all the sub-detectors. LER and HER Touschek simulations have been performed following the lattice evolutions; loss rates and relative lifetime for each new lattice have changed consistently with the lattice developments and the parameters changes. We present here loss rates and lifetimes for the optics design named V12. This lattice has been studied in detail, especially the interaction region, which is essential for the particle losses simulations.

Synchrotron radiation evaluation, beam stay clear constraints, and, mostly important, physical aperture constraints given by the QD0 and QF1 design have been implemented in the IR

Table 5.2: Pair cross sections and estimation of the losses in the beam pipe for a sample of 10^6 events generated with DIAG36 and 3×10^5 with GP++.

	σ_{tot} (mbarn)(GHz)	σ_{BP} (μbarn)(MHz)	σ_{BP} in $\pm 100\ mrad$ (μbarn)(MHz)
DIAG36	7.30 ± 0.03	814 ± 23	430 ± 17
GP++ LL @ creation	7.74 ± 0.29	618 ± 40	346 ± 29
GP++ LL after deflection	7.74 ± 0.29	1027 ± 52	389 ± 31
GP++ IPC @ creation	7.98 ± 0.29	627 ± 40	347 ± 29
GP++ IPC after deflection	7.98 ± 0.29	1052 ± 53	390 ± 31

design, which, in turn, has been implemented in the Touschek simulation. The primary losses at the beam pipe induced by this effect are used for tracking secondaries using a Geant4 detailed model of the Super*B* detector and IR.

The Touschek simulation code is based on the Monte Carlo technique. It has been developed for handling both lifetime and particle losses, which has been very useful for understanding the critical beam parameters and optics knobs. An accurate analysis of the critical positions where Touschek particles are generated—mainly dispersive regions—can be performed, together with the optimization of collimators, both for finding the optimal longitudinal position along the ring and the optimal radial jaw position. IR losses can be studied in detail, like transverse phase space and energy deviation of these off-energy particle losses as a function of different beam parameters, of different optics and for different sets of movable collimators. The generation of the scattering events in the simulation code is done continuously all over the ring. By properly slicing all the elements in the lattice and evaluating the transverse beam size, we obtain a good estimate of the Touschek probability density function along the ring. We have verified that good accuracy is obtained, even in regions where the optical functions change rapidly. We track about 10^6 Touschek scattered macroparticles for a few machine turns; we have checked that five are enough to have stable results. The Touschek lifetime can be evaluated directly from the ratio between the initial number of particles per bunch N and the particles loss rate, $\tau \equiv N/\dot{N}$. A realistic tracking of the off-energy particles includes the main non-linear terms present in the magnetic lattice. Figure 5.8 shows the energy acceptance of the Touschek particles for the two rings for the V12 lattice. The plots represent the loss probability of the Touschek particles as a function of their energy deviation, and each coloured line stands for each machine turn. The energy acceptance found from this technique is in agreement with the one calculated with the MAD [12] program.

The physical aperture is modeled in the simulation code by a circular beam pipe with a radius

Table 5.3: Summary of parameters used for the Touschek simulations for the V12 lattice. Results depend upon horizontal emittance, which is expected to be enlarged by Intra Beam Scattering (IBS) about 40%

	HER	LER
Beam energy (GeV)	6.7	4.18
nominal ϵ_x (nm)	1.97	1.80
ϵ_x with IBS (nm)	2.00	2.46
nominal ϵ_y (pm)	5.00	6.15
particles per bunch	5.08×10^{10}	6.56×10^{10}
number of bunches	978	978
bunch length (mm)	5	5
RF acceptance	0.03	0.04
coupling at full current	0.25%	0.25%

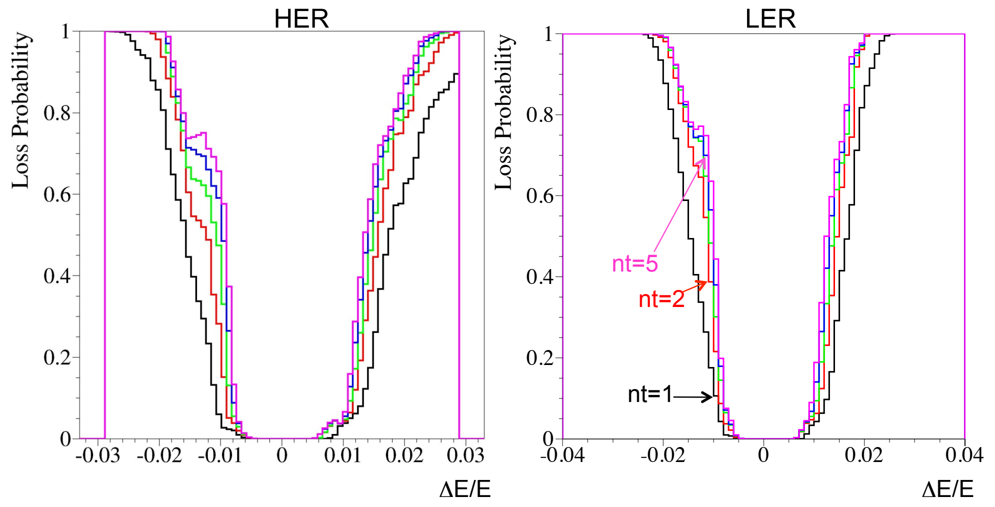

Figure 5.8: Left: Energy acceptance of Touschek scattered particles for the HER (left) and LER (right) for the first five machine turns (nt).

of 2.5 cm everywhere but at the IR, where it is considered elliptical. In fact, in the IR the horizontal and vertical apertures have been carefully evaluated at the QD0 and at the QF1 to allow for a beam-stay-clear of 30 σ_x and 100 σ_y for a full coupled beam. In the simulation code the beam pipe dimensions are given in terms of the aperture that the tracking particles experience through the elements (in figure 5.9 is reported an example for the HER).

The collimator system has been designed to reduce very efficiently IR particle losses to minimize Touschek backgrounds in the experiment. For this source of backgrounds only horizontal collimators are necessary. The collimator system is shown in Figure 5.10 together with the final focus optical functions. The beam direction is from right to left, and 0 m is the IP.

Collimators are modeled in the simulation as perfectly absorbing, and infinitely thin. This is a good approximation, as the closest collimator upstream IP is at −20 m. The primary collimators are in the Final Focus upstream of the IR at −85.8 m and −67.8 m, stopping most of the

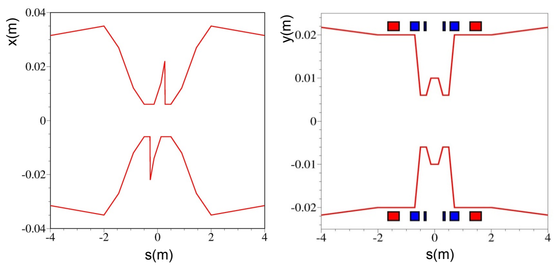

Figure 5.9: The IR dimension experienced by the HER beam moving from left to right.

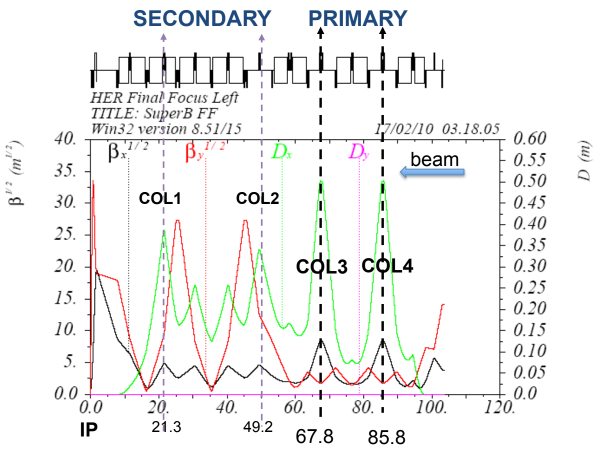

Figure 5.10: Longitudinal position of horizontal collimators upstream the Final Focus. The beam direction is from right to left.

energy-deviated particles that otherwise would be lost at the IR. These two primary collimators are close to two horizontal focusing sextupoles and their location corresponds to a maximum of the dispersion and of the β_x function. The secondary collimators are positioned at -49.2 m and -21.3 m. Simulation indicate that this system is very efficient, reducing IR losses by a factor of about 350 for the HER and about 230 for the LER. This happens at the expenses of Touschek lifetime, which is reduced correspondingly by a factor about 1.2 for the HER and 1.4 for the LER. However, the two horizontal jaws of the collimators have been optimized by simulations to obtain a good trade-off between IR losses and lifetime. Note that the correct position of the jaws will be found experimentally. Also note that in the simulation the orbit is perfectly centered on the beam pipe.

The effectiveness of the collimator system is illustrated in the two lower plots of Figure 5.11, where HER loss distributions are shown without and with the insertion of collimators. The trajectories of the particles that are eventually lost at the IR are shown in the upper plots of Figure 5.11.

The technical solution we propose for the two primary collimators design is to place masks at the two horizontal sextupoles, to intercept the Touschek energy deviated particles that would be lost at the QF1. This is obtained simply by placing masks that give at these locations the same beam stay clear present at QF1. We then propose to add two movable jaws close to these sextupoles as further knobs to tune IR backgrounds.

The trajectories of the Touschek particles that are eventually lost at the IR are shown for the HER (Figure 5.13) and for the LER (Figure 5.12), with a zoomed IR view between -4 m and $+4$ m the IP. Both beams direction in the plots is from left to right, and the physical aperture is the one actually seen by the beam. In this way the actual beam stay clear is taken into account in the tracking simulation. For the LER, the figure shows only the results with collimators. The HER figure shows results both

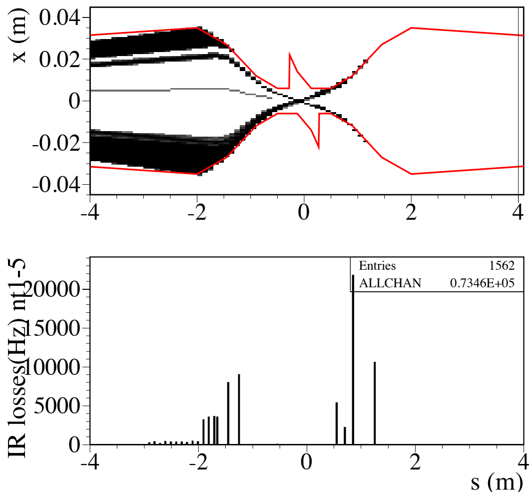

Figure 5.12: LER IR Touschek trajectories with collimators at the optimized locations. Lower plot: corresponding distribution of particle losses at the IR.

and without to illustrate their effectiveness. The simulations also include the vertical collimators optimized for stopping beam gas scattered particles (Sec. 5.6).

The two figures also show the corresponding losses distribution at the IR. These particle losses are tracked into the detector for further investigations. These positions correspond to the locations where Touschek primaries get lost and secondary particles are produced. Figure 5.14 shows the locations in the LER where secondaries are generated.

The background rates seen by the detectors are evaluated by tracking the secondary particles produced by the interaction of the lost primary particles using the full Geant4 simulation. HER and LER particle losses are summarized for the different cases in Table 5.4. Corresponding lifetime predictions are in Table 5.5.

KLOE experiment data and numerical studies have been compared, showing an overall agreement within a factor of two. The shapes of the distributions are well described. The agreement between measured and calculated lifetime with scrapers inserted is good, while the one without scrapers show a disagreement of a factor of

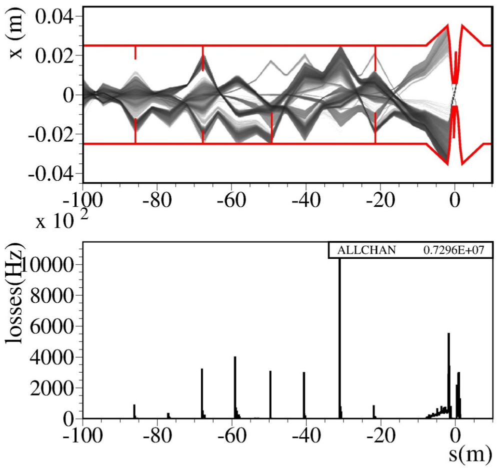

Figure 5.11: Upper plots: HER Touschek trajectories of particles eventually lost at IR without (left) and with (right) collimators. Lower plots: distribution of particle losses in the same region, showing the collimators effectiveness. IP is at 0 m.

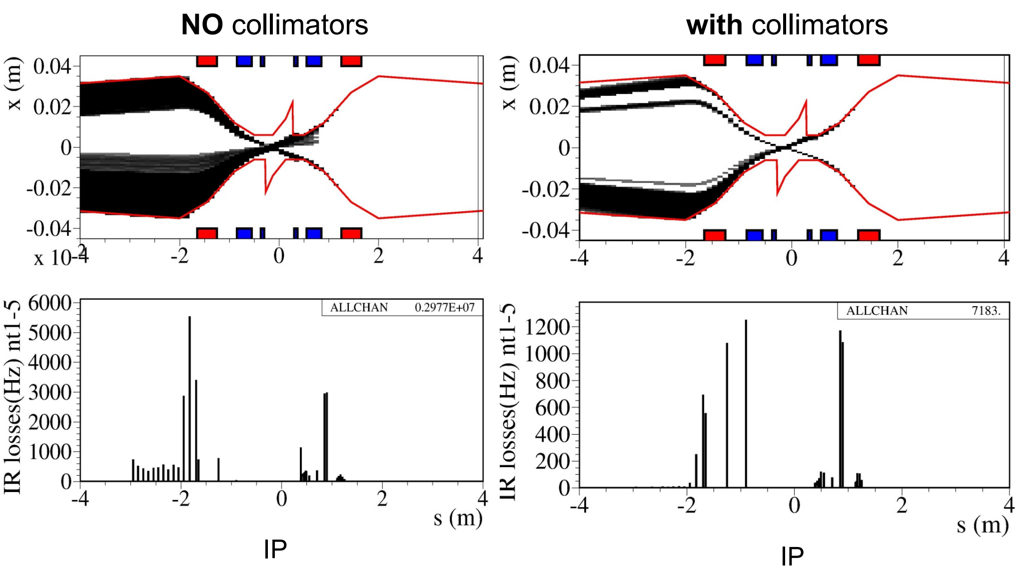

Figure 5.13: Upper plots: HER Touschek trajectories zoomed at the IR without (left plots) and with (right plots) collimators. Lower plots: corresponding distribution of particle losses. IP is at 0 m

Table 5.4: Summary of Touschek particle losses predicted by numerical simulations for the V12 lattice for the HER and LER in the IR within 2 m for the nominal beam current.

	HER	LER
	Loss rate/beam/4m (GHz)	Loss rate/beam/4m (GHz)
no collimators, ϵ_x with IBS	2.4 GHz	17 GHz
with collimators, ϵ_x with IBS	6.8 MHz	72 MHz

Table 5.5: Summary of Touschek lifetimes predicted by numerical simulations for the V12 lattice for the HER and LER.

	HER	LER
	Touschek lifetime (minutes)	Touschek lifetime(minutes)
no collimators, nominal ϵ_x (no IBS)	26	7.4
no collimators, ϵ_x with IBS	26	10.2
with collimators, ϵ_x with IBS	22	7.0

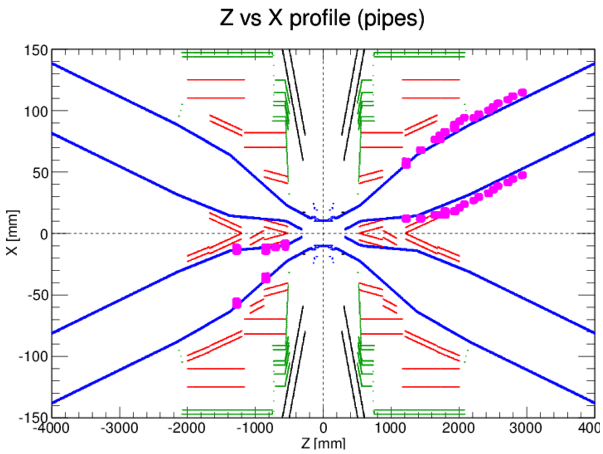

Figure 5.14: x-z profile of the beam pipe and IR with the LER loss position of the Touschek primaries.

two. This could be the result of beam scraping in the opposite ring crossing section; the simulation assumes the beam is perfectly aligned and centered.

To conclude, background rates at the IR due to Touschek scattering are under control with the proposed horizontal collimation system in the final focus. The radiative Bhabha remains the limiting effect for the lifetime. However, LER Touschek lifetime is close to this lower limit, so care has to be paid to this effect and, in particular, to the dynamic aperture. Dedicated simulations have been performed to see the impact of the energy acceptance on the Touschek lifetime. These results have been obtained without tracking, evaluating lifetime while imposing the energy acceptance as input. Figure 5.15 shows the prediction of the LER Touschek lifetime as a function of the energy acceptance for the V12 lattice with emittance enlarged by IBS and with collimators installed. A similar result is obtained for the newer lattice V16. When the IBS effect on emittance is not taken into account, lifetime drops. To have a lifetime larger than 5 minutes, the energy acceptance is required to be larger than 0.9%. This energy acceptance is required even when crab sextupoles are switched on. We remark that earlier optical models have had the crab sextupoles switched off. These calculations show that LER dynamical aperture and energy acceptance are crucial for the LER Touschek lifetime, and that, if not large enough, this single beam effect could be the lower limit for the beam lifetime.

5.6 Beam gas background

Beam gas scattering is a single beam effect that affects lifetime and induces backgrounds in the

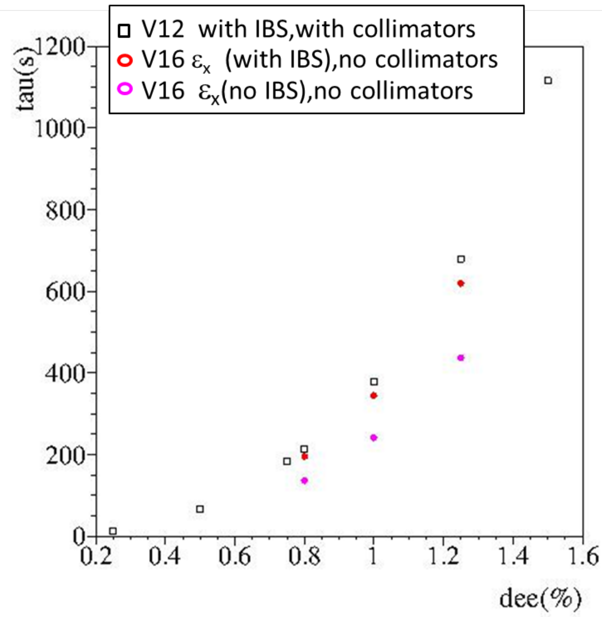

Figure 5.15: LER Touschek lifetime as a function of beam energy acceptance for the V12 lattice (black squares) and V16 (circles).

detectors. At Super*B* this effect has been thoroughly studied with the same Monte Carlo approach used for the Touschek effect. Bunch particles are scattered with the residual gas ions that are present in the vacuum chamber and can get lost. The better the vacuum, the lower will be this effect. However, as a perfect vacuum is not feasible, we need to determine the requirement on the vacuum in order to control lifetime and particle losses at a sustainable level. This beam gas interaction can be elastic or inelastic. In the first case the bunch particle is transversally deflected without losing energy; it increases its betatron oscillation amplitude with the possibility of getting lost, if the gained scattering angle is large enough to exceed the physical aperture or the dynamic aperture. We call this process Coulomb beam gas scattering. In the second case during the scattering with a rest gas atom, the bunch particle also loses energy. Two processes can take place in this case, either Bremsstrahlung, in which the particles emits a photon, or inelastic scattering, in which the bunch particle transfers energy to the atom of the rest gas. Both processes have been included in the inelastic beam gas simulation.

Dedicated Monte Carlo simulations have been performed to evaluate elastic and inelastic scattering, and particle losses and relative lifetime have been found for the V12 lattice. Beam gas scattering is generally estimated from the integrated cross-section, but we have developed a Monte Carlo simulation code that uses the process differential cross-sections and tracks the scattered particles. This technique enables the detailed prediction of the locations where losses occur by hitting the beam pipe, the prediction at which tracking turn these particles are lost and the optimization of a collimator set that intercepts them before they get lost at the IR. As for Touschek simulation, the physical aperture is modeled by a circular beam pipe with a radius of 2.5 cm everywhere but at the IR. In the simulations presented here a constant pressure of 1 nTorr has been assumed, with a gas composition of $Z = 8$.

The bunch particles scattered for the gas Bremsstrahlung process have a behaviour similar to the Touschek particles that lose energy in the scattering. The particles undergoing inelastic scattering are lost by exceeding either the RF bucket or the physical and/or dynamic aperture. We note that when using the integrated cross-section, only the first loss source is taken into account. Although most of the losses happen in the first tracking turn, ten turns have been considered for completeness. The bunch particle that undergoes an elastic scattering increases its betatron oscillation amplitude, so the particle may get lost after some machine turns, as confirmed by the Monte Carlo tracking simulation. The calculated lifetime for the inelastic scattering is in good agreement with the standard integrated cross-section method.

The expected particle loss rates due to elastic beam gas scattering are much higher than the inelastic one, and, accordingly, the lifetime is much shorter (Tables 5.6 and 5.7). This result is an outcome of the crab waist collision scheme, particularly for the small vertical beam size in

Table 5.6: Summary of elastic and inelastic beam gas particle losses for the nominal beam current predicted by numerical simulations for the V12 lattice for the HER and LER in the IR (from -2 m to $+2$ m from IP .

	HER	LER
	Loss rate/beam (MHz)	Loss rate/beam (MHz)
Coulomb no collimators, ϵ_x with IBS	$1.05 \cdot 10^4$	$2.5 \cdot 10^4$
Coulomb with collimators, ϵ_x with IBS	3.7	20
Inelastic no collimators, ϵ_x with IBS	0.6	1.0
Inelastic with collimators, ϵ_x with IBS	0.1	0.4

Table 5.7: Summary of elastic and inelastic beam gas lifetimes predicted by numerical simulations for the V12 lattice for the HER and LER.

	HER	LER
	lifetime (seconds)	lifetime (seconds)
Coulomb no collimators, ϵ_x with IBS	4590	2520
Coulomb with collimators, ϵ_x with IBS	3040	1420
Inelastic no collimators, ϵ_x with IBS	$\sim$ 72hours	$\sim$ 77 hours
Inelastic with collimators, ϵ_x with IBS	$\sim$ 72 hours	$\sim$ 77 hours

QD0 at the IR, which is the hottest location for this process.

Beam gas Coulomb background is proportional to vacuum pressure and to beam current, but also to the betatron function values in the scattering location, as the scattering angle gained by the bunch particles interacting with a residual ion is directly proportional to these values. Therefore, a large fraction of the losses is found to be at QD0 of the IR, corresponding to the maximum β_y position. To cope with this loss source, two vertical collimators have been implemented in the final focus upstream the IR. Only vertical collimators are necessary for this source of backgrounds. However, for a realistic simulation, we have also included the horizontal collimators that intercept Touschek particles.

The collimator system is shown in Figure 5.16, together with the final focus optical functions. The beam direction is from right to left, and the IP is at 0 m. Collimators are modeled in the simulation as perfectly absorbing, and infinitely thin. These two collimators are close to two vertical focusing sextupoles and their location corresponds to a maximum of the β_y function, at about -45 m and -25 m far from IP. Simulation indicates that this system is very efficient, reducing IR beam gas losses by a large factor (Table 5.6). This happens at the expenses of Touschek lifetime, which is reduced by about a factor 1.5 for the HER and 1.8 for the LER. The technical solution we propose for the two vertical collimators is to place masks at the two vertical sextupoles, which intercept the scattered particles that otherwise would be lost at QD0. This is achieved by masks that give at these locations the same beam stay clear that is present at QD0. We also envisage two movable jaws close to these sextupoles as further knobs to tune IR backgrounds. Examples of the HER trajectories of the beam gas Coulomb scattered particles that are eventually lost at the IR are shown in Figure 5.17.

A zoom of the IR (Figure 5.18) shows the the loss position on the beam pipe of these particles. The full Geant simulation is then used to track the resulting secondaries.

In conclusion, elastic and inelastic beam gas backgrounds have been analyzed in detail, showing that these effects are not the main source. As

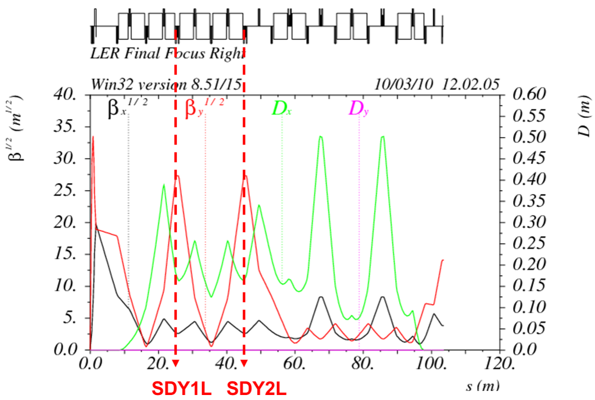

Figure 5.16: Longitudinal position of vertical collimators upstream the Final Focus (red dashed lines). The beam direction is from right to left.

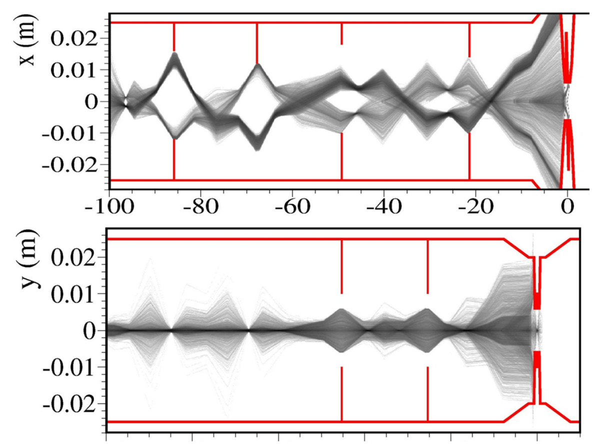

Figure 5.17: Horizontal (upper) and vertical (lower) trajectories of Coulomb gas scattered eventually lost at IR; horizontal (for Touschek) and vertical collimators are inserted

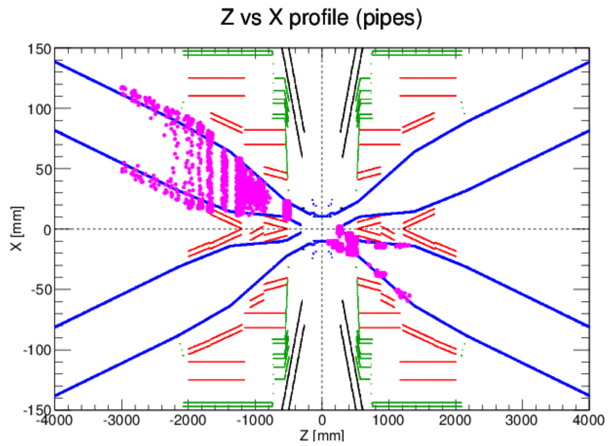

Figure 5.18: HER Coulomb loss particles along the beam pipe at the IR, shown in the horizontal-longitudinal dimensions.

well, the related lifetime is not the limiting one. However, attention has to be paid especially to LER beam gas Coulomb scattering, as the high loss rates expected at QD0 could be dangerous.

5.7 SVT background overview

The background in the detector environment affect the SVT in two separate ways. First, a hit rate higher than the design value can deteriorate the general performances of the tracking system. Second, the silicon layers can be progressively damaged when being exposed to a significant rate of particle for a long period of time. In both cases, accurate simulation of the rates is needed to estimate the performance and the life-span of the SVT.

The main tool used to estimate the rate in the SVT is the simulation of the various background sources using the full simulation described in Sec. 5.3.1.

In the full simulation, the silicon layers are implemented as homogeneous volumes of silicon, and each particle passing through those volumes is recorded, together with additional information about the type of particle, the position, the incident energy, the vector momentum, and the deposited energy. The simulation is not aware of the detector segmentation (strips or striplets).

This choice, even if intensive from the data output point of view, gives us some flexibility in testing different configurations without running the full simulation multiple times. The raw simulation output needs to be further processed to obtain the quantities useful for the tracker design and performance evaluation, such as the rate of "fired" strip per cm^2, the radiation dose, and the 1 MeV neutron equivalent fluence.

A specific application has been develop to analyze the simulation output and produce the relevant quantities and plots. Due to the similarities with other sub-systems, this application has been also extended using multiple modules to produce the same or similar quantities for other sub-detectors. The basic information in the simulation output corresponds to a single step of the particle in GEANT4. A crossing of the volume is defined as a particle entering and exiting the volume once, or as a particle entering the volume and destroyed inside, or as a particle created inside the volume and then exiting, or as a particle created and destroyed inside. Each crossing has a well-defined starting and end point, an incident energy, and a deposited energy. Assuming a specific pitch of the strips (or striplets) in each layer, and approximating the trajectory of the particle with a straight line from the starting point to the end point, we can compute the number of strips (or striplets) crossed by the particle in both directions. Counting the number of strips (or striplets) crossed in all the simulated events, and rescaling by the event frequency, gives a measurement of the rate for each silicon module. Figure 5.19 shows the rate in Layer0, with the different background sources reported separately and summed together.

The rate variations observed as a function of the position can be explained with geometrical or topological considerations. For all the layers the largest contribution to the background in the tracker is given by the pairs production process, where the particles hitting the silicon are coming directly from the IP. This contribution ranges from $\approx 80\%$ for the innermost layer to $\approx 50\%$ for the outermost one. The production of secondaries with low transverse momentum is

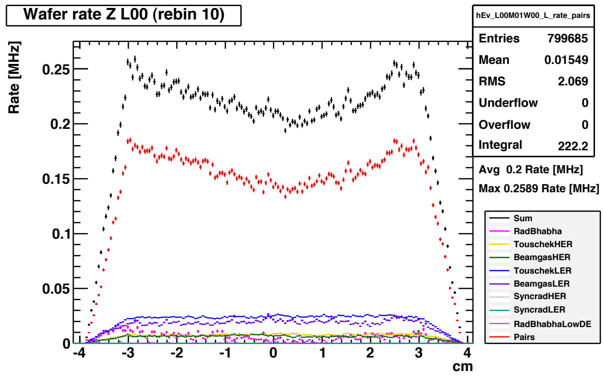

Figure 5.19: Hit rate for the striplet Layer0 option as a funcion of the longitudinal position. The contributions from different background is represented in color code and explained in the legenda.

highly favoured for this process, and the detector magnetic field prevents those particles from reaching the outer layers. The rate is quite high, but it is substantially irreducible, given that it scales with the luminosity and no shielding can be added in between the IP and the SVT.

Together with the strip rate, we can easily compute also the crossing multiplicity and the distribution of deposited energy per strip. All those data are a fundamental input for getting a reliable simulation of the readout electronics, as detailed in Sec. 6.6.4. A similar approach can be used also for the other relevant variables: summing together the deposited energy by all the crossings and dividing by the module mass, we have an estimation of the total ionizing radiation dose; knowing the path length in the volume and the incident energy for each particle, we weight each crossing to get the equivalent damage produced by 1 MeV neutrons [13]. Then, using the appropriate rescaling, we compute the integrated radiation dose, and the fluence by equivalent 1 MeV neutrons after 10 ab^{-1} of collected data. Using previous data or irradiating in a short time a test module with an equivalent amount of particles, we can estimate the deterioration of the tracker performance after a tenth of its designed running period.

Additional details on the impact of the background on the tracker performance can be found in Chap. 6.

5.8 DCH background overview

Background processes are responsible for the largest part of the DCH rate. A rate higher than the design level would affect the charged track reconstruction efficiency and resolution. Additionally, the DAQ electronics can be progressively damaged when being exposed to a significant rate of particle for a long period of time. In both cases, accurate simulation of the rates is needed to estimate the real performances and the life-span of the DCH electronics.

The main tool used to estimate the rate in the DCH is the simulation of the various background sources, described above, using the full simulation described in detail in Sec. 5.3.1. In the full simulation, the gas chamber is implemented as an homogeneous volume with a density corresponding to a weighted value including the gas and the wires. The chamber structure is described accurately including carbon fiber inner and outer wall plus the end-caps with appropriate density. Three silicon plates are included on the backwards side to simulate the amount of material corresponding to the front-end electronics. Each particle going through the gas volume and the silicon plates is recorded, together with additional information about the type of particle, the position, the incident energy, the vector momentum, and the deposited energy. The simulation is not aware of the internal wire structure: this allows us to simulates background events faster, and rates can be computed in each layer for different wire configurations in a post-simulation analysis. The post-simulation analysis also evaluates the radiation dose, the equivalent fluence of 1 MeV neutrons, and fluences of different kind of particles in the plates representing the DAQ electronics.

A specific application has been develop to analyze the simulation output and produce the relevant quantities and plots. Due to the similarities with other sub-systems, this application has been also extended using multiple modules that produce the same or similar quantities, as already described in Sec. 5.7. A given wire structure is provided to the application, with all the information on the cell size and the eventual stereo angles. The application automatically creates a table where the deposited energy is stored for each cell. Given the long path, the curvature of charged tracks in the solenoidal magnetic field cannot be neglected. For each charged track crossing the gas chamber, the helix parameters are computed and the deposited energy in each crossed cell is added in the table. After going through all of the charged tracks in the event, the table is used to fill a plot with one entry for each layer. The number of cells with deposited energy greater than zero in each layer is added into the corresponding entry. The plot is produced for all the background sources and then rescaled for the cross-section/frequency of each process. At the transverse radius of the DCH the tracks produced by background processes are with good approximation isotropic in the azimuthal angle, so no information is lost when averaging the cells over the same layer.

The impact of the background processes on the DCH performances is discussed in Sec. 7.1.5.

5.9 FTOF background overview

The FTOF background has been studied using the Super$B$ full simulation framework `Bruno` in which the quartz tiles (including the Cherenkov physics) and the MCP-PMTs have been simulated in details. The FTOF layout used for these studies is the one optimized during the selection process of the forward PID device and which was driven by the knowledge to date of the Super$B$ forward region. The background samples generated in each Monte-Carlo production have been analyzed and the rates computed in $\mathrm{kHz/cm^2}$, averaged sector by sector. By convention, the sectors are labelled clockwise seen from the IP, with the sector 0 at the top.

The implementation of the Cherenkov physics using GEANT 4 has been tested by comparing the computed photon rates with an independent computation based only on the particle flux incoming to the FTOF and an estimation from *BABAR* data of the optical photon yield per track. The estimates are in good agreement, given the geometry differences between the *BABAR* DIRC and the Super*B* FTOF.

Figure 5.20 shows the contributions of the different background samples sector by sector. The radiative Bhabha is clearly dominant, representing 70–80% of the total rate. Therefore, a dedicated study based on Monte-Carlo truth information has been done to find the origin of this background. The parent genealogy of each Cherenkov photon hitting the FTOF has been followed up to the first daughter of the original radiative Bhabha particle. Its creation vertex has been histogrammed in the plane $R = \sqrt{x^2+y^2}$ vs. z (Figure 5.21). The rectangle at large radius and $z{\sim}175$ cm corresponds to the FTOF location: about 10% of the background comes from positrons from a radiative Bhabha interaction which hit directly the detector. But the largest contribution ($\sim$50%) comes from particles generated at very low radius about 1 meter away from the IP. They correspond to positrons that have lost a significant fraction of their energy by radiating a photon. They leave the HER nominal trajectory and hit the beam-pipe, producing electromagnetic showers whose end products finally reach the FTOF.

As the dominant source of background is well-localized in space, studies have been done to mitigate its impact. In particular, increasing the width of the Tungsten shield from 3 to 4.5 cm has reduced this contribution by a factor 3 (Figure 5.22).

The dose absorbed by the electronics and the corresponding neutron flux have been estimated as 185 Rad and $1.8 \times 10^{11}\mathrm{n/\,cm^2}$ respectively, for 10^7 s at the Super*B* nominal luminosity of $10^{36}\,\mathrm{cm^{-2}s^{-1}}$. The 1 MeV neutron equivalent fluency is 1.0×10^{11}. These values are quite high but still manageable for front-end boards that have been properly designed.

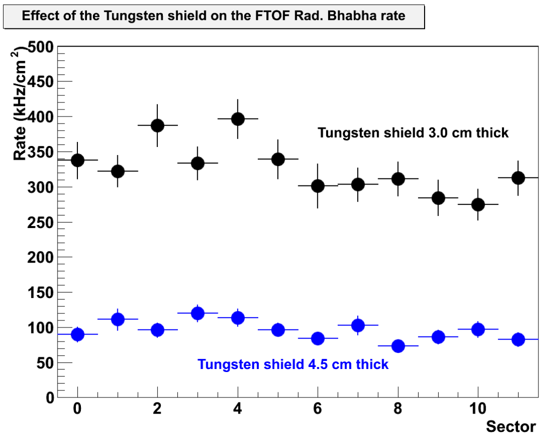

Figure 5.22: Impact of the increase of the width of the Tungsten shield around the beam pipe. Moving from 3 cm (black dots) to 4.5 cm (blue dots) of W made the Rad. Bhabha dominant background rate decrease by almost a factor 3.

5.10 FDIRC background overview

The FDIRC background is mainly due to low energy electrons and positrons that produce Cherenkov light either in the fused silica bars or in the FBLOCK. Some of these photons reach the MaPMT plane where they are detected and combine with the hits coming from the high momentum tracks of the physics events. These low momentum particles are the result of complicated interactions between background primaries and components of the Super*B* detector or machine elements. The primaries come both from luminosity-driven backgrounds, such as radiative Bhabha, and from beam-induced backgrounds, such as Touschek and beam-gas scattering.

As for the other Super*B* systems, the background hits impact the FDIRC in two ways. First, they decrease the performance of the reconstruction algorithm by making the identification of the Cherenkov cones more difficult. More hits mean smaller signal-to-background ratios

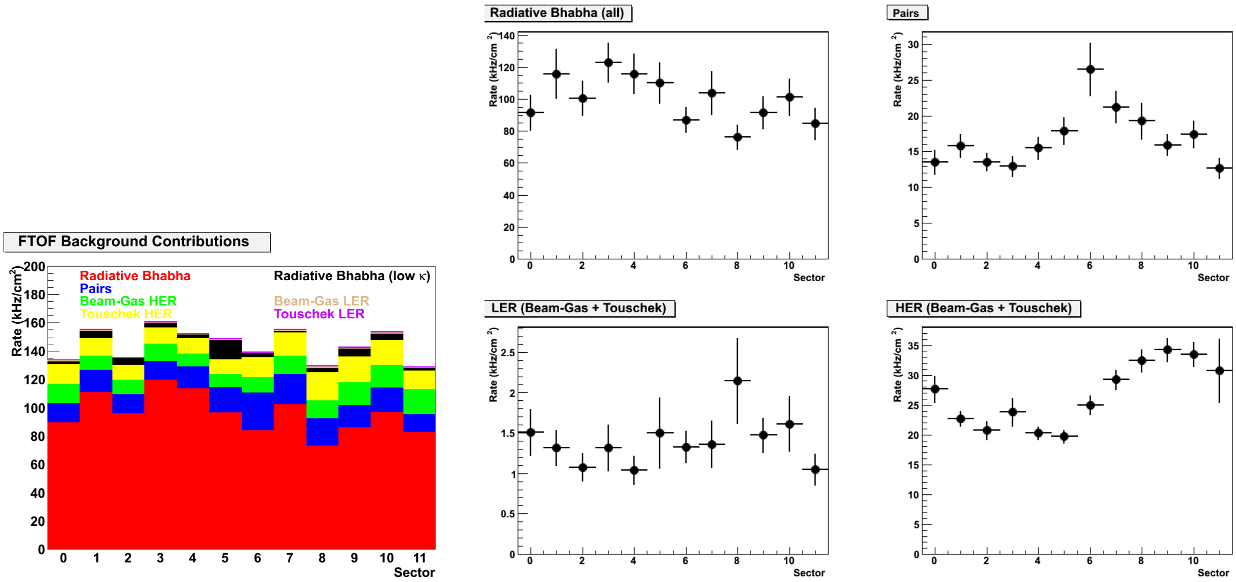

Figure 5.20: Left: contributions of the different background sources to the FTOF rate in each sector; the radiative Bhabha sample (red and black histograms) is clearly dominant. Right: The background rates per sector associated with the four dominant background contributions (radiative Bhabha, Touschek HER, pairs and Touschek LER) are displayed separately.

and more combinatorials. Moreover, real signal photons can be masked by background hits close in time in the same pixel. In addition, the background induces ageing of the FDIRC MaPMTs and front-end electronics.

Therefore, estimating the FDIRC background rates is crucial, not only to validate the choices made at the hardware level but also to define the requirements on the software algorithms. The past experience of the *BABAR* DIRC makes this goal even more important. Less than a year after the beginning of *BABAR* data taking, the DIRC background was significantly exceeding the predictions. The dominant component was few MeV neutrons produced in electromagnetic showers from radiative Bhabha scattering events. These interacted with the SOB water, generating Compton photons which then scattered, producing electrons and positrons finally giving Cherenkov light. A dedicated shield had to be designed to cover the beam line around the *BABAR* backward end-cap. This shield provided a direct reduction of the background by a factor 3 and efficiently protected the DIRC as the PEP-II luminosity rose.

The simulation of the FDIRC background is based on `Bruno` (Sec. 5.3.1), the Super*B* Geant4-based full simulation software. The implementation of the FDIRC hardware components matches the latest design of the detector and has been extensively tested in a dedicated standalone simulation, also based on the `GEANT` framework. The fused silica bars and FBLOCKs have the correct optical properties; the MaPMTs (including the quantum efficiency as a function of the wavelength), mirrors (at the forward bar ends and in the FBLOCKs), and glue joints are simulated as well. Hits on the photon detectors are recorded and stored in ROOT format, along with some truth information about the particles that produced the Cherenkov light. The generation, propagation and detection of the optical photons are completely driven by `GEANT`. Offline, during the analysis phase, the locations of the hits are converted into MaPMT and pixel numbers, taking into account dead areas and the space lost between neighboring photon detectors.

The FDIRC simulation is validated before each major production and dedicated quality

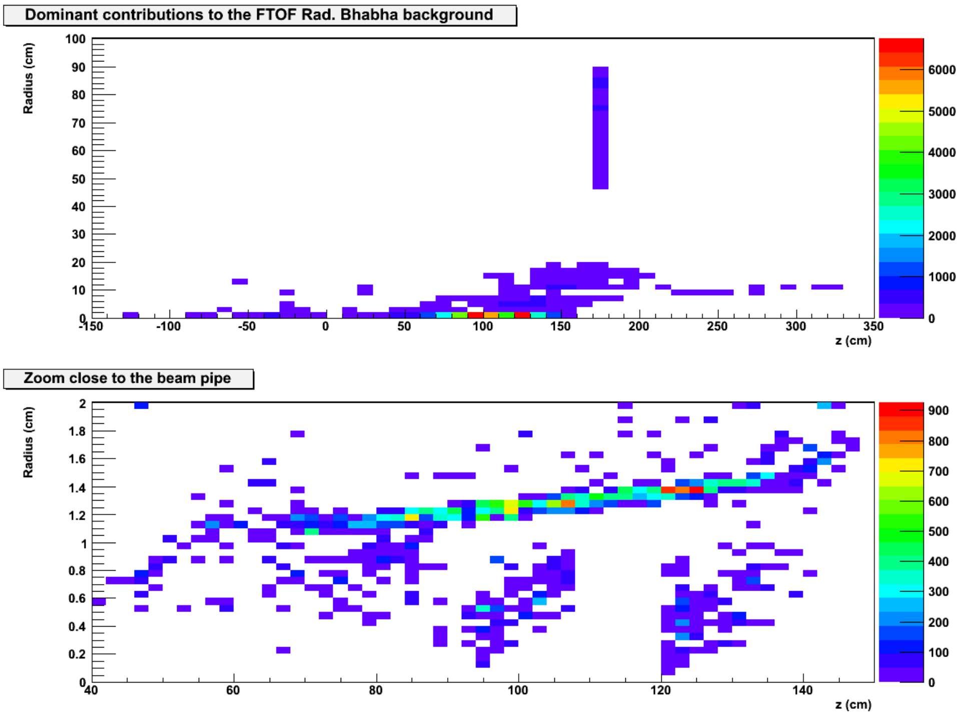

Figure 5.21: Top: distribution in the radius vs. z plane of the decay vertices of the initial radiative Bhabha particles which contribute to the FTOF background. Bottom: zoom of the top map in the low radius region. While about 10% of the background hits originate from radiative Bhabha particles which hit directly the FTOF, the dominant contribution (more than 50%) comes from off-energy positrons which hit the beam-pipe around 1 m away from the IP on the forward side and which generate an electromagnetic shower.

checks are run over the simulated events to test their consistency and track unphysical hits due to mis-modeling of detector components or software issues. This monitoring found, for example, that the simulation of the MaPMT photocathode using BK7 glass was responsible for 10–20% excess hits for the radiative Bhabha background. Changing this material to aluminium made those hits disappear.

5.10.1 Shielding the FDIRC

As explained above, experience based on the *BABAR* DIRC has shown that the FDIRC requires a dedicated shielding to reduce the hit rate. This comes in addition to the design improvements (smaller camera made of quartz instead of water, faster photon detectors and front-end electronics) that aim at mitigating the FDIRC background.

Looking at a side view of the Super*B* detector, the FDIRC can be split into three main regions:

1. $-160\,\mathrm{cm} < z < 220\,\mathrm{cm}$: inside the magnet,
2. $-280\,\mathrm{cm} < z < -160\,\mathrm{cm}$: within the flux return steel, and
3. $-400\,\mathrm{cm} < z < -280\,\mathrm{cm}$: outside the magnet.

The first region cannot include a dedicated FDIRC shielding for obvious reasons. Therefore, its background protection only relies on the W-shield around the beam pipe. The thickness (45 mm) is as large as possible given the maximum allowed weight and the constraints coming from detector integration.

With the W-shielding, simulations show that the dominant background comes from the third region where there is space for a dedicated shield. As the flux of particles entering this area is dominated by photons with energy below 200 MeV, a detailed optimization procedure has lead to the choice of a steel-lead-steel sandwich shielding (2.5-10-2.5 cm-width respectively) which reduces the background by about one order of magnitude. A side effect of this shielding is to roughly double the number of neutrons in this area. Therefore, it is complemented by a 10 cm layer of Boron-loaded (5%) polyethylene.

Without this shielding, the radiative Bhabha events are about one order of magnitude larger than the other background components. This is not the case with the new design, as shown in the following section: most background sources give similar contributions to the total rate.

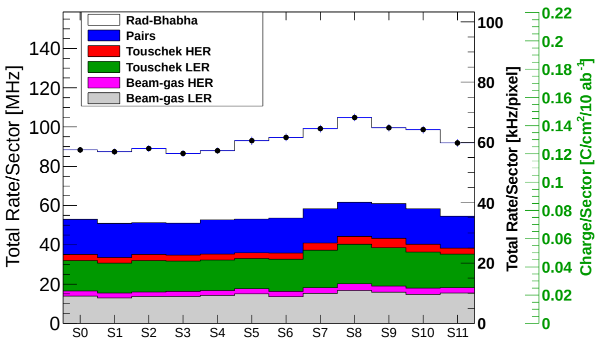

Figure 5.23: Total rates and integrated charge versus sector number on the FDIRC. These rates are the predicted ones and do not include any safety factor.

5.10.2 Background rates in the FDIRC

The backgrounds rates are estimated for each pixel on the focal plane of the FDIRC photo-camera. Simulation shows that the distribution of hits per bunch-crossing within a given sector is rather uniform on the azimuthal angle, but has a small variation with the radius of the pixel location ($R = \sqrt{x^2 + y^2}$), with a maximum around the center of the focal plane. Figure 5.23 shows the total rate of background hits on the FDIRC photo-camera. The horizontal axis labels the FDIRC sectors, counted clockwise as seen from the interaction point. The left-vertical axis shows the total rate on sector and the black right-vertical scale shows the average hit rate per pixel. As can be seen, radiative Bhabha gives the highest background contribution but the other background sources give significant contributions of the same order of magnitude. Also reported on the green right-scale of the plot is the charge integrated on a time period of 10^7 s, which is the time needed to collect 10 ab^{-1} of data at the nominal luminosity (10^{36}Hz/ cm^2). The estimated average hit rate per pixel including a safety factor of 5 is (301.9 ± 1.7) kHz/pixel, which corresponds to an integrated charge of (3.2 ± 0.02) C/ cm^2/(50 ab^{-1}).

5.10.3 Integrated charges and doses

Given the high radiation environment of Super*B*, it is crucial to estimate the amount of ionizing and non-ionizing energy loss (NIEL) on the front-end-electronics (FEE) boards of the FDIRC (Sec. 5.13). In order to accomplish this goal the FDIRC GEANT-4 model includes the FEE boards, which are implemented as 200 μm-thick silicon boards of 34×7 cm^2 area, as specified by the design. Each FDIRC sector has 21 of such FEE boards. Simulations show that there is no variation on the radiation levels within a sector. The numbers reported below correspond then to the total radiation level for each FDIRC sector.

The deposited energy per unit of mass due to ionizing radiation, or dose, is shown on the top plot of Figure 5.24. The horizontal axis labels the FDIRC sector number and the vertical axis is the accumulated dose in krad for every 10 ab^{-1} of integrated luminosity. The color code shows the contribution from the different background sources: radiative Bhabha (white and purple), Touschek from HER/LER (red and green) and beam-gas from HER/LER (magenta and gray). As can be seen, the main radiation source of this kind is radiative Bhabha, the other components giving a negligible contribution. The average dose per sector including a

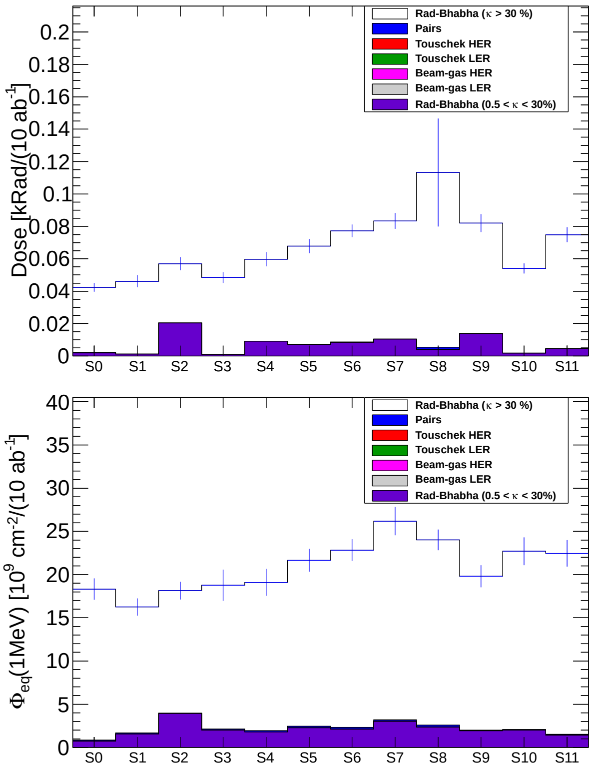

Figure 5.24: Total dose (top) and total equivalent 1 MeV neutron fluency (bottom) per sector on the FDIRC FEE. These rates are the predicted ones and do not include the safety factor of 5.

safety factor of 5 is $(291.2 \pm 5.8)\,\mathrm{rad}/(10\,\mathrm{ab}^{-1})$, which seems to be a bearable level for boards properly designed for the full lifetime of the experiment.

The NIEL is measured in 1 MeV neutron equivalent fluency ($\Phi_{\mathrm{eq}}(1\,\mathrm{MeV}n^0)$). This quantity is the amount of 1 MeV neutrons which would produce the same amount of damage as the actual radiation estimated on the detector, to which particles of different types and energies are contributing. The bottom plot of Figure 5.24 shows the total $\Phi_{\mathrm{eq}}(1\,\mathrm{MeV}n^0)$ for the different FDIRC sectors (horizontal axis). The vertical axis units are $10^9\,\mathrm{cm}^{-2}/(10\,\mathrm{ab}^{-1})$. Again, the dominant contribution to the NIEL are Radiative Bhabha interactions. The average NIEL per sector including a safety factor of 5 is $(10.2 \pm 0.2) \times 10^{10}\mathrm{cm}^{-2}/(10\,\mathrm{ab}^{-1})$, a level within the acceptable range of properly-designed boards.

5.11 EMC background overview.

The main effect of machine background in the EMC is a diffuse energy deposit all over the detector, mainly the result of several low energy deposits per crystal which, given the slow crystal decay time ($\tau \simeq 1.2\mu s$ for the CsI(Tl)) compared to the bunch crossing rate, may result in a significant integrated contribution. The angular (θ) dependence and the overall level for the deposited energy varies with the background source, while the cumulative effect peaks in the forward and backward direction (Figure 5.25).

The Radiative Bhabha background is dominant and determines the shape of the distribution. The sharp change in average deposited energy for the forward EMC (positive θ indexes) between the third and the fourth ring, which is shown by all the background sources, is related to the smaller size of the LYSO crystals whose front face is about $1/4 - 1/5$ with respect to the CsI(Tl) ones in the Barrel and in the outer part of the Endcap. Another geometry related feature is the decrease in energy deposit per crystal for the Barrel-Endcap transition region. This is explained with the fact that the background particles are coming from the beam pipe direction but not directly from the interaction point, so the forward Endcap acts as a shield protecting the above mentioned section of the calorimeter (see Figure 9.1 for a cross section of the relative barrel and Endcap position). Touschek and Beam Gas backgrounds show a similar behaviour.

The sum of all the energy deposit contributions is of the same order as the single Radiative Bhabha one. The maximum difference is the central part of the barrel, the maximum of the Pairs contribution, where a factor of about 2.5 is reached with respect to the single Radiative Bhabha contribution. The mean energy deposit per crystal keeps the peaked shape in the forward and backward directions but, including

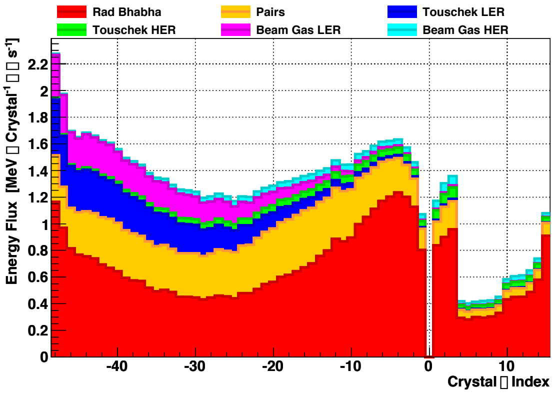

Figure 5.25: Contributions to the total energy deposit rate per crystal vs polar angle (θ) position. Negative indexes are for the CsI(Tl) Barrel crystals, positive indexes are for the forward Endcap which includes three rings of CsI(Tl) crystals in the region close to the Barrel and LYSO crystals in the remaining part; the 0 index corresponds to the Barrel-Endcap transition. The energy deposit shows no dependence on the azimuthal angle.

all the background sources, the maximum of the deposit is in the backward region of the barrel. This shape change is mainly related to the very asymmetric behaviour shown by the Touschek and Beam Gas backgrounds and to the very different rates between the low energy and the high energy rings. It needs to be stressed about the Touschek and Beam Gas backgrounds that, even if their average energy deposit contribution seems almost negligible, the incoming particles energy spectrum is much harder compared to both Pairs and Radiative Bhabha so that, considering only the single energy deposits above 10 MeV, Touschek and Beam Gas rates are comparable with the Radiative Bhabha one. This feature is particularly evident in the forward and backward regions of the barrel and becomes more and more conspicuous for higher deposited energy.

Concerning the effects related to machine backgrounds on the EMC performance, the energy deposited by any particle of physical interest will be superimposed with the diffuse contribution from the backgrounds, whose fluctuations will degrade both the angular and energetic resolution. In addition to this effect, machine backgrounds can create clustered energy deposits which in the reconstruction process may be considered as real particle clusters and therefore spoil the event reconstruction.

In addition to the instantaneous effect of machine background on the event reconstruction, the integrated radiation dose causes a loss of light yield for the scintillating crystals which, if significant, may result in a degradation of the performance. The radiation dose (see Figure 9.16) and the actual impact of the background on the EMC performance which, apart from the overall background level, depends also on the crystal signal processing and on the reconstruction process, are discussed in more details in the dedicated EMC chapter 9.

5.12 IFR background overview

To study the machine related background on the Instrumented Flux Return, the IFR detector has been simulated using Bruno (Sec. 5.3.1.) Radiative Bhabha scattering is the dominant background source for the IFR detector.

All of the background processes produce a high-energy primary $e^{\pm}$ or γ that strikes a beam line element within a few meters of the IP and produces showering secondaries that can be charged or neutral particles with energies ranging from sub-MeV to several tens of MeV. These particles hit the IFR and may affect the detector performance and reduce the photodetector lifetimes.

5.12.1 Neutron Background

In this context there is a non-negligible production of neutrons via giant resonance formation [14]. The neutrons produced with this mechanism have energy of some MeV. These neutrons are moderated by the interaction with the detector material: they scatter back and forth on the nuclei both elastically and inelastically losing energy until they come into thermal equilibrium with the surrounding atoms. At this point they will diffuse through matter un-

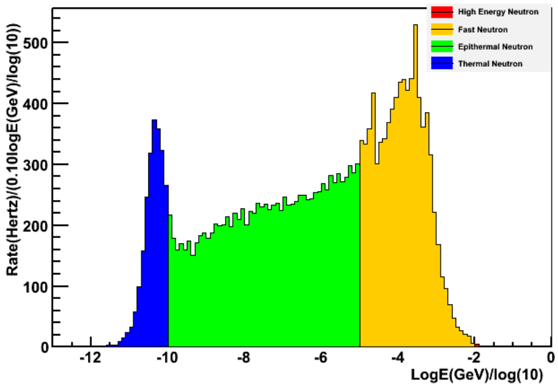

Figure 5.26: Neutron energy spectrum on IFR barrel, the neutron are classified according to their kinetic energy range as high energy neutron, fast, epithermal or thermal.

til they are finally captured by a nucleus. For this reason the neutron energy spectrum in the Super$B$ environment has a very wide range as shown in Figure 5.26, where the neutrons are classified according to their kinetic energy.

Since the neutron spectrum is so wide in energy and the interaction with the matter strongly depends on it, it is customary to characterize the neutron effects in terms of an equivalent mono energetic neutron source [15, 16]. For this reason all the neutron rates in this section are normalized to the equivalent of a 1 MeV neutron.

The neutron background not only contributes to the radiation dose of the IFR detector, but is also particularly dangerous for the SiPM, the devices used for the detector readout, which are quite sensitive to radiation. A fluence of $10^{11} n_{eq}/cm^2$ (n_{eq} is the equivalent number of 1 MeV neutrons on silicon) can severely damaged these devices, producing a loss of efficiency, increasing of dark current, and singles rate [17]). Figure 5.27 shows the neutron rate on layer 0 of the Barrel due to the different background sources, including a safety factor of 5 that takes into account the fact that the simulation may not perfectly reproduce the reality.

The main background source is Radiative Bhabhas. The rate on Barrel layer 0 corresponds to $\sim 6 \times 10^9$ neutrons/ cm^2 for a year. This rate is acceptable for a 10 year run and is the result of the complex shielding system described in Sec. 5.12.3.

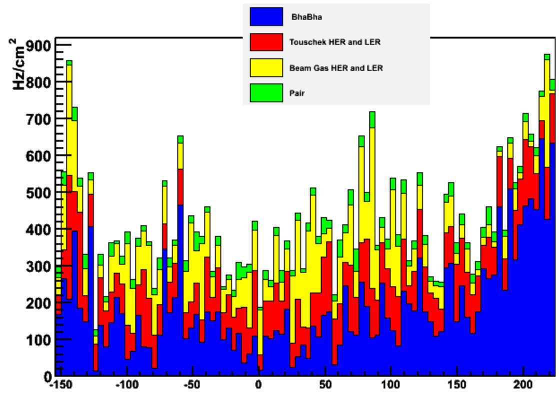

Figure 5.27: Neutron rate on IFR Barrel Layer 0 due to different background sources, normalized to 1 MeV equivalent and multiplied by a safety factor of 5. The different background sources are stacked.

5.12.2 Charged Particles

The background due to charged particles is particularly interesting since it can affect directly the detector performances. It can give fake signals in the detector and affect the track reconstruction and consequently the muon ID. Figure 5.28 shows the rate for electrons and positrons coming from different background sources. As for the neutron case, the dominant source of the background are radiative Bhabha events. The rate shown in Figure 5.28 is for electrons/positrons with energy deposited greater than 150 keV the nominal threshold for the detector.

A high proton rate is observed in the IFR. These protons are produced inside the scintillator in an (n,p) reaction in which the neutron is captured by the scintillator material and a proton is emitted. The cross section for this process falls as $1/v$, so it is more likely to happen when the neutron has low energy. The resulting

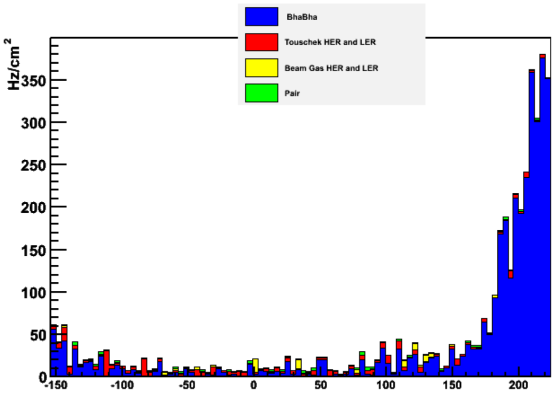

Figure 5.28: Electrons/positron rate for the IFR Barrel layer 0 due to different background sources, multiplied by a safety factor of 5. The deposited energy of the particle is > 150 keV. The different background sources are stacked.

proton has an energy below threshold, and can therefore be neglected.

5.12.3 Background remediation

The rates shown on the previous section are the result of a complex shielding system implemented primarily to significantly reduce the number of neutrons crossing the IFR. Adding shielding material also has the effect of reducing the electron and photon rate. We added a shielding system to the external structure of the IFR and a inner shield to protect the layer 0. The shields are made of Boron Loaded (5%) Polyethylene ($(C_2H_4)_nH_2$). The polyethylene has a high hydrogen density, which slows neutron particles down so they can be absorbed by the Boron. One of the isotopes that comprise natural Boron, B^{10}, has a very high cross section for neutron capture. This shielding design, when implemented in the Super$B$ Full Sim, reduced the neutron rate by an order of magnitude.

5.13 ETD background overview

The high luminosity of the machine and the presence of numerous massive elements close to the interaction region will generate much higher levels of radiation than in *BABAR*, where radiation effects on digital read-out electronics had only been observed after the introduction of FPGAs on the end plate of the drift chamber.

In Super$B$ a large flux of charged particles and photons originating from the interaction point and the beam pipes will cross the detector, and generate large numbers of secondary neutrons as well. Therefore a common general radiation policy has been put in place at the ETD level.

Long term radiation effects are of two types (ionizing and non-ionizing), while short term effects are linked to instantaneous ionization (Single Events). Radiation levels have been simulated, and Total Ionizing Doses (TID) range from 5 kGy down to a few Gy depending on the electronics location. The neutron fluence is required to estimate the effect of the Non-Ionizing Energy Loss (NIEL) and is still under study.

Shielding of sensitive parts of the detector like electronics is a key point of the design, which has been carefully studied. However, all electronics located on the detector have to be able to handle not only the damages linked to TID and NIEL, but also to present minimal sensitivity to Single Event Upsets (SEUs), thanks to the intensive use of mitigation techniques like triple modular redundancy (TMR) for the latches and flip-flops and of safety codes (like parity bits) for data stored in memories. All the components used will be validated for their proven capacity to handle the integrated dose and NIEL foreseen. Power supplies are also designed specifically in order to perform safely in the radiative environment. The architecture of the system has been designed in such a way to reduce as much as possible the risk of failure, especially the critical elements linked to experiment control and readout. In case of failure despite all these precautions, malfunctioning will be detected, experiment control system will be immediately warned, and a fast recovery strategy will be deployed in order to limit as much as possible the dead-time due to these radiation effects.

5.14 SVT radiation monitor

A radiation monitor near the interaction point has been designed to protect the SVT from a high radiation dose and to abort the beam in the presence of a current spike or a prolonged radiation dose. A radiation monitor addresses the following more general issues:

- Allow the protection of the equipment during beam instabilities / accidents;
- Give feedback to the machine, thereby helping it provide optimum conditions; and
- Monitor the instantaneous dose during operation

The primary goal of the SVT radiation-monitoring detector is to measure the interaction rate and the background level in an high radiation environment in order to provide inputs to the background alarm. In addition, it can be used for luminosity measurements and detailed background characterizations during both stable beams and the setting up for collisions. The requirements for a full use of this detector therefore are the following:

- A simple DC (or slow amplification) readout to measure the beam induced DC current.
- Fast electronics with very low noise for detecting minimum ionizing particles and allowing more sophisticated logic coincidences (timing measurements).

The chosen baseline technology is Chemical Vapour Deposition (CVD) diamond sensors[18]. In recent years CVD diamond sensors have been successfully employed as beam monitoring in several experiments: *BABAR* [19], Belle [20], CDF [21], ATLAS [22], CMS [23], LHCb [24], and ALICE [25]. A recent idea is to implement time-of-flight measurements in order to distinguish collision events from background. Very high time resolution (of the order of 100 ps) is required to achieve this goal.

CVD diamond properties Chemical Vapour Deposition (CVD) diamond has a large band-gap (5.5 eV) and a large displacement energy (42 eV/atom) that make it inherently radiation tolerant. It has been extensively tested by the RD42 Diamond Collaboration [26]. The main features of Chemical Vapour Deposition diamonds are:

- Fast timing
- High radiation tolerance (> 1 MGy)
- Single-particle detection and current monitoring capabilities
- Efficiency for charged-particle detection very close to 100%
- 100 pA absorption current for a 500 V applied voltage (low power consumption)
- Leakage current of a few pA, which does not increase with the accumulated dose
- Insensitivity to temperature variations

CVD diamond can be grown on substrate wafers. The deposited films are typically poly-crystalline (pCVD), which have the following drawbacks:

- Many grain boundaries originating defects in the diamond itself
- Non-uniformity of charge-collection properties

Poly-cystalline CVD diamond quality for radiation sensors is typically measured by its charge collection distance (CCD). The CCD is the average separation distance of electron hole pairs under an electric field before they recombine. Current technology allows the growth of pCVD diamonds with CCD of several hundreds of microns. A diamond sensor CCD is dependent on the bias voltage applied to it and increases with the applied bias voltage. For pCVD diamonds, the CCD typically saturates at approximately 1 V per micron.

The development of special substrates allows the homoepitaxial growth of CVD diamond with a mono-crystalline structure (scCVD)[27]. These diamonds offer two major advantages over pCVD diamond. The CCD is substantially larger, ensuring that a nearly fully efficient charge collection is observed, and the maximum charge collection is reached at an applied electric field of 0.2 V/ μm, an order of magnitude lower than poly-crystalline material.

Location of the SVT radiation monitoring The protection system will be made of two rings of CVD diamond sensors placed on opposite sides of the interaction point. Each ring has eight sensors of $4 \times 4\,\mathrm{mm}^2$ dimension. The location of the SVT radiation monitor, between the first silicon layer and the beam pipe, will be between 8 to 12 cm from the interaction point and at about 12 mm from the beam pipe. The available region is very narrow and the read-out electronics need to be placed a few meters away from the detector, making the design of the preamplifier. Figure 5.29 shows a schematic drawing of the read-out system.

Tests at the Tor Vergata INFN laboratory Mono and polycrystalline CVD diamond sensors, purchased by Element Six Ltd[1] have been tested at the Roma Tor Vergata INFN laboratory. The sensors were read-out with three different amplifiers, placed about 4 m away:

[1]Kings Ride Park Kings Ride, Ascot, Berkshire, SL5 8BP, U.K.

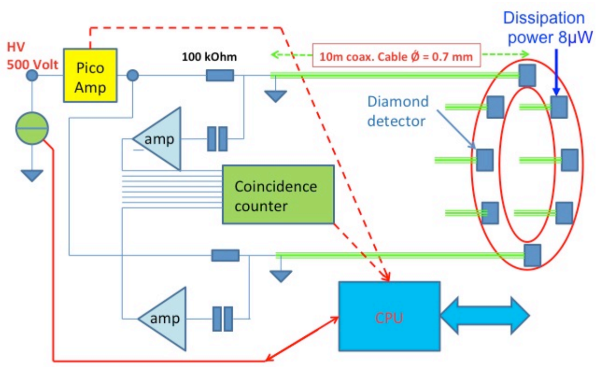

Figure 5.29: Read-out scheme for the SuperB diamond radiation monitor.

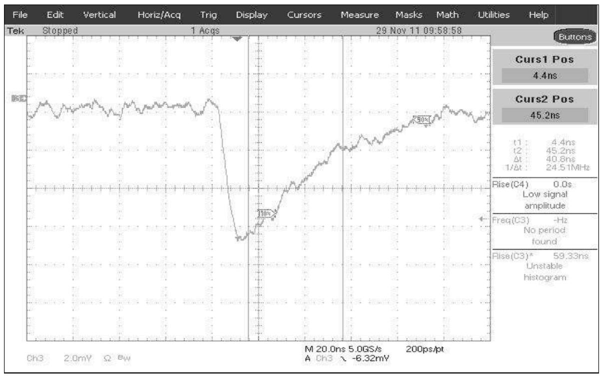

Figure 5.30: Typical signal generated by a minimum-ionizing particle in a CVD diamond detector.

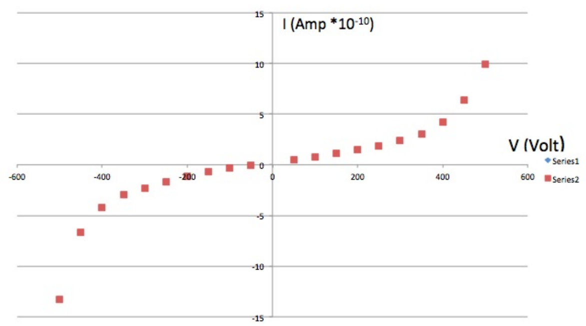

Figure 5.31: I-V curve of a scCVD diamond detector measured with a picoamperometer.

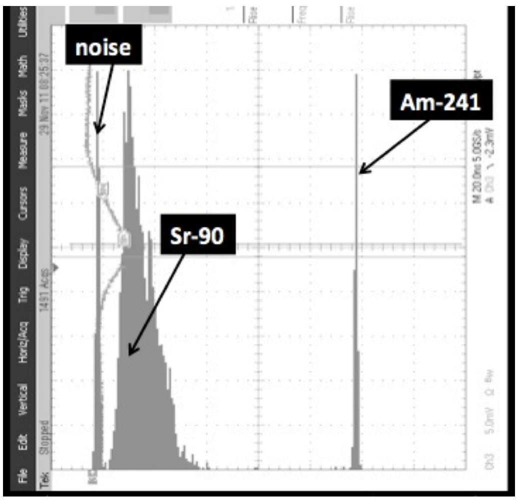

Figure 5.32: 5.5 MeV alpha and electrons signals from a ^{241}Am source and from a ^{90}Str radioactive source respectively, measured with a scCVD diamond sensor.

- Two-stage amplifier, AC, (BJT Si BFQ67)
- AC, (BJT SiGe, BFP650)
- AC, (BJT SiGe, BFP740)

The SiGe transistors have a short transit time in the base because they take advantage of the ballistic effect due to the electric field. This produces an increase in the performance, particularly in the transition frequency, amplification, and noise reduction. The features of the BFP740 amplifier used in the test are:

- Voltage supply: 5 V
- Sensitivity: 6 mV/fC
- Noise: 500 e^- RMS
- Input impedance: 50 Ω
- Band width: 30 MHz
- Power consumption: 10 mW/ch
- Cost: a few €/ch
- Radiation hardness: 50 Mrad, 10^{15} n/cm^{-2}

Figure 5.30 shows an example of a signal from a CVD diamond detector induced by a minimum-ionizing particle. Laboratory tests with ^{241}Am and ^{90}Sr radioactive sources of both mono-crystalline and poly-crystalline CVD diamond sensors gave very promising results in terms of signal-to-noise separation. These amplifiers have already been employed in measurements to read-out CVD diamond sensors for neutron spectroscopy application at the ITER Tokamak project[28]. The detector's signal from radioactive sources has been transported up to the fast charge pre-amplifier by means of a high frequency, single, low attenuation four meters long cable. The preamplifier is able to read, stretch (up to 100 ns) and amplify the small and ultra fast (<100 ps wide) signal produced by the radiation in the diamond detector and has a measured noise of about 500 e^- r.m.s. Figure 5.31 shows the characteristic I-V curve of a scCVD diamond detector measured with a picoammeter. Figure 5.32 shows the signals induced in the scCVD diamond sensor by 5.5 MeV alpha particles from a ^{241}Am radioactive source and electrons from a ^{90}Sr radioactive source. These measurements have demonstrated that adequate performance in terms of SNR can be achieved with the fast high transition frequency SiGe transistor amplifiers.

5.15 Bibliography

[1] M. Bona et al., (Super*B* Collaboration collaboration), "Super*B*: A High-Luminosity Asymmetric e^+e^- Super Flavor Factory. Conceptual Design Report", 2007, arXiv:0709.0451 [hep-ex].

[2] G. Kotkin and V. Serbo, "Beam-size effect and particle losses at Super*B* factory (Italy)", *JINST* 4:P06015, 2009, doi:10.1088/1748-0221/4/06/P06015, arXiv:0903.2907 [hep-ph].

[3] S. Agostinelli et al., (GEANT4 collaboration), "GEANT4: A Simulation toolkit", *Nucl.Instrum.Meth.* A506:250–303, 2003, doi:10.1016/S0168-9002(03)01368-8.

[4] R. Kleiss and H. Burkhardt, "BBBREM: Monte Carlo simulation of radiative Bhabha scattering in the very forward direction", *Comput.Phys.Commun.* 81:372–380, 1994, doi:10.1016/0010-4655(94)90085-X, arXiv:hep-ph/9401333 [hep-ph].

[5] P. Chen, T. Tauchi, and K. Yokoya, "Simulations on pair creation from beam-beam interaction in linear colliders", *Conf.Proc.* C910506:3252–3254, 1991.

[6] F. A. Berends, P. Daverveldt, and R. Kleiss, "Monte Carlo Simulation of Two Photon Processes. 2. Complete Lowest Order Calculations for Four Lepton Production Processes in electron Positron Collisions", *Comput.Phys.Commun.* 40:285–307, 1986, doi:10.1016/0010-4655(86)90115-3.

[7] D. Schulte, Ph. D. Thesis, University of Hamburg 1996. TESLA-97-08.

[8] https://trac.lal.in2p3.fr/GuineaPig.

[9] M. Boscolo and P. Raimondi, "Monte carlo simulation for the touschek effect with the crab-waist scheme", *Phys. Rev. ST Accel. Beams* 15:104201, Oct 2012, doi:10.1103/PhysRevSTAB.15.104201, http://link.aps.org/doi/10.1103/PhysRevSTAB.15.104201.

[10] G. Vignola, S. Bartalucci, M. Bassetti, M. E. Biagini, C. Biscari, et al., "DAPHNE, the Frascati Phi-factory", *Conf.Proc.* C930517:1993–1997, 1993.

[11] C. Milardi, D. Alesini, M. Biagini, C. Biscari, A. Bocci, et al., "Experience with DAFNE upgrade including crab waist", 2009.

[12] H. Grote and F. C. Iselin, "The MAD program (methodical accelerator design) version 8.4: User's reference manual", 1991.

[13] A. Vasilescu (INPE Bucharest) and G. Lindstroem (University of Hamburg), *Displacement damage in silicon*, http://sesam.desy.de/members/gunnar/Si-dfuncs.html.

[14] B. Berman and S. Fultz, "Measurements of the giant dipole resonance with monoenergetic photons", *Rev.Mod.Phys.* 47:713–761, 1975, doi:10.1103/RevModPhys.47.713.

[15] Standard practice for Characterizing Neutron Energy Fluence Spectra in Terms of an Equivalent Mono-energetic Neutron Fluence for Radiation Hardness Testing of Electronics, ASTM E 722 -93.

[16] G. Lindstrom et al., (ROSE Collaboration collaboration), "Developments for radiation hard silicon detectors by defect engineering - Results by the CERN RD48 (ROSE) Collaboration", *Nucl.Instrum.Meth.* A465:60–69, 2000, doi:10.1016/S0168-9002(01)00347-3.

[17] M. Angelone, M. Pillon, R. Faccini, D. Pinci, W. Baldini, et al., "Silicon Photo-Multiplier radiation hardness tests with a beam controlled neutron source", *Nucl.Instrum.Meth.* A623:921–926, 2010, doi:10.1016/j.nima.2010.07.057, arXiv:1002.3480 [physics.ins-det].

[18] W. Adam et al., (RD42 Collaboration collaboration), "New developments in CVD diamond for detector applications", *Eur.Phys.J.* C33:S1014–S1016, 2004, doi:10.1140/epjcd/s2004-03-1798-6.

[19] A. Edwards, M. Bruinsma, P. Burchat, H. Kagan, R. Kass, et al., "Radiation monitoring with CVD diamonds in BABAR", *Nucl.Instrum.Meth.* A552:176–182, 2005, doi:10.1016/j.nima.2005.06.028.

[20] R. S. Wallny, "Status of diamond detectors and their high energy physics application", *Nucl.Instrum.Meth.* A582:824–828, 2007, doi:10.1016/j.nima.2007.07.104.

[21] A. Sfyrla, R. Eusebi, R. Tesarek, P. Dong, C. Schrupp, et al., "Beam Condition Monitoring with Diamonds at CDF", *IEEE Trans.Nucl.Sci.* 55:328–332, 2008, doi:10.1109/TNS.2007.913492.

[22] A. Gorisek, V. Cindro, I. Dolenc, H. Frais-Kolbl, H. Frais-Koelbl, et al., "ATLAS diamond beam condition monitor", *Nucl.Instrum.Meth.* A572:67–69, 2007, doi:10.1016/j.nima.2006.10.348.

[23] L. Fernandez Hernando, D. Chong, R. Gray, C. Ilgner, A. Macpherson, et al., "Development of a CVD diamond beam condition monitor for CMS at the Large Hadron Collider", *Nucl.Instrum.Meth.* A552:183–188, 2005, doi:10.1016/j.nima.2005.06.029.

[24] C. Ilgner, M. Lieng, M. Domke, M. Nedos, J. Sauerbrey, et al., "The Beam Conditions Monitor of the LHCb Experiment", 2010, arXiv:1001.2487 [physics.ins-det].

[25] M. Lechman et al., Protection detectors in ALICE, Proceeding of the 13th International Conference on accelerator and large experimental detector control system, 10-14th October 2011, WTC Grenoble, France, ISSN 2226-0358.

[26] K. Harris et al., RD42 Status Report: Development of Diamond Tracking Detectors for High Luminosity Experiments at the LHC, LHCC-RD-016,CERN-LHCC-2008-005.

[27] J. Isberg, J. Hammersberg, E. Johansson, T. Wikstrom, D. J. Twitchen, et al., "High Carrier Mobility in Single-Crystal Plasma-Deposited Diamond", *Science* 297:1670–1673, 2002, doi:10.1126/science.1074374.

[28] M. Angelone et al., Neutron Spectroscopy by Means of Artificial Diamond Detectors Using a Remote Read Out Scheme IEEE Trans. Nucl. Sci. 57 (2010) 3655–3660.

6 Silicon Vertex Tracker

6.1 Overview

The Silicon Vertex Tracker (SVT), as in *BABAR*, together with the drift chamber (DCH) and the solenoidal magnet provide both track and vertex reconstruction capability for the Super$B$ detector. Precise vertex information, primarily extracted from precise position measurements near the interaction point (IP) by the SVT, is crucial to the measurement of time-dependent CP asymmetries in B^0 decays, which remain a key element of the Super$B$ physics program. In addition, charged particles with transverse momenta lower than 100 MeV/c will not reach the DCH, so for these particles the SVT must provide the complete tracking information.

6.1.1 SVT and Layer0

The above goals where achieved in the *BABAR* detector with a five-layer silicon strip detector with a low mass design, shown schematically in Figure 6.1. The *BABAR* SVT provided excellent performance for the whole life of the experiment, thanks to a robust design [1] that took into account the physics requirements as well as a sufficient safety margin, to cope with the machine background, and redundancy considerations.

The Super$B$ SVT design, shown schematically in Figure 6.2, is based on the *BABAR* vertex detector layout with those modifications needed to operate at an instantaneous luminosity of 10^{36} cm^{-2} s^{-1} or more, and with a reduced center-of-mass boost. In particular the SVT will be equipped with an innermost layer closer to the IP (Layer0) to improve vertex resolution and compensate for the reduced boost at the Super$B$ accelerator, thus retaining an adequate Δt resolution for B decays for time-dependent CP asymmetries. Preliminary studies indicate the same is true for time-dependent mixing and CP asymmetry measurements of charm decays.

Physics studies and background conditions, as explained in detail in the next sections, set stringent requirements on the Layer0 design: radius of about 1.5 cm; resolution of 10-15 μm in both coordinates; low material budget (about 1% X_0); and adequate radiation resistance.

Several options are under study for the Layer0 technology, with different levels of maturity, expected performance and safety margin against background conditions. These include striplet modules based on a high resistivity double-sided silicon detector with short strips, hybrid pixels and other thin pixel sensors based on CMOS Monolithic Active Pixel Sensors (MAPS).

The current baseline configuration of the SVT Layer0 is based on the striplet technology, which has been shown to provide the better physics performance, as detailed in the next sections. However, options based on pixel sensors, which are more robust in high background conditions, are still being developed with specific R&D programs in order to meet the Layer0 requirements (see Section 6.8). These include low pitch and material budget, high readout speed and radiation hardness. If successful, this will allow the replacement of the Layer0 striplets modules in a "second phase" of the experiment. For this purpose, the Super$B$ interaction region and the SVT mechanics will be designed to ensure relatively rapid access to the detector for a replacement of Layer0.

The external SVT layers (1-5), with a radius between 3 and 15 cm, will be built with the same technology used for the *BABAR* SVT (double sided silicon strip sensors), which is adequate for the machine background conditions expected in the Super$B$ accelerator scheme (*i.e.* with low beam currents). Although the SVT module design for layers 1 through 5 will be very similar to that of *BABAR*, albeit with larger solid angle coverage, a completely new readout electronics

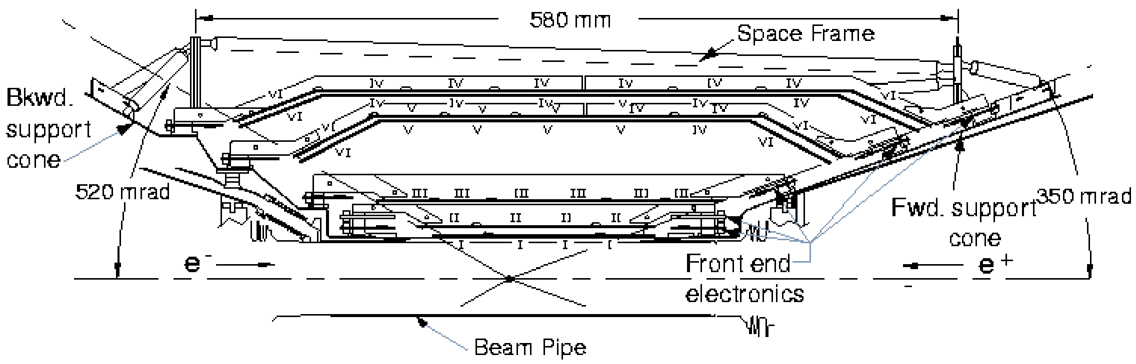

Figure 6.1: Longitudinal section of the *BABAR* SVT.

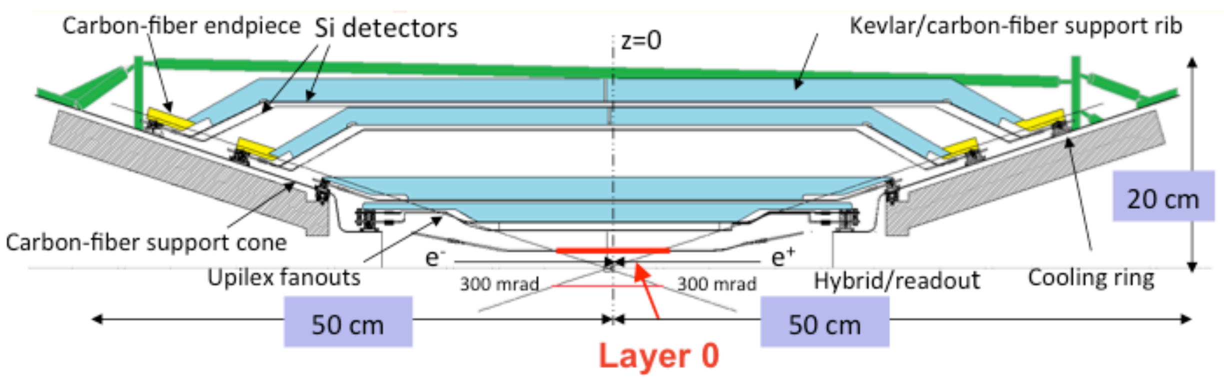

Figure 6.2: Longitudinal section of the Super$B$ SVT.

chain needs to be developed to cope with the higher background rates expected in Super$B$.

A review of the main SVT requirements will be given in the next sections, followed by an overview of the general detector layout. A detailed discussion of all the specific design aspects will be covered in the rest of the chapter.

6.1.2 SVT Requirements

6.1.2.1 Resolution

Without the measurement of the B decay vertex, no useful time-dependent CP asymmetries can be extracted at the $\Upsilon(4S)$. Therefore one of the main goals of the SVT is the determination of the B decay positions, especially along the beam direction (z). Measurements performed in *BABAR*, where the mean separation between B vertices is $\Delta z \simeq \beta\gamma c\tau_B = 250\,\mu$m, demonstrated that good sensitivity to time dependent measurement can be achieved with typical vertex resolution of 50-80 μm in the z coordinate for exclusively reconstructed modes, and 100-150 μm for inclusively modes (tag side in CPV measurements). The reduced Super$B$ boost ($\beta\gamma = 0.24$) with respect to PEP-II ($\beta\gamma = 0.55$) requires an improved vertex resolution, by about a factor of two, in order to maintain a suitable Δt resolution for time dependent analyses.

The *BABAR* resolution was achieved thanks to an intrinsic detector resolution of about 10 μm in the first measured point of the SVT, taken at a radius of about 3 cm, and keeping to the minimum the amount of material between the IP and the first measurement. Multiple scattering affects the resolution on the impact parameter especially for low momentum tracks, and sets a lower limit on the useful intrinsic resolution on the various SVT layers. These correspond to a point resolution of about 10-15 μm for measurements made close to the IP and 30-40 μm for the outer layers [2].

The required improved track impact parameter and vertex resolution can be reached in Super$B$ with the same intrinsic resolution used in *BABAR*, by reducing the radius of the first measured SVT point by a factor of 2 (Layer0 radius at about 1.5 cm) and keeping a very low mass design for the beam pipe and the detector itself.

6.1.2.2 Acceptance

The coverage of the SVT must be as complete as technically feasible, given the constraints of the machine components close to the IP. The SVT angular acceptance, constrained by the Super$B$ interaction region design, will be 300 mrad in both the forward and backward direction. This corresponds to a solid angle coverage of 95% in the e^+e^- center-of-mass (CM) frame, thus increasing the acceptance with respect to the *BABAR* SVT.

There should be as little material as possible within the active tracking volume; minimizing the material between the IP and the first measurement is crucial to reducing the multiple scattering and preserving the impact parameter resolution. The small beam pipe (1 cm radius) requires active cooling with liquid coolant in the detector acceptance to remove the large power deposition due to image beam currents. The total amount of radial material for the actual design of this new beryllium pipe is estimated to be less than 0.5% X_0. Material located beyond the inner layers does not significantly degrade the measurement of track impact parameters, but does affect the performance of the overall tracking system and increases photon conversions in the active region.

6.1.2.3 Efficiency

Our goal is to achieve close-to-perfect track reconstruction efficiency within the active volume of the tracking detectors when information from both the DCH and the SVT is used. The pattern recognition capabilities of the combined tracking system must be robust enough to tolerate background levels up to 5 times the nominal rates, as reported in Table 6.3. Low momentum particles that do not traverse many drift chamber planes, such as many of the charged pions from D^* decays, must be reconstructed in the SVT alone. For this category of tracks, with transverse momentum p_T less than 100 MeV/c, we want to achieve reconstruction efficiencies of at least 80–90%. The SVT must also be efficient for particles such as K_S^0s that decay within the active volume.

The *BABAR* SVT design with 5 layers was optimized to ensure enough redundancy to keep a high tracking efficiency even in the case of failure of some modules or inefficient detectors. The robustness of this choice was demonstrated with the good detector performance over the entire life of the *BABAR* experiment. The Super$B$ SVT design with 6 layers (inserting the Layer0) is inspired by the same philosophy. Simulation studies [3] of a non-perfect/real detector in high background running conditions, indicated that a reduction in the number of layers, from 6 to 5 or 4, yields very modest gains in tracking performance, while showing a sizeable reduction in the reconstruction efficiency for low momentum tracks in D^{*+} decays.

6.1.2.4 Background & Radiation Tolerance

The expected background influences several aspects of the SVT design (segmentation, shaping time, data transmission rates), and sets the requirements for the radiation resistance of the SVT components. The system has been designed to withstand at least 5 times the total expected background rates. Whenever possible, detectors and front-end electronics are specified to be able to survive the entire life of the experiment including a safety factor of 5 on the total dose and equivalent neutron fluence: 7.5 $n_{eq}/\mathrm{cm}^2/\mathrm{yr}\times 5$ yrs at nominal peak luminosity of 10^{36} cm^{-2} s^{-1}.

As described in Section 6.2, the effect of background depends steeply on radius, as shown in Tab. 6.3.

With the high strip rates expected, especially in the inner layers (0-3), the front-end electronics should be fast enough to avoid pulse overlap and consequent hit inefficiency. This requires shaping time in the range 25-150 ns. Furthermore a good time stamp (TS) resolution (30 MHz TS clock) is needed to get a good hit time resolution. The hit time resolution determines the width of the time window cut used in the reconstruction code to accept/reject a hit (offline time window $\simeq 10\sigma_{t-hit}$), and it is then crucial to reduce the offline occupancy to levels acceptable for efficient reconstruction. The offline cluster occupancy in the x5 nominal background scenario, defined as the detector strip occupancy after applying the offline time window cut, divided by the hit multiplicity in a cluster, is on average 2% in each SVT layer. This corresponds to offline time windows of 100-150 ns in layers 0-3, and about 500 ns in layers 4-5, where the longer shaping time is dominating the hit time resolution. See Sections 6.3.5 and 6.6.2 for more details.

In Layer0 the expected integrated dose is about 3 Mrad/yr and the equivalent neutron fluence is about 5×10^{12} $n_{eq}/\mathrm{cm}^2/\mathrm{yr}$ in the sensor area. In the other SVT layers radiation levels are at least one order of magnitude lower: in Layer1 a Total Integrated Dose (TID) $\simeq 0.3$ Mrad/yr and an equivalent neutron fluence of about 8×10^{11} $n_{eq}/\mathrm{cm}^2/\mathrm{yr}$ are expected.

With this expected background in Layer1-5, sensors are proven to be sufficiently radiation hard to survive the entire life of the experiment (with a safety factor 5 included), maintaining acceptable performance, as discussed in Section 6.4.2 and 6.6.2.

For Layer0, where the radiation is an order of magnitude higher, a quick replacement of the entire layer is foreseen, as frequently as necessary, depending on the actual background and the radiation hardness of the technology chosen.

6.1.2.5 Reliability

Although the Super$B$ interaction region and the SVT mechanics will be designed to ensure a relatively rapid access to the detector for replacement of Layer0, access to the SVT is not possible without a major shutdown. The reliability requirements for the SVT are therefore more stringent than usual for such a device, with implications for engineering design at all levels. The detector layout must provide redundant measurements wherever possible; the electronic readout must be very robust, and the functionality of all components must not be compromised by exposure to the expected radiation levels. The detector monitoring and interlock system must serve as a safeguard against major failure in the event of a component malfunction or a human error.

6.1.3 Baseline Detector Concept

6.1.3.1 Technology

The SVT baseline design is based on double-sided silicon microstrip detectors for all layers. The characteristics of this technology that make it attractive for the Super*B* detector are: high precision for measuring the location of charged-particles tracks, tolerance to high background levels, and reduction in mass made possible through double-sided readout. Double-sided silicon detectors have already been employed with success in *BABAR* and in several other large-scale applications, meeting the performance standards outlined above.

6.1.3.2 Layout

The SVT will provide six measurements, in two orthogonal directions, of the positions of all charged particles with polar angles in the region $17° < \theta < 167\,°$. Layer0 has eight detector modules; the rest of the detector keeps the same number modules/layer as in *BABAR*: layers 1-2-3 have six detector modules, arrayed azimuthally around the beam pipe, while the outer two layers consist of 16 and 18 detector modules, respectively. A side view of the detector is shown in Figure 6.2, and an end view is shown in Figure 6.3. A three-dimensional cut-away view of the SVT is shown in Figure 6.4.

The design of the Layer0 striplets module is completely new, and it has quite a complex shape, as shown in Figure 6.5. This is necessary to fit within the 300 mrad acceptance and the very limited space available between Layer1 and the beam pipe. The layout of the other five layers is very similar to the *BABAR* SVT strip modules, shown as a reference in Figure 6.6 and Figure 6.7.

The inner detector modules (layers 0 through 3) are traditional barrel-style structures, while the outer detector modules (layers 4 and 5) employ an arch structure, in which the detectors are electrically connected across an angle. The bends in the arch modules, proven to be functional in *BABAR*, minimize the area of silicon required to cover the solid angle and also avoid very large track incident angles.

In order to satisfy the requirement of minimizing material in the detector acceptance region, one of the main features of the SVT design is the mounting of the readout electronics entirely outside the active detector volume. For this reason signals from the silicon strips are carried to the front-end chips by flexible fanout circuits.

There is a 1 cm space between the 300 mrad stay-clear in the forward and backward directions and the first element of the IR (*i.e.*, the tungsten shield cones) and all of the electronics are mounted here. In both directions, space is very tight, and the electronic and mechanical designs are closely coupled in the narrow region available.

The layout specifications for this six-layer design are given in Table 6.1 and described in more detail in the text.

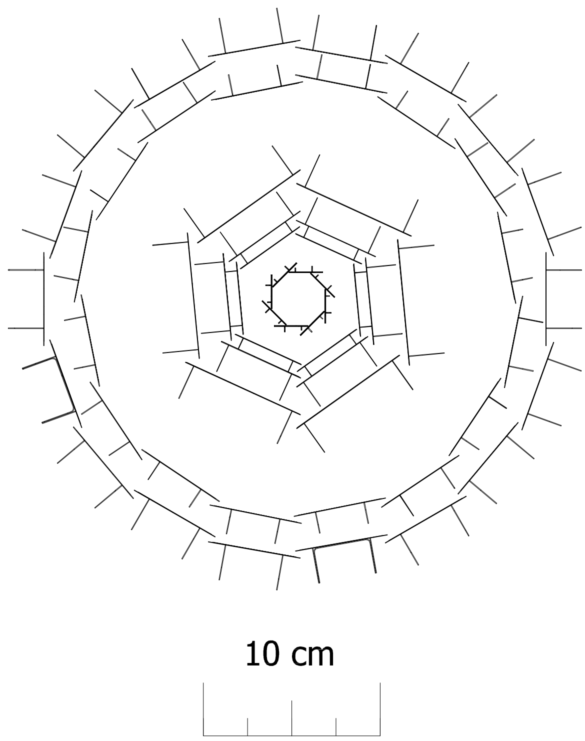

Figure 6.3: Cross section of the SVT in the plane perpendicular to the beam axis. The lines perpendicular to the detectors represent structural support beams.

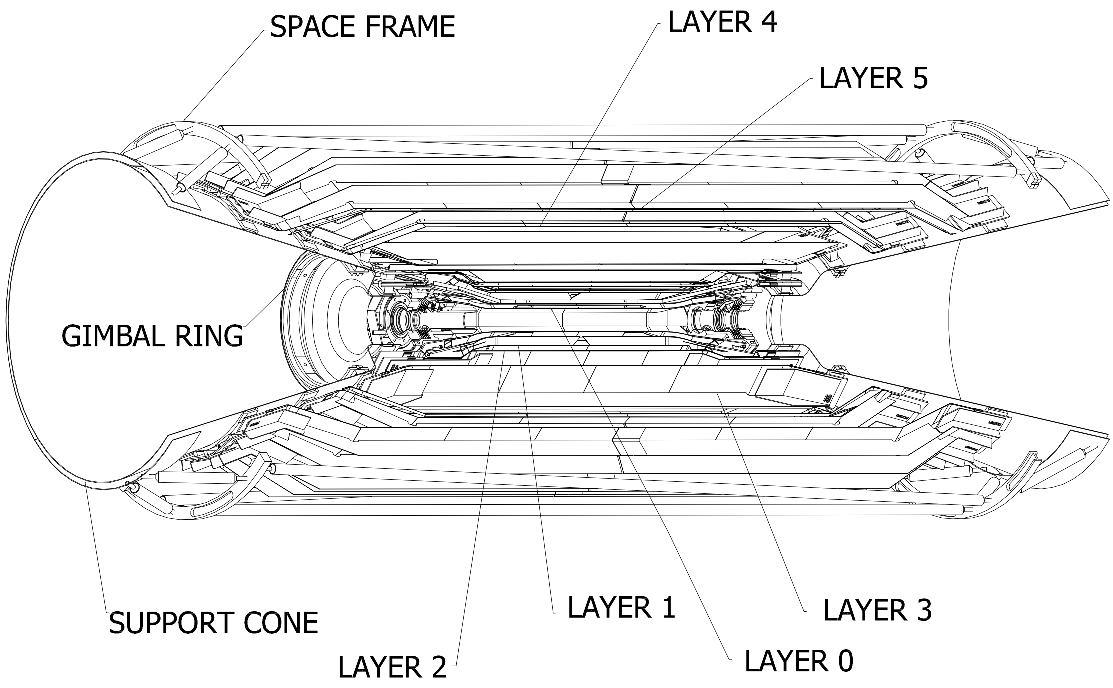

Figure 6.4: Three dimensional cutaway of the SVT.

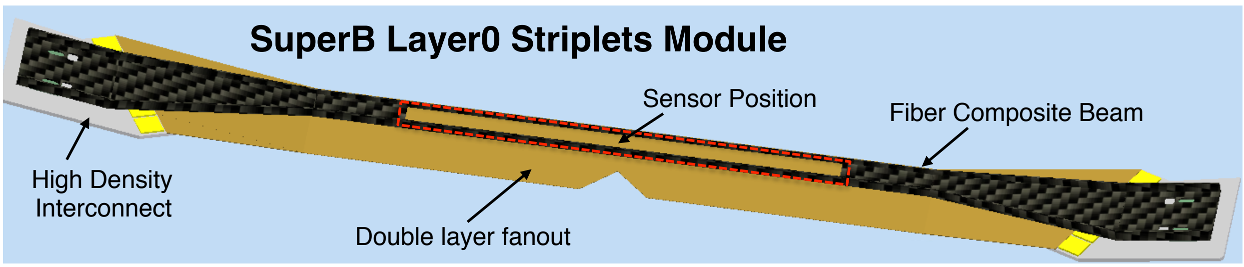

Figure 6.5: Schematic drawing of the Layer0 striplet module.

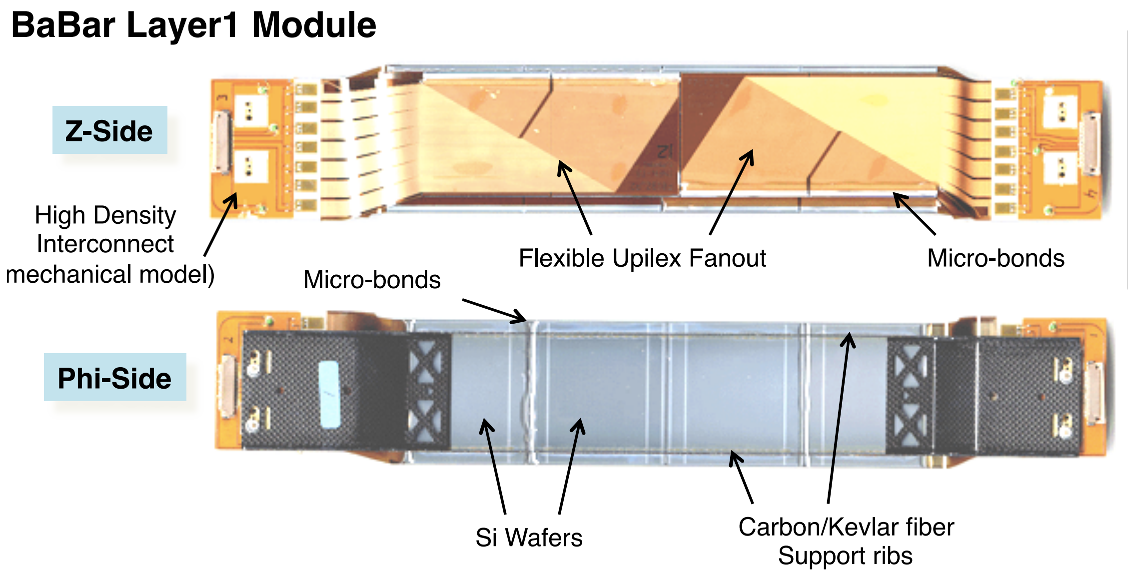

Figure 6.6: Details of the *BABAR* SVT Layer1 module.

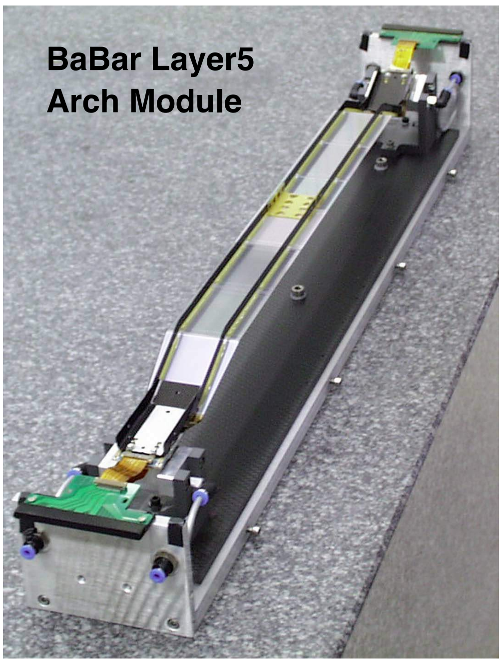

Figure 6.7: Details of the *BABAR* SVT Layer5 arch module.

For Layer0 short strips, oriented at 45 degrees with respect to the detector edges (u, v strips), are adopted on both faces of the sensor in order to reduce the strip length and the related background occupancy to reasonable levels. For layers 1 to 5 the strips on the two sides of the rectangular detectors in the barrel regions are oriented parallel (ϕ strips) or perpendicular (z strips) to the beam line. In the forward and backward regions of the two outer layers, the angle between the strips on the two sides of the trapezoidal detectors is approximately 90°, and the ϕ strips are tapered. Floating strips are used to improve the position resolution for near-perpendicular angles of incidence; the capacitive coupling between the floating strip and the neighboring strips results in increased charge sharing and better interpolation. For larger incident angles the wider readout pitch minimizes the degradation in resolution that occurs because of the limited track path length associated with each strip. These issues are discussed in more detail in section 6.4.2.

The design has a total of 308 silicon detectors of nine different types. The total silicon area in the SVT is about 1.5 m ^{2}, and the number of readout channels is ~170,000.

Table 6.1: See text for more detail on the meaning of the different quantities. The intrinsic resolution, quoted for tracks at 90° incidence angle, is taken from *BABAR* SVT data for Layers 1-5 (pitches are identical). For Layer0, data from a recent beam test on a striplet module prototype are used. The z-ganging/pairing numbers represent the percentage of readout channels connected to the specified strip configuration.

Quantity	Layer 0	Layer 1	Layer 2	Layer 3	Layer 4a	Layer 4b	Layer 5a	Layer 5b
Radius (mm)	15.6	33	40	59	120	124	140	144
Wafers/Module	1	2	4	4	6	6	8	8
Modules/Layer	8	6	6	6	8	8	9	9
Silicon Area (cm^2)	127	554	787	1655	2459	2548	3502	3610
Overlap in ϕ (%)	2.0	2.4	1.8	1.8	4.0	4.0	2.0	2.0
Readout pitch (μm):								
ϕ (u for Layer 0)	54	50	55	100	82–100		82–100	
z (v for Layer 0)	54	100	100	110	210		210	
Floating Strips:								
ϕ (u for Layer 0)	—	—	—	1	1		1	
z (v for Layer 0)	—	1	1	1	1		1	
Intrinsic Resolution (μm):								
ϕ (u for Layer 0)	10	10	10	15	15		15	
z (v for Layer 0)	10	14	14	15	25		25	
Readout Section								
ROS/Module	4	4	4	4	4		4	
ICs/ROS (ϕ-z)	6-6	7-7	7-7	6-10	4-5		4-5	
Readout Channels	24576	21504	21504	24576	36864		41472	
Strip Length Half Module (mm):								
ϕ (u for Layer 0)	20	110	130	190	293	303	369	380
z (v for Layer 0)	20	40	48	70	51–103	103–154	103–154	103–154
Fraction of z-side readout channels with Pairing/Ganging:								
None		77%	55%	65%	4%			
Pairing ×2		23%	45%	35%				
Ganging ×2					73%	74%	25%	16%
Gang.×2 + Pair.×2					23%	24%	41%	43%
Ganging ×3						2%	34%	41%

6.1.3.3 Readout Electronics

As emphasized above, all readout electronics are located outside the active volume, below 300 mrad in the forward and backward regions. To accomplish this, ϕ strips on the forward or backward half of a detector module are electrically connected with wire bonds. This results in total strip lengths associated with a single readout channel of up to ∼19 cm in the inner layers and up to ∼38 cm in the outer two layers.

The signals from striplets for the Layer0 (u and v strips) and the z strips for all the other layers are brought to the readout electronics using fanout circuits consisting of conductive traces on a thin flexible insulator (for example, copper traces on Upilex, as in *BABAR*). The fanout traces are wire-bonded to the ends of the silicon strips.

On the z side of the modules the number of readout strips exceed the number of available electronic channels, constrained by the number of chips that can fit in the limited space available. To reduce the number of readout channels needed, the connection scheme for the z fanout circuits includes "pairing" and "ganging" (described in Section 6.4.2) with two or three strips bonded to a single fanout/readout channel. The length of the z strips is much shorter than ϕ strips, typically 4-7 cm in the inner layers and either 10 or 15 cm in the outer layers, where there is either $\times 2$ or $\times 3$ ganging.

Front-end signal processing is performed by ICs mounted on the High-Density Interconnect (HDI), a thick-film hybrid circuit fabricated on aluminum nitride (AlN) substrate. The HDI provides the physical support; it distributes power and signals, and thermally interfaces the ICs to the cooling system.

New front-end custom-design ICs are currently under development for the Super*B* SVT [4] since none of the existing chips matches all the requirements (Sec. 6.6.2). The signals from the readout strips, after amplification and shaping, are compared to a preset threshold. The time interval during which they exceed the threshold (time over threshold, or ToT) is related to the charge induced on the strip. The ToT technique has a nonlinear input-to-output relationship which is approximately logarithmic. This is an advantage, since it compresses the dynamic range and allows one to achieve good position resolution and large dynamic range with a minimum number of bits. ToT readout has been successfully employed in the front-end chip of the *BABAR* SVT (*i.e.*, Atom chip [1]) providing good analog resolution for position interpolation, time-walk correction, and background rejection.

For each channel with a signal above threshold, the ToT information together with the hit time stamp will be buffered until a trigger is received; it will then be transferred, with the strip number, to an output interface, where data will be serialized and transmitted off chip on output LVDS lines.

The readout IC is expected to be about 6x4 mm^2 and to dissipate about 4.0 mW per channel. The total power that will be generated by the SVT readout chips is ∼700 W.

There are four readout sections (ROS) per detector module: the module is electrically divided in half along z, and the ϕ and z strips are read out separately. The data from one-half of a detector module will be transmitted from the hybrid on a flexible cable to a transition card located approximately 50 cm away, where the signals are converted and transmitted to optical fibers.

6.1.3.4 Module design and Mechanical Support

The silicon detectors and the associated readout electronics are assembled into mechanical units called detector modules. Each module contains from 1 to 8 silicon detectors, the flex circuits to bring the signal from strip to the front-end chips, and a low-mass beam constructed of carbon and Kevlar fiber-epoxy laminates (*i.e.*, ribs) to stiffen the module structure. The ribs are attached through a carbon fiber end-piece to the HDI hybrid circuit. An aluminum nitride substrate for the HDI provides precise mechanical mounting surfaces and heat sink for the electronics.

The Layer0 module has certain unique features (see Figure 6.5). Only one sensor is used; the strips are still orthogonal on both sides but are tilted at a 45° angle with respect to the detector edge. Layer0 is arranged in an octagonal geometry (*i.e.*, not hexagonal. as in layers 1-3) to have shorter strip length. Due to the large number of strips on each side, the fanout circuits must have an extension almost twice the width of the detector and a stack of two fanout layers is required (see details on section 6.5.1). The HDI of Layer0 lies in a plane inclined by 10° with respect to the sensor plane, positioned outside the active region, fitting the constraints on available space. The HDI can fit the necessary 6 read-out chips into its available width by tilting them with a 30° angle with respect to the edges.

The module material budget in the active region is very limited (about 0.45% X_0 per layer) and is similar to *BABAR*. For layers 1 to 5, this is dominated by the silicon sensor thickness of 300 μm; a contribution of about 0.1% X_0 is due to the composite ribs, with about 0.05% X_0 for the z fanout, which isin the active area. For the Layer0 striplets, the contribution of the flex circuit is considerably higher: the total material for the two multilayer flex circuits, now under development, is about 0.15% X_0, while the carbon fiber support structure contributes about 0.1% X_0. Since the sensor thickness of the striplets is only 200 μm, the total material budget for Layer0 is also about 0.45% X_0.

Layer0 modules are supported on the cold flanges, directly coupled to the Be beam-pipe, allowing minimization of the distance to the beam pipe, and quick access to the Layer0 without demounting the other SVT layers. The other five SVT layers are mounted on support cones coupled with the conical tungsten shields with kinematic mounts (*i.e.*, the gimbal rings) that allow relative motion of the forward and backward shielding cones without placing stress on the silicon detectors.

The detector modules from Layers 1 and 2 are glued together with rigid beams, forming sextants that are then mounted from the support cones in the forward and backward directions. Each detector module of layers 3, 4 and 5 is mounted on the support cones independently of the other modules. For layer 4 and 5, there are two different types of modules in each layer, an inner one, labeled a, and an outer one, labeled b, occupying slightly different radial positions. Thus there are eight different types of detector modules.

The support cones are laminated carbon fiber structures which are mounted on the conical tungsten shields, present in the IR region for background reduction. Cooling water flows in brass cooling rings surrounding the outer surface of the support cone. Mounting pins in the hybrid structure provide the alignment between the modules and the brass mounts on the cone, and thermal contact is made to provide cooling for the front-end electronics located on the hybrid. The support cones are divided to allow the vertex detector to be assembled in two halves and then mounted on the shielding cones and the beam pipeby clam-shelling the pieces together. During the assembly/disassembly procedure the splitting of the support cones with the five SVT layers mounted, allows easy access to Layer0 without the need to disassemble the entire SVT.

The stiffness of the overall SVT structure is provided by a very low mass space frame, constructed of carbon fiber tubes, connecting the forward and backward support cones, similar to the one designed for the *BABAR* SVT. The motivation for this space frame stems mainly from the possible relative motion of the two support cones during the assembly/disassembly procedure or in case of an earthquake. Cooling water, power, and signal lines are routed along the support cones to points outside the active region where manifolds for the cooling water, transition cards for wire to optical transition, and power regulation and distribution are located.

6.1.4 Layer0 Pixel Upgrade

6.1.4.1 Motivations

With the machine operating at full luminosity, Layer0 of the SVT may benefit from an upgrade to a pixellated detector that has better performance in high background conditions, thanks to a lower expected background rate per channel. A background rate of about 1 MHz/strip ($\times 5$ safety factor included) is expected with a striplets length of about 2 cm and 50 μm pitch, while only 2.5 kHz/pixel are expected for pixels with a 50x50 μm^2 pixel area.

Possible effects of background hits on performance are: the reduction of the hit reconstruction efficiency (due to pileup), the increase of the effective hit resolution, the reduction of efficiency of the pattern recognition for charged tracks along with the increase of fake tracks. Most of these effects have been included in specific simulation studies performed to evaluate the SVT performance in the high background scenario (*i.e.*, full luminosity including a $\times 5$ safety factor on the nominal background). The results, described in more detail in Sec. 6.3.6 and 6.3.7, showed a significant degradation in the striplet performance with high background occupancy, while the pixel solutions explored showed more stable performance against background conditions. The pixel occupancy is reduced by afactor of at least 200 w.r.t. the striplets, due to the smaller electrode dimensions, even when the possible worse time resolution of the pixels w.r.t. striplets is included.

An example of these studies is shown in Figure 6.8. The impact of machine background on the SVT performance has been studied evaluating the per-event error on the physics parameter S, adding background hits to signal events. S is measured in time-dependent analyses (this corresponds to $\sin(2\beta)$ for $B^0 \to J\psi K^0_S$ decays, or, in the Standard Model, to $B^0 \to \phi K^0_S$ decays) and the per-event error on S is defined as the error on the parameter S normalized to the number of signal events. In Figure 6.8 the impact of background on the physics parameter S is shown for the striplet and pixel solutions, for the case of nominal background and with $\times$ nominal background rates. For the striplets, the reduction in the sensitivity of S w.r.t. *BABAR* is small with the nominal background, only about 3%, but it is up to about 15% with the $5\times$ nominal background. On the contrary, with a pixel option, as the effect of background occupancy is negligible, the reduction to the sensitivity on S is only 3%, even in the high background scenario, and is largely related to the effect of the background in the rest of the SVT.

It is important to stress that in the study reported here the pixel option has the same radius and material budget used for the striplets (r=1.6 cm, 0.45% X_0), and has the same performance without background included. Of course, the advantage of pixels over striplets in a high background environment is reduced if the material budget of the pixel solution is significantly higher. Conversely, if one can achieve a very low material budget with a thin pixel option, below the striplet material budget, then the upgrade to a pixel solution for Layer0 is well-motivated even in nominal background conditions (see for example Figure 6.19).

While for strip modules most of the material budget is due to the silicon of the sensor itself, in pixel modules there are several other important

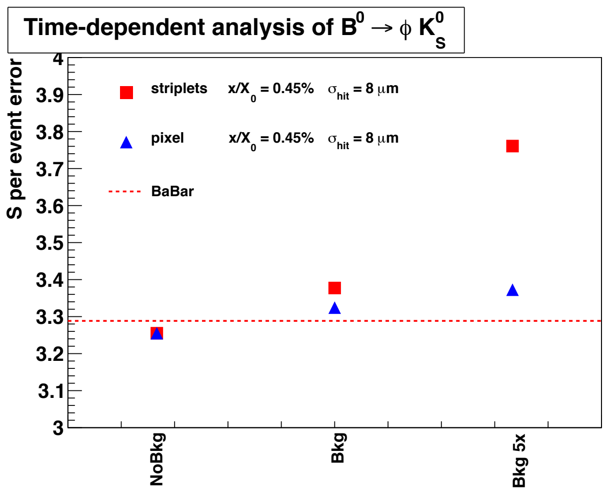

Figure 6.8: Variation of the per-event error S in $B^0 \to \phi K^0_S$ time-dependent analysis in presence of background events, for a Layer0 based on striplets or pixels with the same radius (r=1.6 cm) and material budget. Efficiency and resolution deterioration are both included in the simulation study.

contributions in the active area. Including the readout electronics, cooling, and the pixel bus for the connection of the front-end chips to the periphery of the module, one can easily reach a total material budget for a pixel solution above 1% X_0. A discussion on the material budget for various Layer0 pixel options is presented in the following sections.

6.1.4.2 Technology Options for Layer0 pixel upgrade

Two main technologies are under evaluation for the upgrade of Layer0: hybrid pixel and thinner CMOS Monolithic Active Pixel Sensor (MAPS). Specific R&D programs are ongoing on these options to meet the Layer0 requirements, such as low pitch and material budget, more critical for hybrid pixels, and high readout speed and radiation hardness, challenging aspects for CMOS MAPS sensors.

A short summary of the current status of the R&D on the different pixel options is given below, while a more detailed review is presented in Sec.6.8.

Hybrid Pixel technology represents a mature and viable solution. Reduction in the front-end pitch and in the total material budget, with respect to pixel systems developed for LHC experiments, is required for application in Layer0.

The spatial resolution requirement of 10-15 μm sets a limit to the area of the elementary readout cell and, as a consequence, to the amount of functionalities that can be included in the front-end electronics. For a pixel cell of $50{\times}50$ μm^2, a planar 130 nm CMOS technology may guarantee the required density to implement in-pixel data sparsification and fast time stamping (< 1 μs). This is required for the maximal hit rate in Layer0 of 100 MHz/cm^2 in order to keep the module bandwidth to an acceptable level (<5 Gbit/s).

Denser CMOS technologies, such as the 65 nm technology, can be used to increase the functional density in the readout electronics and include such functions as local threshold adjustment and amplitude measurement and storage. In this case, costs for R&D and production would increase significantly. Vertical integration (or 3D) CMOS technologies may represent a lower cost alternative to sub-100 nm CMOS processes to increase the functional density in the pixel cell [5, 6].

A front-end chip for high resistivity pixel sensors with 50×50 μm^2 pitch is under development for applications to Super$B$. A first prototype chip with 4k pixels has been produced with the ST Microelectronics 130 nm process adopting the same readout architecture, with in-pixel sparsification and timestamping, developed within the SLIM5 Collaboration [7] for CMOS Deep NWell MAPS [8, 9]. The chip bump bonded to a high resistivity sensor matrix has been fully characterized, with charged particle beams, with good results [10].

In this first prototype, only basic functionalities have been implemented. The readout architecture has been recently optimized to efficiently sustain the target Layer0 hit rate of 100 MHz/cm^2 on matrices larger than 50k pixels. The new architecture requires a more complex in-pixel logic and implements a data push and a triggered version of the readout [11].

The design of a 3D front-end chip for hybrid pixels with this new readout architecture, and some improved features, is now in progress with the vertical integration CMOS technology offered by the 130 nm Chartered/Tezzaron process.

CMOS MAPS are very appealing for applications where the material budget is critical: in this technology the sensor and readout electronics share the same substrate that can be thinned down to several tens of microns. Since a fast readout is another crucial aspect for Layer0, a new Deep N-well MAPS design approach has been developed by the SLIM5 Collaboration[7] to improve readout speed in CMOS MAPS sensors. This approach allowed for the first time the implementation of thin CMOS sensors with similar functionalities as in hybrid pixels, such as pixel-level sparsification and fast time stamping [8, 11]

Thanks to an intense R&D program the development of DNW CMOS MAPS (with the ST

Microelectronics 130 nm process) has reached a good level of maturity. A limiting factor in this design is the presence of competitive N-wells, inside the pixel cell, that can subtract charge from the main collecting electrode. The last prototype realized, the APSEL4D chip, a 4k pixel matrix with $50 \times 50\mu\text{m}^2$ pitch has been tested with beams [12] reporting a hit efficiency of 92%. This is related to the pixel cell fill factor (ratio of the DNW area to the total area of N-wells) which is about 90% in the APSEL design. Another critical issue for the application of CMOS MAPS in Layer0 is their radiation hardness, especially as it relates to bulk damage effects. A significant degradation of the charge collected (about 50%) has been measured after irradiation with neutrons up to a fluence of about $7\text{x}10^{12}$ n/cm^2, corresponding to about 1.5 years of Layer0 operation [13].

Improvements of MAPS performance are currently under investigation with two different approaches: the use of INMAPS CMOS process, featuring a quadruple well and a high resistivity substrate, and 3D CMOS MAPS, realized with vertical integration technology.

In order to increase the charge collection efficiency, the INMAPS 180 nm CMOS process is being explored: a deep P-well implant, deposited beneath the competitive N-wells, can prevent them from subtracting charge from the main collecting electrode. Moreover, the use of a high resistivity substrate available in this process can further improve charge collection and radiation resistance with respect to standard CMOS devices. First prototype INMAPS matrices have been realized with the improved readout architecture suitable for the application in the Super*B* Layer0 [10]. The devices, currently under test, have shown promising results, with measured Signal-to-Noise of about 27 for MIPs [14]. Radiation hardness of these devices, at the level required for a safe operation in Layer0 is currently under investigation with encouraging results, as shown in Sec. 6.8.4.

The realization of 3D MAPS, using two CMOS layers interconnected with vertical integration technology, also offer several advantages with respect to standard 2D MAPS. In these devices one CMOS tier is hosting the sensor with the analog front-end and the second tier is dedicated to the in-pixel digital front-end and the peripheral readout logic. With this splitting of functionality the collection efficiency can be improved, significantly reducing the N-well competitve area in the sensor layer. Having more room for the in-pixel logic allows the implementation of a more performant readout architecture. Finally, in 3D MAPS the cross-talk between analog and digital blocks can be minimized.

The characterization of the first 3D MAPS prototypes realized with the 130 nm Chartered/Tezzaron 3D process is under way; first beam test results on the MAPS layer implementing the sensor and the analog front end showed very good hit efficiency (above 98%).

Conclusions Very promising results have been achieved with both evolution of the Apsel DNW MAPS: DNW 3D MAPS with vertical integration and MAPS with quadruple-well process. In particular the encouraging results on Apsel4well sensor seems to suggest that the INMAPS 180 nm CMOS process with high resistivity epitaxial layer might overcome the radiation tolerance issues found in DNW MAPS and become the candidate technology for the Layer0 pixel upgrade. Other developments of CMOS MAPS with quadruple-well 180 nm CMOS process can also be considered for Layer0 application [15, 16, 17, 18, 19, 20]

6.1.4.3 Pixel Module & Material Budget

The schematic drawing of the full Layer0 made of 8 pixel modules mounted around the beam pipe is shown in Figure 6.9. With the pixel option the radius of Layer0 can be slightly reduced (r=1.39 cm), with respect to the one used for the striplets option (r=1.56 cm), thanks to the simpler geometry of the pixel module.

In all the pixel options under evaluation, sharing the same multichip module structure, the material budget of all the components must be kept under control to minimize the detrimental effect of multiple scattering.

Table 6.2: Layer0 module material budget for the different technologies under evaluation.

Layer0 Module Material Budget (X_0)			
	Striplets	Hybrid Pixel	CMOS MAPS
Sensor	0.21%	0.11-0.21%	0.05%
FE-chip+bump bonding		0.14-0.19%	
Multilayer bus or fanout	0.15%	0.15-0.30%	0.15-0.30%
Module Support & ground plane (include cooling for pixels)	0.09%	0.15%	0.15%
Total Material Budget (X_0)	0.45%	0.55-0.85%	0.35-0.50%

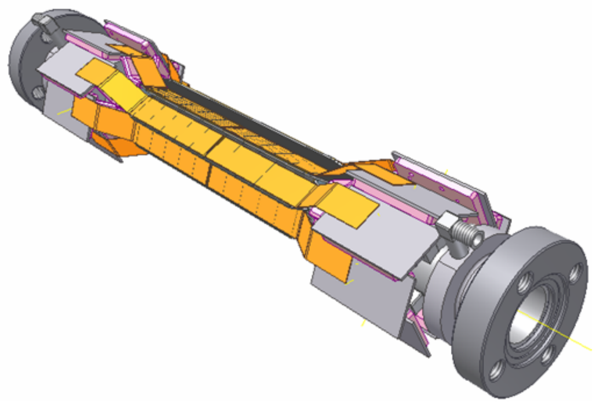

Figure 6.9: Schematic drawing of the full Layer0 made of 8 pixel modules mounted around the beam pipe with a pinwheel arrangement.

The main contributions to the material budget of pixel modules in different technologies are discussed in this section. See Table 6.2 for a summary and a comparison with the striplets option.

In the hybrid pixel solution, the contribution of the silicon of the sensor (100-200 μm) and of the front-end chip (100-150 μm) can be in the range of 0.25-0.4% X_0. In the CMOS MAPS option, the sensor and the front-end electronics are integrated in the same CMOS chip, that could be thinned down to 50 μm reducing this contribution down to 0.05% X_0.

Another important contribution to the material comes from the pixel bus, for the connection of front-end chips to the periphery of the module. This will be realized with an Al/kapton multilayer bus (now under development) and should satisfy the present requirements on speed (high bandwidth due to a hit rate of 100 MHz/cm^2) and power consumption (about 1.5W/cm^2). The estimated material budget for the pixel bus is about 0.15-0.3% X_0, depending on the achievements of present R&D on this item.

The pixel module support structure needs to include a cooling system in the active area to evacuate the power dissipated by the front-end electronics, a total of about 1.5W/cm^2. In order to minimize the material budget, a light carbon fiber support structure with integrated active cooling, based on microchannel technology [21] and forced liquid convection, has been developed. The support with integrated cooling is built with carbon fiber micro-tubes, with a hydraulic diameter of about 200μm, obtained by a pultrusion process. Measurements on the support prototypes, with a total material budget as low as 0.11% X_0, indicate that such approach is a viable solution to the thermal and structural problem of Layer0 [22]. An innovative idea is also under development to integrate the cooling system into the silicon itself and is based on microchannels made by DRIE technology. The embedded microchannels have diameters even below 100μm, and feature a peculiar geometry. In the final step a thin oxide layer is deposited to seal the channels. Results showed this to be reliable for operating in high-pressure conditions. This novel technique permits the integration of the cooling system within the detector with advantages for the efficiency of thermal bridges and reduction of material budget [23].

6.2 Backgrounds

A detailed analysis of background effects is fundamental to having a reliable estimation of performance and expected lifetime of the tracker.

The different sources of background have been simulated with a detailed Geant4-based detector model and beamline description (see Sec. 14.1.1). The detailed simulation is needed because not only the detectors themselves, but also the support structure ("dead material") play an important role in stopping or creating background particles. The raw output of the simulation has then to be processed to obtain information useful for the detector design.

As described in Sec. 5, in addition to well-known background sources, such as Touschek and beam-gas scattering, we have a significant contribution from physics processes that occur in the interaction region. The very high luminosity of the machine produces an unprecedented rate for additional pairs and for radiative Bhabha processes. The effect of those physics processes cannot be mitigated by optimizing the machine optics, because they scale with the luminosity and the machine goal is always to maximize the luminosity. In the SVT the contribution from the radiative Bhabha source is greatly reduced by the tungsten shields that surround the final focus regions. On the contrary, the pair production source of background, with the typical low momentum electrons and positrons coming directly from the IP, cannot be shielded; this represents the main background contribution in the SVT. The relative contribution of the various sources to the total background in the SVT layers is shown in Figure 6.10.

The summary of the relevant variables extracted from background simulation is shown in table 6.3 and defined in the rest of this section.

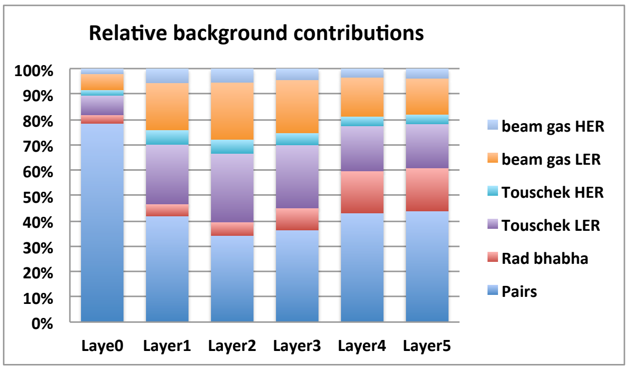

Figure 6.10: Relative contribution of the various background sources to the total track rate in the SVT layers.

From simulation we calculate the track rate per unit area, obtained by counting particles that cross the sensor, normalized to the sensor area. Since a single particle can cross the sensor several times, generating multiple clusters (*i.e.*, low-momentum charged particles that spiral in the detector magnetic field — sometimes referred to as 'loopers'), we also evaluate the cluster rate per unit area, taking into account multiple crossings of the sensor area by the same particle. The simulated cluster rate and the cluster occupancy are the relevant variables used in section 6.3.5 to evaluate the impact of background on tracking performance. For each cluster several strips/pixels can be fired, depending on the incident angle of the particle with the sensor, therefore the strip/pixel rate can be significantly higher than the cluster rate. The strip/pixel rate, which is particularly relevant for the design of the readout electronics, is also evaluated from background simulation and shown in Table 6.3.

The integrated radiation dose, and the 1 MeV neutron equivalent fluence, according to NIEL (non-ionizing energy loss) scaling, are extracted from simulation and are used to determine the radiation damage in the SVT layers over the entire lifetime of the experiment, including a $\times 5$ safety factor on nominal simulated background.

Table 6.3: Summary of expected nominal backgrounds in the sensor area. The SVT has been designed to withstand ×5 the nominal background. Numbers shown do not include the ×5 safety factor. Simulation results for both Layer0 options, striplets and pixels, the latter being at a slightly lower average radius, are reported. The definition of the various quantities shown (track, cluster and strip/pixel rates) is given in section 6.2.

Layer	Radius (mm)	Pitch (ϕ–z) (μm)	Total Rate/Area (MHz/cm^2) Track	Cluster	Strip (ϕ–z)	Total Strip Rate (kHz)	TID (Mrad/yr)	NIEL (n/cm^2/yr)
0 (pixel)	13.9	50–50	2.32	5.86	30	0.8 (pixel)	3.3	5.2×10^{12}
0 (striplets)	15.6	54–54 (u,v)	1.62	4.10	20–20 (u,v)	187–187	2.3	3.6×10^{12}
1	33	50–100	0.217	0.540	3.2–2.7	170–134	0.3	7.9×10^{11}
2	40	55–100	0.163	0.393	2.0–1.9	134–134	0.2	5.1×10^{11}
3	59	100-110	0.079	0.208	0.60–0.83	116–79	0.1	3.0×10^{11}
4	120	100–210	0.022	0.037	0.08–0.06	25–13	0.01	2.0×10^{11}
5	140	100–210	0.014	0.022	0.04–0.03	16–9	0.01	1.8×10^{11}

6.3 Detector Performance Studies

6.3.1 Introduction

The Super*B* vertex detector is an evolution of the *BABAR* SVT. It is capable of maintaining adequate performance for time-dependent measurements in the presence of a lower boost of the center-of-mass (CM) frame ($\beta\gamma = 0.24$ compared to $\beta\gamma = 0.55$ of *BABAR*) and much higher background, mainly related to the increased instantaneous luminosity of about a factor of 100 larger than *BABAR*.

The beam pipe features a reduced radius of about 1.0 cm which allows the positioning of the Layer0 at an average radius of about 1.5 cm. The additional Layer0 measurement, along with the low radial material budget of the beam pipe (0.42% X_0) and of Layer0 (0.45% X_0 with the striplet option), is crucial for improving the decay vertex reconstruction of the B mesons and obtaining adequate proper-time resolution for time-dependent *CP* violation measurements. In addition, the small size of the luminous region, about $(1 \times 1)\,\mu\mathrm{m}^2$ in the transverse plane, also contributes to the improvement of the decay vertex reconstruction when imposing the constraint that the particles originate from the interaction point. The baseline solution for the Layer0 uses short strip (stirplet) technology; an upgrade to a pixel design is foreseen once the machine starts operating at nominal luminosity.

In the following we discuss the baseline layout of the SVT and how the design has been optimized (Section 6.3.2), the impact of the Layer0 on detector performance (Section 6.3.3), and the tracking performance (Section 6.3.4). The impact of the machine background on SVT performance is discussed (Sections 6.3.5 and 6.3.6) and the performance with a Layer0 pixel detector is presented (Section 6.3.7). In Section 6.3.8 the SVT sensor performance for particle identification based on ionization dE/dx is described.

6.3.2 The SVT layout

The baseline SVT is composed by 6 layers of double-sided silicon strip detectors and has a symmetric coverage in the laboratory frame down to 300 mrad (17.2°) with respect to the forward and backward directions, corresponding to asolid angle coverage of 95% in the CM. The inner three layers perform track impact parameter measurements, while the outer layers are required for pattern recognition and for tracking of low transverse momentum (p_t) particles.

The Layer0 strips are short ('striplets') and are oriented at ±45° with respect to the beam direction. The Layer1 to Layer5 silicon strip detectors are very similar to those in *BABAR* in terms of radial position and strip pitches. The optimization of the strip z and ϕ pitches for the strip detectors is discussed in Section 6.4.2. A dedicated study to optimize the SVT layout as a function of number of silicon sensors and radial positions was performed [3]. Several figures of merit were studied: track parameter resolution, reconstruction efficiency, and kinematic variable resolutions of B decays with low momentum tracks using the benchmark channel $B^0 \to D^{*-}K^+$. Since low momentum tracks do not reach the DCH, they are reconstructed only using SVT information. The *BABAR* experiment has shown that at least 4 hits in the ϕ view and 3 hits in the z view are necessary for robust track reconstruction [24, 25]. The main result obtained for Super$B$ is that the 6-layer design is superior and more robust compared to the alternatives investigated, *i.e.* 4- and 5-layer layouts where intermediate layers are removed. Indeed, when accounting for possible inefficiencies in hit reconstruction (by removing intermediate layers), due to damaged modules or high background, the 6-layer design ensures a higher reconstruction efficiency for low momentum tracks compared to the other solutions investigated.

Table 6.4 shows the reconstruction efficiencies for the decay $B^0 \to D^{*-}K^+$ for the 4-, 5- and 6-layer configuration in different running conditions: ideal conditions (A), with a damaged module in Layer3 (B) and with additional hit inefficiency in Layer0 with respect to case B (C). The outer radius of the SVT is ultimately constrained to about 20 cm by the DCH inner radius. It has been demonstrated that there is no real advantage in increasing the outer layer of the SVT with respect to the *BABAR* design (14.4 cm) [26, 27, 28]. Moreover, construction cost and technical difficulties would increase if one attempted to increase this parameter. Radial positions of the Layer1 to Layer4 modules have very little impact on track resolution when comparing a layout with detectors spaced equally or with a *BABAR*-like radial layout.

Table 6.4: Reconstruction efficiencies for $B^0 \to D^{*-}K^+$ decays for different SVT layout (4, 5 ,6 layers) and running conditions (A, B, C). Case A correspond to ideal running conditions, B represents SVT with a damaged module in Layer3 with z hit efficiency of 70%. Case C introduces additional inefficiency with respect to case B in Layer0: 60% hit efficiency for z and ϕ views.

	A	B	C
	eff. (%)	eff. (%)	eff. (%)
6 layers	66.0 ± 0.3	65.0 ± 0.3	64.0 ± 0.3
5 layers	64.0 ± 0.3	62.0 ± 0.3	60.0 ± 0.3
4 layers	60.0 ± 0.3	56.0 ± 0.3	53.0 ± 0.3

6.3.3 Impact of Layer0 on detector performance

The additional Layer0 measurement is crucial for maintaining adequate resolution on the B^0 meson proper-time difference $\Delta t \simeq \Delta z/(\beta\gamma c)$ with the relatively low CM boost value $\beta\gamma = 0.24$ of Super$B$. The average separation Δz between the decay vertex positions of the two B mesons along the z axis is $\Delta z \simeq \beta\gamma c\tau_B = 110$ μm, where τ_B is the B^0 lifetime, which is about 1.5 ps. Hence, in order to be able to separate the B meson decay vertices in Super$B$, their decay positions have to be determined with a significantly better precision than the average separation Δz. In addition in Super$B$ the B vertex separation in the transverse plane, which is about 25 μm, is not completely negligible with respect to the average Δz separation of about 110 μm, and therefore contributes to the determination of Δt. The reference value for the Δt resolution, $\sigma(\Delta t)$, was determined by the resolution obtained in the *BABAR* experiment according to the Fast Simulation (sec. 14.1.2), see Table 6.5. Figure 6.11 shows the dependence of the per-event error on the physics parameter S as a function of $\sigma(\Delta t)$, with the sensitivity obtained in *BABAR* superimposed. In this simplified model $\sigma(\Delta t)$ corresponds to the width of the core Gaussian of the Δt resolution function. The S per-event error is defined as the error on the parameter S normalized to the number of signal events. S is measured in time-dependent analyses and corresponds to $\sin(2\beta)$ for $B^0 \to J/\psi K_S^0$ decays. The resolution σ_z on the z coordinate of

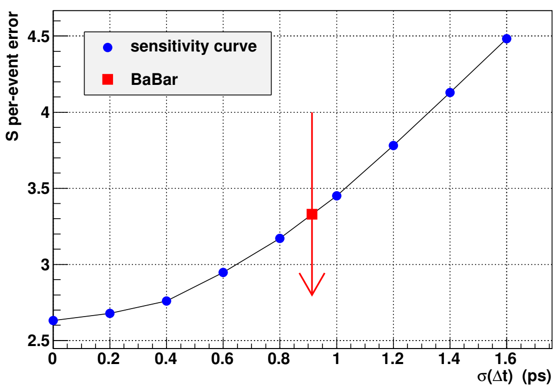

Figure 6.11: The curve represents the dependence of the error on the physics parameter S (*e.g.*, $\sin(2\beta)$) as a function of $\sigma(\Delta t)$. The arrow indicates the $\sigma(\Delta t)$ value obtained in *BABAR* according to the Fast Simulation and the square point is the relative value on the sensitivity curve.

the track depends on the geometry of the vertex detector and the hit resolution. In a simplified model with two hits measured at radii r_0 and r_1 (where $r_1 > r_0$) with z hit resolutions σ_0 and σ_1 respectively, σ_z can be approximated as:

$$\sigma_z = \frac{\sigma_0^2 + (\sigma_1 r_0/r_1)^2}{1-(r_0/r_1)^2}. \tag{6.1}$$

In addition, the tracks undergo multiple scattering interactions with the material in the tracking volume. The scattering angle distribution can be approximated by a Gaussian with a width given by [29]:

$$\theta_{\text{m.s.}} = \frac{13.6\,\text{MeV}/c}{p_t\beta}\sqrt{\frac{x}{X_0}}\left[1+0.0038\ln\left(\frac{x}{X_0}\right)\right] \tag{6.2}$$

where p_t is the transverse momentum, x is the thickness of the material and X_0 is the radiation length. In order to minimize the uncertainty on σ_z it is important to measure the first hit at an r_0 as small as possible with good hit resolution σ_0. Minimizing the material close to the interaction region, *e.g.*, the beam pipe and Layer0 material, is also important.

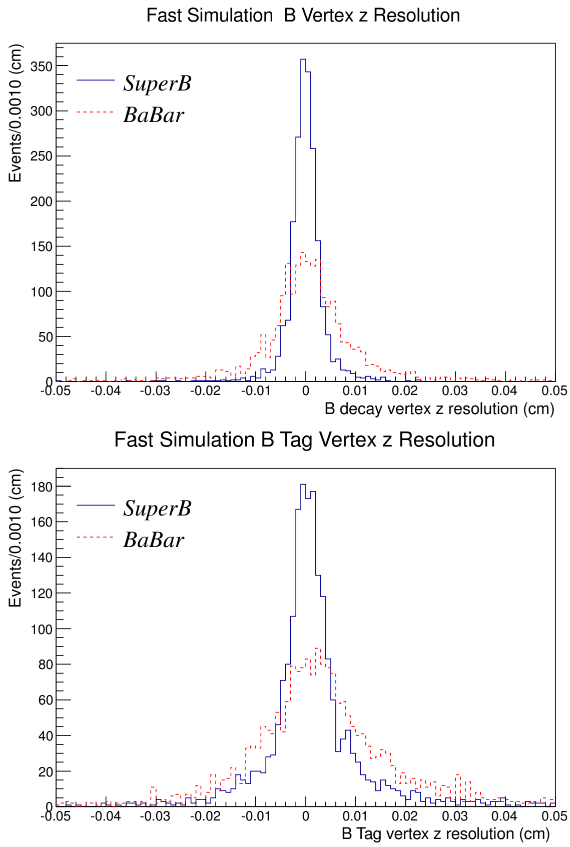

Figure 6.12: B decay vertex z position (top) and B tag z position (bottom) residual distributions in Super$B$ with Layer0 striplets (continuous line) compared with *BABAR* (dashed line) according to Fast Simulation studies.

Figure 6.12 shows the residual distributions of B decay vertex z positions for exclusively (top) and inclusively (bottom) reconstructed B decays. Figure 6.13 shows the Δz (top) and Δt (bottom) residual distributions. One B is exclusively reconstructed in the $B^0 \to \phi K_S^0$ mode (B_{reco}), while the other B is inclusively reconstructed using the remaining tracks of the event and is also used for flavor tagging (B_{tag}). The Fast Simulation results for Super$B$ with Layer0 striplets are compared with the *BABAR* results and summarized in Table 6.5. In Super$B$ we assume $\sigma_0 = 10\,\mu$m for both u and v hits, ex-

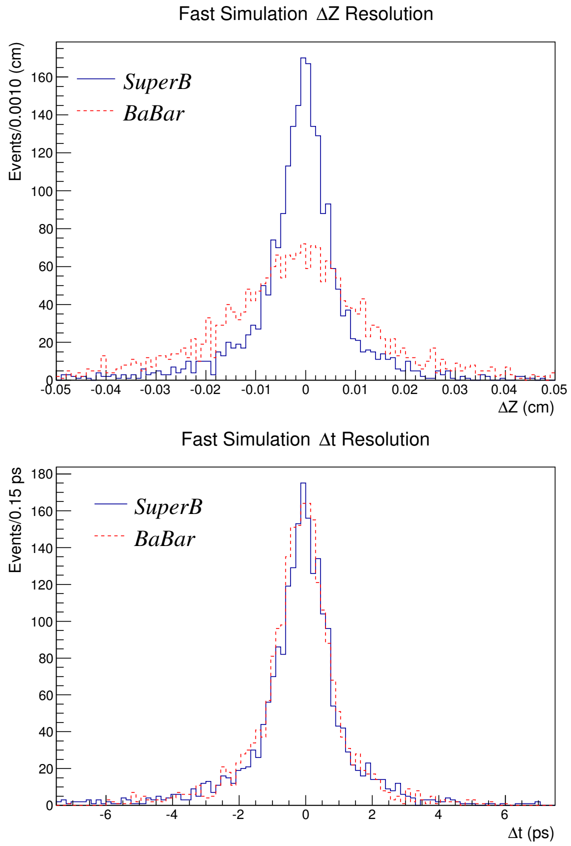

Figure 6.13: Δz (top) and Δt (bottom) residual distributions in Super$B$ with Layer0 striplets (continuous line) compared with *BABAR* (dashed line) according to Fast Simulation studies.

Table 6.5: RMS of the residual distributions for decay vertex z position for exclusively reconstructed $B^0 \to \phi K^0_S$ decays (B_{reco}), inclusively reconstructed B decays (B_{tag}), Δz and Δt at Super$B$ and compared with *BABAR* results, according to Fast Simulation studies.

	Super$B$	*BABAR*
B_{reco} (μm)	40 ± 1	105 ± 1
B_{tag} (μm)	100 ± 2	145 ± 2
Δz (μm)	105 ± 2	165 ± 2
Δt (ps)	1.40 ± 0.02	1.45 ± 0.02

trapolating from data from a recent beam test on a striplets module prototype. The Layer0 has a pinwheel configuration with radii in the range $1.53 - 1.71\,$cm; it is modeled in FastSim as a cylinder with average radius of about $r_0 = 1.6\,$cm. The total material budget for the beam pipe and the Layer0 striplets is about $x/X_0 \simeq 0.9\%$. For striplets detectors, u and v coordinates are oriented at $\pm 45°$ with respect to the z axis and are perpendicular to each other. In *BABAR* we have $\sigma_0 = 14\,\mu$m for the z hits and $10\,\mu$m resolution for the ϕ hits, with $r_0 = 3.32\,$cm and $x/X_0 \simeq 1.6\%$. In Super$B$, the improved Δz resolution is compensated by the reduced boost value, yielding a Δt resolution very similar to *BABAR*. Figure 6.14 shows the Δt resolution obtainable with different Layer0 radii (r_0= 1.4 and 1.6 cm) and material budgets (x/X_0 ranging from 0.1 to 1.0%). The dashed line represents the reference value of *BABAR*.

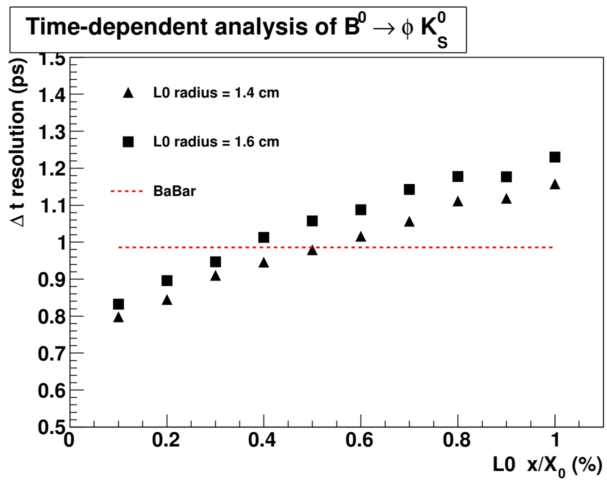

Figure 6.14: Resolution on Δt for different Layer0 configurations in terms of radius (r_0 = 1.4 and 1.6 cm) and material budget (x/X_0 = $0.1 - 1.0\%$) compared with the reference value of *BABAR* (dashed line).

The impact of the hit resolution on the decay vertex reconstruction has also been studied. With $10\,\mu$m hit resolution in both views of Layer0, the error on the vertex position due to multiple scattering interactions with the material dominates the overall vertex uncertainty. This is true even for high momentum tracks from $B^0 \to \pi^+\pi^-$ decays. Hence, without further reduction of the material budget, there is no real advantage in improving the hit resolution with respect to this value. The hit resolution from Layer1 to Layer5 has been chosen according to the *BABAR* SVT design which was optimized for low momentum track reconstruction. The intrinsic detector hit resolution and hit efficiency values used in the Fast Simulation are reported in Table 6.6 for the different SVT layers. The efficiencies have been estimated from simulations taking into account possible hit losses due to the overlap of pulses in the analog section of the FEE with nominal background conditions.

6.3.4 Tracking performance

The tracking performance at Super*B* has been studied considering alternative solutions for the SVT and DCH layout [3, 26, 27]. In particular, we have studied alternative SVT configurations: with different values of the SVT outer radius (from about 14 to 22 cm), without Layer2 modules, different radial positions of the layers (*e.g.*, uniform distance between layers), different hit resolutions accounting for variations of about 50% with respect to the nominal ones reported in Table 6.6. The main result was that the *BABAR*-like layout for Layer1-Layer5 was very close to be the optimal choice in terms of resolution for track parameters. Small improvements in track parameter resolution would have been possible by removing Layer2. On the other hand, the 6-layer layout has been proven to be more robust against possible problems that might cause loss of efficiency in some layers of the detector [3] and was preferred for this reason. Optimization of the strip pitches for the z and ϕ sides of the different layers is discussed in Section 6.4.2. Figure 6.15 shows the resolution on the impact parameter d_0, as a function of p_t with the *BABAR* and Super*B* detectors. The parameter d_0 is defined as the distance of the point of closest approach of the track to the z-axis from the origin of the coordinate system in the $x-y$ plane. Results for alternative configurations of the SVT layout, with extended outer radius, with DCH lower radius, and without Layer2, are also shown. A significant improvement in the d_0 resolution of about a factor 2 is achieved with the Super*B* detector with respect to the *BABAR* one. The alternative SVT layout options investigated give consistent results with the nominal Super*B* solution.

Table 6.6: Intrinsic detector hit resolution and hit efficiency for the ϕ and z sides (Layer0 u and v sides) for the different layers.

	res. u (μm)	res. v (μm)	eff. u (%)	eff. v (%)
Layer0	10	10	99	99
	res. z (μm)	res. ϕ (μm)	eff. z (%)	eff. ϕ (%)
Layer1	14	10	98	98
Layer2	14	10	98	98
Layer3	15	15	98	96
Layer4	25	15	99	98
Layer5	25	15	99	98

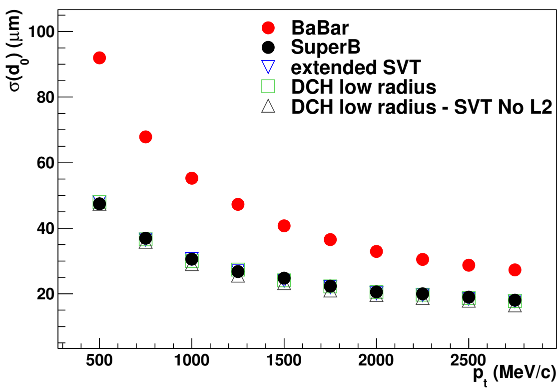

Figure 6.15: Resolution $\sigma(d_0)$ on the impact parameter d_0 as a function of p_t in *BABAR* and for various Super*B* tracking detector configurations.

6.3.5 Impact of machine background on tracking performance

As described in Section 6.2, the background conditions will be more severe in Super*B* than in *BABAR*. The fast front-end electronics of the SVT provides very good resolution on the time of passage of the particle or time of arrival of the hit. The Time over Threshold (ToT) of the shaper output is used to correct for the interval between the arrival of the hit and the time the shaper exceeds threshold. The latter is referred to in the following as time stamp (TS) of the hit, and registered with a TS clock. The resolution on the time of arrival of the hit depends on the SVT layer due to the different shaper peaking times of the front-end electronics, and has been estimated using *adhoc* simulations [30]. Several peaking times summarized in Table 6.16, will be available on the strip detector readout chips. The resolution for all layers and sides is reported in Table 6.7 for the nominal peaking-time configuration and for the shortest peaking times in Layer4 and Layer5. It ranges from about 10 ns for Layer0 up to 50 ns for Layer5. In our studies, hits outside a $\pm 5\sigma$ acceptance time window from the event time (determined by the DCH) are discarded. A similar procedure was used in the reconstruction algorithm used by the *BABAR* experiment.

The Fast Simulation tool does not apply a pattern recognition algorithm. Tracking performance is based on parameterizations tuned on *BABAR* measured performance. Hits from

Table 6.7: Resolution on the time of arrival of the hit for the ϕ and z sides (Layer0 u and v sides) for the different layers with selected peaking times. The "old" detector corresponds to the same detector after 7.5 years of running and includes a safety factor of 5 times the level of radiation with respect to nominal.

	shaper peak. time (ns)	time res. "fresh" det. (ns, ns)	time res. "old" det. (ns, ns)
Layer0	25	(9.7, 9.7)	(9.7, 9.7)
Layer1	75	(10.7,10.2)	(11.0,10.8)
Layer2	100	(11.4,10.5)	(12.0,11.5)
Layer3	150	(12.4,11.7)	(15.1,14.1)
Layer4	500	(28.8,24.2)	(41.6,49.4)
Layer5	750	(42.6,34.3)	(54.6,46.7)
Layer4	250	(17.8,15.9)	(21.1,19.3)
Layer5	375	(24.9,20.5)	(27.6,23.8)

neighboring tracks may be merged or associated with wrong tracks, but all generated tracks with a number of reconstructed hits above a given threshold are reconstructed; no fake tracks are added. This fast simulation tool thus allows one to study track parameter resolution, but not the tracking inefficiency arising from pattern recognition. The impact of background on the resolution of the track impact parameters is shown in Figure 6.16. In order to address the issue of

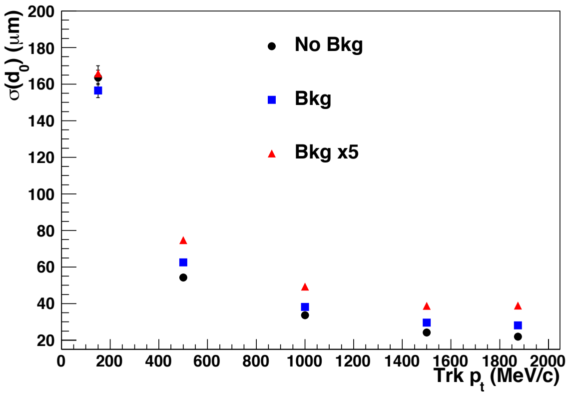

Figure 6.16: Resolution on the impact parameter of the track d_0 as a function of p_t for the Super$B$ detector with Layer0 striplets. The results shown assume no background (points), nominal background (squares) and 5 times the nominal background (triangles).

the pattern recognition capability to reconstruct tracks in the high background environment of Super$B$, SVT detector occupancies estimated in Super$B$ have been compared to those observed in *BABAR*. In particular we compared the cluster occupancy, defined as the detector strip occupancy after applying the time window cut, divided by the hit multiplicity in a cluster. The average cluster occupancy over all layers and sides is estimated to be about 0.4% with nominal background in Super$B$. This cluster occupancy in Super$B$ is smaller than the maximum value of about 0.7% reached at high luminosity in *BABAR*, thanks to the improved hit time resolution. When considering a scenario with an additional $\times 5$ safety factor on background predictions for Super$B$, the estimated average cluster occupancy is about 2% with nominal peaking-time configuration and about 1.5% with the shortest peaking times in Layer4 and Layer5. *BABAR* studies [31] of SVT performance in high background conditions have been used to estimate the efficiency to assign a hit to a track as a function of the cluster occupancy, that was found to be greater than 95% up to a 3% occupancy [32]. These studies indicate that the pattern recognition should be able to function without major problems even in the presence of 5 times the nominal background. Moreover, for low momentum tracks not reaching the DCH, the additional Layer0 measurements should help the pattern recognition when using SVT hits only. Improvements in the pattern recognition algorithm may also be foreseen with respect to that used in *BABAR*.

6.3.6 Sensitivity studies for time-dependent analyses

The sensitivity to the physics parameter S has been considered as a figure of merit for time-dependent analyses of B^0 decays. Several decay modes have been studied: $B^0 \to \phi K^0_S$, $B^0 \to \pi^+\pi^-$, $B^0 \to J/\psi K^0_S$, $B^0 \to D^+D^-$, and, in addition, decay modes such as $B^0 \to K^0_S K^0_S$, $B^0 \to K^0_S\pi^0$, in which the impact of the additional Layer0 measurement is less effective due to the presence of neutral and long-lived particles in the final state. The per-event error on the S parameter estimated in Super$B$ using the Fast Simulation is consistent with that observed with the *BABAR* detector for all decay modes apart from $B^0 \to K^0_S K^0_S$ and $B^0 \to K^0_S\pi^0$ decays, where a reduction in sensitivity of about 15% is observed [26, 28]. Only the impact of the Δt resolution on the measurements has been included in the Fast Simulation studies. In particular, possible improvements of the Super$B$ reconstruction efficiency, due to the 95% angular coverage in the CM frame (with respect to 91% in *BABAR*), and better flavor tagging performance due to improved particle identification, have not been considered in these studies.

In the case of time-dependent analyses for mixing and CP violation in the neutral D meson system, the determination of the proper time t relies on the measurement of the 3-dimensional flight length ($\vec{L}$) and the momentum $\vec{p}$ of the D^0 according to

$$t = \frac{\vec{L} \cdot \hat{p}\, M}{|\vec{p}|}$$

where M is the D^0 nominal mass. D^0 mesons produced in $e^+e^- \to c\bar{c}$ events gain a natural boost in the reaction. Even though the CM boost is reduced with respect to *BABAR*, the resolution on the D^0 proper time in Super$B$ is about 2 times better than that for *BABAR* [33]. Figure 6.17 shows the distribution of the D^0 proper-time error in Super$B$, compared to that obtained from *BABAR*. The average proper-time error is about 0.16 ps in Super$B$ and 0.30 ps in *BABAR* for $D^0 \to K^0_S\pi^+\pi^-$ decays, which should be compared with the D^0 lifetime of about 0.41 ps. Similar results have been obtained for $D^0 \to h^+h^-$ decays, where $h = \pi, K$. It has been shown that the mean per-event error for $D^0 \to h^+h^-$ decays at charm threshold is also about 0.17 ps [34].

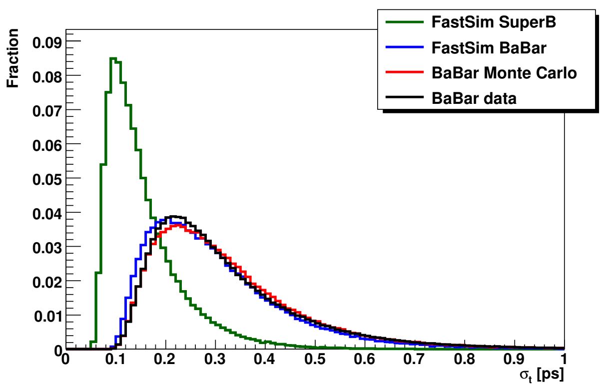

Figure 6.17: D^0 proper-time error distributions obtained with the Super$B$ (green line) and the *BABAR* (blue line) detectors according to Fast Simulation studies. Distributions from *BABAR* Monte Carlo (red line) and data (black line) are also shown in the plot.

The impact of machine background events on the SVT performance has been studied by adding background hits to signal events according to the rates estimated using Full Simulation. Details on the estimates of the machine background can be found in Section 6.2. Background hits may reduce the hit reconstruction efficiency, increase the effective hit resolution, and reduce the efficiency of pattern recognition for charged tracks, along with the increase of fake tracks. Most of the above effects have been included in our Fast Simulation, assuming that the charged track pattern recognition algorithm will work with similar performance to that of *BABAR*, but fake tracks are not simulated. Hit efficiency of the readout chips used in the Fast Simulation studies can be found in Table 6.16 for the case of nominal background and with 5 times the nominal background. Figure 6.18 shows the impact of the machine background events on the physics parameter S for the case of nominal background and with 5 times the nominal background rates. Background hits are rejected if they are not within a time window of $\pm 3\sigma$ ($\pm 5\sigma$) with respect to the time of the event. The values of the hit time resolution (σ) are reported in Table 6.7. The reduction of the sensitivity to S is quite limited with nominal background ($< 3\%$) and is about 9% (14%) with 5 times the nominal background conditions when applying a $\pm 3\sigma$ ($\pm 5\sigma$) time window cut.

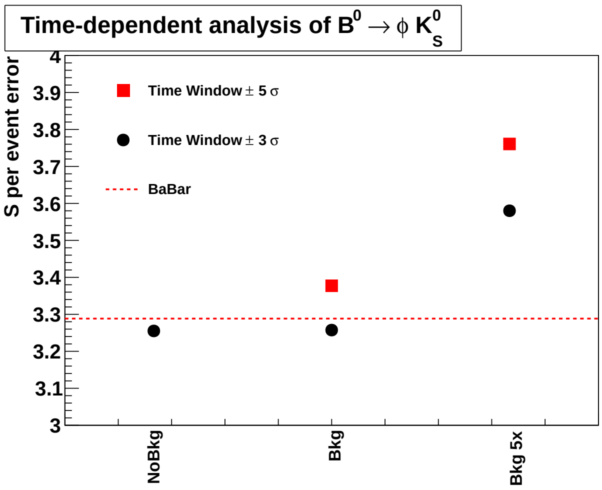

Figure 6.18: Variation of the S per-event error in $B^0 \to \phi K^0_S$ time-dependent analysis in presence of nominal background events and with 5 times the nominal background. A cut on the time of arrival of the hits has been applied at $\pm 3\sigma$ and $\pm 5\sigma$ with respect to the time of the event.

6.3.7 Performance with Layer0 pixel detectors

A Layer0 technology based on a high granularity silicon pixel sensor, *e.g.* with $50 \times 50\ \mu\text{m}^2$ cell, is considered for an upgrade of the baseline striplets solution. The different Layer0 technology options are described in Sec. 6.8 are based on either hybrid pixels or thin CMOS MAPS. These solutions all adopt a digital sparsified readout with the area of the pixel cell of about $2500 - 3000\,\mu\text{m}^2$. The shape of the pixel can be optimized in such a way to reduce the sensor pitch in the z direction and to improve the relative hit resolution while keeping the pixel area constant.

As already discussed in Sec. 6.3.3, the determination of the decay vertex position is driven by the performance of Layer0. The advantage of the Layer0 pixel solution is to guarantee good detector performance in presence of relatively high background. The detector occupancy, defined as the probability of having a noise hit in the sensitive time window, is about two orders of magnitude lower than for the striplet case, taking into account the different detector granularity and resolution on the time of arrival of the hits. Occupancies at the level of $10^{-4} - 10^{-3}$ in a Layer0 pixel detector would correspond to occupancies of $10^{-2} - 10^{-1}$ with the striplet solution, which are about the highest achievable values in the Layer0 striplets at Super$B$. Therefore, the impact of the background hits on the determination of the decay vertex and of the track impact parameters is moderate at Super$B$ with a Layer0 pixel solution.

Figure 6.19 shows the sensitivity to the S parameter in time-dependent CP violation analysis of $B \to \phi K^0_S$ decays as a function of the Layer0 radius (r_0 =1.4 and 1.6 cm) and of its material budget ($x/X_0 = 0.1 - 1.0\%$), in case of nominal background and $\times 5$ the nominal background. The dashed line represents the reference value obtained in *BABAR*. A material budget in the range $x/X_0 = 0.35 - 0.50\%$ ($x/X_0 = 0.55 - 0.85\%$) is achievable for a Layer0 pixel solution based on CMOS monolithic active pixel sensors (hybrid pixels) depending on the results of the ongoing R&D activities. The S sensitivity is very similar to the one obtained in *BABAR*. The maximum difference is about 6% (10%) in the worst case considered (including 5 times the nominal background).

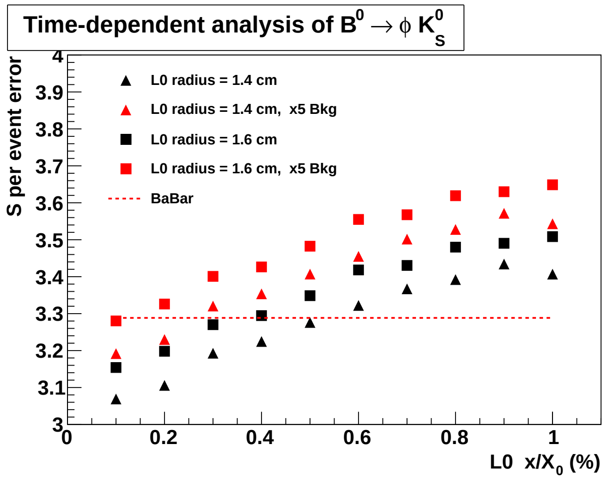

Figure 6.19: S per-event error in $B^0 \to \phi K^0_S$ time-dependent analysis for different Layer0 radii ($r_0 = 1.4$ and 1.6 cm) and material budget ($x/X_0 = 0.1 - 1.0\%$) compared with the reference value of *BABAR* (dashed line). Results in presence of 5 times the nominal background are also shown in the plot.

6.3.8 Particle identification with dE/dx

The measurement of the ToT value by the front-end electronics enables one to obtain the pulse height, and hence the ionization energy loss dE/dx in the SVT sensors. The dynamic range of the analog readout is about 10-15 times the value corresponding to minimum ionizing particles, which is sufficient to make the dE/dx capability of the SVT useful for particle identification [35].

Each sensor will provide 2 measurements of dE/dx, one for each sensor side, for a total of 12 dE/dx measurements in the SVT. In *BABAR*, where a total of 10 dE/dx measurements (5 layers) were available, for every track with signals from at least four sensors in the SVT, a 60% truncated mean dE/dx was calculated. The cluster with the smallest dE/dx energy was also removed to reduce sensitivity to electronic noise. For MIPs a resolution on the truncated mean dE/dx of approximately 14% was obtained.

The intrinsic smearing from the distribution of the energy deposition in the silicon sensors and from the atomic binding effects in the silicon will dominate the uncertainty on the measured dE/dx [35]. The contribution to the dE/dx uncertainty from the electronic noise should be relatively small. Therefore the resolution on dE/dx for MIPs is expected to be similar to that achieved in *BABAR*. However, the dE/dx precision is approximately inversely proportional to the square root of the number of dE/dx samples used for the truncated dE/dx mean calculation [36]. Two additional measurements in the Layer0 should improve the average resolution of a factor $\sqrt{5/6} = 0.9$, where 5 is the average number of dE/dx samples used in *BABAR* and 6 is the expected average number in Super$B$. The e/π separation is expected to be larger than 3σ for momenta lower than 150 MeV/c and will be very useful for rejecting low momentum electrons from background QED processes.

6.4 Silicon Sensors

Layers 1 to 5 of the SVT will be based on 300 μm thick double-sided silicon strip sensors, with integrated AC-coupling capacitors and polysilicon bias resistors. These devices are a technically mature and conservative solution that matches the requirements to be met by the SVT i.e. to provide precise, highly segmented tracking near the interaction point. For the new Layer0, the baseline option also foresees the use of double-sided silicon strip detectors, with short strips ('striplets'), 20 mm long, oriented at ±45 degrees from the beam direction, fabricated on 200 μm thick substrates. The requirements that the sensors must meet are discussed below.

6.4.1 Requirements

Material budget. To achieve good vertex resolution, it is especially important to minimize the material up to and including the first measurement. This requirement, and the need to provide precise vertexing in both z and $r\phi$ views, leads to the choice of double-sided detectors. For Layers 1 to 5 we plan to use 300 μm thick silicon wafers, which are a standard choice and present acceptable handling properties. For Layer0, given the very stringent limitations on the amount of material, we are forced to go to 200 μm thick substrates.

Efficiency. The silicon detectors must maintain high single-point efficiency in order to meet the requirements given in Section 6.1 for high overall track reconstruction efficiency. Loss of efficiency can occur from defective sensor strips, from bad interconnections, or from faulty electronics channels. Sensor related inefficiencies can be due to fabrication defects or handling damage, which can result in strips with high leakage currents, poor insulation or broken AC-coupling capacitor. Our goal is to achieve an overall strip failure rate below 1% for each sensor. The experience gained from a large production of double-sided AC-coupled detectors for the ALICE Inner Tracking System indicates that a total rate of defective strips below 1% can be achieved with reasonable yield ($> 70\%$).

Resolution. As described in Section 6.1, we require the intrinsic point resolution to be 15 μm or better in both z and ϕ for the inner layers (Table 6.2). These are the point resolutions for tracks at near-normal incidence. As the angle between the track and the plane normal to the strip increases, the resolution initially improves, then degrades. We require the resolution to degrade by no more than a factor of ~ 3 for angles up to $75°$ from normal incidence.

Radiation hardness. The sensors must hold up to integrated doses of ionizing radiation and to 1 MeV equivalent neutron fluences as high as reported in Table 6.3. This requirement leads to the use of AC-coupled sensors in order to avoid the problems associated with direct coupling of the large leakage currents caused by the irradiation. It also has implications in the choice of the strip biasing scheme, making the punch-through technique unsuitable and limiting the maximum values of the polysilicon resistors.

Another important effect of the irradiation is a change in the effective dopant concentration of the substrate and, as a consequence, on the minimum bias voltage necessary to deplete the sensor and to achieve full collection of the signal charge. An estimate of these effects is given in the next section.

6.4.2 Sensor design and technology

From the above requirements and from the discussion in Section 6.1, we have arrived at the detector specifications and design parameters described in the following.

Sensor models and sizes. Given the increased module length with respect to the *BABAR* SVT, in order to reduce the insensitive area between adjacent sensors and the complexity of the assembly operations – and to simplify the detector alignment task – we seek to minimize the number of sensors making up each SVT module. Taking into account the constraints on the module sizes coming from the overall SVT design (Section 6.1), this goal can be met by designing a specific sensor model for each module type – plus the wedge shaped sensor – and by having the sensors fabricated on 150 mm diameter wafers.

We are therefore led to nine different sensor models, whose overall sizes are listed in Table 6.8 together with strip numbers and pitches, which will be discussed later.

Although 300 μm thick sensors fabricated on 150 mm substrates are by now an available option from several suppliers, processing the Layer0 double sided sensors on 200 μm thin, 150 mm diameter wafers is a significant challenge, which very few manufacturers are willing to tackle. Unfortunately, while Layers 1-5 could also be assembled from smaller sensors, fitting inside 100 mm wafers, Layer0 sensors require larger wafers. This is due to the requirement to have only one sensor per Layer0 module,

Table 6.8: Physical dimensions, number of strips and pitches for the nine different sensor models. Model VI has a trapezoidal shape.

Sensor Type	0	I	II	III	IVa	IVb	Va	Vb	VI
Dimensions (mm)									
z Length (L)	105.2	111.7	66.4	96.4	114.6	119.8	102.2	106.0	68.0
ϕ Width (W)	15.1	41.3	49.4	71.5	52.8	52.8	52.8	52.8	52.8-43.3
Thickness	0.20	0.30	0.30	0.30	0.30	0.30	0.30	0.30	0.30
PN junction side reads	u	z	z	ϕ	ϕ	ϕ	ϕ	ϕ	ϕ
Strip Pitch (μm)									
z (u for Layer0)	54	50	50	55	105	105	105	105	105
ϕ (v for Layer0)	54	50	55	50	50	50	50	50	$50 \rightarrow 41$
Readout Pitch (μm)									
z (u for Layer0)	54	100	100	110	210	210	210	210	
ϕ (v for Layer0)	54	50	55	100	100	100	100	100	$100 \rightarrow 82$
Number of Readout Strips									
z (u for Layer0)	1536	1104	651	865	540	565	481	499	318
ϕ (v for Layer0)	1536	799	874	701	512	512	512	512	512

which in turn is dictated by the need to minimize insensitive regions and mechanical support structures, and also by limitations on the available number of readout channels. These difficulties are mitigated by the very small number of Layer0 sensors required and the fact that five of them can comfortably fit into a single 150 mm wafer. Because of this, a lower fabrication and assembly yield can be tolerated for Layer0 sensors.

Fabrication technology. The microstrip sensors will be fabricated on n-type wafers, with p^+ strips on the junction side and n^+ strips on the ohmic side, insulated by patterned p^+ implants (p-stops) in between, or by a uniform p-type implant (p-spray). The strips will be AC-coupled, with integrated capacitors and polysilicon bias resistors. The alternative biasing method, exploiting the punch-through effect, does not offer adequate radiation tolerance.
This has proven to be a mature, reliable technology, requiring no R&D.

Substrate resistivity and depletion voltages. The wafer resistivity is assumed to be in the range 6–8 kΩ cm, corresponding to a depletion voltage of 50–38 V for 300 μm thick sensors. These values seem to be a reasonable compromise between the need to limit the initial depletion voltage and peak electric fields on one hand, and on the other hand the desire to delay the onset of type inversion due to radiation damage.
In fact, the relatively high radiation levels expected will cause a significant displacement damage in the substrate. The expected 1 MeV neutron equivalent fluences over 7.5 years of operation at nominal luminosity, both without and with an additional safety factor of 5, are reported in Table 6.9 for the various layers, together with the effective dopant concentration N_{eff} and the total depletion voltage V_{td} expected at the end of the irradiation period. For all Layers the initial (pre-irradiation) resistivity was assumed to be 7 kΩ cm, corresponding to a donor concentration $N_d = 6.3 \times 10^{11}$ cm^{-3} and to a total depletion voltage of 19 V for the 200 μm thick Layer0 sensors and 44 V for the 300 μm thick sensors of the other layers. The changes in effective dopant concentration have been pre-

Table 6.9: Values for the total 1 MeV neutron equivalent fluence Φ_{tot}, effective dopant concentration N_{eff} and total depletion voltage V_{td} after 7.5 years at nominal radiation load, without and with the the $5\times$ safety factor. For all Layers the initial (pre-irradiation) resistivity was assumed to be 7 kΩ cm, corresponding to a donor concentration $N_d = 6.3 \times 10^{11}$ cm^{-3}.

	Pre-Irrad. V_{td}(V)	Nominal radiation load in 7.5 years Φ_{tot} (cm^{-2})	Post-Irrad. N_{eff} (cm^{-3})	Post-Irrad. V_{td}(V)	With $5\times$ safety factor included $5\times\Phi_{tot}$ (cm^{-2})	Post-Irrad. N_{eff} (cm^{-3})	Post-Irrad. V_{td}(V)
Layer0	19	2.7 10^{13}	–1.3 10^{12}	40	1.4 10^{14}	–7.3 10^{12}	220
Layer1	44	5.9 10^{12}	–6.4 10^{10}	4.4	3.0 10^{13}	–1.4 10^{12}	100
Layer2	44	3.8 10^{12}	+1.2 10^{11}	8.1	1.9 10^{13}	–8.7 10^{11}	60
Layer3	44	2.3 10^{12}	+2.9 10^{11}	20	1.1 10^{13}	–4.2 10^{11}	29
Layer4	44	1.5 10^{12}	+3.9 10^{11}	27	7.5 10^{12}	–1.8 10^{11}	12
Layer5	44	1.3 10^{12}	+4.1 10^{11}	29	6.6 10^{12}	–1.2 10^{11}	8.0

dicted using the model and the data given in [37, 38, 39, 40]. Due to the long exposure time, the damage component undergoing short-therm anneal has been neglected; the reverse anneal component has been estimated taking into account, for each operation year, the remaining time until the end of the 7.5 year operation period. An operational temperature of 20 °C has been assumed. Although the possibility of cooling the SVT sensors to lower temperatures (in the range 8-12 °C) is being evaluated for the purpose of reducing the leakage current, the beneficial effect on the reverse annealing would not be very significant, considering also the fact that the detector would in any case stay at room temperature for extended periods.
With the $5\times$ factor included, the resulting final depletion voltage is still comfortable (below 100 V), except for the Layer0 sensors, for which it would reach 220 V. While this is not an unbearable value, it must be kept in mind that the Layer0 is designed to be replaceable and that the striplet detectors are foreseen to be superseded by pixels in the later part of the Super*B* operation.

Configuration of z and ϕ readout strips. The choices regarding the strip readout pitch and which side of the detector (junction or ohmic) should read which coordinate (z or ϕ) largely follow those adopted for the *BABAR* SVT.

At equal pitch, the strip capacitance and, consequently, its noise contribution is somewhat smaller on the junction side than on the ohmic side. Furthermore, the series resistance of the metal strip can be made lower, because the absence of p-stops leaves room for a wider metal readout strip. For these reasons, and because the z vertex measurement is more important from the point of view of physics, we use the junction side for the z strips on the inner Layers 1 and 2 (in Layer0 the two sides read equivalent coordinates, being oriented at ±45° from the beam direction).

The choice of the strip pitch is influenced by several factors, such as the number of available readout channels, the strip capacitance, series resistance and leakage current, the limited area available for the bias resistors, the need to maintain a large enough signal from angled tracks. Profiting from the optimization work made for the *BABAR* SVT, and the experience gained from its operation, the following choices have been made:

Table 6.10: Estimated strip capacitance and series resistance for the different sensor models.

Detector Model	z readout side (u for model 0)			ϕ readout side (v for model 0)		
	C_{strip}/ℓ (pF/cm)	C_{AC}/ℓ (pF/cm)	R_{series}/ℓ (Ω/cm)	C_{strip}/ℓ (pF/cm)	C_{AC}/ℓ (pF/cm)	R_{series}/ℓ (Ω/cm)
0	2.5	40	9	2.5	30	14
I	1.7	40	5	2.5	30	9
II	1.7	40	4	2.5	30	7
III	1.7	30	7	1.7	40	4
IVa,IVb,Va,Vb	1.7	60	3	1.7	40	4
VI	1.7	60	3	1.7	30	4.5

- both sides of Layer0 are read by strips with a 54 μm pitch, without intermediate floating strips;
- the z-side of Layers 1, 2 is read by p-type strips with a 100 μm pitch with one intermediate floating strip;
- the z-side of Layer3 is read by n-type strips with a 110 μm pitch with one intermediate floating strip;
- the z-side of Layers 4, 5 is read by n-type strips with a 210 μm pitch with one intermediate floating strip;
- the ϕ-side of Layer1 is read by n-type strips with a 50 μm pitch without intermediate floating strips;
- the ϕ-side of Layer2 is read by n-type strips with a 55 μm pitch without intermediate floating strips;
- the ϕ-side of Layers 3, 4, 5 is read by p-type strips with a 100 μm pitch with one intermediate floating strip.

The strip pitches and the resulting numbers of strips for the various sensor models are listed in Table 6.8.

Strip capacitance and resistance. Important strip parameters are the capacitance, the series resistance and the leakage current, all of which are proportional to the strip length ℓ. For long strips, as will be those of the SVT, the noise contribution of the strip resistance becomes more important, because it is proportional to the strip capacitance multiplied by the square root of the resistance. This gives an $\ell^{3/2}$ dependence on the strip length, to be compared with an ℓ dependence for the noise contribution of the strip capacitance and an $\ell^{1/2}$ dependence for that of the leakage current. In order to reduce the series resistance of the strips, we plan to increase the thickness of the aluminum metallization beyond the standard value of ~ 1 μm.

Table 6.10 reports the expected values for the strip capacitance – as deduced from measurements on *BABAR* sensors and other strip sensors – and for the strip series resistance, as calculated from the design width of the strips and a metallization thickness of 2.5 μm.

Strip leakage current. After an initial period of operation, the strip leakage current will be dominated by carrier generation at radiation-induced defects. Table 6.11 reports the total 1 MeV neutron equivalent fluence for the different layers and the maximum leakage current expected for ϕ and z-side strips, after 7.5 years at nominal radiation load, without and with the $5\times$ safety factor. Because of the long irradiation time, spanning 7.5 years, the currents are calculated taking into account the effect of the annealing, by assuming a current damage coeffi-

Table 6.11: Total 1 MeV neutron equivalent fluence Φ_{tot} for the different layers and maximum leakage current I_{leak} for ϕ and z-side strips of a module, after 7.5 years at nominal radiation load, without and with the 5× safety factor. An operational temperature of 20 °C is assumed.

	Nominal radiation load in 7.5 years			With 5× safety factor included		
	Φ_{tot} (cm^{-2})	ϕ strips I_{leak} (μA)	z strips I_{leak} (μA)	$5\times\Phi_{tot}$ (cm^{-2})	ϕ strips I_{leak} (μA)	z strips I_{leak} (μA)
Layer0	2.7 10^{13}	0.15	0.15	1.4 10^{14}	0.75	0.75
Layer1	5.9 10^{12}	0.28	0.40	3.0 10^{13}	1.4	2.0
Layer2	3.8 10^{12}	0.23	0.31	1.9 10^{13}	1.2	1.6
Layer3	2.3 10^{12}	0.37	0.30	1.1 10^{13}	1.8	1.5
Layer4	1.5 10^{12}	0.39	0.41	7.5 10^{12}	1.9	2.0
Layer5	1.3 10^{12}	0.43	0.36	6.6 10^{12}	2.1	1.8

cient $\alpha = 2.8\times10^{-17}$ A/cm. The values reported in the table refer to a module strip, composed of a few sensor strips daisy-chained together into a readout channel, by direct bonding on the ϕ-side and by using the fanout circuits on z-side. For the z-side, different numbers of strips (up to three) can be connected together to a single readout channel within the same module; in this case the table reports are the maximum value of the current.

AC coupling capacitors. The strips are connected to the preamplifiers through a decoupling capacitor, integrated on the detector by interposing a dielectric layer between the p or n-doped strip and the metal strip. AC coupling prevents the amplifier from integrating the leakage current with the signal; handling the high leakage currents due to radiation damage imposes an additional heavy burden on the preamplifier design. On each sensor, the value of the decoupling capacitance must be much larger than the total strip capacitance on the same sensor, a requirement which is easily met by the current fabrication technologies.

Bias resistors. The bias resistor values will range between 1 and 8 MΩ, depending on the layer and the detector side. The choice of the R_B value is constrained by two requirements. A lower limit is determined by the need to limit the noise contribution, which has a $\sqrt{\tau/R_B}$ dependence, and if several strips are ganged together the effective resistance is correspondingly decreased. The requirement that, for floating strips, the product $R_B \cdot C_{TOT}$ must be much larger than the amplifier peaking time in order to allow for capacitive charge partition is fulfilled with ample margin for any reasonable values of R_B. An upper limit to R_B is dictated by the allowable potential drop due to the strip leakage current, which depends mainly on the irradiation level and decreases going from inner to outer layers. The maximum resistance value is also limited in practice by the need to limit the area occupied on the wafer. Values of 40 kΩ/square for the sheet resistance of polysilicon can be achieved with sufficient reproducibility. Thus, it is possible to fabricate a 10 MΩ resistor with a 6 μm wide, 1500 μm long polysilicon resistor. With a suitable shaping of the polysilicon line, the space required by the resistor will be less than 200 μm at 100 μm pitch (corresponding to strips at 50 μm pitch with resistors placed at alternate ends). A final requirement is that the bias resistance be sufficiently stable against the expected radiation exposure, a condition that is easily satisfied by polysilicon resistors.

Table 6.12: Number of the different sensor types per module, area of the installed sensors, number of installed sensors and number of sensors including spares. Spare sensors include one spare module per module type (two for Layer0), plus additional sensors accounting for possible losses during the whole SVT assembly process.

Sensor Type	0	I	II	III	IVa	IVb	Va	Vb	VI	All
Layer0	1	-	-	-	-	-	-	-	-	1
Layer1	-	2	-	-	-	-	-	-	-	2
Layer2	-	-	4	-	-	-	-	-	-	4
Layer3	-	-	-	4	-	-	-	-		4
Layer4a	-	-	-	-	4	-	-	-	2	6
Layer4b	-	-	-	-	-	4	-	-	2	6
Layer5a	-	-	-	-	-	-	6	-	2	8
Layer5b	-	-	-	-	-	-	-	6	2	8
Silicon Area (m^2)	0.013	0.055	0.079	0.167	0.194	0.203	0.291	0.302	0.222	1.52
Nr. of Sensors	8	12	24	24	32	32	54	54	68	308
Nr. Including Spares	20	20	40	35	44	44	72	72	92	439

Edge region and active area. Considering the space needed to accommodate the bias resistors and to prevent the depletion region from reaching the cut edge of the sensor, we specify the active region of the detectors to be 1.4 mm smaller than the physical dimensions, that is, the dead region along each edge has to be no more than 700 μm wide. This is the same specification chosen for the *BABAR* strip detectors and, although stricter than adopted by most silicon sensor designs, has proven to be feasible without difficulty, thanks to the choice of placing the polysilicon resistors in the edge region, outside the guard ring. For Layer0 sensors, which have a reduced thickness of 200 μm and smaller value, shorter bias resistors, we specify a 600 μm wide inactive edge region.

6.4.3 z-side strip connection options

On z-side, the readout pitch is set to 100 μm in Layers 1 and 2, 110 μm in Layer3 and 210 μm in Layers 4 and 5, with a 'floating' strip in between, to improve spatial resolution for particle tracks with close to normal incidence. Since the number of readout strips exceeds the number of available electronic channels, it is necessary to 'gang' together up to three (depending on the SVT layer) strips. The 'ganging' scheme – adopted in the *BABAR* SVT – connects two or three far apart strips to the same readout channel (Figure 6.23), thus preserving the strip pitch at the expense of a higher capacitance and series resistance (both resulting in higher noise), in addition to introducing ambiguities in the hit position.

For tracks at small θ angles with respect to the beam direction (that is, large incidence angles on the sensor), the signal-to-noise ratio is further degraded by the fact that a track traverses several z-strips (up to nine in the inner layers) and the signal becomes approximately proportional to the strip readout pitch (only 1/3 the wafer thickness in Layers 1 to 3). This suggests that one should adopt an alternative connection scheme, in which two (or more, at large incidence angles) *adjacent* strips are bonded to a single fanout trace, effectively increasing the strip pitch and the signal into a readout channel, with a less than proportional increase in capacitance, and no increase in series resistance. We call this connection scheme 'pairing'.

At small θ angles, this gives better S/N and, consequently, higher detection efficiency when

Table 6.13: List of different mask sets for 150 mm wafers, specifying the content of each wafer layout, the minimum value of the distance between the sensors and the wafer edge, the number of wafers required for each design and the total number of wafers. The numbers quoted include the spare sensors, but not the fabrication yield.

Mask Design	Wafer content	Min. Clearance to Wafer Edge (mm)	Number of Wafers
A	5×Mod 0	10.2	5
B	Mod I + Mod VI	8.2	20
C	Mod III	15.0	35
D	Mod IVa	11.9	44
E	Mod IVb	9.5	44
F	Mod Va + Mod VI	9.8	72
G	Mod Vb + Mod II	6.9	72
Total			287

compared to individually connected strips. The improvement is even more important in comparison to the 'ganging' scheme, where the strip capacitance is proportional to the number of strips ganged together, but the signal remains that of a single strip. Moreover, for paired strips also the fanout capacitance and resistance can be made lower, because of the larger trace pitch.
Due to the lower noise, at small θ angles pairing is also expected to give better spatial resolution with respect to ganging. In order to avoid a significant increase of the input capacitance, pairing will be made between the 'readout' strips (at 100 μm pitch) so that a 'floating' strip is always present *between* two adjacent groups of paired strips. However, we are evaluating the option of connecting also the intermediate (otherwise floating) strips *within* a group of paired strips.

Strip capacitance measurements performed on test sensors [41] confirm that pairing yields significantly lower capacitance with respect to ganging the same number of strips; the advantage in capacitance of pairing with respect to ganging increases for higher pairing/ganging multiplicity. The additional increase in total capacitance when connecting also the intermediate strips is $4-5\%$ on the$p$-side, and $\sim 6\%$ on the n-side. In addition to this, a better charge collection efficiency is expected.

For Layers 1-3 the combination of track incidence angles and strip pitch is such that all strips can be connected to the available readout channels using a pairing-only scheme. For Layers 4-5, in part because of the 'lampshade' SVT design (limiting the track incidence angles for large $|z|$ in Layer4 and Layer5) and in part because of the larger ratio of strip to channel numbers, it is necessary to adopt a combined pairing/ganging scheme, as indicated in Table 6.1.

6.4.4 Wafer layout and quantities

Table 6.12 reports the sensor composition of the different detector modules, the number of installed sensors of each type, with the corresponding silicon areas, and the total numbers of sensors including spares. Spare sensors account for one spare module of each type (two for Layer0), plus an additional 20% to compensate for possible losses during the assembly process. We see that the current design employs nine different types of sensors, for a total of 308 installed sensors covering 1.52 m^2. Using 150 mm diameter wafers and a dedicated sensor model for each module type allows one to cover the ~ 1.5 times larger area with a smaller number of sensors with respect to *BABAR*, at the expense of having nine different models of sensors. However, through optimized usage of the wafer area it is possible to accommodate all nine sensor types in seven different wafer layouts, i.e. seven mask sets, and to fabricate all 439 sensors (spares included) on 287 wafers. This is illustrated in Table 6.13.

6.4.5 Prototyping and tests

Although both the design and the technology of double-sided microstrip sensors are well developed, and the Super*B* SVT is a direct evolution of the proven *BABAR* design, some specific aspects need to be tested on prototypes before starting the sensor production.

Prototypes of the striplet sensors for Layer0, absent in *BABAR*, have been thoroughly tested with beam at CERN in 2008 and 2011 [12, 42], showing adequate performance for use in the Super*B* SVT.

Additional tests will be required to check the performance of sensors irradiated up to the maximum levels expected at Super*B* which, although much lower than those relevant for LHC detectors, significantly exceed the radiation load experienced in *BABAR*. We plan to irradiate existing prototype sensors with designs similar to that forseen for the Super*B* SVT with neutrons and/or charged particles, as well as some spare modules remaining from the *BABAR* production.

At least one small batch of dedicated prototype sensors will be ordered and qualified before issuing the tender for the sensor supply. Given the quite different demands posed by processing double sided sensors on thin 150 mm diameter substrates, and the very small number of wafers required, fabrication of striplet sensors for Layer0 could likely be awarded to a different company than the one supplying the other sensors. Because of their special characteristics and their fragility, the striplet sensors will also follow a different, dedicated testing procedure.

A limited number of pre-series sensors will be qualified by a full electrical test using a probe station before releasing the series production. Testing double-sided sensors with automatic loading from a cassette, besides requiring a very specialized custom-made prober, would not allow sufficient flexibility for testing the many different sensor sizes equipping the SVT. The experience gained from testing *BABAR* sensors and, more recently, those for the ALICE experiment [43] shows that the routine parametric test of a double-sided sensor can be performed in about two hours using a semiautomatic probe station, with manual mounting and positioning of the sensors on dedicated support jigs designed and made in house. The time increases, of course, if some peculiar results of the test require additional dedicated measurements.

The number and the detailed characteristics of the measurements that will be included in the routine acceptance test of production sensors will depend on the results of the tests themselves. Starting from a full test on the first batches, it is possible that the set of parameters tested could be reduced if the quality and consistency of the measured characteristics will indicate that one would be advised to do so.

Overall, based on past experience, we estimate that the testing of all production sensors will take about one year if performed at a single location.

6.5 Fanout Circuits

The routing of the signals from the silicon sensors to the HDIs is performed by the so-called *fanout circuits*; they consist in flexible circuits that bring the signals from the end of the detector module (where they are wire bonded) to the front-end electronics IC (located a few tens of centimeters from the IP).

The fanout for the ϕ and z coordinates are designed to minimize the material crossed by the particle within the angular acceptance. However, while the ϕ fanout circuits are just one-to-one connections, the z ones are more complicated since they cover the full length of the detector modules (up to $\sim$40 cm for the outer layers) and have to provide the interconnection (ganging or pairing) where the number of readout strips exceeds the available readout channels.

In the following sections the details about the chosen technology and the geometrical and electrical properties of the fanout circuits are described; the layer 0 fanout will be analyzed in a dedicated section.

6.5.1 Fanouts for Layer0

The fanout circuit for the innermost layer of the SVT vertex detector is part of the striplet module and is shown in Figure 6.5. The complex shape of this passive circuit is derived from the geometry of the vertex detector. The Layer0 sensor is closely surrounded by the other layers of the vertex detector as shown in Figure 6.2 and Figure 6.3. From the mechanical model of the vertex detector it can be seen that the clearance between two adjacent detector layers is not constant along the z direction. They generally have a minimum in the center of the detector and increase slightly moving away from the center. Such geometries have been studied for each layer and the shape of the fanout maximizes the area available for the circuits, avoiding mechanical interference between the modules. The resulting outline of the Layer0 fanout is shown in Figure 6.20. The minimum width of the circuit is 29 mm while the overall length is approximately 300 mm. Each detector has one fanout. Half of the strips (768) are read from each end of the circuit.

6.5.1.1 Requirements and Technology

Due to the size, the number of lines and the shape of the fanout, the requirement of reducing the radiation length of each component of the striplet module to a minimum affects the choice of the technology as well as the line pitch to be used in the design. The technology proposed for the Super*B* fanout is similar to the one used in the past for the *BABAR* fanouts. The base material is 50 μm polyimide with metal directly deposited on the dielectric, 5 μm of copper or 10 μm of aluminum. The direct deposit of the metal on the polyimide improves the ease with which the circuit can be manufactured. The maximum trace resolutions for copper or aluminum are different and depend also on the technique used to expose the photo-resist that defines the pattern to be etched. Moreover, the maximum trace resolution depends also on the length of the lines to be etched. Typically, with the presently available best technology, the minimum line width/space is about 15/15 μm for copper and approximately 65/65 μm for aluminum on short traces (up to few centimeters), being on the contrary up to 20/20 μm for copper and 70/70 μm for aluminum on long traces (up to tens of centimeters). The feasibility of the quoted pitch values has been verified on prototypes. The use of aluminum instead of copper has the advantage of significantly reducing the radiation length of the fanout and represents a novelty to be pursued even though a larger fanout is needed to accommodate the same number of connections.

A two-layer fanout design has been preferred to a single-layer solution for the following reasons:

- the orientation of the sensor strips at ± 45 degrees from the beam axis and the aspect ratio of the circuit, long and narrow, requires that the strips are bonded to the fanout along the two long sides of the sensor, in order to keep the width of the circuit within 29 mm;
- the minimum line width/space is approximately 68/68 μm for a two-layer solution, while is of the order of 20/20 μm for the single-layer one. The former is a standard consolidated solution at least for a copper fanout, while the latter is at the present technology limit over the length of the Layer0 fanout (300 mm);
- the Layer0 fanout has to be partially bent to be installed in the detector, as shown in Figure 6.41. The bending takes place outside the sensor area and close to the region where the circuit width increases in a funnel like shape. Having 68 μm lines instead of ~ 20 μm lines increases reliability;
- the two-layer fanout can be made either in copper or in aluminum. The aluminum solution has not been manufactured before and therefore has to be considered as an R&D effort;

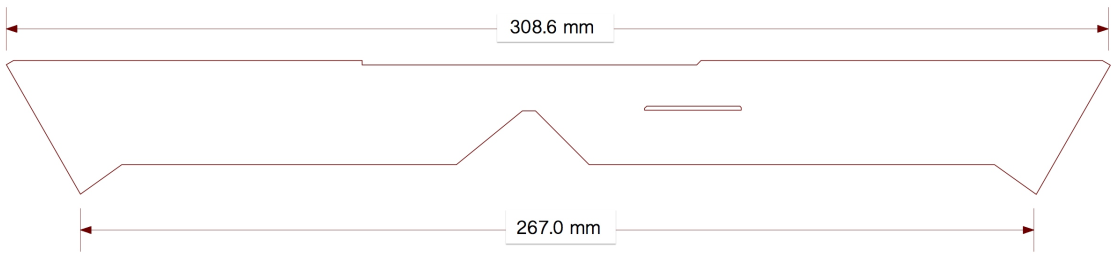

Figure 6.20: Layer0 fanout outline.

- the length of the fanout does not present any particular technological challenge.

6.5.1.2 Design

The CAD drawing of the module and the layout of one of the two layers of the fanout are shown in Figure 6.21 and Figure 6.22, respectively. The stack up of the fanout is reported in Table 6.14.

From the figures it can be seen that a cut-out, 1 mm wide, is needed in the central area of each layer to bond some of the strips and at the same time to properly route the traces without violating the 68 μm minimum pitch rule. The traces are also tapered and bent at the extremities of the circuit to match the pitch of the front end electronics pads, to which the fanout lines are wire bonded. Only in the pad region the traces are gold plated (1.5 μm) for bonding. This solution has been adopted to minimize the radiation length of the assembly. The relaxed 68 μm pitch should result in a simulated crosstalk of about 1% on adjacent traces of the same layer.

Table 6.14: Material breakdown of Layer0 fanout, surface coverage and equivalent radiation length x/X_0. The coverage of the surface area is very small for gold since it is present only on the pads.

Material	Thickness (μm)	Coverage	x/X_0 (%)
Kapton	50	1	0.017
Cu (Al)	5 (10)	0.5	0.018 (0.006)
Glue	10	1	0.003
Kapton	50	1	0.017
Cu (Al)	5 (10)	0.5	0.018 (0.006)
Au	1.5	$\leq 10^{-2}$	≤ 0.001
Total	120 (130)		0.073 (0.049)

Each layer can be individually manufactured, tested and qualified before assembly. After an initial optical inspection to spot defects, the electrical characteristics of each trace of the circuit will be measured, using a "bed of nails" to contact a group of adjacent strips. Only defect-free layers will be glued together to build the two-layer fanout assembly. Repairs of defective layers are not foreseen at the moment. The small number of fanouts to be produced, 16 pieces, justifies the request of having 100% or more redundancy during production. Moreover the copper solution does not represent a real technological challenge and so it is considered the baseline solution until the aluminum solution is proved feasible and reliable.

6.5.1.3 Prototyping and tests

All fanout assemblies will be tested against shorts and opens. Each trace will be measured in terms of resistance and capacitance to the neighbor traces and the data saved for further analysis. No repairs are foreseen on the fanout. A first batch of prototypes is in production at the CERN PCB facility. They have the previously shown layout and will be used not only to validate the design and the test procedure but also for assembling ‘mechanical’ versions of the striplet modules.

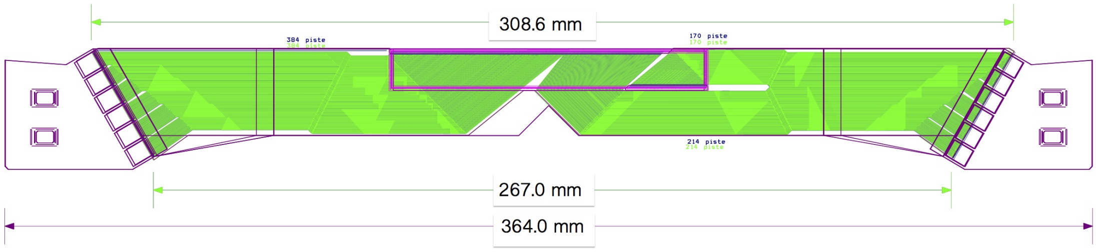

Figure 6.21: CAD drawing of the Layer0 module.

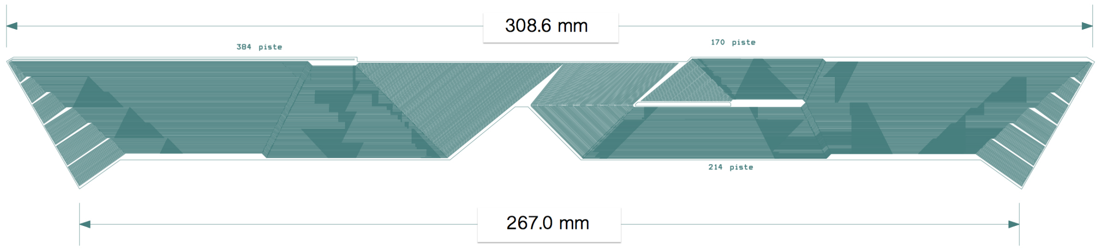

Figure 6.22: Layout of the Layer0 fanout.

6.5.2 Fanouts for outer layers

6.5.2.1 Requirements

The geometrical requirements will be fixed by the detector designs. From the technological point of view, the design requires a typical line width/space of 45/45 μm and a small region of 15/15 μm. This region (corresponding to the bonding area) is 1.5 mm long and it extends to the total width of the fanout itself. No constraints are present on the fanout length given the same machines used for the micro-pattern gas detector production will be used.

6.5.2.2 Material and production technique

The *BABAR* fanouts were produced on 50 μm Upilex substrates (manufactured by UBE Industries, Ltd.[1]) with a deposit of 150 nm of Cr, 4.5 μm of copper followed by a layer of 150 nm of Cr and 1.5 μm of amorphous gold. The Super$B$ SVT fanouts will be produced on a similar material by UBE (50 μm of polyimide with 5 μm of copper directly deposited on the base material) which should ensure fewer defects and thus a better yield. This material will be tested in the prototype phase. The old Upilex is anyway still available if the new material would prove to be inadequate.

A new fabrication technique will be implemented in order to reduce the production time. In the *BABAR* production line, the photo-resist was exposed through a mask after being deposited on the Upilex, which requires working in a clean room. For Super$B$, the idea is to expose the photo-resist directly with a scanned laser beam, without a photo-mask; the photo-resist is solid and the whole procedure, performed in a clean micro-environment inside a machine, becomes much faster. This technique has already been tested on samples with the same pitches foreseen for the Super$B$ SVT fanouts.

The increase in the production speed allows one to repeat the fabrication of pieces with defects without delaying the SVT assembly. All the fanouts will be gold plated with 1.5 μm of amorphous gold for bonding.

[1] http://www.ube-ind.co.jp/english/about/index.htm

6.5.2.3 Design

The design will follow the same rules of the *BABAR* fanouts adapting it to the different length of the modules. Unlike the *BABAR* pieces, no test-tree is foreseen (see next section). To allow the gold plating, all the lines will be shorted together by a small extension of the circuit. A suitable cutting device will be developed to cut away the shorting extension after visual inspection.

Table 6.15 summarizes the geometrical parameters[2] as well as the number of readout strips and channels, the typical pitch and the total number of required circuits per layer and type.

Figure 6.23 presents a sketch of the ganging principle proposed for the design of layers z 3-4-5.

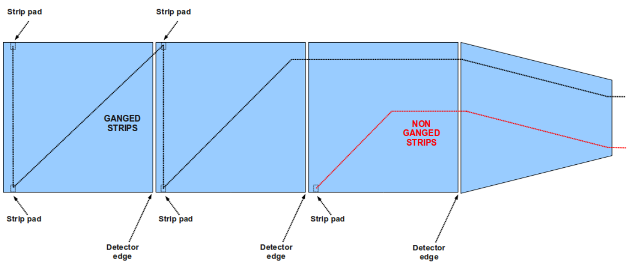

Figure 6.23: Schematic view of two z strips ganged through the fanout circuit.

6.5.2.4 Tests and prototyping

All the fanouts will be automatically optically checked by a dedicated machine which will use the CAD layout files of the fanouts to find shorted or open lines. The machine can work with 25 μm lines; the region with smaller lines (15 μm with a 15 μm space) will have to be controlled manually.

Given the short time needed for the production, no correction is foreseen for shorted or open lines; the damaged pieces will be produced again. However, if a short is present in the larger pitch region, the same correction procedure used for *BABAR* (involving the use of a micro-probe to remove the short) can be implemented.

As far as the tests are concerned, two batches of prototypes have been manufactured up to now. The first batch (designed starting from the *BABAR* layout) has been used to check the performance of the fabrication machine and the whole production chain. The second batch, conforming to the Super*B* Layer3 design (shown in Figure 6.24), has been used to estimate the trace capacitance and resistance: values of C/l ∼0.6 pF/cm and of R/l ∼1.2 Ω/cm have been found. These pieces in principle can be used with working detectors to test also the assembly procedure.

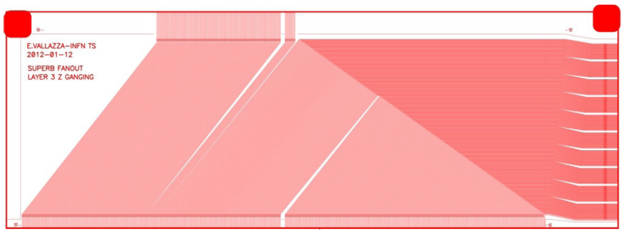

Figure 6.24: Design of a z fanout prototype of layer 3.

Figures 6.25 and 6.26 show a picture of the prototype of the layer 3 z and a step of the cutting procedure.

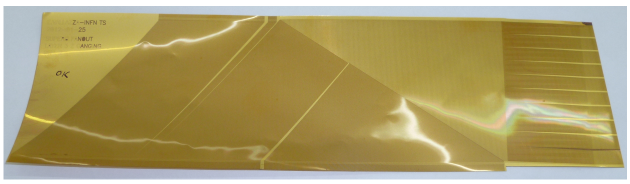

Figure 6.25: Picture of the prototype of the layer 3 z.

6.6 Readout Electronics

The SVT electronics chain consists of various separate hardware components. Starting from the detector and going to the ROM boards, the chain contains: a) the readout chips mounted

[2]The fanouts dimensions have been taken from the SVT Mechanics talk presented at the 4^{th} Super*B* Collaboration Meeting (June 2012, La Biodola - Elba IT).

Table 6.15: Summary of fanout circuit characteristics.

Layer	Fanout	Length (mm)		Number of Readout		Typical Pitch at (μm)		Number
	Type	Left	Right	Strips	Channels	Input	Output	of Circuits
1	z	216.76	217.52	1104	896	100	45	12
	ϕ	105.60	105.82	799	896	50	45	12
2	z	209.00	208.80	1302	896	100	45	12
	ϕ	76.20	76.00	874	896	55	45	12
3	z	250.26	246.26	1730	1280	110	45	12
	ϕ	54.76	53.46	701	1280	100	45	12
4a	z	332.91	328.60	1398	640	210	45	16
	ϕ	35.71	31.40	512	640	82	45	16
4b	z	332.15	327.97	1448	640	210	45	16
	ϕ	24.55	20.37	512	640	82	45	16
5a	z	407.13	411.40	1761	640	210	45	18
	ϕ	32.53	36.80	512	640	82	45	18
5b	z	406.63	411.00	1815	640	210	45	18
	ϕ	20.63	25.00	512	640	82	45	18

on an HDI placed at the end of the sensor modules; b) wire connections to a transition card (signals in both directions and power lines); c) a transition card, placed about 50-70 cm from the end of the sensors, hosting the wire-to-optical conversion; d) a bidirectional optical line running above 1 Gbit/s; e) a receiver programmable board (front-end board: FEB). A sketch of the full data chain is given in Figure 6.27

6.6.1 Readout chips for Strip and Striplet Detectors

The front-end processing of the signals from the silicon strip detectors will be performed by custom-designed ICs mounted on hybrid circuits that distribute power and signals, and thermally interface the ICs to the cooling system. As discussed below, the very different features of the inner (Layer 0-3) and outer layers (4 and 5) of the SVT set different requirements on the readout chip, which makes it necessary to include programmable features in the readout ICs, in order to adjust operating parameters over a wide range. This obviously also holds in the case that a different technology (pixels) is adopted for Layer 0 instead of short strips (striplets). Generally speaking, the ICs will consist of 128 channels, each connected to a detector strip. The signals from the strips, after amplification and shaping will be compared to a preset threshold. If a signal exceeding the threshold is detected, a 4 bit analog information about the signal amplitude will be provided with the Time Over Threshold technique. The analog infor-

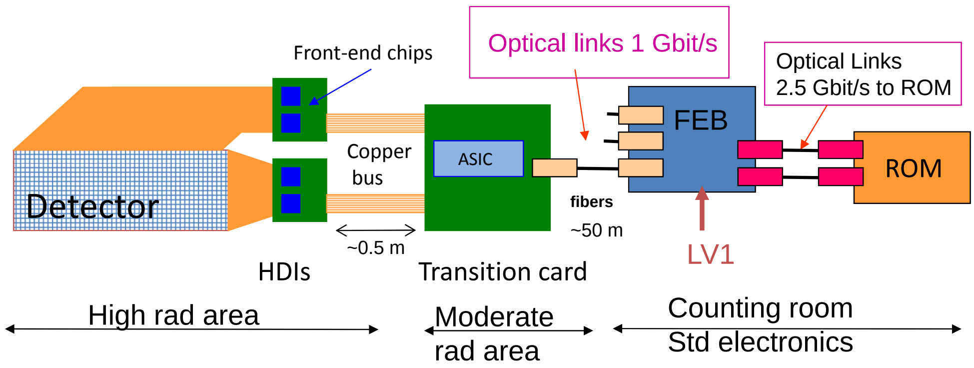

Figure 6.27: Schematic drawing of the full SVT data chain.

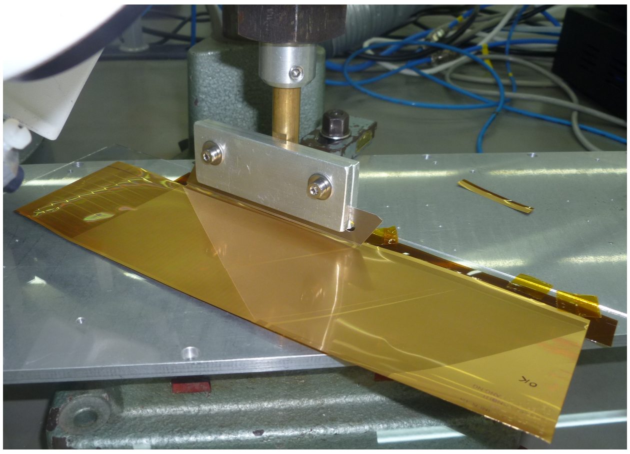

Figure 6.26: Picture of the prototype of the layer 3 z during the cutting procedure.

mation is useful for position interpolation, time walk correction, dE/dx measurements, as well as for calibration and monitoring purpose. The dimensions of the readout IC are expected to be about 6×4 mm^2. As discussed in the SVT HDI subsection of this TDR, the dimensions of the HDI set a 6 mm upper limit on the side of the chip with the bonding pads for the interconnection with the strip sensors. The power dissipation will be below 4 mW/channel including both analog and digital sections. For each channel with a signal above threshold, the strip number, the amplitude information, the chip identification number and the related time stamp will be stored inside the chip waiting for a trigger signal for a time corresponding to the trigger latency (about 6 μs, with 150 kHz trigger rate). When a trigger is received, data will be read out and transmitted off chip, otherwise they will be discarded. The data output from the microstrip detector will be sparsified, i.e. will consist only of those channels generating a hit. The readout integrated circuits must remain functional up to 5 times nominal background.

The option of operating in a data push fashion could be preserved for the external layers, where this is feasible as a result of the low strip hit rate. This will provide the possibility to feed data from these layers to the trigger system.

6.6.2 Readout chips requirements

The microstrip electronics must ensure that the detector system operates with adequate efficiency, but also must be robust and easy to test, and must facilitate testing and monitoring of the microstrip sensors. AC coupling is assumed between the strips and the readout electronics. The following summarises the required characteristics:

- **Mechanical Requirements:**
  Number of channels per chip: 128
  Chip size: width ≤6 mm, length ≤4 mm
  Pitch of input bonding pads: <45 μm

- **Operational Requirements:** Operating temperature: <40 °C
  Radiation tolerance: >3 Mrad/year,

>5·10^{12} n_{eq}/cm^2/year (these are the expected values in Layer 0; in outer layers, radiation levels are at least one order of magnitude lower)
Power dissipation: <4 mW/channel
Detector and fanout capacitance: 10 pF $\leq C_D \leq$ 70 pF (the chip must be stable when sensor strips are disconnected from the input pads of the analog channels)

- **Dynamic range:** The front-end chips must accept signals from either P or N-side of the strip detectors. A linear response of the analog processing section is required from a minimum input charge corresponding to 0.2 MIP up to a full dynamic range of 10-15 MIP charge for dE/dx measurements.

- **Analog Resolution:** The front-end chips have to provide analog information about the charge collected by the detector, which will be also used for calibrating and monitoring the system. A resolution of 0.2 MIP charge is required for dE/dx measurements. In the case of a compression-type ADC, based on the time-over-threshold technique (ToT), this may translate into 4 bits of information.

- **Efficiency:** At design luminosity, the microstrip readout must have a hit efficiency of at least 90% during its entire operational lifetime. This includes any loss of data by readout electronics or readout dead time.

- **Readout bandwidth:** Data coming out of the chip will be substantially reduced by operating in a triggered mode. The chips can use up to 2 output LVDS lines with 180 MHz clock, as it is needed to handle the higher data throughput in inner SVT layers.

- **Radiation Tolerance:** All the components of the microstrip readout system must remain operational over the entire lifetime of the experiment, including a safety factor of 5 on the nominal background expected, this corresponds to 7.5×5 years at nominal peak luminosity of 10^{36}.

- **Operational lifetime:** Up to 10 years of Super$B$ running at the nominal luminosity.

- **Peaking Time:** The constraints for the peaking time of the signal at the shaper output are dictated by different needs in inner and outer layers. In Layer 0, the high occupancy due to background and the need to avoid pulse overlap and consequent hit inefficiencies set the required peaking time in the range of t_p=25-50 ns, which also allows for a high time resolution (see below). In the external layers 4 and 5, where background hit frequency is much smaller and where strips are longer and have a larger capacitance, the peaking time will be mostly determined by the need to reduce series noise contributions and will be in the range of 0.5-1.0 μs.

- **Signal-to-Noise Ratio:** Concerning the signal, this requirement has to take into account the different thickness of silicon detectors in inner (200 μm) and outer (300 μm) layers, as well the signal spread among various strips that depends on the track angle inside detectors and that, again, may vary in different SVT layers. Noise-related parameters (strip capacitance and distributed resistance) also vary significantly across the SVT. A signal-to noise ratio of 20 has to be ensured across the whole SVT and should not decrease significantly after irradiation. Here are the two extreme cases (where the equivalent noise charge ENC includes the thermal noise contribution from the distributed resistance of the strips):

  - Layer 0 striplets: ENC ≈900 e- at C_D=14.9 pF and at t_p=25 ns
  - Layer 5 strips: ENC ≈1100 e- at C_D=66.2 pF and at t_p=750 ns

- **Threshold and Dispersion:** Each microstrip channel will be read out by comparing its signal to a settable threshold around 0.2 MIP. Threshold dispersion must be low enough that the noise hit rate and the efficiency are degraded to a negligible extent. Typically, this should be 300 rms electrons at most and should be stable during its entire operational lifetime.

- **Comparator Time Resolution:** The comparator must be fast enough to guarantee that the output can be latched in the right time stamp period.

- **Time Stamp:** A 30 ns time stamp clock is required for inner layers to get a good hit time resolution in order to reduce the occupancy in the target offline time window (100-150 ns). In the outer layers the time stamp resolution is less critical since the hit time resolution will be dominated by the long pulse shaping time. A single 30 ns time stamp clock in all layers will be used.

- **Chip clock frequency:** Two main clocks will be used inside the readout chip, the time stamp clock (about 30 MHz) and the readout clock (120 MHz or 180 MHz). These clocks will be synchronized with the 60 MHz Super$B$ system clock. In the case that the analog-to-digital conversion is based on the Time-Over-Threshold method, a ToT clock has to be generated inside the chip. The ToT clock period should at least match the pulse shaping time to get a good analog resolution. A faster ToT clock could slightly improve the analog resolution but an upper limit (≈3.5) on the ratio between ToT clock frequency and the shaping time frequency is imposed by the required dynamic range needed for low momentum particle dE/dx measurements (≈10-15 MIP) and the number of bits available for ToT. With the experience of the *BABAR* Atom chip a ToT clock frequency 3 times higher than the pulse shaping frequency could be used.

- **Mask, Kill and Inject:** Each micro-strip channel must be testable by charge injection to the front-end amplifier. By digital control, it shall be possible to turn off any micro-strip element from the readout chain.

- **Maximum data rate:** Simulations show that machine-related backgrounds dominate the overall rates. At nominal background levels (including a safety factor of 5), the maximum hit rate per strip goes from about 1 MHz/strip in Layer 0 to about 50 kHz/strip in Layer 5, z-side.

- **Deadtime limits:** The maximum total deadtime of the system must not exceed 10 % at a 150 kHz trigger rate and background 5 times the nominal expected rate.

- **Trigger specifications:** The trigger has a nominal latency of about 6 μs, a maximum jitter of 0.1 μs, and the minimum time between triggers is 70 ns. The maximum Level 1 Trigger rate is 150 kHz.

- **Cross-talk:** Must be less than 2 %.

- **Control of Analog Circuitry on Power-Up:** Upon power-up, the readout chip shall be operational at default settings.

- **Memory of Downloaded Control of Analog Circuitry:** Changes to default settings shall be downloadable via the readout chip control circuitry, and stored by the readout chip until a new power-up cycle or additional change to default settings.

- **Read-back of Downloadable Information:** All the data that can be downloaded also shall be readable. This includes data that has been modified from the default values and the default values as applied on each chip when not modified.

- **Data Sparsification:** The data output from the microstrip detector shall be only of those channels that are above the settable threshold.

- **Microstrip output data content:** The microstrip hit data must include the time stamp and the microstrip hits (strip number and relevant signal amplitude) for that time stamp. The output data word for each strip hit should contain 16 bits (7 strip addresses, 4 ToT, 1 type (Hit or Time Stamp) 4 bits to be defined). A 10-bit time stamp (with 6 additional bits: 1 type, 5 bits to be defined) will be attached to each group of hits associated to a given time stamp (hit readout will be time-ordered).

6.6.3 Readout Chip Implementation

The Super*B* SVT readout chips are mixed-signal integrated circuits in a 130 nm CMOS technology and are being designed to comply with the requirements discussed above. Each chip comprises 128 analog channels, each consisting of a charge-sensitive preamplifier, a unipolar semi-Gaussian shaper and a hit discriminator. A polarity selection stage will allow the chip to operate with signals delivered both from n- and p-sides of the SVT double-sided strip detectors. A symmetric baseline restorer may be included to achieve baseline shift suppression. When a hit is detected, a 4 bit analog-to-digital conversion will be performed by means of a Time-Over-Threshold (ToT) detection. The hit information will be buffered until a trigger is received; together with the hit time stamp, it will then be transferred to an output interface, where data will be serialized and transmitted off chip on LVDS output lines. An n-bit data output word will be generated for each hit on a strip. A programming interface accepts commands and data from a serial input bus and programmable registers are used to hold input values for DACs that provide currents and voltages required by the analog section. These registers have other functions, such as controlling data output speed and selecting the pattern for charge injection tests.

Given the very different requirements of inner and outer layers, in terms both of detector parameters and hit frequency, several programmable features will be included in the chips such as the peaking time, the gain and the size of the input device. The block diagram of the analog channel is shown in Figure 6.28.

The digital readout of the matrix will exploit the architecture that was originally devised for a high-rate, high-efficiency readout of a large CMOS pixel sensor matrix. A schematic concept of the FE chip readout is shown in Figure 6.29. Each strip has a dedicated array of pre-trigger buffers, which can be filled by hits with different time stamps. The size of this buffer array is determined by the maximum strip hit rate (inner layers) and by the trigger latency. After arrival of a trigger, only hits with the same time stamp as the one provided by the triggering system send their information to the back-end. The array of 128 strips is divided in four sections, each with a dedicated sparsifier encoding the hits in a single clock cycle. The storage element next to each sparsifier (barrel level-2) acts like a FIFO memory conveying data to a barrel-L1 by a concentrator which merges the flux of data and preserves the time order of the hits. This barrel-L1 will drive the output data bus which will use up to 2 output lines depending on

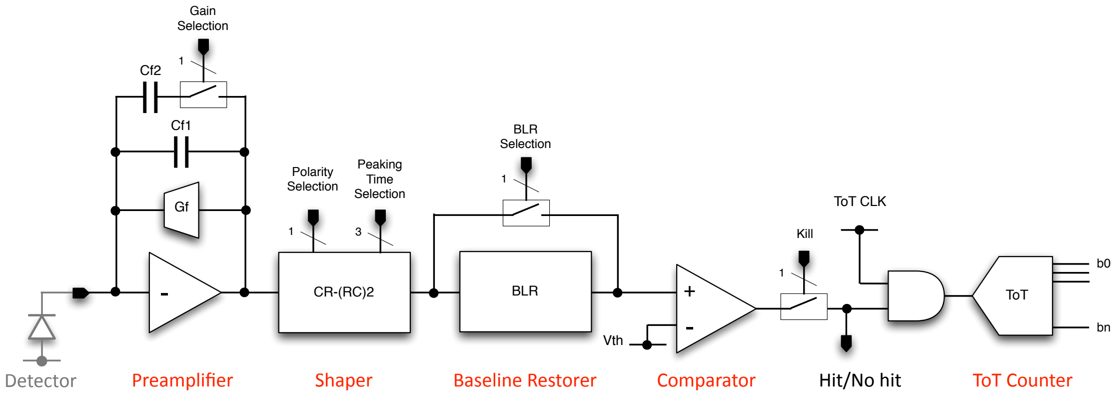

Figure 6.28: Analog channel block diagram.

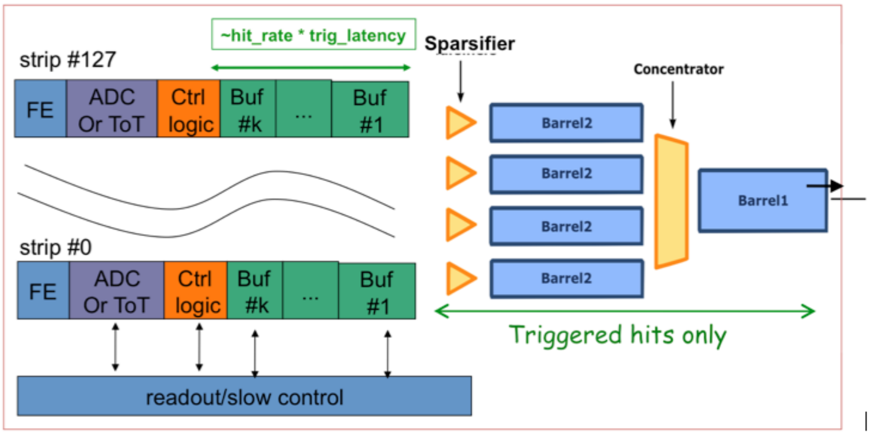

Figure 6.29: Readout architecture of the SVT strip readout chips.

the data throughput and will be synchronous to a 180 MHz clock.

6.6.4 R&D for strip readout chips

The R&D to support the development of the Super*B* strip readout chips began in 2011. The chosen technology for integration is a 130 nm CMOS process: this has an intrinsically high degree of radiation resistance, which can be enhanced with some proper layout prescriptions such as enclosed NMOS transistors and guard rings. There is a large degree of experience with mixed-signal design in this CMOS node that was gained in the last few years inside the HEP community.

The readout architecture is being tested with inputs generated by the detailed Monte Carlo simulation of the expected backgrounds in the SVT. Verilog simulations demonstrate that the chip will be able to operate with a 99 % digital readout efficiency in the worst case scenario, which includes a safety factor of 5 in the background levels.

The analog section of the chip is being optimized from the standpoint of noise, comparator threshold dispersion and sensitivity to variations of process parameters. It will be possible to select the peaking time of the signal at the shaper output in a wide range (25-200 ns typical values for inner layers, 350-750 ns typical values for outer layers) by changing the value of capacitors in the shaper. In this way the noise performance of the chip can be optimized according to the background occupancy, in order to preserve

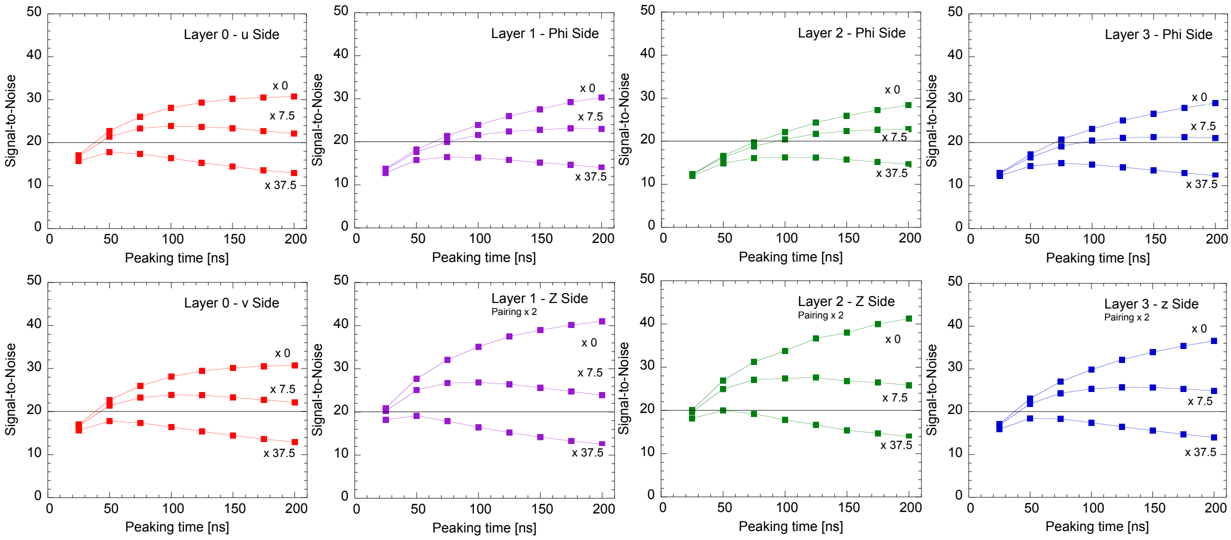

Figure 6.30: Simulated S/N for Layer0-3, as a function of the shaping time. Results are shown for un-irradiated detectors, with negligible noise contribution from leakage current (x0), and for irradiated detectors (higher leakage current noise contribution) with nominal background (x7.5, after 7.5 years) and with a safety factor x5 on nominal background applied (x37.5).

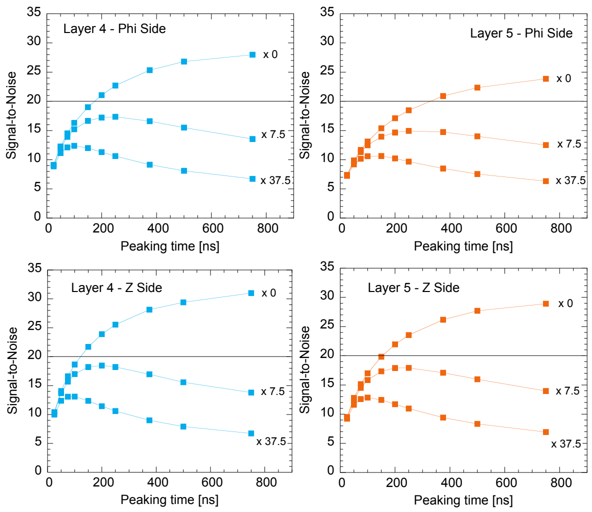

Figure 6.31: Simulated S/N for Layer4-5, as a function of the shaping time, for un-irradiated detectors, with negligible noise contribution from leakage current (x0), and for irradiated detectors (higher leakage current noise contribution) with nominal background (x7.5, after 7.5 years) and with a safety factor x5 on nominal background applied (x37.5).

the required efficiency. The shaping times can be varied with time to take into account the radiation damage and the related increase in the sensor leakage current. Figures 6.30 and 6.31 show the simulated S/N for all the layers as a function of the shaping time with different background conditions and related sensor radiation damage. Table 6.16 shows the main parameters of the analog section, for some reference shaping times, according to simulation estimates for realistic values of detector parameters and strip hit rates. The loss in efficiency is determined by the limits in the double pulse resolution of the analog section, which depends on the signal peaking time. An acceptable compromise will be found here with the noise performance. Although the safety factor of 5 used in noise estimation after 7.5 years represents a really worst case, different strategies will be pursued to mitigate the noise increase after irradiation. In particular, especially for Layer4 and 5, S/N may benefit from moving to shorter peaking times after irradiation, as shown in Figure 6.31, and from reducing the temperature of a few degrees with respect to the ambient temperature. As a further possibility, the replacement of the irradiated detectors with un-irradiated ones can also be considered.

In 2012, the submission of a chip prototype including 64 analog channels and a reduced-scale version of the readout architecture is foreseen.

The submission of the full-scale, 128-channel chip prototypes is scheduled for late 2013. This version will have the full functionality of the final production chip.

6.6.5 Hybrid Design

The Super*B* SVT hybrid is conceptually similar to the High Density Interconnect (HDI) hybrid of the *BABAR* SVT. It is a multipurpose structure that has to satisfy essentially three different types of requirements: mechanical, thermal and electrical. Each of the six detector layers of the SVT is readout by the readout chips described in the previous section. The readout chips will be mounted on a custom designed ceramic circuit called HDI hybrid. The HDI is a thick-film ceramic circuit fabricated from aluminum nitride (AlN). Since the strip sensors are double sided, the readout chips are mounted on both sides of the HDI together with external passive components. The HDIs are mounted through "two bushings" on metal cooling rings which are fixed on the carbon fiber support cones. The HDI is connected to the detector by the flexible fanout circuits, described earlier, and to the so called tail, which will be described in the following section. The HDI provides the physical support for the readout chip, the thermal interface between the chips and the cooling system, the electrical interconnects among the chips and the electrical connections with other components. It also represents the mechanical interface between modules and the support cone.

6.6.5.1 Hybrid mechanical requirements

The HDI is located outside the active region in a very limited space (approximately 1 cm thick) between the tracking acceptance cone and the accelerator stay-clear volume as shown in Figure 6.2. The limited space forces the need for different types of HDI. Currently 4 different models of hybrids are foreseen and they substantially differ in the number of front-end chip (4 to 10) mounted on the hybrid as well as in shape and dimension. An additional reduction in number of types will be studied only when final readout electronics will be available. The approximate dimensions of the HDIs and the quantity of each HDI type to be installed are summarized in the Table 6.17.

Chips are mounted on both sides of the HDI in order to read the ϕ and z strip of half of the detector module. The number of chips and the association with the layer is summarized in Table 6.17. An important parameter in the design is the total thickness of the HDI including the external mounted components. Based on the *BABAR* experience the thickness should be no more than 8 mm. The HDI is the mechanical interface between the detector module and the support cone. Special care must be taken for the mechanical requirements of the AlN substrate and of the technical realization of the circuit:

- accuracy in chip positioning: $\pm 50\,\mu$m;
- planarity tolerance in the stay-clear regions for the contact with the "buttons": $\pm 10\,\mu$m;
- accuracy of the positions of holes for "buttons" and vias: $\pm 50\,\mu$m;
- accuracy in the cut of the substrate: $\pm 100\,\mu$m;
- stay-clear region on the front part of the HDI for gluing the fanout (minimum value): 5 mm;
- stay-clear region on the four corners of the HDIs for mechanical tools access: $\sim 2.5 \times 1\,\text{mm}^2$.

On the opposite side to the fanout, a low profile multi-pin Panasonics connector is mounted in order to contact the HDI to the tail. As a result the mounting requirements of these connectors also have to be respected.

A picture of the layer 0 HDI is shown in Figure 6.32.

Table 6.16: Main parameters of the analog section of the SVT strip readout chips. The total ENC and the efficiency of the analog section has been evaluated with different background conditions: nominal and with the safety factor ×5 applied (×5 bckg.).

Layer	C_D [pF]	t_p [ns]	t_p [ns]	Total ENC [e rms]	Total ENC [e rms]	Total ENC [e rms]	Hit rate/strip [kHz]	Efficiency 1-N	Efficiency 1-N
	with fanout & ganging	Available	Selected		after 7.5 years	after 7.5 years & ×5 bckg.	nominal	nominal	×5 bckg.
0-side u	14.9		25	936	952	1016	187	0.99	095
0-side v	14.9		25	939	956	1019	187	0.99	0.97
1 phi	33.4		75	1122	1197	1457	170	0.98	0.92
1 z	16.2	25-200	75	748	899	1342	134	0.98	0.91
2 phi	37.2		100	1085	1174	1476	134	0.98	0.90
2 z	18.0		100	711	876	1346	134	0.98	0.88
3 phi	35.7		150	897	1125	1763	116	0.96	0.82
3 z	24.6		150	707	935	1540	79	0.98	0.90
4 phi	53.1		500	1086	1709	3090	25	0.98	0.92
4 z	47.2	375, 500	500	819	1555	3041	13.4	0.99	0.95
5 phi	66.2	750	750	1106	2099	3859	16.2	0.98	0.93
5 z	52.2		750	808	1727	3375	8.8	0.99	0.95

Table 6.17: HDI dimensions and quantities for each SVT layer. The dimensions of the width (w) and the length (l) are in mm.

Layer	View	Module	HDI	Chip	w, l (mm)	type
L0	u v	8	16	6 6	$w = 40$ $l = 55$	Type 0
L1	z ϕ	6	12	7 7	$w = 47$ $l = 41$	Type I
L2	z ϕ	6	12	7 7	$w = 47$ $l = 41$	Type I
L3	z ϕ	6	12	10 6	$w = 66$ $l = 38$	Type II
L4	z ϕ	16	32	5 4	$w = 34$ $l = 44$	Type III
L5	z ϕ	18	36	5 4	$w = 34$ $l = 44$	Type III

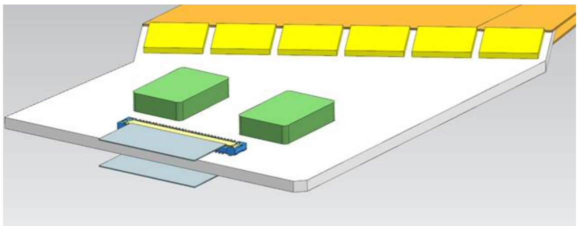

Figure 6.32: In the picture the yellow rectangles represent readout chips, the green boxes are the thermal contacts ("bushing") and the Panasonics connectors are in blue. Two connectors per HDI are needed.

6.6.5.2 Hybrid Electrical requirements

The HDI must allow all functionality of the readout chip. In particular:

- provide separate analog and digital power through low impedance planes;
- two different current returns, one for the digital current and one for the analog current;
- each power line must be locally filtered;
- differential command, control and data lines have to be distributed from each chip to the Panasonics connector;
- impedance of differential lines have to be controlled at 5% to guarantee LVDS communication between front-end chip and transition card;
- whenever possible control and command lines need to be redundant;
- the detector bias voltage must be capacitively coupled to the analog power (representing the analog reference voltage of the readout chip);
- the two readout sections (ϕ and z) of the HDI must be capacitively coupled;
- each HDI must host and provide connection to one resistive temperature monitor;
- each HDI must provide connections for remote sensing lines for all the supply voltages;
- detector fan-outs are glued on the hybrid edge and chip inputs are wire bonded to the fan-outs.

6.6.5.3 Layout requirements and implementation

The layout has to fulfill the electrical requirements. The preamplifier, which is the first step in the signal processing, is particularly sensitive to noise. For this reason as a general rule, the layout must be developed to minimize the coupling of the analog and digital sections. Crosstalk and noise coming from the power planes must also be minimized. Furthermore power supplies have to be distributed in wide planes to reduce trace induction as much as possible and achieve good coupling with current return. Each power line is filtered locally with capacitors to the common return. The capacitors have to be reliable for high frequency behavior, aging effects, temperature coefficients, dimension and values. Following the *BABAR* experience, SMD capacitors with X5R dielectric are proposed. To suppress common mode noise coming from the detector, the two HDI readout sections (ϕ and z) need to be coupled. The connection between the two HDI sides will be realized with a via close to the Panasonics connector, i.e. in an area where space is not critical. Four or more layers (depending on the specific electric layout) on each side will allow electrical connections between the detector and chips from one side and the chips and the transition cards and power supplies on the other side. The thick film technology proposed for the realization of the HDI is a well known industrial solution so that no R&D is required. All fabrication processes are completely under control and there is also possibility of some rework. Such a kind of hybrid is a robust solution and has proven long-term reliability. Based on the *BABAR* HDI, shown in Figure 6.33, it is reasonable to assume that each layer has a thickness of about 65 μm (15 μm conductor and 50 μm dielectric), traces are 15 μm thick, 250 μm wide, traces pitch is 400 μm and pad dimensions are $250 \times 400\,\mu\text{m}^2$. The minimum distance between two vias is 400 μm. It is likely that some of these technological parameters will need to be tuned during the final layout implementation either to take advantage of the latest available technology or to improve some of the electrical parameters, for example the impedance of the differential lines.

Because multiple layers must be screened on the HDI high quality workmanship has to be followed and layer per layer full inspection will be implemented in close collaboration with the manufacturer. For a good isolation of two conductive layers the dielectric layer must have a minimum thickness of $45 - 50\,\mu$m. This will be realized with three different dielectric depositions (printing and thermal processes) and two via fillings:

- deposition of a conductive layer ($10-15\,\mu$m thick);
- first dielectric deposition (15 μm thick);
- first via filling;
- second dielectric deposition (15 μm thick);
- last dielectric deposition (15 μm thick);
- second via filling;
- deposition of another conductive layer.

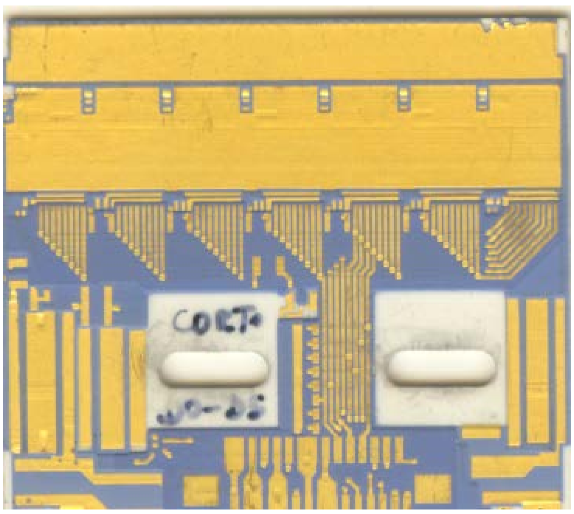

Figure 6.33: *BABAR* HDI, shown as an example of the technology to be used.

Moreover component placement and electrical association of layers will play an important role in design. Again using the experience gained in *BABAR*, the following criteria will be followed:

- separation of components connected to the analog and digital part: the components "linked" to the analog part are mostly placed close to the border of the HDI. The other components are placed in between the mechanical supports;
- dedicated layer/s for clock, control lines and data lines;
- dedicated layers for power/return lines;
- dedicated layer for component mounting. It will contain most of the traces and pads for soldering components. Power sense lines and temperature monitoring will also be on this plane;
- shielding layer will be added if necessary.

Final layout of the HDI will need detail knowledge of IC pinout which is not yet available.

6.6.6 Data Transmission

The SVT data transmission consists of various separate hardware components: the HDIs, the tails, the transition cards and the Front end Boards (FEBs). The characteristics and functionality of the FEBs are described in Sec. 13.1.1.

A simplified drawing of the data transmission chain with the locations of the various components up to the transition card is shown in Figure 6.34.

The FEBs are connected to the transition card output via optical fibers and are located after the radiation wall. As explained in the previous section in the HDI, the signals generated in the detector are processed and translated in digital data, properly formatted, by the readout ICs. The output data from the ICs are transferred from the HDI to the next component of the data transmission, the tail, without further processing. The limited space available for the HDI prevents mounting additional electronics on the hybrid. The specification/characteristics of the data lines can be summarized as follow:

- the data signals follow a LVDS standard, consequently they are differential signals;
- the number of data lines, per IC, varies from:
  - 1 to 3 if synchronized to a 120 MHz clock
  - 1 to 2 if synchronized to a 180 MHz clock

  depending from the data throughput;
- the data are serialized and encoded using a 8b/10b protocol in the readout chip.

The data lines needed for the different HDIs (reference clock of 120 and 180 MHz) are summarized in Table 6.18.

The large number of data lines suggests that the reference clock should be the 180 MHz one, so that the maximum number of lines is 14 for one side of the Type I HDI. Together with the data lines (and always to LVDS standards) all the ICs of same HDI share 6 input lines (Reset, Clock, FastClock, Timestamp, Trigger, RegIn) and 1 output line (RegOut).

6.6.6.1 The Tail

The total number of differential lines to be transferred from a HDI to the next processing block of the chain is 21 or less. As the data rate per line is not excessively high ($\sim$ 180 Mbps) and a custom designed shielded, multilayer copper bus could be used to connect the output of the HDI with the input of the transition card. The length of this bus, called the "tail", is between 50 to 70 cm and changes slightly from layer to layer. The tail should have a rectangular section not exceeding $10 \times 4\,\text{mm}^2$, because it has to be pulled along the supporting cone and below the HDI itself during detector integration. In many cases the tail has to pass between the HDI thermal standoff, the "buttons". Similar dimensional constraints apply to the tail terminating connectors. A very low profile (0.8 mm) narrow pitch (0.35 mm) Panasonics connector (series AXE, 70

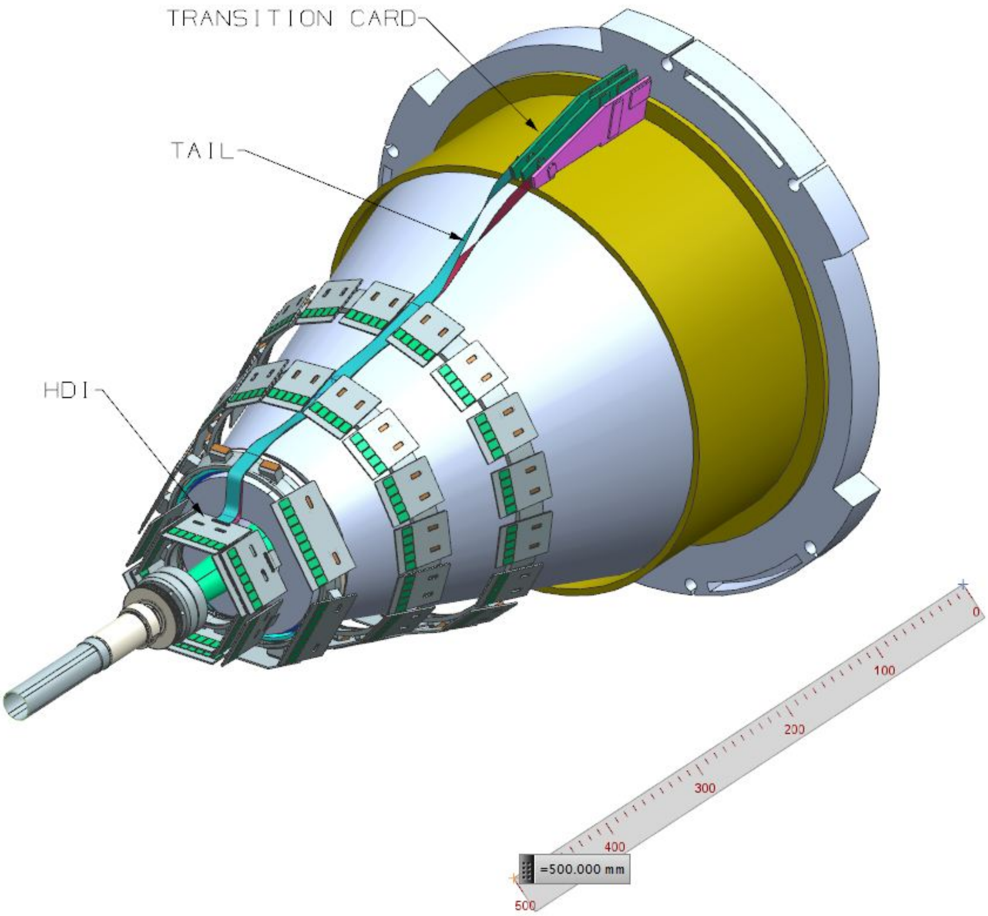

Figure 6.34: Axonometric view of the combination HDI, tail and transition card.

Table 6.18: Number of data lines, tails, transition cards (TCs) and optical fibers for the six layers of the SVT detector.

Layer	View	Modules	HDIs	HDI Type	Chips	Data lines per HDI side (120 MHz)	Data lines per HDI side (180 MHz)	Tails (Cu Bus)	TCs	Optical Fibers
L0	top bottom	8	16	Type 0	6 6	18 18	12 12	32	32	32
L1	z ϕ	6	12	Type I	7 7	14 21	7 14	24	24	24
L2	z ϕ	6	12	Type I	7 7	14 14	7 14	24	24	24
L3	z ϕ	6	12	Type II	10 6	20 12	10 6	24	24	24
L4	z ϕ	16	32	Type III	5 4	10 8	5 4	64	32	32
L5	z ϕ	18	36	Type III	5 4	5 4	5 4	72	36	36

pins) can be utilized for this purpose (see Figure 6.35). By using the repetitive pin sequence Gnd/D+/D-/Gnd it is possible to connect up to 22 LVDS lines (11 per side) to this connector. Each LVDS line is individually shielded if the lines are realized as strip-lines.

The socket (2.5 mm wide) is mounted on the HDI and the transition card, while the header (2.0 mm wide) is mounted on the tail. The dimensions of this surface mount connector are compatible with the space reserved on the HDI for the output connectors. The retention mechanism of this connector provides a holding force of at least 0.20 N/contact, which ensures a reliable lock between the elements of the data chains. This connector is also adequate for the transition card as explained in the following section. In the present design, the tail is a multilayer flexible katpon circuit, whose main electrical parameters are the following:

- five layer circuit. Stack-up plane/signal/plane/signal/plane;
- LVDS lines: strip lines on the two signal layers;
- LVDS line width/space: 100/100 μm;
- LVDS copper thickness $\sim 20\,\mu$m;
- dielectric thickness: ~ 2.5 mm ;
- Zdiff: ~ 100 Ohm;
- kapton thickness: $50\,\mu$m;
- via diameter: $250 - 300\,\mu$m;

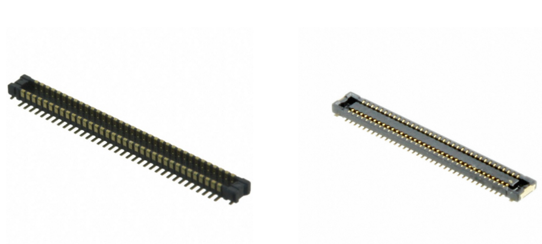

Figure 6.35: Panasonics AXE series connector. Header (left) and socket (right).

- via clearance: $150\,\mu$m;
- width: 10 mm min, 15.8 mm max (at the connector).

The plane layers available in the stack-up can be used both as a shield for the LVDS traces as well as Power/Ground planes. The tail does not only carry the digital signals but also the power for the readout ICs. The parameters for the plane segmentation of the prototype design are:

- power plane width: ~ 4.7 mm;
- ground plane width: ~ 9.4 mm;
- metal thickness: $> 50\,\mu$m;
- current capability: $\sim 3 - 3.5$ Amps;
- voltage drop (both ways): ~ 250 mV.

The minimum bending radius of the resulting multilayer circuit has to be carefully evaluated to verify that during installation the tail can be bent into the required shape.

6.6.6.2 The transition card

The next element of the transmission chain is a printed circuit board made of halogen free material, called transition card (TC). The geometrical aspect, dimensions and shape are defined by the detector geometry as shown in Figure 6.34 and in more detail in Figure 6.36.

The transition cards are located approximately 50 cm from the detector sensors and they are electrically connected inbound to the HDI by means of the tail. They are also connected outbound by optical fibers to the FEBs and by cables to the remote power supplies (both low and high voltage).

A transition card has various functions:

- it will receive and distribute the input and control signals for the front-end chip through the optical fiber from the FEB;
- it will receive, format and serialize, the data coming from the front-end chips;

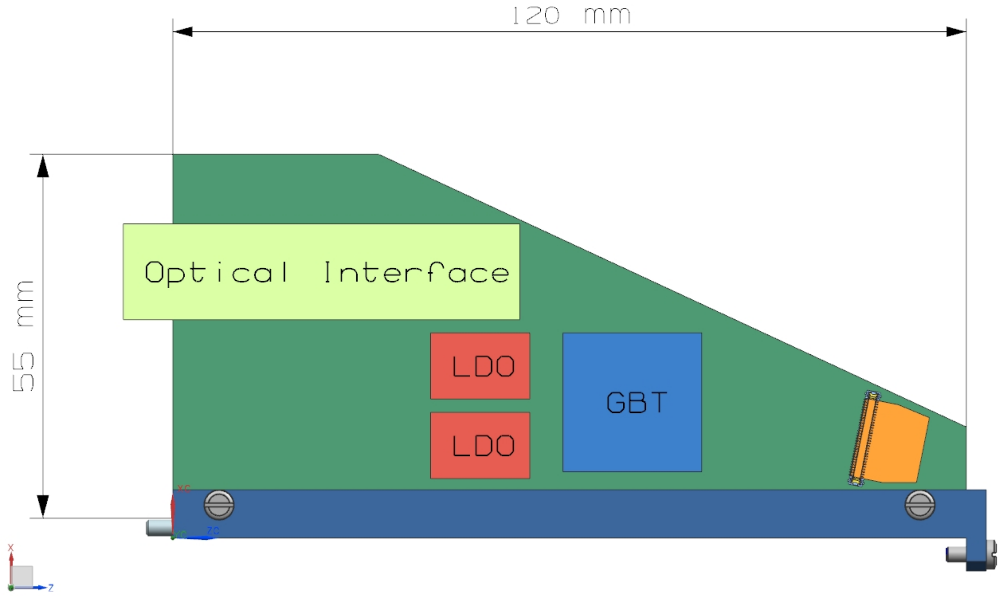

Figure 6.36: Shape/dimensions of a transition card. The main active components to be mounted on the PCB are also shown (GBT, LDOs, optical transmitter) as well as the mechanical support required to mount the board (visible at the bottom) of the figure.

- it will perform the electrical-to-optical conversion of the data and it will transmit the data to the FEB to begin the data acquisition;
- it will regulate and distribute the power to the front-end chip on the HDIs as well as the HV power for the microstrip detectors. It also filters the supplies to have low ripple voltages sent to the HDIs.

Because the data volume decreases substantially from the innermost to the outermost detector layer (from $\sim$ 1 Gbits/trig, to $\sim$ 0.25 Gbits/trig per TC), one transition card will be used per HDI side for the layers 0 to 3. Instead one transition card will serve both sides of the same HDI for layers 4 and 5.

Such a reduction in total number of TC is advantageous both in having a uniform data link speed (<2Gbit/s) with reasonable link utilization for all TCs but also in maximizing the surface area available per TC and increasing the space between two adjacent TCs.

The typical geometrical disposition of the TCs is shown in Figure 6.37. The minimum space between two cards is 3.6 mm, barely enough to mount the tail. The total number of TC is 86 per detector side (172 in total).

The TC requirements can be fulfilled by having at least the following logic blocks:

- an interface circuit to group, before serialization, the LVDS data lines coming from the HDI;
- a serializer/deserializer;
- an optical transmitter/receiver;

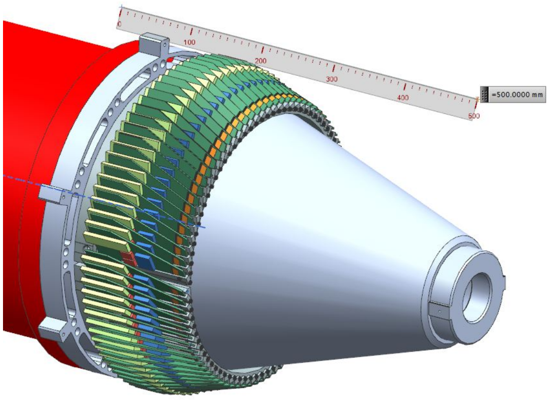

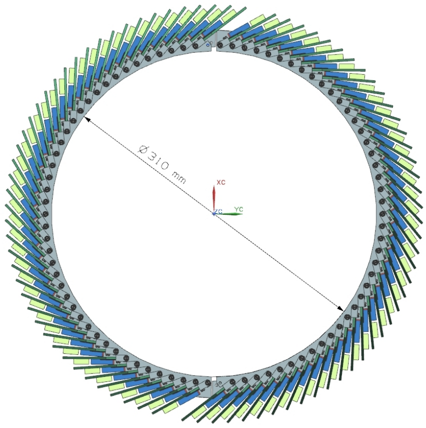

Figure 6.37: Turbine arrangement of the TC on the support cone.

- slow control interface for handling the detector control signals.

This device has not been designed yet, however we are closely following various CERN designs to take advantage of the development already started. In particular the CERN GBT project which is well advanced and which is trying to address very similar needs for the LHC experiments [44], is our baseline design for signal transmission.

The contact undertaken with CERN designers have indicated that the GBT IC characteristics match and even exceed SVT requirements in term of data link, being the GBT project intended to operate up to 4.8 Gbit/s.

The physical dimension of the IC, less than 400 mm^2, the power ($\sim$ 2 W/chip) and the expected delivery time (not later than 2013) are compatible with the TC design, construction and testing. Moreover the CERN design has been proved to be radiation tolerant up to radiation levels well exceeding the ones expected in Super*B*.

The maximum reference clock of the GBT IC is related to the LHC machine clock (40 MHz). Such a frequency will need to be locally generated at the level of the transition card to properly operate the device. If this reference clock, as recently discussed could be an option at Super*B* level, the TC design will take advantage of this possibility.

Similarly, the design of the optical interface and the choice of the optical fibers will take advantage of the results obtained by the CERN VERSATILE LINK project [45], which again is well suited for the SVT application. In particular the new “versatile small form factor transceiver”, the design of which is ongoing at CERN, could fit dimensionally in the TC and has provision for connecting two optical fibers in the same package, one fiber for control signals, the other for data.

Finally, at the present stage, the regulation of the low voltages needed for the front-end IC will be implemented by using the same adjustable low dropout voltage regulators (LDOs) widely adopted at the LHC: LHC4913. This component, manufactured by ST, has been thoroughly tested against radiation and can generate a clean reference voltage down to 1.25 Volts. It also has remote sense capability to compensate voltage drops between the point of regulation and the point of load due to cables. In the baseline design two LDOs, one for the analog and the other for the digital supply, will be used for each HDI.

A preliminary thermal analysis of the transition card has been performed based on the typical heat dissipation of the various electrical blocks mounted on it. A conservative 5 Watt per TC has been used.

A dedicated cooling system is being designed to effectively remove the heat without increasing the temperature of the surroundings. The thermal connection between the board and the cooling system can be achieved by means of the TC mounting support, the design of which is shown in Figure 6.37.

6.7 Mechanical Support and Assembly

An overview of the mechanical support and assembly is provided in section 6.1. In this section we provide a more detailed account of the constraints of the mechanical design due to the accelerator components of the Interaction Region (IR) and describe the details of the detector assembly, installation, survey, and monitoring.

6.7.1 IR Components & Constraints

The support structure design of the SVT is dictated by the configuration and assembly procedure of the IR machine components, as well as by the SVT geometry. A schematic drawing of the IR assembly with all the components described in the rest of this section is shown in Figure 6.38. The whole IR assembly consists of the Beryllium beam-pipe, the SVT, the forward and backward Final Focus (FF) permanent magnets, the conical Tungsten shields for background reduction and the cryostats of the FF superconducting magnet system.

The background conditions impose the need for a pair of conical Tungsten shields located about 25 cm from the IP on either side. There are two further Tungsten shields of cylindrical shape that are located symmetrically with respect to the IP, starting just at the end of the conical ones. The cylindrical shields are rigidly attached to the iron structure of the return yoke of the detector magnet in the forward and backward barrel face of the detector. The conical shields and the final focus permanent magnets occupy most of the region below 17.2° (300 mrad) on both sides of the IP . In order to minimize the mass inside the active tracking volume, all of the electronics are mounted below the 300 mrad cone. This requires that in backward and forward directions electronics, cooling, cabling and supports must be confined in a volume of about one centimeter thick around the conical shields. The use of this tight space below 300 mrad must be carefully arranged with the needs of the accelerator. The angular acceptance in the laboratory frame of the SVT is therefore restricted to the region $17.2° < \theta < 162.8°$, where θ is the polar angle. The radial position of the SVT fiducial volume is imposed by the inner radius of the DCH at about 27 cm.

The Be beam-pipe, cooled by liquid forced convection, is about 2 cm in diameter and 40 cm long. It is positioned symmetrically with respect to the IP and it directly supports the Layer0 modules. The eight striplet modules, arranged in a pin wheel geometry, are mounted on the two cooled flanges. The Layer0 is mechanically decoupled from the other SVT layers to allow its replacement without a complete disassembling of the other SVT modules. The SVT layers from 1 to 5 are supported on the backward and forward sides on the conical shields by two gimbal rings, the kinematic mounts that allow the necessary degree of freedom to prevent SVT over-constraints during the installation/removal operations. The central Be beam-pipe is connected at each end through a bellow and a flange to the beam-pipe coming out of the cryostat of the FF superconducting magnets. In this region the beam pipe is split in two arms: the LER and HER pipes represent the warm internal vessel of the FF cryostats. The forward and backward cryostats are symmetrically positioned around the IP and they are the extreme components of the IR, with the cryostat beam-pipe terminal flanges placed at about 2.2 m away from the IP, as shown in Figure 6.38. The cryostat is rigidly connected to the conical shield flanges and, through the terminal back flange, at a very rigid coaxial external tube, allowing a free space of about 2 cm in radius along its extension for routing the SVT cables out of the inner detector region.

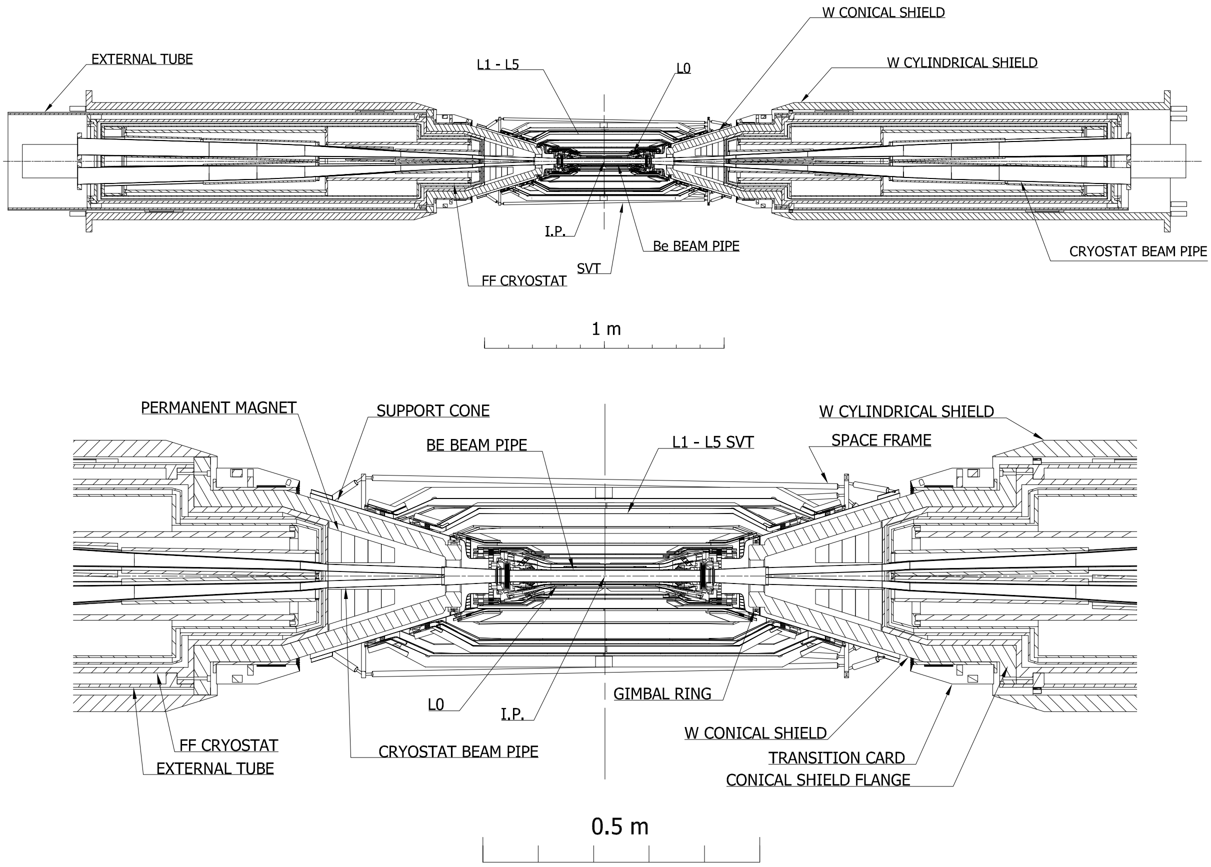

Figure 6.38: Longitudinal section of the IR in the x-z plane (top) with a detailed view (bottom).

Since the L1-L5 and the Layer0 must be installed with all the components of IR system in place, they must be split in two halves and then clam-shelled around the beam-pipe. The whole IR system, just described, will be assembled and aligned in a clean area outside the experimental hall and then transported and installed inside the Super*B* detector. From the mechanical point of view, the IR system consists of two very rigid systems (conical shield + cryostat + external tube) joined by a very weak system (the Be beam-pipe and the SVT) that could be damaged during the transportation and installation/removal operation. On the other hand in order to reduce the passive material between the SVT and the DCH, and improve the detector performance, no permanent stiffening structure (i.e. a support tube as in the *BABAR* detector) is foreseen in Super*B* to rigidly connect these systems. Therefore a removable structural support has been designed, in the following called temporary cage, to connect rigidly the backward and forward conical shields. The temporary cage will be inserted to absorb the mechanical stress present at the moment of the first transportation to the experimental hall and during all the installation/removal operations of the IR assembly/SVT/Layer0, and it will be removed for the data taking (see Sec. 6.7.6.2).

6.7.2 Module Layout & Assembly

The SVT is built with detector modules, each mechanically and electrically independent. Each module consists of silicon wafers glued to fiber composite beams, with a high density interconnect (HDI) hybrid circuit at each end. The HDIs are electrically connected to the silicon strips by means of flexible circuits and they are mechan-

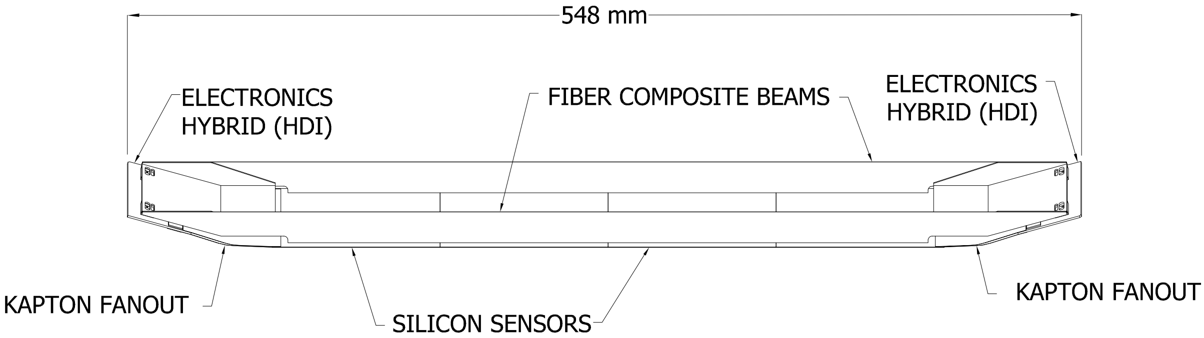

Figure 6.39: Drawing of a layer 3 silicon strip module.

ically supported by the fiber composite beam. The entire module assembly is a rigid structure that can be tested and transported in its case. As an example a drawing of a detector module from layer 3 is shown in Figure 6.39.
The assembly of a detector module will follow the procedure used for the *BABAR* SVT modules [1] and begins after the preparation of all the necessary parts. The silicon detectors must be fully tested, including a long-term stability (burn-in) test under full bias voltage. The fanout circuits will be optically inspected and single trace tested for spotting shorts or opens. The readout hybrid must be assembled and tested, with the HDI supports, the front-end chips and additional passive components. Finally, the completed beam structure, which provide mechanical stiffness, must be inspected to ensure it meets the specifications. These individual parts will be fabricated by different laboratories and then shipped to the place where the module assembly is carried out. The hybrids will be tested again after shipment.
The assembly of the inner barrel-shaped modules and the outer arch-shaped modules is necessarily different. However, there are common steps. The procedure is the following:

1. each silicon detector is precisely aligned using its reference crosses and then head to head glued to the adjacent to form the module;

2. the z and ϕ fanouts are glued to the detectors and wire-bonded to the strips. The ganging bonds between ϕ strips are then performed. Electrical tests, including an infrared laser strip scan, are performed to assess the quality of the detector-fanout assembly (DFAs);

3. the silicon detectors and the readout hybrid are held on a suitable fixture and aligned. The fanouts are glued to the hybrids and wire bonded to the input channels of the readout ICs;

4. the final assembly stage is different for different layers. The module of the layer 1 and 2 are then joined together by gluing the beams on the top of layer 1 to the bottom of layer 2 to give a combined structure called the "sextant". For the layer 3, the DFA is bonded flat to the fiber composite beams. For the modules of layer 4 and 5, the flat module is held in a suitable fixture

and bent on a very precise mask at the corners of the arch and at the connection to the HDI. The fiber composite beams are glued to the module with fixtures insuring alignment between the silicon detectors and the mounting surfaces on the HDI. This procedure has been already successfully adopted for the external modules of the SVT of the *BABAR* experiment;

5. once completed, these detector modules are extremely rigid ladders that can be stored and submitted to the final electrical characterization. They are then stored in their shipping boxes for the final installation on the detector.

A drawing of an arch-shaped module is shown in Figure 6.40.

The assembly procedures for a Layer0 module (shown in Figure 6.41) in general follow that reported for the other SVT layers, although the smaller sensor dimensions represent a greater difficulty in the handling. The procedure is the following:

1. no detector alignment is required because there is only one detector;

2. the u and v fanouts are glued on each face of the detector on both sides and wire-bonded to the strips. A two-layer fanout is necessary to read out each face;

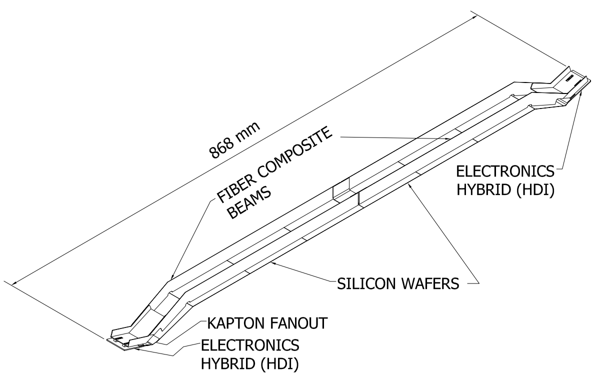

Figure 6.40: Drawing of a layer5 silicon strip arch-module.

3. the silicon detectors and the readout hybrid are held on a suitable fixture and aligned. The fanouts are glued to the hybrids and wire bonded to the input channels of the readout ICs. Electrical tests, including an infrared laser strip scan, are performed;

4. in the final assembly stage for Layer0 module there is the requirement for a mask that is able to position the HDI in a very precise position in a plane inclined at 10° in order to be positioned outside the active region. The fiber composite beams are glued to the module with fixtures assuring alignment between the silicon detectors and the mounting surfaces on the HDI.

6.7.3 L1-L5 Half detector assembly

The L1-L5 detector is assembled in two halves in order to allow the device to be mounted around the beam pipe. The detector modules are supported at each end by cooling/support rings in brass that are attached on the support cone realized in laminated carbon-fiber. Water circulates in the cooling rings and cools the mounting protruded pieces (buttons) in thermal contact with the HDIs. The cones are split along a vertical plane and have alignment pins and latches that allow them to be connected together around the conical shield. See Figure 6.42 for a drawing of the support cone.

During the half detector assembly, the two half-cones will be held in a fixture which holds them in a precise position relative to each other. The detector modules are then mounted on the half-cones to each end. A fixture holds the detector modules during this operation and allows for well-controlled positioning of the module on the half-cones. Pins located in the buttons provide precise positioning of the modules, which are then screwed down. Accurate alignment of the mounting with respect to the silicon wafers is achieved by a pair of mating fixtures. One is a dummy module (mistress mask) and the other simulates the mating surface of the cone (master mask). These fixtures are constructed together and mate perfectly. One is used to verify the correct machining of the mounting of the cool-

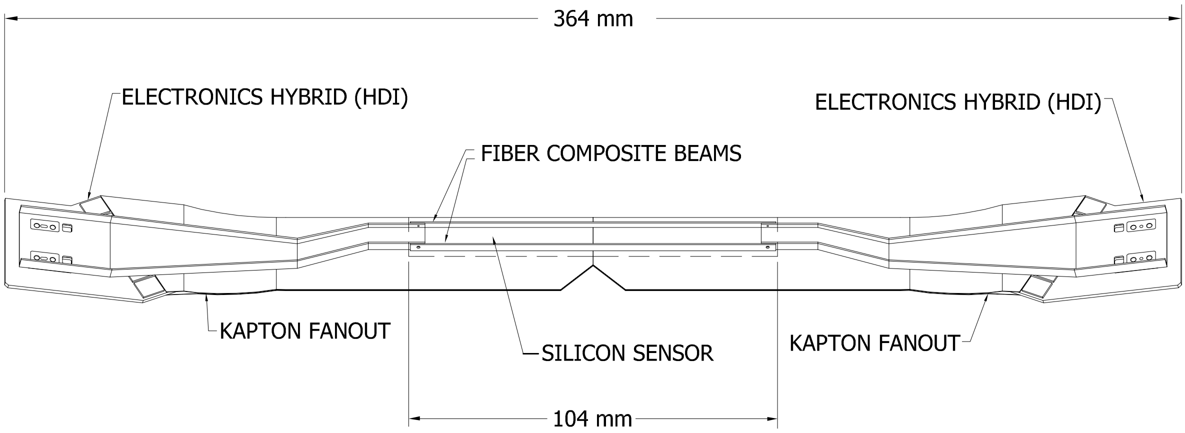

Figure 6.41: Drawing of a Layer0 striplets module.

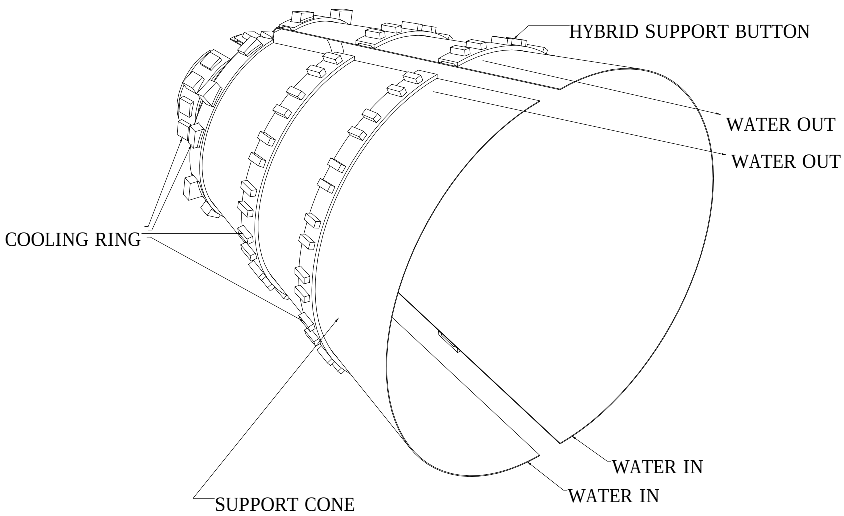

Figure 6.42: The support cone with the four cooling rings for layers 5, 4, 3 and for the sextants of layers 1 and 2.

ing ring on the cones. The other is used to position the mounting points on the HDIs during the assembly of the module.
The connection between the module and the cone (called a foot) provides both accurate alignment of the module and a thermal bridge from the HDI to the coolant. A schematic of the forward foot region, which contains the readout electronics and the cooling ring with the mounting buttons is shown in Figure 6.43.

On the backward side, the foot region is more complicated: in case of bad mounting or temperature variations the elongation of the module in the horizontal plane must be allowed, avoiding over constraint due to the inclined geometry. A schematic of the backward foot region is shown in Figure 6.44.

After verification of the alignment, the connection between the two HDIs and the support beam is permanently glued. The glue joint allows for the correction of small errors in the construction of either the cones or the module. After the beam is glued, the module may be removed and re-mounted on the cone as necessary. The design of the foot allows this glue joint to be cleaved and remade should major repair of the module be required. After the detector module is mounted, it is electrically tested to verify its functionality. As each layer is completed, it is optically surveyed and the data are entered in a database. Finally, the two cones are connected together with the space frame, resulting

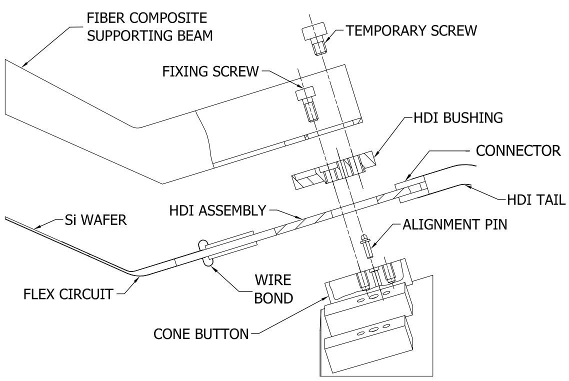

Figure 6.43: The forward foot region.

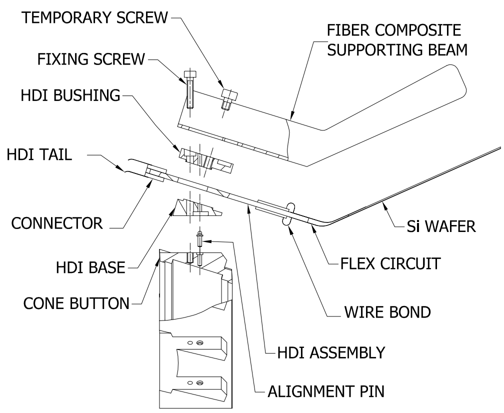

Figure 6.44: The backward foot region.

in a completed detector assembly ready to be opened and re-mounted around the layer0.

Space Frame The two carbon fiber support cones are mechanically connected by a low mass carbon fiber space frame (see Figure 6.45).
The struts of the frame are made of carbon fiber tubing and the rings are carbon fiber skins with foam core. The frame is constructed by gluing the pieces together while they are held rigidly in fixtures. The joints between the struts and the rings use end pieces of carbon fiber material machined to fit the inner diameter of the strut. The space frame must split into two halves just as the cones do. The rings at the ends of the space frame are sections of cones to match the attaching surfaces of the support cones.

6.7.4 Layer0 Half Detector Assembly

Also the Layer0 detector is assembled in halves in order to be clam shelled around the Be beampipe. The detector modules are supported at each end by the cooled half flanges. Cooling water circulates inside each half-flange and cools the protruded mounting wing-pieces supporting the HDIs and comes in thermal contact with them. The Layer0 half-flanges are mated in the vertical plane and have alignment screw-pins to be wrapped in a precise and reproducible way on the robust stainless steel part of the Be beam-

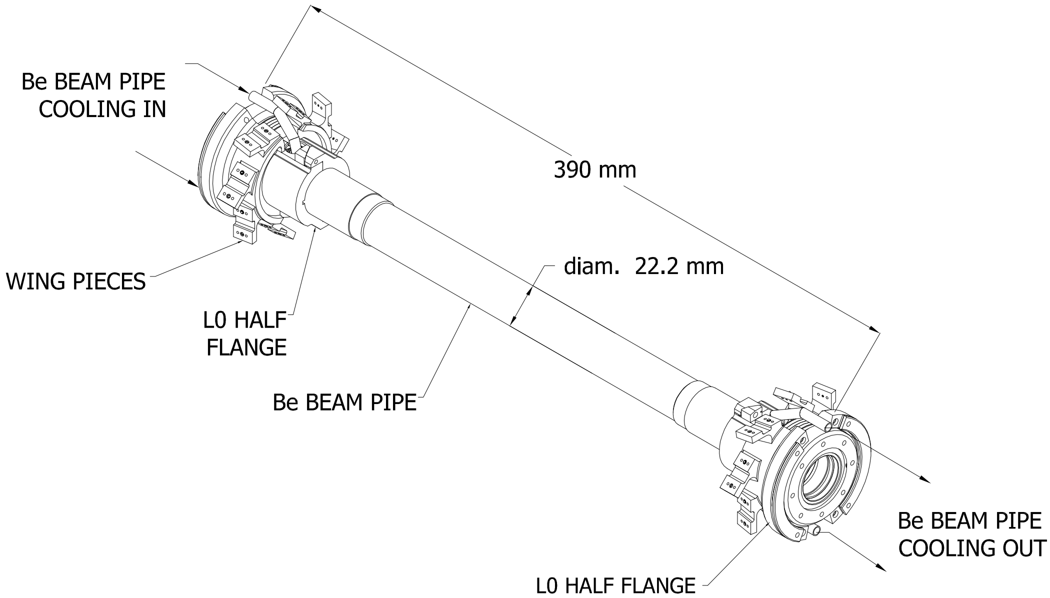

Figure 6.46: The Layer0 half-flanges fixed on the Be beam-pipe.

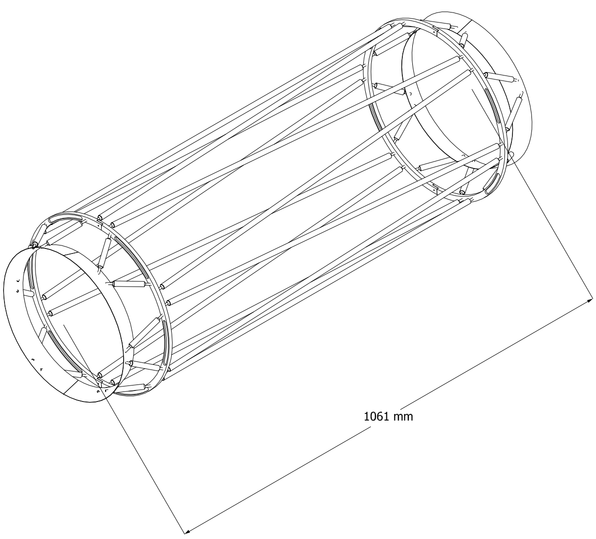

Figure 6.45: The carbon fiber space frame.

pipe. See Figure 6.46 for a drawing of the Layer0 half-flanges fixed on Be beam-pipe.

During the half detector assembly, the two half-flanges will be held in a fixture in a precise relative position. The detector modules are then mounted to the half-flange wing pieces and positioned through precision pins and then screwed down. The procedure to mount a Layer0 module is the same as that used for the L1-L5 modules, using similar fixtures that function in the same way as those for L1-L5. The connection between the modules and the half-flange wing piece feet provides accurate and reproducible alignment of a module and conduction of heat from the HDI heat sink to the cooling water circulating in the half-flanges. The technique to mount and connect the HDI to the support beam is the same as that described for L1-L5 modules. Also in this case, the glue joint allows for the correction of small errors in the construction of either the half-flange or the module. After each Layer0 detector module is mounted it is electrically tested to verify its functionality. Once the Layer 0 is complete, it is optically surveyed and the data are entered in a database. Finally the two half-

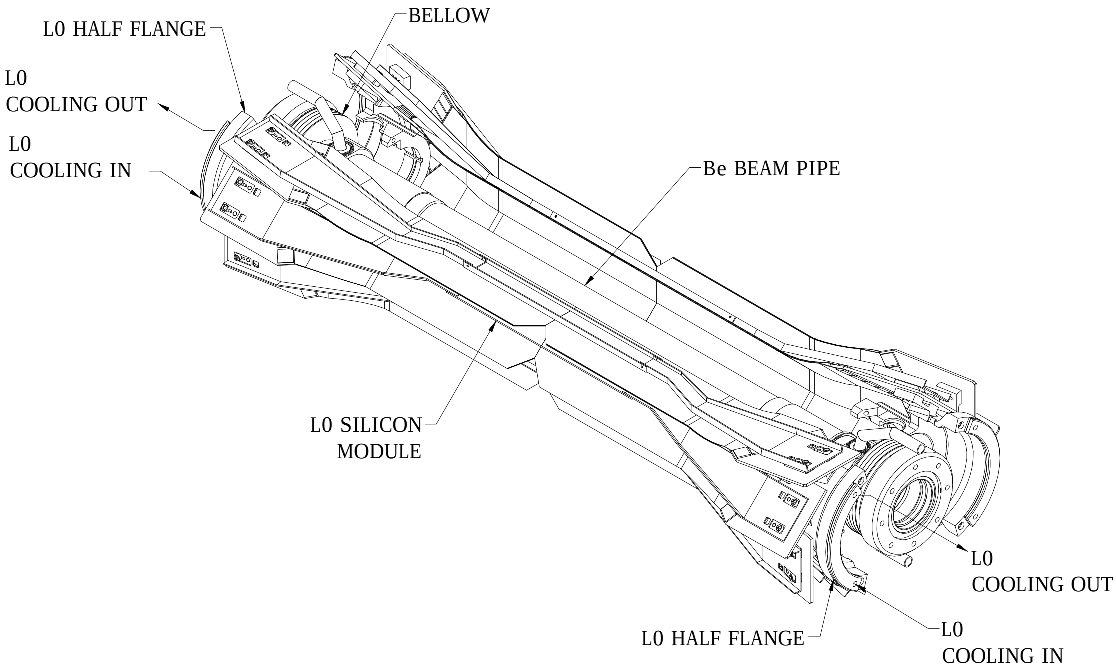

Figure 6.47: The two Layer0 half-shells around the Be beam-pipe.

flanges are connected together with a proper fixture forming a rigid half shell and are then ready to be assembled around the Be beam pipe. An illustration of the two Layer0 half-shells around the Be beam-pipe is shown Figure 6.47.

6.7.5 Mount Layer0 on the Be-pipe and L1-L5 on the conical shield

When the two Layer0 half detector assemblies are completed, they are brought to the staging area where the Be beam pipe, conical shields and cryostats are already mounted. The assembly fixture used to hold Layer0 half-shells, is also used to bring together and clam-shell them around the Be beam-pipe. An isostatic mounting of the Layer0 with respect to the Be beam-pipe is equipped, to allow relative motion due to differential thermal expansion. Radial and circumferential keys ensure precise and reproducible positioning of the Layer0 flanges and thus of the detectors with respect to the Be beam-pipe. The two half detectors are mated and locked together with pin-screws. The cables from HDIs are attached to the conical shields and routed to the transition cards, which are mounted in cooling support flanges at the end of the conical shield. An optical survey is performed and the detector is tested. In the same way, when the two L1-L5 half-detector assemblies are completed, they are brought to the staging area where both conical shield and Final Focus superconducting Magnet Cryostat are mounted and Layer0 has been assembled on the Be beam-pipe. Fixtures are employed to hold the cones as they are brought together and clam-shelled around the Layer0 and Be beam-pipe. The two half detector assemblies are mated and the latches between them are closed. The cables from HDIs are attached on the cones and routed to the transition cards. The entire detector is then thoroughly tested. Afterwards the Temporary Cage Sectors are mounted on the Conical Shield flanges and rigidly fixed in place. At this point the assembly is relatively rigid and can be transported to the interaction hall and installed in the experiment.

6.7.5.1 Gimbal Rings

The detector assembly as described above forms a rigid structure as long as the cones and space frame are connected together. This structure is supported on the conical shields. During the transportation of the IR Assembly to the interaction hall, it is possible for the forward side of the IR Assembly to move by as much as 1 mm relative to the backward side. This motion is reversible, and they will return to their original alignment when installed under normal conditions. In addition, differential thermal expansion may affect the relative alignment of the magnets during periods in which the temperature is not controlled, and relative motion of the magnet and the beam-pipe may occur should there be seismic activity.

The support of the detector on the conical shield must allow for this motion without placing stress on the silicon wafers. In addition, the position relative to the IR must be reproducible when installed. These constraints are met by mounting the support cones on a pairs of Gimbal Rings. One gimbal ring connects the forward cone to the Conical Shield to constrain its center, while allowing rotation about the x and y axes. A second set of Gimbal Rings supports the cone in the backward direction in a similar manner, with an additional sleeve that allows both for motion along z and rotation about the z axis.

6.7.6 Installation & Removal of the Complete IR Assembly in Super*B*

The clearance between the SVT Layer0 and the beam pipe is of the order of 1 to 2 mm. During the transportation of the IR Assembly, the critical clearances must be monitored in real time to ensure that no accidental damage to the detectors occurs. In its final position, the IR Assembly will be supported along the External Tube on the Cylindrical Shield.
One possible installation/removal scenario employs a crane that handles a long stiff beam that rigidly supports the entire IR Assembly through the forward and backward external tube and it is able to carefully lay this system on the external cradle support shown in Fig: 6.48. This support is aligned with respect to the Cylindrical Shield and positioned in front of the forward end of the detector.
With this procedure it will be possible to slide the IR Assembly (in or out) within the DCH using the translation system of the cylindrical shield, described in Sec. 6.7.6.2, which has been previously aligned with respect to the Super*B* detector. Once the IR assembly is in the final position the External Mechanical Cradle is removed.

6.7.6.1 Quick Demounting of the SVT, Layer0 and Be beam-pipe

For a rapid access to some of the IR components (SVT, Layer0 and the Be beam-pipe) the so called quick demounting procedure has been developed to allow experts to operate on these components inside the experimental hall, avoiding the complete removal of the IR assembly from the Super*B* detector, and then reducing the associated down time with respect to what was needed in *BABAR* (several months). This operation can be followed in case that Layer0 needs to be repaired or replaced with a new detector in a short amount of time, as well as for a rapid access to the SVT or the Be beam pipe. As shown in Figure 6.48 the procedure foresees that one slide the IR Assembly only partially outside the detector, leaving it close to the forward door, in order to access the central region of the IR and perform any necessary work, and then slide the entire IR Assembly back inside the detector. The quick demounting operation plans to rigidly move all the IR Assembly components along the z axis in the forward direction up to a position that allows the SVT detector to be completely out of the forward side of the iron of the magnet return yoke (forward end plug open), at z=+2650 mm. In this hypothesis it is assumed that the cylindrical backward and forward shields are rigidly attached on a solid structure and perfectly aligned along the z axis direction, having a supporting function in the IR translation.
The stroke necessary for the SVT demounting position is about 3200 mm. The total weight of the IR assembly components is of about 1.65 t.

A beam profile box of about 3×4×3 m^3 volume will be mounted on the forward end of the

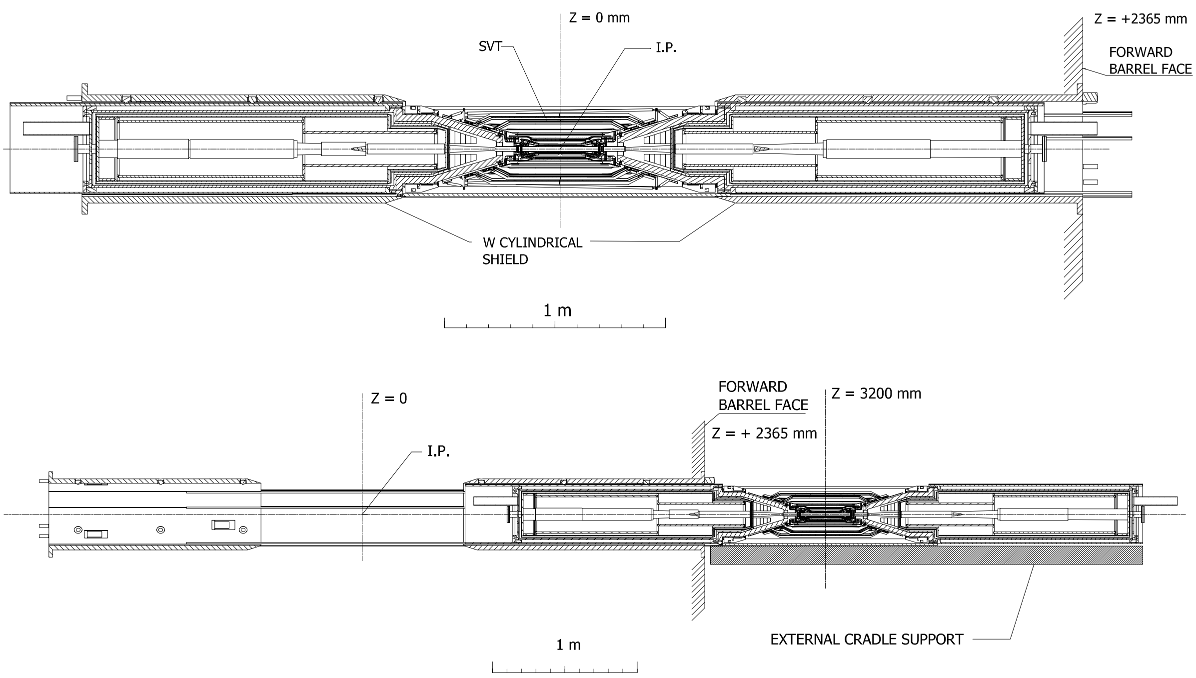

Figure 6.48: Quick demounting operation: a longitudinal section in the y-z plane of the IR system in the initial (top) and final (bottom) position.

detector and it will be equipped with the proper filters and fans to maintain ISO 8 cleanness conditions for a four-person team working on the SVT, Layer0, beam-pipe.

6.7.6.2 Temporary Cage and Translation System

The SVT system represents the weak ring of the the IR assembly mechanical chain. The Be-beam pipe is joined to the Cryostat beam-pipe through a system of flexible bellow flanges. In a different way from *BABAR* where the SVT region was stiffened by the CF support tube, in Super*B* it was decided not to insert any stiffening structure that would add passive material in front of the DCH. Therefore it was necessary to design a temporary and removable structural support (the temporary cage). This rigidly fixes the forward and backward conical shields around the SVT region; it is able to absorb all the mechanical stress that could be present during all the installation/removal operations; it can be removed by operating from the forward end region of the detector, once the SVT is in data-taking position. On doing so one removes the passive material of the temporary cage from between the SVT and the DCH in preparation for data taking.

When the temporary cage is mounted and rigidly connects the two opposite conical shields, the whole IR assembly (forward side + backward sides + SVT) can be considered a rigid body supported by several recirculating spheres. These spheres are embedded in the cylindrical shields, acting on the three rails positioned at 120° that are formed on the external tube profile. The translation system is able to guide the entire IR assembly and prevent any rotation during the installation/removal. The cylindrical shields also include a mechanical system (the Radial Blocking Device) able to rigidly block the IR assembly at the correct position with respect to the IP. This blocking is enacted by longitudinal bars that push on a mechanical conical device embedded in the cylindrical shield, able to block radially the external tube with respect to the cylindrical shield. This blocking system is also useful at the moment of the temporary cage mounting/demounting on the conical shield flange operations, in order not to transfer any mechanical stress to the SVT detector and the Be beam-pipe.

Due to the presence of translation rails on the external tube, the temporary cage is cylindrically shaped in three independent separate sectors, confined in a radial space of about 2 cm between the external tube and the cylindrical shield. The temporary cage sectors are made from a metal sandwich structure with very high flexural resistance. Each temporary cage sector is moved towards the IP position supported by two removable beam-rails mounted and embedded in the cylindrical shield. The beam-rails have sufficient length in order to be fixed on the opposite cylindrical shields in order to support the temporary cage sector. The temporary cage sector has a special mechanical connection on the front side in order to perform a coupling in a secure conical way on the backward conical shield flange. On the backward side it has a special radial bushing device able to be fixed to the forward conical flange avoiding any mechanical stress to the SVT detector. The temporary cage sector fixing screws are tightened with a long special screw driver by acting at the working area in front of the forward end of the detector and in front of the Horse Shoe region (backward side). A mechanical Support Cradle Facility has the function of extending the rail and support for the IR Assembly when it is slid in to the final working position outside the forward end of the Super$B$ detector (see Figure 6.48). An illustration of the IR Assembly showing some components of the installation/removal operation is represented in Figure 6.49. To enable the sliding of the IR Assembly an extension with flexible pipe connections has to be foreseen for the cryogenic service to the Cryostat Final Focus Superconductor Magnets. Monitoring position devices are planned to be installed on the cylindrical backward and forward Shields in order to control the distances of the various components during the mounting-demounting operations. Also a strain-gauge set is planned to be mounted on the Temporary Cage Sectors to monitor the mechanical stress in the different positions during the translation process.

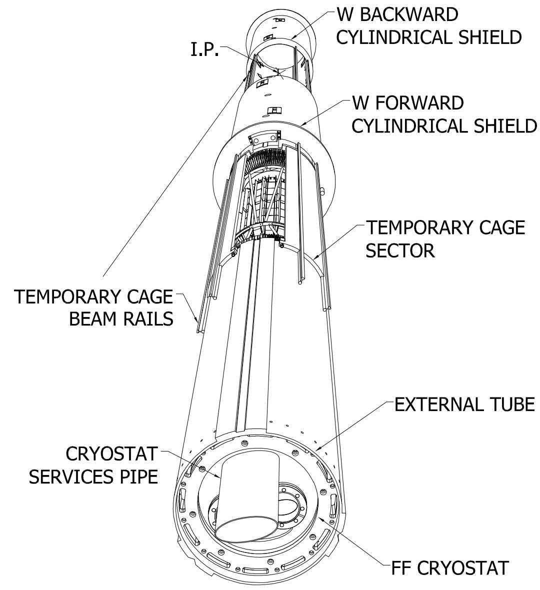

Figure 6.49: An artistic view of the IR Assembly outside the forward end of the Super$B$ detector, showing some components used for the installation/removal operation.

6.7.7 Detector Placement and Survey

The SVT must provide a spatial resolution of the order of 10 μm. The final location of each of the wafers relative to each other (local alignment) and to the DCH (global alignment) will be determined by alignment with charged-particle tracks. This requires a certain degree of overlap of the modules within a layer. There must be overlap in z as well as ϕ, so as to accurately locate the z position of the wafer in a single module with respect to each other.

Mechanical tolerance and measurements must be such that the process of detector alignment with charged-particle tracks converges in a reasonable time. In *BABAR* the optical survey precision was estimated to be 5 μm in the wafer plane and 20 μm out of the plane.

This leads to the requirement that the relative position of the various wafers be stable to the 5 μm level over long periods of time (months or more). The position of the entire detector structure with respect to the DCH can be followed more easily, so that variations of the order of few hours can be tracked.

The relative positions of silicon wafers should be stable in order to avoid the need for frequent local alignments with tracks. Preliminary calculations of the thermal expansion of the entire structure predict of the order of 1 μm/°C change over the length of the detector active region. If the temperature inside the SVT is maintained constant within 1 °C, thermal expansion is not a problem.

6.7.8 Detector Monitoring

Position Monitoring System Although the final placement of the silicon wafer will be measured and monitored with charged particle tracks which traverse the silicon detector and drift chamber, two displacement monitor systems will be designed to measure relative changes in the position of the silicon detector with respect to the machine elements and the cylindrical shield. One displacement monitoring system will be used to monitor the relative position during transportation of the IR Assembly with the silicon detector inside it and during data taking. This system consists of either a capacitive displacement monitor or a LED-photodiode reflection monitor which are sensitive to relative displacements between the silicon detector and the machine components such as the beam pipe, magnet and Cylindrical Shield.
In addition, a laser system will monitor the displacement of the outer layer of detectors with respect to the drift chamber during data taking. Given that the SVT layers are not mounted on the same support as the drift chamber, it is possible that motion between the two will occur. To monitor this motion, short infrared laser pulses are brought in with fiber optics (e.g., 50 μm core diameter) which are attached to the drift chamber. The laser light shines in the active region and reaches the outer layers of the silicon detector to calibrate the relative position of the DCH and SVT.

Radiation Monitoring To protect the silicon detector system against potentially damaging beam losses and to monitor the total radiation dose that the detectors and electronics receive, diamond detectors will be installed on a crown around the beam-pipe, in the vicinity of Layer0. If the radiation dose exceeds a certain threshold, a beam dump signal will be sent to the accelerator control-room. This sort of radiation protection system has already been used successfully in the *BABAR* experiment and it is described in detail in Sec.5.14.

6.7.9 R&D Program

The following R&D projects are planned before the final design of the SVT mechanical configuration is finalized.

Cables Prototypes of the cable from the hybrid to the transition card will be constructed. This allows one to verify the detail of cable routing plans and mechanical robustness. It will also allow the electrical properties to be measured to verify simulations.

Hybrid Realistic mechanical models of the High Density Interconnect (HDI) are required. The HDI is a critical element both in the cooling of the electronics and the mounting of the detector modules. Models will be tested for heat transfer capability and for the module mounting schemes.

Be Beam pipe A full scale of Be beam pipe will be constructed with the cooling design actually available. The part in Be will be realized in a light Aluminum alloy and the cooling and structural tests performed will be renormalized towards Be material.

Layer0 Module A full-scale mock-up of the Layer0 module and its cooled supporting flanges will be constructed. This will be used to verify thermal stability calculations and to investigate the effect of nonuniform beam pipe cooling. It will also be used to design Layer0 assembly fixtures and test and practice the assembly technique.

Inner layer sextant A full-scale mock-up of the L1-L2 layer sextants will be constructed. This will also be used to test and practice assembly technique.

Arch modules Full-scale mock-ups of the arch detector module will also be constructed and used with the prototype cones to verify mechanical stability and mounting techniques.

Cones and space frame A set of prototype cones and space frame will be built to provide realistic test of cooling, mechanical rigidity and thermal stability. In addition they will be used to design L1-L5 assembly fixture and test the assembly technique.

Full-scale model of IR and Cylindrical Shield A model of the entire IR Assembly with the beam pipe near the IP and forward/backward tungsten cylindrical shield will be constructed. This will allow the identification of any interference problems and verify mounting schemes. It will also provide a test bench for the design of various installation fixtures.

Quick Demounting test Tests of the Quick Demounting operation will be made using the full scale model of IR Assembly and cylindrical shield. Sensor gauges will be installed on the SVT mock up module to measure stress and deformation eventually induced by relative movement of the forward/backward cryostat, although blocked by temporary cage sectors. Also the translation mount/demount stages and blocking of the IR Assembly with respect to the Cylindrical shield will be tested.

6.8 Layer0 Upgrade Options

With the machine operating at full luminosity, the SVT Layer0 may benefit from being upgraded to a pixellated detector that has a more stable performance in high background conditions than the baseline striplet option, as discussed in Sec. 6.1.4. In particular:

- the occupancy per detector element from machine background is expected to fall to a few kHz, with a major impact on the speed specifications for the front-end electronics, mainly set by the background hit rate in the case of the striplet readout chip;
- better accuracy in vertex reconstruction can be achieved in presence of relatively high background; the shape of the pixel can be optimized in such a way to reduce the sensor pitch in the z direction while keeping the area in the range of 2500-3000 μm^2, which guarantees enough room for sparse readout functionality.

Two main technologies are under evaluation for the upgrade of Layer0: hybrid pixel and thinner CMOS Monolithic Active Pixel Sensor (MAPS). The first option, mature and with adequate radiation hardness and readout speed capability for application in Layer0, tends to be too thick and has too large a pitch in the detectors presently operated at the LHC. On the contrary for CMOS MAPS, that can be realized with small pitch and material budget, the requirements on readout speed and radiation hardness are more challenging.

Specific R&D activities are in progress to understand advantages and potential issues of the different options described in the following sections.

6.8.1 Hybrid pixels

Hybrid pixel technology has reached quite a mature stage of development. Hybrid pixel detectors are currently used in the LHC experiments [46, 47, 48, 49], with a pitch in the range from 100 μm to a few hundred μm, and miniaturization is being further pushed forward in view of the upgrade of the same experiments at the High Luminosity LHC (HL-LHC) [50, 51, 52]. Hybrid pixel systems are based on the interconnection between a sensor matrix fabricated in a high resistivity substrate and a readout chip. Bump-bonding with indium or indium-tin or tin-lead alloys is the mainstream technology for readout chip-to-sensor interconnection.

The design of a hybrid pixel detector for the SVT innermost layer has to meet some challenging specifications in terms of material budget and spatial resolution. Since the readout chip and the sensor are laid one upon the other, hybrid pixels are intrinsically thicker detectors than microstrips. Interconnect material may further degrade the performance, significantly increasing the radiation length equivalent thickness of the detector (see Table 6.2). As far as the readout and sensor chips are concerned, substrate thinning to 100-150 μm and subsequent interconnection are within the present technological reach. Further thinning may pose some issues in terms of mechanical stability and, as the detector thickness is reduced, of signal-to-noise ratio and/or front-end chip power dissipation. Concerning interconnection, the vertical integration processes currently under investigation in the high energy physics community might help reduce the amount of material. Among the commercially available technologies, the ones provided by the Japanese T-Micro (formerly known as ZyCube), based on so called micro-bumps, and by the US based company Ziptronix, denoted as direct bonding technique, seem the most promising [53]. The Fraunhofer EMFT has developed a bonding technique called SLID and based on a very thin eutectic Cu-Sn alloy to interconnect the chips [54].

The spatial resolution constraints set a limit to the area of the elementary readout cell and, as a consequence, to the amount of functionalities that can be included in the front-end electronics. A planar, 130 nm CMOS technology may guarantee the required density for data sparsification and in-pixel time stamping in a $50{\times}50$ μm^2 pixel area (as already observed, a different aspect ratio might be preferred to improve the resolution performance in one particular direction). The above mentioned interconnection techniques can fully comply with the detector pitch requirements (in the case of the T-Micro technology, pitches as small as 8 μm can be achieved). A fine pitch (30 μm minimum), more standard bump-bonding technology is also provided by IZM. This technology has actually been successfully used to bond the SuperPIX0 front-end chip (to be described later on in this section) to a 200 μm thick pixel detector.

Denser CMOS technologies belonging to the 90 or 65 nm technology can be used to increase the functional density in the readout electronics and include such functions as gain calibration, local threshold adjustment and amplitude measurement and storage. In this case, costs for R&D (and, eventually, production) would increase significantly.

Vertical integration (or 3D) CMOS technologies may represent a lower cost alternative to sub-100 nm CMOS processes. The technology cross section shown in Figure 6.50 in particular points to the main features of the extremely cost-effective process provided by Tezzaron Semiconductor [55]. The Tezzaron process can be used to vertically integrate two or more layers, specifically fabricated and processed for this purpose by Chartered Semiconductor (now Globalfoundry) in a 130 nm CMOS technology. In the Tezzaron/Chartered process, wafers are face-to-face bonded by means of thermo-compression techniques. Bond pads on each

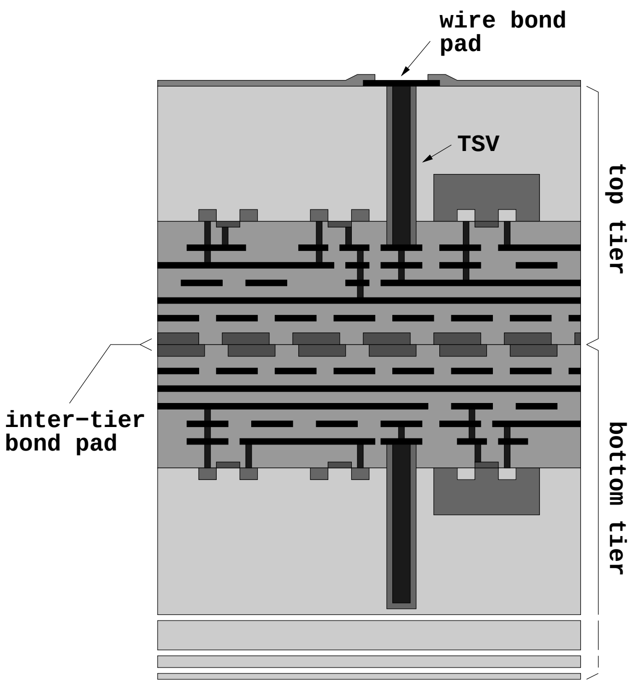

Figure 6.50: Cross-sectional view of a double-layer 3D process.

wafer are laid out on the copper top metal layer and provide the electrical contacts between devices integrated in the two layers. The top tier is thinned down to about 12 μm to expose the through silicon vias (TSV), therefore making possible the connection to the buried circuits. Among the options available in the Chartered technology, the low power (1.5 V supply voltage) transistor option is considered the most suitable for detector front-end applications. The technology also provides 6 metal layers (including two top, thick metals), dual gate option (3.3 V I/O transistors) and N- and P-channel devices with multiple threshold voltages.

The main advantages deriving from a vertical integration approach to the design of a hybrid pixel front-end chip can be summarized as follows:

- since the effective area is twice the area of a planar technology from the same CMOS node, a better trade-off can be found between the amount of integrated functionalities and the detector pitch;
- separating the digital from the analog section of the front-end electronics can effectively prevent digital blocks from interfering with the analog section and from capacitively coupling to the sensor through the bump bond pad.

The design of a 3D front-end chip for pixel detectors is in progress in the framework of the VIPIX experiment funded by INFN [56].

6.8.2 CMOS monolithic sensor options

6.8.2.1 Deep N-well CMOS MAPS

Deep N-well (DNW) CMOS monolithic active pixel sensors (MAPS) are based on an original design approach proposed a few years ago and developed in the framework of the SLIM5 INFN experiment [7]. The DNW MAPS approach takes advantage of the properties of triple well structures to lay out a sensor with relatively large area (as compared to standard three transistor MAPS [57]) read out by a classical processing chain for capacitive detectors. This new design allowed for the first time the implementation of thin CMOS sensors with similar functionalities as in hybrid pixels, such as pixel-level sparsification and fast time stamping in order to match the readout speed requirements for application in Super*B*.

As shown by the technology cross section in Figure 6.51, the sensor, featuring a buried N-type layer with N-wells (NW) on its contour according to a typical deep N-well scheme, collects the charge released by the impinging particle and diffusing through the substrate, whose active volume is limited to the uppermost 20-30 μm thick layer below the collecting electrode. Therefore, within this extent, substrate thinning is not expected to significantly affect charge collection efficiency, while improving resolution performance in charged particle tracking applications. As mentioned above, DNW MAPS have been proposed chiefly to comply with the intense data rates foreseen for tracking applications at the future HEP facilities. The area taken by the deep N-well collecting electrode can actually be exploited to integrate the NMOS parts of the analog front-end inside the internal P-well. A small amount of standard N-well area can be used for PMOS devices, instrumental to the design of high performance analog and digital blocks taking full advantage of CMOS technology properties. In this way, both analog functions, such as signal shaping, and digital functions, such as time stamping and data storing, buffering and sparsification, can be included in the pixel operation. Note that the presence of N-wells other than the sensor is instead strongly discouraged in standard MAPS design, where the operation of the tiny collecting electrode would be jeopardized by the presence of any N-type diffusion in the surrounding. Based on the concept of the DNW monolithic sensor, the MAPS detectors of the Apsel series (see Section 6.8.3.2), which are among the first monolithic sensors with pixel-level data sparsification [58, 17], have been developed in a planar, 130 nm CMOS technology. In 2008, the Apsel4D, a DNW MAPS with 128×32 elements

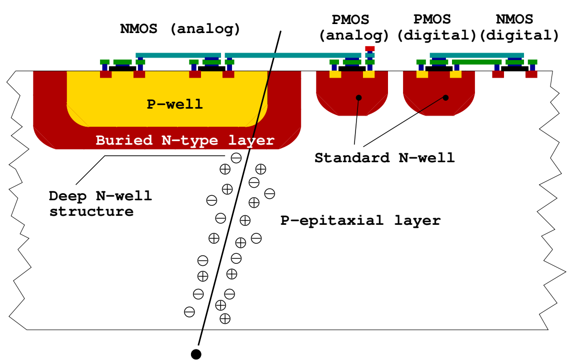

Figure 6.51: Simplified cross-sectional view of a DNW MAPS. NMOS devices belonging to the analog section may be built inside the sensor, while the other transistors cover the remaining area of the elementary cell, with PMOSFETs integrated inside standard N-wells.

has been successfully tested at the Proton Synchrotron facility at CERN [59].

6.8.2.2 DNW MAPS in vertical integration technologies

More recently, vertical integration technologies, like the ones discussed in the previous section for hybrid pixels, have been considered for the design of 3D DNW monolithic sensors. Some specific advantages can derive from the vertical integration approach to DNW MAPS. In particular, all the PMOS devices used in digital blocks can be integrated in a different substrate from the sensor, therefore significantly reducing the amount of N-well area (with its parasitic charge collection effects) in the surroundings of the collecting electrode and improving the detector charge collection efficiency. The first prototypes of 3D DNW MAPS [60, 61] have been submitted in the framework of the 3D-IC collaboration [62]. Characterization has started in the last quarter of 2011.

6.8.2.3 Monolithic pixels in quadruple-well CMOS technology

In DNW MAPS, charge collection efficiency can be negatively affected, although to a limited extent, by the presence of competitive N-wells including the PMOS transistors of the pixel readout chain, which may subtract charge from the collecting electrode. Inefficiency is related to the relative weight of N-well area with respect to the DNW collecting electrode area. An efficiency of about 92% was demonstrated in the aforementioned test beam at CERN [59].

A novel approach for isolating PMOS N-wells has been made available with a planar 180 nm CMOS process called INMAPS, featuring a quadruple well structure [17]. Figure 6.52 shows a simplified cross section of a pixel fabricated with the INMAPS process. By means of an additional processing step, a high energy deep P-well implant is deposited beneath the PMOS N-well (and not under the N-well diode acting as collecting electrode). This implant creates a barrier to charge diffusing in the epitaxial layer, preventing it from being collected by the positively biased N-wells of in-pixel circuits and enabling a theoretical charge collection efficiency of 100%. The NMOS transistors are designed in heavily doped P-wells located in a P-doped epitaxial layer which has been grown upon the low resistivity substrate.

The epitaxial layer is obviously expected to play an important role in improving charge collection performance. Actually, carriers released in the epitaxial layer are kept there by the potential barriers at the P-well/epi-layer and epi-layer/substrate junctions. The use of high resistivity epitaxial layer, also available in this pro-

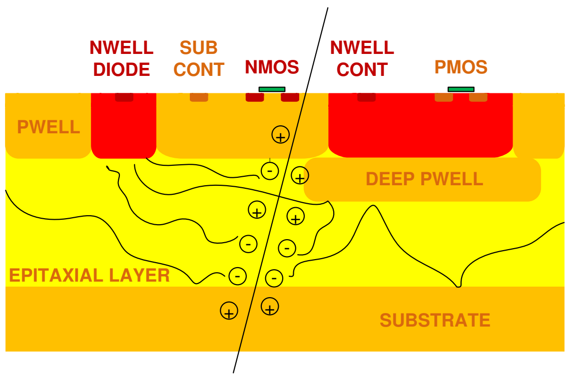

Figure 6.52: Cross-sectional view of the INMAPS CMOS technology; emphasis is put on the deep P-well layer.

cess, can further improve charge collection and radiation resistance of INMAPS sensors with respect to standard CMOS devices.

Epitaxial layers with different thickness (5, 12 or 18 μm) and resistivity (standard, about 10 Ω·cm, and high resistivity, 1 kΩ·cm) are available. A test chip, including several different test structures to characterize both the readout electronics and the collecting electrode performance has been submitted in the third quarter of 2011. Results from the preliminary characterization of the prototypes are discussed in Section 6.8.3.3.

6.8.3 Overview of the R&D activity

6.8.3.1 Front-end electronics for hybrid pixel detectors in 130 nm CMOS technology

A prototype hybrid pixel detector named SuperPIX0 has been designed as a first iteration step aimed at the development of a device to be used for the layer0 upgrade. The main novelties of this approach are the sensor pitch size (50×50 μm) and thickness (200 μm) as well as the custom front-end chip architecture providing a sparsified and data-driven readout. The SuperPIX0 pixel sensor is made of n-type, Float Zone, high-resistivity silicon wafers, with a nominal resistivity larger than 10 kΩ·cm. The SuperPIX0 chip, fabricated in the STMicroelectronics 130nm CMOS technology, is composed of 4096 channels (50×50 μm^2) arranged into 128 columns by 32 rows. Each cell contains an analog charge processor (shown in Figure 6.53) where the sensor charge signal is amplified and compared to a chip-wide preset threshold by a discriminator. The in-pixel digital logic, which follows the comparator, stores the hit in an edge-triggered set reset flip-flop and notifies the periphery of the hit. The charge sensitive amplifier uses a single-ended folded cascode topology, which is a common choice for low-voltage, high gain amplifiers. The 20 fF MOS feedback capacitor is discharged by a constant current which can be externally adjusted, giving an output pulse shape that is dependent upon the input charge. The peaking time increases with the collected charge and is of the order of 100 ns for 16000 electrons injected. The charge collected in the detector pixel reaches the preamplifier input via the bump bond connection. Alternatively, a calibration charge can be injected at the preamplifier input through a 10 fF internal injection capacitance so that threshold, noise and crosstalk measurements can be performed. The calibration voltage step is provided externally by a dedicated line. Channel selection is performed by means of a control section implemented in each pixel. This control block, which is a cell of a shift register, enables the injection of the charge through the calibration capacitance. Each pixel features a digital mask used to isolate single noisy channels. This mask is implemented in the readout logic. The input device (whose dimensions were chosen based on detection efficiency optimization criteria [63]) featuring an aspect ratio W/L=18/0.3 and a drain current of about 0.5 μA, is biased in the weak inversion region. A non-minimum length has been chosen to avoid short channel effects. The PMOS current source in the input branch has been chosen to have a smaller transconductance than the input transistor. The analog front-end cell uses two power supplies. The analog supply (AVDD) is referenced to AGND, while the digital supply is referenced to DGND. Both supplies have a nominal operating value of 1.2 V. Since single-ended amplifiers are sensitive to voltage fluctuations on the supply lines, the charge preamplifier is connected to the AVDD. The threshold discriminator and voltage references are connected to the AVDD and AGND as well. The in-pixel digital

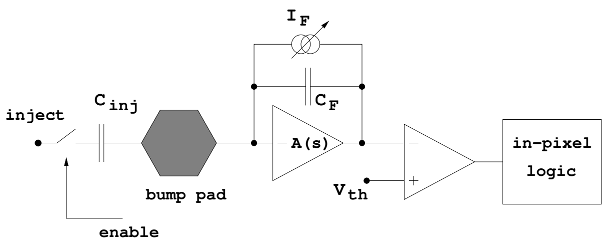

Figure 6.53: Block diagram of the analog front-end electronics for the elementary cell of the SuperPIX0 readout chip.

logic is connected to the digital supply. The substrate of the transistors is connected to a separate net and merged to the analog ground at the border of the matrix. The SuperPIX0 chip has been fabricated in a six metal level technology. Special attention has been paid to layout the channel with a proper shielding scheme. Two levels of metal have been used to route the analog signals, two for the digital ones and two for distributing the analog and digital supplies. The supply lines, at the same time, shield the analog signals from the digital activity. For nominal bias conditions the power consumption is about 1.5 μW per channel. More details on the design of the analog front-end can be found in the literature [64]. The measured threshold dispersion in the chip is around 490 e^- with an average pixel noise of about 60 e^- (without the sensor connected). Since the threshold dispersion is a crucial characteristic to be considered in order to meet the required specifications in terms of noise occupancy and efficiency, circuits for threshold fine-adjusting have to be implemented in the next version of the chip. These results have been extracted using the gain measured with an internal calibration circuit, implemented in the pixel, injecting a charge from 0 to 12 fC in each channel preamplifier. An average gain of about 40 mV/fC with a dispersion at the level of 5% has been obtained. The front-end chip has been connected by bump-bonding to a high resistivity pixel sensor matrix of 200 μm thickness. The bump-bonding process has been performed by the Fraunhofer IZM with electroplating of SnAg solder bumps. Measurements on the bump-bonded chip show a working sensor and a good quality of the interconnection at 50 μm pitch. The measured gain and threshold dispersion are compatible with the ones extracted from the front-end chip only. We observe an increase of the noise of around 20%, up to about 76 e^-, due to the added capacitive load of the sensor connected. The Superpix0 chip, bump bonded to a high resistivity silicon pixel detector, was also tested on the beam of the Proton Synchrotron (PS) at CERN. The measured efficiency is shown in Figure 6.54 as a function of the voltage threshold in the discriminator. Efficiencies larger than 99% were obtained for thresholds up to 1/4 of a MIP, corresponding to more than 10 times the pixel noise.

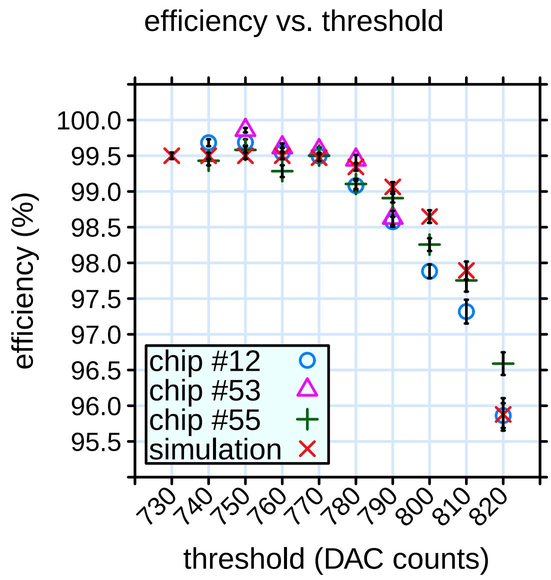

Figure 6.54: Superpix0 efficiency as a function of the voltage discriminator threshold in the case of normal incidence angle.

6.8.3.2 The Apsel DNW MAPS series

DNW MAPS in planar CMOS technology Deep N-well MAPS were proposed a few years ago as possible candidates for charged-particle tracking applications. The Apsel4D chip is a 4096 element prototype MAPS detector with data-driven readout architecture, implementing twofold sparsification at the pixel level and at the chip periphery. In each elementary cell of the MAPS matrix integrated in the Apsel4D chip, a mixed signal circuit is used to read out and process the charge coming from a DNW detector. This design approach, relying upon the properties of the triple well structures included in modern CMOS processes, has been described in Section 6.8.2.1. In the so called DNW MAPS is integrated with a relatively large (as compared to standard three transistor MAPS) collecting electrode, featuring a buried N-type layer, with a classical readout chain for time invariant charge amplification and shaping. In the Apsel4D prototype, the elementary MAPS cells feature a 50 μm pitch and a power dissipation of about 30 μW/channel. The block diagram of the pixel analog front-end electronics is shown in Figure 6.55. The first block of the processing chain, a charge preamplifier, uses a complementary cascode scheme as its forward gain stage, and is responsible for most of the power consumption in the analog section. The feedback capacitor C_F is continuously reset by an NMOS transistor, biased in the deep sub-threshold region through the gate voltage V_f. The preamplifier input device, featuring an aspect ratio $W/L = 14\ \mu m/0.25 \mu m$ and a drain current of 20 μA, was optimized for a DNW detector about 900 μm^2 in area and with a capacitance C_D of about 300 fF. The charge preamplifier is followed by a CR-RC, bandpass filtering stage, with open loop gain $T(s)$, featuring a programmable peaking time which can be set to 200 or 400 ns. C_1 is a differentiating capacitor at the CR-RC shaper input, while G_m and C_2 are the transconductance and the capacitance in its feedback network. A discriminator is used to compare the processed signal to a global voltage reference V_t, thereby providing hit/no-hit information to the cell digital section. More details on the design of the analog front-end can be found in the literature [65].

A dedicated readout architecture to perform on-chip data sparsification has been implemented in the Apsel4D prototype. The readout logic provides the timestamp information for the hits. The timestamp (TS), which is necessary to identify the event to which the hit belongs, is generated by a TS clock signal (also called Bunch-Crossing clock for historical reasons). The key requirements in this development are 1) to minimize logical blocks with PMOS inside the active area, thus preserving the collection efficiency, 2) to reduce to a minimum the number of digital lines crossing the sensor area, in particular its dependence on detector size to allow the readout scalability to larger matrices and to reduce the residual crosstalk effects, and

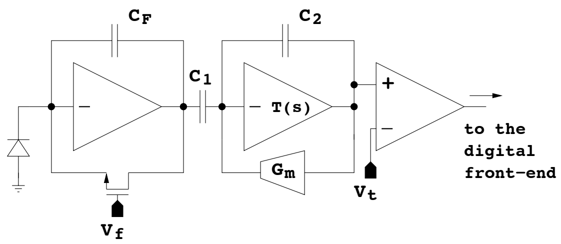

Figure 6.55: Block diagram of the analog front-end electronics for the elementary cell of the Apsel4D prototype.

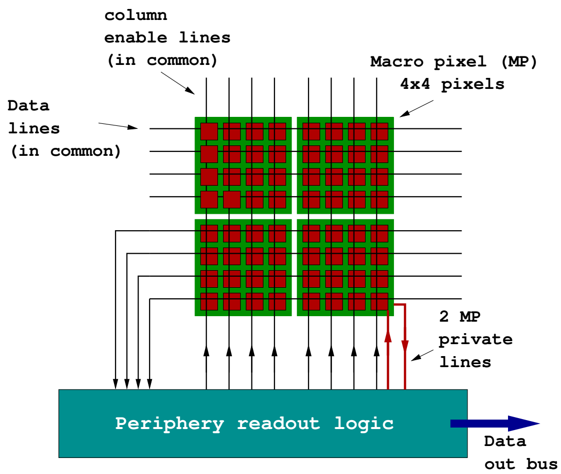

Figure 6.56: Schematic concept of the architecture for MAPS matrix readout.

3) to minimize the pixel dead time by reading hit pixels out of the matrix as soon as possible.

With these criteria a readout logic in the periphery of the matrix has been developed, as schematically shown in Fig 6.56. To minimize the number of digital lines crossing the active area the matrix is organized in MacroPixels (MP) with 4x4 pixels. Each MP has only two private lines for point-to-point connection to the peripheral logic: one line is used to communicate that the MP has got hits, while the second private line is used to freeze the MP until it has been read out. When the matrix has some hits, the columns containing fired MPs are enabled, one at a time, by vertical lines. Common horizontal lines are shared among pixels in the same row to bring data from the pixels to the periphery, where the association with the proper timestamp is performed before sending the formatted data word to the output bus. The chip has been designed with a mixed mode design approach. While the pixel matrix has a full custom design and layout, the periphery readout architecture has been synthesized in standard cell starting from a VHDL model; automatic place-and-route tools have been used for the layout of the read-out logic [58]. The chip has been designed to run with a readout clock up to 100 MHz (20 MHz in test beam), a maximum matrix readout rate of 32 hit pixels/clock cycle and a local buffer of maximum 160 hits to minimize the matrix sweep time.

Apsel4D, together with smaller test matrices 3x3 with full analog output, have been successfully tested with 12 GeV/c protons at the PS-T9 beam line at CERN [12]. On the analog test structures the measured most probable value for the cluster signal for MIPs was about 1000 electrons with a Signal-to-Noise ratio of about 20. The efficiency of the Apsel4D DNW MAPS as a function of threshold for two devices with different silicon thickness (100 μm and 300 μm thick) has also been measured. Figure 6.57 shows the measured hit efficiency, determined as described in a published work [12]. At the lowest thresholds a maximum efficiency of approximately 92% and the expected general behavior of decreasing efficiency with increasing threshold can be observed. The noise occupancy for this range of thresholds was found to vary from 2.5×10^{-3} to 1×10^{-6}. The low efficiency observed for the 300 μm chip at the lowest threshold appears to have been caused by a readout malfunction. Investigations have shown that a small localized area on the detector had very low efficiency, while the rest of the detector behaved normally with good efficiency. Additionally, the efficiency for detecting hits as a function of the track extrapolation point within a pixel has been studied. Since the pixel has internal structures, with some areas less sensitive than others, we expect the efficiency to vary as a function of position within the cell. The uncertainty on the track position including multiple scattering effects is roughly 10 microns, to be compared to the 50 μm pixel dimension. The pixel has been divided into nine square sub-cells of equal area and the hit efficiency within each sub-cell has been measured. The efficiencies thus obtained are "polluted" in some sense due to the migration of tracks among cells. We obtain the true sub-cell efficiencies by unfolding the raw results, taking

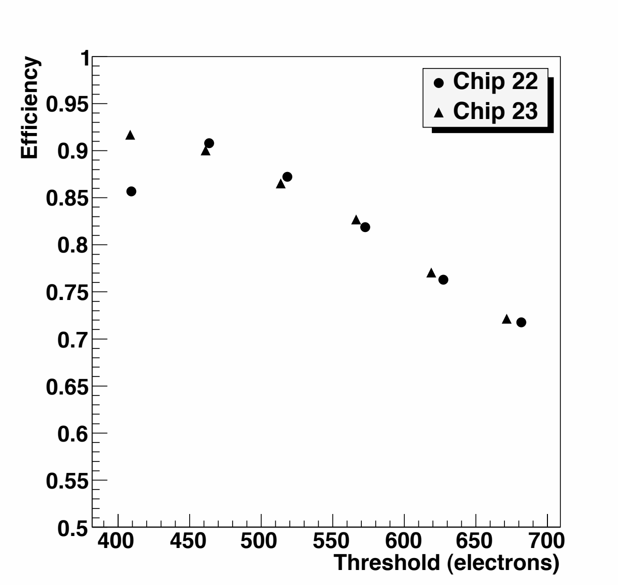

Figure 6.57: Efficiency results for two MAPS detectors. Chip 22 is 300 μm thick while Chip 23 is 100 μm thick. The statistical uncertainty on each point is smaller than the size of the plotting symbol.

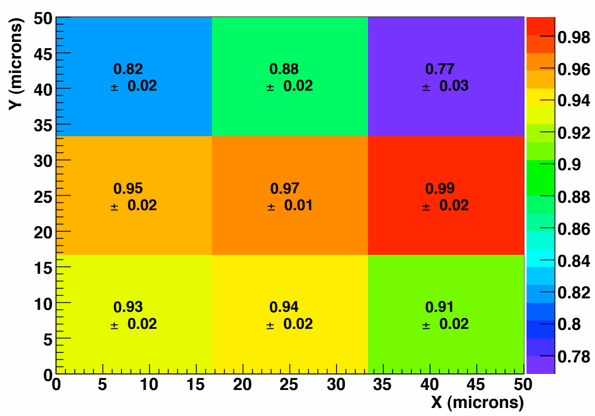

Figure 6.58: Hit efficiencies measured as a function of position within the pixel (the picture, which is not to scale, represents a single pixel divided into nine sub-cells).

into account this migration, which we characterize using a simple simulation. The result can be seen in Figure 6.58, where the efficiency measured in each sub-cell is shown. A significant variation in sensitivity within the pixel area can be observed, as expected. In particular, the central region is seen to be virtually 100% efficient, while the upper part of the pixel, especially the upper right-hand sub-cell, shows lower efficiency due to the presence of competitive n-wells. The position of this pixel map relative to the physical pixel is not fixed. This is a consequence of the alignment, which determines the absolute detector position by minimizing track-hit residuals, as described above. If the pixel area is not uniformly efficient, the pixel center as determined by the alignment will correspond to the barycenter of the pixel efficiency map. Thus, it is not possible to overlay Figure 6.58 on a drawing of the pixel layout, without adding additional information, for example a simulation of internal pixel efficiency. The efficiency as a function of position on the MAPS matrix has also been investigated, since non-uniformity could indicate inefficiencies caused by the readout. Generally, a uniform efficiency across the area of the MAPS matrix was observed. The intrinsic resolution σ_{hit} for the MAPS devices was measured as already described in a published paper [12]. The expected resolution for cases where the hit consists of a single pixel is given by $50/\sqrt{12} = 14.4$ μm, where 50 microns is the pixel dimension.

DNW MAPS in 3D CMOS technology As already mentioned in Section 6.8.2.1, the DNW monolithic sensors have been designed and fabricated also in the Tezzaron/Globalfoundry technology, based on the vertical integration of two 130 nm CMOS layers. The conceptual step from the DNW MAPS in a planar CMOS technology to its vertically integrated version is illustrated in Fig 6.59, showing a cross-sectional view of a 2D MAPS and of its 3D translation. The prototype includes two small 3×3 matrices for analog readout and charge collection characterization and a larger one, 8×32 in size, equipped with a digital readout circuit with data sparsification and time stamping features. In the 3D pixel cell, with 40 μm pitch, the fill factor has been increased up to 94% (90% in 2D DNW MAPS version) and the sensor layout has been optimized; according to device simulation, where a collection efficiency in excess of 98% is expected.

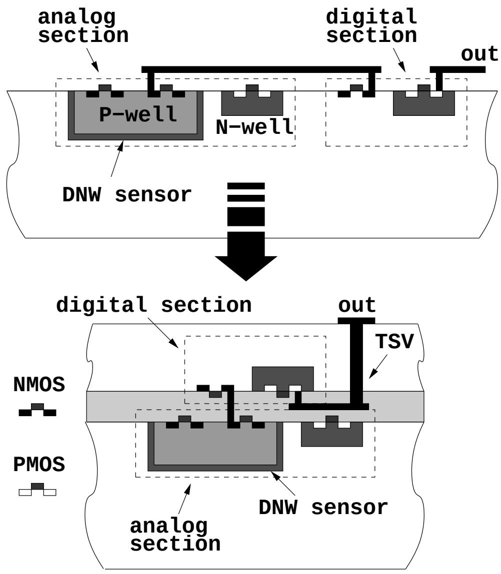

Figure 6.59: Cross-sectional view of a DNW CMOS MAPS: from a planar CMOS technology to a 3D process.

A number of different problems were encountered during fabrication of the first device batch. Among them, the misalignment between the two tiers prevented the analog and digital sections in each pixel cell to communicate to each other [66]. At the time of the TDR writing, other 3D wafers are being processed and devices from the first run are undergoing characterization.

Figure 6.60 shows the analog front-end channel of the 3D DNW MAPS (quite similar to the analog processor of the SuperPIX0 chip, see Figure 6.53), simply consisting of a charge preamplifier, whose bandwidth was intentionally limited to improve the signal-to-noise ratio (the so called shaper-less configuration).

Tests on the CMOS layer hosting the sensor and the analog front-end, already available, allowed a first characterization of the process. Equivalent noise charge of between 30 and 40 electrons (in good agreement with circuit

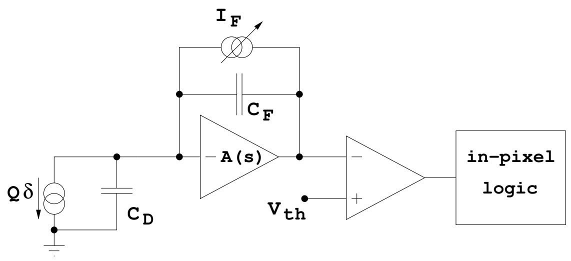

Figure 6.60: Block diagram of the analog front-end electronics for the elementary cell of the 3D DNW MAPS of the apsel family.

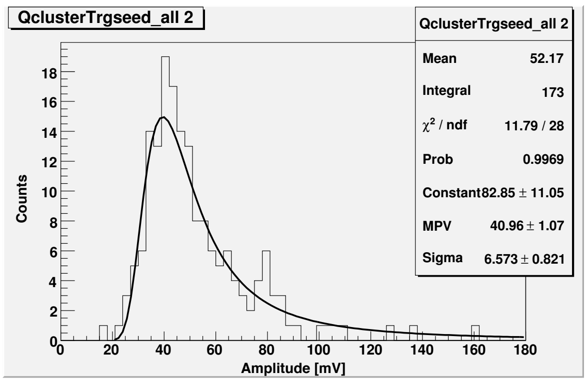

Figure 6.61: 3×3 cluster signal for electrons from a ^{90}Sr source for the 3D DNW MAPS.

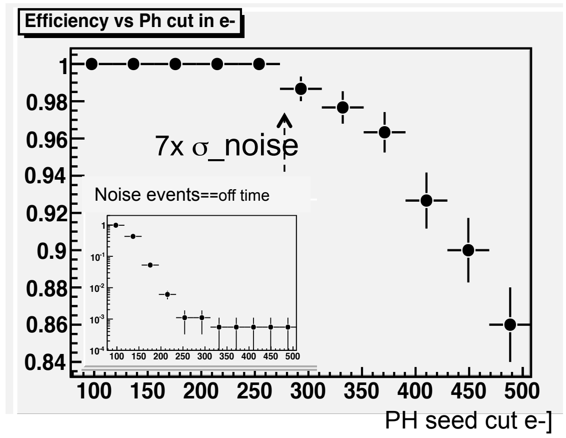

Figure 6.62: Detection efficiency of a pseudo-3D DNW MAPS as a function of the cut on the pulse height of the detected events. The efficiency is 1 up to threshold values of 7 times the pixel noise.

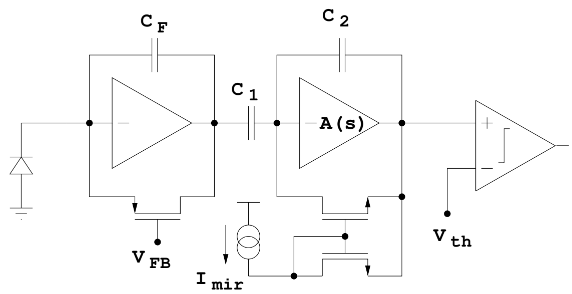

Figure 6.63: Block diagram of the analog front-end electronics for the elementary cell of Apsel4well monolithic sensor.

simulations) and a charge sensitivity of about 300 mV/fC (a factor of 2 smaller than in simulations) were obtained. Figure 6.61 shows the ^{90}Sr spectrum detected by the cluster of 3×3 pixels in a small matrix. The most probable value of the collected charge is about 1000 electrons. Pseudo-3D DNW MAPS have been tested also on the PS beam at CERN. Here, the term pseudo-3D refers to devices consisting of just one tier but suitable for 3D integration. Very promising results were obtained with hit detection efficiency above 98%, as displayed in Figure 6.62.

6.8.3.3 The Apsel4well quadruple well monolithic sensor

As already mentioned in section 6.8.2.3, a test chip in the INMAPS, 180 nm CMOS technology, called Apsel4well, has been submitted in August 2011. The chip includes four 3×3 matrices with different number (2 or 4) of the collecting electrodes (each consisting of a 1.5 μm×1.5 μm N-well diffusion), with or without the shielding deep P-well implant, with or without enclosed layout transistors as the input device of the charge preamplifier. The prototype also contains a 32×32 matrix with sparsified digital readout, with an improved version of the architecture developed for the DNW MAPS and now optimized for the Layer0 target hit rate of 100 MHz/cm^2.

The first test chips have been realized with different thicknesses (5-12 μm) and epitaxial layer resistivity (standard, about 10 Ω·cm, and high resistivity, 1 kΩ·cm).

In the Apsel4well pixel (50 μm pitch) the collecting electrode is readout by a channel similar to previous versions of DNW MAPS, including charge preamplifier, a shaping stage with a current mirror in the feedback network and a two-stage threshold discriminator (Figure 6.63), followed by the in-pixel logic needed to implement the new readout architecture described in section 6.8.3.4. With the new pixel design the total sensor capacitance is only about 40 fF, an order of magnitude smaller than in previous DNW pixels, allowing a reduction of almost a factor of 2 in power consumption (now 18 μW/pixel).

Preliminary results on the different INMAPS test structures realized showed very promising results. Figure 6.64 shows the signal at the shaper output as a response to an input charge signal with varying amplitude. In the 3x3 analog matrix an average equivalent noise charge of 38 e^- and a gain of about 900 mV/fC were measured, both in good agreement with post layout simulation.

The characterization with laser and radioactive sources confirmed that the deep p-well is beneficial in preserving charge collection by the small Nwell diodes, although a much larger area inside the pixel is now covered by competitive Nwells with the deep p-well implant beneath. The plot in Figure 6.65 represents the collected charge in a Apsel4well pixel (12 μm epitaxial layer thickness, standard resistivity) illuminated with an infrared laser source. The layout of the N-wells (both the collecting electrodes and the N-wells for PMOS transistors) included in the elementary cell is superimposed onto the plot. The position of the collecting electrodes is easily detectable.

Measurements with electrons from a ^{90}Sr source are shown in Figure 6.66, for a chip with 12μm high resistivity epitaxial layer. The cluster signal has been fitted with a Landau distribution with a MPV corresponding to about 930 electrons. The Signal-to-Noise ratio of the samples featuring a high resistivity epitaxial layer ranges from 20 to 25.

Evaluation of the threshold dispersion and of the noise variation among pixels has been performed on the 32x32 digital matrix, measuring the hit rate as a function of the discriminator threshold. With a fit to the turn-on curve we report a threshold dispersion of about 2 times the average pixel noise, and a noise variation of about 35-40% inside the matrix. These figures were obtained with a readout clock of 10 MHz, with no significant change in the performance

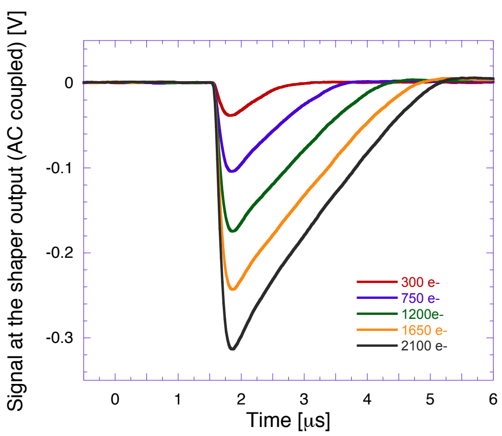

Figure 6.64: Signal at the shaper output as a response to an input charge signal with varying amplitude in an Apsel4well sensor.

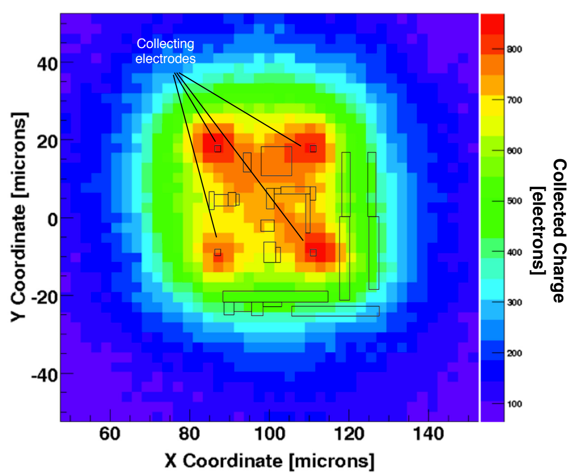

Figure 6.65: Collected charge in a Apsel4well pixel illuminated with an infrared laser source.

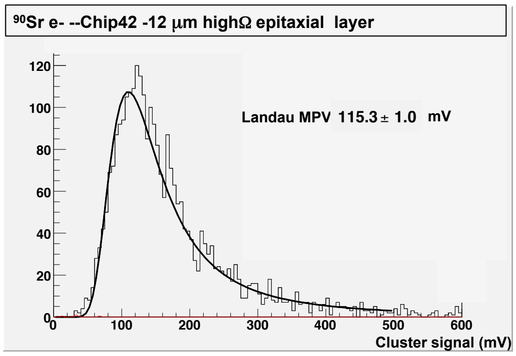

Figure 6.66: Cluster signal for electrons from a ^{90}Sr source detected by a 3×3 matrix of the Apsel4well chip with high resistivity epitaxial layer.

with measurements done up to 100 MHz readout clock.

Specific tests on the 32x32 digital matrix were also performed to verify the new readout architecture in both the operation modes available on chip: data push and triggered. Both functionalities are working as expected with very similar performance verified with measurements of the pixel turn-on curve.

Radiation hardness of these devices is being investigated for application in Super$B$. Irradiation with neutrons up to 10^{14} n/cm^2 has been performed and devices are currently under measurement with laser and radioactive sources (see section 6.8.4).

6.8.3.4 Fast readout architecture for MAPS pixel matrices

An evolution of the readout architecture implemented in the 2D DNW MAPS was developed [11] to benefit from the larger area available for the in-pixel logic in some technologies: 3D MAPS with vertical integration and INMAPS realized with the deep p-well implant. Having more room for the in-pixel logic makes it possible to latch the TS at the pixel level when a hit occurs. When a TS request is sent to the matrix, a pixel FastOR signal activates if the latched TS is the same as the requested one. The columns with an active FastOR signal are enabled and read out in a sequence; 1 clock cycle per column is needed. A conceptual view of the digital readout architecture is shown in Figure 6.67. The matrix readout is timestamp sorted and can be operated either in data push mode (selecting all the TS) or in triggered mode, where only triggered TS are readout. The readout periphery takes care of encoding, buffering and serializing/sorting the hits retrieved from the sensor matrix. In order to achieve the remarkably high readout frequency set by the Super$B$ experiment, the architecture can be subdivided in a number of modules, each serving a submatrix. This choice improves the scalability features of the readout section and makes it suitable for experiment scale detectors.

With this architecture, a TimeStamp of 100 ns can be used, greatly reducing the TS resolution with respect to standard CMOS sensor readout, where large frame readouts are needed. For application in Layer0, where high rates are expected, a fast TS ($< 1\mu$s) is needed to reduce the module readout bandwidth to an acceptable level (<5 Gbit/s). Full VHDL simulation of the readout has been implemented to test the performance on the full size matrix (1.3 cm^2) with a target Layer0 hit rate of 100 MHz/cm^2. Results from simulation showed that with a TS clock of 100 ns and a 50 MHz readout clock one can achieve efficiency above 99% for the data push architecture. Studies on the triggered architecture showed an efficiency of about 98%, for 6 μs trigger latency: in this configuration, where the pixel cell acts as a single memory during the trigger latency, the associated pixel dead time dominates the inefficiency.

This new readout has been implemented in the Apsel4well test chip as well as in two devices in preparation for next 3D submission: a second prototype of a front-end chip for hybrid pixels (Superpix1, 32x128 pixels with 50×50 μm^2 pitch) and a large DNW MAPS matrix with the cell optimized for the vertical integration process (APSELVI, 128x100 pixels with 50×50 μm^2 pitch).

6.8.4 Radiation tolerance

Hybrid pixels. The high degree of radiation tolerance of modern CMOS technologies, com-

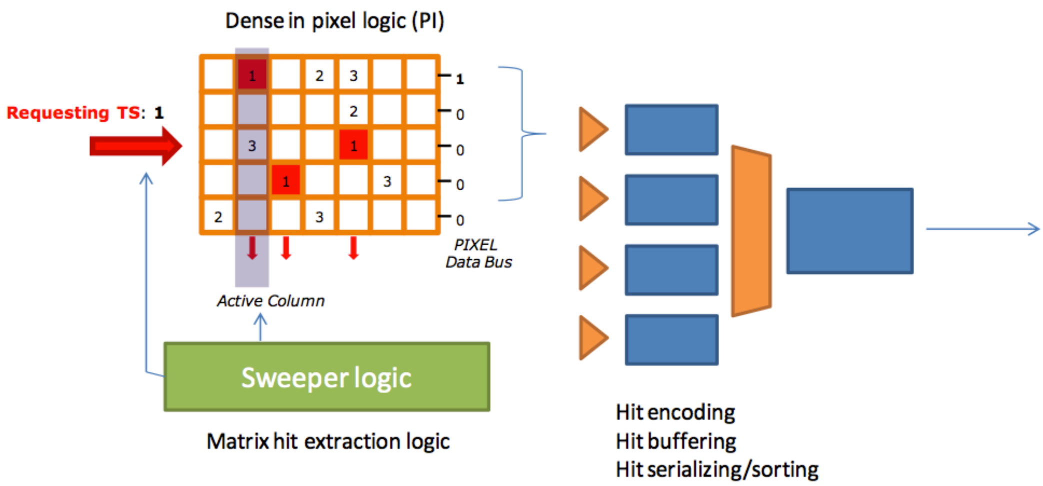

Figure 6.67: Conceptual view of the new pixel readout architecture implemented in the Apsel4well chip.

ing as a byproduct of the aggressive scaling down of device minimum feature size, is having a beneficial impact in high energy physics applications. Beginning with the 130 nm CMOS processes, which entered the sub-3 nm gate oxide thickness regime, direct tunneling contribution to the gate current has assumed a significant role as compared to trap assisted mechanisms [67]. This may account for the very high degree of radiation hardness featured by devices belonging to the most recent technology nodes, which might benefit from relatively fast annealing of holes trapped in the ultra-thin gate oxides. Tolerance to a few hundred of Mrad(SiO_2) has been recently proven in front-end circuits for hybrid pixel detectors [50]. Charge trapping in the thicker shallow trench isolation (STI) oxides is considered as the main residual damage mechanism in 130 nm N-channel MOSFETs exposed to ionizing radiation [68, 69], especially in narrow channel transistors [70]. Ionizing radiation was found to affect also the 90 nm and 65 nm CMOS nodes, although to an ever slighter extent, this is likely to be due to a decrease in the substrate doping concentration and/or in the STI thickness. As far as analog front-end design is concerned, ionizing radiation damage mainly results in an increase in low frequency noise, which is more significant in multifinger devices operated at a small current density. This might be a concern in the case of the front-end electronics for hybrid pixel detectors, where the input device of the charge preamplifier is operated at drain currents in the few μA range owing to low power constraints. However, at short peaking times, typically below 100 ns, the effects of the increase in low frequency noise on the readout channel performance is negligible. Also, use of enclosed layout techniques for the design of the preamplifier input transistor (and of devices in other critical parts of the front-end) minimizes the device sensitivity to radiation [71]. For this purpose, Figure 6.68 shows the noise voltage spectrum for a 130 nm NMOS transistor with enclosed layout, featuring no significant changes after irradiation with a 100 Mrad(SiO_2) total ionizing dose. On the other hand, CMOS technologies are virtually insensitive to bulk damage, since MOSFET transistor operation is based on the drift of majority carriers in a surface channel.

DNW CMOS MAPS. DNW MAPS have been thoroughly characterized from the standpoint of radiation hardness to evaluate their limitations in harsh radiation environments. In particular, the effects of ionizing radiation, with total doses of about 10 Mrad(SiO_2), have been inves-

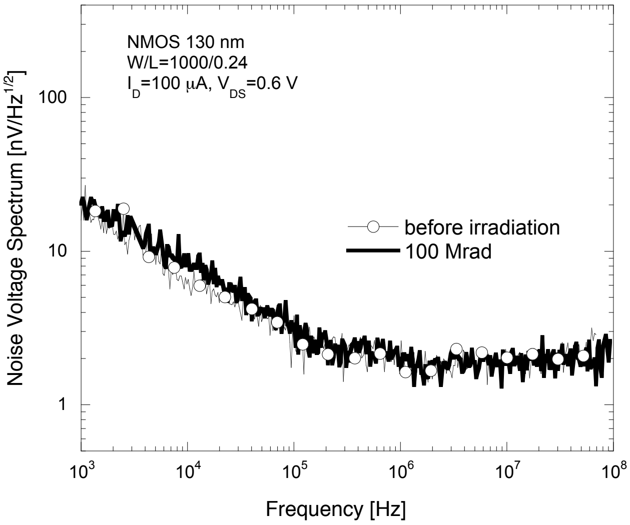

Figure 6.68: Noise voltage spectrum for a 130 nm NMOS device with enclosed layout.

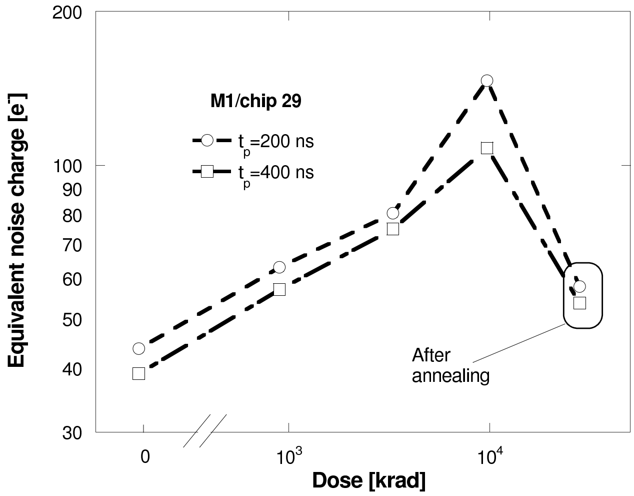

Figure 6.69: Equivalent noise charge as a function of the absorbed dose and after the annealing cycle for DNW monolithic sensor. ENC is plotted for the two available peaking times.

tigated by exposing DNW MAPS sensors to a ^{60}Co source [72]. In that case, some performance degradation was detected in the noise and gain of the front-end electronics and in the sensor leakage current, while no significant change was observed as far as the charge collection properties are concerned. Figure 6.69 shows the equivalent noise charge as a function of the absorbed dose and after the annealing cycle for a DNW monolithic sensor. The significant change can be ascribed to the increase in the flicker noise of the preamplifier input device as a consequence of parasitic lateral transistors being turned on by positive charge buildup in the shallow trench isolation oxides and contributing to the overall noise. Use of an enclosed layout approach is expected to significantly reduce the effect of ionizing radiation.

Figure 6.70 shows event count rate for a DNW monolithic sensor exposed to a ^{55}Fe source before irradiation, after exposure to γ-rays and after the annealing cycle. As the absorbed dose increases, the 5.9 keV peak gets broader as a consequence of the noise increase (in fair agreement with data in Figure 6.69. At the same time, the peak is shifted towards lower amplitude values, as a result of a decrease in the front-end charge

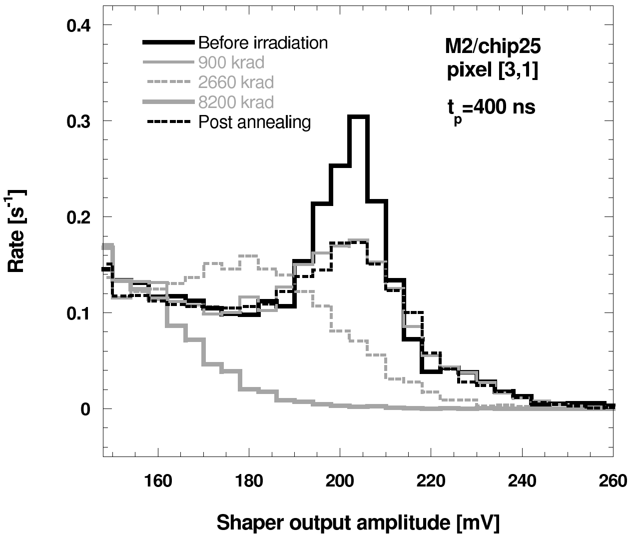

Figure 6.70: Event count rate for a DNW monolithic sensor exposed to a ^{55}Fe source before irradiation, after exposure to γ-rays and after the annealing cycle.

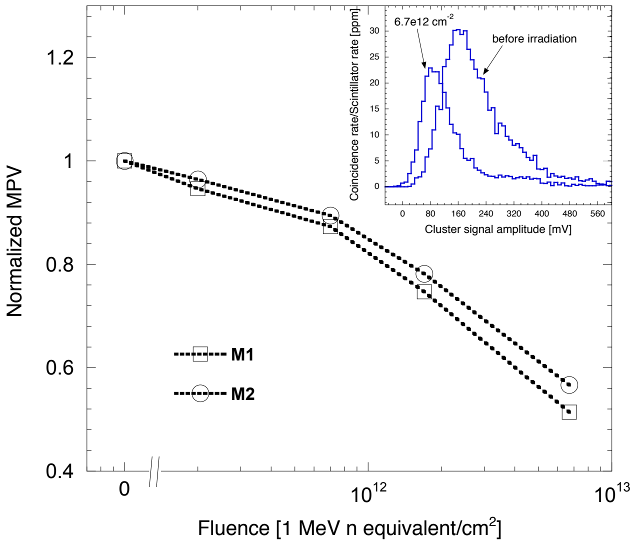

Figure 6.71: Most probable value (MPV) of the ^{90}Sr spectra (shown in the inset for one of the tested chips before irradiation and after exposure to a $6.7{\times}10^{12}$ cm^{-2} neutron fluence) normalized to the pre-irradiation value as a function of the fluence for DNW MAPS with different sensor layout.

sensitivity also due to charge build up in the STI of some critical devices.

DNW MAPS of the same kind have also been irradiated with neutrons from a Triga MARK II nuclear reactor to test bulk damage effects [73]. The final fluence, $6.7{\times}10^{12}$ 1-MeV-neutron equivalent/cm^2, was reached after a few, intermediate steps. The devices under test (DUT) were characterized by means of several different techniques, including charge injection at the front-end input through an external pulser, sensor stimulation with an infrared laser and spectral measurements with ^{55}Fe and ^{90}Sr radioactive sources. Neutron irradiation was found to have no sizable effects on the front-end electronics performance. This can be reasonably expected from CMOS devices, whose operation is based on the drift of majority carriers in a surface channel, resulting in a high degree of tolerance to bulk damage. Exposure to neutrons was instead found to affect mainly the charge collection properties of the sensors with a reduction in the order of 50% at the maximum integrated fluence. Figure 6.71 shows the most probable value (MPV) of the ^{90}Sr spectra normalized to the pre-irradiation value as a function of the fluence for DNW MAPS with different sensor layout. A substantial decrease can be observed, to be ascribed to a degradation in the minority carrier lifetime. A higher degree of tolerance was instead demonstrated in monolithic sensors with high resistivity (1 kΩ·cm) epitaxial layer [74]. Actually, doping concentration plays a role in determining the equilibrium Fermi level, which in turn influences the effectiveness of neutron-induced defects as recombination centers [75].

Quadruple-well CMOS MAPS. Radiation hardness study of quadruple-well MAPS (see sections 6.8.2.3 and 6.8.3.3) is in progress during the writing of this TDR. The preliminary results, shown in the following, are quite encouraging and suggest that the INMAPS 180 nm CMOS process might overcome the radiation tolerance issues found in DNW MAPS and become the candidate technology for the Layer0 pixel upgrade. A number of Apsel4well chips, featuring a high resistivity, 12 μm thick epitaxial layer, have been irradiated with neutrons from the same source as the one used for DNW MAPS tests. Also samples with standard resistivity epitaxial layer (same epilayer thickness) have been irradiated for the sake of comparison. The maximum fluence was 10^{14} 1-MeV-equivalent neutron/cm^2. The irradiated devices where tested with bench top instrumentation and with laser and radioactive sources. As already discussed in the case of DNW MAPS, irradiation with neutrons was found to affect mainly the collecting electrode performance. Figure 6.72 shows the MPV (open square markers) of the measured ^{90}Sr spectra, normalized to the MPV obtained in the non-irradiated device, as a function of the fluence, for quadruple-well MAPS with high resistivity epitaxial layer. Note that at a fluence of about 7×10^{12} cm^{-2}, the loss in collected charge is about 32% of the pre-irradiation value. Data in Figure 6.71, relevant to DNW MAPS, show a charge loss of about 50% at a slightly smaller

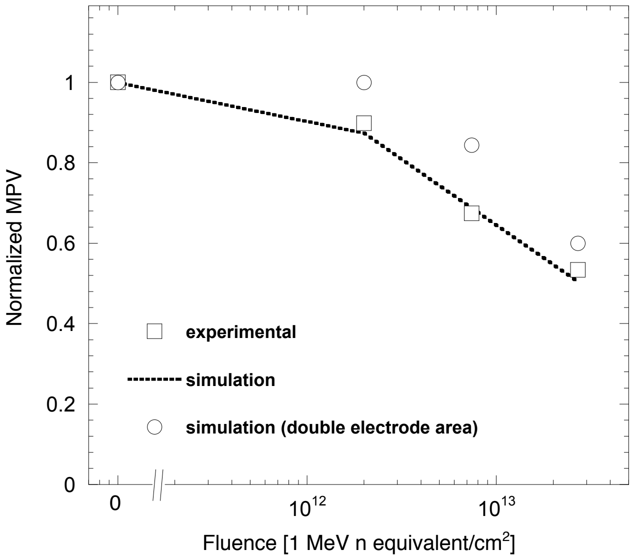

Figure 6.72: Most probable value (MPV) of the ^{90}Sr spectra as a function of the fluence for quadruple-well MAPS with high resistivity epitaxial layer. Data are normalized to the MPV measured in the non-irradiated device.

fluence. In Figure 6.72, results from device simulations, based on a purposely developed Monte Carlo model [76], are also shown. Simulations performed on devices with the same electrode geometry as in the test structures (dashed line in Figure 6.72) reproduce the experimental data with good accuracy. The same Monte Carlo model (see the plot with circle markers again in Figure 6.72) anticipates that, by doubling the collecting electrode area, the charge loss should be about 40% at a fluence of 2.5×10^{13} cm^{-2}, which is the expected fluence, including a $\times 5$ safety factor, for a 1 year operation in the Layer0. Optimization of the collecting diode dimensions is under evaluation to further improve S/N performance for irradiated devices. In addition, the characterization of monolithic sensors developed in a very similar 180 nm CMOS technology (including deep P-well and high resistivity epitaxial layer options), but featuring a different readout approach, has recently provided some promising results in terms of radiation hardness [15, 16]. In this case, less than 10% loss in collected charge and a slight increase in the noise (about 20%) were detected in MAPS samples irradiated with a neutron fluence of 3×10^{13} cm^{-2}.

6.9 Services and Utilities

The vertex detector requires the following services, which must be brought inside the support tube to a location near the outboard of the W conical shield.

Power Supply The readout ICs require two low-voltage power supply lines (analog and digital); the silicon sensors need the bias voltage. Each power supply board must provide a unique low voltage level for each HDI side (referenced to the bias level of the silicon sensor's side). The further split between the analog and digital power takes place on the HDI. The bias voltage will be raised during the experiment life up to 200 V for the Layer0, to fully deplete the sensor in presence of radiation damage. The power supplies will be specially procured to match the vertex detector specifications to take under control the electronic noise.

Cooling water The readout electronics and transition card will be water cooled. Two sets of water connections for each cone (since each cone is constructed from two halves) and two set for each L0 cold flange (since each flange is constructed from two halves) will be required. In the same way, since each transition card support is constructed in two halves, two water connections for each transition card support is required. Also a connection for the cooled Be beam pipe is needed. The cooling water will be supplied by a special low volume chiller system dedicated to the vertex detector system.

Dry air or nitrogen The vertex detector requires a dry, stable environment. Cooled and dry air or nitrogen from each side is planned to be passed through the internal volume of the SVT. The airflow needed will be planned in relation to the silicon detector temperature required, as based on results of background simulation studies and thermal finite element analysis.

6.10 Bibliography

[1] C. Bozzi et al., (*BABAR* collaboration), "The design and construction of the *BABAR* silicon vertex tracker", *Nucl.Instrum.Meth.* A447:15–25, 2000, doi:10.1016/S0168-9002(00)00168-6.

[2] D. Boutigny et al., "*BABAR* technical design report", SLAC-R-0457.

[3] J. Walsh, "Performance with different SVT configurations", *XI SuperB Workshop*, december 2009, http://agenda.infn.it/getFile.py/access?contribId=132&sessionId=19&resId=0&materialId=slides&confId=1165.

[4] F. Giorgi et al., "The front-end chip of the Super*B* SVT detector", *Proceedings of the 12th Pisa Meeting on Advanced Detectors, La Biodola, Isola d'Elba, Italy*, May 2012, to be published in Nucl. Instrum. Meth.

[5] R. Yarema, D. Christian, M. Demarteau, G. Deptuch, J. Hoff, et al., "3D IC pixel electronics - the next challenge", pp. 183-187, 2008, report CERN-2008-008, FERMILAB-PUB-08-422-E.

[6] http://eil.unipv.it/vipix/, VIPIX Collaboration - Vertically Integrated PIXels.

[7] http://www.pi.infn.it/slim5/, SLIM5 Collaboration - Silicon detectors with Low Interaction with Material.

[8] (SLIM5 collaboration), G. Rizzo, "Development of Deep N-Well MAPS in a 130 nm CMOS Technology and Beam Test Results on a 4k-Pixel Matrix with Digital Sparsified Readout", *IEEE Nuclear Science Symposium, Dresden, Germany*, October 2008.

[9] A. Gabrielli, (SLIM5 collaboration), "Development of a triple well CMOS MAPS device with in-pixel signal processing and sparsified readout capabilities", *Nucl.Instrum.Meth.* A581:303–305, 2007, doi:10.1016/j.nima.2007.07.135.

[10] F. Giorgi et al., "2D and 3D Thin Pixel Technologies for the Layer0 of the Super*B* Silicon Vertex Tracker", *IEEE Nuclear Science Symposium, Valencia, Spain*, October 2011.

[11] A. Gabrielli, F. Giorgi, F. Morsani, G. Rizzo, and M. Villa, "High efficiency readout circuits for large matrices of pixels", *Nucl.Instrum.Meth.* A658:141–144, 2011, doi:10.1016/j.nima.2011.04.048.

[12] S. Bettarini, G. Rizzo, J. Walsh, C. Avanzini, G. Batignani, et al., "The SLIM5 low mass silicon tracker demonstrator", *Nucl.Instrum.Meth.* A623:942–953, 2010, doi:10.1016/j.nima.2010.08.026.

[13] S. Zucca, L. Ratti, G. Traversi, S. Bettarini, F. Morsani, G. Rizzo, L. Bosisio, I. Rashevskaya, and V. Cindro, "Characterization of bulk damage in cmos maps with deep n-well collecting electrode", *Radiation and Its Effects on Components and Systems (RADECS), 2011 12th European Conference on*, pp. 297 -304, sept. 2011, doi:10.1109/RADECS.2011.6131308.

[14] G. Rizzo et al., "Recent Development on CMOS MAPS for the Super*B* Silicon Vertex Tracker", *Proceedings of the 12th Pisa Meeting on Advanced Detectors, La Biodola, Isola d'Elba, Italy*, May 2012, to be published in Nucl. Instrum. Meth.

[15] (ALICE collaboration), L. Musa, "Upgrade of the inner tracking system conceptual design report. conceptual design report for the upgrade of the alice its", Tech. rep., CERN, Aug 2012, report CERN-LHCC-2012-013. LHCC-P-005.

[16] S. Senyukov, "Charged particle detection performances of CMOS pixel sensors produced in a 0.18μm process with a high resistivity epitaxial layer", *9^{th} International Conference on Radiation Effects on Semiconductor Materials Detectors and Devices, RSMDD'12, Firenze*, October 2012, To be published in the conference proceedings.

[17] M. Stanitzki, J. Ballin, J. Crooks, P. Dauncey, A. Magnan, Y. Mikami, O. Miller, M. Noy, V. Rajovic, K. Stefanov, R. Turchetta, M. Tyndel, E. Villani, N. Watson, and J. Wilson, "A tera-pixel calorimeter for the ilc", *Nuclear Science Symposium Conference Record, 2007. NSS '07. IEEE*, vol. 1, pp. 254 -258, 26 2007-nov. 3 2007, doi:10.1109/NSSMIC.2007.4436326.

[18] J. Crooks, J. Ballin, P. Dauncey, A.-M. Magnan, Y. Mikami, O. Miller, M. Noy, V. Rajovic, M. Stanitzki, K. Stefanov, R. Turchetta, M. Tyndel, E. Villani, N. Watson, and J. Wilson, "A novel cmos monolithic active pixel sensor with analog signal processing and 100% fill factor", *Nuclear Science Symposium Conference Record, 2007. NSS '07. IEEE*, vol. 2, pp. 931 -935, 26 2007-nov. 3 2007, doi:10.1109/NSSMIC.2007.4437171.

[19] J. A. Ballin, J. P. Crooks, P. D. Dauncey, A.-M. Magnan, Y. Mikami, O. D. Miller, M. Noy, V. Rajovic, M. Stanitzki, K. Stefanov, R. Turchetta, M. Tyndel, E. G. Villani, N. K. Watson, and J. A. Wilson, "Monolithic Active Pixel Sensors (MAPS) in a Quadruple Well Technology for Nearly 100% Fill Factor and Full CMOS Pixels", *Sensors* 8(9):5336–5351, 2008, http://www.mdpi.com/1424-8220/8/9/5336.

[20] J. Mylroie-Smith et al., "First tests of CHERWELL, a Monolithic Active Pixel Sensor. A CMOS Image Sensor (CIS) using 180 nm technology", *Proceedings of Pixel 2012*.

[21] F. Bosi, G. Balestri, M. Ceccanti, P. Mammini, M. Massa, et al., "Light prototype support using micro-channel technology as high efficiency system for silicon pixel detector cooling", *Nucl.Instrum.Meth.* A650:213–217, 2011, doi:10.1016/j.nima.2010.12.187.

[22] F. Bosi et al., "The micro-cooled light support of the pixel modules for the Super*B* experiment", *Proceedings of the 12th Pisa Meeting on Advanced Detectors, La Biodola, Isola d'Elba, Italy*, May 2012, to be published in Nucl. Instrum. Meth.

[23] M. Boscardin et al., "Silicon buried channels for Pixel Detector Cooling", *Proceedings of the 12th Pisa Meeting on Advanced Detectors, La Biodola, Isola d'Elba, Italy*, May 2012, to be published in Nucl. Instrum. Meth.

[24] B. Aubert et al., (*BABAR* collaboration), "The *BABAR* detector", *Nucl.Instrum.Meth.* A479:1–116, 2002, doi:10.1016/S0168-9002(01)02012-5, arXiv:hep-ex/0105044 [hep-ex], SLAC-PUB-8569, BABAR-PUB-01-08.

[25] O. Long, "An alternative algorithm for stand-alone SVT pattern recognition, *BABAR* Note #499 (1999)".

[26] N. Neri, "Tracking Performance with the SVT baseline configuration", http://agenda.infn.it/getFile.py/access?contribId=162&sessionId=25&resId=0&materialId=slides&confId=1161.

[27] M. Rama, "Performance studies with different SVT and DCH configurations", http://agenda.infn.it/getFile.py/access?contribId=161&sessionId=25&resId=2&materialId=slides&confId=1161.

[28] G. Simi, "$B^0 \to K^0_S\pi^0$ vs. SVT radius", http://agenda.infn.it/getFile.py/access?contribId=164&sessionId=25&resId=3&materialId=slides&confId=1161.

[29] K. Nakamura et al., (Particle Data Group collaboration), "Review of particle physics", *J.Phys.* G37:075021, 2010, doi:10.1088/0954-3899/37/7A/075021.

[30] L. Ratti, "Update on time resolution studies", http://agenda.infn.it/getFile.py/access?contribId=0&resId=0&materialId=slides&confId=5315.

[31] "Final Report of the SVT Long Term Task Force", *BABAR* Analysis Document #707, February 24, 2004.

[32] I. Ripp-Baudot, "Update on activities in Strasbourg & tracking in high occupancy", http://agenda.infn.it/getFile.py/access?contribId=63&sessionId=2&resId=2&materialId=slides&confId=4880.

[33] R. Andreassen, "Progress with charm mixing measurements at the 4S", http://agenda.infn.it/materialDisplay.py?contribId=301&sessionId=34&materialId=slides&confId=1742.

[34] G. Inguglia and A. Bevan, "Super*B* Preliminary Vertexing Sensitivity Studies at the Charm Threshold", SuperB Note: SB-PHY-2012-020.

[35] B. Schumm, *BABAR* Note #126, February 15, 1994.

[36] A. V. Telnov, "Detailed Track-Level dE/dx Calibration for the *BABAR* Drift Chamber and Silicon Vertex Tracker", *BABAR* Analysis Document #1500, July 30, 2007.

[37] G. Lindstrom et al., (ROSE collaboration), "Radiation hard silicon detectors developments by the RD48 (ROSE) Collaboration", *Nucl.Instrum.Meth.* A466:308–326, 2001, doi:10.1016/S0168-9002(01)00560-5.

[38] G. Lindstrom, "Radiation damage in silicon detectors", *Nucl.Instrum.Meth.* A512:30–43, 2003, doi:10.1016/S0168-9002(03)01874-6.

[39] S. Dittongo, L. Bosisio, M. Ciacchi, D. Contarato, G. D'Auria, et al., "Radiation hardness of different silicon materials after high-energy electron irradiation", *Nucl.Instrum.Meth.* A530:110–116, 2004, doi:10.1016/j.nima.2004.05.057.

[40] H. Spieler, "Semiconductor Detector Systems", Oxford University Press, 2005.

[41] I. Rashevkaya et al., "Characterization of strip detector parameters for the Super*B* Silicon Vertex Tracker", *Proceedings of the 12th Pisa Meeting on Advanced Detectors, La Biodola, Isola d'Elba, Italy*, May 2012, to be published in Nucl. Instrum. Meth.

[42] L. Fabbri et al., "Beam test results for the Super*B* SVT thin striplet detector", *Proceedings of the 12th Pisa Meeting on Advanced Detectors, La Biodola, Isola d'Elba, Italy*, May 2012, to be published in Nucl. Instrum. Meth.

[43] I. Rachevskaya, L. Bosisio, S. Potin, and O. Starodubtsev, "Test and quality control of double-sided silicon microstrip sensors for the ALICE experiment", *Nucl.Instrum.Meth.* A530:59–64, 2004, doi:10.1016/j.nima.2004.05.048.

[44] P. Moreira and J. Troska, "Radiation-Hard Optical Link for Experiments", http://ph-dep.web.cern.ch/ph-dep/NewsMeetings/FM/FM25Apr08/Troska_Moreira.pdf.

[45] C. Soos, V. Bobillier, S. Detraz, S. Papadopoulos, C. Sigaud, et al., "Versatile transceiver development status", *JINST* 7:C01094, 2012, doi:10.1088/1748-0221/7/01/C01094.

[46] I. Peric, L. Blanquart, G. Comes, P. Denes, K. Einsweiler, et al., "The FEI3 readout chip for the ATLAS pixel detector", *Nucl.Instrum.Meth.* A565:178–187, 2006, doi:10.1016/j.nima.2006.05.032.

[47] R. Klingenberg, (ATLAS Pixel collaboration), "The ATLAS pixel detector", *Nucl.Instrum.Meth.* A579:664–668, 2007, doi:10.1016/j.nima.2007.05.269.

[48] D. Bortoletto, *The CMS pixel system*, Nucl. Instrum. and Meth., vol. A636, pp. 559-674, 2007.

[49] A. Kluge, G. Anelli, F. Antinori, A. Badala, A. Boccardi, G. Bruno, M. Burns, I. Cali, M. Campbell, M. Caselle, S. Ceresa, P. Chochula, M. Cinausero, J. Conrad,

R. Dima, D. Eliad, D. Fabris, R. Fini, E. Fioretto, F. Formenti, S. Kapusta, M. Krivda, V. Lenti, F. Librizzi, M. Lunardon, V. Manzari, M. Morel, S. Moretto, F. Osmic, G. Pappalardo, V. Paticchio, A. Pepato, G. Prete, A. Pulvirenti, P. Riedler, F. Riggi, L. Sandor, R. Santoro, F. Scarlassara, G. Segato, F. Soramel, G. Stefanini, C. Matos, R. Turrisi, L. Vannucci, G. Viesti, and T. Virgili, "The ALICE silicon pixel detector: electronics system integration", *Nuclear Science Symposium Conference Record, 2005 IEEE*, vol. 2, pp. 761-764, oct. 2005, doi:10.1109/NSSMIC.2005.1596367.

[50] M. Garcia-Sciveres, D. Arutinov, M. Barbero, R. Beccherle, S. Dube, et al., "The FE-I4 pixel readout integrated circuit", *Nucl.Instrum.Meth.* A636:S155–S159, 2011, doi:10.1016/j.nima.2010.04.101.

[51] F. Hugging, (ATLAS collaboration), "The ATLAS Pixel Insertable B-Layer (IBL)", *Nucl.Instrum.Meth.* A650:45–49, 2011, doi:10.1016/j.nima.2010.12.113, arXiv:1012.2742 [physics.ins-det].

[52] C. Favaro, (CMS collaboration), "A New CMS pixel detector for the LHC luminosity upgrade", *Nucl.Instrum.Meth.* A658:41–45, 2011, doi:10.1016/j.nima.2011.04.062, arXiv:1104.1288 [physics.ins-det].

[53] *Handbook of 3D Integration: Technology and Applications of 3D Integrated Circuits.* Edited by P. Garrou, C. Bower and P. Ramm. Wiley-VCH, Weinheim, 2008.

[54] A. Klumpp et al., "Vertical System Integration by Using Inter-Chip Vias and Solid-Liquid Interdiffusion Bonding", *Jpn. J. Appl. Phys.* 43:829–830, 2004.

[55] R. Patti, "Three-dimensional integrated circuits and the future of system-on-chip designs", *Proceedings of the IEEE* 94(6):1214 –1224, june 2006, doi:10.1109/JPROC.2006.873612.

[56] F. Giorgi, C. Avanzini, G. Batignani, S. Bettarini, F. Bosi, G. Casarosa, M. Ceccanti, A. Cervelli, F. Forti, M. Giorgi, P. Mammini, F. Morsani, B. Oberhof, E. Paoloni, A. Perez, A. Profeti, G. Rizzo, J. Walsh, A. Lusiani, M. Manghisoni, V. Re, G. Traversi, R. Di Sipio, L. Fabbri, A. Gabrielli, C. Sbarra, N. Semprini, S. Valentinetti, M. Villa, A. Zoccoli, M. Citterio, V. Liberali, A. Stabile, N. Neri, F. Palombo, L. Gaioni, A. Manazza, L. Ratti, V. Speziali, S. Zucca, G.-F. Dalla Betta, G. Soncini, G. Fontana, M. Bomben, L. Bosisio, P. Cristaudo, B. Liberti, D. Jugovaz, L. Lanceri, I. Rashevskayai, L. Vitale, G. Vernier, and R. Cenci, "2D and 3D thin pixel technologies for the Layer0 of the Super*B* Silicon Vertex Tracker", *Nuclear Science Symposium and Medical Imaging Conference (NSS/MIC), 2011 IEEE*, pp. 1324-1328, oct. 2011, doi:10.1109/NSSMIC.2011.6154335.

[57] Y. Degerli, M. Besancon, A. Besson, G. Claus, G. Deptuch, et al., "Performance of a fast binary readout CMOS active pixel sensor chip designed for charged particle detection", *IEEE Trans.Nucl.Sci.* 53:3949–3955, 2006, doi:10.1109/TNS.2006.886151.

[58] A. Gabrielli, G. Batignani, S. Bettarini, F. Bosi, G. Calderini, R. Cenci, M. Dell'Orso, F. Forti, P. Giannetti, M. Giorgi, A. Lusiani, G. Marchiori, F. Morsani, N. Neri, E. Paoloni, G. Rizzo, J. Walsh, M. Massa, A. Cervelli, C. Andreoli, E. Pozzati, L. Ratti, V. Speziali, M. Manghisoni, V. Re, G. Traversi, L. Bosisio, G. Giacomini, L. Lanceri, I. Rachevskaia, L. Vitale, G. Dalla Betta, G. Soncini, G. Fontana, L. Pancheri, G. Verzellesi, D. Gamba, G. Giraudo, P. Mereu, M. Bruschi, B. Giacobbe, N. Semprini, R. Spighi, M. Villa, and A. Zoccoli, "Proposal of a data sparsification unit for a mixed-mode maps detector", *Nuclear Science Symposium Conference Record, 2007. NSS '07. IEEE*, vol. 2,

pp. 1471 -1473, 26 2007-nov. 3 2007, doi:10.1109/NSSMIC.2007.4437277.

[59] S. Bettarini, G. Rizzo, J. Walsh, C. Avanzini, G. Batignani, et al., "The SLIM5 low mass silicon tracker demonstrator", *Nucl.Instrum.Meth.* A623:942–953, 2010, doi:10.1016/j.nima.2010.08.026.

[60] G. Casarosa, C. Avanzini, G. Batignani, S. Bettarini, F. Bosi, M. Ceccanti, R. Cenci, A. Cervelli, F. Crescioli, M. Dell'Orso, F. Forti, P. Giannetti, M. Giorgi, A. Lusiani, S. Gregucci, P. Mammini, G. Marchiori, M. Massa, F. Morsani, N. Neri, E. Paoloni, M. Piendibene, A. Profeti, L. Sartori, J. Walsh, E. Yurtsev, M. Manghisoni, V. Re, G. Traversi, M. Bruschi, R. Di Sipio, B. Giacobbe, A. Gabrielli, F. Giorgi, G. Pellegrini, C. Sbarra, N. Semprini, R. Spighi, S. Valentinetti, M. Villa, A. Zoccoli, M. Citterio, V. Liberali, A. Stabile, F. Palombo, L. Gaioni, A. Manazza, L. Ratti, V. Speziali, S. Zucca, G. Betta, G. Soncini, G. Fontana, M. Bomben, L. Bosisio, P. Cristaudo, D. Jugovaz, L. Lanceri, I. Rashevskaya, L. Vitale, and G. Venier, "Thin pixel development for the Layer0 of the Super*B* Silicon Vertex Tracker", *Nuclear Science Symposium Conference Record (NSS/MIC), 2010 IEEE*, pp. 1901-1905, 30 2010-nov. 6 2010, doi:10.1109/NSSMIC.2010.5874105.

[61] L. Ratti, L. Gaioni, M. Manghisoni, V. Re, and G. Traversi, "Vertically integrated deep n-well cmos maps with sparsification and time stamping capabilities for thin charged particle trackers", *Nuclear Instruments and Methods in Physics Research Section A: Accelerators, Spectrometers, Detectors and Associated Equipment* 624(2):379 – 386, 2010, doi:10.1016/j.nima.2010.05.039, http://www.sciencedirect.com/science/article/pii/S016890021001140X, New Developments in Radiation Detectors, Proceedings of the 11th European Symposium on Semiconductor Detectors.

[62] http://3dic.fnal.gov.

[63] L. Ratti, M. Manghisoni, V. Re, and G. Traversi, "Design of time invariant analog front-end circuits for deep n-well cmos maps", *Nuclear Science, IEEE Transactions on* 56(4):2360 –2373, aug. 2009, doi:10.1109/TNS.2009.2024536.

[64] G. Traversi, "Charge signal processors in a 130 nm CMOS technology for the sparse readout of small pitch monolithic and hybrid pixel sensors", *IEEE Trans.Nucl.Sci.* 58:2391–2400, 2011, doi:10.1109/TNS.2011.2164811.

[65] L. Ratti, "Continuous Time-Charge Amplification and Shaping in CMOS Monolithic Sensors for Particle Tracking", *IEEE Trans.Nucl.Sci.* 53:3918–3928, 2006, doi:10.1109/TNS.2006.886048.

[66] L. Ratti, L. Gaioni, A. Manazza, M. Manghisoni, V. Re, and G. Traversi, "First results from the characterization of a three-dimensional deep n-well maps prototype for vertexing applications", *Nuclear Instruments and Methods in Physics Research Section A: Accelerators, Spectrometers, Detectors and Associated Equipment* 699(0):41 – 46, 2013, doi:10.1016/j.nima.2012.03.021, http://www.sciencedirect.com/science/article/pii/S0168900212002963, Proceedings of the 8th International "Hiroshima" Symposium on the Development and Application of Semiconductor Tracking Detectors. Academia Sinica, Taipei, Taiwan, December 5 – 8, 2011.

[67] A. Ghetti, E. Sangiorgi, J. Bude, T.W. Sorsch, G. Weber, *Tunneling into Interface States as Reliability Monitor for Ultrathin Oxides*, IEEE Trans. El. Dev., vol. 47, no. 12, pp. 2358-2365, Dec. 2000.

[68] V. Re, M. Manghisoni, L. Ratti, V. Speziali, G. Traversi, *Total Ionizing Dose Effects on the Noise Performances of a*

0.13 μm CMOS Technology, IEEE Trans. Nucl. Sci., vol. 53, no. 3, pp. 1599-1606, Jun. 2006.

[69] L. Ratti, L. Gaioni, M. Manghisoni, G. Traversi, and D. Pantano, "Investigating degradation mechanisms in 130 nm and 90 nm commercial cmos technologies under extreme radiation conditions", *Nuclear Science, IEEE Transactions on* 55(4):1992 –2000, aug. 2008, doi:10.1109/TNS.2008.921935.

[70] F. Faccio and G. Cervelli, "Radiation-induced edge effects in deep submicron cmos transistors", *Nuclear Science, IEEE Transactions on* 52(6):2413 – 2420, dec. 2005, doi:10.1109/TNS.2005.860698.

[71] W. Snoeys, T. Gutierrez, and G. Anelli, "A new NMOS layout structure for radiation tolerance", *Nuclear Science Symposium Conference Record, 2001 IEEE*, vol. 2, pp. 822 - 826 vol.2, nov. 2001, doi:10.1109/NSSMIC.2001.1009683.

[72] L. Ratti, M. Manghisoni, V. Re, G. Traversi, S. Zucca, S. Bettarini, F. Morsani, and G. Rizzo, "Front-End Performance and Charge Collection Properties of Heavily Irradiated DNW MAPS", *Nuclear Science, IEEE Transactions on* 57(4):1781 –1789, aug. 2010, doi:10.1109/TNS.2009.2039003.

[73] S. Zucca, L. Ratti, G. Traversi, S. Bettarini, F. Morsani, G. Rizzo, L. Bosisio, I. Rashevskaya, and V. Cindro, "Characterization of bulk damage in CMOS MAPS with deep N-well collecting electrode", *Radiation and Its Effects on Components and Systems (RADECS), 2011 12th European Conference on*, pp. 297 -304, sept. 2011, doi:10.1109/RADECS.2011.6131308.

[74] M. Deveaux, J. Baudot, N. Chon-Sen, G. Claus, C. Colledani, R. De Masi, et al., "Radiation tolerance of a column parallel CMOS sensor with high resistivity epitaxial layer", *Journal of Instrumentation* 6(02):C02004, 2011, doi:10.1088/1748-022/6/02/C02004, http://stacks.iop.org/1748-0221/6/i=02/a=C02004.

[75] G. Messenger, "A summary review of displacement damage from high energy radiation in silicon semiconductors and semiconductor devices", *Nuclear Science, IEEE Transactions on* 39(3):468 –473, jun 1992, doi:10.1109/23.277547.

[76] L. Ratti, L. Gaioni, G. Traversi, S. Zucca, S. Bettarini, F. Morsani, et al., "Modeling charge loss in CMOS MAPS exposed to non-ionizing radiation", *Radiation and Its Effects on Components and Systems (RADECS), 2012 European Conference on, Biarritz, France*, sept. 2012, To be published in the conference proceedings.

7 Drift Chamber

7.1 Introduction

The Super$B$ Drift Chamber (DCH) is the main tracking detector of the Super$B$ experiment. Immersed in a 1.5 T solenoidal magnetic field, the DCH provides several position measurements along the track for a precise reconstruction of the particle momentum. It also measures the ionization energy loss used for particle identification. In fact, the DCH is the primary device in Super$B$ to measure velocities of particles having momenta below approximately 700 MeV/c and, at least in the initial phase of the experiment when no forward PID device is foreseen, it is the the only particle identification device for tracks with $\vartheta \leq 25°$.

Finally the drift chamber, together with the electromagnetic calorimeter, will provide the trigger of the experiment (Sec. 12.3.1.1).

7.1.1 Physics Requirements

Similarly to *BABAR* [1], one of the goals of the Super$B$ experiment is to reconstruct exclusive and inclusive final states with high and well-controlled efficiency. This requirement implies maximal solid angle coverage and highly efficient reconstruction of tracks with $p_\perp$ as low as 100 MeV/c, the minimum transverse momentum for a track produced at the interaction point to leave enough hits to be reconstructed in the drift chamber.

Background rejection requires excellent momentum resolution over the full momentum spectrum. In *BABAR* the momentum resolution has been measured [1] on muon tracks to be $\sigma_{p_\perp}/p_\perp = (0.13 p_\perp + 0.45)\%$, $p_\perp$ in GeV/c. In the Super$B$ drift chamber we aim at obtaining a similar result, or better.

The average charged particle momentum in Super$B$ is less than 1 GeV/c, smaller than in *BABAR* due to the reduced boost. Multiple scattering will therefore be the main limiting factor to track parameter resolution for the majority of charged tracks in Super$B$. The effect is controlled by keeping to a minimum the material budget in the DCH. A thin inner wall helps matching tracks reconstructed inside the vertex detector with those in the DCH and improves the $p_\perp$ and the ϑ resolution by effectively increasing the lever arm of the tracking system when adding high precision measurement points from the vertex detector. It also reduces photon conversion thus minimizing background in the chamber. Low-mass endplates and outer wall limit photon conversions and multiple scattering which could degrade the performance of the detectors surrounding the DCH.

Finally, although the track dip angle is measured with high precision by the vertex detector, the DCH must provide an independent measurement of this angle to allow the reconstruction of secondary vertices of long-lived particles decaying outside the vertex detector region, such as K_S^0 mesons or Λ baryons. The DCH must also provide a measurement of the hit z coordinate. A stand-alone full 3D tracking in the DCH helps in extrapolating tracks to the calorimeter, to the FDIRC detector and back to the vertex tracker, and allows their use in the L1 trigger.

7.1.2 Design Overview

The physics requirements outlined in the previous section can be met with a cylindrical drift chamber with performance similar to the *BABAR* one. We have therefore taken the *BABAR* drift chamber [2] as a starting point, seeking improvements in two main areas: reduction of the detector material and improvement of the dE/dx measurement.

We shall show that the first goal can be met with the adoption of modern construction techniques for the mechanical structure involving the use of composite materials (Sec. 7.3), together with the use of lighter gas mixtures and reduced wire material (Sec. 7.2). Improvements in the energy loss measurements could be achieved by adopting the cluster counting (CC) technique [3, 4, 5, 6] for the DCH readout. These two solutions constitute the baseline of the present design and will be discussed in detail in the remaining sections of this chapter.

We note that a fallback solution for the readout is represented by the standard TDC/ADC readout chain discussed in Sec. 7.4.2.

To reach its ambitious goal on the integrated luminosity, the Super*B* experiment will work in "factory-mode", taking data continuously over extended run periods. This poses stringent requirements on the reliability of all its subdetectors, including the DCH. The *BABAR* drift chamber already met these requirements, and we expect that our choice of separating the signal digitization electronics from the on-detector preamplification boards will further improve the system reliability.

7.1.3 Cluster Counting

Signals in drift chambers are usually split to an analog chain which integrates the charge, and to a digital chain recording the arrival time of the first electron, discriminated with a given threshold. The cluster counting technique consists instead in digitizing the full waveform to count and measure the time of all individual peaks. On the assumption that these peaks can be associated to the primary ionization acts along the track, the energy loss and to some extent the spatial coordinate measurements can be substantially improved. In counting the individual clusters, one indeed removes the sensitivity of the specific energy loss measurement to fluctuations in the amplification gain and in the number of electrons produced in each cluster, fluctuations which significantly limit the intrinsic resolution of conventional dE/dx measurements.

The ability to count the individual ionization clusters and measure their drift times strongly depends on the average time separation between them, which is, in general, relatively large in He-based gas mixtures thanks to their low primary yield and slow drift velocity. Other requirements for efficient cluster counting include good signal-to noise ratio with no or limited gas-gain saturation, high preamplifier bandwidth, and digitization of the signal with a sampling speed of the order of 1Gs/sec. Finally, it is necessary to extract online the relevant signal features (*i.e.* the cluster times), because the DAQ system of the experiment would not be able to manage the enormous amount of data from the digitized waveforms of the about 10 000 drift chamber channels.

7.1.4 Geometrical Constraints

A side view of the drift chamber is shown in Fig. 7.1. The DCH inner radius is constrained by the final focus cooling system, by the Tungsten shield surrounding it and by the SVT service space to $R_{inner} = 270$ mm. The outer radius is constrained to $R_{outer} = 809$ mm by the DIRC quartz bars, as in *BABAR*. The total length available for the DCH is $L = 3092$ mm, including the space for front-end electronics, signal and high voltage cables, and the needed services (*e.g.* cooling, gas pipes). The space necessary for possible future upgrades of the Super*B* detector such as the backward electromagnetic calorimeter (Section 9.49.4) and the forward PID system (Sec. 8.4) has already been taken into account.

The drift chamber is shifted with respect to the interaction point by an offset of 333 mm, resulting from the fact that we want to exploit all the available space in the backward and forward regions (Figure 7.1). .

7.1.5 Machine Background Considerations

Background processes are responsible for the largest part of the DCH rate. A rate higher than the design level would affect the charged track reconstruction, due to spurious hits, and generally degrade tracking performance. Additionally, the DAQ electronics can be progressively damaged when being exposed to a significant rate of particle for a long period of time. In both cases, an accurate simulation of the radiation rates is needed to estimate the real performances and the life-span of the electronics.

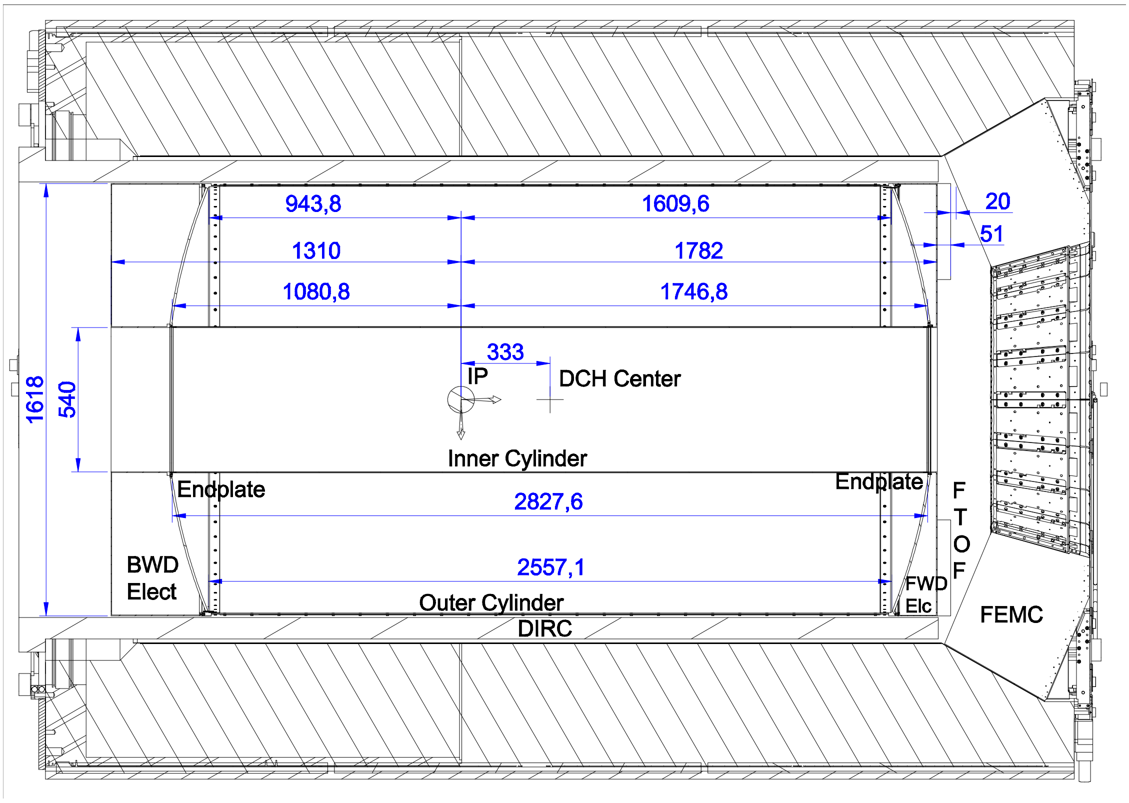

Figure 7.1: Longitudinal section of the DCH with principal dimensions.

The main tool used to perform this estimate is the full simulation program described in detail in Sec. 14.1.1. The chamber gas volume is described as a homogeneous medium with a density corresponding to the weighed average of the gas and the wires densities. The chamber structure is instead accurately described including carbon fiber inner and outer walls and endcaps, each with the appropriate density. Three silicon plates are included on the backwards side to simulate the amount of material corresponding to the front-end electronics. The basic information in the simulation output corresponds to a single interaction (or step) of the particle simulated by GEANT4 [7]. Each particle step inside the gas volume and silicon plates is recorded, together with additional information about the type of particle, its position, incident energy, vector momentum, and deposited energy. The simulation is not aware of the internal wire structure: this allows us to simulate background events faster, and rates can be computed in each layer for different wire configurations in a post-simulation analysis, as described below. The post-simulation analysis evaluates also the radiation dose, the equivalent fluence of 1 MeV neutrons, and fluences of different kind of particles in the plates representing the DAQ electronics.

A dedicated application has been developed to analyze the simulation output and produce the relevant quantities and plots. A given wire structure is provided as input to the application, with all the information on the cell size and stereo angles. For each step, the helix parameters of the track trajectory are computed starting from the initial and final points, and the momentum. Assuming $\mathrm{d}E/\mathrm{d}x$ constant along the step, the total deposit energy is divided between each cell crossed by the track proportionally to the path length inside the cell itself. After having analyzed all the steps from charged tracks in the event, the table is used to fill a histogram with one entry for each layer: the number of cells with deposited energy greater than zero in each layer is added into the corresponding interval. A histogram is produced for all the background sources and then rescaled for the cross-section/frequency of each process. For each given transverse radius of the DCH, the tracks produced by background processes are with good approximation isotropic in azimuthal angle, so no information is lost when averaging the cells fired over the same layer.

The largest contributions to the rate are from radiative Bhabha and Pair productions. The simulation includes also contributions from Touschek scattering and beam scattering with residual gas. Photons from synchrotron radiation give a negligible contribution to the DCH rate and radiation levels, so they are omitted in the following. Figure 7.2 shows the total rate and the separate contribution for each background source assuming a typical configuration with axial cells only. Most of the background activity is

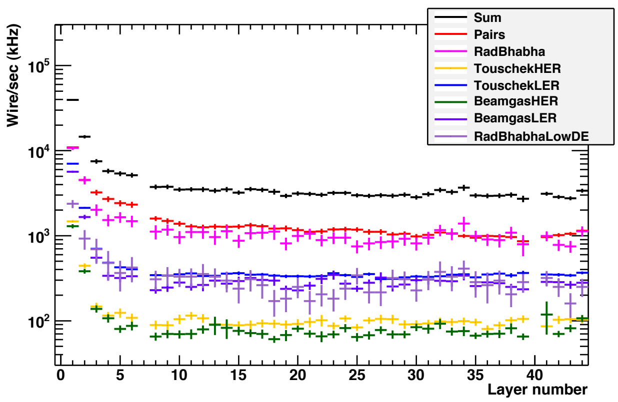

Figure 7.2: Total rate for each DCH layer for a typical axial configuration. The empty intervals correspond to empty spaces between groups of layers. The separate contributions from each background source are shown in different colors (color online, see Table 5.1 for more details on the samples).

located around the interaction point, so the rate decreases fast when moving to outer layers. No significant difference in the shape of the rate is observed between different background sources, because most of the particles that hit the chamber are not primaries, but particles that exit the final focus shielding after many interactions, as explained below.

We found that the DCH rate had a significant dependence on the maximum step length allowed in the GEANT4 simulation. A dedicated study showed that this is due to a poor simulation of the multiple scattering over long distances in low density materials. For this reason the maximum step length in the gas chamber has been fixed to 1 mm, reducing this dependence to a negligible level.

The studies showed that the largest part of the rate is not due to charged tracks coming directly from the interaction point, but mostly from photons coming out of the shielding and kicking out electrons off the chamber walls when they enter the chamber. Looking specifically at those photons coming out of the final focus elements, we were able to detect some areas where the number of particles was higher than usual. The shielding has been subsequently optimized to reduce the number particles from those areas.

Photons impinging on the DCH wall produce low energy electrons that can still travel long distances in the gas. If their transverse momentum is small, they can even traverse the whole chamber spiraling along the z coordinate. In the case of stereo layers, one such a particle travelling along the longitudinal direction can thus cross multiple cells, explaining the higher rate observed in the stereo layers shown in Figure 7.3. The wires in the central block from layer 11 to 34 have a stereo angle from 70 to 90 mrad, and show clearly a rate higher than the neighbor axial wires. The higher rate in the first layers observed in the plot of Figure 7.2, is not present here because, for this configuration, the first layer is 2 cm far from the inner wall.

With the geometry used for the simulation, a typical configuration with a central section of stereo layers, and an integration time of 1μs, the occupancy is estimated at $\sim 5\%$.

The radiation levels estimated in the region where the electronics will be located are gener-

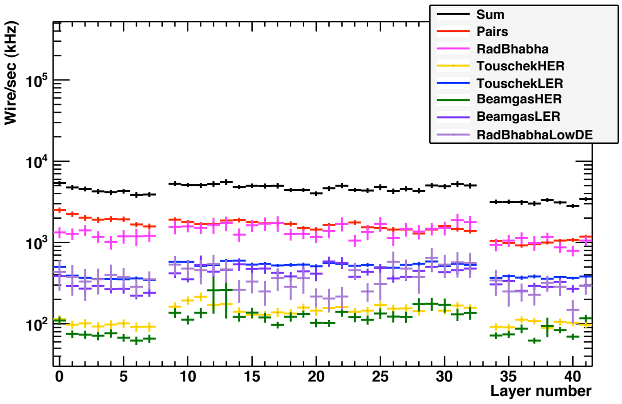

Figure 7.3: Total rate for each DCH layer for a typical stereo configuration (layer 11–34, stereo angle of 70–90 mrad; the other layers are axial). The empty intervals correspond to empty spaces between groups of layers. The separate contributions from each background source are shown using different colors (color online, see Table 5.1 for more details on the samples).

ally low. For a period corresponding to an integrated luminosity of 10 ab^{-1} the estimated dose is below 8 Gy, the equivalent 1 MeV neutron fluence is below 3×10^{11} $n_{eq}/cm^2/yr$, and the fluence due to hadrons with kinetic energy larger than 20 MeV is below 7×10^{10} $n_{eq}/cm^2/yr$.

7.2 Design Optimization

The *BABAR* drift chamber operational record has been quite good, both for performance and reliability. For this reason, several features of the Super$B$ DCH, which will operate in a similar environment, derive from the *BABAR* drift chamber.

However, given that its design and construction dates back over fifteen years, we have looked for possible technological advances and design improvements to build a drift chamber with performances even better than *BABAR*.

7.2.1 Performance Studies

We have made extensive simulation studies to evaluate the impact on track reconstruction of a number of design choices concerning both the external structure (radius and material of the inner cylinder, position and shape of the endplates) and the internal layout (cell shape, wire orientation). The studies have been performed using the Super$B$ fast simulation tool *FastSim*, whose main features are described in Chapter 14. The main results of these studies are summarized in the following sections.

7.2.1.1 Radius and Thickness of the Inner Wall

The simulation of several signal samples with both high (*e.g.* $B \to \pi^+\pi^-$), and medium-low (*e.g.* $B^0 \to D^{*-}K^+$) momentum tracks indicates that, as expected, the momentum resolution improves as the minimum drift chamber radius R_{min} decreases, as long as the hit rate per layer is low enough not to significantly impact the reconstruction. However, as discussed in Sect. 7.1.4, R_{min} is actually limited by mechanical constraints from the cryostats and radiation shields, and is set to $R_{min} = 270$ mm.

The thickness of the inner wall can affect significantly the reconstruction of charged particles, especially those with lower momentum where multiple scattering is larger. For example, the width of the ΔE distribution in $B^0 \to D^{*-}K^+$ events gets about 7% narrower if the thickness of the carbon fiber inner wall is decreased from 1 mm—equal to 0.4% X_0, comparable to the 1 mm of Beryllium used in *BABAR*—to about 0.2 mm (0.1% X_0). A carbon fiber, 0.2 mm-thick inner cylinder is the current baseline, although an even thinner solution is being considered as discussed in Sec. 7.3.1.

7.2.1.2 Endcap shape and position

A study was carried out to compare the momentum and dE/dx measurement resolution of tracks reconstructed in the forward or backward directions as a function of the endcap shape (convex or concave) and its position along the beam (z) axis. Figure 7.4 shows two of these configurations together with the definition of the forward and backward regions. We simulated samples of single charged pions with flat p and $\cos\theta$ distributions and samples of $B^0 \to D^{*-}K^+$ decays. We compared the $p_\perp$ resolution, the

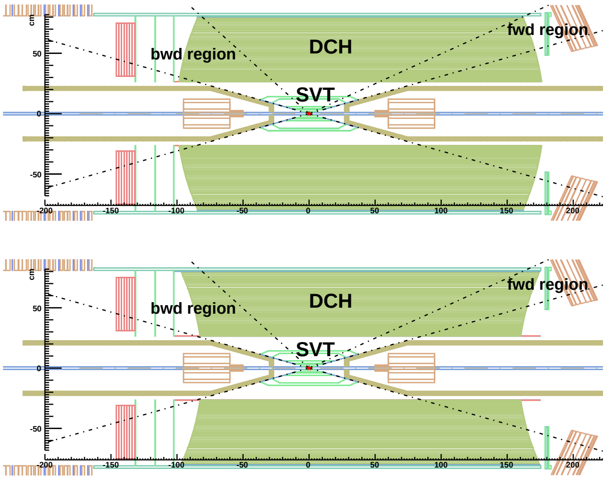

Figure 7.4: Example of DCH configurations where the endcaps are placed in the same position (same z_{min} and z_{max}) but their shape is different: convex (top) and concave (bottom). The forward and backward regions are indicated.

K/π separation based on dE/dx and the reconstruction efficiency of $B^0 \to D^{*-}K^+$ for different configurations. At fixed z position, the average $p_\perp$ resolutions for the concave and convex shapes are consistent within a 3% relative uncertainty in both the forward and backward regions. The average K/π separations are also consistent within 1–2%. Differences of this order of magnitude depend on the specific polar angle distribution of the tracks. The reconstruction efficiency of $B^0 \to D^{*-}K^+$ events is not affected by the endcap shape in the forward region, while it is slightly higher ($\approx 1\%$) when the endcap in the backward region is convex. The average variation of $\sigma(p_\perp)/p_\perp$ as a function of the endcap position is roughly consistent with 1% (1.5–2.0%) per additional cm of DCH length in the forward (backward) direction. Similarly, the average K/π separation based on dE/dx increases by about 0.5% (1%) per additional cm of DCH length in the forward (backward) region. This asymmetry between the forward and backward direction is ascribed to the different average number of crossed layers.

To summarize, also as a result of weighing the effects discussed above for the fraction of tracks crossing these regions (typically below 10% of the total), little difference in terms of performance is observed between the concave and convex endplate shapes *per se*, while the length does have a significant impact. Due to the details of mechanical design of the endplate outer flanges, convex endplates allow for a longer DCH.

7.2.1.3 Wire and Gas Material

The *BABAR* drift chamber featured concentric layers of hexagonal cells, organized in axial (A), positive stereo (U) or negative stereo (V) super-layers. This choice was motivated by the good symmetry of the hexagonal cells, and by the small number of field wires per sense wire (field-to-sense wire ratio $\mathcal{R}_{f:s} = 2$) because many field wires are shared among adjacent cells. However, such a small value $\mathcal{R}_{f:s}$ required larger wire diameters—and therefore more material in the tracking volume and more force on the endplates—to avoid gas amplification at the field wires. In addition, the advantage of stringing fewer field wires was outbalanced by the guard wire layers needed at every super-layer transition to keep the electric field homogeneous across layers (hexagonal cells with different stereo angles cannot intersect radially and must be separated). In Table 7.1 we report the material budget for the hexagonal *BABAR*-like layout and for two alternative solutions using rectangular cell geometry with different values for $\mathcal{R}_{f:s}$. All the numbers shown in Table 7.1 and used in the simulations below were obtained for an inner DCH radius of $R_{min} = 210$ mm and a cell height of 12 mm (the final configuration will have cells of slightly different heights, as dis-

Table 7.1: Combined gas+wires material budget for different cell geometries in a 80%He $-$ 20%iC_4H_{10} mixture. Values from the *BABAR* DCH are shown in boldface.

Cell layout	$\rho(g/cm^3)$ $\times 10^4$	X_0 (m)	# layers
	coat/nocoat	coat/nocoat	
Hex 2:1	**10.0**/9.5	**270**/350	40
Sqr 3:1	9.8/8.5	310/400	44
Sqr 4:1	8.5/8.1	320/430	44

cussed in Sec. 7.2.2). The case in which the field Aluminum wires are coated with a 0.5 μm thick gold plating is compared to the case where the coating is absent. The hexagonal configuration has 40 layers while the other two have 44 layers. Since in the square cell configurations there is no need to leave space between superlayers with different stereo orientation, for a given cell size it is possible to allocate more measurement layers compared to the hexagonal configuration. The average single hit spatial resolutions are estimated to be similar in all configurations. Figure 7.5 compares $\sigma(p_\perp)/p_\perp$ vs $p_\perp$ for the configurations in Tab. 7.1. The average $p_\perp$ resolution in the $\mathcal{R}_{f:s}$=4 square cell configuration is about 5% better than in the hexagonal cell scenario. Both the material and the wire count is optimized with rectangular cells.

The effect of the material budget of different gas mixtures was also studied. We considered square cell configurations with $\mathcal{R}_{f:s}$=3 and three gas mixtures: He80-Ibu20, He90-Ibu10 and He80-Met20. Figure 7.6 shows $\sigma(p_\perp)/p_\perp$ vs $p_\perp$ for the three scenarios. $\sigma(p_\perp)/p_\perp$ for the He80-Ibu20 configuration is 10-15% worse than in the He80-Met20 mixture.

7.2.1.4 Stereo Angle Layout

The impact of the stereo angle layout on tracking performance was studied by comparing the reconstruction of $B \to \pi^+\pi^-$ and $B \to D^*K$ events in four different configurations: *i)* a BABAR-like AUVAUVAUVAUVA; *ii)* a completely axial DCH; *iii)* a "mostly stereo SL" layout in which the innermost and outermost superlayers are axial, and the remaining ones alternate positive and negative stereo orientations, AUVUVUVUVA; and *iv)* a "stereo layers" configuration in which two axial superlayers placed in the innermost and outermost position surround a set of alternate stereo angle layers (alternate stereo angle layers were *e.g.* used in the KLOE drift chamber). The outcome of this study is that since the Silicon Vertex Tracker largely dominates the polar angle measurement, the arrangement of the stereo layers does not impose tight constraints on tracking: for example both the $p_\perp$ and the ΔE resolution are almost identical in the four configurations (configuration *iii)* is slightly better for the case of relatively softer tracks in $B \to D^*K$ events). Compared to the completely axial configuration, however, configurations with stereo layers are preferred because they can provide – in addition to 3D trigger information – some constraints on the polar direction of those few tracks that are not reconstructed in the SVT.

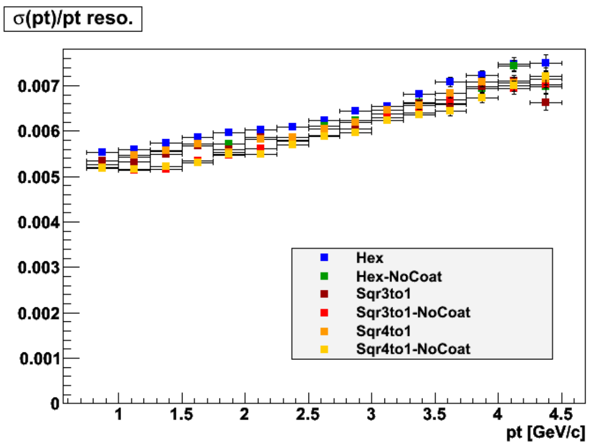

Figure 7.5: Relative $p_\perp$ resolution for different cell geometries. The color codes refer to the configurations in Table 7.1.

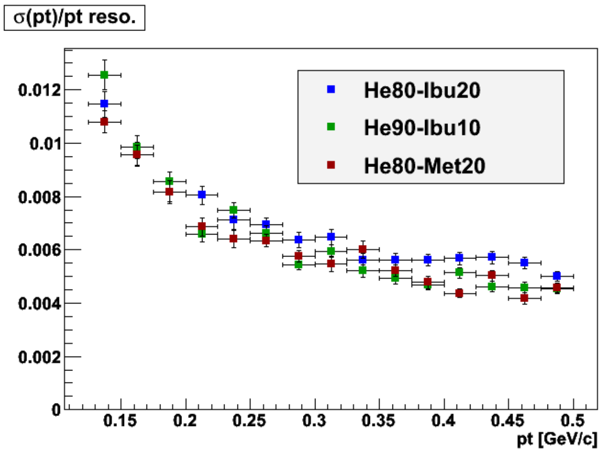

Figure 7.6: Relative $p_\perp$ resolution for different gas mixtures in the configuration with rectangular cells and $\mathcal{R}_{f:s} = 3$.

7.2.1.5 Cluster Counting

We introduced in Sect. 7.1.2 the possibility of enhancing the performance of particle identification (PID) in the Drift Chamber by counting the individual ionization clusters. In general, an improved PID would have several advantages, including better reconstruction efficiency in inclusive and exclusive modes, better tagging efficiency, and reduced backgrounds.

In order to estimate the benefits of the cluster counting technique, we evaluated the efficiency of the semi-exclusive hadronic B reconstruction ("$B_{\rm reco}$"), a technique developed by *BABAR* to obtain high-statistics samples of B candidates used in recoil analysis, *e.g.* of rare decays.

We generated four different samples of 10 million generic $B^{\pm}$ decays each in which at least one K is present in the final state. In one sample the dE/dx performance is set equal to the *BABAR* one and used as a reference. To simulate the improvement due to cluster counting, in the other three samples S_1, S_2, S_3 the momentum- and ϑ angle-averaged K/π separation is set to be higher than the reference one by a factor of 1.3, 1.5 and 1.7, respectively. The results, given in terms of the ratios of their $B_{\rm reco}$ reconstruction efficiency with respect to the reference, are summarized in Figure 7.7. It is observed that this ratio improves by 4–6% when cluster counting is used. The figure shows that the improvement is present also if kinematical cuts on m_{ES} and ΔE are used in conjunction with particle ID information.

The actual improvement achievable with the use of cluster counting must be determined experimentally. Preliminary results from test beam data are discussed in Section 7.2.4.3.

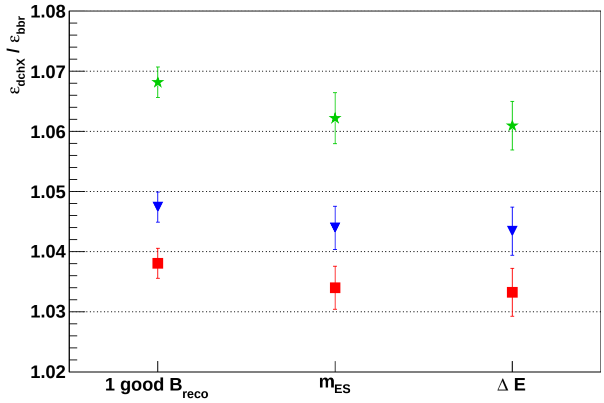

Figure 7.7: Ratio of the $B_{\rm reco}$ reconstruction efficiency with cluster counting to the reference sample for the S_1 (red squares), S_2 (blue triangles) and S_3 (green asterisks) samples described in the text.

7.2.2 Cell Design and Layer Arrangement

The cell must be designed to optimize the homogeneity of the electric field inside it; this is particularly relevant with the non-saturated mixture we intend to use. Other critical parameters are the wire material and an optimal use of the drift chamber volume for accommodating as many measurement points as possible.

The design for the Super$B$ drift chamber employs small rectangular cells arranged in concentric layers about the axis of the chamber. The z coordinate of the track hits is measured by orienting a subset of the wire layers at a small positive or negative stereo angle, ε, relative to the chamber axis. Such a measurement is performed with precision $\sigma_z \simeq \sigma_{R\phi}/\tan\varepsilon$. As in *BABAR*, four consecutive cell layers are grouped radially into a superlayer (SL). This will allow to keep the same *BABAR* algorithms for track-segment finding, both in the track reconstruction and in the formation of the drift chamber trigger.

The rectangular cell layout ensures the most efficient filling of the drift chamber volume, because the transition between superlayers of opposite stereo angles does not require to leave free radial space, nor layers of field-shaping guard wires. Indeed, the latter are only used at a radius inside the innermost SL and at a radius outside the outermost SL. Such guard wires also serve the purpose to electrostatically contain very low momentum electrons produced from background particles showering in the DCH inner cylinder and in the SVT, or background-related backsplash from detector material just beyond the outer SL.

Simulations [8] have shown that a field:sense wire ratio of 3:1 ensures good homogeneity of the electric field inside the cells. In this configuration, used successfully by previous experiments [9, 10], each sense wire is surrounded by 8 field wires.

The radial positions of the stereo wires in the j-th layer vary with the z coordinate, being larger at the endplates than at the center of the chamber by the "stereo drop" $\delta_j \equiv R_j^{\mathrm{EP}} - R_j$. The cell shapes are most uniform when $\delta_j = \delta$ is a constant for all layers: this is obtained by changing the stereo angle with the radius, by the relation $\tan \varepsilon_j = 2\delta/L_j\sqrt{2R_j^{\mathrm{EP}}/\delta - 1}$ (L_j is the chamber length at layer j).

Additional constraints used to determine the cell layout include:

a) the number of cells of width w_j on the j-th sense wire layer, $N_j = 2\pi R_j/w_j$, must be an integer number;

b) to keep a fixed periodicity in signal and high voltage distribution, it is convenient that the number of cells per layer is incremented of a fixed quantity ΔN when passing from a SL to the next one.

c) since the density of both physical tracks and background hits is higher at smaller radii, we choose to have smaller cells in the innermost layers of the drift chamber.

A possible choice for the drift chamber layout, obtained for $\delta = 8\,\mathrm{mm}$ and $\Delta N = 16$ is shown in Table 7.2 and 7.3. In this arrangement the two innermost SL's contain 1472 cells with height $h = 10\,\mathrm{mm}$ and widths $w = (10.2 - 11.7)\,\mathrm{mm}$. The cells in the remaining superlayers have $h = 12.85\,\mathrm{mm}$ and $w = (16.1 - 19.1)\,\mathrm{mm}$. There are a total of 7872 cells in the drift chamber. The first two superlayers have an axial orientation; this minimizes the occupancy from background hits due to low-momentum spiraling electrons which traverse the drift chamber along its axis (see Sec.7.1.5). The two outermost superlayers are also axial. The fact that the innermost and outermost superlayers do not exhibit the stereo drop deformation δ matches the axial symmetry of the inner and outer drift chamber cylinders. The six internal SL's have a stereo arrangement, with angles as shown in the Table.

Table 7.2: A possible drift chamber SL structure, specifying the number of cells per layer, the radius at the center of the chamber of the innermost sense wire layer in the SL, the cell widths, and wire stereo angles, which vary over the four layers in a SL as indicated.

SL	N_{cells}	R [mm]	width [mm]	Angle [mrad]
1	176	292.5	10.4 – 11.5	0
2	192	332.5	10.9 – 11.9	0
3	144	375.4	16.4 – 18.1	+(60 – 63)
4	160	426.8	16.8 – 18.3	−(63 – 66)
5	176	478.2	17.1 – 18.4	+(67 – 69)
6	192	529.6	17.3 – 18.6	−(69 – 71)
7	208	581.0	17.5 – 18.7	+(72 – 73)
8	224	632.4	17.7 – 18.8	−(74 – 75)
9	240	691.8	18.1 – 19.1	0
10	256	743.2	18.2 – 19.2	0

With this wire layout and using a 90%He – 10%$i\mathrm{C_4H_{10}}$ gas mixture (see Sec.7.2.3) , the total radiation length inside the drift chamber is $35.1\,g/\,\mathrm{cm}^2$ (545 m).

The corresponding wire map in the region with angle $|\varphi| < 10^\circ$ is shown in Figure 7.8 at the center of the chamber (a) and at the endplates (b).

It is seen that the axial-stereo transition between SL 2 and SL 3 creates some additional radial space close to the endplates, which disappears at the DCH center. The opposite happens at the stereo-axial transition between SL 8 and SL 9. It is clear that the electric field should be as uniform as possible across layers to ease the drift chamber calibration; however, simulation studies have shown that the field distortion at the two transition radii is moderate and does not require compensation by layers of guard wires, which would add material and reduce the sensitive volume.

In Figure 7.9 we show the drift lines and the isochrone curves for two sample rectangular cells of the proposed Super$B$ drift chamber with a 90%He – 10%$i\mathrm{C_4H_{10}}$ gas mixture, in a 1.5 T magnetic field. The rectangular cells with field:sense wire ratio of 3:1 are indeed a satisfactory compromise, ensuring that the field lines are sufficiently contained within the cell and the isochrone lines are isotropic for most of the drift region, while at the same time the number of field wires is not excessively large.

7.2.3 Gas Mixture

The gas mixture for the Super$B$ drift chamber is chosen to allow optimal resolution in the measurement of both momentum and energy loss. It must also be operationally stable (*e.g.*, have a wide high voltage plateau), and be little sensitive to photons with $E \leq 10\,\text{keV}$ to help controlling the rate of background hits (see Sec. 7.1.5). Finally, aging in the chamber should be slow enough to match the projected lifetime of a typical High Energy Physics experiment (about 15 years). These requirements already concurred to the definition of the *BABAR* drift chamber gas mixture (80%He $-$ 20%iC_4H_{10}). Indeed, a high Helium content reduces the gas density and thus the multiple scattering contribution to the momentum resolution. Good spatial resolution calls for high single electron efficiency and for small diffusion coefficient. The effective drift velocity in Helium-based gas mixtures is typically non saturated. It thereofore depends on the local electric field, and on the Lorentz angle. These dependences can be taken into account by a proper calibration of the space-time relations and in principle do not pose limits to attaining the required spatial resolution. In practice, a careful choice of the cell shape (see the discussion in Sec. 7.2.2), and a small value of the Lorentz angle are an advantage.

To match the more stringent requirements on occupancy rates of Super$B$, it could be useful to select a gas mixture with a higher drift velocity in order to reduce ion collection times and so the probability of hits overlapping from unrelated events. The cluster counting option would instead call for a gas with low drift velocity and primary ionization. As detailed in Section 7.2.4, R&D work is ongoing to optimize the gas mixture.

7.2.4 R&D and Prototype Studies

In order to optimize the gas mixture for the Super$B$ environment, and to asses both the feasibility and the operational improvements for the cluster counting technique a complete R&D program has been proposed. The program includes both beam tests and cosmic ray stands to monitor performances of *ad hoc* built prototypes. While the $\mathrm{d}E/\mathrm{d}x$ resolution gain of the cluster counting method is in principle quite sizable compared to the traditional total charge collection, the actual capability of the measured number of clusters might not retain the same analyzing power, due to a pletora of experimental effects that should be studied in detail so that the energy loss measurement derating should be assessed and, if possible, cured.

A number of prototypes were built and operated to answer the above mentioned questions.

7.2.4.1 Prototype 1

The first one is a small aluminum chamber, 40 cm long, with a geometry resembling the original *BABAR* drift chamber. It consists of 24 hexagonal cells organized in six layers with four cells each. A frame of guard wires with appropriate high voltage settings surrounds the cell array to ensure uniformity of the electric field among the cells. The device was operated in a cosmic ray test stand in conjunction with an external telescope, used to extrapolate the track trajectories with a precision of $80\,\mu$m or better. Different gas mixtures have been tried in the prototype: starting with the original *BABAR* mixture (80%He-20%iC_4H_{10}) used as a calibration point, both different quencher proportions and different quenchers have been tested in order to assess the viability of lighter and possibly faster operating gases.

As an example, the correlation between the extrapolated drift distance and the measured drift time is shown in Figure 7.10 for a 75%He-25%C_2H_6 gas mixture. The result of a fit to a 5^{th}-order Chebychev polynomial is superimposed to the experimental points. Track-fit residuals and spatial resolution as a function of

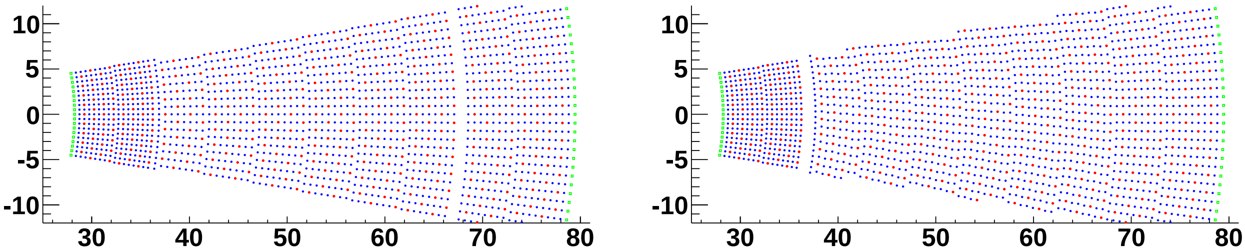

(a) Cell layout at the drift chamber center.

(b) Cell layout at the drift chamber endplates.

Figure 7.8: A possible cell layout of the Super$B$ drift chamber with $h_{\mathrm{in}} = 10\,\mathrm{mm}$, $h_{\mathrm{out}} = 12.85\,\mathrm{mm}$. Open green squares: guard wires; open blue circles: field wires; full red circles: sense wires. Note how the boundary regions after the first 8 layers of axially strung wires in the inner part of the chamber and after the following 24 layers of stereo layers map differently at the drift chamber center and at the endplates.

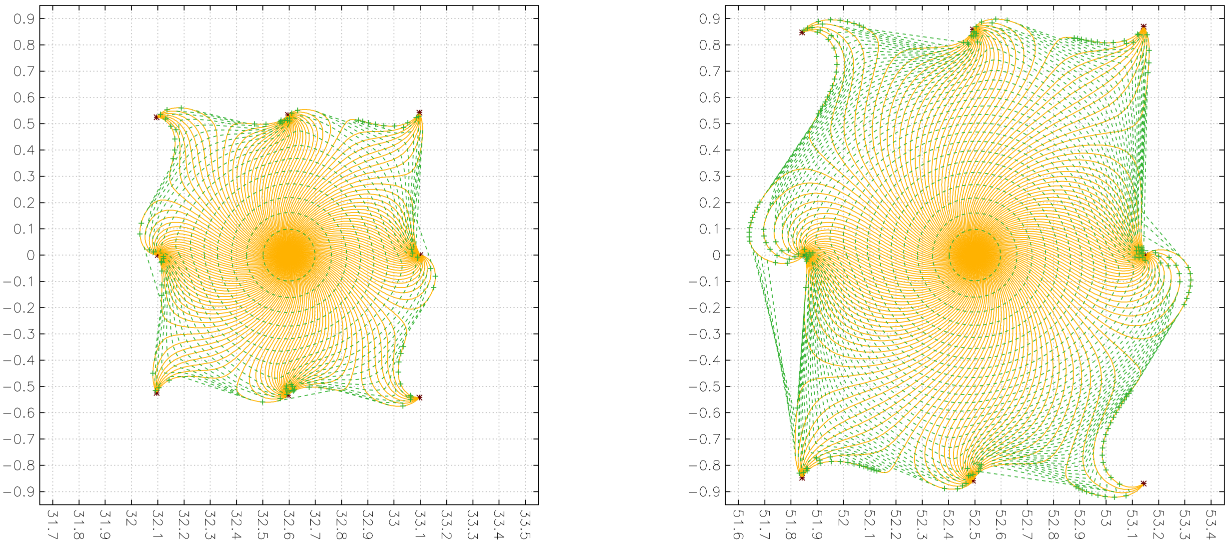

(a) Field and isochrone lines in a sample "small" cell, layer 6. Horizontal and vertical dimensions are in cm.

(b) Field and isochrone lines in a sample "big" cell, layer 22. Horizontal and vertical dimensions are in cm.

Figure 7.9: Field lines and isochrone curves (shown with a 25 ns step) in a cell belonging to the first 8 layers (left) and in a larger cell of the outermost 32 layers (right).

Table 7.3: A possible drift chamber layer structure, specifying the number of cells per layer, the wire layer radius at the center of the chamber, the cell width and the wire stereo angle.

layer	N_{cells}	R [mm]	width [mm]	Angle [mrad]	layer	N_{cells}	R [mm]	width [mm]	Angle [mrad]
1	176	292.5	10.4	0.0	21	192	529.6	17.3	-67.7
2	176	302.5	10.8	0.0	22	192	542.4	17.7	-68.6
3	176	312.5	11.2	0.0	23	192	555.3	18.2	-69.6
4	176	322.5	11.5	0.0	24	192	568.1	18.6	-70.6
5	192	332.5	10.9	0.0	25	208	581.0	17.5	71.6
6	192	342.5	11.2	0.0	26	208	593.8	17.9	72.6
7	192	352.5	11.5	0.0	27	208	606.7	18.3	73.5
8	192	362.5	11.9	0.0	28	208	619.5	18.7	74.5
9	144	375.4	16.4	55.7	29	224	632.4	17.7	-75.5
10	144	388.2	16.9	56.7	30	224	645.2	18.1	-76.5
11	144	401.1	17.5	57.7	31	224	658.1	18.5	-77.5
12	144	413.9	18.1	58.7	32	224	670.9	18.8	-78.5
13	160	426.8	16.8	−59.7	33	240	691.8	18.1	0.0
14	160	439.6	17.3	−60.7	34	240	704.6	18.4	0.0
15	160	452.5	17.8	−61.7	35	240	717.5	18.8	0.0
16	160	465.3	18.3	−62.7	36	240	730.3	19.1	0.0
17	176	478.2	17.1	63.7	37	256	743.2	18.2	0.0
18	176	491.0	17.5	64.7	38	256	756.0	18.6	0.0
19	176	503.9	18.0	65.7	39	256	768.9	18.9	0.0
20	176	516.7	18.4	66.7	40	256	781.7	19.2	0.0

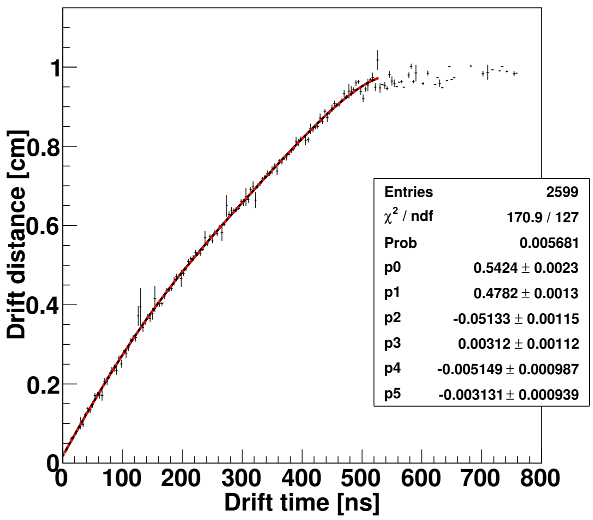

Figure 7.10: Track distance vs. drift time in a cell of the prototype. The line is the result of a fit with a 5^{th}-order Chebychev polynomial.

the drift distance for the same gas mixture are show in Figure 7.11.

The results obtained with this prototype with the *BABAR* gas mixture, agree well with the operating performances of the *BABAR* drift chamber and constitute therefore a reliable reference for our studies.

7.2.4.2 Prototype 2

A full-length drift chamber prototype was designed, built and commissioned to study cluster counting in a realistic environment, including signal distortion and attenuation along 2.5 meter long wires. The prototype, which is also meant to serve as a test bench for the final Front-End electronics and for the drift chamber trigger, is composed by 28 square cells with 1.4 cm side, arranged in eight layers and—as in the final Super*B* drift chamber—with a field-to-sense wire ratio of 3:1. The eight layers have either 3 or 4

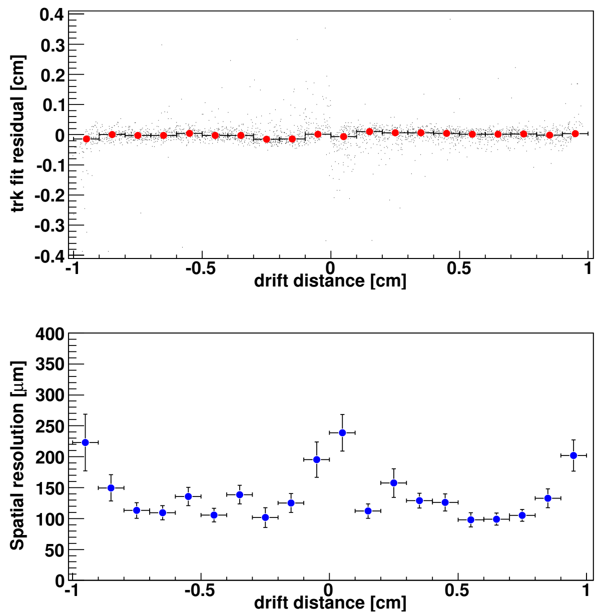

Figure 7.11: Track fit residuals (top) and spatial resolution (bottom) as a function of the drift distance.

Figure 7.12: Prototype 2: detail of the strung wires.

cells each, and are staggered by half a cell side to help reduce the left-right ambiguity. Tracks with angle $|\vartheta| \leq \pm 20^\circ$ cross all the eight layers of the chamber. A set of guard wires surrounds the matrix of 28 cells to obtain a well-behaved field distribution at the boundary of the active detector volume. Most of the cells feature a $25\,\mu$m gold-plated Molybdenum sense wire, while for reference seven cells in two adjacent layers are strung with a $25\,\mu$m gold-plated Tungsten wire, traditionally used in drift chambers. The reason for using the Molybdenum wire is its lower resistivity, which produces smaller dispersion for pulses travelling along the wires. A picture of the chamber after stringing completion is shown in Figure 7.12. The entire wire structure is enclosed in an Aluminum container 3 mm thick; three pairs of thin windows have been carved in the middle and at the extremities in order to have smaller amount of material in the path of low energy particles measured by the device. Four preamplifier boards are used to extract the cell signals. Each board serves seven channels, each with a transimpedence preamplifier (rise time of about 2.4ns), at a nominal gain of 8mV/fC and a noise of 2200 e rms. Each board also has a test input, both unipolar and differential outputs ($50\,\Omega$ and $110\,\Omega$). The latter are used for a test implementation of the Drift Chamber first-level trigger.

The data collected with this prototype are fed into a switch capacitor array digitizer[1], which samples the wire signals at 1 Gs/sec with and input BW$\geq$ 500 MHz. The challenge of detecting the ionization clusters in signals with a wide dynamic range and non-zero noise levels is apparent from the two sample waveforms shown in Fig. 7.13, recorded in the cosmic-ray setup. Hits associated to cosmic ray tracks reconstructed in the drift chamber prototype are used to compare the performances in the energy loss measurement of the traditional truncated mean algorithm and of the cluster counting method. Preliminary results when 10 samples from a single prototype cell are used to form a 70% truncated

[1] `CAEN V1742`: http://www.caen.it/csite/CaenProfList.jsp?parent=13&Type=WOCateg

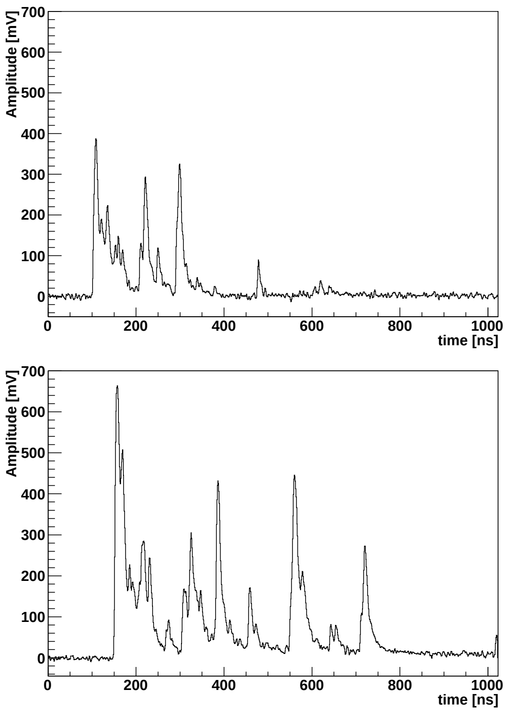

Figure 7.13: Sample waveforms from two different cells of the full-length drift chamber prototype.

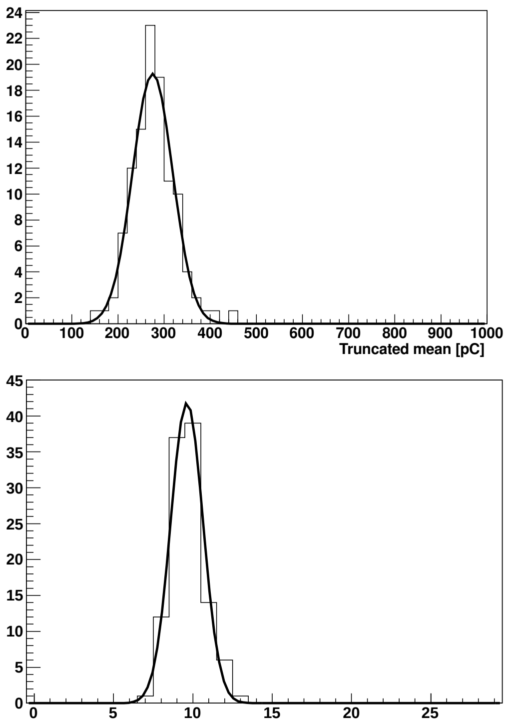

Figure 7.14: Average truncated mean dE/dx (top) and number of clusters (bottom) from 10 samples of a single cell belonging to a track reconstructed in the prototype.

mean or to count the average number of clusters are shown in Figure 7.14. In the experimental conditions of our test, cluster counting yields a 40–50% better relative resolution than the truncated mean method. Additional R&D efforts are ongoing to extend this encouraging result to different momentum regions, and to study how the $K-\pi$ resolving power in the range of interest of Super$B$ ($|p| \leq 5\,\text{GeV}/c$) improves with the cluster counting technique.

The spatial resolution measured in the rectangular cells of the prototype operated in a 90%He-10%iC_4H_{10} gas mixture is shown in Figure 7.15 as a function of the drift distance.

7.2.4.3 Single Cell Prototypes

Two beam tests of single-cell drift chamber prototypes have been carried out at the TRIUMF M11 beam line. The goals of the tests were:

- to establish the benefits of clusters counting for particle identification;
- to study the suitability for cluster counting of various amplifier prototypes provided by the University of Montreal
- to quantify the impact on particle identification performance of various design choices, including sense wire diameter, cable for transmitting the analog signal, connectors, termination, and gas gain.

The beam test in November 2011 used a single prototype, with 25 μm diameter sense wire, while the test in summer 2012 used two prototypes, one with 20 μm sense wire, and the other with either 25 or 30 μm. The prototypes were 2.7m long, and consisted of a single 15 mm square cell surrounded by an array of bias wires that adjusted the electric field distribution within the cell to be that expected for a large drift chamber [Figure 7.16]. A 90% helium / 10% isobutane (90:10) mixture was used for the summer 2012 tests, while the November 2011 test also tested 80:20 and 95:5.

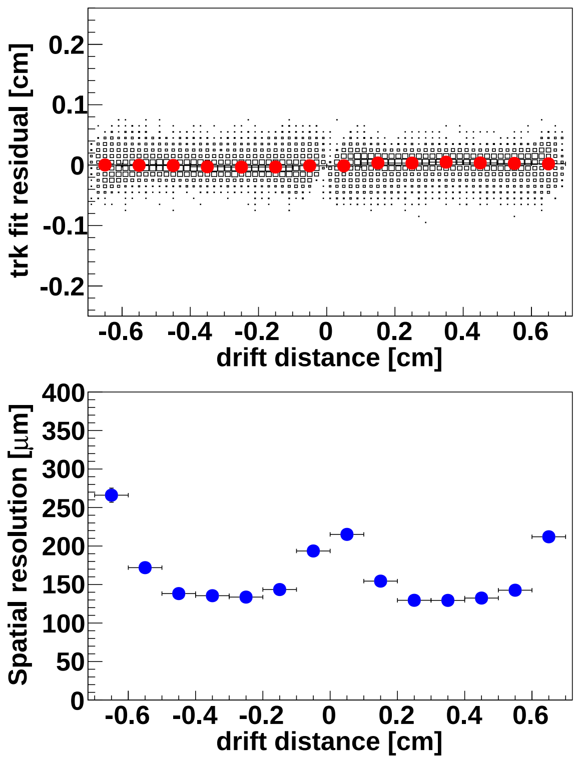

Figure 7.15: Track fit residuals (top) and spatial resolution (bottom) as a function of the drift distance in the rectangular cells of prototype 2 operated in a 90%He-10%iC_4H_{10} gas mixture.

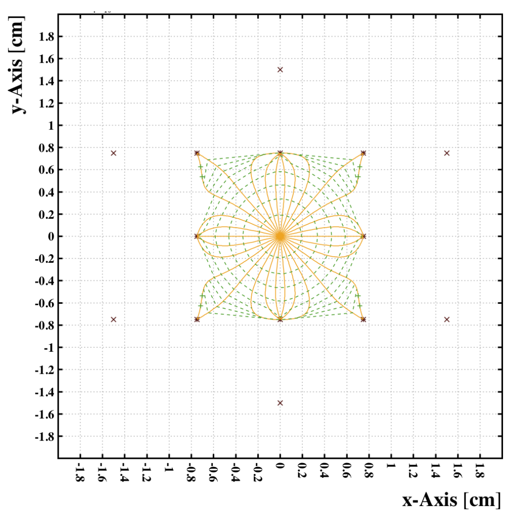

Figure 7.16: Cell design of the single cell prototypes. Isochrones are in 50 ns steps.

Five different amplifier prototypes were built for the test, with three different input impedances: 50, 170, and 380Ω. The impedance of the cell is 380Ω, and for most tests, the cell was terminated at this value on the non-readout end. The 170 and 380Ω consisted of an impedance-matching front end, followed by a 100× gain stage (of 50Ω input impedance); the 50Ω amplifier consisted only of this gain stage.

The TRIUMF M11 beam line delivers positively-charged electrons, muons, and pions, with momenta ranging from 140 to 350 MeV/c. In this momentum range, the particle identification separation between muons and pions is comparable to that between pions and kaons at the 2–3 GeV/c range relevant for Super$B$. The trigger and time-of-flight (TOF) system consisted of two scintillator counters, each with a pair of Burle micro-channel plate phototubes. The trigger rate was typically tens of Hertz, and the TOF resolution was 130 ps, providing clean separation between the particle species.

In the November 2011 test, the drift chamber waveforms were digitized using a CAEN switched-capacitor array, read out using the MIDAS data acquisition system. The bandwidth of this module is 300 MHz, which may be less than required for cluster counting, so in the Summer of 2012, a 4 GHz bandwidth LeCroy oscilloscope was instead used for digitization. In both cases, the amplifier and digitizer were connected by a 10 m long cable, the distance expected in the final design. Events were written to disk at 10–15 Hz.

The benefits of cluster counting on particle ID performance are characterized by comparing the separation between muon and pion tracks using dE/dx only to the combination of dE/dx and cluster counting. Analysis is in progress, and results shown here are preliminary.

A track is formed by randomly selecting 40 samples of the same particle species as determined by the TOF system. The track dE/dx is obtained by discarding the largest 30% of the samples. Clusters are identified by a simple threshold on a smoothed version of the waveform. This algorithm is not necessarily optimal,

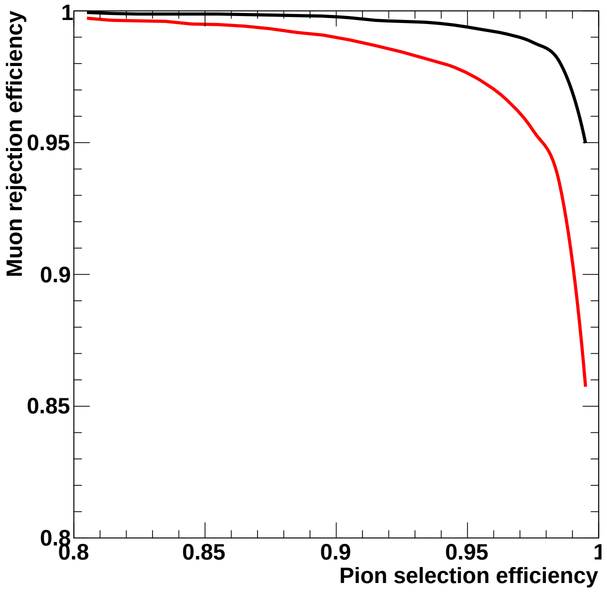

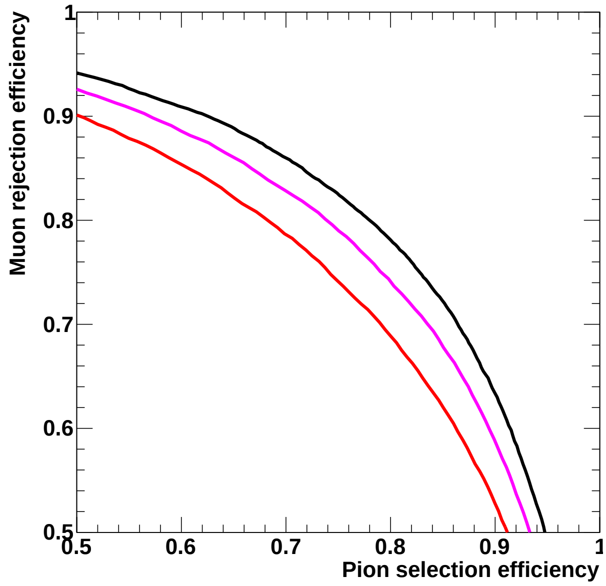

Figure 7.17: Muon rejection efficiency versus the fraction of pions satisfying the selection criteria, for dE/dx only (red), cluster counting only (magenta, not available in left plot), and for the combination of dE/dx and cluster counting (black). Left: 140 MeV/c data, November 2011 test. Right: 210 MeV/c data, summer 2012 test.

and other methods are under study. Conversely, adequate performance may be achieved using a simpler algorithm that could be implemented in hardware, as opposed to an FPGA. The track is characterized by the average of the number of clusters in the 40 samples. The track dE/dx and cluster counting values are combined in a likelihood ratio that is used to label the track as a muon or pion. Figure 7.17 shows examples of the results from the two beam tests.

The data seem to indicate that the use of cluster counting in combination with dE/dx leads to a significant improvement in the pion efficiency. At 210 MeV/c, for example, for a misidentification probability of 10% the pion selection efficiency increases from 50% to 64%, an improvement of $\simeq$ 30%. As the μ/π separation at 210 MeV/c is approximately the same as the K/π at 2 GeV/c, a similar improvement can thus be expected for real physics channels relevant at Super$B$. The Monte Carlo study discussed in Section 7.2.1.5 shows that a 30% improvement in K/π separation leads to about 4% increase in the $B_{\rm reco}$ efficiency. This result, albeit preliminary, is encouraging because it translates directly into an equivalent gain in the statistics collected for a given integrated luminosity.

7.2.4.4 Aging studies

The goal of the aging studies is to establish that the proposed drift chamber can survive for a lifetime of at least 100 ab^{-1}.

These studies use an ^{55}Fe source both to age a test chamber, and to characterize its performance. The initial studies are using a 30 cm long chamber containing a single *BABAR*-like hexagonal-shaped cell, and an 80% helium 20% isobutane gas mixture. The sense wire is 20 micron gold-coated tungsten, and the field and bias wires are 120 micron gold-coated aluminum. The chamber is exposed to a 100 mCi ^{55}Fe source. The resulting current is monitored, along with temperature and atmospheric pressure, as a way to characterize gain as a function of accumulated charge. Once per week, the hot source is replaced with a low-intensity one and the pulse-height spectrum is recorded (Figure 7.18). The location of the ^{55}Fe peak is an additional measurement of gain. The number of very small pulses is sensitive to the Malter effect [11], a form of aging of the field wires in which they accumulate an insulating coating. A second single-cell chamber, which is not exposed to the hot source, is used to calibrate out any possible gain effects due to gas variations, and to verify the gas density corrections. The chamber is operated at a voltage such that the electric field on the field wires is less than 20 kV/cm in order to minimize the Malter effect.

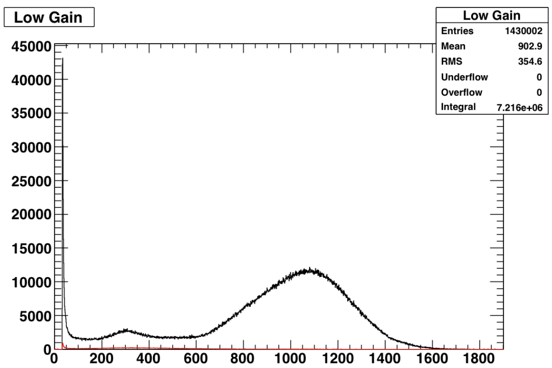

Figure 7.18: Pulse height spectrum (arbitrary units) recorded from an ^{55}Fe source by an aging chamber. The red curve is the underlying cosmic ray background.

The aging chamber shows a gain drop of 25% after accumulating 310 mC/cm over the last 20 months. This lifetime is significantly in excess of the 34 mC/cm accumulated by the *BABAR* drift chamber. The *BABAR* chamber saw a 10% loss of gain over that time.

The next aging chamber is currently under construction. It will include seven square cells, so that the central field wires are surrounded by sense wires, and will therefore accumulate the correct amount of charge. It will use Super*B* materials, gold-coated 20 micron Molybdenum sense wires, and 80 or 90 micron bare aluminum field wires, and 90:10 helium-isobutane gas. The structure of the chamber will be aluminum, as for the current aging chamber, but the walls will be covered by samples of the carbon-fiber material that will be used in the actual chamber.

The amount of charge per cm expected for the Super*B* chamber is a function of the chamber occupancy, the gas gain, and the total running time. Current background calculations indicate occupancy levels comparable to *BABAR*, including a five-times safety factor. The Super*B* running time will also be comparable to *BABAR*. The gas gain may be higher, due to the requirements of cluster counting. The gas gain required is a function of the amplifier; the 50 ohm input impedance amplifier prototypes require four times the gas gain of the 370 ohm amplifiers, due to the impedance mismatch between the amplifier and the drift cell. The field wire diameter is, in turn, a function of the sense wire operating voltage, given the need to keep the electric field at the surface of the field wire below 20 kV/cm.

7.2.5 R&D Future Developments

At the time of this writing, a two week test beam data taking campaign has been completed with the full scale prototype (Prototype 2) at the M11 beam line in the TRIUMF laboratory, Canada. Data were collected with a beam of e, μ, and π particles with momenta between 120 and 210 MeV/c.

The goal of this test is to reproduce and study in further details, with a more realistic full length, multiple cell prototype, the promising preliminary results on cluster counting and dE/dx obtained with the single cell prototype described in Sec. 7.2.4.3. The analysis of these data has just started and will be the object of a future paper.

Another line of future development is centered in the realization of a prototype on-board feature extraction.

7.3 Mechanical Design

The drift chamber mechanical structure must sustain the wire load with small deformations, while at the same time be as light as possible to minimize the degradation of the performances of the surrounding detectors. The structure is also required to ensure tightness for the gas filling the drift volume. We opted for a structure entirely in Carbon Fiber (CF) composite, with an approximately cylindrical geometry. Given the studies shown in Subsec. 7.2.1.2, the active length of the chamber has been maximized. In particular the length in the backward direction is increased with respect to *BABAR* despite the 160 mm reserved in Super*B* for the possible backward EMC to be installed at a later stage; this is possible thanks to the new design of the drift chamber front-end electronics (Sect.7.4), which require substantially less space than *BABAR*.

7.3.1 Endplates

The wires defining the cell layout are strung between the two endplates, which are required to:

a) sustain the total wire load of about 2 tons (see sec. 7.2.2) with minimal deformations;

b) be as transparent as possible to avoid degrading the performances of the forward calorimeter.

c) have 33,000 precisely machined holes to allow positioning the crimp feedthroughs with tolerances better than 50 μm;

The endplates are two identical pieces of 8 mm thick CF composite with inner radius of 270 mm and outer radius of 809 mm. Deformations under load can be minimized using a shaped profile. An optimization taking into account different constraints resulted in spherical convex endplates, with a radius of curvature of 2100 mm. Two CF stiffening rings (the outer one shown in Figure 7.19) on the inner and outer rims help minimize radial (axial) deformations. In the calculation an intermediate modulus carbon fiber (T300, with a Young modulus of 45 GPa) was used. The 8 mm CF laminate is built using stacks of 250 μm plain weave plies with a $[0/45/45/0]_8$ structure. It was conservatively assumed that the average material characteristics are degraded by about 30 % after drilling the 33,000 holes on each endplate; detailed studies on this aspect will be performed on custom samples. The maximum displacements on the endplates is calculated to be less than 600 μm (Figure 7.20). As a comparison, the thickness of flat endplates to have such small deformations under the wire load would be 52 mm.

7.3.2 Inner cylinder

The drift chamber inner cylinder should be as transparent as possible to minimize the multiple scattering degradation to the p_T measurement. For this reason it was designed as a non-load-bearing structure: it must only guarantee gas tightness, and sustain possible differential pressures of about 20 mbar[2] between the inside and outside of the chamber. The 270 mm radius cylinder is composed by two 90 μm CF sheets sandwiching a 3 mm thick honeycomb structure to increase the moment of inertia and improve the buckling load. A 25 μm thick aluminum foil

[2] The nominal differential pressure in normal operation of the Super*B* DCH will be 2 mbar or less, but the cylinder has been designed to sustain 20 mbar.

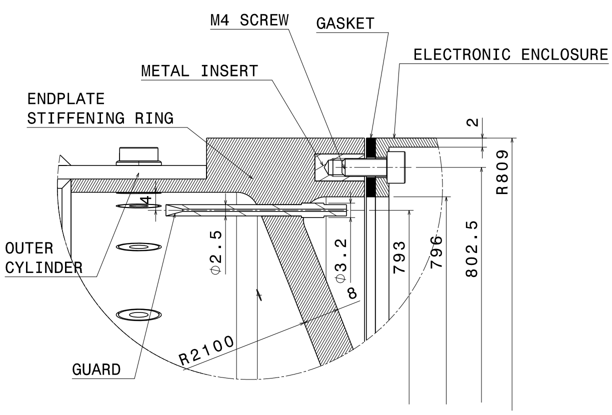

Figure 7.19: Detail of the outer flange of the DCH endplates.

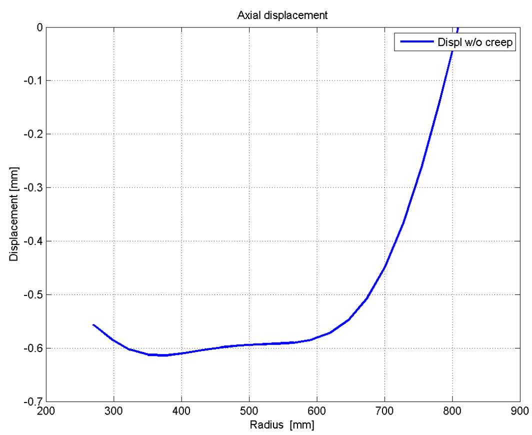

Figure 7.20: Displacement of each endplate due to the wire load.

is glued on each CF skin for RF shielding. The possibility is being explored to build an even thinner inner cylinder, replacing the two 90 μm CF plies with two 50 μm Kapton foils. During the stringing phase the inner cylinder will be free to move longitudinally, being fixed only to one endplate. Only after stringing, when all endplate deformations are settled, will the cylinder be glued to the second endplate. A detail of the interface between the inner cylinder and the endplate is shown in Figure 7.21.

7.3.3 Outer Cylinder

In addition to guaranteeing gas tightness and withstanding a differential pressure as the inner cylinder, the outer cylinder will also carry the entire wire load. It will be installed after completion of the wire stringing. To ease the construction and the mounting procedures, the cylinder is longitudinally divided in two half shells. Each shell consists of two 1 mm-thick CF skins laminated on a 6 mm-thick honeycomb core. A 25 μm thick aluminum foil is glued to each CF skin to ensure the RF shield. The sandwich structure guarantees a high bending stiffness and a high safety factor for global buckling.

7.3.4 Analysis of Buckling Instabilities

The buckling stability of the system was studied for all elements working under compression with the ANSYS Finite Element Analysis Program. Different methodologies were used for the main system elements, as described below.

7.3.4.1 Endplates

The results of a buckling linear analysis performed varying the endplate curvature radius are summarized in Table 7.4. The first buckling mode for the configuration with the nominal endplate curvature radius (2100 mm) is shown in Figure 7.22.

The nominal configuration with $R_{E.P.} = 2100$ mm is observed not only to minimize the displacement, but also to show the best buckling safety factor. We consider a safety factor above 10 adequate even after the uncertainties due to material imperfections and the effect of holes on the endplates are taken into account.

7.3.4.2 Inner Cylinder

A linear buckling analysis was carried out on the inner cylinder structure which, as discussed in Sect. 7.3.2, is only expected to sustain a gas overpressure of a few mbar. The first buckling modes of a perfect structure are shown in Figure 7.23, for a very high load of 120 mbar.

It is well known that cylindrical thin shells are sensitive to geometrical imperfections. In order to realistically estimate the buckling safety factor, we have introduced such imperfections in our model, evaluating the critical load in each case with a non linear analysis. The results are

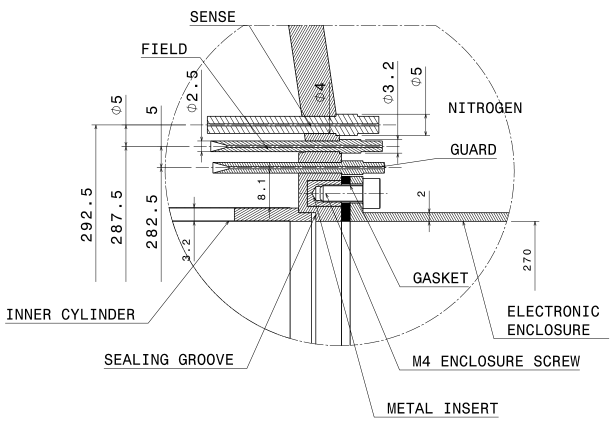

Figure 7.21: Coupling of the DCH inner cylinder to the endplate.

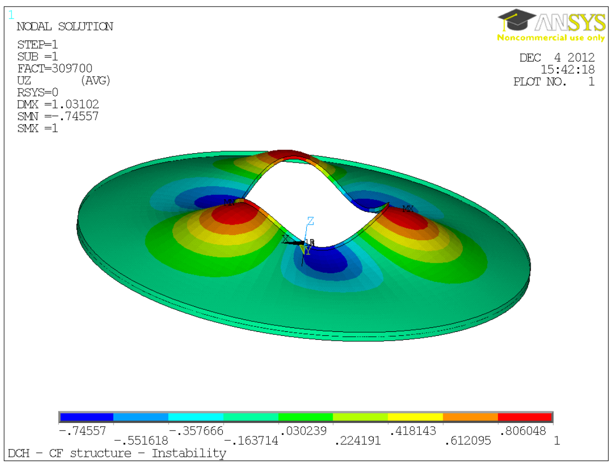

Figure 7.22: Calculated first buckling shape of the endplates.

Table 7.4: Maximum endplate deformations δ_{max}, static and buckling safety factors as a function of the endplate curvature radius $R_{E.P.}$.

$R_{E.P.}$ mm	Thickness [mm]	δ_{max} [mm]	Static S.F.	Buckling S.F.
2100	8	0.6	16.0	16.0
3000	8	1.1	12.4	8.0
4000	8	1.8	10.0	4.8

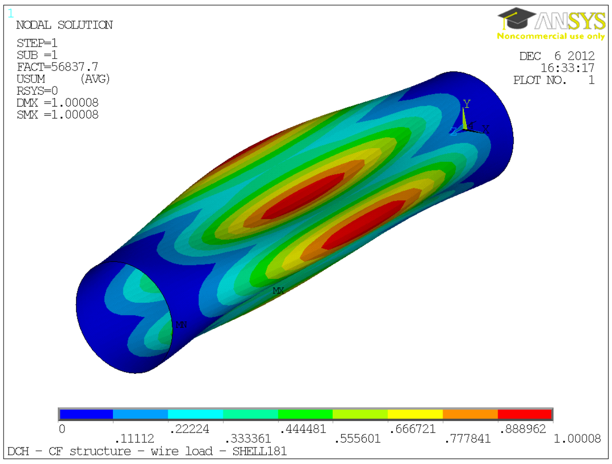

Figure 7.23: Calculated first buckling shape of the inner cylinder.

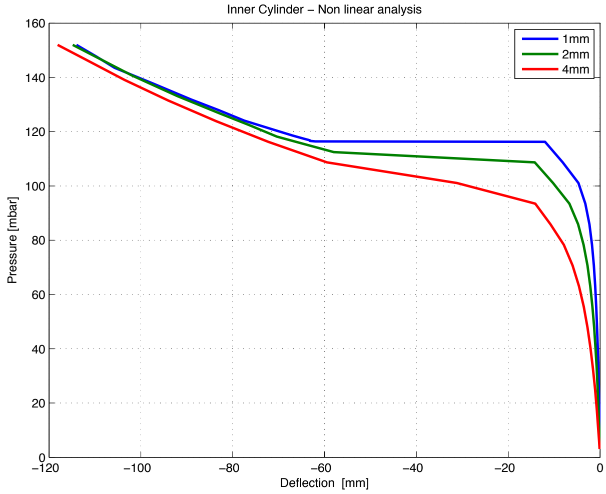

Figure 7.24: Inner cylinder critical load for different values of the geometrical imperfections.

Table 7.5: Buckling load [mbar] as a function of the maximum size [mm] of geometrical imperfections in the inner cylinder.

Max. size [mm] / Config	0	1	2	4
0.09/0.09	0.84	0.74	0.68	0.56
0.09/3/0.09	120	108	99	86

shown in Figure 7.24 and in Table 7.5: as expected, the larger the geometrical imperfections, the smaller the critical load.

The table also shows that very small values are obtained when the inner cylinder is only made of two (0.09 thick) CF skins. The maximum load dramatically increases when a 3 mm thick honeycomb structure is inserted between the CF skins. An acceptance threshold on the geometrical imperfections at the level of $2-4$ mm can certainly be imposed, which leaves a reassuring factor 30 on the buckling load of the inner cylinder.

7.3.4.3 Outer Cylinder

A linear buckling analysis was performed on the outer load-bearing structure similarly to what discussed in the previous subsection. Also in this case geometrical imperfections were included, evaluating the safety factor under an axial load of about 21 kN.

These results are shown in Figure 7.25 for the final structure (1CF 6HC 1CF) and summarized in Table 7.6 for different carbon fiber sandwiches.

7.3.5 Choice of wire

As described in Section 7.2.2, each cell has one sense wire surrounded by a rectangular grid of eight field wires. A smaller value for the sense wire diameter is generally preferred for several reasons: any given gas amplification, therefore electric field, can be reached with smaller applied high voltage; and the avalanche starts closer to the wire, with smaller space-charge effects. In practice the wire diameter is limited by ease of handling, and by the mechanical resistance. For sense wires, we intend to use 20 μm gold-plated Molybdenum wires. Molyb-

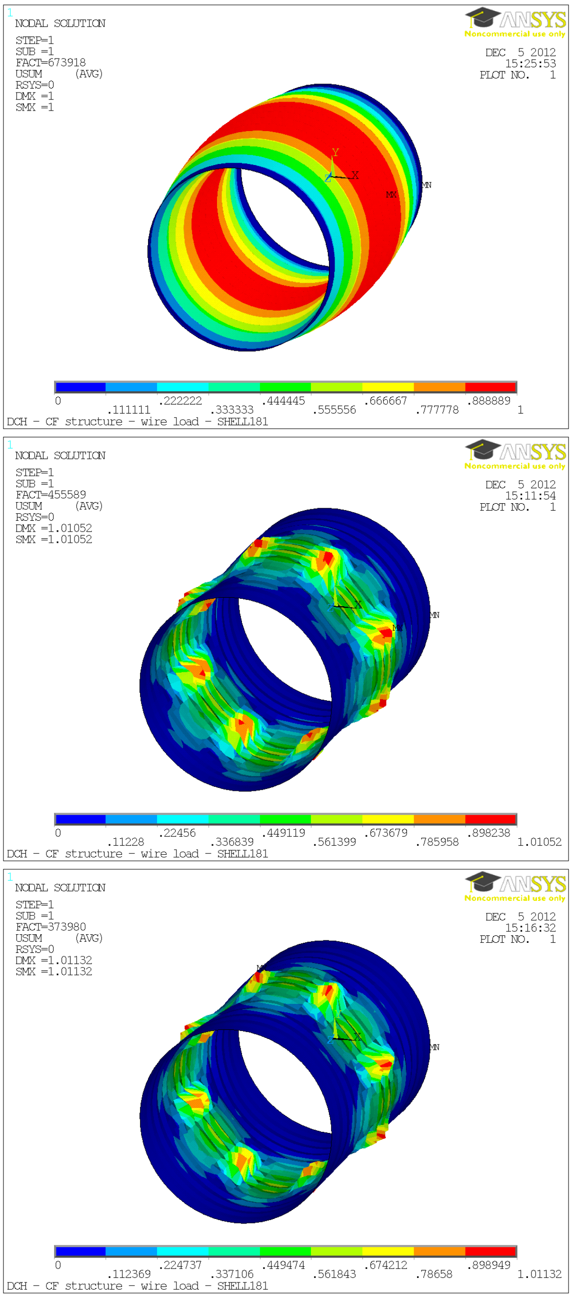

Figure 7.25: Calculated outer cylinder 1st buckling shape for (a) no imperfections, (b) 2 mm imperfections, or (c) 4 mm imperfections.

Table 7.6: Outer cylinder safety factors for different thickness in mm of the Carbon Fiber (CF) and honeycomb (HC) components, and for different sizes of the geometrical imperfections.

Config	Nominal S.F.	2 mm S.F.	4 mm S.F.
2CF	24.0	10.8	8.0
1CF 3HC 1CF	22.0	12.8	8.3
1CF 4HC 1CF	33.6	13.5	9.0
1CF 6HC 1CF	33.6	22.8	18.6

denum has lower resistivity than the more conventional W-Rh alloy, therefore smaller dispersion for pulses traveling along the wires. The density is also smaller than for Tungsten wires, resulting in slightly less tension (160 kg) on the endplates, and more importantly in less material in the tracking volume. The radiation length for all wires (field + sense + guard) increases from 4.25 cm with W-Rh wires to 6.95 cm with Mo wires, while X_0 for the wires and the 90%He − 10%iC_4H_{10} gas mixture increases from 480 m to 545 m. A mechanical tension of approximately 23 g will be applied to each wire, needed for it to show a gravitational sag of 200 μm. Such a tension is consistent with electrostatic stability and with the yield strength of the wire.

The field wires are chosen to be 90 μm diameter Al-5056 wires with a "stress-relieved" temper. The selected diameter keeps the electric field at the cathode surface below the limit of 20 kV/cm, considered a safe value in drift chambers not to trigger gas multiplication and help suppressing the Malter effect. The temper considerably increases the wire tensile and yield strength, and reduces the loss of tension due to the creep effect. A nominal tension of 73 g will be needed to equalize the gravitational sag of sense and field wires (in the stringing phase the latter will be pulled at a slightly higher tension to compensate for the creep effect). Again, this tension is well within the elastic limit of the wires.

7.3.6 Feedthrough design

The feedthroughs locate the wires to within the specified tolerances, hold the wire tension, and, in the case of the sense wires, insulate against the high voltage. They must achieve these goals while maintaining a helium-tight gas seal.

A feedthrough is made from two components, a plastic outer insulator, and a conducting crimp pin (Figure 7.26). The insulators are injection-molded parts formed from Celenex 3300-2, chosen for its low shrinkage during molding, dimensional stability, and high dielectric strength. The crimp pins for the aluminum field wires are aluminum 6063. Studies are planned to determine whether copper or aluminum crimp pins are more suitable for the molybdenum sense wires. The crimp pins will have a gold-flash coating with a nickel underlayment.

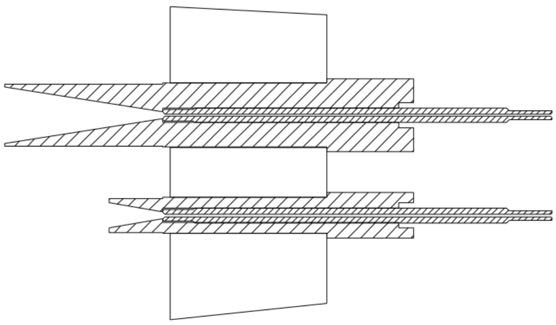

Figure 7.26: Sense wire (top) and field wire (bottom) feedthroughs from the *BABAR* drift chamber. The Super*B* parts will be similar.

The two parts are glued together with an epoxy that is dyed so that extraneous epoxy on the crimp pin can be identified and removed.

The tolerances are specified to ensure that the contribution to cell resolution is small, with tolerances on the sense wire parts significantly tighter than those on the field wires. Inner diameter of sense wire crimp pins at the wire release point will be 100 microns, and 200 microns for field wires. Concentricity of the pin hole with respect to the shaft diameter will be less than 30 microns, and eccentricity of the shaft will be less than 25 microns.

Each of the approximately 75000 feedthroughs will be individually tested against the specifications. Sense wire feedthroughs will have an additional test to verify HV performance.

7.3.7 Endplate systems

7.3.7.1 Electronics enclosures

The amplifiers mounted on the backward endplate of the drift chamber, and the high-voltage components mounted on the forward endplate are covered by the electronics enclosures. The volumes are filled with nitrogen to ensure that a leak of the flammable drift gas through the endplate cannot form an explosive mixture. The enclosures also protect the components inside, and provide the mounting points for the chamber as a whole.

The enclosures are light aluminum structures (Figure 7.27). The main features are feedthroughs for the various signals and services used by the chamber: chamber gas, nitrogen, cooling water, amplifier power and signal, and high voltage. Each 1/16$^{\text{th}}$ sector corresponds to approximately 500 signal cables, arranged into 8-channel ribbon cables and feedthroughs. These feedthroughs may also carry the power and control lines for each amplifier. The feedthroughs are mounted on removable panels, while the cooling lines are on the fixed ribs. The panels allow access for installation and repairs, although such accesses are expected to be rare. Although the endplates are curved, the panels can be flat, reflecting the geometries of the backward calorimeter and the forward time-of-flight system on either side of the drift chamber. This will greatly simplify the necessary gas seals.

7.3.7.2 Cooling

The fast amplifiers mounted on the drift chamber endplates produce approximately 1200 W of heat. This heat must be removed to keep the temperature of the drift chamber and nearby detectors stable and uniform. The cooling system to accomplish this will be water based, operating at a pressure below atmospheric pressure. Small leaks will therefore cause air to leak into the water, rather than leading to water leaking into the

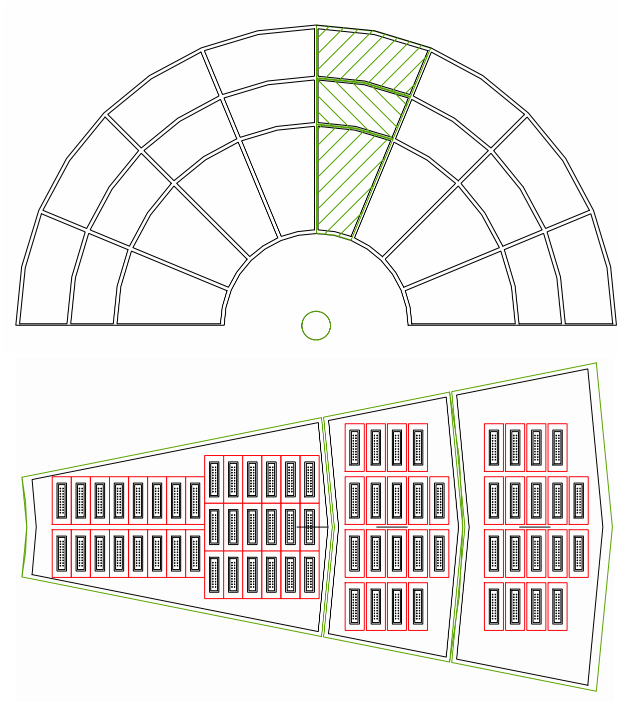

Figure 7.27: (a) The rib structure of each enclosure is machined from a solid piece of aluminum. (b) The feedthroughs are on panels mounted to the ribs.

electronics enclosure. The system is quite similar to one recently built for the near detector of the T2K experiment [12].

The major components of the system include two water reservoirs, one at atmospheric pressure, and the other maintained at an absolute pressure of 0.3 atmospheres; a pump to move water between the systems; cooling lines to the drift chamber and inside the electronics enclosures; valves and gauges; a heat exchanger that connects to the laboratory chilled water system; and a control system to maintain the desired water temperature. Appropriate corrosion inhibitors and microbiocides will be added to the water. The lines within the enclosures will be mounted to the fixed ribs, and may include fins or other features to increase the surface area. These features, combined with turbulent nitrogen flow in the enclosure, may generate sufficient thermal flow from the amplifiers to keep the temperatures at an acceptable level. Mock-ups and thermal calculations will be undertaken to test this concept. The alternative will be cooling straps.

Although there is no heat generated on the forward endplate, cooling lines will be run to ensure a uniform temperature across the drift chamber.

7.3.7.3 Shielding

The aluminum structure of the electronics enclosures, together with the aluminum skins on the outer and inner cylinders, form a Faraday cage that encloses the amplifiers and the chamber wires. A 25 micron thick aluminum skin bonded to the endplates provides additional shielding between the chamber wires and the enclosure volumes.

7.3.7.4 Electromechanical boards

Electrical connections to the crimp pins are required at both ends of every wire. At the forward end, the HV distribution boards ground the field wires and provide HV to the sense wires via the circuit described in Sec. 7.5, and terminate the sense wire at the characteristic impedance of the cell. At the backwards end, service boards ground the field wires, and gather the signals from eight sense wires onto a single multi-conductor connector. The only active components on the service boards are the HV blocking capacitors.

Each of the ten superlayers requires a different size of HV distribution board and service board. Only a single style of 8-channel preamp card is required. Each board will service eight cells (four in radius by two in azimuth), typically corresponding to 32 crimp pins. A number of crimp pin connections much larger than this would make the board difficult to insert and remove.

The connections to the crimp pins are made using low-insertion-force connectors, such as the Hypertronics connectors used for *BABAR*. The details of how the curvature of the endplate is handled in the design of the cards will require prototypes and mockups.

Jumpers between adjacent boards will connect the ground planes. At the HV end, jumpers will distribute the HV among the typically three boards serviced by a single HV channel.

The endplate will include two blind holes per board that will be used with dowel pins to align the boards during insertion. We do not anticipate using pull-down screws, which would require a large number of tapped holes in the endplates. Each board will have two threaded holes that will be used to push against the endplate if it is necessary to remove the board. The boards will be removed rarely, if ever. One of the two holes will be used during normal operations to provide an electrical connection to the aluminum RF shield on the endplate via a low-force spring connection.

7.3.8 Stringing

The chamber will be strung horizontally, with the inner cylinder in place (but not under load), and the outer cylinder absent. The wire load is held by a mechanical structure that attaches to the outer radius of each endplate and to a central shaft inserted through the inner cylinder. The chamber can be rotated about this shaft.

There will be two stringing shifts per day, five days per week. Each shift will have two teams consisting of two stringers plus a wire-transport robot. The robot is used to carry the wire between the endplates, reducing the chance of errors or damage to the previously strung wires, and keeping the interior of the chamber clean by eliminating the need for people to work in that area. The work will be done in a class 10000 or better clean room, with the interior of the chamber (including the robots and the previously strung wires) curtained off for greater cleanliness.

An abbreviated sequence of steps involved in stringing a wire is:

- A stringer attaches the wire to a steel needle and inserts it through a plastic sleeve into the appropriate feedthrough hole, where it is captured by the magnetic head of the robot.

- The robot carries the wire to the other endplate, where the needle is taken by the second stringer, who pulls the additional wire needed. The robot moves into position for the next wire when the second stringer indicates that they have finished pulling the wire. Both ends of the wire are then placed in wire holders before being cut.

- Each stringer feeds the wire through a feedthrough, places a ring of glue around the shaft of the feedthrough, and inserts it in the hole. The glue will be thixotropic gel cyanoacrylate adhesive such as Loctite 454 or 455, dyed red for ease of inspection.

- The second stringer crimps her crimp pin using a foot-operated pneumatic tool, such as the Simonds MSP-1 Squeeze Pliers. The first stringer then applies the appropriate tension using a pulley and weight, and crimps her crimp pin. Because the deflection of the endplate is negligible under the wire load (Figure 7.20), wires can be tensioned at their nominal values. Excess wire is cut at both ends, leaving 1 mm protruding for inspection purposes.

- Once both teams have finished ten wires, the chamber is rotated into position for the next set of ten.

The third shift each day is used for quality control. The steps include measuring the tension, visually inspecting the glue seals around the feedthroughs, looking for excess glue on crimp pins, and straightening bent crimp pins. Wire that have tension out of tolerance (a gravitational sag more than 15 microns from nominal) are removed, and the holes cleaned. These wires are restrung at the start of the next stringing shift. The third shift also makes the gas seal between the wire and crimp pin using a low-viscosity cyanoacrylate adhesive such as Loctite 493, dyed red for easier inspection.

One stringer starts work an hour before the others to prepare the glues, lay out the parts needed that day, and to verify that all crimp tools are producing crimps of the correct size.

Each team is expected to complete 80–100 wires per shift, for a total of approximately 350 per day.

7.4 Electronics

7.4.1 Design Goals

The Super$B$ Drift Chamber front-end electronics is designed to extract and process approximately 8000 sense wire signals to:

- measure the electrons drift times to characterize a track (momentum of charged particles)
- measure the energy loss of particles per unit length, dE/dx (particle identification)
- provide hit information to the trigger system (trigger primitives)

Two methods will be discussed for the energy loss measurements. We first present a solution already widely used in existing drift chambers, based on the measurement of the integrated charge on each sense wire (standard readout, SR). Then we present the baseline of our choice, which is based on the counting of the primary ionization clusters (CC), which has never been used in a large scale drift chamber before. Because the front-end requirements for the two options are quite different, we shall discuss them in separate sections.

7.4.2 Standard Readout

7.4.2.1 Charge measurement

The method is based on an integrated charge measurement, which allows the use of relatively low bandwidth preamplifiers. This makes the front-end chain less sensitive to noise pickup and instabilities, a condition quite useful in a system with a large number of channels. The three main specifications for a charge measurement are: resolution, dynamic range and linearity.

Resolution The goal of a charge measurement to be used for particle identification is to determine the most probable energy loss per unit length to a precision of the order of 7.5%. This can be achieved, despite the large fluctuations present the ionization process, by sampling the collected charge many times (once per DCH hit cell) and by applying the "truncated mean" method to obtain the peak value of the resulting distribution to a precision of several percent.

The Super$B$ drift chamber design parameters and expected working conditions aim at obtaining an overall single cell energy loss resolution (σ_E) of about $25-30\%$, mainly driven by the detector contribution. To make the contribution of the front-end electronics σ_{EL} negligible, we set a limit at $\sigma_{EL} \leq\sim 5\%$.

Finally, if we assume that the charge collection due to a minimum ionizing particle crossing orthogonally the cell is about 50 fC ($\sim 2fC/e$ @ 10^5 nominal gas gain), we can infer a limit to the Equivalent Noise Charge (ENC) for a single front-end channel of about 50 $fC \cdot 0.05 \simeq$ 2.5 fC.

Dynamic range With 8 bits ADCs the dynamic range is $2.5-500$ fC. This is more than enough to satisfy the system requirements.

Linearity As stated above, a single cell energy resolution is about $25-30\%$. Therefore, a linearity of the order of 2% largely satisfies the system requirements.

7.4.2.2 Time measurement

As for the charge measurement, we have three main specifications: resolution, dynamic range and linearity.

Resolution One of the Super$B$ drift chamber requirements is the reconstruction of charged particle tracks. The measurement consists of recording the arrival time at the sense wire of the first ionization electron. The spatial resolution (σ_S) is strictly related to the time resolution and gets contributions from primary ionization statistics, electrons diffusion time and time measurement accuracy. To achieve the required point resolution of $\sigma_S \sim 110\mu m$, and assuming that the first two effects account for about 100 μm, the upper limit for the electronic contribution can be deduced to be $\sigma_{EL} \leq\sim$ 50 μm. Because helium based gas mixtures are characterized by a non saturated drift velocity up to high fields [13], this velocity rapidly increases as the electrons approach the sense wire. A value of 2.5 $cm/\mu s$ (25 $\mu m/ns$) [14]

has been used to evaluate the maximum acceptable error in a time measurement, that is $\sigma_t \leq 50[\mu m]/25[\mu m/ns] \simeq 2\ ns$.

Discarding the bunch length contribution (tenths of ps), there are two main error sources in time measurements: the discriminator jitter and the TDC resolution (digitization noise). The discriminator jitter, in turn, has two main contributions: signal noise and time-walk.

The signal noise contribution is generally small and can be evaluated according to $\Delta t = \sigma_{noise}/(dV/dt) \simeq \sigma_{noise} \cdot \tau/V_{max}$ where τ is the preamplifier-shaper peaking time. Assuming that a single electron cluster generates a signal of amplitude $\sim 20\ mV$, and that the noise and the peaking time associated with the signal are $\sigma_{noise} \sim 3\ mV(rms)$ and $\tau \sim 5\ ns$, we get a noise contribution to the time resolution of about $0.8\ ns$.

The time-walk effect is caused by the signal amplitude variation. With a peaking time of about 5 ns, a time-walk contribution for a low-threshold leading-edge discriminator can be estimated to be about $1.5\ ns$.

Finally, the digitization noise depends on the digitization unit Δ according to the formula $\sigma = \Delta/\sqrt(12)$. Using $\Delta \simeq 1.5\ ns$ a digitizing noise of about $0.45\ ns$ is obtained.

In summary, without corrections, the time resolution is dominated by time-slewing effects. It can thus be estimated to be about $1.8\ ns$ (including all contributions). Nevertheless corrections can be applied using digitized signals to minimize time-slewing effects thereby reducing the time walk contribution (Figure 13.3).

Dynamic range The TDC range depends on the drift velocity and on the cell size. A maximum drift time of about $600\ ns$ has been estimated for Super$B$ drift chamber cells. Providing some safety factor, a TDC range of about $1\ \mu s$ is enough to include any jitter in trigger generation and distribution.

Linearity A linearity of the order of 1% fully satisfies time measurement requirements.

7.4.2.3 Front End Electronics

The drift chamber FEE chain (Figure 13.2) is split in two blocks: on-detector and off-detector electronics.

In the following paragraphs we will give a description of the on-detector electronics while the description of the Off Detector Electronics can be found in Sec. 13.1.2.

On Detector Electronics Preamplifier boards will contain HV blocking capacitors, protection networks, preamplifiers and (possibly) shapers-amplifiers. Because of the small cell dimensions, many cells can be grouped in a single, multi-channel preamplifier-shaper board. Signals and power supply cables will be connected to the boards by means of suitable connectors.

In addition to the requirements on the Signal to Noise Ratio (SNR), each preamplifier should be characterized by enough bandwidth to preserve signal time information meeting the power requirement of not more than 20–30 mW per channel, to limit the total power dissipation on the backward end-plate to 160–240 W. This will allow the use of a simpler and safer forced-air based cooling system (no risk of leak).

Table 7.7: Preamplifier main specifications

Non-linearity	$< 2\%\ (1--100fC)$
Output Signal Umbalance	$< 2\%\ (1--100fC)$
Gain (Differential)	~ 5.2 mV/fC
Z_{IN}	110 Ω
Z_{OUT}	50 Ω
Rise time	~ 2 ns $(C_D = 24pF)$
Fall time	~ 13 ns $(C_D = 24pF)$
Noise	1350 erms $(C_D = 24pF)$
V_{SUPPLY}	4V
P_D	$\sim$ 30mW

Concerning the circuit implementation, since the channel density is low and a simple circuit topology can be used, an approach based on SMT technology can be adopted thus avoiding a specially designed (and expensive) ASIC development.

As an example, the simulation of a three stages transimpedance preamplifier based on SiGe transistors has been carried out. The first

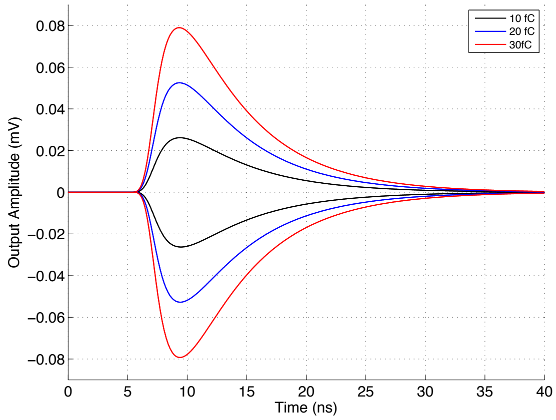

Figure 7.28: Preamplifier output for a 10, 20 and 30 fC test pulse ($C_{DET} = 24\ pF$)

stage dominant pole is around 26 MHz while other stages have been designed with wider bandwidth thus resulting in a good separation in terms of cutoff frequencies. The simulation results are given in Table 7.7 while Figure 7.28 shows the (simulated) output waveforms for 3 different input charges (10, 20 and 30 fC) injected through the test input.

7.4.3 Cluster Counting

The cluster counting technique is very powerful as it leads to an improved particle identification. To fully exploit the technique, individual ionization clusters must be identified.

In our system we use slow drift gas mixtures ($\sim$1 $\mu s/cm$), state of the art high sampling frequency digitizers (at least 1 GSPS) and fast processing (data throughput must sustain the Super$B$ expected 150 kHz average trigger rate). These modules require a large amount of power, forcing us to limit the number of channels to 8–16 channels per Amplifier Digitizing Board (ADB).

Moreover, fast amplifiers must be used on the preamplifier boards, which results in a larger power requirement than that of the SR. As a consequence, we are considering the use of a local liquid cooling system. The wide bandwidth requirement also impacts on the type of cables used to interconnect the preamplifiers with the ADBs and on the noise pick-up sensitivity of the full system . In addition, the use of cluster counting requires that the signal reflection in the sense wires must be eliminated. This is done by mean of termination resistors (R_T), which results in a lower limit on the system intrinsic noise.

Provided the cluster detection efficiency is sufficiently high, information from the cluster counting measurements can be used for tracking purposes. This requires storing the time of arrival at the sense wires of all the clusters, instead of simply counting them.

Specifications for the CC measurements, as for the SR, must be given on resolution, dynamic range and linearity.

Resolution The resolution of the digitizers depends on the lowest signal amplitude to be sampled and the system baseline noise. Assuming an average input signal of $\sim 6fC/e$ @ $3 \cdot 10^5$ gas gain, a preamplifier-shaper gain of 10 mV/fC and a safety factor of 2 to account for gas gain fluctuations, the average cluster signal is about 30 mV for a single electron. We can estimate the preamplifier ENC from that of the dominant noise source, which is the termination resistor. Assuming a $CR-RC$ shaping circuit and a 3 ns peaking time, we get an ENC of about 0.2 fC, that is about 2 mV rms for a preamplifier gain of 10 mV/fC. Thus a voltage resolution of about 2 mV allows good control of the system noise and of the cluster signals reconstruction.

Dynamic range The cluster counting method requires the observation of peaks (corresponding to the clusters) in the digitized signals. An upper limit of the signal dynamic range (discarding gas fluctuations) is then given by the expected total ionization. Helium based gas mixture have already been well characterized [15]. We can assume that a minimum ionizing particle (m.i.p.) crossing orthogonally a 1.2 cm square cell filled with a 90%He $-$ 10%iC_4H_{10} gas mixture, will generate on average about 22 electrons. Thus the dynamic range of an 8 bits ADC is fully adequate for cluster counting measurements.

Linearity As we are interested in finding (and tagging) signal peaks, a linearity of 2% fully satisfies the requirements.

7.4.3.1 Front End Electronics

The drift chamber FEE chain for cluster counting is similar to that for the SR. In this scenario, the electronics modules will be connected with mini coaxial cables. Because of the smaller number of channels per ADB, both the number of crates and ADBs will increases significantly (Tables 13.4 and 13.6).

On Detector Electronics Because preamplifier boards will host high bandwidth ($\sim$ 350 MHz) amplifiers, the layout and assembly are more difficult compared to the SR scenario. Particularly, special attention must be provided to avoid ground loops to minimize instabilities and external noise pickup. The baseline solution is the use of commercially available fast transimpedance amplifiers, but the design of a preamplifier based on high bandwidth and low-noise SiGe SMT transistors will be investigated as well.

7.5 High Voltage system

7.5.1 Main System and HV Distribution Boards

The high voltage distribution network will be located on the forward end-plate. The distribution board modularity will match the preamplifier modularity while the number of distribution boards connected to a single HV channel will depend on the layer (example: inner layers = 2 boards, outer layers = 5 boards).

The HV distribution system consists of power supplies and distribution boards, along with associated cables. The voltage will be supplied by a CAEN SY4527 Universal Multichannel System supply with 16 A1535N distribution boards, giving a total of 384 channels. This is sufficient granularity that a single channel failure will have a very small impact on detector performance. Spares of both the SY4527 and the A1535N will be available. The A1535N permits individual channels to operate in current-generator mode in case of over-currents. This feature was found to be extremely useful for the *BABAR* drift chamber as it permitted the chamber to handle locally high background rates without ramping down the chamber HV.

Individual HV channels are brought to the drift chamber from the A1535N boards via multistrand cables with A996 52 pin Radiall connectors at both ends.

The multiconductor cable connects to a filter box containing a low-pass filter, located at the inner radius of the forward enclosure. The individual channels are fanned out within the enclosure to the HV distribution boards (Sec. 7.3.7). Each HV channel supplies two or three 8-channel distribution boards, depending on the superlayer.

The HV distribution and sense wire termination circuit is shown in Figure 7.29. If termination is not used, the termination resistor (R_T) and the 500 pF capacitor per sense wire are removed.

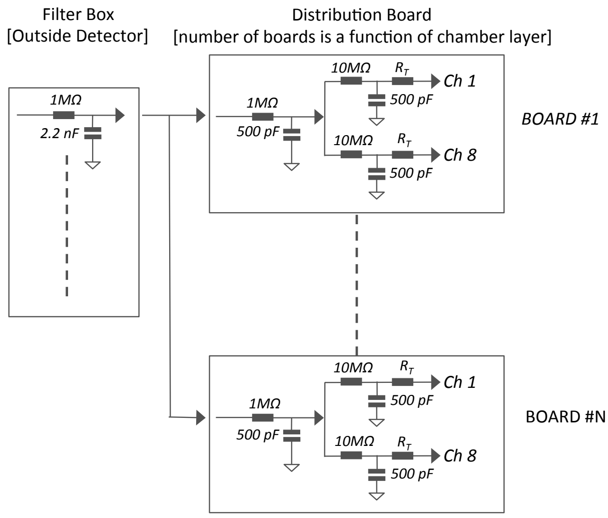

Figure 7.29: HV distribution network.

7.6 Gas system

The drift chamber is filled with a gas mixture of 90% helium and 10% isobutane. The gas system supplies the appropriate gas mixture to the chamber, while maintaining the required flow rate, pressure, purity, and composition stability. It includes safety items such as flammable gas sensors and release valves to protect the gas system, detector, and personnel from dangerous conditions caused by component failures or operator errors. To reduce the operating costs, 85% of the gas will be purified and recirculated.

The mixing will be done using mass flow controllers that will maintain the isobutane fraction at $(10.0 \pm 0.1)\%$. A parallel set of rotameters may be included to allow for high flow rate flushing. The system will allow a fraction of the flow to pass through a temperature-controlled water bath, which will be used if we decide to add water to help control the symptoms of aging.

The gas composition is verified using a set of analyzers to measure isobutane, oxygen, and water. The analyzer set will be able to sample gas at a variety of points in the gas system, such as before or after the gas enters the chamber or the filters.

This will be a recirculating gas system, which reduces operating costs and air pollution from the isobutane. The total flow will be 15 liters per minute, of which 2.5 liters per minute will be fresh gas. For a chamber volume of 5000 liters, this corresponds to four volume changes per day, or one volume of fresh gas every 1.5 days. The flow is controlled by an explosion-proof compressor, which is regulated to maintain a chamber pressure of 4.00 ± 0.05 mbar (0.4% of an atmosphere) above atmospheric pressure.

The primary gas lines between the gas mixing station and the detector will be welded and pressure-tested stainless pipe, 1.5 inches diameter. This will be reduced to 0.75 inch diameter in the cable trays through the detector. The input line is fanned out to 8 lines of 5 mm diameter on the rear endplate, while the output line is fanned out to 16 lines of 5 mm diameter on the forward endplate.

The gas returning from the detector passes through a palladium catalytic filter which removes oxygen by the reaction $13O_2 + 2C_4H_{10} \rightarrow 8CO_2 + 10H_2O$. The resulting water is removed by an alumino-silicate molecular sieve. The system contains two such sieves, so that one can be regenerated (i.e., have the absorbed water removed) by flushing with helium at elevated temperature without stopping operations. This filter system was originally built for the *BABAR* drift chamber and will be reused for Super*B*.

The gas temperature and pressure will be monitored at various points in the system, along with atmospheric pressure. These quantities will be used to calculate gain correction due to gas density. We will also monitor gas gain using a small, single-cell chamber that will be mounted on the return line from the chamber. Any variations in the current induced by an ^{55}Fe source after applying the density correction would indicate gain variations due to gas composition or chamber aging.

The majority of the gas system components will be in the gas hut (or room), which will be located at an exterior wall of the interaction hall. Two additional racks close to the detector will contain bubblers, pressure sensors, and valves. The gas storage areas will be outside, under cover, immediately adjacent to the hut. The isobutane, since it is flammable, will be stored in a physically separate area from the other gases. The isobutane tanks and lines will be heated and insulated.

The gas system includes an extensive safety system to protect personnel and equipment. This system will be reviewed and approved by the laboratory. Aspects of the safety system include:

- ventilation in the gas hut, which, when combined with flow restrictors on the lines into the hut, ensure that a leak cannot create an asphyxiation hazard.
- nitrogen flows in the exhaust lines and into the electronics enclosures on both endplates.
- flammable gas sensors in the gas hut and the bubbler rack.
- an oxygen sensor on the return line.
- bubblers and redundant pressure sensors to protect the chamber against over pressure.

- an independent helium line and regulator to protect the chamber against subatmospheric pressures.
- administrative controls on changes to the gas system.

The system is designed such that it will remain safe even during extended power outages. We will undertake regular maintenance and keep sufficient spare parts to ensure reliable operations.

7.7 Monitoring and Calibration

7.7.1 Monitoring

Environmental and systems-related parameters that are potentially time dependent will be continuously monitored while Super*B* is taking data. These will be collected asynchronously from the e^+e^- collision data stream within the experiment's "slow controls" system. The parameters will be redundantly monitored and include:

- temperature: four in the experimental hall; four on the outside of each gas enclosure bulkhead; four inside the gas enclosure at each end
- pressure: two in the experimental hall; two in each gas enclosure volume
- high voltage and current (read for each HV card)
- high voltage crate voltages, currents and temperatures (read for each HV card)
- preamplifier low voltage and current (read for each read-out board)
- digital electronics voltages, currents and temperature (read for each crate)
- discriminator levels set for cluster counting either in the FPGA or local derivative discriminator (one per channel)
- oxygen, helium, isobutane and H_2O concentrations in the gas system at the input and output lines of the drift chamber
- average ^{55}Fe pulse heights from two gas quality monitoring chambers, one on the input the other on the output gas line of the drift chamber
- cooling system monitors: temperature and pressure on the input and output lines and immediately before and after the chamber

The quantities will be averaged over each minute and made available to the data-taking shift crew and drift chamber experts in the form of digital "strip charts". These will be actively monitored by specialized software and stored in a database for future examination. The annual data volume will, at most, be a few Gigabytes. The active monitoring will read the quantities and determine if a quantity is outside tolerance. If a monitored quantity falls outside its tolerance band, the shift crew will be alerted by an alarm alerting them to the need for action.

The gas quality will be monitored using the pulse height information from the ^{55}Fe source in the two monitoring chambers. Problems with the gas mixture will be revealed by changes in the gas gain after correcting for expected changes in gas density associated with atmospheric pressure, or perhaps experimental hall temperature, changes.

In addition to these environmental and systems-related parameters, the drift chamber will be actively monitored to ensure that it is operating properly. Histograms of the number of hits per cell integrated over 10 minutes for High Level Trigger events will provide on the order of 10^3 hits per cell for an event rate of 25 kHz (based on the High Level Trigger accepting a cross-section of about 25 nb for the $10^{36}\mathrm{cm}^{-2}\mathrm{s}^{-1}$ design luminosity). This will provide the ability to monitor if any given cell's occupancy deviates by more than about 10% from nominal every ten minutes. In addition, histograms of the number of hits per layer can be used to monitor if a drift chamber layer's occupancy deviates by more than a percent every minute. Specialized software will alert the shift crew if cell and layer occupancies fall outside tolerances. Trigger rates for triggers using the drift chamber will also be monitored and used to establish that the drift chamber is operating as expected.

The monitoring of some quantities made available by the online reconstruction, such as D^0 and K^0_S mass peaks, m_{ES}, and ΔE will also be used to validate drift chamber operational integrity.

7.7.2 Calibration

The time-to-distance relations will be calibrated initially with cosmic ray muons. Each cell will have its own calibration, although cells with a common electrostatic configuration are expected to have the same time-to-distance parameters. Comparisons of parameters of those families of cells will provide a measure of quality assurance of the calibration process.

When beams are colliding, low multiplicity physics events, such as $e^+e^- \to \mu^+\mu^-$ and Bhabha events, will be used to calibrate the time-to-distance relations and the calibrations will be continuously updated at a rate determined by the luminosity. The dE/dx calibrations will use physics events in which kinematics provide a cleanly identified particle. For example, $\phi \to K^+K^-$, $K^0_S \to \pi^+\pi^-$, and $D^{*+} \to \pi^+D^0$, $D^0 \to K^-\pi^+$ can be used to select kaons and pions; and $\Lambda \to p\pi^-$ can be used to select protons. Control samples of leptons for particle identification calibration are provided by $e^+e^- \to \mu^+\mu^-\gamma$ and $e^+e^- \to e^+e^-\gamma$ events. These same control samples will be used to calibrate the optimal parameters in the cluster counting algorithm used for particle identification.

7.8 Integration

7.8.1 Overall geometry and mechanical support

The envelope of the drift chamber is determined by the tungsten shield and the DIRC at the inner and outer radii, and by the backward calorimeter and the FTOF in the negative and positive z directions. There are 5 mm radial clearances between the drift chamber and the surrounding components, and 5 mm clearance between the drift chamber envelope and the backward calorimeter. The FTOF is directly mounted onto the drift chamber. The envelope in the backward direction includes the space occupied by the signal cables after they exit the enclosure.

In *BABAR*, the chamber was supported at the backward end by turnbuckles connected to the inner surface of the DIRC central support tube (CST). We envision using a similar system, although the actual mounting points used by *BABAR* will be obscured by the backward calorimeter.

In the forward direction, the drift chamber and FTOF form an integrated mechanical package supported by the CST. Figure 7.30 shows the mounting components used by the *BABAR* drift chamber. Note that the support point on the DIRC is on the z end surface of the CST, not the inner radius. Because the Super*B* chamber is shorter in the forward direction than *BABAR*, the corresponding support tabs will be on the FTOF, not the chamber.

7.8.2 Installation and alignment

The chamber and FTOF will be installed prior to the forward and backward calorimeters and the tungsten shielding. The installation will reuse the existing *BABAR* equipment, which is currently stored at SLAC. The chamber is supported at the inner radius and slid along a supporting beam that passes through the inner cylinder (Figure 7.31).

Both forward and backward enclosures will contain a number of precision 6 mm dowel holes into which target holders for corner-cube reflectors can be mounted. The enclosures in turn are doweled to precise reference holes on the endplates, referencing the target locations to the sense wire locations.

The mounting systems at both ends allow for several mm of adjustment in x and y. The chamber location will be adjusted to center the chamber in x and y on the interaction point and to align the sense wire direction with the magnetic field. The tolerances on these alignments have not yet been specified. The mounting system fixes the chamber location in z at the forward end, but permits a small amount of motion at

Figure 7.30: Mechanical mounting points for the *BABAR* drift chamber on the forward (Top) and backward ends (Bottom). Both ends are attached to the DIRC central support tube.

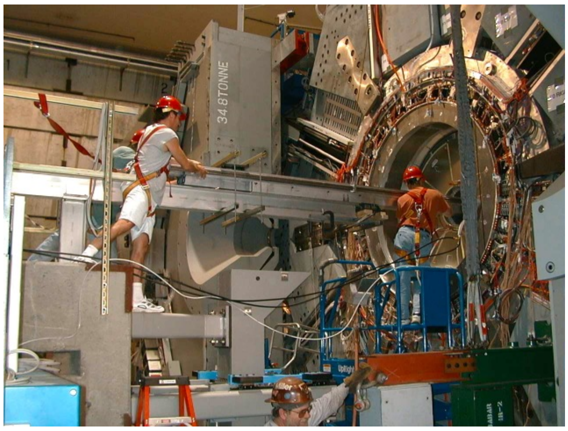

Figure 7.31: *BABAR* drift chamber during installation. The same tooling is available for use by Super*B*.

the backwards end in case of relative thermal expansion. The tolerance on the location in z will be significantly looser than those on x and y.

7.8.3 Services

The services required for the backward end are listed below. These will reach the backward enclosure via 16 slots in the outer radius of the steel plug located within the DIRC strong tube. Each slot will be approximately 50 mm in radius by 250 mm wide. Cables continuing to the digitizing crates, located on the top of the detector, will be routed to wireways at the end of the IFR iron immediately after exiting the DIRC strong tube.

Note that within the radial extent of the backward calorimeter, the signal cables (and all other services) are routed to stay within the drift chamber envelope.

- Signal cables: approximately 8000 coaxial cables, RG-179, 2.54 mm in diameter, organized into 8-cable ribbons. These are 10 m in length, and travel to the digitizing electronics crates.

- Calibration cables: RG-179, one for every eight signal channels. Also originate at the digitizer crates.

- Low-voltage power: Four 1/0 welding cables, 14.7 mm diameter. Originate in the electronics hut.

- Cooling lines: 16 lines (8 separate circuits, each with a supply and a return line), 26.2 mm reinforced PVC. The sub-atmospheric water-based cooling system (Sec. 7.3.7) will be close to the detector, but outside of the radiation area.

- Drift gas: one line, 19 mm diameter stainless steel. Originates in the gas hut. This line increases to 38 mm diameter after exiting the detector.

- Nitrogen flush gas: two lines, 19 mm diameter stainless steel. Also from the gas hut.

The services for the forward end will exit the detector in the radial space between the tungsten shield and the FCAL. The services for the forward region are:

- High voltage: 16 56-conductor cables, 14 mm diameter. Originate at the HV supplies in the electronics hut.
- Drift gas: one line, 19 mm diameter stainless steel. Originates in the gas hut. This line increases to 38 mm diameter after exiting the detector.
- Nitrogen flush gas: two lines, 19 mm diameter stainless steel. From the gas hut.
- Cooling lines: 2 lines, 19 mm reinforced PVC. From the cooling system.

7.9 Bibliography

[1] B. Aubert et al., (BABAR collaboration), "The BABAR detector", *Nucl. Instrum. Meth.* A479:1–116, 2002, doi:10.1016/S0168-9002(01)02012-5, arXiv:hep-ex/0105044 [hep-ex].

[2] G. Sciolla et al., (BABAR Drift Chamber collaboration), "The BABAR Drift Chamber", *Nucl. Instrum. Meth.* A419:310–314, 1998, doi:10.1016/S0168-9002(98)00804-3.

[3] A. H. Walenta, "The time expansion chamber and single ionization cluster measurement (talk)", *IEEE Trans. Nucl. Sci.* 26:73–80, 1979.

[4] P. Rehak and A. Walenta, "Relativitic rise measurement by cluster counting method in time expansion chamber (talk)", *IEEE Trans. Nucl. Sci.* 27:54–58, 1980.

[5] C. Fabjan, W. Willis, I. Gavrilenko, S. Maiburov, A. Shmeleva, et al., "Practical prototype of a cluster counting transition radiation detector", *Nucl. Instrum. Meth.* 185:119, 1981, doi:10.1016/0029-554X(81)91202-7.

[6] A. H. Walenta, "Performance and development of dE/dx counters (talk)", *Phys. Scripta* 23:354–370, 1981, doi:10.1088/0031-8949/23/4A/006.

[7] A. Dellacqua, G. Parrour, S. Giani, P. Kent, A. Osborne, et al., "GEANT-4: An Object oriented toolkit for simulation in HEP", 1994.

[8] R. Veenhof, *Garfield - simulation of gaseous detectors* CERN-W5050, Version 9.

[9] D. Peterson et al., "The CLEO III drift chamber", *Nuclear Instruments and Methods in Physics Research Section A: Accelerators, Spectrometers, Detectors and Associated Equipment* 478(1-2):142 – 146, 2002.

[10] M. Adinolfi, F. Ambrosino, A. Andryakov, A. Antonelli, M. Antonelli, et al., "The tracking detector of the KLOE experiment", *Nucl. Instrum. Meth.* A488:51–73, 2002.

[11] L. Malter, "Thin film field emission", *Phys. Rev.* 50:48–58, Jul 1936, doi:10.1103/PhysRev.50.48.

[12] "The T2K experiment", *Nuclear Instruments and Methods in Physics Research Section A: Accelerators, Spectrometers, Detectors and Associated Equipment* 659(1):106 – 135, 2011, doi:10.1016/j.nima.2011.06.067.

[13] A. Sharma and F. Sauli, "Low mass gas mixtures for drift chambers operation", *Nucl. Instrum. Meth.* A350:470–477, 1994, doi:10.1016/0168-9002(94)91246-7.

[14] C. Avanzini et al., (KLOE collaboration), "Test of a small prototype of the KLOE drift chamber in magnetic field", *Nucl. Instrum. Meth.* A449:237–247, 2000, doi:10.1016/S0168-9002(99)01372-8.

[15] P. Burchat and J. Hiser, "Studies of helium gas mixtures in drift chambers", September 1991, report SLAC-PUB-5626, SCIPP 91/25.

8 Particle Identification

8.1 Summary of Detector Performance goals

8.1.1 DIRC Detector concept

The DIRC (Detector of Internally Reflected Cherenkov light) [1, 2] is an innovative detector technology that has been crucial to the performance of the *BABAR* science program. The main DIRC performance parameters are the following: (a) measured time resolution of $\sim$1.7 ns per photon, driven by the photomultiplier (PMT) transit time spread (TTS) of 1.5 ns; (b) single photon Cherenkov angle resolution of 9.6 mrad for tracks from di-muon events; (c) Cherenkov angle resolution of 2.5 mrad per track in di-muon events; and (d) π/K separation greater than 2.5σ over the entire track momentum range, from the pion Cherenkov threshold ($\sim$130 MeV/c for fused silica) up to 4.2 GeV/c. The *BABAR* DIRC performed reliably and efficiently over the whole *BABAR* data taking period (1999-2008). Its physics performance remained consistent throughout the whole period, although some upgrades, such as the addition of shielding and replacement of electronics, were necessary to cope with evolving machine conditions.

This excellent DIRC performance did not come without substantial effort, and this experience is useful when designing the next DIRC-like detector. To maintain the background at an acceptable level in *BABAR*, it was necessary to: (a) apply a tight timing cut of $\pm$8 ns around the expected arrival time of each Cherenkov photon; (b) add substantial shielding around the beam pipe under the DIRC, which reduced the PMT background by at least a factor of $\sim$6; (c) install many background detectors (here we found, for example, that the rate in neutron detectors correlates with the DIRC background very well, indicating a common origin); and (d) improve operation of the machine.

After $\sim$10 years of operation, the PMT gain was reduced by $\sim$45% in total, but the tubes operated well until the end, requiring only a few voltage adjustments to correct for the gain loss [3]. The electronics dead time was limited to $\sim$1% at a rate of a few MHz per PMT [4].

Excellent flavor tagging will continue to be essential for the program of physics anticipated at Super$B$, and the gold standard of particle identification in this energy region is that provided by internally reflecting ring-imaging devices (the DIRC class of ring imaging detectors). The challenge for Super$B$ is to retain (or even improve) the outstanding performance attained by the *BABAR* DIRC [4], while also gaining an essential factor of at least 100 in background rejection to deal with the much higher luminosity.

A new Cherenkov ring imaging detector is being planned for the Super$B$ barrel; it is called the Focusing DIRC, or FDIRC. It will reuse the existing *BABAR* bar boxes and mechanical support structure. Each bar box will be attached to a new photon 'camera', which will be optically coupled to the bar box exit window. The new camera design combines a small modular focusing structure that images the photons onto a focal plane instrumented with very fast, highly pixelated PMTs [5].

To cope with the higher luminosity, the sensitivity of the FDIRC photon camera to background will be reduced by an overall factor of 250 compared to the *BABAR* DIRC. Indeed,

- it is 25× smaller in volume than the DIRC water-based camera;
- its new, highly pixelated photon detectors will be about 10× faster;
- the photon camera is built using radiation-resistant fused silica material – instead of

water or oil which is more sensitive to neutron background.

Other important characteristics of the FDIRC are the following: (a) the entire system will have $\sim$18,000 pixels (each photon detector includes 32 pixels with 48 detectors per photon camera and 12 sectors total); (b) it will reconstruct photons in 3D (two space coordinates and time); (c) although the Cherenkov angle can be reconstructed using the pixel information only, time will be included in the final PID likelihood hypothesis, which incorporates both particle time of flight and photon propagation time in the FDRC system; (d) time also plays an important role in FDIRC to reduce the background, and (e) the expected timing resolution of $\sigma\sim$200 ps makes it possible to reduce the chromatic broadening of the Cherenkov angle resolution by 0.5-1 mrad, depending on the photon propagation path angle and length.

Although *BABAR* had no PID in the forward direction, several options have been considered for a possible PID detector for Super$B$ to cover the acceptance hole in the forward direction: (a) "DIRC-like TOF" time-of-flight (FTOF) [6, 7], (b) pixelated TOF [8] and (c) Aerogel RICH [9]. As discussed later in this chapter, the Super$B$ collaboration has determined there is physics merit in reserving a longitudinal gap of $\sim 5-10$ cm for a forward PID device and tentatively identified the Dirc-like FTOF, which is based upon the TOF technique, as the leading candidate technology. Tests of a full-scale prototype of one sector of the FTOF detector are foreseen for the near future; if they are successful, the FTOF will be included in the Super$B$ baseline. See section 8.4 for more information on this topic.

8.1.2 Charged Particle Identification

Charged particle identification at Super$B$ relies on the same framework as the *BABAR* experiment, utilizing several detectors in addition to the specific PID systems being described in this chapter. Electrons and muons are identified by the EMC and the IFR respectively, aided by dE/dx measurements in the inner trackers (SVT and DCH). Separation for low-momentum hadrons is primarily provided by dE/dx. At higher momenta (above 0.7 GeV/c for pions and kaons, above 1.3 GeV/c for protons) the dedicated systems being described here, the FDIRC – inspired by the successful *BABAR* DIRC – will perform most of the π/K separation in the barrel region, aided by dE/dx information from the tracking devices. The forward system, if included, would utilize similar combinations of detectors. The FDIRC and possible FTOF are described in the remainder of this chapter. More details about the properties of other Super$B$ detectors can be found in the corresponding TDR chapters.

8.2 Particle Identification Overview

8.2.1 Experience with the *BABAR* DIRC

The *BABAR* DIRC – see Figure 8.1 – is a novel ring-imaging Cherenkov detector. The Cherenkov light angular information, produced in ultra-pure synthetic fused silica bars (average refraction index 1.473), is preserved while propagating along the bar via internal reflections to the camera (called the 'StandOff Box' in the figure, SOB for short) where an image is produced and detected.

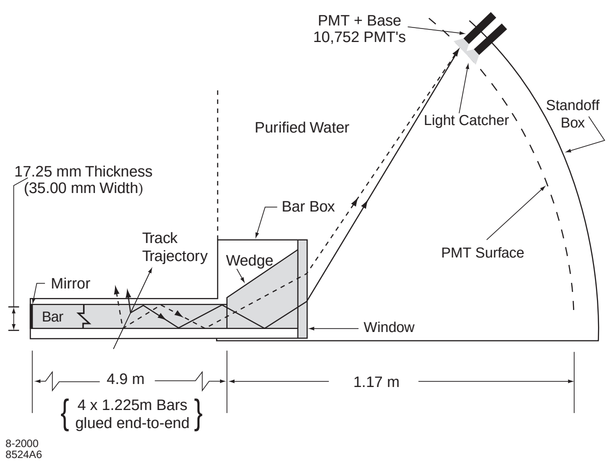

Figure 8.1: Schematic of the *BABAR* DIRC.

The entire DIRC contains 144 quartz bars, each 4.9 m long. They are aligned along the beam line and cover the whole azimuthal range. Thanks to an internal reflection coefficient of ~0.9997, a small absorption coefficient in the bulk material, and orthogonal bar faces, Cherenkov photons are transported to the back end of the bars with the magnitude of their angles conserved with only a modest loss of photons. They exit into a pinhole camera consisting of a large volume of purified water (a medium chosen because it is inexpensive, transparent, and easy to clean, with average index of refraction and relative chromatic dispersion reasonably close to those of the fused silica). The photon detector PMTs are located at the rear of the SOB, about 1.2 m away from the quartz bar exit window.

The reconstruction of the Cherenkov angle uses information from the tracking system together with the positions of the PMT hits in the DIRC. Information on the time of arrival of hits is used to reject background; to resolve ambiguities due to the unknown path of a given photon in the quartz; and also provides some limited direct PID information.

8.2.2 Barrel PID: Focusing DIRC (FDIRC)

As discussed above, the PID system in Super$B$ must cope with much higher luminosity-related background rates than in *BABAR* – current estimates are on the order of 100 times higher. The basic strategy is to make the camera much smaller and faster. A new photon camera imaging concept, based on focusing optics, is therefore envisioned. The focusing blocks (FBLOCK), responsible for imaging the Cherenkov photons onto the PMT cathode surfaces, will be machined from radiation-hard pieces of fused silica. The major design constraints for the new camera are the following: (a) it must be consistent with the existing *BABAR* bar box design, as these invaluable components will be reused in Super$B$; (b) it must coexist with the *BABAR* mechanical support and the Super$B$ magnetic field constraints; (c) it requires very fine photon detector pixelation and fast photon detectors.

Imaging is provided by a mirror structure focusing onto an image plane containing highly pixelated PMTs. The reduced volume of the new camera and the use of fused silica for coupling to the bar boxes (in place of water as in the *BABAR* SOB), is expected to reduce the sensitivity to background by about a factor of ~25 compared to *BABAR* DIRC. The very fast timing of the new PMTs and of the associated readout chain is expected to provide many additional advantages: (a) improvement of the Cherenkov resolution using the combination of photon propagation time and particle time of flight; (b) a measure of the chromatic dispersion term in the radiator [10, 11, 12] which leads to improved performance; (c) better separation of ambiguous solutions in the folded optical system; and (d), an additional factor of 10 in background rejection.

Figure 8.2 shows the new FDIRC photon camera design (see Ref. [5, 13, 14, 15] for more details). It consists of two parts: (a) a focusing block (FBLOCK) with cylindrical and flat mirror surfaces, and (b) a new wedge. The wedge at the end of the bar rotates rays with large transverse angles in the focusing plane before they emerge into the focusing structure. The old *BABAR* wedge is too short so that an additional wedge element must be added to insure that all rays strike the cylindrical mirror. The cylindrical mirror reflects all rays onto the FBLOCK flat mirror, preventing reflections back into the bar box itself; the flat mirror then reflects rays onto the detector focal plane with an incidence angle of almost 90°, thus avoiding reflections. The photon detector plane is located in a slightly under-focused position to reduce the FBLOCK size and therefore its weight. Precise focusing is unnecessary, as the finite pixel size would not take advantage of it. The total weight of a bare solid fused silica FBLOCK is about 80 kg. This substantial weight requires good mechanical support.

There are several important advantages gained in moving from the *BABAR* pinhole focused design with water coupling to a focused

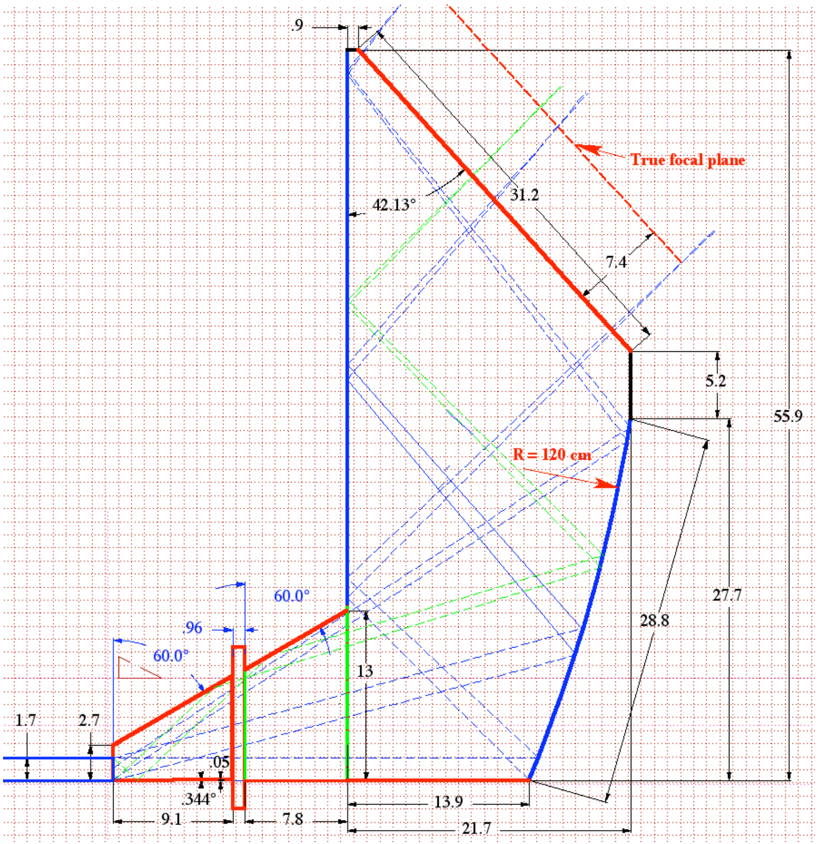

(a) FDIRC optical design (dimensions in cm).

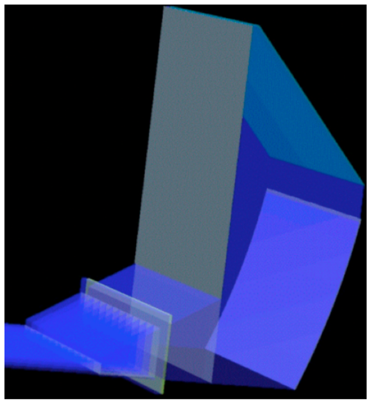

(b) Its equivalent in the GEANT4 MC model.

Figure 8.2: Barrel FDIRC Design.

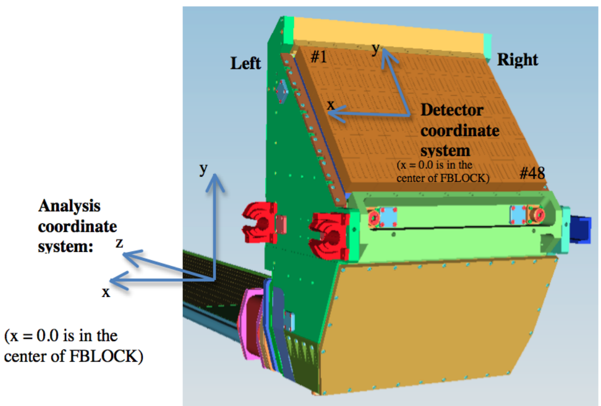

Figure 8.3: FDIRC coordinate systems used in this chapter.

optical design made of solid fused silica: (a) the design is modular; (b) as explained above, the sensitivity to background, especially to neutrons, is significantly reduced; (c) the pinhole-size component of the angular resolution in the focusing plane is removed by focusing with a cylindrical mirror; (d) the total number of photomultipliers is reduced by about one half compared to a non-focusing design with equivalent performance; (e) there is no risk of water leaks into the Super*B* detector, and no time-consuming maintenance of a water system, as was required to operate *BABAR* safely.

Figure 8.3 shows the FDIRC coordinate system as used in this document.

Each new camera will be attached to its *BABAR* bar box with optical RTV glue, which will be injected in a liquid form between the bar

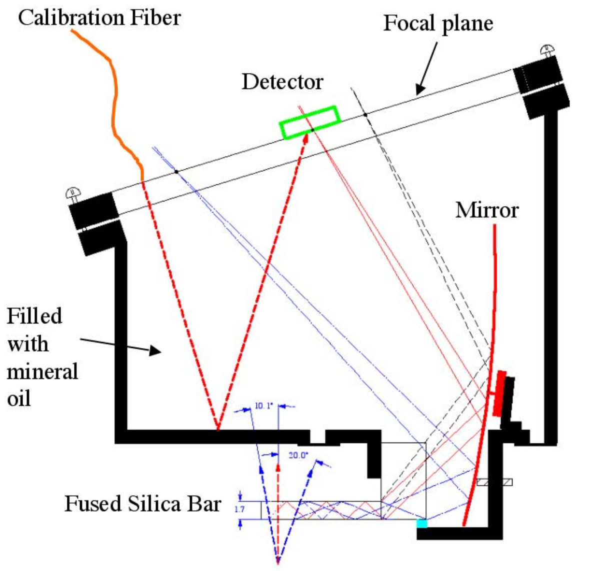

Figure 8.4: The first FDIRC single-bar prototype employing a spherical mirror, an oil-filled photon camera, and highly-pixelated photon detectors [10, 11, 12].

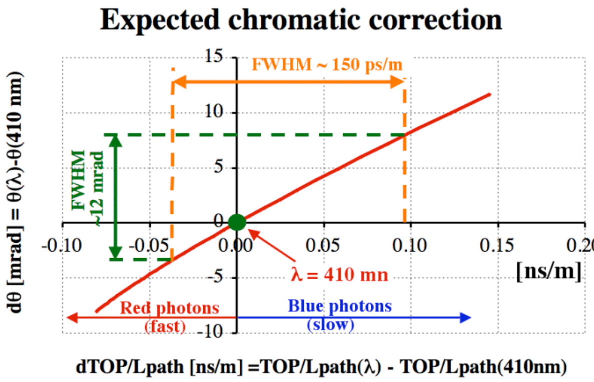

Figure 8.5: Analytical correlation between the variation of the Cherenkov angle and the change in time-of-propagation (TOP), relative to the mean wavelength of 410 nm [10, 12].

box window and the new camera, and cured in place. As Figure 8.2 shows, the cylindrical mirror focuses in the radial y-direction, while pinhole focusing is used in the direction out of the plane of the schematic (the x-direction). Photons that enter the FBLOCK at large x-angles reflect from the parallel sides, leading to additional ambiguities. However, the folded design makes the optical piece small, and places the photon detectors in an accessible location, improving both the mechanics and the background sensitivity. Since the optical mapping is 1 to 1 in the y-direction, this "folding" reflection does not create an additional ambiguity. Since a given photon bounces inside the FBLOCK only 2-4 times, the requirements on surface quality and polishing for these optical pieces are much less stringent than those required for the DIRC bar box radiator bars.

As an intermediate step towards an upgrade of DIRC for the Super$B$ detector, we have built and tested a first FDIRC prototype (see Figure 8.4), in order to learn how to design a more compact 'DIRC' with new highly-pixelated fast

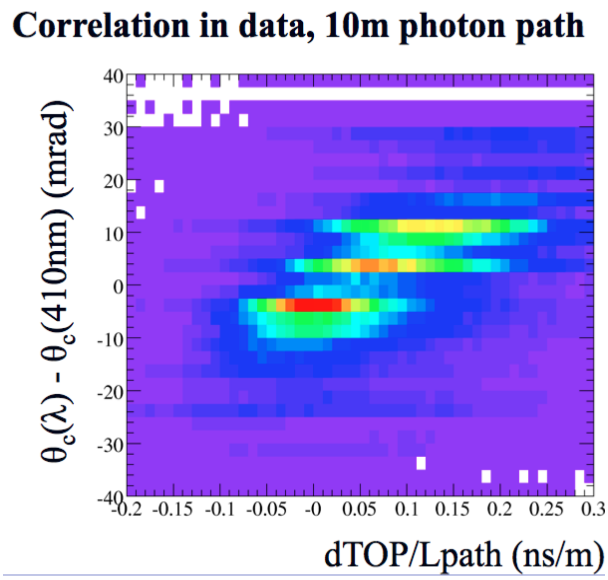

Figure 8.6: The same correlation between the change of the Cherenkov angle and the change in TOP for photons propagating 10 meters in the bar, as seen in the beam test data in the first FDIRC prototype [10, 12].

PMTs [10, 12]. This prototype demonstrated for the first time that chromatic correction could be done with timing. The principle is displayed in Figure 8.5, showing the analytical correlation between the change of the Cherenkov angle and the change in time-of-propagation (TOP), relative to the mean wavelength of 410 nm. Figure 8.6 shows the same plot using data from photons propagating 10 meters in the bar. Figure 8.7 shows the final result of the chromatic correction in the beam test data. One can see that the chromatic correction improves the Cherenkov angle resolution by 0.5-2 mrad depending on the photon propagation path length: the longer the path, the more efficient the correction. To achieve such result, a single photoelectron timing resolution of ~200 ps (provided by H-8500 or H-9500 multi-anode PMTs, MaPMTs) is required.

We also demonstrated from the first prototype that the Cherenkov ring has worse resolution in the wings than in the center, due to the optical aberration caused by the bar, which is amplified by the mirror. Figures 8.8 and 8.9 show that this simulated error contribution goes from 0 mrad (at ring center) to ~9 mrad (near the ring wings) and that it is z-dependent. This

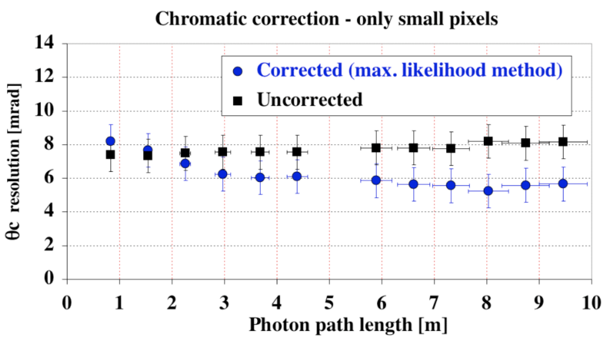

Figure 8.7: Beam test data showing the effect of the chromatic correction for 3 mm × 12 mm pixels obtained with H-9500 MaPMTs in the first FDIRC prototype. Note that the Super$B$ active region starts over 2 meters away from the camera detector end. Results with the H-8500 MaPMTs are similar, but with slightly worse resolution [10, 12].

aberration is present in the non-focusing *BABAR* DIRC as well, but it is smaller, *i.e.*, the mirror amplifies this effect. The effect is similar for spherical, parabolic and spherical mirrors. For more details see Ref. [13, 14, 15].

Each DIRC wedge inside an existing bar box has a 6 mrad angle at the bottom. This was done intentionally in *BABAR* to provide simple stepwise "focusing" of rays leaving the bar towards negative y to reduce the effect of bar thickness. However, in the new optical system, having this angle on the inner wedge somewhat worsens the design FDIRC optics resolution. Figure 8.10 shows the result of a simulation with Mathematica [13, 14, 15]; it shows three images, one from the bottom of bar, one from the bottom of the old wedge, which has inclined surface, and one from top of the old wedge. There are two choices: (a) either leave it as it is, or (b) glue a micro-wedge at the bottom of the old wedge, inside the bar box, to correct for this angle. Though (b) is possible in principle, it is far from trivial, as the bar box must be opened. Because of this difficulty we have decided to exercise option (a).

Figure 8.11 shows a Cherenkov ring image for one of the central bars in the new FDIRC. The ring image is more complicated than those from the *BABAR* DIRC or from the first FDIRC prototype. This is due to reflections from the sides of the FBLOCK, and the pattern is different for each bar in a given bar box. The ring radius is not used in the analysis; instead, we use a dictionary of MC assignments for each pixel. These assignments are generated by placing a

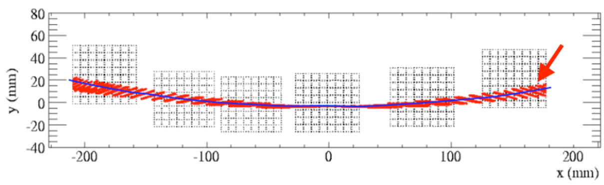

Figure 8.8: Simulated optical ring aberration near the ring wings for the first FDIRC prototype with overlaid detectors and their pixels showing that it is a substantial effect [10].

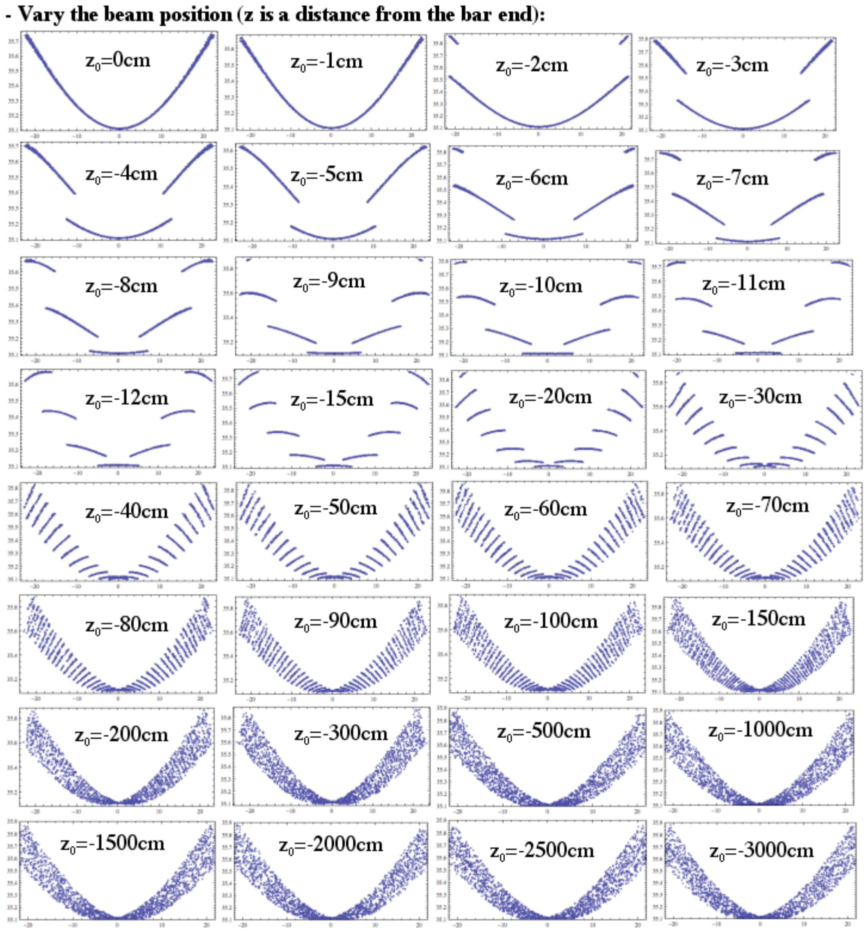

Figure 8.9: Simulated optical ring aberration near the ring wings for the first FDIRC prototype as a function of the beam position along the bar (z coordinate) [13, 14, 15].

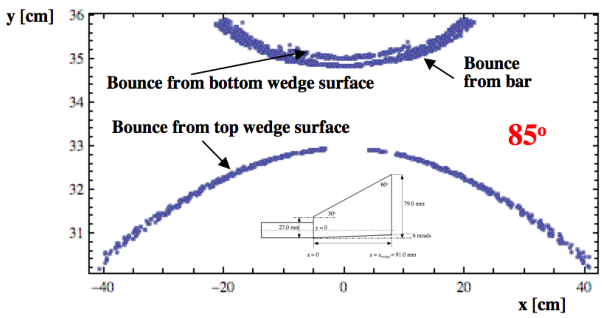

Figure 8.10: Split of Cherenkov ring caused by the inclined bottom surface of the old (*BABAR*) wedge [13, 14, 15].

random photon source in one bar at a time and checking which pixels were hit by these photons. In this way, we create pixel assignments of $\hat{k}_{\mathrm{pixel}} = (k_x, k_y, k_z)$. One can also generate time-of-propagation for direct and indirect photons $\mathrm{TOP}_{\mathrm{direct}}$ and $\mathrm{TOP}_{\mathrm{indirect}}$ for tracks with $\theta_{dip} = 90°$ and crossing each bar at $z = z_{\mathrm{middle}}$. For any track direction $\hat{k}_{\mathrm{track}}$, one can then calculate the Cherenkov angle simply as a dot product of two vectors: $\cos\theta_C = \hat{k}_{\mathrm{track}} \cdot \hat{k}_{\mathrm{pixel}}$. This procedure has been used successfully with the first FDIRC prototype in the cosmic ray telescope with 3D tracking [16]. In the final physics analysis, the measured photons for each track will be tested against probability distribution functions (PDFs) for each particle hypothesis.

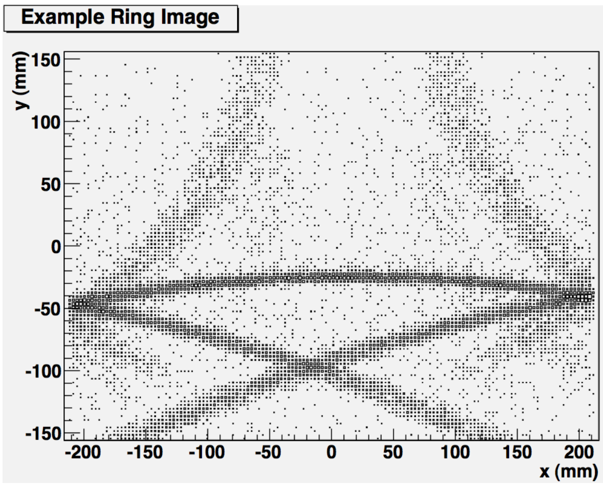

Figure 8.11: Cherenkov ring image from GEANT4 for tracks with $\theta_{\text{dip}} = 90°$ in the central bar at 4 GeV/c [17].

8.3 The Barrel FDIRC Detector Overview

8.3.1 Photodetectors

Photon Detector choice There were three photon detectors under consideration: the H-8500 (64 pixels), the H-9500 (256 pixels) and the R-11265-00-M64 (64 pixels) multi-anode PMTs (MaPMT) by Hamamatsu. At present, we have selected the 12-dynode H-8500 tube from several reasons: a) it is the tube preferred by the medical community and is therefore produced in a larger quantity, b) it has a much smaller unit price than the H-9500 MaPMT, c) it has a smaller single electron timing spread (σ_{TTS} ~140 − 160 ps for H-8500 vs. σ_{TTS} ~220 ps for H-9500), d) it can be obtained with somewhat enhanced quantum efficiency (QE~24% for H-8500 vs. ~20% for H-9500), e) it has more uniform gain response across its face (2:1 for H-8500 vs. 5:1 for H-9500), and f) Hamamatsu strongly recommends not to consider H-9500 tube to keep a reasonable delivery schedule of large quantities. On the other hand, the H-9500 MaPMT can provide finer sampling in the y-direction and thus a significantly better Cherenkov angle resolution. We should keep it on the list of possible tube choices.

The Hamamatsu tube, R-11265-00-M64, came up recently for a consideration [18]. Its main attractions are (a) Super-bialkali QE of 36%, (b) small 2.8 mm pixels, which would allow a thiner binning in y-direction, and therefore a better Cherenkov angle resolution, and (c) small dead space around tube boundaries. We would combine 8 small pixels horizontally to create wide pixels in the x-direction, where we do not have focusing; at the same time we would keep the same total number of electronics channels in the system. We will test this tube and decide later. It would require 2304 tubes (12 photon cameras and 48 × 4 tubes per camera) of this type in the FDIRC system. One should add that Hamamatsu also makes R-11265-00-M16 tube, which has the same pixel size as H-8500 tube. It would still be useful to consider this tube as it has a Super Bialkali QE, and we would benefit from using it. But smaller pixel size tubes are preferred at given QE.

The performance of the new FDIRC is simulated with a GEANT4 based program [17]. Preliminary results for the expected Cherenkov angle resolution (for single photons) are shown in Table 8.1 for different layouts [5]. Design #1 (a 3 mm × 12 mm pixel size with the micro-wedge glued in) gives a resolution of σ~8.1 mrad per photon for 4 GeV/c pions at 90° dip angle. As explained earlier, the micro-wedge option was supposed to remove a ~6 mrad inclined surface on the old wedge. Since the micro-wedge will not be used, options #1 and #3 are excluded. Option #3 is still considered and possibly chosen if a suitable PMT candidate is found in future. Presently, the selected option is #4, which would give σ~9.6 mrad per photon. This would be a performance about the same as in *BABAR* DIRC [4]. However, if the chromatic correction would be implemented successfully, one could reduce the error by 0.5-2 mrad depending on the photon path length [12].

During the prototyping stage we used the H-8500C version of the H-8500 tube, which has an internal resistor chain and a HV cable. In the

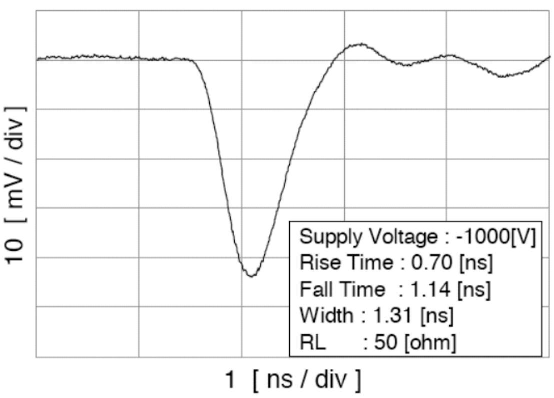

(a) H-8500 MaPMT single electron pulse without an amplifier (response to a 30 ps laser pulse at 407 nm).

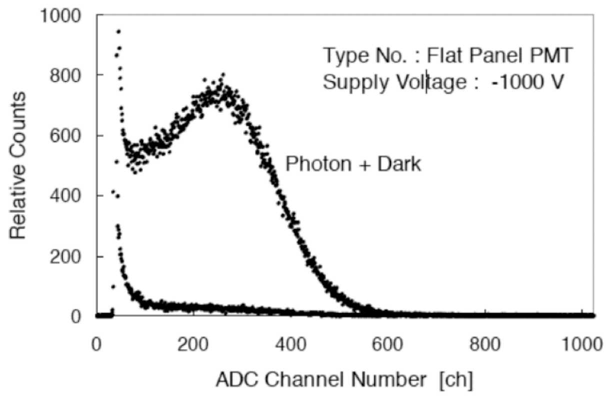

(b) H-8500 MaPMT single electron pulse height spectrum.

Figure 8.12: H-8500 MaPMT single electron pulse, noise and single electron pulse height distribution, Hamamatsu data [19].

Table 8.1: GEANT4 MC simulation of the FDIRC performance (single photon resolution) [17].

FDIRC Design	Option	θ_C resolution [mrad]
1	3 mm×12 mm pixels with a micro-wedge	8.1
2	3 mm×12 mm pixels and no micro-wedge	8.8
3	6 mm×12 mm pixels with a micro-wedge	9.0
4	6 mm×12 mm pixels and no micro-wedge	9.6

final application, we plan to use the H-8500D version of this tube, which receives HV via local pins, which allows an easy distribution of HV among 48 tubes in the photon camera. This tube comes with a 1.5 mm-thick Borosilicate glass window with a spectral sensitivity between 300 and 650 nm. We would ask Hamamatsu to select a minimum QE of ∼24%. The dark anode current of this tube is very low (0.1 nA per pixel and 6 nA total), and the after-pulse rate is also almost negligible. Given the design of the dynode structure of H-8500 MaPMT preventing direct ion back-flow to the photocathode, we expect an usual cathode PMT aging behavior. It is not as good as in a classical PMT dynode structure, but expected to be close to it. We should confirm this by doing aging tests in the future.

It is important to state that all measurements presented in the following section were done with various electronics setups, which are not the Super*B* final electronics, *i.e.* many conclusions are somewhat preliminary.

Figure 8.12 shows (a) a single photoelectron pulse from H-8500 before the amplification at ∼1.0 kV, (b) a single electron pulse height spectrum. As one can see on the plot, the rise time of H-8500 tube is about 0.7 ns. Figure 8.13 shows the SLAC amplifier used for these tests. Hamamatsu points out that the pulse height spectra

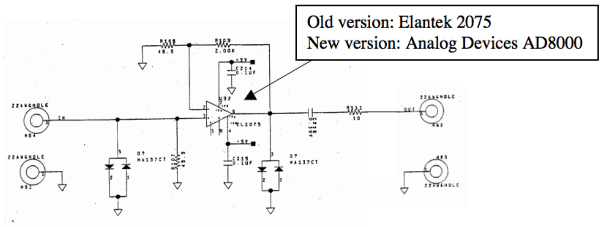

Figure 8.13: SLAC amplifier used in all FDIRC prototypes, both in the SLAC test beam or for the CRT tests. The amplifier has a rise time of about 1.5 ns and a gain of $\sim$40×.

are not uniform across all pixels in the H-8500 tube. How this effect translates into the detection efficiency depends on the type of electronics, noise level and threshold; it will be studied in detail in the FDIRC prototype, first using the SLAC amplifier with the IRS-2 waveform digitizing electronics [20], and then be compared to the Super*B* CFD electronics [21]. One should pay attention to areas in between pixels where pulse height is smaller due to charge sharing. One needs a sufficient electronics gain to get full efficiency.

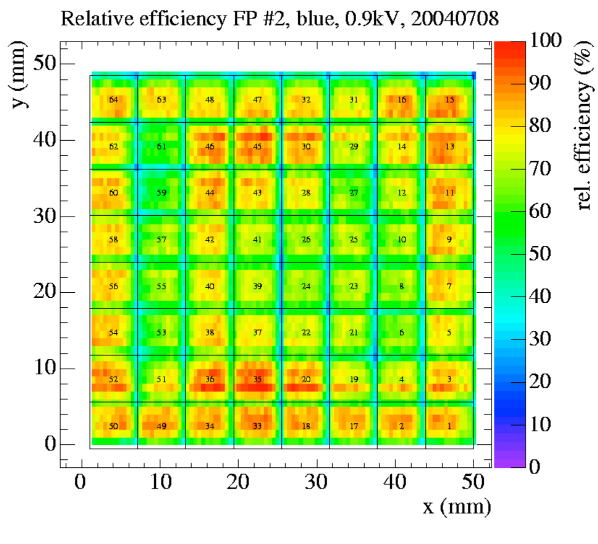

Figure 8.14: Single photoelectron efficiency of an entire H-8500 tube, normalized to the highest efficiency spot within this particular tube [22].

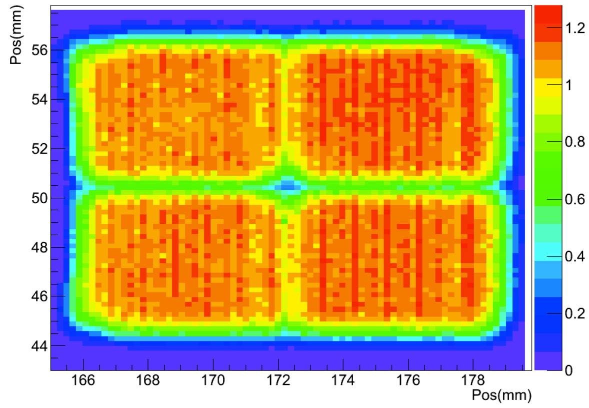

Figure 8.15: Detailed efficiency scan of four pixels in H-8500 tube, normalized to the XP2020 tube [23].

Figure 8.14 shows the single photoelectron efficiency of a H-8500 tube, operating at -0.9 kV and normalized to the highest efficiency spot within this particular tube [22]. This plot was obtained with a SLAC amplifier, a version with two Elantek 2075 chips (a voltage gain of 130×); notice that there is no significant drop in the detection efficiency around pixel edges. There is the efficiency drop in between pixels. This has been recently confirmed with another detailed scan [23] shown on Figure 8.15. The data analysis and scope measurements indicate that some photoelectrons are lost due to the focusing electrode. Figure 8.18 shows the focusing electrode geometry; it can steer electrons one way or another relative to the pixel boundary, and somewhat diminishes the effect of charge sharing. All these issues need to be evaluated carefully with the final electronics and for final tube deliveries.

We plan to short two neighboring pixels in the x-direction, as there is only pinhole focusing available, and thus create 6 mm × 12 mm pixels (H-8500), providing 32 readout channels per tube. Each photon camera would have 48 H-8500 MaPMT detectors, which corresponds to a total of 576 tubes for the entire Super*B* FDIRC, resulting in 18432 pixels total. Figure 8.16 shows the H-8500 tube pixel geometrical layout.

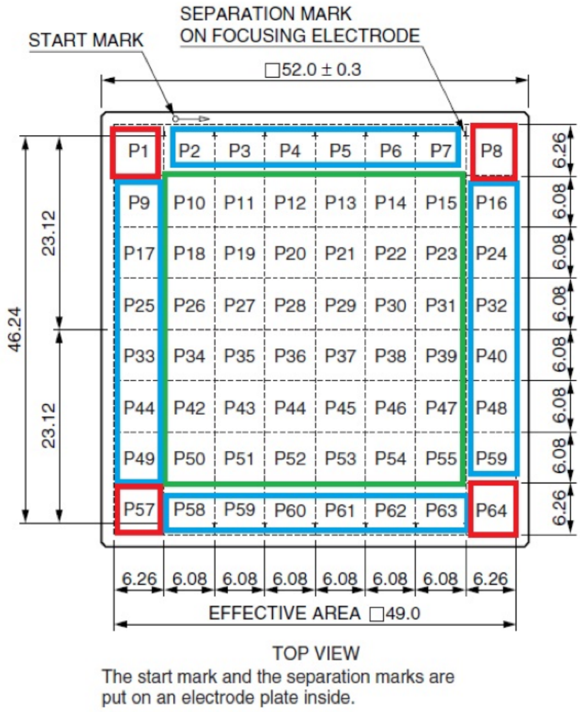

Figure 8.16: The nominal H-8500 pixel geometry.

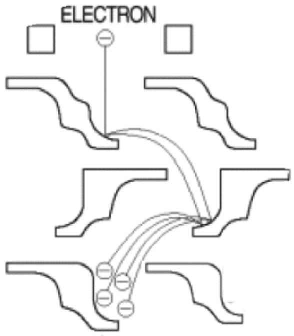

Figure 8.18: The H-8500 electrode structure including focusing electrodes.

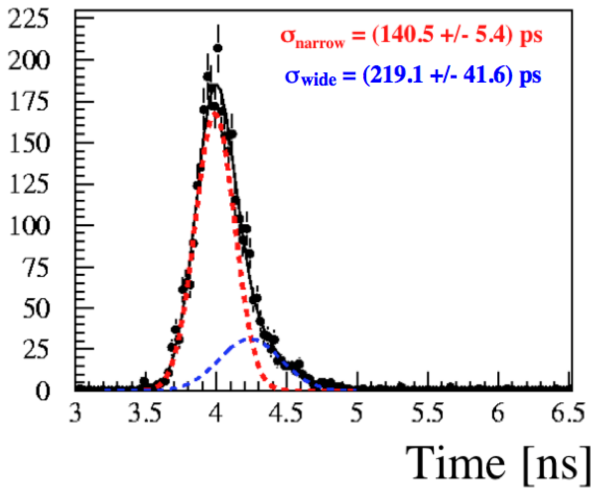

Figure 8.17: The H-8500 single photoelectron transit time resolution is σ_{TTS}~140 ps [22], if one fits the distribution with a double-Gaussian function.

Figure 8.17 shows the H-8500C tube TTS timing resolution with single photoelectrons, indicating σ_{TTS} ~140 ps [22], obtained with a laser pointing to the center of a pixel. Hamamatsu data sheets for H-8500 tube indicates a value for the full width at half maximum (FWHM) of ~400 ps, which gives σ_{TTS} ~170 ps, using a single Gaussian fit. Another measurement comes from R. Montgomery showing an average H-8500 tube TTS resolution of σ_{TTS} ~154 ps [24]. We measured σ_{narrow} ~140 ps and σ_{wide} ~270 ps [23]. They also show that the TTS resolution depends on the position within a given pixel [25], which is driven by the PMT electrode structure, shown on Figure 8.18.

The electrode structure and PMT edge effects and gain variation generally degrade the overall TTS resolution, so one should probably assume that the single photoelectron timing resolution is more like 200-250 ps. This agrees with Figure 8.19 where we plot TTS timing resolution in the first FDIRC prototype [22], where laser photons populate the entire H-8500 face, *i.e.*, pixels were hit uniformly, including their edges. Figure 8.4 shows how the laser calibration was done in the first FDIRC prototype. This plot probably represents what will be a real TTS performance in practice. Notice also that edge pixels tend to have worse resolution.

This timing performance, coupled to the electronics timing resolution contribution of $\sigma_{\mathrm{Electronics}}$ ~100 ps, allows corrections of the chromatic error for photon path length of more than 2 meters [12].

There are two effects to take into account when considering interaction between two neighboring pixels: the pixel-to-pixel cross-talk, and the charge sharing avalanche between two pixels. The neighbor pixel-to-pixel single photoelectron cross-talk was measured to be ~3% of the primary pixel signal, when a laser light was placed on the center of a pixel while looking at its neighbor – see Figure 8.20. This test used a newer SLAC amplifier with AD8000 chip – see Figure 8.13. However, the pixel-to-pixel cross-talk is even more complex in multi-anode tubes [24]. Figure 8.21 shows that the cross-talk depends on the position within a pixel. This will clearly require more study with the FDIRC final electronics. We had hoped to use the charge sharing, which is related to the avalanche size, to reduce the size of pixels in the y-direction by charge interpolation. However, the attempt to use charge sharing was not successful for this particular tube as it has entrance focusing electrodes defining pixel boundaries, which sweep electrons away from pixel boundaries, *i.e.* Hamamatsu has designed the MaPMT electrode structure in such a way to suppress the charge sharing in these tubes. Both H-8500 and H-9500 have this charge sharing-suppressing feature. Such feature does not exist in MCP-PMT detectors.

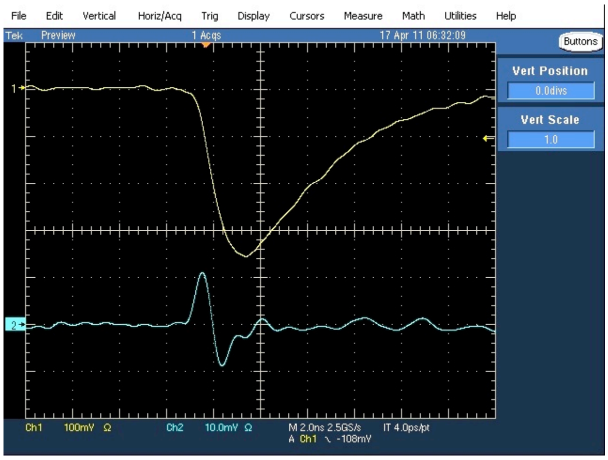

Figure 8.20: The H-8500 tube pixel-to-pixel single electron cross-talk was measured to be ~3%, when the laser light was placed on the center of a pixel while looking at its neighbor [26].

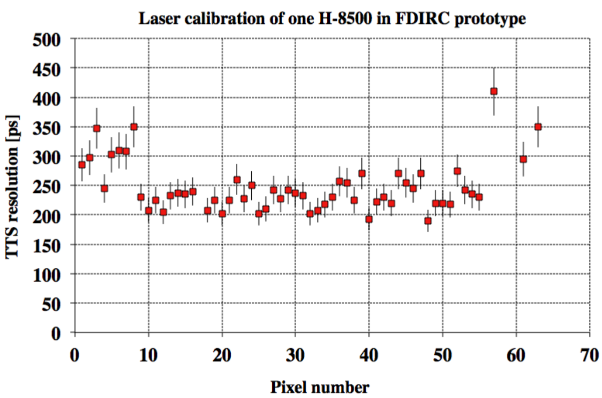

Figure 8.19: The H-8500 single photoelectron transit time resolution across all pixels from a particular tube [22].

Another special feature of all MaPMT detectors is a double Polya distribution, one corresponding to a photoelectron produced at the cathode and the amplification using all 12 dynodes (this is the nominal distribution), and another one corresponding to a case that a photon produces a photoelectron striking the very first dynode rather than at the photocathode, and the amplification is only using 11 dynodes instead of 12. Missing one amplification stage produces a gain 2-3 smaller than the nominal amplification process, while the pulses arrive 2-2.5 ns earlier (see Figure 8.23 [26]). Figure 8.24 shows a time spectrum of normal photoelectrons produced at the cathode, pre-pulse spectrum produced at the first dynode arriving ~2.5 ns earlier, and back-scattered photoelectrons arriving ~6 ns later [29]. Similar measurements indicate that this timing spectrum depends on the position within the pixel [23], *i.e.* whether the photoelectron hits the focusing electrode or moves in between two – see Figure 8.25. However, one should point out that we are dealing with logarithmic scale and that the total rate of off-time pulses is less than a few percents. Figures 8.22 show the resulting single electron

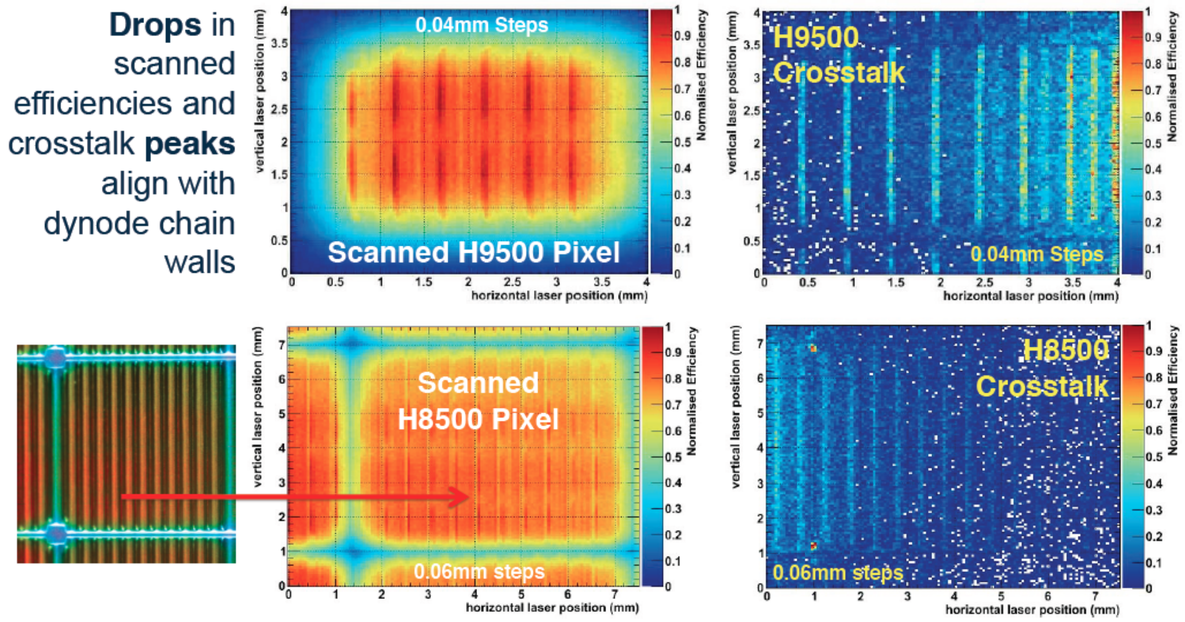

Figure 8.21: The observed periodicities in single electron efficiencies and cross-talk are aligned with the dynode electrode structure [24].

pulse height spectra which exhibit either a small shoulder near the pedestal at lower gain [28], or a clear double-Polya distribution at higher gain [27]. Although the pre-pulses are a nuisance, they can be used as normal photoelectrons in the Cherenkov ring analysis and their time can be calibrated out.

Figure 8.26 shows that the H-8500 tube gain range is $1-3\times10^6$ for nominal operating voltage of $-1.0\,\mathrm{kV}$ [26]. There is a variation of gain from pixel-to-pixel due to non-uniformities in the multi-anode structure.

Figure 8.27 shows scans of 15 tubes [26], operating at -1.0 kV and -1.1 kV, amplifier gain of $\sim$40$\times$, a threshold electronics of -25 mV, and indicates that typically the best-to-worst single electron detection efficiency might vary as much as 2:1 across the H-8500 PMT face. This is compared to the anode current response across all pixels to a fixed high photon flux (Hamamatsu data). This figure also shows the efficiency maps of 15 tubes [26], all operating at -1.0 kV, with an amplifier gain of 40$\times$, with a simple threshold electronics, and normalized to the Photonis Quantacon XP2262/B PMT. It indicates that the best-to-worst detection efficiency variation is as much as 2:1 across the H-8500 PMT face. One should stress that the detection efficiency relative to the Quantacon XP2262/B PMT is typically at a level of 40-50% for the worst pixels, and 80-100% for the best pixels.

Figure 8.28 shows how the H-8500 tube single electron detection efficiency depends on voltage [26]. One can see that the detection efficiency can be improved by 10-20% per 100 V increase.

There are three possible ways to deal with the pixel-based gain non-uniformity: (a) process each tube, equipped with the final electronics, in a scanning setup; record the individual relative efficiency values and store them into an analysis database, or (b) adjust a discriminator threshold on each pixel, or (c) adjust an amplifier gain on each pixel. This concept has yet to be worked out in detail as this effect depends on details of the final electronics. When doing the overall gain adjustment, one should remember that the absolute maximum voltage on H-8500 is -1.1 kV (Hamamatsu recommendation). We want to set the initial voltage low enough to

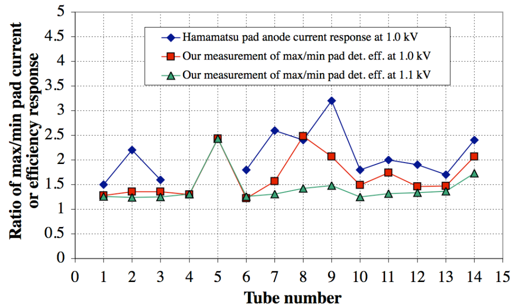

(a) Max-min efficiency uniformity across pixels of 15 PMTs. This is compared to anode current max-min response across 64 pixels to a fixed photon flux.

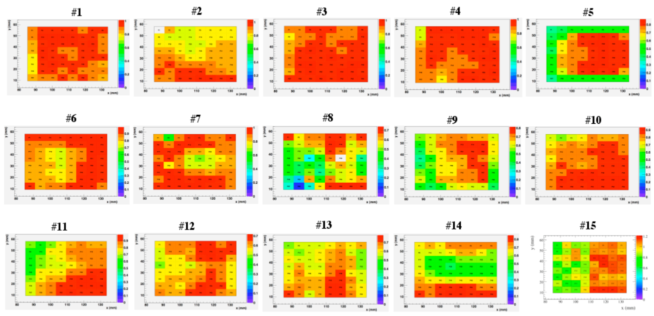

(b) Relative efficiency scan of H-8500 tubes operating at −1.0 kV, normalized to XP2262/B PMT.

Figure 8.27: 2D single electron detection efficiency across pixels of 15 H-8500 tubes [26].

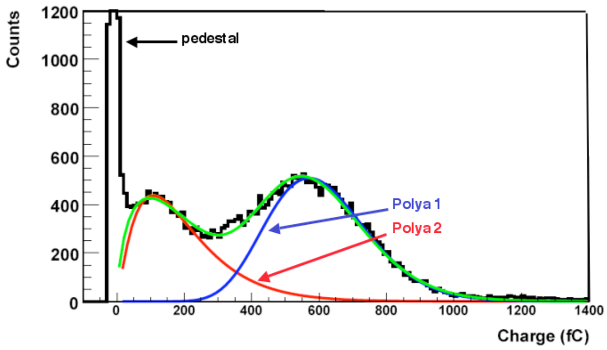

(a) Double-Polya fit to single electron distribution as observed in R7600-03-M16 MaPMT. The lower peak originates from photoelectrons which are missing one amplification stage in the MaPMT [27].

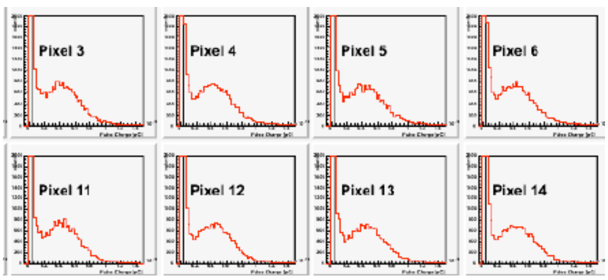

(b) Single electron distributions in H-8500 MaPMT. The lower peak shows up only as a shoulder [28].

Figure 8.22: Single electron pulse height distribution in MaPMTs.

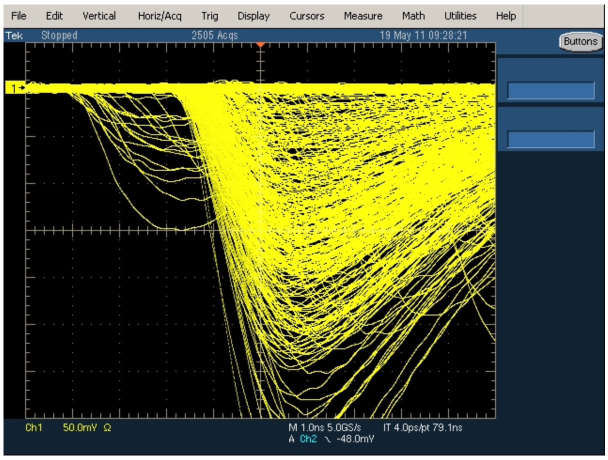

Figure 8.23: The H-8500 single electron prepulses corresponding to a case when a photon produces a photoelectron at the very first dynode rather than at the photocathode, and the amplification is using only 11 dynodes instead of 12 [26].

have some headroom for later period, when the detector will loose gain due to aging.

Prediction of number of photoelectrons per ring Figure 8.29 shows the FDIRC wavelength bandwidth [5]. One can see that we operate in the visible wavelength region and that the effective filter is the Epotek 301-2 epoxy. Assuming a peak QE of 24%, and no optical grease

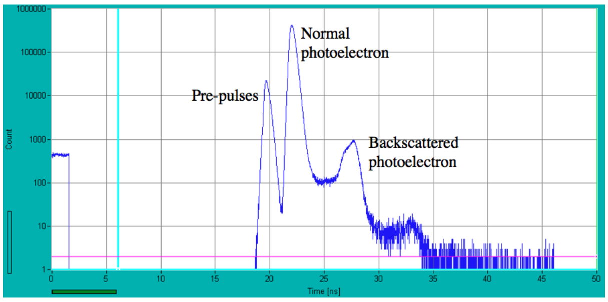

Figure 8.24: The H-8500 single electron time spectrum showing normal photoelectrons, pre-pulses and the back-scattered photoelectrons [29].

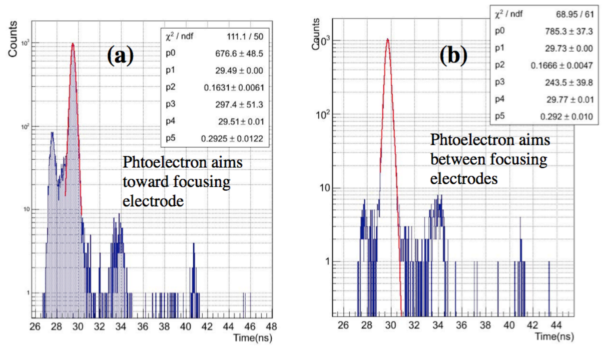

Figure 8.25: The H-8500 single electron time spectrum depends on the photoelectron position relative to the focusing electrodes [23].

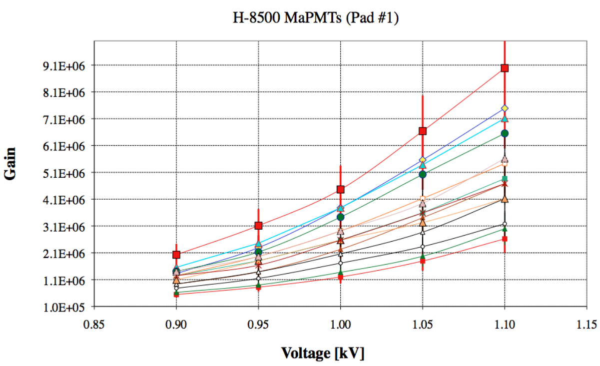

Figure 8.26: The H-8500 tube gain range and dependence on voltage for 14 tubes using pixel 1 (see Figure 8.16 for its location) in each tube [26].

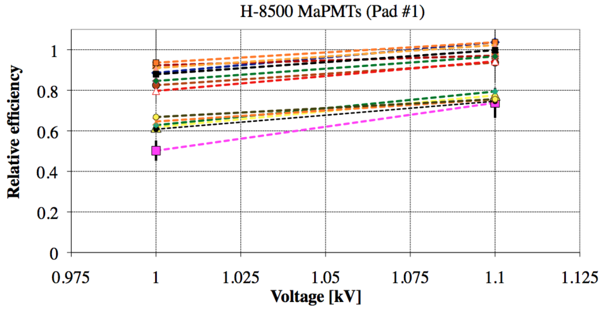

Figure 8.28: The H-8500 single electron detection efficiency dependence on voltage [26].

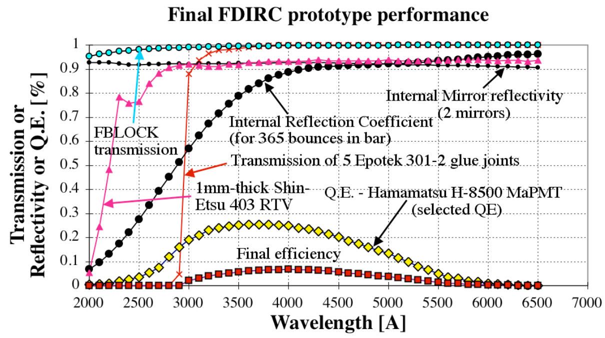

Figure 8.29: The FDIRC wavelength response is limited on low wavelength side by the Epotek 301-2 glue used to glue bars together [5].

coupling between PMTs and the FBLOCK, one obtains ∼32 photoelectrons for di-muon tracks with $\theta_{\text{dip}} = 90°$ using a simple spreadsheet calculation. Figure 8.31 shows the MC simulation of the number of photoelectrons as a function of the dip angle [17]. At $\theta_{\text{dip}} = 90°$ it predicts ∼27 photoelectrons.

Modularity: photodetector mechanical packing fraction There are two factors to consider when determining the photon coverage: (a) detection coverage in the focal plane of the photon camera, and (b) coverage within each tube (we will consider detection losses within the dynode structure later). Figure 8.30 shows the H-8500 matrix of 48 tubes in one photon camera. The size of each H-8500 tube is 52.0 ± 0.3 mm, and the gap between each tube is ∼0.5 mm; this gives a contribution to the packing fraction of

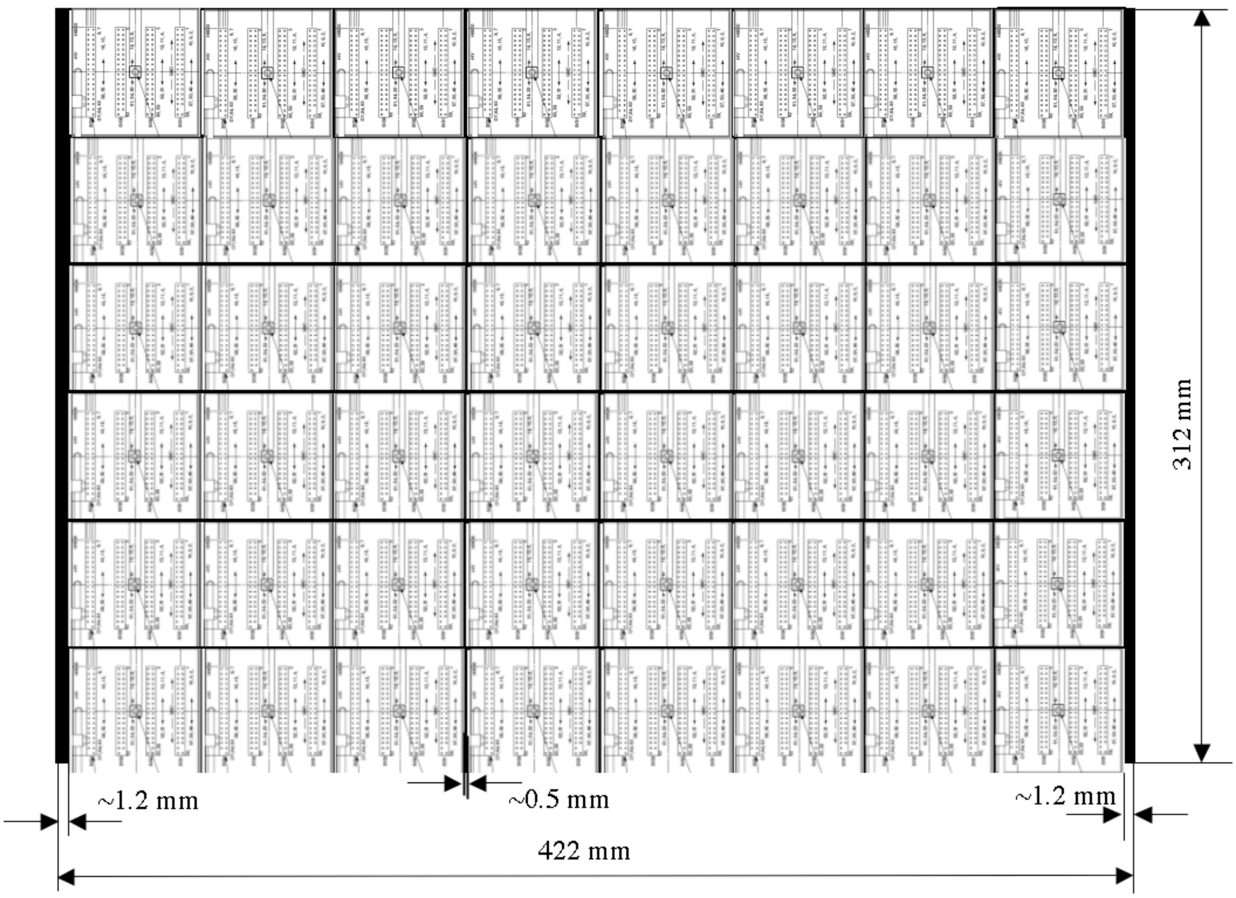

Figure 8.30: Detector matrix on one FDIRC detector camera with 48 H-8500 MaPMTs. The entire FDIRC system needs 576 such tubes for a total of 18,432 pixels [5].

~98.6%. The photon packing density (effective area/external size) within each tube is ~89%. These factors give the overall photon packing efficiency of ~88% for the photon camera based on 48 H-8500 tubes.

Optical coupling of detectors to FBLOCK MC simulation shows (see Figure 8.31) that we loose 8-25% of photons if we do not optically couple PMTs to the FBLOCK [17]. The event Cherenkov angle resolution (σ~2.94 mrad) improves by ~10% with optical coupling [17]. On the other hand, an access to a single failed detector would become complicated. If we use optical coupling, we are considering eight vertical segments, each handling six detectors; each segment could be removable by sliding it vertically off the FBLOCK. In addition, we have not yet selected the optical coupling grease. One should realize that any leak of the grease on the FBLOCK side optical surfaces, would result in a serious loss of photoelectrons. The optical coupling concept has yet to be tested to investigate its practicality, reliability and radiation hardness, and therefore this remains an open issue.

Temperature requirements There are two major sources of heat in the detector enclosure: (a) HV resistor dividers, and (b) electronics. Each tube has a HV divider. All dividers together draw ~9 W per 48 tubes, which is a small amount of heat. Assuming for now that the electronics will dissipate ~500 W per 48 detectors. We will need a water-cooled heat exchanger.

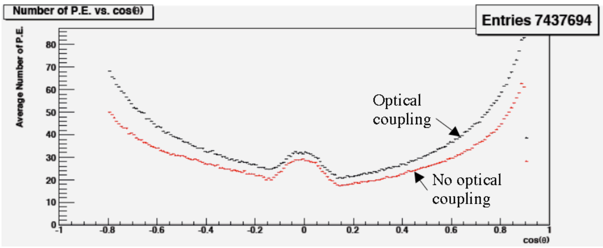

Figure 8.31: Simulated (GEANT4 MC) number of detected photoelectrons as a function of the polar angle for two cases: with and without optical coupling between detector face and the FBLOCK [17].

Another worry is what happens if we loose cooling. Based on tests with the FDIRC prototype detector enclosure, the temperature would rapidly climb beyond ~80°C. That would be dangerous for tubes, optical grease coupling, glues and that could also create mechanical stresses. Therefore, we need an automatic power shutoff system.

Rates and aging issues in H-8500 PMTs One strong point of our design is that we share a total photon background load from a single bar box among 48 H-8500 detectors, and this results in acceptable rates, even at the highest luminosity, and an acceptable total charge load after 10 years of operation.

We use two methods to estimate the FDIRC rates: (a) an empirical scaling (ES) from Belle-I Aerogel counter rates, assuming that the background rate scales as the luminosity. (b) We use the Super*B* MC simulation, which simulates all physics background processes involved in the background production and includes the precise modeling of beam line magnet components all the way up to 16 meters from the interaction point (IP) in either direction. It uses the correct FDIRC geometry with a proper handling of optical photons and includes all background shielding of the photon camera. The ES method is rather close to the MC prediction: 75 kHz (ES) vs. 60 kHz (MC) per double-pixel, or 2.4 MHz (ES) vs. 1.9 MHz (MC) per tube, which would correspond to the total accumulated charge of 1.3 C/cm^2 (ES) vs. 1.2 C/cm^2 (MC) for a total integrated luminosity of L_{int} ~50 ab^{-1}. Table 8.2 summarizes rates under various conditions. Figure 8.33 shows the FDIRC shielding design.

As far as the neutron background on the FDIRC front end electronics (FEE), the MC predicts a rate of 3.3×10^{10} n/cm^2/year of 1 MeV-equivalent neutrons with our up-to-date shielding. This makes the use of SiPMTs detectors for the photon camera impossible. However, this rate is tolerable for the FDIRC electronics.

One should point out that it is very crucial to shield the FDIRC photon camera, located outside of the magnet. Its contribution would be 550 kHz (MC) per double-pixel without shielding. Before the final shielding was put into the MC simulation, the dominating background was due to the Bhabha scattering, and the contribution of the Touschek effect was one order of magnitude smaller. After the shielding was added, all background contributions are at similar level.

Given the design of the H-8500 dynode structure, which aims at preventing a direct ion backflow to the photocathode, we expect that MaPMT tube cathode-aging rate to be similar to usual PMT aging behavior, which means that the above numbers appear to be safe. For example, *BABAR* DIRC PMTs accumulated at least ~150 C per tube during ~10 years of *BABAR* operation, the PMT gain was reduced by ~45% in total, but tubes operated well until the end, with a few voltage adjustments to correct for the gain loss [3]. The above estimates mean that each H-8500 tube would accumulate about 1.3 C of charge during the Super*B* data taking, which is considered a relatively small amount. However, one should point out that aging tests are yet to be done for the H-8500 tube. Figure 8.32 shows the Hamamatsu aging data for R8400-00-M64 MaPMT running at 100 μA for 10,000 hours and operating at -1.0 kV. There is no obvious large effect which could not be corrected by a voltage adjustment.

One should also worry about unusual background conditions caused by the machine misbehavior, changes in tune, beam losses, etc., especially in the early periods before reaching the full luminosity. Hamamatsu recommends that the absolute maximum current be $\sim$100μA per tube or $\sim$2μA per pixel. Another constraint is the capability of the electronics to cope with high rates. The Super*B* FDIRC electronics can handle rates up to $\sim$20 MHz per pixel, if one pixel is firing, and up to $\sim$2.5 MHz per tube if all pixels are firing.

Background shielding to protect FDIRC electronics & photon detectors The aim of this shield is to reduce the background contribution from the FBLOCK, located outside of the magnet. To design the shielding, two main constraints have to be taken into account: first, to allow an easy access to detectors and electronics, and then to minimize the overall weight of the shielding. Figure 8.33 shows the FBLOCK shielding design, which was also modeled in the MC simulation. It consists of 10 cm of Boron-loaded polyethylene layer sitting on 10-15 cm lead-steel sandwich, both located on inner radius and front side of the FBLOCK with its detectors and electronics. The front section of the shielding is moving on the magnetic door allowing a quick access to electronics and detectors – see Figure 8.33.

Magnetic shield of H-8500 PMTs For *BABAR* DIRC PMTs, which have a classical PMT dynode design, it was necessary to keep the magnetic field below $\sim$1 gauss in the SOB to prevent a serious degradation of pulse height spectra [4].

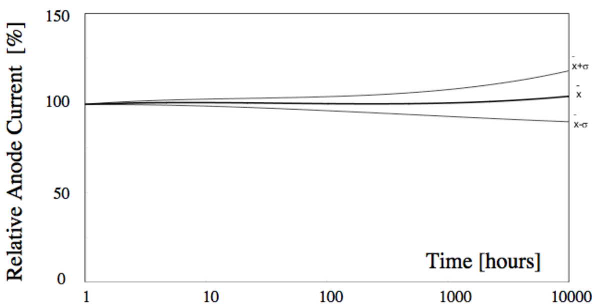

Figure 8.32: Hamamatsu data for R8400-00-M64 MaPMT showing that there is no large drop in photo-current when running 100μA for 10,000 hours ($\sim$400 days).

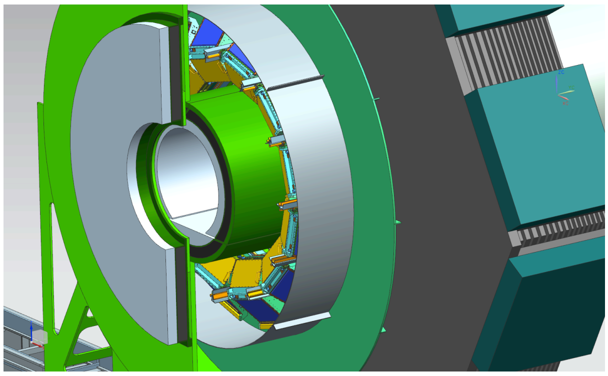

Figure 8.33: Details of local shielding around the FDIRC photon camera (a layer of 10 cm of Boron loaded polyethylene followed by 10-15 cm of lead-steel sandwich, located both on inner and front sides of the FBLOCK with its detectors and electronics).

To do that, it was necessary to enclose the entire photon camera into a large magnetic shield. Figure 8.34 shows the effect of the magnetic field on the H-8500 tube pulse height. One can notice that the effect is different near the tube boundary compared to its central region. We conclude that we can tolerate a residual magnetic field up to a level of a few gauss with no effect on the pulse height. We plan to use a magnetic shield similar to that of *BABAR*.

Radiation damage of optical components We used a ^{60}Co source for the irradiation of the glue samples. First, we have investigated the radiation damage of Corning 7980 Fused Silica 3 mm-thick coupons used for support of glue samples and, as expected, found no loss of transmission up to 250 krad. Figure 8.35 shows the irradiation of the Epotek 301-2 epoxy, used for coupling of the new Wedge to the bar box window, and the Shin-Etsu 403 RTV, used for coupling of the FBLOCK and the new Wedge. We show that these glues are acceptable, although the Epotek 301-2 shows a loss of transmission at $\sim$ 245 krad [30].

8.3.2 Laser calibration system

Optics of calibration The aim of this calibration is twofold: (a) to check the opera-

Table 8.2: MC prediction of FDIRC pixel rates, integrated charge dose and tube current, with and without shielding at tube gain of 10^6.

Shielding	Double-pixel rate	Tube rate	Total charge dose	Current
Yes	60 kHz	1.9 MHz	$1.3\ \mathrm{C/cm^2/50\ ab^{-1}}$	$0.3\ \mu\mathrm{A/tube}$
No	550 kHz	17.8 MHz	$12.7\ \mathrm{C/cm^2/50\ ab^{-1}}$	$2.8\ \mu\mathrm{A/tube}$

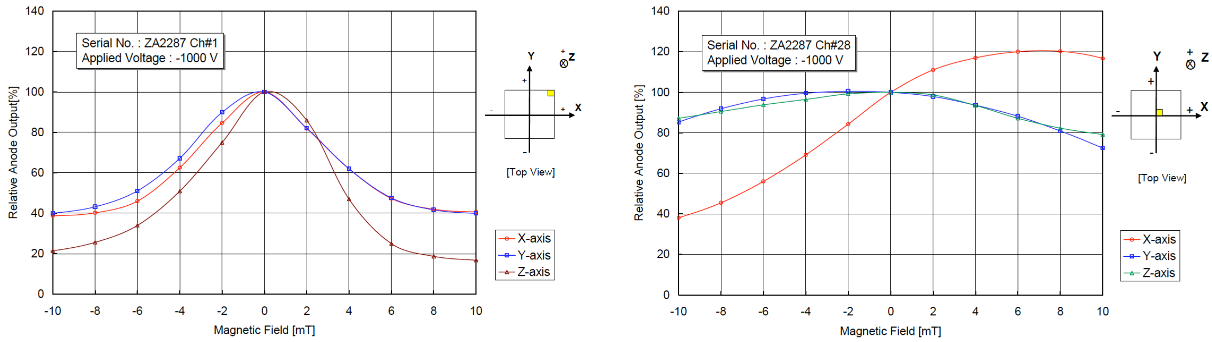

(a) The effect on boundary pixels.

(b) The effect on pixels near center.

Figure 8.34: Magnetic field effect on the H-8500 MaPMT pulse height (Hamamatsu data).

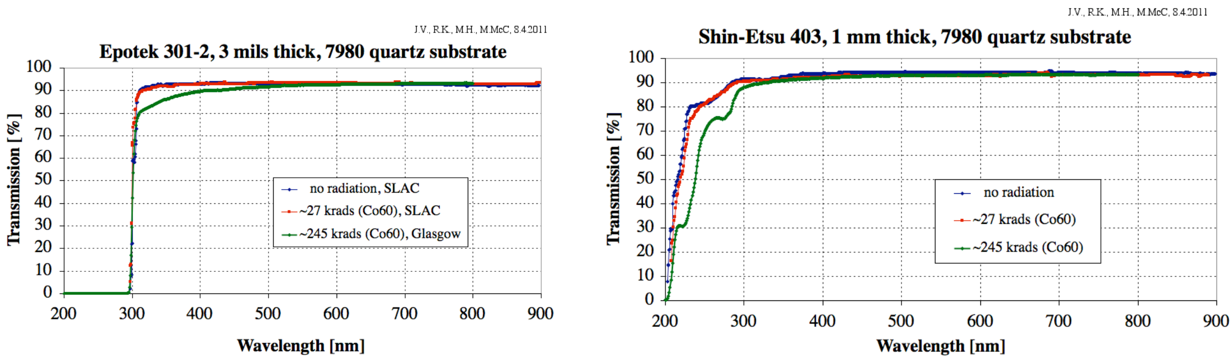

(a) Transmission of Epotek 301-2 epoxy (50-75 microns thick).

(b) Transmission of Shin-Etsu 403 RTV (1 mm thick).

Figure 8.35: Radiation damage by a ^{60}Co source on glues used in the construction of the photon camera [30].

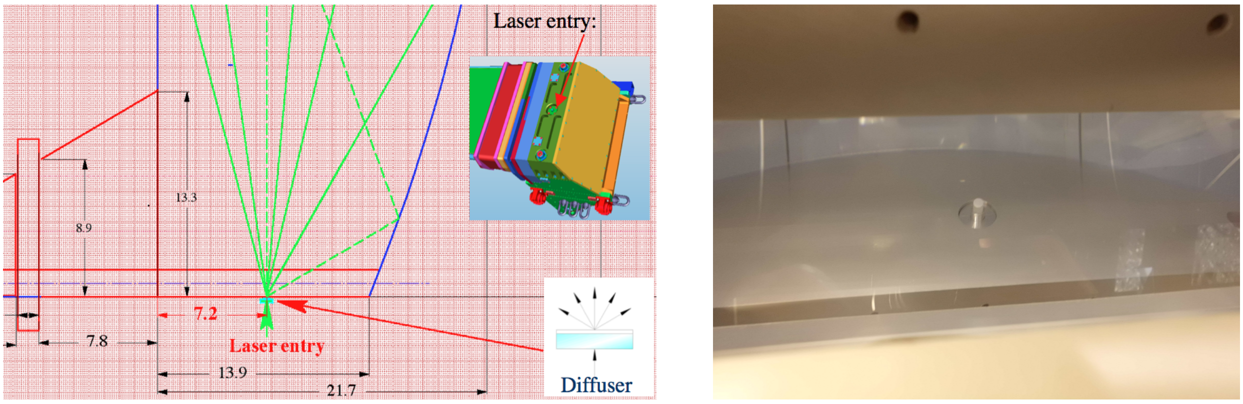

(a) Optical details of laser entry [26].

(b) OPAL diffuser used to spray laser photons into the FBLOCK.

Figure 8.36: Laser entry into the FBLOCK.

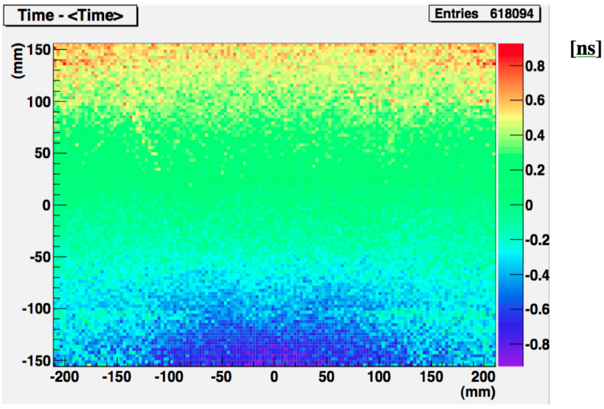

Figure 8.37: The laser time spread across the focal plane is at a few ns level [17].

tion of tubes and electronics, (b) to provide pixel offset constants for FDIRC timing calibration, which was found to be useful in the first FDIRC prototype when doing the chromatic corrections [26]. Figure 8.36 shows the laser entry into the FBLOCK as implemented in the final FDIRC prototype. The fiber plugs into a connector with a lens (F230FC-A), which makes a parallel laser beam, which then strikes a 5 mm diameter Opal diffuser, which was selected out of several choices for its uniform light diffusing effect. The small diameter diffuser is necessary to limit losses of real Cherenkov photons. We found experimentally that the best arrangement is if the diffuser is pressing against the bottom surface of the FBLOCK with the help of a spring (no gluing as it affects the uniformity of the scattered light). There is one fiber entry per photon camera serving one bar box. Figure 8.37 shows a MC simulation indicating that there is a time spread across the focal plane of about 2 ns. The aim is to determine this offset for each pixel and correct any deviation from the expected time. One this correction is determined, we align all pixels to a single reference time, called t_0.

Laser and fiber optics choice We will use PiLas laser diodes providing a light of 407 nm wavelength. We would like to split the light from one PiLas source into 2 branches. Each branch has to be adjusted to provide the same intensity, which should be low enough to generate single photoelectrons in each pixels. If this works, we will need six PiLas control units serving the entire system.

8.3.3 FDIRC Mechanical Design

Description of *BABAR* bars, bar boxes We will reuse the DIRC bar boxes. They will not be modified as it is considered too difficult to do, as discussed before. One potential problem is that the Epotek 301-2 glue has seen ~10 years of radiation during the *BABAR* experiment. Extensive studies were performed with the *BABAR* di-muon data and no detrimental effect was found on the glue transmission [31]. However, we do need to be extra careful when transporting bar boxes, as it is not known if the Epotek 301-2 glue strength was not affected. Similarly we will have to verify that Hexel panels used to build bar boxes can be transported by air (their Hexel-cells are sealed by glue and therefore will be affected by the pressure variation).

Figure 8.38 shows the *BABAR* DIRC bar box with its 12 Fused silica bars – each glued out of four 122 cm-long bar segments – and the nominal dimensions of each bar including the wedge [4]. In the real life, it is somewhat more complicated, as bar dimensions vary and each bar box is slightly different. This has been recorded in spreadsheets [32]. Figure 8.39 shows the cross-section of a bar box containing 12 fused silica bars. Figure 8.40 shows the bar forward end with a mirror. There are altogether 12 bar boxes and 144 full-length bars in the entire system.

Fused silica optics: New Wedge and FBLOCK The new Wedge and the FBLOCK will most probaby be made of radiation hard Fused silica Corning 7980 – this is the material used for the new FDIRC prototype which tests are starting at SLAC. Corning Co. makes fused silica 7980 material in a form of boules of up to 60" diameter – see Figure 8.41. The striae

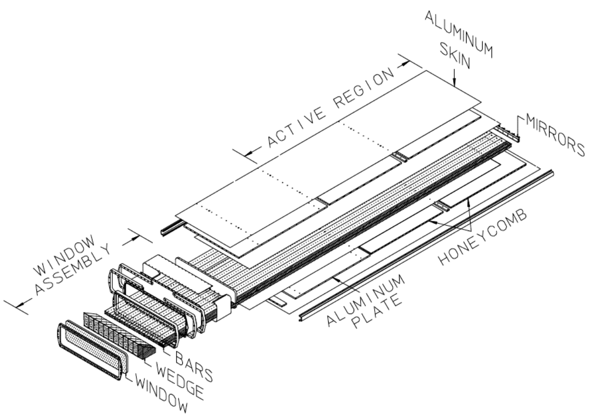

(a) *BABAR* DIRC bar box.

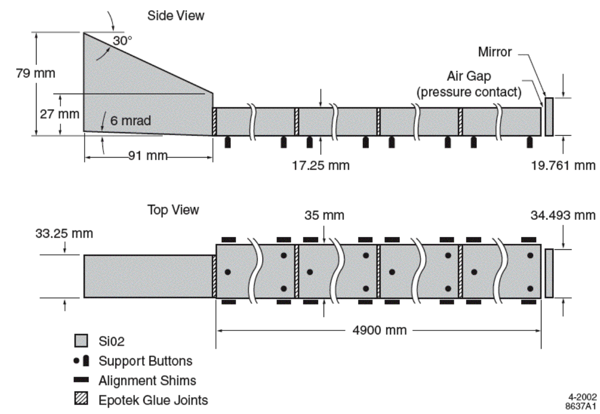

(b) One bar segment with nominal dimensions.

Figure 8.38: Bar box and bar dimensions [4].

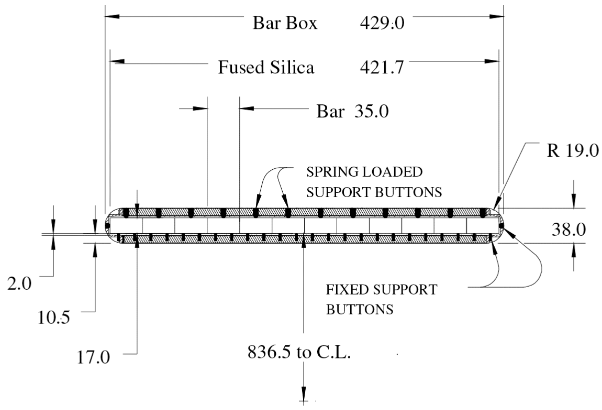

Figure 8.39: Cross-section of a bar box with its 12 fused silica bars [4].

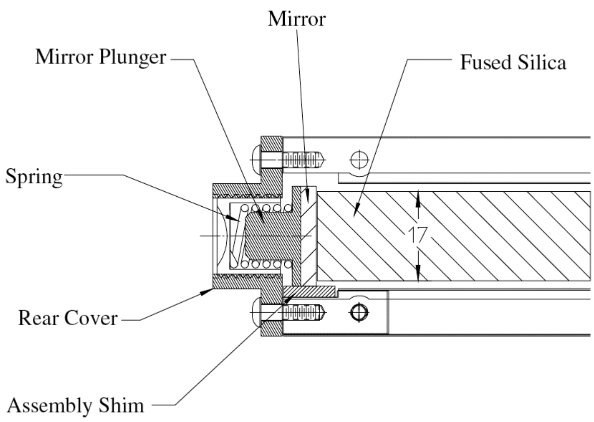

Figure 8.40: Bar end with a mirror (forward side of Super*B*) [4].

Figure 8.41: An example of the fused silica 7980 material in the form of a 60 inch dia. boule made by Corning.

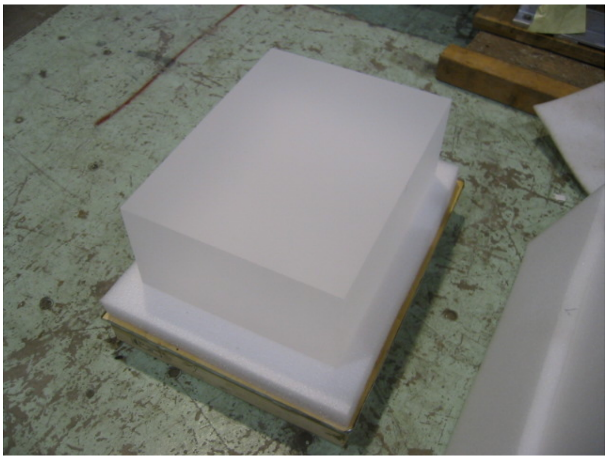

Figure 8.42: Fused silica 7980 material in a form of block ready for machining; the FLOCK used for the FDIRC prototype has been machined from this piece of quartz.

are running typically perpendicular to axis of a 60 inch dia. boule. The best homogeneity of the refraction index dn/n is along the axis of the boule. There are two types of 7980 material: (a) standard (much less characterized and therefore requiring more checks), and (b) the so-called KrF (very characterized material; Corning qualifies striae with an optical interferometer). We chose the "standard" material, as the cost of the KrF material is about 2-3 times higher. For the standard fused silica material these are typical specifications: (a) dn/n is less than 1 ppm over the scale of a mm; (b) the bottom-to-top of the boule along the axis: the refraction index uniformity dn/n is less than 5 ppm at 200 nm and better at longer wavelengths; c) dn/n is about 5-7 ppm in the direction perpendicular to the boule axis. Part-to-part variation is expected at a level of $dn/n \sim 20$ ppm in the visible wavelength range.

One should avoid the very bottom and top of the boule as there could be larger stria. Therefore, one should buy thicker boule, and this issue should be remembered for the final production. We visited this company and tested the material for stria with a laser. None was detected. Out of one boule, one expects to make three blocks such as the one shown in Figure 8.42. One has to pay attention to orientation of the FBLOCK within the raw block. The back side of the FBLOCK needs to be at the bottom of the boule as contamination from sand used as a seed of fused silica material deposition is more likely in this area.

The manufacturing was split into four steps done in three different companies: (a) grinding final shapes about 1-2 mm oversized, (b) polishing to final size and surface polish of better than 30 Å rms, (c) coating two FBLOCK reflecting surfaces with aluminum with SiO_2 overcoat to protect it, and (d) the final quality control (QC) of the completed pieces. Figure 8.43 shows the finished new Wedge and FBLOCK (before the two mirror plating step). These optical pieces were successfully produced, which demonstrates that the new camera optics is doable. However, there is a number of critical steps where error can be made, for example: (a) damages when handling, (b) surface pollution either before plating or in a final assembly, (c) stria problem needs to be checked, (d) accidental swaps of correct and wrong materials, etc.

FBLOCK mirror surfaces It is absolute mandatory to have a very good surface cleanliness before the aluminum plating is attempted.

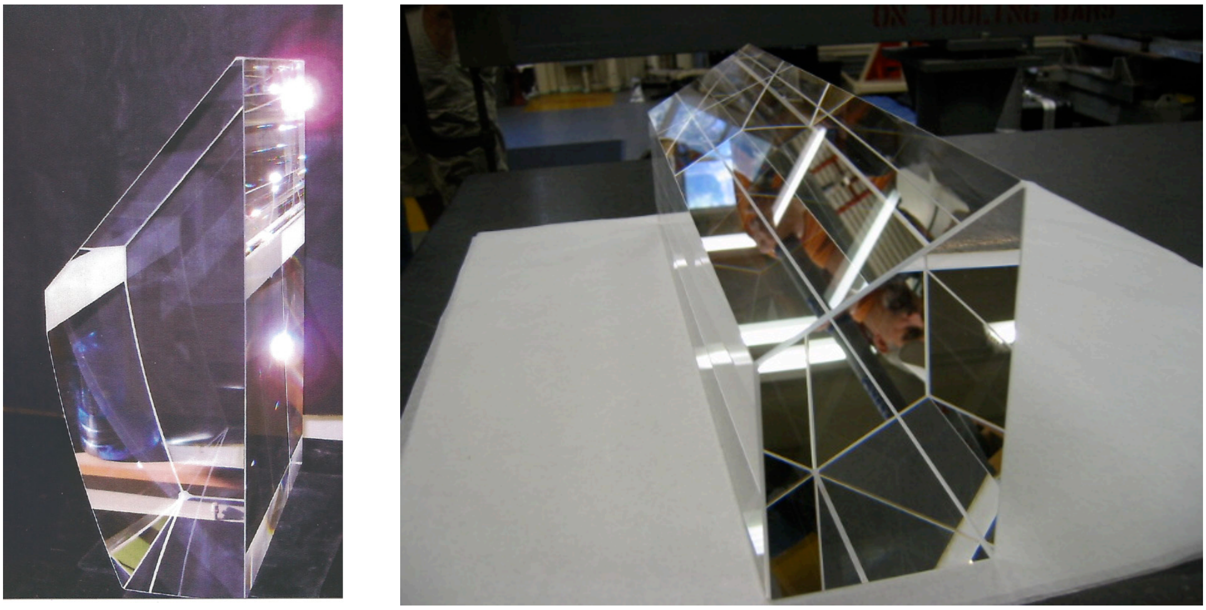

(a) FBLOCK after polishing but before plating.

(b) New Wedge after polishing.

Figure 8.43: New photon camera parts: New Wedge and FBLOCK.

Any contamination will result in peeling problems. The two FBLOCK aluminum-plated mirror surfaces are protected by a SiO_2 layer. Even though there is this protection layer, mirror surfaces are still fragile, especially if the surface is polluted during handling.

Another complicated issue is the FBLOCK shipping from the polishing company to the laboratory where it will be used. The FBLOCK is very heavy; its polished surfaces and the two mirrored sides can be easily damaged by a rubbing motion created by shipping. Surfaces have to be protected by a plastic film during the shipment, but the film must not stick to mirror surface to cause peeling problems. Based on our tests, we have decided to use the Grafix plastic vinyl film in future, which adheres to surfaces via electrostatic forces, does not remove plated layer, and does not leave a surface pollution, which would be difficult to clean.

Gluing the new Wedge to the Bar Box Window This optical coupling of Wedge to bar box window is done in the clean room. Figure 8.44 shows a detail of coupling of the new Wedge to the bar box. The coupling is done with the Epotek 301-2 optical epoxy of 25-50 micron thickness. The bottom of the new Wedge is aligned to the bottom bar surface, *i.e.*, not to the old wedge as it has a $\sim$6 mrad angle. The new Wedge is centered left-right in the bar box window. This coupling is not possible to remove in the future, as one would risk damaging the bar box.

FBLOCK mechanical enclosure: the Fbox Figure 8.45 shows the Fbox enclosure of the optics. Figures 8.46 and 8.47 show details of how the FBLOCK is supported by plastic buttons. Plastic buttons, made of PET (polyethylene terephthalate), prevent FBLOCK optical surfaces from touching the aluminum surface of Fbox. Some buttons are fixed and some are spring-loaded. The spring loading is made using a stack of 8 belleville washers, which is the most compact way to produce predictable force. They are set to offset the total weight of FBLOCK and to take into account thermal effects. Placing the FBLOCK into the Fbox requires a very careful procedure as it is very heavy ($\sim$80 kg)

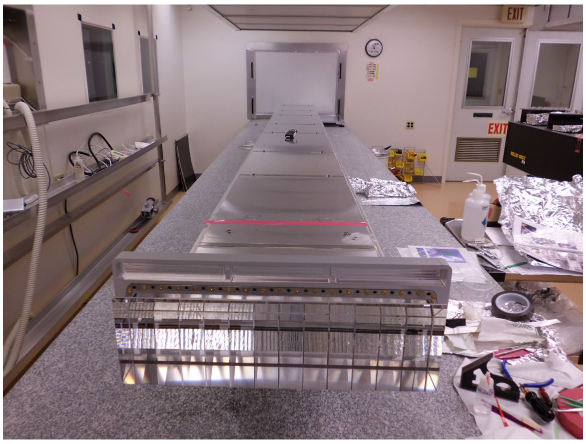

(a) The bar box with the new Wedge in the SLAC clean room.

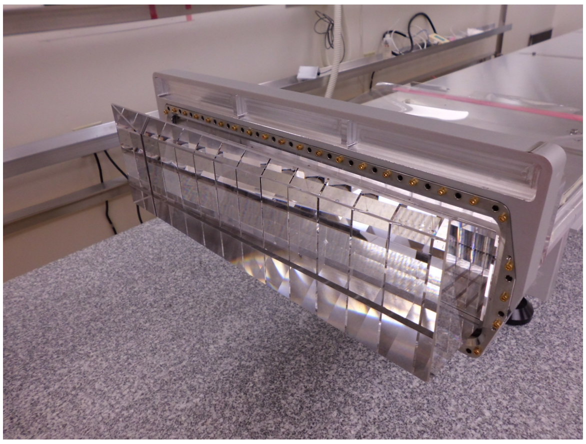

(b) Detailed view of the new Wedge and the bar box window.

Figure 8.44: Coupling of the new Wedge to the bar box.

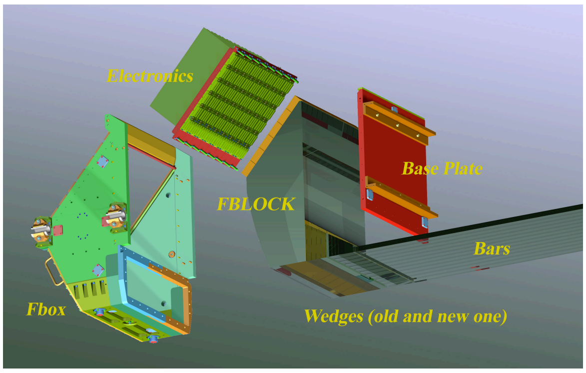

(a) Various components for the optics enclosure.

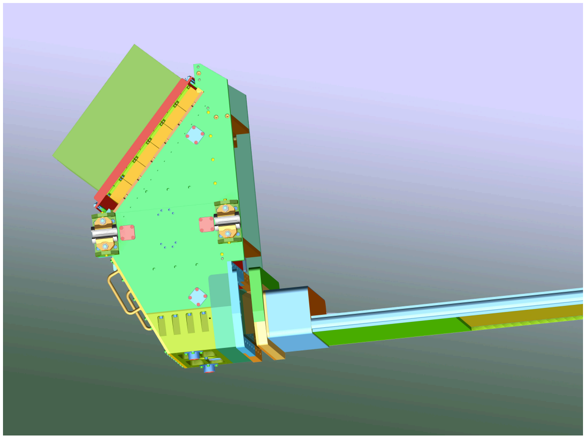

(b) Complete Fbox enclosure, including bar box.

Figure 8.45: Fbox enclosure of FBLOCK optics, including wedges, bars, detectors and electronics.

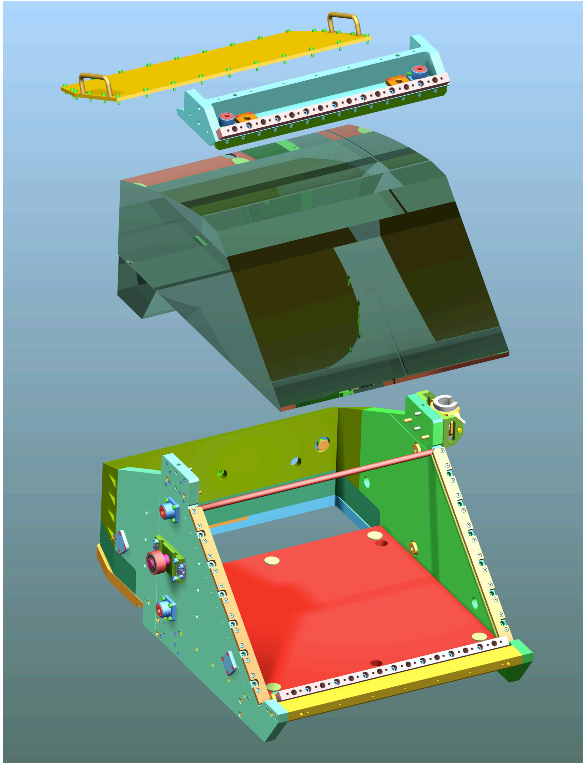

(a) Top view.

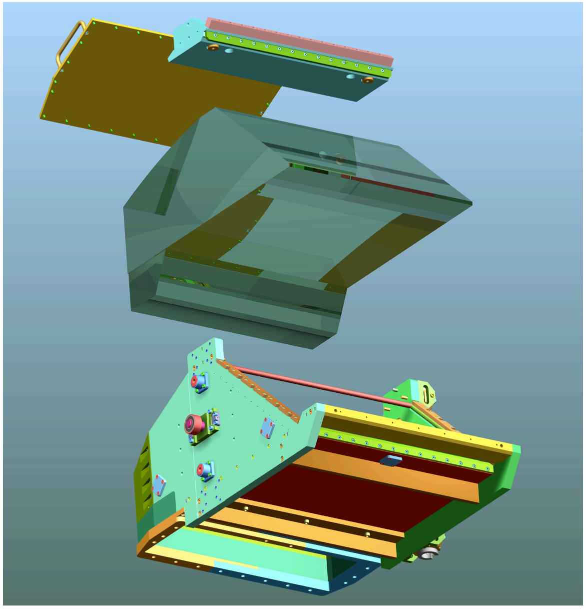

(b) Bottoms view.

Figure 8.46: Button support of FBLOCK optics in Fbox.

and easy to be damaged. It was very useful to work out a step-by-step procedure [33] with a dummy plastic FBLOCK [34].

We already have the experience of putting together the real photon camera with the Fused Silica FBLOCK. Figure 8.48(a) shows the first step of Fbox assembly where we placed the FBLOCK on four plastic support buttons. We have chosen a four-point support rather than a three-point one because it was judged to be easier to place the FBLOCK on the Fbox base plate, which is actually a very tricky operation. The front mirror surface is protected by four quartz coupons about 1.5 mm-thick, glued to the flat mirror surface by Epotek 301-2 epoxy. These four coupons are then touching plastic buttons located in the Fbox. The idea is that a rubbing motion due to thermal effects will be better dealt with if plastic buttons slide on quartz coupons rather than on the mirror plating directly. Figure 8.48 (b) shows a fully assembled Fbox with the real Fused Silica FBLOCK.

The Fbox and its bar box have to be optically coupled. Figure 8.49 shows an example of how this is done in the CRT setup.

Protection of optical surfaces As one deals with internal reflections, all optical surfaces have to be very clean, and therefore every part of the Fbox was very carefully cleaned before final assembly to prevent outgassing. In addition, optical surfaces are protected against environmental pollution and moisture condensation by flowing a boil-off N_2 through the sealed Fbox. Fbox is sealed with a combination of Viton flat gaskets, Viton O-ring and Gore gasket tape (near the detector area), and in some difficult sections simply with DP-190 glue. Based on experience in *BABAR*, each bar box requires a flow of about 100 cc/min.

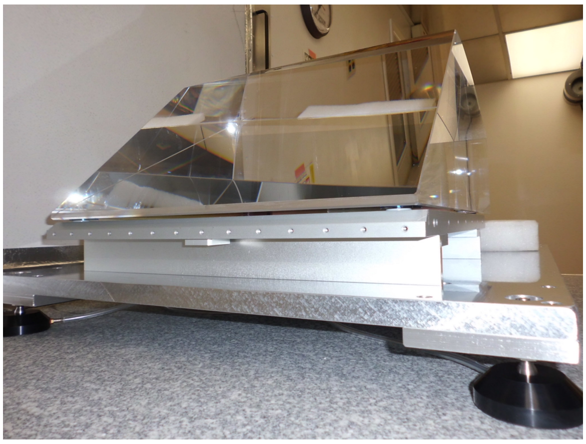

(a) FBLOCK placed on the base plate of Fbox.

(b) Assembled Fbox in front of bar box.

Figure 8.48: Fbox assembly around the real Fused Silica FBLOCK.

(a) Fbox and bar box in the CRT setup.

(b) Details of coupling of new Wedge to FBLOCK.

Figure 8.49: Fbox coupling to bar box in the CRT setup.

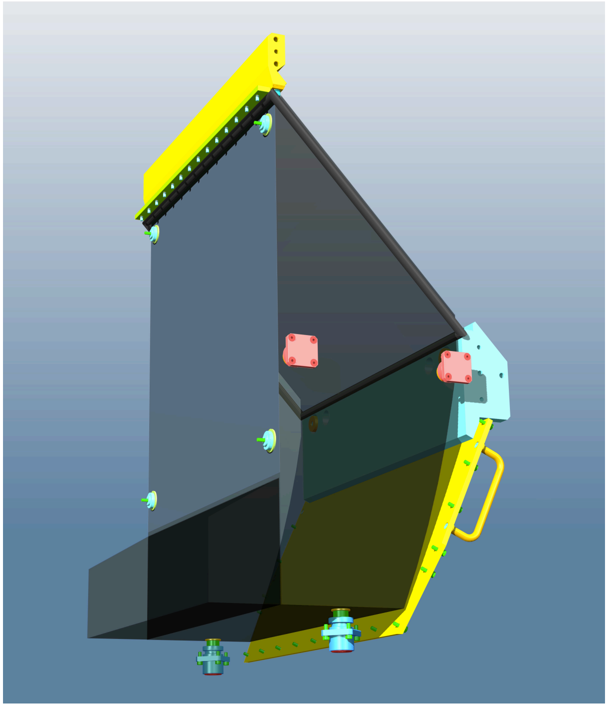

Figure 8.47: FBLOCK support buttons: the small buttons are fixed while the larger ones (two from the bottom and two from one side) are adjustable to keep the FBLOCK stable even if the Fbox, made of aluminum, expands due to thermal effects.

Bar box storage at SLAC Figure 8.50 shows the present storage of the 12 DIRC bar boxes. They are supported on pre-aligned shelves to prevent mechanical stresses due to support distortions. They are under a constant flow of boil-off N_2 and thermally insulated. The storage box is kept at a nominal temperature of 18°C. In addition, there is no light to prevent yellowing of the Epotek 301-2 glue, an important issue to consider in future.

Gluing FBLOCK to Wedge The optical coupling between the new Wedge and the FBLOCK is done in situ, and is in principle removable. We set the gap between the new Wedge and the FBLOCK to 1 mm, and fill it with Shin-Etsu 403 RTV. In case of problems with the Fbox, one can first separate the two pieces using a thin razor wire, then clean the surfaces and finally couple them again. The penalty for this option is that an RTV joint is not as strong as an epoxy joint. The breaking force of this RTV coupling was measured to be ∼520 kg using glass windows of the correct size; it was found that this value depends strongly on the glass cleaning procedure. See Figure 8.51 and chapter "Support of Fbox in the Super*B* magnet" below for more details on the installation procedure.

Figure 8.50: Bar box storage at SLAC.

Support of Fbox in the Super*B* magnet The plan is to install bar boxes with the new Wedge already glued to the bar box windows. The Fbox will be installed in situ. Figure 8.51 shows the procedure. The space between bar boxes is very tight. Therefore, the bar box has to be moved beyond the neighboring already installed Fboxes, so one has enough room for gluing. With a temporary rail support it is possible to bring the Fbox close to the bar box; in that way the Wedge and the FBLOCK surfaces are parallel and the gap is set to 1 mm, bottom surfaces of FBLOCK and the new Wedge are aligned, and both are centered left-right. The gap between FBLOCK and the new Wedge is then filled with the Shin-Etsu 403 RTV. Once the RTV is cured, the gas sealing is made, the Fbox is pushed on the rail to its final position, and the earthquake bracing is installed. The temporary rail support is then removed. Fig-

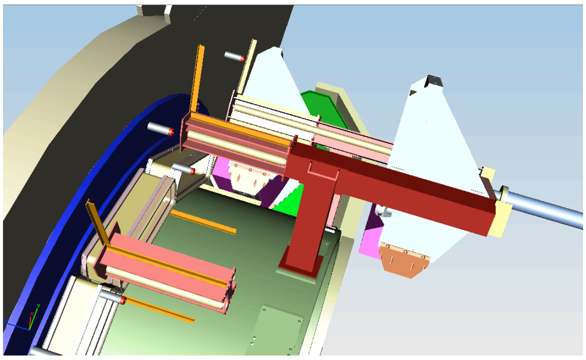

(a) Fbox installation fixture for position pointing up.

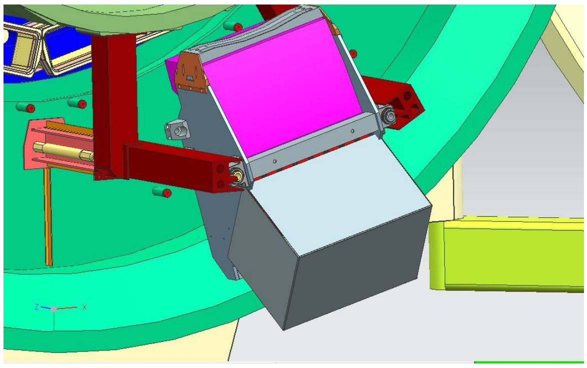

(b) Fbox installation fixture for position pointing down.

Figure 8.51: Fbox installation in the Super$B$ magnet.

ure 8.52 shows the camera after the installation procedure has been completed.

Figure 8.53 shows the overall FDIRC detector schematic layout with its 12 bar boxes, and the 12 corresponding photon cameras. Figures 8.54 and 8.55 show overall mechanical views of the FDIRC in the Super$B$ experiment. Details of the shielding are shown on Figure 8.33.

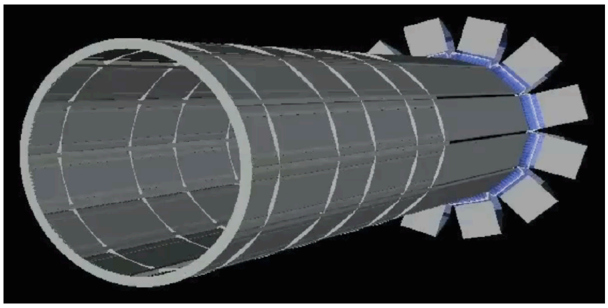

Figure 8.53: Overall view of the FDIRC layout with 12 bar boxes and 12 photon cameras.

Experience with shipping FBLOCK It is useful to share experience with shipping of finished FBLOCK. The polishing company worried about this step because the FBLOCK is very heavy and any rubbing even against a foam padding could cause problems. They decided to cover all surfaces with a protective tape resembling a masking tape. We found that the tape adhesion was too strong and a small section of mirror plating was removed when the tape was peeled off. This triggered a small R&D effort to find out what type of protection tape would not cause this problem. We found that the best result was achieved with the electrostatically-adhered vinyl tape (Grafix Plasics, S-C2436, Cling vinyl). We also found that if one such problem occurs, the best way to fix it is to use a small section of aluminized Mylar sheet pressed uniformly by a foam on its entire surface. Any other method of stretching the aluminized Mylar sheet created wrinkles.

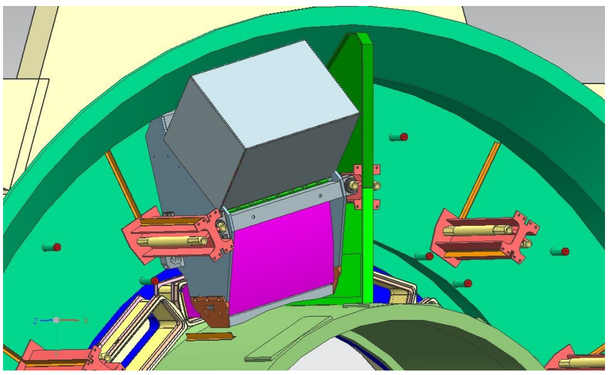

Figure 8.52: Camera after completion of the installation procedure.

Bar box shipment to Italy There are several issues to consider: (a) vibration and mechanical shocks, (b) thermal effects, (c) pressure changes,

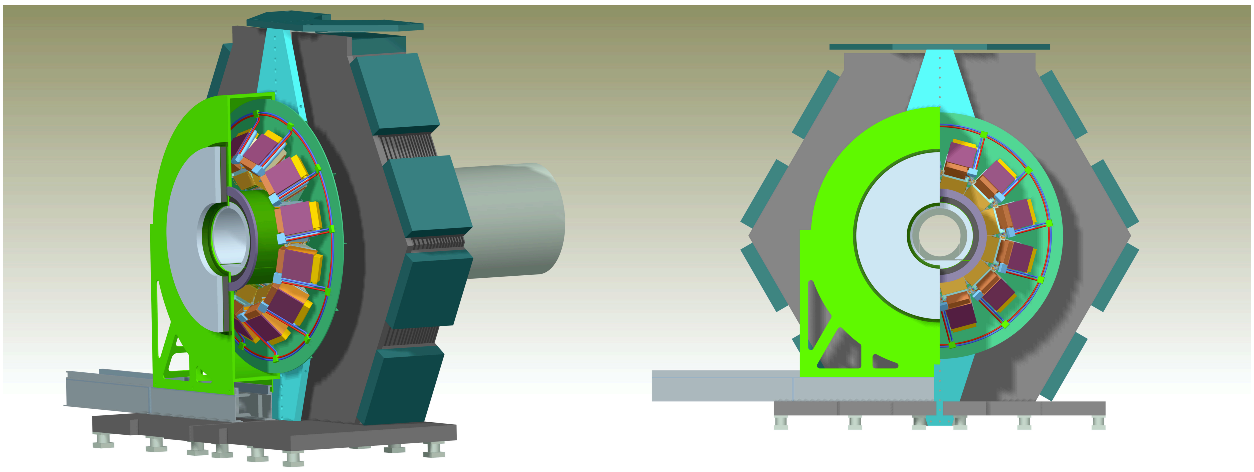

(a) A 3D view showing the new magnetic shield and background shields, and Fboxes.

(b) Front view showing six Fboxes, the rest is hidden behind the magnetic and background shields.

Figure 8.54: FDIRC in the magnet.

and (d) light exposure. Each bar box will have a container providing mechanical support and constant thermal environment. The vibrations and mechanical shocks will be mitigated by placing bar boxes on a precisely leveled support with a foam on top of it. The support structure will need telescopic mount to suppress large shocks. They will be thermally isolated and equipped with active thermal blankets to keep temperature constant. We will also provide a N_2 boil-off gas flow. Another important issue is pressure changes if air transport is used. The Hexel panels, used to construct bar boxes, do not have perforated walls, and therefore some stresses will be created, if one wants to ship bar boxes by air. The present thinking is to construct a container to ship two bar boxes at a time. This container would be air-shipped by a commercial company Fedex or DHL. The shipment has to be insured for full value of bar box replacement (presently we think that the cost of such insurance is about 15% of the total cost of shipment, judging from experience of Nagoya group). Finally, bar boxes must not be left exposed to a strong light as it could yellow the Epotek 301-2 epoxy.

8.3.4 Electronics readout, High and Low voltage

The electronics for the FDIRC can be seen as an upgrade of the electronics of the *BABAR* DIRC. The new requirements of the experiment (trigger rate, background, radiation environment) and FDIRC specific requirements (resolution, number of channels and topology) have led to a similar but new design of the electronics chain.

The FDIRC electronics will handle 18,432 channels in total. The electronics chain is based on a high resolution and high count rate TDC, a time-associated charge measurement with 12-bit resolution, and an event data packing, sending data frames to the data acquisition system (DAQ). The target timing performance of the overall electronics chain is a time resolution of 100 ps rms. It has to deal with hit rates of 100 kHz per channel, a level-1 (L1) trigger rate up to 150 kHz, and a minimum spacing between triggers of about 50 ns.

The radiation level is expected to be about 1 gray per year, thus the use of radiation tolerant or off-the-shelf radiation-qualified components is necessary. However, the expected energy of the particles may make the latch-up effect almost impossible. Thus, the design has only to take

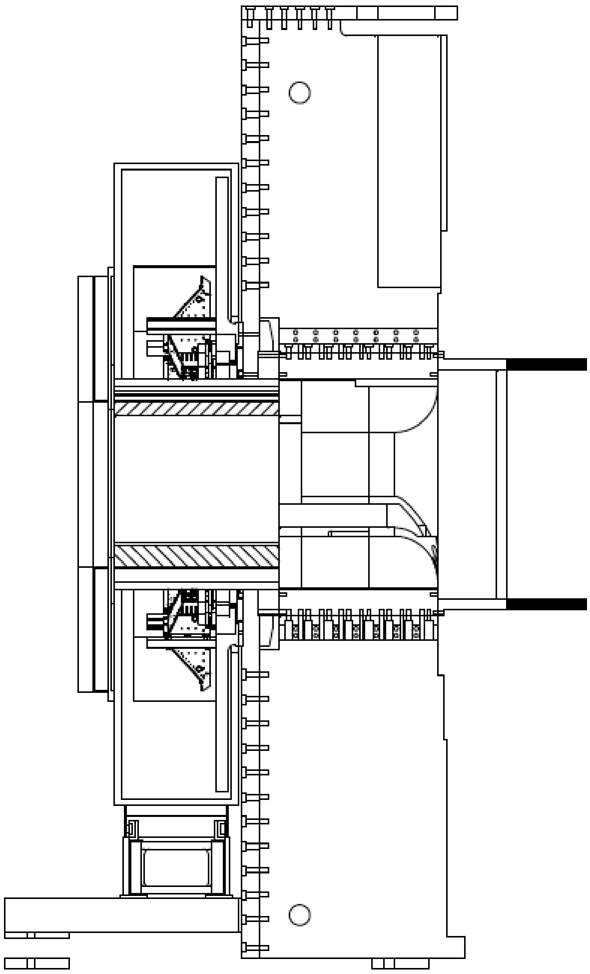

Figure 8.55: Side view of the FDIRC showing magnetic and background shields, and rails on which they move.

into account Single-Event-Upsets (SEUs). We selected the Actel family FPGA components for their non-volatile flash technology configuration memories, which are well-adapted to low level radiation environment.

Several architectures have been considered: (a) all electronics directly mounted on the FBLOCK, (b) all electronics mounted next to the detector and linked to PMTs by cables, and (c) a part of it on the detector (the Front-end boards) and the other part, called 'crate concentrator', is located close to the detector (this board is in charge of interfacing with the Front-end, reading out event data, packing and sending it to the DAQ).

The first solution has been chosen as baseline for the TDR for two main reasons. (a) The cost of cables (PMT to Front-end boards) is estimated to be close to 200 kEuros (1/3 of the price of the overall electronics cost), making this design too expensive. Moreover, the possible option to have pre-amps on the PMT bases does not prevent from having electronics and power supplies on the detector. (b) The large amount of data per channel leads to have the L1 trigger derandomizer and buffer on the Front-end boards. The Fast Control and Timing System (FCTS) receiver could be individually located on each Front end board but the number of cables needed pushes to distribute all the control signals on a backplane. Consequently, the board dedicated to receiving and transmitting FCTS signals on the backplane naturally tends to also become the event data concentrator and the link to the DAQ.

The baseline design assumes a 16-channel TDC ASIC, offering the required precision of $\sim$100 ps rms, embedding an analog pipeline in order to provide an amplitude measurement transmitted with the hit time. Thanks to a 12-bit ADC, the charge measurement will be used for electronics calibration, monitoring and survey purposes. The Front-end board FPGA synchronizes the process, associates the time and charge information, and finally packs them into a data frame which is sent via the backplane to the FBLOCK control board (FBC). The FBC is in charge of distributing signals coming from the FCTS and the Experiment Control System (ECS), packing the data received from the front-end (FE) boards to a n-event frame including control bits and transferring it to the DAQ.

The FDIRC electronics The FDIRC electronics consists of a front-end analog part and a TDC both integrated in a common ASIC called CATS, and of an external ADC. The front-end analog part will soon be validated in a prototype chip called PIF (PId Front end chip), which will contain an amplifier and a peak detector for the amplitude measurement (digitization will be performed by the external ADC), and a low walk discriminator (called "Discri") to drive the TDC inputs. This TDC has already been developed and tested in a prototype called SCATS. Figure 8.56 shows the concept of one channel of the PIF chip and the principle of the "Discri". The latter is mainly based on an high gain amplifier and a discriminator with a programmable threshold . The overall aim is to measure single electron pulses with a resolution of ∼100 ps rms. The TDC chip is derived from a design realized for the SuperNemo experiment [35]. It provides a time measurement with steps of 200 ps offering both a high resolution (70 ps rms) and a large dynamic range (53 bits). The architecture of this chip is based on the association of Delay Locked Loops (DLLs) and of a digital counter, all of these components being synchronized to a 178.5 MHz external clock, multiple of the global system clock (59.5 MHz).

The Super*B* TDC chip (CATS) will keep the same philosophy, but the high input rate requirement leads to a complete re-design of the digital part, in order to minimize the dead time per channel and to increase the output data rate. The solution chosen consists in transforming the former architecture, where data was read out by the FPGA, into one where data goes to FPGA via TDC. Moreover, instead of using registers for memorizing the hits, the new circuit makes use of individual FIFO memories in each channel in order to internally de-randomize the potential high frequency bursts on the chip inputs. With this architecture, data from the DLLs and the coarse counters is now written into this FIFO memory. When the writing is complete, the channel is automatically reset and ready for the next hit, within a delay lower than 50 ns. Simulations of the readout state machine showed an output FIFO data rate capability of up to 100 MHz, thus permitting a safe readout at a frequency of either 59.5 or 89.25 MHz. Time ranges for the DLLs and the coarse counter can be easily customized by adjusting the output data format (16, 32, 48 or 64 bits). Therefore, this chip is actually suitable for various applications with either high count rate and short integration time, or low count rate and long integration time. Figure 8.57 shows the block diagram of the Super*B* FDIRC TDC chip (CATS).

A FIFO depth of 8 words (32-bit each) has been selected after simulation with a exponential distribution model of delta time between hits (mean rate ∼1 MHz) applied to inputs. To design this FIFO, a full custom RAM has been developed. In addition to increasing its speed, it permits reducing the size of the chip and consequently its cost. The chip is designed using known and proved mitigation techniques to face SEU issues due to the low-level radiation environment. The prototype version of the chip (called SCATS), which does not include the analog FIFO and the discriminator, has been submitted in November 2011. We plan to submit by end 2012 another prototype chip (PIF) – see Figure 8.56 – dedicated to the currently main missing parts: (a) a low walk discriminator receiving the PM outputs and able to send a logic signal to the TDC part of the chip, and (b) an amplifier followed by a peak detector and an output buffer. After testing and validation, a final version of the CATS chip including all these functions will then be assembled and submitted by end 2013.

Front-end Crate
The board input will fit the topological distribution of the PMT on the FBLOCK – see Figure 8.58. In each sector, the PMTs are arranged as a matrix of 6 in vertical direction by 8 in horizontal direction. Each column of 6 PMTs will be readout by two FE boards. One vertical moth-

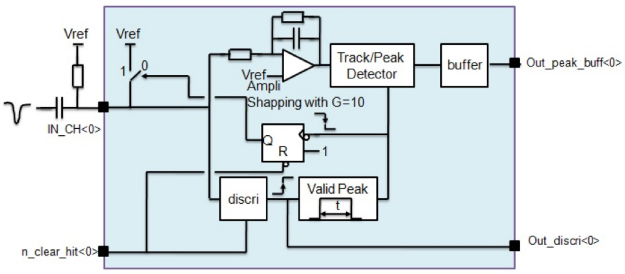

(a) One-channel concept of PIF chip.

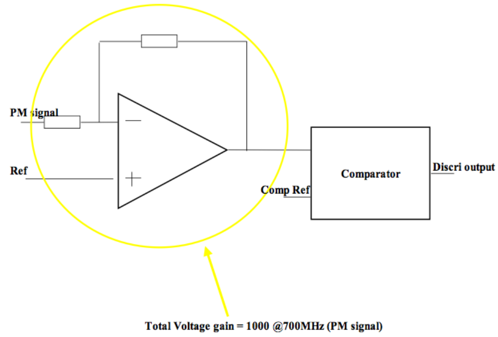

(b) The principle of the "discri".

Figure 8.56: FDIRC front-end analog electronics

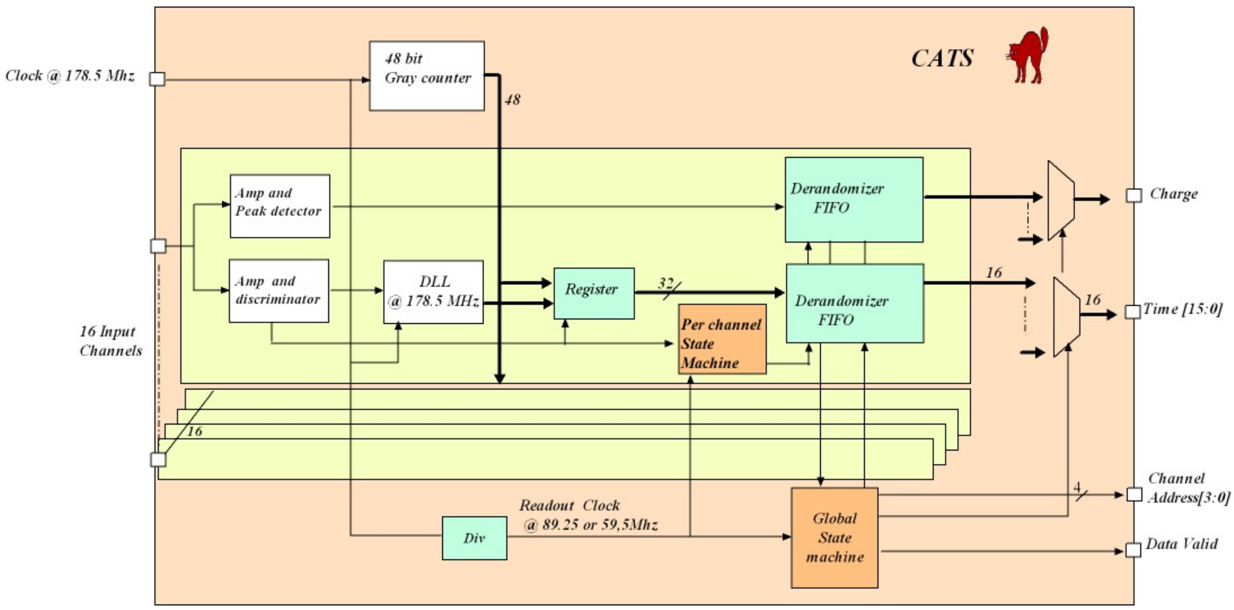

Figure 8.57: Super$B$ FDIRC TDC chip block diagram.

erboard will couple one front-end board to one half column of 6 PMTs. There will be a total of 8 motherboards. For each PMT, the motherboard will convert 4 H-8500 connectors into two other connectors, each connected to a FE board. Figure 8.59 shows the Fbox with the front-end electronics.

The motherboard will also distribute High Voltage to the PMT if we use H-8500D. However, in case that we choose the H-8500C PMT, each PMT will have its own HV cable and HV distribution will be separate. In addition to the 8 motherboards, the backplanes receives one communication board for distributing control signals and data between FE boards and the FBLOCK control board. The FB-crate will use many features of commercial crates, such as board guides, rails, etc.

Communication Backplane
The communication backplane distributes the ECS and FCTS signals from the FBC to the 8 FE boards thanks to point to point LVDS links, and connects each FE board to the FBC for data transfer. A serial protocol will be used between FE board and the FBC in order to reduce the number of wires and consequently improve the reliability. It will also distribute JTAG signals for FPGA board reprogramming, and all signals for the monitoring and control of the crate.

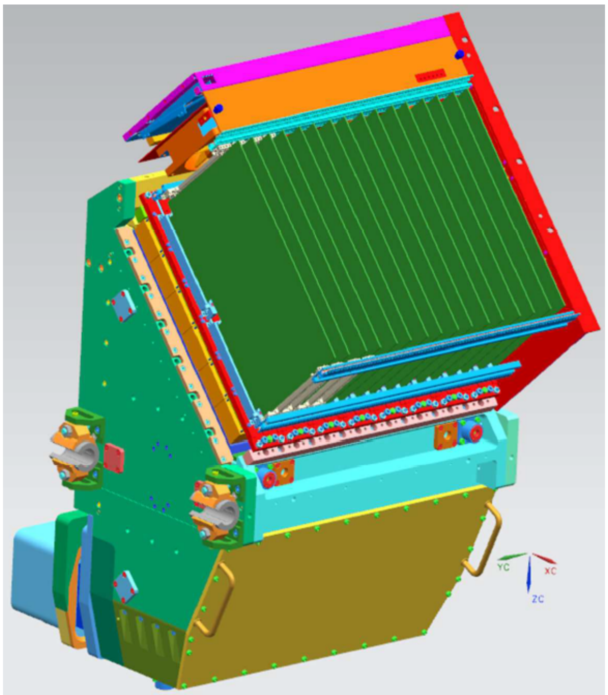

Figure 8.59: Fbox equipped with electronics and its cooling.

PMT Backplane
It is an assembly of 8 motherboards, each one corresponding to a column of 6 PMTs. One motherboard receives 2 FE boards. The 64 channels from 4 connectors per PMT are merged on the motherboard into two connectors to get into the Front end board to get 16 channels per half PMT, *i.e.*, 6 PMTs correspond to 96 channels per FE board. It also insures the ground continuity between the FE boards, the FE crate and the FBLOCK.

The Front-end Board
One FE board is constituted of many 6-channel processing blocks handling the board 96 channels. The channel-processing block is constituted of one TDC chip, one ADC, one small Actel FPGA and glue logics. The FPGA receives event data from the TDC and the converted associated charge from the ADC. The 16-bit input bus carrying data from the 16 channels of the TDC is split into 16 individual trigger latency buffers where events are kept waiting for the level 1 trigger selection. Upon its reception, event data from the 6-channel processing blocks is sent to the master FPGA which packs the event and stores it into the readout derandomizer. The FE board then transfers the event frame in differential LVDS to the FBC via the communication backplane. Figure 8.60 shows the architecture of the FE-board connected to the backplanes.

The crate controller board (FBC)
The FBC board gathers front-end data and transfers it via optical fibers to the DAQ system. There will be one FBC board per crate. The board is separated in several functionalities: (a) acquisition from the front-end boards and DAQ interface to ROM, (b) building of spy-data, (c) ECS interface, (d) deserialization of clock and control signal from FCTS, and (e) monitoring

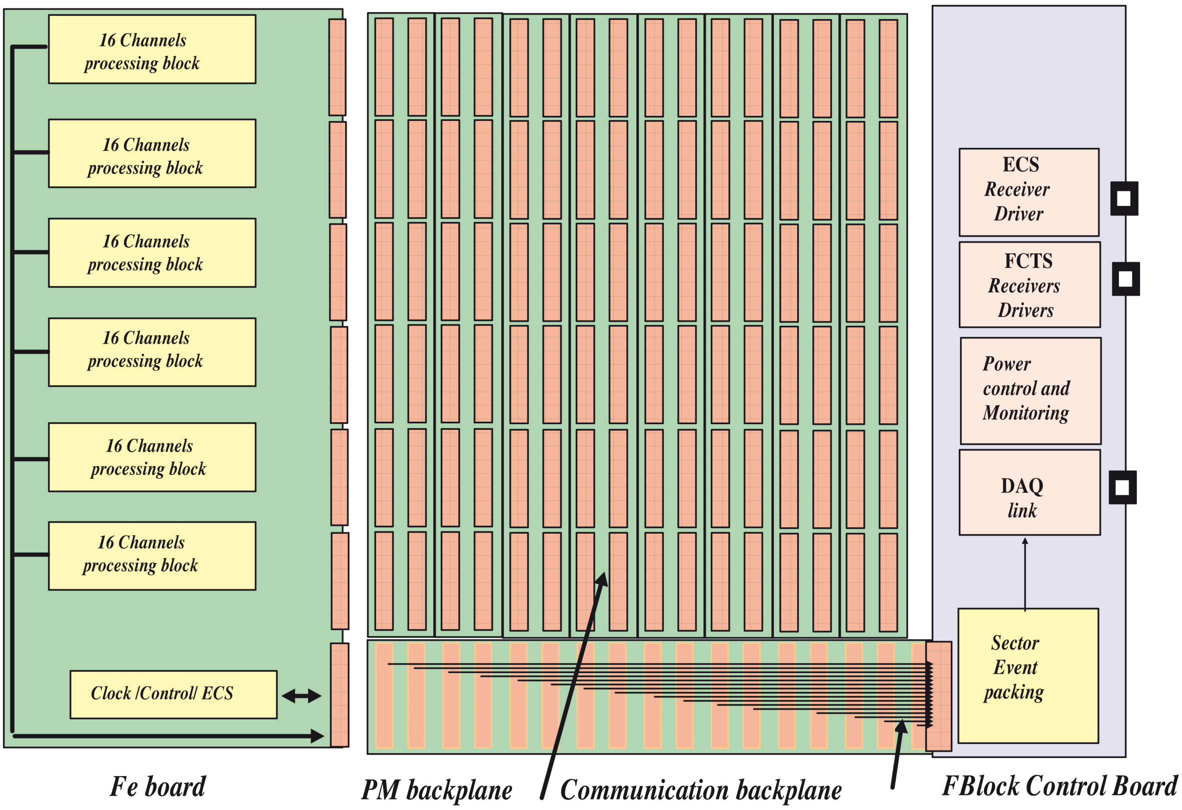

Figure 8.58: Front-end crate: PMT backplane, communication backplane, FE-board, FBLOCK controller (FBC).

of the crate temperature, power supplies, fans, etc.

Cooling and Power Supply
Electronics is located on the detector in a place enclosed by the magnetic doors. There are two major consequences: one is the problem of cooling, which must be carefully studied in terms of reliability and capability, and the second is that the location is "naturally" shielded against magnetic field. Consequently, the use of magnetic sensitive components as coils or fan trays is possible. An estimate of the overall electronics consumption lead to ~6.1 kW, not including the external power supplies. This can be broken down to individual contributions as follows: (a) electronics: 0.325 W/channel, hence 500 W/sector, 6 kW for the whole FDIRC; (b) HV resistor chain: 0.19 W/tube, hence 9.1 W/sector and 109 W for the whole FDIRC. The cooling system must be designed in order to maintain the electronics located inside at a constant temperature close to the optimum of 30 degrees. The air inside the volume must be extracted while dry, clean and temperature-controlled air will be flowing inside. Each FB crate will have its own fan tray like in a commercial crate. Targeting a difference of 10 degrees between inside and outside temperature drives to a rough estimate value of 300 m^3 per hour per crate. 4000 m^3 per hour can be considered as the baseline value for the whole detector.

H-8500 PMT has an AC-connection to the last dynode, and this can be used either for triggering or calibration purposes. One can do the calibration with HV off by injecting a pulse and looking at response of all anodes. Figure 8.61 shows a relative pulse height response of 64 anodes to such pulse injection [29]. It is not uni-

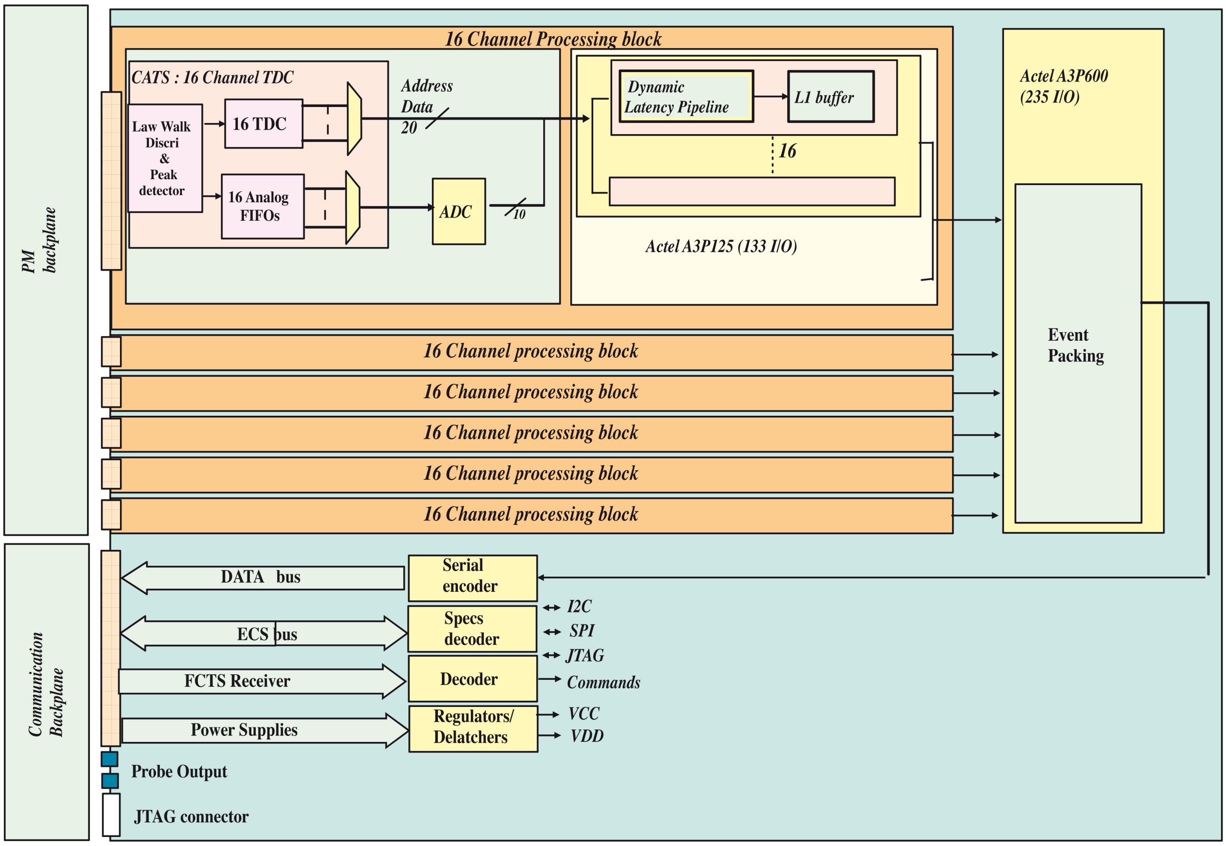

Figure 8.60: Front-end board connected to backplanes.

form, but it could be useful in order to identify possible electronics problems.

Motherboard We presently consider two choices for motherboard geometry: (a) a PC-board combining a group of 6 PMTs (see Figure 8.62), *i.e.*, we need altogether 8 such motherboard per photon camera, or (b) a single PMT PC-board. The nominal choice is the 6-PMT motherboard. The total insertion force is 160N/FE board with ERNI connectors. To make sure that we do not bend pins in connectors, we will need guiding pins. We were considering also zero-insertion connectors (ZIF connectors), however, they are being discontinued and we were advised by the TYCO company not to use them. There will be 16 FE boards per FBLOCK. These boards will either be inserted or extracted with a help of tools and rails, a similar procedure as in some commercial crates.

Figure 8.63 shows the complete photon camera with the electronics for 48 H-8500 PMTs and 1536 double-pixels.

HV distribution and HV power supplies If the H-8500C tube is selected, HV cables will be routed under the motherboard as shown on Figure 8.64. The drawback of this solution is that we will have 48 HV cables in a relatively small volume, and tubes will have to be rotated to fit HV cables in an efficient way.

The resistor chain of each H-8500 tube draws $\sim$150μA at -1.0 kV. The HV power supply will be CAEN, Model A1835, or equivalent. It has 12 independent channels per module, each channel being able to provide up to 1.5 kV and either 7 mA or 0.2 mA (selectable by a jumper). The current monitor has 20 nA resolution. The entire FDIRC HV system would need 48 such HV power supplies, *i.e.*, four per photon cam-

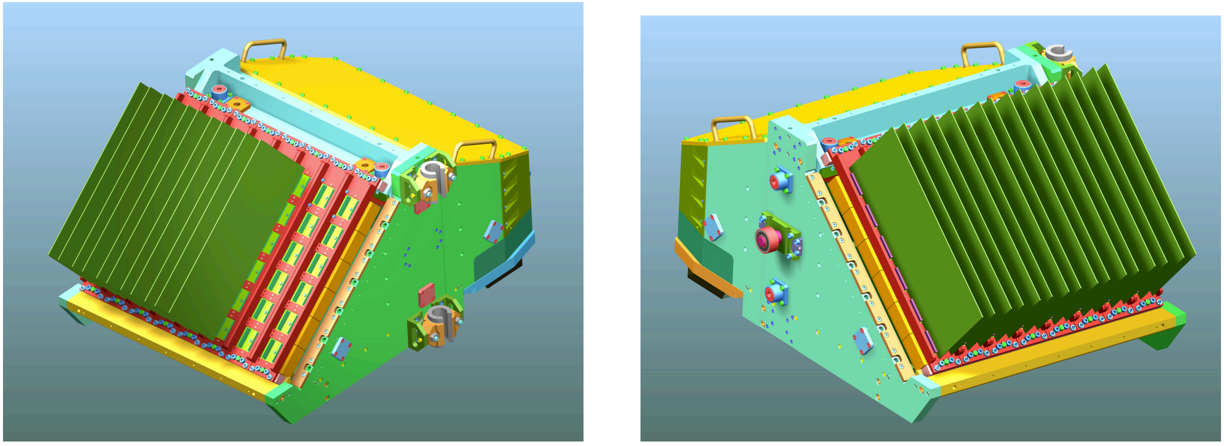

(a) Photon camera with its electronics.

(b) Photon camera with its electronics.

Figure 8.63: Photon camera with high density electronics reading out 48 H-8500 PMTs.

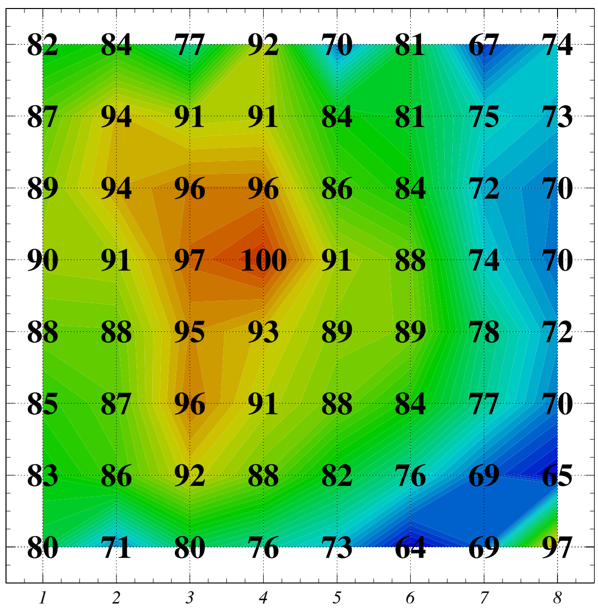

Figure 8.61: A relative pulse height response of H-8500 anodes to a pulse coupled to the last dynode [29].

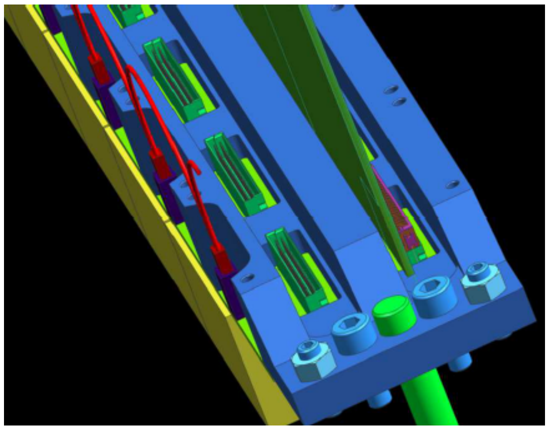

Figure 8.62: A motherboard for six H-8500D tubes, which uses ERNI SMC-Q64004 press fit connectors to couple to FE boards. The total insertion force is 160N/FE board.

era. They will be located behind the background shield in the non-radiation area.

If the H-8500D tube is selected instead, HV will be distributed on the board as shown on Figure 8.65. The drawback of this solution is that we would be grouping six PMTs on one HV power supply channel, which would have to supply 1 A.

Support services FDIRC detector will need these services:

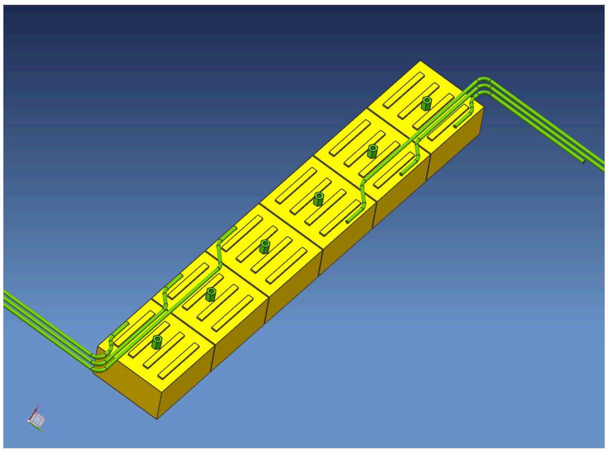

Figure 8.64: HV distribution to H-8500C tubes along the vertical column. Half of tubes are rotated to pack cables efficiently.

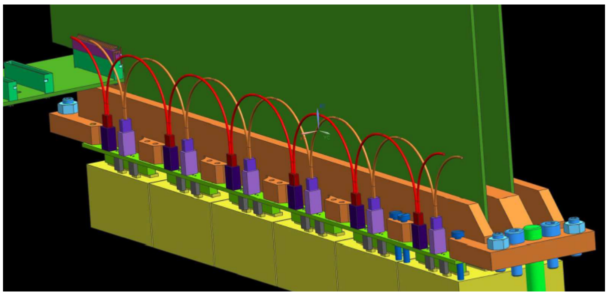

Figure 8.65: HV distribution to H-8500D tubes along the vertical column.

- A boil-off N_2 flow in each bar box up to 100 cc/min per bar box. The N_2 gas has to be distributed in stainless steel electropolished tubing. No oil bubbles to be used.

- The total power dissipation in the entire system is about 6.1 kW. The cooling will be done with water-based heat exchangers and forced air.

8.3.5 Integration issues

Background shield and access to detector maintenance Because the front part of the FBLOCK background shield is mounted on the magnetic door, which is on rails, it will be easy to move it sideways to allow a quick access to the detectors and electronics – see Figure 8.33.

Earthquake analysis of FBLOCK & bar box structure Bar box axial and radial constraints will be equivalent to *BABAR* DIRC setup. The Fbox system itself is not critical, being compact, rigid, and with very limited lever arms. Of course the support disk and the support rails structures of the Fbox must be adequately stiff to avoid resonance in the typical quake range. Axially, the Fbox must be constrained as the bar box. The increased risk relative to *BABAR* DIRC consists in the coupling of Fbox and bar box. However, the presence of a RTV gluing layer instead of a rigid coupling and an adequately stiff support of the Fbox should prevent risks due to this coupling. Calculations are in progress.

PMT protection (helium, large backgrounds) It is well-known that the PMT operation can be affected by a helium contamination, which can penetrate the PMT glass. These atoms convert to ions in the avalanche process, which can drift back to the photocathode creating secondary photoelectrons, often called 'after pulses'. Therefore, just like in case of the *BABAR* DIRC (which had ∼10751 PMTs) we should worry about any leak checking close to the Super*B* detector and using helium – for vacuum purpose. Even if it is done far away in the tunnel, air draft could bring it to the detector. We will need a helium detector to monitor this.

Reference [36] summarizes the effect of helium contamination on a PMT. We should stress, however, that we did not do any experimental study with the H-8500 tube up to this point.

The ion contamination in a PMT can be estimated by measuring the after-pulse rate. Figure 8.66 shows how the H^+, H_2^+ and He^+ ion contamination [29] affects a time spectrum of afterpulses in a H-8500 tube. The total measured rate of after pulses was less than ∼1% rate for this tube. This measurement will have to be part of PMT QC procedure to weed out bad tubes. It will be useful to repeat it periodically on some tubes during the Super*B* data taking.

8.3.6 FDIRC R&D Results

Test beam results from the first FDIRC prototype Figure 8.4 shows the prototype. This

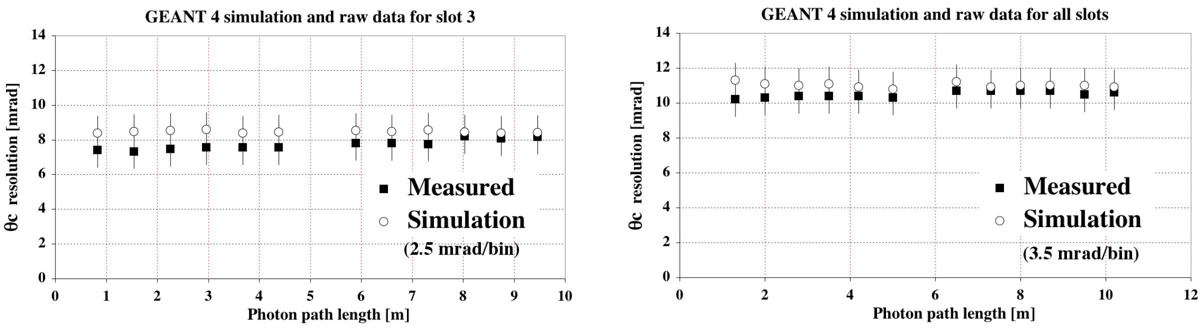

(a) Resolution with 3 mm pixels.

(b) Resolution with 6 mm pixels.

Figure 8.67: Measured and simulated Cherenkov angle resolution without chromatic correction. It is clear that 3 mm pixel choice would improve the FDIRC PID performance [12]

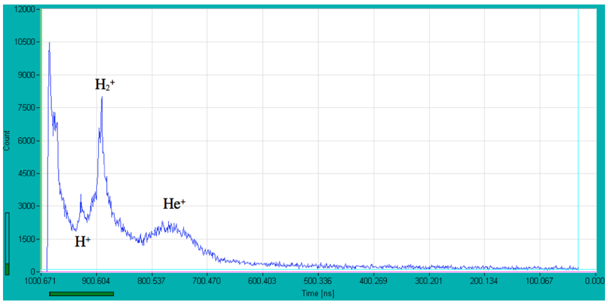

Figure 8.66: A time spectrum of after pulses showing H^+, H_2^+ and He^+ contamination [29].

prototype was tested in a 10 GeV electron test beam at SLAC. This beam entered the bar perpendicularly. It was a very successful R&D program, resulting in a number of very useful results [10, 11, 12], which can be summarized as follows:

- We learned how to operate new fast highly pixelated detectors (Hamamatsu H-8500 and H-9500 MaPMTs; Burle MCP-PMTs). The H-9500 MaPMT was arranged to have 3 mm × 12 mm pixel size, while the other two tubes had 6 mm × 6 mm pixels.

- Test achieved ∼10× better single-electron timing resolution than DIRC: $\sigma_{\mathrm{H-8500}}$∼240 ps, $\sigma_{\mathrm{H-9500}}$∼235 ps, and $\sigma_{\mathrm{MCP-PMT}}$∼170 ps.

- We learned how to design a new optics, which is a combination of pin hole coupled to focusing optics, resulting in ∼25× smaller photon camera that the *BABAR* DIRC SOB.

- This was the very first RICH detector establishing that the chromatic error can be corrected by timing – see Figure 8.7. To be able to do such correction, one needs to achieve a timing resolution at a level of ∼200 ps per single photon, and the photon path length needs to be longer than 2-3 meters. The (F)DIRC bars are indeed longer – due to the bar extra length in the magnet iron –, which helps to improve this correction.

- With 6 mm size pixels we could reproduce *BABAR* DIRC performance of Cherenkov angle resolution of ∼10 mrad per single photon if we do not perform the chromatic correction. With the chromatic correction, one could improve this resolution by 0.5-2 mrad for photon path lengths longer than 2-3 meters – see Figure 8.6.

- With 3 mm size pixels, we could substantially improve on the FDIRC performance – see Figure 8.67. Figure 8.68 shows the overall PID performance for various detector schemes. Clearly, smaller binning in the y-direction would be beneficial to improve the overall performance. Hamamatsu encouraged to use R11256 tube, which would give use 3 mm × 12 mm pad sizes, and possibly QE ∼36%. The comparison also includes the new Hamamatsu 8×8 SiPMT array, where we assumed PDE ∼52%; this is shown for comparative purposes only, as we do not assume to use it due to its large random noise rate at room temperature and further worsening by a possible neutron damage.

- Discovered a new Cherenkov ring aberration, which worsens the resolution near the Cherenkov wings – see Figures 8.8, 8.9.

CRT test results from the first FDIRC prototype We have built the cosmic ray telescope (CRT) to study the FDIRC prototype and various versions of TOF counters using 3D tracking [37]. Figure 8.69 shows the CRT setup [37] which provides a muon energy cutoff of 2 GeV in its latest version.

The first prototype was also tested in the CRT setup. The SLAC CRT setup consists of energy absorber made of 4 feet-thick iron, which provides a muon energy lower cut-off of ∼ 2 GeV. It also provides tracking with 1.5 mrad resolution over an angular range of dip angles within 15 degrees from the vertical. This was also a significant test because it allowed to investigate the Cherenkov angle resolution with 3D tracks [16]. Results can be summarized as follows:

- We learned how to handle 3D tracks in the Cherenkov angle analysis (during the beam test tracks entered perpendicularly [10, 11, 12]).

- Tail in the Cherenkov angle distribution is related to the ambiguity treatment and it is more significant for 3D tracks. The first FDIRC prototype [16] only had two ambiguities: we could not tell a sign of photon vector in the x-direction for photons exiting the bar end, and therefore in the analysis we had to consider both signs. In the final FDIRC prototype, we will have more ambiguities than in the first FDIRC prototype as there are more photon reflections in the new optics. This ambiguity effect enhances the tail as one cannot always reject wrong solution, and it is magnified by a presence of background such as knock-on electrons (delta-rays) or showers accompanying CRT muons. The CRT setup is very good to learn how to deal with these ambiguities. The main conclusion of the studies is that one has to use the quantity dTOP = $\mathrm{TOP}_{\mathrm{measured}}$ - $\mathrm{TOP}_{\mathrm{expected}}$, where TOP is the photon time-of-propagation in the bar. One can make a tight cut on dTOP to help rejecting the background.

- Running CRT continuously allowed to test various versions of electronics very conveniently, and to produce the Cherenkov angle resolution under real conditions.

- The CRT trigger was also used to trigger a PiLas laser diode, which provided a single photoelectron monitoring of all pixels all the time while we were running. The laser trigger did not overlap with the CRT data to avoid any confusion. This allowed to study the stability of FDIRC timing.

- We plan to test the Final FDIRC prototype at high rate background in the CRT setup. This will be done by admixing an asynchronous random light source to the laser calibration signal, while taking regular CRT data. This task will be accomplished with a fiber mixer, which will mix the laser signal with the random light source. In this way we can study the reconstructed Cherenkov resolution as a function of the random background in a controlled way, and see at what point the reconstruction algorithm breaks down. At the same time, we will be monitoring the timing resolution deterioration using the laser signal.

Scanning setups to test H-8500 PMTs and Electronics We have several PMT scanning setups located at SLAC, Maryland, Bari, Padova and LAL-Orsay. These setups differ in their

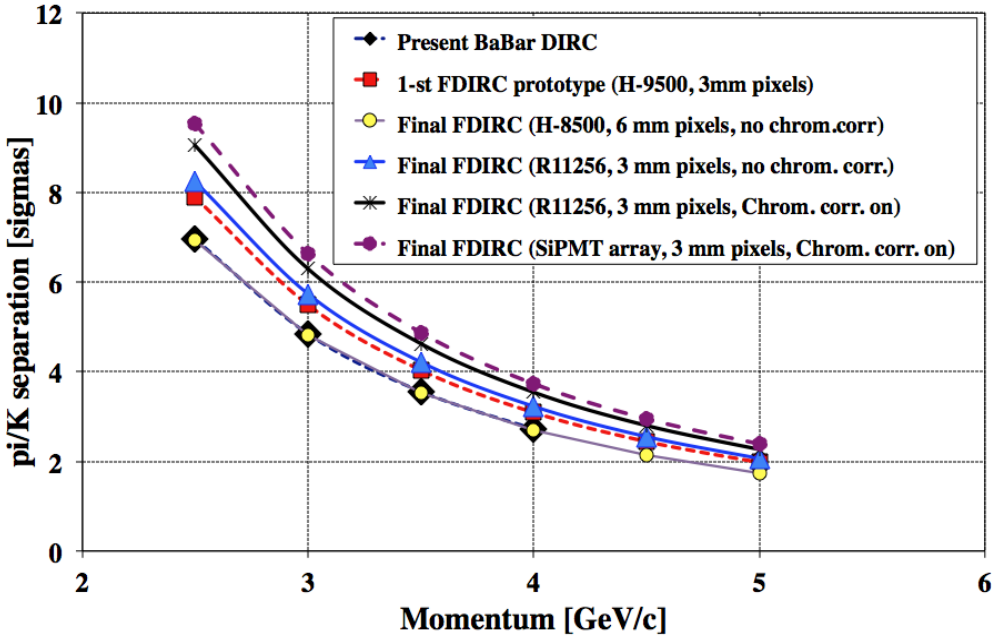

Figure 8.68: Expected $K - \pi$ separation as a function of momentum for various detector schemes, including R11265 PMT and a SiPMT 8×8 array (3 mm pixel sizes).

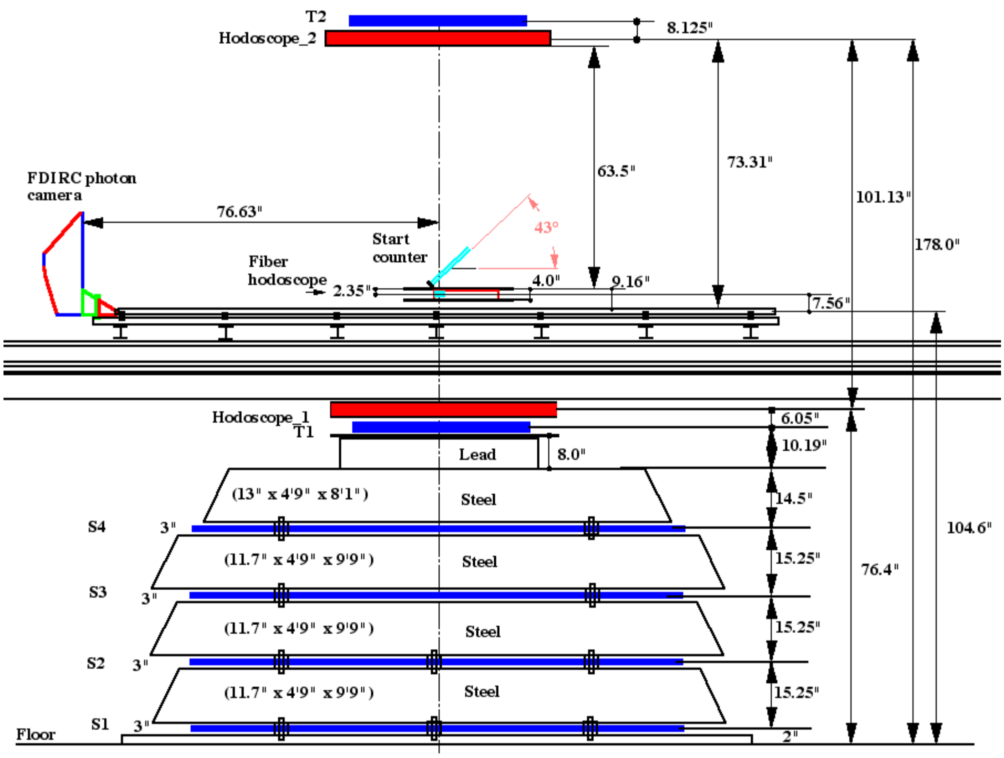

Figure 8.69: The final FDIRC prototype in the CRT setup (shown is its latest version with addition of 8 inches of lead absorber).

capabilities, designs and electronics. Although these setups do not use the final electronics yet, they were nevertheless already very useful to reveal many H-8500 detector details. So far, the following topics have been studied in some details: (a) efficiency uniformity across PMT for 15 tubes, (b) gain uniformity for 15 tubes, (c) cross-talk, (d) charge sharing, (e) after-pulses, (f) pre-pulses (amplification starts on first dynode), (g) anode response to pulses on the last dynode (for calibration purposes), etc. We used many results from these tests throughout this TDR chapter.

In these studies we learned that:

- Based on a study of 15 tubes (960 pixels), the gain uniformity among pixels is typically better than 2.5:1.
- The single photoelectron timing resolution (TTS) has a structure within each pad.
- The charge sharing effect is very small in this particular tube due to its electrode structure, and it is not worthwhile to use it to reduce the effective pixel size, which would help to improve the Cherenkov angle resolution.
- Although one could find a good spot in a H-8500 PMT giving a TTS resolution of $\sim$140 ps (see Figure 8.17), averaging over an entire pixel area gives a TTS resolution more like $\sim$200 − 250 ps, with edge pixels being worse (see Figure 8.19).
- A typical pixel-to-pixel cross-talk in H-8500 tube is about 3%, judging from the scope measurement of pulse amplitudes on neighboring pixels using the SLAC amplifier – see Figure 8.20.

8.3.7 Conclusion and ongoing FDIRC R&D

Experience with the final FDIRC prototype in CRT During its construction we learned the following major points:

- It is possible to build this kind of optics, for affordable cost and within the required tolerances.
- It is possible to handle heavy FBLOCK fragile optics and to assemble Fbox around it.
- We learned how to couple bar box window to the new wedge with Epotek-301 glue.
- We learned how to couple optically the FBLOCK to the new Wedge. It is done with a 1 mm-thick RTV. It is a very large area optical coupling and we learned how to develop a bubble-free coupling. We have demonstrated that this RTV coupling can be cut by a razor wire, the surfaces cleaned and glued again.
- The full size FDIRC prototype is now being studied in the SLAC cosmic ray telescope. The main aim is to verify the optical design and learn how to perform the data analysis.

Detector studies in various scanning setups The study of the H-8500 PMT continues in all scanning setups. So far all tests used various kinds of electronics. It is essential to repeat some of these studies with the final electronics. This, however, cannot be done sooner than in 2013. We also want to make a decision of other possible tube choices, namely Hamamatsu H-9500 and R-11256.

Electronics R&D The final electronics is being developed at LAL. The detector motherboard is being designed at LAL, Padova and Bari. The final electronics will be then tested in the CRT setup at SLAC.

8.3.8 System Responsibilities and Management

Management board structure The PID group has a management board, where each institution has a representative. The role of this management board is to resolve monetary, manpower and other global issues within various institutions as they come during the construction stage.

8.3.9 Cost, Schedule and Funding Profile

Cost The cost of the FDIRC construction, assembly and integration in the Super$B$ detector is given in Chapter 17.

Schedule and Milestones The FBLOCK production determines the entire production time line, *i.e.*, all other tasks take less time. Figure 8.70 shows the present time-flow estimate of the FBLOCK production (for clarity we show only two FBLOCK production cycles). The manufacturing speed is limited by FBLOCK machining and polishing. The total duration of FBLOCK production, as it stands now, is ~28 months. The next longest part of the project is the PMT production, which will take about 2 years, including procurement, delivery and testing.

Critical path items Clearly, the most critical path items are: (a) machining and polishing of the FBLOCK optics and (b) delivery of 600 Hamamatsu H-8500 PMTs. The FBLOCK delivery is controlled by the production capacity, which limits deliveries to one FBLOCK every 6-8 weeks. We will try to find a way to speed it up, or find a parallel production possibility, but it is generally difficult to replicate relevant experience with different companies when one deals with a non-standard optics. Hamamatsu company told us that they can deliver 600 H-8500 tubes over a period of 2 years, which is about 25 tubes per month. It is important that we check that delivered tubes have required performance. We may have to split testing into at least two different scanning setups to be able to cope with a delivery rate of 25 tubes per month.

8.4 A possible PID detector on the Super$B$ forward side

8.4.1 Physics motivation and detector requirements

The Super$B$ barrel region is covered by a dedicated PID detector: the FDIRC, described in the previous sections of this report. The information from this detector, combined with the energy losses from the DCH, ensures a good K/π separation up to about 4 GeV/c. On the other hand, PID in the Super$B$ endcaps only relies on dE/dx measurements from the tracking system without the addition of a dedicated device. In the high momentum region, pions and kaons are only separated at the $\sim 2\sigma$ level – however, the use of the cluster counting method in the DCH would increase this separation 7.1.3. Moreover, dE/dx distributions exhibit a 'cross-over' K/π ambiguity region around 1 GeV/c, inside which charged hadrons cannot be properly identified as the energy loss curves overlap – see Figure 8.71. One can see that a time-of-flight (TOF) resolution of only ~100 ps is good enough in the cross-over region. Though, a better timing accuracy is needed if one wants to be sensitive to higher momenta.

Improving PID in the two endcap regions requires thus new dedicated detectors which should be both powerful and relatively small. The latter characteristic is needed in order to fit in the limited space available in the endcap regions.

In the backward side (where the particle momentum is quite low in average), the EMC group is proposing to install a veto calorimeter to improve the Super$B$ energy measurement – see section 9.4. Should this device be fast enough, it would allow one to separate kaons from pions using the particle TOF.

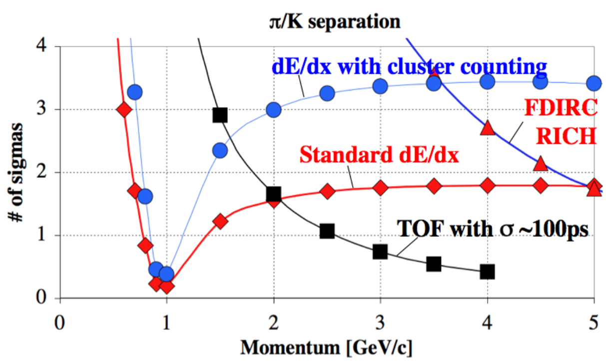

Figure 8.71: Role of a TOF system with ~100 ps timing resolution for K/π separation at low momentum [38, 39].

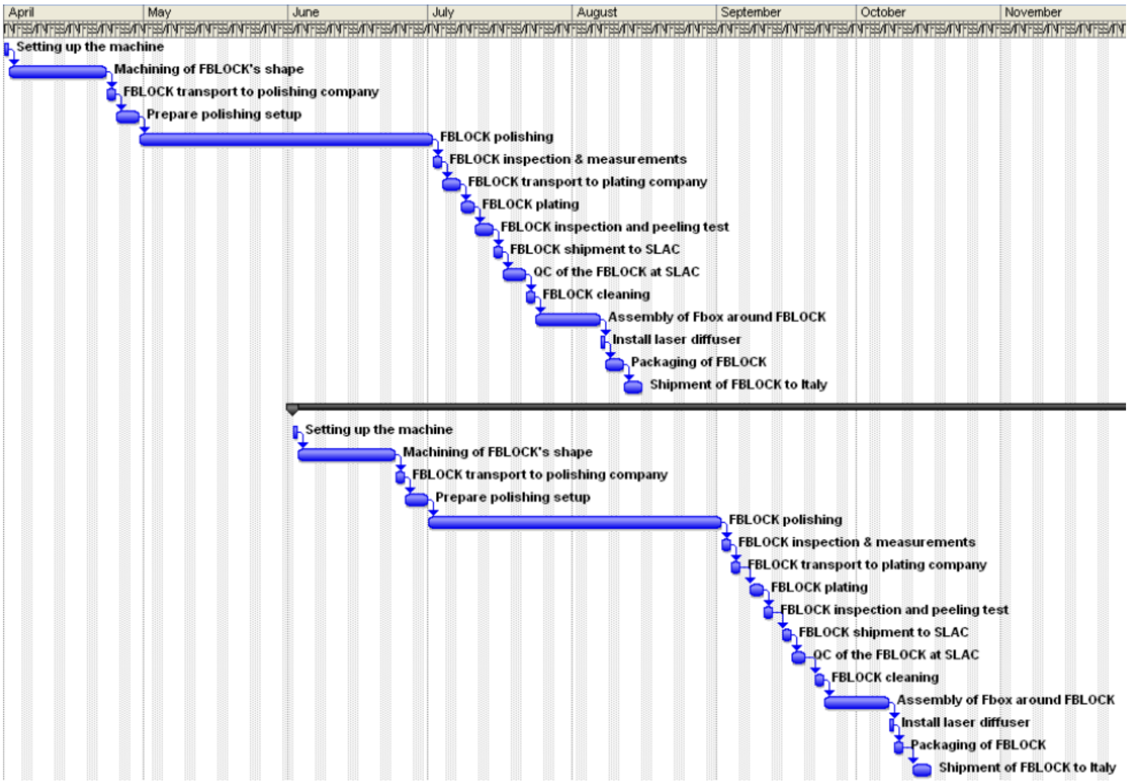

Figure 8.70: FBLOCK production schedule (2 FBLOCK production cycles only).

Due to the Super$B$ boost, the forward region of the detector corresponds to a fraction of the geometrical acceptance larger than its angular coverage in the laboratory frame – about $[17°; 25°]$ in polar angle – while the particles have higher momentum in average. Therefore, a forward PID detector has to be efficient from about 1 GeV/c to 3 GeV/c.

Physics-wise, the Super$B$ performance would benefit from improved PID in many areas:

- larger efficiency in various rare and exclusive B decays;
- reduced background;
- better B tagging;
- improved exclusive reconstruction of hadronic and semileptonic B channels. This technique is used for recoil physics analysis of rare and hard-to-reconstruct decays. Based on the coherent production of a $B\overline{B}$ pair at the $\Upsilon(4S)$, it first identifies events for which one of the B's, the B_{tag}, is fully reconstructed. Once this is done, the rest of the event automatically corresponds to the (other) signal B: B_{sig}. This constraint provides additional kinematical information on B_{sig} decays which would otherwise be underconstrained – e.g. because of undetected neutrinos in the final state. Each of the hundreds of exclusive modes used by this method to reconstruct the B_{tag} meson is characterized by two numbers: its reconstruction efficiency and the purity of the selected sample. Both numbers increase with an improved PID and the larger the number of particles in the final state, the faster the gain.

Given the integration constraints in the Super$B$ forward region, a forward PID detector must be compact. A total thickness around 10 cm would likely put some constraints on the position and dimensions of the DCH and of the forward EMC, but studies – see section 8.4.2 below for a summary – have shown that such changes would only have a limited impact on the performances of these two devices. Yet, the forward PID detector should add the smallest possible X_0 fraction in front of the calorimeter to limit preshowers.

Finally, the cost of the forward PID detector should be moderate in comparison to the one of the FDIRC as it covers a much smaller fraction of the Super$B$ acceptance.

8.4.2 The Forward task force and the selection of a forward PID technology

From early 2009, several possible designs of forward PID detectors have been studied within the PID group. The proposals were submitted to a task force representative of the whole collaboration. It was charged to review the different designs and to make recommendations to the Super$B$ Technical Board, which would then take the final decision. This step was completed in June 2011 and lead to the choice of a technology, as reported in the remainder of this section.

Four main technologies were extensively studied:

- the focusing aerogel RICH (FARICH);
- a pixelated time-of-flight detector with Cherenkov radiators;
- a scintillating detector coupled to G-APD arrays;
- the DIRC-like forward time-of-flight detector (FTOF), finally selected – see section 8.4.3 for the description of this detector.

More details about the first three forward PID concepts can be found in appendix 8.4.4.

Charge and activities of the Forward task force In July 2010, a taskforce on a possible forward PID system in the Super$B$ detector was formed. Its primary charge was to provide an assessment of

- the physics impact of a PID system in the forward region of the Super$B$ detector, roughly defined by the polar angle range 17° to 25°;
- the feasibility of the proposed detector technologies for the forward PID system.

The taskforce considered a list of questions and criteria for both physics and technology assessments, as discussed below.

- Physics evaluation
  - A list of key benchmark physics channels that are affected by a forward PID system were evaluated for both the gain and any potential negative impact due to the added material before the forward EMC or any required change to the DCH dimensions.
  - A preliminary performance evaluation was made of some of the proposed technologies, in the presence of background hits.
  - The impact of each proposed forward PID technology on π^0 efficiency, and momentum and dE/dx resolutions in the DCH was performed.
- Detector technology issues
  - Estimates of cost, required manpower, and construction schedule for each of the proposed technologies were performed. These include information on the availability of components on the time scale of the Super$B$ construction schedule.
  - The need for a proof-of-principle was considered for each of the proposed technologies – at least with cosmic rays and if possible with beam tests. Issues common to nearly all devices are: performance in presence of background; the effect of the Super$B$ magnetic field on the photodetectors and on the overall performance of the device; photodetector aging.

– Integration issues.

The taskforce met with forward PID proponents at all Super$B$ workshops between September 2010 and May 2011 when the committee recommendation was released. There were also phone meetings in between workshops.

Summary and taskforce recommendation

Note: This report has been written in May 2011. Since then, both the SuperB design as a whole and the design of the FTOF (the selected technology) have evolved. For instance, the width of the Tungsten shield around the beam pipe has been increased from 3 to 4.5 cm, leading to a dramatic reduction of the FTOF background. More information can be found in the following section (8.4.3), where the current status of the FTOF R&D activities is described.

The physics gain from a forward PID device is around 4-5% for the benchmark channel $B \to K^{(*)}\nu\bar{\nu}$: roughly 2%/kaon. No physics channel with higher gain has been identified. Results based on simulation and beam test (1 GeV/c electrons) show no significant degradation of resolution & efficiency for γ and π^0 in the EMC. In addition, the impact on tracking resolution due to a shortened DCH has been estimated to be $\sim$1% degradation in momentum resolution/cm cut.

The overall assessments for the proposed detector technologies are the following.

- FARICH. On the whole, this technology is likely to yield the most powerful – and robust – PID performance, extending well above the nominal 4 GeV/c for B decays. The expected performance is verified by impressive beam test results. However, no physics channel that would significantly gain from the extended performance has been identified. Moreover, the required cut of $\sim$17 cm to DCH length significantly degrades momentum resolution in this angular region. This is an unacceptably large negative impact on the detector performance and a too severe constraint on the tracking system. Hence, the taskforce does not see this technology appropriate for forward PID in the Super$B$ detector

- Pixelated TOF (LYSO plus G-APD array option). This technique, due to its potential minimal disturbance on the rest of the detector and likely modest cost, was deemed very attractive. At the aimed resolution of $\sim$100 ps, it would complement the dE/dx measurements for K/π coverage below 2 GeV/c. However, with the obtained time resolution ($\sim$230 ps) for a full size LYSO crystal in cosmic ray tests, the proponent & taskforce have concluded that this technique will not deliver the required performance.

- FTOF. Simulation studies and cosmic ray tests – see section 8.4.3 – have demonstrated that key aspects of this technique can be attained – including the goal of a time resolution of $\sim$90 ps/hit. But there remains significant uncertainties on the expected background level and its impact on PMT lifetime. The taskforce believes this technique could be appropriate for the forward PID system provided that background (and radiation) issues are understood – which may require further studies of the IR design and shielding – and that a full prototype of the system is developed and tested, to verify the expected performance, in particular the pattern recognition in the presence of background hits.

The final recommendation for the forward Super$B$ region is the following: the importance of hermeticity (and redundancy) in PID coverage will increase as we approach the systematics-dominated era in the Super$B$ physics program. Hence, the taskforce members believe – independently of the outcome of the current technology evaluation – that there is physics merit to allowing a gap of $\sim 5-10$ cm in the forward region for a PID device. This would allow for introduction of a system at a later stage of the experiment, in case the detector studies are not completed in time for the initial installation of the Super$B$ detector.

8.4.3 The DIRC-like forward time-of-flight detector (FTOF)

As indicated by its name, the FTOF [6, 7, 40] belongs to the family of the DIRC detectors [1, 2]. One should also say that this particular geometry is close to the TOP concept, which is proposed for the Belle-II barrel detector [41]. Charged particles cross a thin layer of fused silica; provided that their momentum is high enough, they emit Cherenkov light along their trajectories. Part of these photons are trapped by total internal reflection and propagate inside the quartz until an array of MCP-PMT where they are detected. Unlike the (F)DIRC, no attempt is made to reconstruct Cherenkov angles: K/π separation is provided by time-of-flight – at given momentum, kaons fly more slowly than pions as they are heavier.

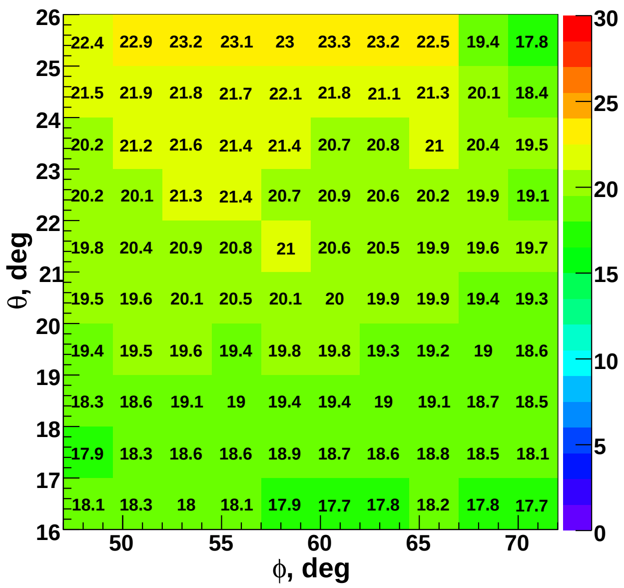

Figure 8.72: Map giving the mean number of detected photoelectrons in a FTOF sector as a function of the track polar (θ) and azimuthal (ϕ) angles at origin. This map is drawn for 800 MeV/c kaons shot from the IP in a simplified detector model including the 1.5 tesla longitudinal solenoid field.

Given the short flight distance between the IP and the FTOF (about 2 meters, hence a 90 ps difference for 3 GeV/c particles), the whole detector chain must make measurements accurate at the 30 ps level or better. This is one of the main challenges of this design, the others being the photon yield, the sensitivity to the background (including ageing effects due to the charge integrated over time by the photon detectors) and the event reconstruction. Regarding the latter point, one should emphasize that the FTOF is in fact a two-dimensional device: the PID separation uses both the timing and spatial distributions of the photons detected in the MCP-PMT arrays.

Design optimization The performances of the FTOF depend on two main parameters which should be optimized simultaneously [40]. One is the photon yield per track, which should be as high as possible; the other is the photon timing jitter, which should be minimized in order to efficiently separate kaons from pions. Both are strongly related to the geometry of the detector.

The number of Cherenkov photons produced by a given track scales linearly with its path length in fused silica. Simulations show that a 1.5 cm thickness for the quartz tile is a good compromise between light yield and detector thickness in term of X_0. This finite size introduces an irreducible component of the photon time jitter (about 50 ps), as Cherenkov photons are emitted uniformly along the track path inside the tile. Their initial directions lie on a cone which opening angle depends on the track velocity (which is a function of the particle measured momentum and of its unknown mass) and on the medium optical index ($n \approx 1.47$ in fused silica). The main axis of the cone is aligned with the track direction. With the FTOF design extensively used to prepare this report, tracks originating from the IP all give a large-enough number of photoelectrons, as shown on Figure 8.72 which is drawn using low-momentum kaon tracks – the most unfavourable case as the Cherenkov photon yield increases with the particle velocity.

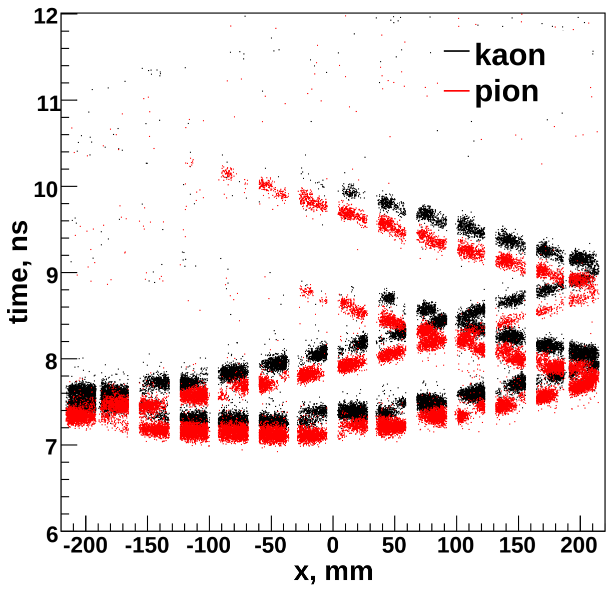

Figure 8.73: The FTOF is a 2D-device: in addition to the photoelectron timing, the distribution of hits in the MCP-PMT channels is also a discriminating variable to separate kaons from pions, as shown on the two plots superimposed in this figure. Both show the time versus position of hits generated by 2 GeV/c kaons (black) and pions (red). $t = 0$ corresponds to the particle generation at the IP while x is an axis along the tile width which shows the MCP-PMT position. The 14 photodetectors are clearly visible just as the small gaps between them.

Therefore, it is clear that photons from a given track can follow several different paths before being detected in a MCP-PMT channel. This is another source of time jitter which has to be taken into account. One way to mitigate it is to select only the 'most-direct' photons which reach the detectors after at most few reflections on the tile front and back faces. This can be done by covering the tile sides by photon absorber, but the loss in photon yield is then too high. In the current design, only the tile inner radius is covered by absorber to stop the 'downward-going' photons whose paths are too long and make their timing unusable. Indeed, with tiles perpendicular to the beam axis, photons are mainly 'upward-going': they are travelling towards the tile outer radius, which is why the MCP-PMTs are located in this area.

Given the accuracy of the timing measurements required by the FTOF, chromaticity is another effect which cannot be neglected: the smaller the photon wavelength the larger its speed – 'red' photons are faster than 'blue' ones.

The FTOF photon yield also depends on the tile orientation as only Cherenkov photons trapped inside the quartz by total internal reflection can be detected. Using vertical tiles as reference, simulations show that a 10° tilt in the forward (backward) direction increases (decreases) the yield by about 15% in average. But configurations in which the FTOF is bent forward are impossible in practice, due to integration constraints on the Super$B$ forward side.

One point worth mentioning is that the FTOF is a 2D-device, as shown on Figure 8.73. This means that the K/π separation is not only coming from the photoelectron timing but also from the spatial distribution of the photon hits on the MCP-PMTs.

FTOF design The DIRC-like forward time-of-flight detector is made of 12 thin fused silica tiles (1.5 cm thick each, which corresponds to 12% X_0) located perpendicularly to the beam axis and covering 30° in azimuth each – see conceptual drawings on Figure 8.74. The requirements for the tile dimension accuracy and the fused silica polishing quality are less stringent than for the *BABAR* DIRC bars, as the Cherenkov photons will bounce much less in the quartz. Therefore, building the FTOF tiles should not be an issue given the knowledge accumulated in this area over the past two decades.

Each FTOF tile will be placed into a light aluminum box which is the equivalent of the DIRC bar boxes for the DIRC quartz bars. To keep the fused silica tiles as clean as possible, the tile box should not contain any other detector component; there will just be an optical contact between the quartz and the MCP-PMTs. Both the tile box and the box enclosing the MCP-PMTs will be light-tight; in addition, the tile box will

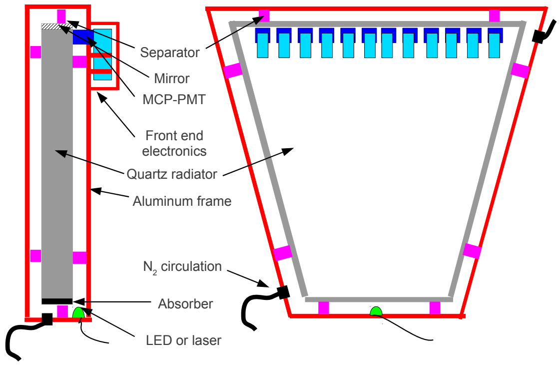

Figure 8.74: Sketch of a FTOF sector: side (left) and back (right) views. These drawings are not to scale: the width of a FTOF sector is about 5 cm (frame included) while its height is a few tens of cm.

Figure 8.75: The 16-channel Wavecatcher board.

be leak-tight and N_2 will flow continuously inside it to avoid any moisture.

The prototype FTOF front-end electronics is based on the new 'WaveCatcher' boards commonly developed by LAL Orsay and CEA/Irfu Saclay [42, 43]. They are 12-bit 3.2 GS/s low power and low cost waveform digitizers based on the SAMLONG ultra-fast analog memory. The sampling time precision is as good as 10 ps rms, a value measured at the level of a crate hosting eight 2-channel boards. The photon arrival time is extracted via digital Constant Fraction Discrimination (CFD). A new 16-channel board – see Figure 8.75 – recently designed has been characterized: it exhibits the same timing performances.

The final electronics will be highly integrated and based on a new principle of TDC, called SAMPIC – see Figure 8.76. The latter, designed in AMS CMOS 0.18 μm technology, will be able to tag the arrival time of 16 analog signals with a precision of a few ps thanks to its embedded analog memory (running between 5 and 10 GS/s) and its embedded ADC. This will permit housing at least 64 channels in a final front-end board. In the current FTOF design, a single 64-channel Wavecatcher board will be enough to

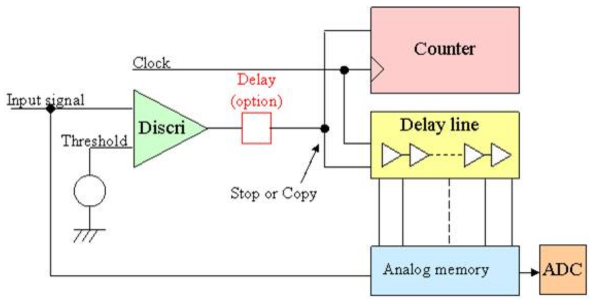

Figure 8.76: Scheme of the new TDC for the FTOF electronics.

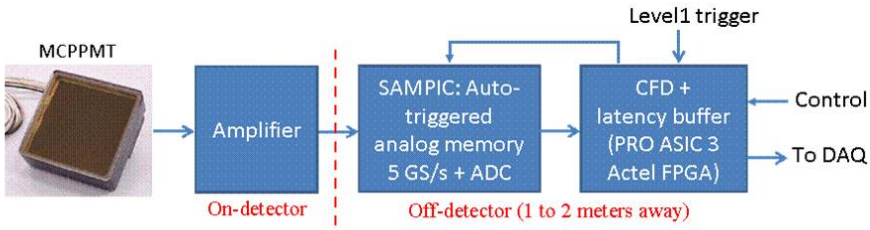

Figure 8.77: Schematics of the FTOF whole electronics chain.

readout a sector (hence 12 boards will be needed in total for the whole FTOF).

The FTOF front-end boards will be located outside the detector, both for protection from background and radiation, and to allow easy access for repair. The analog signal will be amplified right behind the MCP-PMTs and then transferred to the front-end board via signal cables. Figure 8.77 shows the schematics of the FTOF electronics chain.

As explained above, the whole FTOF measurement & processing chain must be ultra-fast. The time resolution per photon must be at the level of 100 ps or better, which makes the use of MCP-PMTs mandatory. Among the products available on the market, the Hamamatsu SL-10 is currently our baseline. With a time-transit-spread (TTS) of 70 ps (FWHM), an active area of 22×22 mm^2, a quantum efficiency of 17% [44] and a lifetime of $\sim$2 C/ cm^2 [44], it offers a good compromise given the FTOF requirements. Two such photon detectors will be characterized at LAL-Orsay in the coming months. In the design used during the TDR preparation period, one needs 14 SL-10 per sector, hence 168 in total; each MCP-PMT will host 4 different channels which will all have their own HV channel. The HV power supplies will be located behind the detector shield wall and could then be accessed 24/7.

A fully instrumented FTOF sector is expected to be very light: about 12 kg total.

Tests with the first FTOF prototype A test of the FTOF detection concept was run at SLAC in the Cosmic Ray Telescope (CRT) between Fall 2010 and Spring 2011 [40]. The SLAC group

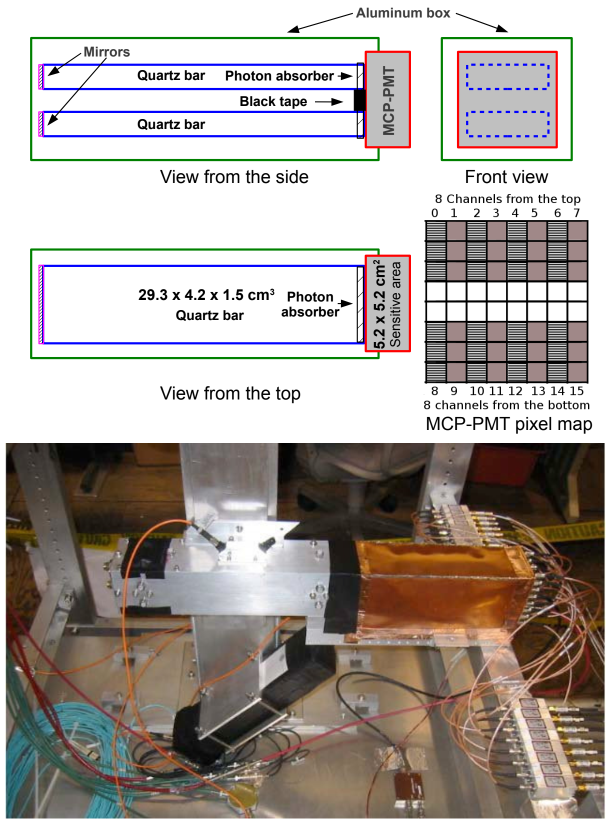

Figure 8.78: Top: side and top views of the 2-bar setup; the 16 channels readout by the USBWC boards are shown on the right-hand side. Bottom: picture of the apparatus in the SLAC CRT. The orange box is a Faraday cage containing the USBWC electronics while the grey box contains the prototype. Under these items, one can see the enclosure of the sloping fast quartz counter which is used to trigger the CRT in coincidence with the hodoscopes.

provided the detector hardware (two short rectangular fused silica bars readout by a Photonis MCP-PMT [45]) and the CRT test facility; the LAL team brought new 2-channel USBWC boards [46]. The test setup is shown in Figure 8.78. Cosmic muons cross two bars located on top one another. The Cherenkov light propagates to the instrumented end of the bars. By shorting and grounding pixels, one defines 16 MCP-PMT vertical pads – 8 for each bar – which are connected to the USBWC electronics.

The CRT trigger start time is defined by a fast Cherenkov counter located under the two bars. For each trigger, the 16 USBWC analog buffers are readout to see if photons have been detected by one or more pads. If this is the case, the USBWC event is written to disk. To handle overlapping waveforms in a given pixel, a photon absorber was placed in front of the MCP-PMT. The waveform time was measured by a CFD-based software algorithm.

The CRT setup does not provide a sufficiently good start time (unless one would severely restrict tracking phase space). Therefore, the current determination of the prototype time resolution is based on time difference between channels, one chosen in the top bar and the other in the bottom bar. All pairs of channels have been considered but they are studied separately as the resulting timing distributions depend on the photon paths compatible with the particular two MCP-PMT pads considered. The interpretation of these data is not straightforward as photons emitted by a muon track can follow several different paths to reach a particular pad. At present, a 3D-tracking treatment is not included in the current analysis. Ideally, one should use

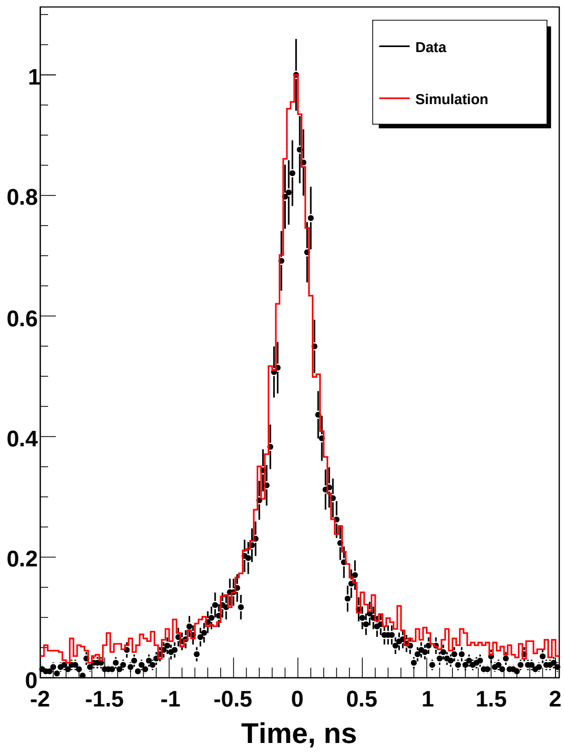

Figure 8.79: Comparison between data (bullets) and simulation (solid-line histogram) for the time difference between two MCP-PMT channels among the 16 readout by the USBWC boards. All distributions are scaled so that their peak is equal to 1 in arbitrary units. The data-MC agreement is impressive, both for the core and the tails of the distributions. Similar results are achieved for all pairs of channels studied.

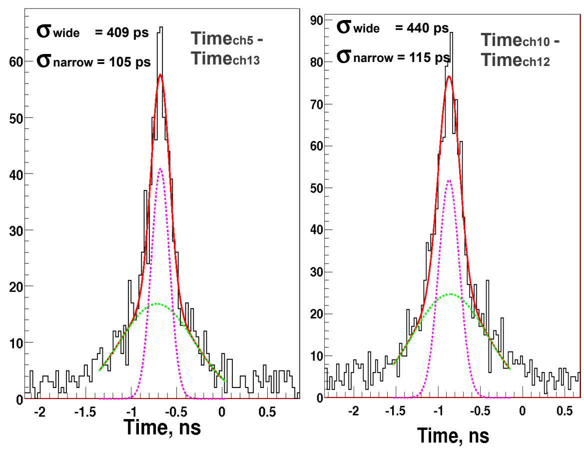

Figure 8.80: Double Gaussian fits to two representative distributions of the time difference between two channels. In both cases, the width of the narrow component is interpreted as the prototype device while the wide component accounts for multiple photon paths (and hence multiple timings) between pads.

a variable dTOP = TOP$_{measured}$ - TOP$_{expected}$, to determine the ultimate timing resolution; this is not easy in CRT as one deals with 3D tracks; the absence of the right treatment of the variable dTOP broadens the timing distribution and increases the size of tails. Yet, a good data-Monte-Carlo agreement – see Figure 8.79 – makes us confident that this analysis is valid. As shown in Figure 8.80, the measured single photon timing accuracy is in the range 80-100 ps, dominated by detector effects (spread of the Cherenkov photon emission time due to the finite quartz tile width; multiple photon paths inside the fused silica to the MCP-PMTs; variation of the cosmic muon track parameters, chromatic effects, etc.). This preliminary result should be confirmed by a re-analysis of the data based on 3D-tracking and aiming at comparing the photon measured and expected times.

Background and aging studies The FTOF sensitivity to background can be seen in two ways. First, background hits could affect the CFD timing algorithm and add to confusion in the pattern reconstruction algorithms. In addition, the background rate will increase the MCP-PMT total charge. The consequence of the latter will be a slow decrease of the MCP-PMT quantum efficiency; at an integrated charge around 2 C/ cm^2 [44], the photon detectors will cease working properly. Therefore, it is crucial to estimate the FTOF background accurately and to find ways to decrease it as much as possible. In addition, the MCP-PMT gain should be high enough to keep the TTS low, but not too high as it limits the MCP-PMT rate.

Full GEANT4 simulations of the Super$B$ interaction region (detector included) simulating the main backgrounds – radiative Bhabha, Touschek particles, etc. – have shown that the dominant FTOF background is due to off-energy positrons which hit the beam pipe about one meter away from the IP on the forward side. This localized background source can be mitigated by increasing the thickness of the tungsten shield which protects the detector. Initial studies have shown that going from 3 cm to 4.5 cm (currently the nominal value) decreases the FTOF rate by a factor 3 to about 115 kHz/ cm^2. As shown in Eq. 8.1, the background rate can be directly related to the gain at which MCP-PMTs can be operated, assuming 15 ab^{-1} collected per year during five years. Therefore, work is ongoing to refine the FTOF background estimate.

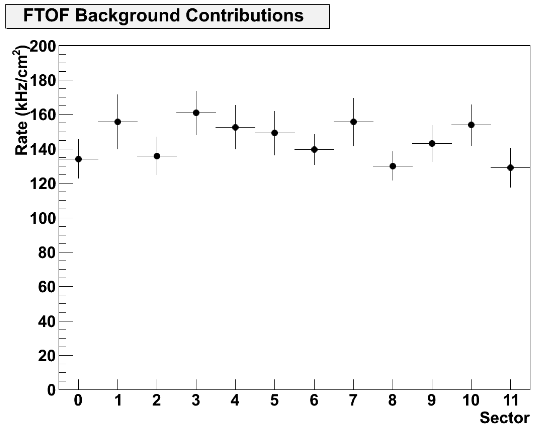

Figure 8.81: Sum of all background contributions in the 12 FTOF sectors – no safety factor included.

$$\begin{aligned}\text{Maximum gain} = {} & 2.8\,10^5 \\ & \times \left(\frac{2.5\,\mathrm{C/\,cm^2}}{\text{Maximum integrated charge}}\right) \\ & \times \left(\frac{150\,\mathrm{kHz/\,cm^2}}{\text{Background rate}}\right) \\ & \times \left(\frac{5}{\text{Safety factor}}\right) \\ & \times \left(\frac{75\,\mathrm{ab^{-1}}}{\text{Integrated luminosity}}\right)\end{aligned} \tag{8.1}$$

Figure 8.81 shows the simulated background rates (summing up the contributions from all sources) in all 12 FTOF sectors, labelled clockwise as seen from the IP – sector 0 is at the top of the FTOF.

Ongoing activities and future plans As explained above, the FTOF technology has been chosen by the Super$B$ collaboration for the forward PID detector. Therefore, if one such device is to be built, that will be the FTOF. Yet,

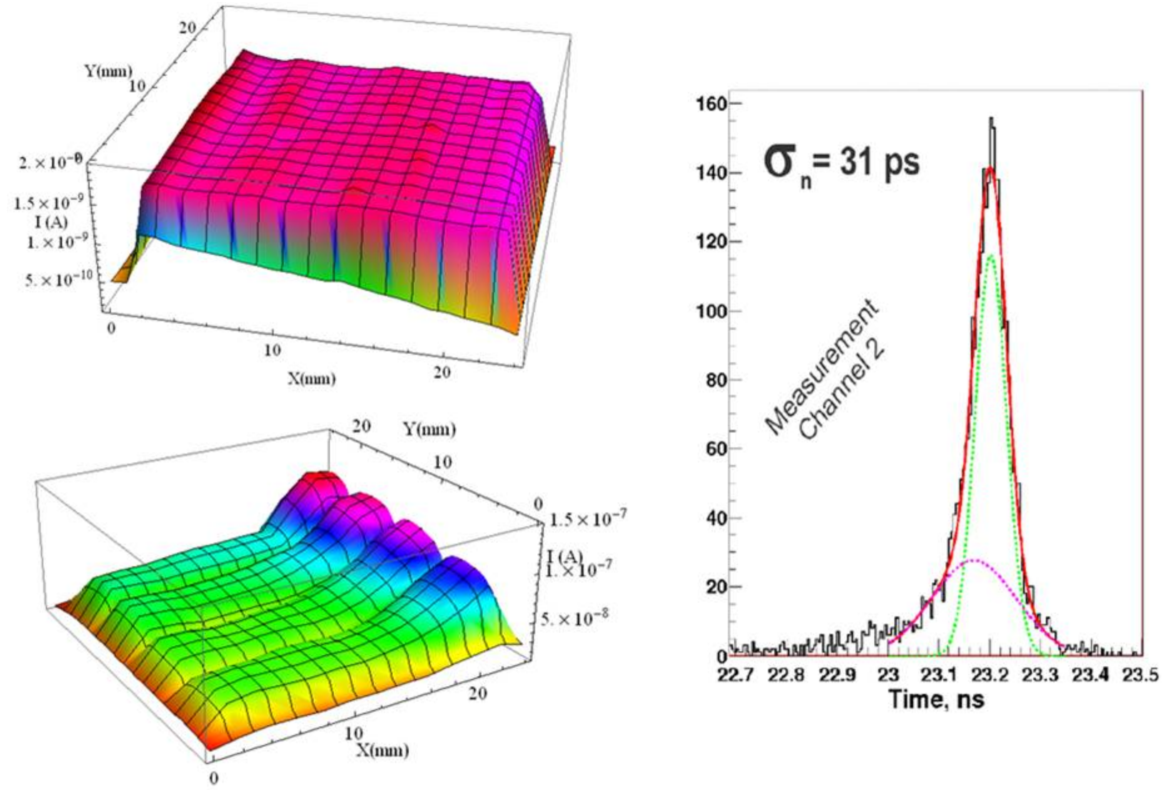

Figure 8.82: Top left plot: SL-10 photocathode response mapping; bottom left plot: 4 anode response mapping; right plot: single photoelectron timing resolution (FWHM).

to be included in the detector baseline, a full-size prototype of a FTOF sector must be built and validated, both in cosmics and test beam.

As a first step, a fused silica tile (Spectrosil 2000 from Heraeus) has been purchased by the LPSC Grenoble group (which joined the FTOF development in 2011). It will be placed in a local cosmic ray telescope specifically designed for the FTOF geometry with an active area of 0.23 m^2 and good resolution on position ($\sim$0.3 − 0.6 cm) and angle ($\sim$0.2 deg). Different absorber thicknesses are used to select 7 momentum ranges of the muons from 300 MeV/c, the thicker absorber giving a lower cut at 1.7 GeV/c. The yield of this telescope is 1 Hz for the full momentum spectra and only 0.2 Hz for the higher energy bin. The main purpose of this setup is to study the photon yield versus the muon impact position and incident angle, using several coatings on edges and faces. The goals of these studies are to measure the photon collection efficiency and timing in various configurations. These data will allow one to validate the full Geant4-based optical simulations.

In addition, the FTOF effort will benefit from another cosmic ray telescope: CORTO. This R&D facility, which is being built at LAL, will be used by different labs of the Orsay campus to test detectors. At CORTO, the FTOF-like fused silica tile will be tested with different MCP-PMTs: R10754X (SL-10) from Hamamatsu and XP85112 from Photonis. Table 8.3 shows a comparison of these two devices. Measurements of the characteristics of these photon detectors are in progress, as shown in Fig 8.82. In addition, we may test in the future MCP-PMTs developed jointly by the Ekran company and BINP [48]. They are much cheaper than the two models mentioned above. But they also need to be stud-

Table 8.3: Comparison of two MCP-PMTs candidate for the FTOF [47].

MCP-PMT	Effective area (mm^2)	Quantum efficiency (QE) @ 400 nm	Typical gain	Transit time spread (FWHM)	QE reduction after 2 C/cm^2 accumulated charge
R10754X-01-L4	22×22	17%	10^6	70 ps	20%
XP85112/A1	53×53	22%	10^5	82 ps	Unaffected

ied in details to see if they would match the SuperB requirements.

In the meantime, the FTOF design will go on, benefiting from improved simulations and progress on the geometry of the crowded SuperB forward region. Discussions are also ongoing about the best location of the MCP-PMTs: at the outermost radius they are subject to less background but accessing them for repair would be extremely difficult. On the other hand, putting the MCP-PMTs at the innermost radius would require tilting the FTOF significantly (to have a larger fraction of Cherenkov photons downward-oriented), which is not possible given the integration constraints on the SuperB forward side.

Following a meeting at SLAC in July which was dedicated to detector integration issues, the geometry of the SuperB forward region has been updated [49] at the September 2012 SuperB meeting in Pisa. Space constraints at large radii make impossible the extension of the FTOF beyond the DCH outer diameter. Therefore, its maximum diameter has to be reduced by about 10 cm with respect to the design which was used for all the studies reported in this document. The new design is being propagated to all SuperB software and will be used as baseline from now on.

Mechanical drawings have then been produced to present the new shape of the FTOF. Figure 8.83 shows the front view of a FTOF sector embedded inside its 'tile box'. Then, Figure 8.84 shows the dimensions of one such sector. Finally, Figure 8.85 shows the corresponding side view of the sector.

The main parameters of the FTOF structure are the following.

- Aluminium side frame thickness: 3 mm
- Aluminium front frame thickness: 1 mm
- Absorber thickness: 3 mm
- Mirror thickness: 3 mm – this mirror is used to reflect back photons which miss the MCP-PMT line initially. It increases significantly the photon yield per track.
- Mass of the quartz tile is around 2.5 kg

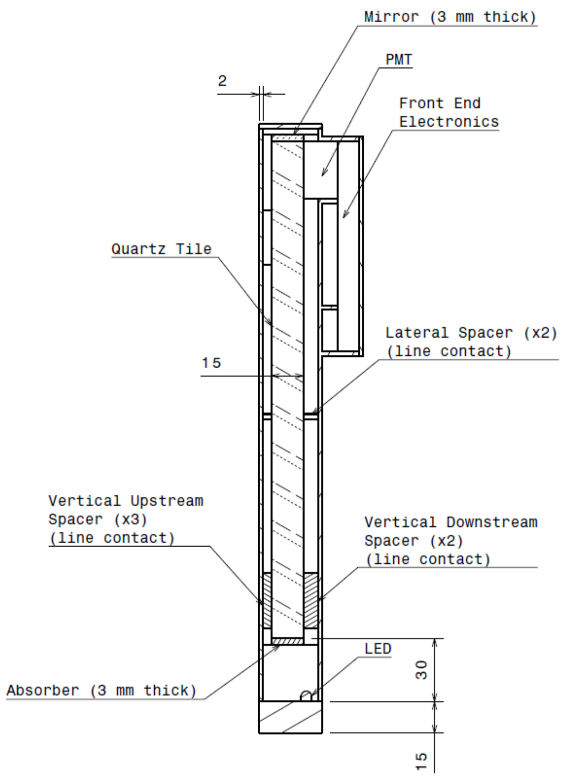

Figure 8.85: Side view of a FTOF sector. On this drawing, the rear of the tile is on the right.

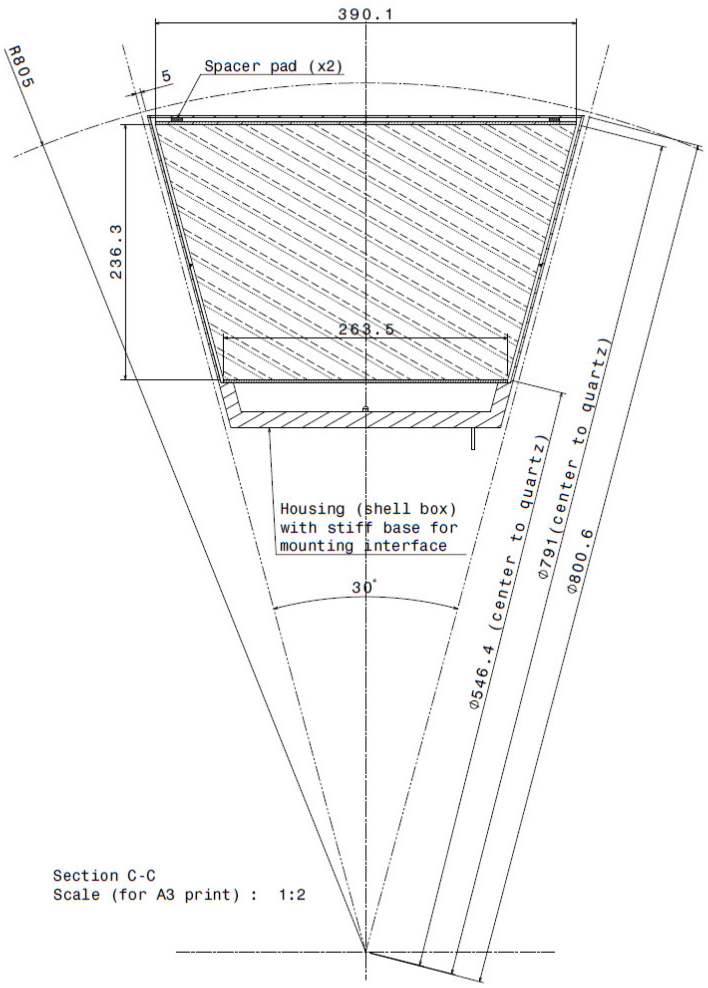

Figure 8.83: Front view of a sector of the FTOF detector inside its 'tile box'. The quoted dimensions are in millimeters and correspond to diameters.

Once the FTOF design is frozen, the building of the prototype will start – its cost is strongly dominated by the MCP-PMT price. Assuming that the whole project proceeds smoothly and that the FTOF is accepted by Super$B$, a detailed appendix of the present detector TDR will be published to provide all the needed information to support this innovative detector.

8.4.4 Appendix: forward PID R&D activities

In the following paragraphs, the main characteristics of the three proposals which have not been selected by the Forward task force are briefly summarized, such as their advantages and drawbacks.

Focusing aerogel RICH (FARICH) Ring Imaging Cherenkov detectors are the most powerful instruments for charged hadron identification in a wide momentum region, ranging from $\sim$0.5 to $\sim$100 GeV/c. The use of multilayer aerogel radiators in proximity focusing RICH detectors significantly improves PID performances with respect to a single layer aerogel RICH device. To provide PID at momenta below 0.6 GeV/c, an additional radiator with high refractive index is added.

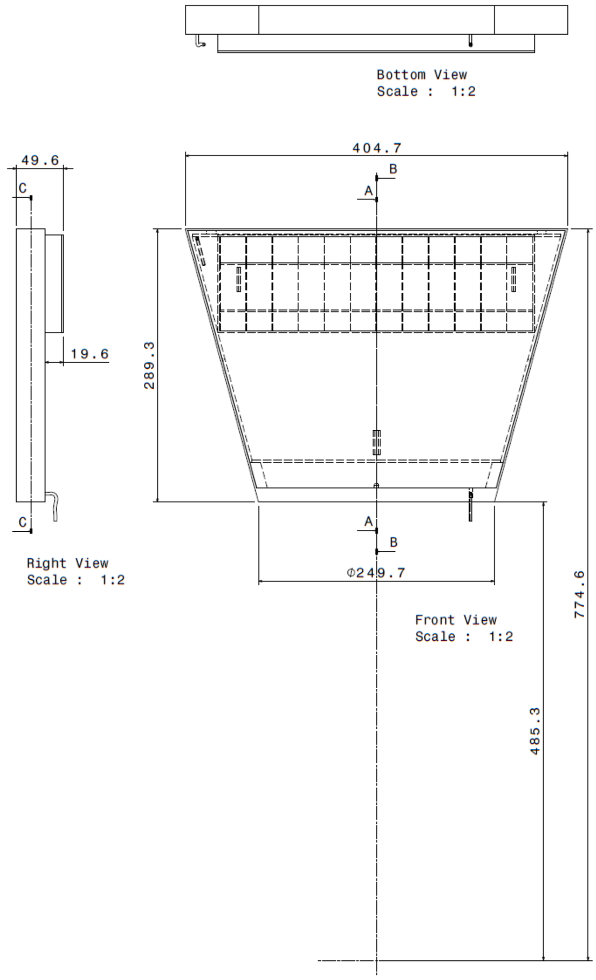

Figure 8.84: Front view of a single FTOF sector showing its dimensions.

From the beginning, it was known that the main drawbacks of the FARICH were integration issues (the free space on the forward side of the detector is limited) and cost. One of the factors which drives the latter is the number of channels. Therefore, the design was optimized to minimize the number of channels, such as the total thickness of the system, while keeping the PID performance high. The FARICH design is presented in Figure 8.86; its main parameters are given below.

- Expansion gap: 65 mm (total thickness of the system ∼150 mm).
- Photon detector: the Photonis Multi-Channel Plate Photomultiplier (MCP-PMT) with 6×6 mm^2 anodes (8×8 matrix); photoelectron collection efficiency: 70%; packing efficiency: 80%.
- A 2-layer 'focusing' aerogel (n_1=1.039, n_2=1.050) of total thickness 30 mm.
- One additional layer of NaF radiator: n=1.33, 5 mm thickness.
- Number of PMTs: 312.
- Number of channels: 20000.
- Amount of material (X/X_0): 25% = 2.4% (aerogel) + 4.3% (NaF) + 10% (MCP PMT) + ∼8% (support, electronics, cables).

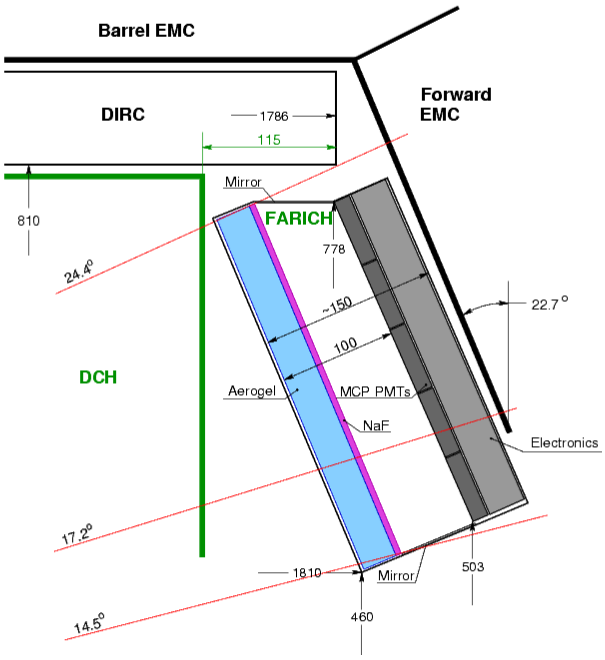

Figure 8.86: Possible FARICH detector layout in the Super$B$ detector.

A Monte Carlo simulation was developed for the proposed configuration. The number of detected photons for $\beta = 1$ particles are 16 from the aerogel radiator and 10 from the NaF one. The FARICH detector is able to perform K/π separation at the 3σ level and better from 0.2 to 5 GeV/c, μ/π separation from 0.13 to 1 GeV/c and π/p separation from 1 to 8 GeV/c.

In addition, a prototype was tested in a beam. The main goal of this test was to demonstrate the 'focusing' capabilities of a real multilayer aerogel radiator at short expansion gap and to measure the contribution from aerogel radiator to the resolution on the Cherenkov angle. The measured aerogel tile had 4 layers, with a maximum layer index of refraction of 1.05 and a total thickness of 30 mm. The FARICH prototype used 32 MRS-APDs (SiPMs) from the CPTA company (Moscow, Russia) as photon detectors. Their active area was $2.1 \times 2.1\,\mathrm{mm}^2$ and they were selected as photodetectors for the prototype because of their good spatial resolution ($\sigma_{\text{pixel}} = 2.1/\sqrt{12} = 0.6$ mm). But such APDs could not be used for the Super$B$ FARICH because of fast damage by neutrons. Custom-made discriminator boards and the CAEN V1190B multi-hit TDC were used for the signal readout.

The test beam facility was constructed at the VEPP-4M collider at the Budker INP in Novosibirsk. This apparatus also included a trigger, some veto scintillation counters, coordinate drift chambers and a NaI calorimeter.

During this experiment, we measured simultaneously the parameters of 1 GeV/c electron tracks and the coordinates of the associated Cherenkov photons detected in the multilayer aerogel radiator. The density of photoelectrons vs. radius for one of the SiPMs used by the prototype is presented in Figure 8.87. As one can see, the distribution of Cherenkov photons vs. radius is well-described by the sum of a signal Gaussian plus a linear background due to random coincidences with SiPM noise, at least within $\pm 5\sigma$ of the signal peak. The measured radial resolution σ_r for the Cherenkov photons is equal to 1.1 mm.

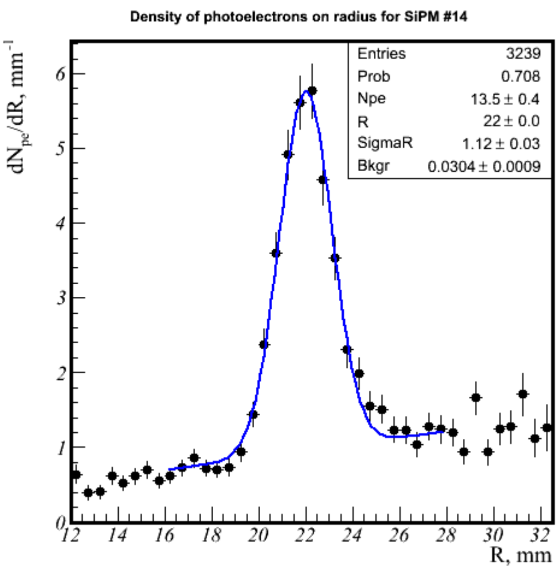

Figure 8.87: Density of photoelectrons vs. radius for SiPM #14.

With this input, we estimate the contribution to the single photon resolution from an aerogel radiator to be $\sigma_{\text{Aerogel}} = \sqrt{\sigma_r^2 - \sigma_{\text{pixel}}^2} = 0.91$ mm. The expected K/π separation based on σ_{Aerogel} (taken from the test beam data) and data provided by Photonis (MCP-PMT provider) is presented in Figure 8.88.

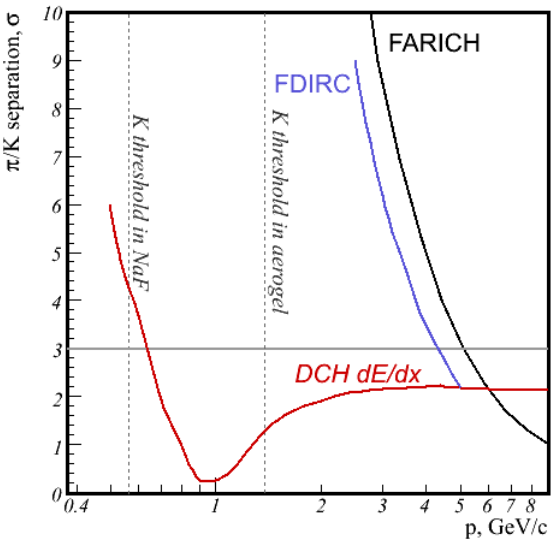

Figure 8.88: The expected FARICH K/π separation based on σ_{Aerogel} from test beam data together with the expected Super$B$ FDIRC and dE/dx K/π separations.

Our study has shown that a FARICH-based PID system could be used by an experiment like Super$B$. First, multilayer 'focusing' aerogel radiators are now available on the market; moreover, the estimated backgrounds are on the low-level side for this detection technology. Finally, the expected life time of the PMTs during the experiment is about 10 years or more.

After detailed investigations, it was concluded that the gain in detection efficiency was not significant enough, in comparison with the cost of the system and the necessity to cut the forward end of the Super$B$ drift chamber in order to give the FARICH enough space.

Pixelated time-of-flight detector with Cherenkov radiators Figure 8.89 shows a possible concept of a TOF detector. It uses polished and side-coated fused silica radiator cubes, which are optically isolated from each other. The radiator cubes are coupled to a MCP-PMT detector with 10 micron holes. This concept is the most simple of all TOF detector designs, as it avoids complicated 3D data analysis and minimizes chromatic effects. On the other hand, it requires a large number of MCP-PMT detectors, which increases the cost prohibitively at present. However, if such detectors would become cheap at some point in future, one could revive this concept again.

Figure 8.90 shows a prototype of the pixelated TOF concept, with a coated fused silica radiator cylinder. The detector had a fiber allowing calibration and laser-based bench-top tests. The radiator was coupled to a Photonis MCP-PMT with 10 micron holes. There were two identical detectors placed in the test beam, allowing to use one as a start and the other as a stop in the timing measurement, and therefore the quoted resolution is the measured resolution divided by $\sqrt{2}$. Reference [50, 8, 42, 51] summarizes all work towards this concept.

Figure 8.91 shows the best resolution obtained with the TOF prototype in the Fermilab test beam. The detector operated at low gain, which means it did not achieve the ultimate resolution. The low gain operation was intentional to avoid aging in the Super$B$ environment.

Figure 8.92 shows all our test results both in the test beams and laser-based bench-top experiments. These results were obtained with Ortec 9327 CFD electronics, WaveCatcher [52] – see section 8.4.3 –, DRS4 [53] and Target [54] waveform digitizers. One can see that waveform

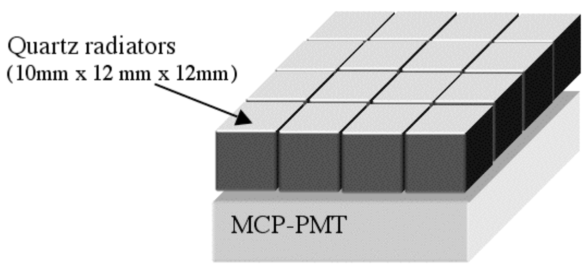

Figure 8.89: A possible geometry for a pixelated TOF detector: polished and side-coated fused silica cubes coupled to a MCP-PMT detector.

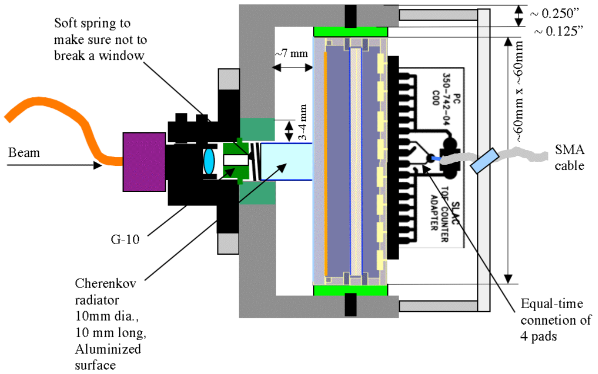

Figure 8.90: The geometry of a pixelated TOF prototype detector used in our tests (two such detectors were actually used for the measurements).

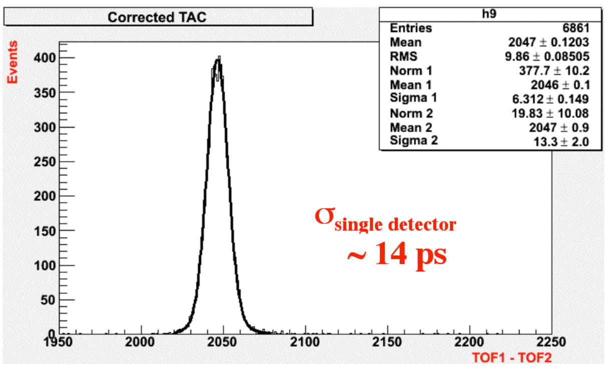

Figure 8.91: The best result obtained in the Fermilab test beam with the Ortec 9327 electronics.

digitizers "almost" reach the resolution of the classical CFD electronics, but not quite.

Figure 8.93 shows the laser-based test results as a function of the signal-to-noise ratio (S/N). A large value of S/N ratio is essential to achieve a good timing resolution. In these tests we achieved $\sigma_{\text{electronics}}{\sim}2.42$ ps with Ortec 9327 CFD electronics. Therefore the detector contribution to the final ultimate timing resolution was $\sigma_{\text{detector}}{\sim}3.6$ ps for S/N of ~1400. To achieve such a high value of S/N ratio in practice is difficult, as there are many limitations. The most important one is due to MCP detector aging, which requires a low gain operation. One could also have to avoid using an amplifier

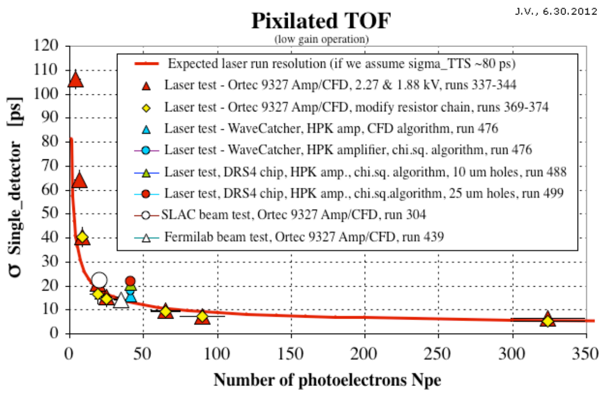

Figure 8.92: A summary of all results with the pixelated TOF prototype, including beam and laser tests.

to improve the S/N ratio, as the amplifier is contributing significantly to the noise (Ortec 9327 CFD electronics has internal 10× amplifier). It is probably more realistic in practice to target S/N ~200, *i.e.*, a 10-12 ps resolution.

Scintillating detector coupled to G-APD arrays Because of the prohibitive cost of MCP-PMT detectors for the entire forward pixelated TOF detector design at present, we considered other possible "pixelated" schemes based on scintillators and G-APDs. We used the SLAC CRT to test various options using 3D muon

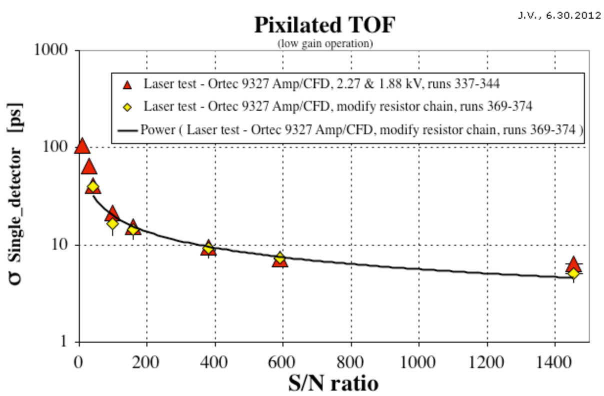

Figure 8.93: A summary of our laser-based results with the pixelated TOF prototype with the Ortec 9327 CFD electronics as a function of signal to noise ratio (S/N).

tracks. The 3D tracks with dip angle up to 20 degrees will somewhat worsen the timing resolution, however, they provide more realistic results compared to test beam. We used various types of scintillators (BC-404, BC-420, a small LYSO crystal and a full size one) as radiator. The logic for the full size LYSO radiator was to see if one could "parasite" the endcap calorimeter by adding a 4×4 G-APD array on its front face. The photon detection in these tests was provided by either MCP-PMT (for a reference run only), or Hamamatsu 4×4 G-APD array (each pixel size is 3 mm $\times$ 3 mm), or simply a pair of single 3 mm $\times$ 3 mm G-APDs (either MEHTI or Hamamatsu MCCP) coupled to the side of the small scintillator. The overall goal was to reach a resolution of $\sim$100 ps only, in order to provide a PID identification in the dE/dx cross-over region. Table 8.4 shows a summary of all results [38, 39]. One can see that we could reach resolutions between 110 and 180 ps for several small scintillators. However, the full size LYSO crystal results were considerably worse. Although one could search for some further improvements in future, it was felt that this type of TOF counter cannot compete with the FTOF concept at present.

8.5 Bibliography

[1] B. Ratcliff, "The B factory detector for PEP-II: A Status report", *AIP Conf.Proc.* 272:1889–1896, 1993, report SLAC-PUB-5946, C92-08-06.

[2] B. Ratcliff, "Simple considerations for the SOB Redesign for Super*B*", *SuperB PID Meeting*, March 2008, http://agenda.infn.it/conferenceDisplay.py?confId=458.

[3] The *BABAR* collaboration, "The *BABAR* Detector: Upgrades, Operation and Performance", 2013, arXiv:1305.3560 [physics.ins-det], Submitted to Nucl. Instrum. Meth. A.

[4] I. Adam et al., (*BABAR*-DIRC Collaboration collaboration), "The DIRC particle identification system for the *BABAR* experiment", *Nucl.Instrum.Meth.* A538:281–357, 2005, doi:10.1016/j.nima.2004.08.129, report SLAC-PUB-10516.

[5] J. Va'vra, D. Roberts, and B. Ratcliff, "FDIRC design for Super*B*", *Nucl.Instrum.Meth.* A639:282–286, 2011, doi:10.1016/j.nima.2010.10.105, report SLAC-PUB-14282.

[6] J. Va'vra, "Forward PID: geometry, attachment schemes, services", *IX SuperB General Meeting, Perugia*, June 2009, http://agenda.infn.it/conferenceDisplay.py?confId=1161.

[7] J. Va'vra, "Forward TOF: update on photocathode choice and the waveform electronics performance", *X SuperB General Meeting, SLAC*, October 2009, http://agenda.infn.it/conferenceDisplay.py?confId=1742.

[8] J. Va'vra, D. Leith, B. Ratcliff, E. Ramberg, M. Albrow, et al., "Beam Test of a Time-of-Flight Detector Prototype", *Nucl.Instrum.Meth.* A606:404–410, 2009, doi:10.1016/j.nima.2009.04.053, reports FERMILAB-PUB-09-387-E, SLAC-PUB-13573.

[9] E. Kravchenko, "Status report of the Novosibirsk activities", *IX SuperB General Meeting, Perugia*, June 2009, http://agenda.infn.it/conferenceDisplay.py?confId=1161.

[10] J. Benitez, I. Bedajanek, D. Leith, G. Mazaheri, B. Ratcliff, et al., "Development of a Focusing DIRC", 2006, report SLAC-PUB-12236.

[11] J. Va'vra, J. Benitez, D. W. Leith, G. Mazaheri, B. N. Ratcliff, et al., "The Focusing DIRC - the First RICH Detector to Correct the Chromatic Error by Timing, and the Development of a New TOF Detector Concept", *Nucl.Instrum.Meth.*, 2007, report SLAC-PUB-12803.

[12] J. Benitez, D. Leith, G. Mazaheri, B. Ratcliff, J. Schwiening, et al., "Status of the Fast Focusing DIRC (FDIRC)", *Nucl.Instrum.Meth.* A595:104–107, 2008,

Table 8.4: Results with TOF pixelated detectors using scintillator radiators and 3D tracks in the SLAC CRT.

Radiator	Detector	Measured resolution
Small LYSO ($17 \times 17 \times 17$ mm^3)	MCP-PMT	109 & 159 ps
Small LYSO ($17 \times 17 \times 17$ mm^3)	4×4 G-APD array (pixel 3 mm^2)	140 ps
Large LYSO ($25 \times 25 \times 200$ mm^3)	4×4 G-APD array (pixel 3 mm^2)	220 ps
Scintillator ($17 \times 17 \times 17$ mm^3)	4×4 G-APD array (pixel 3 mm^2)	136 ps
BC-404 scintillator ($38 \times 38 \times 25$ mm^3)	Two single 3 mm^2 G-APDs	156 ps
BC-420 scintillator ($38 \times 38 \times 10$ mm^3)	Two single 3 mm^2 G-APDs	177 ps

doi:10.1016/j.nima.2008.07.042, report SLAC-PUB-13104.

[13] J. Va'vra, "Simulation of the Focusing DIRC Optics with Mathematica", *Conference Records*, 2008, report SLAC-PUB-13464.

[14] J. Va'vra, "Focusing DIRC Design for Super*B*", 2009, report SLAC-PUB-13763.

[15] I. Wolfram Research, "Mathematica, version 6.0", 2007.

[16] K. Nishimura, B. Dey, D. Aston, D. Leith, B. Ratcliff, et al., "A Detailed Study of FDIRC Prototype with Waveform Digitizing Electronics in Cosmic Ray Telescope Using 3D Tracks", 2012, report SLAC-PUB-15202.

[17] D. Roberts, "Geant4 model of FDIRC", *X SuperB General Meeting, SLAC*, October 2009, http://agenda.infn.it/conferenceDisplay.py?confId=1742.

[18] M. Maino, "Characterisation of Multi-Anode Photomultiplier Tubes in Milano-Bicocca", *3rd SuperB Collaboration Meeting, Frascati*, March 2012, http://agenda.infn.it/conferenceDisplay.py?confId=4441.

[19] H. Kyushima et al., "The Development of Flat Panel PMT", *IEEE Nuclear Science Symposium Conference Record, Vol. 1, NJ, USA 7/3-7/7*, 2000.

[20] G. Varner, "Deeper Sampling CMOS Transient Waveform Recording ASICs", *TIPP conference, Chicago*, June 2011, http://www.phys.hawaii.edu/~varner/TIPP_DeeperWFS_ASICs_10jun2011_varner.pdf.

[21] C. Beigbeder, "Status of FDIRC electronics", *XVII SuperB workshop and Kick Off Meeting, Elba*, May 2011, http://agenda.infn.it/conferenceDisplay.py?confId=3352.

[22] C. Field, T. Hadig, D. W. Leith, G. Mazaheri, B. Ratcliff, et al., "Development of Photon Detectors for a Fast Focusing DIRC", *Nucl.Instrum.Meth.* A553:96–106, 2005, doi:10.1016/j.nima.2005.08.046, report SLAC-PUB-11107.

[23] F. Gargano, "Update on Bari activities", *5th SuperB Collaboration Meeting, Pisa*, September 2012, http://agenda.infn.it/conferenceDisplay.py?confId=4437.

[24] R. Montgomery et al., "Multianode Photomultiplier Tube Studies for Imaging Applications", 2011, Presented as NDIP conference poster, Lyon, France.

[25] F. Gargano, "Update on H8500 test in Bari", *3rd SuperB Collaboration Meeting, Frascati*, March 2012, http://agenda.infn.it/conferenceDisplay.py?confId=4441.

[26] J. Va'vra, "FDIRC status", *XVII SuperB Workshop and Kick Off Meeting, Elba*, May 2011, http://agenda.infn.it/conferenceDisplay.py?confId=3352.

[27] P. Abbon et al., (COMPASS RICH Upgrade collaboration), "The Fast read-out system for the MAPMTs of COMPASS RICH-1", *Nucl.Instrum.Meth.* A595:204–207, 2008, doi:10.1016/j.nima.2008.07.063, arXiv:0712.1964 [physics.ins-det].

[28] C. Pauly, "Single photon detection with H-8500 MaPMTs for the CBM RICH detector", *DPG Munster*, March 2011, http://www.gsi.de/documents/DOC-2011-Mar-233-1.pdf.

[29] G. Simi, "H-8500 studies", *2nd SuperB Collaboration Meeting, Frascati*, December 2011, http://agenda.infn.it/conferenceDisplay.py?confId=4107.

[30] J. Va'vra, "FDIRC status", *1rst SuperB Collaboration Meeting, London*, September 2011, http://agenda.infn.it/conferenceDisplay.py?confId=3827.

[31] N. Arnaud, "Study of the glue transmission with di-muon *BABAR* data", 2009.

[32] J. Va'vra, "Spreadsheet accompanying each bar box construction", 1999.

[33] M. Benettoni, "Fbox assembly procedure", *XVII SuperB Workshop and Kick Off Meeting, Elba*, May 2011, http://agenda.infn.it/conferenceDisplay.py?confId=3352.

[34] N. Mazziota, "Activity in Bari", *1rst SuperB Collaboration Meeting, London*, September 2011, http://agenda.infn.it/conferenceDisplay.py?confId=3827.

[35] R. B. Pahlka, (SuperNEMO Collaboration collaboration), "The SuperNEMO Experiment", 2008, arXiv:0810.3169 [hep-ex].

[36] N. Mazziotta, "A study of after-pulse effect due to Helium permeation in the H8500 MaPMT", *2nd SuperB Collaboration Meeting, Frascati*, December 2011, http://agenda.infn.it/conferenceDisplay.py?confId=4107.

[37] J. Va'vra, "SLAC Cosmic Ray Telescope Facility", 2009, report SLAC-PUB-13873.

[38] J. Va'vra, "TOF with LYSO and G-APD", *XVI SuperB Workshop, Frascati*, April 2011, http://agenda.infn.it/conferenceDisplay.py?confId=3410.

[39] J. Va'vra, "Pixilated TOF options", *1rst SuperB Collaboration Meeting, London*, September 2011, http://agenda.infn.it/conferenceDisplay.py?confId=2303.

[40] L. Burmistrov, *A detector for charged particle indentification in the forward region of SuperB*, Ph.D. thesis, Université Paris Sud, 2011, http://tel.archives-ouvertes.fr/tel-00673482, report LAL-11-299.

[41] T. Iijima, "Status and perspectives of vacuum-based photon detectors", *Nucl.Instrum.Meth.* A639:137–143, 2011, doi:10.1016/j.nima.2010.11.127.

[42] D. Breton, E. Delagnes, J. Maalmi, K. Nishimura, L. Ruckman, et al., "High resolution photon timing with MCP-PMTs: a comparison of commercial constant fraction discriminator (CFD) with ASIC-based waveform digitizers TARGET and WaveCatcher", *Nucl.Instrum.Meth.* A629:123–132, 2011, doi:10.1016/j.nima.2010.10.087, report SLAC-PUB-14048.

[43] D. Breton, E. Delagnes, and J. Maalmi, "Using ultra fast analog memories for fast photodetector readout", *Nuclear Instruments and Methods in Physics Research Section A: Accelerators, Spectrometers, Detectors and Associated Equipment* 695(0):61 – 67, 2012, doi:10.1016/j.nima.2011.12.007, http://www.sciencedirect.com/science/article/pii/S0168900211021668, New Developments in Photodetection NDIP11.

[44] K. Inami, "TOP counter prototype R&D", *RICH Conference, Cassis and private communication*, 2010, http://rich2010.in2p3.fr/indico/Research_&_Development_for_future_experiments/49-inami.html.

[45] J. Va'vra, "Ongoing tests of TOF counters in CRT", *XIV SuperB General Meeting, Frascati*, September 2010, https://agenda.infn.it/conferenceDisplay.py?confId=2303.

[46] J. Maalmi, "The Electronics of the CRT experiment", *XIV SuperB General Meeting, Frascati*, September 2010, https://agenda.infn.it/conferenceDisplay.py?confId=2303.

[47] V. Puill, "Private communication", 2012.

[48] M. Y. Barnyakov and A. Mironov, "Photocathode aging in MCP PMT", *JINST* 6:C12026, 2011, doi:10.1088/1748-0221/6/12/C12026.

[49] F. Raffaelli, "Detector integration", *5th SuperB Collaboration Meeting, Pisa*, September 2011, http://agenda.infn.it/conferenceDisplay.py?confId=4437.

[50] J. Va'vra, C. Ertley, D. Leith, B. Ratcliff, and J. Schwiening, "A High-resolution TOF Detector: A Possible Way to Compete with a RICH Detector", *Nucl.Instrum.Meth.* A595:270–273, 2008, doi:10.1016/j.nima.2008.07.021, report SLAC-PUB-13073.

[51] J. Va'vra, "Development of pixilated TOF concept: an overall summary", July 2012, http://www.slac.stanford.edu/~jjv/activity/fdirc/Vavra_DOE_review_detectorRD_2012.pdf, DOE, OHEP Review of Laboratory Detector R&D.

[52] D. Breton, E. Delagnes, and J. Maalmi, "Picosecond time measurement using ultra fast analog memories", *TWEPP-09, proceedings of the Topical Workshop on Electronics for Particle Physics, Paris, France, 21-25 September 2009*, 2009, report CERN-2009-006.

[53] S. Ritt, "DRS4 documentation", 2009, http://drs.web.psi.ch/evaluation.

[54] G. Varner, L. Ruckman, P. Gorham, J. Nam, R. Nichol, et al., "The large analog bandwidth recorder and digitizer with ordered readout (LABRADOR) ASIC", *Nucl.Instrum.Meth.* A583:447–460, 2007, doi:10.1016/j.nima.2007.09.013, arXiv:physics/0509023 [physics].

9 Electromagnetic Calorimeter

As was the case with *BABAR*, the Super$B$ electromagnetic calorimeter (EMC) will play an essential role in the study of flavor physics, especially in the study of B meson decays involving neutral particles. The calorimeter provides energy and direction measurement of photons and electrons, reconstruction of neutral hadrons such as π^0's, and discrimination between electrons and charged hadrons. Channels containing missing energy due to the presence of neutrinos will rely on information from the EMC to discriminate against backgrounds.

9.1 Overview

The electromagnetic calorimeter has three major components: a CsI(Tl) "barrel" calorimeter covering the central region, a "hybrid" CsI(Tl)/LYSO(Ce) "forward" calorimeter covering the small angle region in the direction of the high energy beam, and a lead-scintillator "backward" calorimeter covering the small angle region in the direction of the low energy beam. Table 9.1 shows the solid angle coverage for the three components of the Super$B$ EMC.

The Super$B$ EMC reuses the barrel part of the *BABAR* EMC detector consisting of 5760 CsI(Tl) crystals (Fig. 9.1). Due to the increased rates and radiation dose at Super$B$ compared with PEP-II, the *BABAR* forward calorimeter must be modified: the innermost CsI(Tl) rings of the forward endcap will be replaced by new LYSO crystals better-matched to the Super$B$ environment.

Reuse of the *BABAR* barrel calorimeter still requires a substantial effort. There is an ongoing engineering investigation of whether the barrel structure can be shipped as a unit, or whether it is necessary to disassemble it into its 280 individual modules for safe shipment. In either eventuality, due to the substantial increase in background and signal rates at Super$B$ compared to PEP-II, it will be necessary to replace the crystal-mounted preamplifier-shapers with versions having a shorter integration time.

After an intensive R&D program, the baseline choice for the forward endcap is to replace the inner rings of the *BABAR* forward calorimeter with faster and more radiation resistant LYSO crystals. As will be discussed below, this is the clear favorite in terms of performance and radiation hardness over the alternatives we have considered. The faster response time and smaller Molière radius serve together to address the higher event and background rates at Super$B$. LYSO is a fast scintillator heretofore used principally in small sizes in medical applications. Our R&D program has concentrated on the optimization of the performance of large crystals (2 cm $\times$ 2 cm $\times$ 20 cm). This entails having high light yield, optimized cerium doping to ensure the greatest possible uniformity of light output along the crystal, and surface treatment to refine the uniformity of response to meet a stringent specification. Thanks to this effort, there are now at least four producers able to grow LYSO crystals for high energy physics applications. Table 9.3 is a comparison of LYSO and other crystals used in high resolution electromagnetic calorimeters. The main issue with LYSO is cost. The hybrid design is a compromise, aimed at balancing the performance and cost of the forward endcap. We have studied several additional alternatives, described below.

A lead-scintillator-sandwich backward endcap calorimeter improves the hermeticity of the detector. Its main purpose is to act as a veto for events having "extra" energy in the backward region, which is particularly important for studying decay channels with neutrinos in the final state. The backward EMC has excellent time resolution, and may thus also have a role in particle identification by providing time-of-flight for

Table 9.1: Solid angle coverage of the electromagnetic calorimeters. Due the lower boost, the barrel calorimeter is displaced 10 cm in the backward direction with respect to the position in *BABAR*. The CM angular coverage and solid angle are for massless particles and nominal 4 on 7 GeV beam energies.

Calorimeter	$\cos\theta$ (lab)		$\cos\theta$ (CM)		Ω (CM)(%)
	minimum	maximum	minimum	maximum	
Backward	-0.98	-0.88	-0.99	-0.93	2.9
Barrel	-0.79	0.89	-0.87	0.81	84
Forward	0.89	0.97	0.81	0.94	6.8

the relatively slow backward-going charged particles.

The EMC calorimeter plays an important role in the experiment's trigger. which is discussed in Chapter 12.

9.1.1 Background and radiation issues

One of the major concerns for the electromagnetic calorimeter is its capability to sustain the radiation dose, which is larger than in *BABAR* due to the increased luminosity. The dominant contribution to the radiation dose in Super*B* comes from radiative Bhabha events that produce a large number of low energy photons at an extremely high rate. The high photon rate has two main effects on the performance of the detector: the integrated radiation dose can reduce the transmittance of the crystals and therefore alter the calibration of the detector over time, and the large number of background photons can produce pile-up, degrading the energy resolution.

The impact of these effects have been simulated in detail; this is discussed in Sec. 5.11. The energy deposited by background events in each crystal is simulated at each beam crossing. The resulting rates of energy deposit are shown in Fig. 5.25. The simulations show that there is no significant difference in the radiation dose to individual crystals between the barrel and the forward endcap. This is by construction. Due to the different Molière radii of CsI(Tl) and LYSO, the transverse dimensions of the LYSO crystals are chosen to be about half the size of the CsI(Tl) crystals and the overall volume of a LYSO crystal is 6.7 times smaller (120 cm^3 vs 800 cm^3) than a typical CsI(Tl) crystal. Thus the background rates and radiation dose per crystal are compensated by the change in volume.

The radiation dose to which the crystals are subjected is defined as the total energy deposited in a crystal per unit mass. The dose expected per year, conventionally taken as a "New Snowmass Year" having 1.5×10^7 s, was estimated to range between 0.15 and 0.3 krad. Conservatively, assuming 10 years of operations, the crystals must be radiation resistant up to at least 4.5 krad. The impact on the energy resolution of a ~ 0.045 rad/hour dose rate needs to be considered. In contrast to $PbWO_4$, the light output of neither CsI(Tl) or LYSO is rate-dependent.

9.1.2 Simulation tools

9.1.2.1 FastSim

A fast simulation (FastSim) tool based on the *BABAR* software framework has been developed to evaluate the detector performance, optimize the geometry and study the physics reach. The detector geometry is modeled as two-dimensional "shells" of basic topologies such as cylinders, disks, cones, and rectangles. The event generators are identical to those in *BABAR*. Each particle is tracked in the detector volume. When it crosses a detector element, the interaction type and the energy loss are determined according to the particle type, detector material

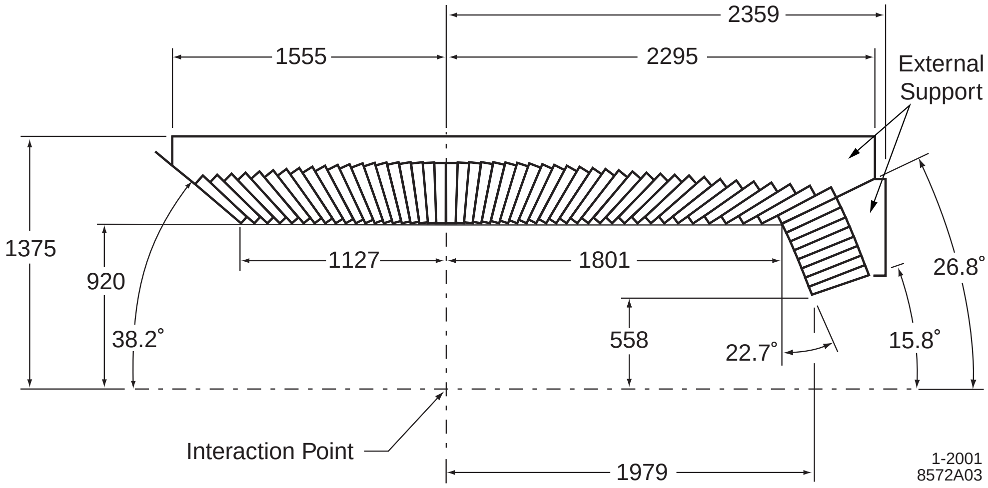

Figure 9.1: Longitudinal *BABAR* EMC cross-section (top half) showing the arrangement of the 48 barrel and 8 endcap crystal rings. The detector is axially symmetric around the z-axis. Dimensions are in mm.

and thickness. Secondary particles are created if necessary. Particle showers are represented by a quasi-particle instead of a (large) number of individual shower particles.

Charged track hits are fitted with a Kalman filter. EMC clusters are created based on the Molière radius, interaction type (EM shower, hadron shower or minimum ionizing), detector segmentation, and parameterized shower shape. Geometry and model parameters can be easily set up and modified. The high level data structure of an event is the same as that in *BABAR*, including tracks, clusters, and particle identification objects, so we were able to directly apply available *BABAR* analysis tools.

Background cannot be simulated with FastSim because it is highly sensitive to the details of the beam line and interaction region geometries, magnetic fields, and beam trajectories. The secondary particles from beam and material interactions must be simulated precisely, which can only be done with a complete GEANT4 simulation. Thus in order for the FastSim to include background effects, periodic "background frame" productions are carried out with GEANT4, including beamlines up to ± 5 meters from the interaction point. For each bunch crossing, background particles that cross the boundary between the beamline elements and the detector volume are recorded and stored in a background frame file. In FastSim, for each signal event, background particles of a number of bunch crossings are read in from the background frame file and are appended to the list of signal particles. FastSim then proceeds as usual. The number of bunch crossings per signal event is determined by the crossing frequency and an overall sensitive time window. Each sub-detector has its own response timing structure to model the appropriate signal pulse.

9.1.2.2 FullSim

The calorimeter full simulation tool (FullSim) is based on GEANT4 and the Bruno tool (Sec. 14.1.1), which is used to simulate particle interactions and energy deposits. The geometry description includes all of the Super*B* sub-detectors. In the case of the calorimeter, it contains all the crystals and support structures. The Bruno output information for the calorimeter is the deposited energy per crystal. Each single source of machine background is simulated separately for the entire Super*B* detector and, if needed, these are combined in a second step of the analysis.

At the present stage of development the FullSim does not perform the digitization of signals and the reconstruction of clusters, which are instead obtained with a two-step procedure through stand-alone programs. During the digitization stage, which is overlaid on the GEANT4 simulation output, the electronic signal shape is generated for each crystal with an energy deposit. Photostatistics, electronic noise and time resolution effects are added using extrapolations from BABAR, or using actual measurements when possible. To study the calorimeter performance, signal particles events are overlapped with machine background events, following the time structure of the bunch crossing rate in a time window centered on the signal particle arrival time. This allows the emulation of effects of the background, including electronic signal pile-up. The different sources of background are mixed according to their probability and time behavior.

Starting from the outcome of the digitization step, energy clusters are created following the BABAR algorithm [1]; a random 1% intercalibration error is applied when the cluster energy is computed (see for example [2]). To be accepted for clustering, the signal from a crystal is required to peak within a time window centered on the expected signal time.

9.2 Barrel Calorimeter

We propose to reuse the barrel portion of the BABAR EMC [3], retaining the mechanical structures and the 5760 CsI(Tl) crystals and the pair of photodiodes mounted on each crystal, after carrying out modifications of the electronics required for optimal performance at Super*B*.

We first describe below the condition, as of the end of BABAR running, of the CsI(Tl) crystals. We then discuss the Super*B* environment, which produces high pile-up and backgrounds. These must be addressed to optimize the energy resolution. Next, we describe the mechanical design and calibration systems for the barrel, each of which will be minimally changed from their current configurations, as well as the detector readout system, which will be upgraded. We then discuss the resulting barrel energy and position resolution, as well as the $\gamma\gamma$ mass resolution, and the effects of long-term radiation exposure at BABAR. These results are extrapolated to estimate the effect on performance to be expected over the lifetime of Super*B*.

We then describe the existing barrel crystal photodiodes, which will not be replaced, and the changes proposed for the on-crystal preamplifier package and the front-end electronics. Finally we present the proposed plan for disassembly of the barrel EMC down to its component structures, their packaging and shipping and local storage before and reassembly at a facility at or near Tor Vergata.

9.2.1 Requirements for the Super*B* Environment

9.2.1.1 Crystal Aging in BABAR at PEP-II

Over the span of BABAR running at PEP-II, the EMC crystal light yield has decreased due to exposure to high levels of radiation, which is monitored by 116 RadFETs distributed on the front face of the calorimeter. The most common form of radiation damage [4] comes from the development of absorption bands that reduce the crystal's light yield by reducing the transmittance. Although crystals in the EMC endcap experienced higher levels of radiation than those in the barrel, all EMC crystals from the furthest backward to those more forward received non-negligible integrated doses. The resulting changes in crystal light yields were monitored and corrected for during BABAR operation using calibrations performed at both ends of the dynamic range of the detector: a low-energy calibration using a 6.13 MeV radioactive photon source, discussed in Sec. 9.2.2.3, and a high-energy calibration with Bhabha events.

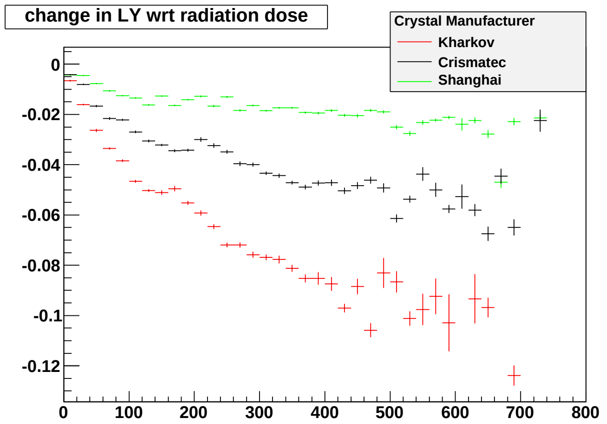

(a) Change in light yield versus dose (Rad.), for barrel backward

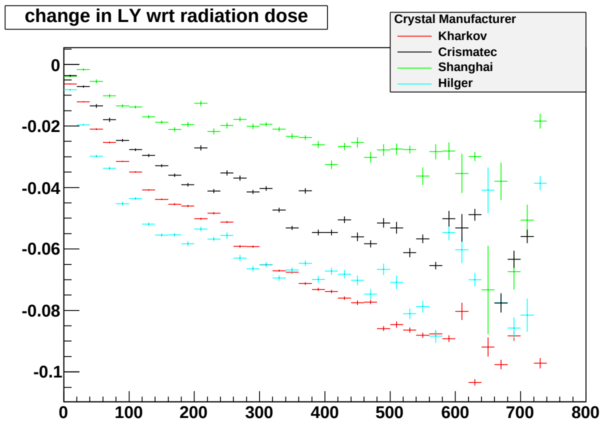

(b) Change in light yield versus dose (Rad.), for barrel forward

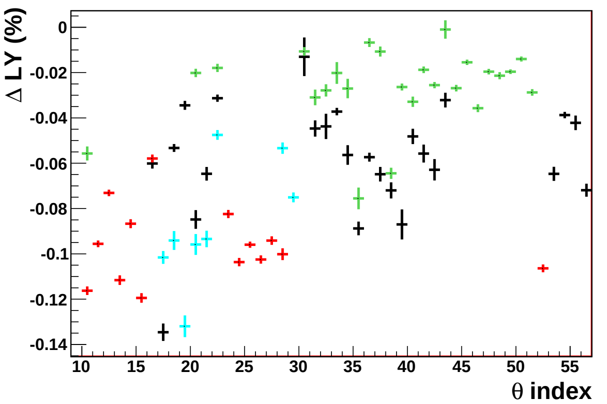

(c) Δ LY vs theta. The forward endcap is 6–9; the barrel starts at 10, with the backward barrel at large values of the index.

Figure 9.2: Backward and forward barrel crystal light yield decreases with absorbed radiation dose, with the different crystal providers indicated. The bottom plot shows the light yield decrease as a function of polar angle index for each manufacturer using the same color legend.

The change in light yield for barrel crystals as a function of absorbed radiation dose, based on the low-energy calibration data, is shown categorized by crystal manufacturer in Fig. 9.2. Though the crystals were initially set up to have a relatively uniform response before they were integrated into the detector, there have been varying degrees of degradation in performance over time. Depending on the manufacturer, the total decrease in light yield can be up to ∼10%. Much of the decrease occurred during the initial years of PEP-II running. As the integrated dose increased, there was less light loss per unit dose received. However, as can be seen in Fig. 9.2, in the Super*B* environment, the eventual loss in light yield for the worst-performing barrel crystals—generally those provided by Kharkov and Hilger—is substantial. The relatively poor performance of the crystals provided by these manufacturers was known at the time of barrel construction. To the extent possible, these manufacturers' crystals were placed as far backwards in polar angle as possible (Fig. 9.2).

9.2.1.2 Backgrounds

In addition to crystal aging, backgrounds can degrade energy resolution by causing electronic signal pile-up. The dominant source in Super*B* is expected to be photons and neutrons from radiative Bhabha events. This effect was negligible in *BABAR*, but could be substantial in Super*B*, especially in the low energy range.

The pile-up effect is a function of signal pulse shape. Since Super*B* is reusing the *BABAR* barrel, the limitation of the long decay time of CsI(Tl) scintillation light must be accepted. Readout and electronics can, nonetheless, be optimized to minimize the impact of the pile-up effect. To ensure similar physics sensitivity as *BABAR*, the requirement is that background pile-up should have a negligible effect on the energy resolution of high energy photons, and should not dominate the energy resolution at low energy, which is approximately 4.5% at 100 MeV in *BABAR*.

9.2.2 Description of *BABAR* Barrel Calorimeter

9.2.2.1 Mechanical design

The *BABAR* barrel EMC consists of a cylindrical shell with full azimuthal coverage, extending in polar angle from 26.8° to 141.8°. A longitudinal cross-section, including the forward endcap, is shown in Fig. 9.1. The barrel EMC contains 5,760 crystals arranged in 48 azimuthal rings, with 120 identically dimensioned crystals in each ring. Each crystal has a tapered trapezoidal cross section, with length increasing from 29.6 cm furthest backward to 32.4 cm furthest forward in order to minimize the effects of shower leakage from increasingly higher energy particles. To minimize the probability of pre-showers, the crystals are supported entirely at the outer radius, with only a thin gas seal at the front. The amount of material in front of the crystal faces is $0.3-0.6X_0$, mostly from material in the beampipe, SVT, DCH, and DIRC.

Figure 9.3 is a schematic of a single crystal, showing the layered crystal wrappings, silicon photodiodes, diode carrier plate, preamplifier, and the aluminum housing.

The barrel crystals are inserted into carbon fiber modules that are supported individually from an external cylindrical support structure that carries the load of the barrel modules and the forward endcap to the magnet steel through four flexible supports, which decouple and dampen any motion relative to the magnet steel during an earthquake.

The crystal modules are tapered, trapezoidal compartments made from carbon-fiber-epoxy composite (CFC) with 300 μm-thick walls. Each compartment loosely holds a single wrapped and instrumented crystal, assuring that the forces on the crystal never exceed its own weight. Each module is surrounded by a second layer of 300 μm CFC to provide additional strength. The modules are bonded to an aluminum strong-back that is mounted on the external support structure. Figure 9.4 shows some details of a module and its mounting to the support cylinder. This scheme minimizes inter-crystal material while exerting minimal force on the crystal surfaces, preventing geometric deformations and surface degradation that could compromise performance.

The barrel is composed of 280 separate modules, each holding 21 crystals (7×3 in $\theta \times \phi$), except for the furthest backward modules which contain only 6×3 crystals. After insertion of the crystals, the aluminum readout frames, which also stiffen the module, are attached with thermally-conducting epoxy to each of the CFC compartments. The entire ~ 100 kg module is then bolted and glued with conducting epoxy to an aluminum strong-back (Fig. 9.4). The strong-back contains alignment features, as well as channels that couple it to the cooling system. Each module is installed into the 2.5 cm-thick, 4 m-long aluminum support cylinder, and sub-

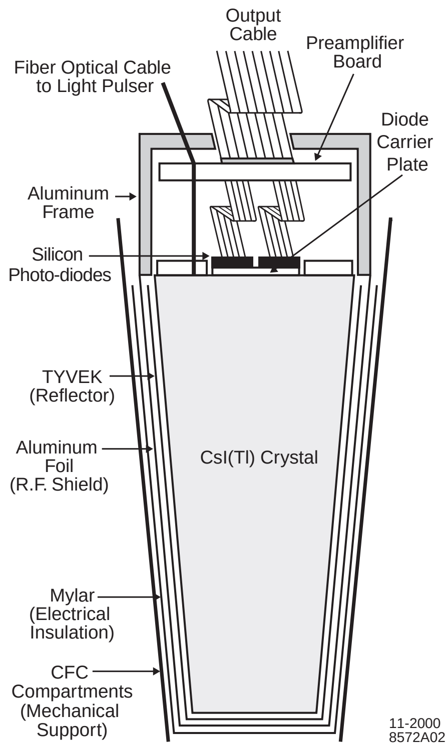

Figure 9.3: A schematic (not to scale) of a wrapped barrel crystal and the front-end readout package mounted on the rear face. Also indicated is the tapered, trapezoidal CFC compartment, which is open at the front.

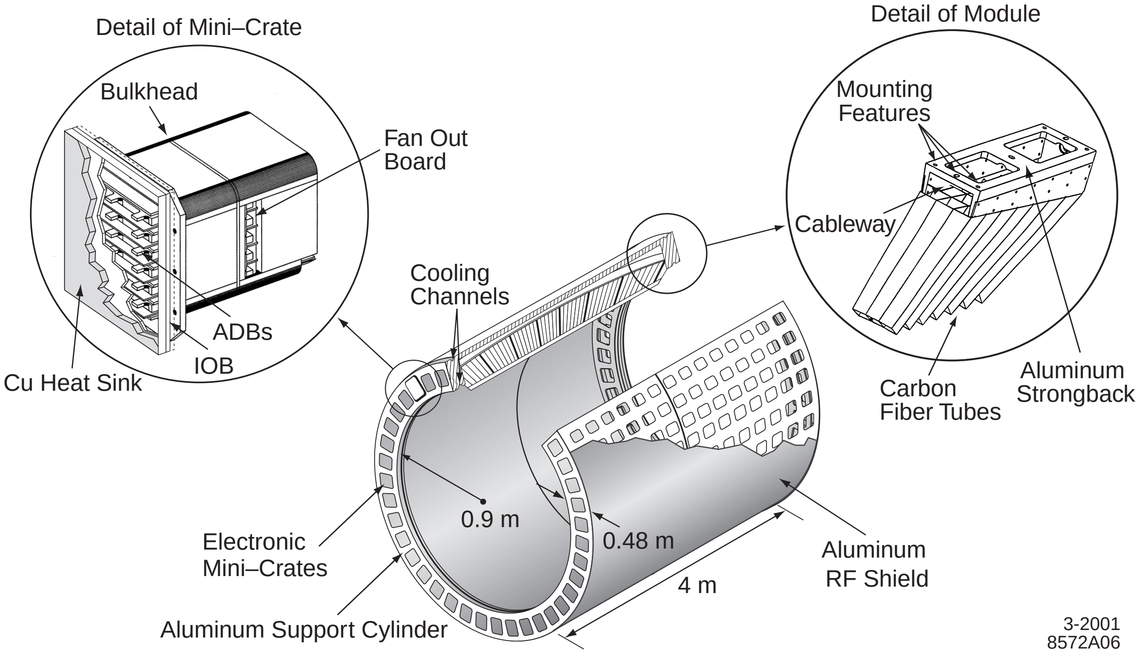

Figure 9.4: The EMC barrel support structure, with details on the modules and electronics crates (not to scale).

sequently aligned. On each of the thick annular end-flanges, the support cylinder contains access ports for digitizing electronics crates with associated cooling channels, as well as mounting features and alignment dowels for the forward endcap. Figure 9.4 shows details of an electronics mini-crate situated within the support cylinder.

The primary heat sources internal to the calorimeter are the preamplifiers (2×50 mW/crystal) and the digitizing electronics (3 kW per end-flange). In the barrel, the heat generated by the preamplifiers is removed by conduction to the module strong backs, which are directly cooled by Fluorinert (polychlorotrifluoroethylene). The digitizing electronics are housed in 80 mini-crates mounted on the end-flanges of the cylindrical support structure. These crates are indirectly cooled by chilled water pumped through channels milled into the end-flanges close to the inner and outer radii.

The barrel is surrounded by a double Faraday shield composed of two 1 mm-thick aluminum sheets, further shielding the diodes and preamplifiers from external noise. This cage also serves as the environmental barrier, keeping the slightly hygroscopic crystals in a dry, temperature-controlled, nitrogen atmosphere.

The stability of the photodiode leakage current, which rises exponentially with temperature, and the crystal light yield, which is weakly temperature-dependent, were of particular concern during *BABAR* data-taking. The most important issue for the upgrade to Super*B* is that the diode-crystal epoxy joints experience as little stress as possible due to differential thermal expansion during disassembly, transport and reassembly. Studies performed prior to the construction of the EMC showed that preserving the integrity of these joints requires that crystals be kept at a temperature of (20 ± 5) C. The barrel and endcap are currently maintained in this state, with temperatures monitored in real-time and recorded in the conditions database. Figure 9.5 shows the temperature history for one year for the four quadrants of the barrel and the two halves of the endcap.

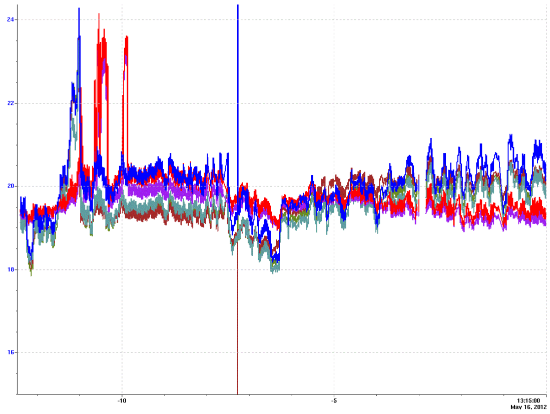

Figure 9.5: Barrel and endcap thermal history for one year. The four barrel quadrants are blue, brown, and dark and light green; the endcap halves are purple and red. The horizontal axis shows months prior to 16 May 2012. The vertical line extending the full range of the plot is an artifact due to a bad database record.

9.2.2.2 Readout

Each CsI(Tl) barrel and endcap crystal is read out using two $2 \times 1\,\mathrm{cm}^2$ silicon PIN diodes glued to a transparent 1.2 mm-thick polystyrene substrate that is in turn glued to the center of the rear face of the crystal with an optical epoxy to maximize light transmission. The surrounding area of the crystal back face is covered by a plastic plate coated with white reflective paint, which has two 3 mm-diameter penetrations for the fibers of the light pulser monitoring system.

The signal from each of the diodes is transmitted to a low-noise preamplifier through a cable terminated in a connector that allows the preamplifier to be detached from the photodiodes. The preamplifier characteristics are discussed below in Sec. 9.2.4. The entire diode/electronics assembly is enclosed in an aluminum fixture (Fig. 9.3). This fixture is electrically coupled to the aluminum foil wrapped around the crystal silver-conductive epoxy and thermally coupled to the support frame to dissipate the heat load from the preamplifiers.

9.2.2.3 Low-energy Source Calibration

Achieving the best possible performance of the EMC requires careful calibration and monitoring during data-taking. The low-energy calibration system devised for *BABAR* produces a 6.13 MeV photon line from a short-lived ^{16}O transition that can be activated as required. This system was successfully used for routine biweekly calibrations of the *BABAR* calorimeter, and is an ideal match to the Super*B* requirements. We will therefore refurbish the *BABAR* system for use in Super*B*. The final *BABAR* calibration run was taken on 3 July 2008, and records of this run, as well as a few earlier ones, will be maintained for comparison with the refurbished Super*B* EMC.

In this system, ^{19}F, a component of Fluorinert$^{\mathrm{TM}}$ (polychlorotrifluoroethylene) coolant liquid, is activated with a neutron source to produce ^{16}N, which β-decays to an excited state of ^{16}O. This state in turn emits a 6.13 MeV photon as it cascades to its ground state. The source spectrum, as seen with a CsI(Tl) crystal with the PIN diode readout used in *BABAR*, is shown in Fig. 9.6. There are three principal contributions to the overall peak, one at 6.13 MeV, another at 5.62 MeV, and the third at 5.11 MeV. The latter two represent e^+e^- 0.511 MeV annihilation-photon escape peaks. Since all three peaks have well-defined energies, they simultaneously provide an absolute calibration and an energy scale at the low end of the energy spectrum.

The fluorine is activated by neutrons produced by a commercial deuterium-tritium (DT) generator that produces 14.2 MeV neutrons by accelerating deuterons onto a tritium target. Typical rates are several times 10^8 neutrons/second. The DT generator is surrounded with a bath of the fluorine-containing liquid, which is then circulated in a manifold to the barrel and endcap crystals. There are many suitable fluorine-containing liquids available; Fluorinert FC77 [5], was used in *BABAR*. The half-life of the activated liquid is 7 s, hence residual radioactivity is not a substantial concern when the DT generator is not operating.

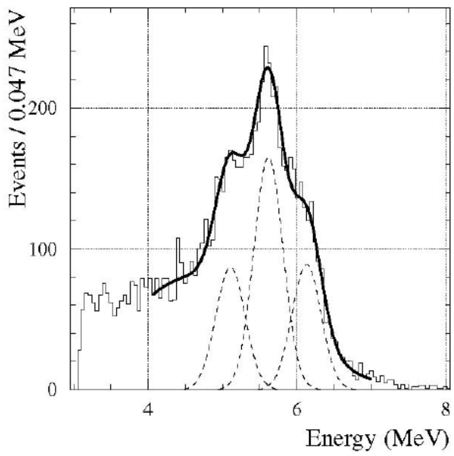

Figure 9.6: Energy spectrum in a single *BABAR* CsI(Tl) crystal irradiated with 6.13 MeV photons from an $^{16}O^*$ source, read out with a PIN diode. The solid curve is a fit to the spectrum, including Gaussian contributions at 6.13 MeV, 5.62 MeV, and 5.11 MeV, indicated by the dashed curves. [3]

The Fluorinert is stored in a reservoir near the DT generator. When a calibration run is started, the generator and a circulating pump are turned on. Fluid is pumped from the reservoir through the DT bath to be activated, and then to the calorimeter. The system is closed, with fluid returning from the calorimeter to the reservoir (Fig. 9.7). In *BABAR*, the fluid is pumped at 3.5 l/s, producing a rate of approximately 40 Hz in each of 6500 crystals. This produces a calibration with a statistical uncertainty of 0.35% on peak positions in a single crystal in a 10-minute calibration run [3, 6]. The crystals are approximately 12 m from the DT generator. Although Fluorinert FC-77 is no longer manufactured, an adequate supply is on hand. Should it be necessary to substitute a commercially available coolant liquid (all of which have slightly reduced fractions of fluorine), the pumping rate or neutron source intensity would have to be adjusted accordingly.

In *BABAR*, the fluid transport manifold consisted of thin-wall (0.5 mm) aluminum tubing (3/8 inch diameter), flattened to meet space constraints. One millimeter of Al represents 1.2% of a radiation length. This material is located in front of the *BABAR* crystals, as is an additional 2 mm of Al in the structural support of the tube assemblies, which are deployed as a set of curved panels. This system can be reused for the barrel in Super*B*, or it could be rebuilt to better integrate into the barrel structure, reducing the amount of material and providing additional radial space.

The DT generator is a small accelerator; radiation safety protocols factor into the mechanical design of the system. For example, operation of the source will be done remotely, in a no-access condition. It will be shielded according to INFN radiation safety regulations. The shielding will be interlocked such that the DT generator cannot be operated if the shielding is not in place. The reservoir is capable of holding the entire volume of Fluorinert fluid. The system is anticipated to be operated approximately weekly. In the event of a fluid leak, the maximum exposure for the similar *BABAR* system was calculated to result in an integrated dose of less than 1 mrem. A detailed hazard analysis will be performed in collaboration with INFN radiation safety experts.

9.2.2.4 Light Pulser

The light response of the individual crystals was measured daily during *BABAR* running using a light-pulser system, which transmitted spectrally filtered light from a xenon flash lamp through optical fibers to the rear of each crystal. We propose to refurbish the *BABAR* system for use in Super*B*. The light pulse is similar in spectrum, rise-time and shape to the scintillation light in the CsI(Tl) crystals. The pulses were varied in intensity by neutral-density filters, allowing a precise measurement of the linearity of light collection, conversion to charge, amplification, and digitization. The intensity was monitored pulse-to-pulse by comparison to a reference system with two radioactive sources, ^{241}Am and ^{148}Gd. Each of these was attached to a small CsI(Tl) crystal read out by both a photodiode and a photomultiplier tube. The response was stable to 0.15% over a period of one week.

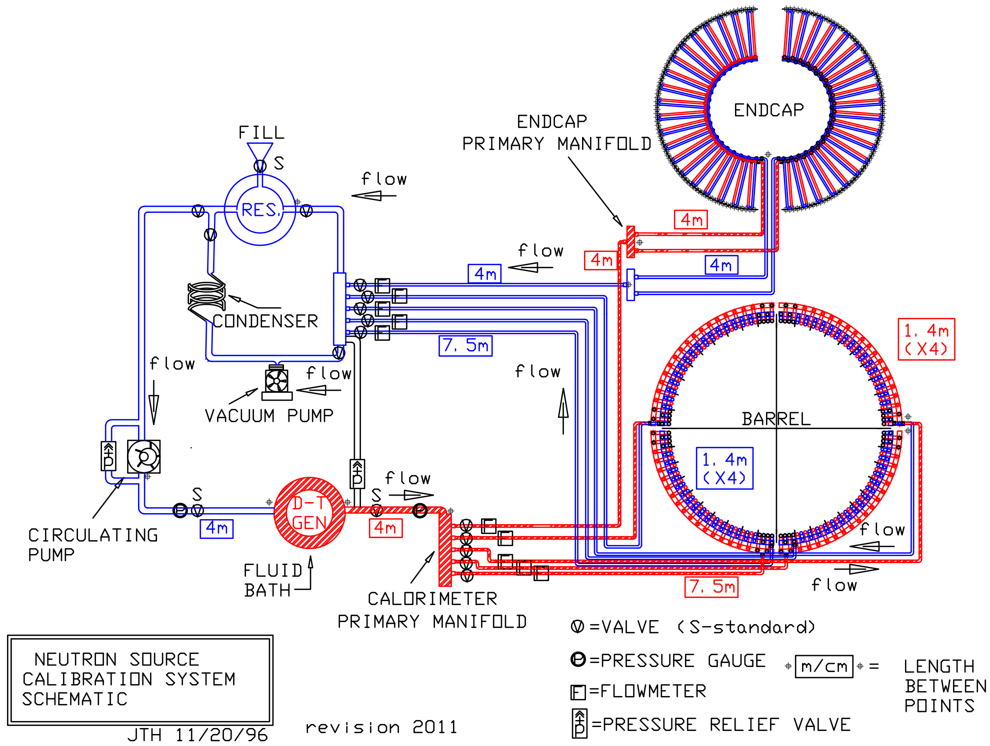

Figure 9.7: Schematic of the *BABAR* calibration system, which produces ^{19}F 6.13 MeV photons from an ^{16}O* source, as updated for Super$B$. The system is used for both the barrel and forward endcap calorimeters.

9.2.3 Performance of the *BABAR* barrel

9.2.3.1 Energy and position resolution

The energy dependence of the energy resolution of a homogeneous crystal calorimeter is generally empirically described by two terms summed in quadrature:

$$\frac{\sigma_E}{E} = \frac{a}{\sqrt[4]{E(\mathrm{GeV})}} \oplus b, \tag{9.1}$$

where E and σ_E refer to the energy of a photon and its *rms* error in GeV. The energy-dependent term arises from fluctuations in photon statistics, electronics noise, and beam background-generated noise. The constant term arises from non-uniformity in light collection, shower leakage, calibration uncertainties, and energy deposited in the non-sensitive material between and in front of the crystals. The angular resolution is primarily determined by the crystals' transverse dimension and is also described empirically with energy-dependent and energy-independent contributions. Figure 9.8 shows the energy and angular resolution of the *BABAR* calorimeter derived from various data control samples. The performance may be parameterized as [3]:

$$\frac{\sigma_E}{E} = \frac{(2.32 \pm 0.3)\%}{\sqrt[4]{E(\mathrm{GeV})}} \oplus (1.85 \pm 0.12)\% \tag{9.2}$$

$$\sigma_\theta = \sigma_\phi = \frac{(3.87 \pm 0.07)\ \mathrm{mrad}}{\sqrt{E(\mathrm{GeV})}} \oplus (0.0 \pm 0.04)\ \mathrm{mrad} \tag{9.3}$$

9.2.3.2 $\gamma\gamma$ mass resolution

Figure 9.9 shows a two-photon invariant mass distribution in the π^0 and η mass ranges for selected *BABAR* data multi-hadron events from 2001. Photons are required to have energy $>$ 30 MeV, with π^0 candidate energy $>$ 300 MeV, and η candidate energy $>$ 1 GeV. The reconstructed π^0 mass is found to be 134.9 MeV/c^2,

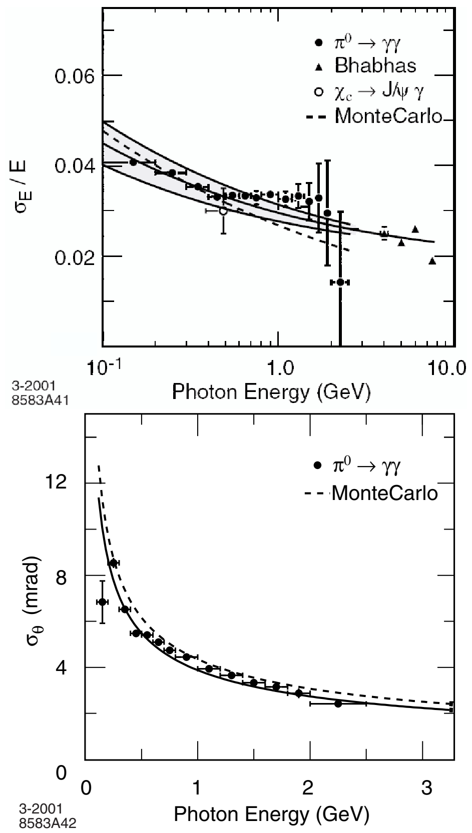

Figure 9.8: Photon energy (top) and angular (bottom) *BABAR* EMC resolutions [3]. Solid curves are fits to the data (eq. 9.2); dashed lines are simulation.

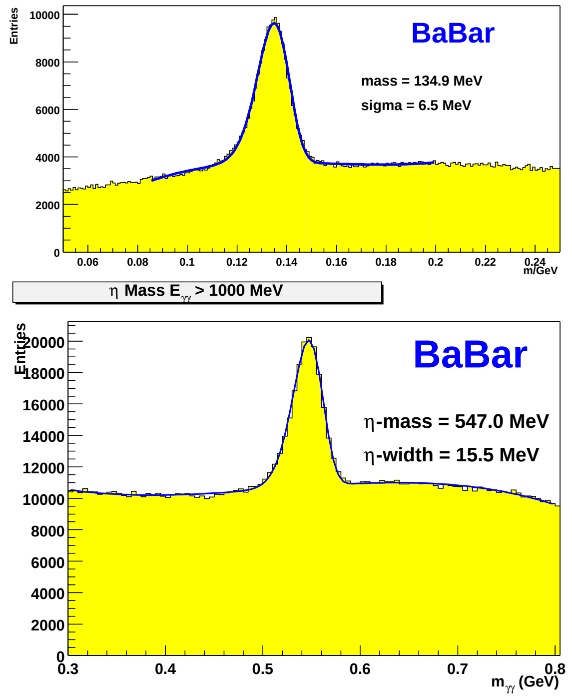

Figure 9.9: Two-photon invariant mass distribution in π^0 (top) and η (bottom) mass ranges.

with a width of 6.5 MeV/c^2. The fitted η mass is 547 MeV/c^2, with a width of 15.5 MeV/c^2.

9.2.3.3 Radiation Damage Effects on Resolution

Beam-generated backgrounds are the major cause of reduction in the light yield of the crystals over time. In order to monitor this source of background, 116 RadFETs are placed in front of the calorimeter barrel and endcap crystals. These RadFETs, real-time integrating dosimeters based on solid-state MOS technology, are integrated into the EPICS monitoring system. As can be seen in Fig. 9.10, the integrated dose is largest in the endcap, which is closer the the beam line, as well as more forward in polar angle, making it more susceptible to beam-generated background photons from small angle radiative Bhabha events in which an $e^\pm$ strikes a machine element.

Radiation damage impacts CsI(Tl) through the creation of color centers in the crystals, inducing absorption bands, resulting in a degradation of response uniformity and light yield. The nominal dose budget for the *BABAR* CsI(Tl) calorimeter is 10 krad over the lifetime of the detector. The dominant contribution to the dose arises from luminosity and single-beam background sources, and hence is due to MeV photons and presumably neutrons. The integrated dose does not scale with integrated beam current, but does scale approximately linearly with integrated luminosity.

A total dose of about 1.2 krad was received in the most heavily irradiated regions for an integrated luminosity of 400 fb^{-1}, resulting in a loss of about $\sim 15\%$ of the total light yield, but with no measurable impact on physics performance. It is notable that most of the observed light loss occurred relatively early in *BABAR* running, although the radiation dose accumulated relatively steadily, and that crystals from different manufacturers have responded somewhat differently to irradiation.

In order for the barrel calorimeter to function in the Super$B$ environment, beam background rates must be maintained at a level of approximately 1 MeV/μs or less per CsI(Tl) crystal. If this condition is achieved, then radiation dose rates are anticipated to be roughly comparable to current *BABAR* levels. A dose budget of well under 1 krad/year is expected to be achievable. At this a level, the CsI(Tl) barrel would survive for the duration of Super$B$ operations. This assumption will, however, need to be verified by detailed simulation.

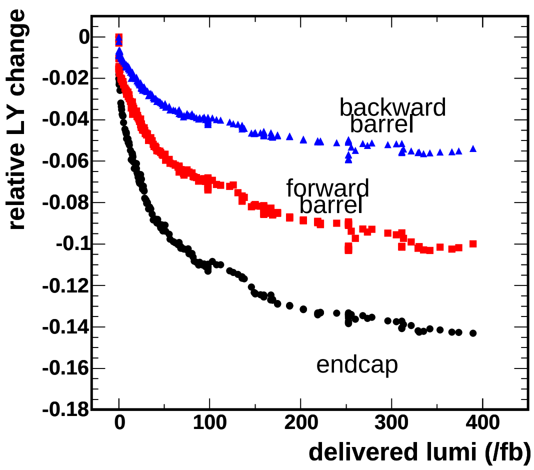

Figure 9.10: The light yield loss in the *BABAR* CsI(Tl) crystals due to radiation damage as a function of integrated luminosity. The total dose received after 300 fb^{-1} is 1.2 krad in the endcap and 750 rad in the barrel.

9.2.3.4 Expected Changes in Performance at Super$B$

The CsI(Tl) crystals used in the barrel calorimeters of both *BABAR* and Belle are the most expensive elements of the two detectors. Based on the performance that has been achieved, and the radiation damage that has been observed so far, both collaborations have concluded that the re-use of the barrel crystals is possible at a Super B Factory.

The baseline assumption is that the geometry of the crystals is unchanged from that of the current *BABAR* detector. The one change that should be made is to move the position of the interaction point from -5 cm to $+5$ cm relative to the position of the crystal gap normal to the beam axis. This adjustment retains the current non-pointing geometry, but, in view of the reduced energy asymmetry, moves the barrel to a slightly more symmetric position. The effect of the change in boost from $\gamma\beta = 0.56$ to 0.28 and the shift of the IP is to increase the angular coverage of the barrel from 80% ($\cos\theta = -0.93$ to $+0.66$) to 84% ($\cos\theta = -0.87$ to $+0.81$).

The higher background rates will impact the performance of the barrel calorimeter. This effect will be mitigated with the electronics changes described below in Section 9.2.4. FastSim studies modeling the new electronics and background rates indicate that the barrel performance will continue to be acceptable. Figure 9.11 shows the expected single-photon energy resolution in the barrel at Super$B$, obtained with FastSim. Little change from the *BABAR* experience is expected, except at the lowest photon energies. Considering generic $B^0\bar{B}^0$ events at predicted backgrounds, we obtain the $\gamma\gamma$ mass plots in the π^0 and η regions in Fig. 9.12. There is a slight shift in the mass from the expected peak positions; the FastSim absolute calibration is undergoing further tuning. The $\gamma\gamma$ mass resolution in the MC could be somewhat underestimated, partly due to inaccurate modeling of the angular resolution compared with data, which slightly affects the $\gamma\gamma$ mass resolution here. It is clear, however, that the effect of the changes at Super$B$ is not large.

A possible change to improve the coverage in the backward region would be to add one or two additional rings of crystals to the last module ring in θ, which currently only contains 6 rings of crystals. This would require, however, major changes in the mechanical support structure and a redesign of the electronics readout, so it

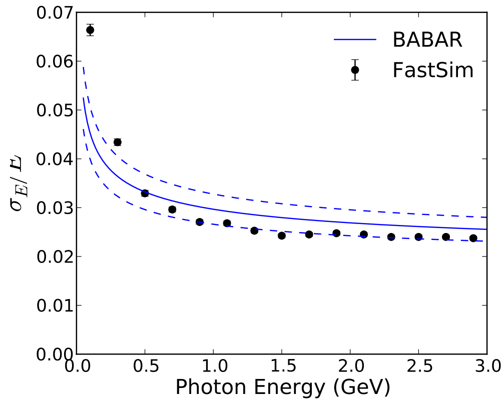

Figure 9.11: FastSim Super*B* single photon energy resolution in the barrel at expected background. The curves show the *BABAR* resolution, with error bands, according to Eq. 9.2

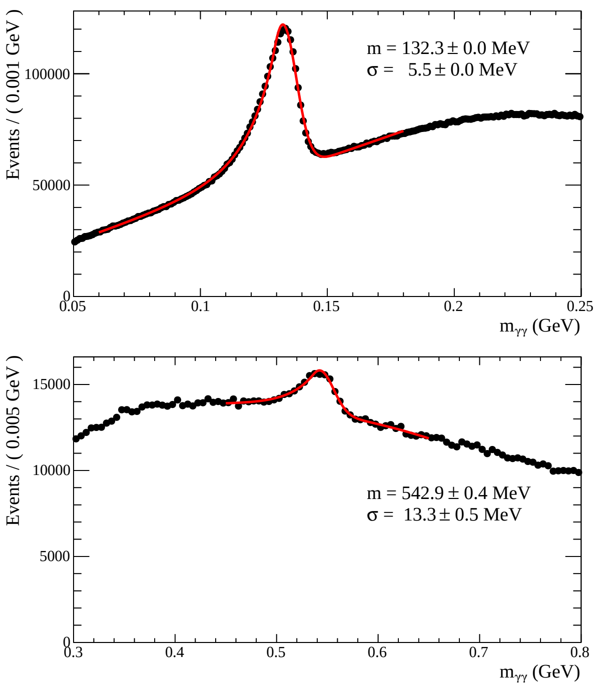

Figure 9.12: FastSim Super*B* $\gamma\gamma$ mass spectra for generic $B^0\bar{B}^0$ events in the π^0 and η meson mass regions, with both photons in the barrel, at expected background rates.

will not be undertaken unless there is a significant gain from the extra ring(s). Changes to the rear section of the barrel also interact strongly with the possible addition of a backward endcap calorimeter (Sec. 9.4).

9.2.4 Electronics changes

The *BABAR* EMC barrel crystals are coupled to two PIN diodes (Hamamatsu S2744-08) glued to the rear face of each crystal. The possibility of replacing these photo-detectors with new devices was investigated but discarded, due to the strong mechanical constraints and the difficulty of removing the PIN photodiodes from the crystals without the risk of damage. Each PIN diode is read with a separate electronic chain composed of a charge-sensitive preamplifier and a CR-RC-RC shaper, with 800 ns−250 ns−250 ns shaping times. To achieve the required dynamic range, the output of each channel is amplified in two chains, having gains of 1 and 32, respectively.

9.2.4.1 Requirements

The increased background radiation in the Super*B* environment calls for a shorter integration time, at the price of a reduction of the integrated light, and a corresponding worsening of the electronics signal-to-noise ratio. The signal shaping time must also be reduced to a few hundred nanoseconds; this increases the bandwidth of the shaper and consequently the electronic noise. Finally, the need to have good timing response for use in the EMC trigger led us to replace the charge sensitive preamplifier with a transimpedence amplifier with a low feedback capacitance.

Achieving the desired signal-to-noise performance with this design requires the use of low noise components. The new Front End Boards will also have increased power consumption, due to the larger bandwidth operational amplifiers and the use of off-the-shelf components.

The final design choices will result from a compromise between rate capability and electronic noise performance.

9.2.4.2 Electronic noise measurements

A test stand has been setup in the Electronics Laboratory (LABE) of the INFN in Rome in order to study the electronic noise of the FEE of the Barrel EMC. The aim of this test is to study the effect of short integration times, of the order of 100 ns, by measuring the noise level for different FEE configurations. To this end, a CsI(Tl) crystal from the *BABAR* calorimeter, with dimensions of $\sim 6 \times 6 \times 30$ cm^3, has been equipped with the photosensor under test on one side, and with an EMI9814B PMT on the opposite side to provide a trigger. Two photosensors have been tested: standard PIN diodes from *BABAR* with sensitive area 1×2 cm^2 (only one of the pair is read out), operated at 60 V, and the avalanche photodiodes (APD) used in the CMS calorimeter (Hamamatsu S8664), with a sensitive area 0.5×0.5 cm^2, operated at two different voltages, 340 and 380 V.

The signal is provided by a ^{60}Co radioactive source having two well-defined γ lines of 1.17 and 1.33 MeV. The photosensor is read out with a charge-sensitive preamplifier (CSP) followed by a Gaussian shaper. Both the photosensor and the PMT signals are viewed with a LeCroy 12 bit digital oscilloscope. The waveforms have been recorded at a sampling rate of 20 GSamples/s; 50000 events were collected for each configuration studied. For each event, the maximum amplitude of the photosensor signal after the trigger time is found; the region before the trigger is used to evaluate the baseline.

The CSP is the Hamamatsu H4083 with 100 ns integration time, in combination with a Gaussian shaper with shaping times ranging from 100 to 500 ns.

A prototype amplifier (LNA02V0) developed at LABE has also been tested. This prototype is very similar to the Hamamatsu CSP, but has slower output signal rise time (400 *vs.* 300 ns), and narrower bandwidth.

As a benchmark, a CSP with very large integration time, 140 μs, similar to that used in the *BABAR* readout chain, has also been used. Finally a test of a PIN diode with the original *BABAR* FEE has also been performed, to check the performance of our experimental setup.

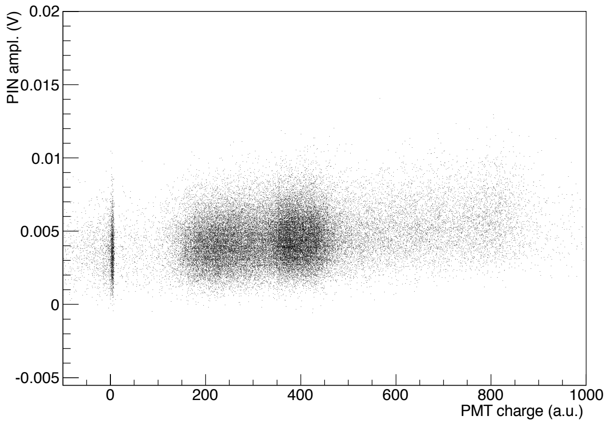

Figure 9.13: APD maximum amplitude vs PMT response.

The two γ lines of ^{60}Co are clearly visible in the charge spectrum of the PMT, as is the small sum peak at 2.5 MeV. The basic idea is to use the two γ lines and their sum to calibrate the energy response of the photosensor, and to then use this calibration to evaluate the equivalent electronic noise (in MeV) starting from the absolute noise (expressed in mV).

The scatter plot of Fig. 9.13, shows an example of the APD maximum amplitude as a function of PMT charge. This scatter plot is divided into six regions: the pedestal around $Q_{PMT} = 0$, the crystal background, the two γ lines, the tail of the crystal background and the region of the sum of the two γs. The calibration of the energy scale is obtained from a linear fit of the peaks of the distributions as function of the photon energy (Fig. 9.14). The dependence of the widths of the same distributions on photon energy is also shown in Fig. 9.14; as an estimate of the electronic noise, the average of the first four points is taken, and the equivalent noise is obtained by dividing by the calibration factor. For the example shown:

$$\frac{1.5 \text{ mV}}{0.8 \text{ mV/MeV}} = 1.9 \text{ MeV} \qquad (9.4)$$

The same analysis has been repeated for all the configurations studied . Table 9.2 shows the absolute noise level. The shortening of the shaping time increases the noise level; therefore in the study of the PIN, only 500 ns shaping is considered.

The energy calibration factors are related to the overall gain of the sensor/FEE chain, and the shortening of the shaping time corresponds to a decrease of the effective gain. Note also that the gain of the APDs at 380 V is about three times the gain at 340 V, while the absolute noise is only slightly higher.

Table 9.2 shows the equivalent noise for each chain. In this test, only one PIN of the two paired together is read out. If both PINs were used, the signal would double, while the electronic noise would increase by a factor of $\sqrt{2}$,improving the equivalent noise performance by the same factor. In this case, the *BABAR* FEE noise would go from 0.78 to 0.55 MeV; the Hamamatsu noise from 2.5 to 1.8 MeV; and the prototype LNA02V0 noise from 1.9 to 1.3 MeV.

The impact of the reduction in integration and shaping time on noise performance is significant. The search for further options and optimization of the system including all effects is therefore still ongoing.

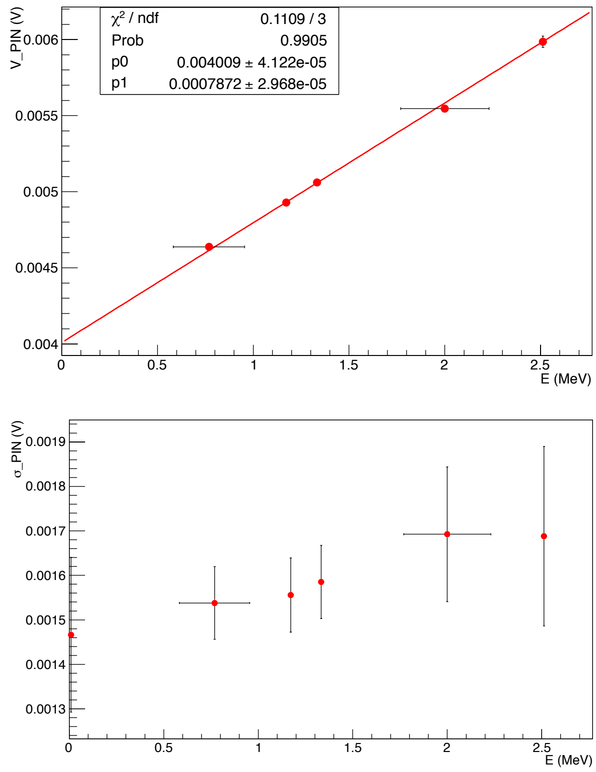

Figure 9.14: (a) Calibration plot for the electronic noise measurements: average APD response vs energy measured by the PMT. (b) Resolution as a function of the deposited energy.

9.2.4.3 Readout design

The readout of each PIN diode is done using two separate channels. This choice is motivated by the need for redundancy and to minimize the possibility of dead crystal channels in the event of a PIN diode failure. In order to minimize the noise of the Front End Boards, we provide two outputs for each channel, one for the low energy range and the other for the high energy range, with a gain of 1 and 32 as in *BABAR*. The four signals for each crystal (two channels with two different gains) are combined in the digitizer board; normally the mean signal from two PIN diodes is used, but in case of failure of one PIN diode, the signal from the remaining diode can be selected.

9.2.5 Disassembly at SLAC and Transport to Italy

The *BABAR* barrel calorimeter was assembled at SLAC and then inserted and supported in the magnet flux return structure. The EMC design did not, therefore take into consideration the requirements of the long-haul transportation that will be required to move it to Cabibbo Lab. We have studied two scenarios for shipment, electronics refurbishment and final installation:

a) Ship the barrel calorimeter as a unit, in one piece, and then do the refurbishment of the front end electronics in a suitable environment as close as possible to the Super*B* interaction area.

b) Disassemble the calorimeter at SLAC, shipping the 280 individual modules and the supporting structures for refurbishment in Naples, followed by transport of modules and structures to the Super*B* assembly hall at Cabibbo Lab.

Table 9.2: Absolute noise (mV) and equivalent noise (MeV) for several electronic solutions

CSP - integration time - shaping time	$V_{APD} = 340$ V	$V_{APD} = 380$ V	PIN diode
Cremat - 140 μs - 500 ns	2.4/1.3	3.3/0.62	1.5/0.56
Hamamatsu - 100 ns - 500 ns	2.9/1.3	4.5/0.85	2.5/2.5
Hamamatsu - 100 ns - 250 ns	5.1/3.4	6.0/1.3	-
Hamamatsu - 100 ns - 100 ns	5.3/4.4	6.0/1.5	-
LNA02V0 - 100 ns - 500 ns	-	3.0/0.57	1.5/1.9
BaBar FEE	-	-	0.7/0.78

Each option has pros and cons, which have been carefully evaluated, leading to the decision to adopt scenario b) as the baseline. To evaluate the risks associated with the transport of the complete barrel EMC, the original structural analysis calculations would have to be updated, and some critical information, such as the current condition of glued parts and internal structures, is difficult, and in some cases impossible, to ascertain. Moreover, design and construction of a complex and expensive support structure able to damp motions occasioned by an intercontinental air shipment, with subsequent ground transportation, would be required. Air shipment of the 30 ton barrel structure, with a volume of the order of 4×4 cubic meters, requires the use of large cargo planes. The cost of such a shipment has not been evaluated.

Shipping is simpler and safer in scenario b), at the cost of complex disassembly and reassembly efforts. Some disassembly is still necessary in scenario a) in order to reach the front end electronics. In scenario b), refurbishing work is much easier, allowing repairs such as re-gluing of loose PIN diodes, that are difficult if the modules are mounted in the cylindrical support structure. Last, but not least, costs and availability of space resources and manpower have been compared, tending in favor of the chosen baseline.

A well-coordinated effort to disassemble the barrel EMC is underway at SLAC. Most of of the tooling, from jigs and supporting structure to critical tools like the robotic arm for module handling (Fig. 9.15), has been located, and parts are being tested and refurbished. Procedures and schedules are well-advanced, with the goal of readiness for shipment in summer 2014.

9.2.6 Electronics refurbishment

The guiding principle in the upgrade of the barrel electronics is to retain the mechanics of the electronics components of *BaBar*, using the same form factor for the revised electronics boards so that they fit into the existing mechanical structures.

The front end preamplifiers are located at the rear of each crystal, inside a brass shield. The shield cages are connected to the crystal photodiode assembly, which is very difficult to unglue and disassemble. The brass cages themselves are robust, and can be dismounted and reused without risk of damage.

With the intent to reuse this brass housing, we will design the preamplifier form factor to fit, retaining as well the form factor of the connector and cable.

The barrel digital electronics in *BaBar* is housed inside 48 small custom-built crates (minicrates) located on either side of the ends of the cylindrical structure. Each minicrate contains a backplane that divides the connection board from the digitizer boards and a fiber optic signal transmission board.

We plan to reuse the mechanical structure of the minicrates, retaining the same form factors for the four replacement electronics boards (connection boards, backplane, digitizer board, and fiber optic transmission board).

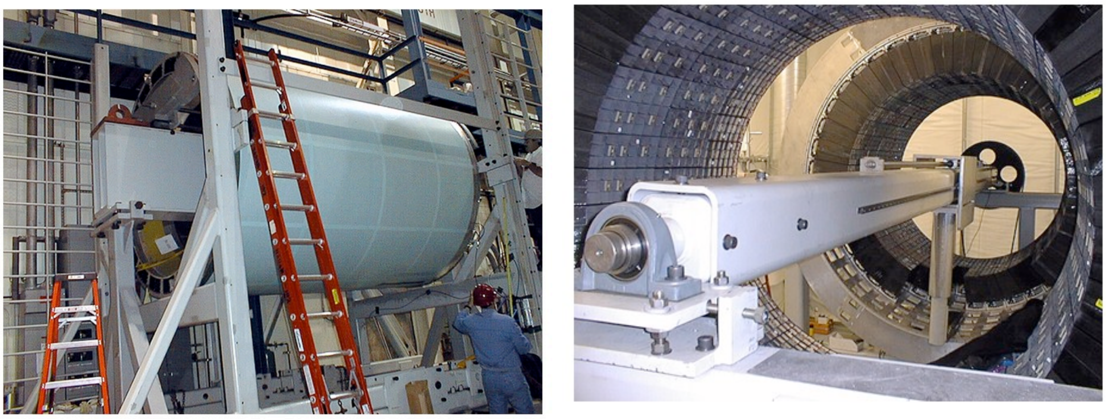

Figure 9.15: Examples of tooling equipment for the EMC Barrel.

9.2.7 Shipment, Refurbishing and Reassembly

The CsI(Tl) crystals are sensitive to humidity, and the PIN sensors glue joint can be broken by temperature excursions. Tests in *BABAR* have shown that temperature variations must be limited to $\pm 5^\circ$ C. Accordingly, the module shipping containers must be provide controlled temperature, a dry atmosphere, and protection against mechanical and thermal shocks. Shipment by air is foreseen in order to shorten travel times and consequently decrease risks.

In due time, decisions on shipment and storage location of the rest of the EMC mechanical components (such as the main support cylinders, jigs, and tooling) will be taken. To ensure controlled ambient conditions during module refurbishment in Naples, at the end of 2013 part of the dedicated hall will be enclosed in a protective tent (10×10 m^2 area), whose temperature and humidity will be actively controlled by a new air conditioning system that will work in parallel with the already existing plant, as insurance against failures. In this tent, the front end electronics will be refurbished by teams working in parallel. Completed modules will be individually tested with radioactive sources, light pulsers through optical fibers reaching each crystal, and cosmic ray data taken inside an existing telescope with tracking resolution in the millimeter range. Queued and completed modules will be stored in the same tent on layered scaffolding.

Estimated refurbishing and test time, based on *BABAR* experience, is of the order of one year, placing the end of refurbishing work in Naples approximately a year after the new preamps are available. Depending on the status of the Tor Vergata site, shipment and the remounting phase will start in 2016, or perhaps in 2015, using modules already completed. At Tor Vergata, in the construction hall close to the interaction region, again in a air conditioned tent, modules will be inserted into the steel support cylinder, cables and readout electronics will be added, and calibration systems (light pulses on an optical fiber distribution system, fluorine activation and distribution system) will be implemented and tested during the commissioning phase before detector assembly.

9.3 Forward Calorimeter

The Forward Calorimeter extends the coverage of the electromagnetic calorimeter to low forward polar angles, as detailed in Tab. 9.1. To be effective, its performance must therefore be comparable with the barrel calorimeter, despite the higher rates seen in the forward direction. Hence the design choice is a crystal calorimeter read out by compact photodetectors capable of operating in magnetic field.

Taking as a performance objective the *BABAR* calorimeter, the new endcap should have a relative energy resolution of at most 4.3% at 100 MeV and 2.7% at 1 GeV. In order to retain appropriate resolution on the π^0 invariant mass, and to allow $\pi^0 \to \gamma\gamma$ reconstruction up to sufficiently high energies, segmentation at least comparable to that of *BABAR* is needed. Since the transverse crystal size is dictated by the Molière radius of the material, only crystals with a Molière radius no larger than CsI(Tl) can be considered. Finally hermeticity is also important, so the requirement on mechanics is that the fraction of particles originating from the interaction point passing through the cracks between the crystals be minimal, comparable with the barrel.

As already described for the barrel calorimeter, the most stringent constraints arise from the presence of large backgrounds due to the extremely high luminosity. As shown in Fig. 9.16, the expected radiation dose integrated in a year ranges from $\sim$ 250 rad for the outermost rings to $\sim$ 320 rad for the innermost ones. Consequently, the dose rate the crystals must tolerate is about $\sim$ 0.1 rad/h.

As described in Sec. 9.1.1, the large rate of low energy photons can also damage the crystals themselves, reducing the longitudinal transmission, and thus the light yield. The *BABAR* experience is that this is worse in the endcap than in the barrel (Fig. 9.10), and this is expected to be true in Super$B$ as well. The large rate in the forward direction can degrade the energy resolution by causing signal pile-up. This is a serious concern, as shown in Fig. 9.17, and in particular, the performance of the *BABAR* CsI(Tl) endcap is not adequate. The chosen crystal must therefore have a stable light yield in the expected radiation environment and the signal shape produced by the readout must be compatible with the expected rates.

We have investigated several combinations of crystals and electronics, as described below. The option yielding the best performance is crystals made of LYSO, with readout by avalanche photodiodes (APD), in a new low-mass mounting structure. This configuration has been studied in detail. However, budget restrictions force us to adopt as our baseline a "hybrid" scheme, making use of LYSO at the smallest radii, while retaining the *BABAR* CsI(Tl) crystals in the three outermost endcap layers. This results in a significant reduction in cost, while maintaining the benefits of LYSO where it is needed most, where the rate and radiation issues are most severe. As part of this cost compromise, the structural support of the *BABAR* endcap will also be reused, rather than adopting a lower mass structure that would improve performance.

9.3.1 LYSO Crystals

Over the last two decades, cerium-doped lutetium oxyorthosilicate (Lu_2SiO_5 or LSO) [7] and lutetium yttrium oxyorthosilicate ($Lu_{2(1-x)}Y_{2x}SiO_5$ or LYSO) [8, 9] have been developed for the petroleum and medical industries; mass production capabilities are firmly established. This section addresses the crystal properties, specifications, production and testing.

Table 9.3 [10] lists basic properties of several heavy scintillating crystals: NaI(Tl), CsI(Tl), pure CsI, bismuth germanate ($Bi_4Ge_3O_{12}$ or BGO), lead tungstate ($PbWO_4$ or PWO) and LSO/LYSO. All have either been used in, or are actively being pursued for, high energy and nuclear physics experiments, which are also listed in the table. The experiment names in bold refer to future crystal calorimeters. NaI(Tl), CsI(Tl), BGO, LSO and LYSO crystals are also widely used in the medical and oil industries. Mass production capabilities exist for all these crystals.

Because of their high stopping power, high light yield, fast decay time, small temperature coefficient and excellent radiation hardness, LSO and LYSO crystals have attracted broad interest for new intensity frontier projects in high energy physics (HEP) [11, 12, 13, 14, 15]. They are the best choice for the Super$B$ forward calorimeter, either the full uncompromised version or the adopted hybrid design. Full size LSO and LYSO crystals from the following vendors have been tested during the R&D phase of

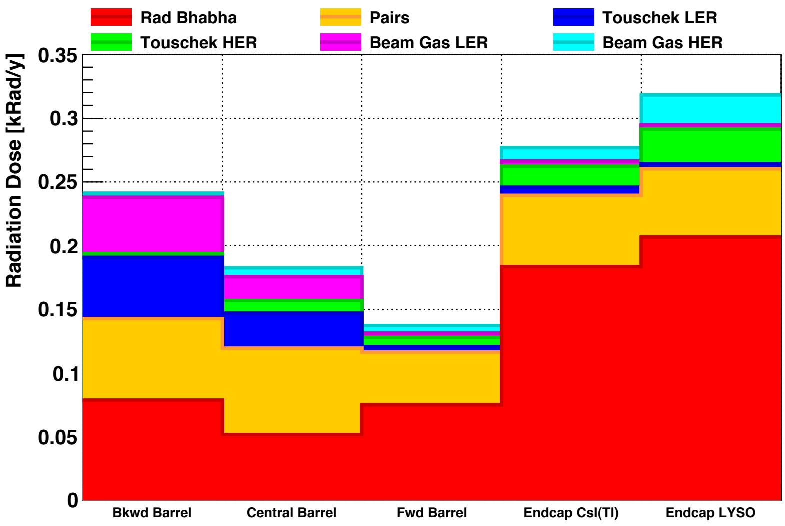

Figure 9.16: Expected radiation dose per year as a function of the calorimeter region.

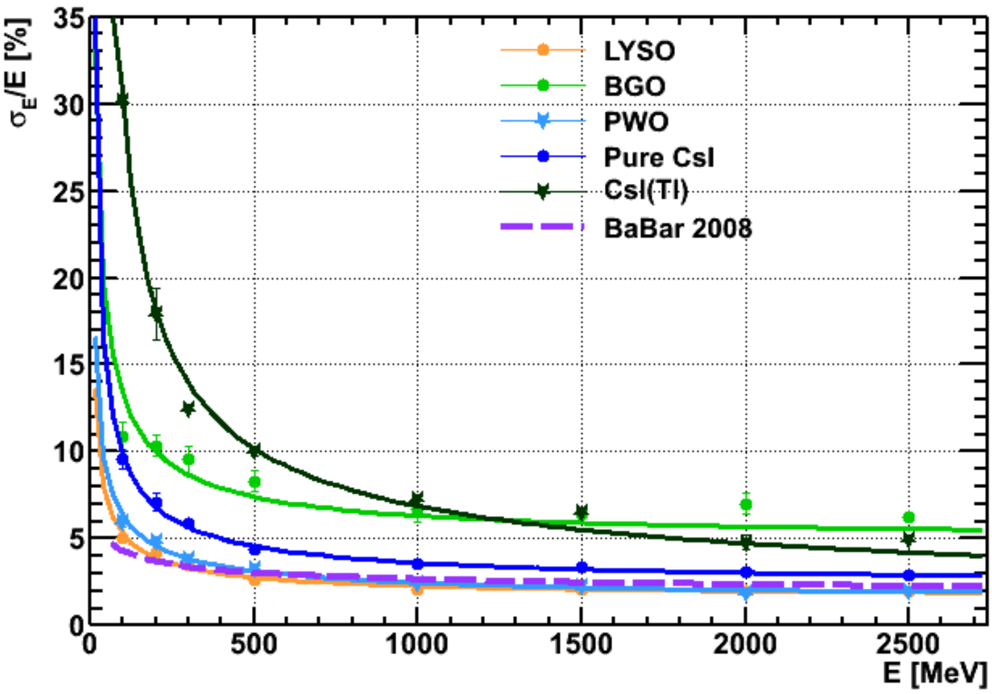

Figure 9.17: Comparison of resolution in the forward calorimeter for several different crystals, at 5 times nominal background.

Table 9.3: Properties of Heavy Crystal with Mass Production Capability

Crystal	NaI(Tl)	CsI(Tl)	CsI	BGO	$PbWO_4$	LSO/LYSO(Ce)
Density (g/cm^3)	3.67	4.51	4.51	7.13	8.3	7.40
Melting Point (°CC)	651	621	621	1050	1123	2050
Radiation Length (cm)	2.59	1.86	1.86	1.12	0.89	1.14
Molière Radius (cm)	4.13	3.57	3.57	2.23	2.00	2.07
Interaction Length (cm)	42.9	39.3	39.3	22.7	20.7	20.9
Refractive Index[a]	1.85	1.79	1.95	2.15	2.20	1.82
Hygroscopicity	Yes	Slight	Slight	No	No	No
Luminescence[b] (nm) (at Peak)	410	560	420 310	480	425 420	420
Decay Time[b] (ns)	245	1220	30 6	300	30 10	40
Light Yield[b,c]	100	165	3.6 1.1	21	0.30 0.077	85
d(LY)/dT[b,d] (%/°CC)	−0.2	0.4	−1.4	−0.9	−2.5	−0.2
Experiment	Crystal Ball	CLEO *BABAR* BELLE BES III	KTeV E787	L3 BELLE	CMS ALICE PrimEx **Panda**	**Mu2e** **Super*B*** **HL-LHC?**

a At the wavelength of the emission maximum.
b Top line: slow component, bottom line: fast component.
c Relative light yield of samples of 1.5 X_0 and with the PMT quantum efficiency taken out.
d At room temperature.

Super*B*: CTI Molecular Imaging (CTI), Crystal Photonics, Inc. (CPI), Saint-Gobain (SG), Sichuan Institute of Piezoelectric and Acousto-optic Technology (SIPAT) and Shanghai Institute of Ceramics (SIC). Our development efforts over the past several years have served to effect a substantial reduction in the price of large LYSO crystals.

9.3.1.1 Transmittance and Emission

Large LYSO crystals with good transmittance characteristics are now routinely produced in industry. The left plot of Fig. 9.18 shows the longitudinal (green) and transverse (red) transmittance spectra measured for a rectangular LYSO sample with dimensions 2.5 × 2.5 × 20 cm (18 X_0). Significant red shift, caused by internal absorption, is observed in the absorption edge of the longitudinal transmittance, as compared to the transverse transmittance. The black point are a fit to the theoretical limit of transmittance calculated by using the refractive index, assuming multiple bounces between two end surfaces and no internal absorption [16]. It overlaps with the transverse transmittance spectrum at wavelengths longer than 420 nm, indicating the excellent optical quality of the crystal. Also shown is the photo-luminescence spectrum (blue) [17]. The fact that a part of the emission spectrum is at wavelengths below the absorption edge in-

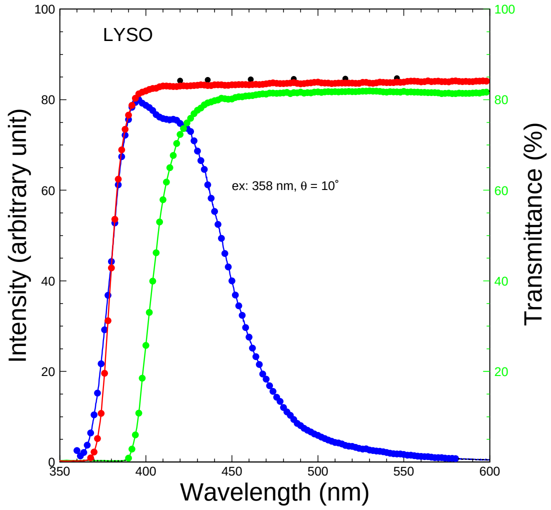

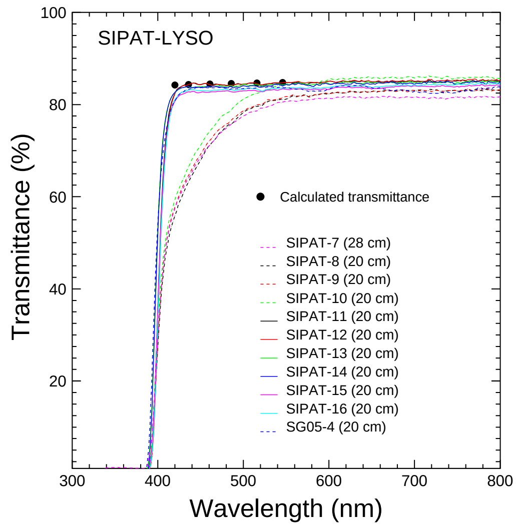

Figure 9.18: Left: The longitudinal (green) and transverse (red) transmittance spectra and the photo-luminescence (blue) spectrum as a function of wavelength for a rectangular LYSO sample with dimensions 2.5 $\times$ 2.5 $\times$ 20 cm. Right: Longitudinal transmittance spectra as a function of wavelength for eleven LYSO crystals: ten from SIPAT and one from Saint-Gobain. All except SIPAT-7 are 20 cm long.

Table 9.4: Photo Luminescence-Weighted Quantum Efficiencies (%)

Photo Luminescence	LSO/LYSO	BGO	CsI(Tl)
Hamamatsu R1306 PMT	12.9±0.6	8.0±0.4	5.0±0.3
Hamamatsu R2059 PMT	13.6±0.7	8.0±0.4	5.0±0.3
Photonis XP2254b	7.2±0.4	4.7±0.2	3.5±0.2
Hamamatsu S2744 PD	59±4	75±4	80±4
Hamamatsu S8664 APD	75±4	82±4	84±4

dicates that this part of the scintillation light is absorbed internally in the crystal bulk; this is usually referred to as the self-absorption effect. There is no such self-absorption effect in other scintillation crystals commonly used for HEP calorimeters, such as BGO, CsI(Tl) and PWO [10]. While this self-absorption has little consequence in the 6 mm long pixels used in medical instruments, it can affect the light response uniformity for the 20 cm long crystals used in the Super*B* calorimeter. This will be discussed in section 9.3.1.3.

During the R&D phase for crystal development poor longitudinal transmittance was observed in some samples [18]. The right plot of Fig. 9.18 shows that four samples (SIPAT-7 to SIPAT-10) have poor longitudinal transmittance between 380 nm and 500 nm, showing an absorption band. Further investigation revealed that this absorption band is located at the seed end, and is caused by point defects [17] associated with a poor quality seed crystal used in their growth. With rigorous quality control, LYSO crystals grown later at SIPAT (SIPAT-11 to SIPAT-16) show no absorption band at the seed end (Fig. 9.18). An increase of light output of about 30% was found after this problem was resolved. It is thus important to include in crystal specifications a requirement on the crystal's longitudinal transmittance.

The left plot of Fig. 9.19 shows typical quantum efficiencies of a PMT with multi-alkali cathode (Photonis XP2254b) and an APD (Hamamatsu S8664) [19]. The photoluminescence spectra of LSO/LYSO, BGO and CsI(Tl) crystals are also shown; the area under the luminescence spectra is roughly proportional to the corresponding absolute light output. Table 9.4 summarizes the numerical values of the photoluminescence-weighted average quantum efficiencies for various readout devices. These numbers can be used to convert the measured photo-electron numbers to the absolute light output in photon numbers.

A significant red component was observed in the γ-ray induced luminescence spectra in the CTI LSO samples; this was not seen in the LYSO samples from the other suppliers [17]. This red component disappeared after a γ-ray irradiation with an accumulated dose of 5×10^3 rad. This is the only significant difference observed between the large size LSO and LYSO samples [17], indicating that LYSO is the preferred choice.

9.3.1.2 Decay time and Light Output

The right plot of Fig. 9.19 shows the light output for six crystal scintillators in units of photoelectrons/ MeV, measured using a Photonis XP2254 PMT as a function of integration time [10]. The light output can be fit to the following function to determine the fast and slow components and the decay kinetics:

$$LO(t) = F + S(1 - e^{-t/\tau_s}), \qquad (9.5)$$

where F is the fast component of the scintillation light with a decay time of less than 10 ns, and S is the slow component with a decay time of τ_s longer than 10 ns. The decay time of both LSO and LYSO crystals is about 40 ns.

As shown in Table 9.3 LSO and LYSO crystals have high light output, about 85% and 50% of NaI(Tl) and CsI(Tl) respectively, and about 18, 4, and more than 200 times that of pure CsI, BGO, and PWO, respectively. Figure 9.20 shows 0.511 γ-ray pulse height spectra measured by a Hamamatsu R1306 PMT (left) and two Hamamatsu S8664-55 APDs (right) for four LSO and LYSO samples of $2.5 \times 2.5 \times 20$ cm^3 from CTI, CPI, SG, and SIPAT. The equivalent noise energy for the APD readout is less than 40 keV [19]. The CPI LYSO sample showed poor energy resolution; the other samples did not. According to the grower this was caused by intrinsic non-uniformity, which may be improved by appropriate thermal annealing. It thus is important to include in crystal specifications a requirement on the crystal's energy resolution.

Because of their fast decay time and high light output, LSO and LYSO crystals have also been used in time of flight (TOF) measurements for medical applications, such as TOF PET (positron emission tomography). Better than 500 ps FWHM was achieved for the time

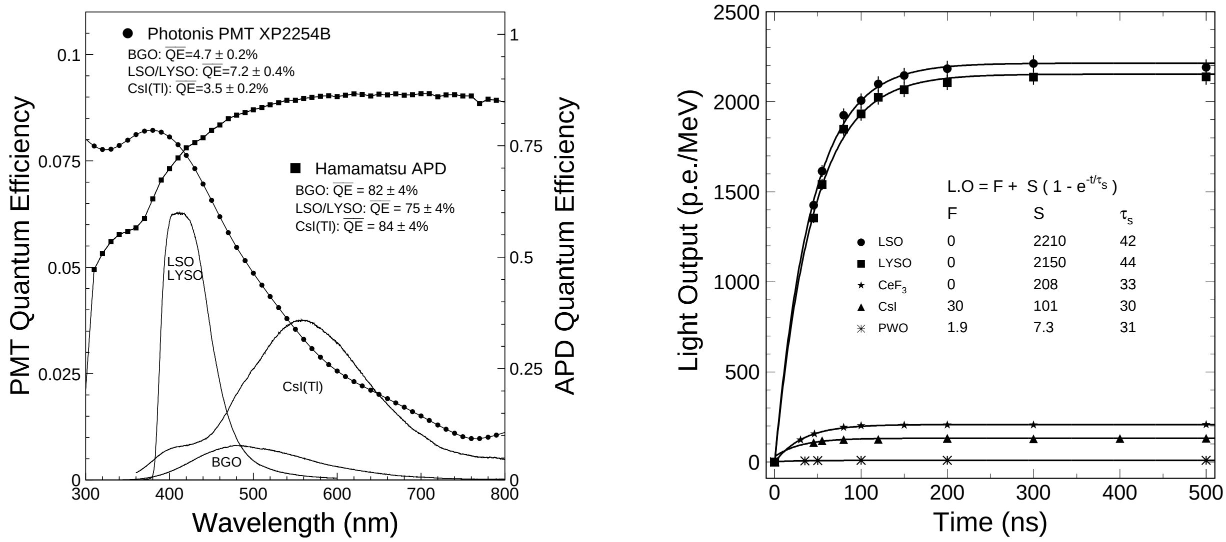

Figure 9.19: Left: The quantum efficiencies of a Hamamatsu R2059 PMT (solid dots) and a Hamamatsu S8664 APD (solid squares) are shown as a function of wavelength together with photoluminescence spectra of the LSO/LYSO, BGO and CsI(Tl) samples, where the area under the luminescence spectra is roughly propotional to the corresponding absolute light output. Right: Light output measured by using a Photonis XP2254 PMT is shown as a function of integration time for six crystal scintillators.

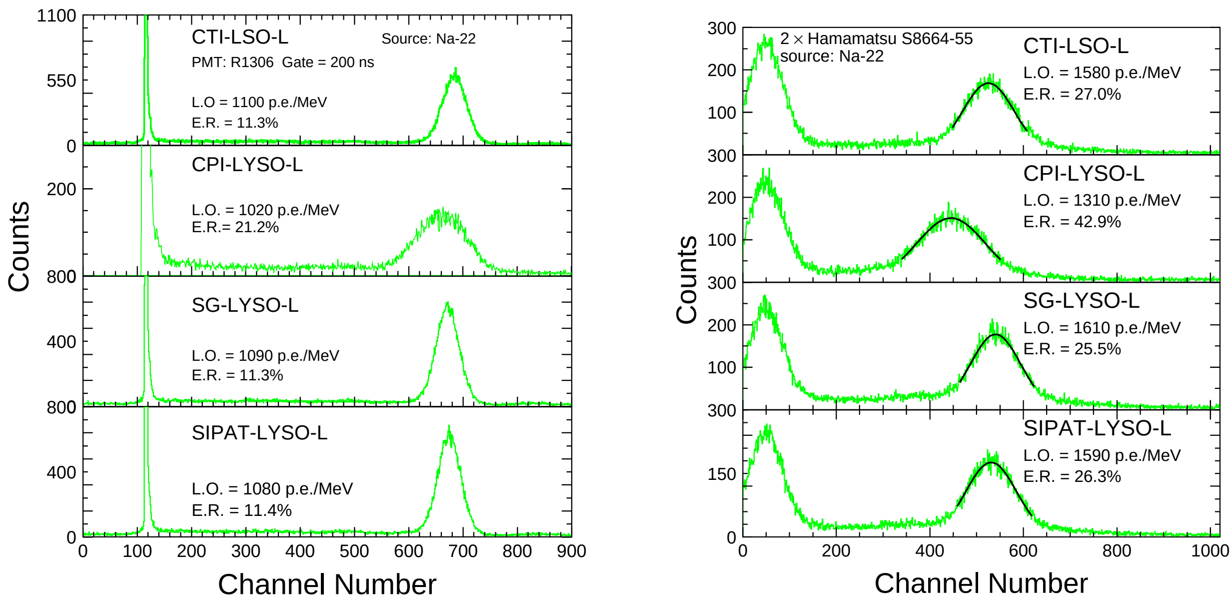

Figure 9.20: 0.511 MeV γ-ray spectra from a ^{22}Na source, measured by a Hamamatsu R1306 PMT (Left) and two Hamamatsu S8664-55 APDs (Right), with a coincidence trigger for four long LSO and LYSO samples of $2.5 \times 2.5 \times 20$ cm^3.

difference between two photons. In HEP experiments, an *rms* time resolution of better than 150 ps may be achieved for TOF measurements for single particles. Since the intrinsic rise time of scintillation light is about 30 ps for LSO and LYSO crystals [20], the measured time resolution for LSO and LYSO is affected mainly by the response speed of the readout device and the choice of time pick-off [21]. Calcium doping of LSO and LYSO has been reported to reduce the decay time to about 20 ns [22], which would help to improve the time resolution.

9.3.1.3 Response Uniformity

Adequate light response uniformity along the crystal length is key to maintaining the precision offered by a total absorption crystal calorimeter at high energies [23]. The light response uniformity of a long crystal is parameterized as a linear function,

$$\frac{LY}{LY_{\mathrm{mid}}} = 1 + \delta(x/x_{\mathrm{mid}} - 1), \qquad (9.6)$$

where (LY_{mid}) represents the light output measured at the middle point of the crystal, δ represents the deviation from the flat response and x is the distance from the photo-detector. To achieve good energy resolution, the corresponding $|\delta|$ value for Super$B$ LYSO crystals of 18 X_0 length must be kept to less than 3% [24].

Effective light collection requires good light reflection. The glass fiber-based supporting structure designed for the originally envisioned Super$B$ full LYSO forward calorimeter was coated with a thin layer of aluminum as reflector. All measurements and simulations discussed in this section were therefore carried out with an aluminum-coated glass fiber supporting structure cell, referred to as the RIBA Cell, around the crystal. In the baseline hybrid design, the BABAR endcap mechanical structure is retained; an equivalent reflective wrapping to the four LYSO crystals that will occupy each existing cell must be developed.

The light response uniformity of a long tapered LYSO crystal is affected by three factors. First, the tapered crystal geometry leads to an optical focusing effect, *i.e.,* the response for scintillation light originating at the small end far away from the photodetector would be higher than that at the large end, which is coupled to the photodetector. This is caused by the light propagation inside the crystal, and is common to any optical object with this tapered geometry. Second, there is a self-absorption effect in LYSO crystals, as discussed in section 9.3.1.1, since a part of the emission spectrum is self-absorbed in the crystal bulk (left plot of Fig. 9.18). This effect is specific to LYSO crystals. Last, there is a non-uniform light yield along the longitudinal axis of the crystal, caused by segregation of the cerium activator in LYSO crystals during growth. Because of the small segregation coefficient (about 0.2) the cerium concentration increases from the seed end to the tail end of the crystal. This effect is common to all Czochralski method crystals doped with an activator, *e.g.*, CsI(Tl).

The left plot of Fig. 9.21 shows the light response uniformities calculated using a ray-tracing program [23] for a Super$B$ LYSO crystal with tapered geometry and dual Hamamatsu S8664-55 APD readout. The blue dots show the uniformity with only the optical focusing effect; the red dots include, in addition, the self-absorption. Numerically, the optical focusing effect alone causes a δ value of 17%, which is reduced to 13% with self-absorption included. This indicates that the self-absorption effect can provide partial compensation for the optical focusing effect, provided that knowledge of the crystal growth orientation is retained.

The right plot of Fig. 9.21 shows the light output measured for two batches of 17 mm LSO/LYSO crystal cubes (red and blue) as a function of the cerium concentrations determined by Glow Discharge Mass Spectroscopy (GDMS) analysis. It shows that the optimized cerium doping level is between 150 and 450 ppmw because of the interplay between the cerium activator density and the self absorption caused by overdoping. Also shown in the plot is a second order polynomial fit. By adjusting the cerium doping concentration, the light yield difference along the crystal can be minimized. A difference at the level of 10% is more or less the maximum, which may provide a variation of the δ value up to 5%. Taking this into account, the initial δ value of the Super$B$ LYSO crystals may vary between 8% and 18%.

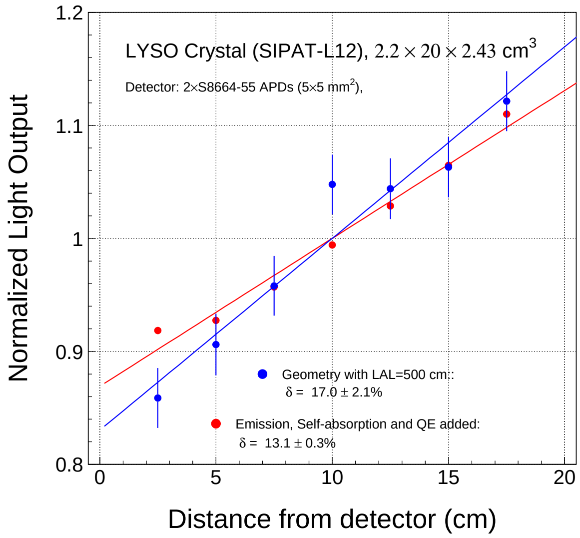

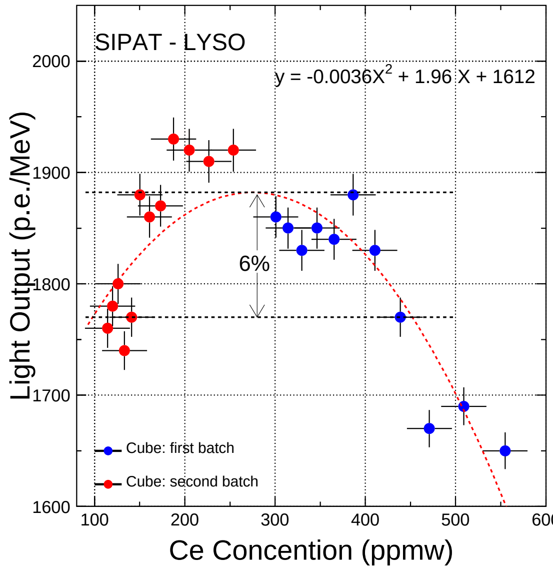

Figure 9.21: Left: Light response uniformities without (blue) and with (red) self-absorption effects, calculated by a ray-tracing program, shown for a 20 cm long crystal with tapered geometry and two Hamamatsu S8664-55 APD readout. Right: Light output measured for 17 mm LSO/LYSO crystal cubes shown as a function of the cerium concentration.

Following the experiences of previous crystal calorimeters, such as L3 BGO and CMS PWO, a $|\delta|$ value of less than 3% may be achieved by roughening one side surface of the crystal to an appropriate roughness [25]. The left plot of Fig. 9.22 shows the light response uniformities measured with dual Hamamatsu S8664-55 APD readout for a tapered Super*B* LYSO crystal, SIC-L3. The δ value is reduced from 15% before (red) to -1.9% after (blue) roughening the smallest side surface to Ra = 0.3. The right plot of Fig. 9.22 shows a comparison of the δ values before (top) and after (bottom) roughening for all 25 Super*B* test beam crystals, showing a reduction of the average δ value from 10% to 0.26%. All 25 $|\delta|$ values after uniformization are within 3%. The reduction of light collection efficiency caused by this uniformization is about 17%. It is expected that one or two Ra values would be sufficient to uniformize the full cohort of mass produced LYSO crystals to achieve $|\delta|$ values of less than 3%.

9.3.1.4 Radiation Hardness

The radiation hardness of long LSO and LYSO samples has been investigated with γ-rays [26, 27] and neutrons [28]. It is found that the scintillation mechanism of this material is not damaged. The damage to light transmission does not recover at room temperature, indicating no dose rate dependence [23], but can be completely eliminated by thermally annealing at 300°C. Studies also show that LYSO is also more radiation-hard against charged hadrons [29] than other crystals.

Figure 9.23 shows the longitudinal transmittance (left) and normalized average light output (right) for four 20 cm LSO and LYSO samples from CTI, CPI, SG and SIPAT. The light output was measured by using a XP2254 PMT (top) and two S8664-55 APDs (bottom). All samples tested have a consistent radiation resistance, with degradations of the emission-weighted longitudinal transmittance (EWLT) and the light output of approximately 12% for a γ-ray dose of 1 MRad. This radiation hardness is much better than other scintillation crystals, such as BGO, CsI(Tl) and PWO.

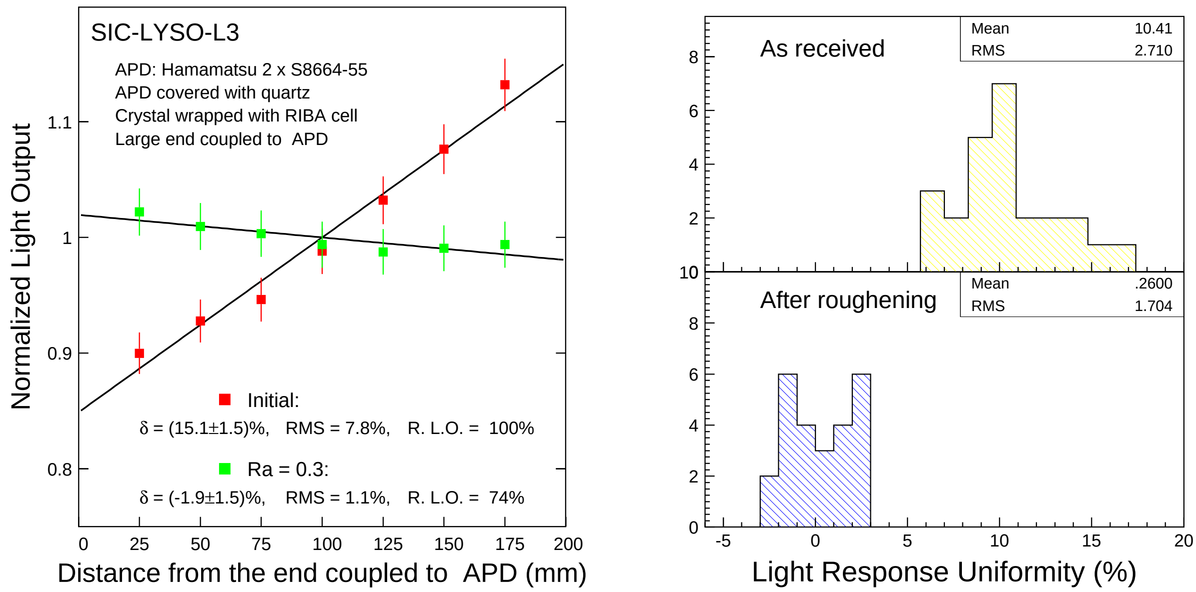

Figure 9.22: Left: Light response uniformity measured with two Hamamatsu S8664-55 APD readout for a tapered Super*B* LYSO crystal SIC-L3 before (red dots) and after (green dots) uniformization by roughening the smallest side surface to Ra = 0.3. Right: The distributions of light response uniformity (δ values) are shown for 25 Super*B* test beam crystals before (top) and after (bottom) uniformization by roughening the surface of the smallest side.

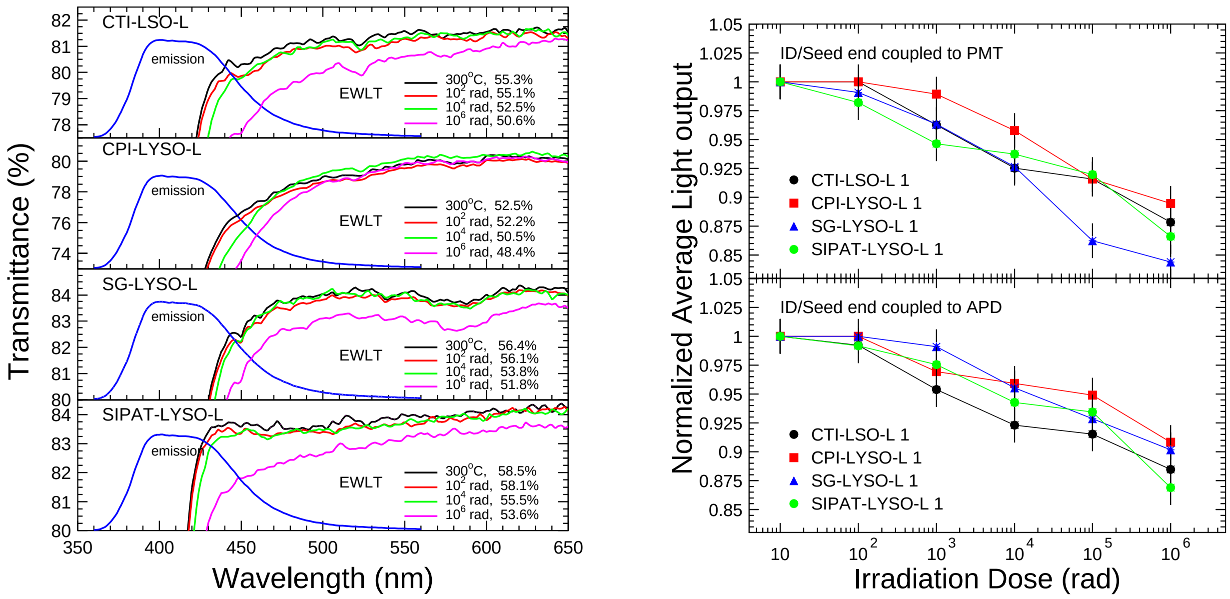

Figure 9.23: The longitudinal transmittance spectra in an expanded view (left) and the normalized light output (right) are shown as a function of the integrated dose up to 1 Mrad for four LSO and LYSO samples of $2.5 \times 2.5 \times 20$ cm^3. Also shown in the left plot is the photoluminescence spectrum (blue) in arbitrary units. The EWLT is listed in the legend.

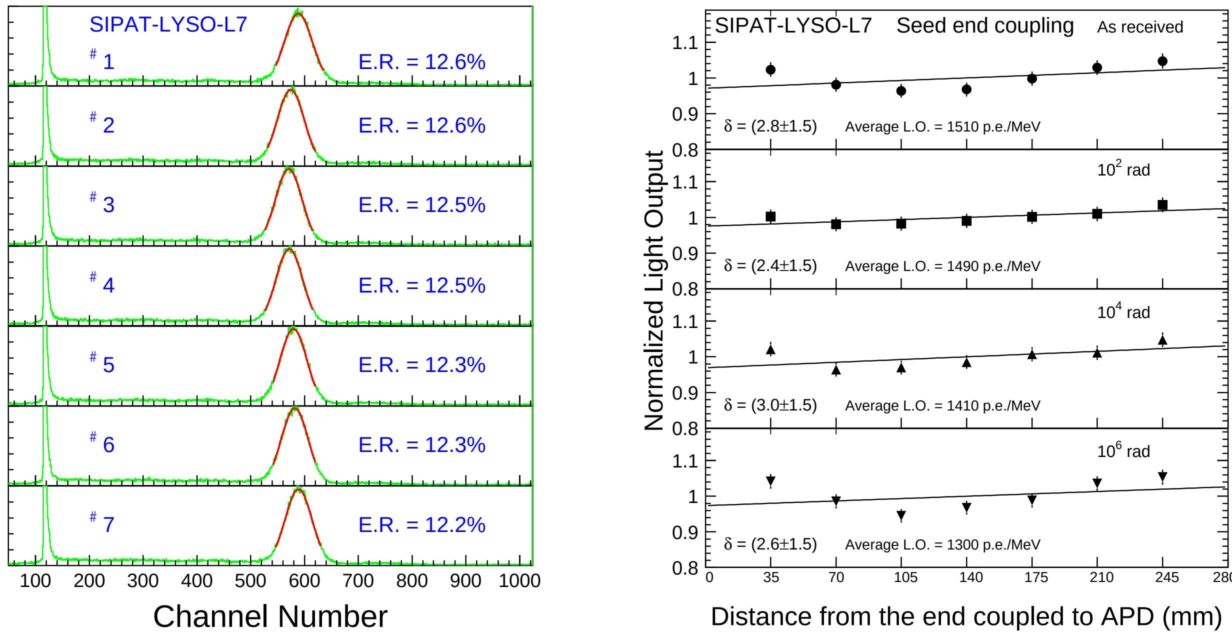

Figure 9.24: Left: The pulse height spectra of 0.511 MeV γ-ray peaks (green) and corresponding Gaussian fits (red) measured by a Hamamatsu R1306 PMT are shown at seven points evenly distributed along SIPAT-LYSO-L7. Also shown are the numerical values of the FWHM energy resolutions (E.R.). Right: Normalized light output and light response uniformity measured by two Hamamatsu S8664-1010 APDs, before and after γ-ray irradiations in several steps up to 1 Mrad are shown for SIPAT-LYSO-L7.

Recently, a 28 cm (25 X_0) LYSO crystal (SIPAT-LYSO-L7) was grown at SIPAT. This LYSO sample has consistent emission, adequate light response uniformity and good radiation hardness against γ-rays up to 1 Mrad [18]. The left plot of Fig. 9.24 shows the pulse height spectra measured by a Hamamatsu R1306 PMT at seven points evenly distributed along SIPAT-LYSO-L7. The FWHM resolutions obtained for 0.511 MeV γ-rays from the ^{22}Na source are about 12.5%. This is quite good for crystals of such length. The right plot of Fig. 9.24 shows normalized light output and response uniformity measured by two Hamamatsu S8664-55 APD before and after γ-ray irradiations with an integrated dose of 10^2, 10^4 and 10^6 rad. The degradation of the light output was found to be about 13% after 1 Mrad dose. The light response uniformity of SIPAT-LYSO-L7 does not change even after a 1 Mrad dose, indicating that its energy resolution will be maintained [23].

In summary, LSO and LYSO crystals are radiation hard crystal scintillators, well-suited to the Super*B* rate and radiation environment at forward polar angles. These crystals are also likely to find application in other severe radiation environments.

9.3.1.5 Specifications, Production and Testing

Following our extensive R&D on LYSO crystals, the following specifications have been defined for the procurement of high quality LYSO crystals from various vendors for the Super*B* forward calorimeter.

- Dimension: $+0.0/-0.1$ mm.
- Longitudinal transmission at 420 nm: greater than 75%.
- FWHM energy resolution: $<$ 12.5% for 0.511 MeV γ-rays measured by a Hama-

matsu R1306 with Dow-Corning 200 fluid coupling at 7 points along the crystal.

- Light output will be required to be more than a defined percentage of a small crystal standard candle with air-gap coupling to the PMT.

- Light Response uniformity ($|\delta|$): $< 3\%$ measured with dual Hamamatsu S8864-55 APDs.

Crystals will be produced by various vendors. The total LYSO crystal volume for the hybrid LYSO Super*B* forward calorimeter, which retains the outer three CsI(Tl) rings) of the *BABAR* endcap, is 0.24 m^3, which is small compared to the volume of LYSO crystals grown for the medical industry.

The following instruments are needed at each of the crystal vendors as well as in the Super*B* crystal laboratory.

- A station to measure crystal dimensions.

- A photospectrometer with a large sample compartment to measure the longitudinal transmission along a 20 cm path.

- A PMT-based pulse height spectrometer to measure light output and FWHM energy resolution with 0.511 MeV γ-rays from a ^{22}Na source.

- An APD-based pulse height spectrometer to measure light response uniformity with 0.511 MeV γ-rays from a ^{22}Na source.

9.3.2 Readout and Electronics

9.3.2.1 APD Readout

The photosensors chosen for readout of the LYSO crystals of the forward endcap are an independent pair of 10×10 mm avalanche photodiodes (APDs). The APDs have several advantages over photodiodes in this application: they are a better match to the emission spectrum of LYSO, providing a quantum efficiency integrated over the spectrum of 75% (Fig. 9.25); they provide useful gain (of the order of 75) with low noise; and, as they have a thinner sensitive region, they suffer less from the nuclear counter effect, in which a hadron interaction in the sensitive region produces a large anomalous signal.

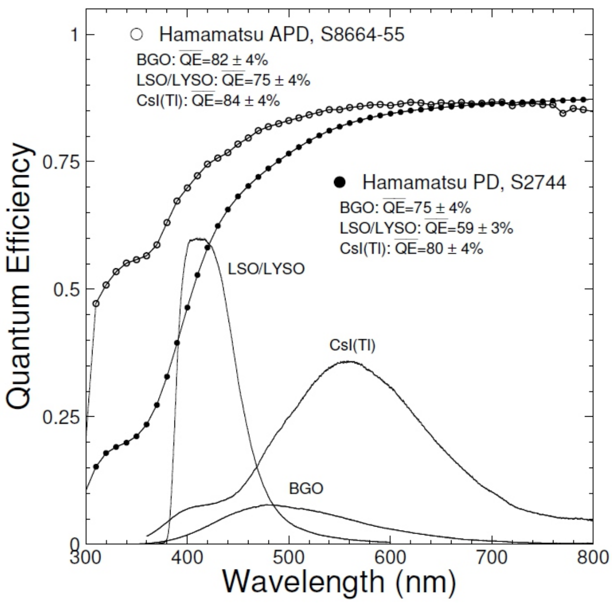

Figure 9.25: Quantum efficiency of a Hamamatsu APD and photodiode, together with the emission spectra of LYSO, BGO and CsI(Tl) crystals.

The gain with low noise of the APDs presents two additional advantages: it allows a reduction of the shaping and integration time constants, variables that can be used optimize the signal-to-noise ratio in the presence of machine background; it also improves the signal-to-noise ratio for the signals used for calibration, allowing a crystal-by-crystal calibration (see Sec. 9.3.3).

9.3.2.2 Electronics Block diagram

The electronics of the forward calorimeter uses the same components as the barrel calorimeter. In the hybrid design the 360 retained CsI(Tl) crystals use exactly the same electronics as the barrel. The different characteristics of LYSO crystals require a different preamplifier and shaper, and a faster sampling time.

9.3.2.3 Preamplifier and shaper

LYSO has a faster scintillation decay time than CsI(Tl), typically 40 ns. The design of the preamplifier uses the same active components as the CsI(Tl) case, but with a different time constants in the passive network. Instead of a transimpedance amplifier configuration as for the slower CsI(Tl), in the LYSO case we use a CSP (charge sensitive preamplifier) with a integration constant of 1 μs, which guarantees complete charge collection. The charge sensitive amplifier noise performance is dominated by the low noise field effect transistor used as the first stage, and by the APD capacitance of about 100 pf. The preamplifier directly drives the shaper, which is also used as a buffer. The shaper circuit is the same as that of the CsI(Tl) circuit, with a different passive time network. The shaper uses a 4 pole circuit CR-RC^4 with a constant time of 100 ns, that produces a near-Gaussian output shape for digital sampling. The shorter shaping time avoids pile up and better uses the decay time characteristics of the LYSO crystal. After the shaping, as with the CsI(Tl), there are two separate drivers, one with unitary gain and the other one with a gain of 32. Four signals, two for each independent photodiode, go to the digitizer board.

9.3.2.4 Digitization

The digitizer board is the same as the one used for the CsI(Tl) crystal readout, but with a higher sampling rate due to the shorter signal shape. The sampling frequency chosen is 39.66 MHz (1/12 of the accelerator RF) using 32 samples in a total time window of 806 ns.

9.3.2.5 Requirements on mechanics

There are two major differences with respect to the *BABAR* setup as far as mechanics is concerned.

On one side the power consumption of the electronics of each individual crystal increases from 100 mW to approximately 180 mW per crystal. This should not be a problem for the alveola where the crystals is not changed. In the 540 alveola where the single CsI(Tl) crystal is replaced by 4 LYSO crystals there are additional mechanical and cooling issues to be addressed. On one side, four channels instead of one need to be lodged on the back of the crystals. To this aim one can exploit the volume left free by the fact that the LYSO crystals are shorter by about 10 cm. Nonetheless, dissipating 720 mW from cards placed within the last 10cm of the alveola is a problem that still needs to be addressed.

9.3.3 Calibration

9.3.3.1 Initial LYSO calibration with sources

A goal of the initial source calibration procedure is that the signal rate and the signal-to-noise ratio with a typical radioactive source such as ^{137}Cs be sufficient to allow individual calibration of each crystal with the readout device with which it will actually be paired. As was the case with the *BABAR* CsI(Tl) crystals, photodiode readout of large crystals does not allow the use of sources for calibration and setup. This is typically done with a reference photomultiplier, with the results then convoluted with measurements of the individually-calibrated photosensors. This procedure does not, of course, fully account for the effects of surface oxidation of the crystal or glue joint losses. With APD readout of the LYSO crystals, however, the response of the entire chain can be measured.

The full setup of each crystal assembly requires each crystal/readout package to be individually adjusted to meet the uniformity requirements *in situ* and the characteristics of each object to be entered into a reference database. This involves appropriate roughening of, typically, one crystal surface to conform to a light collection uniformity specification, as discussed in 9.3.1. The output of this setup/calibration procedure is then entered into a reference database, which serves as the initial set of calibration constants for the calorimeter system.

The fully-assembled calorimeter is then calibrated with the circulated Fluorinert system retained from *BABAR* (see Sec. 9.2.2.3) at appropriate intervals (one to four weeks in the case of *BABAR*). A substantial advantage of this approach is that one obtains an individual pedestal and gain constant for each crystal. A limitation is that the source is at a relatively low energy, although it is at a higher energy than that of long-lived radioactive sources. Calibration with radiative Bhabhas can provide calibration over the full energy range, but it requires development of a complex matrix unfolding procedure, since high energy electrons deposit shower energy in many crystals, not in a single crystal as in the case of source calibration. if using crystals with intrinsic radioactivity, such as for instance the LYSO. For such a crystal the properly designed to achieve the required accuracy in a sustainable time. Since LYSO is intrinsically radioactive, some of the endcap crystals will have an irreducible background, and a configurable trigger threshold is planned. Estimates imply that the issue is small. However a test with LYSO crystals using 6.13 MeV photons from an ^{16}O* state produced with neutrons from a ^{252}Cf source will be made.

9.3.3.2 Temperature monitoring and correction

The characteristics of APDs place fairly stringent requirements on the temperature control of the system, greater than those imposed by the temperature variation of light output of the crystals, as well as on the stability of the APD power supply voltage.

The Hamamatsu S-8664 APDs specified for the crystal readout have a temperature coefficient of gain of $\Delta G/\Delta T$ of 2.5%/°C, while the LYSO light output varies −0.2%/°C. A specification of an APD gain stability of ±0.5% requires knowledge of the temperature to ±0.2°C. which is more stringent than that required by light output variation. The CERN beam test demonstrated that a measurement of the calorimeter temperature to 0.2°C can be easily achieved. Note that this specification is not on the stability of the temperature with time, but rather on the knowledge of the temperature, as long as temporal variations are slow.

The overall mechanical structure of the *BABAR* calorimeter will be retained. The entire calorimeter is surrounded by a double Faraday shield and environmental enclosure composed of two 1mm-thick aluminum walls. The diodes and preamplifiers are thus shielded from external noise, and the slightly hygroscopic CsI(Tl) crystals reside in a dry, temperature controlled nitrogen atmosphere. The preamplifiers (2×50 mW/crystal) and the digitizing electronics ($\sim$3 kW per end-flange) are the primary internal heat sources. The temperature was monitored by 256 thermal sensors distributed throughout the calorimeter. This system maintains the crystal environment at a temperature of 20 ± 0.5°C. Dry nitrogen circulation stabilizes the relative humidity at 1 ± 0.5%.

The gain stability of the APDs, for a gain of $\sim$75, with a reverse bias voltage of $\sim$375 V, requires a voltage stability of better than 1 volt. This requirement can be met by commercially available computer-controlled high voltage supplies, such as those used for the CMS calorimeter.

9.3.4 Mechanical Structure

To reduce cost, the mounting structure of the *BABAR* forward endcap will be reused (Fig. 9.26). The *BABAR* structure was designed to minimize inactive materials, as was done for the barrel, and to provide hermeticity and precision alignment at the barrel/endcap interface. The design is conceptually different from that of the barrel. While the barrel remained unopened for the lifetime of *BABAR*, the endcap had to be designed to be capable of rapid mounting and dismounting while retaining the precision of the mating to the barrel itself. The forward endcap is a conic section, with front and back surfaces tilted at 22.7° to the vertical, matching the drift chamber endplate. The total weight is approximately four tons. It is built in two monolithic D-shaped halves, each containing ten carbon fiber crystal mounting structures, to allow quick dismounting for access to the inner components of the detector; It is supported from and precisely aligned with the calorimeter barrel structure.

9.3.4.1 Crystals

The *BABAR* forward endcap structure contains cells for a total of 900 CsI(Tl) crystals, arranged

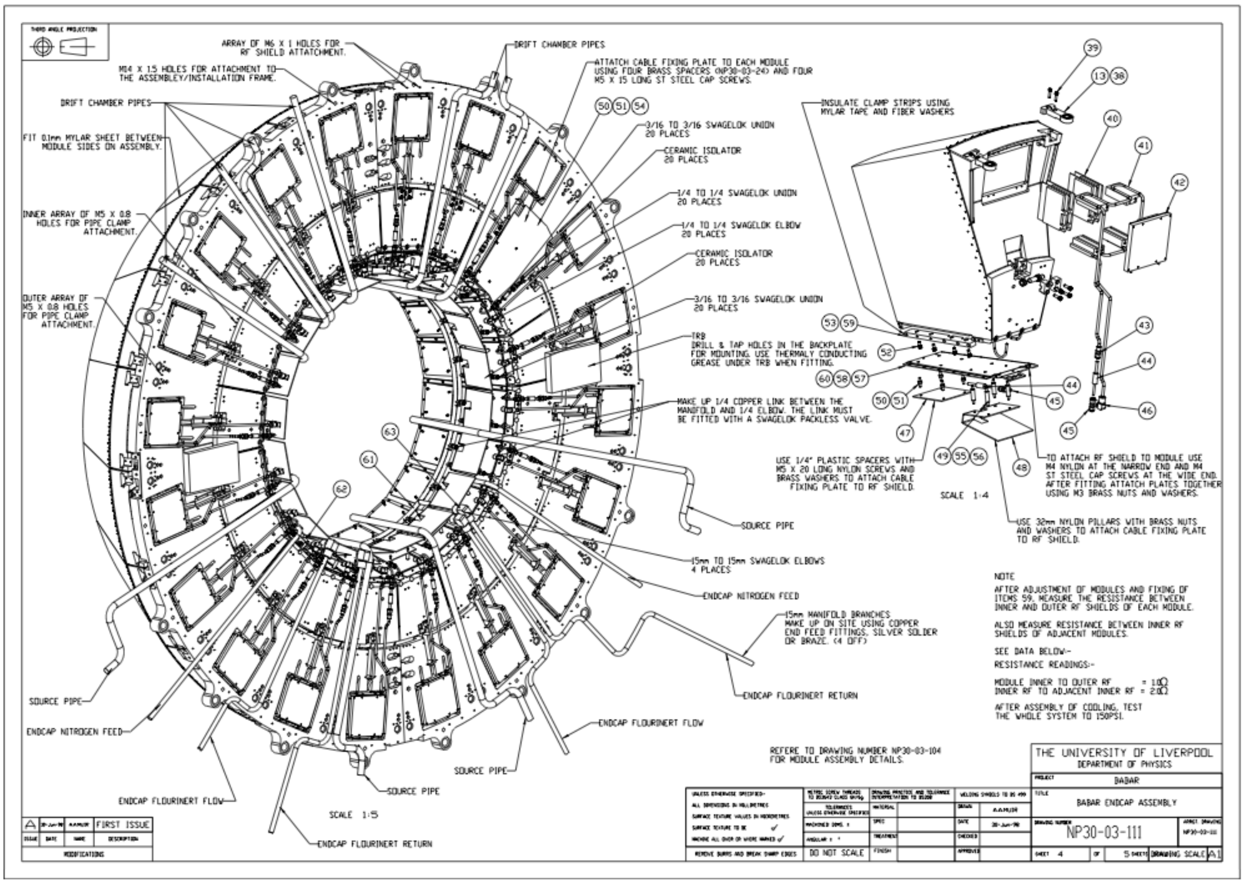

Figure 9.26: Forward assembly drawing

nine distinct radial rings (3×120, 3×100, 3×80), with approximately the same crystal dimensions everywhere; total crystal volume for the 900 compartments is 0.7 m^3. In *BABAR*, the inner ring of 80 cells was used to hold lead shielding.

The outer eight rings hold the CsI(Tl) crystals. CsI(Tl) is a soft material that cannot support substantial loads; for this reason the CFC structure is designed to support the individual crystals without transferring the load to neighboring cells; the CFC wall thickness of 250 μm wall thickness is chosen for adequate strength with minimum radiation length. The design and dimensions of these crystals are described in Fig. 9.27.

The CsI(Tl) crystals, produced with a tolerance on transverse dimensions of $\sim$225 μm, fit loosely into their compartments. Each crystal is read out with 2 large areas photodiodes (Hamamatsu S2744-08) glued onto a 1 mm polystyrene coupling plate, that itself is glued to the rear crystal surface. The crystals (Fig. 9.3) are wrapped with a double layer of Tyvek (150 μm each) to improve the light yield, a layer of aluminum foil for electrical shielding (75 μm) and a layer of mylar (12 μm) for insulation and mechanical protection of the Al foil. A small aluminum box covering the photodiodes at the back of crystals contains the preamplifiers.

In the hybrid scheme, we will populate the inner six rings of the endcap structure with LYSO crystals. As the Molière radius of LYSO is approximately half that of CsI(Tl), the replacement will be four LYSO crystals for each compartment. In this way, the same structure is used, with four LYSO crystals per CFC cell. LYSO is a very mechanically strong crystal; no additional support is required within the com-

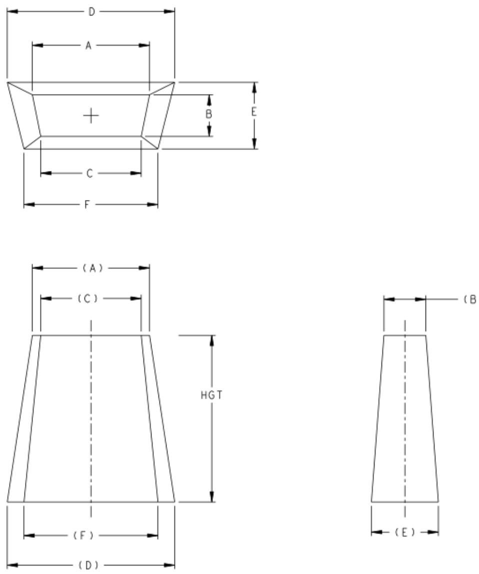

θ Row	Number Needed	Volume (cc)	A (cm)	B (cm)	C (cm)	D (cm)	E (cm)	F (cm)	Height (cm)
1	80	741.0	4.298	4.670	3.944	4.995	5.426	4.583	32.55
2	80	802.4	4.641	4.670	4.289	5.394	5.428	4.985	32.55
3	80	863.6	4.982	4.670	4.632	5.792	5.430	5.386	32.55
4	100	739.6	4.247	4.670	3.970	4.941	5.432	4.618	32.55
5	100	788.3	4.519	4.670	4.244	5.257	5.433	4.937	32.55
6	100	836.9	4.790	4.670	4.517	5.573	5.433	5.256	32.55
7	120	737.7	4.209	4.670	3.984	4.898	5.434	4.636	32.55
8	120	778.4	4.437	4.670	4.214	5.162	5.433	4.903	32.55
9	120	819.1	4.665	4.670	4.445	5.427	5.432	5.171	32.55

Figure 9.27: Geometry of the projective crystals and their dimensions in the forward calorimeter of *BABAR*.

partment. Were further cost savings in the initial implementation to be necessary, additional rings of CsI)Tl) may be retained from the *BABAR* endcap. A future upgrade of the detector could include replacing more rings of CsI(Tl) with LYSO.

9.3.4.2 Modules

The endcap consists of twenty individual modules (Fig. 9.28). The geometry is essentially projective, with the compartments aligned so that the crystal axes point to an axial position 5 cm from the interaction point. In order to preserve optimum light collection and both spatial and energy resolution, similar-sized crystals have been used, arranged in a layout of nine rings of trapezoidal shaped compartments grouped in three super-rings.

As described above, for Super$B$ we populate the six inner rings of the endcap with LYSO, retaining the existing outer three rings of CsI(Tl) (Fig. 9.29).

9.3.4.3 Installation

The installation tools and instruments used at *BABAR* to install the twenty modules and two D structures still exist at SLAC. Detailed procedures for moving and installing the forward calorimeter are derived from *BABAR* are being prepared. Fig. 9.30 shows the existing Installation Bridge, able to move individually each one of the two monolithic endcap halves.

9.3.4.4 Refurbishment of the *BABAR* structure

As with the *BABAR* barrel, the endcap will be disassembled to the module level for transport. The alternative of transporting each half with modules installed carries mechanical risks, but will be investigated further.

For the CsI(Tl) rings that are retained, each crystal diode pair and preamps will be tested and measured for signal strength, before and after shipment; repairs will be made as necessary. The testing in Italy may be done at a remote site at the module level, for both the CsI(Tl) and LYSO crystals. Final assembly of the endcap and installation into the detector will be done at Tor Vergata.

The electronics for the retained Cs(Tl) rings will be refurbished as for the barrel (Sec. 9.2.4. The LYSO readout with APDs requires new electronics (9.3.2).

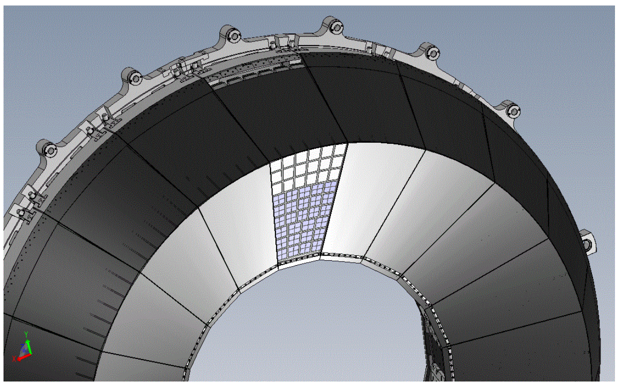

Figure 9.29: Layout of a module in the forward endcap in the hybrid plan.

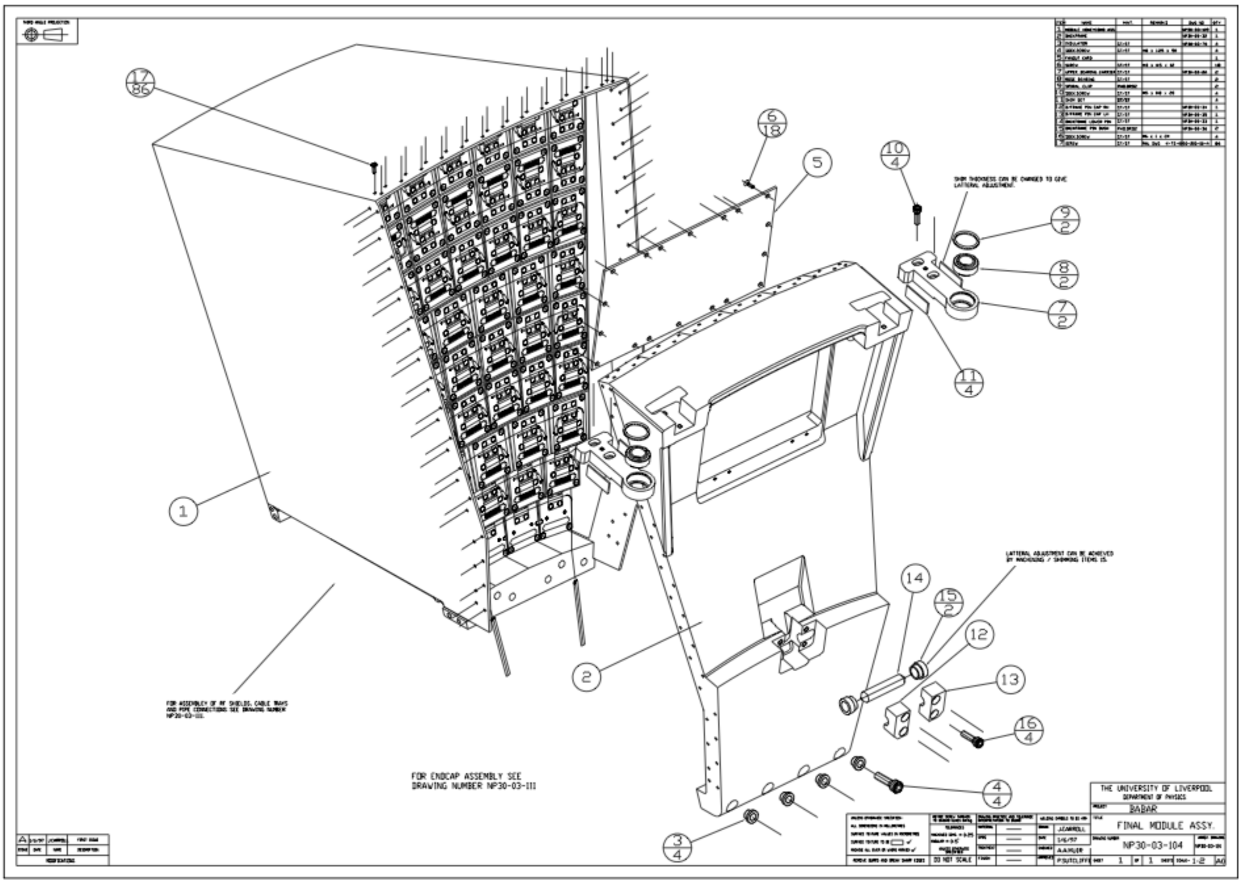

Figure 9.28: Forward module assembly drawing

9.3.4.5 Tests of the Spare FWD modules

In order to study the changes required to accommodate the new LYSO crystals, two spare *BABAR* endcap structural modules have been shipped to Italy. Tests and measurements on them will be necessary to define a procedure for the insertion of the new LYSO crystals, as well as to understand any problems (in mounting the electronics, for example), and to validate the existing technical information, particular regarding the strength of the CFC compartments.

9.3.5 Beam Tests

Two beam tests have been performed with a prototype LYSO matrix, one at CERN in October 2010 and one at the Beam Test Facility (BTF) in Frascati in May 2011.

9.3.5.1 Description of the apparatus

In both cases, the prototype matrix was composed of 25 LYSO crystals of pyramidal shape with dimensions 2.3 cm$\times$2.3 cm$\times$22 cm inserted into a support structure, described in detail in Sec. 9.3.4, that was fabricated at the RIBA company (Faenza, Italy). To improve light output uniformity along the length of each crystal, a 15 mm wide black band was painted at the end of its smallest face. The area of the face not covered by the APD (or PIN) was painted with a reflective white paint. The mounting structure is made of glass fiber, where each cell consists of the wrapping of several layers of pre-impregnated glass fiber epoxy composite, a single inner layer of a reflecting aluminum foil and a composite bottom insert. Electrical connection is made to copper foils 35 μm thick at the

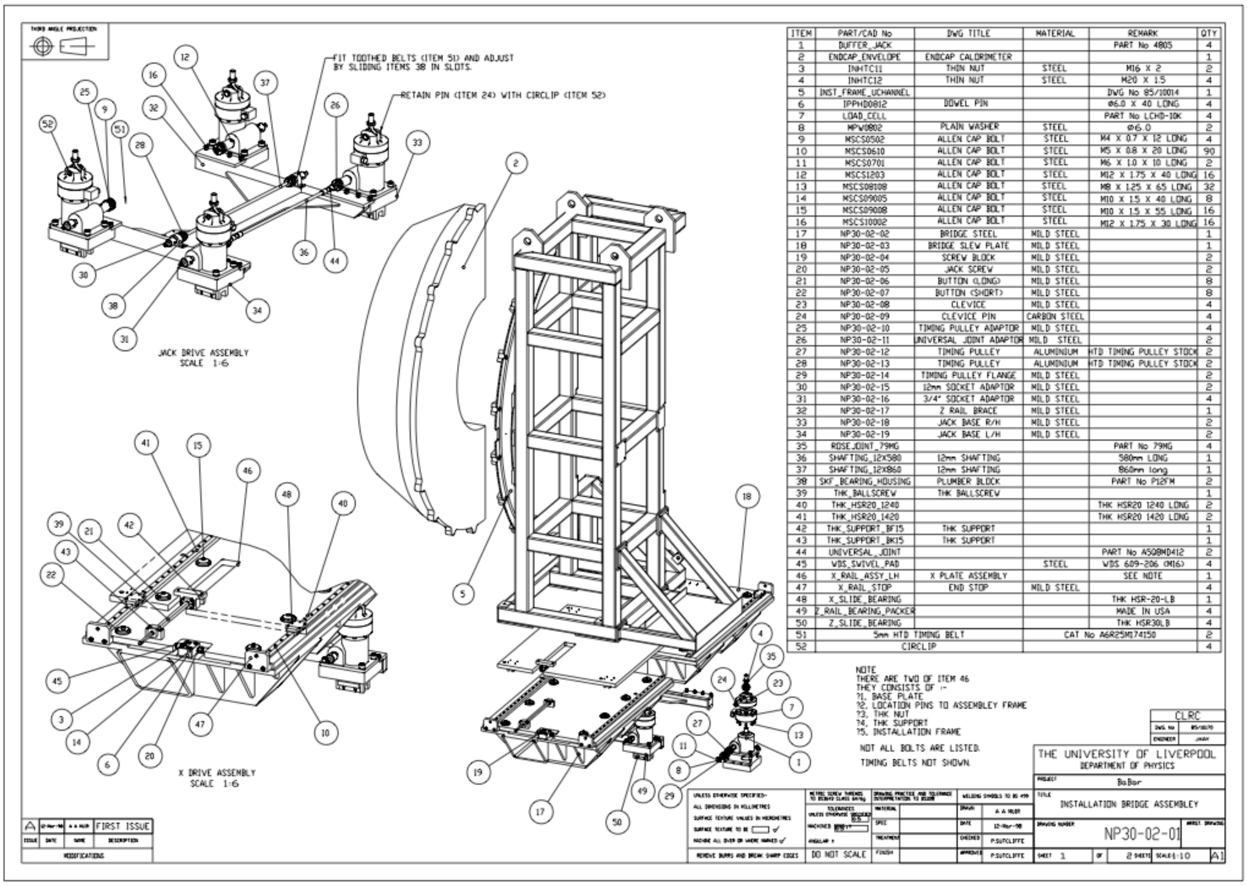

Figure 9.30: The forward endcap installation tooling.

back each compartment. Between one cell and the other there is a nominal thickness of 200 μm, while the external walls are 135 μm thick. Figure 9.31 shows a picture of the test beam structure with one row of crystals inserted.

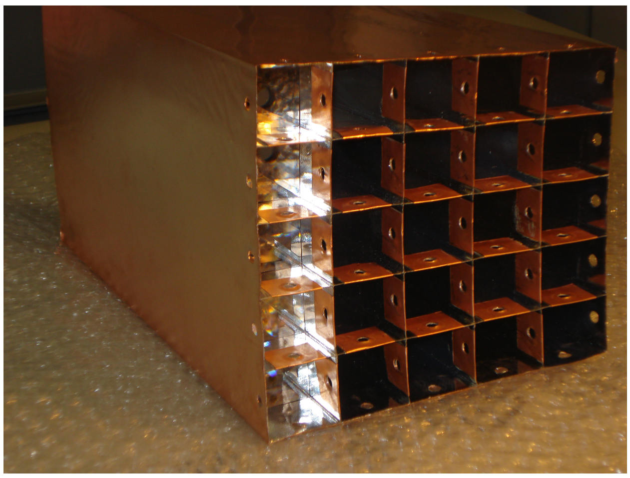

Figure 9.31: The test beam mechanical structure with one row of LYSO crystals installed.

Twenty of the crystals were read out with an Avalanche Photodiode (APD) in both tests; the remaining five were read out with PIN Diodes at CERN and with APDs at the BTF. The readout chain was composed of a front end board (VFE) containing a charge shaper preamplifier (CSP); a shaper range board that further shapes the signal, and then divides the signals according to the energy (Fig. 9.32). Two different ranges are foreseen in the treatment of the signals, for energies lower than 200 MeV and for energies greater than 200 MeV, although in the beam tests the amplification was adjusted to use only a single range. A 12 bit CAEN ADC digitized

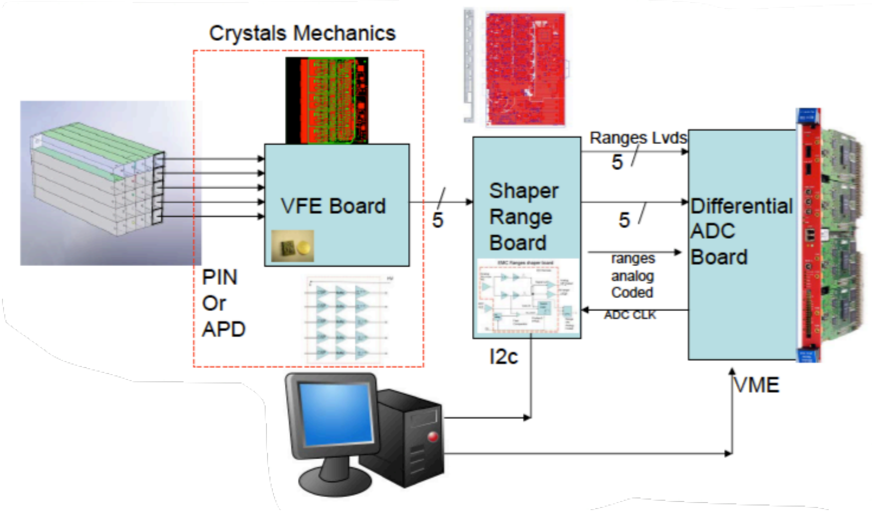

Figure 9.32: Schematic view of the electronics chain for the forward EMC beam tests.

the analog outputs. The APDs were biased at 308 V to avoid saturation effects.

9.3.5.2 Description of the beams

The beam test at CERN took place at the T10 beam line in the East Area. The beam was composed mainly of electrons, muons and pions produced by protons on aluminum and tungsten targets. The composition of the beam is highly dependent on the energy: for electrons it ranges from 60% at 1 GeV to 1% at 6 GeV. The maximum energy reachable at this beam line is 7 GeV with a nominal momentum spread $\Delta p/p \simeq 1\%$. The distance between the end of the beam line and the crystal matrix was about 15 m. The event rate was of the order of 1 Hz. Figure 9.33 shows the experimental setup used at CERN, composed of a Cherenkov detector for electron-pion discrimination, two scintillators (finger counters) $2{\times}2$ cm^2, the box containing the matrix and the VFE boards.

Signals from the two finger counters formed the trigger. The Cherenkov detector information was stored in order to select Minimum Ionizing Particles (MIP) offline, and was also used for calibration and to prescale the triggers.

The Beam Test Facility at the INFN Frascati Laboratory (LNF) is part of the ΦFactory, DaΦne, composed of a linear accelerator

Figure 9.33: Schematic view of the test beam setup used at CERN.

LINAC, a spectrometer, and two circular accelerators of electrons and positrons at 510 MeV. The LINAC that fills the rings also supplies the test beam line at the BTF. The pulsed beam of the LINAC circulates electrons up to 800 MeV at a maximum current of 550 mA/pulse and positrons at a maximum energy of 550 MeV with a current of 100 mA/pulse. The typical pulse duration is 10 ns, with a repetition rate of 50 Hz. A bending magnet selects the electron momentum, and a system of slits controls the particle flux. The beam energy spread is 1% at 500 MeV. The setup of the beam test of the crystal matrix at the BTF is shown in Fig. 9.34.

The setup drawing shows the end of the electron beam line, four planes of silicon strip detector (two measurements in x and two measure-

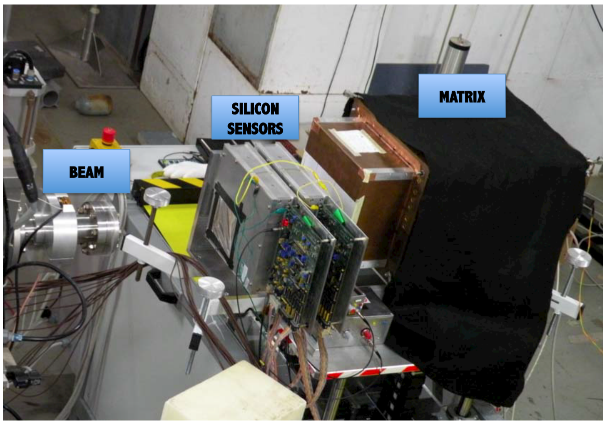

Figure 9.34: Schematic view of the test beam setup used at the BTF LNF.

ments in y) and the box containing the crystal matrix and the VFE boards. As mentioned above, at the BTF all the crystals are equipped with APDs. The gain of the VFE was changed from 0.5 to 1, and an amplification factor was also introduced. To control the position of the beam with respect to the matrix, a detector composed of 16×16 3 mm scintillating fibers was used. The LINAC RF pulse signal (25 Hz) was included in the trigger.

Based on the performance at BTF, we suspect that the beam energy spread at the CERN facility was larger than the specification. Thus, we use the CERN TB data only to study the linearity at high energy; resolution studies are performed exclusively on the BTF data.

9.3.5.3 Description of data and calibration

For each triggered event, the output of the readout is 384 samples of the waveforms of the 25 channels. The signal amplitude in each channel was defined as the maximum of the waveform, extracted from a Gaussian fit to the sampling distribution, with pedestal subtracted. The pedestal is calculated for each crystal by averaging the first 60 samples on a reference run. The pedestal-subtracted amplitude is taken as the measurement of the energy deposit, provided it is above a threshold, chosen to be three times the *rms* noise, whose value is determined from a run taken with random triggers where no signal is present. After calibration, the energy of the electron that initiated the shower was determined by summing all the energy deposits in all crystals ("cluster energy").

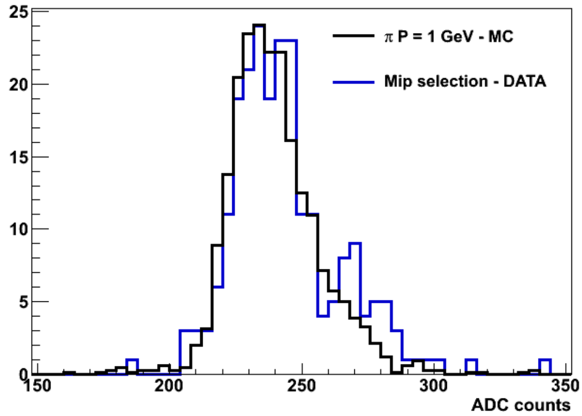

Figure 9.35: Comparison between data and MC of the energy deposited in the MIPs sample. The hypothesis that after the selection, the beam is dominated by pions is made.

At the CERN test beam hadrons traversing the crystals horizontally were selected as Minimum Ionizing Particles (MIPs) by requiring no significant signal in the other crystals and a signal consistent with a hadron in the Cherenkov detector. Profiting from the fact that MIPs deposit a constant energy in the crystal regardless of their energy, the amplitude spectra of each crystal was fitted to extract the most likely value. We determined by GEANT4 simulation the expected energy deposit in each crystal (Fig 9.35); the corresponding calibration constants could then be extracted.

At the BTF test beam, where no hadrons were available, the relative intercalibration constants were obtained from the electron sample itself. The relative cluster energy resolution was minimized by floating a constant for each crystal except the central one. The overall energy scale was then determined from the knowledge of the beam energy. This procedure was applied on a small fraction of the runs where the electrons were approximately 500 MeV (the highest energy reached in the tests) and the corresponding constants used in all other runs. This intercalibration was also cross-checked using cosmic-ray data obtained with an *ad hoc* trigger derived from two plastic scintillator pads positioned above and below the crystal matrix. The channels where there is a significant difference are those where the electron data shows very little energy, because they are far from the center of the matrix. In such cases, which have little impact on the resolution studies since they contribute little to the total energy measurement, the calibration constants estimated from the MIPs are used.

9.3.5.4 Electronics noise measurements

The first information we could extract from the data are the characteristics of the electronic noise. From the signal distribution in a random trigger run at the BTF we estimated (Fig. 9.36) that apart from two channels, the noise is on average 2 ADC counts. After applying the calibration, this noise corresponds to approximately 0.4 MeV. To understand if there were resonant components, we analyzed the power spectrum (PS) of the noise of each crystal i using waveforms acquired with a random trigger:

$$\mathrm{PS}_i(\omega_k) = \langle n_i(\omega_k) n_i^*(\omega_k) \rangle, \qquad (9.7)$$

where $n(\omega_k)$ is the k-th component of the discrete Fourier transform (DFT) of a noise waveform, and <> denotes the average taken over a large number of waveforms.

The estimated power spectrum of a representative channel is shown in Fig. 9.36, where it can be seen that the dominant source of noise is in the range 0–8 MHz, which corresponds to the bandwidth of the shaper. Sources of noise occurring after the shaper give a negligible contribution; the dominant contributions occur before the shaper transfer function filter. Correlations among the noise in the crystals was also estimated and found to be negligible.

9.3.5.5 Temperature corrections

A temperature dependence of several percent per degree is expected in the light yield of the LYSO crystals and in the gain of the APDs. At the CERN test beam the position of the MIP peak as a function of the temperature measured by sensors placed on the rear of the crystals has

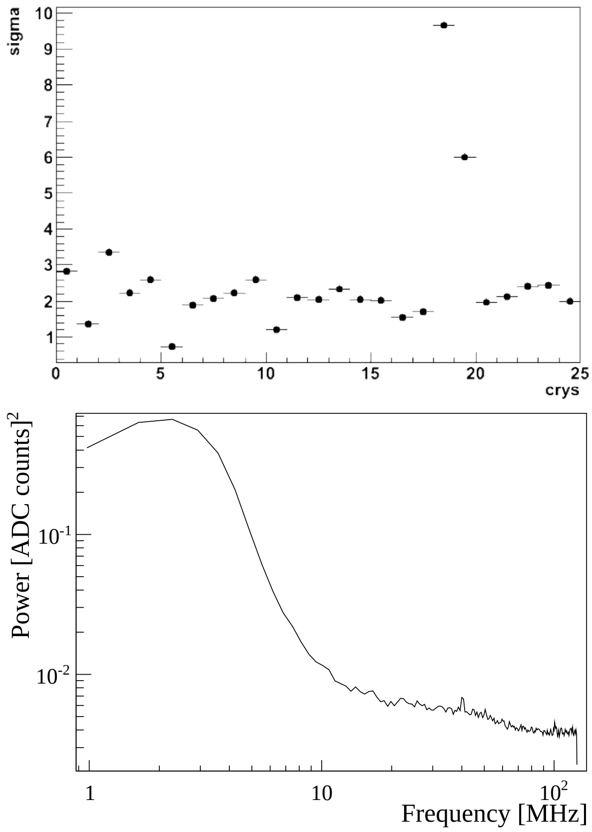

Figure 9.36: Top: Noise (*rms*) for each channel of the BTF test beam calorimeter. Bottom: power spectrum of a representative channel.

been used to extract the temperature correction: $E_{\mathrm{corr}} = E_{\mathrm{raw}}/(1 - p_0(T - T_0))$ where E_{corr} and E_{raw} are the corrected and uncorrected energies, $p_0 = (2.8 \pm 0.2) \times 10^{-3}$, and $T_0 = 34$ K.

This correction proved irrelevant at the BTF test beam where the room was climate-controlled and the temperature variation was negligible.

9.3.5.6 Results

In order to determine the linearity of the crystal matrix response and the energy resolution, the distribution of the cluster energy was fitted for each beam configuration with a Crystal Ball function. The mean value of the Gaussian component is taken as the estimate of the energy, while the resolution is evaluated from the FWHM of the entire distribution.

Figure 9.37 shows the mean value as a function of the energy for the data collected during the CERN beam test. The linearity of the response is thus clear.

At the BTF, the beam was configured to allow as many as three simultaneous electrons impacting the crystal matrix within the DAQ dynamic range. This allowed us to have more than one resolution measurement for each beam energy configuration (Fig. 9.37). This in turn allowed us to estimate the dependence of the beam spread on the energy by comparing measurements of the same amount of deposited energy, but obtained with different beam energies. The intrinsic resolution obtained by subtracting the measured beam spreads in quadrature from the average resolutions is also shown in Fig. 9.37.

These intrinsic resolutions were then compared with the results of a full simulation of the experimental setup (Sec. 9.1.2). There is good agreement, with a resolution smaller than 2% at 1 GeV.

9.3.6 Alternatives

We have described above the baseline design adopted for the Forward EMC: a hybrid design that retains the existing *BABAR* mounting structure and the outer three rings of CsI(Tl) crystals, and populates the six inner rings of the structure with LYSO crystals.

The best technical choice for the forward calorimeter would have been to construct a totally new device using LYSO crystals throughout, with a new thinner mechanical support structure to reduce non-sensitive material. We have pursued extensive R&D on this option. Cost considerations do not, however, permit us to choose this device as the baseline; it remains an alternative should adequate funding materialize. This section describes the original full LYSO design as well as other alternatives that have been considered.

9.3.6.1 Full LYSO calorimeter

The driving design principles are the same as were used for the *BABAR* Electromagnetic Calorimeter (see Sec. 9.3.4), the biggest changes resulting from the use of higher density LYSO crystals that have a Molière radius (2.07 cm) nearly a factor two smaller than that of CsI (Tl) (3.57 cm). The radiation length is also significantly smaller (1.14 cm vs 1.86 cm). This changes both the optimal transverse dimensions of the cells and the position of the center of gravity of the modules, thus significantly altering the original *BABAR* design. A detailed report of the studies that have been carried out can be found in Ref. [30]. We stress herein only the relevant points.

The new support structure would be subdivided into four rings in theta (Fig. 9.38) each composed of 36, 42, 48, and 54 modules respectively. The cells are designed in order to keep the dimensions of the front of each crystal as close to identical as possible.

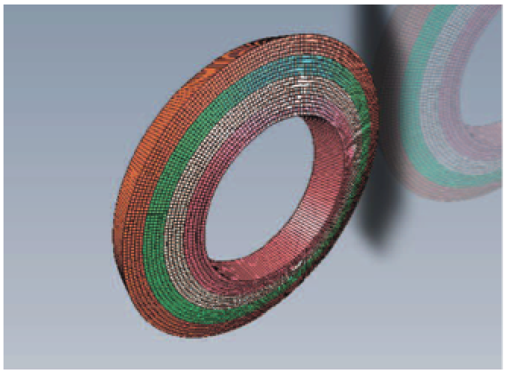

Figure 9.38: Overview of the structure of the FWD EMC.

The detailed placement of electrical, calibration and cooling services was not studied in detail, but the *BABAR* solutions would be well-suited to the new geometry; the reduced crystal lengths leaves further room for them.

The basic modular unit is a 5×5 alveolar matrix (*i.e.*, a sort of egg-crate structure, with a cell for each crystal) of crystals with dimensions of approximately $110 \times 110 \times 230$ mm^3. The total weight of the crystals is about 25 kg. The requirements on the thickness and the material of the walls constrain the module to be held in a very light container of 220 g, thus making the mechanical requirements challenging.

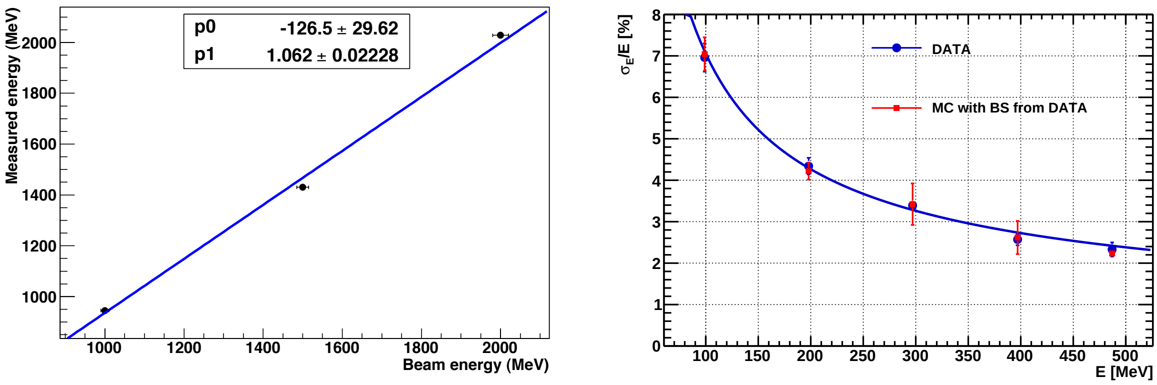

Figure 9.37: Left: Measured mean value of the energy as a function of the beam energy at the CERN test beam. Right: relative resolution as a function of the deposited energy on data and MC simulation. Error bars in MC contains the contribution of the beam energy spread evaluated from data.

The ϕ and θ symmetries of the design require only twenty distinct types of crystals. To achieve the required energy resolution, crystal-to-crystal separation must be less than or equal to 500 microns. The design guarantees a maximum distance between crystal faces of 400 microns within a module and of 600 microns across two modules,in both the ϕ and θ directions. The tolerance on the transverse dimensions of the crystals is specified as $^{+0}_{-100}$ microns.

Alveolar modules are assembled into a shell support structure, with the front face positioned by 5 tubular carbon-fiber reinforced plastic (CFRP) setpins and then glued to the structures front plate (Fig. 9.39).

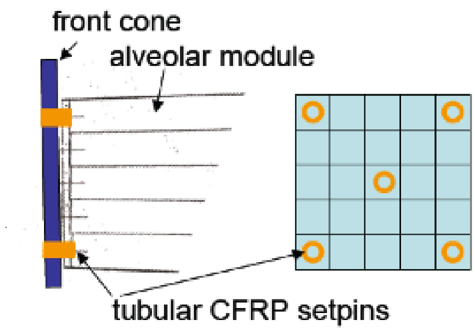

Figure 9.39: Alveolar supports.

To validate the submodule design, two prototypes of the alveolar module were constructed (see a photo in Fig. 9.31). The first prototype (Proto1) was produced to validate the cell structure concept and understand possible economies in the construction. It was then used to hold the 25 LYSO crystals in the beam tests for physics validation. Proto1 provided validation of the whole production process. A 3D dimensional inspection performed showed that dimensional tolerances could be met. Wall thickness measurements at the cell open edge produced the following values. For internal walls: nominal 200 microns, actual 150–220 microns; for external walls: nominal 135 microns, actual 130–170 microns.

A second prototype, Proto2, identical to Proto 1, was produced in September 2011 to confirm the process repeatability and to evaluate the global mechanical properties of the structure. Global deformations of the alveolar array are significant, and a load test is essential to check for lack of interference between modules and the absence of stress on the crystals. As shown in Fig. 9.40, the cells were loaded with dummy crystals to simulate the mass, and different gravity vectors were investigated. The mechanical tests performed on the modular structure provided basic input data to a finite element analysis of the complete support structure.

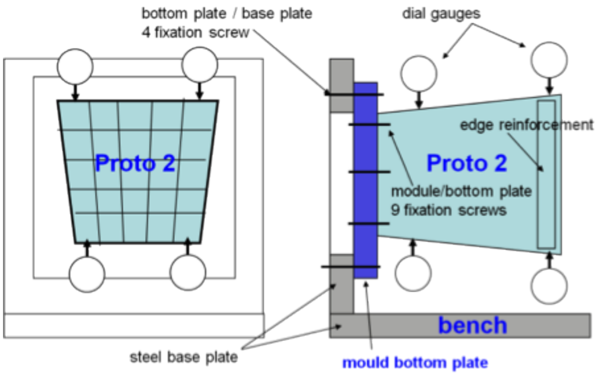

Figure 9.40: Alveolar module test setup

A detailed finite element analysis was performed on the alveolar structure. An approximate module based on surfaces was used as a reference to validate the Global Finite element model of the whole EMC (Fig. 9.41). On the external wall two laminates of total thickness 200 microns were used, together with four internal walls laminates at 0°, 90°, 0°, and 90°. The base was composed of 600 microns aluminium, equivalent to the CFRP. Five constraint points simulated the setpin constraints that connect the module to the mechanical structure.

The load is the 1 kg weight of each crystal, simulated by a "rigid bar" with five nodes along the center alveolar cell, and a "lumped mass" having 1/5 of the crystal weight at each of the nodes. These nodes are then rigidly connected with certain others near the alveolar walls, and from there to the alveolar wall nodes with "gap and spring" elements.

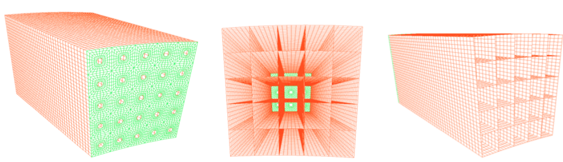

Figure 9.41: Alveolar module finite element model

The resulting stresses predicted on the structures are depicted for the 0° case in Fig. 9.42. The corresponding values for the ply stresses and for the index failure (*i.e.*, the ratio between the predicted stress and the breakdown) are summarized in Table 9.5.

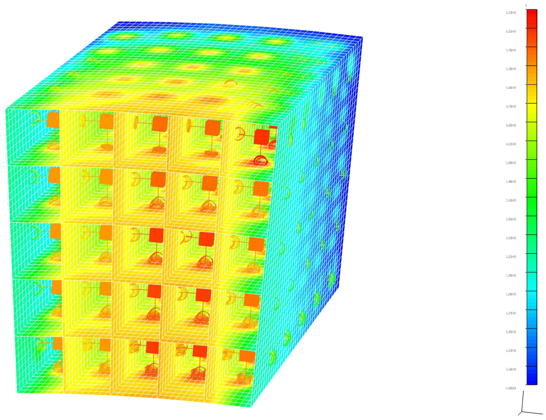

Figure 9.42: Results of the module finite element model at 0°. Scale ranges from 0 (dark blue) to 6.3×10^{-5} (Red).

The shell, shown in Fig. 9.43, consists of the outer cone and front cone as a single unit of CFRP. The inner cone is a 20 mm section of 7075 Al. The back plate is retained from *BABAR*. The volume is defined by the lines AB, AD, and CD.

The outer cone is composed of 6 to 10 mm of CFRP, while the front cone is either CFRP or a sandwich plate 20 mm thick. The back plate provides the EMC interface with the bearing points for position reference and transmis-

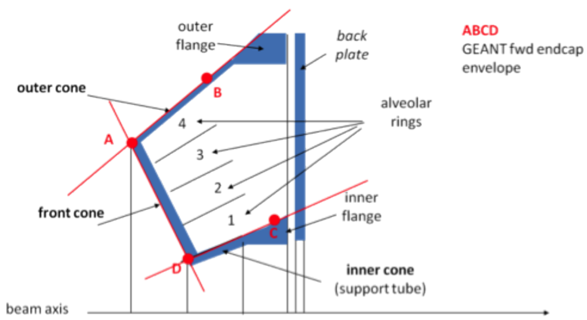

Figure 9.43: Support shell structure

Table 9.5: Expected ply stresses and index failures.

case (°)/ coordinate	Ply Stress(MPa)	index failure
0/x	35	1/48
0/y	2.6	1/10
0/z	1.4	1/16
90/x	5	1/342
90/y	10	1/2.6
90/z	1.7	1/13
180/x	30	1/57
180/y	7	1/4
180/z	1.5	1/15

sion of loads. The alveolar array is cantilevered from the shell front cone as detailed in Fig. 9.44.

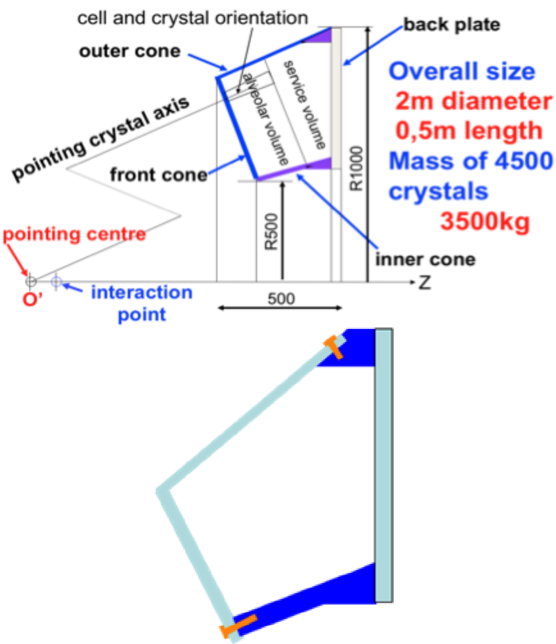

Figure 9.44: Support shell assembly

9.3.6.2 Pure CsI

Crystals of pure CsI have been used as fast scintillators in electromagnetic calorimeters at high counting rates. The scintillation spectrum has two components: the fast component, at 310 nm has a decay time of 6 ns, with a light output 1.1% that of NaI(Tl), while the slow component at 420 nm has a decay time of 30 ns and a 3.6% relative light output. The temperature dependence of the CsI light yield is $-1.4\%/°C$. CsI has a relatively high resistance to radiation damage. Table 9.3 [10] compares the main properties of pure CsI with other scintillators. The scintillation spectrum matches the sensitivity of typical PMTs better than it matches solid state readout devices.

Tests of pure full size ($5 \times 5 \times 30$ cm^3) CsI crystals have been carried out to measure the light yield and signal-to-noise ratio. Due to the low light yield of pure CsI crystals, it is important to achieve the best possible electronic noise performance. The crystals were read out with a PMT on one end and one or two APDs on the other, using the electronics developed for the LYSO readout. The measurement of the light output has been done with a Photonis XP2266b PMT, integrating the signal in a 500 ns window, with the crystal wrapped with Tyvek. A ^{137}Cs source (0.667 MeV photons) was used. A light output of 21 photoelectrons/MeV has been measured, in agreement with the PDG-quoted value. Figure 9.45 shows the distribution of the measured charge.

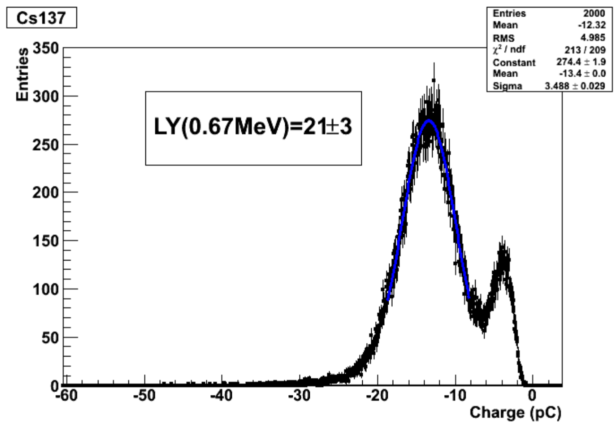

Figure 9.45: Distribution of the measured charge.

The noise was measured using either one or two Large Area APDs (LAAPD) (10mm × 10 mm) to read the crystal. The signal was sent to a charge shaper preamplifier and a shaper. A PMT on the opposite side of the crystal provided the trigger. A calibration of the system has been performed using cosmics collected with a PMT, selecting events which passed completely through the crystal. Three measurements were made with APD voltages at 365, 380, and 390 V; the noise was measured to be 11, 12 and 13 MeV, respectively. In the same configuration, but with two LAAPD's, a noise of about 6 MeV has been measured. A second setup used the front end developed for the LYSO measurement and beam test. In this configuration, the trigger was provided by the coincidence of two scintillator bars. In this case the best signal-to-noise ratio of 8.2 was obtained at 390 V (Fig. 9.46).

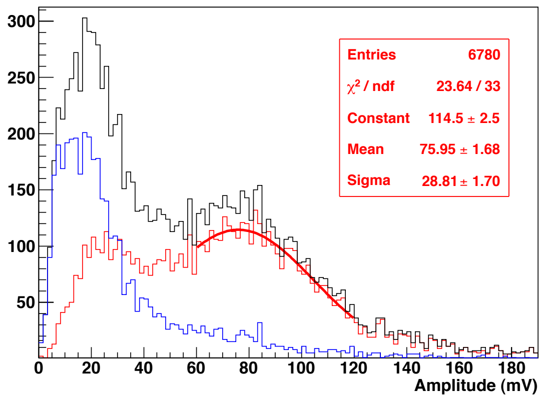

Figure 9.46: Distribution of the cosmic ray signal measured with two LAAPDs (red curve). The blue curve is the measured noise and the black is the total signal.

The energy deposited by 1 GeV muons through the 5 cm thickness of pure CsI has been calculated with simulations and is ∼30 MeV, leading to a total measured noise of 3.7 MeV. This is a substantial improvement with respect to the previous setup. It has, however, been shown with simulations, that the performance of the calorimeter would be adversely affected if the noise is higher than 1 MeV. To reach this level of noise, further improvements in the electronics are being developed, as well as a better selection of the events. A new front end will also be developed to try a readout with a phototopentode instead of the LAAPD. In this case the gain of the photodetector would be higher (120 to be compared with 50 for the LAAPD), but the noise level has to be controlled a dedicated readout electronics. R&D is continuing. Radiation hardness measurements are foreseen before the end of the year and a beam test with a pure CsI matrix of 25 crystals is in preparation for 2013.

The option of the forward calorimeter using pure CsI crystals does not require any particular change in the mechanical structure supporting the detector. Due to the fact that the material is the same except for the doping, pure CsI crystals will be of the same dimensions and of the same shape of the original forward *BABAR* CsI(Tl) calorimeter.

9.3.6.3 BGO

Prior experience with calorimeters made of BGO crystals in high energy physics come from L3 [31] and Belle [32]. In the first case BGO was used for both barrel and endcaps, while Belle used BGO to build the Extreme Forward Calorimeter for the purpose of improving hermeticity close to the beam line and to monitor beam background. The information gained will be summarized here, supplemented by tests performed to account for the particular operating conditions expected at Super$B$: short integration time, needed to reduce pile-up, and large radiation doses.

The properties of the BGO crystals are summarized in Tab. 9.3: the mechanical properties are similar to LYSO, but with a light yield four times smaller. The scintillation decay time is intermediate between that of LYSO and CsI(Tl); acceptable performance in a high rate environment is therefore possible.

The performance of the L3 calorimeter, read by PIN diodes, was $\sigma_E/E = (1.6/\sqrt{(E)} \oplus 0.35)\%$ and $\sigma_\theta = ((6/\sqrt{(E)} \oplus 0.3)$ mrad), i.e., the statistical term of the resolution at 100 MeV was 4%. Later studies with APDs [33] show that the system produces $\sim$ 420 p.e./ MeV, i.e., the statistical term at 100 MeV would be 0.5%, well within the requirements.

Nonetheless, due to the requirements dictated by machine background (Sec. 9.1.1) we would not be able to operate the detector with an integrate that captures the entire light output of the crystal. The degradation in resolution caused by the shorter integration time was tested specifically for this application in the INFN-Roma1 electronics laboratory with a single $2 \times 2 \times 18$ cm^3 crystal. 0.667 MeV photons from a ^{137}Cs radioactive source were detected with a crystal read at both ends by two EMI-9814B PMTs. The waveforms of the signals provided by the PMTs were acquired by a LeCroy digital oscilloscope having a bandwidth of 300 MHz and used with a sampling rate of 250 Ms/s. One of the two signals was used to trigger the oscilloscope. The other signal was processed with an Ortec-474 and acquired by the scope. The Ortec-474 module has an integration time (RC) that can be chosen between 20, 50, 100, 200, and 500 ns.

For each value of RC and for each pulse shape both the total charge, independent of the total time, and the maximum amplitude, the quantity that will eventually be used in the experiment, were recorded. The resolution on the charge was found to be 9.5%, consistent with 130 p.e./ MeV after detection and independent of the integration time of the ORTEC shaper. The resolution on the amplitude depends instead on the latter, as shown in Fig. 9.47 and compared with the expectations from a simple Monte Carlo simulation in which only the effect of the photo-electron statistics is included [34]. The results show that shortening the integration time worsens the resolution, but only moderately. For instance, even integrating only for 20 ns, compared with the 300 ns scintillation time of the crystal, the contribution to resolution due to the photo-statistics worsens only by 60%.

A test to measure the electronic noise of the read out for BGO crystals has been performed with the same experimental setup described in Sec. 9.2.4: a $2 \times 2 \times 18$ cm^3 BGO crystal read out with an 0.5×0.5 cm^2 APD followed by a CSP and a Gaussian shaper. The test procedure is slightly different from the one previously described: instead of using a ^{60}Co source to excite the crystal scintillation, the intrinsic background of the BGO, due to the presence in the crystal of ^{207}Bi, which decays into ^{207}Pb with the emission photons of different energies [35] has been exploited. Since the PMT resolution is much better than the APD, the PMT signal, after the calibration of the energy scale, is used as the "true" energy to calibrate the APD response. The scatter plot of the distribution of the APD amplitude as a function of the PMT charge has been divided into slices and for each slice the peak of the distribution is obtained. These peaks show a linear behavior with energy that has been fitted to obtain the calibration of the APD response. An estimate of the equivalent noise has been obtained from the widths of the distributions of the difference of the APD and PMT signals both measured in MeV. In the case of the Hamamatsu H4083 CSP with 100 ns integration time, with a shaping time of 500 ns, the equivalent noise is measured to be about 2.2 MeV. To compare this result with a CSP with a longer integration time, a measurement with a Cremat CSP with 140 μs integration time

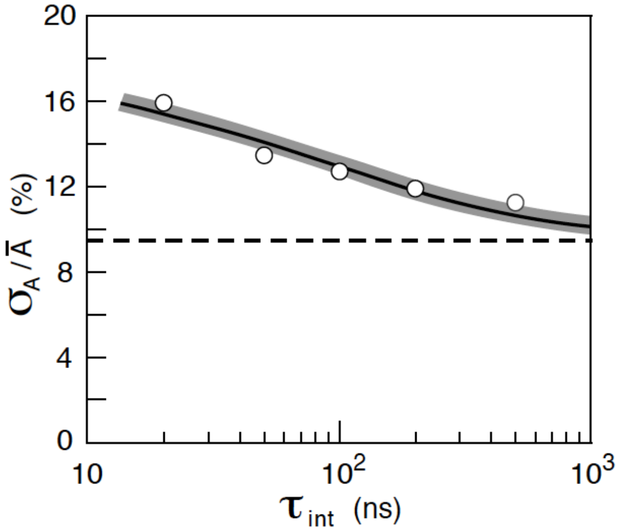

Figure 9.47: Resolution on the measurement of the total charge (dashed line) and the amplitude of the pulse shapes (dots)as a function of the integration time. The results of a Monte Carlo simulation are superimposed (shaded line).

was also performed and the equivalent noise in this case was about 1.7 MeV.

The BGO radiation hardness was tested up to 90Mrad [32]. After a drop of about 30% in the first 20 Mrad of integrated dose the crystal light yield plateaus. It will nonetheless recover up to 90% of the original light yield in approximately 10 hours; it is not documented what will happen if after this pre-irradiation the crystal receives a small additional dose. For non irradiated crystals, a dose of 115 krad implies a light yield loss of 30% that fully recovers with a lifetime of ∼1 hour. These results refer to undoped, recently produced crystals; they also depend strongly on the level of doping and on the manufacturer.

To customize the radiation hardness study to our case, we exposed four samples of BGO crystals to γ-rays from a high-activity ^{60}Co radioactive source. Two crystals of $2.2 \times 2.2 \times 18$ cm^3 have been previously used in the L3 experiment at CERN, other two crystals of $2.5\times2.5\times20$ cm^3 were recently supplied by the Shanghai Institute of Ceramics (SIC).

Irradiations and measurements took place at the Calliope Gamma Irradiation Facility at ENEA-Casaccia center (Rome) (Fig. 9.48). The irradiation source is a cylindrical array of ^{60}Co source rods emitting γ-rays of 1.17 and 1.33 MeV, in an irradiation cell of $6\times7\times3.9$ m^3 plus an attached gangway. Depending on the placement of the samples, dose rates from few rad/h up to 230 krad/h are available. The source can be moved outside or inside its shielding pool in less than two minutes.

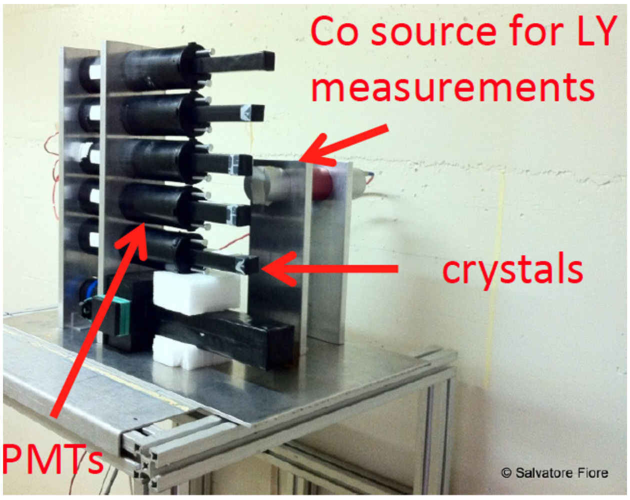

Figure 9.48: Experimental set-up for light yield measurements. Crystal samples are shown while mounted on the PMTs. Crystals were coupled to the PMTs during low-dose irradiation, and data were acquired by shutting down the source for few minutes.

Plastic mechanical supports for the crystals, not shielding them from the radiation, allowed us to expose the samples to different dose rates, and to couple them to EMI 9814B Photomultiplier Tubes (PMT) to perform the light yield (LY) measurements using a low-activity ^{60}Co calibration source. PMTs were read out by a CAEN VME ADC.

We started our irradiation campaign by exposing the crystals to 5–10 rad/h dose rate for a few hours. We were able to measure the LY once every 20 minutes of irradiation, with only two minutes delay after the source was shut down. Using this approach we measured the progressive LY reduction at different dose rates. We measured the LY recovery after 15–30 rad and 170 rad doses, and evaluated the recovery time constant for the different samples by fitting the time evolution of the LY after irradiation with the sum of two exponential functions. The results summarized in Tab. 9.6 show that the LY loss are important, and that there are several components in the recovery time. The most relevant one, due to 5–10 rad/h dose rate is about four hours.

Table 9.6: Effect of irradiation on a BGO crystal: relative LY loss after irradiation and recovery times as measured with a fit to the time evolution with two exponential components.

dose (rad)	rate (rad/h)	LY *drop*	τ_1 hr	τ_2 hr
15	5	25%	2.7 ± 0.4	–
170	10	67%	4.7 ± 0.2	380 (fixed)
12×10^6	23×10^4	90%	5.0 ± 2.4	381.9 ± 3.5

We then exposed some crystals to a massive dose rate of 230 krad/h for a total dose of 12 Mrad, and then to small doses with 1.5 rad/h rate, to measure the sensitivity to small dose rates after strong delivered doses. We measured LY reductions up to 1/10 of the pre-irradiation LY value. A long-term recovery was then analyzed and exploited to measure the recovery time constant. We fit the LY recovery data with a double-exponential function, yielding a short time constant of (5.0±2.4) h and a long time constant of (381.9±3.5) h. BGO crystals from L3 experiment showed a larger damage after each irradiation, but also a faster recovery capability, while crystals from SIC hardly recovered from radiation damage.

Light transmission spectra have been acquired before and after irradiation, in order to identify the nature of the LY reduction. As previously stated, the radiation-induced LY reduction could be due either to a decrease of the light transmittance, or to a damage of the scintillation mechanism itself. By comparing the LY and transmittance measurements, we observed that the main effect of the radiation damage was a reduction of the light transmission due to color center formation.

9.3.6.4 Comparison among options

The decision on the technology to be used for the forward calorimeter must weigh physics performance, technical feasibility and cost. On this basis the baseline was chosen to be a hybrid design, with three rings of CsI(Tl) and six rings of LYSO hybrid. Other options considered were the use of a full LYSO design, retaining the existing structure or constructing an improved one, pure CsI, or BGO crystals, as described above, and the use of lead tungstate ($PbWO_4$) crystals, for which the study was based on the existing literature.

In order to compare the physics performance of the various options, we set up a full GEANT4 simulation that included the correct detector geometry, the electronic noise obtained from beam or lab tests, when available, and extrapolations from them when needed. The signal shape was obtained from detailed simulation of the expected electronic chain, using signal extraction algorithms that reproduced the actual electronics and a clustering algorithm based on the one used by *BABAR*.

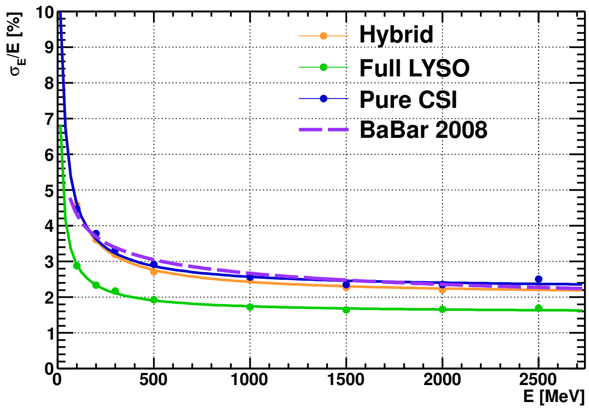

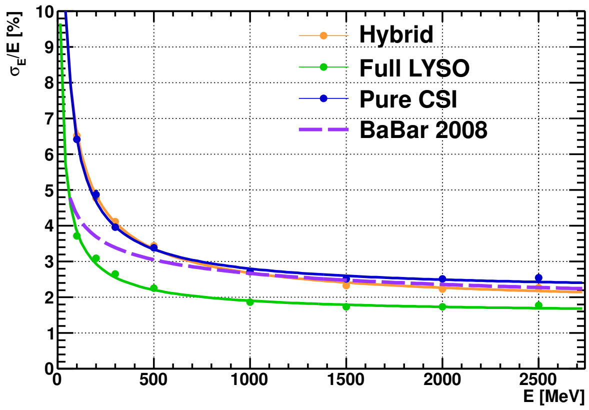

Figure 9.49: Comparison of the relative energy resolution between several options of the forward EMC. Top: nominal machine background. Bottom: machine background increased by a safety factor of five.

For each option, and for several energies, the response of the detector to monochromatic photons was fitted with a Gaussian with exponential tails. The relative energy resolution was computed as the FWHM of the fitted shape for several values of photon energy. The results for different options are compared in Fig. 9.49 for the current estimate of the machine background and for a scenario in which the background is increased by a safety factor of five (5× background).

The best forward endcap option is clearly to use LYSO crystals everywhere; the option suf-

Table 9.7: Comparison of crystal volume and calorimeter structural and calibration costs for the baseline forward endcap configuration and several options.

Option	Number of new crystals	New crystal volume (cm^3)	Crystal cost/cm^3 (k€)	Crystal cost (M€)	Photo-detectors (M€)	Calibration system (M€)	Total structure (M€)	Total Cost (M€)
Baseline - Hybrid								
3 CsI(Tl) + 6 LYSO	2160	245	19.23	4.76	0.38	-	0.19	5.33
LYSO new structure	4500	402	19.23	7.72	0.44	-	1.75	9.91
LYSO old structure	3600	402	19.23	7.72	0.44	-	0.19	8.35
Reduced Hybrid								
4 CsI(Tl) + 5 LYSO	1760	198	19.23	3.81	0.31	-	0.19	4.31
5 CsI(Tl) + 4 LYSO	1360	154	19.23	2.93	0.24	-	0.19	3.38
Alternative crystals								
Pure CsI	900	692	3.92	2.71	0.43	-	0.19	3.33
BGO	4500	392	6.92	2.72	0.44	0.92-2.31	1.75	5.82-7.21
$PbWO_4$	4500	306	2.96	1.18	0.44	0.92-2.31	1.75	4.28-5.67

fering for the most problems is BGO. The latter is very sensitive to the 5× background, most likely due to the non-optimal geometry of the simulation, which was done *ad-hoc*. The hybrid solution also suffers from background; the effect is comparable with the expected degradation in resolution of the barrel. All other options have comparable performance, intermediate between the full LYSO and the hybrid options.

To complete the picture, Tab. 9.7 shows a comparison of the volume and total cost of the scintillating crystals, the cost of the photodetectors, the calibration system, and the mounting structure, all of which must be included in evaluating options.

Photo-detectors have roughly similar costs for all options. Some saving can be achieved with the hybrid option by reusing existing readout channels. A more precise (and more expensive) calibration system is needed only for those crystals whose light output degrades under irradiation with a short recovery time, namely BGO and $PbWO_4$. Finally, the carbon fiber mechanical support needs to be redone only for the LYSO, BGO and PWO options; in the other options, the only costs are the shipping and the refurbishment of the present structure.

The table also lists three hybrid options, in which differing numbers of the outer CsI(Tl) rings of the endcap are retained, the inner rings being replaced by LYSO crystals.

The two least expensive options are the CsI(Tl)/LYSO hybrid and the pure CsI solutions. Simulations show that the hybrid option has a somewhat worse resolution. It is, however, technically the best-studied, has a proven readout scheme and is ready for construction. The properties of pure CsI crystals and their readout are still under study, and therefore the conservative TDR baseline choice was the hybrid design. The budget has been based on this option.

9.4 Backward Calorimeter

The backward electromagnetic calorimeter for Super$B$ is a new device designed to improve the hermeticity of the detector at modest cost. Excellent energy resolution is not a requirement, since there is significant material from the drift chamber in front of it. Thus, a high-quality crystal calorimeter is not planned for the backward region. The proposed device is based on a multi-layer lead-scintillator sampling calorimeter with longitudinal segmentation providing capability for π/e and K/π separation at low momenta. The design is derived from the analog hadron calorimeter for the ILC [36].

The active region of the backward calorimeter is located behind the drift chamber starting at $z = -1320$ mm (Figure 3.1) allowing room for the drift chamber front end electronics. The inner radius is 310 mm, the outer radius is $r_0 = 750$ mm and its total thickness is less than 180 mm covering $12X_0$. It is constructed from a sandwich of 2.8 mm Pb plates ($0.5X_0$) alternating with 3 mm plastic scintillator strips (*e.g.*, BC-404 or BC-408). The scintillation light of each strip is collected by a wavelength-shifting fiber (WLS) coupled to a photodetector located at the outer radius. The scintillator strips come in three different geometries, right-handed logarithmic spirals, left-handed logarithmic spirals and radial wedges (Figure 9.50). This pattern alternates eight times. Each layer contains 48 strips producing a total of 1152 readout channels.

The WLS fibers, Y11 fibers from Kuraray, are embedded in grooves milled into the center of the scintillator strips. Each fiber is read out at the outer radius with a $1 \times 1\,\mathrm{mm}^2$ multi-pixel photon counter (SiPM/MPPC) [37]. A mirror is glued to each fiber at the inner radius to maximize light collection. A preamplifier is coupled to the SPM/MPPC, then the signal is transmitted to readout boards mounted in a convenient location. The PID electronics is used, providing 12 bit ADCs and 200 ps TDCs.

9.4.1 Requirements

The main goal of the backward EMC is to increase the calorimeter coverage by recording any charged or neutral particle in the backward region. This information is important in particular for analyses that utilize the recoil method with hadronic and semileptonic tags to select B meson decays with neutrinos in the final state. The backward EMC helps to increase the selection efficiency and to improve background rejection. For this task, excellent energy resolution is not necessary. It is more important to keep the costs moderate. With moderate energy resolution and good angular resolution, it will also be possible to use the backward EMC in π^0 reconstruction. Furthermore, the backward EMC has the capability to measure time-of-flight and the energy loss via ionization of charged particle well. This information is useful for particle identification, in particular π/e and K/π separation at low momenta.

9.4.1.1 Energy and angular resolution

Since the backward EMC prototype is still in the construction phase, we do not yet have results on energy resolution and angular resolution. However, electromagnetic sampling calorimeter prototypes with plastic scintillator strips and tiles have been tested in test beams within the CALICE collaboration [38]. The energy resolution for the stochastic term is $15\%\sqrt{E[\,\mathrm{GeV}]}$ and for the constant term is around 1%. For the CALICE analog hadron calorimeter which has a non-optimized geometry for electromagnetic showers, the stochastic term was measured to be around $20\%/\sqrt{E[\,\mathrm{GeV}]}$. For low photon energies, an additional noise term of $\sim 130\,\mathrm{MeV}/E$ contributes. Thus, the backward endcap EMC is expected to have a similar performance with a stochastic term of $15-20\%/\sqrt{E[\,\mathrm{GeV}]}$.

A left-handed logarithmic spiral is defined by

$$x(t) = re^{b\cdot t}\cos t - r \tag{9.8}$$
$$y(t) = re^{b\cdot t}\sin t, \tag{9.9}$$

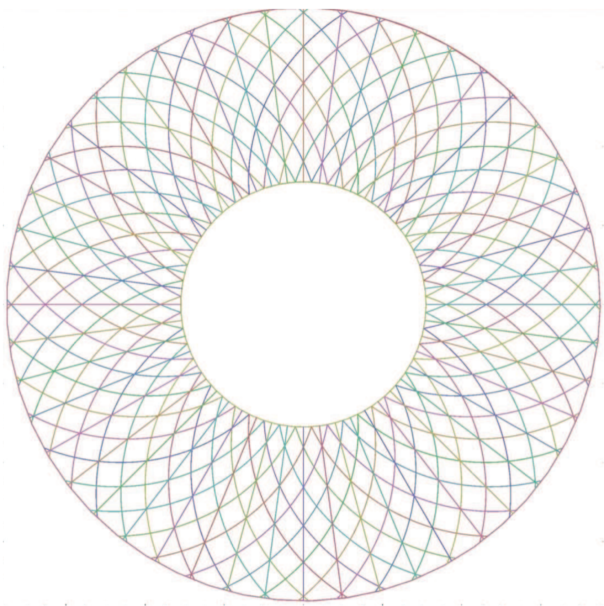

Figure 9.50: The backward EMC, showing the scintillator strip geometry for pattern recognition.

where t is a arbitrary parameter, $r = r_o/2 = 37.5$ cm, and $b = 0.2$. Eight left-handed spiral strips overlap with eight right-handed spiral strips defining a tile-shaped region. The radial strips overlap with five left-handed and right-handed spiral strips. In the worst case, the resolution is estimated to be $\sigma_r = \sigma_\phi \simeq 29\,\mathrm{mm}$ for a single tile in the outer region. This is improved to $\sigma_r = \sigma_\phi \simeq 12\,\mathrm{mm}$ in the inner region. If the shower is distributed over several adjacent tiles, the center-of-gravity method will improve the position resolution significantly.

9.4.1.2 Background rates

Present background simulations indicate that the worst rates for all energies of $3\ \mathrm{kHz/\,cm^{-2}s^{-1}}$ occur in the inner most region. In ten years of running this amounts to $6.1 \times 10^9\ n/\,\mathrm{mm}^2$ in the region near the inner radius. The background rates drop significantly toward the outer radius. At the location of the photodetector, the rate is reduced by more than a factor of 10. Further simulation studies are needed to study the impact on occupancy. To deal with this issue we may either subtract a higher average background energy from each strip or divide the strips into two segments at the cost of doubling the number of photodetectors. The former solution has an effect on the energy resolution since the background energy deposit has a wide distribution. The latter solution is preferable, but is about 75k Euros more expensive.

9.4.1.3 Radiation hardness

Irradiation of Si detectors causes the dark current to increase linearly with flux neutron flux Φ:

$$\Delta I = \alpha \Phi V_{\mathrm{eff}} G, \tag{9.10}$$

where $\alpha = 6 \times 10^{-17}\ \mathrm{A/\,cm}$ $V_{\mathrm{eff}} \sim 0.004\,\mathrm{mm}^3$, Φ is the flux, V_{eff} is the bias voltage and G is the gain. Since the initial resolution of MPPCs/SiPMs of ~ 0.15 photoelectrons (pe) is much better than that of other Si detectors, radiation effects start at lower fluxes. For example, at a flux $\Phi = 10^{10}\ n/\,\mathrm{cm^{-2}s^{-1}}$ the individual single pe signals are smeared out. The MIP peak is still visible at $\Phi \sim 10^{11}\ n/\,\mathrm{cm^{-2}s^{-1}}$. The number of observed hot spots and the noise rate increases after irradiation of $3 \times 10^9\ n/\,\mathrm{cm^{-2}s^{-1}}$. No significant changes are observed on the cross talk probability as well as no significant change on the saturation curves. The main effect is an increase in noise after exposure to high n dose. Hamamatsu has produced new SiPM/MPPCs with $20\,\mu\mathrm{m} \times 20\,\mu\mathrm{m}$ and $15\,\mu\mathrm{m} \times 15\,\mu\mathrm{m}$, which have lower detection efficiency than the $25\,\mu\mathrm{m} \times 25\,\mu\mathrm{m}$ version due to additional boundaries and thus need a higher bias voltage to compensate for losses. Figure 9.51 shows the detection efficiency as a function of bias voltage for $15\,\mu\mathrm{m} \times 15\,\mu\mathrm{m}$ detectors before and after irradiation with $10^{13}\ n/\,\mathrm{cm^{-2}s^{-1}}$. For the new detectors, signal/noise and the equivalent noise charge look fine after irradiation. We expect the backward endcap EMC will record $10^{11}\ n/\,\mathrm{cm^{-2}s^{-1}}$ after 10 years operation. If the $25\,\mu\mathrm{m} \times 25\,\mu\mathrm{m}$ pixel SiPM/MPPC is problematic we may switch to one of the new SiPM/MPPCs with smaller pixel size.

9.4.1.4 Solid angle, transition to barrel

In the laboratory frame, the backward EMC covers a full polar angle region from 231 mrad to 473 mrad. Partial coverage extends the polar angle region from 209 mrad to 517 mrad. In the present design, there is a gap between the backward EMC and the barrel covering the region

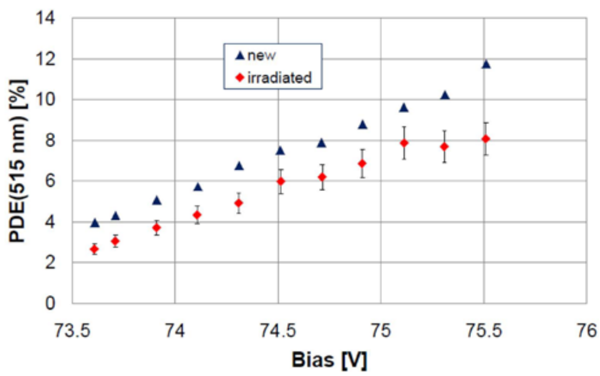

Figure 9.51: The photon detection efficiency (PDE) of $15\,\mu\mathrm{m} \times 15\,\mu\mathrm{m}$ pixel MPPCs as a function of the bias voltage before and after irradiation with $10^{13}\ n/\,\mathrm{cm^{-2}s^{-1}}$.

517 mrad to 694 mrad in the laboratory frame. In the center-of mass frame, full coverage of the backward EMC is in the region 215 mrad to 442 mrad, while partial coverage exists in the region from 194 mrad to 482 mrad. If the backward EMC could move closer to the IR, the gap to the barrel calorimeter would be reduced.

9.4.2 Mechanical design

The 3 mm thick scintillator strips are cut individually from a scintillator plate. Thus, the plate size and the cutting procedure need to be carefully thought through to minimize the amount of waste. For the spiral strips the least waste and fastest production is obtained by fabricating a mould. However, this approach may be too expensive, since the total number of spiral strips is rather small. The preferred scintillator material is BC-404 from St. Gobain, since it has the smallest decay time for TOF capability and its emission spectrum is reasonably matched to the Y11 absorption spectrum. The strip width is 38 mm at the inner edge increasing to 98 mm at the outer edge. The strip sides are painted with a white diffuse reflector. Front and back faces are covered with reflectors sheets (3M, Tyvek). Test bench measurements have shown that the yield along the strips varies by more than a factor of two. To restore uniformity, a pattern of black dots is printed onto the white reflector sheets.

In the center of each strip, a 1.1 mm deep groove is milled into which the 1 mm thick Y11 WLS fiber is inserted. At the outer edge of the strip, the groove is cut 0.4 mm deeper so that the active area of the SiPM/MPPC fully covers the fiber. The SiPM/MPPC is housed in a small precisely cut pocket. Especially fabricated fixtures out of Teflon or Nylon will hold a strip. The fiber groove at the outer edge is closed with a plug at the position of the photodetector. The Y11 fiber is pressed against the plug and held with a drop of glue. After removing the plug the SiPM/MPPC is inserted and is glued onto the Y11 fiber to match refractive indices. A mirror is placed at the other end of the fiber to detect the light that moves away from the photodetector. So tolerances in the length of the Y11 fiber are picked up at the mirror end. The strip layout is shown in Figure 9.52.

To hold the strips in each layer in place 1.5 mm deep and 1 mm wide grooves are cut into the lead plates. The shape of groove matches that of the strip. A 3 mm thick and 1 m wide and 550 mm long plastic strip is inserted into the groove and is glued. This structure is strong enough to hold the scintillator strips in place. The calorimeter can be rotated by 90°. This is needed for operation with cosmic muons that yield a MIP calibration and allows for testing the calorimeter before installing it into the Super*B* detector.

The entire calorimeter weighs about 1300 kg. An aluminum frame with a strong rear plate and a strong inner cylinder will hold the backward EMC in the Super*B* detector. The front plate and outer cylinder needed for closure and shielding can be thin. Considering cost and performance it is advantageous to build the backward EMC as a single unit. This requires the calorimeter to slide back on the beam pipe supported on the tunnel walls. It needs to be fixed at the tunnel and rolled in. Since the inner radius is 31 cm, there is sufficient clearance for pumps and other beam elements. The design of this capability requires a detailed drawing of the beam pipe and the position and size of machine elements.

It is possible, however, to build the backward EMC in two halves with a vertical split. The impact of such a design is that ten strips per layer have to be cut into two segments. The

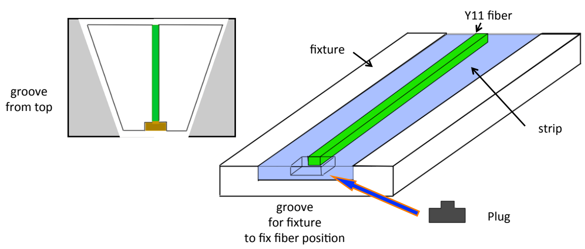

Figure 9.52: Schematic of holding the scintillator strip in a fixture for mounting the MPPC to the Y11 fiber.

inner segments of these strips have to be read out at the inner radius. This increases the number of channels by 240, requiring 240 additional SiPM/MPPCs, additional readout boards and four extra calibration boards. This layout will deteriorate the performance near the vertical boundary. The effect needs to be studied in simulations. This also adds approximately 20% to the cost.

9.4.2.1 Calorimeter construction

Each completed strip with Y11 fiber and MPPC mounted is tested in the lab with a ^{106}Ru source. All important properties, such as bias voltage, gain, noise, and MIP position are recorded in a data base. Stacking will start from the rear to the front. The rear Al plate rotated by 90° is placed on the mounting table and the inner cylinder is bolted on to it. The back plate requires 48 radially milled grooves into which the plastic strips are inserted that will hold the scintillator strips. Next, all scintillator strips are mounted, the MPPCs are connected to preamplifiers and a Pb plate with right-handed logarithmic spiral grooves is placed on top completing layer 24. This procedure is repeated 24 times. Finally, another scintillator layer with radial strips and the front plate are stacked. The scintillator layer 0 yields information on the shower origin.

Before the outer cylinder is bolted on, temperature sensors and clear fibers need to be installed at the outer ring that transport light from a UV LED to the strips. Each fiber illuminates 13 strips via a notch spaced equidistantly every 12 mm,requiring a total of 96 fibers. The fibers run through small holes in the back plate from the rear to the front. Attaching four fibers per LED, 24 LEDs housed outside the rear plate are needed.

9.4.2.2 Support and services

The preferred option is to build the backward EMC as one unit. In order to avoid breaking the beam pipe when access is required to the drift chamber endplate, the backward EMC must be be able to slide back far enough. The explicit design requires a detailed design of the IR with all machine elements in place. In the detector position, the weight is supported by two brackets that are fixed at the rear endplate and on the inner wall of the IFR backward endcap. When rolling back the weight could be supported by the tunnel wall. To facilitate sliding back, rollers are mounted on the inner support cylinder.

The readout and calibration boards (CMBs) are mounted on the rear support plate of the EMC. Each readout board has a multiplexed output cable to the DAQ, a cable providing low voltage inputs, a cable for the MPPC bias voltage of 70 V, an electronic calibration input and an analog output.

The four CMBs are also mounted on the rear support plate. Each CMB holds six LEDs and six PIN photodiodes and needs to read out four thermocouples. Including the low voltage supplies for the CMB electronics, 80 cables are needed for the CMBs, yielding 272 cables in total.

9.4.3 SiPM/MPPC readout

The photodetectors are SiPM/MPPCs from Hamamatsu (type S10362-11-025P) with a sensitive area of $1\,\mathrm{mm} \times 1\,\mathrm{mm}$ holding 1600 pixels with a size of $25\,\mu\mathrm{m} \times 25\,\mu\mathrm{m}$. These detectors are avalanche photodiodes operated in the Geiger mode with a bias voltage slightly above the breakdown, $50 - 70$ V, providing a gain of a few times 10^5. They are insensitive to magnetic fields. Each pixel typically has a quenching resistor of a few MΩ so it recovers within 100 ns. The efficiency is of the order of $10 - 15\%$. Since the SiPM/MPPCs record single photoelectrons (Figure 9.53), they are autocalibrating. SiPM/MPPCs are non-linear requiring non-linearity corrections for higher energies. As an example, Fig. 9.54 shows the response curves of 10,000 SiPMs measured at ITEP, most of which were installed in the CALICE analog hadron calorimeter [36]. The dynamic range is determined by the number of pixels. Properties of several SiPM/MPPCs are listed in Table 9.8.

A concern with SiPM/MPPCs is radiation hardness. Degradation in performance is observed in studies performed for the Super$B$ IFR,

Table 9.8: Properties of Hamamatsu MPPCs

MPPC type	# cells $1/\text{mm}^2$	C [pF]	R_{cell} kΩ]	C_{cell} [fF]	$\tau = R_c \times C_c$ [ns]	$V_{\text{break down}}$ [V] at T=23 C	V_{op} [V] at T=23 C	Gain [10^5]
15 μm	4489	30	1690	6.75	11.4	72.75	76.4	2.0
20 μm	2500	31	305	12.4	3.8	73.05	75	2.0
25 μm	1600	32	301	20	6.0	72.95	74.75	2.75
50 μm	400	36	141	90	12.7	69.6	70.75	7.5

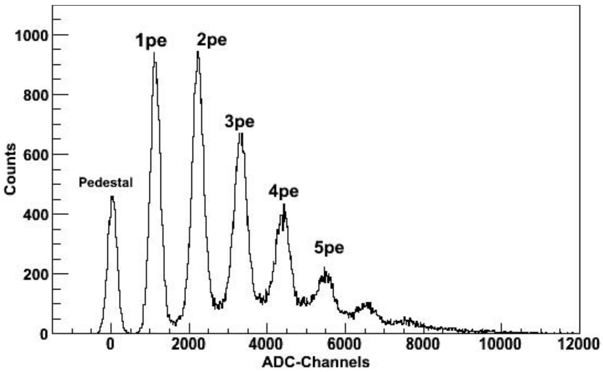

Figure 9.53: Single photoelectron spectrum measured with a Hamamatsu S10362-11-025P MPPC.

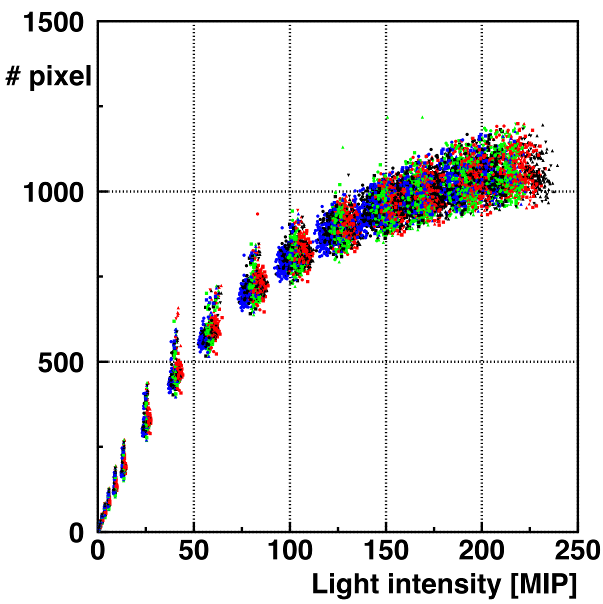

Figure 9.54: Saturation curves of 10,000 SiPMs measured in the CALICE analog hadron calorimeter.

beginning at integrated doses of order 10^8 1-MeV-equivalent neutrons/ cm^2 [39]. This needs to be studied further, and possibly mitigated with shielding. Another alternative is to select a different photodetector. Recently, Hamamatsu has produced SiPM/MPPCs with pixel sizes of 20 μm $\times$ 20 μm and 15 μm $\times$ 15 μm (see Table 9.8). A study by CMS shows that the performance of these new photodetectors deteriorates only slightly after an irradiation of $10^{13} n/\text{cm}^{-2}\text{s}^{-1}$.

9.4.4 Electronics

For tests so far, the signal of the SiPM/MPPC is first amplified with a charge-sensitive preamplifier then fed into an auto-triggered, bi-gain SPIROC ASIC [40]. The SPIROC board has 36 channels. Each channel has a variable-gain charge preamplifier, variable shaper and a 12-bit Wilkinson ADC. It can measure the charge Q from one photoelectron (pe) to 2000 pe and the time t with 100 ps accuracy. A high-level state machine is integrated to manage all these tasks automatically and to control the data transfer to the DAQ. The SPIROC ASIC was designed to supply the high voltage for the SiPM/MPPC. Using a DAC, individual high voltages can be supplied to each photodetector within a range of ± 5 V.

The SPIROC ASIC gives Gaussian signals with no tails, shows excellent linearity and low noise. The endcap requires 32 ASIC readout boards. The boards are mounted in two layers behind the endcap. The first layer holds 20 boards and the second layer the remaining 12 boards. Each board connects to 36 SiPM/MPPCs via a ribbon cable that has been designed for the ILC.

It is unclear whether a version of the SPIROC board can be designed to meet the data acquisition requirements at Super$B$. Thus, we have adopted the electronics of the PID system as our baseline. This provides 12 bit ADCs and 200 ps TDCs. Further details are in section 13.1.3. To match the PID electronics, the preamplifier will produce a negative pulse. Seventy-two of the 16-channel PID ASICs are required for the backward EMC. The circuit boards are placed behind the backward EMC.

9.4.5 Calibration

An LED-based calibration system with fixed LED intensities is used to monitor the stability of the strip-fiber-SiPM/MPPC system between MIP calibrations, to perform gain calibrations, determine intercalibration constants, and to measure the SiPM/MPPC response functions. This is necessary since the SiPM/MPPCs have a temperature and voltage dependence of the gain of

$$\frac{dG}{dT} \sim -1.7\%/^{\circ}\text{K}, \tag{9.11}$$

$$\frac{dG}{dV} \sim 2.5\%/0.1\text{ V}. \tag{9.12}$$

The temperature and voltage dependence of the scintillation signal is

$$\frac{dQ}{dT} \sim -4.5\%/^{\circ}\text{K} \tag{9.13}$$

$$\frac{dQ}{dV} \sim 7\%/0.1\text{ V}. \tag{9.14}$$

The calibration system is based on a new design for the analog hadron calorimeter. Light from a UV LED is coupled to clear fibers, notched at equidistant positions. The shape of each notch changes such that it emits about the same intensity of light. For the backward EMC, 96 fibers with 12 notches each are sufficient to illuminate all strips. If four notched fibers and one untouched fiber are coupled to one LED, 24 LEDs are needed whose light is monitored by a PIN photodiode via the untouched fiber. A few thermocouples distributed throughout the outer edge of the EMC near MPPCs measure temperature. Both temperature and bias voltage are recorded regularly by the slow control system. After temperature and PIN diode correction the stability of LED system is better than 1%.

The calibration boards are 40 mm × 140 mm in dimension and house one LED, one PIN diode, the electronics to read out the PIN diode, and monitor temperature and MPPC voltage. The boards are sufficiently small to be mounted at the backplate near the outer radius. They can be arranged such that the fibers are nearly straight.

9.4.6 Backward simulation

A backward EMC model exists in the GEANT4 detector simulation, modeling 24 layers of scintillator and lead. Each layer is modeled by a complete disc without physical strip segmentations in r-ϕ. Support structure, fibers, electronics, and cables are presently ignored.

In the fast simulation, the model does not separate lead from scintillator. It uses instead an artificial material that approximates the overall density, radiation length, interaction length and Molière radius of the mixture of lead and plastic. The volume is divided into eight rings, each of which is divided into 60 segments. The logarithmic spirals and the lead-scintillator layers, however, are not modeled explicitly to avoid a complicated shower reconstruction and the modeling of longitudinal shower energy distribution. The energy resolution is set to $\sigma_E/E = 14\%/\sqrt{E(\text{ GeV})} \oplus 3\%$.

9.4.7 Performance in simulations

A GEANT4 simulation is performed to study the energy resolution under the simplified conditions, ignoring the rest of the detector and shooting mono-energetic photons perpendicular to the face of the disc. All energy deposited in the scintillator is collected. No clustering algorithm is performed. Figure 9.55 shows the energy deposition for five different photons energies, 0.1 GeV, 0.2 GeV, 0.5 GeV, 1 GeV, and 2 GeV. For 0.1 GeV photons, approximately 9.5% of the photon energy is deposited in the scintillator on average. This percentage drops to 9.0% for 2 GeV photons.

The energy dependence of the energy resolutions on generated energy is shown in Figure 9.56. The distribution can be fitted with the function $\sigma_E/E = 10\%/E(\text{ GeV})^{0.485} \oplus 6\%$.

9.4.8 Impact on physics results

Fast simulation studies have been conducted to investigate the performance gain achieved by the addition of the backward calorimeter. The channels chosen to evaluate the impact of this detector are $B \to \tau\nu$ and $B \to K^{(*)}\nu\bar{\nu}$, since both are benchmark channels for the Super$B$ physics program and greater detector hermeticity improves signal reconstruction efficiencies and background rejection.

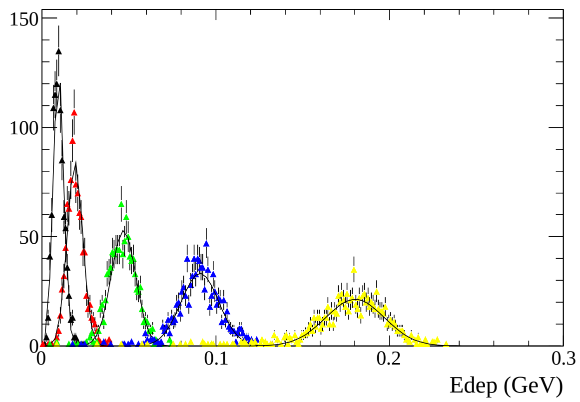

Figure 9.55: Simulated energy depositions from mono-energetic photons (0.1 GeV, 0.2 GeV, 0.5 GeV, 1 GeV, and 2 GeV) observed in the scintillators of the backward EMC.

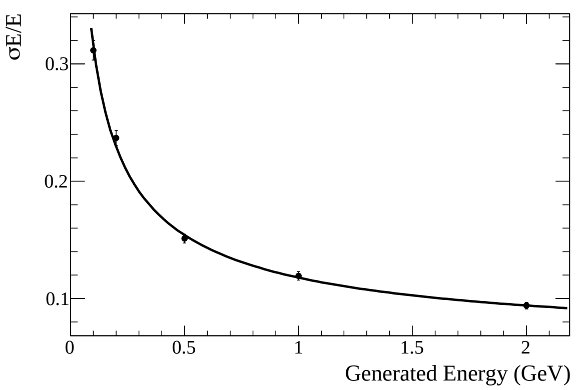

Figure 9.56: The backward EMC energy resolutions, σ_E/E, where σ_E and E are the Gaussian width and mean in Figure 9.55, as a function of generated photon energy.

The study of the leptonic decay $B \to \tau\nu$ is of particular interest as a test of the Standard Model (SM) and a probe for New Physics [41]. The presence of a charged Higgs boson (in *e.g.*, a Two Higgs Doublet Model) as a decay mediator could significantly modify the branching ratio with respect to the SM value, depending on the Higgs mass and couplings. A detailed analysis of this channel is therefore quite important in searches for physics beyond the SM. A complementary search for new physics can be performed using $B \to K^{(*)}\nu\bar{\nu}$ decays [42], [43]. Being mediated by a flavor-changing neutral current, these processes are prohibited at tree level in the SM and the higher order diagrams may receive contribution from a non-standard mechanism. Moreover, new sources of missing energy may replace the neutrinos in the final state.

The reconstruction of both decay modes is challenging, since the final state contains more than one neutrino and thus is only partially reconstructible. Signal events are selected using a recoil method analysis, in which the signal B-meson (B_{sig}) is identified as the system recoiling against the other tag B meson (B_{reco}). The tag B meson is either reconstructed fully via its hadronic decays or partially reconstructed from its semileptonic final states [44]. The rest of the event is assigned to the $B \to \tau\nu$ candidate, if it is compatible with one of the following decay modes of the tau lepton: $\mu\nu_\mu\nu_\tau$, $e\nu_e\nu_\tau$, $\pi\nu_\tau$, $\pi\pi^0\nu_\tau$, $\pi\pi^0\pi^0\nu_\tau$, $\pi\pi\pi\nu_\tau$, or $\pi\pi\pi\pi^0\nu_\tau$. These final states cover about 95% of all τ decays, and have one charged particle (1-prong) or three charged particles (3-prong), with the possible addition of one or two π^0s. Since final states containing one or more π^0 cover about 40% of the tau decay modes, an increase in the EMC coverage improves substantially the efficiency of tau identification.

Candidates for the $B \to K^{(*)}\nu\bar{\nu}$ sample must be compatible with one of the following final states: $K^{*+} \to K_S(\pi^+\pi^-)\pi^+$, $K^+\pi^0$; $K^{*0} \to K^+\pi^-$; K^+; or $K_S \to \pi^+\pi^-$ (semileptonic analysis only). In the analyses with a $K^{(*)}$ in the final state, further selection criteria are applied using kinematic quantities related to the goodness of the $B_{\rm reco}$ and $K^{(*)}$ reconstruction and event shape variables that test the energy balancing in the event and the presence of missing energy due to the neutrinos in the final state. The present level of the analyses is very similar to that in Refs. [44] and [45].

Backgrounds are further rejected using $E_{\rm extra}$, the total neutral energy in the calorimeter of particles not associated with either B meson. Signal events peak at low values of $E_{\rm extra}$, while background events which contain additional sources of neutral showers tend to have higher values of $E_{\rm extra}$. The discriminating power of this observable obviously increases with the calorimeter coverage.

The performance of the backward EMC is assessed by comparing the signal-to-background ratio, S/B, and the statistical precision, $S/\sqrt{S+B}$, of the expected signal with and without the backward EMC used as a veto device for extra-neutral energy. For this task, the extra neutral energy reconstruction is split into two disjoint calorimeter regions: $E^{\rm extra}_{\rm brrfwd}$ covering the barrel and the forward region and $E^{\rm extra}_{\rm bwd}$ covering the backward region only. Furthermore, the effects of machine backgrounds (Sec. 14.1.2) superimposed on physics events are taken into account.

The results for both rare decay channels are summarized in Table 9.9. For $B \to \tau\nu$ reconstructed in hadronic tags, the improvements in $S/\sqrt{S+B}$ are shown as a range sampling over the individual τ final states. For $B \to \tau\nu$ reconstructed in semileptonic tags, the improvement in $S/\sqrt{S+B}$ is presented as an average over all τ final states. Combining $S/\sqrt{S+B}$ of both tags, the net gain is of the order of 10%. For $B \to K^*\nu\bar{\nu}$, the net gain for hadronic and semileptonic tags combined ranges between 8% and 16% depending on the final state. For $B \to K\nu\bar{\nu}$ the net gain is about 6%.

These improvements in turn yield improvements in the precision of measured physical observables For $\mathcal{B}(B \to K^+\nu\bar{\nu})$ and $\mathcal{B}(B \to K^*\nu\bar{\nu})$ the 3σ significance for evidence without the backward EMC is reached at 5 ab^{-1} and 51 ab^{-1}, respectively. When adding the backward EMC, the 3 σ significance is already reached at 4.5 ab^{-1} and 42 ab^{-1}, respectively.

The signal-to-background ratio for reconstruction of the rare decay $B \to \tau\nu_\tau$ with and without a backward endcap in shown in Figure 9.57 (left). The ratio of S/B with and without a backward endcap is shown on the right.

In addition to the measurement of neutral clusters, the backward EMC can be used to improve the π^0 reconstruction efficiency. If one photon is reconstructed in the backward EMC, the $\gamma\gamma$ invariant-mass resolution ranges from $\sim$ 24 MeV for 200 MeV/c π^0s to $\sim$ 13 MeV for 1 GeV/c π^0s.

It is worth mentioning that the inclusion of the backward EMC not only improves the background rejection, but also the B-tagging efficiency. The impact on the B reconstruction efficiency is determined by using the decays $B^- \to D^0\pi^-, D^0 \to K^-\pi^+\pi^0$. Events are separated into two groups: the first uses only photons from the barrel and forward endcap, while the second includes photons from the backward EMC with polar angle between $-0.96 < \cos\theta < -0.89$ as well. The π^0 mass window is defined as 120–145 MeV (100–180 MeV) for the first (second) group. For B candidates, D^0 s are selected by $1.830 < m_{K\pi\pi^0} < 1.880$ GeV and $-80 < \Delta E < 50$ GeV. The $m_{\rm ES}$ distribution is fitted to determine the B reconstruction efficiency. Including the backward EMC, the signal efficiency increases by nearly 4% in this particular channel (see Figure 9.58).

9.4.9 Use for particle identification

Charged particles moving in the backward direction typically have lower momentum. Thus, ionization loss and time-of-flight measurements may provide useful information for particle identification, *e.g.* for e/π and K/π separation.

A preliminary time-of-flight study is performed with fast simulation. Single kaons or

Table 9.9: Relative gain in $S/\sqrt{S+B}$ by including the backward EMC in the event selection for $B \to K^{(*)}\nu\bar{\nu}$ and $B \to \tau\nu$ decay channels reconstructed in the recoil of B semileptonic and hadronic tags. The first uncertainty is statistical and the second is systematic.

channel	Semileptonic	Hadronic
$B \to \tau\nu$	$(6.1 \pm 0.1 \pm 0.7)\%$	$\simeq 3 - -5\%$
$B \to K^{+}\nu\bar{\nu}$	$(5.8 \pm 1.0 \pm 0.6)\%$	-
$B \to K_S\nu\bar{\nu}$	$(6.0 \pm 0.4 \pm 0.6)\%$	-
$B \to K^{*+}(K^{+}\pi^{0})\nu\bar{\nu}$	$(7.0 \pm 0.2 \pm 0.7)\%$	$(5.9 \pm 2.5 \pm 0.5)\%$
$B \to K^{*+}(K_S\pi^{+})\nu\bar{\nu}$		$(6.2 \pm 2.1 - 0.5)\%$
$B \to K^{*0}\nu\bar{\nu}$	$(9.1 \pm 0.4 \pm 0.7)\%$	$(7.3 \pm 1.8 \pm 0.5)\%$

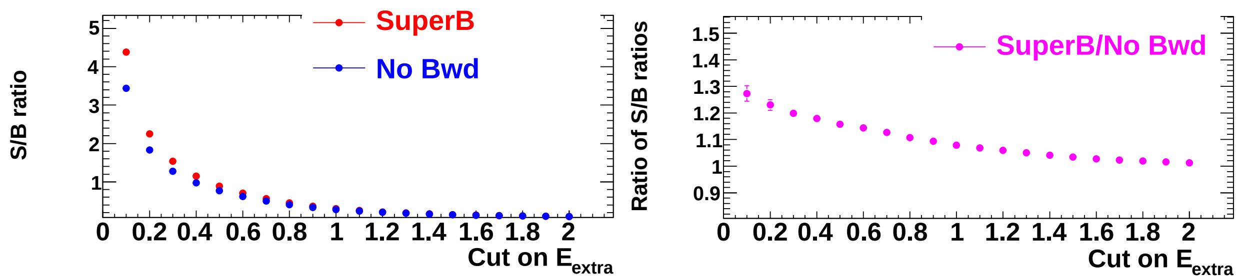

Figure 9.57: Left: Signal-to-background ratio with and without a backward EMC, as a function of the E_{extra} selection. Right: Ratio of the S/B ratio with a backward EMC to the S/B ratio without a backward calorimeter, as a function of the E_{extra} selection.

pions are generated that move towards the backward EMC. The true arrival time calculated at the first layer is smeared with a Gaussian resolution to simulate the measured time distribution. Velocity distributions are obtained for kaons and pions at a given momentum from the measured time and reconstructed track path length. Both mean and RMS values are extracted from these distributions to determine K/π separation in standard deviation units (σ) as a function of momentum for different time resolutions, in which uncertainties in the momentum measurement and path length reconstruction are included. Figure 9.59 shows K/π separation in units of standard deviations as a function of momentum for time resolutions of 100 ps, 50 ps, 20 ps, 10 ps, and perfect timing. For example, for a 100 ps time resolution, a K/π separation of more than three σ can be achieved for momenta up to 1 GeV/c and approximately 1.5σ up to 1.5 GeV/c.

Since each layer measures the time distribution, 24 measurements will be averaged. In addition to timing, the ionization is measured in each layer. For MIP-like particles, the average energy loss per layer is $dE_{Pb} = 4.3$ MeV and $dE_{\text{scintillator}} = 0.6$ MeV. A 0.5 GeV/c π is at the ionization minimum, a 0.5 GeV/c K is below the minimum and a 0.5 GeV/c e is at the relativistic plateau. For MIP particles, the ionization loss in the 24 layers is $\Delta E = 117$ MeV. Since the energy loss below the minimum increases with decreasing momenta as $1/\beta^2$, dE/dx measurements in the endcap can be combined with the dE/dx information from the SVT and DCH. Figure 9.60 shows the ionization curves for e, μ, π, K and p as a function of momentum. A $> 3\sigma$ K/π separation is achievable for momenta up to $0.6 - 0.7$ GeV.

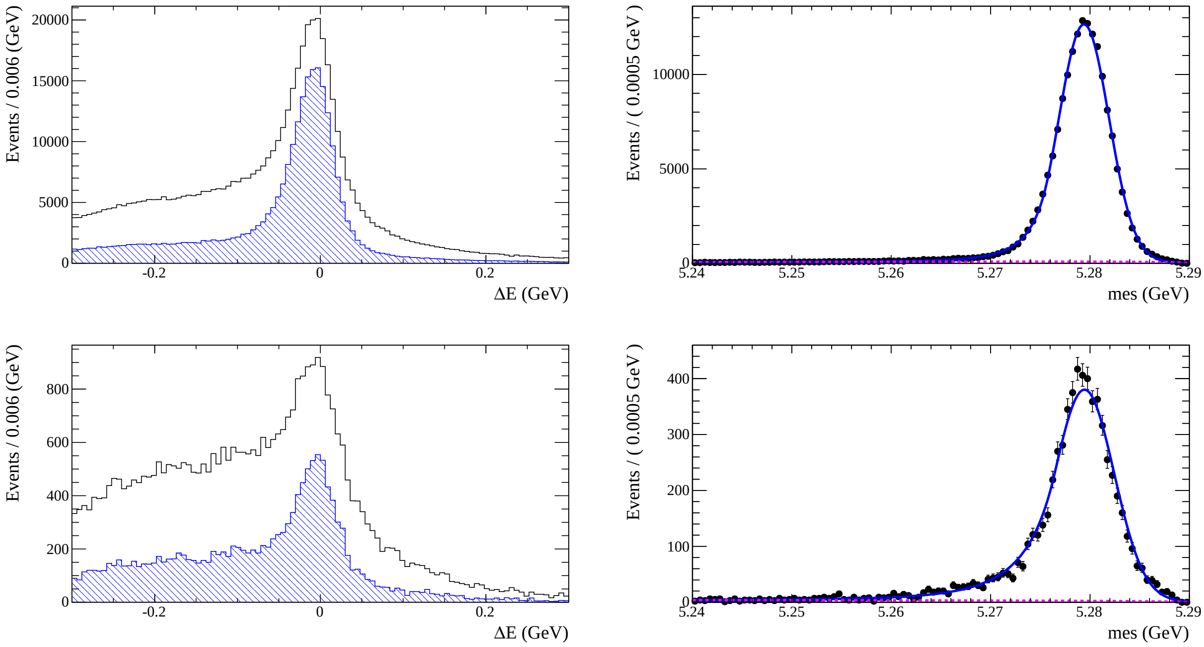

Figure 9.58: (left) ΔE and (right) m_{ES} distributions for the decay $B^- \to D^0\pi^-$ with $D^0 \to K^-\pi^+\pi^0$ reconstruction for (top) both γ's in barrel and forward endcap and (bottom) one γ in the backward EMC. The two histograms in each ΔE distribution are before and after a requirement on the D^0 mass.

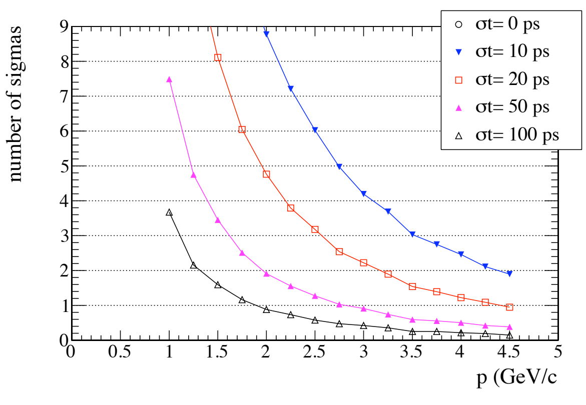

Figure 9.59: K/π separation versus measured momentum for different timing resolutions in the backward EMC. The $\sigma_t = 0$ curve is offscale. The finite separation in this case is caused by uncertainties in the momentum measurement.

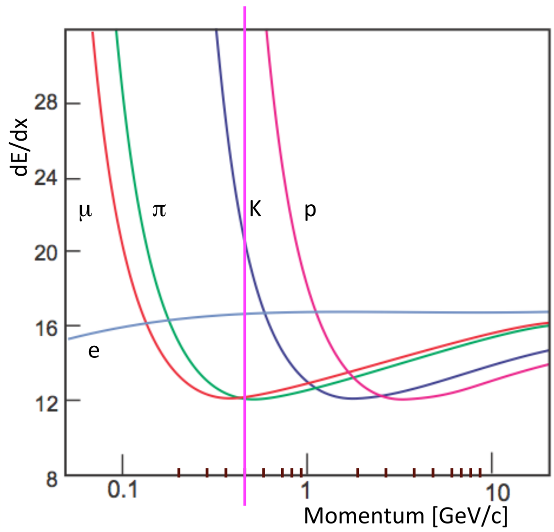

Figure 9.60: Calculated energy loss curves versus momentum for e, μ, π, K, and p in one layer of the backward EMC.

9.4.10 Discussion of task force conclusions

- The device adds to the physics program in important channels through the increased hermeticity.
- The design is technically plausible and cost-effective. However, operation of the readout in the radiation environment should be studied further, and a prototype should be demonstrated in a beam test.
- The possibility of using the backward EMC for PID through time-of-flight is attractive and should be pursued with further R&D.
- The capability to install this device should be preserved, as opposed to, for example, extending the drift chamber.

9.5 Environmental monitoring

The calorimeter must be protected from various hazards. We summarize these hazards in this section.

The principal heat loads in the EMC are from the electronics. The main barrel readout electronics is water-cooled. Fluorinert is the coolant for the barrel and endcap preamps and the endcap digital electronics. Thermal stability is important: the CsI(Tl) light output, the PIN diode leakage current and the APD gain are all temperature-dependent. In addition, the PIN diode and APD glue joints can be broken due to differential expansion. Temperature excursions of greater than $\pm 10^{\circ}$ are known to be capable of breaking the PIN diode glue joint. A specification that variations be less than $\pm 5^{\circ}$ has a comfortable safety margin. In *BABAR*, the temperature was monitored with 256 sensors on the barrel, and 100 sensors on the forward endcap. Figure 9.5 provides an example of the data on the thermal stability. This system will be retained in Super*B*. The backward endcap requires additional temperature monitoring and control.

The CsI crystals are slightly hygroscopic, so they must be kept dry. This is achieved by flowing nitrogen through the crystal volume. In addition, both oxygen level and humidity are monitored. The readout for these sensors, as well as the temperature sensors is via a CANbus General Monitoring Board [46].

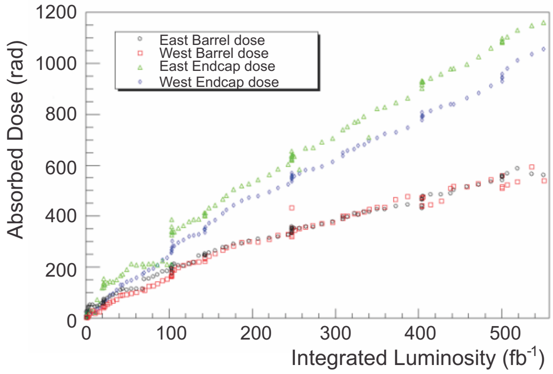

Figure 9.61: Radiation dose in rads as measured by radFETs in the *BABAR* barrel and endcap. The horizontal axis is the integrated luminosity in fb^{-1}. The curves show the barrel and endcap doses, divided into east and west sides of the detector.

The CsI(Tl) crystal light output and uniformity also degrade with radiation so the radiation exposure must be monitored. Two radiation monitoring systems for the EMC have been in use in *BABAR*, and will be reused in Super*B*. First is a set of small CsI(Tl) crystals with PIN diode readout for prompt monitoring and protection, and second is a set of RadFET dosimeters to track long term exposure.

There are 16 CsI(Tl) crystal/PIN diode packages installed at both forward and backward locations on the detector (4 backward and 12 forward; the 12 forward being in the inner and outer faces and the inner radius of the forward EMC). The crystals are approximately $4 \times 4 \times 1$ cm^3 with Hamamatsu S3590-01 PIN diodes. The diodes are run unbiased, in order to have a more stable leakage current pedestal. In the current configuration at *BABAR*, the signals from the four packages at the forward EMC inner radius are summed and used to provide an injection inhibit signal when the signal exceeds 0.7

V. This corresponds to a dose rate around 0.2 mRad/s.

The radiation dose over the long term is monitored by a set of 56 real-time integrating dosimeters (radFETs) placed in front of the barrel and 60 radFETs in front of the endcap. Readout of the radFETs is performed with a RadFET Monitoring Board (RMB). The RMB ties the radFETs to ground except during a reading, at which time a constant current source injects a current and the resulting radFET voltage is digitized [47]. The accumulated dose measured by these radFETs over the life of the *BABAR* detector is shown in Fig. 9.61, separately for the endcap, the forward, and the backward barrel of the calorimeter. These dose measurements may be used to understand the changing light yields shown in Fig. 9.2.

9.6 Bibliography

[1] P. D. Strother, "Design and application of the reconstruction software for the *BABAR* calorimeter", 1998, report SLAC-R-828.

[2] J. Bauer, "The *BABAR* electromagnetic calorimeter: status and performance improvements", *Nuclear Science Symposium Conference Record, 2005 IEEE*, vol. 2, pp. 1038 - 1042, oct. 2005, doi:10.1109/NSSMIC.2005.1596430.

[3] B. Aubert et al., (*BABAR* Collaboration collaboration), "The *BABAR* detector", *Nucl.Instrum.Meth.* A479:1–116, 2002, doi:10.1016/S0168-9002(01)02012-5, arXiv:hep-ex/0105044 [hep-ex], report SLAC-PUB-8569, BABAR-PUB-01-08.

[4] R. Zhu, "Radiation damage in scintillating crystals", *Nucl.Instrum.Meth.* A413:297–311, 1998, doi:10.1016/S0168-9002(98)00498-7.

[5] Fluorinert is the trademark for polychlorotrifluoroethylene, manufactured by 3M corporation, St. Paul, MN.

[6] M. Weaver, private communication (2011).

[7] C. Melcher and J. Schweitzer, "Cerium-doped lutetium oxyorthosilicate: a fast, efficient new scintillator", *Nuclear Science, IEEE Transactions on* 39(4):502 –505, aug 1992, doi:10.1109/23.159655.

[8] D. Cooke, K. McClellan, B. Bennett, M. Roper, J.M.and Whittaker, and R. Muenchausen, "Crystal Growth and Optical Characterization of Cerium-doped $Lu_{1.8}Y_{0.2}SiO_5$ ", *J. Appl. Phys.* 88, 2000.

[9] T. Kimble, M. Chou, and B. Chai, "Scintillation properties of LYSO crystals", *Nuclear Science Symposium Conference Record, 2002 IEEE*, vol. 3, pp. 1434 - 1437 vol.3, nov. 2002, doi:10.1109/NSSMIC.2002.1239590.

[10] R. Mao, L. Zhang, and R.-Y. Zhu, "Optical and Scintillation Properties of Inorganic Scintillators in High Energy Physics", *Nuclear Science, IEEE Transactions on* 55(4):2425 –2431, aug. 2008, doi:10.1109/TNS.2008.2000776.

[11] W. Wisniewski, "Consideration for Calorimetry at a Super *B* Factory", *Proceedings of Tenth International Conference on Calorimetry in Particle Physics*, 2002.

[12] C. Cecchi, "A LYSO Calorimeter for a Super *B* Factory", *Proceedings of Fourteenth International Conference on Calorimetry in Particle Physics*, 2010.

[13] F. Happacher, "CCALT: Crystal Calorimeter at KLOE2", *Proceedings of Fourteenth International Conference on Calorimetry in Particle Physics*, 2010.

[14] R. Abrams et al., (Mu2e collaboration), "Mu2e Conceptual Design Report", 2012, arXiv:1211.7019 [physics.ins-det].

[15] R.-Y. Zhu, *CMS Forward Calorimetry Task Force Meeting at CERN*, June 2010, http://indico.cern.ch/getFile.py/access?sessionId=0&resId=4&materialId=0&confId=97272.

[16] D.-a. Ma and R.-y. Zhu, "Light attenuation length of barium fluoride crystals", *Nucl.Instrum.Meth.* A333:422–424, 1993, doi:10.1016/0168-9002(93)91185-P.

[17] R. Mao, L. Zhang, and R.-Y. Zhu, "Emission Spectra of LSO and LYSO Crystals Excited by UV Light, X-Ray and γ-ray", *Nuclear Science, IEEE Transactions on* 55(3):1759 –1766, june 2008, doi:10.1109/TNS.2008.921877.

[18] R. Mao, L. Zhang, and R.-Y. Zhu, "Quality of a 28 cm long LYSO crystal and progress on optical and scintillation properties", *Nuclear Science Symposium Conference Record (NSS/MIC), 2010 IEEE*, pp. 1030 -1034, 30 2010-nov. 6 2010, doi:10.1109/NSSMIC.2010.5873922.

[19] J. Chen, R. Mao, L. Zhang, and R.-Y. Zhu, "Large Size LSO and LYSO Crystals for Future High Energy Physics Experiments", *Nuclear Science, IEEE Transactions on* 54(3):718 –724, june 2007, doi:10.1109/TNS.2007.897823.

[20] S. Derenzo, M. Weber, W. Moses, and C. Dujardin, "Measurements of the intrinsic rise times of common inorganic scintillators", *Nuclear Science, IEEE Transactions on* 47(3):860 –864, jun 2000, doi:10.1109/23.856531.

[21] R.-Y. Zhu, *Time Resolution Workshop at University of Chicago*, April 2011, http://www.hep.caltech.edu/~zhu/talks/ryz_110428_time_resolution.pdf.

[22] T. Szczesniak, M. Moszynski, A. Synfeld-Kazuch, L. Swiderski, M. Koschan, and C. Melcher, "Timing Resolution and Decay Time of LSO Crystals Co-Doped With Calcium", *Nuclear Science, IEEE Transactions on* 57(3):1329 –1334, june 2010, doi:10.1109/TNS.2009.2035620.

[23] R. Zhu, "Radiation damage in scintillating crystals", *Nucl.Instrum.Meth.* A413:297–311, 1998, doi:10.1016/S0168-9002(98)00498-7.

[24] "The CMS Electromagnetic Calorimeter Project", 1997, CERN/LHCC 97-33.

[25] R.-Y. Mao, L. Zhang, and R.-Y. Zhu, "Optimization of Light Response Uniformity for Super*B* Tapered LYSO Crystals with APD Readout", Paper N29-6, booktitle=Nuclear Science Symposium Conference Record, 2011 IEEE, year =.

[26] J. Chen, R. Mao, L. Zhang, and R.-Y. Zhu, "Gamma-Ray Induced Radiation Damage in Large Size LSO and LYSO Crystal Samples", *Nuclear Science, IEEE Transactions on* 54(4):1319 –1326, aug. 2007, doi:10.1109/TNS.2007.902370.

[27] R. Mao, L. Zhang, and R.-Y. Zhu, "Gamma ray induced radiation damage in PWO and LSO/LYSO crystals", *Nuclear Science Symposium Conference Record (NSS/MIC), 2009 IEEE*, pp. 2045 -2049, 24 2009-nov. 1 2009, doi:10.1109/NSSMIC.2009.5402126.

[28] L. Zhang, R. Mao, and R.-Y. Zhu, "Effects of neutron irradiations in various crystal samples of large size for future crystal calorimeter", *Nuclear Science Symposium Conference Record (NSS/MIC), 2009 IEEE*, pp. 2041 -2044, 24 2009-nov. 1 2009, doi:10.1109/NSSMIC.2009.5402125.

[29] F. Nessi-Tedaldi, G. Dissertori, P. Lecomte, D. Luckey and F. Pauss, "Studies of Cerium Fluoride, LYSO and Lead Tungstate Crystals Exposed to High Hadron Fluences," Paper N32-3, 2009 IEEE NSS Conference.

[30] R. Faccini, C. Gargiulo, F. Pellegrino, V. Pettinacci, and A. Zullo, "EMC Forward Mechanical Design", Super*B* Technical Note SB-DET-2012-006.

[31] B. Adeva et al., (L3 collaboration), "The Construction of the L3 Experiment", *Nucl.Instrum.Meth.* A289:35–102, 1990, doi:10.1016/0168-9002(90)90250-A.

[32] S. Sahu et al., (Belle collaboration), "Radiation hardness of undoped BGO crystals", *Nucl.Instrum.Meth.* A388:144–148, 1997, doi:10.1016/S0168-9002(97)00333-1.

[33] J. Chen, R. Mao, L. Zhang, and R.-Y. Zhu, "Large Size LSO and LYSO Crystals for Future High Energy Physics Experiments", june 2007, doi:10.1109/TNS.2007.897823.

[34] V. Bocci, D. Chao, G. Chiodi, R. Faccini, F. Ferroni, et al., "Dependence of the energy resolution of a scintillating crystal on the readout integration time", *JINST* 7:P09014, 2012, doi:10.1088/1748-0221/7/09/P09014, arXiv:1207.4902 [physics.ins-det].

[35] T. Lewis, "The Reduction Of Background Signal In Bismuth Germanate Scintillators", *Nucl.Instrum.Meth.* A264:534–535, 1988, doi:10.1016/0168-9002(88)90955-2.

[36] C. Adloff *et al.* [CALICE Collaboration] "Construction and Commissioning of the CALICE Analog Hadron Calorimeter Prototype," JINST 5:P05004 (2010).

[37] V. Andreev, V. Balagura, B. Bobchenko, P. Buzhan, J. Cvach, et al., "A high granularity scintillator hadronic-calorimeter with SiPM readout for a linear collider detector", *Nucl.Instrum.Meth.* A540:368–380, 2005, doi:10.1016/j.nima.2004.12.002.

[38] H. Ono, H. Miyata, S. Iba, N. Nakajima, A. Sanchez, et al., "Beam test results of a high-granularity tile/fiber electromagnetic calorimeter", *Nucl.Instrum.Meth.* A600:398–407, 2009, doi:10.1016/j.nima.2008.11.100.

[39] M. Angelone, M. Pillon, R. Faccini, D. Pinci, W. Baldini, et al., "Silicon Photo-Multiplier radiation hardness tests with a beam controlled neutron source", 2010, doi:10.1016/j.nima.2010.07.057, arXiv:1002.3480 [physics.ins-det].

[40] M. Bouchel, S. Callier, F. Dulucq, J. Fleury, J. Jaeger, et al., "SPIROC (SiPM Integrated Read-Out Chip): Dedicated very front-end electronics for an ILC prototype hadronic calorimeter with SiPM read-out", *JINST* 6:C01098, 2011, doi:10.1088/1748-0221/6/01/C01098.

[41] W.-S. Hou, "Enhanced charged Higgs boson effects in $B^- \to \tau\bar{\nu}$, $\mu\bar{\nu}$ and $b \to \tau\bar{\nu} + X$", *Phys.Rev.* D48:2342–2344, 1993, doi:10.1103/PhysRevD.48.2342.

[42] W. Altmannshofer, A. J. Buras, D. M. Straub, and M. Wick, "New strategies for New Physics search in $B \to K^*\nu\bar{\nu}$, $B \to K\nu\bar{\nu}$ and $B \to X_s\nu\bar{\nu}$ decays", *JHEP* 0904:022, 2009, doi:10.1088/1126-6708/2009/04/022, arXiv:0902.0160 [hep-ph], report TUM-HEP-709-09.

[43] T. Barakat, "The $B \to K^*\nu\bar{\nu}$ rare decay in the two-Higgs doublet model", *J.Phys.* G24:1903–1912, 1998, doi:10.1088/0954-3899/24/10/007.

[44] B. Aubert et al., (*BABAR* collaboration), "Search for $B \to K^*\nu\bar{\nu}$ decays", *Phys.Rev.* D78:072007, 2008, doi:10.1103/PhysRevD.78.072007, arXiv:0808.1338 [hep-ex].

[45] P. del Amo Sanchez et al., (*BABAR* collaboration), "Search for the Rare Decay $B \to K\nu\bar{\nu}$", *Phys.Rev.* D82:112002, 2010, doi:10.1103/PhysRevD.82.112002, arXiv:1009.1529 [hep-ex].

[46] P. Anthony, H. Crawley, P.-A. Fischer, R. McKay, and W. Meyer, "CANbus and microcontroller use in the *BABAR* detector at SLAC", *Nuclear Science, IEEE Transactions on* 47(2):166 –169, apr 2000, doi:10.1109/23.846140.

[47] A. Khan, W. Meyer, J. Stelzer, and J. Yi, "The radiation dose measurement system for the *BABAR* electromagnetic calorimeter", *Nuclear Science Symposium Conference Record, 2005 IEEE*, vol. 1, pp. 486 - 489, oct. 2005, doi:10.1109/NSSMIC.2005.1596299.

10 Instrumented Flux Return

10.1 Physics Goals and Performance Requirements

The principal task of the Instrumental Flux Return (IFR) detector is the detection of muons and neutral hadrons. The detector is integrated into the large iron structure that forms the magnet return yoke.

Reliable muon detection is vital for searches of New Physics in processes like $b \to s\mu^+\mu^-$, $\tau \to \mu\gamma$, $\tau^+ \to \mu^+\mu^-\mu^+$, $\tau \to \mu X$, (with $X = \rho, \eta^{(\prime)}, f_0, ...$), $B_{d,s} \to \mu^+\mu^-$, $D^0 \to \mu^+\mu^-$, to name but a few [1] [2]. Moreover, efficient muon identification identification is crucial for a substantial part of studies related to the determination of sides and angles of the unitarity triangle, which are based on semileptonic decays of B mesons. In these decays, the sign of the lepton charge determines the flavour of the parent heavy meson, thus providing one of the tags for the CP-asymmetry measurements.

The asymmetry of the machine results in a strong correlation between momenta and production angles of the final state particles. The absolute population and the shape of the momentum spectra are quite different in the backward, central and forward regions of the detector. In this regard, the different Super$B$ boost with respect to *BABAR* (see Chapter 3) plays an important role and must be taken into account for the detector optimization. Figure 10.1 shows the momentum distribution versus the polar angle for muons coming from B semileptonic decays in *BABAR* and Super$B$: with the lower Super$B$ boost the momentum distribution is flatter and the barrel and backward regions gain importance. Almost one fifth of all B decays contain at least one muon in the Super$B$ detector acceptance region. Most of them are either produced directly from the B meson or from the cascade Ds. τ decays and $e^+e^- \to \mu^+\mu^-$ processes are an addtional small source of muons. High momentum ($p > 1\,\mathrm{GeV}/c$) muons come mostly from direct decays, while muons from D decays peak at lower momenta. Figure 10.2 presents the momentum and angular distributions for muons coming from the decays $B \to K^{(*)}\mu^+\mu^-$, $B \to \mu\nu$ and from $D \to K\mu\nu$, where D mesons originate from $B \to D\ell\nu$ events. Pions are very abundant in B decays and their momenta peak below $1\,\mathrm{GeV}/c$, as shown in Figure 10.3.

The muon momenta to be covered by the IFR range from a few hundred MeV/c up to a few GeV/c. The lower limit of this range is set by the magnetic bending in the barrel region and by energy losses in the inner detectors of the two endcap regions.

Charged tracks found with the internal tracking system will be matched to the tracks in the IFR. Their identification as muons or hadrons will result from detailed analysis of the hit patterns in the active detector. The maximum tolerable level of hadron misidentification will

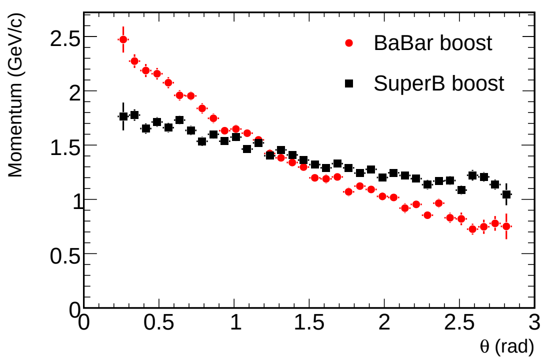

Figure 10.1: Average momentum of muons coming from the semileptonic decay $B \to D^{(*)}\ell\nu$ as s function of the polar angle with the *BABAR* and Super$B$ boost.

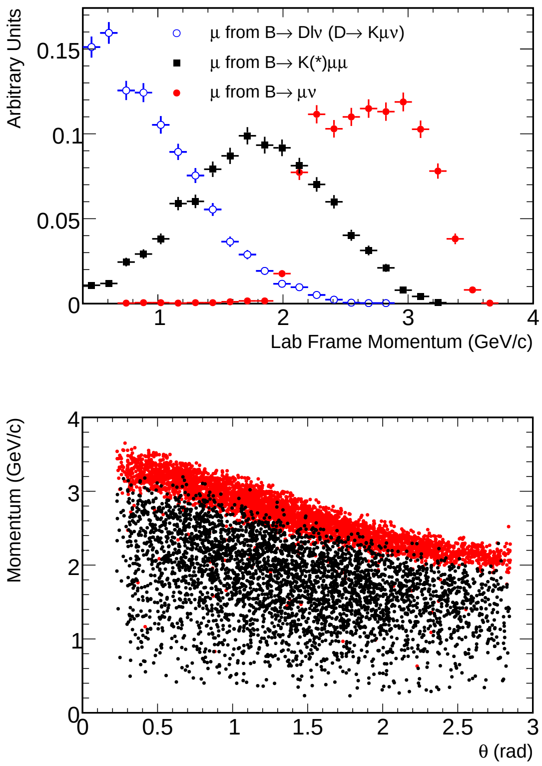

Figure 10.2: Top: momentum distributions for muons coming from $B \to K^{(*)}\mu\mu$, from $B \to \mu\nu$ and from the D decays $D \to K\mu\nu$ (where the D meson originates from $B \to D\ell\nu$). Bottom: momentum versus the polar angle for muons coming from $B \to K^{(*)}\mu\mu$ (black) and from $B \to \mu\nu$ (red).

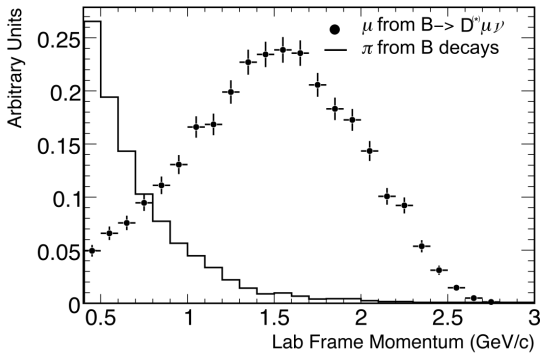

Figure 10.3: Momentum distributions for muons coming from $B \to D^{(*)}\ell\nu$ (data points) decay and for pions coming from generic B decays (black line).

depend on the physics topic under study.

The IFR will also act as a hadronic calorimeter for the detection of neutral hadrons. Special attention is paid to the reconstruction of K^0_L mesons which is performed by using IFR information in conjunction with information provided by the electromagnetic calorimeter. The ability to reconstruct the K^0_L mesons allows, in particular, to compare CP-violation effects in the decay channel $B \to J/\psi K^0_L$ with those in $B \to J/\psi K^0_S$. In other analyses, the IFR will be used to veto events where a K^0_L is present. These events are an important source of background for the decays whose signature is characterized by a large missing-momentum, like $B \to \tau\nu$ or $B \to \pi\tau\nu$. About 60 % of the K^0_L interact before reaching the IFR and can be detected with the EMC, the remaining 40 % interact only within the IFR. Figure 10.4 shows the momentum and angular distributions for K^0_L coming from B generic decays and from $B \to J/\psi K^0_L$.

10.2 Detector Overview

10.2.1 The Absorber Structure

The Super$B$ flux return structure, used as absorber material to identify muons, will be composed of an hexagonal iron yoke with a barrel and two endcaps (see Figure 10.5). The barrel is the assembly of six sextants, each one composed of an inner and an outer wedge, while each of the two endcaps comprises two doors. All these components are made of welded steel plates with a thickness ranging from 20 mm to 100 mm. The geometry of the absorber will be almost identical to the *BABAR* IFR, except for the overall thickness of the steel layers, which will be increased in Super$B$.

The thickness of the *BABAR* IFR amounted to 650 mm (600 mm) for the barrel (endcaps), respectively. The overall thickness of the steel in Super$B$ should be upgraded to 920 mm in order

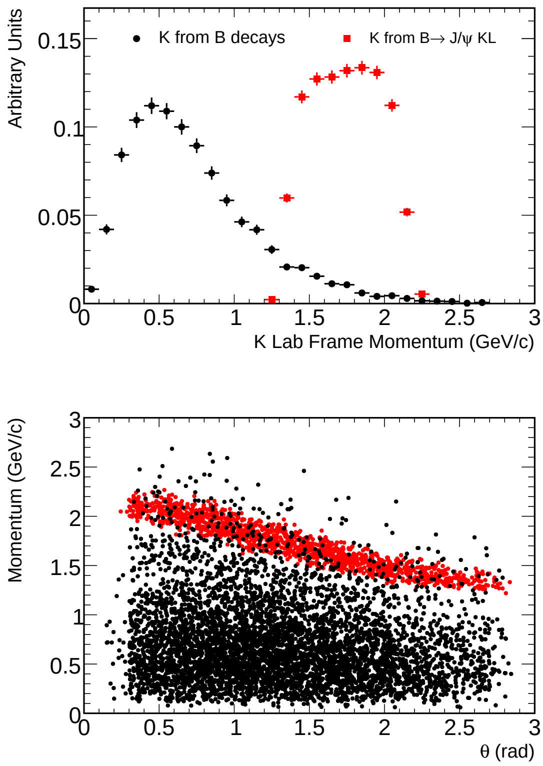

Figure 10.4: Top: momentum distributions for K_L^0 coming from B generic decays (black) and from $B \to J/\psi K_L^0$ (red). Bottom: momentum versus the polar angle for the K_L^0 coming from the same events.

to increase the particle identification capability of the flux return.

In Super*B* 9 layers of scintillator (instead of the 17 detector layers in *BABAR*) will be installed into slots of the flux return. In the barrel, the first layer of detectors will be mounted in front of the first layer of steel and the last layer will be outside the outer wedge plates, therefore only 7 slots will be needed for the detector layers inside the steel. This arrangement is shown in Figure 10.6.

In the doors 7 or 8 gaps will be used for detectors for the forward or backward endcaps, respectively. On the backward side the available space is limited by the horsecollar structure.

In order to minimize the cost, the baseline design foresees the reuse of all the *BABAR* structure, and the increase of the steel thickness by inserting metal plates in those of the 17 slots that are left empty. The nominal thickness of each detector plane is of the order of 25 mm, while the gap width of the *BABAR* wedges and doors have nominal dimension between 30 mm and 35 mm.

The gaps not used by scintillators will be filled with metal plates. To reach the 920 mm of the designed thickness there are 270 mm missing from the *BABAR* parts in the barrel, thus the gaps should be filled with plates of 27 mm. According to preliminary measurements of the *BABAR* barrel gaps, 25 mm plates should fit in all the barrel, except for maybe one or two gaps of the lower sextant. The feasibility of the insertion of 27 mm thick plates should be checked by measuring the gaps with adequate resolution and proper gauges.

The baseline design of the barrel foresees the reuse of the brass plates of *BABAR* and the insertion of 25 mm thick metal plates in the remaining unused gaps; this allows to reach 882 mm of overall metal thickness. The reuse of the six *BABAR* brass layers inside the barrel implies a reduction of the overall thickness by 18 mm compared to the possible use of 25 mm plates. To still reach the design thickness, the insertion of thin (3–5 mm) plates into the gaps where the brass is already located, could be investigated.

For the doors the overall amount of steel can reach the thickness of 850 mm by filling the unused gaps. The geometry of the doors allows for the increase of their overall thickness by adding

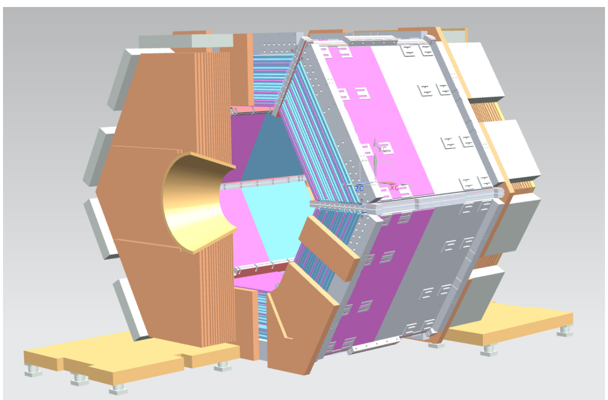

Figure 10.5: The IFR flux return structure.

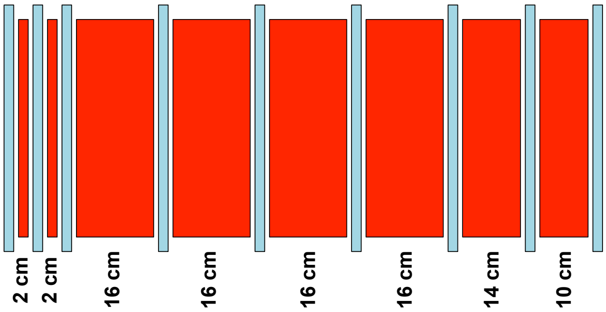

Figure 10.6: Schematic of a possible IFR stratigraphy with 8 active layers; incoming particles travel from left to right.

metal plates on the outer face, as it was done in the forward doors of BABAR, where a plate of 100 mm (4 inches) was added on the outer face to increase the shielding with respect to background. This additional slab can also be reused in Super$B$ to reach the nominal thickness of 900 mm. In the backward door the addition of an external plate 100 mm thick could be incompatible with the presence of the horsecollar, as it would limit the movements needed for the opening and closing of the doors. The thickness that can be added could be of the order of 50 mm, thus the overall thickness can be 900 mm. In order to define the maximum thickness that can be added on the outer face of the backward door, the opening movements of the doors need to be detailed and actual dimensions of the horsecollar must be measured.

The metal composing the plates to be inserted in the unused gaps should match the following criteria:

- non-magnetic material in order to avoid the increase of magnetic forces on the coil;
- small interaction length;
- acceptable flatness;
- reasonable cost.

In BABAR a few layers were filled with brass plates, but nowadays this choice would be very expensive due to the cost of copper, which suffered a strong increase in the last years. A viable alternative choice could be a stainless steel 304L with certified low magnetic permeability. While a reasonable value for the magnetic permeability would be less than 1.04, it might be possible to reach a certified permeability smaller than 1.02, depending on the production process and eventual machining. The flatness of the plates is also important and shall be checked and, if needed, corrected in order to easily fit the plates in the gaps. The weight of the 25 mm stainless steel plates to be inserted is about 110 ton, in addition to the brass already available from BABAR. A large part of this additional mass is due to the filling of the backward doors and the barrel. Another difference of the Super$B$ IFR with respect to BABAR will be in the connection between the barrel wedges and the outer frame (cradle and arches). As the last detector layer will be located outside the wedges, a useful gap for detectors will be realized in between the structure and the wedges, reducing as much as possible the connection between the two parts. The connections will be made only at the corners of the wedges leaving available the substantial part of the top surface of outer wedges to lay down scintillators. As a result, all the parts involved (cradle, arches, outer wedges) might require some workshop intervention in order to modify the relative coupling. The increasing of thickness also results in an increased weight of the structure and the reduction of connections between the outer structure and the wedges reduces the strength and stiffness of the overall steel body. Therefore, the overall deformation of the structure will be verified in detail to ensure that stresses are not critical and deformations are compatible with the required overall precision. The installation procedure is well defined: It will be similar to the BABAR installation, but in addition it can also rely on the procedures that have been documented during the dismantling of BABAR.

During disassembly the BABAR barrel has been measured with a laser tracker. As a result, it will be possible to reference the Super$B$ assembly to what was done in the past. The filling of the gaps in the doors and wedges with plates could be done before the assembly of these parts in the detector, allowing to save some time since those processes can be parallelized. Once inserted, the plates will be fixed in position by welding or by provisional brackets in order to prevent their displacements during handling. Plate insertion could be assigned to an external company and be performed either on the Super$B$ site or in a company workshop, depending on the incidence of costs of the special transportation. The tools like spread beams, scaffolding, platforms, etc., used to assemble and dismount *BABAR* could also be reused for Super$B$, provided that they are reviewed and certified according to Italian law. In this case the cost of shipping, modifying and certifying the tools should be evaluated and compared with the cost for the production of brand new items. A preliminary offer for filling the gaps of *BABAR* with 110 tons of stainless steel plates is around 600 kEuro. The shipping cost of large pieces (wedges, doors, cradle, arches) from the US to Italy is estimated to be about 500 kEuro due to the non-standard dimensions, while import taxes and duty are neglected for the purpose of this document. Other costs encompass the shipping of the various IFR parts that can fit in containers or open-rack platforms and the modifications to cradle, arches and outer wedges that would be required to allow the addition of the outmost layer of detectors.

According to these estimates, the overall cost of reusing the flux return from *BABAR* for Super$B$ will be of the order of 1.5 MEuro.

10.2.2 The Active Detector Choice

The IFR active detectors will cover a surface of approximately 1200 m^2. They will be inserted in the gaps between the iron plates, where access and replacement will be very difficult and in some cases impossible. It is, therefore, necessary that the chosen detector technology is simple and reliable as well as low in cost.

In the Super$B$ environment, the critical regions for backgrounds are the small polar angle sections of the endcaps and the edges of the barrel internal layers, where we estimate that in the hottest regions the rates are of the order of a few 100 $\mathrm{Hz/cm}^2$. These rates are too high for gaseous detectors. While the *BABAR* experience with both RPCs and LSTs has been, in the end, positive, detectors with high rate characteristics are required for the high background regions of Super$B$. A scintillator-based system provides much higher rate capability than the gaseous detectors. For this reason, the baseline technology choice for the Super$B$ detector is extruded plastic scintillator read out through WLS fiber and avalanche photodiode pixels operated in Geiger mode.

Several detection modules will be joined together to fill each IFR layer. Each module will be composed of orthogonal scintillator strips, so that by combining their information each layer can measure space points. A baseline design that guarantees sufficient performance to match the physics requirements has already been established, however the actual design of the modules is not completed yet. The optimization of the number of WLS fibers for each bar and their position as well as some mechanical details will be finalized in the near future based on current R&D studies. The total number of channels in the current design is about 22,000.

For each layer, the modules will be inserted into the iron gaps using appropriate tooling. The front end stage of the readout system will be positioned in the IFR cable conduits near the detector, where they will be readily accessible for testing and maintenance.

10.3 Backgrounds

Machine-related backgrounds are one of the challenges for the Super$B$ detector and background considerations influence several aspects of its design. The IFR detector has been simulated using Super$B$ FullSim based on GEANT4 (see Section 14.1.1). The results of these simulations show that the primary source of background are: radiative Bhabha events, Touschek scattering, pair production, beam-gas scattering, and photons from synchrotron radiation. For a detailed description of the background sources see Chapter 5. For the IFR detector the dominant background source is radiative

Bhabha scattering as will be explained later in this section.

10.3.1 Neutron Background

In this context there is a non-negligible production of neutrons via giant resonances formation [3]. The neutrons produced with this mechanism have energies of some MeV but are moderated when interacting with the detector material. For this reason the neutron energy spectrum in the Super$B$ environment has a very wide range as shown in Figure 5.26 of Sec. 5.12.1 where the neutrons are classified according to their kinetic energy.

Since the neutron spectrum has such a large range, and the interaction with matter strongly depends on it, it is standard to characterize the neutron fluence from a source in terms of an equivalent mono-energetic neutron (1 MeV) fluence [4, 5]. For this reason all neutron rates in this section are normalized to the equivalent of a 1 MeV neutron (n_{eq}).

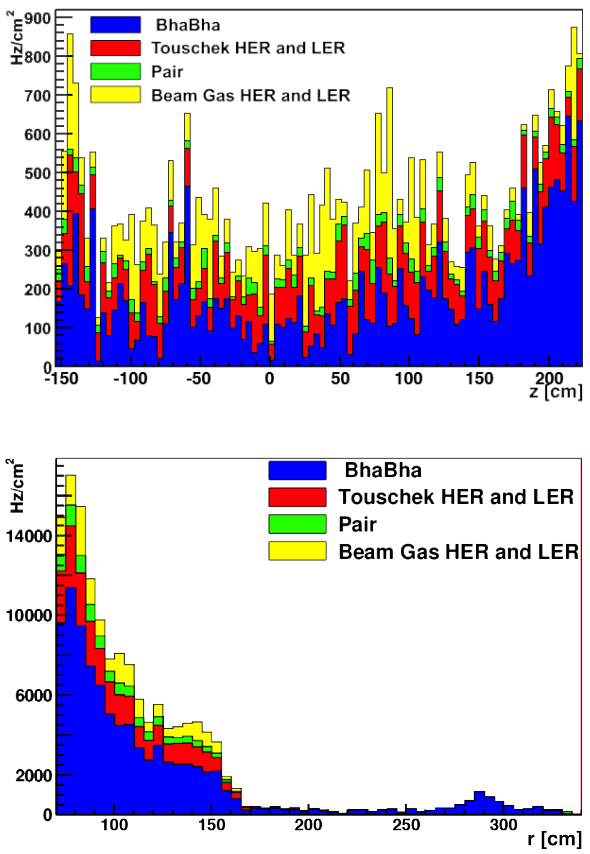

Figure 10.7: Neutron rate on IFR Barrel (top) and Forward Endcap (bottom) innermost layer for different background sources. The rates are normalized to 1 MeV equivalent [4] .

Figure 10.7 shows the neutron rate on the innermost layer (layer 0) for the Barrel and Forward Endcap for the different background sources. The rates are normalized to 1 MeV as explained above, and they include a safety factor ($\times 5$) that takes into account the fact that the simulation could underestimate the real background contribution. The rate on the Forward Endcap layer 0 is higher compared to that of the Barrel layer 0; this is due to the fact that this layer cannot be shielded because of mechanical constraints. The rate corresponding to small radii amounts to 2.5×10^{11} n_{eq}/cm^2 per year, while for larger radii it is 6×10^9 n_{eq}/cm^2.

10.3.2 Charged Particles

Charged-particle backgrounds can directly affect detector performance, since they can produce additional signals in the detector, thus modifying the track reconstruction and consequently the muon identification. Figure 10.8 shows the rate for electrons and positrons coming from different background sources: as for the neutrons, the dominant source of background is radiative Bhabha scattering. The rates shown in Figure 10.8 are for electrons/positrons that deposit more than 150 keV, the nominal energy threshold we have chosen for the detector.

10.3.3 Photon Background

Since all background sources come from QED processes, we also studied the background contribution coming from photons. The photon energy spectrum has a very broad energy range as shown in Figure 10.9. The lines from neutron capture on Hydrogen (2.223 MeV), from annihilation radiation (0.512 MeV), and from neutron capture on ^{10}B (0.48 MeV) are clearly visible (the ^{10}B is used for radiation shielding, see Sec. 5.12.3).

For the IFR, the photon rate contributes only to the radiation dose on the scintillator, since

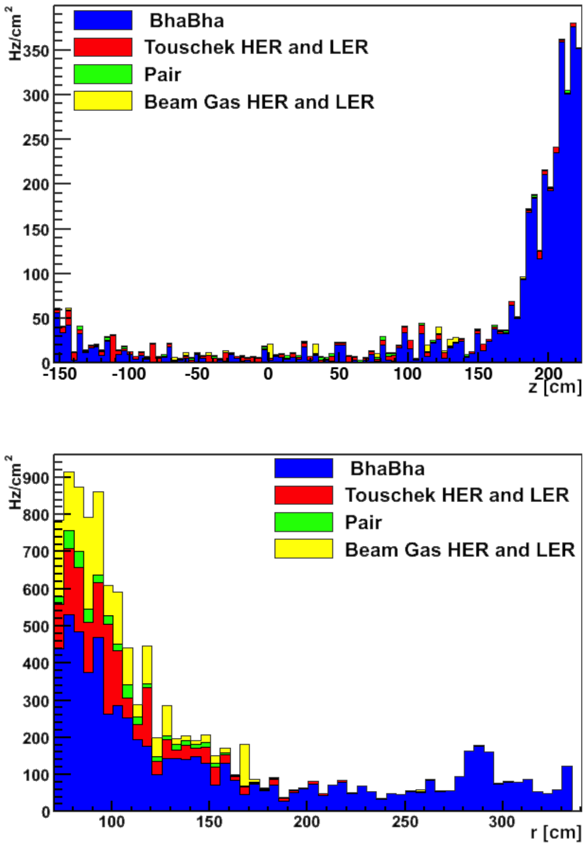

Figure 10.8: Electron/Positron rate for the IFR Barrel (top) and Forward Endcap (bottom) innermost layer due to different background sources. The threshold for the deposited energy is 150 keV.

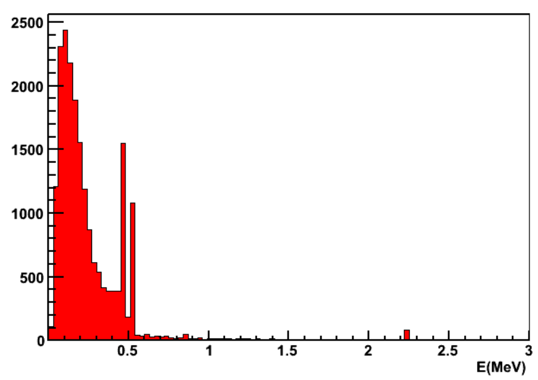

Figure 10.9: Photon energy spectrum for IFR Barrel Layer 0.

the contribution from high energy photons that convert is already taken into account in the rate of charged particles. The photon rates in the innermost layer of the barrel and forward endcap are shown in Fig. 10.10 and, even though high, are not expected to affect detector performance.

10.4 Identification Performance

10.4.1 Muon Detection

Muons are identified by their penetration range in the iron. Above 1.5–2.0 GeV/c, depending on the incident angle, muons penetrate all layers. Non-penetrating muons can be identified from the measured range. More generally, separation of pions from muons is achieved by using a combination of range and hit pattern information.

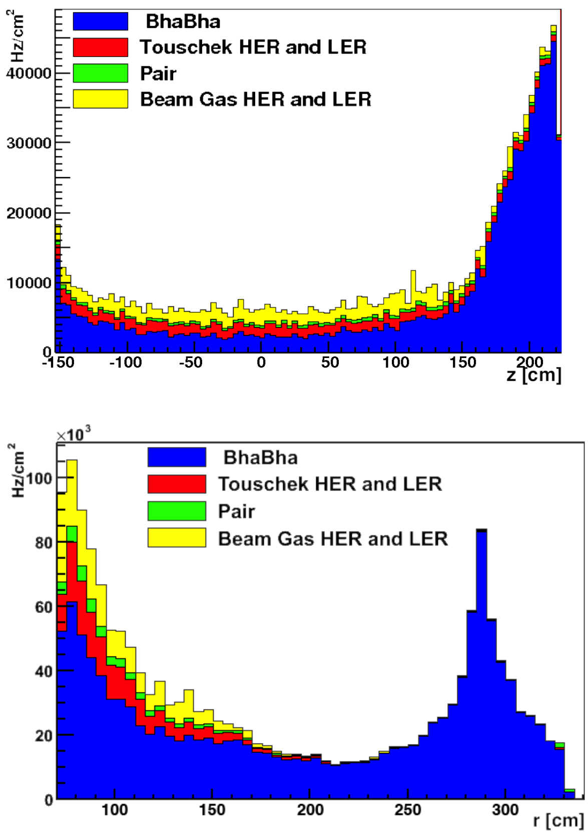

Figure 10.10: Photon rate on IFR Barrel (top) and Forward Endcap (bottom) innermost layer due to different background sources.

In the Super$B$ baseline design the iron from *BABAR* will be reused, so many design parameters are fixed. The main questions that should be addressed (and were already outlined in the *CDR* [6]) are:

- total amount of iron;
- number of active layers;
- size of the scintillation bars.

The Super$B$ full simulation (section 14.1.1) based on GEANT4 is used to properly simulate the detector geometry and the interaction of the particles with the elements of the detector.

The data taken with the IFR prototype have been used to validate the simulation, in particular the algorithm of digitization needed to generate actual hits from the hits generated by GEANT4 (see the prototype data analysis Section 10.5.2.3).

We focus our studies on the forward detector (FWD), but the performance is the same in the other part of the setup. We simulate the binary readout (see section 10.6.1 for details) assuming that each layer is constructed from a set of orthogonal bars of 5 cm size. For each layer the information we have are the coordinate of the scintillator bars traversed by the charged track, for the two orthogonal views, called *X-view* and *Y-view* in the following. Figure 10.11 shows the Y-view hit positions for typical muons or pions fired into the FWD.

As already outlined before, the criteria for distinguishing muons from hadrons are based on the differences in their interaction with matter. A muon track typically generates just one hit in each layer, while hadrons can interact strongly in the iron, resulting in a hadron shower with several lower momentum particles and yieldig multiple hits per layer. It is also possible that few neutrals (neutrons) are produced in the hadronic interaction, travelling long distance before generating a hit. In general, for pion tracks, the number of consecutive active layers is smaller than for muon tracks, and the average number of hits per each hit layer is higher.

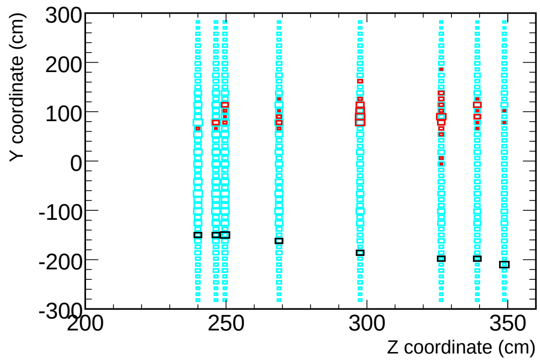

Figure 10.11: Hit position in the Y-view of the FWD detector. The particles come from the nominal interaction point located at (0,0), and are directed to the right. The hit patterns due to a muon (bottom hits) and a pion (top hits) are very different.

The hit positions associated with a track are fitted separately for the X- and Y-view, with the functional form $y = Y(z)$ and $x = X(z)$, where z is the longitudinal coordinate (essentially the layer number) and x and y are the two transverse coordinates given by the bar position for the X- and Y-view, respectively. The functions $Y(z)$ and $X(z)$ are parameterized as second order polynomials.

The sum of the hit residuals squared, called χ^2, and the fitted parameters are used for the muon selection. In particular, the difference between the fit direction and a prediction extrapolated from the inner tracking subdetectors is a very useful variable to suppress part of the contamination from the pion and kaon decays in fly before the first layer of the IFR. So far we take the truth direction information from the MC but these information will also be available when the full track reconstruction will be available.

The amount of the energy released in the EMC, which has a slightly different distribution for muons and pions, can also be used to reduce the pion contamination. The DIRC response could in principle also be used to improve muon detection at lower momenta—so far we have not exploited this option.

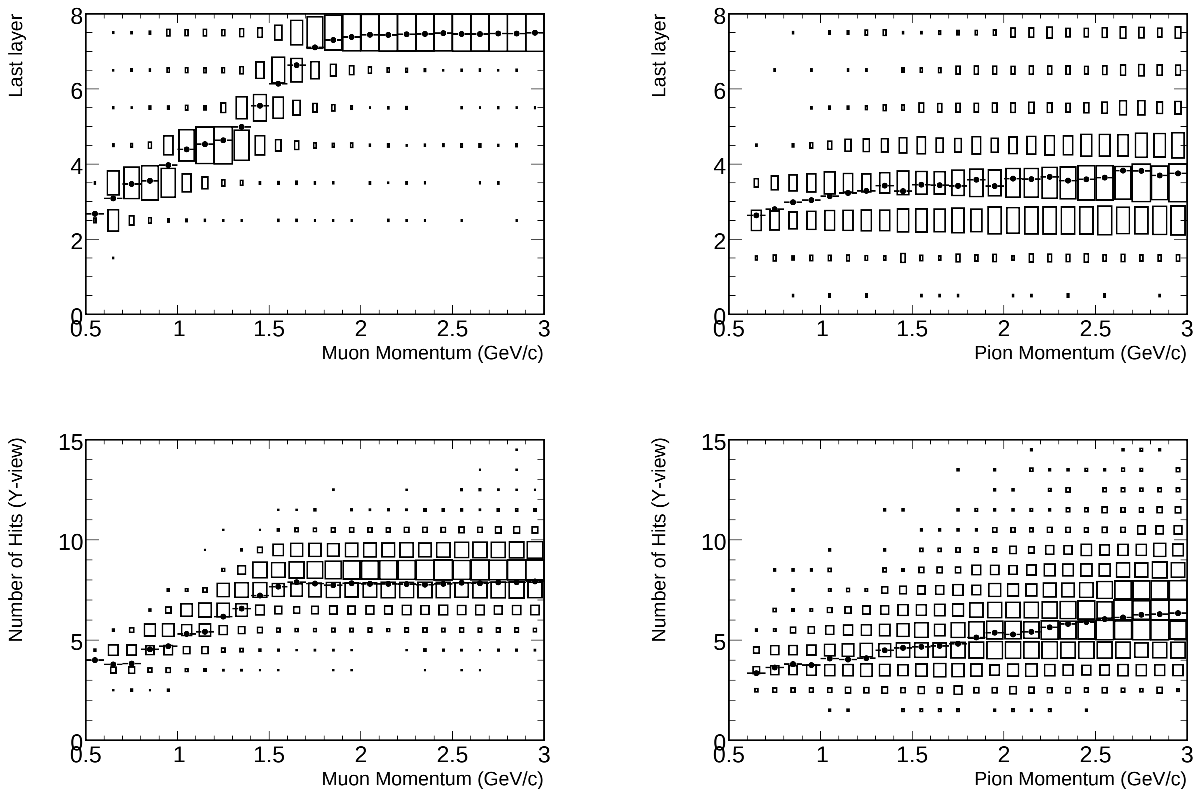

Figure 10.12: Distribution of the last detected layer reached (top), and the number of hits (bottom), as a function of the μ (left) and π (right) momentum. The dots represent the average value of the distribution.

To summarize, we study the muon identification performance, using a consistent set of the following variables:

1. number of hits in the X- and Y-view;
2. number of active layers for the X- and Y-view;
3. the last layer containing hits, which is translated in the number of interaction lengths, λ_{int};
4. track continuity;
5. χ^2 of the hits to the tracks for the X- and Y-view;
6. parameters of the fit track;
7. the total energy released in the EMC.

The average distribution of some of the above variables, as a function of the track momentum, are shown in Figure 10.12. Even simple sequential cuts on these variables, provide a good pion rejection. The experience gained in *BABAR* shows that a multivariate approach gives the best performance for muon identification, even at lower energy when the muons stop inside the IFR volume. Because of the non-trivial correlations between the reconstructed quantities, we used a non-linear multivariate approach, in particular a boosted decision tree (BDT), which turned out to be very powerful and robust with respect to changes in the input parameters.

The BDTs are trained in 7 bins of momentum, ranging from 0.5 to 4 GeV/c. π rejection as functions of μ efficiency for the 0.5–1.0 GeV/c and 1.5–2.0 GeV/c momentum ranges obtained after training are shown in Figure 10.13. The performance can be judged either by comparing these curves or by fixing the level of π rejection and comparing the μ efficiency.

Plots of the μ efficiency as a function of the momentum, with the π-misidentification probability, fixed at 2 % and 5 %, are shown in Figure 10.14.

Muon efficiencies in bins of lepton momentum are also shown in Table 10.1. The performance matches the expectations. Above 1.5 GeV/c, the efficiency is close to 100 % for muons that hit the detector. As expected, there is a drop in the signal efficiency below 1.5 GeV/c, where the muons stop within the IFR volume. With the segmentation and granularity studied so far, about half of the pion contamination is due to the irreducible background from pions decaying in flight.

We also studied different configurations and compared the response with the default configuration, evaluating the impact of the following factors:

- efficiency lost: an overall drop in the single layer efficiency (ϵ_{layer}) to 50 % and 80 %;
- occurrence of a dead layer: ϵ_{layer} = 80 % and absence of the last layer (total amount of the absorber equivalent to 820 mm of iron);
- background: the effect of the background from radiative Bhabhas;

Table 10.1: The efficiency for muon identification (in %) in 7 bins of momentum between 0.5 and 4 GeV/c and for two different value of the pion efficiency.

P(GeV/c)	ϵ_μ ($\epsilon_\pi = 2\,\%$)	ϵ_μ ($\epsilon_\pi = 5\,\%$)
0.5-1.0	27.6±0.6	52.8±0.8
1.0-1.5	50.2±0.4	91.9±0.5
1.5-2.0	96.3±0.3	99.6±0.5
2.0-2.5	97.1±0.3	99.9±0.5
2.5-3.0	96.4±0.3	99.8±0.5
3.0-3.5	97.9±0.3	99.9±0.5
3.5-4.0	95.7±0.3	99.9±0.5

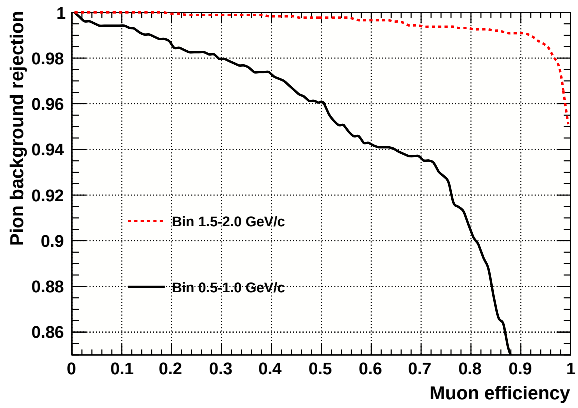

Figure 10.13: Plot of the pion rejection as a function of the muon efficiency. The curves are reported for tracks in the 0.5–1.0 GeV/c (solid line) and 1.5–2.0 GeV/c range (dashed line).

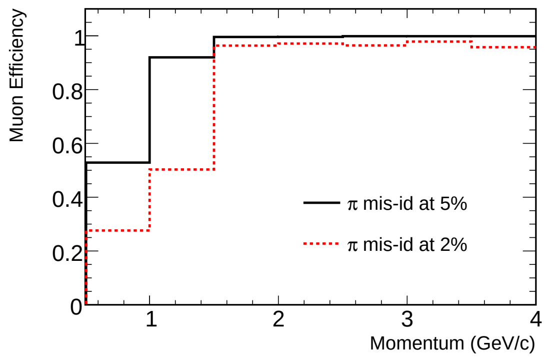

Figure 10.14: Muon efficiency as a function of the momentum, with π mis-identification rate fixed in each momentum bin at 2 % (dashed line) and 5 % (solid line).

- background and efficiency lost: the effect of the machine background and ϵ_{layer} = 80 %.

The resulting efficiencies are compared with the above default values in Tab. 10.2 and Figure 10.15, where we require a π misidentification rate of 5 %. It is evident that for momenta above 1.5 GeV/c, the impact of an average drop in the single layer efficiency at ϵ_{layer} = 80 % is negligible. Moreover, the additional occurrence of the dead last layer does not lead to a significant deterioration of the performance If the average

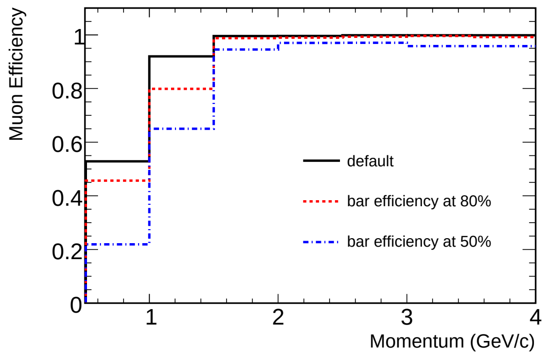

Figure 10.15: Muon efficiency as a function of the momentum, with π misidentification rate fixed at 5 % for the default configuration (solid), compared with the assumpition of a layer efficiency at 80 % (dashed) and 50 % (dashed-dot).

efficiency drop is reduced to 50 %, we observe a large impact at lower momenta. This drop in the μ efficieny can be compensated only by requiring a larger π mis-identification rate.

We studied the impact of the background from Bhabha events by adding samples of background hit events corresponding to five times the expected Bhabha rate to events with single pions and muons. We repeat the optimization of the μ selector obtaining the efficiencies reported in the last two rows of Tab. 10.2. This background contribution reduces the detector performance mainly at lower momenta. Because we limit our study to the forward region, where the background from Bhabha events is more important, the drop in efficiency of about 10 % can be considered the worst case.

10.4.2 K_L Detection

The identification of the K_L mesons in exclusive B decays requires the selection of the IFR hits belonging to the K_L and the determination of the K_L direction from these hits. In the real case, all the clusters near the extrapolation of charged tracks from the inner detectors are eliminated. The remaining clusters are due to neutral particles and mis-associated charged hadrons. A good angular resolution is important to reduce the backgrounds. To study our capability to identify the K_L, and the K_L angular resolution, we fired single K_L with momenta between 0 and 4 GeV/c towards the forward endcap. In Figure 10.16 we show the distribution of the last detector layer reached. About 65 % of the K_L interact in the EMC, and the debris of the interaction generates hits in the IFR. The hit pattern can be used to disentangle the K_L from background, mainly γ from π^0 and merged π^0 in the EMC and charged hadrons.

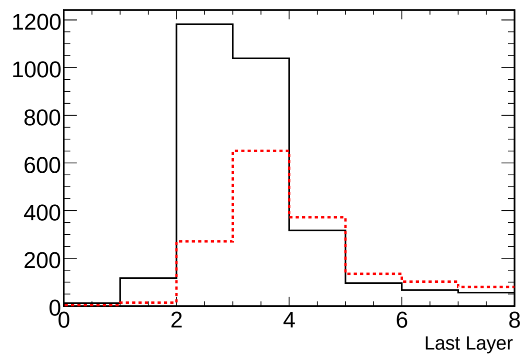

Figure 10.16: Distribution of the last-layer reached for a sample of K_L in the momentum range 0–3 GeV/c for K_L that interact in the EMC (solid) or after the EMC (dashed).

The distribution of the last layer hit is on average higher when the K_L does not interact with the EMC, as can be seen in Figure 10.17. There is a correlation between last-layer and the K_L momentum, but the distribution is quite wide due to the large fluctuations in the hadron interactions, and cannot be used to infer the K_L momentum.

The information that can be extracted by combining measurements from EMC and IFR is limited to the K_L direction. This is very useful when one needs to reconstruct exclusive decays with a K_L in the final state, like the $B \to J/\psi K_L$. The knowledge of the K_L direction allows to constrain the decay kinematics. Moreover, the reconstruction of the K_L in the event is very important for identifying rare decays whose signature is a large missing momentum (e.g., $B \to \tau\nu_\tau$ or $B \to \pi\tau\nu_\tau$). The angular

Table 10.2: Muon efficiency (in %) in 6 different bins of momentum between 0.5 and 3.5 GeV/c for some configurations studied in the simulations. The muon efficiencies are obtained assuming $\epsilon_\pi = 5\,\%$. The statistical uncertainty is 2-5 % in the 0.5-1.0 GeV/c bin, and is less than 1 % for the other bins.

Momentum [GeV/c]	0.5-1.0	1.0-1.5	1.5-2.0	2.0-2.5	2.5-3.0	3.0-3.5
Default	52.5±0.7	91.9±0.5	99.6±0.5	99.6±0.5	99.6±0.5	99.8±0.06
Eff. at 80 %	45.7	79.9	98.8	98.9	99.3	99.6
Eff. at 50 %	21.9	65.0	94.5	97.0	97.1	95.8
Eff. at 80 % and layer 8 dead	44.9	81.9	98.6	98.7	99.2	99.4
Background	53.5	73.5	97.0	98.5	98.8	98.6
Background and eff. at 80 %	36.3	71.3	95.0	96.7	96.2	97.5

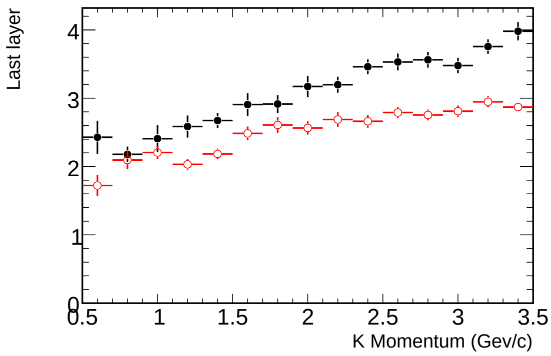

Figure 10.17: The last-layer variable distribution as a function of the K_L momentum. On average, the last-layer is larger when the K_L does not interact in the EMC (○) than when it interacts in the EMC (●).

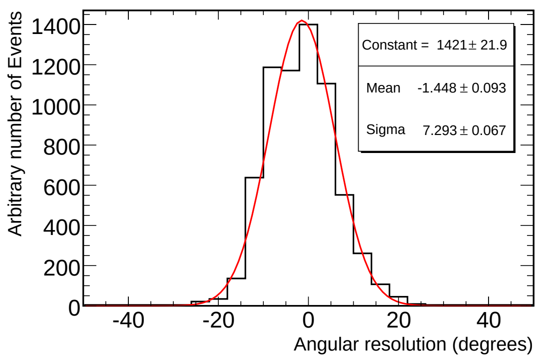

Figure 10.18: K_L angular resolution.

resolution is about 7.3° for K_L generated with a flat momentum distribution between 0 and 4 GeV/c (Figure 10.18).

The impact of the machine background, that affects mainly the first layers in both the forward and the barrel regions, can be important for the K_L identification efficiency and background reduction. These studies require full pattern recognition that has not been performed yet.

10.5 Detector R&D

10.5.1 Module Tests and Results

The IFR detector technology is the result of an extensive R&D program, carried out in the last years and devoted to the choice of the most effective component for each detector component. In more detail, the initial studies were mainly dedicated to:

- scintillators;
- fibers;
- photodetectors.

For practical reasons, due to the many possible combinations, our R&D studies proceeded by comparing two different configurations in which only one element was changed. At the end, the decision was made by balancing the performance and reliability of the detection system with the cost and complexity of the mechanical implementation.

Scintillators

Given the large amount of scintillator needed ($\simeq$ 20 tons), our attention was, since the beginning, focused on rather inexpensive scintillators produced in large quantities by the FNAL-NICADD facility at Fermilab [7]. They are fabricated by extrusion and a thin layer of TiO_2 is co-extruded around the active core. This production method suits particularly well our needs to provide long and thin scintillator strips in the desired shape.

We tested several samples of scintillator strips of external dimensions $1.0 \times 4.5\,\mathrm{cm}^2$ (already available at the FNAL -NICADD facility) and $2.0 \times 4.0\,\mathrm{cm}^2$, considering two options on the positioning of the fibers: those placed in an embedded hole or in surface grooves. The difference in light yield has been measured to be about 10 % higher for the embedded hole option. This relatively small improvement in light yield is offset by the greater difficulty of filling the embedded holes with optical glue. We have therefore chosen the surface grooves as the baseline option.

For the barrel readout, larger strips of dimensions $1 \times 10\,\mathrm{cm}^2$ and $1 \times 5\,\mathrm{cm}^2$, produced by the Vladimir factory near Moscow [8], have been studied. In terms of light yield and attenuation length the Russian scintillators are very similar to the above-mentioned FNAL-NICADD ones.

Optical fibers

Since the attenuation length of the scintillator is rather short ($\simeq$ 35 cm), the light produced by the particle interaction has to be collected and transported to the photodetectors efficiently by Wave Length Shifting (WLS) fibers, In our application the fibers should have a good light yield to ensure a high detection efficiency for fiber lengths in the range between 0.6 and 3 m. The time response was also studied, since originally a TDC readout option was considered (extracting one coordinate from the hit arrival time). While the TDC option could match the required performance, it was deemed to be not reliable enough for implementation on the detector.

We tested WLS fibers from Saint-Gobain (BCF92) [9] and from Kuraray (Y11-300) [10] factories. Both companies produce multiclad fibers with good attenuation length ($\lambda \simeq 3.5$ m) and trapping efficiency ($\varepsilon \simeq 5$ %). The fibers from Kuraray have a higher light yield (about 40 % more), while Saint-Gobain fibers have a faster response ($\simeq$ 2.7 ns versus $\simeq$ 9 ns of the Kuraray), which ensures a better time resolution.

Photodetectors

For the IFR detector the photodetectors converting the light signal from the WLS fibers need to work efficiently in tight spaces and in a high magnetic field environment. Geiger mode avalanche photodiodes (GMAPDs) have been selected as they meet these needs. GMAPDs have high gain ($\simeq 10^5$), low bias voltage ($<$ 100 V), good detection efficiency ($\simeq$ 30 %), fast response (risetime below ns), and are very small (few mm^2) and insensitive to magnetic fields. On the downside they have a relatively high dark count rate (few 100 kHz/mm^2 at 1.5 p.e.) and non-negligible sensitivity to radiation. Among several GMAPDs which are now on the market we concentrated our efforts on the following devices: Silicon Photomultipliers (SiPMs) from IRST-FBK [11], and Multi Pixel Photon Counters (MPPCs) from Hamamatsu [12].

At first, small ($1 \times 1\,\mathrm{mm}^2$) photodetectors had been considered. However, given the small amount of light extracted out of the scintillator with just one fiber, it was soon realized that larger devices are needed to couple more readout fibers, while keeping the active surface (and so the noise) as low as possible. The studies, that led to the prototype design and construction were then performed with $2 \times 2\,\mathrm{mm}^2$ FBK devices. The detection efficiency of such devices is related to the operating parameters and the tolerable dark noise. FBK devices are in general noisier and have a better time resolution than MPPCs. MPPCs have a better light yield and are more sensitive to bias and temperature variations. Additional important parameters to be taken into account for photodetectors are the rate of aging and radiation hardness.

Custom devices from the FBK company with a rectangular active area optimized for our needs ($1.2 \times 3.2\,\mathrm{mm}^2$, and $1.4 \times 3.8\,\mathrm{mm}^2$) were produced and tested for the IFR prototype together with the TDC readout. After we dropped the TDC readout, the Hamamatsu devices seemed to guarantee the best performance and are currently our baseline. Since this technology is rapidly evolving the final choice will depend on the state of the art when this choice is made.

10.5.1.1 Detection module R&D

Number of fibers and geometry. The light collected with cosmics data using one, two or three fibers placed on a scintillator bar has been studied in order to determine the most effective number of fibers. As shown in Figure 10.19, going from one to two fibers provides the gain in light yield of the order of 100 %. The application of three instead of two fibers increases the light yield by another $\sim 50\,\%$, a total gain of three times with respect to one fiber. Using more than three fibers per scintillator bar results in only in small increases of light that will not compensate the increase of the dark count and of the cost. The studies of this issue are still ongoing. From Table 10.3, which summarizes all the results, we can also deduce that the scintillator geometry has a sizable impact on the light output.

Table 10.3: Light yield (the number of photo-electrons) for different readout configurations.

	$1 \times 5\,\mathrm{cm}^2$ strip	$1 \times 10\,\mathrm{cm}^2$ strip
1 fiber	37±3	19±3
2 fibers	71±4	34±3
3 fibers	105±5	60±4

Module length. The studies described above have been performed with the cosmic trigger located at about 40 cm from the photodetector. On the other side the amount of light collected by the SipM is dependent on the path traversed by photons in the fibers (Figure 10.20). The

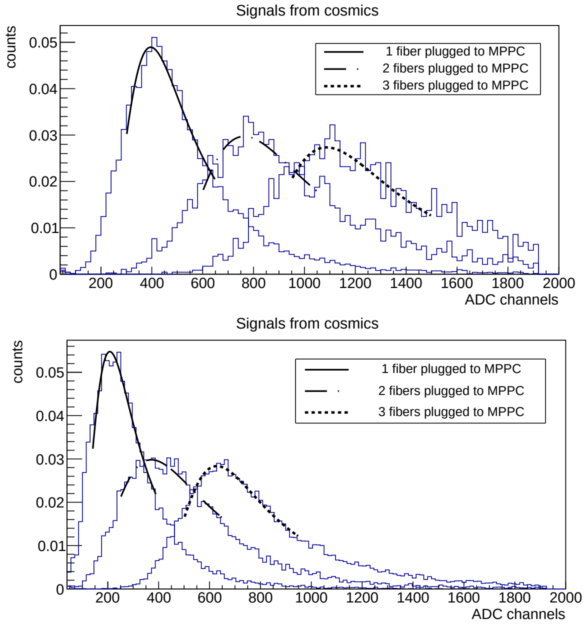

Figure 10.19: Comparison of the light yield with one, two and three fibers readout for 5 cm strip (top) and for 10 cm strip (bottom). All the above plots correspond to data collected with cosmic rays.

dependence of the light yield on the distance of the muon impact point from the photodetector is the result of the light attenuation inside the WLS fiber and the photon propagation and collection along the scintillator strip. The attenuation inside the WLS fibers has been extensively studied in [13]. It can be modeled by the superimposition of two exponentials, one with a short attenuation length of about 0.8 m and another of about 10 m. The long attenuation length is typical for polystyrene fibers and it is rather independent of the wavelength. The component with short attenuation length is due a mechanism of self absorption. In this case the absorption spectrum of the fiber overlaps with the emission spectrum. In particular for the Kuraray fiber this corresponds to relatively low wavelengths from the range between 450 nm and 470 nm. The attenuation due to the self absorption mechanism is dependent on the wavelength and it is greater in the blue-violet region. This mechanism has to be taken into account when coupling the WLS fiber to the photodetector. Generally, devices with more sensitivity in the blue part of the spectrum are more affected by the fiber attenuation length.

Other related studies. Performance required several other studies which will be briefly discussed below. Among them is **gluing** of the fiber to the scintillator groove. It would certainly improve the light collection, but at the price of additional mechanical complications in the production of the modules. The studies revealed that the usage of a Bicron optical epoxy resin provides the gain in light output at the level of almost 50 % higher with respect to the non glued module.

The **polishing** of the fiber surface was investigated in order to understand which material and type of blade would be optimal in order to obtain the best quality of the surface and optimal light transmission. We compared the quality of fiber polishing for natural and synthetic diamond blades; the tests showed a 10 % higher light transmission for the natural diamond option.

Studies have been also performed on the coverage of the free end of the fiber with aluminum (through a sputtering process) in order to reflect back the light which would be lost otherwise. It was estimated that the above technique yields a reflection coefficient of the order of 50 %. Thus we are considering the possibility to aluminize the free end of the fibers to recover part of the light and to reduce the light yield loss as a function of the length.

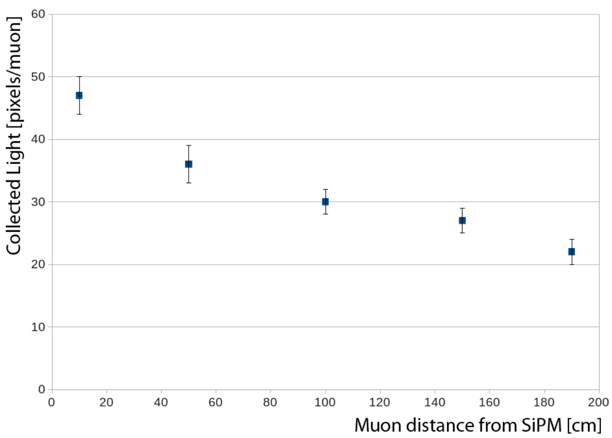

Figure 10.20: Light output as a function of the distance of the cosmic trigger from the photodetector.

10.5.1.2 Radiation damage of photodetectors

Similar to most other solid state devices, SiPMs are rather sensitive to radiation. In the Super*B* environment we expect neutrons to be the main source of background that can cause the aging of IFR photodetectors. An extensive program, started in 2009 with a first test at the ENEA FNG (Frascati Neutron Generator) [14] is currently ongoing to understand the effects of intense neutrons fluxes on SiPMs. A test with low energy neutrons ($\leq$ keV) has just been carried out at the GELINA (GEel LINear Accelerator) [15] facility in Belgium. The next test with higher energy neutrons is foreseen in the following months. The first irradiation test [16] was carried out at the Frascati Neutron Generator facility with neutrons of 2.5 MeV energy [14]. In this test we observed an increase in dark current by a factor of 30 after a dose of $7.3 \times 10^{10}\,\mathrm{n}_{eq}/\mathrm{cm}^2$(1 MeV equivalent). At the same time, the dark count rate increased by a factor of 10 and the average output signal (charge) was reduced to one third. While the increase in the dark current is not a major issue by itself, the increase in dark count and the reduction of the output signal might cause a significant deterioration of the detection efficiency. This reduction was studied by comparing the SiPM signal from cosmics before and after the irradiation and it was estimated to be about 15 % in the worst case (see Figure 10.21). These results are not conclusive yet because the SiPM techology is rapidly improving with time and new tests of recently produced devices (e.g. with an initial dark count rate $\simeq$ a factor 10 lower) are needed.

Since an important fraction of neutrons expected at Super*B* would be in the range of thermal energies, a test at the GELINA facility, where a neutron beam is available with energy

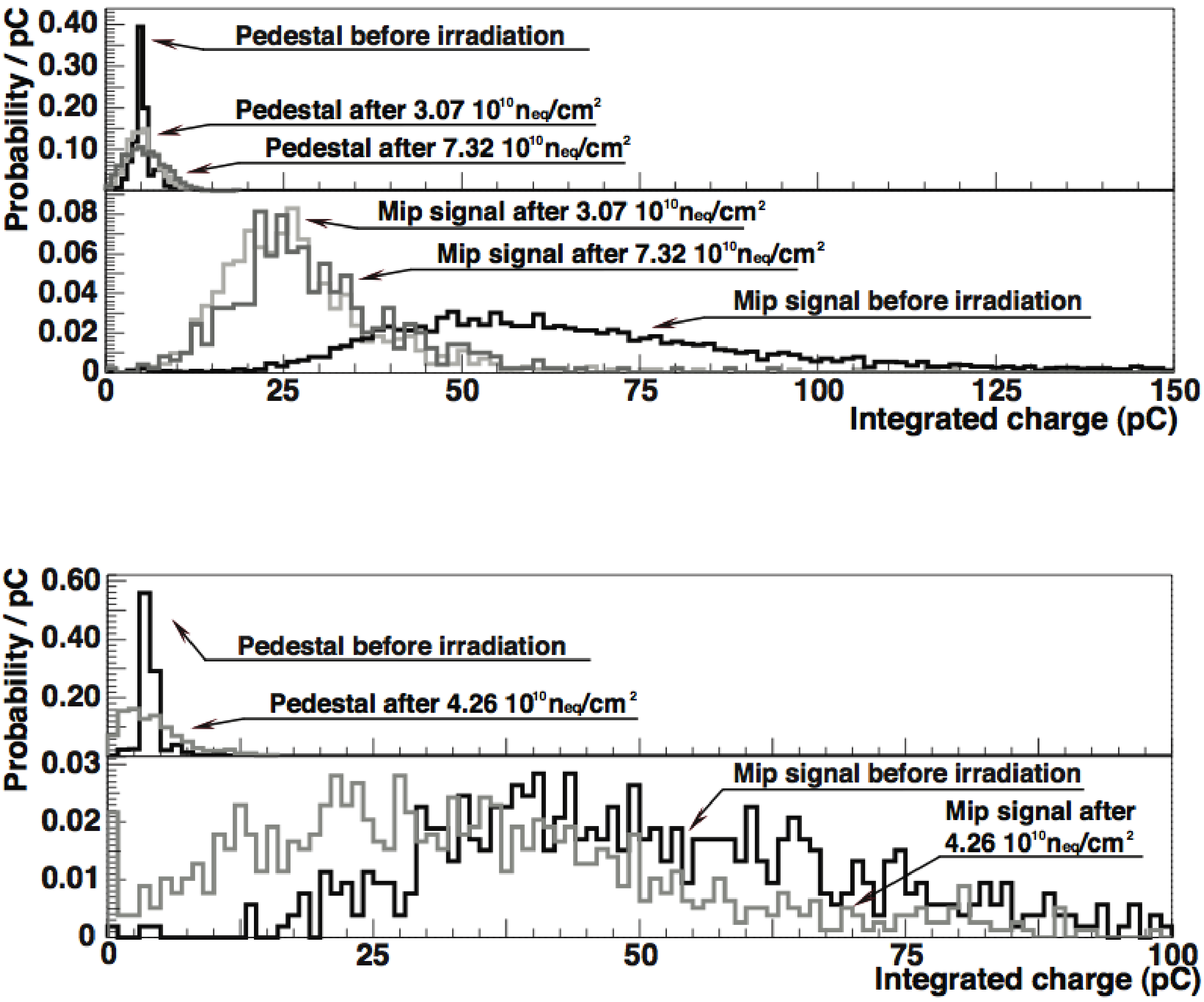

Figure 10.21: Comparison of the cosmic signal distribution before and after the irradiation, for a FBK 1 mm^2 (top) and a MPPC 1 mm^2 (bottom) device.

ranging from tens of meV to about one MeV [15], has been recently carried out on a set of about 25 SiPM devices from AdvanSiD, Hamamatsu and SenSL. For each device, the dark rate and dark current were measured every minute and I-V (*i.e.* current versus voltage) curve and dark rate threshold scan were performed every hour. For some of the devices the dark noise charge spectra have also been acquired. The data analysis is ongoing and preliminary results indicate that the dark current and dark count increase almost linearly starting from about 10^{8} n/cm^2. Figure 10.22 reports the different behavior of the three technologies we tested: the Hamamatsu device seems to be the most sensitive to the radiation. In addition to standard devices, two Hamamatsu radiation hard devices have been tested. The results are still very preliminary, but while the current behavior is not so different with respect to the standard devices, the charge spectra seem to be less affected by the radiation.

10.5.2 Prototype Test and Results

Once a baseline design of the IFR detector was established, a full depth prototype was built and beam-tested at the Fermilab Test Beam Facility [17] using muon and pion beams in the range of interest for Super*B*. The main goal of the beam test was to measure the detector performance: mainly the detection efficiency, the time resolution and the particle identification capability as a function of the beam momentum. The test was also the source of useful experience concerning the future strategy of the construction and assembly of the full detector. In addition, the prototype was used to test two different readout modes for the detection modules. The first one is the "Binary ReadOut" (BiRO), where the SiPM signals, once discriminated, are sampled and digitized, so that the hit coordinate is given only by the scintillator bar position. The BiRO detection modules are composed of two orthogonal layers of strips. The second readout is the "Time Readout", where the discriminated SiPM signals are read by a TDC system: this way one coordinate is given by the strip position and the other by the hit arrival time. Therefore, only one layer of strips is needed for the Time Readout.

10.5.2.1 Design and construction of the IFR prototype

Figure 10.23 shows a picture of the prototype. It represents a section of $60 \times 60\,\mathrm{cm}^2$ of the IFR detector, with the full depth, and an iron structure designed to have the possibility of moving the active layers in different positions, in order to change the scintillator-iron segmentation and determine the configuration being the most effective for particle identification.

Twelve active modules were assembled in the prototype (as summarized in Table 10.4): four of them were "standard" in terms of the readout (BiRO and TDC) and designed according to our baseline approach. The remaining four were "special" *i.e.* designed to estimate the impact of individual components (larger fibers, different photodetector, etc.).

Figure 10.24 shows the general internal structure of an active module of the prototype. It is composed of two layers of orthogonal scintillating bars, 5 cm wide and 50 cm long with three fibers in each bar. One of the fibers is housed in surface grooves and the remaining two in embedded holes. For the TDC modules, the scintillator bars were 2 cm thick, so a single layer was present. The fibers are collected on cylindrical supports and then coupled to the SiPM by means of custom made plastic (plexiglas) cou-

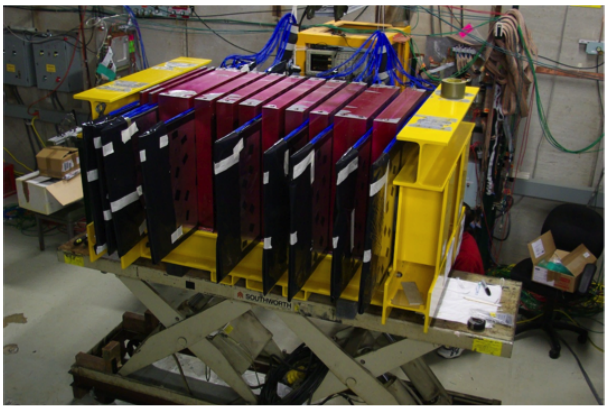

Figure 10.23: A picture of the IFR prototype during the beam test a Fermilab.

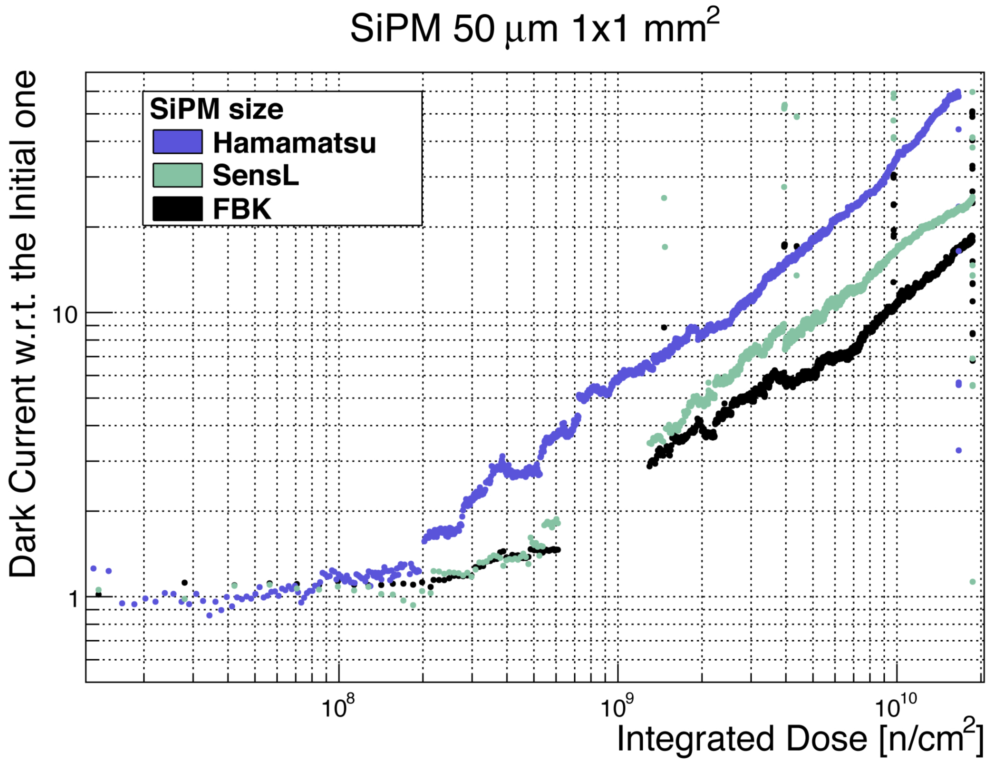

Figure 10.22: Dark current as function of the integrated neutron dose during the GELINA test.

Table 10.4: Parameters of the modules built for the IFR prototype.

Id. #	Scint. (mm^2)	Fibers type - ϕ (mm)	SiPM $\mathcal{A}$(mm^2)	Readout
1	20×40	Bc - 1.0	1.2×3.2	TDC
2	20×40	Bc - 1.0	1.2×3.2	TDC
3	20×40	Bc - 1.0	1.2×3.2	TDC
4	20×40	Bc - 1.0	1.2×3.2	TDC
5	20×40	Bc - 1.2	1.4×3.8	TDC
6	20×40	Bc - 1.2	round	TDC
7	20×40	Bc - 1.0	MPPC	TDC
8	10×45	Ku - 1.2	1.4×3.8	BiRO
9	10×45	Ku - 1.2	1.4×3.8	BiRO
10	10×45	Ku - 1.2	1.4×3.8	BiRO
11	10×45	Ku - 1.2	1.4×3.8	BiRO
12	10×45	Ku - 1.2	round	BiRO

plers. Their lengths range from 45 to 370 cm for BiRO readout; the fibers for the TDC readout have a fixed length of 4 m.

The front-end electronics providing the bias to the SiPMs and amplification and discrimination of signals was based on commercial amplifiers MMIC BGA2748 and BGA 2716. The data acquisition and online control systems were custom-designed specifically for the experimental setup of the test beam.

10.5.2.2 Beam Tests

Beam Test Setup and data taking. To assess the detection and identification performance the prototype has been extensively tested with a muon and pion beam delivered by the Fermilab Test Beam Facility at FNAL [17]. Muons and pions were produced by means of a proton beam impingingon an Aluminum target. The range of particle momenta was selected by two dipoles with a spread of about 5-10 % at 10 GeV/c and getting worse at lower momenta. In the mo-

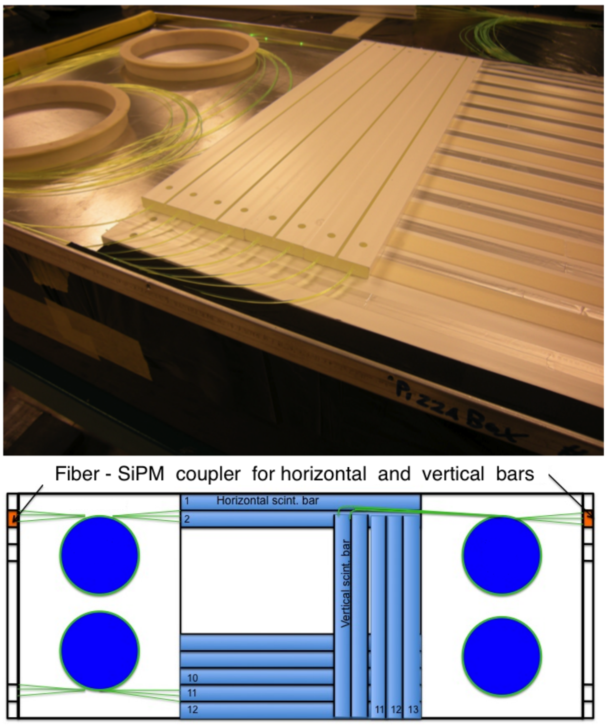

Figure 10.24: A picture and a scheme of a BiRO active module of the prototype.

mentum range we explored (1–10 GeV/c) the resulting beam is composed mainly of electrons and pions, with a small admixture of muons (less than 5 %). Electrons were removed based on the veto trigger from the Cherenkov counter (Figure 10.25). Muons and pions with momenta above 2 GeV/c were selected using another Cherenkov signal. For momenta below 2 GeV/c no external particle identification information was available, so these data have been used only for cross checks. The tagging capabilities of the Cherenkov counters were deteriorating at smaller momenta. This was caused mainly by the increase in the beam diameter from a few cm at 8 GeV/c to 20–30 cm at 1 GeV/c as well as by the spread in the beam momentum. As a result it was hard to select clean muon and pion samples below 5 GeV/c.

Four beam tests have been performed between December 2010 and March 2012. While the basic concept, shown in Figure 10.25, remained stable, the apparatus was modified for each test, taking into account the experience gathered in the previous runs.

The setup encompassed:

- Cherenkov counters for particle identification, placed about 20 m upstream the prototype;
- a slab of 16 cm of iron upstream of the apparatus to “simulate” the material in front of the IFR detector in the Super$B$ experiment and to get rid of most of the electrons;
- two or three scintillator detectors with photomultipliers (PMT) readout placed between the iron and the IFR prototype as trigger;
- the IFR prototype;
- another set of scintillator detectors placed behind the prototype to select tracks going through the prototype.

All the signals from PMTs and Cherenkov counters were acquired with the prototype TDC system in order to refine trigger requests offline.

Table 10.5 shows the data samples collected at different energies during the four beam tests along with the trigger used to select the events.

Table 10.5: Beam test data sample.

beam mom. (MeV/c)	min. bias (k evt)	muon trigger (k evt)	pion trigger (k evt)	μ/π trigger (k evt)
1	50	-	-	386
2	60	-	-	236
3	126	134	89	155
4	101	106	76	129
5	262	87	158	25
6	230	218	230	100
8	236	375	413	125

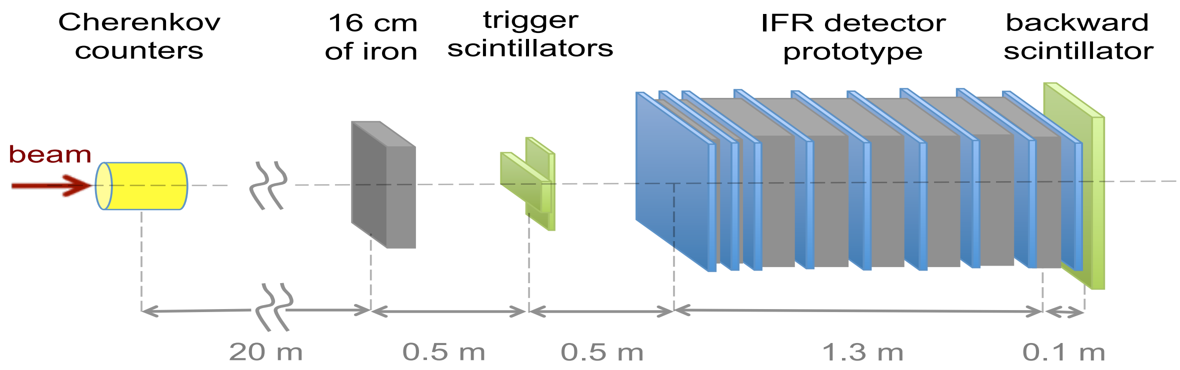

Figure 10.25: The layout of the Fermilab beam test setup.

10.5.2.3 Tests Results

Data from different runs have been analyzed in order to study the detection performance and the muon identification capability of the IFR prototype. The resuts are described in detail in the following paragraphs.

During all four tests the full setup, including the prototype detector was working reliably with almost 100 % data taking efficiency. After almost 18 months of tests (both with the accelerator beam and cosmics) only three channels out of 237 failed; their damage was caused by shipping and handling of the detector during installation and dismounting.

Detection Performance. One of the major goals of beam tests was to confirm the R&D results on a larger scale to assure that the system is capable not only to detect particle hits but also to reconstruct three dimensional tracks passing through it. Therefore, not only the high detection efficiency, but also the spatial resolution is of a paramount importance; correspondingly for the TDC readout modules the time resolution has also been also evaluated.

The detection efficiency has been evaluated using muon events passing through the entire prototype and selected using the backward scintillators. Results are shown in Figure 10.26 both for the binary and time readout modules. The detection efficiency is clearly dependent on the length of the light path inside the fibers, which varies from module to module, but its value exceeds 95 % in almost any case. The only exception is for the module in layer number two for which the light path amounted to almost 4 meters, however, such long light paths are not foreseen in the final detector design. The detection efficiency depends also on the electronic threshold. Figure 10.27 shows that, except for the module with the long fibers (layer number two), there is room to raise the threshold from the current nominal value, that is 3.5 photoelectrons, to 4.5 in order to reduce the SiPM dark count with very small efficiency loss. All these conclusions are consistent with the R&D results.

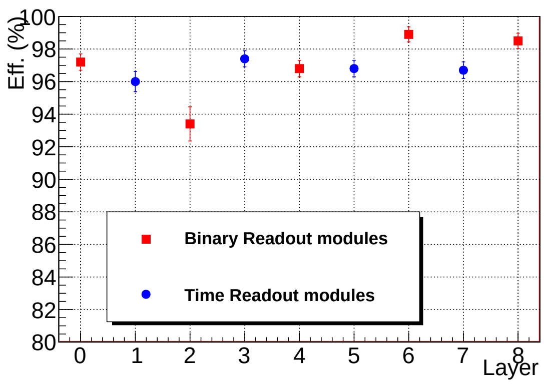

Figure 10.26: The detection efficiency of each individual layer of the prototype as measured during the first beam test at Fermilab in December 2010.

The beam tests have also shown that the time resolution linearly depends on the fiber length, in agreement with our R&D results. The average time resolution was measured to be about

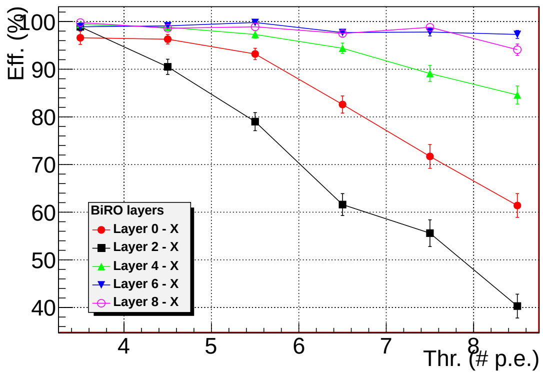

Figure 10.27: The detection efficiency of each individual layer of the prototype as a function of the electronic threshold (measured in the number of photoelectrons) for the BiRO modules.

1.2 ns, which would be sufficient to guarantee the spatial resolution needed to match the physics performance requirements. On the other hand, there is very little space for improvements in the time resolution and moreover the risk of worsening the performance with the aging of the photodetectors is rather high.

The last important factor estimated during beam tests was the average strip occupancy caused by the SiPM dark noise. It was evaluated to be about 1.7 % both with a random trigger and using out-of-time hits.

Muon Identification Results The IFR muon identification performance described in section 10.4.1 is based on studies with Monte Carlo (MC) events. The prototype data have been compared with the respective MC samples and the simulation parameters have been tuned in order to ensure that the MC reproduces the prototype behavior (hit and particle multiplicity, noise, detection efficiency and time response). The extensive data-MC comparisons and tuning have been done in order to reproduce the prototype particle identification performance with the MC. For the reasons explained above, only the subsample of data collected at 8 GeV/c have been used in the tuning procedure (to improve the purity of the sample offline cuts on the hits arrival time in the Cherenkov and in the trigger scintillators have been performed).

Therefore a complete simulation of the prototype has been implemented within the Super*B* Full Simulation (see Sec. 14.1.1) framework. The simulation included the Cherenkov counters and the scintillators used in the trigger, the prototype iron structure and the position of the momentum-selecting magnet (about 70 m upstream with respect to the prototype) — important for taking into account the particles decaying in flight.

Beam background and SiPM dark count are parameters of paramount importance to reproduce the beam test conditions. To estimate their contribution we used the sampling feature of the BiRO readout with muon events to disentangle the signal, beam and electronic components of the hit occupancy as shown in Figure 10.28: each sample corresponds to a 12.5 ns interval. The electronic component, due to SiPM dark rate, is flat and is estimated using the last three samples. Muon hits arrive within few nanoseconds and the hit time depends also on the light path into the fibers: the signal component peaks between sample number 1, 2 and 3; the beam-related background (mainly tails from electron showers) is distributed around the signal peak, for its estimation we considered samples 0 and from 4 to 6; Beam and electronic background have been evaluated strip by strip on all the prototype channels and their occupancy has been added to the simulation.

Similarly, the detection efficiency has been studied layer by layer using 8 GeV muon data; the layer inefficiency has been added to the simulation by tuning a cut on the MC hit energy loss.

As last part of the tuning procedure we simulate a multi-particle component: the beam composition, given by the beam test facility [17], is made of about 10 % of multi-particle events, in our case mostly pions; we randomly added pion events to the 10 % of each MC sample. The effect of this addition is shown in Figure 10.29.

After the tuning, the data-MC agreement of all the variables we used as BDT input for muon and pion samples was good, see Section 10.4.1 for a complete description of the BDT selec-

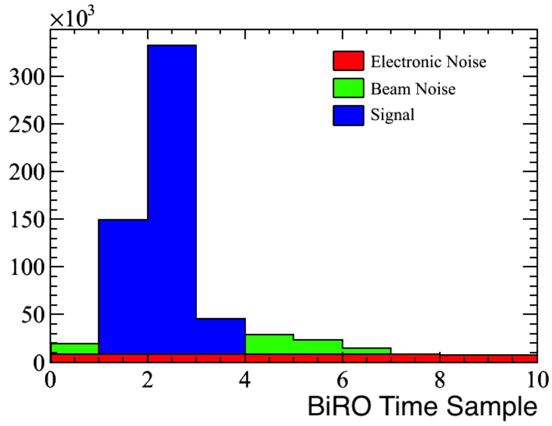

Figure 10.28: Hit occupancy for muon events as a function of the binary readout sample; each sample corresponds to 12.5 ns. Muon hits peak around sample number 2, the noise due to the SiPM dark count is flat over entire region while the remaining component is ascribed to beam background.

tor. The BDT was then trained separately on data and MC sub-samples and applied to the remaining datasets; the signal efficiency - background rejection curves (ROC) are reported in Figure 10.30: the consistency between data and MC is within 5 % in the worst case. Therefore, we can conclude that the tuned MC at 8 GeV is a good description of the beam test data and we can use the tuning information to extend particle identification studies with MC to increase the statistics and using the Super$B$ geometry.

10.6 Baseline Design of the IFR Detector

10.6.1 Detector Layout

The layout of the IFR detector takes into account several requirements and limitations. They will be underlined below before the detailed discussion of the detector design.

The IFR system must have high efficiency for selecting penetrating particles such as muons, while at the same time rejecting charged hadrons (mostly pions and kaons) in a wide momentum range, from approximately 0.5 GeV/c to 5 GeV/c.

The possibility of reusing the *BABAR* iron offers a cheap solution for the flux return struc-

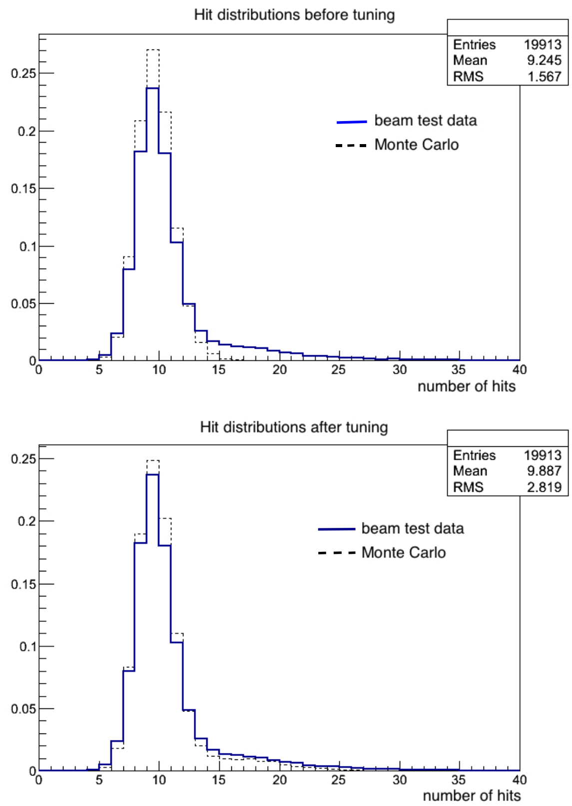

Figure 10.29: Data - Monte Carlo comparisons for the hit multiplicity before (top) and after (bottom) the addition of a secondary particle to the Monte Carlo sample.

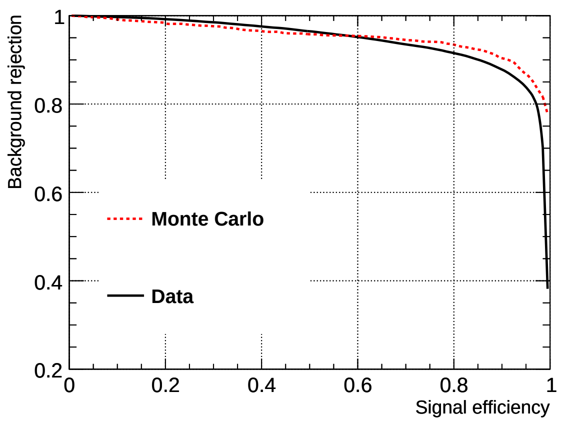

Figure 10.30: ROC curve for BDT selector with prototype data (solid line) and Monte Carlo (dashed line).

ture, but it introduces some mechanical constraints which have a significant influence on the detector design. In particular, the available space for the detection modules is limited by the dimension of the existing gaps (25 mm). Also, the thickness of the absorber material is restricted to about 90 cm of iron and the clearances and paths for cables and other utilities must follow the existing structure of the flux return.

The design of the IFR detector should also take into account the presence of the accelerator-induced backgrounds that can potentially reduce the quality of particle identification as well as speed up aging of the system components. These two issues are discussed in the next paragraphs.

The maximum rate of the accelerator-induced background is expected in the forward endcap of the IFR. A detailed Monte Carlo simulation yielded that the above background should not exceed 1 kHz/cm^2 and that it decreases rapidly with the distance from the beam axis. It was checked that with the above background estimation multiplied by a safety factor of five, the performance of muon identification is still acceptable.

For what concerns the aging of the photodetectors the main hazard comes from the high flux of neutrons originating from radiative Bhabha events. Recent neutron irradiation tests yielded [16, 18] that SiPM devices continue to work at least up to a fluence of $\sim 10^{11} - 10^{12}\,\mathrm{n}_{eq}/\mathrm{cm}^2$. However, they suffer a considerable increase of dark rate and dark current and an associated loss in the light yield lower than 20 %, depending on the cell size. The neutron flux in the part of the IFR where the SiPMs will be located was estimated from Monte Carlo simulations to be in the range from 50 Hz/cm^2 to 500 Hz/cm^2. We use such information to identify the safest place for the SiPM.

R&D results have revealed that using $1 \times 5\,\mathrm{cm}^2$ ($1 \times 10\,\mathrm{cm}^2$) strips, and with three fibers for each strip, it is feasible to build a detection module of 2.5 m (1 m) length. For such a module the detection efficiency would exceed 95 % and the increase of the dark count rate due to the neutron irradiation damage could be kept under control by applying a sufficiently high threshold. Moreover, beam tests on a large scale prototype have demonstrated that the muon identification capability and the reliability of the system are fully acceptable.

The design of the IFR detector should also take into account its abilities to provide a reasonable reconstruction of K_L^0s mesons. Monte Carlo simulations and previous experience with the *BABAR* experiment led to the conclusion that maintaining the existing fine segmentation of the three internal layers is sufficient for this goal.

Module concept. The basic element of the IFR detector is composed of an extruded plastic scintillator with three WLS fibers located in machined grooves and a SiPM installed as shown in Figure 10.31a. The scintillator will be the one produced by the FNAL-NICADD facility and the fibers will be produced by the Kuraray company (Y11-300, with a diameter of 1.2 mm). The $3\times3\,\mathrm{mm}^2$ MPPCs produced by Hamamatsu with a cell size of 50 μm have been chosen as photodetectors.

From one end of each scintillator bar the WLS fibers are brought in front of a SiPM mounted on a PCB. A coaxial cable then connects the PCB with the front-end stage of the IFR readout. The scintillator is wrapped with an aluminum foil reflecting the light toward the fibers. The detector is composed of two perpendicular layers of scintillators. The scintillator bars, together with the SiPM carrier PCBs and the signal cables, will be enclosed in aluminum dark boxes. Their main purpose will be to shield the assembly from the ambient light and to provide the necessary mechanical robustness. The above structure will be, in the following, referred to as ”module”.

The modules will be inserted, in nine gaps of the iron structure, both in the barrel and endcap sections of the IFR. Each of these gaps instrumented with modules will be referred as an "active layer". Figure 10.31b shows a few modules installed in the barrel section of the IFR, with the aluminum ”envelopes” removed in or-

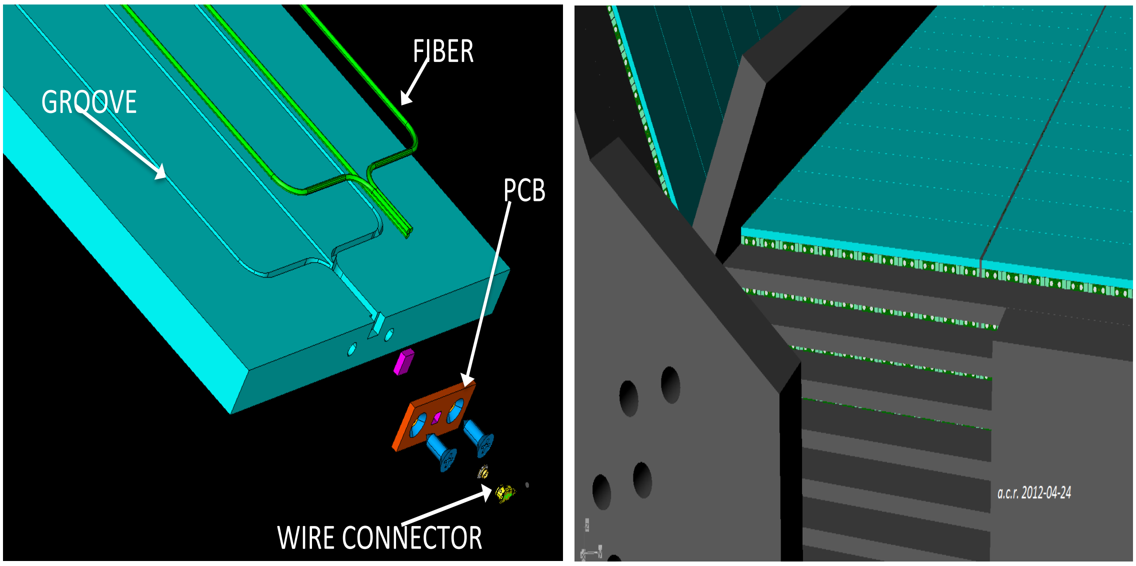

(a) Layout of the module, showing details of the fiber geometry and of the SiPM-PCB connection.

(b) Location of the scintillator bars and SiPMs inside the IFR barrel. The innermost layer is shown with the modules' enclosure removed.

Figure 10.31: Concept of the IFR module design.

der to show the scintillator's orientation. The tight coupling of the SiPM to the WLS fibers has been decided as it maximizes the number of converted photoelectrons. This choice determines in turn that the coupling between the SiPMs and the first stage of the IFR signal processing chain must be done through coaxial cables and connectors.

The barrel modules will be of rectangular shape and each module will be composed of a layer of ϕ-strips superimposed on a layer of z-strips. The ϕ-strips will be 10 mm thick, 50 mm wide, and 1800 mm long. The number of these strips will vary from layer to layer. The z-strips will be 10 mm thick, 106 mm wide and their length varies from 650 mm to 800 mm. The number of strips for each module is 17 except for the two outermost layers that will be shorter and will contain 15 strips. The number of modules of each active layer is 6 or 8, depending on the gap width. Since each module covers half of the gap length along the beam direction, we will have half of the modules facing forward and half on the backward side. As a result the cables will be routed on both sides of the barrel. Figure 10.32 shows the innermost and the outermost layers instrumented with forward modules. Modules of the outermost layer will have a special design due to the details of the mechanical connection between the last iron plate and the external structure.

Gap dimensions as well as the number of channels and modules for each barrel layer are collected in Table 10.6.

The endcap modules. There will be six wide endcap modules with each active layer as dictated by the reuse of the *BABAR* flux return (Figure 10.33). While top and bottom modules will have the same size, the dimensions of the middle ones will depend on the internal radius of the hole, that is conical for the forward and cylindrical for the backward endcap. Each module will be instrumented with x and y strips of the same thickness (10 mm) and width (50 mm). The strip lengths will range from about 500 mm up to about 2500 mm. Table 10.7 provides the information about the number of strips in the endcap modules.

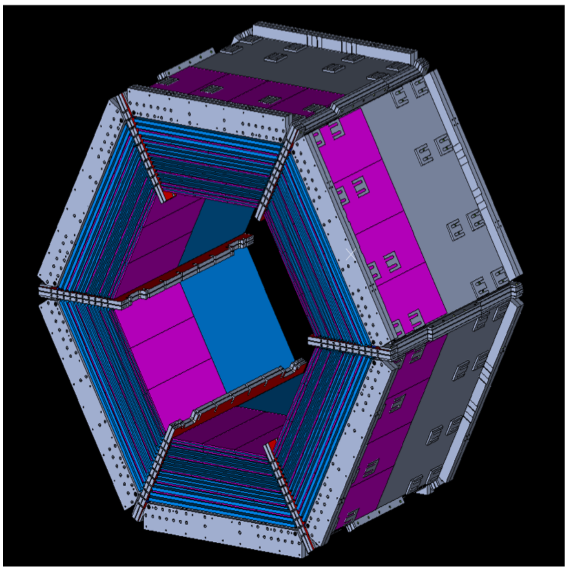

Figure 10.32: Layout of the barrel modules of the IFR detector.

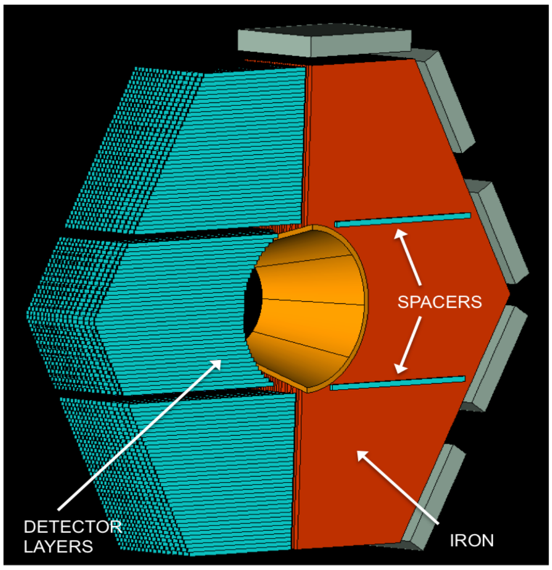

Figure 10.33: Layout of the endcap modules of the IFR detector.

Table 10.6: The numbers of modules and strips per modules in layers of the barrel part of the IFR detector.

Layer	n. of modules	ϕ-strips per modules	z-strips per modules
1	6	13	17 (65 cm)
2	6	13	17 (65 cm)
3	6	13	17 (65 cm)
4	6	15	17 (75 cm)
5	8	12	17 (60 cm)
6	8	13	17 (65 cm)
7	8	14	17 (70 cm)
8	8	15	15 (75 cm)
9	8	16	15 (80 cm)

Table 10.7: The numbers of strips in endcap modules.

	Top modules	Middle modules	Bottom modules
x strips	51	64	51
y strips	37	36	37
Total strips	88	100	88

10.6.2 Chamber Construction, Assembly and Quality Control

Module assembly procedure

The assembly of the modules requires a careful production plan, defining, in particular, the requirements for the place, timing, tooling and quality control. The procedure can be split into different operations, some of which are sequential, while others will occur in parallel. The main steps of the assembly will be described below.

Manufacturing of the scintillators encompasses their cutting the scintillator to the proper length, labeling and stocking. It can be divided into the following operations:

1. positioning of the scintillator on the machine;
2. machining the linear grooves;
3. machining the curved grooves;
4. cleaning of the grooves and the scintillator;
5. checking the grooves quality;
6. stocking the scintillator.

The operations 2 and 3 are to be done in parallel on the same machine equipped with two heads; the first one with a cutting disk making the linear grooves, and the second one with a cylindrical milling cutter making the curved grooves.

Preparation of the WLS fibers: the three fibers belonging to the same strip are to be inserted and clamped into a plexiglass connector, machined and polished. All the fibers and connectors comprising a single module are to be polished at the same time. The manufacturing of the scintillators and the preparation of the fibers have to be done in parallel.

Scintillators and fibers assembly. This operation encompasses :

1. the positioning of the scintillator on the machine, inserting the plexiglass connector and fibers into the grooves;
2. glueing the fibers into the grooves;
3. checking the quality of the glueing (diffusion of the resin and air bubbles);
4. stocking in the curing station.

A two component optical epoxy resin is used for the glueing processes. The resin is characterized by low viscosity and by a liquid consistency. These features facilitate the diffusion and avoids the air bubbles due to the gluing not under vacuum. The curing time lasts three days and when the production is started the steps which will be described in the following are to be shifted by this time period.

Covering scintillators and fibers with thin aluminum foils. The scintillators with the fibers are to be wrapped with a thin reflecting aluminum foil in order to maximize the light collected by the fibers themselves.

The module assembly. The wrapped scintillators are accommodated into the box defining the module. The scintillators are, one by one, secured by double sided ribbons into the box comprising both the longitudinal and the transversal layer. The PCB and the SiPM are assembled in front of the polished surfaces of the fibers by screws. Finally, the read-out cables are connected to the PCB connector. Thus, the module assembly will proceed as follows:

1. fixing the ribbon into the inner surfaces of the box;
2. positioning the scintillator;
3. mounting the PCB and SiPM;
4. checking the reference position;
5. connecting the read-out cable;
6. fixing the ribbon between the two layers;
7. closing the box;
8. checking the module.

Tooling for module assembly. Proper tooling will be developed to automate some of the steps of the module preparation, in particular for:

- manufacturing of the scintillators;
- polishing of the fibers;
- dispensing the resin on the fibers.

Quality Control procedures

Quality Control (QC) encompasses a set of tests to be performed in scheduled phases during production and assembly of the modules. These are:

1. **QC on finished scintillators** to validate the quality of fiber grooves by visual inspection in search for any macroscopic defects.
2. **QC test on finished fibers** to check the quality of polished surfaces. This plays a crucial role as far as the efficiency of the detected light is concerned. The quality of samples of polished fibers will be tested versus the aging time of the polishing tool. The sample to be tested will be inserted in a black box and will be illuminated with a source of light like a pulsed LED or a laser. Then, in order to determine the status of the polished surface and of the tool, the efficiency of light collection will be measured using the photodetectors coupled to fibers.

3. **QC test on finished bars** to verify a global status of various couplings like the ones between the following pairs of components: scintillator-glued fibers, photodetector-fibers and photodetectors-PCB-cables. In order to isolate the bars from external light, a cap will be placed on the test table and the QC will be performed on a group of bars. During the test the photodetector will be powered on and the single rate and dark current will be monitored in order to determine the status of channels. In addition a scan test will be done by passing a radioactive source orthogonally over a set of scintillator bars close to the PCB side.

4. **QC test on finished modules** performed in groups of predefined number of them in a cosmic ray station. Taking into account the planned production rate, five modules per week would be a reasonable number. Then a QC test lasting a week would allow to obtain precise information about the status of the modules. A cosmic ray station is equipped with two extra layers for triggering cosmic events and allows for tests of of the status of each channel together with the verification of their efficiency and uniformity, based on reconstructed tracks.

10.7 Photodetectors and PCB

The baseline design for the IFR detector foresees that the photodetector would be applied at the end of each bar. A suitable PCB will be designed to support the photodetector as well as the miniature connector to a thin coaxial cable.

10.7.1 Photodetector PCB and optical coupling to fibers

The details of the assembly to be installed at the end of each scintillator bar are shown in Figure 10.34. The SiPM is viewed (from the solder pad side) suspended in front of the machined notch where it is lodged once the PCB assembly is fastened. The WLS fibers are guided by grooves machined at the scintillator surface. The WLS fibers are glued in the position in which their diamond-cut ends are as close as possible to the SiPM active surface. As the SiPM should guarantee an efficient collection of light from all three fibers, its size will be chosen to meet this requirement. Suitable SiPMs with an area of up to 9 mm^2 have been tested during the detector R&D in order to evaluate their efficiency and radiation tolerance properties.

Figure 10.34 shows also the assembly in operation: a micro coaxial jack such as the Amphenol A-1 JB, soldered on the PCB, allows for connection of a small-diameter coaxial cable. All coaxial cables are routed out of the detector assembly enclosure and reach the front end cards to which they are connected via a mass-terminated high density connector as shown in Figure 10.35.

As shown in Figure 10.34, the coupling of the WLS fibers to the SiPM is defined by means of machined grooves for the fibers, of a machined notch for the SiPM and of threaded holes for

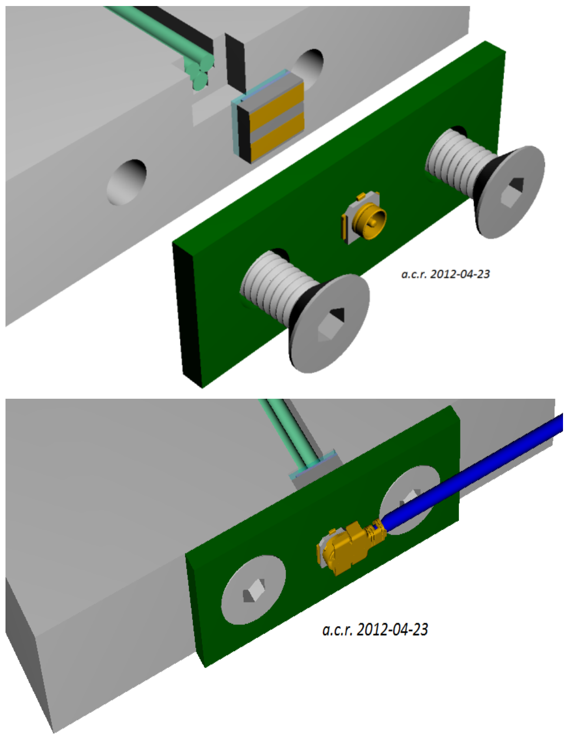

Figure 10.34: Detailed view of the three WLS fibers and the PCB.

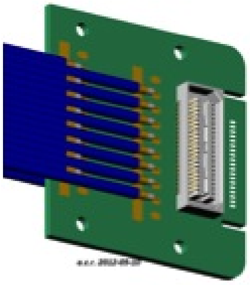

Figure 10.35: Detailed view of the multi coaxial connector assembly

the PCB mounting screws (and eventually with a hole for precision positioning pins). Based on the experience acquired during the R&D and prototype construction it was estimated that the relative positions of the fiber ends and the surface of the photodetector can be controlled with a precision in the order of 100 μm. The optical grease or silicon pads can be used to improve the optical matching.

10.7.2 Photodetector location

As described before, the scintillator bars, fitted with the photodetectors, will be enclosed in light-tight sheet-aluminum boxes, which will also provide mechanical rigidity to the assemblies, or modules.

It is to be said that once the modules are installed inside the IFR it will be impossible to perform any maintenance on the majority of them without a major overhaul of the detector; this is especially true for the barrel part of the detector. In Figure 10.31b we have shown a view of the barrel section of the IFR with a few modules of the innermost layer (the modules' envelopes are not drawn, to show the locations of the SiPMs for the barrel). A similar arrangement is foreseen for the active layers of the endcaps. The SiPMs are distributed throughout the entire surface of an active layer, they are expected to operate reliably. This assessment of the radiation tolerance of the SiPMs has already been carried out for the devices available at the time the IFR prototype was assembled. More R&D and irradiation tests have to be planned before the final SiPM choice is made, to characterize and possibly select devices built with the latest and most promising technologies. For the modules that will be subjected to the highest intensities of background radiation a special layout is also being investigated in which the SiPMs are relocated at more suitable positions by extending the length of WLS fibers.

10.7.3 Photodetector choice

Different solid-state single photon detectors have been and are being evaluated for the IFR application. The technology of these devices is rapidly evolving and it would be reasonable to commit to a specific device as late as possible.

Devices tested so far by the Super*B* collaboration include SiPM manufactured by the Fondazione Bruno Kessler (FBK), Hamamatsu MPPC and SiPM by SensL [19, 20, 21, 22, 23]. The key parameters describing the performance of a single photon detector are:

- the photon detector efficiency at the WLS fiber characteristic wavelength;
- the fill factor;
- the optical cross-talk ;
- the dark count rate;

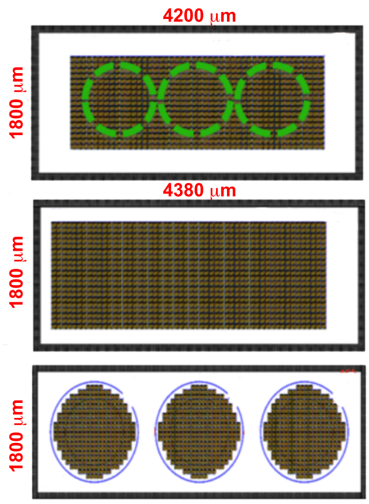

Figure 10.36: The custom SiPM manufactured by FBK company for the IFR prototype.

- the sensitivity of breakdown voltage to temperature variations;
- the gain and its sensitivity to temperature variations.

The SiPM suited for the IFR application should guarantee a detection efficiency better than 95 % when installed in a detector assembly and should yield a dark count rate at 0.5 p.e. threshold in the range of a few 100 kHz/mm^2 at room temperature and nominal bias voltage. SiPM devices satisfying these requirements and showing, after irradiation, the least perturbation of their original performance will be finally selected for the instrumentation of the IFR detector.

Another parameter which will be considered for the SiPM device selection would be the availability of detector geometries which minimize the unused surface area to optimize the ratio of dark count rate over signal rate. For the instrumentation of the IFR prototype a special device run was commissioned to the FBK and devices tailored to the IFR prototype needs were manufactured (see Figure 10.36 and 10.37). The IFR prototype had the majority of the channels equipped with the FBK SiPMs, but also had channels equipped with MPPCs and both types of silicon photomultipliers performed very well.

10.7.4 Aging and background issues

The SiPMs manufactured by FBK and the MPPC by Hamamatsu have been irradiated with neutrons at the Laboratori Nazionali di Legnaro [24] and at the Frascati Neutron Generator to evaluate the effect of radiation on the devices' key parameters [16]. These tests have shown that for neutron fluences above a few $10^8\,\mathrm{n}_{eq}/\mathrm{cm}^2$ the dark current and the dark count rate begin to increase. It was determined that after exceeding a few $10^{10}\,\mathrm{n}_{eq}/\mathrm{cm}^2$ the number of photons detected by an irradiated silicon photomultiplier instrumenting a cosmic muon detector may drop to about 80 % of the initial value [16]. As a reference, the fluence

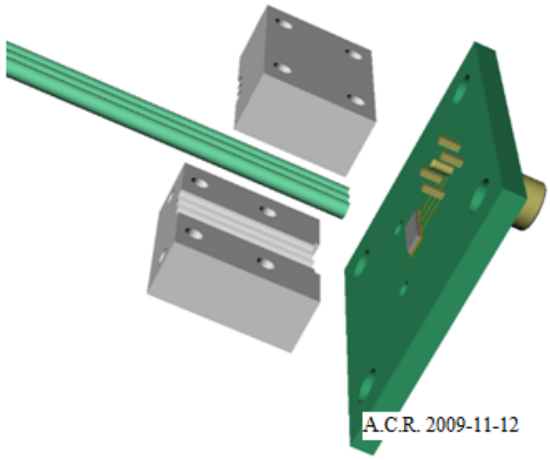

Figure 10.37: A detail of the SiPM carrier PCB with the MMCX connector.

of 1 MeV-equivalent neutrons expected [25] at the hottest location of the IFR barrel is about $3 \times 10^9\,\mathrm{n}_{eq}/\mathrm{cm}^2$ per year. The outcome of the irradiation tests results would seem to advise against installing the SiPM inside the IFR steel, where a possible replacement would require a major overhaul of the detector and a long downtime. On the other hand the positioning of the silicon photomultipliers in accessible locations would require to carry scintillation light to them via long clear fibers spliced to the WLS fibers. The latter would yield increasing costs, increasing dead space and loss of the photons available at the SiPM, with similar effects on the overall efficiency. Other topic to consider is that the signal processing foreseen for the binary mode readout of the detector is more tolerant to device performance degradation than the alternative "timing mode" readout [23] and that new silicon photomultiplier devices are being introduced, which feature an improved radiation tolerance. The dose received by the sensors could also be reduced by inserting multiple and shielding layers within the IFR, which would thermalize the neutrons from the beam halo, capture the thermal neutrons and finally absorb the energetic photons resulting from these processes. These considerations lead the IFR collaboration to maintain the baseline design described above, while scheduling more irradiation tests to evaluate the radiation tolerance of the newest SiPMs and the effectiveness of the shielding techniques.

10.7.5 Temperature requirements

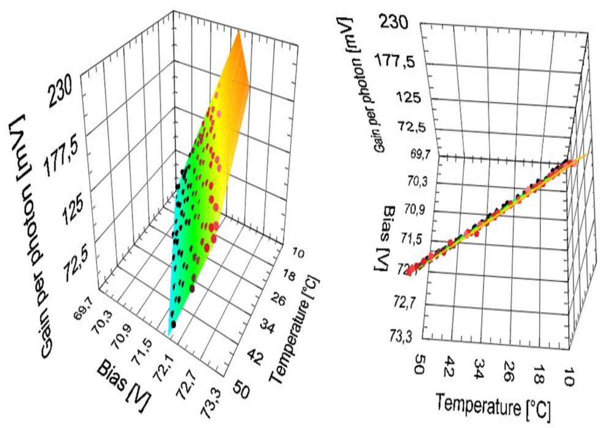

Figure 10.38: The measured points and the fitting plane representing the SiPM gain vs. bias voltage and temperature relationship

Both the operating point and the parameters of SiPMs are influenced by temperature. In the case of the IFR detector it is not foreseeable to refrigerate the devices by means of thermoelectric coolers. As result we assume that the devices will operate at the temperature of the flux return steel, which was controlled, in *BABAR*, by means of a chiller system. Rather than controlling the temperature of the silicon photomultiplier devices, the IFR environmental control system will periodically correct the bias point of each device to compensate for local temperature variations. This technique was used in the latest beam tests of the IFR prototypes [26].

The results of extensive studies on the compensation of temperature induced SiPM gain variations [27]. Figure 10.38 illustrates the distribution of measurements points in the (gain, bias, temperature) space, while Figure 10.39 shows the effectiveness of the compensation techniques against temperature variation for two types of silicon photomultipliers.

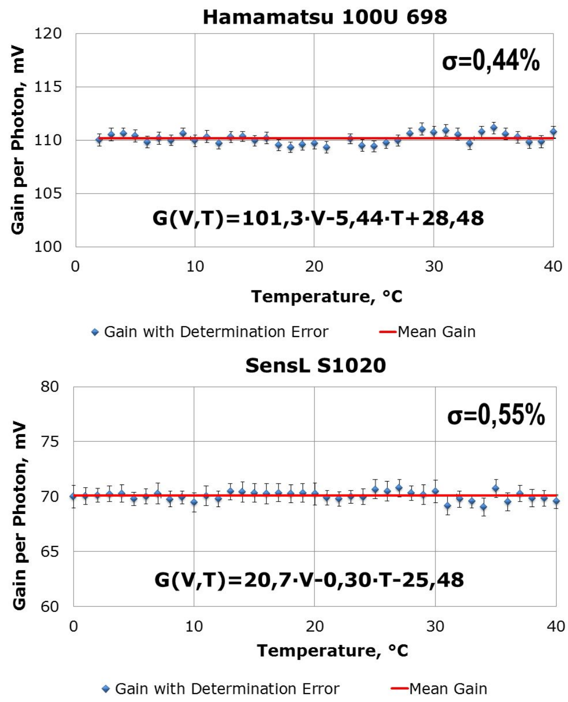

Figure 10.39: Gain stabilization results obtained at the AGH Krakow for Hamamatsu (top) and SensL (bottom) devices.

10.8 Front-End Electronics

This section describes the features and the design of the IFR readout system. At first, an estimation of the number of electronic channels, of the event size and the data bandwidth at the nominal Super*B* trigger rate are presented. The design constraints determined by the expected background radiation are then reviewed, along with the results of irradiation tests on existing ASICs and off-the-shelf devices suited for the implementation of some functional blocks of the readout chain. This chapter describes, finally, the baseline IFR readout system, going from the basic requirements of a dedicated IFR front end ASIC to the proposed installation locations of the IFR electronics building blocks and to the services required in the detector hall.

10.8.1 IFR channel count estimation

The active layers of the IFR detectors are equipped with modules in which the detector bars (of different widths for the ϕ and the z

views in the barrel) are assembled in two orthogonal layers. Table 10.8 summarizes the current number of electronic channels based on the figures reported in Table 10.6 end Table 10.7; the result is a total of 11640 channels for the IFR barrel and 9936 for the endcaps, considering 9 equipped gaps.

Table 10.8: Estimation of the electronics channels count for the IFR detector.

Barrel		Endcaps	
ϕ ch per sxt	884	x ch per door	1494
z ch per sxt	1056	y ch per door	990
Ch. per sxt	1940	Ch. per door	2484
Tot. ch.	11640	Tot. ch.	9936

10.8.2 Estimations of the IFR event size and data bandwidth

The IFR detector will be read out in binary mode: the output of each SiPM device will be amplified, shaped and compared to a threshold; the binary status of each comparator output being the variable to be recorded to reconstruct the particle tracks within the IFR detector. The downstream stages of the IFR electronics are the digitizers which sample the comparators outputs at Super$B$ clock rate and store the samples into local "on-detector" circular memories. These buffers are designed to keep the data for a time interval equal at least to the Super$B$ trigger command latency. The last stage of the "on-detector" readout system is based on Finite State Machines (FSM) which extract, from the local latency buffers, the data selected by the trigger command coming from the Fast Control and Timing System (FCTS). The IFR channels will be processed by functional blocks with a modularity of 32 ("MOD32").

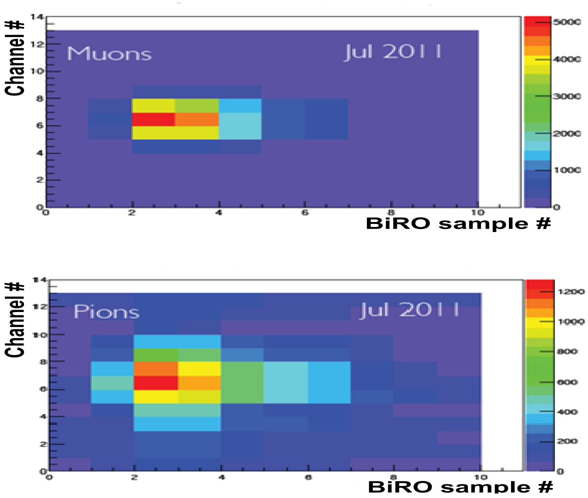

Figure 10.40: Time evolution of muons and pions evaluated across the 10 samples taken for each BiRO event (plots from [28] corresponding to a sampling period of 12.5 ns).

Such a straightforward scheme has been successfully applied to the IFR prototype, which has been tested with cosmic muons and with the beam provided by the Fermilab Test Beam Facility [28, 29]. The beam tests have shown that the time window for the extraction of data matched to a trigger should be about 120 ns wide (see Figure 10.40), in order to recover the entire signal from the shower initiated in the detector by an impinging hadron.

Tables 10.9 and 10.10 contain all information relevant for the computation of the expected IFR event size and data bandwidth at the nominal Super$B$ trigger rate. In these tables the number of samples has been set to 16 to account also for a trigger jitter of the order of 100 ns. The event size and required bandwidth could be reduced by applying the data reduction scheme proposed by the ETD group. In this approach, if a new trigger would select data that has already been sent in response to a previous one, the repeating data is not transmitted and a pointer to the start of the repeating data within the previous packet would be sent instead.

10.8.3 Background radiation and electronics design constraints

The current knowledge of the radiation environment at Super$B$ comes from detector simulations—constantly improving as far as the details of the structure being simulated and thus the accuracy of the results, are concerned. The simulations [30, 31] allowed, in particular, for the analysis of the known sources of radiation

Table 10.9: Estimation of the event size and data bandwidth for the Barrel.

Max channel count per module	32
# of MOD32 units per module	1
Tot. # of barrel modules	384
Tot. # of MOD32 units	384
Sampling period ($\frac{1}{FCTS_{clk}}$ ns)	17.86
# of samples in the trigger window	16
Barrel event size (kByte)	24.580
Trigger rate (kHz)	150
Total barrel bandwidth (Gbit/s)	36.860
# of data links for the barrel	24
Bandwidth per link (Gbit/s)	1.536

Table 10.10: Estimation of the event size and data bandwidth for the Endcap.

Max channel count per module	92
# of MOD32 units per module	3
Tot. # of endcap modules	108
Tot. # of MOD32 units	324
Sampling period ($\frac{1}{FCTS_{clk}}$ ns)	17.86
# of samples in the trigger window	16
Endcap event size (kByte)	20.736
Trigger rate (kHz)	150
Total endcap bandwidth (Gbit/s)	31.104
# of data links from the endcap	16
Bandwidth per link (Gbit/s)	1.944

background in Super*B* and for the evaluation of the doses in silicon at the locations of the SiPMs and at the positions of the FEE. The largest fraction of the total dose absorbed by the IFR electronics is deposited by neutrons originating back to the radiative Bhabha and the Touschek processes. The neutron energy spectrum shown in Figure 5.26 in Sec. 5.12.1 is quite wide-spread and so different types of interaction processes have to be considered to assess the effects of the background neutrons on the performance of the sensors and of the readout components. As a reference location for the neutron rate estimation one could take innermost layer of the barrel where the neutron rate is shown in Figure 5.27. The rates presented in this plot are reported separately for the different background sources, are normalized to 1 MeV-equivalent neutrons in silicon and include a *safety factor* that takes into account the fact that the simulation may not reproduce perfectly the reality (as explained in Sec. 10.3). A reference flux of 500 $\mathrm{n}_{eq}/\mathrm{cm}^2/\mathrm{s}$ would result in a fluence of about $1.6 \times 10^{10}\,\mathrm{n}_{eq}/\mathrm{cm}^2$ per solar year.

The background simulations provided also information on the total dose in silicon at locations around the IFR steel where "on detector" components of the electronic readout system could be located. Figure 10.41 gives information on the dose absorbed at the different locations in evidence. The highest dose is found at the C2 locations of the forward endcap and it is about 140 krad/year.

Electronic devices and systems, which must reliably and durably operate under these radiation conditions, must be designed or selected according to guidelines which have already been drawn, among others, by the LHC community. As an example one could refer to the "ATLAS Radiation Tolerance Criteria" for electronics [32] to see that the neutron fluence expected for the Super*B* IFR is of the same order of magnitude simulated for the ATLAS MDT muon spectrometer.

We could then, if not exploit exactly the same technical solutions adopted there, at least follow the design guidelines established by the cited document and by similar papers. A more general approach to the subject of radiation effects in silicon devices is described in [33, 34, 35, 36]. The R&D activity for the preparation of the Super*B* TDR has included the evaluation of the ra-

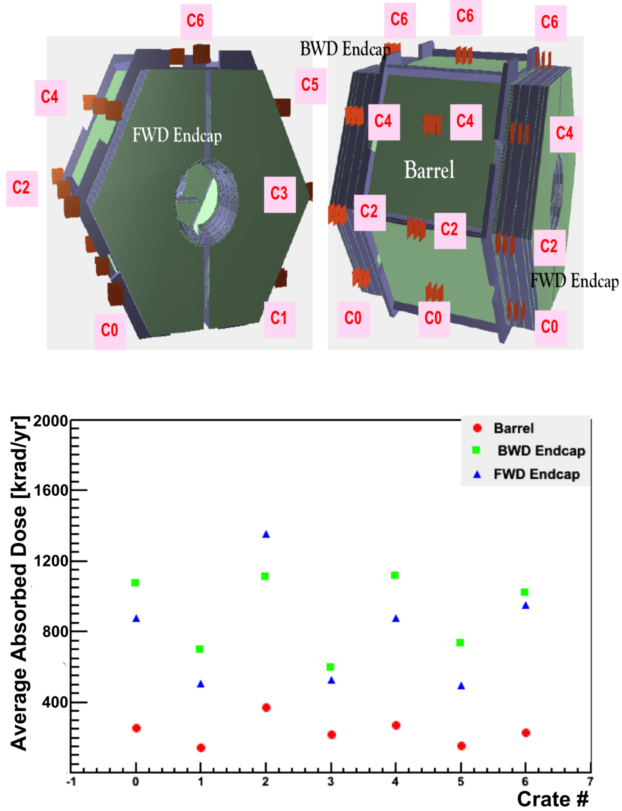

Figure 10.41: Location of the IFR FEE crates as simulated (top). Doses (krad/year) measured at some relevant locations around the detector (bottom).

diation effects on SiPM [37, 38, 39, 40, 41] and on electronics devices used to implement the basic functions of the readout system. Irradiation tests were performed at the CN facility of the INFN Laboratori Nazionali di Legnaro (LNL) on samples of:

- low power, current feedback, operational amplifiers (op amp), to be used, if necessary, for "on detector" buffers, active summing junctions and so on;
- ACTEL proASIC3E FPGA (backup solution for the implementation of digital functions of the IFR readout chain);
- the "EASIROC" ASIC developed by the Omega group of the LAL, Orsay, France [42, 43];
- the "RAPSODI" ASIC developed by W. Kucewicz and his group at the AGH University, Krakow, Poland [44];
- the "CLARO" ASIC developed by G. Pessina and his group at INFN Milano-Bicocca, Milano, Italy [45].

The CN facility of the LNL has a beam line delivering 4 MeV $^{2}H^{+}$ ions interacting on a beryllium target. The energy spectra of the neutrons produced in the $^{9}Be(d,n)^{10}B$ reaction are shown in Figure 10.42. Figure 10.43 shows the stack of boards carrying, in the first of the irradiation tests performed, the EASIROC, the FPGA and the op amps installed right in front of the beampipe, and a thermally isolated SiPM box located behind it, at about 4 cm from the beam pipe. Some results of this irradiation tests are presented in Tab. 10.11. The OMEGA EASIROC ASIC, manufactured in the 0.35 μm SiGe technology of Austria Micro Systems, was exposed to an estimated total of 1.7×10^{11} neutrons, equivalent to a few year's exposition to the Super*B* IFR operating conditions.

The outcome of the test was that, as expected, while the FPGA configuration memory contents was not corrupted, the on-chip SRAM blocks and the registers in the FPGA fabric were subjected to upsets. Therefore, any critical part of the FPGA design should include suitable protection against Single Event Effects (SEE), which include Single Event Upset (SEU) and Single Event Latchup (SEL). It is worth to notice that no SEU afflicted the EASIROC configuration registers, no latch-up occurred and finally that no evidence of Total Ionizing Dose (TID) damage was found while comparing the current consumption and the analog performance before and after the irradiation test [41]. The op amps to be tested had been fastened to the top of the FPGA and have thus been irradiated with a fluence of the order of 10^{12} n_{eq}/cm^2 with no noticeable effect on their current consumption or DC offset.

On a later occasion, in June 2012, the RAPSODI ASIC-2 and the CLARO ASICs were also irradiated at the CN facility, using similar se-

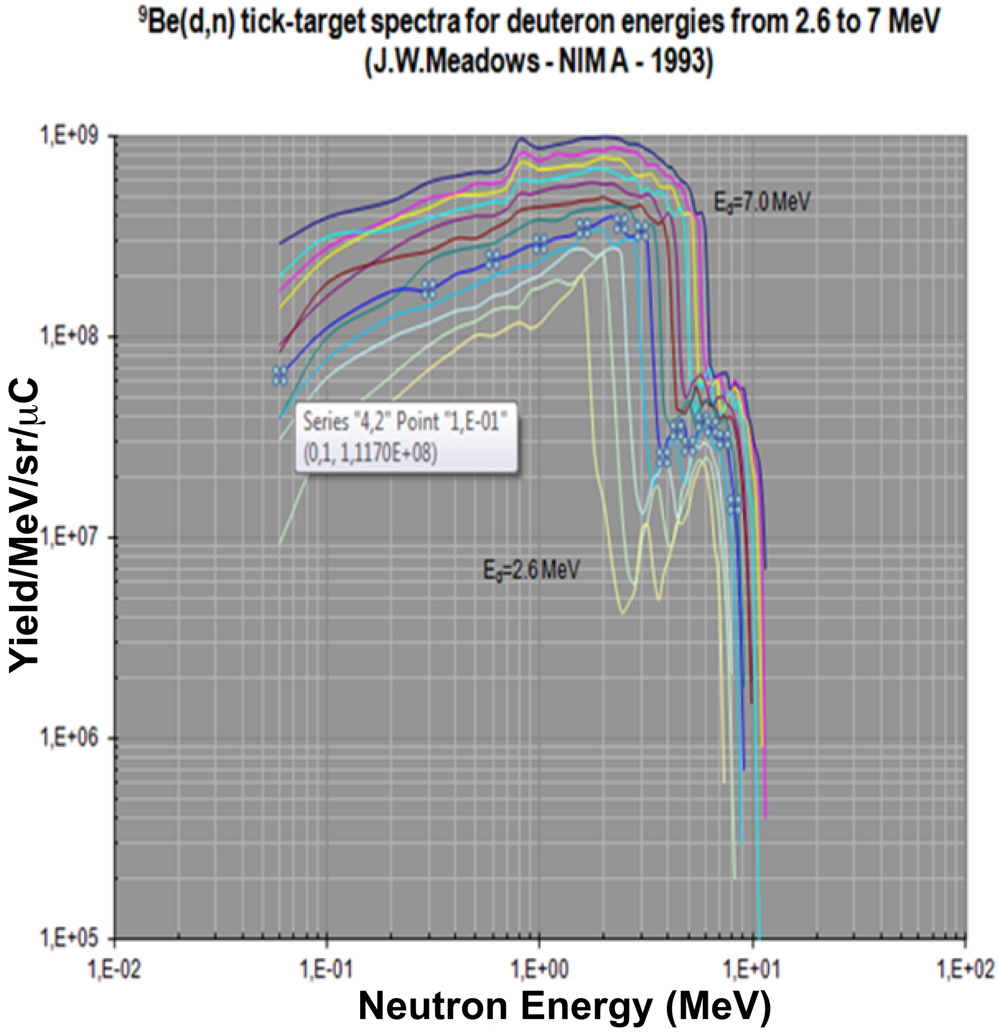

Figure 10.42: Energy spectra of the neutron beam delivered by CN at LNL).

tups as the one illustrated above. Figure 10.44 sketches the relative positions of the neutron source and the devices under test (DUTs). No SEL were detected both for the CLARO and the RAPSODI ASIC-2, which were powered at nominal operating voltage during the irradiation. Also a little effect was measured on the ASIC performance such as DAC transfer functions, gain and comparator offset [46, 47]. As an example, the comparison between transfer function measurements performed before and after irradiation are shown in Figure 10.45 for one of the CLARO DACs. Also, the comparison between linearity measurements performed before and after irradiation is presented in Figure 10.46 for one of the irradiated RAPSODI chips.

The neutron fluences delivered to the devices under test, *i.e.* two samples of the CLARO ASIC and two samples of the RAPSODY ASIC-2, were:

- CLARO sample n. 1: $1.28 \times 10^{12}\,\mathrm{n}_{eq}/\mathrm{cm}^2$;
- CLARO sample n. 2: $1.32 \times 10^{12}\,\mathrm{n}_{eq}/\mathrm{cm}^2$;
- RAPSODY sample n. 1: $3.3{\times}10^{13}\,\mathrm{n}_{eq}/\mathrm{cm}^2$;
- RAPSODY sample n. 2: $1.32 \times 10^{12}\,\mathrm{n}_{eq}/\mathrm{cm}^2$.

The results of the irradiation tests supported the decision on how to build and where to install

Table 10.11: Results of the EASIROC irradiation tests at CN-LNL.

total integration time (sec)	60683			
total charge (μC)	4104			
	ACTEL A3PE250-PQ208			**EASIROC**
distance from source (mm)	7			20
fluence at target (n/cm^2)	6.12×10^{12}			1.03×10^{12}
fluence at DUT (n)	4.95×10^{12}			1.69×10^{11}
	Configuration memory bits	SRAM bits	Flip flop	Flip flop
total memory elements monitored	N.A.	32768	5824	456
number of SEU detected	0	752	26	0
number of SEL detected	0	0	0	0

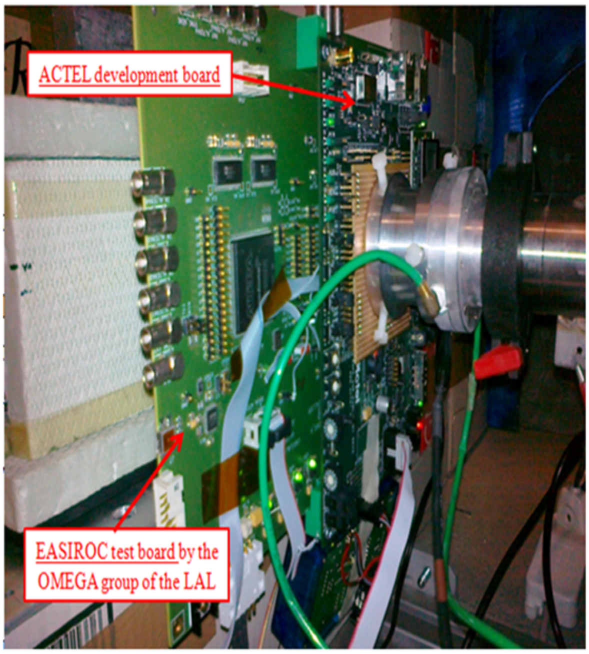

Figure 10.43: Irradiation test setup at the CN-LNL facility.

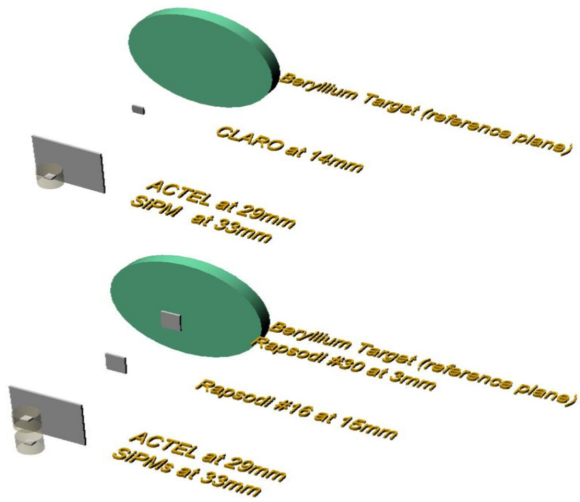

Figure 10.44: Schematic representation of the CLARO and RAPSODI irradiation test setup at INFN-LNL.

the front end stages of the IFR readout system. As more neutron irradiation tests on SiPM are planned to assess the radiation tolerance of the latest generation devices, there will be more occasions to test, at the same time, more samples of ASICs built in the AMS 0.35 μm technology at different neutron energies and with different beam orientations with respect to the device under test. The 0.35 μm CMOS technology from AMS is being tested because it represents the preferred choice for the development of a dedicated ASIC, as described in the next chapter.

10.8.4 The IFR readout system

IFR readout basics: outline of the IFR prototype readout. The basic principles of the IFR readout system design have been tested with the IFR prototype, which was read out in the binary mode described above. For the prototype readout, a dedicated front end board, the ABCD, was built from off-the-shelf components (COTs). Figure 10.47 shows the ABCD block diagram.

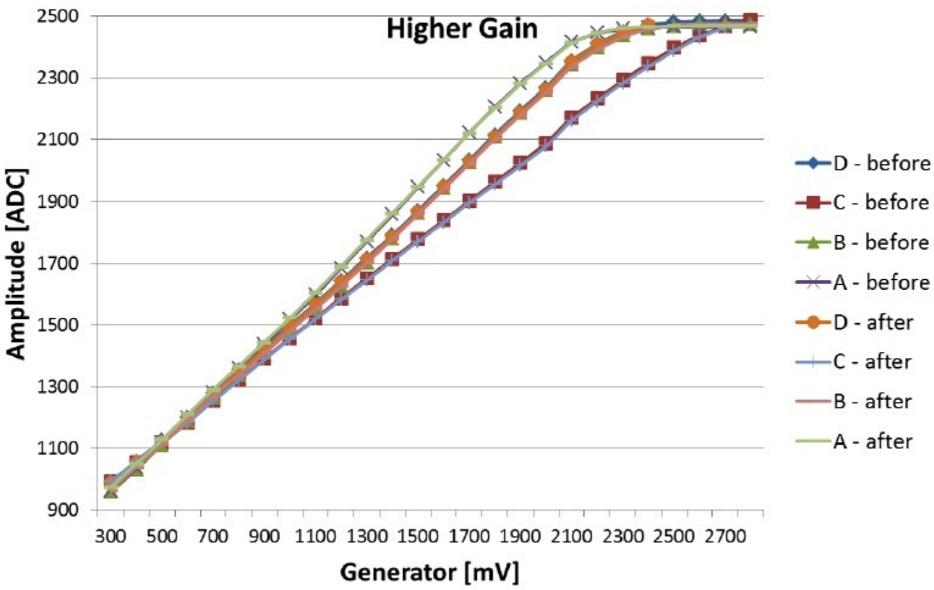

Figure 10.46: RAPSODY linearity test performed before and after the irradiation.

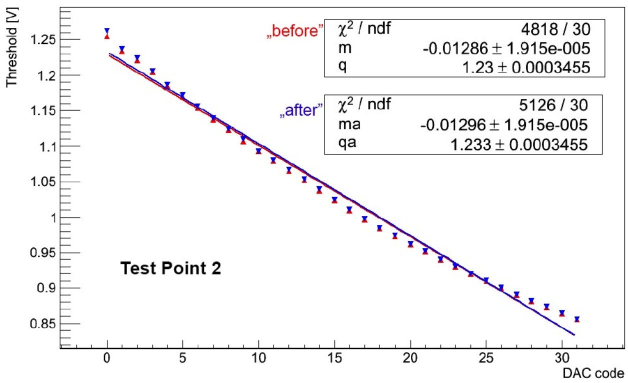

Figure 10.45: CLARO DAC test performed before and after the irradiation.

The main functions which were implemented on the 32 channel ABCD board are:

- individual "high side" regulation (with 12 bit resolution) of the SiPM bias voltage; bias voltage and SiPM signal are carried by the inner conductor of the coaxial cable, whose outer conductor is at true ground potential;
- wideband (-3 dB frequency of 1.5 GHz) amplification of the SiPM signal;
- discrimination of each SiPM signal to an individually programmable (with 12 bit resolution) threshold voltages; the discriminators (two per channel) used AC coupled feedback to stretch the output pulse to a width of about 20 ns;
- sampling of the discriminators outputs and storing of samples onto local memories to accommodate for the latency of the trigger signal; an ALTERA Cyclone III FPGA was used to sample the discriminated SiPM signals and store them in an internal latency pipeline running at 80 MHz;
- trigger processing: with each trigger a set of 10 samples was extracted from the latency pipeline and transferred to an output buffer (along with suitable framing words) from where they reached the "BiRO Trigger Logic Unit (TLU) Interface board" [48] acting as a crate-wide data-collector and interface to the DAQ PC and to the experiment TLU.

The DAQ system developed for the IFR prototype readout performed also functions which would, in Super*B*, be carried on by the

Experiment Control System (ECS). Among the latter there are: room temperature acquisition, calculation and download to the ABCD DACs of new set points for the bias voltages (needed to stabilize the SiPM gain against variations of the operating temperature) [28]. The Fermilab beam tests of the IFR prototype have demonstrated, among other things, that connecting the SiPMs to the front end cards by means of long (4 m) coaxial cables, although not optimal, was possible and resulted in a reliably operating system. This result supported the current baseline choice of locating the SiPMs near the scintillator bars and far from the front end cards, so that the latter can be installed at more convenient (better accessible) locations.

ASIC based front end readout. The COTS-based design of the ABCD card met goals such as short development time and flexibility (especially needed for tuning the parameters of the channels to be read out in the "timing" mode [49]) but it wouldn't be convenient for large volume production. A search for existing ASICs suited for binary mode processing of SiPM signals was started and a good candidate was found in the "*Extended Analogue Silicon PM Integrated Read Out Chip*" or EASIROC which had many features already suited for the IFR readout application [42, 43]. The EASIROC has been used, thanks to the test board and utilities provided by the LAL/OMEGA group, to test different SiPM technologies and coupling schemes [50]. Figures 10.48 and 10.49 show, for instance, the pulse height histograms obtained from a 1 mm^2 SensL SiPM connected to the EASIROC via:

- different lengths of coaxial cables, up to 12 m (Figure 10.48);
- one differential pair of a high density, double shielded, multi twisted pair cable 8 m long (Figure 10.49).

The features of the EASIROC which would suite the IFR readout application are:

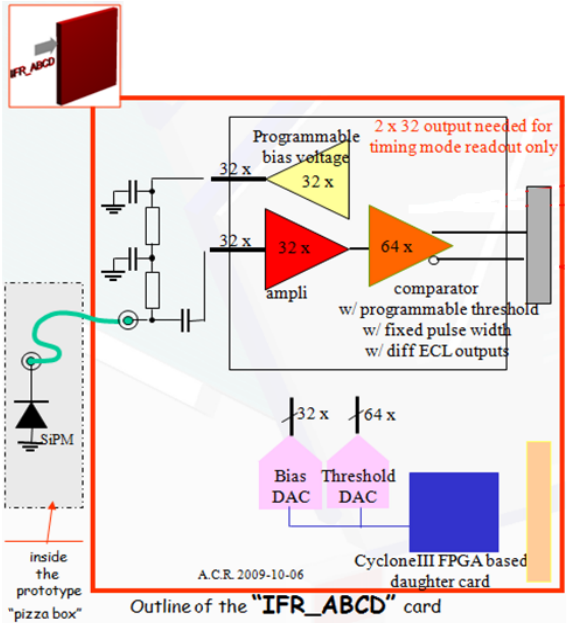

Figure 10.47: Basic features of the ABCD card designed for the IFR prototype readout.

- the integration of 8 bit DACs, one per channel, for "low side" adjustments of the SiPM bias voltage;
- one fast (15 ns peaking time) shaper stage for each channel driving the trigger comparators;
- the integration of a 10 bit DAC, common to all channels, for setting the threshold of the fast trigger comparators;
- the availability of all 32 trigger outputs at the I/O pins (with single ended LV-TTL level) of the EASIROC;
- low power consumption;
- no sign of performance degradation or SEE detected during or after the irradiation tests described above.

These suitable features are partially offset by other characteristics which make the EASIROC not quite usable as it is. The most important is the 15 ns peaking time of the fast shaper: a lower value is necessary to cope with the increasing dark count rate for SiPMs operating in the Super*B* radiation environment. As the

IFR collaboration has been growing in the last year to include groups experienced in VLSI design [36][44][45] [51, 52, 53, 54], the development of an ASIC implementing the front end stages of the IFR readout system has become within reach. The EASIROC and an auxiliary flash based FPGA could still be considered as building blocks for a backup solution.

The new IFR front end ASIC should implement a set of basic features as follows:

- a preamplifier and shaper chain suited for positive and negative input signals and characterized by a dynamic range of about 100 times the single photon response signal;
- a shaper peaking time not larger than 10 ns to minimize the pulse pile-up effects at high input rates;
- individual DACs to set, with a few mV resolution, the DC level of each input and thus the "low side" bias voltage for the DC-coupled SiPM; the current compliance of the DAC should be specified considering that the dark current of a SiPM could increase two orders of magnitude during its operational life in Super$B$;
- a fast comparator design, possibly differential;
- one threshold setting DAC with a resolution of at least one fourth of the single photon response signal and a linear range one fourth of the shaper linear dynamic range;
- a configurable test pulse injection circuits;
- a slow control interface logic: a simple serial protocol should be implemented in order to perform write and non destructive readback to/from all register controlling the ASIC's programmable features;
- a clock interface unit: to avoid the need of on-chip PLLs the ASIC will receive an LVDS clock with a multiple of the Super$B$ clock frequency; the timing unit will derive from it all on-board timing signals; a suitable fast reset signal input should also be foreseen;
- a trigger primitives generator: a Lookup Table (LUT) based block combining signals from a programmable set of the on-chip comparators and driving one or two trigger outputs;
- SEU protection through TMR or Hamming coding for all key registers and state machines in the ASIC.

The IFR front end ASIC should also possess a set of application specific features such as:

- a configurable latency buffer: a dual ported memory whose width would be equal to the number of channels and whose depth would be determined by the Super$B$ trigger latency time interval. The constant (but configurable) offset between the write pointer and the read pointer would equal the trigger latency time expressed in terms of Super$B$ clock periods;
- a trigger interface: a trigger matching logic would detect a trigger pulse from the experiment, then wait for the relevant data to be extracted from the latency buffer and forward the trigger-matched data packet to the output serializer;
- a set of low power serializers clocked by the input clock (which has a pace multiple of the sampling clock) needed to transfer the trigger matched data to the downstream data collector units; the serial output data could be 8b/10b encoded to allow the usage of AC coupled transmission links requiring DC-balancing.

The features listed above are differentiated into a first set, mainly analog, and a mainly digital second set to point out that it might be convenient to implement the two lists of functions in two different ASICs, to increase the flexibility of the overall system. Figure 10.50 shows a block diagram of the new IFR

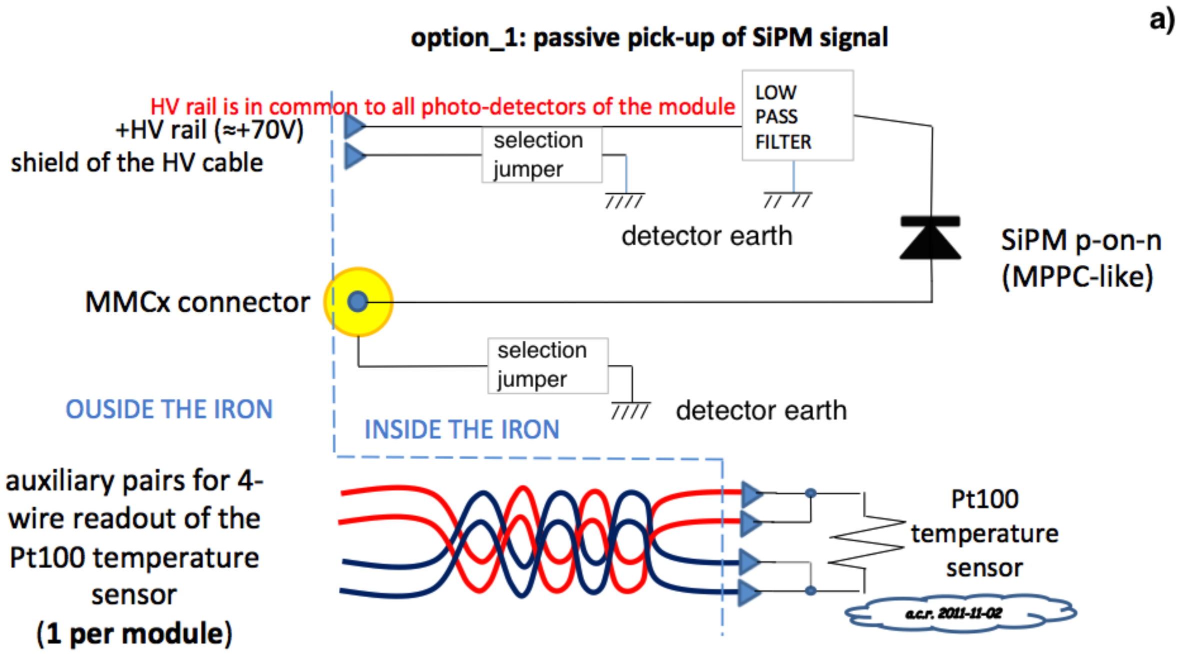

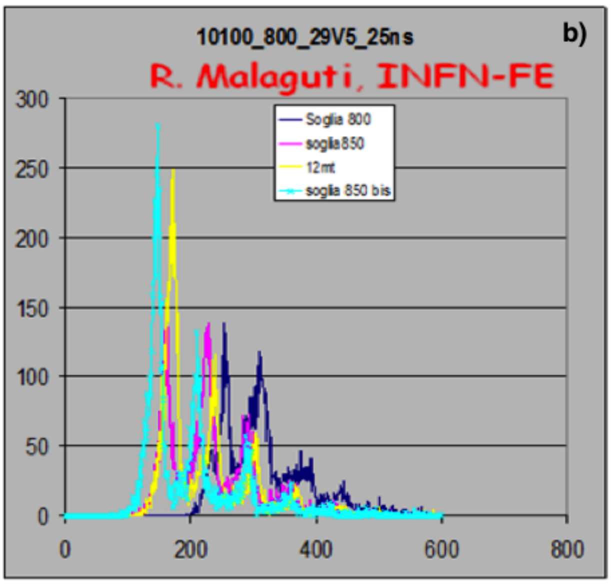

Figure 10.48: a) Schematic view of the "passive pick-up" coupling. b) Histogram (counts vs. ADC bins) of the signal amplitude at the monitor output of the EASIROC. The SiPM was connected with coaxial cables up to 12 m.

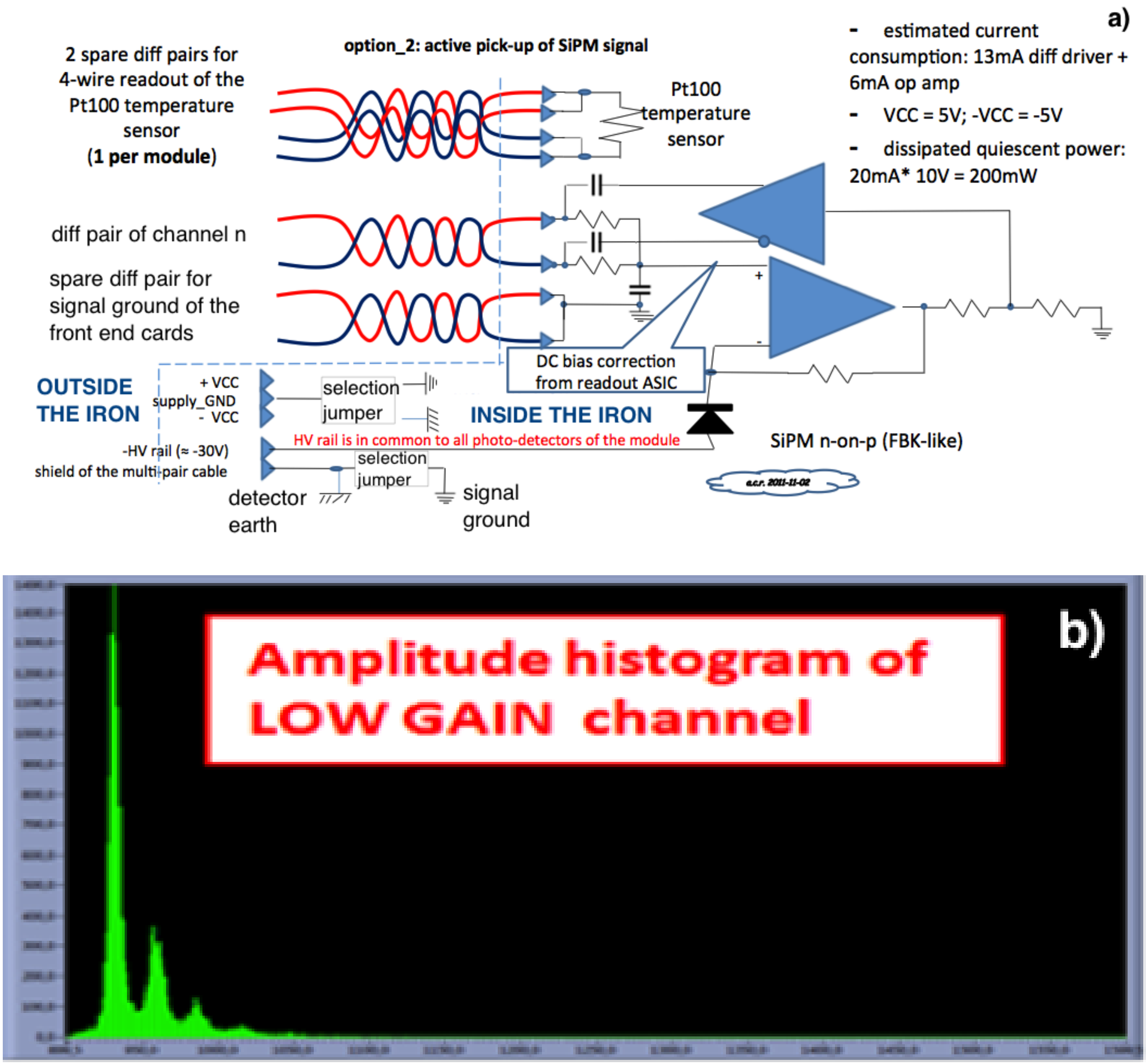

Figure 10.49: a) Schematic view of the "active pick-up" coupling. b) Histogram (counts vs. ADC bins) of the signal amplitude at the monitor output of the EASIROC. The SiPM was connected with one differential pair of a high density cable 8 m long.

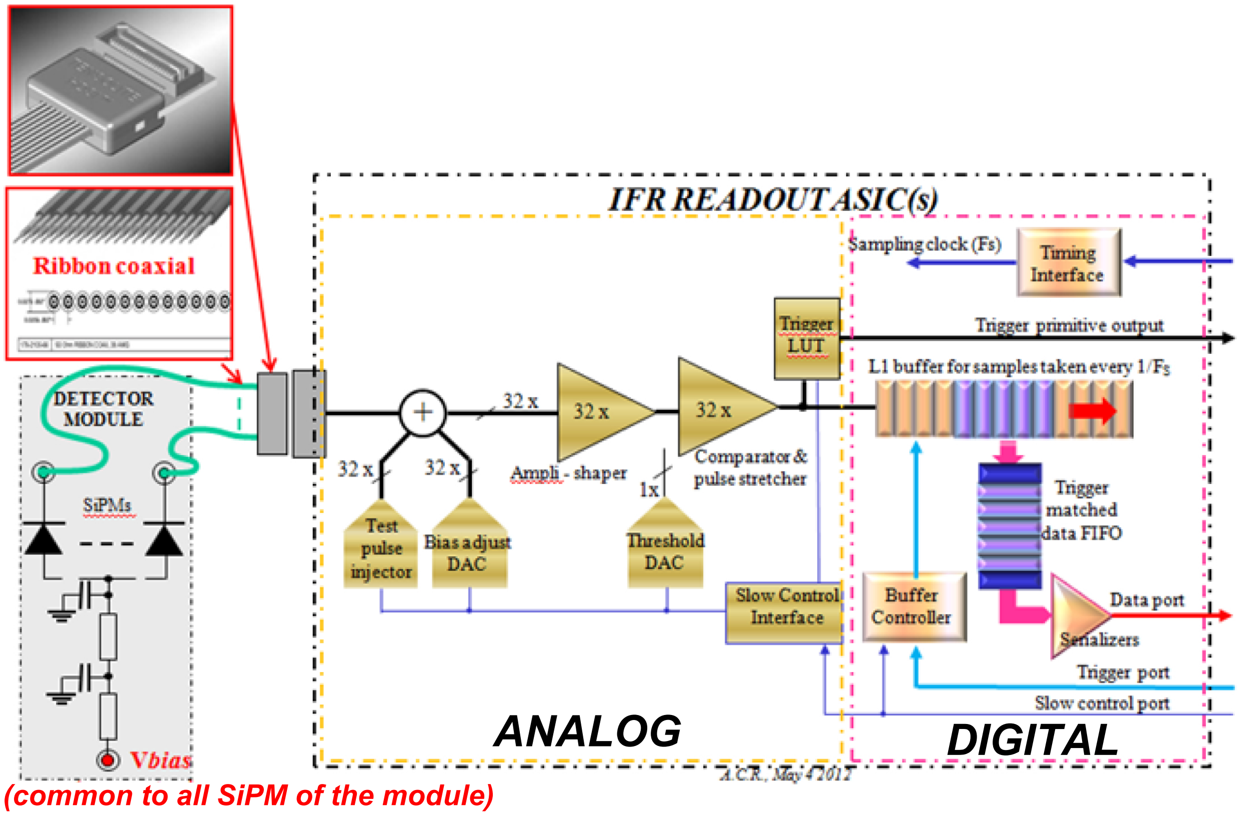

Figure 10.50: Block diagram of the IFR readout ASIC.

readout ASIC and its connection to the SiPMs in the detector module. An IFR ASIC with a modularity of 32 channels would be able to readout all SiPMs in one module of the barrel. As shown in the inlay of Figure 10.50 a ribbon-coaxial cable, mass terminated to a high density connector, could be used to carry the signals from the sensors to the IFR readout ASICs and the ancillary components on the IFR front end cards. At the right side of the ASIC diagram, Figure 10.50 shows the input and output ports for the connections between the IFR ASIC and the downstream data merger cards.

Location of the front end stages of the IFR readout system. The SiPMs would be installed, according to the baseline design, directly on the scintillator bars and thus distributed at different locations inside the modules. The ASIC based front end stages would be installed outside the modules, at the closest accessible locations. The reason behind this choice is that even if we were to install the front end ASICs inside the modules, we would not still be able to directly connect the SiPMs to the ASICs (in order to maximize the signal/noise ratio). This, in turn, would make it more difficult to remove the heat dissipated by the front end and it would make it impossible to access the front end cards, to replace faulty ones for instance, without disassembling large parts of the IFR system.

The position of two of the 5” × 3” conduits through which the IFR detector signal and power cables are routed are shown in Figure 10.51. The printed circuit boards for the front end stages of the IFR signal processing chain could be located in these cable conduits. They would be accessible, if needed, without removing structural elements of the IFR structure. Figure 10.52 shows a section of one IFR cable conduit

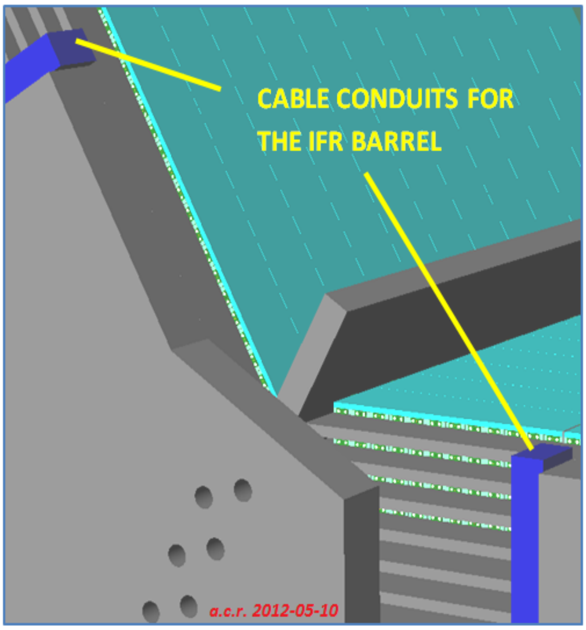

Figure 10.51: The IFR cable conduits for two sextants.

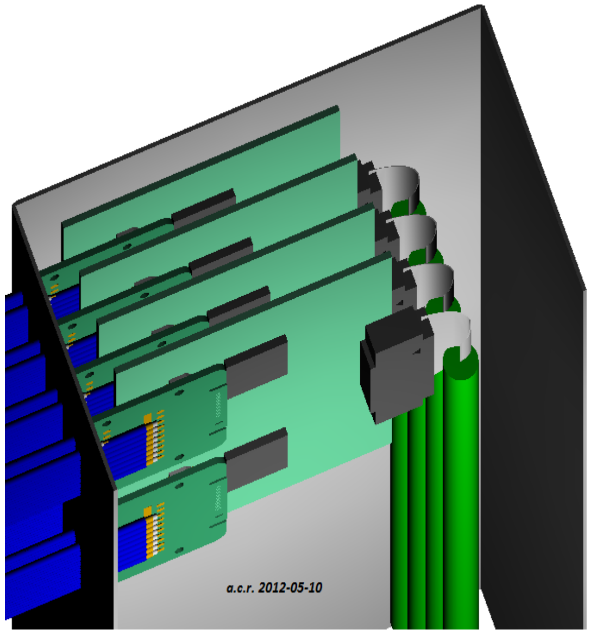

Figure 10.52: Detailed view of the front end cards installed in the IFR cable conduit.

with a stack of 4 boards in evidence. Each IFR front end board could host 2 ASICs with 32 input channels each and since the IFR modules in the barrel are equipped with 32 SiPM at most, a stack of three to four IFR front end cards can handle all SiPMs installed in an active layer; 9 active layers are foreseen in the IFR detector. All digital signals to and from the two front end ASICs on a board are coming from the data merger cards downstream, physically located as close as possible to the end of the cable conduit emerging from the IFR, as illustrated in the next paragraph. The interconnection cables are shown on the right side of the Figure 10.52: they are double shielded, 17 pairs, Amphenol SpectraStrip part number 425-3006-034 fitted with connectors by KEL (part no. KEL 8825E-034-175D). The mating connectors on the front end and the data merger PCBs are KEL 8831E-034-170LD. The power cables for the SiPM bias (one common bias voltage per detector module) and for the front end card supply voltage are not shown in Figure 10.52.

The cable conduits have a big enough cross-section to accommodate all boards and cables needed for the 9 active layers of each barrel sextant. Not shown in Figure 10.52 are also the copper pillars which are foreseen to build a thermal conduction path from the IFR front end card to the IFR steel, to which the cable conduit is fastened. If individual coaxial cables were used to carry the SiPM signals instead of ribbonized coaxial cables, then the signal cables from the module could be soldered onto a suitable interface PCB, as it was shown in Figure 10.35. The multi coaxial assembly, shown in this 3D drawing, features a SAMTEC QSE-20-01-F-D high density connector which mates to a QTE-020-01-F-D installed on the IFR front end PCB.

The above description concerned the instrumentation of the barrel section of the IFR detector. Figure 10.53 shows a perspective view of a pair of endcaps. Here the yellow callouts indicate the openings in the side lining steel through which the signal and power cables for the detector modules can be routed. The signal cables emerging from these openings are routed to the crates marked by the red callouts. For the endcap section of the IFR, the front end cards carrying the IFR read out ASIC could be installed directly in the crate and connected to the data merger boards through the crate's backplane interconnections.

The IFR data merger crates. The IFR data merger crates are interfaced to the Super*B* FCTS and ECS from which they receive and execute the commands controlling the data acquisition and the detector configuration, respectively. The data merger units also collect the trigger matched data from the front end cards and merge the input streams into the output packets sent to the Super*B* ROM (ReadOut Modules) via the high speed optical data links. Figure 10.54 shows the main functions performed by the units installed in a data-merger crate:

- FCTS interface: the key element of this functional unit is the FCTS receiver module which is linked via optical fiber to the Super*B* Fast Control and Timing System; the FCTS interface unit fans out to the IFR front end cards the timing (clock and reset) and the trigger commands decoded by the "receiver of the FCTS protocol" block;

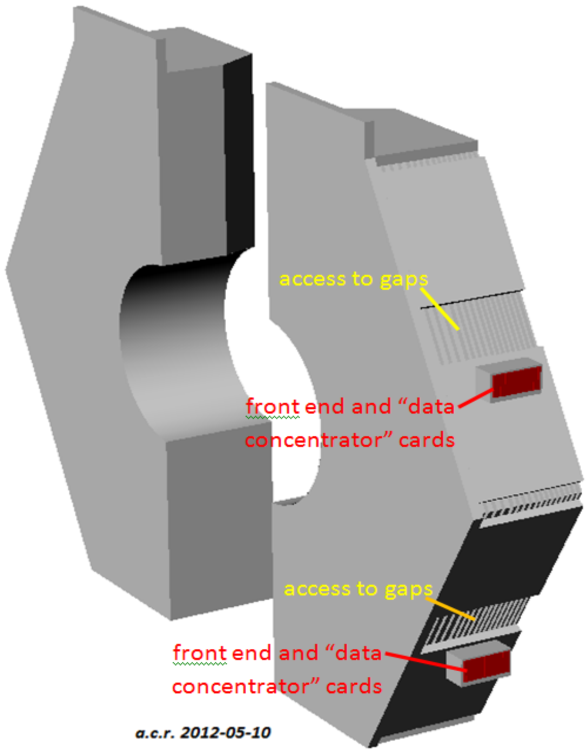

Figure 10.53: Perspective view of IFR endcaps.

- muon trigger module: this unit receives the trigger primitives generated by the IFR front end cards and combines them to generate a muon trigger for local debugging purposes;

- data link: each data-merger crate is supposed, according to the baseline design, to receive and combine the serial streams of trigger matched data coming from the front end cards connected to it and to drive a suitable number of high speed optical data links (four for the barrel section, two for the endcap ones) to the ROMs. This functional unit will exploit the common TX link driver module to reliably send data to the ROM, even in the radiation environment of the IFR;

- ECS interface: the key element of this functional unit is the ECS receiver module, which is linked via optical fiber to the Super*B* Experiment Control System. The ECS unit translates commands and status information back and forth between the ECS system and the serial configuration controllers implemented in the front end ASICs.

For the endcap section of the IFR the physical links between the front end and the data merger boards are composed of the differential lines provided by the backplane in which the front end and the data-merger units are installed. An ATCA or Micro-TCA crate [36] provides a large number of such interconnection resources and the IFR data merger crates could conveniently conform to one of these TCA specifications.

Because of the Super*B* radiation environment it is likely that in the IFR data merger crates the standard xTCA IPM ("Intelligent Platform Management") controller will be replaced by some ad-hoc interface card connected to the Super*B* ECS. The power supply units of the IFR data merger crate would have to be radiation tolerant or simply to be installed at a larger distance from the crates. The power entry module integrated into a xTCA crate are fit to both options. The xTCA fans will have to be tested for

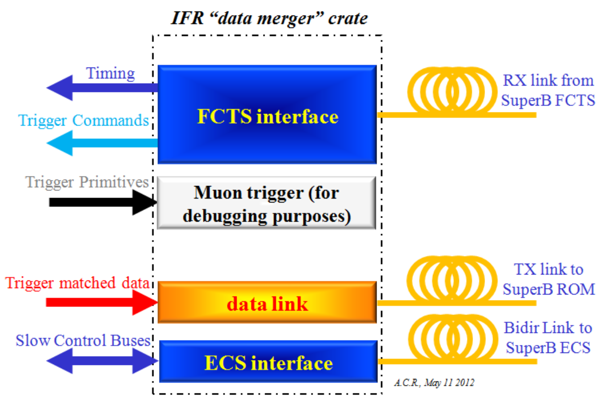

Figure 10.54: Illustration of the main functions performed by the electronic units in the data-merger crate.

operation in a radiation environment or replaced with qualified units. On the other hand, the convection cooling specification could be somewhat relaxed, since the data merger crates will most likely dissipate much less than the allowed 150–200 W per slot. Figure 10.55 shows the proposed location for one of the barrel data merger crates.

Two other such crates would be placed at 120° on the forward end of the barrel while three

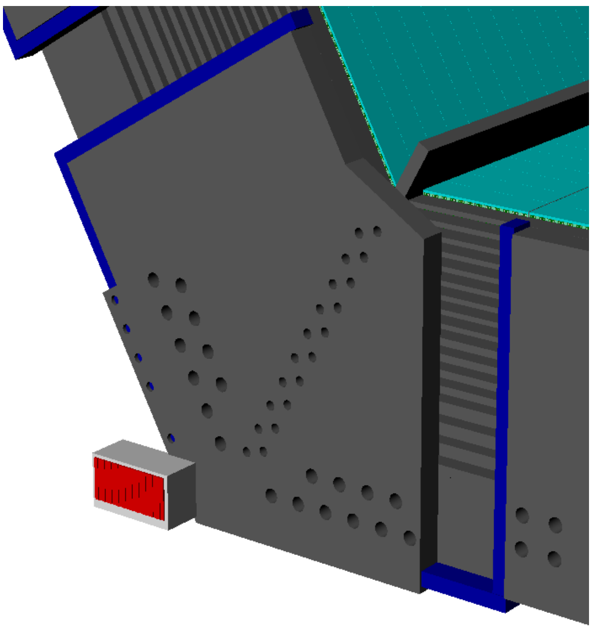

Figure 10.55: The location of one of the six data merger crates for the Barrel part of the detector

crates will be located in a similar arrangement at the backward end of the barrel. Each data merger crate serves two sextants.

Services needed for the IFR readout in the experimental hall. The elements of the IFR readout system need to be properly powered, monitored and refrigerated. This paragraph summarizes the main requirements for a readout system built according to the baseline design:

- HV SiPM supply: since the SiPMs are handled in groups of 32 by the front end ASICs which set the individual correction to the SiPM bias, it is preferable to bias each group of 32 SiPMs from a single "high side" supply channel; the IFR needs then 384 programmable HV supply channels for the barrel and 324 for the endcaps, for a total of 708 HV independent supply voltages. An HV supply channel should feature: a programmable (with at least 10 bit resolution) output voltage ranging from 0 to 100 V (actual range and polarity depend on the final SiPM technology chosen) and a current compliance of 25 mA. The power dissipated by the SiPMs in the whole IFR under nominal operating conditions is of the order of a few tens of Watts;

- LV front end cards supply: in the baseline design a front end card hosts two ASICs, powered at 3.3 V and drawing 50 mA each and, eventually, one FPGA powered at 3.3 V and drawing about 150 mA. If optional ancillary op amp stages were installed, these would draw, for each group of 32 channels, a current of 350 mA from both the positive and negative 3.3 V supply rails. In summary the current consumption for a front end card would be: 600 mA at +3.3 V, 350 mA at -3.3 V, resulting in a total power consumption of about 2.7 W for a 32 channel group. The IFR would then need 354 + 354 LV supply channels with 1 A compliance and +3.3 V and -3.3 V output voltage, respectively. Lower core voltages for the ASIC could be derived on-board by means of low-drop out regulators; the radiation tolerance of suitable LDO regulators is being characterized;

- cooling: the temperature of the IFR steel should be controlled to within ±2°, as it was for *BABAR*; the design of the barrel cooling system should then take into account the estimated 1140 W dissipated in total by the front end stages of the IFR barrel and endcap electronics.

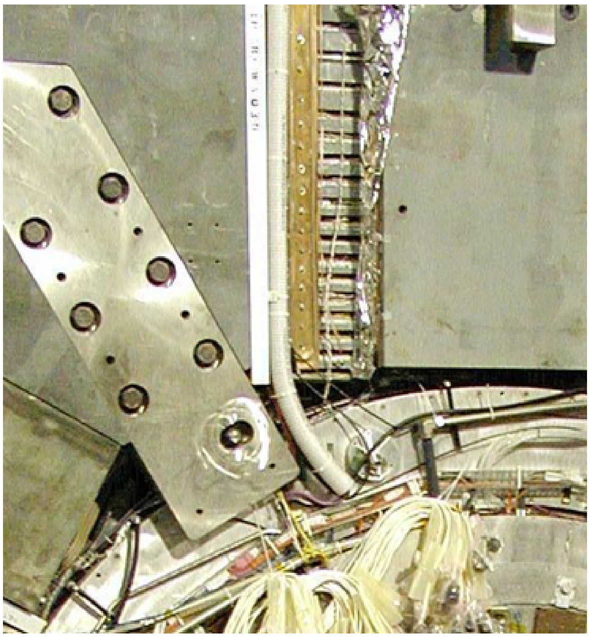

Figure 10.56: A picture from *BABAR* showing one of the elements of the cooling system for the IFR steel

10.9 Final assembly and installation

The assembly of the detector modules in the experimental area has to take into account the space needed for the modules, the installation tooling and the people involved. Safety rules have to be followed. The average weight is 50 kg for the barrel modules and 100 kg for the endcap modules. For the insertion of the absorber plates into the gaps the structure used in *BABAR* could be adapted. Following the IFR structure, the installation is divided between the barrel and the end caps.

Barrel installation. The barrel is composed of six wedges called sextants. The top and bottom sextants are horizontal, while the lateral sextants are inclined at an angle of 60°. For the assembly a lifting structure will be used which will allow the positioning of the module in front of the gap and the insertion of the module itself. The module covers half the length of the barrel and the insertion will take place on both sides. The plane of the lifting structure supporting the modules can be rotatated in order to be parallel to the gaps of the angled sextants. The barrel is supported by arches connected to the external plate of the sextants. This reduces the plates deformation and leaves the dimension of the gaps within the mounting tolerance. The external layers of the detector have to be sized in order to cover the maximum detector area. The external layers of the three bottom sextants need a supporting frame connected to the barrel structure. Figure 10.57 and 10.58 show a schematic and a picture of the *BABAR* muon detector disassembly: the same kind of tooling can be used to install the IFR modules into the Super*B* detector.

Endcap installation. The lifting structure used for the installation of the modules in the barrel will be used for the installation in the endcaps. The endcap modules are heavier than the barrel modules and bigger in size: the lifting connections have to be chosen in a way to avoid deformation and damages during the handling and the insertion.

Installation tests both for the barrel and the endcaps have to be done in order to optimize the procedure and the schedule.

10.10 Bibliography

[1] B. O'Leary et al., (Super*B* collaboration), "Super*B* Progress Reports – Physics", 2010,

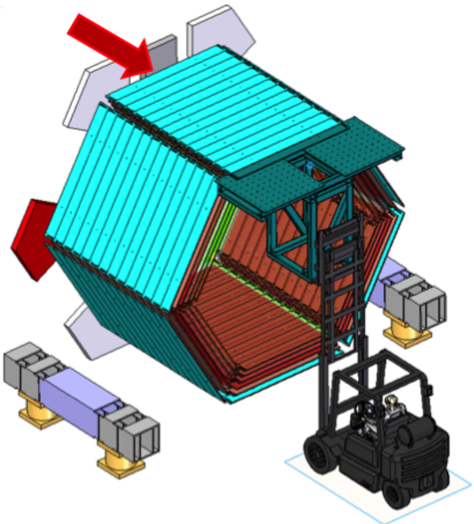

Figure 10.57: Scheme of the *BABAR* brass removal tooling that can be reused for the IFR module installation.

Figure 10.58: Picture taken during the removal of the brass from a diagonal sextant of the *BABAR* barrel.

arXiv:1008.1541 [hep-ex], report INFN-AE-10-2, LAL-110, SLAC-R-952.

[2] A. J. Bevan, "The Physics of Heavy Flavours at Super*B*", *J.Phys.* G39:023001, 2012, doi:10.1088/0954-3899/39/2/023001, arXiv:1110.3901 [hep-ex].

[3] B. Berman and S. Fultz, "Measurements of the giant dipole resonance with monoenergetic photons", *Rev.Mod.Phys.* 47:713–761, 1975, doi:10.1103/RevModPhys.47.713.

[4] Standard practice for Characterizing Neutron Energy Fluence Spectra in Terms of an Equivalent Mono-energetic Neutron Fluence for Radiation Hardness Testing of Electronics, ASTM E 722 -93.

[5] G. Lindstrom et al., (ROSE collaboration), "Developments for radiation hard silicon detectors by defect engineering - Results by the CERN RD48 (ROSE) Collaboration", *Nucl.Instrum.Meth.* A465:60–69, 2000, doi:10.1016/S0168-9002(01)00347-3.

[6] M. Bona et al., "Super*B*: A High-Luminosity Heavy Flavour Factory. Conceptual Design Report", arXiv:0709.0451v2, http://www.pi.infn.it/SuperB/CDR, report INFN/AE-07/2, SLAC-R-856, LAL 07-15.

[7] http://nicadd.niu.edu/fnpl/, FNAL NICADD Photoinjector Laboratory.

[8] http://uniplast-vladimir.com/, Uniplast Vladimir Factory.

[9] http://www.detectors.saint-gobain.com/fibers.aspx, Bicron specs.

[10] http://www.df.unife.it/u/baldini/superB/Kuraray.pdf, Kuraray specs.

[11] C. Piemonte, R. Battiston, M. Boscardin, G. Dalla Betta, A. Del Guerra, et al., "Development of Silicon PhotoMultipliers at FBK-irst", *Nuovo Cim.* C30:473–482, 2007, doi:10.1393/ncc/i2008-10260-2.

[12] http://sales.hamamatsu.com/en/products/solid-state-division/si-photodiode-series/mppc.php, MPPC specs.

[13] P. Border, P. Cushman, K. J. Heller, D. Maxam, J. Nelson, et al., "A large liquid scintillator detector for a long baseline neutrino oscillation experiment", *Nucl.Instrum.Meth.* A463:194–204, 2001, doi:10.1016/S0168-9002(01)00525-3.

[14] M. Martone et al., "The Frascati Neutron Generator (FNG)", *Proc. SPIE Vol. 2339, p. 208-212, International Conference on Neutrons and Their Applications, George Vourvopoulos; Themis Paradellis; Eds.*

[15] http://irmm.jrc.ec.europa.eu/, GELINA facility at IRMM.

[16] M. Angelone, M. Pillon, R. Faccini, D. Pinci, W. Baldini, et al., "Silicon Photo-Multiplier radiation hardness tests with a beam controlled neutron source", *Nucl.Instrum.Meth.* A623:921–926, 2010, doi:10.1016/j.nima.2010.07.057, arXiv:1002.3480 [physics.ins-det].

[17] http://www-ppd.fnal.gov/MTBF-w/, Fermilab Test Beam Facility.

[18] A. H. Heering, P. Bohn, A. Clough, E. Hazen, J. Rohlf, S. Los, J. Freeman, E. Cascio, Y. Musienko, and C. Piemonte, "Radiation damage studies on SiPMs for calorimetry at the Super LHC", *Nuclear Science Symposium Conference Record, 2008. NSS '08. IEEE*, pp. 1523 -1526, oct. 2008, doi:10.1109/NSSMIC.2008.4774702.

[19] N. Dinu, Z. Amara, C. Bazin, V. Chaumat, C. Cheikali, et al., "Electro-optical characterization of SiPM: A comparative study", *Nucl.Instrum.Meth.* A610:423–426, 2009, doi:10.1016/j.nima.2009.05.101.

[20] G. Llosa, N. Belcari, M. Bisogni, G. Collazuol, S. Marcatili, S. Moehrs, F. Morsani, C. Piemonte, and A. Del Guerra, "Energy and Timing Resolution Studies With Silicon Photomultipliers (SiPMs) and 4-Pixel

SiPM Matrices for PET", *Nuclear Science, IEEE Transactions on* 56(3):543 –548, june 2009, doi:10.1109/TNS.2009.2015877.

[21] http://www.advansid.com/products/silicon-photomultiplier, AdvanSiD page on FBK SiPM.

[22] http://jp.hamamatsu.com/products/sensor-ssd/4010/indexen.html, Hamamatsu page on MPPC.

[23] http://sensl.com/products/silicon-photomultipliers/microsl/, sensL page on SPM.

[24] F. Dal Corso, "Studies of SiPM at Padova: Neutrons irradiation at LNL 9th, 13th Oct 2009", *XI Super*B *General Meeting, LNF*, Dec. 2009.

[25] V. Santoro, "IFR Background Report", *3rd Super*B *Collaboration Meeting, Frascati*, March 2012.

[26] E. Grauges et al., (Super*B* collaboration), "Super*B* Progress Reports – Detector", 2010, arXiv:1007.4241 [physics.ins-det], report INFN-AE-10-4, LAL-10-115, SLAC-R-954.

[27] P. Dorosz and M. Baszczyk, "Thermal Stabilization of Silicon Photomultiplier measurement system for IFR", *Instrumentation for Muon and K_L^0 Identification at Super Flavor Factories" workshop in Krakow, Poland*, September 2012.

[28] G. Cibinetto, "Something about the prototype", *Super*B *Workshop and Kick Off Meeting, Elba*, May 2011.

[29] G. Cibinetto, "Beam Test: data for analysis", *I Super*B *meeting, London*, Sep 2011.

[30] V. Santoro, "IFR Background Report", *III Super*B *meeting, LNF-Frascati*, Mar 2012.

[31] V. Santoro, "IFR Background Report", *Instrumentation for Muon and K_L^0 Identification at Super Flavor Factories workshop in Krakow, Poland*, Sep 2012.

[32] http://atlas.web.cern.ch/Atlas/GROUPS/FRONTEND/WWW/RAD/RadWebPage/ATLASPolicy/Appendix_1.pdf, ATLAS Policy on Radiation Tolerant Electronics: ATLAS Radiation Tolerance Criteria.

[33] P. Jarron, "Radiation tolerant electronics for the LHC experiments", *Proceedings of the 4th Workshop on Electronics for LHC Experiments, Rome*, Sept 1998.

[34] F. Faccio, "Radiation effects in devices and technologies, IN2P3 school", May 2005.

[35] W. Dabrowski, "Challenges and benefits of designing readout ASICs in advanced technologies", *Nucl.Instrum.Meth.* A579:821–827, 2007, doi:10.1016/j.nima.2007.05.302.

[36] A. L. Rosa and other, "Ionizing radiation effects on a 64-channel charge measurement ASIC designed in CMOS 0.35 um technology", *Nucl.Instrum.Meth.* A593:619–623, 2008.

[37] M. Angelone, M. Pillon, R. Faccini, D. Pinci, W. Baldini, et al., "Silicon Photo-Multiplier radiation hardness tests with a beam controlled neutron source", *Nucl.Instrum.Meth.* A623:921–926, 2010, doi:10.1016/j.nima.2010.07.057, arXiv:1002.3480 [physics.ins-det].

[38] F. Dal Corso, "Studies of SiPM at Padova: Neutrons irradiation at LNL 9-13 Oct 2009", *XI Super*B *General Meeting , LNF, Frascati*, Dec. 2009.

[39] E. Feltresi, "Neutron Damage on SiPMs studies at LNL", *XV Super*B *General Meeting Caltech, Pasadena CA, USA*, Dec. 2010.

[40] F. Dal Corso, "Status of SiPM; studies at Padova", *XVI Super*B *General Meeting , LNF, Frascati*, Apr. 2011.

[41] "Super*B* IFR electronics: update", *2nd Super*B *General Meeting, LNF, Frascati*, Dec. 2011, Cotta Ramusino, A.

[42] Orsay MicroElectronics Group Associated (OMEGA), "EASIROC DATASHEET Version: 5", April 2011.

[43] Orsay MicroElectronics Group Associated (OMEGA), "EASIROC SOFTWARE & TEST BOARD USER GUIDE Version: 11", April 2011.

[44] R. Mos, J. Barszcz, W. M. J. Jastrzb, M. ans Kucewicz, E. Raus, and M. Sapor, "Front-End electronics for Silicon Photomultiplier detectors", *Electrical Review* 11a, 2010.

[45] P. Carniti, A. Giachero, C. Gotti, M. Maino, and G. Pessina, "An introduction to CLARO: A fast Front-End ASIC for Photomultipliers", *2nd Super*B *Collaboration Meeting, LNF Frascati*, Dec 2011.

[46] M. Baszczyk and P. Dorosz, "Characterization of RAPSODI ASICs after Irradiation", *Instrumentation for Muon and K_L^0 Identification at Super Flavor Factories workshop in Krakow, Poland*, Sep 2012.

[47] "CLARO and RAPSODI ASICs irradiation at the CN facility of the INFN-LNL", *Instrumentation for Muon and K_L^0 Identification at Super Flavor Factories workshop in Krakow, Poland*, Sep 2012.

[48] A. Cotta Ramusino, "Super$B$ IFR electronics: update on prototype electronics and IFR_DAQ", *XII Super*B *Workshop - LAPP Annecy*, Mar. 2010.

[49] E. Grauges et al., (Super$B$ Collaboration collaboration), "Super$B$ Progress Reports – Detector", 2010, arXiv:1007.4241 [physics.ins-det], report INFN-AE-10-4, LAL-10-115, SLAC-R-954.

[50] "Super$B$ IFR electronics: update", *3rd Super*B *meeting, LNF, Frascati*, Mar. 2012, Cotta Ramusino, A.

[51] A. Baschirotto, G. Cocciolo, M. De Matteis, A. Giachero, C. Gotti, et al., "A fast and low noise charge sensitive preamplifier in 90-nm CMOS technology", *JINST* 7:C01003, 2012, doi:10.1088/1748-0221/7/01/C01003.

[52] G. Mazza, D. Calvo, P. De Remigis, T. Kugathasan, M. Mignone, et al., "A CMOS 0.13-mu m silicon pixel detector readout ASIC for the PANDA experiment", *JINST* 7:C02015, 2012, doi:10.1088/1748-0221/7/02/C02015.

[53] G. Dellacasa, S. Garbolino, F. Marchetto, S. Martoiu, G. Mazza, et al., "A 130-nm ASIC prototype for the NA62 Gigatracker readout", *Nucl.Instrum.Meth.* A650:115–119, 2011, doi:10.1016/j.nima.2010.12.109.

[54] M. Baszczyk, P. Dorosz, S. Głb, W. Kucewicz, and M. Sapor, "Four channels data acquisition system for silicon photomultipliers", *Elektronika* 12, 2011.

11 Magnet and Flux Return

The magnet for the Super$B$ experiment is a thin superconducting solenoid mounted inside a hexagonal flux return. It was initially designed and built in the 1990s for the *BABAR* experiment [1, 2] where it was successfully operated with a high degree of reliability for approximately ten years. Because of this it has been chosen as the preferred option for the Super$B$ detector. In this chapter the main characteristics of the magnet, the modifications required for its integration into the Super$B$ detector, and a plan for its transport from SLAC to the Tor Vergata site, reassembly and installation are described.

11.1 Magnet main characteristics

The Super$B$ magnet, for which a schematic cross section is shown in Figure 11.1, includes:

1. The superconducting solenoid;
2. The laminated barrel flux return, composed of 18 steel plates of different thickness (from 20 mm to 100 mm);
3. The two doors of the flux return with 19 steel plates of different thickness;
4. An iron end plug shield in the forward end door;
5. An iron end plug shield in the backward end door.

Compared to *BABAR*, the design of the forward end plug shield has been modified to make it as symmetric as possible with respect to the backward end plug. The reason for the asymmetry of the *BABAR* magnet was that the magnetic field had to be shielded from the Q2 final focus quadrupole. This quadrupole is no longer present in in the Super$B$ accelerator lattice, allowing for a more symmetric detector magnet configuration. In the present design the forward door configuration remains the same as in *BABAR*. However, a future option for making the forward door completely symmetric with respect to the backward door is under consideration. Another difference from the *BABAR* magnet is the addition of a 50 mm plate at the external ends of the backward door and of a 100 mm plate at the external side of the forward door. More detailed information about the flux return can be found in Chapter 10.

Figure 11.2: The superconducting solenoid after the cryogenic test at Ansaldo. One can see the annular cryostat enclosing the superconducting solenoid and the turret with proximity cryogenics and current leads.

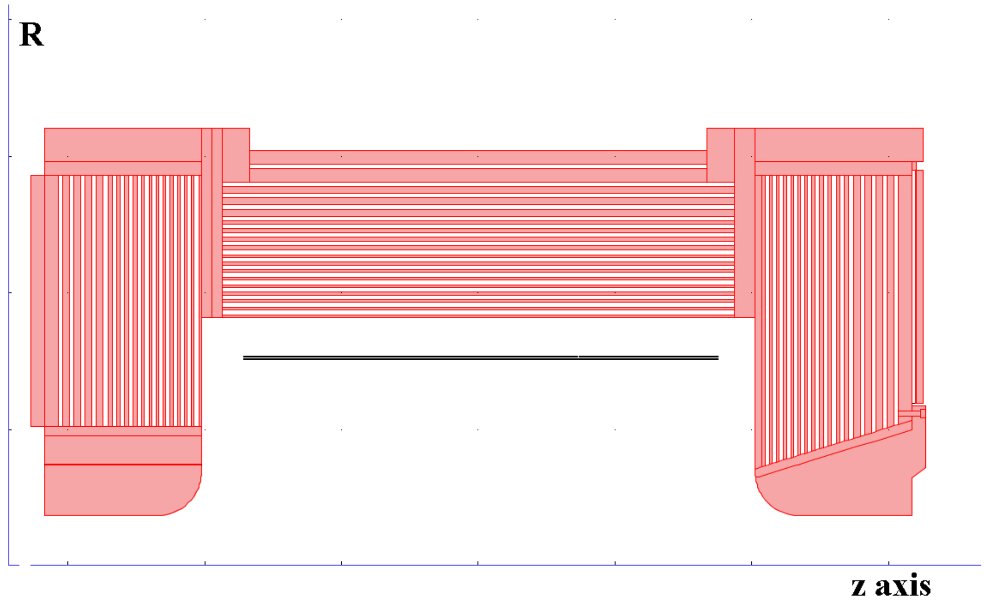

Figure 11.1: Simplified cross-sectional view of the magnet in the plane z-r (cylindrical symmetry with respect the axis shown at the bottom of the figure). This model is used for 2D magnetic computations. The thin black line represents the superconducting solenoid (just the coil, the cryostat is not shown). It is included in the flux return composed of the barrel and two end caps (the doors) including two end plugs. The asymmetry is due to the reuse of the *BABAR* equipment.

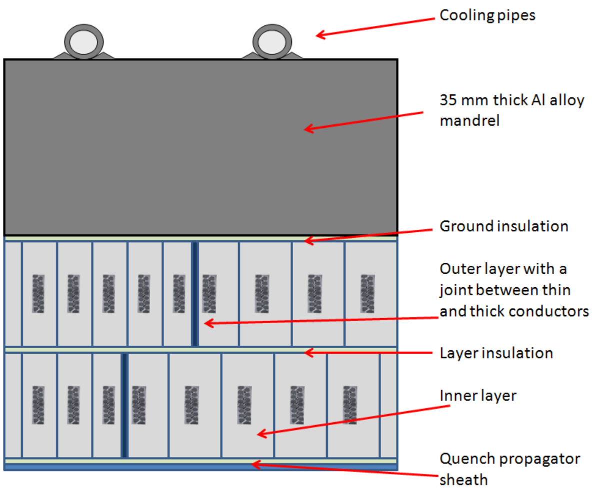

Figure 11.3: Cross section of the cold mass. One can see the two layers made of a two different conductors for grading the axial current density. The two layers were directly wound inside an external mandrel in aluminum alloy 5083. The liquid helium is circulated in pipes directly attached to the external surface of the mandrel.

The core of the magnet is a thin superconducting solenoid with as-built characteristics shown in Table 11.1. Figure 11.2 shows the solenoid just after the preliminary test at Ansaldo in Genova (Italy) [3], where it was built. The design of the solenoid was based on criteria developed and tested with many superconducting detector magnets using aluminum-stabilized thin solenoids [4], including the magnets for the ALEPH [5] and DELPHI [6] experiments at CERN.

The coil is composed of two layers of aluminum-stabilized conductors internally wound in a 35 mm-thick aluminum (alloy 5083) support mandrel. Cooling pipes welded to the outside of the support mandrel form part of a cryogenic thermo-siphon system. Electrical insulation consists of dry wrap fiberglass cloth and epoxy vacuum impregnation. Figure 11.3 shows a schematic cross section of the solenoid's cold mass. The conductors are 20 mm wide and are composed of a superconducting 16-strand Rutherford-type cable embedded in a

Table 11.1: Main characteristics of the Super$B$ solenoid, as built. (R.T. = room temperature).

Central Induction	1.5 T
Conductor peak field	2.3 T
Winding structure	2 layers graded current density
Uniformity in the tracking region	± 3%
Winding axial length	3512 mm at R.T.
Winding mean radius	1530 mm at R.T.
Operating current	4596 A
Inductance	2.57 H
Stored Energy	27 MJ
Total turns	1067
Total length of conductor	10300 m

pure aluminum matrix through a co-extrusion process, which ensures good bonding between the aluminum and the superconductor. In order to achieve a field homogeneity of ±3 % in the large volume required by BABAR (and confirmed for Super$B$), the current density in the winding is graded: It is lower in the central region and higher at the ends. This gradation is obtained by using conductors of two different thicknesses: 8.4 mm in the central region and 5 mm towards the ends. Table 11.2 shows the main characteristics of the conductor. In total six conductor lengths were employed in the construction. The electrical joints between the thin and the tick conductors are integrated into the winding, as it can be seen in Figure 11.3.

11.2 Magnetic forces on the solenoid

The coil is located inside an asymmetric flux return yoke, a heritage of the BABAR configuration. The forward plug design has been modified to make it more symmetric with respect to the backward plug, but axial offset forces are still present. For the BABAR magnet, in order to have an offset force in one direction only (no inversion during the ramp up), the coil was positioned with a 30 mm axial displacement in the forward direction and held in place by three Inconel 718 tie rods on the backward end. These tie rods were designed to hold forces as high as 250 kN with a safety factor of 4. During magnet operation at SLAC the axial force was continuously monitored and measured be no more than 80 kN at 3800 A magnet current. The three similar tie rods on the forward end were never strained.

The modification of the iron yoke introduced for Super$B$ requires an adjustment of the axial coil position inside the cryostat. A preliminary magnetic computation, for which the magnetic field map is shown in Figure 11.4, indicates that the same conditions for the axial forces can be obtained in Super$B$ with a displacement of 20 mm in the forward direction. It has also been determined that the gradient of the axial force is about 15 kN/mm.

11.3 Cryogenics

The coil is indirectly cooled at an operating temperature of 4.5 K using the thermo-siphon technique with the liquid helium being circulated in pipes welded to the support cylinder (Figure 11.3). The piping was designed for a steady-state cooling flow of 30 g/s. In the BABAR magnet, cool down and cryogenic supply to the coil and 40 K radiation shields was accomplished by a modified Linde TCF-200 liquefier/refrigerator [7]. Liquid helium and cold gas from the liquefier/refrigerator and a 4 m^3 storage vessel was supplied to the coil and shields through a 60 m-long, coaxial, return gas-screened, flexible transfer line. A similar, albeit updated system, will be implemented for Super$B$; the proximity cryogenics integrated with the magnet and hosted in the turret will however remain unchanged. The schematic of the cooling system is shown in Figure 11.5. It is possible to cool down the coil by a mixture of warm and cold helium gas or by supplying gas at increasingly lower temperature through the re-

Table 11.2: Summary of strands, Rutherford, and conductor characteristics.

Component	Characteristic	Value
Strand	Material	NbTi
	Composition	Nb $46.5 \pm 1.5\%$ wt
	Filament size	$< 40\,\mu$m
	Twist pitch	25 mm
	Cu/NbTi ratio	> 1.1
	RRR	Final >100
	Wire diameter	0.800 ± 0.005 mm
Rutherford	Transposition pitch	< 90 mm
	Number of strands	16
	Final size	$1.4 \times 6.4\,\text{mm}^2$
Conductor	Al-RRR	>1000
	Thin conductor dimensions	$(4.93 \times 20) \pm 0.02$ mm
	Thick conductor dimensions	$(8.49 \times 20) \pm 0.02$ mm
	Rutherford-Al bonding	> 20 MPa
	Thin conductor Al/Cu/NbTi ratio	23.5:1.1:1
	Thick conductor Al/Cu/NbTi ratio	42.4:1.1:1
	Edge curvature radius	> 0.2 mm
	Critical current ($T = 4.2\,\text{K}; \text{B} = 2.5\,\text{T}$)	12680 A

frigerator. The shields are cooled by part of the gas coming back from the coil. The cool-down at SLAC took about a week.

Refrigerator. The refrigerator consists of a $4\,\text{m}^3$ supply dewar, a helium liquefier, distribution valve box and a compressor facility with three screw compressors. Descriptions of the system design and function can be found in References [8] and [9].

Heat load. In *BABAR* a heat load measurement at 4.5 K was performed by closing the input valve to the $4\,\text{m}^3$ Dewar and then measuring the liquid helium consumption in that vessel. With a 1.58 T magnetic field the mass flow rate per lead (at 40 mV across each lead) was 90 NLP/m corresponding to a heat load of 5 W per lead. Using these data, and considering that a 3 W loss can be attributed to the transfer line, we can calculate that the magnet heat load was between 19 W and 24 W at a flow rate of 14 l/h. Cooling the shields with cold helium gas from the liquid helium reservoir in the Valve Box contributed to keeping the loss rate very low: Shield temperatures ranged from from 37 K to 49 K with a mass flow rate of 0.35 g/s. Since the enthalpy variation of helium gas at atmospheric pressure between 4.5 K and 45 K (average shield temperature) is about 250 J/g, the total load at the shield was 87 W. For the magnet in the Super*B* configuration we can assume the same heat load values.

11.4 Current supply and protection system

The Super*B* magnet will be electrically operated with the same circuit used in the *BABAR* magnet (Figure 11.6). A 5 kA - 20 V two-quadrant power supply supplies current to the solenoid, which is protected by a resistor electrically connected in parallel. If a quench is detected (50 mV unbalance signal between the two volt-

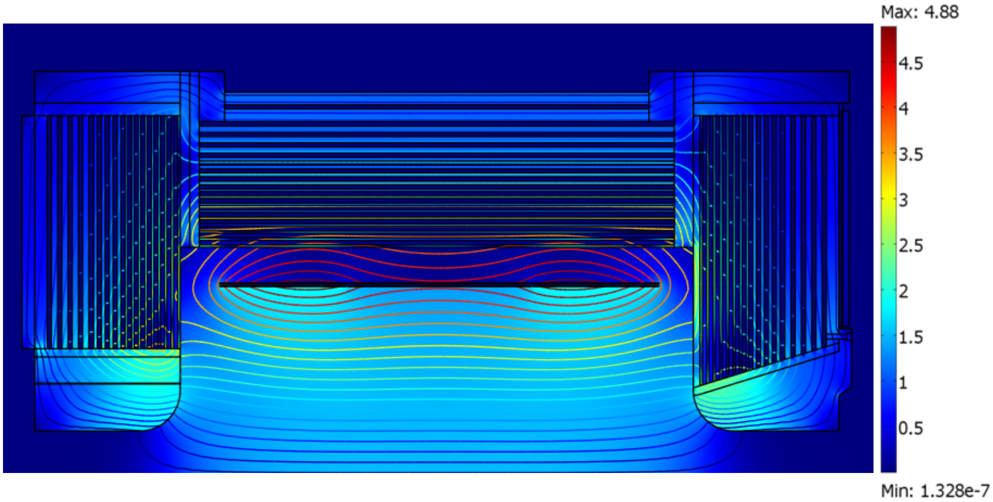

Figure 11.4: Magnetic field map (in T) in the Super$B$ detector region showing that the field in proximity of the magnetic axis will be partially shielded by the anti-solenoids of the final focus. In this simulation the superconducting coil is axially displaced by 20 mm in the forward direction (to the right in the figure).

ages in two layers), the breakers open, allowing the coil to discharge its stored energy into the dump resistor. During this process the peak voltage at the coil ends can reach up to 340 V. The fast discharge of the nominal current causes a quench of the whole coil due to the heating of the supporting cylinder (*Quench Back*) and its temperature increases to 37 K uniformly. About five hours are needed after a quench to cool down the coil and fill the reservoir before the magnet is ready again for ramping up the current.

11.5 Plan for reusing the *BABAR* magnet equipment.

With appropriate refurbishing, the superconducting solenoid and its ancillaries from *BABAR* can largely be reused for Super$B$. The following items are involved:

1. The superconducting coil composed of the cold mass (mass: 7.8 t), the cryostat (3.0 t), and the valve box (0.8 t);
2. the dump resistor (1.2 t);
3. the power supply (5 kA, 20 V);
4. two racks with controls;
5. the vacuum pumps and related systems:
6. the transfer line and quench line;
7. the breaker for 5 kA;
8. cables and miscellaneous hardware;
9. the cold box, the compressors, and the refrigerator controls.

Although some options are still under investigation, the most credible scenario is described below.

Superconducting solenoid. The coil has been disassembled (the turret has been removed) and is currently mounted inside the transportation tool. For transport, the cold mass still needs to be blocked with respect to the cryostat as it was during delivery to SLAC. The supporting system should be able to hold the expected transportation loads (3g vertical, 2g axial and 1.5 g lateral). Prior to transportation the flanges will be removed and the transportation blocks reapplied. The same consideration applies to the valve box enclosed in the turret. A preferred option for the transportation is a dedicated flight

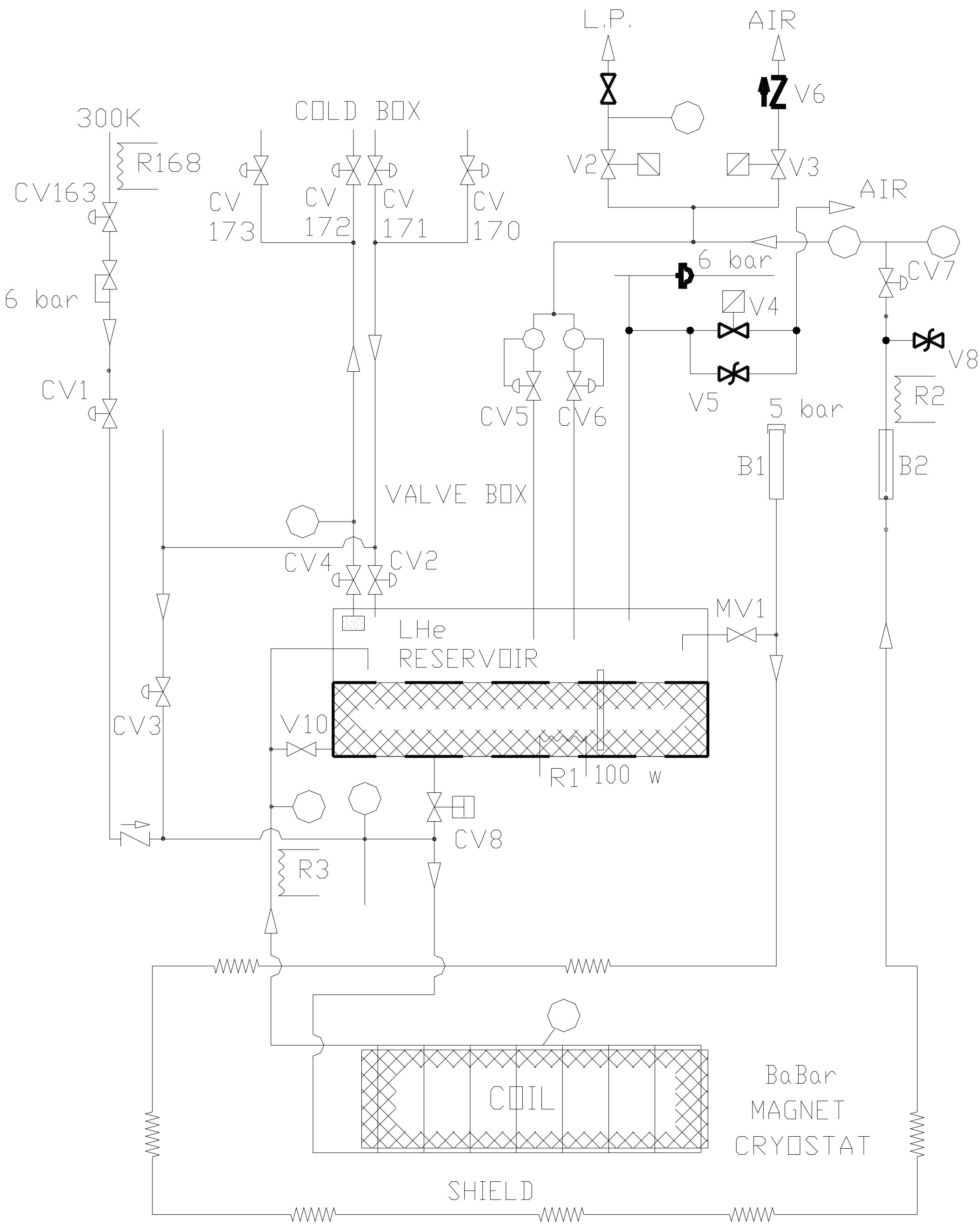

Figure 11.5: Schematic of cryogenic circuit with proximity cryogenics, which is completely integrated with the magnet. The reservoir, the valves and the current leads are hosted in the turret visible in Figure 11.2

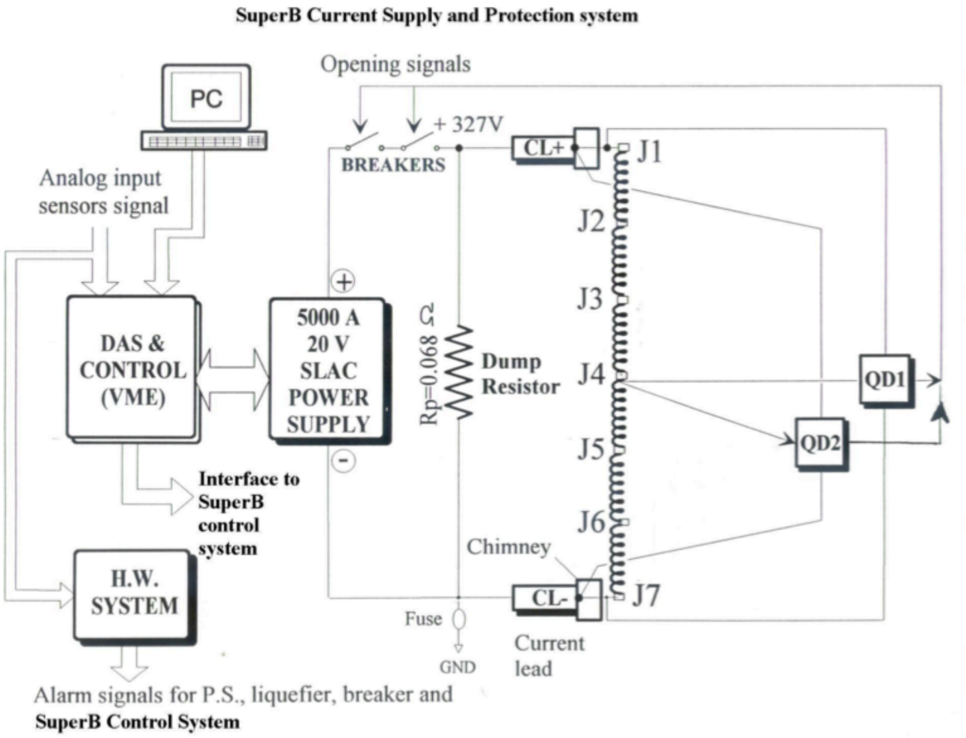

Figure 11.6: Electrical scheme for current supply and protection system

as it was done for the delivery to SLAC, because there is much less risk of damage. Once in Italy the solenoid will be reassembled in an area close to the Super*B* site to perform a cryogenic test before the final installation in the detector. Since the sensors on the tie rods (strain gauges and thermometers) are no longer working, they will need to be replaced before the realignment of the cold mass. Reassembly will also include the reconnection of the current leads and restoration of the electrical insulation.

Dump resistor, quench detectors and breakers. These components are reusable after a check of their conditions. The breakers might require maintenance.

Power supply and control system. The reuse of these components is problematic, partly due to their old age, and partly due to different electrical equipment standards and codes. The plan is to procure them as new.

Cryogenic devices. The refrigerator could in principle be reused, but its reinstallation and commissioning in Italy would require the replacement of the screw compressors and the involvement of personnel from both the manufacturer (Linde) and SLAC, resulting in high costs with large uncertainties. Furthermore, there are significant risks in reusing a 15-year-old machine and expecting it to operate for another 15 years. Similar considerations also apply to all the other cryogenic components with the notable exception of the flexible transfer lines. The option of a new refrigerator, better sized for the solenoid and final focus superconducting magnets, has been studied.

11.6 Bibliography

[1] P. Fabbricatore et al., "The Superconducting magnet for the *BABAR* detector of the PEP-II B factory at SLAC", *IEEE Trans .Magnetics* 32:2210–2213, 1996, doi:10.1109/20.508606.

[2] R. A. Bell et al., "The *BABAR* superconducting coil: design, construction and test",

Nuclear Physics B - Proceedings Supplements 78:559–564, 1999, doi:10.1016/S0920-5632(99)00603-9.

[3] Ansaldo Energia (Genova, Italy), http://www.ansaldoenergia.it.

[4] A. Yamamoto and Y. Makida, "Advances in superconducting magnets for high energy and astroparticle physics", *Nucl. Instrum. Meth.* A494:255–265, 2002, doi:10.1016/S0168-9002(02)01477-8.

[5] D. Decamp et al., "ALEPH: A detector for electron-positron annihilations at LEP", *Nucl. Instrum. Meth.* 294:1–2, 1990, doi:10.1016/0168-9002(90)91831-U.

[6] "The DELPHI detector at LEP", *Nucl. Instrum. Meth.* 303:233–276, 1991, doi:10.1016/0168-9002(91)90793-P.

[7] W. Burgess et al., "Reconfiguration of a B&W/SSC/LINDE liquefier to meet SLAC *BaBar* detector magnet requirements", *SLAC-PUB-7874*, 1998.

[8] D. Boutigny et al., (*BaBar* Collaboration collaboration), "*BaBar* technical design report", *SLAC-R-457*, 1995.

[9] E. Thompson et al., "Failure scenarios and mitigations for the *BaBar* superconducting solenoid.", *AIP Conf.Proc.* 823:71–77, 2006, doi:10.1063/1.2202402.

12 Electronics, Trigger, Data Acquisition and Online

The Super$B$ [1] Electronics, Trigger, Data acquisition and Online system (ETD) comprises the Level-1 trigger, the event data chain, and their support systems. Event data corresponding to accepted Level-1 triggers move from the Front-End Electronics (FEE) through the Read-Out Modules (ROMs) and the network event builder to the High Level Trigger (HLT). Events accepted by the HLT are streamed to a data logging disk buffer from where they are handed over to offline for further processing and archival. ETD also encompasses the hardware and software components that control and monitor the detector and data acquisition systems, and perform near-real-time data quality monitoring and online calibration.

12.1 Trigger Strategy and System Requirements

The *BABAR* and Belle [2] experiments both chose to use "open triggers" that preserved nearly 100% of $B\overline{B}$ events of all topologies, and a very large fraction of $\tau^+\tau^-$ and $c\overline{c}$ events. This choice enabled very broad physics programs at both experiments, albeit at the cost of a large number of events that needed to be logged and reconstructed, since it was so difficult to reliably separate the desired signals from the $q\overline{q}$ $(q = u, d, s)$ continuum and from higher-mass two-photon physics at trigger level. The physics program envisioned for Super$B$ requires very high efficiencies for a wide variety of $B\overline{B}$, $\tau^+\tau^-$, and $c\overline{c}$ events, and depends on continuing the same strategy, since few classes of the relevant decays provide the kinds of clear signatures that allow the construction of specific triggers.

All levels of the trigger system are designed to permit the acquisition of prescaled samples of events that can be used to measure the trigger performance.

The trigger system consists of the following components [1]:

Level 1 (L1) Trigger: A synchronous, fully pipelined L1 trigger receives continuous data streams from the detector independently of the event readout and delivers readout decisions to the FCTS with a fixed latency. Like in *BABAR*, the Super$B$ L1 trigger operates on reduced-data streams from the drift chamber and the calorimeter.

High Level Triggers (HLT) — Level 3 (L3) and Level 4 (L4): The L3 trigger is a software filter that runs on a commodity computer farm and bases its decisions on specialized fast reconstruction of complete events. An additional "Level 4" filter may be implemented to reduce the volume of permanently recorded data if needed. Decisions by L4 would depend on a more complete event reconstruction and analysis. If the worst-case per-event performance of the L4 reconstruction algorithms does not meet the near-real-time requirements of L3, it might become necessary to decouple L4 from L3 – hence, its designation as a separate trigger stage.

12.1.1 Trigger Rate and Event Size Estimation

The Super$B$ L1-accept rate design standard of 150 kHz takes into consideration the experience with *BABAR*. The *BABAR* Level-1 physics configuration produced a trigger of approximately

[1] While at this time we do not foresee a "Level 2" trigger that acts on partial event information in the data path, the data acquisition system architecture would allow the addition of such a trigger stage at a later time, hence the nomenclature.

3 kHz at a luminosity of 10^{34} cm^{-2}sec^{-1}, however changes in background conditions produced large variations in this rate. The *BABAR* DAQ system performed well, with little dead time, up to approximately 4.5 kHz. This 50% headroom was very valuable for maintaining stable and efficient operation and will be retained in Super$B$. In spite of the different energy asymmetry, the Super$B$ geometrical acceptances are very similar to those in *BABAR*, due to changes in detector geometry.

In *BABAR* the output of the offline physics filter corresponded to a cross-section of approximately 20 nb and included a highly efficient Bhabha veto. We take this as an irreducible baseline for an open hardware trigger design; in fact this is somewhat optimistic since the offline filter used results from full event reconstruction. The accepted cross-section for Bhabhas in Super$B$ is also similar to *BABAR*, and approximately 50 nb. At the Super$B$ design luminosity of 10^{36} cm^{-2}sec^{-1} these two components add up to 70 kHz L1-accept rate without backgrounds. The maximum rate of background-related L1 accepts is estimated to be 30 kHz, resulting in a total L1-accept rate of 100 kHz. Without a Bhabha veto at L1 (which is not part of the Super$B$ baseline trigger design) this is the minimum rate the readout system has to handle. By adding a *BABAR*-like reserve of 50% to both accommodate the possibility of higher backgrounds than design (e.g. during machine commissioning), and the possibility that the machine exceeds its initial design luminosity, we set the the Super$B$ design rate at 150 kHz.

The event size estimate still has some uncertainties. The size of raw events that have to be transferred from the FEEs through the ROMs to the HLT is understood well enough to determine the number of data links required, and to size the event building network. Based on initial estimates from the SVT and the EMC we predict a raw event size of 500 kByte. As part of the event processing in the HLT farm, the event size will be reduced by applying zero suppression or feature extracting algorithms. The details of these algorithms and their specific performance for data size reduction are not known yet, so we make a conservative event size estimate of 200 kByte for permanent logging.

12.1.2 Dead Time and Buffer Queue Depth Considerations

The event data chain has been specified to handle the maximum average rate of 150 kHz, and to absorb the expected instantaneous rates, both without incurring dead time of more than 1% under normal operating conditions at design luminosity. Note that this 1% dead time specification does not include event loss due to individual sub-detector's intrinsic dead times or the L1 trigger's limitations in separating events that are very close in time. Dead time is generated and managed centrally in the FCTS based on feedback ("fast throttle") from the FEE: the FCTS drops valid L1 trigger requests when at least one FEE indicates that its rate capabability has been exceeded. The ROMs and the event builder also provide feedback ("slow throttle") to slow down the trigger if they cannot keep up with the L1 accept rate.

The required ability to handle the maximum average rate determines the overall readout system bandwidth; the instantaneous trigger rate requirement affects the FCTS, the data extraction capabilities of the front-end-electronics, and the depth of the de-randomization buffers.

The minimum time interval between bunch crossings at design luminosity is about 2.1 ns—so short in comparison to detector data collection times that we assume "continuous beams" for the purposes of trigger and FCTS design. In this model the inter-event time distribution is exponential and the instantaneous rate is only limited by the capability of the L1 trigger to separate events in time. Therefore, the burst handling capability of the system (i.e. the de-randomization buffer size in the FEEs) is determined by the average L1 trigger rate, minimum time between L1 triggers, and the average data link occupancy between the FEEs and the ROMs. Figure 12.1 shows the result of a simple simulation of the FCTS together with the FEE of a typical subdetector: The minimum buffer depth required to keep the event loss due to a full derandomization buffer below 1% is shown as a function of the average data link utilization.

In Super$B$, we are targeting a link utilization of 90%. According to Figure 12.1, this requires the derandomizer buffers to be able to hold a minimum of 10 events. It is very important to understand that there is no contingency in the target link utilization — all system-wide contingency is contained in the trigger rate headroom.

Additional derandomizer capacity to what is shown in Figure 12.1 is required to absorb triggers generated while the fast throttle signal is propagated from the CFEE to the FCTS. Therefore, we estimate the total derandomizer depth to be at least 16 events.

12.1.3 Choice of Global Clock Frequency

The Super$B$ trigger and data acquisition system requires a global clock that can be distributed to all components that operate synchronously, i.e. FCTS, the L1 trigger and the sub-detector FEEs.

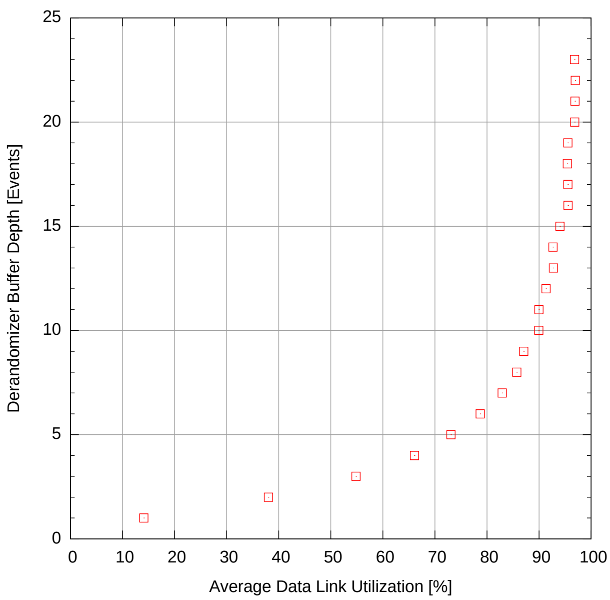

Figure 12.1: Minimum derandomizer buffer depth required to keep the event loss due to "derandomizer full" below 1% as a function of the average data link utilization.

To allow features like selective blanking of triggers for a well-defined part of the revolution of the stored beams, it is critically important that the global clock is in well defined relation with the machine RF of 476 MHz and the revolution phase of the stored beams.

In *BABAR* the global clock was generated by dividing the RF by eight, yielding a 59.5 MHz clock that was distributed to all components of the experiment. In addition, a revolution ("fiducial") signal was fed to the FCTS, giving the system knowledge of the revolution phase of the stored beams.

The baseline for Super$B$ is to use the same parameters and distribute a 59.5 MHz clock throughout the ETD system.

We are investigating to change the RF clock divisor from 8 to 12. This would result in a globally distributed experiment clock of $39\frac{2}{3}$ MHz, allowing us to reduce Super$B$-specific R&D and cost by reusing components and system designs developed and qualified for the 40 MHz clock frequency of the LHC experiments.

12.2 Architecture Overview

The system design takes into account the experience from running *BABAR* [3] and building the LHC experiments [4], [5], [6]. To minimize the complexity of the FEEs and the number of data links, the detector side of the system is synchronous, and the readout of all sub-detectors is triggered by a fixed-latency first-level trigger. Custom hardware components (e.g. specialized data links) are only used where the requirements cannot be met by commercially available off-the-shelf (COTS) components such as e.g. Ethernet.

Radiation levels are significantly higher than in *BABAR*, making it mandatory to design radiation-tolerant on-detector electronics and links (see also Chapter 5). Figure 12.2 shows the control and data flow in the trigger and event data chain, Figure 12.3 gives an overview of the ETD system architecture.

A first-level hardware trigger processes dedicated data streams of reduced primitives from

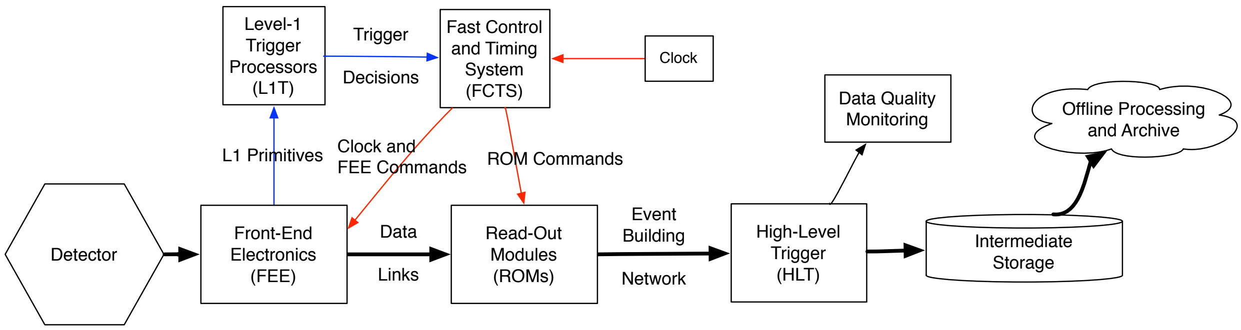

Figure 12.2: Control and data flow in the event data chain

the sub-detectors to provide trigger decisions to the Fast Control and Timing System (FCTS).

The FCTS is the central "bandmaster" of the system; it distributes clock and commands to all elements of the architecture. It initiates the readout of the events by broadcasting "L1-accept" commands to the detector FEEs at a fixed time period ("trigger latency") after the activity in the detector that caused the trigger to be asserted. In response to a L1-accept, the FEEs read out a window of samples ("readout window") from the latency buffer, format the data and transfer these "event fragments" via derandomizer buffers and optical links to the ROMs. The ROMs then perform a first stage internal event build and send the partially constructed events to the HLT farm where they are combined into complete events, and processed by the HLT which reduces the amount of data to be logged permanently by rejecting uninteresting events. Note that the readout window has to be large enough to contain the sub-detector information pertaining to an event, and to accommodate the time uncertainty of the trigger ("trigger jitter") caused by the limited time resolution of the detectors feeding the trigger.

The trigger, data acquisition and support components of the ETD system are described in this chapter, sub-detector electronics, power supplies, grounding and shielding, and the cable plant are described in the next chapter.

12.3 Trigger and Event Data Chain

The systems in the trigger and event data chain manage event selection, event filtering and end-to-end data flow from the detector to the intermediate buffer.

12.3.1 Level-1 Trigger

The baseline for the L1 trigger is to re-implement the *BABAR* L1 trigger [7] with state-of-the-art technology. It is a synchronous pipeline running at the 59.5 MHz system-wide clock (or multiples of 59.5 MHz) that processes primitives produced by dedicated electronics located on the front-end boards or other dedicated boards of the respective sub-detector. The raw L1 decisions are sent to the FCTS which applies a throttle if necessary and then broadcasts them to the FEEs and the ROMs. The standard chosen for the trigger crates will most likely be either ATCA for Physics (Advanced Telecommunications Computing Architecture) for the crates and the backplanes, or a fully custom architecture.

The main elements of the L1 trigger are shown in Figure 12.4 and are described below.

12.3.1.1 Drift chamber trigger (DCT)

The DCT consists of a track segment finder (TSF), a binary link tracker (BLT) and a p_t discriminator (PTD). The DCT also extrapolates tracks to the interaction point (IP); this

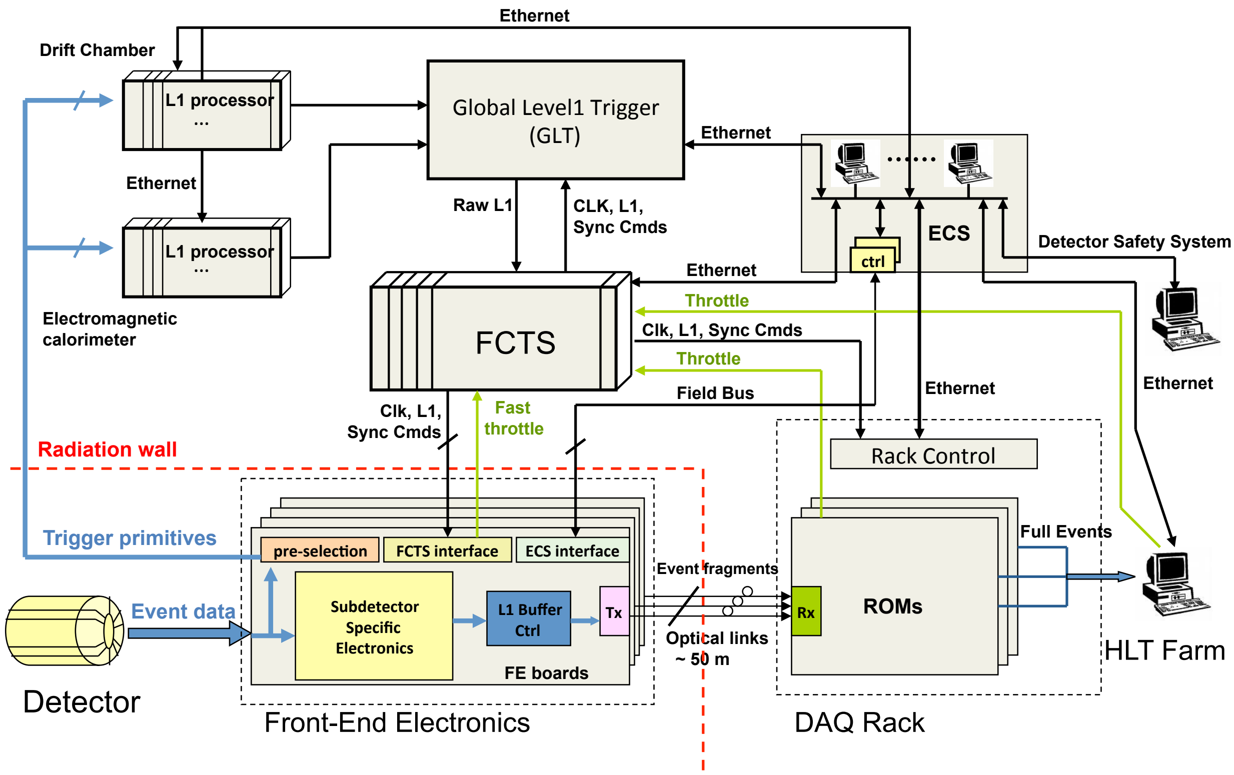

Figure 12.3: Overview of the ETD system architecture

allows to remove backgrounds that do not originate from the IP.

The layout of the DCT is shown in Figure 12.5. Track finding is implemented in two stages: in the first stage, the algorithm locally searches for track segments exploiting the data available at the front-end level. The second stage links the track segments and searches for complete tracks.

Local Segment Finding: Two options are under discussion for the DCH FEE. In the first option time and charge are measured using standard FADCs and TDCs. A second option is instead based on a cluster counting technique that requires very high-speed digitization of the signals. Granularity is 64 channels per front-end board in the first case and 16 channels per front-end board in the second. In the first case data delivered by the front-end boards will be gathered by a single board on the front-end crate and an optical link will connect the crate with the trigger crate. In the other option the DCH electronics has a modularity of 64 channels distributed on 4 contiguous radial planes. This geometry defines the super layer. Table 12.1 shows the super-layer composition for the DCH and the front-end boards necessary for its data acquisition. The track segment finder is partially integrated in the DCH front-end.

The TSF will be implemented either at the crate level or at the mezzanine level; the number of optical links and TSFs will be 118 in the case of ADC/TDC-based DCH electronics or equal to the number of DCH front-end crates in the

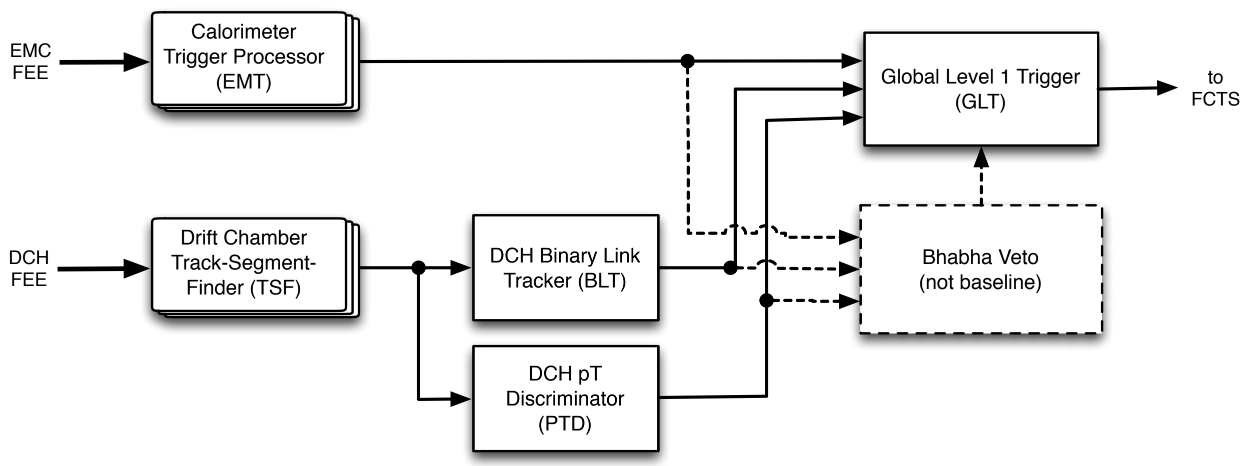

Figure 12.4: Level 1 trigger overview

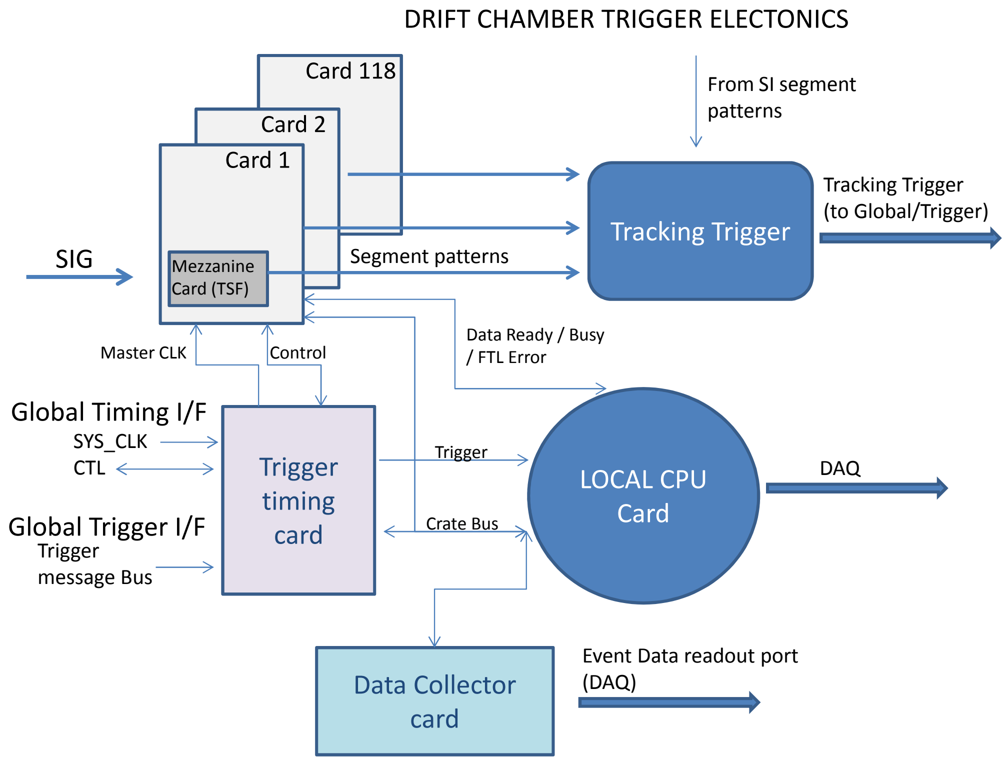

Figure 12.5: DCT Overview

Table 12.1: DCH superlayer (SL) and wire readout

	Sl1	SL2	SL3	SL4	SL5	SL6	SL7	SL8	SL9	SL10	TOT
Planes	4	4	4	4	4	4	4	4	4	4	
Type	A	A	U	V	U	V	U	V	A	A	
n. wires	736	864	496	560	624	688	752	816	896	960	7392
n. TSF	12	14	8	9	10	11	12	13	14	15	118
n. BCD	1	1	1	1	1	1	1	1	1	1	10

case of cluster counting. With cluster counting, data delivered by the FEE will be gathered by a single board in the front-end crate and sent to the trigger processor via an optical link. Each card reads a set of super cells. In order to define a coincidence and define a track segment we need to stretch the signal delivered by every wire for at least one drift time.

The TSF takes decisions at a programmable rate which can be as high as the system clock frequency. A possible track segment is shown in Figure 12.6.

A pattern needs 3 hits to be taken in consideration. The TSF delivers a bit stream to the following DCH stage, whose dimension depends on sampling frequency. This bit stream represents the ϕ of the segment in the super cell. These data are delivered to the trigger crate. To avoid efficiency losses a small number of contiguous channels is collected by all the neighboring cards. It is relevant in this scheme to optimize the sampling frequency as a function of track efficiency and exploited bandwidth.

Transmission links: We will use high speed serial links to deliver trigger data to the trigger crate. Therefore signal aggregation delivered by the TSF is made possible, and a single card in the trigger crate has all the data from the pertaining superlayer.

Global Tracking: A simple and efficient tracking algorithm is the Binary Link Track Finder (BLT) developed within the CLEO collaboration. This method starts from superlayer (SL) 2 and moves radially outward combining the TSFs if in the following SL one of the three contiguous TSF is active. The track length varies from the first to the last super layer. Track charge does not affect the algorithm and it can be implemented on programmable logic. DCT primitives are received by the DCH L1 trigger box. In this crate the optical links exploited by the DCH trigger lines are collected in such a way that each board stores the information of a single SL. A bus with a switch topology interconnects the single boards where the SL information is present with the master where all the DC TSFs are present.

Particle Counter: The BLT outputs are used to count different tracks using a multiplicity logic exploiting also isolation criteria. To define a track we can use associative memory based techniques so that in one clock cycle a pattern can be identified. The very same associative memory can in principle be used to compute the transverse momentum and the perigee parameters of the track. Track counting takes into consideration 4 SL long tracks.

Transverse Momentum: Using TSF positions and their ϕ angle it is possible to measure the multiplicity of tracks above a predefined momentum threshold and their perigee parameters. The data are delivered to the GLT which on the basis of the trigger tables asserts the trigger.

12.3.1.2 Electromagnetic Calorimeter Trigger (EMT)

The EMT (Figure 12.7) processes the trigger output from the calorimeter to find energy clusters. From the trigger point of view the electromagnetic calorimeter in the barrel is composed

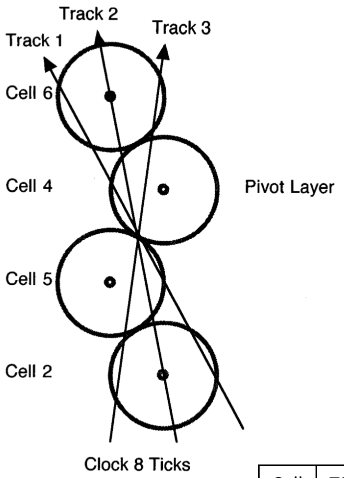

Cell	T0	1	2	3	4	T0	1	2	3	4	T0	1	2	3	4
6	0	0	0	1	2	0	1	2	3	0	0	0	0	1	2
4	0	0	0	1	2	0	0	0	1	2	0	0	1	2	3
5	0	0	0	1	2	0	0	0	1	2	0	0	1	2	3
2	0	0	0	1	2	0	1	2	3	0	0	0	0	1	2
	Track 1					Track 2					Track 3				

Cell	T0	1	2	3	4	5	6	7	8	T0	1	2	3	4	5	6	7	8	T0	1	2	3	4	5	6	7	8
6	0	0	0	0	0	1	2	3	4	0	1	2	3	4	5	6	7	0	0	0	0	0	0	1	2	3	4
4	0	0	0	0	0	1	2	3	4	0	0	0	0	0	1	2	3	4	0	0	0	1	2	3	4	5	6
5	0	0	0	0	0	1	2	3	4	0	0	0	0	0	0	1	2	3	0	0	0	1	2	3	4	5	6
2	0	0	0	0	0	1	2	3	4	0	1	2	3	4	5	6	7	0	0	0	0	0	0	1	2	3	4
	Track 1									Track 2									Track 3								

Figure 12.6: Track segment: *BABAR* vs Super*B* output bitstream. In this example we assumed to double the *BABAR* sampling frequency.

of "towers" of $8(\theta) \times 3(\phi)$ CsI(Tl) crystals, as shown in Figure 12.8.

The number of crystals in the barrel is 5760; this implies that the trigger box will handle 240 towers in the barrel. The trigger-level configuration of the end-cap has not been finalized yet, but we expect a maximum of 60 towers in the end-cap. Two different strategies are under study, both generating analog sums at the tower level. The first strategy uses the signals from the readout pre-amps, the other strategy foresees to equip each crystal with independent photon detectors (such as SiPM).

The tower-level sums are calibrated using look-up tables, encoded, and sent via LVDS links to fiber-optic transceivers shielded from radiation.

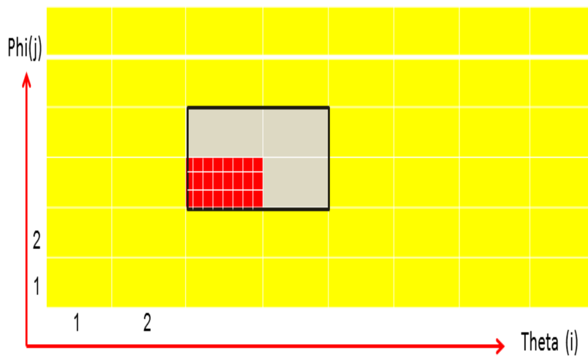

Figure 12.8: EMT trigger tower layout. A tower (shown in red) in the barrel calorimeter is comprised of 24 crystals. The black rectangle shows an example of 4 neighboring towers that need to be considered when calculating cluster energies.

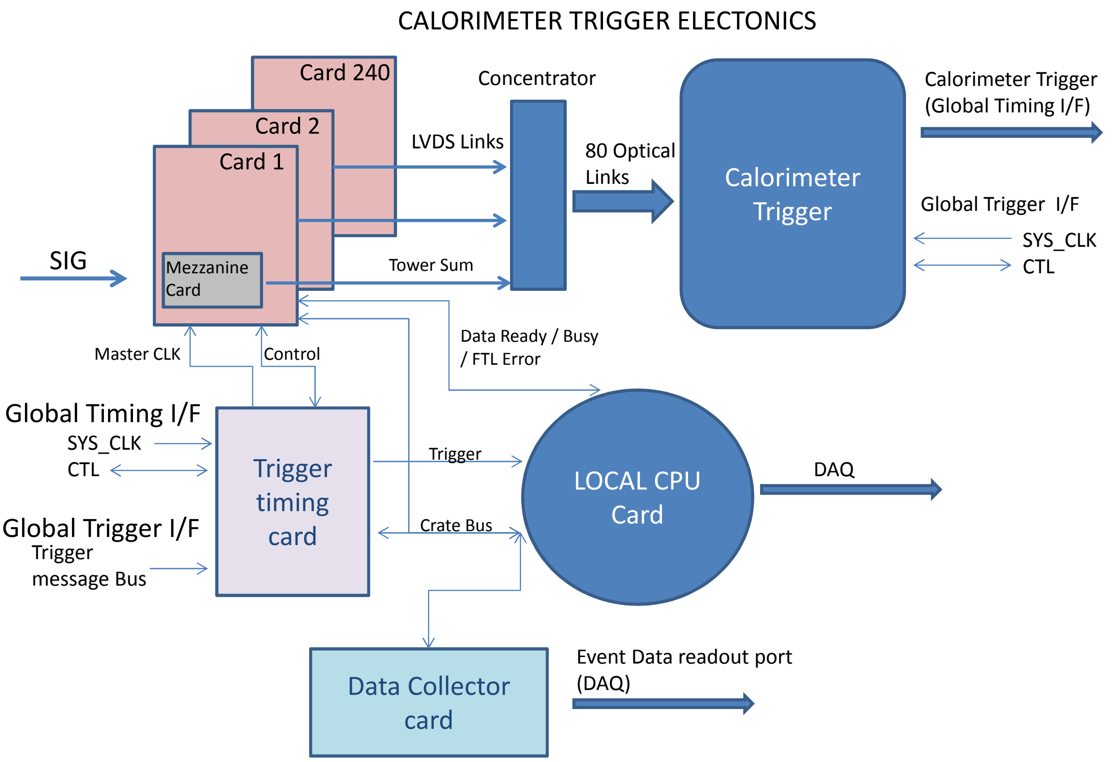

Figure 12.7: EMT overview

Particle Finders and global cluster formation: The energy deposit of a shower can be spread over adjacent towers, therefore, neighboring towers will need to be considered in the calculation of the cluster energy. Neighboring towers are scanned, and if their energy deposit is above a threshold of interest, it is added to the cluster energy.

As in *BABAR*, there will be 3 separate energy thresholds for clusters in the trigger: M cluster (above a low energy consistent with a minimum ionizing), G cluster (above 500-600 MeV) and cluster (electron Bhabha). The thresholds are all programmable. Bhabhas can be vetoed or pre-scaled. This algorithm will be implemented by the L1 EMT processor.

Particle Counters: Since clusters can be dynamically defined this allows to apply isolation cuts on particle definition.

12.3.1.3 L1 DCT and EMT trigger processors

A crate based on VME or ATCA technology will host the L1 processors. They will be based on FPGA technology, will have the same optical and electrical interfaces for both DCT and EMT, and will only differ in firmware. Track finding and dynamic super-cluster definition will be implemented on the L1 processor backplane.

12.3.1.4 Global Trigger (GLT)

The GLT processor combines the information from DCT and EMT (and possibly other inputs such as a Bhabha veto) and forms a final trigger decision that is sent to the FCTS. The GLT receives the information from the sub-detectors participating in the trigger decision through an optical link.

The trigger can be asserted by considering the information delivered by the DCH and the EMC either separately or combined. This module combines the information of the detectors and compares them to pre-defined criteria. Through the use of an FPGA the trigger can be fully programmable and upgradable.

12.3.1.5 L1 Trigger Latency

The *BABAR* L1 trigger had $12\,\mu$s latency. However, since size and cost of the L1 latency buffers in the sub-detectors scale directly with trigger latency, it should be substantially reduced, if possible. L1 trigger latencies of the much larger, more complex, ATLAS, CMS and LHCb experiments range between 2 and $4\,\mu$s, however these experiments only use fast detectors for triggering. Taking into consideration that the DCH adds an irreducible latency of about $1\,\mu$s due to drift-time and read-out, and adding some latency reserve for future upgrades, we currently estimate a total trigger latency of no more than $6\,\mu$s. More detailed engineering studies are required to validate this estimate.

12.3.1.6 Monitoring the Trigger

To debug and monitor the trigger, and to provide cluster and track seed information to the higher trigger levels, data information supporting the trigger decisions is read out on a per-event basis through the regular readout system. In this respect, the low-level trigger acts like just another sub-detector.

12.3.1.7 L1 Trigger R&D

We will study the applicability of this baseline design at Super*B* luminosities and backgrounds, and will investigate improvements, such as adding a Bhabha veto to the L1 trigger. We will also study faster sampling of the DCH and the impact of the forward calorimeter design choice. For the barrel EMC we will need to study how the L1 trigger time resolution can be improved and the trigger jitter can be reduced compared to *BABAR*. In general, improving the trigger event time precision should allow a reduction in readout window and raw event size. Other improvements might include the improvement of tracking and clustering algorithms, or by exploiting better readout granularity in the EMC.

12.3.2 Fast Control and Timing System

The Fast Control and Timing System (FCTS) manages all elements linked to clock, trigger, and event readout, and is responsible for partitioning the detector into independent subsystems for testing and commissioning. Figure 12.9 shows how the FCTS is connected to the L1 trigger, FEE, ROMs and HLT.

The FCTS will be implemented in a crate where the backplane can be used to distribute all the necessary signals in point-to-point mode. This permits the delivery of very clean synchronous signals to all boards — avoiding the use of external cables. Figure 12.10 shows the main functional blocks of the FCTS crate. The Fast Control and Timing Module (FCTM, shown in Figure 12.11) provides the main functions of the FCTS.

Clock and Synchronization: The FCTS synchronizes the experiment with the machine and its bunch timing, buffers the clock and distributes it throughout the experiment, and generates synchronous reset commands.

The baseline configuration is to distribute the clock through the FCTS command links. The deserializers will extract the clock from the serialized bitstream and report any loss of the clock signal or lock. Possible mechanisms to recover from loss-of-clock conditions are still under investigation and might include the capability of individual FEE to regain synchronization without major interruptions of the data taking. Should reliability concerns arise during the final design stage, we will consider a separate, dedicated clock distribution network as a backup solution.

To globally synchronize the system, all FEE must support the ability to reset all clock di-

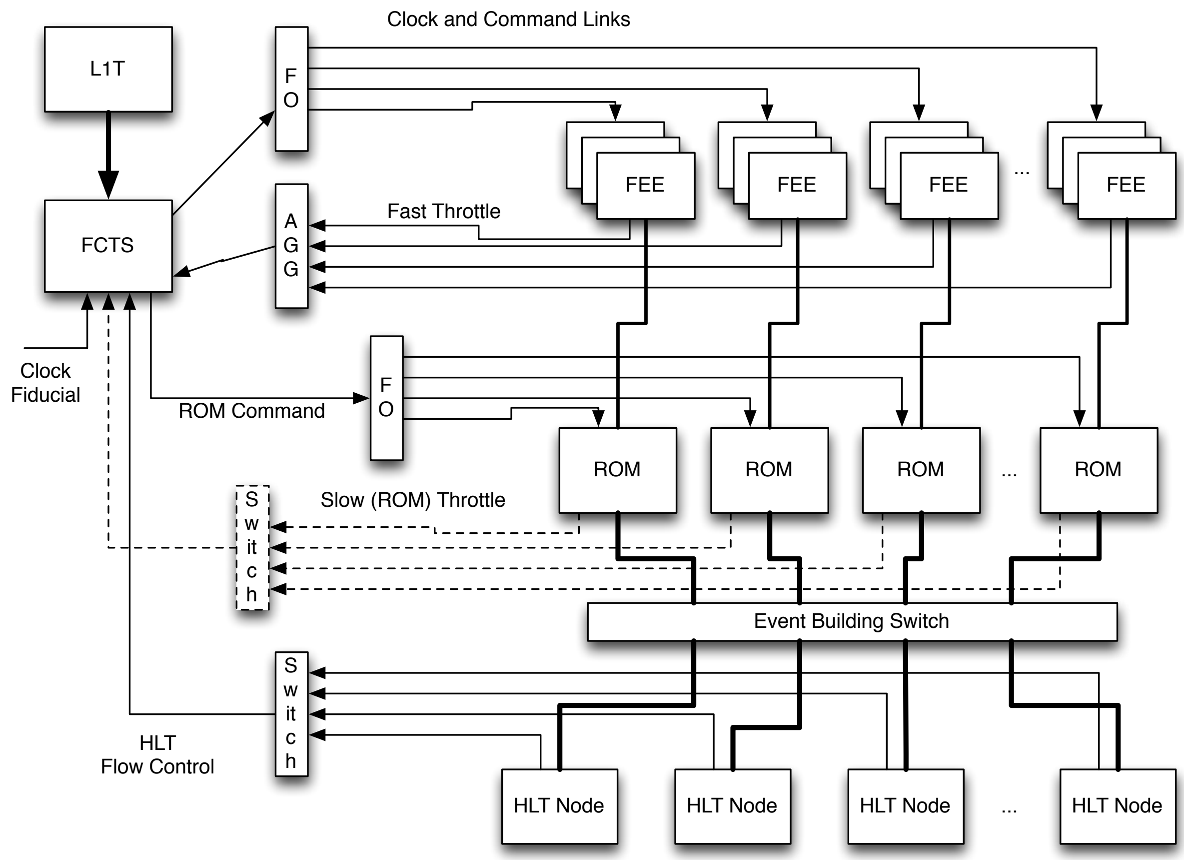

Figure 12.9: Overview of L1T/FCTS/ROM/HLT integration

viders, state machines and pipelines at system initialization or system reset to ensure that all counters and divided versions of the global clock are properly synchronized. This can be achieved through a global reset command broadcast by the FCTS. Alternatively, individual FEEs may be instructed by the ECS to resynchronize.

Trigger Handling and Throttling The FCTS receives the raw L1 trigger decisions, the fast throttle signals from the sub-detector FEE and slow throttle signals from the ROMs, generates readout commands and broadcasts them to the FEEs and the ROMs. The fast throttle is needed because during a spike in instantaneous rate or event size, data generated by the FEE can exceed the bandwidth of the data links and fill up the derandomizer buffers. An FEE generates a throttle signal when the free space in the derandomizer buffer falls below a certain threshold determined by the throttle latency. The throttle signal is removed when enough space in the derandomizer buffer has been freed up.

Assertion of a throttle signal temporarily inhibits the generation of L1-accept commands in the FCTS and thus stops the readout of new events. Any L1-accepts that are already in-flight when a throttle is asserted will still need to be absorbed by the derandomizer buffers. In addition to acting as a rate limiting mechanism, the fast throttle can also be used by the FEEs to request an "emergency stop" of the event readout.

As a baseline, the fast throttle will be implemented as a 1-bit level without any framing or encoding. This minimizes the complexity of generating, aggregating, distributing and monitoring the signals. It also allows to design a simple throttle aggregator device that can easily be standardized across all subsystems.

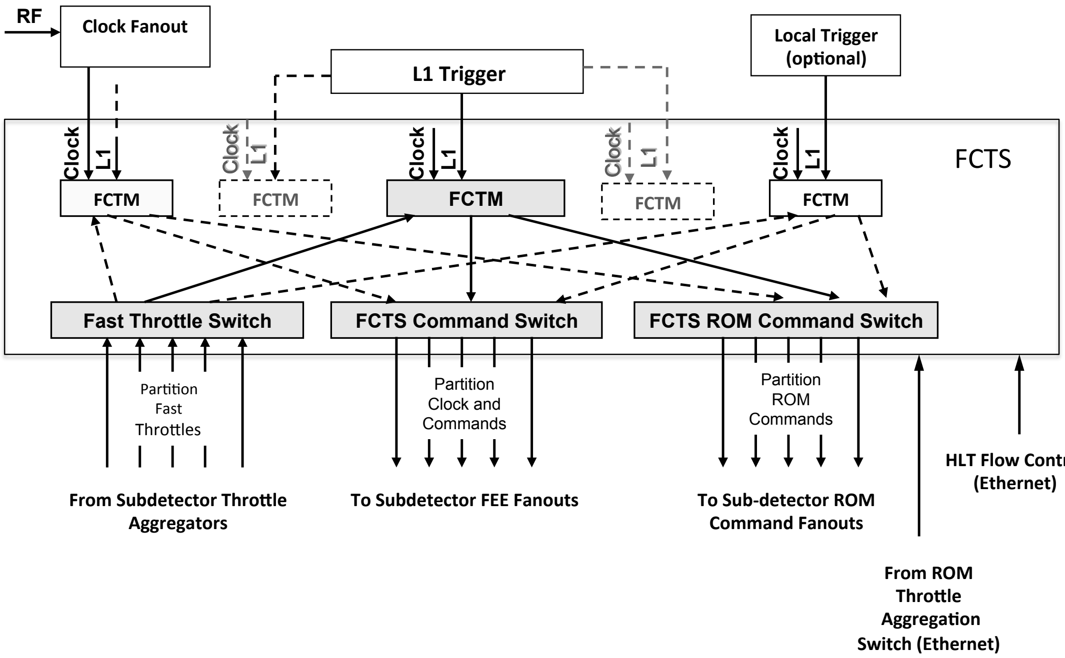

Figure 12.10: The main functional blocks in the FCTS crate

Every throttle line is monitored by measuring the fraction of time a throttle signal is asserted, and by counting the number of throttle on/off transitions. Detailed monitoring of the throttle-aggregation devices and detailed sub-detector specific diagnosis of the reasons for a throttle/stop can be performed through the ECS.

Since there is no further local flow control mechanism on the data links, the ROMs cannot assert backpressure through the FEEs but need a separate path to slow down or stop the trigger when they are unable to offload the data through the event builder. Since there is plenty of buffer space in the ROMs, this throttle ("slow" throttle) does not have stringent latency requirements and can be implemented using Ethernet.

L1-accept Command Format and Distribution The commands broadcast to the FEEs have a strict fixed-latency requirement and are as simple and short as possible to minimize the achievable temporal inter-command spacing during transmission and the amount of decoding required in the FEEs. We foresee a command word of at least 16 bits, that in addition to the front end command code and parameters contains an event tag of at least 8 bits to allow the ROM to match the event fragment with its corresponding ROM command word. The exact number of bits in the event tag (and thus the FEE command word) will depend on the details of the clock and command link protocol for framing and error detection. The FEEs are required to include the FEE command word with each event fragment they send to the ROMs.

The commands distributed to the ROMs are not subject to a fixed-latency requirement. In addition to a copy of the command word sent to the FEEs they contain at least an event timestamp (minimum of 56 bits), the full trigger word (32 bits) and the HLT destination node

(10-12 bits). Additional information such as a per-run event counter or the time since the last trickle injection pulse in the HER or LER might be included in the ROM command word as well. Since latency is variable, the ROM commands can be derandomized by queuing them before transmission; this means that the ROM command links only need to sustain the average rate (150kHz) of ROM commands.

FEE and ROM commands are sent in the same order (parallel pipelines). Suitable ways of handling lost or corrupted FEE commands will have to be developed, however this will depend on the detailed failure modes of clock distribution and command links.

Event Management: The FCTS generates unique event identifiers, manages the assignment of events to nodes in the HLT farm and uses a per-HLT-node sliding window protocol to load-balance the HLT farm and to stop sending events to unresponsive HLT farm nodes. For this, the FCTS manages a per-node counter of events it is still allowed to send to this node. A node's counter gets decremented with each event sent to that node. The FCTS determines the next destination node by searching for the next non-zero counter. Every HLT node asynchronously sends "generic event requests" with the number of events it is willing to take — when the FCTS receives such a request from a node it updates the corresponding counter with the value contained in the request. The ROM/HLT/FCTS protocol is described in more detail in the network event builder section below. Handling the event distribution with the help of the FCTS minimizes the complexity of the ROMs and the event building protocol.

Super$B$ events are large enough that in an Ethernet-based event builder we will not need to batch events into multi-event-packets (MEPs); the system, however, does not preclude the addition of a MEP scheme. Such a scheme might be required to send events that are very close in time to the same HLT node or to accommodate a non-Ethernet event building network that necessitates transmission of data in significantly larger units.

To generate a MEP, the FCTS would simply send the same HLT destination address for subsequent events which would then be packed into the same MEP (the packing can in fact be determined by the individual ROM). Sending a ROM command with a new HLT destination will then close the current MEP and open a new one.

The FCTS also keeps track of all its activity, including an accounting of triggers lost due to FEE throttling or other sources of trigger inhibits.

Calibration and Commissioning: The FCTS can trigger the generation of calibration pulses and flexibly programmable local triggers for calibration and commissioning. To support the EMC source calibration where a meaningful global trigger can not be constructed, the system can run in a special mode in which the readout of individual EMC channels is self-triggered, and the resulting waveforms are aggregated and collected under the control of the FCTS.

Partitioning: The FCTS crate includes as many FCTM boards as required to cover all partitions. One FCTM will be dedicated to the unused sub-systems in order to provide them with the clock and the minimum necessary commands.

As shown in Figure 12.11, three dedicated switches are required for partitioning the system into independent sub-systems or groups of sub-systems: One switch each for FEE clock and commands, ROM commands, and fast throttle feedback from the FEEs.

12.3.3 Control and Data Links

Requirements High-speed optical links will be used for data transfer, triggering and fast control distribution. The clock recovered from the serial streams will be used to synchronize the whole experiment.

Considerations based on event size, average expected trigger rate, topology, and cost of the link components, suggest to choose a per-link throughput in the 1-3 Gbit/s range.

Super$B$ policy explicitly requires the use of COTS components where available, avoiding the

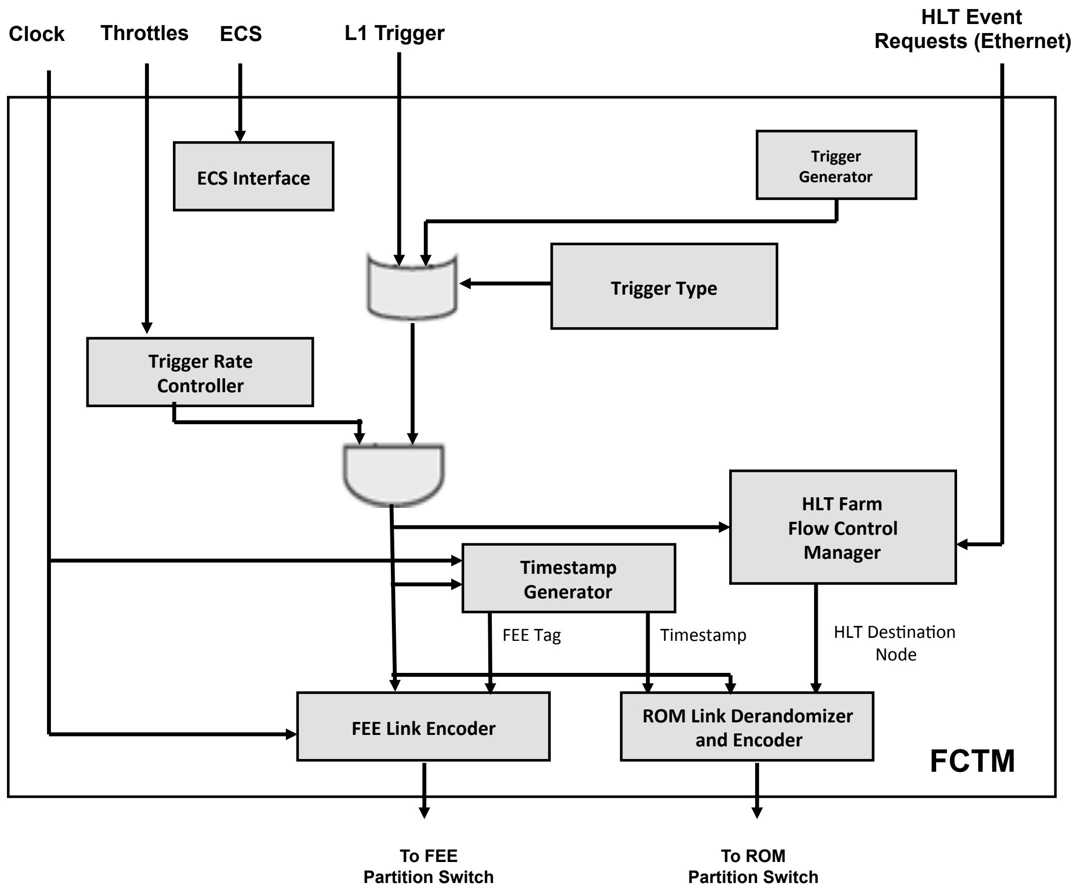

Figure 12.11: Fast Control and Timing Module

design of application specific integrated circuits (ASIC) where possible.

Since the whole ETD is designed to work synchronously with a frequency-divided machine clock, the latency and the recovered clock phase of serial links deployed for trigger and fast control distribution should be fixed and predictable, at a level below 1 unit interval. This requirement does not apply to read-out links, where the latency can be variable.

Moreover, the line coding should be DC-balanced in order to allow AC-coupled transmissions where needed and in such a way not to stress, and consequently not reduce the lifetime of, optical transmitters.

Radiation Tolerance Issues Because the high-speed optical links are a key element of the ETD, their electrical and optical components must withstand the expected radiation levels.

According to preliminary simulations of the luminosity-scaling background component (see Table 5.1), and under the assumption that no links will be installed in the high-radiation regions closer to the beam than the innermost layer of the DCH, the worst-case Total Ionizing Dose (TID) is 7.6 Gy(Si), and the neutron and hadron (E>20 MeV) fluences are $3 \cdot 10^{11}\mathrm{cm}^{-2}$ and $7.6 \cdot 10^{10}\mathrm{cm}^{-2}$, respectively.

R&D has been performed to identify the most reliable devices in terms of radiation tolerance among those compatible with the Super*B* requirements. These included the irradiation testing (with 62 MeV protons) of Serializer-Deserializers (SERDESes), both standalone

(Texas Instruments TLK2711A [8], DS92LV18 [9] and DS92LV2421 -serializer only- [10]), and embedded in SRAM-based FPGAs (Xilinx Virtex-5 [11] and Virtex-6 [12]). The DS92LV18 has also been tested with gamma rays from a ^{60}Co source. For the optical part of the link, a VCSEL-based (Avago AFBR-57R5APZ [13]) transceiver has been tested.

The links implemented with SRAM-based FPGAs have also been protected with triple modular redundancy (TMR) and configuration scrubbing mitigation techniques. The layout of the TMR-protected version has been optimized with placement-hardening algorithms in order to produce different circuit layouts (Figure 12.12), which have been tested.

Before discussing the irradiation results, it is worth remarking that the optical links are a chain of different devices (SERDES, optical transceiver, fiber) and the failure of any component impacts the whole chain. In general the irradiation with 62 MeV protons generates both total ionizing dose and single event effects.

For the different devices the following dose effects were observed:

- **TLK2711A**: failed persistently (not recoverable by cycling power) after absorbing a dose of $\sim$ 400 Gy (Si).

- **DS92LV18**: did not fail either during testing with protons, or with gamma rays. For a total dose of 2.5 kGy(Si) the only effect observed was a moderate ($\sim$ 0.5%) variation in power dissipation.

- **DS92LV2421/22**: did not fail persistently during the testing and did not show any measurable current variation due to TID.

- **Xilinx V5 and V6 FPGAs**: did not exhibit TID-related variations of the power dissipation, however, their power consumption increased gradually during the accumulation of Single Event Upsets (SEUs). Reconfiguration of the devices restored the initial power consumption.

- **Avago AFBR-57R5APZ**: failed persistently at 400 Gy (Si).

Concerning transmission errors related to single event effects, Figure 12.13 shows the expected mean time between failures (MTBF) for each tested device, considering a reference fluence of $3 \cdot 10^{11}\mathrm{cm}^{-2}$ 62 MeV protons per effective year (10^7 s). In the following, we use the word "failure" to refer to the following:

1. for a standalone SERDESes, to a single bit error either in the transmitter or in the receiver (for the DS92LV18 also to a loss of lock);

2. for a FPGA-embedded SERDES, a persistent failure of the link requiring the reconfiguration of the device.

The separate MTBFs for the transmitter and receiver parts of the TLK2711A and of the DS92LV18 are reported. For the DS92LV18, the rate of losses-of-lock is also shown. The Virtex-6 FPGA MTBF is not shown since it is lower than 10^{-1}days.

These results show that optical receivers are expected to be the main source of errors (we did not find any error in the transmitters during testing). For the reference fluence of $3 \cdot 10^{11}\mathrm{cm}^{-2}$62 MeV protons, a MTBF of 2.3 days is expected for errors (either single or burst) in the optical receiver. Among the SERDESes, the most reliable are the DS92LV18 and the GTP embedded in V5 FPGAs, when protected with

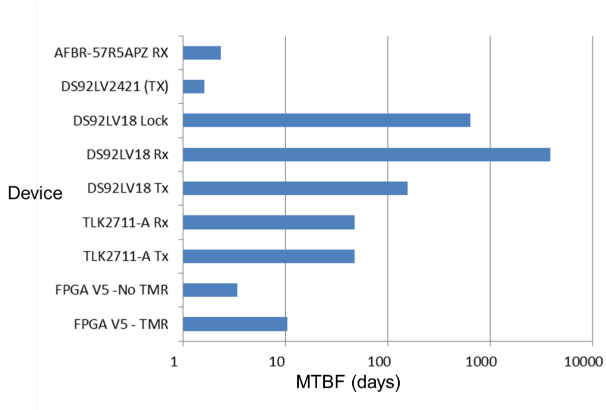

Figure 12.13: Expected failure rates at Super$B$ for a fluence of $3 \cdot 10^{11}\mathrm{cm}^{-2}$ 62 MeV protons in one effective year (10^7s).

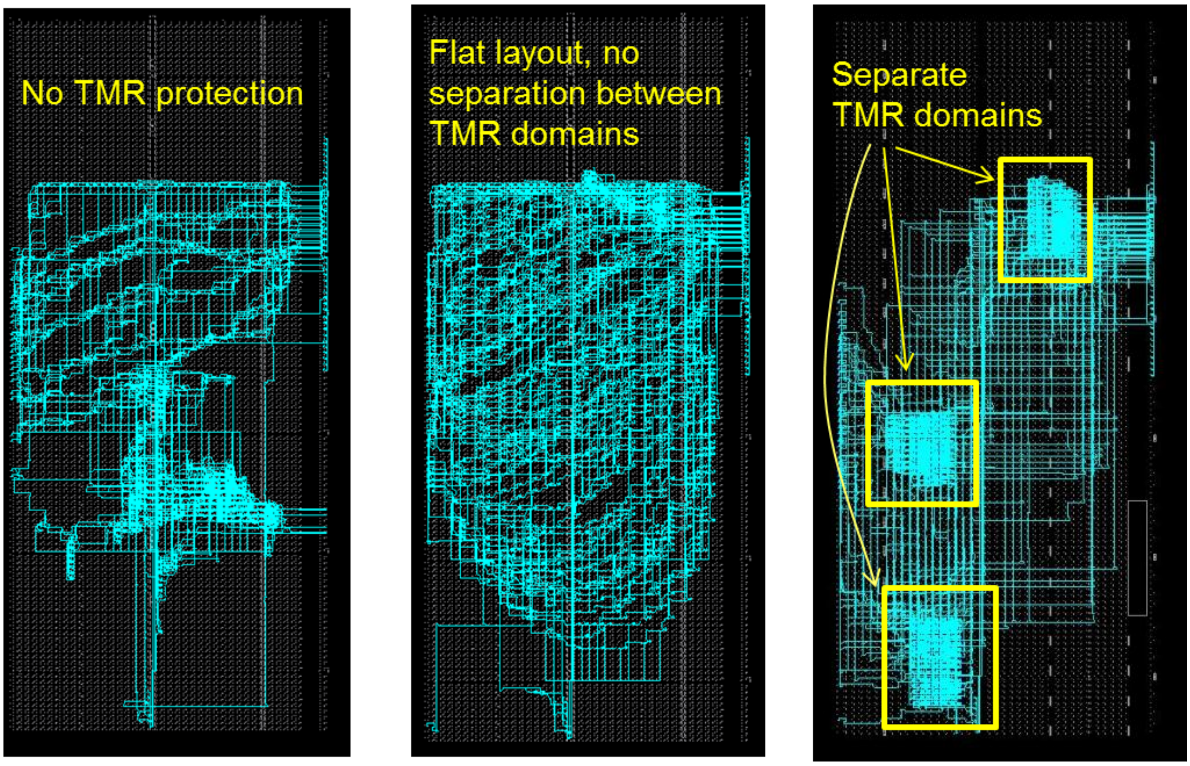

Figure 12.12: Layouts of the serial link implementation in a Xilinx FPGA V5LX50T. Left: link implementation without TMR protection. Center: TMR-protected version with flat layout. Right: TMR-protected version with separation of the TMR domains in distinct areas.

TMR (we do not consider the TLK2711, since it has a low tolerance to TID). The DS92LV18 is limited to 1.32 Gbit/s and it adopts a proprietary line encoding, therefore only the payload, rather than the full frame, can be protected by means of external EDAC components. The line protocol of the device includes a 20-bit symbol consisting of a start bit, an 18-bit payload and a stop bit. When one of these bits is incorrect, the receiver loses the lock to the stream and the recovered clock stops toggling. Since the errors in the optical receiver are uniformly distributed on the parallel symbol, there is a 2/20=0.1 chance of hitting a start or a stop bit and losing the lock at the deserializer level.

Due to the line protocol of the DS92LV18, on average 10% of the incoming bit errors from the optical receiver will result in a loss-of-lock from the stream, also with the loss of the recovered clock. This means that the effective mean time between two losses of lock for the DS92LV18 will be lowered to nearly 23 days (from the value of 640 days related to the SERDES alone). On the other hand, the FPGA-based links do not lose the lock due to single or (short) bursts errors in the optical receiver and for the TMR-protected versions the failure rates are in the order of 10 days. The results in terms of MTBF suggest that link failures are unavoidable and therefore the whole ETD should be implemented as a fault-tolerant machine. This is further discussed in each ETD component subsection.

However, in the light of the present irradiation results the electrical part of the links should be based either on Virtex-5 FPGAs or on the DS92LV18. For both these devices the fixed-latency operation required by the trigger and fast control links is guaranteed. Although tested at a line rate of 2 Gbit/s, the links in V5 FPGAs can run up to 3.125 Gbit/s (limited by the embedded SERDES throughput) and the coding, including also error detection and correction (EDAC) schemes, can be completely customized by implementing the required logic in the fabric.

Error Detection and Correction Two common solutions are error *correcting* codes (ECC) or the simpler error *detecting* codes (EDC). The ECC solution, for example using a Reed Solomon corrector, appears to be too intensive with regard to the computational effort of both encoding and decoding, resulting in increased hardware complexity, longer link latency and reduced reliability. The expected low error rate will permit a simpler and faster solution in the form of a proper EDC code. This will simply flag the occurrence of the error in the transmitted block, so that the block can just be discarded. As shown below, the expected frequency of this kind of error is extremely low, thus, bit errors will not affect data quality and event reconstruction.

As far as the choice of the error detection code is concerned, both cyclic redundancy check and check-sums have been evaluated. Since CRC coding has a complexity that is comparable to a full ECC approach, it is not a viable option.

Checksums have a lower error detection ability than CRCs but have the advantage of a lower hardware complexity that meets the latency requirements and allow for a widespread use in the experiment, increasing the overall reliability. A parameter to be evaluated is the overhead in terms of ratio of the number of check-sum bits added to the useful message bits.

Let us suppose to deploy the DS92LV18 SERDES for the optical links. In this case, the 18 bits block managed as a whole by the SERDES will be buffered in groups of 3 blocks to be protected as a single 54 bit super-block. In order to achieve the best possible DC balance, the super-block will then be scrambled, checksum bits will be added and the data will be transmitted by the SERDES and the optical link. On the receiving end, the inverse process will be applied and possible errors will be flagged.

Tools have been developed in order to evaluate error detecting efficiencies of different check-sums, such as *Parity*, *Modular Sum*, *One Complement Sum* and *Fletcher Sum*. The choice will be the adoption of Fletcher check-sum which provides detection of all 1 bit errors and two bits burst errors. Less frequent 2 or 3 bits errors are also detected even if not with the same 100% efficiency. Hardware complexity is limited to simple binary adders using the so called one's complement addition. Using the 54 bits block including a 6 bits check-sum, overhead is as low as 12.5%. Error detection probability, evaluated by direct simulation mixed with proper analytical approach, provides the following figures for the detection efficiency: 1 bit errors 100%, 2 bits errors 98.7%, 3 bit errors 98.0%, 4 bit errors 98.1%. At the same time complete coverage is provided for burst errors encompassing 2-3-4 bits, an invaluable feature in our case foreseeing these kind of errors. The above figures, for a reference Bit Error Ratio BER=10^{-10} will deliver a probability of undetected error as low as $1.5 \cdot 10^{-19}$. This undetected error rate, in turn, for a reference 2.5 Gbit/s transmission speed, will deliver 8 years average time between undetected errors in a single link; for 1000 links this will deliver 3 days average time between undetected errors in the whole apparatus.

Physical Implementation Serial links could be implemented on a plug-in mezzanine board (a board which plugs onto a carrier mainboard in order to extend its functionality). One of the main advantages of this approach is an easier maintenance and possibility of upgrading the link performance (data rate, power, jitter) by simply replacing mezzanine cards. This also guarantees protection against obsolescence of components. A single design group would be in charge of characterizing performance and testing of the links, while other ETD boards might be designed by other groups independently in the meanwhile. The link-related issues will be decoupled from the logic-related ones, leaving critical issues (latency, jitter) to be solved at the mezzanine level. An higher design efficiency will be achieved since the mezzanine design group will focus on a 'critical but single' board. A single printed circuit board (PCB) will be customized with different components to fit different needs (e.g. jitter cleaners or rad-hard SERDES for on detector nodes, copper and/or optical lanes where needed).

The implementation of serial links, as separate systems, by means of mezzanine cards is a widespread solution. Examples of this trend are the timing trigger and control (TTC) [14] system of the LHC, the S-Link [15] deployed in several CERN experiments, and the SODA [16] timing distribution system adopted in the PANDA experiment. In the TTC system, the implementation on a mezzanine allowed to upgrade the receiver with a VCXO-based PLL for improved output jitter ($\sim$ 20 ps rms), compatible with the requirements of the reference clock of Gbit/s SERDESes and other jitter sensitive devices.

Due to the limited space in the FCTS crate, the mezzanines for the FEE clock, command and throttle links will be housed in dedicated fan-out crates that will also contain the logic to aggregate and monitor the throttle signals.

The ROM PCIe boards have similar space constraints, so a mezzanine solution for the data links will require the mezzanines and circuitry to convert the signals to e.g. LVDS to be housed in external crates.

Backup Solutions In order to optimize the design effort, control and data links should be based on the same components and mezzanine printed circuit boards. Should the tested devices be found not to be compatible with the radiation tolerance requirements of the experiment, the gigabit optical link (GOL) [17] transmitter could be considered as a backup solution for data links. The radiation-hard GBT [18] transceivers could also be considered, if available within a time scale compatible with the links realization phase.

12.3.4 Common Front-End Electronics

It will be beneficial to implement the different functions required to drive the front-end electronics as independent modular elements. These elements can for example be implemented as mezzanines or as circuits directly mounted on the front-end modules. For instance, as shown in Figure 12.14, one mezzanine can be used for FCTS signals and commands decoding, and one for the ECS management.

Depending on the implementation of the FEE, it is also possible to decode the FCTS and ECS signals on one mezzanine board, and to distribute them to neighboring boards, permitting a great reduction in the number of links. Driving the L1 buffers may also be implemented in a dedicated common control circuitry inside a radiation-tolerant FPGA. This circuitry would handle the L1 accept commands and provide the signals necessary to control the data transfer from the latency pipeline into the derandomizer, and finally, the transmission of event fragments to the serializer, as shown in Figure 12.15.

The latency buffers can be implemented either in the same FPGA or directly on the carrier boards, and one such single circuit could be able to drive numerous data links in parallel, thus reducing the amount of electronics on the front-end boards.

The control circuit will also handle events that have overlapping readout windows because they were triggered very close in time. The strategy for this is that data shared between events with overlapping readout windows is only read out and transmitted once. Complete events will then be reconstituted in the ROM by duplicating the data from the overlapping region as necessary.

It is also the responsibility of the CFEE to manage the derandomizer buffer and the fast multiplexer that feeds the data link serializer.

Figure 12.14 shows a possible implementation of the L1 buffers, their control electronics and the outputs towards the optical readout links. The control electronics may be located within a dedicated FPGA.

Another important requirement is that all (rad-tolerant) FPGAs in the FEEs have to be reprogrammable without dismounting a board. While this could be done through dedicated front panel connectors which might be linked to numerous FPGAs, the preferred solution is to program FPGAs through the ECS system

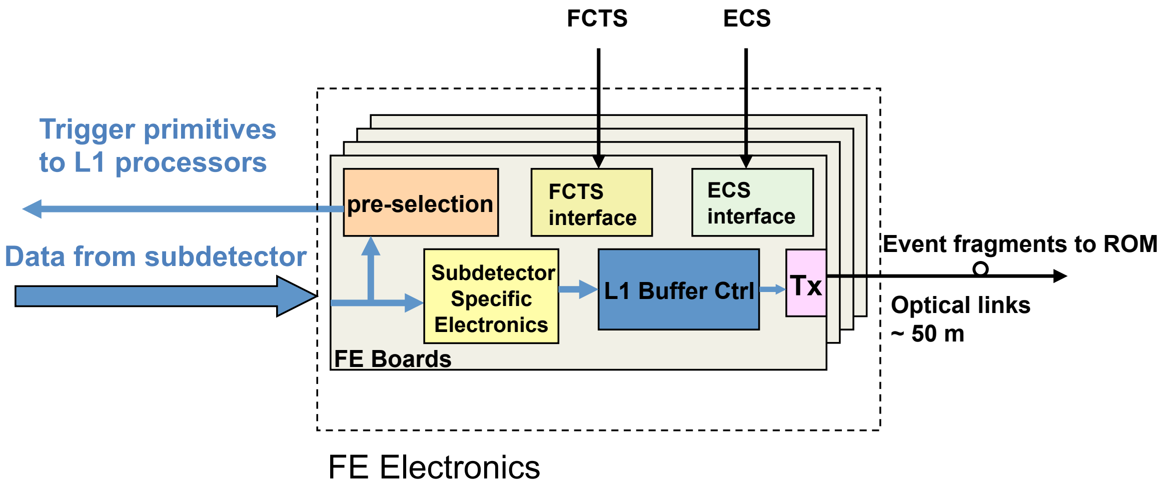

Figure 12.14: Common Front-End Electronics

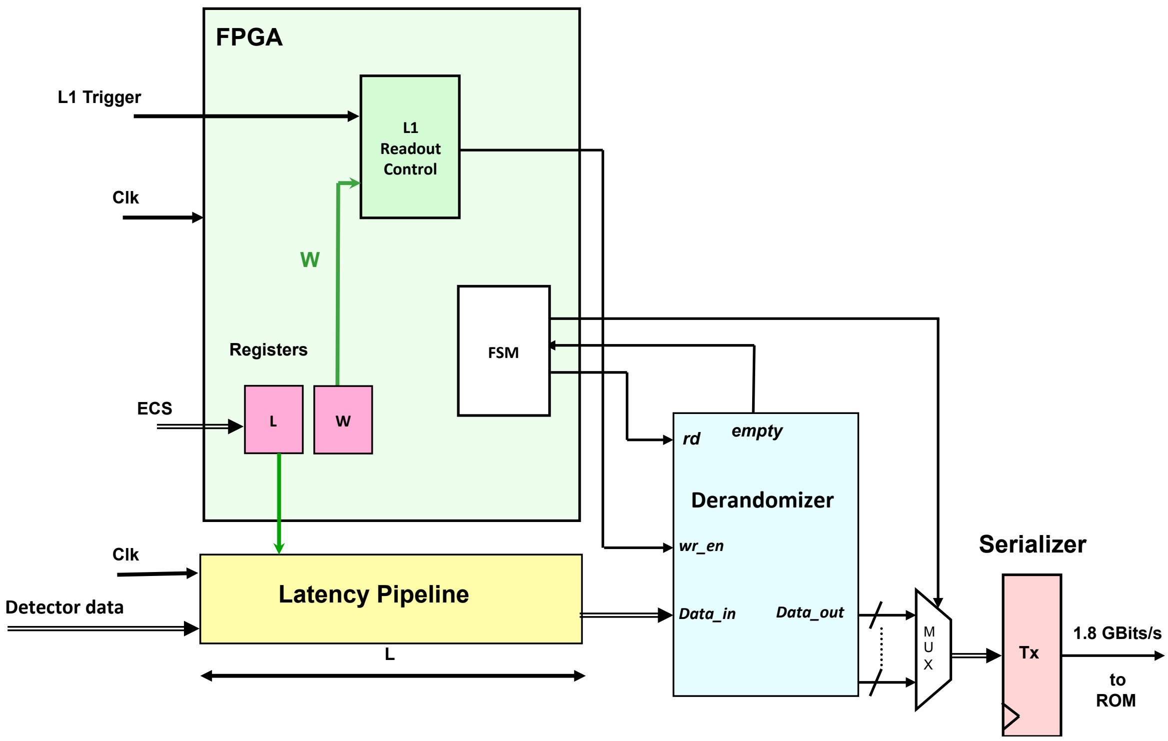

Figure 12.15: Control of latency pipeline and derandomizer in the CFEE

without any manual intervention on the detector side.

12.3.5 Read-Out Modules

The Readout Modules (ROMs) are the hardware interfaces between the FEE and the event builder. The processing flow in the ROM starts with receiving event fragments from the subdetectors' front-end electronics and the corresponding ROM command words from the FCTS. Processing then continues by cross-checking front-end identifiers and absolute time-stamps, buffering the event fragments in derandomizing memories, performing processing (still to be defined) on the fragment data, and eventually injecting the formatted fragment buffers into the event builder and HLT farm. Processing includes duplicating data that are shared between events because of overlapping readout windows.

Connected to the front-end electronics via optical fibers, the ROMs will be located in an easily accessible, no-radiation area. ROM hardware is identical for all sub-detectors, however, if the need arises, the peculiarities of each subdetector can be addressed by customization of the ROM firmware.

A ROM will have 10 or more optical input channels operating at a rate of 1 Gbit/s and at least one output channel at 10 Gbit/s. To exploit flexibility and processing power of computer technology, the ROMs will be manufactured as PCI Express (PCIe) add-on cards for servers in the event-building farm. This approach helps to keep production costs low (when compared to a field-bus based solution), allows the processing of event fragment data with a combination of hardware (FPGA on the ROM) and software (host CPU), and provides the flexibility to address unforeseen changes and upgrades with a low impact on the overall architecture. It is important to note that the space on a PCI express card is rather limited, both for connectors and mezzanines, so the strategy of using mezzanines and the mechanical design has to be reviewed carefully.

To assess the suitability of this approach, a prototype ROM has been manufactured and qualified. It is a PCIe 2.0 add-on card (Figure 12.16) built around a Xilinx Virtex6-250T FPGA with 48 high speed serial transceivers. The plug-in module accommodates 3 SNAP12 optical receivers and 2 QSP optical transceivers for a total of 44 receivers and 8 transmitters each operating at max 6.2 Gbit/s. An 8 MByte true dual-port RAM is used to derandomize incoming event fragments before they are streamed to host server memory.

The prototype ROM features a TDC and a ultra-low jitter PLL for the benefit of the FPGA (Fig 12.17). A 4x PCIe 2.0 interface with an aggregate bandwidth of 20 Gbit/s per direction allows fragment data to be moved to

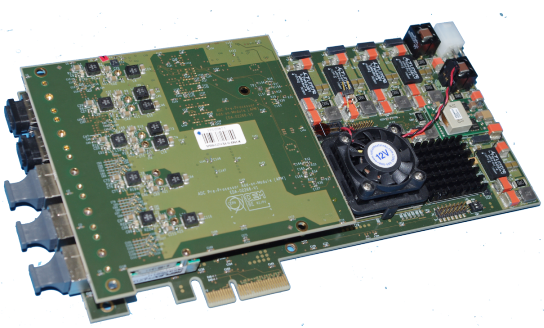

Figure 12.16: Photo of ROM prototype developed and tested for Super*B*.

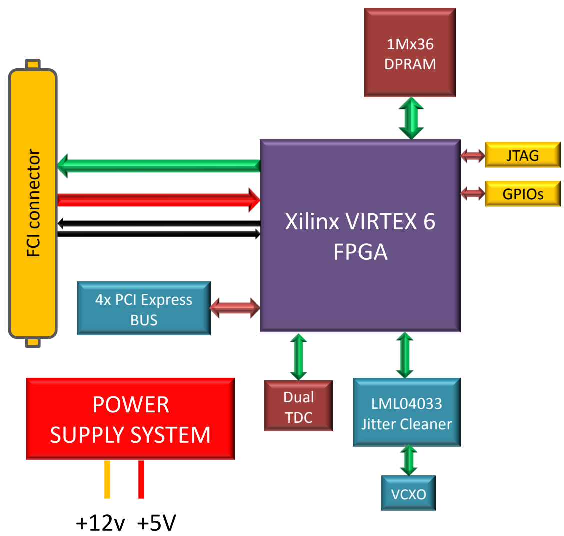

Figure 12.17: Block diagram of a ROM. The fiber-optic receivers are not shown.

host memory efficiently. To measure the worst-case power consumption, the FPGA was configured with 38 input channels at 2.0 Gbit/s, eight FIR filters per input channel for data processing, a 10 Gbit/s PCI-express interface, a scatter-gather DMA engine, and a timing unit, resulting in a total of 92% occupancy of logic resources. With this configuration the board uses 60 W, and does not require any special cooling measures when housed in a low-cost 2U Dell server.

Data transfers from the ROM's dual-port RAM to the host memory were exercised through a custom-developed Linux driver. This driver uses a custom designed scatter-gather DMA engine in the FPGA to efficiently move the fragment data from the ROM directly into user-space buffers. By handling the mapping between virtual pages and physical memory regions, it allows the direct transfer of data from the dual-port RAM into data vectors defined in user space, obviating the need for an additional kernel space to user space copy ("zero-copy").

Bandwidth tests show that with 4x PCIe 1.1, fragment buffers larger than a few hundred bytes can be moved at a rate of approximately 950 MByte/s. With 4x PCIe 2.0 (using a 256 byte PCIe payload), this rate almost doubles. Since these test results by far exceed the requirements for the Super*B* ROMs, we are confident that the PCIe-based ROM approach can be safely adopted.

12.3.6 Network Event Builder

The ROMs receive event fragments in parallel from the sub-detector front-end-electronics, perform a first stage event-build, store the event fragments in memory buffers, and add the corresponding ROM command received from the FTCS on the dedicated ROM-command links. The resulting partially-built events are then encapsulated in UDP datagrams and sent to the HLT node determined by the destination node field in the ROM command word. Thus, all fragments of an event are sent to the same HLT node which completes the event building process by combining them. Full events are passed to the HLT through a queue. To utilize the multiple cores and CPUs on a HLT node, the HLT can be implemented as multithreaded application or, alternatively, as multiple independent processes working in parallel.

As described earlier, the FCTS determines the HLT destination node for every event using a round-robin algorithm that takes into consideration a simple flow control scheme based on a per-node sliding window maintained by the FCTS. Each HLT node maintains a queue of fully built events that is filled by the event building process and drained by the HLT process(es). As long as the event building process is running and the number of events in the queue stays below a high-water mark, the HLT node periodically sends requests for more events to the FCTM that is responsible for the partition. These requests are sent as UDP packets over Ethernet; their aggregate rate can be limited to a fraction of the L1-accept rate, since each request is for multiple events.

If the HLT processes on a node cannot keep up with the incoming events, the node stops sending requests and after the FCTM has exhausted the node's window of outstanding events, no more events are directed to the node. No events are lost in this case, since the node still queues all event fragments that are still in-flight. Only after the FCTM receives a new event request from this HLT node, it considers it as a valid event destination again. This provides a flow-control and load balancing mechanism for the HLT farm. In the case of a complete HLT node failure (or the failure of the event building process) the event loss is less or equal to the number of events last requested.

The overall process of event building is inherently parallel and its rate can be scaled up as needed, up to the bisection bandwidth of the event building network. The baseline technology for the event builder network is standard 10 Gbit/s Ethernet. We will investigate the suitability of end-to-end flow control mechanisms (such as IEEE 802.1Qbb) at the Ethernet layer for avoiding packet loss in the event building network. We will also investigate alternative network technologies and protocols (such as RDMA or Infiniband).

With a L1 trigger rate of 150 kHz and a pre-HLT event size of 500 kByte, the bandwidth in the network event builder is about 75 GByte/s, corresponding to about 750 Gbit/s with network overhead included. To avoid packet loss and to maintain stability, the event building network cannot be operated at 100% link utiliziation, and we need to retain an additional safety factor of ~1.5. Therefore, the minimum bisection bandwidth of the event building network is 1200 Gbit/s. When implemented with 10 Gbit/s Ethernet, this means 120 "source" network interfaces on the ROMs and at least 120 "destination" interfaces on the HLT nodes. Network switches that provide the necessary bandwidth and can host at least 120+120 = 240 10 Gbit/s Ethernet ports are commercially available at the time of the writing of this document.

12.3.7 High-Level Trigger Farm

The HLT farm needs to provide sufficient aggregate network bandwidth and CPU resources to handle the full Level 1 trigger rate on its input side. The Level 3 trigger algorithms should operate and log data entirely free of event time ordering constraints and be able to take full advantage of modern multi-core CPUs (the simplest implementation would be to run multiple identical HLT threads or processes which get their input from a single queue of built events). Extrapolating from *BABAR*, we expect 10 ms core time per event to be more than adequate to implement a software L3 filter, using specialized fast reconstruction algorithms. With such a filter, an output cross-section of 25 nb should be achievable. Using contemporary (as of Summer 2012) hardware and taking into account the CPU overhead for event building, logging and data transfer, a suitable farm could be implemented with approximately 150 nodes.

Level-4 Option To further reduce the amount of permanently stored data, an additional filter stage (L4) could be added that acts only on events accepted by the L3 filter. This L4 stage could be an equivalent (or extension) of the *BABAR* offline physics filter—rejecting events based either on partial or full event reconstruction. If the worst-case behavior of the L4 reconstruction code can be well controlled, it could be run in near real-time as part of, or directly after, the L3 stage. Otherwise, it may be necessary to use deep buffering to decouple the L4 filter from the near real-time performance requirements imposed at the L3 stage. The discussion in the Super*B* CDR [1] about risks and benefits of a L4 filter still applies.

12.3.8 Data Logging

The output of the HLT is written to disk storage. With a cross-section of about 25 nb accepted by the HLT, the event rate is 25 kHz at a luminosity of 10^{36} cm^{-2}sec^{-1}. With an event size of 200 kByte, this corresponds to an aggregate logging rate of 5 GByte/s, or ~430 TByte per day. In a farm of 150 HLT nodes, the per-node rate is approximately 33 MByte/s.

The most likely mode of operation is that every HLT farm node writes a single file at a time and that data from multiple farm nodes is not aggregated into larger files. Instead, the individual files from the farm nodes are maintained in the downstream system. This means that the bookkeeping system and data handling procedures have to manage these files, and also deal with missing or damaged run contribution files.

There will be least a few TByte of usable space per HLT farm node, implemented as directly attached low-cost disks in a redundant (RAID) configuration, a storage system connected through a network or SAN, or as a combination of the two.

A network separate from the event builder one is used to transfer data asynchronously to archival storage and/or near-online farms for further processing. It has not yet been decided where such facilities will be located, or if they will even be on site, since a distributed, virtual Tier-0 computing facility is the Super*B* computing infrastructure baseline. In any case, network connectivity with with adequate bandwidth and reliability is required. At the experiment, enough local storage must be available to allow to continue taking data during periods of link downtime. Many considerations will determine the exact amount of local storage, including cost, expected data collection efficiency, link downtime, and the availability of backup links and facilities.

Data Format While the format for the raw data has yet to be determined, many of the basic requirements are clear, such as efficient sequential writing, compact representation of the data, portability, long-term accessibility, and the freedom to tune file sizes in order to optimize storage system performance.

12.3.9 Data Quality Monitoring System

Event data quality monitoring is based on quantities calculated by the HLT, as well as quantities calculated by a more detailed analysis of a subset of the data. A distributed histogramming system collects the monitoring output histograms from all sources and makes them available to automatic monitoring processes and operator GUIs.

12.4 System Integration and Error Handling

Due to the radiation environment, SEUs and the corresponding rate of link and FEE failures cannot be neglected, as there will likely be at least a few failures per day. For this reason it is very important that detection of and recovery from these failures is reliable and fast. Because we cannot predict all possible failure modes, the system design uses a generic approach to recovery. The FCTS and all FEEs implement mechanisms that allow individual front-ends to detect and report the loss of synchronization, and to resynchronize without the need to restart the whole system. This includes the periodic broadcasting of synchronization frames on the clock and command links, the reporting of FEE problems through the fast throttle, and the ability to diagnose, reset and synchronize individual front-ends under the control of the ECS. Other components in the system that participate in the detection of FEE problems are the ROMs, the HLT, and the data quality monitoring system.

Recovery from failures will be orchestrated by the global control system software and the ECS, this provides maximum flexibility in handling unforeseen failure modes.

12.5 Control Systems

A major lesson learned during BABAR operations was that achieving high operational efficiency and true "factory-mode" data taking required a high degree of automation and control system integration. The traditional approach of separate control systems for different aspects of the experiment (detector control, run control, farm and logging control) designed and implemented with completely separate tools and very limited capability to communicate with each other, greatly limited the amount of automation and automatic error detection and recovery.

In Super$B$, all routine operations will need to be orchestrated across subsystem boundaries. For example, performing a simple calibration might require high voltages to be ramped to a calibration set-point, the FEE and the FCTS to be configured for calibration, farm nodes to be allocated and configured, the calibration run to be performed, calibration data to be analyzed and after completion the system to be returned to its normal data taking configuration.

For Super$B$ we therefore foresee a unified control system that can automatically perform all routine operations. The system comprises the Electronics Control System (ECS), the Detector Control System (DCS), the Farm Control System (FCS), the configuration database, sequencing engines to implement distributed state machines, an archiving and logging system, operator GUIs, and the interface to the accelerator control system. All components are connected by a central virtual control bus ("Global Control System").

All operations are driven by the configuration database and executed under the control of one or more sequencing engines.

A large part of the system, including the central virtual control bus, will be implemented using the !CHAOS [19] control system toolkit which is currently under development for the Super$B$ accelerator. !CHAOS is a state-of-the-art

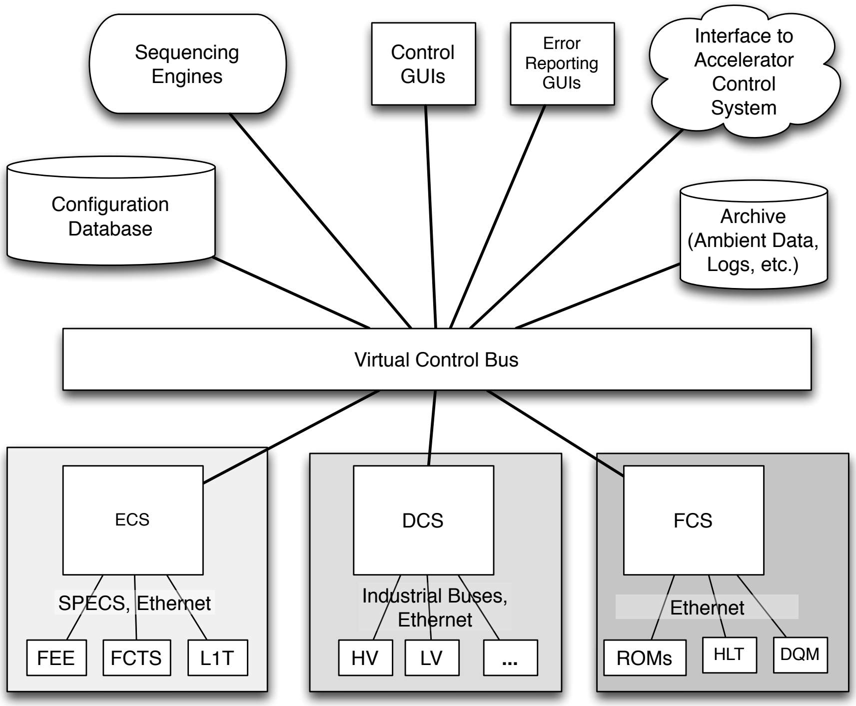

Figure 12.18: The Super$B$ unified control system architecture

scalable distributed control system framework that combines high-performance data acquisition and archiving capabilities with a plug-in architecture to provide low-level controller interfaces and graphical user interfaces (GUIs).

An overview of the unified control system architecture is shown in Fig 12.18; its major components are described below.

12.5.1 Electronics Control System

The Electronics Control System (ECS) controls and monitors the FEE, the FCTS and the Level 1 trigger. Its main responsibilities are:

Configuring the Front-ends: Many front-end parameters must be initialized before the system can work correctly. The number of parameters per channel range from a only a few to large per-channel lookup tables. The ECS may also need to read back parameters from registers in the front-end hardware to check the status or verify that the contents have not changed. For a fast detector configuration and recovery turnaround in factory mode, it is critical to not have bottlenecks either in the ECS itself, or in the ECS' access to the front-end hardware.

Error recovery: The ECS plays a central role in recovering from temporary system failures due to radiation (such as loss-of-clock). It provides the interface to the dead time monitoring system, allows detailed diagnostics of FEE failures and can reset and resynchronize indidividual FEEs without the need for issuing a global reset or resynchronization command.

Calibration: Calibration runs require extended functionality of the ECS. In a typical calibration run, after loading calibration parameters, event data collected with these parameters are sent through the DAQ system and analyzed. Then the ECS loads the parameters for the next calibration cycle into the front-ends and repeats the operation.

Testing the FEE: The ECS is also used to remotely test all FEE electronics modules using dedicated software. This obviates the need for independent self-test capability for all modules.

Monitoring the Experiment: The ECS continuously monitors FEE boards, FCTS and the L1 Trigger to ensure that they function properly. This might include independent spying on event data to verify data quality, and monitoring operational parameters on the boards (such as voltages, currents, temperatures and error flags). By monitoring these parameters, the ECS also participates in protecting the experiment from a variety of hazards. An independent hardware-based detector safety system, which is part of the DCS, protects the experiment against equipment damage in case the software-based ECS is not operating correctly.

ECS support must be built into all electronics modules that are to be controlled by the ECS – this includes the FEE.

Programming the FPGA firmware: Where applicable, the ECS can also be used to program or update FPGA configurations. It is highly desirable to be able to perform such operations without physical access to the boards. Depending on the FPGA this may require appropriate programming voltages to be made available on the boards.

The specific requirements that each of the sub-systems makes on ECS bandwidth and functionality must be determined (or at least estimated) as early as possible so that the ECS can be designed to incorporate them. Development of calibration, test, and monitoring routines must be considered an integral part of sub-system development, as it requires detailed knowledge about sub-system internals.

ECS Implementation: The field bus used for the ECS has to be radiation tolerant on the detector side and provide very high reliability. Such a bus has been designed for the LHCb experiment: it is called SPECS (Serial Protocol for Experiment Control System) [20]. It is a bidirectional 10 Mbit/s bus that runs over standard Ethernet Cat5+ cable and provides all possible facilities for ECS (like JTAG (Joint Test Action Group) and I2C (Inter IC)) on a small mezzanine. It can be easily adapted to the Super*B* requirements. Though SPECS was initially based on PCI boards, it is currently being translated to an Ethernet-based system, as part of an LHCb upgrade, also integrating all the functionalities for the out-of-detector elements. For the electronics located far from the detector, Ethernet will be used for ECS communication. The Super*B* ECS will be implemented using SPECS; an interface to !CHAOS will be developed.

12.5.2 Detector Control System

The Detector Control System (DCS) is responsible for ensuring detector safety, controlling the detector and its support system, and monitoring and recording detector and environmental conditions. The DCS also provides the primary interface between the accelerator and the detector.

Efficient detector operations in factory mode require high levels of automation and automatic recovery from problems. Here, the DCS plays a key role and a tight integration with the Accelerator Control System (ACS) is highly desirable. The DCS in conjunction with the ACS manages the accelerator-detector interlocks and beam and detector states and has access to all information from the accelerator and the detector that is needed to fully automate data taking operations.

The DCS-ACS connection is also used to provide the accelerator with beam measurements performed by the detector (such as beam spot positions or bunch-by-bunch luminosities). Operational experience from *BABAR* has shown that mutual access between machine and detector to their respective archived control system data (such as records of background levels, detector currents, trigger rates on the detector side and vacuum pressures, temperatures and stored currents on the machine side) are invaluable for improving the accelerator and detector performance.

The DCS will be implemented with !CHAOS. Due to its distributed nature and modular storage design, !CHAOS will allow us to federate the independent instances of DCS and ACS and provide a unified query interface for data archived by the respective systems.

Low-level components and interlocks responsible for detector safety (Detector Safety System, DSS) will be implemented as simple circuits or with programmable logic controllers (PLCs).

12.5.3 Farm Control System

Processes on the ROMs and on the HLT farm will be started, controlled and monitored by the Farm Control System (FCS) and will be implemented using the !CHAOS framework or a traditional network inter-process communication system such as DIM [21].

12.6 Support Systems

A number of systems and infrastructure components are needed to support detector and data taking operations, and ETD/Online software development. These include:

Software Infrastructure: The data acquisition and online system is a distributed system built with commodity hardware components and a substantial software design and implementation effort. Taking a homogeneous approach in both the design and implementation phases will help to keep the effort under control and also facilitate maintenance and improvement of the system during the operations phase. An Online software infrastructure framework will be of great help. It should provide basic memory management, communication services, and the environment to execute the Online applications. Specific Online applications will make use of these general services to simplify the performance of their functions. Middleware designed specifically for data acquisition exists, and may provide a simple, consistent, and integrated distributed programming environment.

Electronic Logbook: A web-based logbook, integrated with all major Online components, allows operators to keep an ongoing log of experiment status, activities and changes.

Databases: Online databases such as configuration, conditions, and ambient databases are needed to track, respectively, the intended detector configuration, calibrations, and actual state and time-series information from the DCS.

Configuration Management: The configuration management system defines all hardware and software configuration parameters, and records them in a configuration database.

Software Release Management: Strict software release management is required, as is a tracking system that records the software version (including any patches) that was running at a given time in any part of the ETD/Online system. Release management must cover FPGAs and other firmware as well as software.

Performance Monitoring: The performance monitoring system monitors all components of ETD/Online.

Computing Infrastructure: The Online computing infrastructure (including the specialized and general-purpose networks, file, database and application servers, operator consoles, and other workstations) must be designed to provide high availability, while being self-contained (sufficiently isolated and provided with firewalls) to minimize external dependencies and downtime.

12.7 R&D for Electronics, Trigger and Data Acquisition and Online

The baseline design presented in this chapter can be implemented with technology and components available at the time of writing of this document. However, we expect that by the times when we have to freeze various aspects of the design to start construction or purchasing, components that are significantly more performant and/or cost effective might be available. In order to take advantage of these developments, we will need to develop a detailed plan on when we have to finalize the parts of our design.

Data Links: The data links for Super$B$ require further R&D in the following areas: (1) studying jitter related issues and filtering by means of jitter cleaners; (2) coding patterns for effective error detection and correction; (3) radiation qualification of link components; and (4) performance studies of the serializers/de-serializers embedded in the new generation of FPGAs (Virtex6, Xilinx, etc.). We will also closely follow developments that are in progress for other experiments (e.g. LHC experiment upgrades) to understand their applicability in the Super$B$ system.

Readout Modules: Readout Module R&D requires further investigation of 10 Gbit/s Ethernet and alternative networking technologies, and detailed studies of the I/O sub-system performance in the ROMs.

Trigger: For the L1 trigger, the time resolution, algorithms and their physics performance, pile-up handling, and the achievable mimimum latency will need to be studied in detail. We will also need to investigate the feasibility of a L1 Bhabha veto. For the HLT, studies of achievable physics performance and rejection rates need to be conducted, including understanding the risks and benefits of a possible L4 option.

Event Builder and HLT Farm: The main R&D topics for the Event Builder and HLT Farm are (1) the applicability of existing tools and frameworks for constructing the event builder; (2) the HLT farm framework; and (3), event building protocols and how they map onto network hardware.

Software Infrastructure: To provide the most efficient use of resources, it is important to investigate how much of the software infrastructure, frameworks and code implementation can be shared with Offline computing. This requires us to determine the level of reliability-engineering required in such a shared approach. We also must develop frameworks to take advantage of multi-core CPUs.

12.8 Conclusions

The architecture of the ETD system for Super$B$ is optimized for simplicity and reliability at the lowest possible cost. It builds on substantial in-depth experience with the *BABAR* experiment, as well as more recent developments derived from building and commissioning the LHC experiments. The proposed system is simple and safe. Trigger and data readout are fully synchronous—allowing them to be easily understood and commissioned. Safety margins are specifically included in all designs to deal with uncertainties in backgrounds and radiation levels. Event readout and event building are centrally supervised by a FCTS system which continuously collects all the information necessary to optimize the trigger rate. The hardware trigger design philosophy is similar to that of *BABAR* but with better efficiency and smaller latency. The event size remains modest.

The Online design philosophy is similar—leveraging existing experience, technology, and toolkits developed by *BABAR*, the LHC experiments, and commercial off-the-shelf computing and networking components—leading to a simple and operationally efficient system to serve the needs of Super$B$ factory-mode data taking.

12.9 Bibliography

[1] M. Bona et al., (Super$B$ collaboration), "Super$B$: A High-Luminosity Heavy Flavour Factory. Conceptual Design Report", arXiv:0709.0451v2, http://www.pi.infn.it/SuperB/CDR, report INFN/AE-07/2, SLAC-R-856, LAL 07-15.

[2] A. Abashian et al., (Belle collaboration), "The Belle Detector", *Nucl.Instrum.Meth.* A479:117–232, 2002, doi:10.1016/S0168-9002(01)02013-7.

[3] B. Aubert et al., (*BABAR* collaboration), "The *BABAR* detector", *Nucl.Instrum.Meth.* A479:1–116, 2002, doi:10.1016/S0168-9002(01)02012-5, arXiv:hep-ex/0105044 [hep-ex], report SLAC-PUB-8569, BABAR-PUB-01-08.

[4] (ATLAS collaboration), "ATLAS: Detector and physics performance technical design report", http://atlas.web.cern.ch/Atlas/GROUPS/PHYSICS/TDR/access.html.

[5] (CMS collaboration), "CMS Detector Technical Design Report", http://cmsdoc.cern.ch/cms/cpt/tdr/.

[6] (LHCb collaboration), "LHCb Technical Design Reports", http://cmsdoc.cern.ch/cms/cpt/tdr/.

[7] http://www.slac.stanford.edu/BFROOT/www/Detector/Trigger/index.html, The *BABAR* Trigger Web Pages.

[8] Texas Instruments, "1.6 to 2.7 Gbit/s Transceiver", September 2009, http://www.ti.com/lit/ds/symlink/tlk2711a.pdf.

[9] Texas Instruments, "DS92LV18 18-Bit Bus LVDS Serializer/Deserializer - 15-66 MHz", June 2006, http://www.ti.com/lit/ds/symlink/ds92lv18.pdf, Literature Number: SNLS156D.

[10] Texas Instruments, "DS92LV2421/DS92LV2422 10 to 75 MHz, 24-bit Channel Link II Serializer and Deserializer", January 2011, http://www.ti.com/lit/ds/snls321a/snls321a.pdf.

[11] Xilinx, "Virtex-5 FPGA RocketIO GTP Transceiver User Guide", 2008, http://www.xilinx.com/support/documentation/user_guides/ug196.pdf, Xilinx UG196, v1.7.

[12] Xilinx, "Virtex-6 FPGA GTX Transceivers User Guide", 2011, http://www.xilinx.com/support/documentation/user_guides/ug366.pdf, Xilinx UG366, v2.6.

[13] Avago Technologies, "AFBR-57R5APZ Data Sheet", 2007, http://www.avagotech.com/docs/AV02-0881EN.

[14] P. Moreira and E. Murer, "TTCrx and QPLL Mezzanine Card (TTCrq)", 2003, http://bonner-ntserver.rice.edu/cms/TTCrqSpec.pdf.

[15] O. Boyle, R. McLaren, and E. van der Bij, "The S-LINK Interface Specification", 1997, http://vanderby.web.cern.ch/vanderby/s-link/spec/spec/s-link.pdf.

[16] I. Konorov, H. Angerer, A. Mann, and S. Paul, "SODA: Time distribution system for the PANDA experiment", *Nuclear Science Symposium Conference Record (NSS/MIC), 2009 IEEE*, pp. 1863 -1865, 24 2009-nov. 1 2009, doi:10.1109/NSSMIC.2009.5402172.

[17] P. Moreira, G. Cervelli, J. Christiansen, F. Faccio, A. Kluge, A. Marchioro, T. H. Toifl, J. P. Cachemiche, and M. Menouni, "A radiation tolerant gigabit serializer for LHC data transmission", *Proceedings of the 7th Workshop on Electronics for LHC Experiments, Stockholm, Sweden*, pp. 145-149, Sep 2001.

[18] P. Moreira and J. Troska, "Radiation-Hard Optical Link for Experiments", *PH Faculty Meeting April 25, 2008 CERN, Geneva, Switzerland*.

[19] L. Catani et al., "Exploring a new paradigm for accelerators and large experimental apparatus control systems", *ICALECPS 2011*, 2011, http://accelconf.web.cern.ch/accelconf/icalepcs2011/html/clas013.htm.

[20] https://lhcb.lal.in2p3.fr/Specs/, The SPECS Web Page.

[21] C. Gaspar et al., "The DIM Homepage at CERN", http://dim.web.cern.ch/dim.

12.A Appendix: ETD design rules for the FEE

This appendix outlines the rules for a correct implementation of the FEE.

1. Average and instantaneous rate handling capabilities
   a) Every FEE must be able to handle an average rate of at least 150 kHz
      i. At 150 kHz with equidistant L1-accepts it must not generate any dead time
      ii. At 150 kHz with the standard exponential inter-event time distribution, it must not generate more than 1% dead time
2. Properties of L1-Accepts
   a) L1-accepts are synchronous with the system clock and have fixed latency
      i. L1-accepts arrive at a time $L \pm (J/2)$ after the activity in the detector that caused the trigger to be asserted.
         A. L is the trigger latency (approximately 6 μs in the current design)
         B. $L = N/f$ where N is the trigger pipeline depth in clock cycles, and f the system clock frequency (59.5 MHz in the current design). In other words, L is an integer multiple of the system clock period.
         C. J is the peak-to-peak trigger jitter, caused by the limited time resolution of the detectors feeding the trigger, and by the resynchronization of detector signals to the (global) clock running the trigger system.
         D. $J/2$ is expected to be in the order of few tens of ns.
      i. L1-accepts have no minimum inter-command spacing, so the rate of sending L1-accepts is only limited by the control link wire speed and protocol.
         A. Every FEE must be able to process back-to-back L1-accepts, even if data has to be shared between the successive events (pile-up events). See the discussion about dead time and pile-up below for more details about this requirement.
         B. We expect the time length of an L1-accept command word to be no more than 60 ns.
3. Latency buffer and read-out windows
   a) The latency buffers in the FEE hold the samples during the trigger latency.
      i. They constitute pipelines that run parallel to the trigger pipeline.
      ii. They are filled synchronously and read-out at the same frequency, which can be the global clock or multiples thereof
      iii. When an L1-accept arrives, a time window W of samples around the end of the latency buffers is read out, formatted and transferred to the derandomizer buffers
      iv. W contains all the information pertaining to the particular event
         A. W has to be large enough to also accommodate the trigger jitter J
      v. Alternative implementations are permissible, as long as they do not violate the principle of parallel pipelines and back-to-back L1-accept handling (see item 5 below for a discussion of dead time management)

4. Management of overlapping read-out windows (pile-up)
   a) In case of close consecutive triggers, data can be shared between consecutive events if their readout windows overlap
      i. In this case, the first event is sent in full, for subsequent overlapping events, only the new, non-overlapping data are sent.
      ii. Full events are restored in the ROMs by replicating the shared data.
5. Dead time management
   a) Dead time is centrally managed by the FCTS.
      i. Should the instantaneous rate exceed an FEE's capacity, the FEE must assert a "fast throttle" (FT) signal to the FCTS to temporarily stop L1-accepts
      ii. The FEE must be able to handle all L1-accepts that have already been generated, and are in flight at the time it asserts FT, and absorb any L1-accepts generated during the latency period from asserting the FT signal to stopping the L1-accepts
      iii. The preferred implementation is to only use an "almost full" signal from the derandomizer buffers to generate the throttle. This makes it easy to calculate the derandomizer depth based on the maximum link utilization
         A. Alternative implementations are permissible, however, great care must be taken that none rules outlined in this appendix are violated.
6. Derandomizer buffers and data link utilization
   a) In the standard design, the derandomizer buffers absorb spikes in the instantaneous rate
   b) To be able to catch up after a rate spike, the data link utilization corresponding to the average L1-accept rate must not exceed 90% for every individual link.
   c) Alternative implementations for derandomizing are permissible, however, great care must be taken that no rules outlined in this appendix are violated.
7. Radiation
   a) Each element of the FEE has to be validated to work safely and reliably in its expected radiation environment

13 Subdetector Electronics and Infrastructure

The general design approach is to standardize components across the system as much as possible, implementing common functions on mezzanine boards, and using commercially available common off-the-shelf (COTS) components where viable. In this chapter we will discuss and summarize the aspects of the front-end electronics (FEE) that relate to the central fast control and timing system (FCTS) and data acquisition system. We will also discuss the general infrastructure for power distribution to the FEE.

13.1 Subsystem-specific Electronics

13.1.1 SVT Electronics

The full details of the SVT electronics are given in Sect. 6.6. Here we recall the main features relevant for data collection, trigger distribution, system programming and monitoring.

In the baseline SVT option, all layers will be equipped with double sided silicon strips (or alternatively, striplets). Custom front-end chips will be used to read the analog information of a particle traversing the detector and digitize it as soon as possible, yielding position (layer, strip), energy deposit (signal time over threshold) and time. The different requirements of all SVT layers will be handled by a single chip design with programmable features and operating parameters that are adjustable over a wide range. A possible upgrade of the SVT internal layers might require a pixelated detector and a different custom front-end chip design. The digital architecture of the pixel chips has already been partially developed; it will be based on the same general readout architecture, and will—from the point of view of the trigger and DAQ system—share the same interface.

Common features of all chips will include the capability to work both in data-push and data-pull mode, the presence of internal buffers to allow for a trigger latency of up to $10\,\mu$s, the use of a periodic signal to time-tag the recorded hits, a serialized hit output, and the chip programmability via two digital lines.

The full SVT data chain will therefore be able to provide and distribute all the signals, clocks, triggers, and time-tagging signals to all the front-end chips in a system-wide synchronous way.

A sketch of the data chain is given in Figure 13.1. Starting from the detector and going to the ROM boards, the chain contains: a) the front-end chips mounted on an HDI placed immediately at the end of the sensor modules; b) wire connections to a transition card (signals in both directions and power lines); c) a transition card, placed about 50 cm from the end of the sensors, hosting the wire-to-optical conversion; d) a bidirectional optical line running at or above 1 Gbit/s; e) a programmable Front-End-Board (FEB).

Since the silicon sensors are double sided, the front-end (FE) chips are mounted on both sides of the HDIs. Each HDI side will host from 5 to 10 FE chips servicing a side of the silicon strip module, a read-sut section (ROS). All the chips will share the same input lines (*reset*, *clock*, *fastclock*, *trigger*, *time-stamp*, *registerIn*) and at least a *registerOut* line. The chips can either be programmed individually (by addressing a single chip) or in bulk by sending broadcast commands

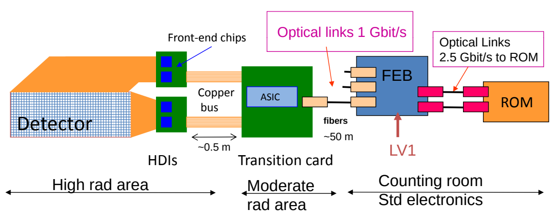

Figure 13.1: Sketch of the SVT Electronics and data chain.

to all chips in an HDI. Hits will be serialized on a programmable number of lines (1 or 2) using the *fastclock* signal. Each HDI will have a maximum number of 14 data output lines running at the *fastclock* rate.

The role of the transition card is threefold: a) it will distribute the power to the HDI; b) it will receive all control signals for the front-end chips via the optical line connected to the FEB; and c) it will ship the data to FEB for data acquisition. For the inner layers (0–3) there will be a transition card for each HDI. For the outer layers (4–5) it will be possible to group the data of the two HDIs servicing the two sides of the same silicon sensor into the same transition card, reducing the total number of optical links needed (Table 6.18).

The FEBs will handle all the communications with the front-end chips, the FTCS, the ECS and the downstream DAQ system. Each FEB will host up to 12 optical links: up to 4 of them could be run at 2.5 Gbit/s and used for communication with the ROMs. The other links will be connected to the transition cards and run at 1 Gbit/s. Important functions of the FEB are clock distribution, trigger handling, and data collection. There are multiple clock signals that need to be distributed in a sub-detector-wide synchronous manner: The experiment clock (59.5 MHz), a fast clock (120–180 MHz), and a time-stamping clock (up to 30 MHz). In order to synchronize the system at the sensor (or front-end) level, the latencies of all serializers and deserializers in the signal and DAQ chain will be measured at each power-up; the phases of the signals will then be adjusted according to the measurements.

The time-stamping clock is used to time-tag the hits; its frequency can be higher for the inner layers, where the high track rates require short signal shaping times and short DAQ time windows. In the outer layers, a lower frequency could be used to adapt to the longer shaping times (800–1000 ns) and correspondingly larger readout time windows.

Data volumes have been estimated assuming a time-stamping clock period of 30 ns in the inner and outer layers. The acquisition window will be defined as a time window centered around the L1 trigger time, and lasting at least 10 time-stamp clock cycles (300 ns) for the inner layers, and 33 time-stamp clock cycles (990 ns) or more for the outer layers. The FEB forwards trigger requests via the transition boards to the FE chips, and also collects their data, both for the main data acquisition and for monitoring. Data are deserialized in the board, redundant information is stripped, and optionally, further data compression algorithms can be applied. Finally, the data will be sent to a ROM via an optical link.

A possible change in the global clock frequency from 59.5 to 39.66 MHz has already been considered in the design; only minor changes in the DAQ chain would be required: In this scenario, a *fastclock* running at 120 or 160 MHz would be used to collect the data, and a time stamping clock at 39.66 MHz would be used to time-tag the hits. No changes would be necessary in other parts of the SVT system, in particular, the number or types of optical links, and the number of transition cars and FEB boards would remain the same.

Data volumes. As discussed in the SVT chapter (see sect. 6.2), the data rates and volumes are dominated by the background. For the SVT front-end chip and DAQ design, the latest background simulations at nominal luminosity were used, and a safety factor of 5 was applied on the results. Due to the strong non-uniformity of the particle rate in the sensors, the front-end chip characteristics have been chosen according to the peak rates, while the data volumes have been calculated from the mean rates for each layer.

To evaluate the data rate, a trigger rate of 150 kHz with 10 μs maximum latency and 100 ns of time jitter has been used. A 16-bit hit size is used as the FE chip output, which becomes 20 bits when serialized with an 8b/10b protocol. The bandwidth needed by the layer-0 ROS in a data-push configuration is of the order of 20 Gbit/s per ROS. This rate is high enough and difficult enough to handle, so we considered a fully triggered SVT. In Table 13.1 the mean ex-

Table 13.1: Electronic load on each layer (assuming a ×5 safety factor on background levels), readout sections and optical links.

Layer	Layer side	chips/ ROS	available channels	Backgnd (MHz/cm^2)	Gbits/trig (per GROS)	FE Boards	Event Size (kHits)
0	u	6	768	100	0.66	2	3.5
0	v	6	768	100	0.66	2	3.5
1	z	7	896	14.0	0.56	2	2.2
1	phi	7	896	16.0	0.64	2	2.6
2	z	7	896	9.6	0.54	2	2.2
2	phi	7	896	10.3	0.58	2	2.3
3	z	10	1280	4.2	0.50	2	2.0
3	phi	6	768	3.0	0.36	2	1.5
4a	z	5	640	0.28	0.26	1	1.4
4a	phi	4	512	0.43	0.38	1	2.0
4b	z	5	640	0.28	0.26	1	1.4
4b	phi	4	512	0.43	0.40	1	2.1
5a	z	5	640	0.15	0.17	1	1.0
5a	phi	4	512	0.22	0.24	1	1.5
5b	z	5	640	0.15	0.17	1	1.0
5b	phi	4	512	0.22	0.24	1	1.5

pected data load for each layer type, evaluated assuming a safety factor of ×5, is shown.

For events accepted by the L1 trigger, the bandwidth requirement is only 1 Gbit/s, and data from each ROS can be transferred on optical links to the FEBs and from there to the ROMs through the 2.5 Gbit/s optical readout links at an average 90% link utilization.

13.1.1.1 SVT Summary

In total, the SVT electronics requires 24 FEBs, 56 optical links at 2.5 Gbit/s for connection to the ROMs and 172 bidirectional links at 1 Gbit/s (radiation hard) for command, trigger and data shipping. The average SVT event size is 79 kByte, 22% coming only from the layer0. Table 13.2 summarizes the SVT specification concerning the DAQ interface requirements.

Table 13.2: SVT summary

Number of Control Links	172
Number of Data Links	56
Total Event Size	79 kByte

13.1.2 DCH Electronics

13.1.2.1 Design Goals

The Super*B* Drift Chamber (DCH) Front End Electronics (FEE) extracts and processes approximately 8000 sense wire signals for tracking and energy loss measurement purposes. Moreover it provides information (trigger primitives) to the L1 trigger processor.

For the dE/dx measurements, two possible scenarios will be investigated. The first one is based on the measurement of the integrated charge on each sense wire (Standard Readout), while the second one is based on the detection of electron clusters in a given cell (Cluster Count-

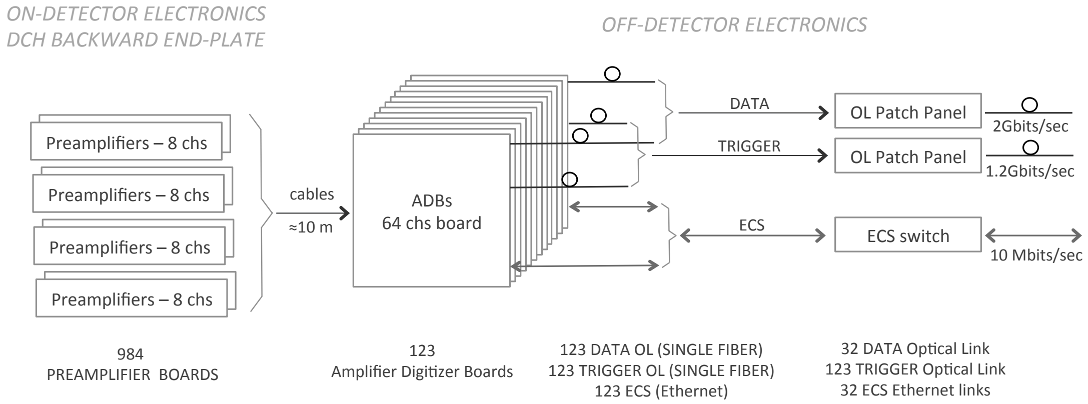

Figure 13.2: DCH front end system (Standard Readout)

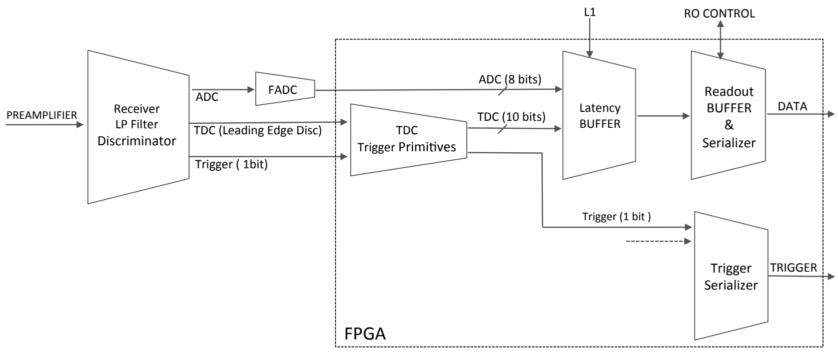

Figure 13.3: Off-Detector Electronics: ADB board (Standard Readout)

ing) A description of the different requirements for the two scenarios can be found in Section 7.

13.1.2.2 DCH FEE (overall design)

The DCH FEE block diagram is very similar for the two options. It is shown in Figure 13.2 for the Standard Readout case. It consists of two subsystems:

- On-Detector Electronics: the HV distribution boards located on the front endplate and the preamplifier cards located on the back endplate.
- Off-Detector Electronics: Amplifier Digitizer Boards (ADBs) and Concentrator boards, located approximately 10 m away.

13.1.2.3 Off Detector Electronics - Standard Readout

ADBs - Overall Design Each ADB will host up to 64 channels and will consist of three stages as shown in Figure 13.3. The first stage receives signals from the preamplifiers and generates analog and discriminated outputs. The second stage provides digitization for charge and time measurements and includes the logic for trigger primitives generation as well. Finally, the third stage contains the latency and readout buffers and the dedicated control logic. The ADBs will also include an interface (not shown in the diagram) that will be used for parameters setting/readout and to test the entire FEE chain.

Input connections will use twisted or mini-coaxial cables, while output connections will use different types of cables depending on the chain. DAQ and Trigger chain will use optical links while the ECS chain will use copper links (see section 12.5.1).

ADBs - Receiver Section This stage is designed to amplify and to split the preamplifier output signal to feed a low-pass filter for charge measurement, and a leading edge discriminator for time measurement.

ADBs - Digitization Section The low-pass filter output signal is routed to an 8-bits, 30 megasamples/s FADC whose outputs are sent to a section of the latency buffer implemented in a FPGA. Upon a L1-accept, the system extracts 32 FADC output samples (corresponding to a time window of about 1 μs, enough to span the full signal development) from the latency buffer and transfers them to a readout buffer.

The comparator output is routed to a FPGA where it is split along two paths. One signal is sent to a TDC, implemented in the FPGA itself (using the oversampling method) for time measurement. The other signal, synchronized with the system clock and stretched appropriately to remove redundant information, is sent to the DCH Trigger Segment Finder (TSF) modules (Figure 12.5). The TDC outputs are also sent to the latency buffer, to be readout in the presence of a L1-accept trigger signal.

Normally, the event data structure will have different lengths since L1 triggers, spaced less than a single event readout time, will extend the time window to include the new event. However, during Feature EXtraction (FEX) implementation (extraction of information from the digitized data), the transferred data stream will have a fixed length. An example of a possible readout data structure is shown in Table 13.3.

In both instances the first, non zero, FADC output signal can be used to correct the discriminator output jitter, thereby minimizing the input signal slewing effects on the timing mesurement.

Table 13.3: FEX based data stream (fixed length structure)

Data stream example
Digitizer Module Address (2 bytes)
Flag (1 byte)
Trigger Tag (1 byte)
Counter (1 byte)
Charge (2 bytes)
Time (2 Bytes)
1st ADC sample (different from baseline) for time walk correction (1 byte)

13.1.2.4 Off Detector Electronics - Cluster Counting

The Cluster Counting technique for dE/dx measurements is based on the detection of electron clusters (primary ionization measurements). This requires high bandwidth devices and digitizers with high sampling frequencies of, at least, 1 gigasamples/s (GSPS). Very fast processing is required to sustain the 150 kHz average L1-accept rate foreseen in Super$B$. With current technology, this results in a very large power dissipation, and as a consequence, the number of channels per ADB board has to be limited in the present design.

If we can detect the electron clusters with an efficiency of 100%, the system can also be used for tracking purposes; all that is needed is to measure and store the cluster arrival times, in addition to counting them.

The DCH FEE system block diagram for Cluster Counting is similar to the one shown in Figure 13.2. However, because of the smaller number of channels per board (16 instead of 64), the number of boards and crates increases significantly (Table 13.4).

ADBs The ADBs will have high-sampling-rate ($\geq$ 1 GSPS) digitizers. To meet the power requirements, only 8 channels working at 1 GSPS can be packaged in a single VME 6U board at this time. However, in the future, we expect to be able to increase the number of channels per board to 16, or even 24, with only a small increase in power requirements.

The circuit structure is very similar to the one shown in Figure 13.3. The digitizing section is different, since no TDC is required for the time measurements, and the trigger primitives are generated from the FADC output instead.

Because of the large amount of data per L1-accept and channel (about 1 kByte), we cannot transfer raw data to the DAQ. This means that the FEX must be implemented on the ADB, that is, for every L1-accept, all event samples must be examined to identify possible clusters. While the time required for cluster identification using current technology is compatible with the L1-accept rate expected at the nominal Super$B$ luminosity, this could become a limiting factor at higher L1-accept rates. Another potential problem may be the radiation sensitivity of the high performance RAM-based FPGA used in the present design.

13.1.2.5 FEE Crates

Each FEE Crate will host up to 16 ADBs, a Power Supply board for the preamplifiers, Data Concentrators and, possibly, a Trigger Patch Panel or Trigger Concentrator. Custom backplanes will be designed to:

- distribute power and common signals to the ADBs
- make use of Interconnection Boards (IB) to gather the preamplifier cables (Fig. 13.4)
- send trigger signals to adjacent boards (Section 12.3.1.1)

13.1.2.6 Number of Crates and Links

Table 13.4 shows the estimate of the number of links, boards and crates required for both the DAQ and Trigger FEE chains. As shown in the table, the number of trigger signals is the same for both options even though the number of ADBs for the Standard Readout scenario is not the same as for the CC scenario. The reason for this is that we intend to also use, in the CC option, a Trigger Concentrator board for the trigger chain to compensate for the limited number of channels per ADB. This board will

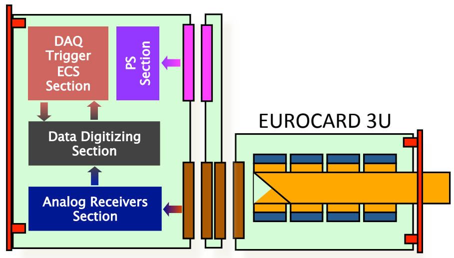

Figure 13.4: On-Off Detector FEE connections (ADB - Custom Backplane - IB)

generate a single trigger output from the trigger inputs coming from several ADBs and will send this single output to the TSF modules.

The estimate has been done assuming about 1 μs sampling window and:

- 150 kHz L1 trigger rate, 7872 sense wires (subdivided in 10 super-layers)
- 10% chamber occupancy in 1 μs time window
- SR - NO FEX option: 50 bytes per channel data transfer (charge: 32 bytes; time: 10 bytes; information: 8 bytes)
- SR - FEX option: 11 bytes per channel data transfer (Table 13.3)
- CC - FEX option (18 clusters - 2 bytes/cluster): 44 bytes per channel data transfer (data: 36 bytes; event information: 8 bytes)
- single link bandwidth of 2 Gbits/sec for the DAQ data path and 1.2 Gbits/sec for the Trigger data path

13.1.2.7 ECS

Each ADB will have an interface section to manage ECS communications. The interface will control the ADB and will provide the capability of data readout for debugging purposes. ECS details can be found in section 12.5.1.

Table 13.4: Number of links (Data, ECS, Trig), ADBs and crates (Cr) for 64 channels Standard Readout (SR) and 16 channels Cluster Counting (CC) boards

	chs	Data	ECS	Trig	ADBs	Cr
SR	64	32	32	123	123	8
CC	16	32	32	123	492	31

13.1.2.8 Cabling

Because of the large number of channels involved, the DCH cable layout must be carefully designed. The main requirement is the possibility to replace failed preamplifier boards without having to disconnect too many cables. Thus, signal and HV cables should be routed to the chamber's outermost layer to minimize the overlap of cables. Table 13.5 gives the expected number of cables and a rough estimate of their sizes.

13.1.2.9 Power Requirements

A very preliminary power requirement estimate is shown in Table 13.6. The estimate for On Detector Electronics is based on preamplifier simulation and prototype tests, while the estimate for Off Detector Electronics comes from the latest available state of the art digitizing boards. Local (preamplifier) voltage regulation is supposed to be implemented by means of linear low-drop rad-hard regulators.

Table 13.5: Estimate of the number and dimension of DCH signal cables (7872 sense wires - Preamplifiers of 8 channels each)

	LVPS	HV	Signal (coax)	Signal (twist)
Quantity	123	16	7872	984
Number of cores	16	28	1	16
Core area (mm^2)	0.5	0.07		
Cable diam. (mm)	12	14	1.8	6.5

Table 13.6: Power requirement estimate for SR and CC (DC = Data Concentrators; TC = Trigger Concentrators)

	Boards	Power Req.
SR Preamplifier	984	0.25 kW
SR ADB	123	5 kW
SR DC	8	0.24 kW
CC Preamplifier	984	1.2 kW
CC ADB	492	20 kW
CC DC	31	1 kW
CC TC	31	1 kW

13.1.2.10 DCH Summary

Table 13.7 summarizes the DCH FEE main specifications concerning the DAQ interface and power requirements. As already stated, the number of links is the same for both SR and CC options, while the power requirement is significantly different for the two options.

Table 13.7: DCH FEE summary

Number of TriggerLinks	123
Number of Control Links	32
Number of Data Links	32
SR Total Event Size (NO FEX)	40 kByte
SR Total Event Size (FEX)	9 kByte
SR On-Detector Power Req.	0.25 kW
SR Off-Detector Power Req.	5 kW
CC Total Event Size	35 kByte
CC On-Detector Power Req.	1.2 kW
CC Off-Detector Power Req.	20 kW

13.1.3 PID Electronics

The PID electronics will read out the 18,432 channels of the 12 sectors of the FDIRC. The electronics chain is based on a high speed TDC, a time-associated charge measurement with 12-bit precision, and an event data packing block, sending event data frames to the data acquisition system (DAQ). The target performance of the overall electronics chain is a time precision of 200 ps rms and a per-channel count rate capability of up to 500 kHz, yet dealing with the global system constraints (average L1-accept rate of up to 150 kHz and a minimum spacing between triggers of about 50 ns).

The estimated radiation level is expected to be about 1 Gray per year, so it is mandatory to use radiation-tolerant or off-the-shelf radiation-qualified components. Latch-up effects are very unlikely at the expected particle energies, so the design has only to take into account Single Event Upsets. The ACTEL family FPGA components have been chosen here for their non-volatile configuration memories based on flash technology, which are well adapted to this kink of radiation environment.

The electronics consists of a front-end analog part and a TDC both integrated in a 16 channel ASIC called CATS. The analog part contains an amplifier, a peak detector, an analog pipeline for the charge measurement and a fast comparator to drive the TDC inputs. The TDC part provides a time measurement with both a high resolution (100 ps RMS) and a large dynamic range (53 bits). Thanks to an external 12-bit ADC, the charge measurement can be used for electronics calibration, monitoring and survey purposes. The front-end (FE) board FPGA synchronizes the process, associates the time and charge information coming from CATS and finally packs them into a data frame which is sent via the backplane to the FBLOCK control board (FBC). The FBC is in charge of distributing signals from the FCTS and ECS, packing the data received from the FE boards to an n-event frame including control bits, and transferring it to the DAQ.

13.1.3.1 The Front-end Crate

The board input will match the topological distribution of the PMTs on the FBLOCK. The PMTs are arranged in a 6 (vertical) by 8 (horizontal) matrix. Each column of 6 PMTs will fit to one FE board. One vertical backplane (PMT Backplane) will interface between the 4 connectors of each PMT base to one connector of the FE board. The PMT Backplane also distributes the High Voltage, thus avoiding HV cables to pass over the electronics. In order to minimize the need for custom-designed elements, such as board guides, the FB crates will use as many commercially available elements as possible.

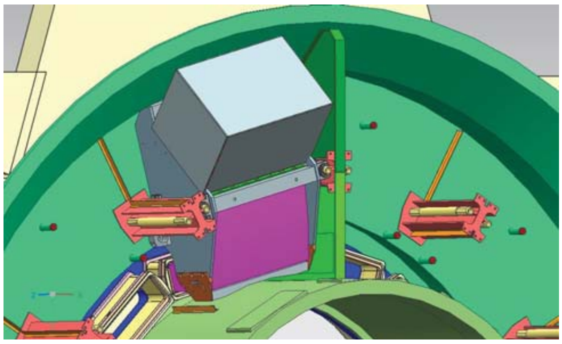

Figure 13.5: The FBLOCK equipped with the boards and fan tray

13.1.3.2 The Communication Backplane

The communication backplane distributes the ECS and FCTS signals from the FBC to the 16 FE boards thanks through point to point LVDS links. It connects each FE board to the FBC for system control and data transfer.

13.1.3.3 The PMT Backplane

The PMT backplane is an assembly of 8 motherboards, each corresponding to a column of 6 PMTs.

13.1.3.4 Cooling and Power Supply

The cooling system must be designed in order to maintain the electronics located inside the FBLOCK at a constant temperature close to the optimum of 30°C.

The air inside the volume will be extracted by dedicated fans while dry, clean, and temperature controlled air will replace it. Like commercial crates, each FB crate will have its own fan tray. 4000 m^3/h can be considered as the baseline value for the whole detector. The crate and boards will be cooled by a water based cooling system.

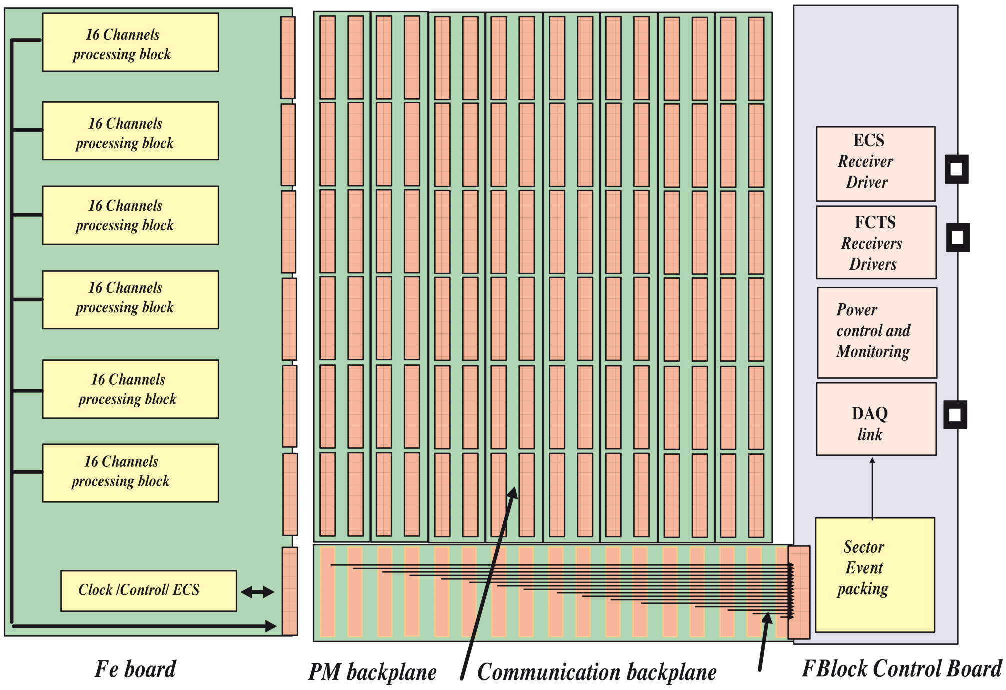

Figure 13.6: The Front end Crate

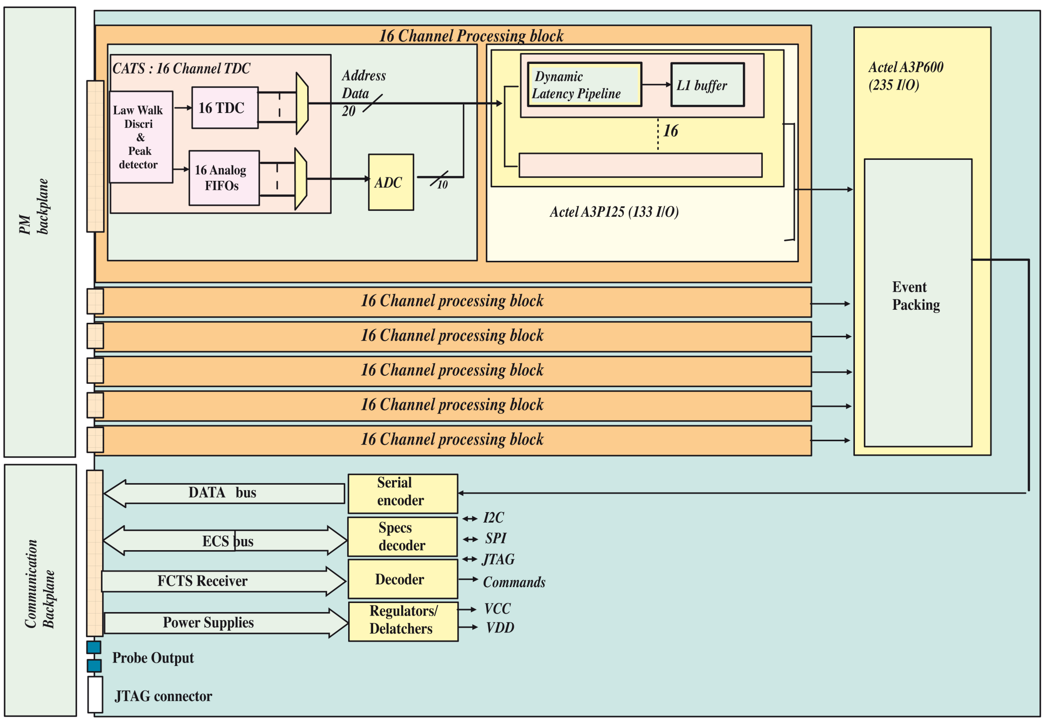

Figure 13.7: The PID Front-end Board

13.1.3.5 The Front-end Board

One FE board (Figure 13.7) handles a total of 96 channels and actually comprises 6 channel-processing blocks.

A channel-processing block consists of one CATS chip, one ADC, one ACTEL FPGA, and the associated ancillary logic. The FPGA receives event data from the CATS and the associated charge data from the ADC. The 16-bit data bus coming out of the CATS is de-serialized and split into 16 separate data buses, each corresponding to one channel. A dedicated mechanism inside the FPGA inserts the events into the latency buffer at their proper position with respect to the hit time. From there on, the design perfectly corresponds to the common ETD proposal for the latency buffer and derandomizer (CFEE). Event data is stored in the event buffer where it is kept until either been thrown away if it is not selected, or sent to the derandomizer located in the master FPGA upon the reception of a L1-accept from the FCTS.

13.1.3.6 The Crate Controller Board (FBC)

The master FPGA receives event data from the 6-channel processing blocks, packs it in a frame with parity bits for data checking and transmits it in a serial differential LVDS format to the FBC via the communication backplane.

13.1.3.7 PID Summary

There is thus one link per sector, leading to a total of 12 readout links for the whole FDIRC. Each link has a mean occupancy of 15 %, far below the limit fixed to 90 % by ETD official rules. The parameters of the PID system concerning the DAQ interface and power consumption are summarized in Table 13.8.

Table 13.8: PID summary

Number of Control Links	12
Number of Data Links	12
Total Event Size	5 kByte
On-Detector Power Consumption	6.1 kW

13.1.4 EMC Electronics

The EMC is fully triggered in order to minimize the number of optical links between FEEs and ROMs, and trigger primitives are sent to the L1 trigger processor on a separate, independent data path. Compared to the untriggered EMC readout system in *BABAR*, the new system keeps the same number of optical links for the barrel EMC, and requires only a very moderate increase in the link count for the new hybrid forward calorimeter design, even with a large increase in trigger rate. The separate trigger data path is mandated by the need for a fast calorimeter trigger. To support the neutron-activated liquid-source calibration (see Sec. 9.2.2.3), where no central trigger can be provided, both the barrel and the end-cap readout systems need to support a free running "self-triggered" mode where only samples associated with an actual signal are sent to the ROM. This may require digital signal processing to suppress noisy channels.

Barrel Calorimeter While the 5760 crystals and PIN diodes from *BABAR* are reused in the barrel EMC, the charge-sensitive preamplifiers and shapers that convert the charge into voltage will be replaced with faster devices that have a 500 ns shaping time and provide a pulse with a FWHM of 1180 ns. Each shaped signal is then amplified with two different gains ($\times 1$ and $\times 32$) and digitized. An auto-range circuit decides on-the-fly which of the two gains will be digitized by a 12-bit pipeline ADC running at 9.915 MHz (1/6 of the Super*B* global clock frequency). Note that a change of the global system frequency to 39.66 MHz can easily be handled by using a divisor of 4 instead of 6. The 12 bits from the ADC plus an additional bit for the selected gain covers the full scale from 10 MeV to 10 GeV with a resolution better than 1%. Storing these 13-bit samples in 16-bit (2 byte) words leaves an additional 3 spare bits per sample that could be used for bit error detection or correction.

In order to optimize the energy scale for the 6 MeV photons produced by the calibration

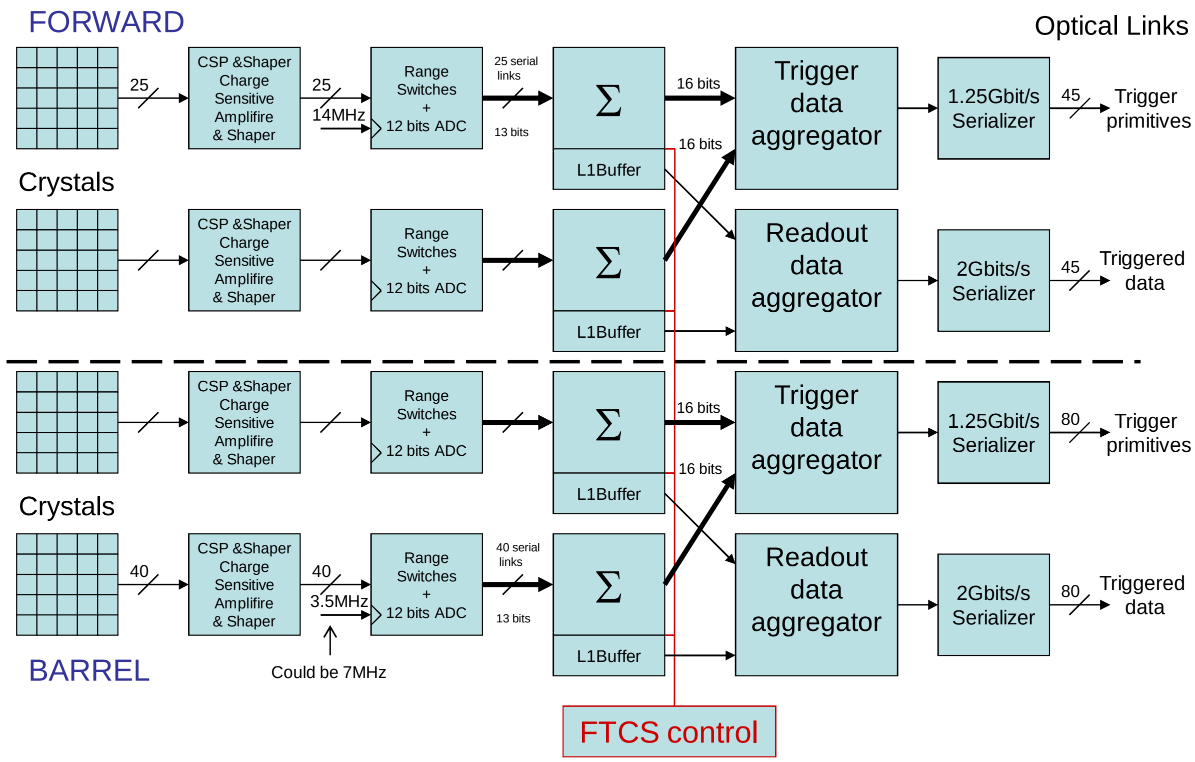

Figure 13.8: EMC Electronics

source, separate programmable gain amplifiers are used during source calibrations.

Each channel is sampled continuously, and the samples are stored in latency buffers in the Data Unit Concentrators (DUTs). Upon a L1-accept, a window of 32 samples (corresponding to approximately $3.3\,\mu$s) around the trigger time is transferred from the latency buffers to the derandomizer buffers that feed the optical links to the ROMs. The mean time interval between two L1-accepts is approximately $6.6\,\mu$s. The triggered system requires only approximately half of the bandwidth of a comparable untriggered system, albeit at the price of moving the latency and derandomizer buffers into the FEE. Additional gains will result from transferring data shared between overlapping events only once.

The Super*B* EMC barrel FEE reuses the *BABAR* topology, mechanics and mechanical specifications: A single digitizer board hosts 12 channels. Each DUT hosts latency buffers, readout logic and derandomizer buffers for 6 digitizer boards, and feeds 2 optical links to the ROMs. This configuration allows complete reuse of the *BABAR* mechanics and form factors, but requires new boards implementing the new electronics specification. There are a total of 80 DUTs (one for each of the 40 ϕ sectors on each end of the barrel), resulting in a total of 160 optical links for the barrel EMC.

Each L1-accept generates 64 bytes of waveform data per channel (32 samples $\times$ 2 bytes/sample). 36 channels feed one optical link, generating a total of 2304 bytes per L1-accept. At a mean trigger rate of 150 kHz, this corresponds to an average bandwidth of 1.38 Gbit/s.

Forward Calorimeter For the forward calorimeter, the proposed baseline configuration consists of a hybrid detector with 360 CsI(Tl) crystals and 2160 LYSO crystal; it was chosen as a trade-off between cost and performance of the forward EMC. The readout scheme for the CsI(Tl) crystals follows the EMC barrel scheme, and uses 5 DUTs and 10 optical links. For the LYSO crystals used in the high-background area, the faster response time requires the shaping time to be shortened to 100 ns, and the sampling frequency to be increased correspondingly. We expect to use the same digitizer boards as in the EMC barrel, increase the sampling frequency to 29.75 MHz (1/2 the baseline Super*B* global system frequency), and to use a readout window of 32 samples, corresponding to 1.08 μs. To read the 2160 LYSO crystals, 30 DUTs with 60 optical links are required. To accommodate a change of the global system clock to 39.66 MHz, one would instead sample at the rate of the system clock, and the readout time window would become 807 ns.

Backward Calorimeter The backward EMC has 1152 readout channels. The inputs are the MPPC signals from the scintillator strips amplified by a charge-sensitive preamplifier. We have been using SPIROC boards in tests and are investigating whether a fast enough version of this technology can be defined. However, our baseline electronics for the detector is the same as for the PID system, with 12 bit ADC and 200 ps TDCs. Further details are in section 13.1.3. To match the PID electronics, the preamplifier will produce a negative pulse. Seventy-two of the 16-channel PID ASICs are required for the backward EMC. The circuit boards are placed behind the backward EMC. For calibration and monitoring we use two calibration boards, each housing 12 LEDs and 12 PIN diodes. Each LED distributes light via four clear fibers that have 12 notches each and span the full calorimeter length. A fifth fiber is coupled to a PIN diode. Thus, with four fibers two full layers (24 tiles each) can be illuminated, while the fifth fiber is used to monitor the LED light.

13.1.4.1 EMC Summary

The parameters of the EMC concerning the DAQ and power consumption are summarized in Table 13.9.

Table 13.9: EMC summary

Number of Control Links	266
Number of Data Links	496
Total Event Size	277 kByte
On-Detector Power Consumption	16.6 kW

13.1.5 IFR Electronics

The full description of the IFR readout electronics, from the design constraints determined by the features of the IFR detector, to the details of the adopted baseline design, is given in the subdetector chapter. In this section, only the features of the IFR electronics related to the common ETD and ECS infrastructure, are described.

The active layers of the IFR are equipped with modules in which the detector elements (of different widths for the ϕ and the Z views in the barrel) are assembled in two orthogonal layers. Assuming that the IFR is instrumented with 9 active layers, the total channel count amounts to 11604 channels for the barrel section, and 9540 channels for the endcaps.

Table 13.10: Estimation of the event size and data bandwidth for the Barrel

Maximum channel count per module:	32
Number of MOD32 processing units per module	1
Total number of modules in the barrel	384
Total number of MOD32 processing units	384
Sampling period (ns)	17.86
Number of samples in the trigger matching window	16
Barrel Event Size (kB)	24.58
Trigger Rate (kHz)	150
Total Barrel Bandwidth (Gbps), including 8b10b encoding overhead	36.86
Number of data links from the barrel detectors	24
Bandwidth per link (Gbps)	1.536

The IFR detector will be read out in "binary mode": the output of each SiPM device will be amplified, shaped and compared to a threshold. The binary outputs of the comparators are then sampled by "digitizers" at the Super*B* clock rate, and the samples are stored into local "on-detector" circular memories. These *latency buffers* are designed to keep the data for a time interval that is at least the L1 trigger latency. The last stage of the "on-detector" readout system is based on Finite State Machines (FSMs); upon arrival of a L1-accept command, it transfers the data corresponding to the L1 trigger from the latency buffers to the derandomizer FIFOs.

Table 13.11: Estimation of the event size and data bandwidth for the Endcaps

Maximum channel count per module:	92
Number of MOD32 processing units per module	3
Total number of modules in the endcaps	108
Total number of MOD32 processing units	324
Sampling period (ns)	17.86
Number of samples in the trigger matching window	16
Endcap Event Size (kB)	20.74
Trigger Rate (kHz)	150
Total Barrel Bandwidth (Gbps), including 8b10b encoding overhead	31.10
Number of data links from the barrel detectors	16
Bandwidth per link (Gbps)	1.944

In this baseline version of the IFR electronics, the digitizer blocks have 32 input channels. In response to a L1-accept, the digitizers send the data corresponding to that trigger via copper serial links to the "data merger" units. The data merger units assemble the data from a number of digitizers into event data packets of suitable size and forward these via the derandomizer buffers and optical links to the ROMs. Parts of this binary readout scheme have already been tested on an IFR prototype detector, allowing the determination and optimization of the readout system parameters, such as the sampling frequency and the number of samples.

Tables 13.10 and 13.11 show the estimated event size and data bandwidth required for the IFR readout at the nominal trigger rate of 150 kHz. These tables assume a readout window that can accommodate a trigger jitter of 100 ns, but do not take into account the data reduction that can be achieved by not sending the shared data of events with overlapping time windows twice.

While a readout system based on COTS was designed and successfully used in the IFR prototype, the front end stages of the readout chain for the final IFR detector will be implemented in an ASIC whose block diagram is shown in Figure 13.9.

The IFR scintillation detectors are each equipped with a silicon photomultiplier (SiPM) capable of counting single photons. They are grouped in modules which are inserted in selected gaps of the flux return steel or around it. The signals from all the SiPMs of a module are carried by thin coaxial cables. These cables exit the module's aluminum enclosure and are mass-terminated to a high density connector on a carrier PCB (printed circuit board). The average length of the coaxial cable bundles is in the order of a few meters to allow the carrier boards to be located in an area conveniently accessible for maintenance.

Figure 13.10 shows the situation for the IFR barrel: in this representation the metal enclosures of the modules are not shown; the closest convenient locations for the ASICs carrying boards are indicated by the yellow callouts. The front end cards are installed inside the 3" x 5" cable conduits as indicated in Figure 13.11. While the figure only shows the double shielded, multi differential-pair cables (green jacket) that are needed to connect the front end cards' output serial lines to the data merger units, the cable conduits are also meant to host cables for the distribution of the SiPM bias voltages (one bias

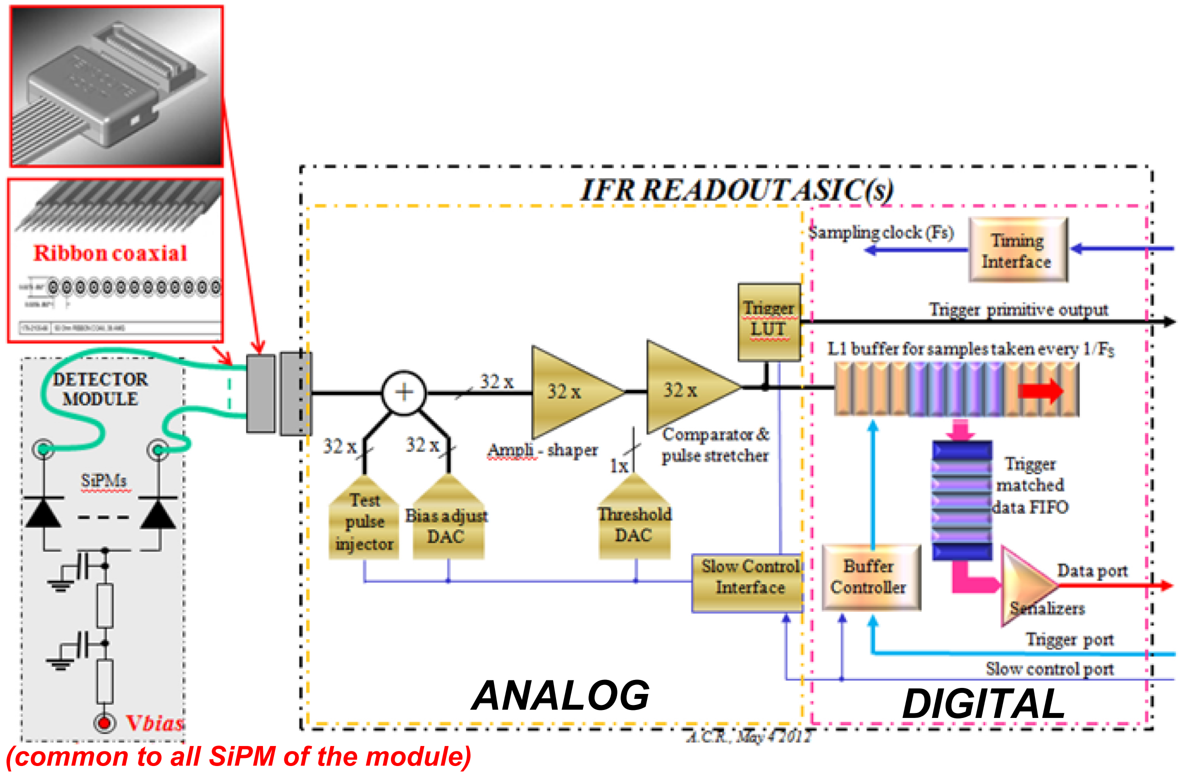

Figure 13.9: Block diagram of the IFR readout

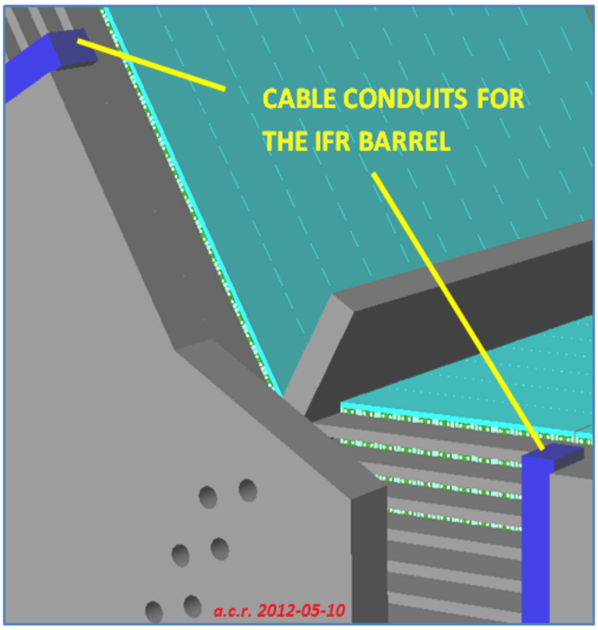

Figure 13.10: The IFR cable conduits for 2 sextants

voltage common to all SiPMs of a module), of the fast (FCS) and slow (ECS) commands and, finally, of the supply voltages for the front end cards.

Figure 13.12 shows the perspective view of the two "doors" of an endcap: the yellow callouts indicate the openings in the side-lining steel through which the data, control and power cables for the detector modules will be routed. The signals emerging from these openings are routed to the crates indicated by the red callouts. For the endcap section of the IFR, the front end cards carrying the IFR read out ASICs could be installed directly in the crate and connected to the data merger cards through the crate's backplane interconnections.

The data merger crates receive the global clock and fast commands from the FCTS and send their merged data to the ROMs, both via optical links. They also have a connection to

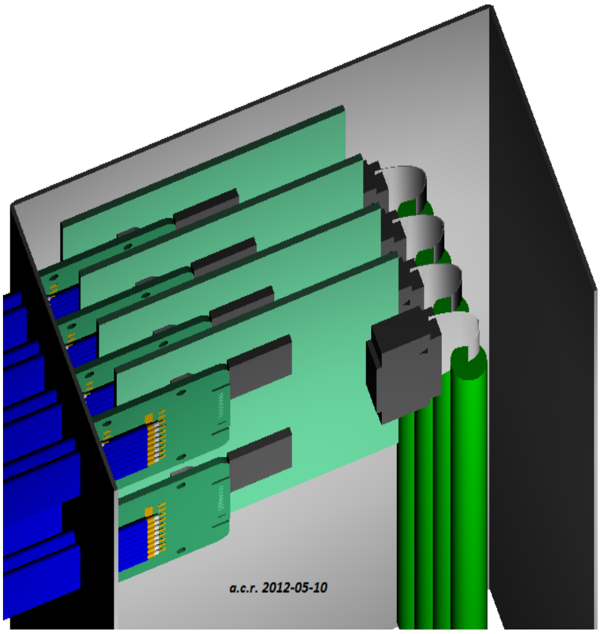

Figure 13.11: Detail of front end cards installed in the IFR cable conduit

the ECS for data acquisition system configuration and diagnostics.

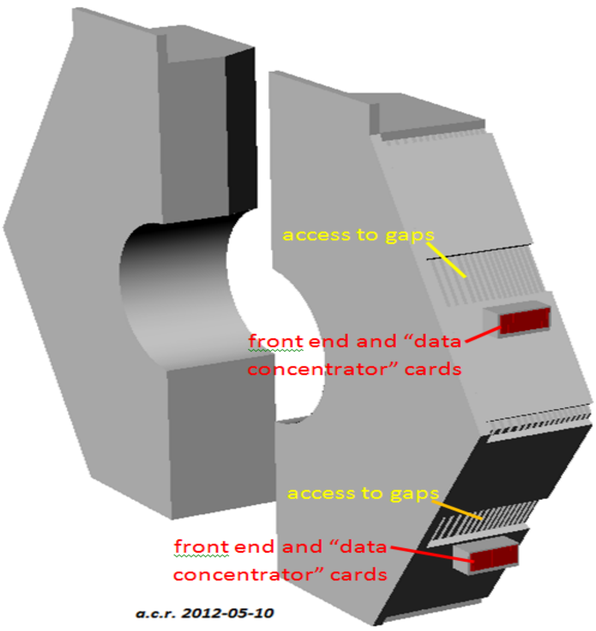

Figure 13.12: Perspective view of IFR endcaps

The IFR barrel will be equipped with a total of 6 data merger crates while 8 crates are foreseen for the endcaps. Further details on partitioning, location and construction of the data merger crates are given in the IFR subdetector chapter, which also provides a description of the services needed by the IFR readout in the experimental hall:

- SiPM supply voltages: 384 (barrel) + 324 (endcaps) = 708 "HV" channels with: maximum output voltage 100 V, 10 bit resolution, maximum output current 25 mA. The power dissipated by the SiPMs in the whole IFR under nominal operating conditions is of the order of a few tens of Watts.

- Front end cards supply voltages: 354 + 354 "LV" supply channels with: +3.3 V or -3.3 V output voltage respectively, maximum output current 1 A, IR drop compensation. The power dissipated by the front end stages for each 32 SiPM group is around 1.6 W and thus the power dissipated by the front end stages is about 620 W for the barrel and 520 W for the endcap.

- Cooling: the temperature of the IFR steel should be controlled to within a few degrees, as it was for *BABAR*; the design of the barrel cooling system should then take into account the estimated 1140 W dissipated in total by the front end stages of the IFR barrel and endcap electronics.

13.1.5.1 IFR Summary

Table 13.12 summarizes the IFR specification concerning the DAQ interface and power requirements.

Table 13.12: IFR summary

Number of Control Links	20
Number of Data Links	40
Total Event Size	45 kByte
On-Detector Power Consumption	1.2 kW

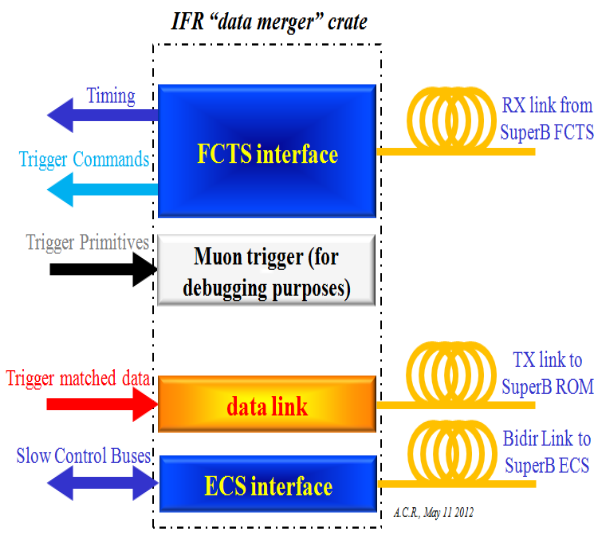

Figure 13.13: Main functions performed by the electronic units in the data merger crate

13.2 Electronics Infrastructure

13.2.1 Power supplies, grounding and cabling

The infrastructure for grounding, shielding and powering the detector is an integral part of the electronics design. As a general rule, the ground has to be as equipotential as possible across the experiment. When constructing the experimental hall, it should be foreseen to connect the iron reinforcement bars sunken in the concrete ground to the experiment's electrical ground in order to create the most perfect possible mesh. Shielding is not limited to cables carrying signals that can cause or are sensitive to electrical interference, but must also extend to electronics sensitive to any kind of interference. Interference can be electric, magnetic or radiative. If possible, power supplies should remain outside of the radiation area, because radiation-tolerant power supplies are more expensive and less reliable than standard ones. This implies long cables. Therefore, power consumption on the detector has to remain reasonable in order to limit the power loss along the cables.

13.2.1.1 Grounding and shielding

Noise in the front-end analog electronics, typically located in or on the detector, is the most dangerous one for the event data quality. For this reason, we need the best possible ground on the detector. One has to avoid high currents flowing back to the power supplies through unforeseen paths, especially through other subdetectors. Ground connections have to be strong everywhere, but the currents they carry have to be very limited. Subdetectors have to be fully equipotential internally; between subdetectors, this requirement can be somewhat relaxed, because there are no analog data connections between them. The choice of having a "perfect" equipotential ground has to be made very early in the experimental hall and detector design, because it is very difficult to retrofit later.

13.2.1.2 Rules for cables

Cable interconnection can use DC or AC coupling. DC coupling requires a perfect grounding, and is sensitive to any kind of currents, whereas AC coupling is only sensitive to AC currents. In all cases, the goal is to try to avoid any kind of parasitic currents. Therefore, the best solution is again to ensure a strong common ground. Moreover, it is strongly advised to also have a common analog and digital ground on electronics boards.

Cables have to be carefully defined and have to be perfectly matched to the required currents and the noise levels tolerated. Such cables have already been designed for other HEP experiments. Shielding mainly concerns remote interconnections. As a rule, in order to be effective, shields must be connected to ground on both ends. Within the electronics house, high-rate serialized data can be transmitted on shielded Cat6 cables with shielded RJ45 connectors on both ends, covering distances of up to about 15 meters.

Generally, we will try to avoid any power consumption local to the receiver side, and favor differential signalling because it offers constant power consumption. In cases where unipolar links are absolutely necessary, serial adaptaion at the source will be used to make the signal return path the same as the forward path, thus avoiding current flow in the cables.

13.2.1.3 Power Supply to the Front-end

Ground is not supposed to be the return path for supply currents, therefore power cables have to offer a very low impedance path for current returns. Moreover, the best solution to avoid having return currents flowing into ground is to let the power supplies float and to fix the ground potential on the sole detector side of the power cables. To avoid voltage drop fluctuations, it is normally better to regulate the power near to its use; this also permits to use cheaper DC/DC main supplies. In the Super$B$ environment, however, this would require radiation-tolerant supplies for many components of the on-detector electronics. Since radiation-tolerant supplies are expensive and less reliable, we will try to avoid them as much as possible by using alternative schemes to power the front-ends.

The voltage supply system is normally composed by a cascade of AC/DC, DC/DC and linear regulators. An example of a scheme for powering front-end electronics is shown in Figure 13.14. The main power supplies are located outside the detector, and linear regulators are used to regulate the power locally. Such as system has of course to be optimized for the power dissipation and noise requirements. In Super$B$, the presence of a strong magnetic field and large particle fluences poses additional constraints, as they can have an impact on the aging and behavior of electronic equipment. Radiation is addressed by adopting only radiation-hardened technology, and by using suitable layouts recipes for monolithic circuits. Magnetic fields generally have less impact, except for AC/DC and DC/DC converters that use inductances and/or transformers with ferromagnetic cores.

Power Supply outside the detector area In the following we will describe our solution that is able to meet the requirements outlined above. The basic strategy is to minimize the amount of power electronics in the detector area with a system design that allows the distance between the main power source and the front-ends to be a few tens of meters. In such as system, the energy stored in the inductive component of a cable can be large, and attention must be paid to protect the electronic equipment from damage in case of an accidental short circuit to ground or a sudden change of the current draw (e.g. in the case of loss and recovery of clock in digital electronics).

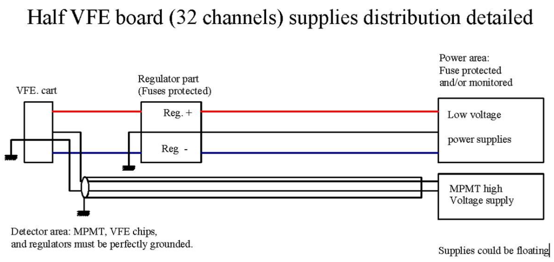

Figure 13.14: Example of implementation for front-end electronics powering.

We have found that most cables with 3 or 4 wires and cross-sections between 1.5 mm^2 and 4 mm^2 have an inductance per unit length, L_M, of the order of 0.7 μH/m from DC to few hundreds of kHz. To limit the voltage at a safe level we add a capacitance in parallel to the load that is able to store the released energy. For instance, we calculated that with 50 m of cable length, I_{short} =20 A and C_{lim} =160 μF, the maximum overvoltage excursion would be less than 9.5 V.

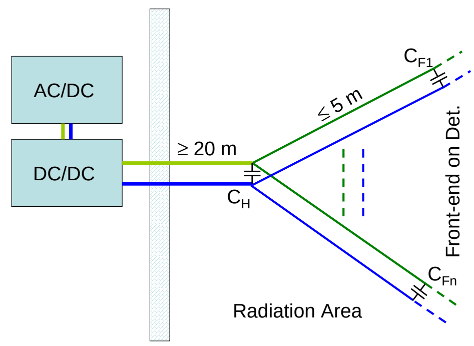

Figure 13.15: Possible voltage supply layout for a sub-detector

Adopting this technique, a hub for distribution to several shorter cables can also be implemented as shown in Figure 13.15. A large value capacitance, C_H, is at the end of the cable that connects the DC/DC regulators from the outside to the inside of the detector area. In our example we continue to assume 50 m cable length and $C_H = 160\,\mu$F. From the distribution hub several shorter cables, or stubs, connect the various parts of the detector or sub-detector front-end. To save space, the cross sections of the stubs can be smaller, since they each only have to carry a smaller current.

At the end of each of these stubs, 5 m in this example, a smaller value capacitance, C_{Fx}, (33 μF) is connected. In case of short at the end of a stub all the current flows into it. But as soon as the short is opened, capacitance C_H absorbs the energy of the longer cable, while the energy of the shorted stub is managed by the corresponding capacitance C_{Fx} (Figure 13.15).

The suppression capacitance must have a very small series resistance and inductance. Capacitors with plastic dielectric such as Metalized Polypropylene Film satisfy this condition. As an example the 160 μF capacitor we have adopted for the test has only 2.2 mΩ of series resistance, but, being big in volume, it shows a series inductance of a few tens of nH. To compensate for this latter effect, a smaller value (and volume) capacitance (1 μF), able to account for the fast part of the rising signal, is put in parallel. Metalized Polypropylene Film capacitances have a range of values limited to a few hundreds of μF. As a consequence, a limited current per cable, 10 A to 20 A, results in a good compromise. Many commercial regulators, also in the form of the so called bricks and half-bricks layouts, are available off the shelf at low cost. This strategy is particularly useful for minimizing the dropout along the cable and it is of particular concern when a low voltage is needed.

An overvoltage can also happen due to a possible malfunctioning of the regulator. To reject rapidly and with good precision this effect a stack of fast diodes is a good choice. For instance with a voltage supply of 10 V, about 20 diodes would allow to maintain a safe operating condition for a while, provided that they are in contact with a heat sink. The diode stacks can be located close to the regulator where space constraints are not an issue.

Noise cabling and shielding The combination of the inductance component of the wires and the suppression capacitance has an additional benefit, as it behaves also as a low pass filter. Figure 13.16 shows the noise at the end of the 50 m cable with two 5 m stubs when 160 μF plus 2×33 μF capacitances load the combination. The applied supply voltage was 10 V and the load 3.3 Ω. In this case a standard commercial regulator was used. Very low noise DC/DC regulators have been designed [1] and Figure 13.17 shows the noise performance under the same conditions. Even better performances can be obtained by cascading the DC/DC to a linear regulator of very good quality [2].

Low noise results can be obtained by careful choice of the type of cable. In all our measurements described so far we used only shielded cables. This protects the supply voltage from outside interferences, and also avoids creating disturbances for the outside world. We intend to adopt this layout for the final Super$B$ setup. In addition, where needed, we intend to add another shield by inserting the cables into a tubular copper mesh.

The connection scheme of Figure 13.15 is, in a natural way, also suitable to route ground. Assume that the ground of every detector or subdetector to which the cables are routed is isolated. We can then route a tinned copper wire (or a copper bar) very close to the power supply cables to reduce the area sensitive to EMI interferences. Such a routing scheme allows a “star” connection with only one ground contact node (recall that AC/DC and DC/DC regulators are floating) which is the standard requirement.

Shielding is considered for those regions where the electric or magnetic field can affect performance. The shields can be considered for the whole sub-detector or individually on a channel by channel basis. This is particularly true for the effect of magnetic field on those detectors that extend on a large volume, such as photomultiplier tubes (PMTs). Past experience shows that in these cases a local shield implemented with mu-metal around every PMT is essential.

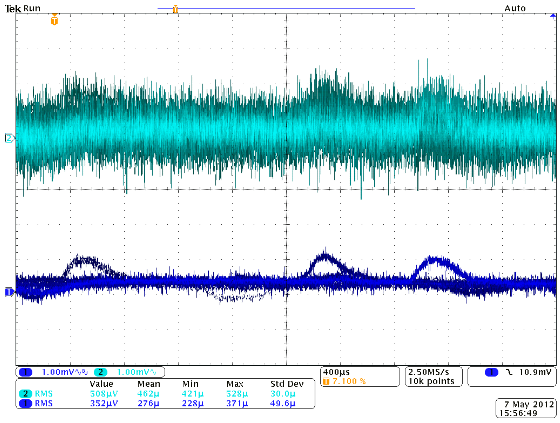

Figure 13.16: Noise after 50 m cable loaded with 160 μF plus $2{\times}33\,\mu$F capacitance at 10 V and with 3.3 Ω load. The upper noise trace is measured with the full 350 MHz bandwidth of the oscilloscope, the lower noise trace has has the scope bandwidth limited to 20 MHz.

Power Supply in the detector area We are considering to use both DC/DC and linear regulators inside the detector area where inductances and transformers cannot use ferromagnetic coils. As a consequence these are limited in their range of values and the switching speed of the DC/DC must be very large. This is the case for the monolithic DC/DC regulator we are considering [3], developed in 0.35 μm CMOS technology based on a rad-hard layout and components. Its modulator has a switching frequency of a few MHz, which allows the use of a coil-free inductance. A linear regulator based on the same technology is also available. [4].

13.2.1.4 High Voltage Power Supply for the Detectors

High voltage power supplies suffer of similar problems as AC/DC and DC/DC regulators. As a consequence these regulators must be located outside the detector, sub-detector area (we do not know about any commercial rad-hard high voltage regulator). The energy released to the load in case of accidental short circuit would be not an issue thanks to the fact that such regulators normally have their driving current limited to a few hundreds of μA. For instance, if we load the line with a 1 nF high voltage capacitor and assume 1 A as the short circuit current, we expect an overvoltage of about 0.2 V. Finally, commercial overvoltage protectors based on gas discharge tubes are very efficient and fast.

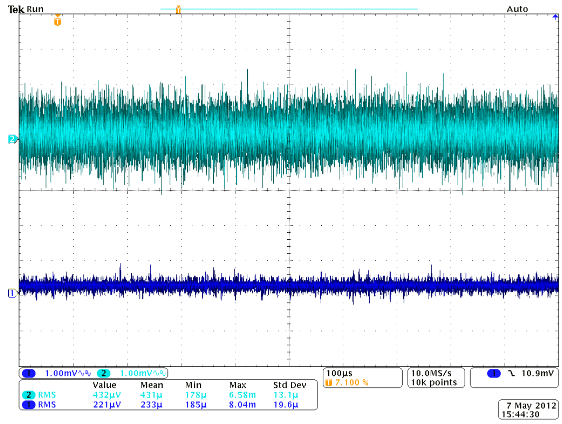

Figure 13.17: Very low noise DC/DC regulator [1]. Measurements condition and setup as for Figure 13.16

13.3 Bibliography

[1] C. Arnaboldi, A. Bau, A. Giachero, C. Gotti, M. Maino, A. Passerini, and G. Pessina, "A very low noise AC/DC Power Supply System for large arrays of cryogenic detectors", *Nuclear Science Symposium and Medical Imaging Conference (NSS/MIC), 2011 IEEE*, pp. 791 -793, oct. 2011, doi:10.1109/NSSMIC.2011.6154540.

[2] G. Pessina, "Low-noise, low drift, high precision linear bipolar (±10 v) voltage supply/reference for cryogenic front-end apparatus", *Rev. Sci. Instrum.* 70:3473, 1999, doi:10.1063/1.1149939.

[3] S. Michelis et al., "DC-DC converters in 0.35μm CMOS technology", *J. of Instrumentation* 7:C01072, 2012.

[4] F. Faccio, P. Moreira, A. Marchioro, and S. Velitchko, "A radiation-tolerant LDO voltage regulator for HEP applications",

Conference proceeding of the TWEPP-2005, Valencia (Spain), 2005.

14 Software and Computing

During 5 years of data taking, the Super$B$ detector will produce more than 500 PByte of raw data. To this, event reconstruction and Monte Carlo simulation will add another 300 PByte.

To cope with these large data volumes, Super$B$ will rely on predictable progress in computing technology to provide cost reduction and performance increase. The effective exploitation of computing resources on the Grid has become well established in the LHC era, and will enable Super$B$ to access a huge pool of world wide distributed computing resources.

Crucial issues for Super$B$ are the ability to efficiently use modern CPU architectures, and to efficiently and reliably access very large amounts of data spread over multiple geographically distributed sites.

So far, the Super$B$ computing effort has been devoted to the development and support of simulation software tools and computing infrastructure needed to design and validate the detector, to the initial definition of a computing model, and to computing R&D.

In the first part of this chapter, the existing software tools are presented. The second part describes the current baseline computing model, gives an estimate of the Super$B$ computing requirements, and presents a possible implementation of the computing infrastructure. The third part describes the dedicated computing R&D program that has been initiated to investigate possible technical solutions to the Super$B$ computing problems.

14.1 Tools to support detector studies

The Super$B$ collaboration has developed a set of tools to perform fairly detailed and sophisticated detector and physics studies. This toolset includes a detailed Monte Carlo simulation (Bruno) based on GEANT4 [1], a fast parametric simulation (FastSim) which directly leverages the existing *BABAR* analysis code base, and a production system that exploits the computing resources available on the European and US Grids to perform very large–scale simulation productions.

In addition, the computing group is providing and supporting the infrastructure and tools to support and coordinate the day-to-day activities of the Super$B$ collaboration: source code management, a portal for document management, and tools to enable and support collaborative work and manage collaboration membership.

A description of the tools made available to the collaboration and their capabilities is presented in the following.

14.1.1 Full Simulation

The availability of reliable full simulation tools is crucial for designing both the accelerator and the detector. First of all, the background rates in the sub-detectors need to be carefully assessed for each proposed accelerator design. Secondly, for a given background scenario, the design of the sub-detectors must be optimized to obtain the best possible performance. Moreover, full simulation software can be used to improve the results of the fast simulation in some particular cases, as discussed below.

Bruno: the Super*B* full simulation software To better profit from both the *BABAR* legacy, and the experience gained in the development of the full simulation softwares for the LHC experiments, the choice was made to rewrite from scratch the core simulation software. Therefore, GEANT4 and the C++ programming language were the natural choice for the underlying technology.

After some years of development, the Super$B$ full simulation software is, in its present state, usable (and, indeed, used) to assist in the design of the accelerator and detector. The basic functionality is in place and well tested; more features are added based on user requests. We will give in the following a short overview of the main characteristics, emphasizing areas where future developments are planned.

Geometry description The need to reuse as much as possible the existing geometrical description of the *BABAR* full simulation, called for some application-independent interchange format to describe the geometry and materials of the sub-detectors. In the present phase of the Super*B* experiment, a human-readable format is preferred, so that it is easy to change the geometry details in order to model different design alternatives.

From the formats currently used in HEP applications, the Geometry Description Markup Language (GDML) was chosen for the following reasons:

- its XML-based structure allows for relatively easy human inspection and editing, while still providing (by construction) a certain level of robustness.
- it provides some level of modularization, by allowing to split the global geometry into smaller files.
- its specification is an independent project, not linked to any specific application
- GEANT4 provides native interfaces to read and write GDML files. This allowed, for example, to export the *BABAR* original geometry, modify it as necessary, and read it back into Bruno.
- ROOT can process GDML geometry as well, allowing for example to easily visualize some simulation result together with the underlying detector geometry using ROOT embedded geometry viewer

The present implementation relies on GDML as the only source of geometry information. The file structure reflects the natural division in subdetectors, with one global file defining only subdetector envelopes, each filled in turn (using a different file) with all needed details. Space allocation is thus centrally managed at the level of the top file, while the sub-detector communities have the freedom of experimenting with different layouts without interfering with each other.

The consistency of the geometry (volume overlaps, volume overshoots) is periodically checked with standard GEANT4 tools. The choice of GDML also brings in some limitations. One example is the limited support for loops and volume parameterization. In the longer term, after the detector layout has finalized, and the ease of inspection is no longer as crucial as it is now, the GDML-based approach might be replaced with a custom solution that allows more flexibility at the cost of reduced human readability.

Simulation input: Event generators Bruno can be interfaced to an event generator in two ways: either by directly embedding the generator code, or by using an intermediate exchange format. In the latter case, the event generator is run as a different process and its results are saved in a file, which is then used to feed the full simulation job. Bruno presently supports two interchange formats: a plain ASCII file and a purely ROOT-based format that uses persisted instances of the TParticle class.

Simulation output: Hits and Monte Carlo Truth Hits in the different sub-detectors are created by specific SensitiveDetectors. The transient representation is managed through instances of custom implementations of the G4VHit interface which are translated into instances of ROOT-based classes for persistency. Presently, all sub-detectors are producing hits, which are then saved in the output (ROOT) file for further processing and analysis. In addition to the simulated event as seen from the detector, the Monte Carlo Truth (MCTruth) describes the event as seen by the simulation engine itself, i.e. with full detail. The same ROOT-native class (TParticle) is used for the transient and persistent representations of MCTruth. Examples of MCTruth information presently handled by Bruno include:

- Full snapshots of the simulation status at different scoring volumes. All particles crossing a given scoring volume are persisted and saved into the output file, allowing easy estimation of the particle flux. Predefined scoring volumes include all sub-detector boundaries, and the list is extensible/modifiable at run time without need to recompile.
- Detailed lists of secondaries produced within a given volume. The secondaries can be filtered based on the particle type or energy
- Full particle trajectories, i.e. the list of steps a particle makes while propagating through the detector. Due to its very high level of detail, this information is of little use without advanced filtering. The present implementation allows, for example, to save the trajectories only for particles of selected type/energy, being produced in a given volume, under the condition that the particle leaves the volume it was created in. This is specifically tailored for studying the effect of shielding components.

Simulation optimization In order to properly optimize the simulation results, several parameters need to be adjusted. The most important parameter is probably the physics list to be used. A conservative choice was made by using QGSP_BERT_HP, which from other experiments is known to provide a good description of both electromagnetic and hadronic physics (including low-energy neutron interactions), but at the cost of more computing time. Tests with different physics lists are foreseen for the near future.

On top of the default physics lists, the user can choose to apply some Super*B*-specific tunings, such as simulation of optical photons or different models of Multiple Coulomb Scattering.

Another crucial aspect is the choice of the production threshold for different particles in different parts of the detector, since this has impact on both computing and physics performance. The present policy is to use the default Geant4 production cut (0.7mm) unless specific studies from sub-detectors require different settings. Such studies are already ongoing, and results will be reflected in the default configuration.

Staged simulation Especially in the design phase, a very common use case is where the layout of a detector is modified and full simulation is used to evaluate the effect of the change, requiring the production of an appropriate number of events. When all sub-detectors are working in parallel on their own implementations, this may result in sub-optimal use of computing resources. One way to ease this situation is the use of staged simulation.

The basic idea is that if the layout of a detector changes, there is no need to re-simulate all the interactions taking place *before* particles hit that detector: the simulation must be redone only for that detector (and the ones downstream). For example, if the IFR wants to test a new layout, all existing simulated events can be re-used up to the electromagnetic calorimeter, and only the very last simulation step needs to be redone.

The infrastructure for this kind of application is already implemented and validated, and it uses features already described above:

- All simulated events save snapshots of the simulation status at sub-detector boundaries in the output ROOT file.
- The resulting TParticles can be read back by Bruno as if they were the output from an event generator, thus seeding the new simulation process.

In the concrete IFR example, one can use the existing simulated events as input to the new simulation, instructing Bruno to consider the snapshot at the exit of the electromagnetic calorimeter as a seed.

Interplay with fast simulation As already mentioned in the introduction, full simulation can also be used in conjunction with the fast simulation programs in certain contexts.

The design of the interaction region in particular has a large impact on the background rates seen by the detector. Simulating such a complex geometry with the required level of detail is beyond the capability of the fast simulation. On the other hand, full simulation is not fast enough to generate the high statistics needed for signal events.

Super$B$ uses a hybrid approach to this problem. Bruno is used to simulate background events up to (and including) the interaction region and a snapshot of the simulation status is saved. In order to save time, the full simulation of the event can optionally be aborted once the relevant information has been saved. The result of this procedure is a set of *background frames*, which can be read back in the fast simulation program which propagates these particles through the simplified detector geometry and overlays the resulting hits with the hits coming from signal events. This approach allows to combine the two simulations and to use each one only for the tasks it performs best.

The interplay between fast and full simulation is also very useful for the evaluation of the neutron background. The idea here is to make Bruno handle all particle interactions within the interaction region, as explained above, *plus* all neutron interactions afterwards. Neutrons are tracked in full simulation until they decay, and the decay products are saved in the output file, as part of the background frame. Fast simulation can then include these interactions in the overlaying procedure. All these functionalities are presently implemented, and have been used in the recent productions.

Long term evolution of the full simulation software While the full simulation software already provides adequate functionality for the design phase of the experiment, it will need to be constantly updated and improved to be ready to support the needs of the data taking period.

Studies of the readout electronics will require a digitization framework and digit persistency. Since digitization is generally not very demanding in terms of CPU, it will be implemented as a separate step from the full simulation and possibly be run in a different job, starting from the persisted hits.

Particular attention will be devoted to performance issues:

Physics performance must be improved, both through a finer tuning of Bruno's internal parameters and by following closely the evolution of the GEANT4 code itself, in order to better profit from improved modeling of the underlying physics processes.

Optimizing the **computing performance** is also of paramount importance, in particular in the context of highly distributed and/or parallelized computing. The present implementation is already capable of running on distributed computing resources, while it still lacks intra-event parallelism. This is mainly due to limitations of the GEANT4 toolkit itself, which will hopefully be overcome in a timescale compatible with the lifespan of the Super$B$ experiment. In order to take advantage of new parallelization features, Bruno will most likely need to be heavily restructured. Similar considerations apply to the optimal exploitation of the new (yet already widespread) computing architectures, such as multi/many core CPUs and GPUs.

14.1.2 Fast Simulation

FastSim relies on simplified models of the detector geometry, materials, response, and reconstruction to achieve an event generation rate a few orders of magnitude faster than is possible with a GEANT4-based detailed simulation, but with sufficient precision and detail to allow realistic physics analyses.

In order to produce more exact results, FastSim incorporates to some degree the effects of expected machine and detector backgrounds. It is easily configurable and allows different detector options to be selected at run time. It is also compatible with the *BABAR* analysis framework, allowing sophisticated analyses to be performed with minimal software development.

A diagram summarizing the structure of FastSim is shown in Figure 14.1. The simulation proceeds through four main steps: particles generation, detector configuration and response, particle reconstruction and analysis of the event.

Event generation Since FastSim is compatible with the *BABAR* analysis framework, we can exploit the same event generation tools used by *BABAR*. On-peak events ($e^+e^- \to \Upsilon(4S) \to B\bar{B}$), with the subsequent decays of the B and $\bar{B}$ mesons, are generated with the EvtGen package [2]. EvtGen also has an interface to JETSET for the generation of continuum $e^+e^- \to q\bar{q}$ events ($q = u, d, s, c$) and the generic hadronic decays that are not explicitly defined in EvtGen. The Super$B$ machine design includes the ability to operate with a $70-80\%$ longitudinally polarized electron beam, which is especially relevant for τ physics studies. Events $e^+e^- \to \tau^+\tau^-$ with polarized electron beam are generated using the KK generator and Tauola[3].

Machine backgrounds are superimposed on top of the physics event at the event generation stage.

Detector description FastSim models Super$B$ as a collection of detector elements that represent medium-scale pieces of the detector. The overall detector geometry is assumed to be cylindrical about the solenoid $\vec{B}$ axis (z axis), which simplifies the particle navigation. The detector's volumes are divided into voxels, defined as cells in the z, ρ, ϕ space with sizes specified in the XML configuration files. Particles are tracked through these voxels. When a particle crosses a voxel, it interacts with all elements inside the voxel without any assumption about the order of these elements.

Individual detector elements are described as sections of two-dimensional surfaces such as cylinders, cones, disks and planes; the effect of physical thickness is modeled parametrically. For example, a barrel layer of Si sensors is modeled as a single cylindrical element. Thick detector components, such as the EMC crystals, are modeled by layering several elements and summing their effects. Gaps and overlaps between the real detector pieces within an element are modeled statistically. Density, radiation length, interaction length, and other physical properties of common materials are described in a simple database. Composite materials are modeled as mixtures of simpler materials. A detector element may be assigned to be composed of any material, or none.

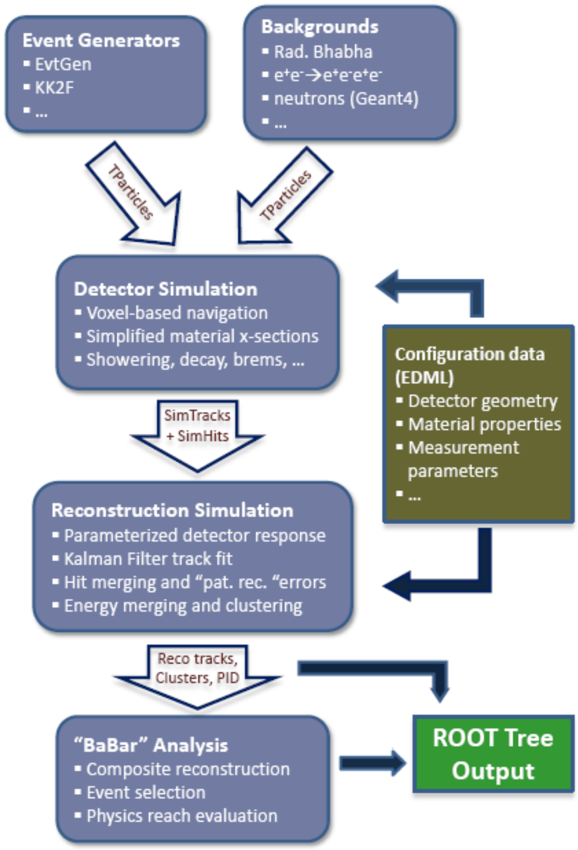

Figure 14.1: Simulation diagram of FastSim.

Sensitive components are modeled by optionally adding a measurement type to an element. Measurement types describing Si strip and pixel sensors, drift wire planes, absorption and sampling calorimeters, Cherenkov light radiators, scintillators, and TOF are available. Specific instances of measurement types with different properties (resolutions) can co-exist. Any measurement type instance can be assigned to any detector element or set of elements. Measurement types also define the time-sensitive window, which is used in the background modeling. The geometry and properties of the detector elements and their associated measurement types are defined through a set of XML files using the EDML (Experimental Data Markup Language) schema invented for Super$B$.

Interaction of particles with matter FastSim models particle interactions using parametric functions. Coulomb scattering and ionization energy loss are modeled using the standard parameterization in terms of radiation length and particle momentum and velocity. Molière and Landau tails are included. Bremsstrahlung and pair production are modeled using simplified cross-sections. Discrete hadronic interactions are modeled using simplified cross-sections extracted from a study of Geant4 output. Electromagnetic showers are modeled using an exponentially-damped power law longitudinal profile (a simplified version of the gamma distribution in [4][5]) and a double Gaussian transverse profile[6], which includes the logarithmic energy dependence and electron-photon differences of shower-max. Hadronic showers are modeled with a simple exponentially-damped longitudinal profile [7][8] tuned using Geant4 output.

Unstable particles are allowed to decay during their traversal of the detector. Decay rates and modes are simulated using the *BaBar* EvtGen code and parameters.

Detector response All measurement types for the detector technologies relevant to Super$B$ are implemented. Tracking measurements are described in terms of the single-hit and two-hit resolution, and the efficiency. Si strip detectors and (optional) pixel detectors are modeled as two independent orthogonal projections, with the efficiency being uncorrelated (correlated) for strips (pixels) respectively. Wire chamber planes are defined as a single projection with the measurement direction oriented at an angle, allowing stereo and axial layers. Ionization measurements (dE/dx) used in particle identification (PID) are modeled using a Bethe-Bloch parameterization.

Cherenkov rings are simulated by using a lookup table to define the number of photons generated based on the properties of the charged particle when it hits the radiator. Timing detectors are modeled based on their intrinsic resolution.

In the EMC the energy deposits are distributed across a grid representing the crystal or pad segmentation, taking into account profile fluctuations and the energy resolution of the crystals. In the IFR the hadronic shower profile produced by charged pions or the ionization energy loss by muons are used to determine the 2-dimensional distribution of hits over the scintillator planes, taking into account the intrinsic spatial resolution. The detector response for charged pions and K_L is also simulated.

Reconstruction On one hand, full reconstruction based on pattern-recognition is beyond the scope of FastSim, on the other hand, a simple smearing of particle properties is insensitive to important effects like backgrounds. As a compromise, FastSim reconstructs high-level detector objects (tracks and clusters) from simulated low-level detector objects (hits and energy deposits), using the simulation truth to associate detector objects. Pattern recognition errors are introduced by perturbing the truth-based association, using models based on observed *BaBar* pattern recognition algorithm performance.

In tracking, hits from different particles within the two-hit resolution of a device are merged, the resolution degraded, and the resulting merged hit is assigned randomly to one particle. Hits overlapping within a region of 'potential pattern recognition confusion' are statistically mis-assigned based on their proximity. The final set of hits associated with a given charged particle are then passed to the *BaBar* Kalman filter track fitting algorithm to obtain reconstructed track parameters at the origin and the outer detector. Outlier hits are pruned during the fitting, based on their contribution to the fit χ^2.

Ionization measurements from the charged particle hits associated with a track are combined using a truncated-mean algorithm; this is done separately for the SVT and DCH hits. The truncated mean and its estimated error are used in PID algorithms. Figure 14.2 shows the reconstructed dE/dx in the drift chamber as a function of the particle momentum for different particle types. The measured Cherenkov angle from the DIRC is smeared according to its intrinsic resolution and the Kalman filter track fit covariance at the radiator.

In the EMC, overlapping signals from different particles are summed across the grid. A simple cluster-finding algorithm based on a local maxima search is run on the grid of calorimeter response. The energies deposited in the cluster cells are used to define the reconstructed cluster parameters (cluster energy and position). Simple track-cluster matching based on proximity of the cluster position to a reconstructed track is used to distinguish charged and neutral clusters.

Hits in IFR are combined into clusters, which are then fitted with a straight line ($\vec{B}$ is zero outside the coil). A number of quantities useful to distinguish pions from muons are computed, such as the number of interaction lengths crossed by the particle. The distribution of this quantity for charged pions crossing the *BABAR* IFR is shown in Figure 14.3. The fast simulation agrees reasonably well with the *BABAR* detailed simulation.

FastSim has its own event display. Figure 14.4 shows a reconstructed $e^+e^- \rightarrow \Upsilon(4S) \rightarrow B\bar{B}$ event with the B mesons decaying to hadrons. The subsystems have cylindrical symmetry. Both charged particles and photons

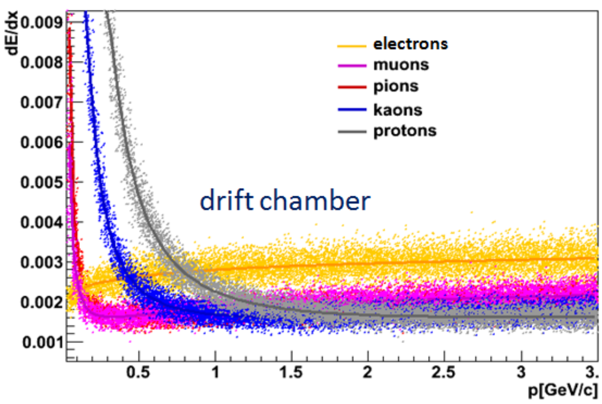

Figure 14.2: Reconstructed dE/dx in the drift chamber as a function of the track momentum for different charged particle types.

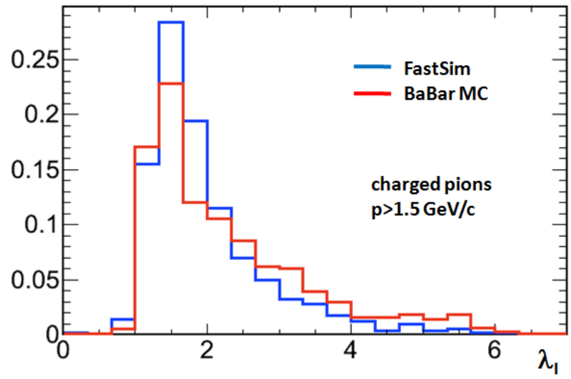

Figure 14.3: Number of interaction lengths for $\pi^{\pm}$ crossing the *BABAR* IFR.

(straight segments) are visible. The green spots are reconstructed clusters in the EMC.

Machine backgrounds The main contributions to machine background at Super*B* are radiative Bhabhas, Pair production ($e^+e^- \rightarrow e^+e^-e^+e^-$), Touschek background and beam-gas interactions. Background events are generated in dedicated full simulation (based on GEANT4) runs, and then superimposed on the FastSim physics events. GEANT4 is needed to model the effect of background showers in the elements of the interaction region, since the detailed description of these elements and the processes involved are beyond the scope of FastSim. Background events are stored as lists of the generated particles (*TParticles* [9]), these lists are then filtered to save only those particles which enter the sensitive detector volume.

Background events from all sources are overlaid on top of each generated physics event during FastSim simulation. The time origin of each background event is assigned randomly across a global window of 0.5 μs (the physics event time origin is defined to be zero). Background events are sampled according to a Poisson distribution whose mean is the rate of the background process times the global time window. Particles from background events are simulated exactly as those from the physics event, except that the response they generate in a sensitive element is modulated by their different time origin. In general, background particle interactions outside the time-sensitive window of a measure-

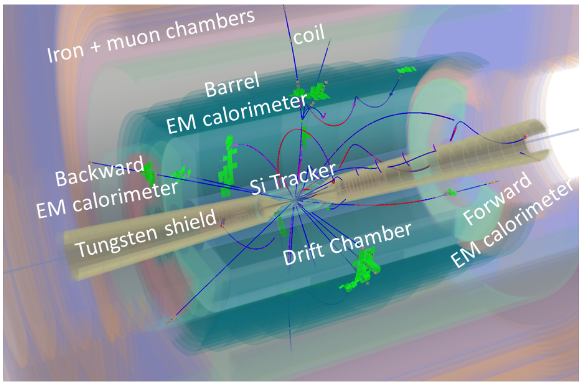

Figure 14.4: Reconstructed $e^+e^- \to \Upsilon(4S) \to B\bar{B}$ event with $B \to$ hadrons represented using the FastSim event display.

ment type do not generate any signal, while those inside the time-sensitive window generate nominal signals. The EMC response to background particles is modeled based on waveform analysis, resulting in exponentially-decaying signals before the time-sensitive window, and nominal signals inside. The hit-merging, pattern recognition confusion and cluster merging described earlier are also applied to background particle signals, so that fake rates and resolution degradation can be estimated from the FastSim output. The mapping between reconstructed objects and particles is kept, allowing analysts to distinguish background effects from other effects.

Background effects on electronics (hit pileup) and sensors (saturation or radiation damage) are also crucial for Super$B$, but are best studied using the full simulation and other tools. Their impact on the measurement performance can be implemented parametrically at the detector response or reconstruction level.

Analysis tools FastSim has been designed to be compatible with the *BABAR* analysis framework, so that existing *BABAR* analysis tools such as vertexing and combinatorics engines can be used in FastSim with small modifications. PID selectors are also available. They provide lists of identified particles (pions, kaons, electrons, etc.) selected by combining the PID information measured in the relevant subsystems and are key ingredients in most of the Super$B$ physics analyses.

User packages have been developed to support the reconstruction and analysis of specific decay modes. For instance, packages are available for the selection of tau decays in $\tau^+\tau^-$ events or the reconstruction of semi-inclusive hadronic and semileptonic B decays for the recoil analysis of rare B decays.

The standard tool used in *BABAR* to store analysis information into a ROOT tuple has been adapted to work in FastSim, allowing even complex analyses to be run in FastSim approximately as in *BABAR*.

Typical per-event processing times on a dual quad core Intel(R) Xeon(R) E5520 CPU (2.27 GHz) are 1 ms for particle generation, 10 ms for propagation of particles through the detector, 100 ms for reconstruction, and 100-1000 ms for composites selection, depending on the event complexity.

Simulation validation and detector studies Many aspects of FastSim have been validated either by simulating the *BABAR* detector and comparing the output with the full simulation or real data of the *BABAR* experiment, or by comparing with the Super$B$ full simulation. In general the outcome of these comparisons is quite satisfactory. The tracking simulation works particularly well, despite the lack of a real pattern recognition.

FastSim is being used extensively to optimize the Super$B$ detector design by studying the performance of different layouts. Since the complete simulation and reconstruction chain is available, including the tools to perform a complete physics analysis of the simulated events, it is possible to compare different detector configurations directly in terms of the physics reach of benchmark channels.

An example is illustrated in Figure 14.5. The top plot shows the reconstructed mass of the tag B mesons selected in hadronic decays, with the FastSim result superimposed to the *BABAR* full simulation. The bottom plot shows how $S/\sqrt{S+B}$ (S and B are the signal and background yields, respectively) scales as a function of the integrated luminosity and detector layouts.

14.1.3 Distributed computing tools

Even at this early stage in its lifetime, the Super$B$ experiment needs very large samples of Monte Carlo simulated events to evaluate the machine background, to optimize the detector design, and to estimate the physics analysis performances. Since producing these samples is beyond the capacity of a single computing farm, the Super$B$ collaboration developed a suite of tools to fully exploit the existing HEP world wide Grid computing infrastructure. [10][11][12]. The Super$B$ distributed computing tools are built upon the LHC Computing Grid (LCG) [12] which is widely adopted in the HEP

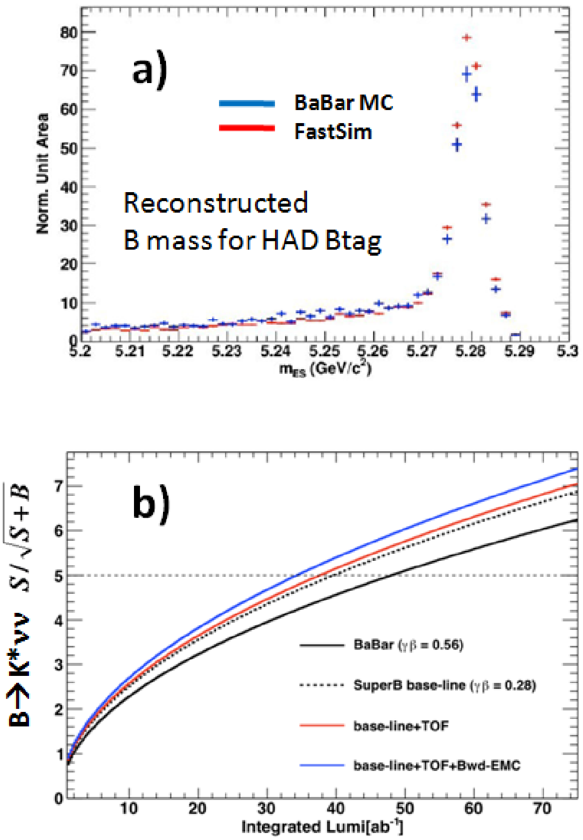

Figure 14.5: Top: Mass of the reconstructed B decays selected into hadronic final states. Bottom: precision of the $B \to K^* \nu \bar{\nu}$ measurement as a function of the integrated luminosity in four different detector configurations.

community and has long term support by the Grid initiatives. The Super$B$ Virtual Organization (VO) is currently enabled at several sites located in countries participating in the project; both Grid flavors, EGI [10] and OSG [11] are in use within the Super$B$ VO, so all services need to be able to support multi-flavor Grid middlewares.

The Super$B$ distributed tools use the following LCG services and applications:

- The *Workload Manager System* (WMS) [13] for job brokering, resource matching and job submission;
- the *Virtual Organization Membership System* (VOMS) [14] to manage user authentication and authorization;
- the *LCG File Catalog* (LFC) [15] to provide logical to physical file mappings;
- the *SRMV2 resource manager layer* [16] to share, access and transfer data among heterogeneous and geographically distributed data centers; and
- the *LCG-Utils* [17] to perform data handling tasks compliant with LCG and SRMV2.

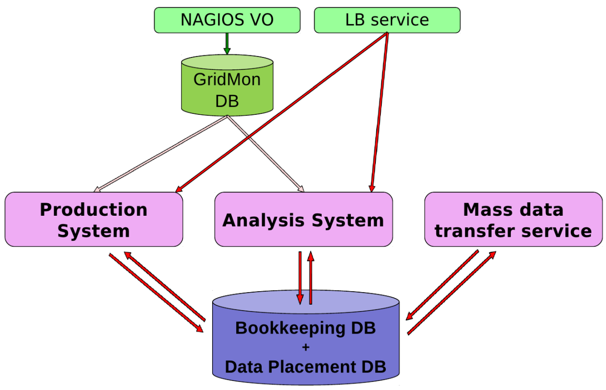

Figure 14.6: Distributed systems bird's-eye view.

Figure 14.6 shows the important elements of the Super$B$ distributed computing system: actual processing and data movement are performed in the *Simulation Production System*, the distributed *Analysis System* and the *Mass data transfer service*. The *Bookkeeping and Data Placement databases* hold metadata related to FastSim and FullSim, and information about dataset structures and data placement on Grid resources. The monitoring system uses the *Nagios* [18] tools suite to implement a *Service Availability Monitoring* (SAM) [19] to maintain a per-VO status of the Grid elements in the GridMon database. Finally, the *Logging and Bookkeeping* (LB) service provides detailed job status information from the Grid-internal processes.

The Simulation Production System has been developed to manage the production of very large Monte Carlo samples in a distributed environment. It supports both FastSim and FullSim, is tightly integrated with the bookkeeping database, permits a fine tuning of operational tasks via web portal, and hides the intrinsic complexity of the Grid infrastructure from the user by providing automated submission procedures and rich monitoring features. Job submission is performed by the Ganga [20] system. A Ganga-specific script has been developed to permit run time customizations and the generation of site-specific job files.

The web interface provides rich monitoring features by means of querying the bookkeeping database and interacting with the Logging and Bookkeeping gLite service. The user can retrieve the list of jobs as a function of their unique identifier (or range of them), their specific parameters, the execution site, status, and so forth. The monitor section provides a per job list of output files and a direct access to the corresponding log files. The output file size, execution time, computing resource load status, and the list of the last finished jobs (successfully or with failures) are also provided.

A simple authentication and authorization layer, based on an LDAP [21] directory service permits to apply a user-role based policy to access the system. A VOMS proxy user authentication has been added to be compliant with Grid Security Infrastructure (GSI) standards.

For a detailed and technical description of the production system framework please refer to [22].

The data analysis system prototype Physicists involved in Monte Carlo simulation productions and in data analysis need to perform job management and basic data transfer operations in a user-friendly way and with minimal training. Ganga has been adopted as the interface layer of this distributed analysis infrastructure and a Super*B*-specific Ganga-plugin has been developed. Two use cases are currently implemented: a private Monte Carlo production and data reduction and analysis of centrally (or privately) produced Monte Carlo datasets. The main components of the Super*B* data analysis suite are the job wrapper, the bookkeeping and data placement database and the Ganga plug-in software layer. The job wrapper allows the management of stage-in, user application execution, monitoring and stage-out phases. It interacts with the Ganga plug-in for monitor purpose only. Bookkeeping and data placement databases are the back end providing the Ganga plug-in with all the information needed regarding distributed resources, dataset structure and placement and output metadata. For a detailed and technical description of the distributed analysis prototype please refer to [23].

Bookkeeping and data placement database Both the distributed production and data analysis systems require a way to identify selected data files and the Storage Elements (SEs) that hold these files in the distributed system. The immediate access to the execution status of jobs and their parameters is crucial for users in order to plan their activities and summarize the results. Therefore, a data bookkeeping system has been developed, that stores the semantic information associated with data files and tracks the relation between jobs, their parameters and their output data.

The bookkeeping database is extensively used by the production job management system itself in order to schedule subsequent submissions, and to keep the information about request completion and site availability up to date. It was modeled after the general requirements of a typical simulation production application; its design uses the relational model, and the current implementation uses the PostgreSQL RDBMS [24] in a centralized way.

The database connections from/to processes running in a Wide Area Network environment are managed via web services, in particular, a RESTful [25] service in front of the database has been developed. Database accesses to the central information systems from jobs running at remote sites are authenticated by VOMS proxy certificates. Local jobs may alternatively use direct connections to PostgreSQL.

The feasibility of integrating and using a schema-free and/or document-oriented information system is under study. Such a system might be required for distributed metadata management and data replication with bi-directional conflict detection and management.

14.1.4 Collaborative tools

The computing group supports a suite of computing tools to facilitate the day-to-day activities of the Super$B$ collaboration, to present the project to the general public, to exchange information among collaborators, to manage and store documents, and to coordinate software development. A short description is presented in the following.

Authorization The need to manage authorization and authentication for the number of people in a Super$B$-size collaboration imposes the use of some kind of database. Since several services (code repository, internal web pages, wiki, etc.) require authentication/authorization, a directory service based on LDAP [21] has been chosen to implement single-sign-on (SSO) access across the Super$B$ service suite, and to manage authorization information such as access permissions and group membership.

Web Portal The web plays a central role for the Super$B$ collaboration. Web services and tools are both used for outreach to the general public, and to provide collaboration space where Super$B$ members can interact, and share content and knowledge. Initially, Super$B$ started out with two separate web content management systems (CMS), one for the general public, the other for the collaboration website. Since then, these services have been consolidated in a portal system. The Super$B$ collaboration portal is based on the *Liferay* portal system [26] and provides both an outreach website, and a collaboration website. For the collaboration website it uses *Jasig CAS* [27] to provide SSO to collaboration members; after authenticating through the portal, they can use collaboration services without the need to sign in to each service individually[1]. Collaboration services include the Super$B$ event calendar, a members directory, and an administrative database to manage collaboration membership, speakers, and service access privileges.

Document Management The Super$B$ document management system is implemented using the *Alfresco* platform [28], an enterprise class suite of applications for document and content management. The repository is fully integrated with the collaboration portal and is accessible both via web interfaces or WebDAV. It provides document workflows, automated actions on documents, user/group based document-level security, Super$B$-specific data dictionaries, fully indexed documents (metadata and content), and auditing and versioning of all documents. The repository can be browsed or searched by category or keywords.

Documentation The document repository notwithstanding, the Super$B$ collaboration has realized from the beginning that it also needs a tool to facilitate the creation and maintenance of web pages to be used as internal documentation. For this, Mediawiki [29] has been chosen, because it combines easy creation and modification of content in a web browser (WYSIWYG or simple markup language) with basic content management features, integrates well with the directory service, and can also handle content like TEX formulas, plots, and pictures.

[1] Not all collaboration services have been converted to SSO yet.

Code repository The Super$B$ collaboration currently uses *Subversion* (SVN) [30] in conjunction with *Trac* [31] to manage the source code for FastSim, FullSim, several component projects, and documentation. SVN provides the management of source code and revisions, while Trac provides add-on services such as code navigation via web browser, a ticketing system, a wiki for the code documentation and a blog.

Code packaging and distribution The Super$B$ software release system is based on the *RPM* [32] packaging system. It has been chosen because it provides an easy way to install, update and uninstall software packages, and also provides a mechanism to declare explicit dependencies on other RPM packages. External packages (e.g. ROOT, GEANT4 and others) are also packaged and distributed in RPM format. Super$B$ code distribution is performed using *yum* [33], an updater and package installer/remover which facilitates the use of RPM by automatically computing and resolving dependencies and orchestrating the download and installation/uninstallation of RPM packages.

14.2 The Super$B$ baseline computing model

The computing models of the *BABAR* and Belle experiments have proven to be very successful in handling the data volume generated by a flavor factory in the $\mathcal{L} = 10^{34}\,\mathrm{cm}^{-2}\mathrm{s}^{-1}$ luminosity regime. The data volumes produced by Super$B$ will be two orders of magnitude larger, nevertheless, we expect that a *BABAR*-like computing model can still apply. In this section we introduce the *BABAR*-inspired data processing strategy and computing model, give an estimate of the extrapolated Super$B$ computing requirements, and finally present a possible computing infrastructure.

14.2.1 Data processing strategy

Data processing in Super$B$ is envisaged to be similar to the strategy used in *BABAR*. An overview of the proposed computing model and data flow is shown in Figure 14.7.

"Raw data" coming from the detector are permanently stored and then reconstructed in a two-step process:

1. a *Prompt Calibration* (PC) pass is performed on a subset of the events to determine various calibration constants.

2. a *full Event Reconstruction* (ER) pass that uses the calibration constants derived in the first step is then performed on all events.

Reconstructed data are permanently stored and data quality is monitored at each step of the process.

A comparable amount of Monte Carlo simulated events are also produced in parallel and processed in the same way. The Monte Carlo simulation incorporates the trigger configuration, the calibration constants, and *background frames* derived from "random" triggers recorded by the data acquisition system.

Reconstructed data (both from the detector and from the simulation) are stored in two different formats: The *Mini* contains reconstructed tracks and energy clusters in the EMC, as well as information from the other subdetectors. Efficient packing of data and noise suppression makes this format relatively compact. The *Micro* contains only information that is essential for physics analyses.

Detector and simulated data are made available for physics analysis in a convenient form through the process of "skimming". This involves the production of selected subsets of the data, the "skims", designed for specific areas of analysis. Skims are very convenient for physics analysis, but they increase the storage requirement because the same events can be present in more than one skim.

From time to time, as improvements in constants, reconstruction code, or simulation are implemented, the data may be "reprocessed", or new simulated data may be generated. When a set of new skims become available, an additional skim cycle can be run on all the reconstructed events.

At the core of the Super$B$ computing model there are two databases, the *configuration*

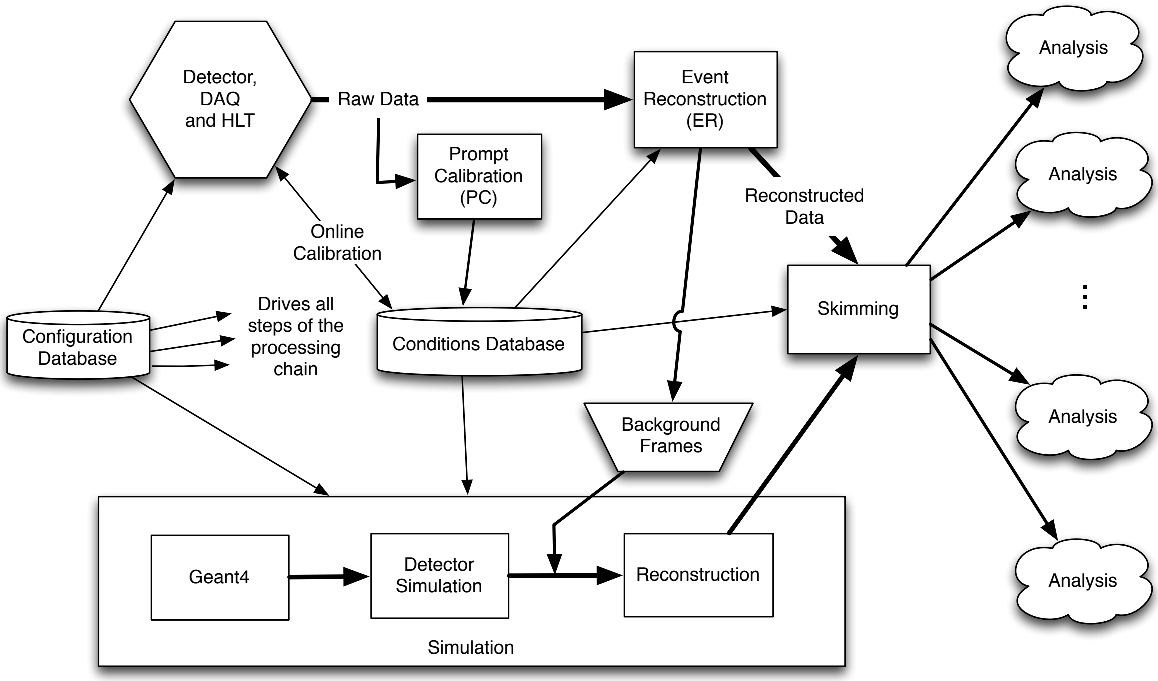

Figure 14.7: Data and control flow in the SuperB baseline computing model.

database that is the authoritative source for the detector, data acquisition system and trigger configuration, and the *conditions database* that records calibration information and provides it to all components of the computing model.

14.2.2 Resource estimate

Computing resource estimates for SuperB are based on the extensive experience with BABAR computing. As described above, the baseline SuperB computing model is very similar to the BABAR one. This allows us to estimate the SuperB computing resource needs by extrapolating from the well-understood BABAR computing parameters. Table 14.1 shows the basic parameters of the BABAR and SuperB computing models.

Compared to BABAR, the SuperB raw data size increases by about a factor of 6, mostly due to detectors with higher granularity and sampling rates, and the projected need to permanently store raw EMC waveforms to recover detector performance during reconstruction. After reconstruction, the event sizes in Mini and Micro are expected to be about twice the corresponding sizes in BABAR.

We expect the CPU needs to increase by a factor of 4 for reconstruction and simulation production, and by a factor of 3 for all other activities. The factor of 3 is an estimate, and is based on the assumption that skimming and analysis will require more CPU compared to BABAR to handle increased combinatorics and for advanced algorithms to handle the larger backgrounds. The factor of 4 reflects the additional penalty imposed by the increased event size.

For storage, we anticipate two copies of the raw data stored at different geographical locations.

Table 14.2 shows the computing resource estimate for the first 5 years of SuperB data taking. The data set and storage sizes include replication factors, contingency, on-disk fractions and support storage. Raw data is processed at the same rate at which it is produced, with no more than 48 hours of latency; the corresponding simulated data sets are produced within a month. As a consequence, the CPU required for these

Parameter	BABAR	SuperB		Factor
Raw event size	35	200	kByte	~ 6
Raw data size	875	5250	TByte/ ab^{-1}	~ 6
Mini/Micro event size	42	84	TByte/ ab^{-1}	2
CPU for Reconstruction	88.4	354	kHS06/ ab^{-1}	4
CPU for Simulation Production	280	1120	kHS06/ ab^{-1}	4
CPU for Skimming (Data)	40.8	122	kHS06/ ab^{-1}	3
CPU for Skimming (MC)	40	120	kHS06/ ab^{-1}	3
CPU for Physics Analysis (Data)	4.8	14.4	kHS06/ ab^{-1}	3
CPU for Physics Analysis (MC)	5.2	15.6	kHS06/ ab^{-1}	3
Number of raw data copies		2		
Number of Mini copies		1		
Number of Micro copies		4		
Skim expansion factor		5		
Fraction of Mini on disk		100% → 10% (Year 5+)		
Reprocessing cycles / year		1		

Table 14.1: Basic Super$B$ computing resource estimate parameters.

activities is proportional to the peak luminosity. The CPU required to reprocess the data collected in the previous years scales with the integrated luminosity.

14.2.3 Computing Infrastructure

Super$B$ will exploit distributed computing resources using Grid or eventually Cloud technologies. At this early stage in the experiment life, the Super$B$ VO is already enabled on more than 26 sites and actively accessing the available hardware. At data taking time we foresee to access pledged resources in Tier-0/1/2 computing centers located in Italy and the other participating countries. In addition to the INFN/CNAF computing center in Bologna, four new centers are under construction in Bari, Catania, Cosenza, and Napoli, funded by the PON ReCaS [34]. As a consequence, only minimal computing resources will be needed at the experiment site to perform the online and near-online computing tasks that are essential for data acquisition, calibration (PC), data quality monitoring, and providing feedback about the detector status and performance.

Raw data will be sent to CNAF and to another center for permanent storage on tape, and to the ReCaS centers for ER. As discussed in 12.3.8, sufficient disk space at the experimental site (Cabibbo Lab) will be provided to allow data collection to temporarily continue during wide area network failures. The ReCaS sites will provide the disk storage to host the raw data for the initial processing, and, after the first year of data taking, for the reprocessing of data collected in the previous years. In this scheme, Cabibbo Lab, CNAF and the ReCaS centers will together act as a distributed Tier-0 center.

In the other participating countries there are already Tier-1/2-sized sites primarily used by the LHC experiments. Pledged resources for Super$B$ are expected to become available and to provide about 50% of the total Super$B$ computing needs.

Monte Carlo production can be performed at all tiers, while skimming will be done only at the Tier-0 and Tier-1 facilities.

Multiple copies of real and Monte Carlo events in Mini and Micro format together with the collections of skimmed events will be stored on disk

	Year	1	2	3	4	5	
Luminosity	Peak	**0.25**	**0.7**	**1.0**	**1.0**	**1.0**	$10^{36}\,\mathrm{cm}^{-2}\mathrm{s}^{-1}$
	per Year	3.75	10.51	15.01	15.01	15.01	ab^{-1}
	integrated	3.75	14.26	29.26	44.27	59.28	ab^{-1}
Data Sets	Raw Data	39.4	149.7	307.3	464.9	622.4	PByte
	Mini	1.2	4.5	9.2	14.0	18.7	PByte
	Micro	2.8	10.6	21.8	33.0	44.1	PByte
	User	0.4	1.3	2.8	4.2	5.6	PByte
Storage	Disk	9.4	31.4	51.3	68.5	77.1	PByte
	Tape	43.7	168.0	348.2	530.7	713.1	PByte
CPU	Reconstruction	0.09	0.34	0.69	1.04	1.40	MHS06
	Simulation	0.28	1.06	2.18	3.30	4.42	MHS06
	Skimming	0.06	0.26	0.59	0.95	1.32	MHS06
	Analysis	0.11	0.43	0.88	1.33	1.78	MHS06
	Total	**0.54**	**2.09**	**4.34**	**6.63**	**8.91**	MHS06

Table 14.2: Computing resource estimate for the first 5 years of Super*B* data taking.

at Tier-1 and Tier-2 sites for physics analysis. The possibility of also performing physics analysis at the Tier-0 is under study. At this stage it is difficult to estimate the amount of data replication needed to mitigate network failures, and to accommodate the analysis load; in our estimate we have used a conservative replication factor of 4.

The network bandwidth required for each member of the distributed Tier-0, and the Tier-1 sites is estimated to be 100 Gbit/s. The GARR-X network [35] and similar networks in other countries will provide that bandwidth.

14.3 The Super*B* Computing R&D program

Computing technology is evolving in several areas. The number of cores per CPU and the amount of storage per disk are rapidly increasing, as are the resilience and bandwidth of Wide Area Network (WAN) links. In addition, gains in computing performance are increasingly being achieved by offloading some computing tasks to specialized co-processors such as graphical processing units (GPUs), or by adopting radically different, highly parallel computing paradigms.

In order to be cost-effective, computing solutions adopted or developed by the Super*B* collaboration will need to take advantage of this evolution as much as possible.

For example, the Super*B* event reconstruction and analysis framework will very likely need to implement an approach based on parallelism as the programming paradigm. Since legacy and current HEP software is not optimized for this, current frameworks and many familiar algorithms will need to be redesigned.

Another requirement for the Super*B* computing system is to be able to reliably and efficiently access large amounts of data that are spread over multiple, geographically disjoint sites. This requires mechanisms to mass-transfer and directly access distributed data in a user-friendly, robust and efficient manner.

In the following, we describe the R&D efforts that are underway to investigate possible technical solutions to these problems.

14.3.1 Exploiting parallelism

Parallelism is one of the most promising programming paradigms to improve the efficiency of data processing and analysis tools for future HEP experiments. The main ways to achieve software parallelization in HEP are to parallelize the *algorithms*, and to parallelize the *data flow*. The computing R&D program aims at understanding the different strategies and techniques to obtain parallelism, and how they can be combined and applied to the Super*B* computing problems.

Algorithm parallelization can be achieved by using architectures that provide a large number of computing units that are tightly connected through low-latency links and execute the same algorithm on a sub-sample of data in each computing unit. Graphical processing units (GPUs) providing several hundred computing units with a very restricted set of operations are currently the most common representatives of this architecture. New architectures, like Intel's MIC [36], that could in principle be more user friendly than GPUs, are also emerging. Typically, all these architectures offer very good internal communication between their computing units, but have relatively high latency and limited bandwidth for the communication with the host CPU and memory.

Obviously, GPU-like approaches are only useful where algorithms are executed in parallel on subsets of the same data.

Although our studies of *MIC* and *GPUs* have shown promising results for some algorithms, they also have shown that neither the programming tools nor the hardware itself are mature. Intel MIC hardware is in a beta test stage and not generally available yet, and can only programmed with a proprietary compiler that still needs optimization. nVidia hardware is more mature, but the combinations of hardware and software we have used so far, still show large latencies in memory handling and data transfer from/to the GPU board.

Another approach is to parallelize the processing of different parts of the data with different and independent software "modules". Here, an HEP program can be thought as being made of modules that operate on sets of data which are generally encapsulated in a container called *event*. Independent parts of the same physical event can then be processed concurrently by independent modules.

Yet another approach that has already being used widely in HEP for a long time, is the concurrent processing of complete events. This approach has the disadvantage of inefficient use of data and instruction caches, especially on modern multi-core CPUs, and in many cases a very large memory footprint.

Almost certainly, the Super*B* software will use a combination of these methods.

GPU R&D GPUs are many-core architectures that provide *Single Instruction, Multiple Thread* (SIMT) parallelism. They allow for interesting scenarios but at the same time require extensive studies and major changes to the existing HEP programming paradigms. Several groups in the HEP community are working on exploiting GPUs for a multitude of use cases. In Super*B*, the GPU-related activities started in 2011 and are ongoing. They have been mainly related to offline analysis software with the goals to assess the effectiveness of GPUs as co-processors for specific analysis tasks, to evaluate the cost-benefit ratio of porting sequential code to GPUs, and to create a prototype that can be integrated in the current Super*B* code.

A first phase of inspection and profiling of the existing physics reconstruction algorithms that are part of the Super*B* fast simulation has started. The focus is on the Super*B* physics software that provides the basic tools for composition of particle hypotheses, fitting of four-momenta, and track vertexing. These high-level reconstruction procedures are performed during central productions when the complete data are filtered and processed into overlapping subsets optimized for particular analyses (skimming). This process is combinatorial in nature and computationally expensive, but has the potential of great gains from parallelization.

A second line of activity aims at the parallelization of maximum likelihood fits of complex physics models, evaluating the probability density functions on the GPU, while the MINUIT algorithm is run on the CPU as usual. The first tests of fitting on simple, simulated datasets already show encouraging results with speed-up factors up to several hundreds with respect to running on a single CPU.

MIC Architecture R&D The Many Integrated Core (MIC) architecture is a multiprocessor architecture developed by Intel, that provides a co-processor composed of many simple x86-compatible cores.Two prototypes have appeared so far, code-named Knights Ferry and Knights Corner, the latter providing up to about 60 CPU cores and a few GBs of memory. Each core supports 4 threads of in-order execution, has 512-bits wide vector units and has its own L2 cache. The L2 caches are nonetheless coherent among all the cores, which are connected through a wide high-speed ring bus.

The above characteristics and the fact that the system runs the Linux operating system make it an appealing target for parallel applications, since at least in principle, very few changes are needed to adapt software to MIC. The Super*B* computing group is collaborating with the COKA [37] project to understand whether and how the MIC architecture might be usable in the HEP computing environment.

The first results of the attempt to port an event generator (written in C++) to the MIC architecture show that the changes to the code are not very intrusive, and that the difference of the MIC platform can easily be handled in the build process. Once the commercial product becomes available, the next steps will be to conduct performance measurements, to identify more code that is suitable for running on MIC, and to investigate how offloading of computing to a MIC co-processor could be transparently integrated into the Super*B* Framework.

Framework Architecture and R&D The efforts on understanding GPUs and MIC are tightly coupled with an investigation of how module-parallelism and these new computing architectures could be exploited in the Super*B* reconstruction and analysis software framework. In the Super*B* Framework (inherited from *BABAR*) modules operate on data generally encapsulated in an event container. Modules communicate through messages and put the result of their computations inside the event container. In general, to produce something, a module needs some input (possibly taken from the container) which is processed by the module's algorithms; the output is stored back inside the container. A common feature of all modules is that there is *required input* and *provided output*. This allows to build an execution schedule based on dependencies which can be represented by a directed graph.

To understand the impact of module-parallelism, performance measurements on a typical configuration of FastSim were performed to establish a baseline, and data and execution dependencies between FastSim modules were studied in detail. Theoretical speedup was determined by developing a dependency-aware scheduling algorithm and using it to simulate code execution and measure the performance gains.

As a next step, the collaboration has decided to build a proof-of-concept parallel Framework prototype using the *Intel Thread Building Block* (TBB) [38] library. A major benefit of TBB is that it has native support for dependency graphs, allowing a near 1:1 mapping of module dependencies to the TBB execution schedule. In parallel to the development of the Framework, there is ongoing work to migrate some analysis modules from the legacy serial environment to the parallel prototype, mainly focusing on improving parallelism at the module level. Efforts are also spent on aspects of the Framework not related to parallelism, for example analysis configuration, so that the finished prototype can be used as a complete test bed.

At the time of writing of this document, work is still in progress, but it is expected to have preliminary measurements of the prototype performance in multi-core environments in the near future.

14.3.2 Distributed computing R&D: DIRAC framework evaluation

As part of the distributed computing R&D, the Super*B* collaboration is evaluating the

DIRAC [39] framework. DIRAC (Distributed Infrastructure with Remote Agent Control) was initially developed as a simulation production tool using pilot jobs for the LHCb experiment. Since then data management functionality has been added, making it a complete Grid-based data and workload management solution for HEP experiments. DIRAC aims to provide a complete distributed computing environment, capable of supplying all features needed in a small VO.

Two realistic use cases have already been successfully tested within Super$B$: distributed analysis and Monte Carlo production. Further integration of Super$B$-specific functions into DIRAC will take place in a new DIRAC module called SuperBDIRAC. Integration between DIRAC and the Super$B$ bookkeeping database is currently under development, and the DIRAC web portal will be extended to include the functions provided by the Super$B$ distributed computing system prototype.

Due to the modular and distributed architecture of DIRAC, it should be straightforward to build up an infrastructure for Super$B$. The minimal set of functionalities included in a DIRAC installation are the DIRAC framework, the configuration service, the data and workload management services, accounting functionalities, the bookkeeping service, log and sandbox storage and the web interface. While DIRAC components can be deployed on several servers, a single well equipped machine can be configured as head node to run all previously cited functionalities.

Future work on DIRAC will be focused on completing the evaluation, testing advanced features, and implementing more Super$B$-specific use cases. For a detailed and technical description of the Dirac evaluation process please refer to [40].

14.3.3 Data management and distributed storage R&D

One of the key drivers for Super$B$ computing R&D activities is the study of data management in a distributed resource environment. Since Super$B$ is at least a few years away, it is important that we investigate the next generation of tools in this field. The main interests are Wide Area Network (WAN) data access, mass data transfer and file catalogs.

WAN data access In this section we will discuss the state of the art in the data management field. For WAN data access our current focus is on the use of HTTP or xrootd as the underlying data transport protocols, and the optimization of remote data access through mechanisms such as pre-fetch and caching.

During the next 2-5 years we expect to be able to exploit remote data access solutions in order to simplify the management of a typical Super$B$ computing center, and to increase the flexibility of data movement and placement.

This approach is supported by the trends in the computing models of other HEP experiments. The LHC experiments are very interested in dynamic and remote data access to augment the data placement models already in place. The Alice [41] experiment has been fully working with this paradigm for the last two years; CMS and ATLAS have recently implemented such solutions for specific use cases [42][43].

Neither the current grid-based data management solutions in EGI and OSG, nor the SRM protocol provide a solid infrastructure for direct remote WAN data access; their model still relies on a data driven computing paradigm.

The ALICE data access strategy uses the xrootd/ROOT suite, which natively provides name spaces and data brokering.

The following use cases will greatly benefit from the adoption of a reliable direct WAN data access design:

- Interactive usage of Super$B$ data, such as event display and single event browsing
- Analysis code development and debugging
- Opportunistic analysis tasks executed on resources not dedicated to Super$B$, for example non-Super$B$ grid computing centers or dynamically allocated cloud resources.

- Job execution on small sites where the experiment does not have an allocation of storage resources (Tier-3-like)
- Improved reliability and availability, especially when recovering from temporary or partial storage failure at SuperB sites

Suitable network protocols for remote data access will have to provide at least the following functionality:

- Support of a minimal Posix-like API (open, read, seek, close)
- Ability to work through routers and firewalls
- Caching and pre-fetching mechanisms to improve performance over high-latency networks ("latency-hiding")
- Native support by ROOT [9] framework

At the present time, the two viable protocol candidates that could fulfill these requirements are xrootd [44] and HTTP.

Xrootd was developed and is being used primarily within the HEP environment, and provides a high level of functionality useful in HEP. In contrast, HTTP is the dominating protocol on the Internet, is very mature, and is collecting huge interest also outside the HEP environment for use as large-scale data distribution and access protocol.

Data access library Like all the other HEP experiments, SuperB is developing its own software framework. As part of this framework, it will be important to implement a library and APIs to standardize and facilitate end user access to data, hiding the complexity of the underlying hardware and software storage implementations, and network contexts.

The development of this general file/data access library is in progress, and it will implement the following features:

- Intelligent pre-fetching and buffering, using the time spent in processing events to read the data from remote storage
- Mapping of logical file names to different and multiple storage URIs.
- Enabling the support of storage protocols not already supported by ROOT
- Read-ahead and caching mechanisms in order to match the performance requirements of different network, application, and storage solution

File Transfer Service evolution In addition to direct remote data access, SuperB will also need mechanisms for pre-determined data placement. Many other HEP experiments use experiment-developed frameworks to move data between sites, that rely on FTS (File Transfer Service, developed within the gLite middleware) as an underlying transport. Currently, FTS can only be used if sites provide an SRM interface for managing the files and a gridftp server to transfer the data. As soon as new protocols like xrootd and HTTP are widely used, it will be important to have an FTS implementation that support these protocols. Within the EMI (European Middleware Initiative) project, there are developments to improve the FTS service, and to add these new protocols.

Dynamic file catalog technology One of the most important components of a distributed data and computing architecture is the File Catalog. Today, each HEP experiment has its own implementation of this. SuperB should consider reusing one of the already available file catalog solutions, choosing the one that best fits the needs of the experiment. Since HTTP does not provide multi-site brokering functionality, its use will require the file catalog to manage and provide lists of replicas in HTTP. The next-generation LFC (LCG File Catalog [15]) will provide this functionality. As soon as it is released, we will start tests to check whether it can fulfill the SuperB requirements.

Storage system evaluation Moving and accessing the large volumes of SuperB data puts significant requirements on the performance of the underlying storage systems and necessitates dedicated storage system R&D. This is particularly important in order to provide adequate guidance to the site admin community that has to manage the experiment's data.

Data Storage During the last few years the evolution of storage and file system technologies provided significant new features in the areas of clustering and distributed data management. Today we have a multitude of available file system solutions, ranging from open-source file systems to commercial products. The large body of experience in the HEP community will facilitate the selection of working solutions that accommodate the most relevant requirements of Super*B* computing. The sites that are already running production systems for Super*B* and other experiments constitute large test beds for specific file systems like GPFS and Lustre. Their experiences provide the starting point for our evaluation campaign.

The expected use of many-core CPUs has a major impact on storage system capabilities; technology is moving towards a computational model built upon clusters of nodes with large amounts of computing power provided by many-core CPUs as well as GPUs. Such configurations place much higher demands on the I/O subsystem and networks and can easily introduce bottlenecks and scalability problems between CPU nodes and storage systems. The availability of cost-effective multi-10 Gbit/s networks in the near future will also affect how we distribute the access to our data.

These new developments could invalidate the current cluster and site configurations and open up new ways of data distribution and analysis techniques. The Super*B* storage R&D program is expected to yield feedback on the best use of these new technologies to support the requirements of the experiment.

The Distributed Storage R&D group is in the process of testing several file systems. This activity has two main goals:

- Provide input to the Super*B* computing centers on the storage technologies that could be used to serve the storage requirements of the experiment.
- Identify storage technologies that are suitable for building one or more "virtual computing centers" from loosely coupled federations of geographically distributed data centers and that can provide complete fail-over solutions for Super*B* data processing.

The main storage technologies currently under test are: GlusterFS [45], HADOOP-FS, NFSv4.1 [46] and EOS/xrootd [47]. The tests primarily focus on:

- Fail-over characteristics;
- Performance in data analysis and simulation production use cases, and;
- Scalability.

The evaluation process will identify the best storage system solutions that will fit within the different computing infrastructures and data management requirements for the various use cases, such as buffering the raw data at the detector site, archiving raw data on tape, and storage of intermediate data products for simulation and analysis.

For a detailed and technical description of the R&D lines in distributed storage field please refer to [48] [49].

14.4 Outlook

So far the effort of the Super*B* computing group has been focused on developing and mantaining the suites of tools to support the detector and physics studies and on investigating possible technical solution to strategic issues with an active R&D program. We expect to complete these R&D activities and to have a first computing and data model design within a year.

The next step will be the coding of a first version of the full set of the software tools of the experiment and this should require two more years. The plan is to have a group of computing experts designing and coding the core software under the leadership of a software architect. Detector and physics analysis experts will provide subsytem and analysis specific code (simulation and reconstruction modules for their subsystems, physics analysis modules, etc.).

One of the challenges to be faced will be that the Reconstruction and Analysis Framework is foreseen to be based on parallel computing and expertise on it is so far scarse in the HEP community and has to be build up. A possible strategy is to have a group of core developers professionally trained. They will then mentor other developers to increase the number of skilled programmers. Some level of familiarity with parallel computing will be required to the core group of expert, but care has to be taken to isolate people contributing detector and analysis specific code from the complexity of parallel computing.

The remaining time before the beginning of the data taking will be devoted to debugging and testing the code. Large scale data challenges are foreseen to stress test the system.

14.5 Bibliography

[1] S. Agostinelli et al., (GEANT4 collaboration), "GEANT4: A Simulation toolkit", *Nucl.Instrum.Meth.* A506:250–303, 2003, doi:10.1016/S0168-9002(03)01368-8, http://geant4.web.cern.ch/geant4.

[2] D. Lange, "The EvtGen particle decay simulation package", *Nucl.Instrum.Meth.* A462:152–155, 2001, doi:10.1016/S0168-9002(01)00089-4, http://robbep.home.cern.ch/robbep/EvtGen/GuideEvtGen.pdf.

[3] S. Jadach, B. Ward, and Z. Was, "The Precision Monte Carlo event generator K K for two fermion final states in e^+e^- collisions", *Comput.Phys.Commun.* 130:260–325, 2000, doi:10.1016/S0010-4655(00)00048-5, arXiv:hep-ph/9912214 [hep-ph], report DESY-99-106, CERN-TH-99-235, UTHEP-99-08-01.

[4] E. Longo and I. Sestili, "Monte Carlo Calculation of Photon Initiated Electromagnetic Showers in Lead Glass", *Nucl.Instrum.Meth.* 128:283, 1975, doi:10.1016/0029-554X(75)90679-5.

[5] K. Nakamura et al., (Particle Data Group collaboration), "Review of particle physics", *J.Phys.* G37:075021, 2010, doi:10.1088/0954-3899/37/7A/075021, chapter 27.

[6] G. Grindhammer *et al.*, in Proceedings of the Workshop on Calorimetry for the Supercollider, Tuscaloosa, AL, March 13-17, 1989, edited by R. Donaldson and M. G. D. Gilchriese (World Scientific, Teaneck, NJ, 1989), p. 151.

[7] R. Bock, T. Hansl-Kozanecka, and T. Shah, "Parametrization of the longitudinal development of hadronic showers in sampling calorimeters", *Nucl.Instrum.Meth.* 186:533, 1981, doi:10.1016/0029-554X(81)90232-9, report CERN-EP/80-206.

[8] D. Acosta et al., November 1990, report CERN-PPE/91-223.

[9] R. Brun and F. Rademakers, "ROOT: An object oriented data analysis framework", *Nucl.Instrum.Meth.* A389:81–86, 1997, doi:10.1016/S0168-9002(97)00048-X, http://root.cern.ch.

[10] http://www.egi.eu.

[11] http://www.opensciencegrid.org.

[12] C. Eck, J. Knobloch, L. Robertson, I. Bird, K. Bos, N. Brook, D. Düllmann, I. Fisk, D. Foster, B. Gibbard, C. Grandi, F. Grey, J. Harvey, A. Heiss, F. Hemmer, S. Jarp, R. Jones, D. Kelsey, M. Lamanna, H. Marten, P. Mato-Vila, F. Ould-Saada, B. Panzer-Steindel, L. Perini, Y. Schutz, U. Schwickerath, J. Shiers, and T. Wenaus, *LHC computing Grid: Technical Design Report. Version 1.06*, Technical Design Report LCG. CERN, Geneva, June 2005, report LCG-TDR-001, CERN-LHCC-2005-024.

[13] http://glite.web.cern.ch/glite.

[14] http://hep-project-grid-scg.web.cern.ch/hep-project-grid-scg/voms.html.

[15] https://twiki.cern.ch/twiki/bin/view/LCG/LfcAdminGuide.

[16] http://sdm.lbl.gov/srm-wg/doc/SRM.v2.2.html.

[17] http://lcg.web.cern.ch/LCG.

[18] http://nagios.org.

[19] https://wiki.egi.eu/wiki/SAM.

[20] http://ganga.web.cern.ch/ganga.

[21] J. Sermersheim, Ed., "RFC4511: Lightweight Directory Access Protocol (LDAP): The Protocol", 2006, http://www.ietf.org/rfc/rfc4511.txt.

[22] F. Bianchi, V. Ciaschini, M. Corvo, D. Delprete, A. Di Simone, G. Donvito, A. Fella, F. Giacomini, A. Gianoli, S. Longo, S. Luitz, E. Luppi, M. Manzali, A. Perez, S. Pardi, M. Rama, G. Russo, B. Santeramo, R. Stroili, and L. Tomassetti, "Super*B* Simulation Production System", *J.Phys.Conf.Ser.* 396, 2012, Proceedings of 19th International Conference on Computing in High Energy and Nuclear Physics (CHEP 2012).

[23] D. Antoniev, Z. Deng, J. Ebke, U. Egede, A. Fella, Y. Han, J. Jakub, A. Galvani, M. Kenyon, E. Luppi, M. Manzali, A. Richards, M. Slater, V. Spinoso, and L. Tomassetti, "BESIII and Super*B*: Distributed job management with Ganga", *J.Phys.Conf.Ser.* 396, 2012, Proceedings of 19th International Conference on Computing in High Energy and Nuclear Physics (CHEP 2012).

[24] http://www.postgresql.org.

[25] R.T. Fielding, *Architectural Styles and the Design of Network-based Software Architectures* , PhD. Thesis, University of California Irvine, 2000.

[26] http://www.liferay.com.

[27] http://www.jasig.org/cas.

[28] http://www.alfresco.com.

[29] http://www.mediawiki.org.

[30] http://subversion.apache.org.

[31] http://trac.edgewall.org.

[32] http://www.rpm.org.

[33] http://yum.baseurl.org.

[34] "ReCaS (Rete di Calcolo per SuperB e altre applicazioni)", http://www.pon-recas.it/.

[35] "The Italian Academic and Research Network", http://www.garr.it/b/eng.

[36] "Intel Many Integrated Core Architecture", http://www.intel.com/content/www/us/en/architecture-and-technology/many-integrated-core/intel-many-integrated-core-architecture.html.

[37] "COKA: COmputing on Knights Architectures", http://web2.infn.it/coka/.

[38] http://threadingbuildingblocks.org.

[39] http://diracgrid.org.

[40] F. Bianchi, V. Ciaschini, M. Corvo, D. Delprete, A. Di Simone, G. Donvito, A. Fella, F. Giacomini, A. Gianoli, S. Longo, S. Luitz, E. Luppi, M. Manzali, A. Perez, S. Pardi, M. Rama, G. Russo, B. Santeramo, R. Stroili, and L. Tomassetti, "DIRAC evaluation for the Super*B* experiment", *J.Phys.Conf.Ser.* 396, 2012, Proceedings of 19th International Conference on Computing in High Energy and Nuclear Physics (CHEP 2012).

[41] K. Aamodt et al., (ALICE collaboration), "The ALICE experiment at the CERN LHC", *Journal of Instrumentation* 3(08):S08002, 2008, http://stacks.iop.org/1748-0221/3/i=08/a=S08002.

[42] T. Maeno, K. De, and S. Panitkin, (ATLAS collaboration), "PD2P: PanDA Dynamic Data Placement for ATLAS", Computing in High Energy and Nuclear Physics 2012, New York, NY, USA, 21–25 May 2012.

[43] D. Giordano, (CMS collaboration), "Implementing data placement strategies for the CMS experiment based on a popularity model", CMS Note, CMS-CR-2012-080; report CERN-CMS-CR-2012-080.

[44] http://xrootd.slac.stanford.edu.

[45] http://www.gluster.org.

[46] http://www.pnfs.com.

[47] http://eos.cern.ch.

[48] F. Bianchi, V. Ciaschini, M. Corvo, D. Delprete, A. Di Simone, G. Donvito, A. Fella, F. Giacomini, A. Gianoli, S. Longo, S. Luitz, E. Luppi, M. Manzali, A. Perez, S. Pardi, M. Rama, G. Russo, B. Santeramo, R. Stroili, and L. Tomassetti, "Super*B* R&D computing program: HTTP direct access to distributed resources", *J.Phys.Conf.Ser.* 396, 2012, Proceedings of 19th International Conference on Computing in High Energy and Nuclear Physics (CHEP 2012).

[49] F. Bianchi, V. Ciaschini, M. Corvo, D. Delprete, A. Di Simone, G. Donvito, A. Fella, F. Giacomini, A. Gianoli, S. Longo, S. Luitz, E. Luppi, M. Manzali, A. Perez, S. Pardi, M. Rama, G. Russo, B. Santeramo, R. Stroili, and L. Tomassetti, "Testing and evaluating storage technology to build a distributed Tier1 for Super*B* in Italy", *J.Phys.Conf.Ser.* 396, 2012, Proceedings of 19th International Conference on Computing in High Energy and Nuclear Physics (CHEP 2012).

15 Facilities, Mechanical Integration and Assembly

15.1 Introduction

The *BABAR* detector was built to a design optimized for operations at a high luminosity asymmetric B meson factory. The detector performed well during the almost nine years of colliding beams operation, at luminosities three times the PEP-II accelerator design. There are substantial cost and schedule benefits that result from reuse of detector components from the *BABAR* detector in the Super$B$ detector in instances where the component performance has not been significantly compromised during the last decade of use. These benefits arise from two sources: one from having a completed detector component which, though it may require limited performance enhancements, will function well at the Super$B$ Factory; and the other from requiring reduced interface engineering, installation planning and tooling manufacture (most of the assembly/disassembly tooling can be reused, with procedures that are mirrors of the disassembly procedures). The latter reduces risk to the overall success of the mechanical integration of the project. Though reuse is very attractive, risks are also introduced. Can the detector be disassembled, transported, and reassembled without compromise? Will components arrive in time to meet the project needs?

The reuse of elements of the PID, EMC and IFR system, and associated support structures have been described in previous chapters. In this section, issues related to the magnet coil and cryostat, and the IFR steel and support structure are discussed as well as the integration and assembly of the Super$B$ detector, which begins with the disassembly of *BABAR*, and includes shipping components to Italy for reassembly there.

15.1.1 Magnet and Instrumented Flux Return

The *BABAR* superconducting coil, its cryostat and cryo-interface box, and the helium compressor and liquefier plant will be reused in whole or in part. The magnet coil, cryostat and cryo-interface box will be used in all scenarios. Use of on-detector pumps and similar components may not be cost effective due to electrical incompatibility. The existing *BABAR* helium liquefier plant, which is halfway through its forty year service life, has sufficient capacity to cool both the detector magnet and the final focus superconducting magnets. The final decision about reuse of other external service components, such as compressors, etc., will take into account electrical compatibility, schedule and cost.

The initial *BABAR* design contained too little steel for quality μ identification at high momentum. Additional brass absorber was added during the lifetime of the experiment to compensate. This will be retained and augmented. The flux return steel is organized into five structures: the barrel portion, and two sets of two end doors. Each of these is, in turn, composed of multiple structures. The substructures were sized to match the 50 ton load limit of the crane in the *BABAR* hall.

Each of the end doors is composed of eighteen steel plates organized into two modules joined together on a thick steel platform. This platform rests on four columns with jacks and Hilman rollers. A counterweight is also located on the platform. There are nine steel layers of 20 mm thickness, four of 30 mm thickness, four of 50 mm thickness, and one of 100 mm thickness. During 2002, five layers of brass absorber were installed in the forward end door slots in order to increase the number of interaction lengths seen by μ candidate tracks. In the baseline, these doors will be retained, including the five 25 mm layers of brass installed in 2002, as well as the outer steel modules which can house two additional layers of detectors. Additional layers of brass or steel will be added, following the specification of the baseline design in the instrumented flux return section. The aperture of the forward plug must be opened to accommodate the accelerator beam pipe. Compensating modifications to the backward plug are likely to be necessary. These modifications to the steel may affect the central field uniformity and the centering forces on the solenoid coil, and so must be carefully re-engineered.

The barrel structure consists of six cradles. These are each composed of eighteen layers of steel. The inner sixteen layers have the same thicknesses as the corresponding end door plates. The two outermost layers are each 100 mm thick. The eighteen layers are organized into two parts; the inner sixteen layers are welded into a single unit along with the two side plates, and the outer two layers are welded together and then bolted into the cradle. The six cradles are in turn suspended from the double I-beam belt that supports the detector. During the 2004/2006 barrel LST upgrade, layers of 22 mm brass were installed, replacing six layers of detectors in the cradles. In the Super$B$ baseline, these brass layers will be retained, as well as all the additional flux return steel attached to the barrel in the gap between the end doors and barrel. As in the end doors, additional layers of absorber will be placed in gaps occupied in BABAR by LSTs. In order to provide more uniform coverage at the largest radius for the μ identification system, modifications to the sextant steel support mechanism are likely to be needed. Finite element analyses will be required to confirm that deflections of the steel structure due to this alternative support mechanism do not reduce inter-plate gaps needed for the tracking detectors.

15.2 Component Extraction

Extraction of components for reuse requires the disassembly of the BABAR detector. This process began after the completion of BABAR operations in April 2008. The first stage of the project was to establish a minimal maintenance state, including stand alone environmental monitoring, that preserves the assets that have reuse value. The transition was complete in August 2008. In order to disassemble the detector into its component systems, it was necessary to move it off the accelerator beam line where it was pinned between the massive supports of accelerator beamline elements into the more open space in the IR2 Hall. This required removal of the concrete radiation shield wall, severing of the cable and services connections to the electronics house which contained the off detector electronics, and roll-back of the electronics house 14 m. Electronics, cables and infrastructure that were located at the periphery of the detector were removed. Beamline elements close to the detector were removed to allow access to the central core of the detector by July 2009, allowing removal of the support tube, which contained the PEP-II accelerator final beamline elements as well as the silicon vertex detector, the following month.

The core disassembly sequence was optimized after the Conceptual Design Report. Completion of disassembly of the detector required fewer steps, less time, and posed fewer risks, with the end doors being disassembled while the detector was on beamline. Tooling that was used in the initial installation of the detector at IR2 was refurbished and additional tooling has been fabricated for the disassembly effort. All of this tooling is available for use on Super$B$. In 2010, the end doors were broken down into component parts, and the EMC forward endcap and the drift chamber were removed. The detector was rolled out for core disassembly in Fall 2010. The DIRC was removed. In Winter 2011 the Barrel EMC and Superconducting Solenoid were removed. Brass was removed from the Barrel Flux Return, and the Barrel Flux Return disassembly completed in August 2011.

This work has been accomplished as a low priority project with a small crew of engineers and technicians. Though the disassembly project is behind schedule, due to laboratory priorities, the earned value compared to actual costs indicates that the level of effort estimated to perform the disassembly is very accurate. The same methodology used to determine the level of effort needed for the *BABAR* disassembly has been applied in estimating the needs for Super$B$ assembly.

The components from *BABAR* that are expected to be reused in Super$B$ were available for transport to Italy in mid-2011. In order to minimize the possibility of damage to the DIRC bar boxes and their fused silica bar content, disassembly proceeded with removal of the bar boxes one by one from the bar box support structure inside the DIRC. The twelve DIRC bar that were removed from the DIRC structure during the disassembly of the core of the detector have been stored in an environmentally controlled container.

15.3 Component Transport

The magnet steel components will be crated for transport to limit damage to mating surfaces and edges. Most, if not all, of these components can be shipped by sea.

The *BABAR* solenoid was shipped via special air transport from Italy to SLAC. It is hoped that this component can be returned to Italy in the same fashion. The original transport frame has been refurbished.

The DIRC and barrel calorimeter present transportation challenges. In both cases transport without full disassembly is preferred. In the case of the DIRC, the central support tube will be separated from the strong support tube and transported as an assembly. The bar boxes storage container provides a dry environment, but is unsuitable for bar box transport. Design and fabrication are required.

In the case of the EMC, there are two environmental constraints on shipment of the device or its components. The glue joint that attaches the photodiode readout package to the back face of the crystal has been tested, in mock-up, to be stable against temperature swings of $\pm 5°$C. During the assembly of the endcap calorimeter, due to a failure of an air conditioning unit, the joints on one module were exposed to double this temperature swing. Several glue joints parted. The introduction of a clean air gap causes a light yield drop of about 25%. In order to avoid this reduction in performance, temperature swings during transport must be kept small. Since the crystals are mildly hygroscopic, it is best that they be transported in a dry environment to avoid changes in the surface reflectivity, and consequent modification in the longitudinal response of the crystal. Individual *BABAR* endcap modules constructed in the UK were successfully shipped to the USA in specially constructed containers that kept the temperature swings and humidity acceptably small.

Disassembly of the barrel calorimeter for shipment presents a substantial challenge. Both the disassembly and assembly sites need to be temperature and humidity controlled. The disassembly process requires removal of the outer and inner cylindrical covers, removal of cables that connect the crystals with the electronics crates at the ends of the cylinder, splitting of the cylinder into its two component parts and removal of the 280 modules for shipment. Though much of the tooling is still in hand, the environmentally conditioned buildings used in calorimeter construction at SLAC no longer exist so that alternative facilities will need to be outfitted. The cooling and drying units used in the module storage/calorimeter assembly building continue to be available.

The clear preference is to ship the barrel calorimeter as a single unit by air. With tooling support stand and environmental conditioning equipment, the load is likely to exceed 30 tons. It is anticipated that such a load could be transported in the same way as the superconducting coil and its cryostat, but verification is needed. Detailed engineering studies, which model accelerations and vibrations involved with flight that might cause the crystal containing carbon fiber modules to strike against one another, are needed to determine if the calorimeter can be safely transported. It may be that a module restraint mechanism will need to be engineered and fabricated. A transport frame must be designed and its performance modeled. Engineering studies have begun, however, it is not unlikely that it will be necessary to transport the barrel calorimeter via air, but disassembled into modules.

15.4 Detector Assembly

Assembly of the Super$B$ detector is the inverse of the disassembly of the *BABAR* detector. Ease of assembly will be influenced by the facilities which are available. In the case of *BABAR*, the use of the IR2 hall, which was "too small", led to engineering compromises in the design of the detector. Assembly was made more complicated by the weight restrictions posed by the 50 ton crane. Upgrades were made more difficult because of limitations in movement imposed by the size of the hall.

The preferred dimensions for the area around the Super$B$ detector when it is located in the accelerator housing are at least 16.2 m transverse to the beamline, 20.0 m along the beamline, 11.0 m from the floor to the bottom of the crane hook, 15.0 m from floor to ceiling, and 3.7 m from the floor to the beamline. The increased floor to beamline height relative to *BABAR*-PEP-II will require redesign effort for the underpinnings of the detector cradle. However, this will permit improved access for installation of cable and piping services for the detector, as well as make possible additional IFR absorption material for improved μ detector performance below the beamline. In order to facilitate detector assembly, the preferred capacity for the two hook bridge crane is 100/25 tons.

16 The Super$B$ Collaboration and Project Management

During the pre-approval phase of the project, the Super$B$ detector was organized as a "Proto-collaboration", with a structure modeled on that of the *BABAR* detector. Leadership was centered in the "Proto-technical" Board which included technical leadership for all subsystems (SVT, DCH, PID, EMC, IFR); the general detectors systems (electronics, DAQ, computing, and simulation), and the machine detector interface (MDI). The "Proto-technical" Board was led by Detector Co-leaders and the Proto-Technical Coordinator who provided executive direction and decision making for the collaboration with the guidance of the Board. Subsystem status and progress were reviewed by the Board at regularly scheduled meetings. Major overall decisions about the detector were also reviewed by the Board, aided in the more challenging cases by recommendations provided by ad-hoc review committees and a geometry working group appointed by the leadership.

Following formal project approval in Dec. 2010, the Super$B$ detector "Proto-Collaboration" began the transition to the Super$B$ detector Collaboration. The inaugural Collaboration forming meeting was held in Elba in May-June 2011. Initial steps were defined to begin to organize the experimental collaboration, while allowing time for new groups to become involved from the worldwide community. The basic model was suggested by the long history of successful experimental collaborations in particle physics with particular reference to the successful experience of the *BABAR* detector. Given the success of the Super$B$ Proto-collaboration to date and its ability to deal with most executive and technical functions, this structure was retained during the interim period until the new executive and technical structures could be defined by the Collaboration and new leadership appointed. This bootstrapping process began by establishing a Proto-council composed of the PIs of the collaborating institutions to provide input to the process, approve default membership and interim leadership, and provide monitoring of the working committees. This Proto-council then approved the appointment of a Governance committee to develop the bylaws of the collaboration, and a continuation of the Proto-speakers bureau to select speakers for conferences to the bridging period.

The Governance committee, in consultation with collaboration membership, Proto-collaboration leadership, and the Laboratory project leadership (now the Cabbibo Laboratory), drafted a Governance document for the collaboration. This document [1] was unanimously approved at the March 2012 meeting of Super$B$ and the Proto-council became the Council of the Collaboration. Following the procedures described in the Governance document, The Council chair was selected and a Council committee is now being appointed to select the leadership of the collaboration. The Council also appointed an Executive Board to deal with issues that go beyond those managed by the Proto-technical board. Given the fact that the collaboration will evolve substantially in the coming months, the initial terms for this Executive Board were set to one year.

In this chapter, we summarize the collaboration organization as detailed in the Governance document.

16.1 Collaboration Membership

The SuperB Detector Collaboration is the organization of scientists belonging to academic or research Institutions worldwide whose goal is the exploitation of the physics potential of the SuperB electron-positron asymmetric collider. Institutions who participate in the Collaboration are expected to make significant contributions to the construction and operation of the SuperB detector, including its computing systems, both hardware and/or software. Participating Institutions are entitled to be represented in the Collaboration Council, and, to preserve their membership, they must actively participate in the SuperB program and comply with the obligations that are defined by the Collaboration in terms of financial and service contributions. Ph.D. physicists, engineers, and Ph.D. thesis students who belong to a participating Institution can become members of the Collaboration if they intend to devote a substantial fraction of their research time to the SuperB program over a period of several years. Participation of an individual in SuperB is at the discretion of the Institution to which he or she is accredited. Members of the Collaboration are eligible to be included in the author list.

16.2 The Collaboration Council

The Collaboration Council, representing the full membership of the Collaboration, is the principal governing body of the Collaboration. Institutions with two or more Collaboration members who are Ph.D. physicists will be directly represented on the Collaboration Council. Members of the Collaboration from Institutions with fewer than two Ph.D. physicists may affiliate with another Institution for the purpose of representation, while larger institutions will be given additional representation. The Council has an elected Chair and Vice-Chair. Council decisions are to be agreed by consensus wherever possible. Should a situation arise where consensus cannot be reached, a time scale shall be set for the decision to be reached at a later date and the matter will then be decided at a subsequent meeting of the Council, by a vote if necessary.

The Council selects and may remove the executive leadership of the collaboration, particularly the Spokesperson and the Executive Board via specific defined procedures of the Governance document. The Spokesperson is the scientific leader of the Collaboration, responsible for financial, scientific, technical, and organizational decisions pertaining to the Collaboration. The Spokesperson is assisted by a Management Team. The Executive Board is responsible for advising the Spokesperson on all scientific, financial, and organizational matters pertaining to the Collaboration. The details of the management structure, including the roles and responsibilities of individual managers, the roles and responsibilities of additional groups such as the Technical Board, the Management Team, the Publication Board, and Physics Analysis Groups will be established in a management plan, proposed by the Spokesperson, endorsed by the Executive Board and ratified by the Council.

The Collaboration Council will concern itself with issues related to the overall framework of the Collaboration. It will ratify the Collaboration by-laws and the organizational structure, insofar as it is specified in the Collaboration Constitution, and vote on proposed amendments, which may be introduced by any Council representative or by the Spokesperson.

The Chairperson, in consultation with the Collaboration, possibly through the appointment of a search committee, will select candidates for ratification by Council for the several boards and committees that are to be established by the Council.

The Collaboration Council will appoint a Membership Committee, which will make recommendations to the Council regarding membership issues, including the admission of new Institutions. Ratification of such recommendations requires a two-thirds majority vote of the Council.

The Collaboration Council will be responsible for developing a publications policy and for appointing a Publications Board to approve papers for publication. The Board will be responsible for maintaining a list of eligible authors for both instrumental and physics papers. The Collaboration Council will also be responsible for appointing a Speakers' Bureau to organize Collaboration presentations at conferences and workshops as appropriate and to determine who will represent the Collaboration at such meetings.

16.3 The Spokesperson

The Collaboration will be led by a single Spokesperson, who is the scientific leader of the Collaboration, responsible for financial, scientific, technical, and organizational decisions pertaining to the Collaboration. The Spokesperson also serves, ex-officio, as Chair of the Executive Board and as an ex-officio member of the international body of agencies organized by the Cabibbo-Lab to support the Super$B$ detector experiment Collaboration through the construction and operation phases (indicated in the following as IFC, International Finance Committee).

The Spokesperson, with the endorsement of the Executive Board, proposes a Management Plan to the Council for ratification, and a Management Team that will assist him/her in the execution of the Super$B$ program. The Spokesperson is expected to devote all his/her research time to the position, and must be willing and able to take up residence at Cabibbo-Lab when detector commissioning begins.

During the construction phase, the initial term for the Super$B$ Spokesperson is 3 years long and renewable, which will allow long-range planning and will provide continuity. Renewal for additional terms will be discussed and endorsed by the Council at least 9 months before the end date. The construction phase, and the Spokesperson term, will end on the September 1 that follows the first year in which the experiment has accumulated at least three months of beam. During the data taking phase, the Spokesperson will serve a single 2 year term, non-renewable, beginning September 1 of the relevant year, during which time he/she must be resident at the laboratory. At the end of his/her term, the retiring spokesperson serves for a year in the management team by mutual agreement with the incoming spokesperson.

16.4 The Executive Board

The Executive Board advises the Spokesperson on all scientific, financial, and organizational matters of the Collaboration. It consists of members distinguished by their scientific judgment, technical expertise, commitment to the experiment, and ability to speak knowledgeably and effectively for the regions they represent.The Spokesperson will chair the Executive Board. The Executive Board will meet at least eight times per year. The Board will also meet at least once each year with ex-officio members not present to review the performance of the management team. By a two-thirds majority vote of the entire Executive Board, the Board may recommend to the Collaboration Council that the Spokesperson be removed.

The number of members reflects the national composition of the collaboration. Initially, the Board will consist of one representative each from Canada, France, Russia, Poland, U.S., and the U.K. and six representatives from Italy. In addition, the Spokesperson, the Spokesperson-Elect, and the Chairperson of the Collaboration Council will be nonvoting ex-officio members of the Executive Board. The Cabibbo-Lab Directorate will appoint a senior scientist who is also a member of the Super$B$ Detector Collaboration to sit on the Executive Board as an ex-officio member. From time to time, the Board will review its regional composition, in consultation with the Cabibbo-Lab management, and will propose changes to the Collaboration Council that it may approve with a qualified majority.

Membership on the Collaboration Council does not preclude membership on the Executive Board. However, members of the Management Team may not serve simultaneously as members of the Executive Board. The normal term of office for the Executive Board will be three years, renewable, with one-third of the members being replaced or renewed each year.

16.5 The Management Team and Management Plan

The overall execution of the Super$B$ program is the responsibility of a Management Team led by the Spokesperson. The Management Team consists of: the Spokesperson, the Physics Analysis Coordinator, the Technical Coordinator, the Computing Coordinator, and the Spokesperson-elect when that office is filled. The Spokesperson may decide to designate at most two additional members to the management team, such as a Deputy Spokesperson, Financial Coordinator, and/or a Senior Advisor.

The Technical Coordinator is in charge of detector operations and hardware development. He/she is responsible for the common project construction and the technical integration of all Super$B$ components. He/she provides oversight for the implementation of Super$B$ engineering standards and procedures and the subsystem construction, commissioning and operations. He/she is assisted by managers responsible for the sub-systems. The Physics Analysis Coordinator is in charge of coordinating the analysis infrastructure and planning for physics analyses leading to publication. He/she is assisted by physics-topic group conveners . The Computing Coordinator is in charge of planning for and coordinating the software and computing activities and resources necessary for data acquisition and analysis.

The precise details of the management structure may evolve with time, including the roles and responsibilities of individual members of the Management Team and of additional groups such as the Technical Board, and Physics Analysis Groups will be established in a Management Plan, proposed by Spokesperson, approved by the Executive Board by a majority vote and ratified by the Council with a majority vote. In particular, the roles of the Technical Board and its members will be at the heart of collaboration activities during the fabrication and commissioning phases of the experiment, but will become less central as time passes. The Technical Coordinator will be nominated with the agreement of the Cabibbo-Lab Management.

16.6 The International Finance Review Committee

An International Finance Review Committee instituted by the Cabibbo Laboratory will monitor the financial aspects of the experiment as detailed in the management plan and agreed between the Cabibbo Laboratory, the collaboration, and the International Funding Agencies. This will be described in Memoranda of Understanding between the participating institutional partners and Cabibbo Laboratory.

16.7 Interaction with the Cabibbo-Lab

The Spokesperson will plan regular meetings with Cabibbo-Lab management. He/she will report to the International Cabibbo-Lab Scientific Committee on different aspects of the experiment in order to converge on the detector design, review the construction, installation and commissioning. He/she will also propose for endorsement to the Cabibbo-Lab and International Finance Committee the annual construction, maintenance and operation budgets of the detector.

16.8 Construction Responsibilities

The design of the Super$B$ detector described in this report began with the excellent BABAR detector. It then went through an extended process of optimization of the design of individual systems and the detector as a whole against the required physics performance, the interests and technical capabilities of the collaborating institutions, and financial constraints. In cases where there were conflicting requirements or competing technologies, task forces were employed to evaluate alternatives and recommend the appropriate choice. These include task forces for the forward PID, the backward EMC, and the forward EMC. All design decisions have been informed by a long term simulation task force (the Geometry Working Group), and background simulation effort.

Specific responsibilities for design and construction of the various detector subsystems have yet to be fully specified, and will be discussed more completely in a later document. We expect that they will be assigned through the traditional process of matching interests, capabilities, and resources. Final responsibilities will be detailed in Memoranda of Understanding. The collaboration expects to finance certain items through a common fund. Details remain under discussion.

16.9 Bibliography

[1] SuperB Detector Collaboration Constitution, http://superb.infn.it/detector-collaboration1.

17 Cost and Schedule

The Super*B* detector cost and schedule estimates, presented in this chapter, rely heavily on experience with the *BABAR* detector at PEP-II. The reuse and refurbishing of existing components has been assumed whenever technically possible and financially advantageous.

The costing model used here is similar to that already used for the Super*B* CDR (2007) and White Paper (2010). In all cases where significant changes have been made to the design, the estimates has been updated to include design changes and new vendor quotes obtained since 2010, but if no such changes have occurred, the estimate from 2010 has sometimes been taken without escalation. Some small cost escalation from 2010 to 2012 is therefore not consistently included, but it is considered to be a small perturbation, well within the contingency levels. The components are estimated in two different general categories; (1) "LABOR" and, (2) M&S (Materials and Services). M&S cost estimates are given in 2010 Euros and include 20% of Value Added Tax (VAT). The "LABOR" estimates comprise two sub categories which are kept and costed separately as they have differing cost profiles;(1) EDIA (Engineering, Design, Inspection, and Administration) and (2) Labor (general labor and technicians). Estimates in both categories are presented in manpower work units (Man-Months) and not monetized, as a monetary conversion can only be attempted after institutional responsibilities have been identified and the project timescale is known. The total project cost estimate can be calculated, once the responsibilities are identified, by summing the monetary value of these three categories.

Given the long term nature of this multinational project, there are several challenging general issues in arriving at appropriate costs including (1) fluctuating currency exchange rates, and (2) escalation. M&S costs and factory quotes that have been directly obtained in Euros can be directly quoted. M&S estimates in US Dollars are translated from Dollars to Euros using the exchange rate as of Jun 1, 2010 (0.8198 Euros/US$). For costs in Euros that were obtained in earlier years, the yearly escalation is rather small. For simplicity, we use a cost escalation rate of 2% per year which is consistent with the long term HICP (Harmonized Index of Consumer Prices) from the European Central Bank. Costs given in 2007 Euros are escalated by the net escalation rate (1.061) for three years to arrive at the 2010 cost estimates given here [1].

For all items whose cost basis is *BABAR*, we accept the procedure outlined in the Super*B* CDR which arrived at the costs given there in 2007 Euros. This procedure escalated the corresponding cost (including manpower) from the PEP-II and *BABAR* projects from 1995 to 2007 using the NASA technical inflation index [2] and then converted from US Dollars to Euros using the average conversion rate over the 1999—2006 period [3]. The overall escalation factor in the CDR from 1995 Dollars to 2007 Euros is thus $1.21 = 1.295 \times 0.9354$.

Similarly, the replacement values ("Rep.Val.") of the reused components, *i.e.*, how much money would be required to build them from scratch, as presented in separate columns of the cost tables, have been obtained by escalating the corresponding *BABAR* project cost (including manpower) from 1995 to 2007. Though it is tempting to sum the two numbers to obtain an estimate of the cost of the project if it were to be built from scratch, this procedure yields somewhat misleading results because of the different treatment of the manpower (rolled up in the replacement value; separated for the new cost estimate) and because of the double counting when the refurbishing costs are added to the initial values.

Contingency is not included in the tables. Given the level of detail of the engineering and the cost estimates, a contingency of about 35% would be appropriate.

17.1 Detector Costs

The costs, detailed in Table 17.1, are presented for the detector subsystem at WBS level 3/4. Although the Super*B* baseline detector is essentially defined, some further options remain open: some components, such as the forward PID, have overall integration and performance implications that need to be carefully studied before deciding to install them; for some other components, such as the SVT Layer0, promising new technologies require additional R&D before they can be definitively used in a full scale detector. The cost estimates list some of the different technologies separately, but the rolled-up value only includes the baseline detector choice. Technologies that are not included in the rolled-up value are shown in italics.

Table 17.1: Super$B$ detector budget.

WBS	Item	EDIA mm	Labor mm	M&S kEuro	Rep.Val. kEuro
1	**SuperB detector**	**3749**	**2464**	**50840**	**48922**
1.0	**Interaction region**	**21**	**12**	**860**	**0**
1.0.1	Be Beampipe	10	4	260	0
1.0.2	Tungsten Shield	9	6	540	0
1.0.3	Radiation monitors	2	2	60	0
1.1	**Tracker (SVT + Strip + MAPS)**	**258**	**364**	**4870**	**0**
1.1.1	**SVT**	**222**	**309**	**4328**	**0**
1.1.1.1	Mechanical	48	129	400	0
1.1.1.2	Cooling	8	10	155	0
1.1.1.3	Silicon Wafers and Fanout	24	120	2642	0
1.1.1.4	On-detector electronics	72	42	1014	0
1.1.1.5	Detector monitoring	4	4	94	0
1.1.1.6	Detector assembly	6	4	0	0
1.1.1.7	System Engineering	60	0	24	0
1.1.2	**L0 Striplet option**	**36**	**55**	**541**	**0**
1.1.2.1	Mechanical	12	30	60	0
1.1.2.2	Cooling	3	3	48	0
1.1.2.3	Silicon Wafers and Fanout	16	18	326	0
1.1.2.4	On-detector electronics	5	4	107	0
1.1.3	***L0 MAPS option***	***150***	***78***	***1576***	***0***
1.1.3.1	*Mechanical*	*18*	*48*	*90*	*0*
1.1.3.2	*Cooling*	*6*	*6*	*96*	*0*
1.1.3.3	*MAPS Modules Components*	*126*	*24*	*1390*	*0*
1.1.4	***L0 Hybrid Pixel option***	***156***	***84***	***1684***	***0***
1.1.4.1	*Mechanical*	*18*	*48*	*90*	*0*
1.1.4.2	*Cooling*	*6*	*6*	*96*	*0*
1.1.4.3	*Hybrid Pixel Modules Components*	*132*	*30*	*1498*	*0*
1.2	**DCH**	**169**	**151**	**3481**	**0**
1.2.1	System engineering	24	0	60	0
1.2.2	Endplates	16	6	660	0
1.2.3	Inner cylinder	8	2	200	0
1.2.4	Outer cylinder	6	2	120	0
1.2.5	Wire	4	6	308	0
1.2.6	Feedthroughs	9	10	439	0
1.2.7	Endplate systems	12	12	445	0
1.2.8	Assembly & Stringing	74	96	960	0
1.2.9	Gas System	10	8	240	0
1.2.A	Test	6	9	48	0
1.3	**FDIRC Barrel (Focusing DIRC)**	**97**	**101**	**4129**	**7138**
1.3.1	Radiator Support Structure (new support disc)	2	1	18	2516
1.3.2	New magnetic door and inner cylinder	4	1	96	0
1.3.3	FDIRC photon camera background shielding	4	1	120	0
1.3.4	Background shield displacement system and rails	4	1	30	0
1.3.5	Bar box transport to Italy	6	1	120	0

Continued on next page

Table 17.1 – continued from previous page

WBS	Item	EDIA mm	Labor mm	M&S kEuro	Rep.Val. kEuro
1.3.6	Radiator box/Photon camera assembly	23	12	1159	4515
1.3.7	Photon Camera mechanical boxes	24	44	282	0
1.3.8	Photodetector assembly	20	20	2004	0
1.3.9	Calibration System	4	0	72	0
1.3.10	Temperature, water, nitrogen and helium leak interlock system	4	2	12	0
1.3.11	Alignment services	2	4	36	0
1.3.12	Mechanical Utilities	0	4	60	107
1.3.13	System Integration	0	10	120	0
1.4	**EMC**	**332**	**578**	**10047**	**31574**
1.4.1	**Barrel EMC**	**110**	**169**	**1802**	**30923**
1.4.1.1	Crystal Procurement	0	0	0	21742
1.4.1.2	Light Sensors & Readout	0	0	0	2654
1.4.1.3	Crystal Support Modules	0	0	0	2875
1.4.1.4	Barrel Structure	0	0	0	3419
1.4.1.5	Transfer to Italy	22	15	1318	0
1.4.1.6	Refurbish and re-assemble	24	42	240	0
1.4.1.7	Electronics	52	88	221	0
1.4.1.8	Project management	12	24	24	233
1.4.2	**Forward EMC**	**127**	**298**	**7268**	**0**
1.4.2.1	Crystals	27	110	5990	0
1.4.2.2	Light sensors and electronics	59	106	654	0
1.4.2.3	Transfer to Italy	6	14	312	0
1.4.2.4	Refurbish and assembly	24	50	288	0
1.4.2.5	Project management	12	18	24	0
1.4.3	**Crystal Calibration Systems**	**46**	**19**	**332**	**650**
1.4.3.1	Source calibration	10	7	116	463
1.4.3.2	Light pulser system	12	12	96	187
1.4.3.3	Project Management	24	0	120	0
1.4.4	**Backward EMC**	**30**	**54**	**600**	**0**
1.4.4.1	Scintillator	2	12	246	0
1.4.4.2	Radiator	1	5	11	0
1.4.4.3	Fibers	4	9	19	0
1.4.4.4	Photodetectors	2	5	47	0
1.4.4.5	Mechanical support	17	15	146	0
1.4.4.6	Electronics	2	6	107	0
1.4.4.7	Project Management	2	2	24	0
1.4.5	**Monitoring**	**4**	**8**	**8**	**0**
1.4.6	**Project Management**	**15**	**30**	**36**	**0**
1.5	**IFR**	**37**	**188**	**2340**	**0**
1.5.1	Scintillators	0	0	516	0
1.5.2	WLS fibers	0	0	600	0
1.5.3	Photodetectors and PCBs	1	6	990	0
1.5.4	Mechanics (Production and QC)	16	62	234	0
1.5.5	Module Installation	20	120	0	0
1.6	**Magnet**	**93**	**59**	**3767**	**10210**
1.6.0	System Management	36	0	0	612
1.6.1	Superconducting solenoid	0	0	0	2421

Continued on next page

Table 17.1 – continued from previous page

WBS	Item	EDIA mm	Labor mm	M&S kEuro	Rep.Val. kEuro
1.6.2	Mag. Power/Protection	0	0	0	181
1.6.3	Cryogenics	34	36	1753	0
1.6.4	Cryo monitor/Control	17	11	214	0
1.6.5	Flux return	6	12	1800	6481
1.6.6	Installation/test equipment	0	0	0	515
1.7	**Electronics**	**719**	**361**	**11476**	**0**
1.7.1	SVT	32	8	470	0
1.7.2	DCH	55	81	4248	0
1.7.3	PID Barrel	136	18	612	0
1.7.4	EMC	110	164	2726	0
1.7.5	IFR	32	48	644	0
1.7.6	Infrastructure	4	36	314	0
1.7.7	Systems Engineering	12	0	0	0
1.7.8	Hardware Trigger	120	0	677	0
1.7.9	ETD (without Trigger)	218	6	1784	0
1.8	**Online System**	**951**	**27**	**2058**	**0**
1.8.1	Event Data Chain	285	3	1594	0
1.8.2	Control Systems	192	0	108	0
1.8.3	Databases, Web, Logbook	114	0	12	0
1.8.4	Infrastructure	48	12	246	0
1.8.5	Software Triggers	216	0	0	0
1.8.6	Coordination and Commissioning	72	12	0	0
1.9	**Installation and integration**	**353**	**624**	**7596**	**0**
1.9.1	Disassembly	95	161	612	0
1.9.2	Assembly	222	463	3984	0
1.9.3	Structural analysis	36	0	0	0
1.9.4	Transportation	0	0	3000	0
1.10	**Project Management**	**720**	**0**	**216**	**0**
1.10.1	Project engineering	300	0	120	0
1.10.2	Budget, Schedule and Procurement	300	0	48	0
1.10.3	ES & H	120	0	48	0

17.2 Basis of Estimate

Vertex Detector and Tracker: System cost is estimated based on experience with the *BABAR* detector and vendor quotes. A detailed estimate is provided for the cost of the main detector (layers 1 to 5). The costs associated with Layer0 are analyzed separately. The costing model assumes that a striplet detector will be installed initially – followed by a second generation upgrade to a pixel detector, which could either be either a MAPs or hybrid pixel device. Substantial R&D on these new technologies is needed in either case before such a detector can be built. The total SVT cost is obtained by using the baseline option with striplets for Layer0, while the MAPS and Hybrid Pixels Layer0 costs are shown as options.

Drift Chamber: The DCH costing model is based on a straightforward extrapolation of the actual costs of the existing *BABAR* chamber to 2010, since, as discussed in Sec. 7 the main design elements are comparable, and many related components, such as the length of wire, number of feedthroughs, duration of wire stringing, etc., can be reliably estimated. Although the cell layout is still being finalized, the total cell count will likely be about 25% larger. The endplates will be fabricated from carbon fiber composites instead of aluminum. Though this will require a somewhat longer period of R&D and engineering design, it is unlikely to result in significantly larger production costs for the final endplates. The DCH electronics on Table 17.1 assumes the cluster counting readout option discussed in Sec. 13.1.2.

Particle Identification: Barrel PID costs and replacement values are derived from *BABAR* costs as extrapolated to 2010, with updated quotes from vendors. The main new component of the barrel FDIRC is its new camera. For each module, the optical portion consists of the focusing block (FBLOCK), an addition to the wedge (the New Wedge) and possibly a Micro-Wedge. We have contacted about twelve optics companies and received four preliminary bids. We use the average bid in the present budget. We hope to continue to refine the values through further R&D. The photon detector cost estimate is based on the Hamamatsu bid for 600 H-8500 MaPMTs. No budget estimate is included at this time for a forward endcap PID.

Electromagnetic Calorimeter: The electromagnetic calorimeter (EMC) consists of a barrel calorimeter, a forward calorimeter, and a backward calorimeter. The barrel and forward calorimeters make substantial reuse of *BABAR* components. The backward EMC is a new lead/scintillator sandwich device. As described in the calorimeter chapter, there are some technical alternatives for the forward EMC. The present cost estimate is for our baseline "hybrid" design. The cost estimate also includes the backward EMC, although a final decision has not been taken on this device; it could become a later upgrade.

There is no cost assigned for the value of the reused *BABAR* components. They are assumed to be available as a scientific transfer or loan of equipment at no cost to the project. However, there are significant costs associated with preparing these items for transport, and for the transport. It is assumed that both the barrel and endcap will be dis-assembled to the module level, although some engineering is included to further study the possibility of shipping the barrel as a whole.

Manpower and costs for engineering and tooling required for the preparation for the move of the barrel EMC from SLAC are engineering estimates. These incorporate substantial experience with the *BABAR* installation as well as current dis-assembly operations of the *BABAR* detector. Engineering and labor provided by SLAC are included in the M&S cost estimate. Engineering and labor from the project are provided separately in man months. The similar estimates for the endcap are not as well developed, but are scaled from the barrel estimates. The labor for the barrel and forward endcap includes 21 man months for module testing that might be provided by physicists (e.g., graduate students).

The transportation cost for the endcap and associated tooling is based on a shipping vendor quote, while the transportation for the barrel is obtained based on the endcap quote.

The main cost driver for the forward endcap is the cost of LYSO crystals. The estimate is based on guideline quotes from vendors, where we assume the six rings of LYSO in the baseline design. The next largest element is the APD photodetectors, with a cost based on a quote from the vendor.

The PIN diodes on the CsI(Tl) crystals will be reused from *BABAR*, but the preamps will all be replaced. The preamp costs for the CsI(Tl) and the LYSO are based on engineering estimates and vendor quotes. The replacement of the barrel preamps is complicated by accessibility, and the labor estimate for this is based on an in situ test.

For the backward endcap, the scintillator, lead, wavelength-shifting fiber, and readout MPPC costs, as well as some other minor materials, are all based on vendor quotes. Other items are based on experience and estimator judgment.

The source calibration system costs are estimated based on experience with the system at *BABAR*, which we anticipate reusing. Due to the half-life of tritium, replacement of the DT generator is included in the cost. Monitoring is planned to be achieved largely with the existing *BABAR* sensors and readout. An estimate of costs for refurbishing and augmentation for the LYSO is included.

Instrumented Flux Return: The IFR cost is based on quotations received for the prototype construction appropriately scaled to the real detector dimensions. While the active part of the detector is quite inexpensive the total cost is driven by the electronics and the photodetectors. The current baseline design allows the reuse of the *BABAR* iron structure with some modification that needs to be taken into account. Manpower and cost for engineering and module installation is based on the *BABAR* experience.

Electronics, Trigger, DAQ and Online: The cost for the Electronics and Trigger subsystems is estimated with a combination of scaling from the *BABAR* experience and from direct estimates. For items expected to be similar to those used in *BABAR* (such as infrastructure, high and low voltage or the L1 trigger) costs are scaled from *BABAR*. The same methodology is used to estimate EDIA and Labor costs for the Online system. However, some modifications based on "lessons learned" are applied. In particular, we are including costs for development work that, in our opinion, should have been centralized across sub-detectors in *BABAR* (but wasn't) and work that should have been done upfront but was only done or completed as part of *BABAR* Online system upgrades.

The readout systems for which the higher data rates require redesigned electronics are estimated from the number of different components and printed circuit boards, and their associated chip and board counts. This methodology is also used for the possible new detectors (forward EMC, backward EMC, forward PID) and for the elements of the overall system architecture that are very different from *BABAR*.

The hardware cost estimates for the Online computing system (including the HLT farm) are, very conservatively, based on the current prices of hardware necessary to build the system, with the assumption that Moore's Law will result in future systems with the same unit costs but higher performance. This is justified by our observation that for COTS components, constraints from system design, topology and networking are more likely to set minimum requirements for the *number* of devices than for the per-device performance.

Magnet The costs were evaluated on the basis of the experience and some market prices (for vacuum system). The cost for a new refrigerator and cryogenic equipment are included. The preferable option for managing the reuse of the solenoid should be a contract to an expert firm, which takes the full responsibility of the operation. An estimated cost for this contract is also included.

Transportation, installation, and commissioning: Installation and commissioning estimates, including disassembling and reassembling *BABAR*, are based on the *BABAR* experience, and engineering estimates use a detailed schedule of activities and corresponding manpower requirements. The transportation costs have been estimated from costs associated with disassembling and transporting *BABAR* components for dispersal, if they were not to be reused.

17.3 Schedule

The detector construction schedule has not been finalized since it depends heavily on the availability of civil and accelerator infrastructures. The fabrication of the detector subsystems can proceed in parallel while the the *BABAR* detector is disassembled, transported to the new site, and reassembled. The detector subsystems will be installed in sequence. An extended detector commissioning period, including a cosmic ray run, will follow to ensure proper operation and calibration of the detector. The total construction and commissioning time is estimated to be a little over five years.

17.4 Bibliography

[1] Euro Inflation Rates, http://www.ecb.int/stats/prices/hicp/html/index.en.html.

[2] NASA Inflation Calculator, http://cost.jsc.nasa.gov/inflation/nasa/inflateNASA.html.

[3] Federal Reserve Foreign Exchange Rates, http://www.federalreserve.gov/releases/g5a/.

SuperB